PRACTICAL HANDBOOK OF

Photovoltaics

Fundamentals and Applications

Tom Markvart & Luis Castañer

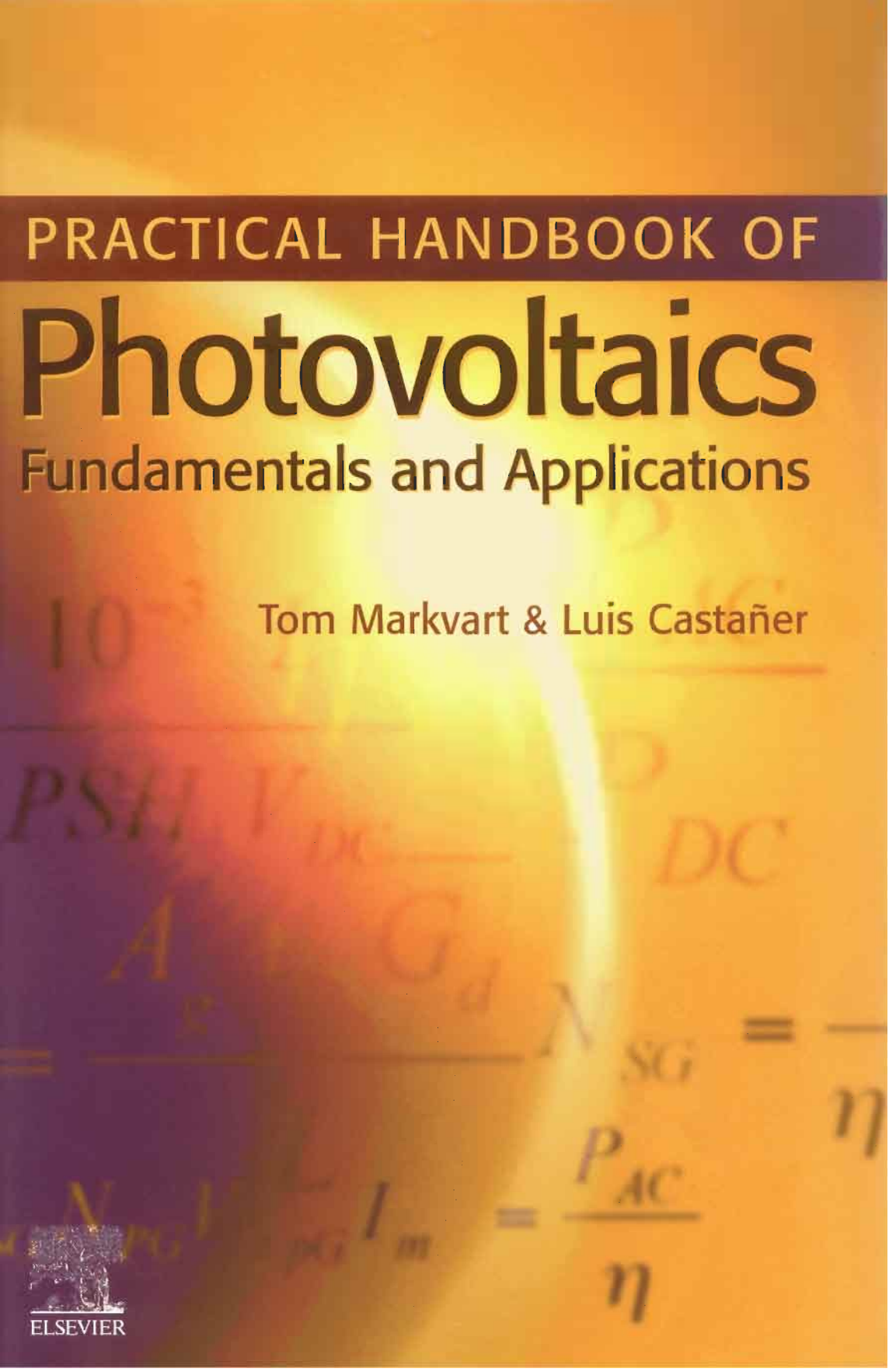

ELSEVIER

Handbook of Photovoltaics: Section Finder

Handbook of Photovoltaics: Section Finder

Practical Handbook of Photovoltaics: Fundamentals and Applications

Practical Handbook of Photovoltaics: Fundamentals and Applications

Edited by:
Tom Markvart and Luis Castañer

ELSEVIER

UK Elsevier Science Ltd, The Boulevard, Langford Lane, Kidlington, Oxford OX5 1GB, UK
USA Elsevier Science Inc, 360 Park Avenue South, New York, NY 10010-1710, USA
JAPAN Elsevier Japan, Tsunashima Building Annex, 3-20-12 Yushima, Bunkyo-ku, Tokyo 113, Japan

British Library Cataloguing in Publication Data
Practical handbook of photovoltaics: fundamentals and applications
1. Photovoltaic power systems 2. Photovoltaic power generation
3. Photovoltaic cells
I. Markvart, Tomas II. Castañer, Luis
621.3'1244

ISBN 1856173909

Library of Congress Cataloging-in-Publication Data
Practical handbook of photovoltaics: fundamentals and applications / edited by Tom Markvart and Luis Castañer.
p. cm.
Includes bibliographical references and index.
ISBN 1-85617-390-9
1. Photovoltaic cells. 2. Photovoltaic power generation. I. Markvart, Tom. II. Luis Castañer.

TK8322.P73 2003
621.3815'42–dc21 2003040758

Published by
Elsevier Advanced Technology, The Boulevard, Langford Lane, Kidlington Oxford OX5 1GB, UK
Tel.: +44(0) 1865 843000
Fax: +44(0) 1865 843971

Typeset by Variorum Publishing Ltd, Lancaster and Rugby
Printed and bound in Great Britain by Biddles Ltd, Guildford and King's Lynn

Preface

Photovoltaics is about to celebrate 50 years of its modern era. During this time, the industry has grown from small satellite power supplies to utility-scale systems that are now routinely installed in many countries of the world. Solar cells capable of producing power in excess of 500 MW were manufactured in 2002, providing electricity to a variety of applications ranging from small consumer products, power systems for isolated dwellings and remote industrial equipment to building-integrated solar arrays and megawatt-size power stations.

This *Practical Handbook of Photovoltaics* addresses the need for a book that summarises the current status of know-how in this field. It represents a detailed source of information across the breadth of solar photovoltaics and is contributed to by top-level specialists from all over the world. Over 1,000 references, bibliographies and web sites guide the reader to further details, be it specific information for industrial production and research or a broad overview for policy makers. Thirty-seven chapters in the handbook cover topics from fundamentals of solar cell operation to industrial production processes, from molecular photovoltaics to system modelling, from a detailed overview of solar radiation to guidelines for installers and power engineers, and from architectural integration of solar cells to energy payback, CO_2 emissions and photovoltaic markets. Appendices include extensive bibliography and lists of standards, journals and other sources of information which can be found in a printed or electronic form.

The main credit for this handbook must go to the 47 contributors who have produced a unique compilation of the contemporary knowledge in photovoltaic science and technology.

Our thanks go to our families for their patience and support without which this book would have never seen the light of day.

Luis Castañer
Barcelona

Tom Markvart
Southampton

Guide to Usage of the Handbook by Professional Groups

	Solar radiation	II. Solar cells					III. Systems					Testing, monitoring & calibration	Economics, environment & business
		Introduction	c-Si	Thin Films	Space &Concentrators	Molecular devices	Introduction	Balance of system	Grid-connected systems	Space &Concentrators	Case studies		
	I	IIa	IIb	IIc	IId	IIe	IIIa	IIIb	IIIc	IIId	IIIe	IV	V
Solar cell - production		✔	✔	✔	✔	✔						✔	✔
Solar cell - R&D		✔	✔	✔	✔	✔						✔	
System design	✔	✔					✔		✔	✔	✔		
Grid connection		✔					✔		✔		✔		
System installers	✔						✔	✔	✔	✔	✔	✔	
Business managers		✔	✔	✔	✔		✔	✔	✔	✔	✔	✔	✔
Sales & marketing		✔					✔						✔
PV equipment manufacturers			✔	✔	✔	✔						✔	✔
Policy and business strategy							✔		✔		✔		✔
Project managers	✔						✔	✔	✔		✔	✔	✔
Space technologists		✔			✔					✔			
Environmentalists	✔										✔		✔
Architects and urban planners		✔					✔				✔		✔
System analysis and evaluation		✔					✔				✔	✔	
Solar energy resource	✔						✔						
PV consumer products		✔									✔		
Venture capitalists and investors							✔						✔

Contents

APPENDICES

List of Contributors

Erik Alsema, Department of Science, Technology and Society, Copernicus Institute for Sustainable Development and Innovation, Utrecht University, Padualaan 14, NL-3584 CH Utrecht, The Netherlands
email: e.a.alsema@chem.uu.nl

Vyacheslav M. Andreev, Ioffe Physico-Technical Institute, 26 Polytekhnicheskaya str., St. Petersburg 194021, Russia
email: vmandreev@mail.ioffe.ru

Sheila Bailey, Photovoltaic and Space Environments Branch/5410, NASA Glenn Research Center, MS 302-1, Cleveland, OH 44135, USA
email: Sheila.Bailey@grc.nasa.gov

Allen Barnett, 19 Nivin Lane, Landenberg, PA 19350, USA
email: ambarnett@aol.com

Sandra Bermejo, GDS, Modulo C4 Campus Nord, Universidad Politecnica de Catalunya, Calle Jordi Girona 1, 08034 Barcelona, Spain
email: sandra@eel.upc.es

Dieter Bonnet, Breslauer Ring 9a, D-61381 Friedrichsdorf, Germany
email: DieterBonnet@aol.com

David E. Carlson, BP Solar, 989 Corporate Boulevard, Linthicum, MD 21090, USA
email: carlsde@bp.com

Luis Castañer, GDS, Modulo C4 Campus Nord, Universidad Politecnica de Catalunya, Calle Jordi Girona 1, 08034 Barcelona, Spain
email: castaner@eel.upc.es

Martin Cotterell, SunDog Energy Ltd, Matterdale End, Penrith, CA11 0LF, UK
email: martin@sundog-energy.co.uk

Bruce Cross, PV Systems / EETS Ltd, Unit 2, Glan-y-Llyn Industrial Estate, Taffs Well, CF15 7JD, UK
email: bcross@eets.co.uk

Andres Cuevas, Department of Engineering, Australian National University, Canberra, Australia 0200
email: Andres.Cuevas@faceng.anu.edu.au

Emilio Fernandez Lisbona, Solar Array Section,ESA-Estec, Keplerlaan 1, 2200 AG Noordwijk, The Netherlands
email: Emilio.Fernandez.Lisbona@esa.int

Francesca Ferrazza, Eurosolare S.p.A. Via Augusto D'Andrea 6, 00048 Nettuno, Italy
email: francesca.ferrazza@eurosolare.agip.it

Katerina Fragaki, School of Engineering Sciences, University of Southampton, Southampton SO17 1BJ, UK
email: A.FRAGAKI@soton.ac.uk

Vasilis M. Fthenakis, National PV EHS Assistance Center , Department of Environmental Sciences, Brookhaven National Laboratory, Upton, NY 11973, USA
email: fthenakis@bnl.gov

Martin A. Green, Centre of Excellence for Advanced Silicon Photovoltaics and Photonics, University of New South Wales, Sydney NSW 2052, Australia
email: m.green@unsw.edu.au

Ulrike Jahn, Institut für Solarenergieforschung GmbH Hameln/Emmerthal (ISFH), Am Ohrberg 1, D-31860 Emmerthal, Germany
email: ujahn@easynet.de

Peter T. Landsberg, Faculty of Mathematical Studies, University of Southampton, Southampton SO17 1BJ, UK
email: ptl@maths.soton.ac.uk

Rogelio Leal Cueva, GESP - Agrupacio Euroregional dels Sistemes Fotovoltaics, Seccio Arquitectura Sostenible, c/Baldiri Reixac 4-6, 08028 Barcelona, Spain
email: rleal@pcb.ub.es

Tom Markvart, School of Engineering Sciences, University of Southampton, Southampton SO17 1BJ, UK
email: t.markvart@soton.ac.uk

Michael Mauk, AstroPower, Inc., 300 Executive Drive, Newark, DE 19702-3316, USA
email: mauk@AstroPower.com

Paul Maycock, PV Energy Systems, 4539 Old Auburn Road, Warrenton, VA 20187, USA
email: pves@pvenergy.com

Augustin McEvoy, Institute for Molecular and Biological Chemistry, Faculty of Basic Sciences, Ecole Polytechnique Fédérale de Lausanne, CH-1015 Lausanne, Switzerland.
email: augustin.mcevoy@epfl.ch

Robert P. Mertens, Interuniversity Microelectronic Center (IMEC), Kapeldreef 75, 3001 Leuven, Belgium
email: robert.mertens@imec.be

Jenny Nelson, Centre for Electronic Materials and Devices, Department of Physics, Imperial College, London SW7 2BW, UK
email: jenny.nelson@ic.ac.uk

Johan F. Nijs, Photovoltech, rue de l'Industrie 52 Nijverheidsstraat, 1040 Brussel, Belgium
email: johan.nijs@photovoltech.be

Carl R. Osterwald, NREL, 1617 Cole Boulevard, Golden, Colorado 80401-3393, USA
email: carl.osterwald@nrel.gov

Roger van Overstraeten (deceased), formerly of Interuniversity Microelectronic Center (IMEC), Kapeldreef 75, Leuven B-3001, Belgium

John Page, 15 Brincliffe Gardens, Sheffield, S11 9BG, UK
email: johnpage@univshef.freeserve.co.uk

Ryne P. Raffaelle, NanoPower Research Labs,85 Lomb Memorial Drive, Rochester, NY 14623, USA
email: rprsps@rit.edu

James Rand, AstroPower, Inc., 300 Executive Drive, Newark, DE 19702-3316, USA
email: jimrand@AstroPower.com

Uwe Rau, Institute of Physical Electronics, University of Stuttgart, Pfaffenwaldring 47, D-70569 Stuttgart, Germany
email: uwe.rau@ipe.uni-stuttgart.de

J. Neil Ross, Department of Electronics and Computer Science, University of Southampton, Southampton SO17 1BJ, UK
email: jnr@ecs.soton.ac.uk

Gabriel Sala, Instituto de Energia Solar, Universidad Politecnica de Madrid, Ciudad Universitaria, 28040 Madrid, Spain
email: sala@ies-def.upm.es

Hans Werner Schock, Institute of Physical Electronics, University of Stuttgart, Pfaffenwaldring 47, D-70569 Stuttgart, Germany
email: schock@ipe.uni-stuttgart.de

Rafael Serra, E.T.S.Arquitectura de Barcelona, Av. Diagonal 649, 08028 Barcelona, Spain.
email: rafael.serra@upc.es

Santiago Silvestre, GDS, Modulo C4 Campus Nord, Universidad Politecnica de Catalunya, Calle Jordi Girona 1, 08034 Barcelona, Spain
email: santi@ecl.upc.es

Paul Sims, AstroPower, Inc., 300 Executive Drive, Newark, DE 19702-3316, USA
email: pesims@AstroPower.com

Ronald A. Sinton, Sinton Consulting, Inc., 1132 Green Circle, Boulder, CO 80305, USA
email: Ron@Sintonconsulting.com

Siva Sivoththaman, University of Waterloo, Faculty of Electrical and Computer Engineering, 200 University Ave, Waterloo, Ontario, Canada N2L 3G1
email: sivoththman@uwaterloo.ca

David Spiers, Naps Systems, PO Box 83, Abingdon, Oxfordshire OX14 2TB, UK
email: david.spiers@napssystems.com

Jozef Szlufcik, Photovoltech, rue de l'Industrie 52 Nijverrheidsstraat, 1040 Brussel, Belgium
email: Jozef.Szlufcik@imec.be

Jim Thornycroft, Halcrow Group Ltd, Burderop Park, Swindon SN4 0QD, UK
email: thornycroftjm@halcrow.com

Pierre J. Verlinden, Origin Energy, GPO Box 1097, Adelaide, SA 5001, Australia
email: Pjverlinden@aol.com

Philip Wolfe, WolfeWare, Rose Cottage, Dunsomer Hill, North Moreton, OX11 9AR, UK
email: philip@wolfeware.com

Christopher R. Wronski, 215 Electrical Engineering West, The Pennsylvania State University, University Park, PA 16802, USA
email: crwece@engr.psu.edu

Kenji Yamamoto, Kaneka Corporation, 2-1-1, Hieitsuji, Otsu, Shiga, 520-0104, Japan
email: yamamoto@pv.kaneka.co.jp

Beatriz Yordi, Directorate General for Energy and Transport, European Commission, 200 Rue de la Loi, BE-1049, Brussels, Belgium
email: beatriz.yordi@cec.eu.int

Introduction

This Practical Handbook of Photovoltaics aims to give a detailed overview of all aspects of solar photovoltaics in a way that can be easily accessed by the expert and non-specialist alike. It reflects the current status of this modern power-generating technology which, despite its mature status, continues to explore new directions to improve performance and reduce costs. A focus on practical aspects, however, does not imply the neglect of fundamental research and theory which are both covered in depth, as are the environmental impacts, commercial aspects and policy views.

Solar cell manufacturing technologies are discussed in Part II. An overview of the principal issues, including the physics of solar cell operation, materials and modelling and the fundamental theoretical framework form an introduction to the device aspects of photovoltaics given in Part IIa. Part IIb gives a detailed account of crystalline silicon technology, from the manufacture and properties of silicon (Chapter IIb-1) to industrial and high-efficiency solar cells based on wafer silicon (Chapters IIb-2 and -5), and thin silicon cells (Chapter IIb-3). Part IIc examines all aspects of thin-film solar cells, including amorphous silicon, cadmium telluride and copper–indium diselenide and its derivatives (Chapters IIc-1, -3 and 4). Chapter IIc-2 describes a novel amorphous/microcrystalline silicon cell which is rapidly gaining ground. Part IId focuses on high-efficiency cells for space and concentrator use. Part IIe deals with devices based on molecular structures.

The testing and calibration of both terrestrial and space solar cells is discussed in Part IV. An overview of material characterisation methods for silicon wafers and devices will be found in Chapter IIb-4.

Solar radiation has been called the fuel of photovoltaics, and its characteristics form the basis of system design, from array construction to the reliability of electricity supply by stand-alone photovoltaic systems. The understanding of solar radiation forms arguably the most ancient part of physical science but it is only recently that the statistical nature of solar energy has been understood in some detail. A number of sophisticated computer models are now available and are described in detail in Part I, which also summarises the relevant aspects of solar radiation as an energy source and examines the principal attributes and limitations of the available computer tools.

System engineering is discussed in Part III. Part IIIa provides an introduction to this field by giving an overview of the generic aspects of photovoltaic system design, including a review of the relevant modelling and simulation tools. The balance of system components is discussed in Part IIIb, providing an in-depth analysis of battery operation in photovoltaic systems (Chapter IIIb-2) and an overview of the electronic control and power conditioning equipment (Chapter IIIb-1).

The rapidly growing area of grid-connected systems is considered from several viewpoints in Part IIIc which examines the technical and regulatory issues of the grid connection, and the building and electrical installation of domestic systems. The International Energy Agency data about user experience and performance indicators are analysed in Chapter IIIe-2; the allied subject of system monitoring is reviewed in Chapter IV-2.

Solar cells as a source of power for consumer products are reviewed in Chapter IIIe-3. Arguably the most exciting aspect of photovoltaics – the visual impact of the new solar architecture – is discussed in Chapter IIIe-1, which also gives numerous breathtaking examples of the new trends.

An in-depth analysis of the world photovoltaic markets is given in Part V alongside an overview of support mechanisms. Part V also reviews the potential hazards in solar cell manufacture, and examines broader environmental issues, including CO_2 emissions and the energy payback times.

The space application of solar cells has always been considered a unique and a special area of photovoltaics. The device aspects, including radiation damage, are discussed in Chapters IId-1 and IIId-2, with a brief introduction to the material aspects in Chapter IIa-2. Chapter IIId-2 gives a thorough review of the operation of solar cells in the space environment together with its history and space mission requirements.

The use of high-efficiency cells is not confined to space but is finding an increasing application in concentrator systems which are examined Chapter IIId-1. The corresponding solar cells are discussed in Part IId.

The handbook contains a number of chapters that contain a strong research element. The ultimate efficiencies that can be reached by a solar cell are discussed in Chapter IIa-3. High-efficiency concepts in crystalline silicon photovoltaics, which have driven the progress in this field over several decades, are reviewed in Chapter IIb-5. The dye-sensitised and organic/plastic solar cells that are attracting a large research investment are examined in Part IIe. Part IId and Chapter IIc-2 cover wide areas at the boundary between industrial production and research, as do many other chapters on thin-film solar cells in Part IIc.

Each chapter gives a self-contained overview of the relevant aspect of photovoltaic science and technology. They can be read on their own although ample cross-referencing provides links that can be followed to build a knowledge base for any particular purpose at hand. For the non-specialist, the introductory chapters of Parts II and III can serve as a starting point before proceeding to explore other parts of the handbook. The supplementary chapters and appendices, including bibliography, solar radiation data for selected sites and the lists of standards, web sites and news sheets, act as pointers to more specific details and textbooks if a more didactic approach is required.

Part I

Solar Radiation

1

The Role of Solar Radiation Climatology in the Design of Photovoltaic Systems

John Page, Emeritus Professor of Building Science,
University of Sheffield, UK
Fellow of the Tyndall Centre for Climate Change at Tyndall North,
UMIST, Manchester, UK

1 Introduction

Climate and solar radiation impact both on system supply side issues and on system demand side issues. Designers need both solar data and temperature data. Temperature affects the performance of photovoltaic devices per se. It also has a strong bearing on the demands of the energy required for heating and cooling. Relating supply and demand within any renewable energy structure requires study of the inter-relationships between supply and demand. One has to establish the resources that need to be devoted to energy storage to achieve an acceptably reliable energy supply from an intermittent supply resource. Ideally one needs long-term time series of solar radiation data and temperature data for each specific site at the hourly level. Such data are relatively rare, so in recent years statistical approaches have been developed to help fill the gap. Long series of daily data are needed for sizing and modelling of stand-alone systems (see Part IIIa, Chapters 2 and 3). Effective statistical approaches have to recognise the links between solar radiation data and temperature data.

Section 2 aims to provide the reader with a brief general overview of the main features of solar radiation climatology that are important for photovoltaics design in different parts of the world. Section 3 discusses in more detail some of the currently available quantitative techniques available for compiling solar radiation design data for specific sites. The goal is to help optimise future photovoltaic design through the application of improved climate knowledge. Sections 4–7 explain in detail the quantitative procedures that are suitable for developing quantitative solar radiation data in the forms needed for the study of the performance of photovoltaic systems.

Attention is drawn throughout to important sources of systematic climate data that are already readily accessible to designers. These modern approaches, aiming to provide the user with specialised meteorological data for specific sites, usually try to deliver information to users through user-friendly PC-based methodologies. The most successful now use advanced CD-ROM-based computational toolboxes as a matter of routine. For example, the digitally based 4th European Solar Radiation Atlas (ESRA) [1] provides an advanced stand-alone CD-ROM toolbox. The ESRA toolbox includes coupled applications modules that enable users to address in a user-friendly way the design of stand-alone and grid-connected PV systems for any site in the mapped area. The efficient climate data supply from the ESRA database is enhanced to meet user needs with a wide range of supporting algorithms. Global coverage based on CD-ROM approaches is available in the Meteonorm system marketed by Meteotest of Switzerland [2–5]. RetScreen® International [6] developed between Canada and the US NASA enhanced with support from UNEP provides another example of a CD-ROM-based design tool. This contains photovoltaic applications tools. A recent UK CD-ROM-based achievement is the Chartered Institution of Building Services Engineers (CIBSE) Guide J Weather, solar and illuminance data [7]. It is published on a CD-ROM in pdf format. Additional supporting quality controlled hour by hour observed climate databases may be purchased for the UK. The pdf format provides opportunities for the intelligent user to extract published

tabulated data into spreadsheets to enhance their practical utility in design, for example for facilitating inter-site interpolation and for creating site specific design graphics.

More recently developed systems provide user friendly live interactive IT methodologies, operating through the World Wide Web. After development, which is costly, such systems allow users to specify their own climate data requirements directly through the Internet and then receive back nearly immediate application oriented answers to their questions for any part of the globe. Designated server sites interacting within organised computational networks offer users intelligently programmed access to the use of various distributed and interlinked data bank systems to provide advanced solar radiation data and other climate design data. The user-requested results are delivered back through the internet. The recently completed EU-funded SoDa project provides a good example of such web-based approaches [8]. The EU-based Satel Light program provides another web-based example, covering the area 34°N to 68°N, 20°W to 50°E with data for five years (1996 to 2000) and specialising in illuminance data information and daylighting design [9, 10].

Extensive use is now made of digital mapping techniques in such programmes. Such maps have the advantage that they can be accessed in very user-friendly ways using computer mouse clicks to extract climate data associated with any specific pixel from the database resource. The data associated with any pixel are arranged in arrays spatially structured to correspond with the mapped pixels maps (see, for example [1, 8]). Both systems enable users to work directly from the maps themselves. The mouse is used to gain computational access to detailed design databanks associated with any specific pixels held in the database. This input data is then used in structured algorithmic systems to supply outputs that match declared user needs like time series of hourly radiation on inclined surfaces of any selected orientation.

This chapter does not attempt to reproduce the advanced technological studies that underlie these new approaches. Readers should consult the above listed publications to find out more about them. These new approaches include the use of satellite technology to estimate radiation data for regions of the world with no ground observational resources for measuring solar radiation [1, 8]. This processed satellite data then becomes part of the organised database resource.

The world is a big place. No one can be familiar with more than a small part of it. There are great dangers in photovoltaics design, if designers attempt to guess in the assessment of design risks the properties of the radiation climate at unfamiliar places. As globally based climatological tools are becoming more widely available, designers should make themselves aware of the powers of the new tools for design assessment in renewable energy design. Such tools should not be looked on as luxuries. They deliver quality controlled programmed results very efficiently to users. This chapter draws heavily on the resources available in the above publications.

2 Key Features of the Radiation Climatology in Various Parts of the World

2.1 Some Definitions and Associated Units

The solar short-wave radiation falling on a horizontal surface from sun and sky combined is known as the global short-wave radiation. The global short-wave radiation flux, i.e. radiant energy flow per unit time, is known as the irradiance, symbol G. The most commonly used unit is watts per square metre (W m^{-2}). The integral of irradiance flux over any period is called the irradiation. Typical integration periods are the hour, which yields the hourly global irradiation, G_h, (units MJ m^{-2} h^{-1} or Wh m^{-2} h^{-1}), the day G_d (units MJ m^{-2} d^{-1} or Wh m^{-2} d^{-1}) and the month G_m (units MJ m^{-2} per month or Wh m^{-2} per month). The monthly daily mean irradiation is written as $(G_d)_m$ in this chapter. The subscripts indicate the integration period. The global radiation may be split into its two components, beam and diffuse. The method of indicating the integration period for these irradiation data corresponds to that used for global irradiation, yielding B_h, B_d, B_m and $(B_d)_m$ as the symbols for the horizontal beam irradiation and D_h, D_d, D_m and $(D_d)_m$ as the symbols for the horizontal diffuse irradiation over the indicated periods, h hour, d day, and m month and monthly mean. The symbols for irradiance, G, B and D carry no time subscripts, so making a clear distinction between irradiance and irradiation.

Solar radiation data are often presented in a dimensionless form called the Clearness Index. The Clearness Index, often called the KT value, is obtained by dividing the global irradiation at the surface on the horizontal plane by the corresponding extraterrestrial irradiation on a horizontal plane for the same time period. Three integration time periods are in common use. The hourly clearness index KT_h is the ratio G_h/G_{oh}. The daily clearness index KT_d is the ratio G_d/G_{od}. The monthly mean clearness index KT_m is $(G_d)_m/(G_{od})_m$. G_{oh}, G_{od} and $(G_{od})_m$ are the corresponding extraterrestrial global irradiation quantities for the time integration periods, as indicated by the subscript.

The solar constant I_o is the extraterrestrial irradiance of the solar beam at mean solar distance. The accepted value is 1367 W m^{-2}. The distance of the earth from the sun varies slightly according time of year. The symbol used for the correction to mean solar distance is ε. It is dimensionless. The extraterrestrial irradiance normal to beam is therefore εI_o W m^{-2}.

2.2 The Variability of Solar Radiation and the Implications for Design

Solar photovoltaic designers are essentially facing the design problem of achieving optimal performance from an input of a natural energy resource of great intrinsic variability. Three basic sky conditions can be identified, cloudless skies, partially clouded skies and overcast skies. Cloud cover is the primary cause of the variability in solar radiation energy supply from one minute to another and from one day to another. The typical patterns of cloud cover vary according

to geographic locations. In desert climates, there may be no cloud cover day after day. In high latitude maritime climates, overcast skies may persist day after day in winter with only rare breaks of sunshine. Statistics of cloud cover and daily sunshine, which are widely available, yield qualitative information that can help inform design. Such statistics are available in a systematic mapped form for Europe [9]. Reliable design, however, needs quantitative data about the actual solar radiation energy fluxes. The starting point is to understand the basic radiation climatology for the three basic conditions: clear sky, partially cloudy skies and overcast skies.

2.3 Cloudless Sky Global Solar Radiation at Different Latitudes

The global irradiation is made up of two components, the horizontal beam irradiation and the horizontal diffuse irradiation coming from the hemispherical sky dome. The cloudless sky global irradiation may be calculated using the improved ESRA clear sky model [1, 11]. The model requires as inputs the latitude of the site, the date in the year, which determines the solar geometry and the clarity of the atmosphere. The clarity of the sky is described by an index known as the Linke turbidity factor. Dust, man-made pollution and water vapour in the cloudless atmosphere deplete the clear sky beam irradiation and increase the clear sky diffuse irradiation. Figure 1 plots the calculated clear sky irradiance normal to the solar beam as a function of the sea level solar altitude for different values of the Linke turbidity factor. Figure 2 plots the corresponding values of the diffuse irradiance on horizontal surfaces. Representative spectra of the clear sky global and diffuse irradiance are shown in Figure 3.

By combining the information in Figures 1 and 2 with the geometric information about the solar altitude, a clear day irradiance plot can be produced.

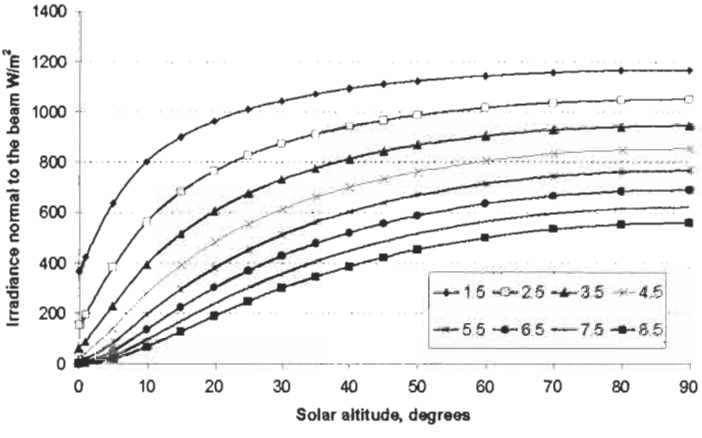

Figure 1 European Solar Radiation Atlas clear sky beam irradiance model [1, 11] estimates of the irradiance normal to the beam in Wh m^{-2} at sea level at mean solar distance for a range of Linke turbidity factors of 1.5–8.5. In practice the sea level Linke turbidity factor is seldom below about 3.5. Values above 6 are common in desert areas due to dust in the atmosphere.

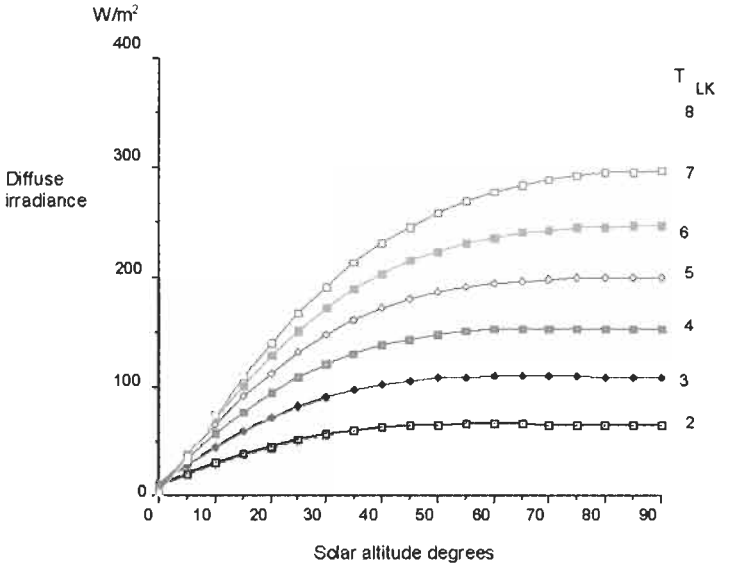

Figure 2 European Solar Radiation Atlas clear sky irradiance model [1, 11] estimates of the diffuse irradiance on a horizontal plane in Wh m^{-2} at sea level at mean solar distance for Linke turbidity factors between 2 and 8. Note the diffuse irradiance increases as the Linke turbidity factor increases, while the beam irradiance decreases.

Figure 4 shows the calculated distribution of the hourly global, beam and diffuse irradiation under clear skies at latitude 45°N on 30 April. The Linke turbidity factor, for this example, has been set at 3. This represents quite a clear sky. The direct beam dominates. Under cloudless sky conditions, the diffuse irradiation forms typically about 10–20% of the global radiation. If one performs the same calculation, day by day throughout the year and then integrates the hourly values, one can estimate the annual pattern of the clear day daily irradiation at this latitude at any reference level of atmospheric clarity. Figure 5 shows the result. The inter-seasonal variations due to the changing day length and the associated changes in solar altitude with time of year are very evident. Figure 6 shows the substantial impact of the Linke turbidity factor on the clear sky daily global radiation at latitude 45°N. It is very rare to encounter a turbidity below about 2.5 at sea level. Large cities have typical turbidity factors around 4.5 in summer. Extremes of dust in the atmosphere may raise the Linke turbidity factor to 6.0 or more. The diffuse proportion of the daily irradiation, which is not plotted, increases as the sky clarity decreases. The hour by hour diffuse proportion also becomes greater as the solar altitude angle gets lower. The available clear sky global radiation becomes extremely low in December at high Northerly latitudes as one is close to the Arctic Circle and the noon sun is low in the sky. Finally Figure 7 plots the influence of latitude on the clear day irradiation as a function of the day number. As the knowledge of the Linke turbidity factor is so important for making solar energy estimates, considerable

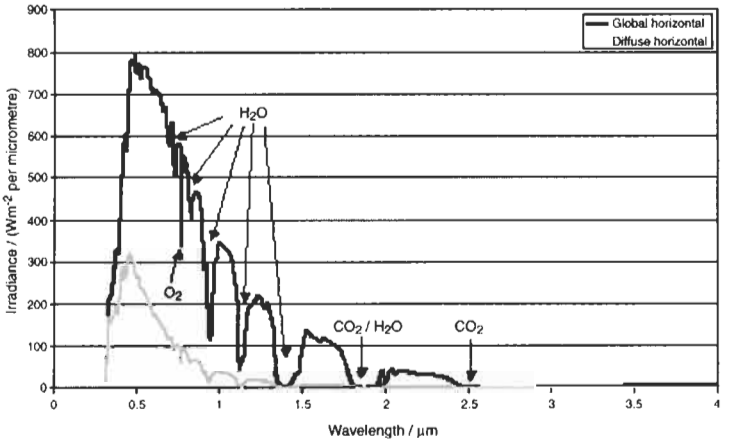

Figure 3 Calculated clear sky global and diffuse spectral irradiances on a horizontal surface for a solar altitude of 30°. The integrated global irradiance was 476 W m^{-2} and the integrated diffuse irradiance was 114 W m^{-2}. Note the dominance of diffuse radiation in the ultraviolet and the contrasting low clear sky diffuse spectral irradiance in the infrared region. Water vapour in the atmosphere is an important absorbing agent in the infrared region. Source: reference [7].

efforts have had to be made within the SoDa program [8, 12, 13] to develop a reliable global database of Linke turbidity factor values.

Note in Figure 7 the bunching of the curves in June around the summer solstice in the northern hemisphere. The Equator values show the maximum values there occur at the Equinoxes, 21 March and 23 September. Figure 7 effectively defines the near maximum global radiation likely to be observed on horizontal planes on any date. Considerable improvements in daily beam irradiation received per unit area can be achieved by tilting the collector surface to face the sun. This helps offset some of the adverse impacts of latitude on solar radiation availability in winter. The quantitative estimation of the cloudless sky irradiation falling on inclined planes is discussed later.

2.3.1 Partially Clouded Conditions

The cloud interrupts the direct beam, so the direct beam irradiance is very variable in partially clouded climates. Dramatic changes in beam irradiance can occur within a few seconds. Skies with a lot of scattered cloud tend to be relatively bright. Consequently the associated diffuse radiation received during such periods can be quite large. However, the short-term variations in the diffuse irradiance are normally not as great as in the case of the beam. The beam irradiance may fall from 750 W m^{-2} to zero within seconds and then, within less than a minute, increase to more than 750 W m^{-2}. Figure 8 shows some detailed observed radiation records for four European sites measuring both global and diffuse radiation on a continuous basis from [15]. The four days were selected as being representative of different types of intermittent cloudiness. The top curve gives the global flux. The bottom curve gives the diffuse flux. When the curves coincide, the weather is overcast ($G = D$). At Vaulx, near Lyon, on 29 September

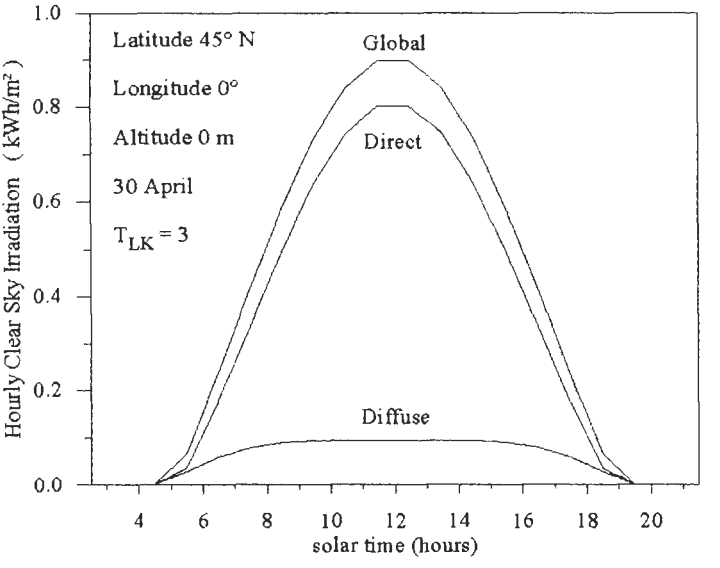

Figure 4 Estimated hourly horizontal irradiation under cloudless skies at sea level at latitude 45°N, showing the split into hourly direct and diffuse irradiation with a fixed Linke turbidity factor of 3. Source: reference [14].

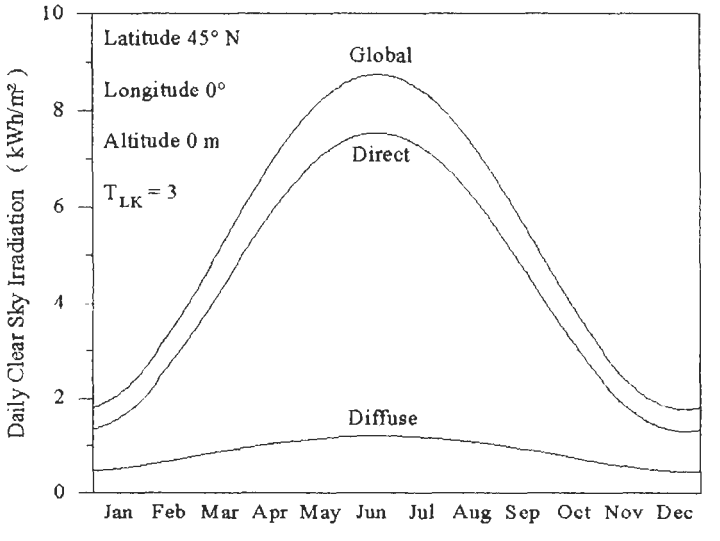

Figure 5 Estimated daily horizontal irradiation under cloudless skies at sea level in different seasons, latitude 45°N, showing the split into daily direct and diffuse irradiation with a fixed Linke turbidity factor of 3. Source: reference [14].

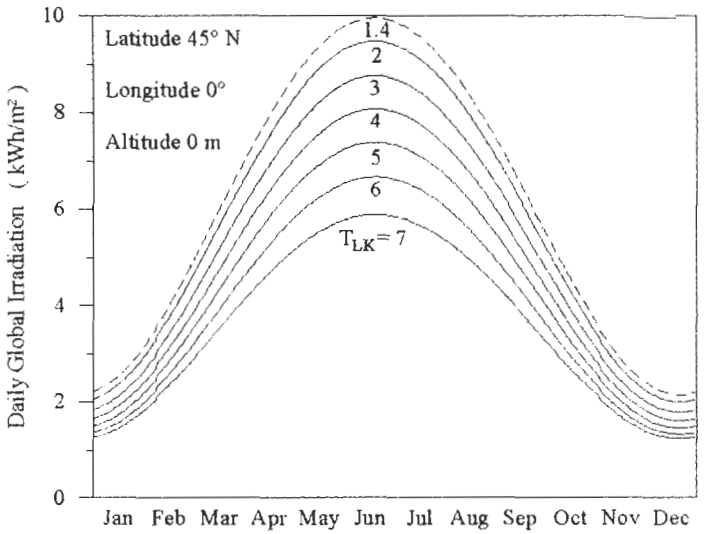

Figure 6 Estimated daily horizontal global irradiation under cloudless skies at sea level, latitude 45°N. The combined impacts of season and of Linke turbidity factor. Source: reference [14].

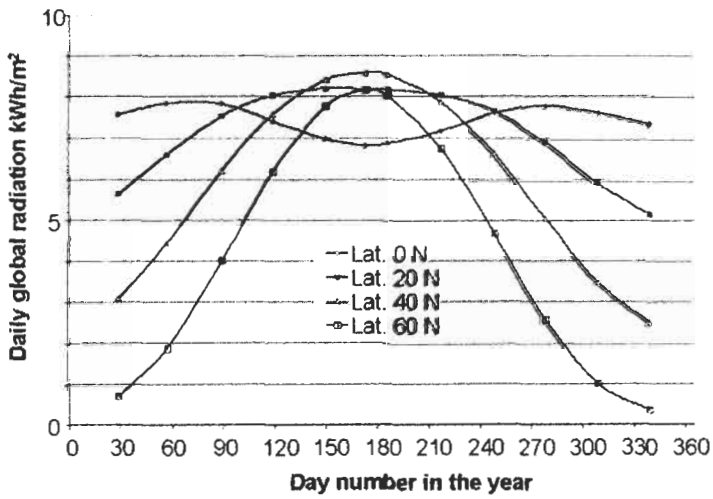

Figure 7 Cloudless day daily global irradiation falling on horizontal surfaces at four different latitudes calculated using a Linke turbidity factor of 3.5. Derived from reference [7].

1994 the morning was cloudy followed with an afternoon of broken cloud. At Nantes on 9 May 1994, very rapid changes were experienced in the afternoon. This is characteristic with broken cloudy under windy conditions. At Nantes on 22 July 1994, the morning was overcast and the afternoon sunny. In Athens on 25 October 1994 there was some thin cloud throughout most of the day

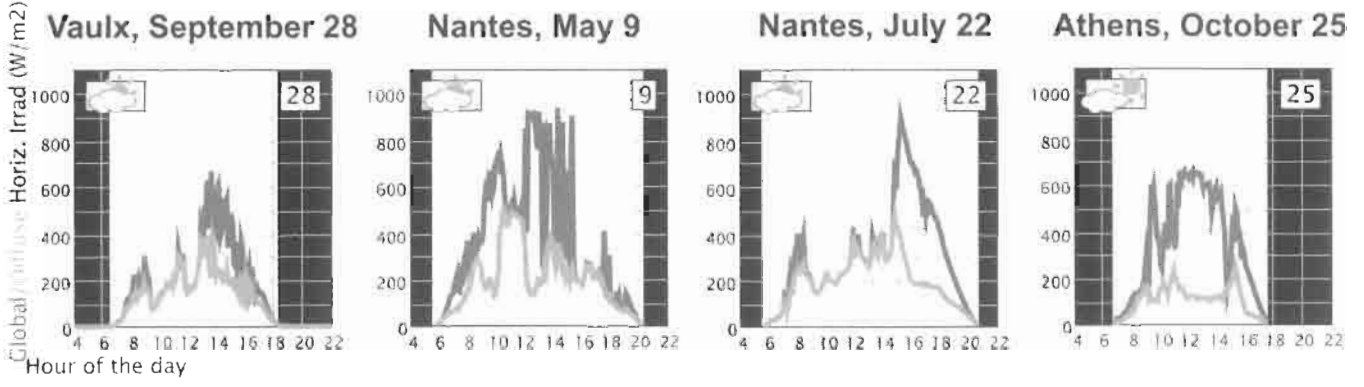

Figure 8 Variation of the global and diffuse horizontal irradiance with time of day for four European sites under conditions of intermediate cloudiness. The bottom line is the diffuse component, the top line is the global component. When the two lines merge into one line it is overcast. Vaulx and Nantes reveal a cloudy morning followed by a sunnier afternoon. The irradiance at Nantes on 9 May 1994 is very variable. Source: reference [15].

followed by a brief overcast period. The day and night periods are indicated using night as black. This presentation makes the changes in day length evident. The numbers at the top right-hand side give the temperatures. The daily global radiation is obtained by integrating the area under the curve. This yields a single variable G_d thus suppressing all knowledge of the detailed variations. The first question is 'Is the detail important for design?' The second question, if it is important, is 'Can the detail be statistically regenerated for design studies?' The answer to the first question is yes, because one is dealing with non-linear systems. The answer to the second question is there are stochastic data generation methods available but they are complex. Stochastic methods are discussed in more detail in Section 4.

2.4 Overcast Sky Conditions

There is no direct beam during overcast periods. The radiation on overcast days is not steady. The height, type and depth of clouds influence the atmospheric transmission. Changes in the cloud cover make the irradiation on overcast days variable but the minute to minute variations in global irradiance tend to be far less than with partially cloudy skies.

Kasten and Czeplak [16] studied the impact of cloud cover type on the global irradiation at Hamburg. They found that the overcast hour diffuse radiation from a given cloud type was roughly a linear function of the sine of the solar altitude. There were strong differences between the different cloud types. They expressed the overcast hour horizontal radiation data with different cloud types as a fraction of the corresponding clear sky global horizontal radiation data found at Hamburg. Their findings are given in Table 1. This table provides a way to link typical overcast day values to the clear day values discussed in Section 2.3. The impact of rain clouds is especially evident. Such days prove serious battery down draw days. The practical risk is such days often occur in prolonged runs of adverse weather rather than single days in isolation.

2.5 Sequences of Global Radiation Data

The experience gained in the production of ESRA 2000 [1] has indicated the great importance in having daily time series of global radiation for making sensibly reliable design decisions. Otherwise, the day to day variability patterns

Table 1 Overcast cloud transmittance relative to clear sky values. Source: reference [16]

Cloud type	Relative transmittance
Cirrus, cirrostratus and cirrocumulus	0.61
Altocumulus and altostratus	0.27
Cumulus	0.25
Stratus	0.18
Nimbostratus	0.16

in solar radiation due to weather change will lost. The daily global radiation can be profiled to match the clear day profile to estimate hourly irradiation values with an acceptable loss in accuracy. The monthly mean values cannot be used with accuracy to simulate daily profiles. Figure 9 shows the advantages of using a profiled daily time series model to simulate performance compared with Figure 10 showing the consequences of using a profiled monthly average model. The differences between the methodologies become even greater when one moves on to estimating slope irradiation.

Another issue is that there is an auto-correlation between the global radiation on successive days because of the common persistence of cyclones and anti-cyclones over several days. Strings of dull days may therefore occur, which may put a serious strain on battery storage resources. These statistical issues are discussed in Section 4.

2.6 Simplified Radiation Climatologies

2.6.1 Typical Components of Simplified Radiation Climatologies

It is useful to have some way of profiling in acceptably simple ways the solar radiation climatology found in different parts of the world. As climate data are compiled on a month by month basis, it is sensible to adopt the calendar month as basic time scale division in climatological summaries. The most important solar radiation climatological value is the long-term monthly mean daily global solar radiation $(G_d)_m$. This should be an average value compiled over several years. For example, ERSA 2000 used the 10-year period 1981–90. It is very useful to have this daily value split into the monthly beam component $(B_d)_m$ and the monthly diffuse component $(D_d)_m$. As diffuse radiation is only measured at a few sites, it usually has to be estimated using the methods described later in Section 6. As knowledge of extremes is useful, it is also valuable to have representative monthly maximum values of daily global irradiation, G_dmax. The third European Solar Radiation Atlas [23] used the mean of the 10 monthly maximum measured values in each 10-year data series for each site to obtain G_dmax. SoDa 2003 generates the clear G_dmax values from terrain height and its

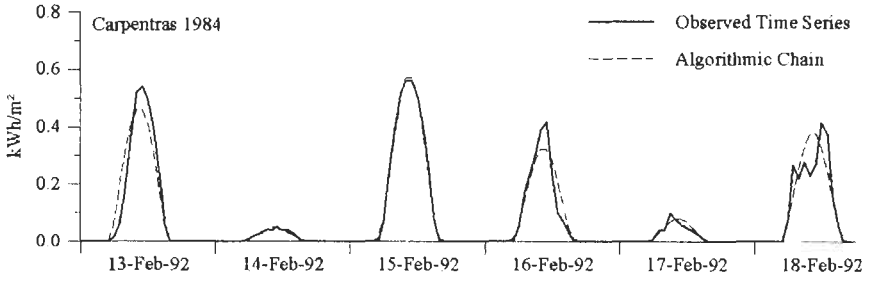

Figure 9 Using an average profile model to generate hourly data, starting with the respective time series of daily global irradiation values G_d. *Source: reference [14].*

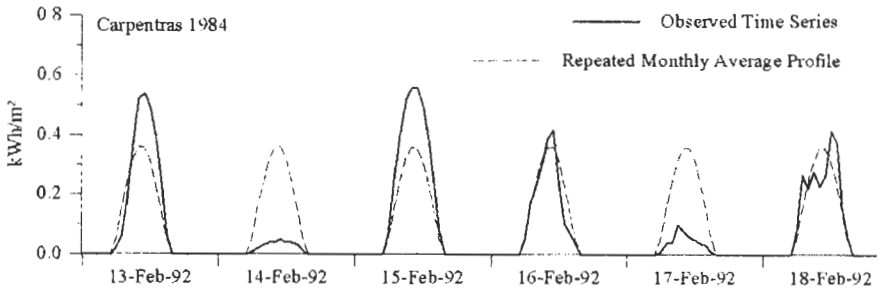

Figure 10 Using a monthly average hourly global radiation profile model to generate hourly data starting with monthly mean daily global radiation (G_d)$_m$ *Source: reference [14].*

global database of monthly mean Linke turbidity factors. However, there is a risk of over-estimation in $G_d max$ in using the SoDa approach when applied to climates where cloudless days have a near zero probability of occurrence, for example in the rainy season months in Equatorial Africa and in the Monsoon months in countries like India. It is also useful to tabulate representative minimum global values $G_d min$. The European Solar Radiation Atlas [23] used the mean of the 10 monthly minimum measured daily values in each 10 year-data series. Sunshine observation data can be usefully added. As the day length varies so much with season, especially at high latitudes, it is useful to express the monthly mean daily bright sunshine in hours as a fraction of the astronomical day length. This ratio is called the relative sunshine duration. Experience with the various European Atlases has also indicated the value of including the monthly mean daily clearness index $(KT_d)_m$ in simplified radiation climatological summaries. Many of the algorithms used in data preparation, described in Section 3 onwards of this chapter, use this dimensionless quantity as an input.

2.6.2 Examples of Simplified Radiation Climatologies for Europe

Figure 11, based on observed data for the period 1981-90 for eight European cities located at different latitudes, presents the latitudinal relationships between daily global radiation, daily diffuse radiation, the ratio diffuse/global radiation and finally the monthly mean KT values for June and December. The data were prepared by the author using reference [1]. Figure 12 (a) to 12 (f) plots month by month the monthly mean global and diffuse radiation for the period 1981-90 for 6 of the 8 sites included in Figure 11. Figure 12 contains one desert site Sde Boker 12 (h) and one humid tropical site, Ilorin in Nigeria. Figure 11(a) immediately makes evident the large latitudinal gradient in monthly mean daily global radiation in winter. In mid-summer this strong latitudinal gradient is absent. This winter gradient reflects the extraterrestrial values shown in Figure 11(a) by the dashed line. A better understanding of exactly what is happening is often achieved by examining the dimensionless $(KT_d)_m$ values. These values are shown in Figure 11(d). For example, the range of $(KT_d)_m$ values in December ranges from 0.150 at Stockholm (latitude 59.35°N) to 0.468 at Nice (latitude

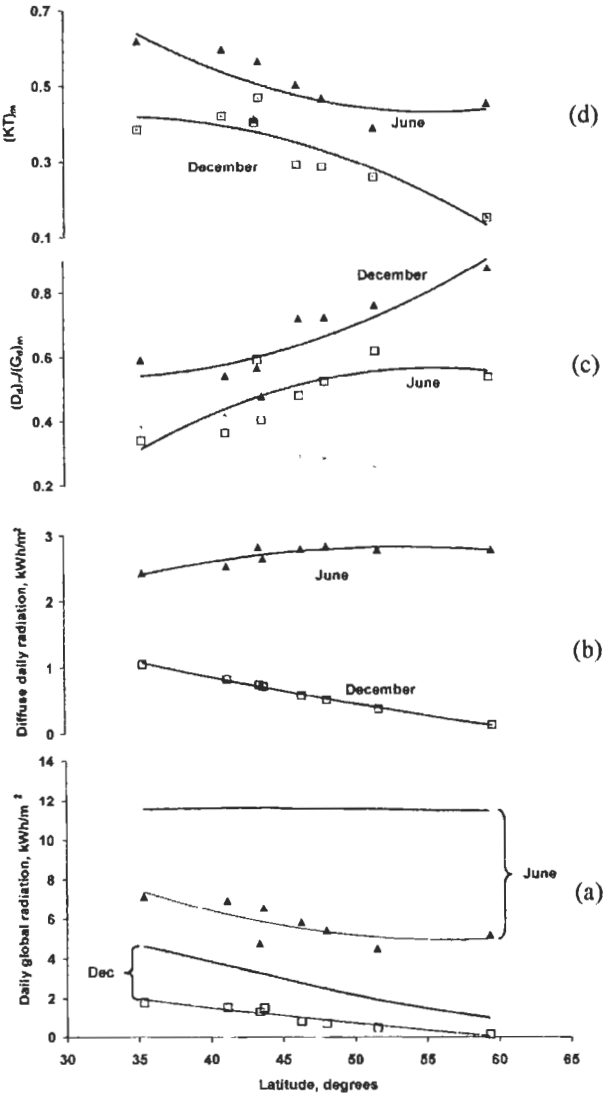

Figure 1.1 Monthly mean climatology of selected European sites 1981–90 in June and December. Prepared from reference [1]. (a) Monthly mean daily global radiation (points and full lines) and the radiation outside the atmosphere (dashed lines); (b) monthly mean diffuse radiation on horizontal surfaces (all in kWh m^{-2}); (c) ratio of mean daily diffuse radiation on horizontal surfaces to the corresponding global values; (d) monthly mean KT values. The graph corresponds to solar radiation data shown in the Appendix.

43.65°N). The sun is scraping the horizon in Sweden in December. The weather is often overcast. In contrast Nice is favoured both by latitude and by its relatively sunny winter climate, due to the protection offered by the mountains immediately to the north. In summer London (latitude 51.52°N) has a cloudier summer climate than Stockholm because of its maritime location and so receives

less radiation than more northerly Stockholm, which has a more continental type of summer.

Figure 11(b) presents the corresponding information about monthly mean daily diffuse irradiation falling on horizontal surfaces. The diffuse radiation is relatively constant across Europe in the period May to August and can be less at southerly latitudes than at northerly latitudes. There are large variations however in the relative proportion of beam irradiation. Figure 11(c) sets down the month by month values of the ratio $(D_d)_m/(G_d)_m$. Of course $(B_d)_m/(G_d)_m = 1 - (D_d)_m/(G_d)_m$. While Figures 11(b) and (c) reveal big variations in the diffuse radiation, it shows that, even in relatively sunny climates, the diffuse radiation is an important resource. In London over 60% of the incoming resource is diffuse radiant energy, so proper attention must be attached to diffuse irradiation analysis. Only the beam radiation can be focused successfully.

A systematic description of the climatology of solar radiation in Europe may be found in the ESRA User Guidebook of reference [1] which identifies three roughly defined climatic categories, Maritime climates, Continental climates and Mediterranean climates, adding a separate category of high mountainous climates. Photovoltaic designers are strongly encouraged to strengthen their understanding of the basic dynamics of climate in the regions in which they plan to work, before embarking on detailed quantitative studies. Such knowledge strengthens understanding of the basic strategic issues that should underlie the detailed engineering design decisions.

2.6.3 Basic Solar Radiation Climatology of the Humid Tropics

The humid tropics are located close to the Equator. The Tropic of Cancer at latitude 22.5°N and the Tropic of Capricorn at latitude 22.5°S give a broad definition to the zone. The equatorial radiation climate is quite different in nature to the climate produced by the varying patterns of cyclones and anti-cyclones, which dominate the typical high latitude solar radiation climates.

For a start, the month to month variations in day length are very small close to the Equator. There are no long summer evenings. There are no long winter nights. So the hours during which indoor lighting is needed do not vary much across the year. This has a bearing on patterns of photovoltaic energy demand.

The noon solar elevation of the sun at low latitudes remains fairly high throughout the year with the consequence that, in the absence of cloud cover, the global solar energy varies very little across the year. Figure 7 in Section 2.3 shows clearly the contrast between the annual pattern of clear sky daily irradiation at latitude 0°N and the corresponding patterns found at higher latitudes. However, cloudless conditions are rare in equatorial areas.

The wet and dry seasons are usually well-defined periods in tropical regions. There is always a considerable amount of cloud during the wet seasons. There is also often quite a lot of cloud in the drier seasons too. The daily pattern of irradiation is often dominated by convective clouds. The clouds build up as the surface temperatures increase. These clouds frequently obstruct the sun and some produce large amounts of rainfall. This rainfall is often associated with

violent thunderstorms. The normal pattern of insolation is therefore an oscillating mix of periods of bright sunshine intermingled with periods of heavy obstruction of the solar beam. The diffuse radiation frequently dominates throughout the year.

The variations in the amount and type of cloud cover associated with the different seasons is the main factor influencing the monthly mean global solar radiation available at different times of the year. The patterns of radiation experienced reflect the impacts of the general circulation of the earth's atmosphere in tropical regions. Surface warming by the sun induces a global atmospheric circulation pattern of ascending air above the equatorial zone. Air from both the northern hemisphere and the southern hemisphere flows horizontally in at the bottom at low levels to drive this vast vertical circulation system in the equatorial zone. This air ascends in massive convection cells that move upwards, cooling and shedding moisture as they ascend. Vertical clouds that may grow to considerable heights in the atmosphere often form producing heavy rain. The air that has ascended, loosing much of its initial moisture on the way up through rainfall, then flows away from the equatorial region towards higher latitudes, moving horizontally at relatively high levels close to the stratosphere. This circulating air eventually descends heated adiabatically by recompression to reach the surface of the land, warm and dry. Such descending dry air overlies the surface of the great deserts of the globe and desiccates them. These regions of descending dry air are essentially regions of high sunshine and small or virtually non-existent rainfall. The rotation of the earth causes a distortion of the convection cells, so, for example, the returning air from the Sahara moving into the west of Africa arrives predominately from a north-east direction.

The zone where the air masses from the south and north merge to form the equatorial convection cells is known as the inter-tropical convergence zone. The position of the inter-tropical convergence zone oscillates north and south as the solar declination changes with season. This movement produces the typical patterns of wet and dry seasons found in tropical climates. There are northern and southern limits to the movement of the inter-tropical convergence zone. If the latitude of any site is close to the latitude of that limit, a single short rainy season will be experienced. Closer to the Equator a pattern of two wet seasons is usually experienced as the rains come up from the Equator and produce the first rainy season. The ITCZ then passes on to a region further from the Equator, the rains yield, only to return later with a second season of rain as the inter-tropical convergence zone falls back later in the year towards the other hemisphere. The northern hemisphere and southern hemisphere tropical rainy seasons typically are about 6 months out of phase from each other, reflecting the annual movements of the inter-tropical convergence zone back and forwards across the Equator.

Global and Diffuse Irradiance Estimates under Partially Clouded Conditions. Maximum diffuse radiation values tend to occur during hours of broken thin cloud. The diffuse radiation from partially clouded skies is normally substantially higher

than the diffuse radiation from clear skies and from typical overcast skies. *It is thus an invalid scientific process to attempt to calculate monthly mean diffuse radiation by linear interpolation between estimated overcast sky and estimated clear sky diffuse radiation values.* The typical hourly sunshine amount producing the highest diffuse irradiation conditions is about 0.3 to 0.5 hours within the hour. Surprisingly high global radiation levels can occur under thin high cloud conditions but the radiation is very diffuse dominated.

An interesting study has recently been published by Gu et al. [17] on the cloud modulation of surface solar irradiance at a pasture site in southern Brazil. They report broken cloud fields typical of humid tropical climates create mosaic radiative landscapes with interchanging cloud shaded and sunlit areas. While clouds attenuate solar radiation incident on cloud shaded areas, sunlit ground surfaces may actually receive more irradiance than under a clear sky due to light scattering and reflection from neighbouring clouds. The authors analysed a high-resolution time series of radiation measurements made in the wet season of 1999 in southern Brazil. Surface solar irradiance frequently (more than 20% of the time) exceeded clear sky levels and occasionally surpassed the extraterrestrial radiation. They found the clouds created a bimodal frequency distribution of surface irradiance, producing an average of approximately 50% attenuation for about 75% of the time and 14% enhancement for about 25% of

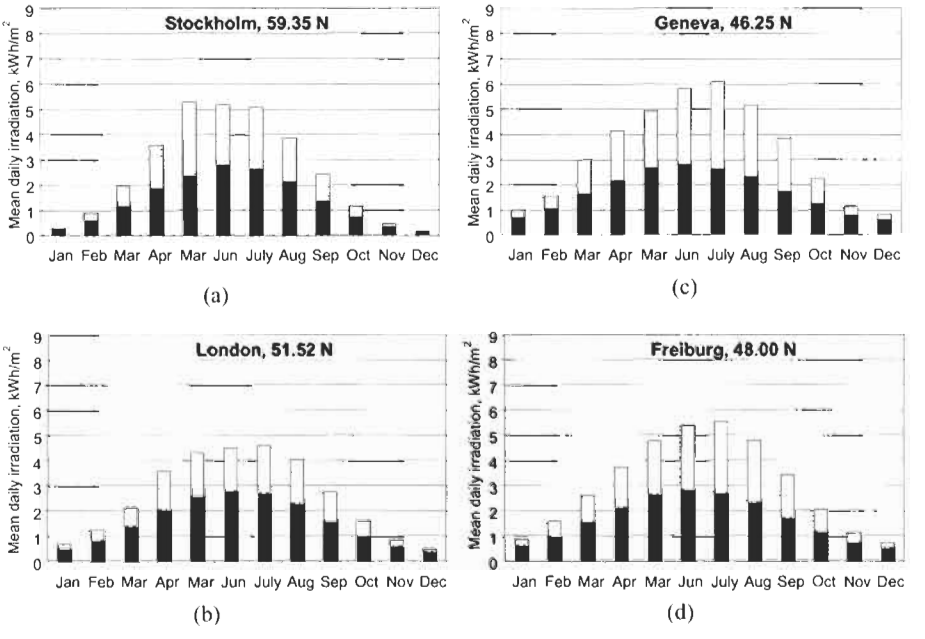

Figure 1.2 (a)–(f) Monthly mean global and diffuse radiation on horizontal surfaces for six European sites, for a humid tropical location (g), and for a desert region (h). The numerical data on which these graphs are based can be found in the Appendix. The shaded bands represent the diffuse irradiation magnitude and the clear bands the beam irradiation magnitude on horizontal surfaces.

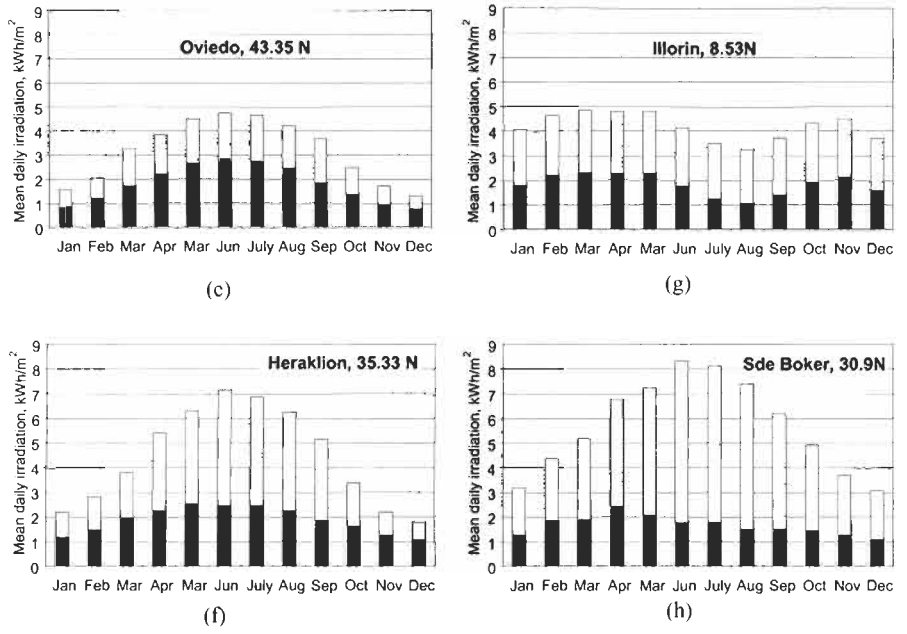

Figure 12 (continued).

the time, respectively, as compared to the corresponding clear sky levels of irradiance. The study is helpful in drawing attention to the actual patterns of irradiance likely to be found on solar cell systems across the humid tropics.

Examples of the Radiative Climatology of a Typical Humid Region. Kumasi, Ghana.

Figure 13 presents observed climatological data for Kumasi in Ghana in West Africa from [18]. Kumasi, located at latitude 6.72°N, longitude 1.6°W at a height of 287 m, is nearly at the centre of the rain forest belt in Ghana. The values of the monthly mean daily clearness index $(KT_d)_m$ reveal the fairly small annual range characteristic of humid tropical climates. The lowest values occur in the rainy season. The double peak in the rainfall in the rainy season in June and September is evident (Figure 12(c)). For most of the year wet moist air moves in from the South Atlantic. However, for a short period around December, the wind tends to blow off the desert regions to the north. These winds, known locally as Harmattan winds, are dry and very dusty especially in December and January. In this season there is very little rainfall for a rain forest area. The Linke turbidity factor is very high in the Harmattan season. It may reach 6 or 7. There is a lot of cloud cover throughout the year. The monthly mean values of $(KT_d)_m$ range from 0.32 in August to 0.47 in February to May and in November. The typical values of KT_dmax are around 0.60, only rising in November to 0.70. In August no cloudless days occur and the KT_dmax value is as low as 0.52. The values of KT_dmin are lowest in the wet season, standing at around 0.10.

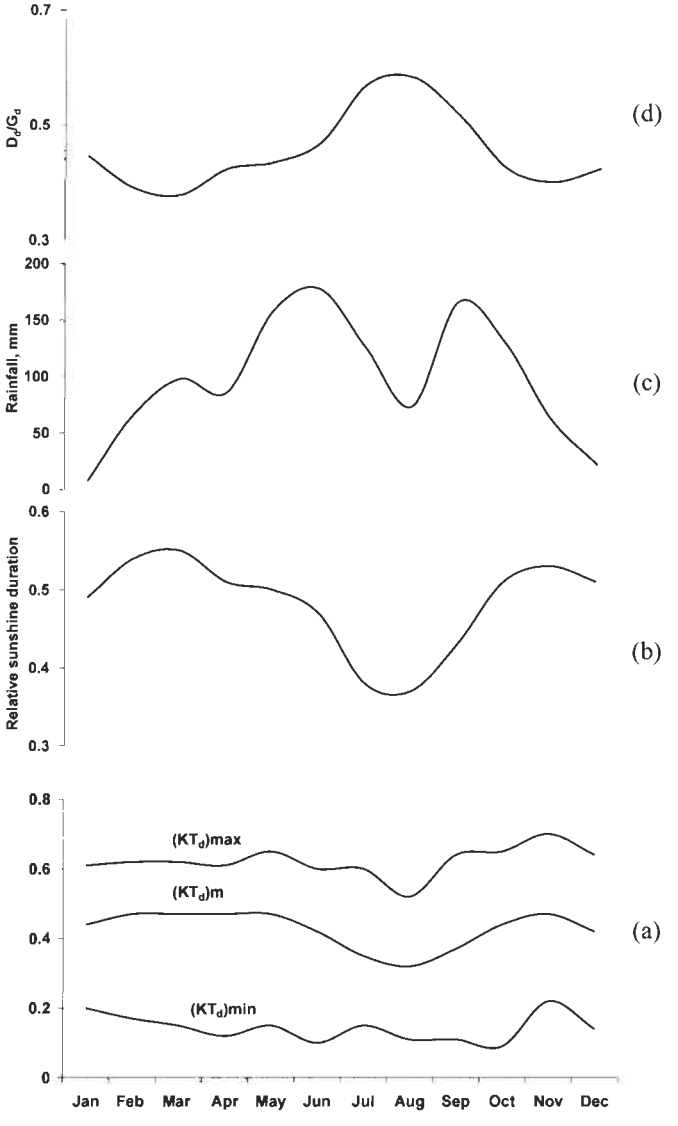

Figure 1 3 (a) Monthly mean daily $(KT_d)_m$ values plotted alongside $(KT_d)max$ and $(KT_d)min$. The monthly mean daily relative sunshine duration values S_d/S_{od} (b), the rainfall (c) and the ratios $(D_d)_m/(G_d)_m$ estimated using Equation (1). The KT_d values are for Kumasi in Ghana, West Africa; the rainfall data, sunshine duration and D_d/G_d are for Ilorin, Nigeria, with a similar climate. Source: references [18] and [19].

Ilorin, Nigeria

The next example is for Ilorin in Nigeria located at 8.53°N, 4.57°E at a height of 375 m based on data from [19], with a very similar radiation climate to that found at Kumasi, but Ilorin being slightly further north. The Ilorin study included relative sunshine duration data. Figure 12(g) shows the rainy season

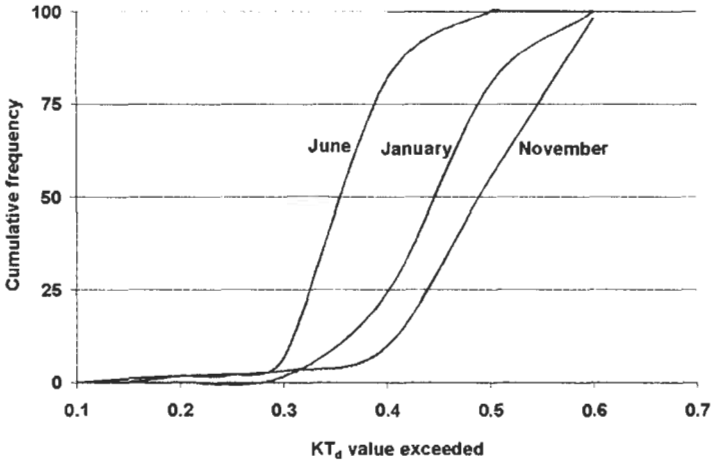

Figure 14 Monthly percentage cumulative frequency of the daily clearness index KT_d *for Ilorin, Nigeria. Source: reference [19].*

causes a strong drop in the relative sunshine duration. The impact of the Harmattan is again evident. Figure 14 gives the monthly percentage cumulative frequency of the KT_d values for the months of January, June and November. There are significant differences in the cumulative frequency curves for different months. In June 50% of the days have a KT_d value of less than 0.36. In November 50% of the days have a KT_d value below 0.50. The seasonal implications for battery storage are obvious. Udo [19] showed the cumulative frequency curves for Ilorin and Kumasi have a much smaller spread of values than typical cumulative frequency curves for higher latitudes. This small spread reflects the low observed values of KT_dmax. Also the observed values of KT_dmin in the humid tropics are high compared with those found in high-latitude climates.

Estimation of diffuse radiation in the Humid Tropics. The diffuse proportion of the monthly mean global irradiation can be estimated approximately using the following simple formula developed by Page [20] widely verified since in many papers:

$$(D_d)_m/(G_d)_m = 1.00 - 1.13(KT_d)_m \tag{1}$$

Monthly mean $(D_d)_m/(G_d)_m$ estimates for Kumasi using Equation (1) are shown in Figure 13(d).

2.6.4 Solar Radiation in Desert-Type Climates

The main hot desert climates of the world lie in those latitudinal regions where the air from the equatorial zone transported aloft at the Equator descends to the surface in a very dry condition. Such climates are characterised by long hours of sunshine, few clouds and very little rain. As there is no water available in the

centre of large deserts like the Sahara, human activity is usually confined to the fringes of such deserts. In some areas water from nearby mountains can flow underground considerable distances and re-emerge at the surface providing the water needed for life in areas without rain. The desert atmosphere however can contain a lot of sand raised by the wind. Consequently, the actual irradiance levels are not as high as those found in many cooler climates with clearer local atmospheres. The Linke turbidity factors are often above 6. High temperatures must not be assumed to provide high irradiation levels from the cloudless sky. Figure 6 in Section 2.3 shows the reductions expected at latitude 45°N as the Linke turbidity factor increases. The clear day daily global radiation may be nearly halved if the Linke turbidity factor rises to 7. The colour of the desert sky is an important indicator of the amount of desert dust. The blue colour may become weak as dust increases. In heavy pollution conditions the sun's disc may become quite red when it is below 30° elevation and cut out altogether when the sun is below 15°. The sky may take on a brown hue. Dust deposition on photovoltaic collectors is likely to impact adversely on performance. Arrangements for achieving effective periodic cleaning of solar panels are essential in desert regions.

Example: The solar radiation climatology of the Negev region of Israel

This example has been selected to bring out the main features of the solar radiation climatology of a relatively dry and sunny area. The data presented by Ianetz et al. for the Negev has been selected [21]. This dataset includes measured beam irradiation data as well as measured global irradiation data. Figure 12(h) shows the monthly mean irradiation data for Sde Boker at 30.90°N, 34.8°E at 470 m. As the latitude in this case is around 30°N, one finds the expected substantial increase from winter to summer. Figure 15 presents the same data in dimensionless forms, as the monthly mean values of the daily clearness index $(KT_d)_m$ and as the monthly mean daily diffuse/monthly mean global irradiation ratio $(D_d)_m/(G_d)_m$. The very high monthly mean values of $(KT_d)_m$ found in the period June to August may be noted. Every day is

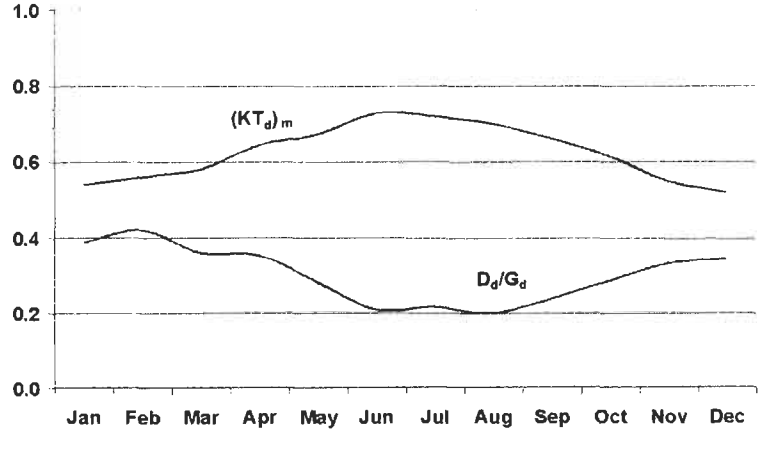

Figure 15 Ratios of $(KT_d)_m$ *and* D_d/G_d *for Sde Boker. Source: reference [21].*

virtually cloudless. The $(KT_d)_m$ ratios are less in the winter period but are still relatively high compared with the humid tropics. The diffuse data are of especial interest as they show there is still a lot of diffuse radiation even in very sunny climates.

2.6.5 Special Issues in Mountainous Areas

Stand-alone photovoltaics applications are becoming quite common at high-level mountain farms and isolated mountain recreational retreats in countries

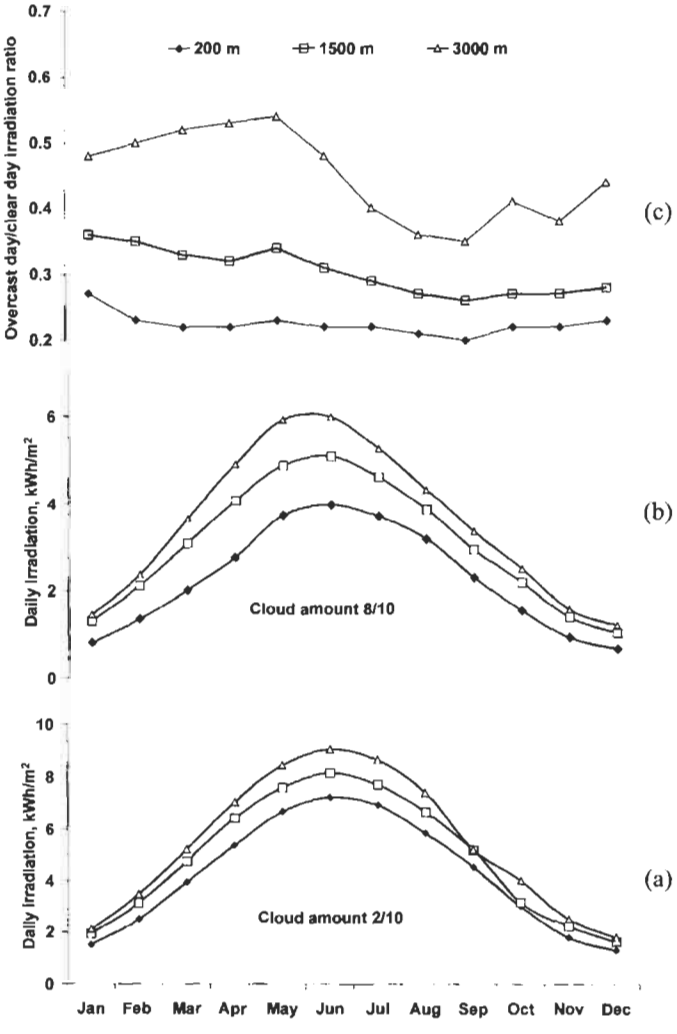

Figure 16 Influence of cloud and site elevation on global solar radiation. (a) The mean daily global irradiation for cloud amounts 2/10 (b) The mean daily global irradiation for cloud amounts 8/10. (c) Overcast day/clear day irradiation ratio at three elevations. A case study from the Austrian Alpine area. Units are kWh m^{-2} d^{-1}. Source: reference [22].

like Norway, Austria and Switzerland. This study, which shows the influence of site height and cloud cover on horizontal surface irradiation in mountainous regions, is drawn from published Austrian data. Figure 16 demonstrates the influence of site elevation and cloud cover on the typical horizontal surface irradiation at different elevations in the Austrian Alps during different months of the year. Detailed examination of Figure 16 shows there are good climatic reasons favouring the use of photovoltaics in mountainous regions. However, designers habituated to sea level living may only partially appreciate these issues, unless they make more focused studies of the radiation climates of such mountainous regions.

Figure 16 will now be discussed in detail. Figure 16 (a) plots the daily irradiation for cloudless and near cloudless conditions. The increase with elevation is evident. The radiation obviously decreases with increase in cloud cover as Figure 16 (b) shows. However there is a substantial elevational effect. The ratio of the overcast day values to the clear values is shown in Figure 16(c). The typical radiation on overcast days at the 200 m level is about 22% of the radiation on cloudless days. At low levels, this reduction is slightly less in the snowy month of January. (Snow in this region is more persistent at higher elevations.) However, in general, the mean overcast sky irradiation reduction at 200 m is relatively constant from month to month. There are, of course, substantial day to day variations in overcast sky radiation due to cloud type.

Let us now examine the effect of height on the irradiation on cloud free days. The ratios of the monthly values at 1500 m and 3000 m to the 200 m monthly values are presented to make the comparison simpler. The clear sky daily radiation increases with site elevation. The increases are greatest in mid-winter when the sun is lowest and least in mid-summer when the sun is highest. The increases are quite substantial, especially at 3000 m; for example a 33% increase in January and a 21% increase in June at 3000 m.

Examining next the impact of site elevation on the corresponding overcast sky data, it is clear that the global radiation on overcast days is substantially greater at higher elevations when compared with the low-level values. The differences are greatest in the mountain snowy period February to May. In March the ratio on overcast days is 1.79 at 1500 m and 3.00 at 3000 m compared with 1.17 and 1.25 on clear days. Two effects are at work. Firstly, as one gets higher, the water content of the clouds above the site gets less. Secondly, as one gets higher, snow is more likely to be lying, especially in winter. Snow increases the diffuse radiation through back-scattering. Some of the reflected energy returns from the atmosphere. The increases become less as the summer melt takes place, with the overcast day ratios falling to 1.48 at 1500 m and 2.13 at 3000 m in August. The consequence is the overcast day/clear day irradiation ratios at 1500 m and 3000 m are substantially greater than those found at lower elevations.

Figure 16 cannot of course bring out the mix of days with different cloud amounts at different mountain sites. However, as is well known, many mountain climates have a high proportion of sunshine in winter months and then become cloudier in summer, as the moisture content of the air rises.

The above factors favour stand-alone photovoltaics in mountainous regions, because the conditions of high sunshine coincide with the seasons of low sun, so easing the issue of battery storage capacity requirements in winter. The atmosphere is not so opaque on cloudy days reducing the energy storage risks associated with runs of cloudy days.

2.7 Radiation Climatology of Inclined Planes for Photovoltaics Applications

While national meteorological services normally concentrate on the provision of horizontal surface data, the practical utilisation of solar energy normally demands detailed design knowledge of the irradiation of inclined planes. Choice of a favourable collector orientation helps to reduce costs by increasing the radiant flux per unit collector area, so enabling a greater energy collection efficacy to be achieved per unit of investment. When the exposure of any site used for harnessing solar energy photovoltaically allows the most favourable orientations tend to be south facing in the northern hemisphere and north facing in the southern hemisphere. However, there are some climates where the afternoons are systematically cloudier than the forenoons. In these cases the true north–south orientation rule may be inappropriate. The appropriate choice of collector tilt and collector orientation is always an important decision. The most appropriate choice is strongly influenced by latitude. A common recommendation is that the ideal exposure is an Equator-facing surface with a tilt equal to the latitude. Accepting this recommendation, this section presents variations in the monthly mean irradiation on equator-facing surfaces on planes

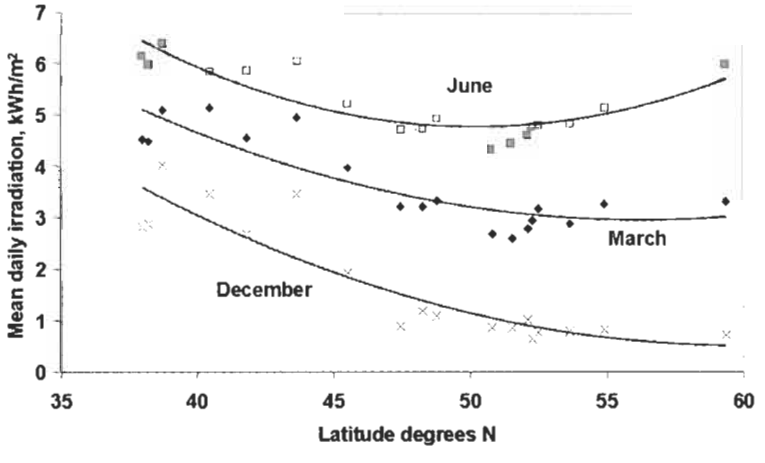

Figure 17 Monthly mean daily global irradiation on a south-facing plane with a slope equal to the latitude plotted against site latitude for 18 European cities of different latitudes in 3 selected months. Period 1966–75. Data source: reference [23]. The ESRA 2000 toolbox [1] contains the tools to enable such calculations for slopes of any orientation and slope in the geographical range covered. This range is from 30° W to 70° E and 29° N to 75° N. The SoDa-IS [8] system provides similar computational systems for the whole world.

with a tilt equal to the latitudes using data from the 3rd European Solar Radiation Atlas [23].

Figure 17 shows the monthly mean daily inclined surface irradiation data for a south facing surface with a tilt equal to the latitude predicted for 18 selected European sites during 3 selected months plotted against latitude. It is clear from Figure 17 that latitude makes a very big impact on expected inclined surface radiation in December. There is very little solar energy available around mid-winter when the latitude is above 45°N. Tilting the collector plane cannot compensate for the longer solar path length through the atmosphere and the greater cloudiness. In December, there is about 4 times as much solar radiation on a latitude-facing south slope around latitude 40°N in Europe than is available for sites above latitude 50°N. The latitudinal slope is less in March than it is in December. However, there is about three times as much solar radiation energy available at high latitudes in March compared with December. At mid-summer the curve becomes U-shaped with a minimum around latitude 50°N. The longer days close to the Arctic Circle and the more continental summer climate found in Sweden increase the plotted mid-summer daily gains at these high latitudes. While there are significant variations between sites, say Nice and Venice at nearly the same latitudes, the latitudinal effects broadly dominate solar radiation availability in Europe.

2.8 Inter-annual Variability

Most of the short-wave radiation variability on cloudless days is the direct result of the apparent movements of the sun as seen from the earth. However, some of the clear sky variability is associated with the varying amounts of water vapour and aerosols in the atmosphere in different seasons in different parts of the world. Imposed on this basic variability is the variability that results from the day to day variations of weather, as cyclones and anti-cyclones pass over the site. These variations are expressed in terms of variations in cloud type and cloud amount in different months. In high latitudes, such disturbances often last three or five days. The dynamics of climatology drives variations in both the total amount of solar energy and in the balance between beam and diffuse radiation received from the sky. There is also usually considerable inter-annual variability. This inter-annual variability in some cases is linked to fundamental oceanic oscillations in sea temperature, for example the impacts of El Nio felt around the world. In Northern Europe, the North Atlantic pressure oscillation is important determining the typical tracks of weather fronts in different years. There are also the occasional impacts of major volcanic eruptions. The consequence of such influences is that there is often a persistence of either radiatively favourable or radiatively unfavourable weather across succeeding months in particular years. These experiences leave behind human memories of excessively hot summers and miserably cold summers, also bright sunny winters and dark overcast winters. Risk analysis of stand-alone photovoltaic systems performance is affected by the impacts of

such inter-annual variations in climate. There is a danger in placing too much reliance on short-term records as the basis of risk assessment. When long-term radiation observations are missing, sunshine data can provide an alternative approach. The method below is based on the use of the Angström regression equation (see Equation (2) below) in conjunction with monthly mean sunshine data selected on a year by year basis. It is based on the 4th European Solar Radiation Atlas [1].

2.8.1 Estimating Daily Radiation from Sunshine Data

The daily global irradiation can be estimated from sunshine data using the Angström formula. Monthly mean sunshine data are first converted into the monthly mean relative sunshine duration, σ_m, by dividing the observed monthly sunshine data, S_m, by the corresponding monthly mean maximum possible sunshine, S_{0m}. S_{0m} can be determined from the sunset hour angle, ω_s; using Equation (11) in Section 5.4.4, as $2\omega_s/15$ hours.

The linear relationship between the monthly mean daily clearness index defined as $(G_d)_m/(G_{od})_m$ and the monthly mean relative sunshine duration is known as the Angström regression formula. The following equation is used to estimate the monthly mean value of $(G_d)_m$ from σ_m:

$$(G_d)_m/(G_{od})_m = a_m + b_m\sigma_m \tag{2}$$

where $(G_{od})_m$ is the monthly mean daily extraterrestrial irradiation on a horizontal plane, and a_m and b_m are site-dependent monthly regression coefficients. G_{od} is calculated using Equation (19) in Section 6.1. The site-dependent Angström regression coefficients a_m and b_m used in [1], were extracted on a month by month basis. They were derived for the period 1981–90 from the quality controlled daily series of global irradiation and sunshine duration data. Such data were available over 500 sites in the ESRA mapped region. The geographical range coverage is from 30°W to 70°E, 29°N to 75°N. The values are stored in two text files on the ESRA CD-ROM, one containing values of a_m and the other the values of b_m. By assuming that these values still hold for nearby sites with the same type of climate, one can make a good approximation of the global irradiation provided there are no major impacting geographical features in the region of interest. These include mountain ranges, large water bodies, etc., which can originate significant climatic gradients.

While site-dependant linear regression coefficients are widely available from the literature for many parts of the world (publications of the national meteorological services, atlases and solar energy journals), the coefficients are not usually derived using the same methodologies, as adopted in the ESRA 2000 project. Caution has to be used in drawing international comparisons based on published Angström coefficients. If a site lies outside the ESRA area and a short-term series of daily global radiation is available, the short-term series can be used can be used month by month to estimate site applicable values of a_m and b_m, following the detailed procedures reported in [1]. These values can then be applied to the long-term records of observed monthly mean sunshine to explore year to year variability.

2.9 Conclusions Concerning Basic Radiation Climatology

It is always wise to aim to achieve a sound understanding of the basic climatic influences driving the local solar radiation at any point of the globe before proceeding to any detailed quantitative technical analysis of system designs. Assessing risk reliably is a difficult task in the design of renewable energy systems. Always try to obtain long-term records where possible.

3 Quantitative Processing of Solar Radiation for Photovoltaic Design

3.1 Introduction

Photovoltaic system designers usually have to aim to extract the maximum economic return from any investment over the lifetime of the installation. One way of doing this is to try to increase the incoming energy density by tilting the solar cell panels towards the sun. However, the optimum tilt for increasing the daily energy density varies with time of year. The value of the collected energy to the user also varies with time of year, particularly for stand-alone photovoltaic systems. For example, if the electrical energy is to be used for lighting, the night time period during which the electric lighting is needed, will vary across the year. So choosing the optimal tilt and orientation of collectors requires careful thought. Design also has to deal with the assessment of the effects of site obstruction on collection performance. Partial shading of photovoltaic panels is also undesirable. So a proper understanding of the geometry of solar movements is needed. The irradiation on inclined surfaces can only be calculated if the global irradiation can first be split into its beam and diffuse radiation components at the hourly level. The designer is handling a three-dimensional energy input system. His/her capacity to be able to inter-relate the solar geometry and the energy fluxes is usually important.

National meteorological services aim to provide generalised data for the regions they cover. Their work has two main components:

- short-range and long-range weather forecasting
- providing climatological advice and data

Climate data needs for solar radiation data were historically met using ground-based observation records. More recently, ever-increasing use is being made of satellite observed data to generate ground level information. Satellite data, for example, form a crucial component of the radiation database material available to users of the SoDa-IS 2003. The ESRA 2000 [1] solar radiation maps are based on a combination of satellite-observed and ground-observed data.

Photovoltaics design depends on the successful harnessing the available climatological information to the detailed task of design. The gap between what

data national meteorological services can provide and what systems designers actually need is currently often quite wide. This part of the chapter considers some of the currently available methodologies for providing photovoltaic designers with quantitative information that they need to address various design tasks.

Performance has to be assessed in the context of risk. Supply and demand have to be matched through appropriate energy storage strategies. This places especial value on the availability of time series of solar radiation data preferably linked to temperature data. The diurnal temperature range is strongly linked to the daily horizontal radiation received. The daily mean temperature is usually dominated by the source of the air passing over the site. Polar air can bring low daily mean temperatures in association with large solar radiation gains and consequently associated big diurnal swings of temperature.

3.2 Assessing Solar Radiation on Inclined Planes: Terminology

In the case of inclined planes, there are three components of the incident radiation: beam radiation, diffuse radiation from the sky and radiation reflected from the ground. The ground reflected component depends on the albedo of the ground surface. The albedo is the surface reflectivity averaged over the whole solar spectrum. Typical values of the albedo are 0.2. Snow cover can raise this to 0.6–0.8 according to the age of the snow. The terminology used here for inclined plane irradiance is $B(\beta,\alpha)$ for the direct beam irradiance falling on a surface with tilt β and azimuth angle α. $D(\beta,\alpha)$ is used for the diffuse radiation received from the sky and $R(\beta,\alpha)$ for the diffuse radiation reflected from the ground alone. Irradiation quantities for different integration periods are indicated by adding the following subscripts: h for hour, d for day and m for month. This practice conforms with the terminology of Section 2. The supplementary subscript cs refers to cloudless sky data.

3.3 An Example: Analysis of the Components of Slope Irradiation for London

A specific graphical study is next presented in order to make the nature of the decision-making issues concerned in deciding collector orientation and tilt clearer. This example is based on the use of numerical monthly mean irradiation data and clear day irradiation values data for London (Bracknell). These data have been extracted from reference [7].

Figure 18(a) shows the estimated monthly means of the daily irradiation on south-facing inclined planes of different inclinations at Bracknell. These data were processed from observed hour by hour global and diffuse horizontal surface irradiation data for the period 1981–92. (UK readers should note that there are corresponding tables for west, south-west, south-east and east surfaces as well in reference [7] for this site, as well as for Edinburgh and Manchester Aughton, all valuable for photovoltaic design purposes in the UK.) The large variation found in the global radiation from winter to summer at high latitudes has already been discussed in Section 2. Figure 18(b) presents the corresponding ratios of the daily slope diffuse radiation to the daily global radiation on that inclined plane. Figure

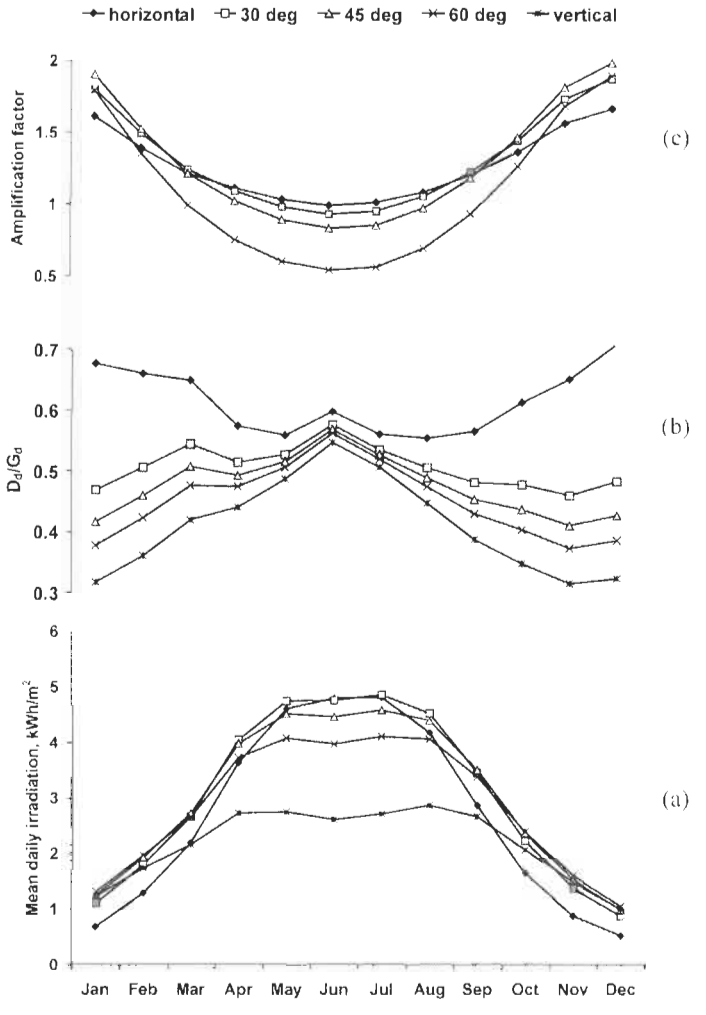

Figure 18 (a) Monthly mean daily irradiation on south-facing inclined planes. (b) The ratio of diffuse to daily global radiation on the inclined plane. (c) The total radiation amplification factor over the horizontal surface. London Bracknell (1981–92). Units are Wh m^{-2} d^{-1}. Latitude 51.38°N, longitude 0.78°W. Site elevation 73 m. Ground albedo 0.2. Source: CIBSE Guide J [7].

18(c) compares the estimated total irradiation values on the various south-facing inclined planes with the corresponding observed global radiation values on the horizontal plane. The ratio *monthly mean irradiation on the inclined plane/ monthly mean irradiation on horizontal plane* has been termed the monthly mean daily amplification factor for that specific slope and orientation. It is usually a design aim to optimise the amplification factor in the context of supply and demand. The monthly mean amplification factors are different for beam radiation, diffuse radiation and total radiation. An important question is 'When is the energy most valuable?' Choice of collector slope and orientation becomes

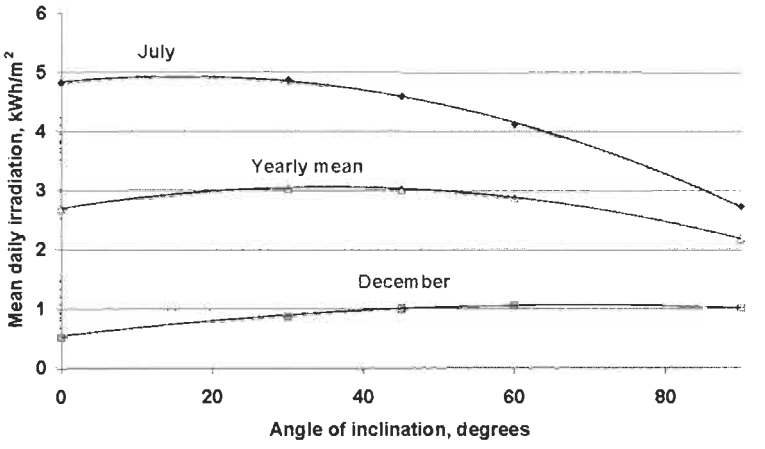

Figure 19 Mean daily irradiation on a south-facing inclined surface in London in July and December and the mean yearly value as a function of the angle of inclination.

especially important for the periods of the year when the solar radiation energy supply is low and the energy demand high.

Figure 18(c) shows the maximum tabulated global amplification factor in January is 1.90 on a south-facing plane with a tilt of 60°. This tilt may be compared with latitude of Bracknell of 51.38°N. The December value is slightly higher at 1.98. It also occurs on a south-facing plane with a tilt of 60°. The maximum tabulated total amplification factor value in June is 1.01 on a south-facing plane with a tilt of 30°. A vertical south-facing surface in June has a monthly mean amplification factor of only 0.56 compared with 1.79 in January.

Figure 19 summarizes the predictions for July and December for south facing slopes of different inclination. The annual mean curve is also included.

3.4 Design Conclusions

This analysis has shown that the interactions between global irradiation and inclined plane irradiation are very complex. This complexity makes it difficult to make sound decisions about photovoltaic design without having simulation methodologies available to explore the issues of optimisation of collector exposure efficiently under different energy demand scenarios.

The monthly mean energy density gains achieved through tilting collection systems vary very much from month to month. Designers have to decide how to match supply and demand best across the whole annual cycle taking account of the economics of energy storage in bridging between periods of favourable and unfavourably energy supply. Decisions about tilt angle are critical.

Compared with horizontal exposures, inclining photovoltaic collectors appropriately towards the sun usually increases the radiation density available on sunny days and reduces it on overcast days. Statistically the variance range in the daily irradiation is increased as a surface is tilted towards the Equator.

Collecting diffuse radiation efficiently is often as important as collecting beam energy efficiently, especially in high-latitude cloudy climates.

Satisfactory time series of hourly slope irradiation can be developed from time series of observed daily horizontal irradiation. It follows that observed daily global radiation data are needed to aid effective simulation. For example, the 4th European Solar Radiation Atlas [1] contains a 10-year time series of quality controlled daily solar radiation observations for the period 1981–90 for nearly 100 European sites. These data can be harnessed to help improving design understanding using suitable simulation models.

User-friendly tools for preparing hourly time series of inclined surface beam and diffuse irradiation data already exist within [1] covering Europe and [8] covering the whole world. The development of these tools has had to address algorithmically a number of issues including the generation of the solar geometry, the estimation of clear sky radiation, the estimation of monthly mean global radiation, the estimation of diffuse radiation, conversion radiation from horizontal surfaces to inclined planes, handling reflections from the ground, and providing tools to examining the geometric impact of obstructions. Considerable attention has had to be given to the development of stochastic tools for the generation of irradiation times series. These statistical approaches are described in Section 4.

4 The Stochastic Generation of Solar Radiation Data

4.1 The Basic Approach and the Implicit Risks

4.1.1 General Principles

Stochastic models for generating time series of solar radiation data use various statistical approaches for the generation of solar radiation data. One type of stochastic model commonly used creates time series of daily global radiation data statistically from values of the monthly mean daily global irradiation. A different type of stochastic model is used for generating time series of hour by hour irradiation statistically from day by day time series of daily global radiation data. Using the principle of the chaining of stochastic models, the day by day models can be used first to process the relatively widely available monthly mean daily irradiation data to provide statistically generated representative time series of daily radiation data. This day by day output then provides the starting statistical daily time series needed as input to drive a second statistical stage to generate, hour by hour, the corresponding more detailed time series of hourly global radiation data. However, before moving to the hour by hour stochastic stage, mean daily profiles of hourly solar irradiation data have to be generated for each day from the generated daily global irradiation time series using some suitable algorithm. Once the daily profile of the mean hourly global irradiation associated with each specific

daily irradiation value has been established, the hour by hour stochastic models, which generate statistically the departures from the expected mean profile for the day can then be applied. This process converts the stochastically generated daily time series of global radiation data into a stochastically generated hourly time series of global radiation data for the simulated period. The most common simulated periods are a month or a whole year. The stochastic generation of a time series of hourly global irradiation data falling on a horizontal surface thus involves three basic stages. The next step for practical applications is to estimate the split of the generated hour by hour global irradiation time series data into their hour by hour beam and diffuse components. This information is essential to make estimates of the irradiation falling on inclined planes. This adds a fourth stage involving the application of another appropriate algorithm to achieve the split.

The definitions of most of the dimensionless quantities used here have been given already in Section 2.1. Following the SoDa project [8], a new objective dimensionless quantity has been added for this section. This is the clear sky KT value, $KT_{d,cs}$. It is simply defined as $G_d/G_{d,cs}$, where $G_{d,cs}$ is the estimated representative daily clear sky irradiation on day d. The SoDa project has a facility for estimating $G_{d,cs}$ for any place in the world.

The Problem of Data Generalisation. The various models in use attempt to generalise the underlying statistical relationships in order to build successful stochastic models. The aim often is to generate acceptable time series data covering the radiative characteristics of a wide range of climates. The methodology used needs to reproduce the distribution of the probabilities and, also, to preserve the degree of auto-correlation between succeeding days [24]. A fine day has a greater probability of being followed by another reasonably fine day than being followed by an overcast day. This is due to the typical persistence of anti-cyclonic weather, which statistically typically lasts several days. There is also the corresponding day to day persistence in overcast day irradiation, because cyclonic disturbances also typically endure more than one day.

Limitations Imposed by Variations in Global Climatology. The various stochastic models proposed do not usually achieve their prediction goals successfully for all geographic locations. Unfortunately, many authors working at specific places tend to believe the aim is to find universal solutions. In following this ambitious aim, they often reveal a lack of detailed knowledge of the complexities of radiation climatology in various parts of the globe. So they risk becoming scientifically exposed through their lack of global climate knowledge.

Most of the available stochastic models have tended to be derived predominately from mid-latitude observed data. The underlying statistical derivation processes are influenced by the predominant use of observed data from the mid-range of latitudes in their generation. This geographically limited approach unfortunately has tended to make the many of the commonly available generalised stochastic models less reliable at high latitudes and at

low latitudes than they are at mid-latitudes. It is therefore important to assess the type of observed data being used in any statistical model development process against the actual latitude of use. Great benefits can still be obtained, however, from the use of stochastic techniques for generating realistic time series of solar radiation data for assessing the performance of photovoltaic systems in various parts of the world, provided these underlying difficulties are recognised.

It is a simple question to ask 'Has this specific stochastic model been validated against radiation observations in my part of the world?' If not, proceed with care.

4.2 Estimating Time Series of Daily Global Radiation from Monthly Means using KT-Based Methods

There is normally considerable variation in the global irradiation from day to day especially at high latitudes. The alternation of anti-cyclonic and cyclonic conditions causes large variations in cloud amount and in sunshine amounts. This results in a highly variable supply in the available daily solar energy in such regions. This is especially true for areas exposed to a strong maritime influence. The desert climates in contrast show much less day to day variation in irradiance. Some humid tropical climates have some cloud nearly every day. In such regions, cloudiness often develops progressively across the day due to vertical convection as the ground warms. Other climates are linked to strongly defined wet and dry seasons, for example the Monsoon climates of South-East Asia. There still remains a lot of work to be done in developing sound stochastic models covering the wide range of climates found across the world.

The model of Aguiar et al. [24] was implemented within METEONORM Version 3.0 [3]. This commonly used algorithm converts the monthly mean global radiation into a statistically generated time series using a library of Markov transition matrices to generate the daily global radiation series. The aim is to make the statistically generated series indistinguishable statistically from the observed time series. This approach provides a way of obtaining radiation sequences for locations where such sequences have not been measured.

The method is based on two observations [24]:

1. There is a significant correlation between radiation values for consecutive days.
2. The probability of occurrence of dimensionless daily radiation KT_d values is the same for months with the same monthly mean KT_m values at different locations in the world.

The basic algorithm generates a statistical time series of daily values of KT_d. The global radiation G_d is then estimated from KT_d as $KT_d.G_{od}$ where G_{od} is the daily extraterrestrial value for day d. The method depends on the availability of a suitable library of monthly Markov Transition Matrices (MTMs), each covering a

defined range of KT_m values. The library [24] of MTMs was built up using daily data from five Portuguese stations, plus Polana in Mozambique, Trappes and Carpentras in France and Macau. There were 300 months of data.

There are a number of shortcomings of the KT_m approach for the stochastic generation of daily global radiation time series. The difficulties at higher latitudes have already been mentioned. Workers at mid-latitudes do not always realise how significant change of latitude can be on the KT_d max values in winter. This factor was not taken into account adequately in the Aguiar et al. [24] mid-latitude studies. The earlier Aguiar approach also produces difficulties at sites elevated well above sea level. For these reasons, the SoDa project has developed the alternative MTM methodology outlined in the next section.

4.3 Improvements in the Stochastic Estimation of Daily Solar Radiation in the SoDa Project

The following important methodological improvement has been recently introduced in the EU supported SoDa program [8, 13]. The SoDa project has produced world maps of the monthly representative Linke turbidity factors across the globe automatically adjusted to site level. The SoDa computational processes also provide the user with accurate information on terrain elevation. These maps and their associated data bases are conjoined to SoDa clear sky modelling programs, so an objective process is now available for estimating the representative value of the clear sky daily global irradiation $G_{d,cs}$ on any day. The whole system of MTMs was therefore changed from a KT_m clearness index basis to a clear sky clearness index basis. Formulated like this, the maximum value of $KT_{d,cs}$ (=1) must correspond automatically to the clear sky model predictions used. $KT_{d,cs}$ is calculated as the ratio $G_d/G_{d,cs}$.

This change required the daily MTM tables to be completely revised to match the new formulation. Data from 121 stations in the world were used [13].

4.3.1 Validation of Daily Irradiation Generation Models

Two sets of validation studies are needed. The first set has to verify that there is a reasonable representation of the overall probability profile. This is normally achieved by accumulating the observed daily time series into bins of defined KT_d or $KT_{d,cs}$ width and comparing these values with the corresponding predicted values, binned in exactly the same manner. A reasonable match should be obtained. The match will never be perfect. A second basic check is to compare the one-day time lapse auto-correlation values between prediction and observation.

The new model was validated at 12 sites and compared the KT estimates against the KT_{cs} observations. Generally the new model was found to be slightly better. The probability profile distributions generated from the two methods are very similar. Generally the clear day KT_{cs} model shows better results for North American sites than for European sites. This result can be explained by the different geographical choice of sites used for making the original Aguiar model

and the new METEONORM/SoDa model developed by Meteotest of Switzerland in conjunction with other EU SoDa project partners.

While the results are very similar in numeric detail, it has to be underlined that good convergence with the clear day observations is only achieved with the new version. The close interaction with the clear sky model is helpful especially when looking at clear day extremes. Additionally the new Meteotest/SoDa model is easier to use (requires no minimum and maximum classes) and runs generally faster (less loops). The auto-correlation also seems to be predicted better with the new $KT_{m,cs}$ model [13].

4.4 Generating Hourly Values of Global Radiation from Daily Values

4.4.1 Generating Mean Daily Profiles of Irradiance from Specific Values of Daily Radiation

The knowledge of the mean daily profiles is essential for many simulation applications. It is also the first step in the generation of hourly values of global radiation from daily values of clearness index or clear sky clearness index. The model of Aguiar and Collares-Pereira [25] was used in METEONORM Version 3.0 [3] to generate the daily profile. Unfortunately, this earlier model is very badly suited for high latitudes. In METEONORM Version 4.0 [4] the hourly integration model of Gueymard [26] was introduced. Gueymard validated different models for 135 stations. One of them was the model of Collares-Pereira and Rabl [27] that was used for ESRA [1]. Gueymard as a result presented a corrected version of Collares–Rabl model that was better adapted to high latitudes. Gueymard's new model and the corrected model of Collares–Rabl showed about the same quality.

In a report by Page [28] a firm recommendation was made to use another daily profile of beam irradiance. This report pointed out that the profile model of Collares-Pereira and Rabl [27] was unsafe, principally for low solar altitudes, a point especially important for high latitudes, where low solar altitudes are much more dominant in solar radiation simulations. Page proposed the hypothesis that the average day beam irradiance profile should mirror the clear day beam profile exactly in the form:

$$B_h = B_d \cdot \frac{B_{h,cs}}{B_{d,cs}} \tag{3}$$

where B_d is the daily beam irradiance, $B_{h,cs}$ the clear sky hourly beam irradiance and $B_{d,cs}$ the daily clear sky beam irradiance.

The clear day hourly beam irradiance and the daily clear day beam irradiation can be calculated any standard clear day formulae. The SoDa project has adopted the improved ESRA clear day model for this calculation [8, 11]. The disadvantage of the model described by Equation (3) is that the daily beam value has to be known first. This value can be calculated for example with Erbs's model as discussed in reference [1]. Page suggested [28] the use of a new model for daily beam values, using a kind of Angström formulae with sunshine data. In order to escape this problem in the estimation the daily beam values, Meteotest

postulated the alternative method for calculating the global mean daily profile directly. This avoids the difficulties mentioned. As the diffuse profile can be calculated from the improved ESRA model, the global profile can be easily calculated as sum of the two components.

4.4.2 Profiling of the Global Irradiance

The following new method for generating mean daily irradiation profiles was proposed and has been incorporated as a standard part of the SoDa stochastic software. The global radiation clear sky profile is used to calculate the global radiation profile from the daily global irradiation using

$$G_h = G_d \cdot \frac{G_{h,cs}}{G_{d,cs}} \tag{4}$$

where G_d is the daily global horizontal irradiance, $G_{h,cs}$ the clear sky hourly global irradiance, $G_{d,cs}$ the daily clear sky global irradiation [29].

The advantage of this model is, that daily values of beam or diffuse do not have to be known in advance. The model, called here Remund–Page (RP), relates perfectly to the upper edge of the distribution, the clear sky profile. This calculation is always needed as the first step in the SoDa chain of algorithms. A short validation of the model has been made and will be published in due course by Meteotest.

4.4.3 Stochastic Generation of Hourly Values of Global Irradiation

The stochastic generation of hourly values of global irradiance in the SoDa program is based on the TAG (time-dependent, auto-regressive Gaussian) model of reference [25]. This model, also used in METEONORM, consists of two parts. The first part calculates an average daily profile. The second part simulates the intermittent hourly variations by superimposing an auto-regressive procedure of the first order (AR(1)-procedure) [30]. The improved chain of stochastic models is implemented in a user accessible way in SoDa [8] and also in the new version of METEONORM [5].

4.5 Splitting the Global Radiation to Diffuse and Beam

Two well-researched models for estimating the fraction of the hourly diffuse radiation in the hourly global radiation, D_h/G_h, are the models of Perez [31], as used in METEONORM Version 4.0 [4], and of Skartveit et al. as used in the Satel-light project [32]. The disadvantage of the use of a model like that of Perez or Skartveit is that the daily values of beam or diffuse the hourly values cannot be determined without stochastically generating hourly values. So the beam and diffuse values depend to a small extent on random numbers. The use of mean daily profiles to calculate the beam and diffuse profile is not really possible, because both the Skartveit and Perez models depend on the hourly variations from one hour to the next. Mean profiles and hourly values with variations do not give the same result.

One advantage of the Skartveit model is that a correction for the impact of high ground albedoes is available for this model. There is also a formula to calculate the hourly variation of global irradiation if this value is not known. The original model was adjusted to observed data from Bergen, Norway. The Perez model is more widely used and is still the standard model. It can be adapted to both US and EU climates.

4.6 Assessment of Progress

- In the past it has been usual to use the KT_m values as the key inputs, taking no detailed account of the impact of local atmospheric transmission variations when assembling data from a wide range of sites. It is now possible to take better account of local variations in atmospheric transmission and, also, of the impacts of site elevation on the division between clear day beam and diffuse radiation, because of the advances achieved in the SoDa project.
- The earlier stochastic work of Aguiar et al. [24] on the estimation of daily global radiation time series has proved very valuable, especially in middle latitudes. It has been available to users of Meteonorm system for some time as a fully working user-friendly programme in METEONORM Version 3.0 [3]. This model, however, has weaknesses in dealing with high-latitude sites, because the impact of latitude on KT max values is not adequately treated. The new Meteotest model for the generation of daily global radiation time series addresses these issues of clear day data generation with greater precision using the SoDa global database of Linke turbidity factor data. The impacts of site elevation also are now treated more scientifically.
- The models for generating the daily profiles of irradiance proposed by Collares-Pereira and Rabl [27] and subsequently used in ESRA 2000 have been shown to be unreliable at higher latitudes. A new improved method for estimating the daily radiation profile has been created based on the use of improved ESRA clear sky model implemented in SoDa-IS and in METEONORM Version 5.0 [5].
- An improved group of stochastic modelling procedures has been developed as part of the work on the SoDa project. The new approach is based of the use of the clear sky KT factor. This approach has required the development of new Markov transition matrices based on the clear sky KT factor. This new stochastic approach has been implemented in a user-friendly way as a key element in the SoDa computing chains (visit http://www.soda-is.com for practical implementation).
- The hour by hour stochastic model of Aguiar and Collares-Pereira [25] was used in METEONORM Version 3.0 [3]. However, this model has significant weaknesses at high latitudes, especially in winter. In version 4 of METEONORM [4] the hourly integration model of Gueymard [26] was introduced. This helped to rectify weaknesses in high latitude estimates.

- These improvements have been implemented in a systematic way with the SoDa-IS and embedded within a global computational structure for generating hourly and daily time series of radiation data.
- A new version of METEONORM 5.0 has been published [5]. This version will contain the algorithmic improvements reported here and in other papers associated with the SoDa project.
- More studies are needed on the stochastic generation of solar radiation data for tropical areas, especially for humid and cloudy climates. The physical patterns of tropical weather generation are essentially different from those encountered at high latitudes. Convectively generated cloud often plays an important role. Additionally there are often considerable asymmetries of global radiation between morning and afternoon.
- Statistically based solar radiation data generation modules are likely to become increasingly important in photovoltaic system design. The models available to users are likely to continue to improve in scientific quality.

5 Computing the Solar Geometry

5.1 Angular Movements of the Sun Across the Seasons

The calculation of the solar geometry is often needed. This knowledge is essential to assist both in the choice of the most effective tilt and orientation of the solar cells and, also, for consideration of the detailed impacts of overshadowing obstructions. This section describes the calculation of the movements of sun as seen from any point on the surface of the earth.

The daily solar path depends on the latitude of the site and the date in the year. The basic input variable in the trigonometric estimation of the solar geometry is the solar declination. The solar declination is the angle between the direction of the centre of the solar disc measured from the centre of the earth and the equatorial plane. The declination is a continuously varying function of time. The summer solstice, i.e. the longest day, occurs when the solar declination reaches its maximum value for that hemisphere. The winter solstice, i.e. the shortest day, occurs when the declination reaches its minimum value for that hemisphere. The declination on any given day in the southern hemisphere has the opposite sign to that in the northern hemisphere on that same day. While any day in the year may be studied, most design manuals select one or two days in each month for detailed reference calculations, for example in the European Solar Radiation Atlas [1] and CIBSE Guide [7]. The mid-month values adopted here are given in Table 2.

The passage of days is described mathematically by numbering the days continuously through the year to produce a Julian day number, J. 1 January, J = 1; 1 February, J = 32; 1 March, J = 57 in a non-leap year and 58 in a leap year; and so on. Each day in the year can be then be expressed in an angular form as a

Table 2 Equation of Time (EOT, expressed both in hours and in minutes) and solar declination values at monthly design dates based on monthly mean declination. Values for 21 June and 22 December are also given. The declination angles are stated for the Northern hemisphere, change the sign for the Southern hemisphere

Date	Jan. 17	Feb. 15	Mar. 16	Apr. 15	May 5	Jun. 11	Jun. 21	Jul. 17	Aug. 16	Sep. 16	Oct. 16	Nov. 15	Dec. 11	Dec. 22
EOT, hour	−0.163	−0.241	−0.157	−0.006	+0.061	+0.009	−0.029	-0.099	−0.070	+0.094	+0.250	+0.252	+0.106	−0.195
EOT, *min*	−9.8	−14.5	−9.4	−0.3	+3.7	+0.5	-1.8	5.9	−4.2	+5.6	+15.0	+15.1	+6.4	−11.7
δ degrees	−20.71	12.81	-1.80	+9.77	+18.83	+23.07	+23.43	+21.16	+13.65	+2.89	−8.72	−18.37	−22.99	23.46

day angle, J', in degrees by multiplying J by $360/365.25$. The day angle is used in the many of the trigonometric expressions that follow.

5.2 Time Systems Used in Conjunction with Solar Geometry and Solar Radiation Predictions

Different time systems are in use. Legal clock time differs from solar time. Solar time is determined from the movements of the sun. The moment when the sun has its highest elevation in the sky is defined as solar noon. Solar noon at any place defines the instant the sun crosses the north–south meridian It is then precisely due south or precisely due north. It is strongly recommended that all calculations of the solar geometry are carried out in solar time. This time system is usually called local apparent time (LAT). Solar time is converted to its angular form, the *solar hour angle*, for trigonometric calculations of the solar path. The solar hour angle is referenced to solar noon. The earth rotates through 15° in each hour. The standard convention used is that the solar hour angle is negative before solar noon. So 14:00 hours LAT represents a solar hour angle of 30°. 10:00 hours LAT represents a solar hour angle of −30°.

5.3 Conversion of Local Mean Time (LMT) to Local Apparent Time (Solar Time)

Local mean time (LMT), often called *clock time* or *civil time*, differs from LAT, often called *solar time*. The difference depends on the longitude of the site, the reference longitude of the time zone system in use at that site and the precise date in the year. Most climate observations are made in synoptic time. This is GMT in the UK. Hour by hour solar irradiation and bright sunshine observations have been important exceptions. They are usually observed in and summarised in LAT. There is also the complication of summer time.

As climatic data are typically provided in two different systems of time, it is sometimes important to be able to inter-relate the two time systems, especially in the case of simulation studies. The solar irradiance is a discontinuous function at sunrise and sunset. The other synoptic weather variables are continuous. So, it is more accurate to interpolate synoptic values into solar time than it is to interpolate irradiation values into synoptic time when compiling consistent data sets for simulation.

The conversion of time systems requires knowledge both of the longitude of the site and the reference longitude of the time system being used. The conversion also requires the application of the Equation of Time, which accounts for certain perturbations in the rotation of the earth about its polar axis. In the UK, LMT is Greenwich Mean Time (GMT) in winter and British Summer Time (BST) in summer. Many countries in the west of the European Union use West European Time (WET) and its summer time variants. Based on longitude 15°E, these nearby countries have time systems one hour ahead of GMT and BST (it is EU policy that all member states change to and from summer time on the same dates). Countries sometimes change their time reference longitudes; for example Portugal switched to WET to align with the European Union and was then forced

by formal public protest to switch back to GMT. Telephone directories and up to date airline timetables are useful sources of current time zone systems in use in different zones of different countries. UK readers should note that the latest UK BT telephone directories contain an excellent colour map showing in detail the local time systems of the world.

The Equation of Time is the difference in time between solar noon at longitude 0° and 12:00 GMT on that day. The calculation of the Equation of Time requires as input the day number in the year. This is then converted into a day angle in the year as explained in Section 5.1. The Equation of Time is calculated as:

$$\text{EOT} = -0.128 \sin(J' - 2.80°) - 0.165 \sin(2J' + 19.7°) \text{ hours} \tag{5}$$

Then

$$\text{LAT} = \text{LMT} + (\lambda - \lambda_R)/15 + \text{EOT} - c \text{ hours} \tag{6}$$

where J' is the day angle in the year in degrees, λ is the longitude of the site, in degrees, east positive, λ_R is the longitude of the time zone in which the site is situated, in degrees, east positive, and c is the correction for summer time, in hours. Values of the Equation of Time for selected dates may be found in Table 2.

Example. Estimate the time of occurrence of solar noon at Belfast on 4 August in BST. The longitude of Belfast is 6.22°W. The time system is BST. The time zone reference longitude is Greenwich 0.00°. A westward displacement of 6.22° yields a value of $(\lambda - \lambda_R)/15 = (-6 - 13/60)/15$ hours = −24.9 minutes. From Equation (5) the Equation of Time on 4 August is −5.9 minutes. LAT is 12:00. In LMT, solar noon will occur at 12:00 − (−24.9 − 5.9) minutes, i.e. 12:32 GMT or at 13:32 BST.

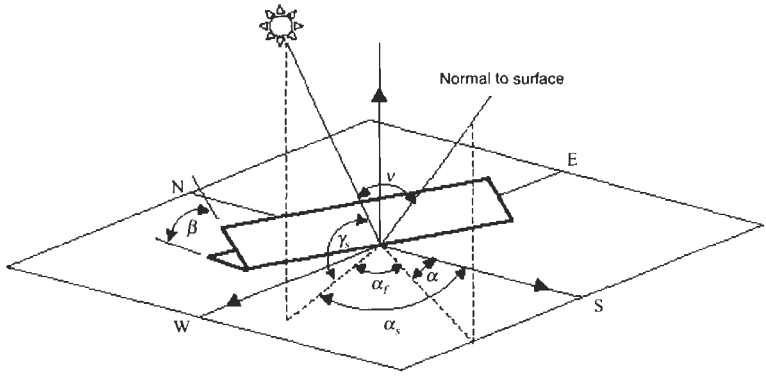

Figure 20 Definition of angles used to describe the solar position (γ_s and α_s), the orientation and tilt of the irradiated plane (α and β), the angle of incidence (ν) and the horizontal shadow angle (α_f). Source: reference [7].

5.4 Trigonometric Determination of the Solar Geometry

5.4.1 Key Angles Describing the Solar Geometry

Two angles are used to define the angular position of the sun as seen from a given point on the surface of the earth (Figure 20):

- Solar altitude (γ_S). This is the angular elevation of the centre of the solar disc above the horizontal plane.
- Solar azimuth (α_S). This is the horizontal angle between the vertical plane containing the centre of the solar disc and the vertical plane running in a true north–south direction. It is measured from due south in the northern hemisphere, clockwise from the true north. It is measured from due north in the southern hemisphere, anticlockwise from true south. Values are negative before solar noon and positive after solar noon.

Four other important solar angles are:

- Solar incidence angle on a plane of tilt α and slope $\beta(\nu(\beta,\alpha))$. This is the angle between the normal to the plane, on which the sun is shining, and the line from the surface passing through the centre of the solar disc. The cosine of $\nu(\beta,\alpha)$ is used to estimate the incident beam irradiance on a surface from the irradiance normal to the beam.
- Vertical shadow angle, sometimes called the vertical profile angle (γ_p). This is the angular direction of the centre of the solar disc, as it appears on a drawn vertical section of specified orientation (see Figure 21).
- Wall solar azimuth angle, sometimes called the horizontal shadow angle (α_F). This is the angle between the vertical plane containing the normal to the surface and the vertical plane passing through the centre of the solar disc. In other words, it is the resolved angle on the horizontal plane

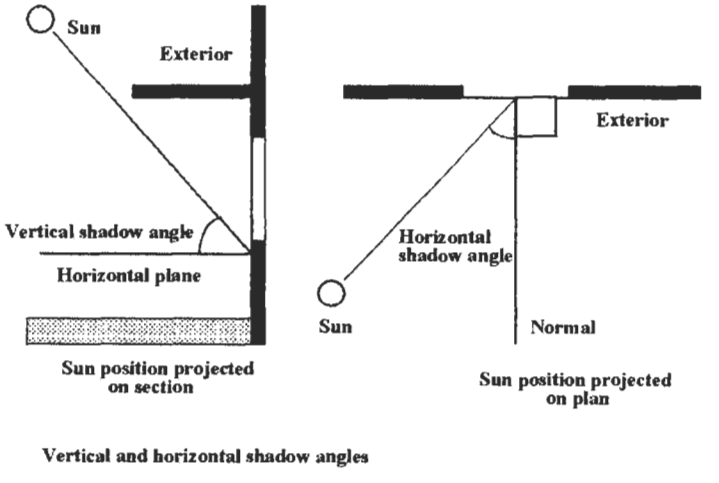

Figure 21 Definition of vertical shadow angle γ_p and the horizontal shadow angle α_F. Source: reference [7].

between the direction of the sun and the direction of the normal to the surface (see Figure 21).

- The sunset hour angle (ω_s). The azimuth angle at astronomical sunset is known the sunset hour angle. It is a quantity used in several algorithmic procedures.

5.4.2 Climatological Algorithms for Estimating Declination

The solar year is approximately 365.24 days long. The calendar is kept reasonably synchronous with the solar-driven seasons through the introduction of leap years. This leap year cycle means that the precise declination for any selected day varies according to the position of the day within the four-year leap cycle. For calculations involving climatological radiation data averaged over several years, it is appropriate to use long-term mean value formulae to estimate the declination. In contrast, if observed data for specifically identifiable days in specific years are available, it is logical to use more accurate declination formulae to calculate the declination for that specific day and longitude, for example in developing the solar geometry to use with simulation tapes based on observed time series. Usually the noon declination values are used. This gives sufficient accuracy for practical calculations. The following equation is used in the European Solar Radiation Atlases to compute representative mean values of the declination based on a 365-day year:

$$\delta = \sin^{-1} 0.3978 \sin[J' - 1.400 + 0.0355 \sin(J' - 0.0489)] \tag{7}$$

where J' is the day angle in radians (Julian day number $\times 2\pi/365.25$).

Monthly mean declination values can be derived for each month by integrating the daily declination values over each month and taking the mean. Each mean can be associated with a monthly mean representative design date. Table 2 tabulates the recommended climatological values of the mean declination for use at the monthly mean level. Table 2 includes the day in the month when the representative declination is closest to the monthly mean value.

More accurate formulae for calculating the solar declination for a specific time at a specific place in a specific year are available, for example the Bourges algorithm [33] is recommended for use by engineers to obtain an accurate assessment of the declination on specific days in specific years [1, 7] (see Section 5.6 for details). Solar cell designers will not normally require this greater accuracy, unless they are using refined beam focusing systems

5.4.3 The Calculation of Solar Altitude and Azimuth Angles, also Astronomical Day Length

These two angles, which are defined in Section 5.4.1, are dependent on the time of day, t, as measured in hours LAT on the 24 hour clock. For solar trigonometric calculations that follow, time is expressed as an hour angle, ω, where

$$\omega = 15(t - 12) \text{ degrees} \tag{8}$$

where t is the solar time in hours (i.e. LAT). The solar altitude angle γ_s is obtained from

$$\begin{aligned} \sin \gamma_s &= \sin \phi \sin \delta + \cos \phi \cos \delta \cos \omega \\ \gamma_s &= \sin^{-1}(\sin \gamma_s) \end{aligned} \tag{9}$$

where ϕ is the latitude of the location. The solar azimuth angle is obtained from

$$\begin{aligned} \cos \alpha_s &= (\sin \phi \sin \gamma_s - \sin \delta)/(\cos \phi \cos \gamma_s) \\ \sin \alpha_s &= \cos \delta \sin \omega / \cos \gamma_s \end{aligned} \tag{10}$$

If $\sin \alpha_s < 0$ then $\alpha_s = -\cos^{-1}(\cos \alpha_s)$; if $\sin \alpha_s > 0$ then $\alpha_s = \cos^{-1}(\cos \alpha_s)$.

Both formulae in Equation (10) are needed to resolve the azimuth angle into the correct quadrant in computer programs. The sunset hour angle, ω_s, is calculated by setting the solar altitude to zero in Equation (9). It follows that ω_s may be calculated as

$$\omega_s = \cos^{-1}(-\tan \phi \tan \delta) \tag{11}$$

The astronomical day length is therefore $2\omega_s/15$ hours. The day length is an important design variable. At high latitudes it changes considerably with time of year. The sun-path diagram for latitude 52°N is shown in Figure 22. The annual variation in day length (shown in Figure 23) is much less at lower latitudes than at higher latitudes. The astronomical day length is 12 hours everyday on the Equator. These facts have a strong bearing of the length of time during which night-time electric lighting is needed at different locations, impinging strongly on the demand side in the analysis of photovoltaic system performance.

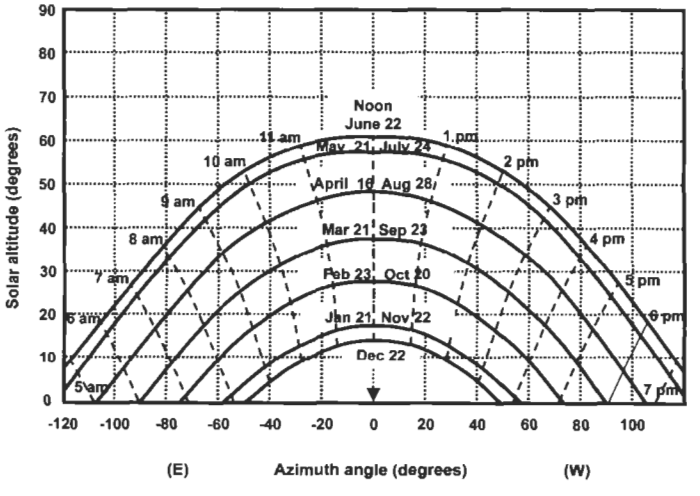

Figure 22 Sun-path diagram for latitude 52°N. The times of day, defined by near vertical lines, are expressed in LAT. Note that, in the earlier and later parts of the day, the sun lies to the north of a south-facing facade during the period between the spring and autumn equinoxes. Source: reference [7].

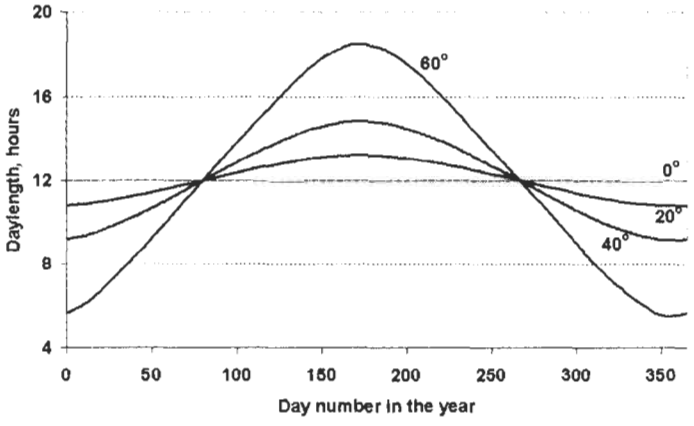

Figure 2.3 Annual variation of astronomical day length for four latitudes.

5.5 The Calculation of the Angle of Incidence and Vertical and Horizontal Shadow Angles

The determination of the exact geometry of the solar movements across the sky is important for many aspects of practical photovoltaic design. The size of the array required to meet a given load can be optimised through appropriate geometric decisions. Knowledge of the solar geometry is also important in the assessment of the periods of partial and total overshadowing. Collection performance may be considerably reduced when collectors are placed within the detailed potentially obstructive structure of their surrounding townscape and landscape. It is often useful to present the geometry on the same projections as those used in standard engineering design.

The angle of incidence of the solar beam, $\nu(\beta,\alpha)$, on a surface of tilt β and surface azimuth angle α is calculated from the solar altitude and solar azimuth angles. The wall solar azimuth angle α_F has to be calculated first using Equation (12). The sign convention adopted for wall solar azimuth angle is the same as that used for the solar azimuth angle. The angle is referenced to due South in the Northern Hemisphere and to due North in the Southern Hemisphere. Values to the East of the North South meridian are negative. Values to the West are positive.

$$\alpha_F = \alpha_s - \alpha \tag{12}$$

where α_s is the solar azimuth angle and α is the azimuth angle of the surface. If $\alpha_F > 180°$ then $\alpha_F = \alpha_F - 360°$; if $\alpha_F < 180°$ then $\alpha_F = \alpha_F + 360°$.

Once the wall solar azimuth angle has been calculated, the angle of incidence $\nu(\beta,\alpha)$ can be calculated using Equation (13). A negative value implies the sun is behind the surface and then the value is usually set to zero:

$$\nu(\beta,\alpha) = \cos^{-1}(\cos\gamma_s \cos\alpha_F \sin\beta + \sin\gamma_s \cos\beta) \tag{13}$$

A particularly useful geometric parameter for engineering design purposes is the vertical shadow angle (see Figure 18) because it aligns with standard engineering projection practice. It may be calculated as:

$$\gamma_p = \tan^{-1}(\tan\gamma_s / \cos\alpha_F) \tag{14}$$

If $\gamma_p < 0$, $\gamma_p = 180 + \gamma_p$ For a vertical surface, if $\gamma_p > 90°$ then the sun is falling on the opposite parallel vertical surface. The horizontal shadow angle is identical with α_F.

5.6 Establishing the Accurate Noon Declination and the Accurate Solar Geometry

Sometimes when working with data for specific days or making live observations it is useful to use a more accurate formula for estimating the declination. The Bourges formula [33] is simple to use. It is adequate to accept the noon declination as representative for the whole day:

$$\begin{aligned}\delta_{noon} = {} & 0.3723 + 23.2567\sin\omega_t + 0.1149\sin 2\omega_t - 0.1712\sin 3\omega_t \\ & - 0.7580\cos\omega_t + 0.3656\cos 2\omega_t - 0.2010\cos 3\omega_t \text{ degrees}\end{aligned} \tag{15}$$

where

$$\omega_t = \omega_o(J - t_1) \text{ radians}, \quad \omega_o = 2\pi/365.2422 \text{ radians},$$
$$t_1 = -0.5 - \lambda/360 - n_o \text{ days}, \quad n_o = 78.8946 + 0.2422(Y - 1957) - \text{INT}[(Y - 1957)/4]$$

in which λ is the longitude (east positive), Y is the year in full, INT is the integer part number of the expression, and J is the Julian day running from 1 to 365 in non-leap years and from 1 to 366 in leap years.

6 The Estimation of Hourly Global and Diffuse Horizontal Irradiation

6.1 The Estimation of the Extraterrestrial Irradiance on Horizontal Planes

Knowledge of the diurnal pattern of extraterrestrial irradiation is needed for establishing the profile of the daily radiation at the surface. The extraterrestrial irradiance normal to the solar beam at the mean solar distance (solar constant, I_o = 1367 W m^{-2}, has already been introduced in Section 2.1). The correction needed to allow for the variation of sun–earth distance from its mean value, ε, can be conveniently expressed as a function of the day angle J' in radians:

$$\varepsilon = 1 + 0.03344\cos(J' - 0.048869) \tag{16}$$

The extraterrestrial irradiation values incident on a horizontal surface can be obtained by numerical integration over time of the extraterrestrial irradiance, given by

$$I_o = \varepsilon \sin \gamma_s$$

But it is also possible [1], and simpler, to make a direct integration, resulting in simplified formulae where, instead of the solar altitude angle γ_s, the three basic angles (latitude ϕ, solar hour angle ω in radians and declination δ, all defined in Section 5) are used as inputs:

- general case

$$G_{o(1\,2)} = I_o\varepsilon(T/2\pi)[\sin\phi\sin\delta(\omega_2 - \omega_1) + \cos\phi\cos\delta(\sin\omega_2 - \sin\omega_1)] \quad (17)$$

- case of hourly values ($|\omega_1 - \omega_2| = \pi/12$), provided γ_s is positive or 0 throughout the hour

$$G_{oh} = I_o\varepsilon(T/2\pi)[\sin\phi\sin\delta(\pi/12) + \cos\phi\cos\delta(\sin\omega_2 - \sin\omega_1)] \quad (18)$$

- case of daily values, the sunrise hour angle values and sunrise hour angle values are used ($\omega_1 = -\omega_s$, $\omega_2 = \omega_s$, inputs in radians (see Section 5, Equation (11) for the calculation of ω_s)

$$G_{od} = I_o\varepsilon(T/\pi)\cos\phi\cos\delta(\sin\omega_s - \omega_s\cos\omega_s) \quad (19)$$

The parameter T is the duration of a rotation of the earth about its axis; an average value of 86400 s (i.e. 24 hours) can be used in practice.

6.2 The Daily Clearness Index (KT_d value)

The daily clearness index is the ratio of the global irradiance at the surface, falling on a horizontal plane, to the corresponding extraterrestrial global irradiance on the horizontal plane. The clearness index value may be extracted at the daily level KT_d or the hourly level KT_h. The daily extraterrestrial irradiation G_{od}, Equation (19), is required to estimate the widely used daily clearness index KT_d. Typical values of KT_d are around 0.68 to 0.72 under cloudless conditions, with lower values at high latitudes in winter. The monthly mean daily clearness index is indicated by $(KT_d)_m$. It is a mapped variable in ESRA [1]. Section 2.8.1 outlines how to calculate the monthly mean daily radiation from sunshine data using the monthly mean daily relative sunshine duration.

6.3 The Estimation of Mean Daily Profiles of Global Solar Irradiation from Monthly Means

Hour by hour irradiation data are essential if the irradiation on inclined planes is to be estimated. Two well-described methodologies are available for estimating

hourly global irradiation data from daily data. One method is based on the use of the diurnal profile of extraterrestrial irradiance. The other is based on the diurnal profile of clear day global irradiance at the surface.

6.3.1 Method 1: Estimating the Monthly Mean Daily Irradiance Profile of $G_h(t)$ from the Monthly Mean Extraterrestrial Irradiance Profile

The mean daily profile of the hourly global horizontal irradiation $G_{hm}(t)$ is estimated from the respective monthly mean daily sum $(G_d)_m$ using the model of Collares-Pereira and Rabl [27]. This model is set down as Eq. (20) below:

$$G_{hm}(t) = (G_d)_m r_{om}[a + b\cos(\omega(t))] \tag{20}$$

with seasonally varying coefficients a and b:

$$a = 0.4090 + 0.5016\sin[(\omega_s)_m - \pi/3]$$
$$b = 0.6609 - 0.4767\sin[(\omega_s)_m - \pi/3]$$

where r_{om} is the monthly mean ratio of hourly to daily extraterrestrial radiation, which is a function of the hour angle $\omega(t)$ (see Section 5.4.3, Equation (8)) and the monthly average sunset hour angle $(\omega_s)_m$ for the month in question (see Section 5.4.3, Equation (11)):

$$r_{om}(t) = \frac{\pi}{24}\left[\frac{\cos\omega(t) - \cos(\omega_s)_m}{\sin(\omega_s)_m - (\omega_s)_m\cos(\omega_s)_m}\right] \tag{21}$$

This model does not perform well at high latitudes [13]. See also Section 4 for further discussion of this point.

6.3.2 Method 2: Estimating the Monthly Mean Daily Profile of $G_h(t)$ from the Clear Sky Irradiance Profile

This method provides more accurate estimates of the value of the hourly surface global irradiation, G_h. However, it needs accurate information is available about the clarity of the atmosphere at the site under consideration in order to estimate $G_{c.cs}$ [8, 13]. More discussion is included in Section 4 and Equation (4).

The clear sky model requires the user to input the site elevation and the Linke turbidity factor. (The Linke turbidity factor and the terrain elevation are mapped variables on a global scale within the SoDa-IS 2003 project making it easy to implement Equation (4) of Section 4 at any selected site.) A comparison by Meteotest found the rmse of the hourly values of KT_h (= G_h/G_{oh}) generated with this second model tested against 10 worldwide sites was 0.072 compared with 0.095 using Method 1, i.e. the Collares-Pereira and Rabl model. Method 2 has the added value that it avoids all risk of generating negative values close to sunrise and sunset, a fault encountered sometimes in the first method.

6.4 The Estimation of Hourly Diffuse Radiation on Horizontal Surfaces

6.4.1 Introduction

The estimation of the irradiation on inclined surfaces can only be achieved through knowledge of hourly values of beam and diffuse radiation. Unfortunately, few observed data sets contain observations of diffuse irradiation. It is frequently necessary to estimate the monthly mean and daily diffuse irradiation algorithmically from the observed monthly mean and daily global radiation. Once this split has been achieved, the monthly mean data and daily data can then be converted to representative daily profiles. The hourly diffuse profile approximately follows the extraterrestrial hourly profile. By using these facts, representative hourly values of diffuse horizontal irradiance can be developed, which are then used to estimate inclined surface values.

6.4.2 Estimating the Monthly Average Daily Diffuse Horizontal Irradiation from the Monthly Average $(KT_d)_m$ Value

ESRA [1] uses the following third order polynomial models to estimate the monthly mean daily diffuse horizontal irradiation $(D_d)_m$ as a fraction of the monthly mean global irradiation $(G_d)_m$ from the monthly mean clearness index $(KT_d)_m$:

$$\frac{(D_d)_m}{(G_d)_m} = c_0 + c_1(KT_d)_m + c_2(KT_d)_m^2 + c_3(KT_d)_m^3 \tag{22}$$

The coefficients c_o, c_1 and c_2 depend on latitude and season. The coefficients of the polynomial are listed in Table 3.

Table 3 Coefficients of the third-order polynomial for estimation of monthly average diffuse horizontal irradiation from (KTd)m values for use in Equation (22). Source: reference [1]. Winter = November to February; spring = March, April; summer = May to August; autumn = September, October

Latitude band	Season	c_0	c_1	c_2	c_3	$(KT_d)_m$ validation range
61°N > ϕ 56°N	Winter	1.061	−0.397	−2.975	2.583	[0.11, 0.50]
	Spring	0.974	−0.553	−1.304	0.877	[0.24, 0.50]
	Summer	1.131	−0.895	−1.616	1.555	[0.26, 0.60]
	Autumn	0.999	−0.788	−0.940	0.788	[0.21, 0.51]
56°N > ϕ > 52°N	Winter	1.002	−0.546	−1.867	1.490	[0.14, 0.49]
	Spring	1.011	−0.607	−1.441	1.075	[0.22, 0.59]
	Summer	1.056	−0.626	−1.676	1.317	[0.29, 0.64]
	Autumn	0.969	−0.624	−1.146	0.811	[0.23, 0.53]
ϕ < 52°N	Winter	1.032	−0.694	−1.771	1.562	[0.15, 0.51]
	Spring	1.049	−0.822	−1.250	1.124	[0.23, 0.61]
	Summer	0.998	−0.583	−1.392	0.995	[0.27, 0.63]
	Autumn	1.019	−0.874	−0.964	0.909	[0.22, 0.55]

It was verified during mapping of the diffuse irradiation over the ESRA geographical range that the discontinuities of the estimated value of $(D_d)_m$ at the two interfaces of the latitude bands selected 56°N and 52°N are very small [1].

6.4.3 Estimating the Daily Diffuse Horizontal Irradiation from the Daily Global Irradiation

A different formula is recommended in ESRA [1] for estimating daily D_d values from daily G_d values. The *overall* test findings were that the models of [34] and [35] were the most appropriate for this purpose. This Erbs *et al.* model allows for seasonal variations (to some extent). So it was selected as the most appropriate current algorithm in ESRA [1]. For sunset hour angle $\omega_s < 81.4°$:

$$\frac{D_d}{G_d} = \begin{cases} 1.0 - 0.2727KT_d + 2.4495KT_d^2 - 11.9514KT_d^3 + 9.3879KT_d^4, & \text{for } KT_d < 0.715 \\ 0.143, & \text{for } KT_d \geqslant 0.715 \end{cases} \tag{23}$$

For sunset hour angle $\omega_s \geqslant 81.4°$:

$$\frac{D_d}{G_d} = \begin{cases} 1.0 - 0.2832KT_d - 2.5557KT_d^2 + 0.8448KT_d^3, & \text{for } KT_d < 0.722 \\ 0.175, & \text{for } KT_d \geqslant 0.722 \end{cases} \tag{24}$$

6.4.4 Estimating the Monthly Mean Daily Profile of $D_h(t)$

The final step is to obtain the respective average daily profile of the hourly diffuse horizontal irradiation $D_{hm}(t)$. This is estimated from the respective daily sum (D_d) found using Section 6.1, Equation (18). This method adopts the simple model of Liu and Jordan [35], developed based on North American data:

$$D_{hm}(t) = (D_d)_m r_{om}(t) \tag{25}$$

and $r_{om}(t)$ is found from Equation (18). Note that because the global and diffuse radiation profiles are generated independently, it is necessary on rare occasions to reset some diffuse radiation values close to sunrise/sunset hours, to make sure that $D_{hm}(t) \leqslant G_{hm}(t)$. When this happens, the $D_{hm}(t)$ profile must be suitably re-normalised to yield the input daily sum $(D_d)_m$.

7 The Estimation of the All Sky Irradiation on Inclined Planes from Hourly Time Series of Horizontal Irradiation

7.1 Estimating the Components of Slope Irradiation from First Principles

This section provides guidance on the conversion of observed hourly time series of global and diffuse irradiation on horizontal surfaces into the corresponding hourly components of irradiation on inclined planes. The method assumes the availability of an hourly time series of global and diffuse horizontal irradiation

derived from a reliable meteorological source. If observed data on diffuse irradiation are not available, they have to filled first using the algorithmic approaches given in Section 6. If an observed time series is to be used for simulation, any gaps in the horizontal data should first be filled, using appropriate techniques [7]. The data may be generated stochastically (see Section 4). Then there should be no gaps.

The tilt of the irradiated surface from the horizontal plane is defined as β. This needs to be stated in radians for some of the algorithms used. The azimuth angle of the surface is α (see Figure 20 in Section 5). The azimuth angle is measured from due south in the northern hemisphere and from due north in the southern hemisphere. Directions to the west of north–south are positive, east is negative.

The inclined surface total short-wave irradiation for any hour is obtained by summation of the three slope irradiation components; the hourly slope beam component $B_h(\beta,\alpha)$, the hourly slope sky diffuse component $D_h(\beta,\alpha)$ and the hourly slope ground reflected component $R_{gh}(\beta,\alpha)$. Each component has to be separately estimated:

$$G_h(\beta, \alpha) = B_h(\beta, \alpha) + D_h(\beta, \alpha) + R_{gh}(\beta, \alpha) \tag{26}$$

The associated hour by hour solar geometry has to be developed first, using the algorithms in Section 5 provide a matching time series of solar geometric data, in order to start the process. When observed data for specific hours are involved, an accurate formula for the declination should be used. The Bourges formula given in Section 5 is accurate and simple in engineering use.

7.2 Direct Beam Irradiation on Inclined Planes

Knowing the mid-hour observational times of the input data, the detailed solar geometry can be established using Section 5, making appropriate adjustments in the sunrise and sunset hour. The astronomical sunrise and sunset times must be calculated each day first to do this. The angle of incidence of the beam on the plane is also a required geometrical input (see Equation (13)).

The estimation of the slope beam irradiance from the beam normal irradiance is straightforward, once the cosine of the angle of incidence of the solar beam for the inclined plane under consideration has been established:

$$\begin{aligned} B(\beta, \alpha) &= B_n \cos \nu(\beta, \alpha) \quad \text{for} \cos \nu(\beta, \alpha) > 0 \\ B(\beta, \alpha) &= 0 \qquad\qquad\qquad\quad \text{otherwise} \end{aligned} \tag{27}$$

However, this process is dealing with observed irradiation data summarised on an hour by hour basis. The sun is not necessarily on the selected surface for the whole of the summation period. Outside the sunrise and sunset hour, the hourly mean beam normal irradiation B_{nh} may be estimated as

$$B_{nh} = (G_h - D_h)/\sin \gamma_s \tag{28}$$

where γ_s is the mid-hour solar altitude. In the sunrise and sunset hour, account must be taken of the proportion of the hour when the sun is above the horizon. Then

$$B_{nh} = (G_h - D_h)\Delta T / \sin \gamma_s \tag{29}$$

where γ_s is now the solar altitude at a time halfway between sunrise and the end of the sunrise hour or halfway between the beginning of the sunset hour and sunset, and ΔT is the length of time during the sunrise or sunset hour during which the sun is above the horizon.

The accurate estimation of beam irradiation on inclined planes using standard observational time periods of 1 hour also raises complications, because, undetected in the hour by hour calculation process, the sun may move off the surface during the hour in question. A simple irradiation approximation can be achieved for hours when the sun is on the surface for the whole hour by using the mid-hour angle of incidence, and setting the hourly irradiation equal to the mid-hour irradiance. Thus

$$B_h(\beta, \alpha) = B_{nh} \cos \nu(\beta, \alpha) \tag{30}$$

The ESRA Atlas methodology [1] reduces the risk of errors by calculating at 6 minute intervals throughout each hour.

7.3 The Estimation of the Hourly Diffuse Irradiation on Inclined Surfaces from the Hourly Horizontal Diffuse Irradiation

This section is based on research by Muneer [36]. It includes some recent small improvements both by Muneer himself and by the CEC ESRA team [1]. The method requires, as inputs, hourly values of global and diffuse horizontal irradiation, G_h and D_h. The method has been tested and selected as a recommended algorithm in the CEC European Solar Radiation Atlas project. It gave better results in tests using a set of European-wide observed inclined surface data than the currently widely used Perez model [31]. European tests showed, for sun-facing surfaces, that the model yields similar values to the Perez model at the day by day hourly level. It yielded better results at the monthly mean level. It gave more accurate values for surfaces facing away from the sun than the algorithm developed by Perez et al. [31], both for monthly mean hourly values and also for daily hour by hour values.

The algorithms distinguish between potentially sunlit surfaces and surfaces which are not potentially sunlit. For sun-facing surfaces, there are different algorithms for low sun (below 5.7°) and high sun (above 5.7°). For potentially insolated surfaces, a distinction is also made between overcast hours and non-overcast hours. An overcast sky hour is defined as an hour having $G_h - D_h < 5$ Wh m^{-2}. A modulating function K_b is first calculated as

$$K_b = B_h/(\varepsilon I_o \sin \gamma_s) = (G_h - D_h)/(\varepsilon \times 1367 \sin \gamma_s) \tag{31}$$

where I_o is the solar constant (1367 W m^{-2}), ε is the correction to mean solar distance on day J, and γ_s is the solar altitude angle. These angles have been defined previously. K_b expresses the horizontal beam irradiance as a ratio to the extraterrestrial horizontal irradiance, corrected to mean solar distance. Then a diffuse function $f(\beta)$ for slope β is calculated. β *must be expressed in radians*. This function is defined as

$$f(\beta) = \cos^2(\beta/2) + [2b/\pi(3 + 2b)][\sin\beta - \beta\cos\beta - \pi\sin^2(\beta/2)] \tag{32}$$

where b takes the following values: shaded surface, 5.73; sunlit surface under overcast sky, 1.68; sunlit surface under non-overcast sky, −0.62.

As an improvement, for certain specific areas where appropriate observed data exist, Muneer has suggested an alternative way of evaluating $2b/\pi(3 + 2b)$ to be applied to the sunlit surface cases only.

Northern Europe considered represented by Bracknell:

$$\text{Replace } 2b/\pi(3 + 2b) \text{ with } 0.00333 - 0.4150K_b - 0.6987K_b^2 \tag{33}$$

Southern Europe considered represented by Geneva:

$$\text{Replace } 2b/\pi(3 + 2b) \text{ with } 0.00263 - 0.7120K_b - 0.6883K_b^2 \tag{34}$$

Equation (32) for a vertical surface reduces to

$$f(\beta) = 0.5 + [2b/\pi(3 + 2b)](1 - 0.5\pi) \tag{35}$$

For a sunlit vertical surface, under the non-overcast sky conditions, using $b = -0.62$:

$$f(\beta) = 0.5 + [2(-0.62)/\pi(3 - 2 \times 0.62)](1 - 0.5\pi) = 0.628$$

If the vertical surface is not potentially sunlit, i.e. cos ν(β,α) is zero or less, then Equation (35) must be evaluated using $b = 5.73$, and one obtains for a vertical surface

$$f(\beta) = 0.5 + [2 \times 5.73/\pi(3 + 2 \times 5.73)](1 - 0.5\pi) - 0.357$$

For *a potentially sunlit surface under an overcast sky*, using $b = 1.68$, one obtains for a vertical surface

$$f(\beta) = 0.5 + [2 \times 1.68/\pi(3 + 2 \times 1.68)](1 - 0.5\pi) = 0.404$$

For *sunlit surfaces*, with $\gamma_s > 5.7$ degrees, $D_h(\beta,\alpha)$ is found using the following formula:

$$\begin{aligned} D_h(\beta,\alpha)/D_h &= f(\beta)(1 - K_b) + K_b\cos\nu(\beta,\alpha)/\sin\gamma_s \\ &= 0.628(1 - K_b) + K_b\cos\nu(\beta,\alpha)/\sin\gamma_s \text{ for a vertical surface} \end{aligned} \tag{36}$$

where D_h is the hourly diffuse irradiation on the horizontal plane, and cos ν(β,α) is the angle of incidence on the surface.

For *a potentially sunlit surface with an overcast sky* $K_b = 0$ and for all solar altitudes:

$$D_h(\beta, \alpha)/D_h = f(\beta) = 0.404 \text{ for a vertical surface} \tag{37}$$

For *surfaces in shade*, i.e. cos ν(β,α) =0, and for all solar altitudes:

$$D_h(\beta, \alpha)/D_h = f(\beta) = 0.357 \text{ for a vertical surface} \tag{38}$$

As there is not a perfect conjunction in the functions at the instant the sun changes from being just on the surface to being just off the surface, a small adjustment was made in the program for the CEC ESRA project to ensure continuity in estimation. Linear interpolation was used to achieve a smooth transition in this zone, using a zone of 20° width either side of the on–off sun switch position.

7.4 The Estimation Process for Sunlit Sun-Facing Surfaces for Solar Altitudes below 5.7°

The above Muneer algorithm is not suitable for sunlit surfaces below a solar elevation of 5.7°. In this region Muneer has proposed applying an adjustment based on the Temps and Coulson algorithms. The original Temps and Coulson algorithm [37] for cloudless skies is

$$D_c(\beta, \alpha)/D_c = \cos^2(\beta/2)[1 + sin^3(\beta/2)][1 + \cos^2 \nu(\beta, \alpha) \sin^3(90 - \gamma_s)] \tag{39}$$

This formula was modified by Klucher [38] to become an all sky model by introducing a modulating function $F2$. $F2$ was set by Klucher as $1 - (D_h/G_h)^2$. Muneer substituted K_b in Equation (39) giving:

Table 4 Typical albedo values for various ground types

Surface type	Albedo
Grass (July, August, UK)	0.25
Lawns	0.18–0.23
Dry grass	0.28–0.32
Uncultivated fields	0.26
Bare soil	0.17
Macadam	0.18
Asphalt	0.15
Concrete new before weathering	0.55
Concrete weathered industrial city	0.20
Fresh snow	0.80–0.90
Old snow	0.45–0.70
Water surfaces for different values of solar altitude	
$\gamma_s > 45°$	0.05
$\gamma_s = 30°$	0.08
$\gamma_s = 20°$	0.12
$\gamma_s = 10°$	0.22

$$D_c(\beta, \alpha)/D_c = \cos^2(\beta/2)[1 + K_b \sin^3(\beta/2)][1 + K_b \cos^2 \nu(\beta, \alpha) \sin^3(90 - \gamma_s)] \quad (40)$$

7.5 Ground-Reflected Irradiation

Three assumptions are implicit in the method adopted for making estimates of the irradiation reflected from the ground. The first is that the ground surface reflects isotropically. The second assumption is that the ground surface is fully irradiated. The third is that there is no reflected energy other than that directly reflected from the level ground. A ground albedo of 0.2 has been adopted in the ESRA [1] and CIBSE Guide J [7] tables. This value can be changed if better knowledge exists about the ground cover in different months. Table 4 provides typical values of the ground albedo for different types of surface. The most important albedo change is that due to snow cover. Table 4 also demonstrates the directional reflection characteristics of water surfaces at different solar altitudes. Late afternoon water reflected gains can be important in some locations.

Additional information about ground-reflected irradiation in the UK may be found in [39]. The reflected irradiance $R_{gh}(\beta,\alpha)$, which is assumed independent of orientation α, is simply estimated as

$$R_{gh}(\beta, \alpha) = r_g \rho_g G_h \quad (41)$$

where ρ_g is the ground albedo, r_g is ground slope factor, with $r_g = (1 - \cos \beta)/2$, and G_h is the hourly irradiation falling on the ground.

8. Conclusion

All the detailed climatological algorithmic procedures discussed here are accessible as pre-programmed computational chains in user-friendly forms in ESRA [1] and SoDa-IS [8]. ESRA is a European-based resource. SoDa-IS is an international resource. Additionally considering specifically PV built in applications modules, the SoDa-IS contains (a) a Daylighting Service for SoDa, (b) an Advanced User Application: Grid-connected PV System, (c) an Advanced User Application: Solar Home System (PV non-grid connected) and (d) a daily Temperature Information Database covering the domain latitude 34°N to 68°N longitude 20°W to 50°W on a grid of 5 minutes of arc between 1996 and 2001. The ESRA computational toolbox contains a facility for the assessment of PV grid-connected systems and a PV stand-alone system with batteries. The SoDa-IS system also contains a facility for estimating ultraviolet irradiation on inclined planes coupled to the internationally based solar radiation data generation facility. This facility could be useful in the assessment of the long-term weather exposure risks of PV systems. The latest version of the METEONORM CD-ROM [5] is closely related to SoDa-IS and incorporates many new facilities which have evolved from the participation of METEOTEST in the European Commission supported program SoDa-IS, including the estimation of UV irradiation. It also incorporates the latest advanced stochastic models to aid the effective simulation

of climate variability so enabling effective performance risk assessment of photovoltaic systems at any place across the world.

Acknowledgements

The material in this chapter has drawn very heavily on the research sponsored by the Commission of the European Communities. It reflects some 25 years of EC research support to the systematic study solar radiation climatology, in which the author has been deeply involved. Two especially important recent EC contracts in which the author has participated have been:

- 4th European Solar Radiation Atlas (EC Contract JOULE II Project Number JOU2-CT-94-00305).
- Integration and Exploitation of Networked Solar Radiation Databases for Environmental Monitoring (SoDa); funded in part under the Information Societies Technology Programme (EC Contract IST-1999-122245 SoDa). The SoDa project was led by Professor Lucien Wald, Ecole des Mines de Paris, BP 207, 06904 Sophia Antipolis cedex, France.

On the personal level, I would especially like to express my thanks to my key Swiss collaborator in the SoDa project *Jan Remund* of Meteotest, Bern, Switzerland, and to my two academic colleagues, who have worked with me on the EU SoDa programme in the Department of Physics at UMIST Manchester, *Dr Ann Webb* and *Richard Kift*. I thank them for their considerable help and advice over the last three years.

References

[1] ESRA, 2000. European Solar Radiation Atlas, 4th Edition. Scharmer, K. and Grief, J., co-ordinators. Les Presses de l'Ecole des Mines de Paris, Vol. 2. Database and exploitation software contains photovoltaics applications module.

[2] Remund, J. and Kunz, S., 1995. METEONORM – a comprehensive meteorological database and planning tool for system design. *Proc. 13th European Photovoltaic Solar Energy Conf.*, Nice, pp. 733–735.

[3] Remund, J. and Kunz, S., 1997. METEONORM Version 3.0. Nova Energie GmbH, Schachenallee 29, CH-5000 Aarrau, Switzerland.

[4] Remund, J. and Kunz, S., 1999. METEONORM Version 4.0. Nova Energie GmbH, Schachenallee 29, CH-5000 Aarrau, Switzerland.

[5] Remund, J. and Kunz, S., 2003. METEONORM Version 5.0. METEOTEST, Fabrikstrasse 14, 3012 Bern, Switzerland.

[6] RETSCREEN®INTERNATIONAL, 2003. Prepared by CANMET Energy Technology Centre, Varennes Canada on behalf of National Resources

Canada. Visit http:/www.retscreen.net. These programs include a PV module.

[7] CIBSE Guide J Weather, Solar and Illuminance Data, 2002. Chartered Institution of Building Services Engineers, 222 Balham High Road, London SW12 9BS, UK.

[8] SoDa-IS, 2003. Integration and exploitation of networked solar radiation databases for environmental monitoring. Either contact the welcome website at http://www.helioclim.net/ or consult http://www.soda-is.com. Contains photovoltaic applications modules.

[9] SATELLIGHT, 1995. Fontoynont, M., Dumortier, D., Heinemann, D., Hammer, A., Olseth, J., Skartveit, A., Ineichen, P., Reise, C., Page, J., Roche, L., Beyer, H.G. and Wald, L. Processing of Meteosat data for the production of high-quality daylight and solar radiation data available on a web server. Application to Western and Central Europe. JOR3-CT95-0041.

[10] Fontoynont, M., Dumortier, D., Heinemann, D., Hammer, A., Olseth, J., Skartveit, A., Ineichen, P., Reise, C., Page, J., Roche, L., Beyer, H.G. and Wald, L.,1998. Satellight: a WWW server which provides-high quality daylight and solar radiation data for Western and Central Europe. *Proc. 9th Conf. On Satellite Meteorology and Oceanography*, Darmstadt, Germany, EUM P22, Vol. 1, pp. 434–435.

[11] Rigollier, C., Bauer, O. and Wald, L., 2000. On the clear sky model of the ESRA with respect to the heliostat method, *Solar Energy*, Vol. 68, pp. 33–48.

[12] Remund, J. Levevre, M., Ranchin, T. and Wald, L. 2002. *Constructing maps of the Linke turbidity factor*, SoDa project deliverable D5-2-1, Internal Document, Meteotest, Bern. SoDa project working paper for European Commission. Refer also Remund, J., Wald L. Lefevre M., Ranchin T. and Page J. 2003 Worldwide Linke Turbidity Information. Proc. of World Solar Congress, Götebourg, Sweden, June 14-19, 2003, In the press.

[13] Remund, J and Page, J.K., 2002. *Integration and exploitation of networked Solar radiation Databases for environmental monitoring* (SoDa Project). Advanced parameters: WP 5.2b: Deliverable D5-2-2 and D5-2-3. Chain of algorithms: short- and long-wave radiation with associated temperature prediction resources. SoDa project working paper for European Commission.

[14] Aguiar and Page, 2000. Chapter 3 in reference [1].

[15] Dumortier, D., 2002. *Prediction of air temperatures from solar radiation.* SoDa project Working Partnership WP-5-2.c, deliverable 5-2-4. CNRS-ENTPE, Department Genie Civil et Batiment, Rue Maurice Audin, 69518 Vaulx-en-Velin, near Lyons, France. E-mail: dominique.dumortier@entpe.fr.

[16] Kasten, F. and Czeplak, G.,1980. Solar radiation and terrestrial radiation dependent on the amount and type of cloud. *Solar Energy*, Vol. 24, pp. 117–189.

[17] Gu, L. Fuentes, J.D., Garstang, M., Tota da Silva, J. Heitz, R., Sigler, J. and Shugart, H.H., 2001. Cloud modulation of surface solar irradiance

at a pasture site in southern Brazil, *Agricultural and Forest Meteorology*, Vol. 106, pp. 117–129.

[18] Akuffo, F.O. and Brew-Hammond, A., 1993. The frequency distribution of daily global irradiation at Kumasi, *Solar Energy*, Vol. 50, pp.145-154.

[19] Udo S.O., 2000. Sky conditions at Ilorin as characterized by clearness index and relative sunshine, *Solar Energy*, Vol. 69, pp. 45–53.

[20] Page, J.K., 1964. The estimation of monthly mean values of daily total short wave radiation on vertical and inclined surfaces from sunshine records for latitudes 40°N to 40°S. *Proc. UN Conf. on New Sources of Energy*, Rome, Vol. 4, pp. 378–390.

[21] Ianetz, A., Lyubansky, I., Setter, I., Evseev, E.G. and Kudish, A.I., 2000. A method for characterization and inter-comparison of sites with regard to solar energy utilization by statistical analysis of their solar radiation data as performed for three sites in the Israel Negev region. *Solar Energy*, Vol. 69, pp. 283–294.

[22] Dirmhirn, I. Quoted by P. Valko, Swiss Meteorological Institute, Zurich, 1983, in IEA programme to develop and test solar heating and cooling systems, Task V Use of existing meteorological information for solar energy applications, Final draft. A literature search has showed that US DoE funded I. Dirmhirn to produce the report Solar energy potential, ultraviolet radiation, temperature and wind conditions in mountainous areas, DoE Grant Number EG-77-S-07-1656, completed 1982.

[23] Palz, W. and Grief, J., Eds., 1996. *European Solar Radiation Atlas*, 3rd Edition. *Solar Radiation on Horizontal and Inclined Surfaces*. Commission of the European Communities, Springer-Verlag, Berlin, Heidelberg, New York.

[24] Aguiar, R., Collares-Pereira, M. and Conde, J.P., 1988. A simple procedure for generating sequences of daily radiation values using a library of Markov transition matrices. *Solar Energy*, Vol. 40(3), pp. 269–279.

[25] Aguiar, R. and Collares-Pereira, M., 1992. TAG: A time-dependent auto-regressive, Gaussian model. *Solar Energy*, Vol. 49(3), pp. 167–174.

[26] Gueymard, C. 2000. Prediction and performance assessment of mean hourly global radiation. *Solar Energy*, Vol. 68(3), pp. 285–303.

[27] Collares-Pereira, M. and Rabl, A. 1979. The average distribution of solar radiation – correlations between diffuse and hemispherical and between daily and hourly insolation values. *Solar Energy*, Vol. 22, pp. 155–164.

[28] Page, J., 2000. ESRA Task II Technical Report Number 14. Internal project report.

[29] Remund, J., Wald L. and Page J. 2003 Chain of algorithms to calculate advanced radiation parameters. Proc. of World Solar Congress, Götebourg, Sweden, June 14-19, 2003, In the press. This paper contains the new Markov transition matrices based on the used of the clear sky clearness index.

[30] Box E. P. and Jenkins, G.M., 1970. Time series analysis. Forecasting and control. Holden Day, San Francisco.

[31] Perez, R., Seals, R., Ineichen, P., Stewart, R. and Menicucci, D., 1987. A new simplified version of the Perez Diffuse Irradiance Model for tilted surfaces. *Solar Energy*, Vol. 39(3), pp. 221–231.

[32] Skartveit, A., Olsen, J.A. and Tuft, M.E., 1998. An hourly diffuse fraction model with correction for variability and surface albedo. *Solar Energy*, Vol. 63, pp. 173–183.

[33] Bourges B., 1985. Improvement in solar declination calculations. *Solar Energy*, Vol. 35, pp. 367–369.

[34] Erbs, K. and Duffie, 1982. Estimation of the diffuse radiation fraction for hourly, daily and monthly-average global radiation. *Solar Energy*, Vol. 28, pp. 293–302.

[35] Liu, B. and Jordan, R., 1960. The interrelationship and characteristic distributions of direct, diffuse and total solar radiation. *Solar Energy*, Vol. 4, pp. 1–19.

[36] Muncer, T., 1990. Solar radiation model for Europe. *Building Serv. Eng. Res. Technol.*, Vol. 11(4), pp. 153–163.

[37] Temps, R.C. and Coulsen, K.L., 1977. Solar radiation incident on slopes of different orientations. *Solar Energy*, Vol. 19, pp. 179–184.

[38] Klucher, T.M., 1979. Evaluation of models to predict insolation on inclined surfaces. *Solar Energy*, Vol. 23, pp. 111–114.

[39] Saluja, G.S. and Muneer, T., 1988. Estimation of ground-reflected radiation for the United Kingdom. *Building Serv. Eng. Res. Technol.*, Vol. 9(4), pp. 189–196.

US Data may be found in the following references:

[40] NSRDB, 1992. User's Manual, National Solar Radiation Data Base (1961–1990), Vol. 1. National Renewable Energy Laboratory, Golden, CO, USA.

[41] NSRDB, 1995. Final Technical Report, National Solar Radiation Data Base (1961–1990), Vol. 2. National Renewable Energy Laboratory, Golden, CO, USA. NERL/TP-463-5784.

[42] Garrison, J.D., 2003. A programme for calculation of solar energy collection by fixed and tracking collectors. *Solar Energy*, Vol. 73, pp. 241–255.

Appendix

Solar Energy Data for Selected Sites

Monthly mean daily global radiation on horizontal surfaces (Wh m ^{2})

	Jan.	Feb.	Mar.	Apr.	May	Jun.	July	Aug.	Sep.	Oct.	Nov.	Dec.	Year
Stockholm, 59.35°N	292	892	1947	3583	5289	5175	5072	3847	2431	1156	453	144	2523
London, 51.52°N	683	1222	2119	3561	4294	4481	4572	4022	2719	1617	853	486	2552
Freiburg, 48.00°N	869	1539	2603	3731	4736	5406	5528	4789	3411	2031	1122	708	3039
Geneva, 46.25°N	975	1553	2978	4153	4933	5819	6083	5178	3847	2228	1133	803	3307
Nice, 43.65°N	1758	2325	3658	4708	5906	6556	6681	5903	4514	2917	1878	1506	4026
Oviedo, 43.35°N	1589	2039	3272	3864	4497	4753	4678	4217	3681	2492	1717	1311	3176
Porto, 41.13°N	1928	2511	4069	5036	6189	6931	6683	6200	4781	3258	2011	1533	4261
Heraklion, 35.33°N	2189	2819	3797	5392	6319	7136	6853	6228	5153	3369	2203	1781	4437
Sde Boker, 30.90°N	3175	4361	5169	6767	7231	8333	8106	7381	6211	4908	3689	3056	5699
Ilorin, 8.58°N	4031	4631	4867	4803	4806	4156	3511	3253	3733	4317	4478	3725	4192

Monthly mean daily diffuse radiation on horizontal surfaces (Wh m^{-2})

	Jan.	Feb.	Mar.	Apr.	May	Jun.	July	Aug.	Sep.	Oct.	Nov.	Dec.	Year
Stockholm, 59.35°N	226	573	1147	1849	2348	2774	2613	2116	1358	720	317	126	1347
London, 51.52°N	483	823	1381	2023	2563	2773	2693	2286	1574	1001	577	369	1545
Freiburg, 48.00°N	610	976	1543	2109	2625	2826	2699	2324	1691	1156	721	511	1649
Geneva, 46.25°N	679	1027	1612	2142	2641	2791	2614	2299	1709	1225	769	577	1673
Nice, 43.65°N	800	1147	1647	2147	2542	2643	2462	2167	1680	1291	887	716	1677
Oviedo, 43.35°N	835	1172	1702	2208	2652	2820	2741	2436	1822	1332	917	742	1781
Porto, 41.13°N	903	1239	1674	2153	2498	2526	2475	2126	1715	1354	993	828	1707
Heraklion, 35.33°N	1146	1454	1939	2219	2506	2431	2423	2237	1835	1590	1225	1052	1838
Sde Boker, 30.90°N	1236	1836	1875	2400	2053	1747	1750	1472	1486	1414	1225	1058	1629
Ilorin, 8.58°N	1799	1805	1842	2035	2091	1949	2004	1893	1919	1829	1796	1578	1878

Part II

Solar Cells

Part IIa

Introduction

Principles of Solar Cell Operation

Tom Markvart, School of Engineering Sciences,
University of Southampton, UK
Luis Castañer, Universidad Politecnica de Catalunya,
Barcelona, Spain

1 Introduction

Photovoltaic energy conversion in solar cells consists of two essential steps. First, absorption of light generates an electron–hole pair. The electron and hole are then separated by the structure of the device – electrons to the negative terminal and holes to the positive terminal – thus generating electrical power.

This process is illustrated in Figure 1 which shows, at a glance, the principal features of the typical solar cells in use today. Each cell is depicted in two ways. One diagram shows the physical structure of the device and the dominant electron transport processes that contribute to the energy conversion process. The same processes are shown on the band diagram of the semiconductor, or energy levels in the molecular devices.

The diagrams in Figure 1 are schematic in nature, and a word of warning is in place regarding the differences in scale: whilst the thickness of crystalline silicon cells (shown in Figures (a) and (f)) is of the order of a hundred micrometres or more, the thickness of the various devices in Figures (b)–(e) (thin film and GaAs based cells) might be several micrometres or less. The top surface of the semiconductor structures shown in Figure 1 would normally be covered with antireflection coating. The figure caption can also be used to locate the specific chapter in this book where full details for each type of device can be found.

2 Electrical Characteristics

2.1 The Ideal Solar Cell

An ideal solar cell can be represented by a current source connected in parallel with a rectifying diode, as shown in the equivalent circuit of Figure 2. The corresponding I–V characteristic is described by the Shockley solar cell equation

$$I = I_{ph} - Io\left(e^{\frac{qV}{k_B T}} - 1\right) \tag{1}$$

where k_B is the Boltzmann constant, T is the absolute temperature, q (>0) is the electron charge, and V is the voltage at the terminals of the cell. I_0 is well known to electronic device engineers as the diode saturation current (see, for example, [1]) serving as a reminder that a solar cell in the dark is simply a semiconductor current rectifier, or diode. The photogenerated current I_{ph} is closely related to the photon flux incident on the cell and its dependence on the wavelength of light is frequently discussed in terms of the quantum efficiency or spectral response (see Section 2.3). The photogenerated current is usually independent of the applied voltage with possible exceptions in the case of a-Si and some other thin film materials [2–4].

Figure 3(a) shows the I–V characteristic (Equation (1)). In the ideal case, the short circuit current I_{sc} is equal to the photogenerated current I_{ph}, and the open circuit voltage V_{oc} is given by

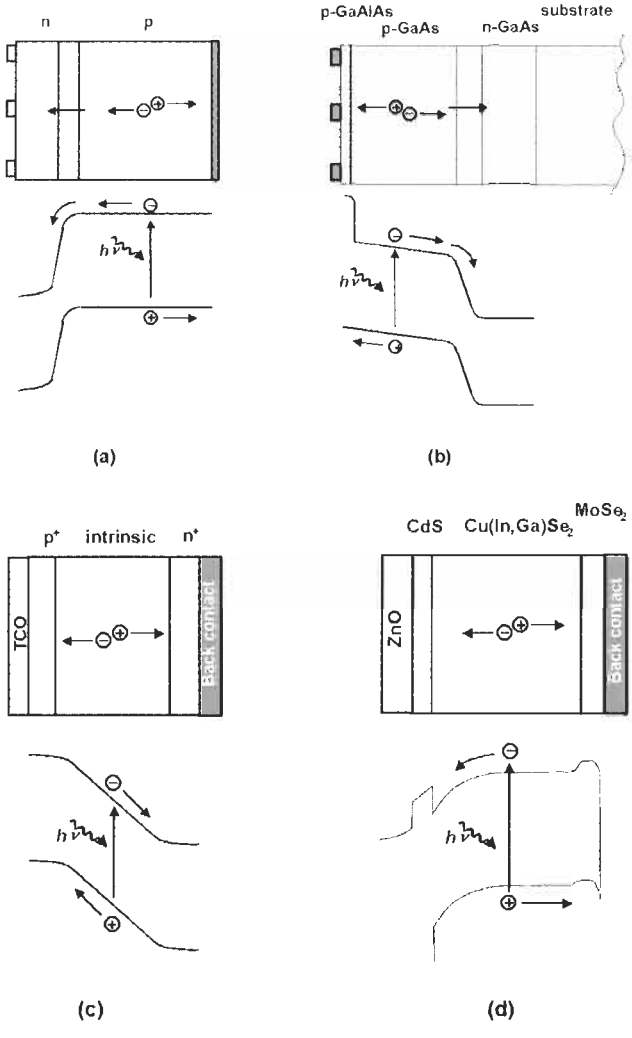

Figure 1 (a) The structure of crystalline silicon solar cell – the typical solar cell in use today. The bulk of the cell is formed by a thick p-type base where most of the incident light is absorbed and most power is generated. After light absorption, the minority carriers (electrons) diffuse to the junction where they are swept across by the strong built-in electric field. The electrical power is collected by metal contacts to the front and back of the cell (Chapters IIb-2 and -5). (b) The typical gallium arsenide solar cell has what is sometimes called a heteroface structure, by virtue of the thin passivating GaAlAs layer which covers the top surface. The GaAlAs 'window' layer prevents minority carriers from the emitter (electrons) to reach the surface and recombine but transmits most of the incident light into the emitter layer where most of the power is generated. The operation of this p–n junction solar cell is similar in many respects to the operation of the crystalline silicon solar cell in (a) but the substantial difference in thickness should be noted. (Chapter IId-1). (c) The structure of a typical single-junction amorphous silicon solar cells. Based on p–i–n junction, this cell contains a layer of intrinsic semiconductor which separates two heavily doped p and n regions near the contacts. Generation of electrons and holes occurs principally within the space-charge region, with the advantage that charge separation can be assisted by the built-in electric field, thus enhancing the collection efficiency. The contacts are usually formed by a transparent conducting oxide (TCO), at the top of the cell, and a metal contact at the back. Light trapping features in TCO can help reduce the thickness and reduce degradation. The thickness of a-Si solar cells ranges typically from a fraction

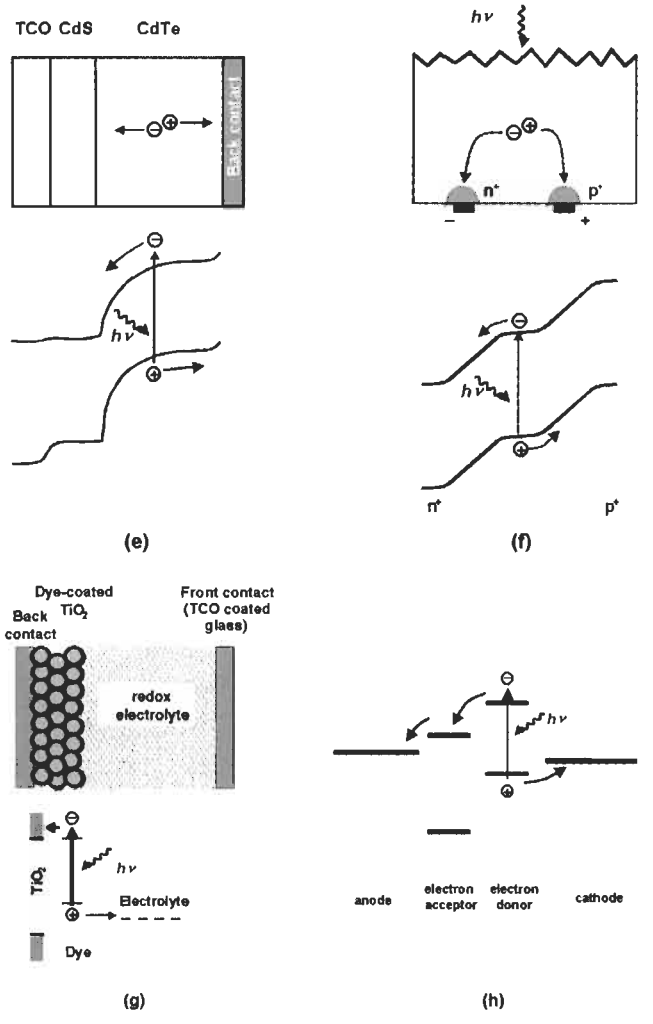

of a micrometer to several micrometers. (Chapter IIc-1). (d), (e) The typical structures of solar cells based on compound semiconductors copper indium–gallium diselenide (d) and cadmium telluride (e). The front part of the junction is formed by a wide band gap material (CdS 'window') which transmits most of the incident light to the absorber layer (Cu(In,Ga)Se_2 or CdTe) where virtually all electron–hole pairs are produced. The top contact is formed by a transparent conducting oxide. These solar cells are typically a few micrometers thick. (Chapters IIc-3 and -4). (f) Contacts can be arranged on the same side of the solar cell, as in this point contact solar cell. The electron–hole pairs are generated in the bulk of this crystalline silicon cell which is near intrinsic, usually slightly n-type. Slightly thinner than the usual crystalline silicon solar cell, efficient light absorption is aided here by light trapping: a textured top surface and a reflecting back surface (Chapter IId-2). (g), (h) The most recent types of solar cell are based on molecular materials. In these cells, light is absorbed by a dye molecule, transferring an electron from the ground state to an excited state, rather than from the valence band to the conduction band, as in the semiconductor cells. The electron is subsequently removed to an electron acceptor and the electron deficiency (hole) in the ground state is replenished from an electron donor. A number of choices exist for the electron acceptor and donor. In the dye sensitised cell (g, Chapter IIe-1), the electron donor is a redox electrolyte and the role of electron acceptor is the conduction band of titanium dioxide. In plastic solar cells (h, Chapter IIe-2), both electron donor and electron acceptor are molecular materials.

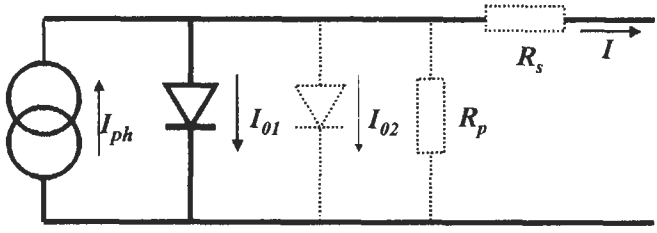

Figure 2 The equivalent circuit of an ideal solar cell (full lines). Non-ideal components are shown by the dotted line.

$$V_{oc} = \frac{k_B T}{q} \ln\left(1 + \frac{I_{ph}}{I_0}\right) \tag{2}$$

The maximum theoretically achievable values of the short circuit current density J_{ph} and of the open circuit voltage for different materials are discussed and compared with the best measured values in Chapter IIa-3.

The power $P = IV$ produced by the cell is shown in Figure 3(b). The cell generates the maximum power P_{max} at a voltage V_m and current I_m, and it is convenient to define the fill factor FF by

$$FF = \frac{I_m V_m}{I_{sc} V_{oc}} = \frac{P_{max}}{I_{sc} V_{oc}} \tag{3}$$

The fill factor FF of a solar cell with the ideal characteristic (1) will be furnished by the subscript 0. It cannot be determined analytically but it can be shown that FF_0 depends only on the ratio $v_{oc} = V_{oc}/k_B T$. FF_0 is determined, to an excellent accuracy, by the approximate expression [5]

$$FF_0 = \frac{v_{oc} - \ln(v_{oc} + 0.72)}{V_{oc} + 1}$$

The I–V characteristics of an ideal solar cell complies with the *superposition principle*: the functional dependence (1) can be obtained from the corresponding characteristic of a diode in the dark by shifting the diode characteristic along the current axis by I_{ph} (Figure 4).

2.2 Solar Cell Characteristics in Practice

The I–V characteristic of a solar cell in practice usually differs to some extent from the ideal characteristic (1). A two-diode model is often used to fit an observed curve, with the second diode containing an 'ideality factor' of 2 in the denominator of the argument of the exponential term. The solar cell (or circuit) may also contain series (R_s) and parallel (or shunt, R_p) resistances, leading to a characteristic of the form

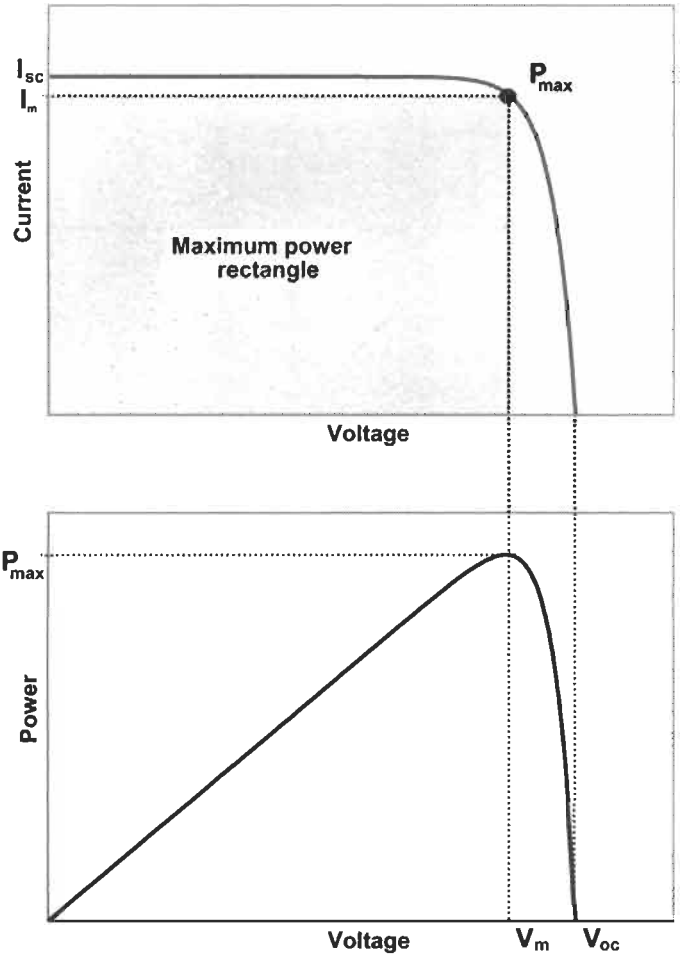

Figure 3 The I–V characteristic of an ideal solar cell (a) and the power produced by the cell (b). The power generated at the maximum power point is equal to the shaded rectangle in (a).

$$I = I_{ph} - I_{o1}\left\{exp\left(\frac{V + IR_s}{k_B T}\right) - 1\right\} - I_{o2}\left\{exp\left(\frac{V + IR_s}{2k_B T}\right) - 1\right\} - \frac{V + IR_s}{R_p} \tag{4}$$

where the light-generated current I_{ph} may, in some instances, depend on the voltage, as we have already noted. These features are shown in the equivalent circuit of Figure 2 by the dotted lines. The effect of the second diode, and of the series and parallel resistances, on the I–V characteristic of the solar cell is shown in Figures 5 and 6, respectively; further information about these parameters can be obtained from the dark characteristic (Figure 7). The effect of the series resistance on the fill factor can be allowed for by writing

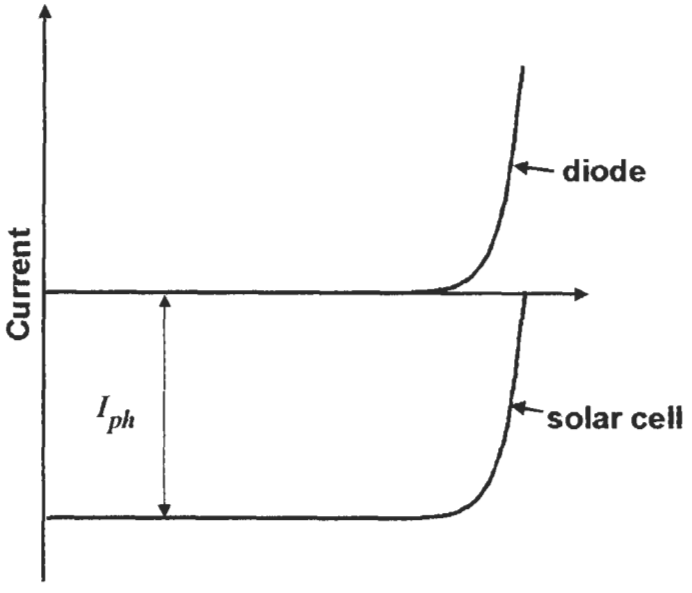

Figure 4 The superposition principle for solar cells.

$$FF = FF_0(1 - r_S) \tag{5}$$

where $r_s = R_s\, I_{sc}/V_{oc}$. An analogous expression exists also for the parallel resistance (see Chapter IIc-4). Instead of the two-diode equation (4), an empirical non-ideality factor n_{id} can be introduced in the single-diode equation (1) which usually lies between 1 and 2. Two among a number of possible sources of non-ideal behaviour – recombination in the depletion region and series resistance – are discussed in Sections 4.1.1 and 4.4.

2.3 The Quantum Efficiency and Spectral Response

The quantum efficiency of a solar cell is defined as the ratio of the number of electrons in the external circuit produced by an incident photon of a given wavelength. Thus, one can define external and internal quantum efficiencie (denoted by $EQE(\lambda)$ and $IQE(\lambda)$, respectively). They differ in the treatment of photons reflected from the cell: all photons impinging on the cell surface are taken into account in the value of the EQE but only photons that are not reflected are considered in the value of IQE.

If the internal quantum efficiency is known, the total photogenerated current is given by

$$I_{ph} = q\int_{(\lambda)} \Phi(\lambda)\{1 - \mathcal{R}(\lambda)\}IQE(\lambda)d\lambda \tag{6}$$

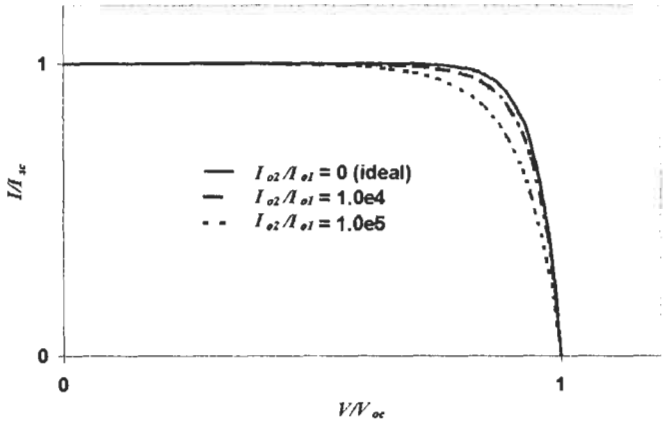

Figure 5 *The I–V characteristic of the solar cell in the two diode model for three values of the ratio* I_{02}/I_{01}.

where $\Phi(\lambda)$ is the photon flux incident on the cell at wavelength λ, $\mathcal{R}(\lambda)$ is the reflection coefficient from the top surface (see Section 3.1), and the integration is carried out over all wavelength λ of light absorbed by the solar cell. The values of the internal and external quantum efficiency are routinely measured to assess the performance of a solar cell by using interference filters or monochromators.

The *spectral response* (denoted by $SR(\lambda)$, with the units A/W) is defined as the ratio of the photocurrent generated by a solar cell under monochromatic illumination of a given wavelength, to the value of the spectral irradiance at the same wavelength. Since the number of photons and irradiance are related, the spectral response can be written in terms of the quantum efficiency as (see, for instance, [6])

$$SR(\lambda) = \frac{q\lambda}{hc} QE(\lambda) = 0.808 \cdot \lambda \cdot QE(\lambda) \tag{7}$$

where λ is in micrometres. Spectral response in (7) can be either internal or external, depending on which value is used for the quantum efficiency.

3 Optical Properties

3.1 The Antireflection Coating

Most solar cells rely on a thin layer of a dielectric (an antireflection coating) to reduce the reflection of light from the front surface of the cell. This section gives a brief description of the reflection of light from a bare semiconductor, and from a semiconductor with a single-layer antireflection coating. The discussion is confined to the case of normal incidence of light onto a smooth planar surface.

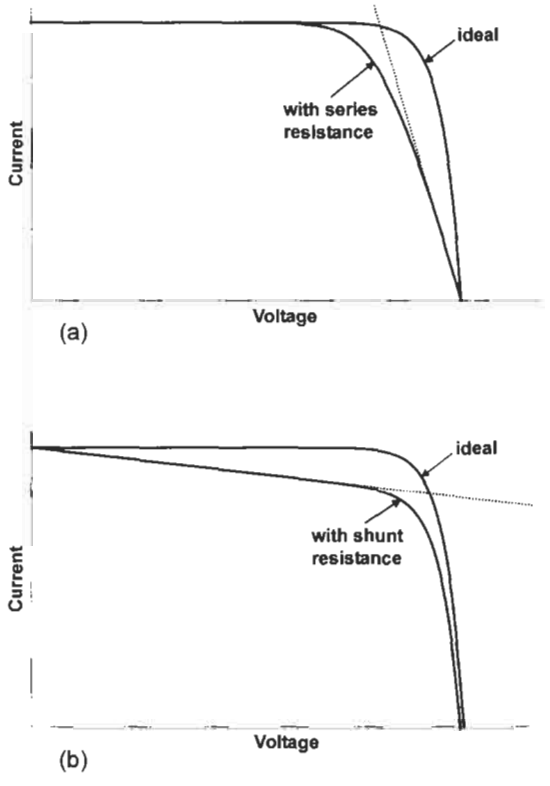

Figure 6 The effect of series (a) and parallel (b) resistance on the I–V characteristic of the solar cell.

The reflection coefficient from bare silicon for light incident from air is given by

$$\mathcal{R} = \frac{(\mathbf{n}-1)^2 + \kappa^2}{(\mathbf{n}+1)^2 + \kappa^2} \tag{8}$$

where $\mathbf{n}$ and κ are the refractive index and extinction coefficient of the semiconductor, both in general functions of the wavelength λ of light in vacuum. The extinction coefficient is related to the absorption coefficient α by

$$\kappa = \frac{\alpha\lambda}{4\pi\mathbf{n}} \tag{9}$$

For single-layer antireflection coating of refractive index $\mathbf{n}_{ar}$ between a top medium of refractive index $\mathbf{n}_0$ (for example, glass or air) and semiconductor, the reflection coefficient becomes, neglecting light absorption in the semiconductor

$$\mathcal{R} = \frac{r_0^2 + r_{sc}^2 + 2r_0 r_{sc}\cos 2\beta}{1 + r_0^2 r_{sc}^2 + 2r_0 r_{sc}\cos 2\beta} \tag{10}$$

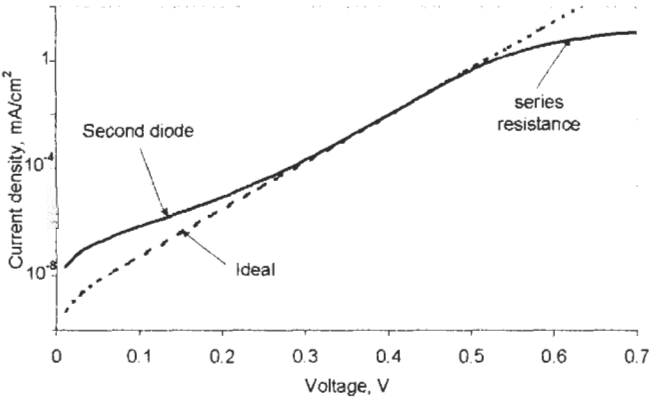

Figure 7 The dark I–V characteristic of a solar cell for the two-diode model including the series resistance. The shunt resistance has a similar effect to the second diode.

where

$$r_0 = \frac{\mathbf{n}_{ar} - \mathbf{n}_0}{\mathbf{n}_{ar} + \mathbf{n}_0}; \qquad r_{sc} = \frac{\mathbf{n}_{sc} - \mathbf{n}_{ar}}{\mathbf{n}_{sc} + \mathbf{n}_{ar}} \qquad \beta = \frac{2\pi}{\lambda}\mathbf{n}_{ar}d$$

and d denotes the thickness of the coating. The transmission coefficient is, in both cases, simply

$$\mathcal{T} = 1 - \mathcal{R} \tag{11}$$

In most cases of interest, both r_{sc} and r_0 are positive and $\mathcal{R}$ vanishes when

$$d = \frac{\lambda}{4\mathbf{n}_{ar}}; \qquad \frac{3\lambda}{4\mathbf{n}_{ar}}; \qquad \frac{5\lambda}{4\mathbf{n}_{ar}}; \ldots \tag{12}$$

and

$$\mathbf{n}_{ar} = \sqrt{\mathbf{n}_0\mathbf{n}_{sc}} \tag{13}$$

The first value of d in (12) is often used in practice under the name of *quarter-wavelength rule* since $\lambda/\mathbf{n}_{ar}$ is the wavelength of light in the antireflection coating.

Reflection from the top surface can be reduced further by the use of a multilayer coating. The details of such coatings as well as a general theory for an oblique incidence of light can be found, for example, in [7]. Figure 8 compares the reflection coefficients for a smooth bare silicon surface, a smooth surface covered with antireflection coating, and a textured surface with antireflection coating.

3.2 Light Trapping

In solar cells with a simple geometry, light rays enter the cell through the front surface and, if not absorbed, leave through the rear surface of the cell. More sophisticated arrangements exist which extend the path of light inside the

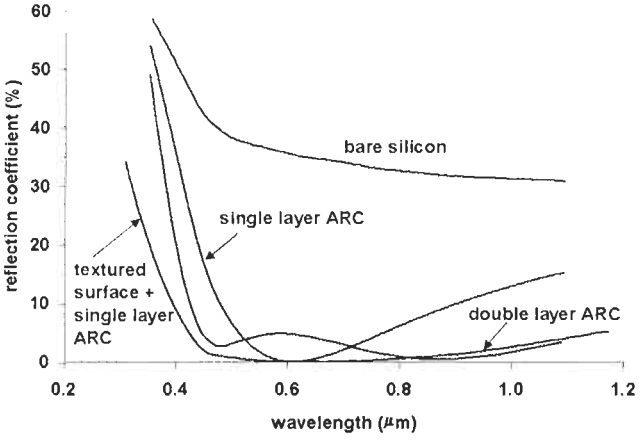

Figure 8 The reflection coefficient from polished bare silicon, and from a polished silicon surface covered with a single and double layer antireflection coating (after [31, 33]). The reflection coefficient for a textured surface is also shown.

cell, and are usually referred to as optical confinement or light trapping. In crystalline or amorphous silicon solar cells, light trapping is used to reduce the thickness of the cell without lowering the light absorption within the cell. Light trapping can also be used to enhance the open circuit voltage [8, 9].

The most common light trapping features include a textured top surface combined with an optically reflecting back surface (Figure 9). In the ideal case, Yablonovich [10, 11] (see also [12]) has shown that a randomly textured (so called Lambertian) top surface in combination with a perfect back-surface reflector produces a light trapping scheme which enhances the light intensity inside the cell by a factor of $\mathbf{n}_{sc}^2$ where, as in Section 3.1, $\mathbf{n}_{sc}$ is the refractive index of the solar cell material. This arrangement also increases the average path length of light rays inside the cell from $2W$, in the case of single pass through the cell, to $4\mathbf{n}_{sc}^2 W$ in the case of complete light trapping, where W the cell thickness. Schemes have been developed to enhance the operation of practical devices including crystalline, polycrystalline and amorphous silicon cells (discussed in Chapters IIb-2, -3 and -5, and Chapters IIc-1 and -2). With application to the latter cells, Schropp and Zeman [13] consider the trapping and scattering of light at rough interfaces in some detail. In gallium arsenide cells, multilayer Bragg reflectors (in place of the back-surface reflector) have been used with success (see Chapter IId-1).

4 Typical Solar Cell Structures

4.1 The p–n Junction Solar Cell

The planar p–n junction solar cell under low injection is usually singled out for special analysis since realistic approximations exist that allow analytic solutions

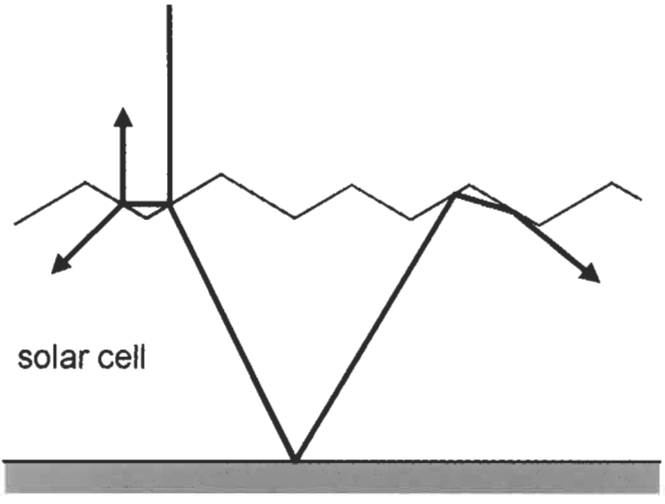

Figure 9 The textured top surface reduces reflection from the solar cell and, when combined with a reflecting back surface, helps to confine or 'trap' light within the cell.

to be developed and used successfully for the description of practical devices. The success of this model is due, to a large extent, on the clear way the cell can be divided into three regions – emitter, junction region and base – which serve a different purpose in solar cell operation.

The emitter and base – which remain largely neutral during the cell operation – absorb the main part of the incident light and transport the photogenerated minority carriers to the junction. The p–n junction – which contains a strong electric field and a fixed space charge – separates the minority carriers that are collected from the emitter and base. The junction is effectively devoid of mobile charge carriers and is sometimes called the depletion region.

4.1.1 The p–n Junction

Figure 10 shows the principal parameters of a p–n junction in equilibrium along the spatial coordinate perpendicular to the junction. In operation, the Fermi level E_F splits into two quasi-Fermi levels E_{Fn} and E_{Fp}, one each for the electrons and holes, with the corresponding potentials $\phi_n = -q/E_{Fn}$ and $\phi_p = -q/E_{Fp}$. Near the open circuit, the quasi-Fermi levels are parallel in the junction, their gradients are small, and their splitting is equal to the observed voltage at the junction (Figure 11). The charge carrier statistics in terms of the quasi-Fermi levels is discussed in Section 3 of Chapter IIa-2.

Under illumination or under applied bias in the dark, the electrostatic potential difference $\Delta\psi$ between the two sides of the junction is a difference of two terms: the equilibrium built-in voltage V_{bi} and the voltage V at the junction edges:

$$\Delta\psi = V_{bi} - V \tag{14}$$

$$qV_{bi} = k_B T \ln\left(\frac{N_D N_A}{n_i^2}\right) \tag{15}$$

where N_A and N_D are the acceptor and donor concentrations on the p- and n-sides of the junction, respectively. In the absence of resistive losses, V is equal to the voltage measured at the terminals of the cell. The junction width W_j is given by

$$W_j = L_D \sqrt{\frac{2q\Delta\psi}{k_B T}} \tag{16}$$

Here, L_D is the Debye length,

$$L_D = \frac{\sqrt{\varepsilon k_B T}}{q^2 N_B} \tag{17}$$

where ε is the static dielectric constant and

$$N_B = \frac{N_A N_D}{N_A + N_D}$$

In an ideal p-n junction solar cell, the junction (or depletion) region serves as a lossless mechanism for extracting and separating the minority carriers from the quasi-neutral regions – the base and the emitter. The function of the junction can then be summarised in the form of boundary conditions which link the majority carrier concentration on one side of the junction with the minority carrier concentration on the other. For an n-type emitter and p-type base, for example, the following relations hold:

$$n(base) = n_0(base) e^{qV/k_B T} = n_0(emitter) e^{q(V-V_{bi})/k_B T} \tag{18}$$

Equation (18) relates the electron concentration n(base) at the edge of the depletion region of the base to its equilibrium value n_0(base), and to the equilibrium electron concentration n_0(emitter) at junction edge of the emitter. A similar relationship exists for the hole concentration at the junction edge of the emitter and base:

$$p(emitter) = p_0(emitter) e^{qV/k_B T} = p_0(base) e^{q(V-V_{bi})/k_B T} \tag{19}$$

Equations (18) and (19) are the boundary conditions for an analytical solution of the transport equations (discussed in Chapter IIa-2, Section 4) in the quasi-neutral regions. A rigorous discussion of this *depletion approximation* which forms the basis for the analytical treatment can be found in reference [14].

The photogenerated and dark saturation currents for the cell are obtained by adding the relevant quantities for the base and the emitter:

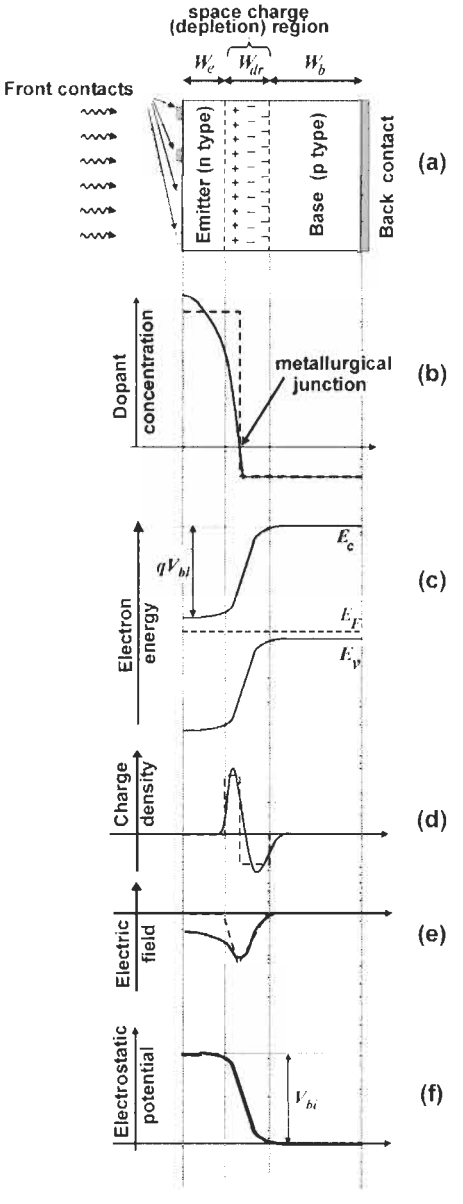

Figure 10 The p–n junction solar cell in equilibrium. (a) The physical layout (not to scale); (b) the difference of dopant concentrations $N_D - N_A$*; (c) the band diagram; (d) charge density; (e) electric field; (f) electrostatic potential. The quantities shown by the dashed line correspond to an idealised abrupt junction with constant dopant concentrations in the base and in the emitter; the full line corresponds to a typical industrial solar cell with a diffused emitter.*

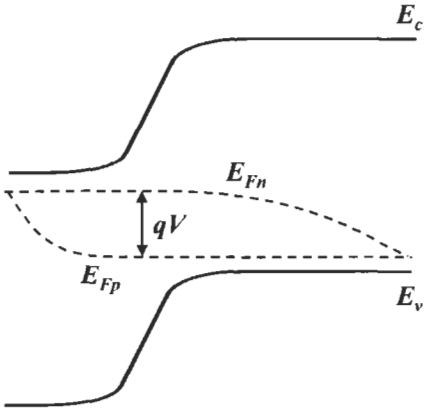

Figure 11 The p–n junction at open circuit.

$$I_{ph} = I_{phb} + I_{phe}$$
$$I_0 = I_{0b} + I_{0e} \tag{20}$$

A similar results holds also for the quantum efficiency. It is sometimes convenient to define the collection efficiency ϑ_i for a region i (where i stands for the base, emitter or the depletion region) as the probability that an electron–hole pair generated in this region reaches the junction:

$$EQE_i(\lambda) = a_i(\lambda)\vartheta_i(\lambda) \tag{21}$$

where $a_i(\lambda)$ is the (fractional) number of electron–hole pairs generated by each photon of incident light in region i.

No recombination occurs in an ideal p–n junction but the (small) light generated current produced here can be added to the first Equation (20). Recombination is included in more realistic analytical theories: the original treatment by Sah et al. [15] uses the Shockley–Read–Hall model of recombination via defects (see Chapter IIa-2, Section 7) with the principal result that the current in (1) is reduced by a term of the form

$$I_{02}\left(e^{\frac{qV}{2k_BT}} - 1\right) \tag{22}$$

In other words, recombination in the depletion region gives rise to an additional dark current corresponding to the second diode in the I–V characteristic (4), as already discussed in Section 2.2.

4.1.2 Uniform Emitter and Base

Analytical expressions for the photogenerated and dark saturation current densities for the emitter or base can be obtained if the dopant concentration and all other parameters are assumed constant. To this end we define

$$\zeta = \frac{SL}{D} \tag{23}$$

$$\gamma_+ = (\zeta + 1)e^{W/L} + (\zeta - 1)e^{-W/L} \tag{24}$$

$$\gamma_- = (\zeta + 1)e^{W/L} - (\zeta - 1)e^{-W/L} \tag{25}$$

where S is the surface recombination velocity at external surface (front surface in the case of emitter and rear surface in the case of base), W is the width of the relevant region (W_e for the emitter and W_b for the base), $L = \sqrt{D\tau}$ is the minority-carrier diffusion length, τ is the minority carrier lifetime, and D is the minority carrier diffusion constant. The photogenerated and dark saturation currents for each region are then given by

$$J_0 = \frac{qD}{L}\frac{n_i^2}{N_{dop}}\frac{\gamma_+}{\gamma_-} \tag{26}$$

where N_{dop} is the dopant concentration N_A or N_D appropriate for the relevant region. The internal quantum efficiency for each region is given in Table 1.

4.1.3 Diffused Emitter

In practical silicon solar cells the emitter is generally fabricated by diffusion of impurities into the semiconductor wafer. This creates a thin layer where the impurity gradient is very high and the approximation of constant doping concentration does not hold. Simultaneously, the continuity and current equations do not combine into a second-order differential equation with constant coefficients, and a simple analytical solution cannot be found. Several approaches have been followed besides the numerical integration of the equations [16] to reach a reasonably simple analytical or truncated series solutions. Analytical solutions were reviewed in reference [17] where the errors have been estimated for the transparent emitter [18] and quasi-transparent emitter [19] solutions. An emitter is considered transparent when the recombination inside the emitter bulk is negligible and quasi-transparent when this recombination can be considered as a perturbation to the transparent solution. Solutions based on an infinite series which can be truncated to provide different order approximations were proposed in reference [20] and extended as a succession of asymptotic expansions in [21]. One of the simplest yet accurate solutions is given in [22] based on the superposition of a zero-input and a zero-state solutions of the continuity equation with a boundary condition at the surface given by a surface recombination velocity S as follows:

$$J_0 = \frac{qn_i^2}{\int_0^{w_e} \frac{N_{eff}}{D}dx + \frac{N_{eff}(W_e)}{S}} + qn_i^2 \int_0^{w_e} \frac{dx}{N_{eff}\tau} \tag{27}$$

Table 1 The internal quantum efficiency for the emitter and base in the uniform doping model. The subscripts *e* or *b* of γ, ζ, *L* and *W* refers to the emitter or base, respectively. In the case of base, IQE is understood per unit photon entering from the junction

	$IQE(\lambda)$	
Base	$\frac{\alpha L_b}{\gamma_{b-}}\left\{\frac{\zeta_b+1}{1+\alpha L_b}\left(e^{W_b/L_b}-e^{-\alpha W_b}\right)+\frac{\zeta_b-1}{1-\alpha L_b}\left(e^{-W_b/L_b}-e^{-\alpha W_b}\right)\right\} \rightarrow \frac{\alpha L_b}{1+\alpha L_b}$	*for an infinite base* ($W_b \rightarrow \infty$)
Emitter	$\frac{\alpha L_b e^{-\alpha W_e}}{\gamma_{e-}}\left\{\frac{\zeta_e+1}{1+\alpha L_e}\left(e^{-W_e/L_e}-e^{+\alpha W_e}\right)+\frac{\zeta_e-1}{1-\alpha L_e}\left(e^{+W_e/L_e}-e^{+\alpha W_e}\right)\right\}$	

where $N_{eff}(x)$ is the effective doping concentration at depth x taking into account the effect of band gap narrowing. A systematic and general formulation of the several approximations is given in [23]. An elegant formalism to deal with inhomogeneously doped emitters can be found in [24].

When the emitter in illuminated, the problem can be solved using the same approaches as used in the dark, computing the emitter collection efficiency ϑ_{em} equal, as in (21), to the ratio of the photogenerated current at the emitter boundary of the space charge region divided by the integrated carrier generation in the emitter. Bisschop et al [25] extended Park's solution in the dark [20] to illuminated emitters. Cuevas et al. [23] provided a formulation in terms of a series expansion and Pons et al. extended the dark superposition model [22]. The first-order result for the photocurrent is given by (see, for instance, [23])

$$J_{ph} = \frac{q\int_0^{W_e} g(x)dx}{1+\frac{s}{N_{eff}(W_e)}\int_o^{W_e}\frac{N_{eff}}{D}dx+\frac{N_{eff}(W_e)}{S}} \tag{28}$$

where $g(x)$ is the generation rate (see Section 6.1, Chapter IIa-2).

4.2 Heterojunction Cells

Heterostructures represent an opportunity to manufacture efficient solar cells from highly absorbing thin-film materials without substantial losses through electron–hole recombination at the front surface. This is illustrated by the structures of the CdS/CdTe and CdS/CIGS solar cells where a wide band gap semiconductor (here, CdS) serves as a 'window' partner to a lower band gap 'absorber' where most of the power is generated.

An important consideration in the heterojunction design includes the band gap line-ups at the interface between the two semiconductors. Figure 12 shows the equilibrium band diagrams of typical heterojunctions between a wide-gap window A and an absorber B. The band diagram corresponds the usual situation encountered in CdTe and CIGS solar cells where an n-type wide-gap window and a p-type emitter are the most common arrangements. Similarly to the p–n junction, the built-in potentials V_{bi}(A) and V_{bi}(B) on the two sides of the junction

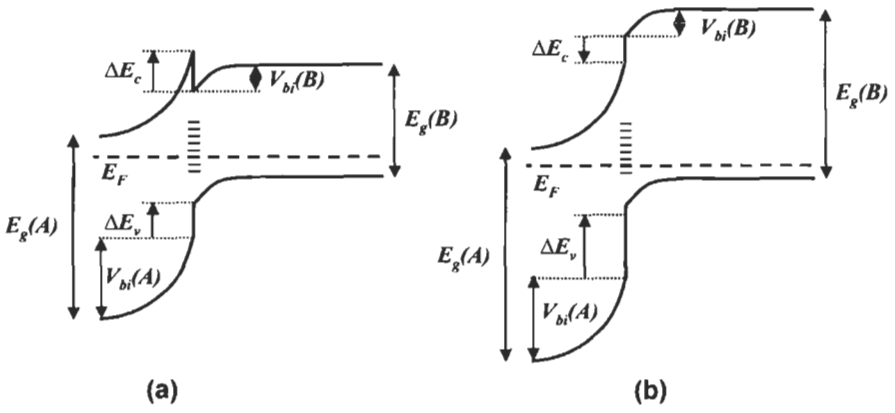

Figure 12 The band diagrams of typical heterojunction solar cells consisting of a window layer of wide-gap n-type semiconductor A, and an absorber of p-type semiconductor B. The energy levels of an interface defect layer, and the band-bending potential V_{bi}*(A) and* V_{bi}*(B) are also shown. A spike in the conduction band occurs for positive* ΔE_c*, as shown in the structure (a).*

can be determined by solution of the Poisson equation (see Equation (7) in Chapter IIa-2). The band gap discontinuities ΔE_c and ΔE_v have been subject to much discussion over the years, and a number of theories have evolved that provide an understanding in terms of electron affinities and the electron dipole moments at the interface. The discontinuity in the conduction band edge, for example, can be written in the form

$$\Delta E_c = \chi_B - \chi_A + \text{interface dipole terms}$$

where χ_A and χ_B are the electron affinities of semiconductors A and B [26].The classical Shockley–Anderson model [27] neglects the interface dipole terms. Its limited validity has been discussed extensively (see, for example, [28]) although it does seem to provide a reasonable description for some heterojunctions (Figure 13). In the application to solar cells, a full understanding of the problem is hindered further by the polycrystalline nature of the materials, and frequently the presence of more than two layers that need to be considered in the analysis.

On account of the wide band gap and weak generation in the window material, both the dark and photogenerated currents from the emitter are significantly smaller that the corresponding quantities from the base. In addition, dark current may contain a component due to recombination at the interface defect states; less frequently, these states also reduce the collection probability and the photogenerated current.

Because of the short-minority carrier diffusion lengths, it is desirable to ensure that minority carriers are generated predominantly in a region where electric field assists collection through drift rather than diffusion. As in the homojunction cell, this can be achieved by employing sufficiently low doping concentrations in the absorber to obtain a wide depletion region; a similar philosophy is also employed in amorphous silicon solar cells, as discussed in

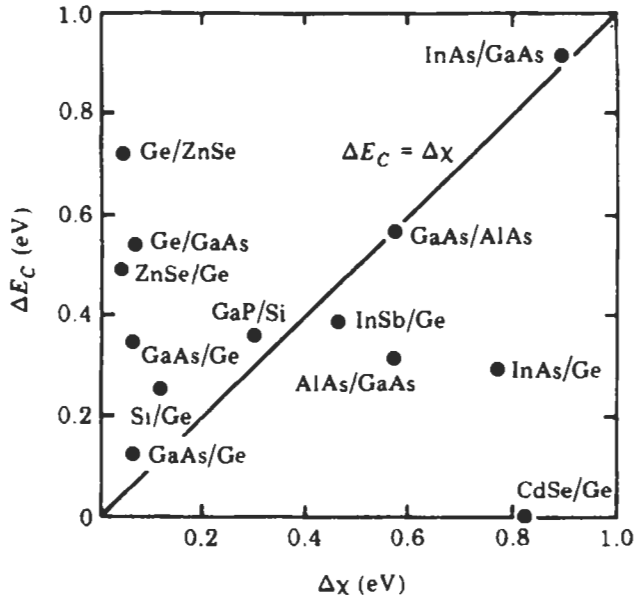

Figure 13 The conduction band discontinuity ΔE_c and the difference of electron affinities $\Delta\chi$ for a number of heterojunctions. (reference [26], p. 391). © Elsevier. Reprinted with permission.

Section 4.3 and Chapter IIc-1. More detailed description of heterojunctions in application to practical solar cells will be found in Chapters IIc-3 and -4.

Somewhat similar to heterojunction is the *heteroface* solar cell; a common structure in GaAs solar cells where a thin layer of wide-gap GaAlAs is deposited to reduce recombination at the top surface. It is more convenient, however, to describe this structure as a homojunction cell with surface passivation which can be treated by the methods described in Section 4.1.

4.3 The p–i–n Structure

The analysis of p–i–n junction solar cells is of considerable importance for the understanding of operation of amorphous silicon solar cells. Furthermore, similar principles have been invoked in the description of other thin film solar cells where carrier diffusion is ineffective and electric field is used to enhance carrier transport and collection. Despite this importance, however, the theoretical understanding of these structures is limited, hampered by the fundamental complexity of the problem. Indeed, the less-than-complete knowledge of the parameters of amorphous or polycrystalline material is compounded by mathematical difficulties arising principally from the need to solve the non-linear transport equations. Although a detailed description is possible only with the use of numerical computational techniques, a broad understanding can be gained through judicious approximations based on a physical insight [29].

A schematic band diagram of a p–i–n structure is shown in Figure 14. Noting that the carrier transport dominant chiefly by drift in the electric field of the

junction rather than by diffusion, carrier collection will be described by the drift lengths ℓ_n and ℓ_p rather than by the diffusion lengths L_n and L_p (see Chapter IIa-2, Section 7.3). The recombination can be conveniently approximated with the use of minority carrier lifetimes τ_n and τ_p on the two sides of the junction where electrons and holes are minority carriers, respectively. The use of constant electric field $\mathcal{E}$ is obviously an approximation, but it is usually a good one if carrier injection is not too high. A reasonably simple analysis is then possible which, in the limit of weak absorption, results in an analytical expression in the form

$$J = qg\ell_c(1 - e^{-W_i/\ell_c}) \tag{29}$$

for the current density produced by illumination. In Equation (29), W_i is the width of the intrinsic region, and

$$\ell_c = \ell_n + \ell_p \tag{30}$$

is the collection length, d is the width of the i layer and g is the generation function which is assumed here to be constant. Equations similar to (29) have been used with success to interpret various characteristics of p–i–n solar cells (see, for example, [4]).

An extension of this theory was later proposed which allows for the three charge states of the dangling bonds in amorphous silicon rather than the two charge states usually considered in the Shockley–Read–Hall theory [30].

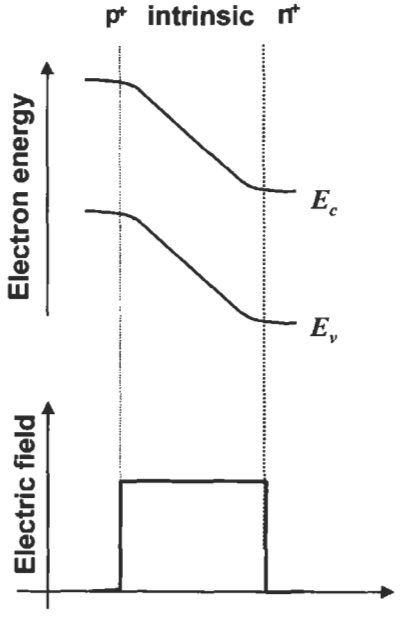

Figure 14 An idealised model of a p–i–n junction amorphous silicon solar cell with a constant electric field in the intrinsic region.

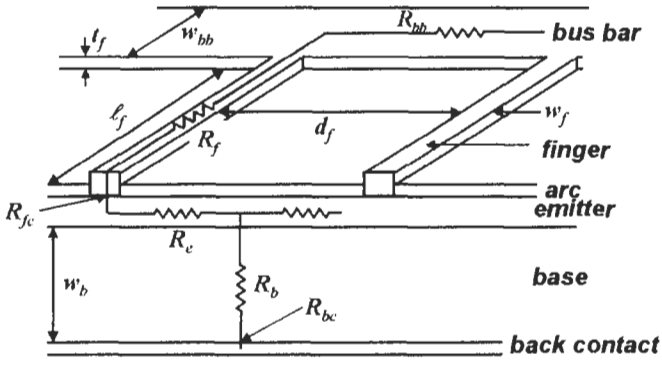

Figure 15 Components of the series resistance in a p–n junction solar cell (after [32] and [33]).

Table 2 Expressions for the various components of the series resistance; the bus bar resistance assumes that connection is made at one end. Here, R_{sp} is the sheet resistance of the emitter layer (in ohm/square), ρ_{cf} and ρ_{cr} are the contact resistances (in ohm/cm²) of the front and rear contact, respectively, ρ_b is the base resistivity, and ρ_m is the resistivity of the front metallisation. The geometrical dimensions are defined in Figure 15

Component of resistance	Notation	Expression
Emitter resistance	R_e	$R_e = \frac{R_{sp} d_f}{7\ell_f}$
Resistance of the base	R_b	$R_b = AW_b\rho_b$
Contact resistance: front contact	R_{fc}	$R_{fc} = \frac{\sqrt{R_{sp}\rho_{cf}}}{\ell_f} coth\left(W_f\sqrt{\frac{R_{sp}}{\rho_{cf}}}\right)$
Contact resistance: rear contact	R_{bc}	$R_{bc} = A\rho_{cr}$
Resistance of the finger contact	R_f	$R_f = \frac{\ell_f \rho_m}{3t_f W_f}$
Resistance of the collecting busbar (per unit length)	R_{bb}	$R_{bb} = \frac{\rho_m}{3t_f W_{bb}}$

4.4 Series Resistance

Considerations regarding series resistance form an important part of the solar cell design. The main components of the series resistance of a typical crystalline silicon solar cell are shown in Figure 15 and expressions given in Table 2.

References

[1] Sze, S.M., 1981. *Physics of Semiconductor Devices* (2nd edition), John Wiley & Sons, New York.

[2] Hishikawa, Y., Imura, Y. and Oshiro, T., 2000. Irradiance dependence and translation of the I-V characteristics of crystalline silicon solar

cells, *Proc. 28th IEEE Photovoltaic Specialists Conf.*, Anchorage, pp. 1464–1467.

[3] Philips, J.E., Titus J. and Hofmann, D., 1997. Determining the voltage dependence of the light generated current in $CuInSe_2$-based solar cells using I-V measurements made at different light intensities, *Proc. 26th IEEE Photovoltaic Specialist Conf.*, Anaheim, pp. 463–466.

[4] Hegedus, S.S., 1997. Current-voltage analysis of a-Si and a-SiGe solar cells including voltage-dependent photocurrent collection, *Prog. Photovolt: Res. Appl.*, Vol. 5, pp. 151–168.

[5] Green, M.A., 1995. *Silicon Solar Cells: Advanced Principles and Practice.* Centre for Photovoltaic Devices and Systems, University of New South Wales.

[6] Castañer L. and Silvestre, S., 2002. *Modelling Photovoltaic Systems Using Pspice*, John Wiley & Sons, Chichester, 2002.

[7] Born, M. and Wolf, E., 1999. Principles of Optics (7th edition), Cambridge University Press, Cambridge, Section 1.6.

[8] Brendel, R. and Queisser, H.J., 1993. On the thickness dependence of open circuit voltages of p-n junction solar cells, *Sol. Energy Mater. Sol. Cells*, Vol. 29, p. 397.

[9] Markvart, T., 2000. Light harvesting for quantum solar energy conversion, *Prog. Quantum Electronics*, Vol. 24, p. 107.

[10] Yablonovich, E., 1982. Statistical ray optics. *J. Opt. Soc. Am.*, Vol. 72, p. 899.

[11] Yablonovich, E. and Cody, G.C., 1982. Intensity enhancement in textured optical sheets for solar cells, *IEEE Trans. Electron Devices*, Vol. ED-29, p. 300.

[12] Miñano, J.C., 1990. Optical confinement in photovoltaics, in A. Luque and G.L. Araujo Eds., *Physical Limitations to Photovoltaic Energy Conversion*, Adam Hilger, Bristol, p. 50.

[13] Schropp, R. and Zeman, M., 1998. *Amorphous and Microcystalline Silicon Solar Cells: Modelling, Materials and Device Technology*, Kluwer, Boston.

[14] Selberherr, S., 1984. *Analysis and Simulation of Semiconductors Devices*, Springer, Vienna, New York, 1984, pp. 141-146.

[15] Sah, C.T., Noyce, R.N. and Shockley, W., 1957. Carrier generation and recombination in p-n junctions and p-n junction characteristics, *Proc. IRE*, Vol. 45, p. 1228.

[16] Rover, D.T., Basore, P.A. and Thorson, G.M., 1985. *Proc. 18th IEEE Photovoltaic Specialist Conf.*, Las Vegas, pp. 703–709.

[17] Cuevas, A. and Balbuena, M., 1989. Review of analytical models for the study of highly doped regions of silicon devices. *IEEE Trans. Electron Devices*, Vol. ED-31, pp. 553–560.

[18] Shibib, M.A., Lindholm, F.A. and Therez, F., 1978. *IEEE Trans. Electron Devices*, Vol. ED-26, p.958.

[19] del Alamo, J.A. and Swanson, R.M., 1984. *Proc. 17th IEEE Photovoltaic Specialist Conf.*, Orlando, pp. 1303–1308.

[20] Park, J.S., Neugroschel, A. and Lindholm, F.A., 1986. *IEEE Trans. Electron Devices*, Vol. ED-33, p. 240.

[21] Rinaldi, N., 1993. Modelling of minority carrier transport in non-uniformly doped silicon regions with asymptotic expansions, *IEEE Trans. Electron Devices*, Vol. ED-40, pp. 2307–2317.

[22] Alcubilla, R., Pons J. and Castañer, L., 1992. Superposition solution for minority carrier current in the emitter of bipolar devices, *Solid State Electronics*, Vol. 35, pp. 529–533.

[23] Cuevas, A., Merchan, R. and Ramos, J.C., 1993. On the systematic analytical solutions for minority carrier transport in non-uniform doped semiconductors: application to solar cells, *IEEE Trans. Electron Devices*, Vol. ED-40, pp. 1181–1183.

[24] del Alamo, J.A. and Swanson, R.M., 1984. The physics and modelling of heavily doped emitters, *IEEE Trans. Electron Devices*, Vol. ED-31, p. 1878.

[25] Bisschop, F.J., Verhoef, L.A. and Sinke, W.C., 1990. An analytical solution for the collection efficiency of solar cell emitters with arbitrary doping profile. *IEEE Trans. Electron Devices*, Vol. ED-37, pp. 358–364.

[26] Brillson, L.J., 1992. Surfaces and interfaces: atomic-scale structure, band bending and band offsets. In: P.T. Landsberg Ed., *Handbook of Semiconductors*, Vol. 1, Elsevier, pp. 281–417.

[27] Anderson, R.L., 1962. Experiments on Ge–As heterojunctions, *Solid State Electronics*, Vol. 5, pp. 341–351.

[28] Kroemer, H., 1983. Heterostructure devices: a device physicist looks at interfaces, *Surface Science*, Vol. 132, pp. 543–576.

[29] Crandall, R.S., 1983. Modelling of thin film solar cells: uniform field approximation, *J. Appl. Phys.* Vol. 54, p. 7176.

[30] Hubin, J. and Shah, A.V., 1995. Effect of the recombination function on the collection in a p-i-n solar cell, *Phil. Mag.*, Vol. B72, p. 589.

[31] Zweibel, K. and Hersch, P. 1984. *Basic Photovoltaic Principles and Methods*, Van Nostrand Reinhold, New York.

[32] Overstraeten, R. van and Mertens, R.P., 1986. *Physics, Technology and Use of Photovoltaics*, Adam Hilger, Bristol.

[33] Goetzberger, A., Knobloch, J. and Voss, B. 1998. *Crystalline Silicon Solar Cells*, John Wiley & Sons, Chichester.

Semiconductor Materials and Modelling

Tom Markvart, School of Engineering Sciences,
University of Southampton, UK
Luis Castañer, Universidad Politecnica de Catalunya,
Barcelona, Spain

1 Introduction

Solar cell modelling is fundamental to a detailed understanding of the device operation, and a comprehensive model require a detailed knowledge of the material parameters. A brief overview of the semiconductor properties relevant to solar cell operation is given in this chapter, including the semiconductor band structure and carrier statistics, transport and optical properties, recombination processes, material aspects of radiation damage to solar cells in space and effects observed under heavy doping, with special attention given to the properties of hydrogenated amorphous silicon. The principal semiconductor parameters encountered in photovoltaic applications are summarised in Tables 1 and 2. The refractive indices of materials used for antireflection coating can be found in Table 3.

Numerous computer programs that use the material parameters to model solar cell operation have been developed over the years, and several are now available commercially:

- PC1D developed by P.A. Basore and colleagues at the University of New South Wales, Australia, is the standard one-dimensional simulator used by the PV community.
- ATLAS, a Device Simulation Software by SILVACO International, uses physical models in two and three dimensions. It includes the Luminous tool which computes ray tracing and response of solar cells. It allows the use of monochromatic or multi-spectral sources of light.
- MEDICI by Technology Modelling Associates models the two-dimensional distribution of potential and carrier concentration in a semiconductor device. It also includes an Optical device advanced application module where photogeneration can be computed for multi-spectral sources.

Some programs are available free of charge. These include, for example, SimWindows which can be downloaded from http://www-ocs.colorado.edu/SimWindows/simwin.html.

A discussion of the main principles of the numerical techniques can be found in specialised texts which deal with the modelling of solar cells (see, for example, the review [1]) or with the modelling of semiconductor devices in general [2].

2 Semiconductor Band Structure

The energy gap (or band gap) E_g and its structure as a function of the wave vector are key characteristics of the semiconductor material and of fundamental importance to the operation of the solar cell (see Figure 1). The principal features of interest are the temperature variation of the band gap energy E_g and the magnitude of wave vector associated with low-energy transitions.

The variation of the band gap with temperature can be described by an expression originally suggested by Varshni [10]

Table 1 Properties of the principal semiconductors with photovoltaic applications (all at 300 K). Bandgap: d = direct; i = indirect. Crystal structure: dia = diamond, zb = zinc blende, ch = chalcopyrite. The refractive index is given at the wavelength 590 nm (2.1 eV) unless otherwise stated. Principal sources of data: c-Si [20]; GaAs [3]; InP [4, 41]; a-Si [5] and Section 10; CdTe [6]; CIS [7]; $Al_xGa_{1-x}As$ [9]. Details of the absorption coefficient and refractive index, including the wavelength dependence, can be found in references [27] and [28]. χ is the electron affinity and TEC stands for thermal expansion coefficient

	E_g (eV)	Crystal strucure	ε	n	χ (eV)	Lattice const. (Å)	Density (g/cm^{-3})	TEC ($10^{-6}\,K^{-1}$)	Melting point (K)	Comments
c-Si	1.12 (i)	dia	11.9	3.97	4.05	5.431	2.328	2.6	1687	Cell material (Part IIb)
GaAs	1.424 (d)	zb	13.18	3.90	4.07	5.653	5.32	6.03	1510	Cell material (Ch. IId-1)
InP	1.35 (d)	zb	12.56	3.60	4.38	5.869	4.787	4.55	1340	Cell material (Ch. IId-1)
a-Si	~1.8 (d)	–	~11	3.32						Cell material, invariably Si:H alloy; sometimes also alloyed with germanium or carbon (Chs. IIc-1, -2)
CdTe	1.45–1.5 (d)	zb	10.2	2.89*	4.28	6.477	6.2	4.9	1365	Cell material (Ch. IIc-3)
$CuInSe_2$ (CIS)	0.96–1.04 (d)	ch			4.58			6.6	~1600	Cell material, often alloyed with gallium (Ch. IIc-4)
$Al_xGa_{1-x}As$ ($0 \leqslant x \leqslant 0.45$)	$1.424 + 1.247x$ (d)	zb	$13.18 - 3.12x$		$4.07 - 1.1x$	$5.653 + 0.0078x$	$5.36 - 1.6x$	$6.4 - 1.2x$		Window layer for GaAs solar cells
($0.45 < x \leqslant 1$)	$1.9 + 0.125x + 0.143x^2$ (i)				$3.64 - 0.14x$					

* At 600 nm.

Table 2 The energy gap E_g, refractive index n and the electron affinity χ of transparent conducting semiconductors used as window layers in thin-film solar cells

Material	E_g (eV)	n	χ
CdS	2.42	2.5	4.5
ZnS	3.58	2.4	3.9
$Zn_{0.3}Cd_{0.7}S$	2.8		4.3
ZnO	3.3	2.02	4.35
In_2O_3:Sn	3.7–4.4		4.5
SnO_2:F	3.9–4.6		4.8

Table 3 The refractive index at 590 nm (2.1 eV) of the common materials used for antireflection coating. The full wavelength dependence of most of these substances can be found in references [27] and [28]

Material	n
MgF_2	1.38
SiO_2	1.46
Al_2O_3	1.76
Si_3N_4	2.05
Ta_2O_5	2.2
ZnS	2.36
SiO_x	1.8–1.9
TiO_2	2.62

$$E_g(T) = E_{g0} - \frac{\alpha T^2}{T + \beta} \tag{1}$$

where T is the absolute temperature and the parameters α and β are given in Table 4.

The current produced by solar cells is generated by optical transitions across the band gap. Two types of such transitions can be distinguished: direct transitions where the momentum of the resulting electron–hole pair is very close to zero, and indirect transitions where the resulting electron hole pair has a finite momentum. The latter transitions require the assistance of a phonon (quantum of lattice vibration). Thus, there are two types of semiconductors:

- ***Direct gap semiconductors*** where the top of the valence band and the bottom of the conduction band lie at the Γ point of the first Brillouin zone (i.e., at zero wave vector $\mathbf{k} = 0$).
- ***Indirect gap semiconductors*** where the minima of the conduction band (in general, more than one) lie at a another point of the first Brillouin zone, with a different value of the wave vector $\mathbf{k}$.

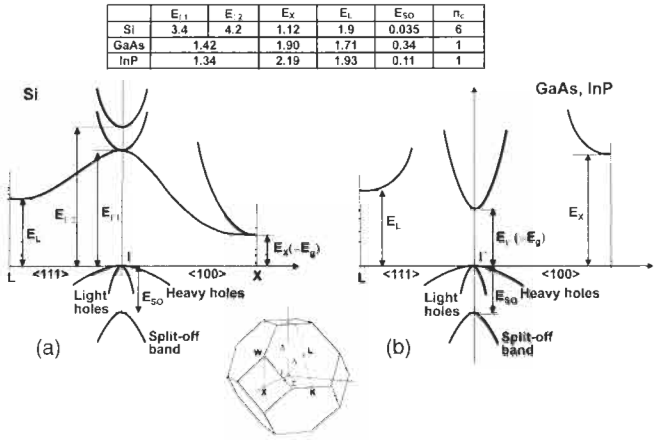

	$E_{\Gamma 1}$	$E_{\Gamma 2}$	E_X	E_L	E_{SO}	n_c
Si	3.4	4.2	1.12	1.9	0.035	6
GaAs	1.42		1.90	1.71	0.34	1
InP	1.34		2.19	1.93	0.11	1

Figure 1 The energy gaps in Si (a), and GaAs and InP (b) as functions of the wave vector $\mathbf{k}$*. The inset shows the Brillouin zone of the corresponding face-centred cubic crystal lattice.*

Table 4 The parameters E_{g0}, α and β in Equation (1). Sources of data: (a) Thurmond [11]; (b) Varshni [10]

	E_g ($T = 0$ K), eV	$\alpha \times 10^{-4}$, eV/K^2	β, K
Si (a)	1.17	4.730	636
GaAs (a)	1.52	5.405	204
InP (b)	1.42	4.906	327

The optical absorption in indirect-gap semiconductors is considerably weaker than in direct gap semiconductors, as shown in Figure 2 on the example of silicon and gallium arsenide.

3 Carrier Statistics in Semiconductors

In thermal equilibrium the temperature and electrochemical potential (the Fermi level, denoted by E_F) are constant throughout the device. The product of the electron concentration n and the hole concentration p is then independent of doping and obeys the mass action law

$$np = n_i^2 = \mathcal{N}_c \mathcal{N}_v \exp\left(-\frac{E_g}{k_B T}\right) \tag{2}$$

where k_B is the Boltzmann constant, n_i is the electron (or hole) concentration in the intrinsic semiconductor, and the effective densities of states $\mathcal{N}_c$ and $\mathcal{N}_v$ are given by

$$\mathcal{N}_c = 2\left(\frac{2\pi m_e k_B T}{h^2}\right)^{3/2} \qquad \mathcal{N}_v = 2\left(\frac{2\pi m_h k_B T}{h^2}\right)^{3/2} \tag{3}$$

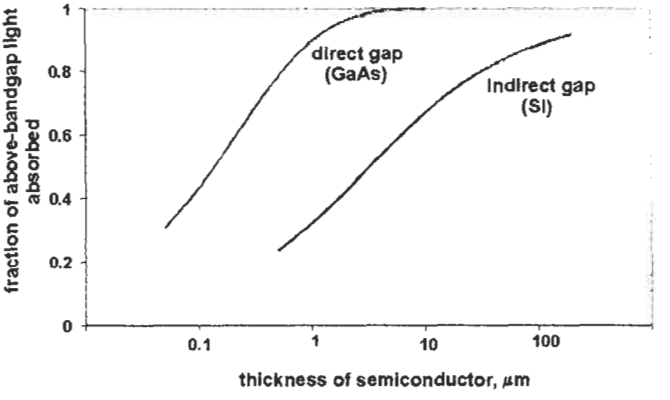

Figure 2 A comparison of the difference in strength of the optical absorption in direct and indirect semiconductors, illustrated on the examples of silicon and gallium arsenide.

Here, h is the Planck constant and m_e and m_h are the electron and hole density-of-states effective masses (see Table 6). In Equation (3), the effective mass m_e includes a factor which allows for several equivalent minima of the conduction band in indirect-gap semiconductors (see Figure 1).

Equation (2) does not hold for a solar cell in operation. Current flow as well as electron transitions between different bands and/or other quantum states are induced by differences and gradients of the electrochemical potentials, and temperature gradients may also exist. It is then usual to assign a quasi-Fermi level to each band which describes the appropriate type of carriers. Thus, electrons in the conduction band will be described by the quasi-Fermi level E_{Fn}, and holes by E_{Fp}. It is convenient to define also the appropriate potentials ϕ_n and ϕ_p by

$$\begin{aligned} E_{Fn} &= -q\phi_n \\ E_{Fp} &= -q\phi_p \end{aligned} \tag{4}$$

The use of quasi-Fermi levels to describe solar cell operation was already mentioned in Section 4.1 of Chapter IIa-1. The formalism leads to expressions for electron and hole concentrations which are summarised in Table 5.

4 The Transport Equations

The electron and hole current densities $\boldsymbol{J}_n$ and $\boldsymbol{J}_p$ are governed transport by the transport equations

$$\begin{aligned} \boldsymbol{J}_n &= q\mu_n n\boldsymbol{\mathcal{E}} + qD_n\nabla n \\ \boldsymbol{J}_p &= q\mu_p p\boldsymbol{\mathcal{E}} - qD_p\nabla p \end{aligned} \tag{5}$$

Table 5 Carrier concentration in degenerate and non-degenerate semiconductors. $F_{1/2}$ denotes the integral $F_{1/2}(z) = \frac{2}{\sqrt{\pi}} \int_0^\infty \frac{x^{1/2}}{1+exp(x-z)} dx$

	Non-degenerate semiconductors		General expressions
	In terms of the band parameters	In terms of the parameters of intrinsic semiconductor	
n	$\mathcal{N}_c exp\left(\frac{E_{Fn} - E_c}{k_B T}\right)$	$n_i exp\left\{\frac{q(\psi - \varphi_n)}{k_B T}\right\}$	$\mathcal{N}_c F_{1/2}\left(\frac{E_{Fn} - E_c}{k_B T}\right)$
p	$\mathcal{N}_v exp\left(\frac{E_v - E_{Fp}}{k_B T}\right)$	$n_i exp\left\{\frac{q(\varphi_p - \psi)}{k_B T}\right\}$	$\mathcal{N}_v F_{1/2}\left(\frac{E_v - E_{Fp}}{k_B T}\right)$

Table 6 The densities of states in the conduction and valence band ($\mathcal{N}_c$ and $\mathcal{N}_v$, respectively), the intrinsic carrier concentration n_i and the density-of-states effective masses m_e and m_h (all at 300 K) in Si, GaAs and InP. m_o denotes the free-electron mass. Data from references [20, 35]; intrinsic carrier concentration in Si from reference [12]

	$\mathcal{N}_c$ (cm^{-3})	$\mathcal{N}_v$ (cm^{-3})	n_i (cm^{-3})	m_e/m_o	m_h/m_o
Si	2.8×10^{19}	1.04×10^{19}	1.00×10^{10}	1.08	0.55
GaAs	4.7×10^{17}	7.0×10^{18}	1.79×10^{6}	0.063	0.53
InP	5.7×10^{17}	1.1×10^{19}	1.3×10^{7}	0.08	0.6

where n and p are the electron and hole the concentrations, μ_n and μ_p are the electron and hole mobilities, D_n and D_p are the electron and hole diffusion constants, and $\boldsymbol{\mathcal{E}}$ is the electric field. The first term in each equation is due to drift in the electric field $\boldsymbol{\mathcal{E}}$, and the second term corresponds to carrier diffusion. With the help of the quasi-Fermi levels, Equations (5) can be written as

$$\begin{aligned} \boldsymbol{J}_n &= -q\mu_n n \nabla \phi_n \\ \boldsymbol{J}_p &= -q\mu_p n \nabla \phi_p \end{aligned} \tag{6}$$

Equations (6) are valid for a semiconductor with a homogeneous composition but position-dependent dopant concentration is included. A generalisation to semiconductors with position-dependent band gap can be found, for example, in [13].

In a region where space charge exists (for example, in the junction), the *Poisson equation* is needed to link the electrostatic potential ψ with the charge density ρ:

$$\nabla \cdot \boldsymbol{\mathcal{E}} = \frac{\rho}{\varepsilon} \tag{7}$$

with

$$\rho = q(p - n + N_D - N_A) \tag{8}$$

$$\mathcal{E} = -\nabla \cdot \psi \tag{9}$$

where ε is the static dielectric constant of the semiconductor (see Table 1).

In non-degenerate semiconductors, the diffusion constants are related to mobilities by the *Einstein relations*

$$D_n = \frac{kT}{q}\mu_n; \qquad D_p = \frac{kT}{q}\mu_p \tag{10}$$

The generalisation of the Einstein relations to degenerate semiconductors is discussed, for example, in [14].

The conservation of electrons and holes is expressed by the *continuity equations*

$$\begin{aligned} \frac{\partial n}{\partial t} &= G - U + \frac{1}{q}\nabla \cdot \boldsymbol{J}_n \\ \frac{\partial p}{\partial t} &= G - U + \frac{1}{q}\nabla \cdot \boldsymbol{J}_p \end{aligned} \tag{11}$$

where G and U are the generation and recombination rates which may be different for electrons and holes if there are transitions into or from localised states.

5 Carrier Mobility

In weak fields, the drift mobilities in Equations (5) represent the ratio between the mean carrier velocity and the electric field. The mobilities – which are generally different for majority and minority carriers – depend on the concentration of charged impurities and on the temperature. For silicon, these empirical dependencies are generally expressed in the Caughey–Thomas form [15]:

$$\mu = \mu_{min} + \frac{\mu_0}{1 + \left(\dfrac{N}{N_{ref}}\right)^{\alpha}} \tag{12}$$

The values of the various constants for majority and minority carriers are given in Tables 7 and 8. A full model which includes the effects of lattice scattering, impurity scattering, carrier-carrier scattering and impurity clustering effects at high concentration is described in [16] where the reader can find further details.

In strong fields, the mobility of carriers accelerated in an electric field parallel to the current flow is reduced since the carrier velocity saturates. The field dependence of the mean velocity v (only quoted reliably for majority carriers) is given by

Table 7 The values of parameters in Equations (12) for majority-carrier mobility in silicon (from reference [17]; $T_n = T/300$)

	$\mu_{min} = AT_n^{-\beta}$		$\mu_0 = BT^{-\beta_2}$		$N_{ref} = CT_n^{\beta_3}$		$\alpha = DT_n^{-\beta_4}$	
	A	β_1	B	β_2	C	β_3	D	β_4
Electrons	88	0.57	7.4×10^8	2.33	1.26×10^{17}	2.4	0.88	0.146
Holes	54.3		1.36×10^8		2.35×10^{17}			

Table 8 The values of parameters in Equations (12) for minority-carrier mobility in silicon (from references [18, 19])

	μ_{min}	μ_0	N_{ref}	α
Electrons	232	1180	8×10^{16}	0.9
Holes	130	370	8×10^{17}	1.25

$$v = \frac{\mu_{lf}}{\left(1 + \left(\frac{\mu_{lf}\mathcal{E}}{v_{sat}}\right)^{\beta}\right)^{1/\beta}} \tag{13}$$

where μ_{lf} is the appropriate low field value of the mobility (Equation (12)), the parameter $\beta = 2$ for electrons and $\beta = 1$ for holes, and v_{sat} is the saturation velocity, identical for electrons and holes [20]:

$$v_{sat} = \frac{2.4 \times 10^7}{1 + 0.8e^{T/600}} \tag{14}$$

In gallium arsenide, the empirical fitting of the mobility data is of a more complex nature, and the reader is referred to the reference [21] for more information regarding the majority-carrier mobility. The temperature and dopant concentration dependences of the minority-carrier mobility are shown in Figures 3 and 4.

The electric field dependence of carrier mobility in GaAs is different from silicon as the velocity has an 'overshoot' which is normally modelled by the following equation [24]:

$$\mu_n = \frac{\mu_{lf}\mathcal{E} + v_{sat}(\mathcal{E}/\mathcal{E}_0)^{\beta}}{1 + (\mathcal{E}/\mathcal{E}_0)^{\beta}} \tag{15}$$

where μ_{lf} is the appropriate low-field mobility, $\mathcal{E}_0 = 4 \times 10^3$ V/cm, β equals 4 for electrons and 1 for holes, and v_{sat} is given by [25]

$$v_{sat} = 11.3 \times 10^6 - 1.2 \times 10^4 T \tag{16}$$

where T is the temperature in K.

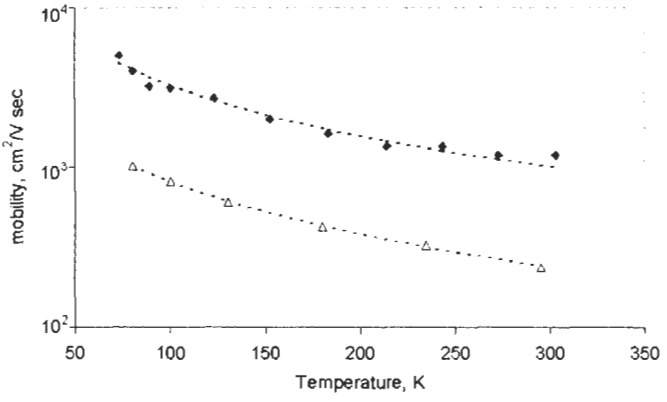

Figure 3 The temperature dependence of the minority-carrier mobility in GaAs. Full symbols: electron mobility in p-type GaAs ($N_A = 4 \times 10^{18}$ cm^{-3}); data from [22]. Empty symbols: hole mobility in n-type GaAs ($N_D = 1.8 \times 10^{18}$ cm^{-3}) [23]. The dashed lines show fits to the data with expressions

$$\mu_n = \frac{337\,100}{T} - 116; \qquad \mu_p = \frac{85\,980}{T} - 49.84;$$

where T is the temperature in K.

The majority carrier mobility in indium phosphide reported in reference [26] is shown in Figure 5.

6 Carrier Generation by Optical Absorption

6.1 Band-to-Band Transitions

The principal means of carrier generation in solar cells is the absorption of light. For a planar slab (Figure 6), a photon which enters the semiconductor generates $g(x)\ \delta x$ electron hole pairs in a thin layer at depth $x \rightarrow x + \delta x$. The generation function $g(x)$ is given by

$$g(x) = \alpha(\lambda) exp\{-\alpha(\lambda)x\} \tag{17}$$

where $\alpha(\lambda)$ is the absorption coefficient, shown in Figure 7 for a number of semiconductors with photovoltaic applications. The generation rate G per unit volume which appears in Equation (11) is related to the generation function g in Equation (17) by $G = g/A$, where A is the illuminated area of the sample.

A useful formula for the absorption coefficient of silicon is provided by the expression of Rajkanan et al. [29]:

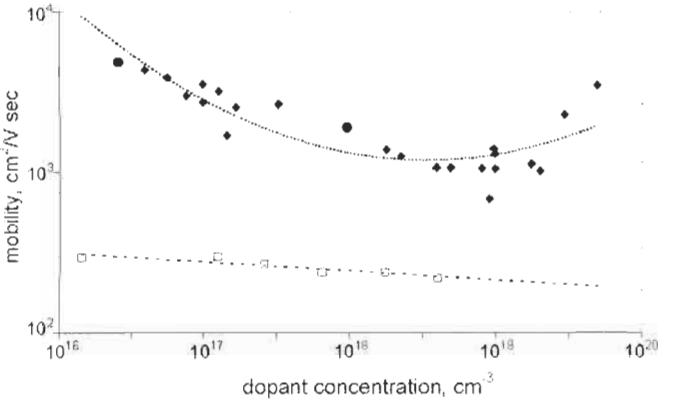

Figure 4 The dopant concentration dependence of the room-temperature minority-carrier mobility in GaAs. Full symbols: electron mobility in p-type GaAs; data from [21]. Empty symbols: hole mobility in n-type GaAs [23]. The dashed lines show fits to the data with the expressions

$$log\ \mu_n = 0.16(log\ N_A)^2 - 5.93 log\ N_A + 58$$
$$log\ \mu_p = -0.0575 log\ N_D + 3.416$$

where N_D *and* N_A *are the donor and acceptor concentrations in* cm^{-3}.

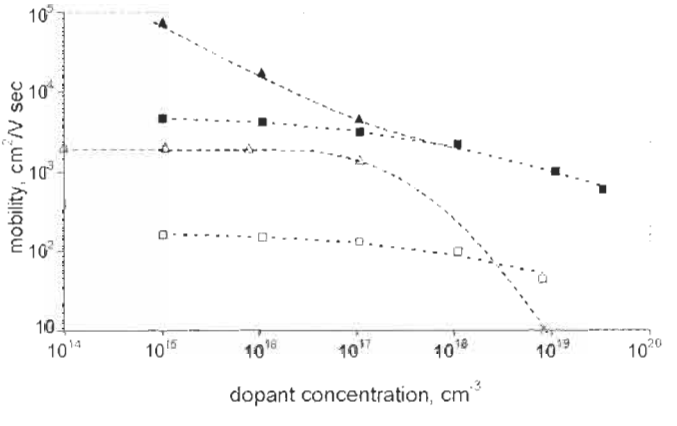

Figure 5 The majority-carrier mobilities in InP [26]. Full symbols correspond to electron mobility, empty symbols to hole mobility. Room temperature (300 K) data are shown by squares; data at 77 K by triangles. The room-temperature data were fitted with a Caughey–Thomas-type expression with parameters shown in Table 9.

$$\alpha(T) = \sum_{\substack{i=1,2 \\ j=1,2}} C_i A_j \left[\frac{\{h\nu - E_{gj}(T) + E_{pi}\}^2}{\{exp(E_{pi}kT) - 1\}} + \frac{\{h\nu - E_{gj}(T) - E_{pi}\}^2}{\{1 - exp(-E_{pi}kT)\}} \right] + A_d\{h\nu - E_{gd}(t)\}^{1/2} \tag{18}$$

Table 9 Parameters in Equation (12) which were used to fit the room-temperature electron and hole mobilities in InP

	μ_{min}	μ_0	N_{ref}	α
Electrons	0	4990	4.02×10^{17}	0.433
Holes		168	1.24×10^{18}	

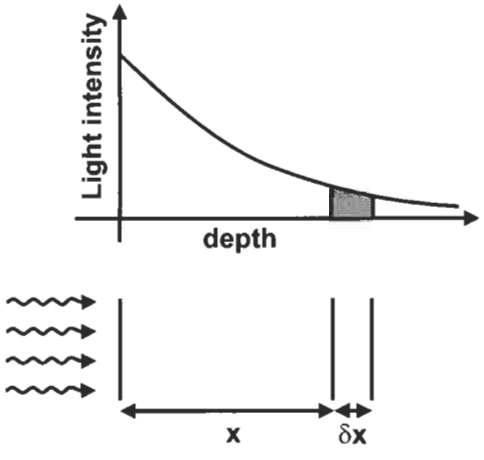

Figure 6 The geometry used to discuss the light absorption in semiconductors.

where $h\nu$ is the photon energy, $E_{g1}(0) = 1.1557$ eV, $E_{g2}(0) = 2.5$ eV and $E_{gd}(0) = 3.2$ eV are the two lowest indirect and the lowest direct band gap, respectively (used here as parameters to obtain a fit to the spectrum), $E_{p1} = 1.827 \times 10^{-2}$ eV and $E_{p2} = 5.773 \times 10^{-2}$ eV are the Debye frequencies of the transverse optical and transverse acoustic phonons, respectively, $C_1 = 5.5$, $C_2 = 4.0$, $A_1 = 3.231 \times 10^2$ cm^{-1} eV^{-2}, $A_2 = 7.237 \times 10^3$ cm^{-1} eV^{-2} and $A_1 = 1.052 \times 10^6$ cm^{-1} eV^{-2}. The temperature variation of the band gaps is described by Equation (1) where the original Varshni coefficients $\alpha = 7.021 \times 10^{-4}$, eV/K^2 and $\beta = 1108$ K are used for all three band gaps E_{g1}, E_{g2} and E_{gd}.

6.2 Free-Carrier Absorption

In regions with high-carrier concentration (due to doping or strong illumination, for example) photon absorption can also occur by electron transitions with initial and final states inside the same band. This free-carrier absorption does not generate electron–hole pairs and competes with the band-to-band transitions that produce the photogenerated current which were discussed above. Free carrier absorption might be significant in the case of photon energies near the band gap, and should not be included in the absorption coefficient α in front of the exponential in Equation (17). Figure 8 illustrates the different phenomena that occur near the band edge for high doping concentrations.

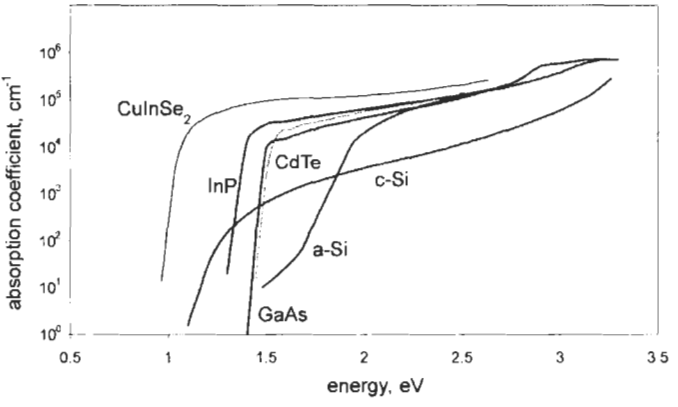

Figure 7 The absorption coefficients of the principal semiconductors used in the manufacture of solar cells. Full details of these and other semiconductors can be found in references [27] and [28]. Further details of silicon absorption are given in the text.

Table 10. The constants for the free carrier absorption coefficient in Equation (19)

	K_1	a	K_2	b
Si	2.6×10^{-27}	3	2.7×10^{-24}	2
GaAs	4×10^{-29}	3	–	–
InP	5×10^{-27}	2.5	–	–

Based on experimental data of [30] and [31], the PC1D model, for example, uses the following expression for the absorption coefficient due to free carrier absorption:

$$\alpha_{FC} = K_1 n \lambda^a + K_2 p \lambda^b \tag{19}$$

where λ is in nanometres and the empirically determined constants K_1, K_2, a, and b are given in Table 10.

7 Recombination

Recombination processes can be classified in a number of ways. Most texts distinguish between bulk and surface recombination, and between band-to-band recombination as opposed to transitions with the participation of defect levels within the band gap. Recombination processes can also be classified according to the medium which absorbs the energy of the recombining electron–hole pair: radiative recombination (associated with photon emission), or the two principal non-radiative mechanisms by Auger and multi-phonon transitions, where the recombination energy is absorbed by a free charge carrier or by lattice vibrations, respectively. An opposite process to Auger recombination (where an electron hole pair is generated rather than consumed) is called impact ionisation.

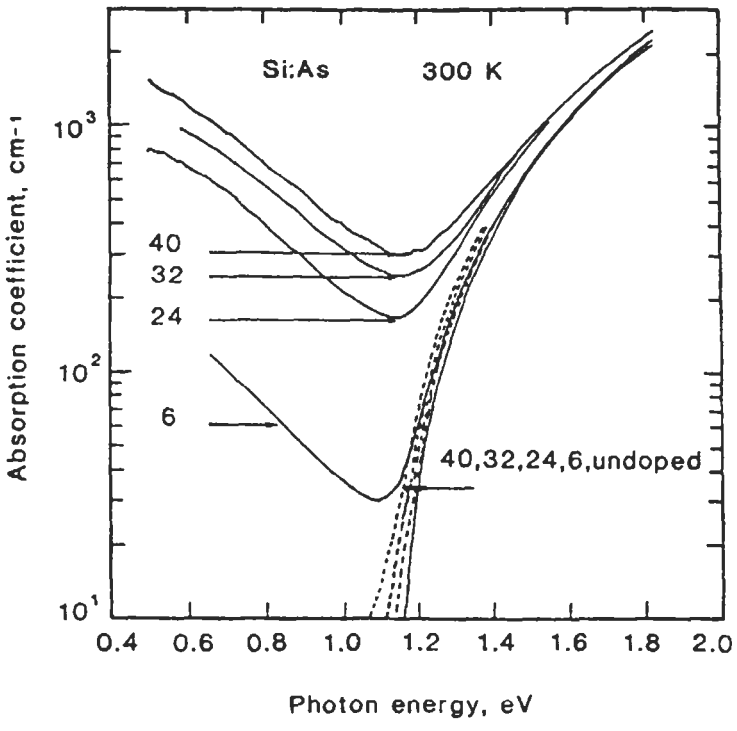

Figure 8 The effects observed near the absorption edge at high doping concentrations, illustrated here on the example of n-type silicon (from reference [30], as adapted by M.A. Green, Silicon Solar Cells – See Bibliography).

The following sections give a brief summary of the main recombination mechanisms with relevance to solar cell operation which are summarised schematically in Figure 9.

7.1 Bulk Recombination Processes

A detailed discussion of the variety of the bulk recombination mechanisms can be found in [32]. Here, we confine ourselves to a brief overview of the radiative, Auger and defect-assisted recombination processes which are most frequently encountered in practical operation of solar cells. These processes are depicted schematically in Figure 9 which also shows the notation used to describe the relevant parameters.

The rate of *band-to-band radiative recombination* can be written in the form

$$U_{rad} = B(np - n_i^2) \tag{20}$$

where the coefficient B is sometimes written as R/n_i^2. Radiative transitions between a free electron and a localised state within the band gap may also be important in certain situations, for example in novel concepts such as the

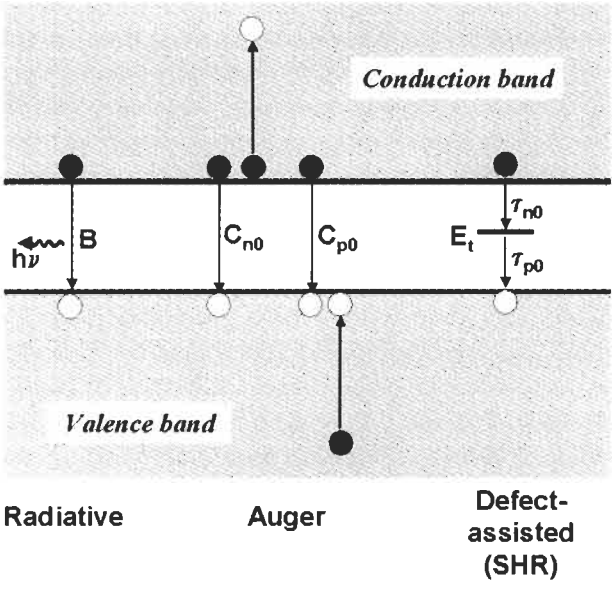

Figure 9 A schematic diagram of the principal recombination processes in semiconductors, and the notation for the rate constant adopted in this book. The direction of arrows indicates electron transitions.

impurity photovoltaic effect. The values of B for silicon, gallium arsenide and indium phosphide can be found in Table 11. In other situations, the radiative recombination coefficient B can be determined from optical absorption using the detailed balance argument due to van Roosbroeck and Shockley [33].

The rate of *band-to-band Auger recombination* can be written as

$$U_{Auger} = (C_{p0}p + C_{n0}n)(np - n_i^2) \tag{21}$$

where the first bracket gives the two, usually most important, Auger terms. Table 11 gives values of the coefficients C_{po} and C_{no} for Si, GaAs and InP.

The *recombination rate via defects* of concentration N_t with a level at energy E_t within the band gap is described by the Shockley–Read–Hall formula [36, 37]:

$$U_{SHR} = \frac{np - n_i^2}{\tau_p(n + n_1) + \tau_n(p + p_1)} \tag{22}$$

where

$$n_1 = n_i \, exp\left(\frac{E_t - E_i}{k_B T}\right) \qquad p_1 = p_i \, exp\left(\frac{E_t - E_i}{k_B T}\right) \tag{23}$$

and τ_n, τ_p are parameters, proportional to the defect concentration N_t, which are characteristic for the particular defect and energy level. At low injection, τ_n and τ_p assume the meaning of minority carrier lifetimes. With an appropriate

Table 11 The coefficients B of the radiative recombination rate (Equation (20)) and C_{n0} and C_{p0} of the Auger recombination rate (Equation (21)). Sources of data: (a) [34]; (b) [32]; (c) [35]; (d) [26]

	B, $cm^3 s^{-1}$	C_{n0}, $cm^6 s^{-1}$	C_{p0}, $cm^6 s^{-1}$
Si	1.8×10^{-15} (a)	2.8×10^{-31} (b)	0.99×10^{-31} (b)
GaAs	7.2×10^{-10} (a)	$\sim 10^{-30}$ (c)	
InP	6.25×10^{-10} (d)	$\sim 9 \times 10^{-31}$ (c)	

dependence on the doping concentration and temperature, τ_n and τ_p are also used extensively in material and device modelling (see reference [20], Section 1.5.3 and Section 7.3 below for a fuller discussion).

7.2 Surface Recombination

Surface recombination velocity is an important parameter which affects the dark saturation current and the quantum efficiency of solar cells. Similarly to dislocations and planar defects such as grain boundaries, surfaces (and interfaces in general) introduce band of electronic states in the band gap which can be ascribed to broken (or strained) bonds and impurities. A complete characterisation of surface recombination must also take into account the surface charge which may give rise to band bending. To achieve optimal operation, surface recombination is reduced by a passivating or window layer which prevents minority carriers from reaching the surface. Passivation of silicon surface by an oxide layer, or the deposition of a thin 'window' layer of GaAlAs on GaAs solar cells are just two examples of such practice.

For an oxidised silicon surface, surface recombination velocity is strongly dependent on the surface roughness, contamination, ambient gases used during oxidation and the annealing conditions. Under identical process parameters, however, one can identify trends in the dependence of the surface recombination velocity on the surface doping concentration. Cuevas et al. [38] proposed the following analytical relationship between surface recombination velocity and doping concentration:

$$S = 70 \text{ cm/s} \quad \text{for } N < 7 \times 10^{17} \text{cm}^{-3}$$

$$S = 70\left(\frac{N}{7 \times 10^{17}}\right) \quad \text{for } N > 7 \times 10^{17} \text{ cm}^{-3} \tag{24}$$

Equation (24) models several experimental results such as those reported in [39].

In gallium arsenide, the surface recombination velocity is very high (of the order of 10^6 cm/s). The deposition of a thin layer of GaAlAs, however, reduces the recombination velocity at the interface to 10–10^3 cm/s (see reference [40], p. 41). Coutts and Yamaguchi [41] quote the values of 10^3–2×10^4 cm/s and 1.5×10^5 cm/s for the surface recombination velocity in n- and p-type InP, respectively.

7.3 Minority-Carrier Lifetime

Under low injection – a regime of particular importance for solar cell operation – the majority-carrier concentration can be assumed excitation independent, and the effect of recombination can be discussed in terms of minority-carrier lifetime. In p-type material, for example, and the recombination rate can be written as

$$U = \frac{1}{\tau_n}(n - n_0) \tag{25}$$

where τ_n is the minority-carrier (electron) lifetime. An analogous equation can be written for the hole lifetime τ_p in n-type material. The inverse of the lifetime – the rate constant – is a sum of the different contributions to the lifetime:

$$\frac{1}{\tau} = \frac{1}{\tau_{rad}} + \frac{1}{\tau_{Auger}} + \frac{1}{\tau_{SRH}} \tag{26}$$

where τ stands for τ_n or τ_p, as appropriate. This additive nature of the recombination rate constant is also useful when discussing the radiation damage (see Section 8).

The effect of lifetime on transport properties by carrier diffusion can be discussed in terms of the diffusion length defined by

$$L = \sqrt{D\tau} \tag{27}$$

where D is the diffusion constant for the minority carriers in question. If, however, drift in electric field $\mathcal{E}$ is the dominant transport mechanism, it is appropriate to define the drift length as

$$\ell_n = \mathcal{E}\tau_n\mu_n; \qquad \ell_p = \mathcal{E}\tau_p\mu_p \tag{28}$$

for electrons and holes as minority carriers. This parameter plays an important role in the analysis of p–i–n junction solar cells (see Section 4.3 in Chapter IIa-1).

The wealth of available data for crystalline silicon has made it possible to arrive at a consensus as to the magnitude as well as the temperature and doping concentration dependence of the contributions (26) to minority carrier lifetime [42] The contribution to lifetime due to defects, when combined with recombination in intrinsic material, has been empirically observed to follow the equations

$$\begin{aligned} \frac{1}{\tau_{n,SRH}} &= \left(\frac{1}{2.5 \times 10^{-3}} + 3 \times 10^{-13} N_D\right)\left(\frac{300}{T}\right)^{1.77} \\ \frac{1}{\tau_{p,SRH}} &= \left(\frac{1}{2.5 \times 10^{-3}} + 11.76 \times 10^{-13} N_A\right)\left(\frac{300}{T}\right)^{0.57} \end{aligned} \tag{29}$$

where the first term in the brackets applies for recombination in intrinsic semiconductor. Similarly, the contribution to Equation (26) by Auger recombination can be described by the expressions

$$\begin{aligned}\frac{1}{\tau_{n,Auger}} &= 1.83 \times 10^{-31} p^2 \left(\frac{T}{300}\right)^{1.18} \\ \frac{1}{\tau_{p,Auger}} &= 2.78 \times 10^{-31} n^2 \left(\frac{T}{300}\right)^{0.72}\end{aligned} \tag{30}$$

Although the concept of minority carrier lifetime is most commonly applied to bulk recombination, a similar notion can be relevant for surface processes. For example, the effective lifetime observed of minority carriers with uniform concentration in a wafer can be written as

$$\frac{1}{\tau_{eff}} = \frac{1}{\tau_{SRH}} + \frac{2W}{A} S \tag{31}$$

where S is the value of the recombination velocity, W is the wafer thickness and A is the area of the sample.

8 Radiation Damage

Solar cells which operate on board of a satellite in an orbit which passes through the van Allen belts are subjected to fluxes of energetic electrons and protons trapped in the magnetic field of the earth and by fluxes of particles associated with high solar activity [43, 44] (see Chapter IIId-2). When slowed down in matter, most of the energy of the incident proton or electron is dissipated by interaction with the electron cloud. A relatively small fraction of this energy is dissipated in collisions with the nuclei, resulting in the formation of a lattice defect when energy in excess of a minimum threshold value is transferred to the nucleus [45, 46]. A proton with energy in excess of this threshold causes the most damage (typically, of the order of 10–100 atomic displacements) near the end of its range in the crystal. At high energy, on the other hand, a proton creates simple point defects, and the displacement rate decreases with increasing proton energy. In contrast, the displacement rate by electrons increases rapidly with energy and approaches a constant value at higher energies. Electron damage can usually be assumed to be uniform throughout the crystal.

Some defects which are thus created act as recombination centres and reduce the minority-carrier lifetime τ. Thus, it is the lifetime τ (or, equivalently, the diffusion length L) which is the principal quantity of concern when the cell is subjected to the particle radiation in space. Under low injection, the reduction of the diffusion length L is described by the Messenger–Spratt equation (see, for example, [47], p. 151):

$$\frac{1}{L^2} = \frac{1}{L_0^2} + K_L \phi \tag{32}$$

where L_o is the diffusion length in the unirradiated cell, ϕ is the particle fluence (integrated flux), and K_L is a (dimensionless) diffusion-length damage constant characteristic for the material and the type of irradiation.

The damage constant K_L generally depends on the type of dopant and, even in single-junction cells, a different damage constant should therefore be introduced for each region of the cell. Moreover, care should be exercised when dealing with low-energy protons (with energy of the order of 0.1–1 MeV) which are stopped near the surface and may create non-uniform damage near the junction. Figures 10 and 11 show the doping concentration and energy dependence of the damage constant K_L for electrons and protons in p-type silicon. Details of the damage constants for other materials can be found in references [43], [44], [48] and [49].

Damage constants are usually quoted for 1 MeV electrons, and converted to other energies and particles (such as protons) by using the concept of damage equivalent. Conversion tables are available in the Solar Radiation Handbooks which will suit most circumstances. Radiation damage equivalence works well when applied to uniform damage throughout the cell but care should be exercised in the case of non-uniform damage, for example, for low-frequency protons.

The reduction of the diffusion length describes usually the most significant part of the damage but changes in other parameters on irradiation also sometimes need to be considered. The dark diode current I_o may increase as a result of compensation by the radiation-induced defects. This, however, occurs

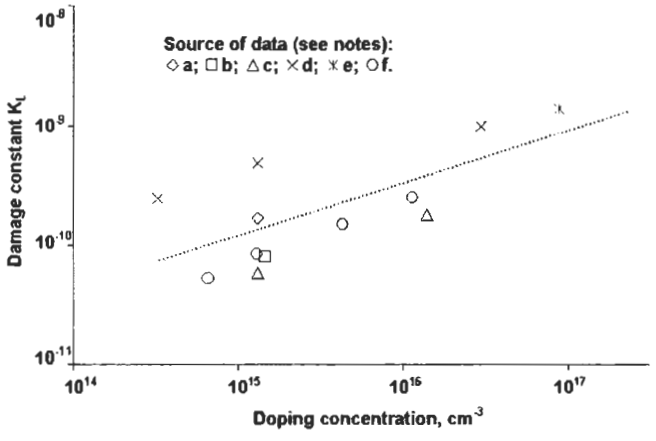

Figure 10 The radiation damage constant K_L for 1 MeV electrons in p-type silicon as a function of the dopant concentration. Source of data: (a) [50]; (b) [51]; (c) [52]; (d) [53]; (e) [54]; (f) [55]. The dashed line shows a fit to the data with the formula $K_L = 3.43 \times 10^{-17} N_A^{0.436}$, where N_A is the acceptor concentration in cm^{-3}.

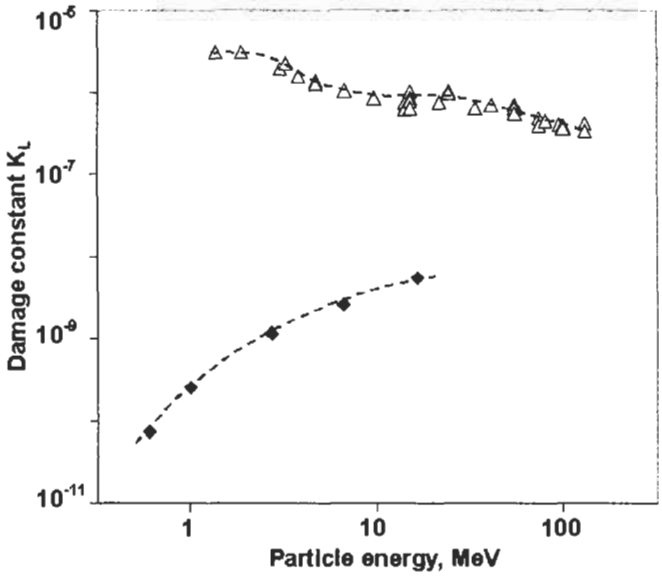

Figure 11 The energy dependence of the damage constant K_L *in 1 Ω cm p-type silicon by electron (full symbols, [55]) and protons (empty symbols, [56]).*

usually at a fluence orders of magnitude higher than that which degrades τ or L. Other source of degradation may be defects created in the depletion region, at the interfaces between different regions of the cell, or at the external surfaces.

9 Heavy Doping Effects

At high doping densities the picture of independent electrons interacting with isolated impurities becomes insufficient to describe the electron properties of semiconductors. As doping concentration increases, an impurity band is formed from the separate Coulomb wave functions located at individual doping impurities. This band gradually merges with the parent band and eventually gives rise to a tail of localised states. Electron–electron interaction becomes important, and the exchange and correlation energy terms have to be taken into account for a satisfactory description of the optical parameters and semiconductor device operation. An early overview of this multi-faceted physical problem can be found in [57].

In practical situations, this complex phenomenon is usually described in terms of band-gap narrowing, with a possible correction to effective masses and band anisotropy. Different manifestations of this effect are normally found by optical measurements (including absorption and low-temperature luminescence) and from data which pertain to device operation. Parameters which have been inferred from the latter are usually referred to as apparent band gap narrowing denoted by ΔE_g. For n-type material, for example,

$$\Delta E_g = kT \ln\left(\frac{p_0 N_D}{n_i^2}\right) \tag{33}$$

where p_0 is the minority-carrier (hole) concentration and N_D is the dopant (donor) concentration.

The experimental data obtained by various methods have been reviewed in [58] where the reader can find references to much of the earlier work. Jain et al. [59, 60] obtain a fit for band-gap narrowing in various materials using a relatively simple and physically transparent expression which, however, is less easy to apply to device modelling. Values for silicon which are now frequently used in semiconductor devices modelling are based on the work of Klaasen et al. [61] After reviewing the existing experimental data and correcting for the new mobility models and a new value for the intrinsic concentration, Klaasen et al. show that the apparent band gap narrowing of n- and p-type silicon can be accurately modelled by a single expression:

$$\Delta E_g(meV) = 6.92\left[\ln\left(\frac{N_{dop}}{1.3 \times 10^{17}}\right) + \sqrt{\left(\ln\frac{N_{dop}}{1.3 \times 10^{17}}\right)^2 + 0.5}\right] \tag{34}$$

where N_{dop} is the dopant concentration

For gallium arsenide, Lundstrom et al. [62] recommend the following formula based on fitting empirical data:

$$\Delta E_g = A N_{dop}^{1/3} + k_B T \ln\{F_{1/2}(E_F)\} - E_F$$

where E_F is the Fermi energy, the function $F_{1/2}$ is defined in the caption to Table 5, and

$$A = \begin{cases} 2.55 \times 10^{-8} eV & (p - GaAs) \\ 3.23 \times 10^{-8} eV & (n - GaAs) \end{cases}$$

10 Properties of Hydrogenated Amorphous Silicon[1]

In hydrogenated amorphous silicon (a-Si:H), the effective band gap between the conduction and valence band edges is around 1.8 eV but a thermal shrinking of the band gap with temperature has been reported [63]:

$$E_g = E_{go} - \gamma(T - T_o) \quad \gamma \approx 5k_B \tag{35}$$

[1] A rigorous description of the band structure and charge carrier transport in amorphous silicon is a complex matter well beyond the scope of this Handbook. This section gives a simplified picture in terms of effective parameters which has been used in success in semiconductor device modelling.

For statistical calculations, the corresponding effective densities of states can be approximated by $\mathcal{N}_c \approx \mathcal{N}_V \approx 4 \times 10^{19}\,\mathrm{cm}^{-3}$. In contrast to crystalline silicon, the conduction and valence bands show evidence of exponential tails of localised states within the band gap [64]:

$$\begin{aligned} D_{Ct} &= D_{CO}\, exp\left(\frac{E - E_C}{kT_C}\right) \quad D_{CO} \approx 0.8 \times 10^{21} cm^{-3} \quad kT_C \approx 30\ meV \\ D_{Vt} &= D_{VO}\, exp\left(\frac{E_V - E}{kT_V}\right) \quad D_{VO} \approx 1.1 \times 10^{21} cm^{-3} \quad kT_V \approx 50\ meV \end{aligned} \tag{36}$$

In addition, there is a Gaussian distribution of dangling bond states (states corresponding to non-saturated silicon bonds) around mid gap (Figure 12):

$$D_{DB} = \frac{N_{DB}}{\sqrt{2\pi w^2}}\, exp\left(-\frac{(E - E_{DB})^2}{2w^2}\right) \quad w \approx 100\ meV \quad E_{DB} = \frac{E_C + E_V}{2} \tag{37}$$

In device-quality intrinsic a-Si:H films, the density of dangling bonds N_{DB} ranges from 10^{15} to $10^{16}\,\mathrm{cm}^{-3}$.

The carrier mobility in the localised states (band tails and dangling bonds) is negligible. The accepted values for extended states in the valence and conduction band are μ_p = 0.5 cm^2/V-s and μ_n = 10 cm^2/V-s, respectively. As in other

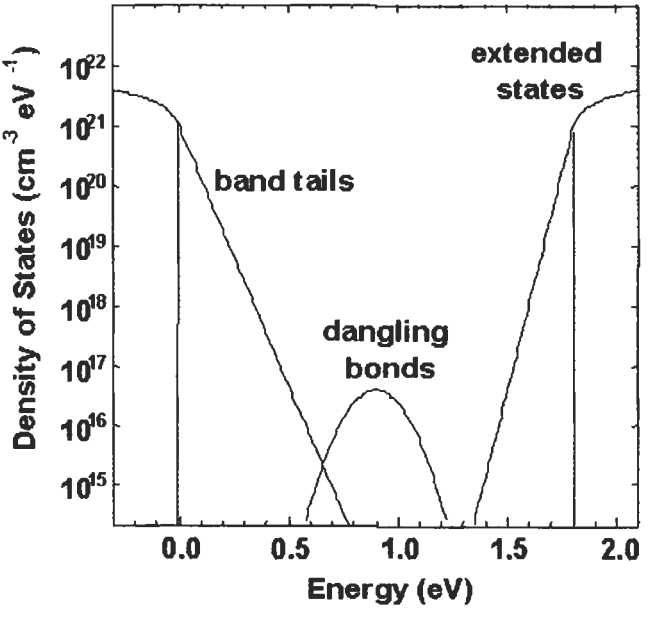

Figure 12 Typical density of states in a-Si:H. The states in the band tails behave as carrier traps whereas dangling bonds are recombination centres. Only those carriers in the extended states contribute to the electron transport [65].

semiconductors, the electron transport is given by the drift-diffusion equations (5) where the Einstein relations (10) apply.

The optical absorption coefficient shows three different zones (Figure 13):

- Band-to-band transitions (Tauc plot) for photon energies in excess of the band gap (> 1.8 eV).
- Transitions involving tail states (Urbach's front) for photon energies in the range 1.5–1.8 eV.
- Transitions involving dangling bonds for photon energies below 1.5 eV.

Once the optical absorption coefficient is known, the carrier generation can be easily calculated according to Equation (17) but it is important to note that only photons with energies in excess of the band gap yield useful electron-hole pairs for photovoltaic conversion.

Finally, the dominant recombination mechanism in intrinsic a-Si:H is given by the modified Shockley–Read–Hall equation, as applied to the amphoteric distribution of dangling bonds:

$$U = v_{th}\left(n\sigma_n^o + p\sigma_p^o\right)\frac{N_{DB}}{1 + \dfrac{p}{n}\dfrac{\sigma_p^o}{\sigma_n^+} + \dfrac{n}{p}\dfrac{\sigma_n^o}{\sigma_p^-}} \tag{38}$$

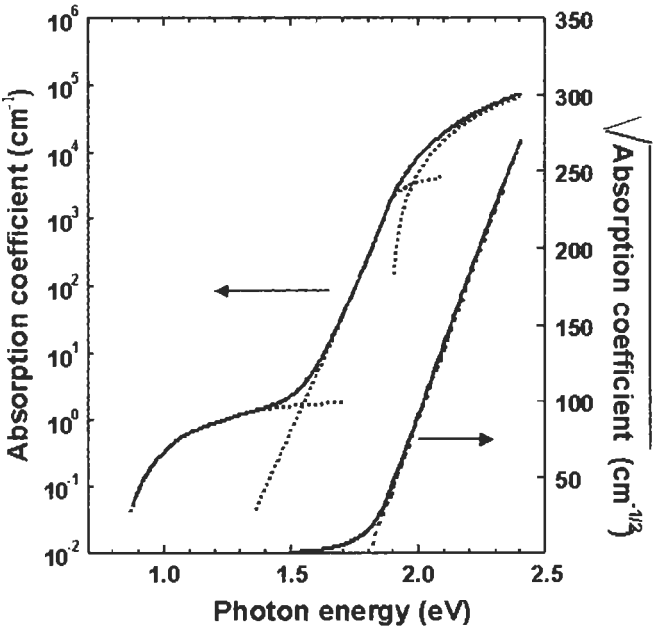

Figure 13 Typical optical absorption coefficient in a-Si:H. Three different regions can be observed corresponding to band-to-band absorption, transitions involving tail states and defect-associated absorption [65].

Table 12 Recombination parameters in amorphous silicon

v_{th} (cm · s^{-1})	σ_n^o (cm^2)	σ_p^o (cm^2)	σ_n^+ (cm^2)	σ_p^- (cm^2)
10^7	10^{-15}	$\sigma_n^o/3$	$50\sigma_n^o$	$50\sigma_p^o$

where the parameters are given in Table 12 [66].

Acknowledgements

We are grateful to J. Puigdollers and C. Voz for providing graphs of the absorption coefficient and density of states in amorphous silicon.

References

[1] Schwartz, R.J. 1990. The application of numerical techniques to the analysis and design of solar cells, in T.J. Coutts and J.D. Meakin, Eds., *Current Topics in Photovoltaics*, Vol. 4, p. 25.

[2] Selberherr, S. 1984. *Analysis and Simulation of Semiconductor Devices*, Springer, Vienna, New York.

[3] Brozel, M.R. and Stillman, G.E., Eds. 1996. *Properties of Gallium Arsenide* (3rd edition), IEE/INSPEC, Institution of Electrical Engineers, London.

[4] Pearsall, T.P., Ed. 2000. *Properties, Processing and Applications of Indium Phosphide*, INSPEC/IEE, London.

[5] Shur, M. 1990. *Physics of Semiconductor Devices*, Prentice Hall, Englewood Cliffs, NJ.

[6] Chu, T.L. 1988. Cadmium telluride solar cells, in T.J. Coutts and J.D. Meakin, Eds., *Current Topics in Photovoltaics*, Vol. 3, p. 235.

[7] Kazmerski, L.L. and Wagner, S. 1985. Cu-ternary chalcopyrite solar cells, in Coutts, T.J. and Meakin, J.D., Eds., *Current Topics in Photovoltaics*, Vol. 1, p. 41.

[8] *Handbook of Physics and Chemistry of Solids* (82nd edition), CRC Press, Boca Raton, 2001.

[9] Adachi, S. 1985. GaAs, AlAs and $Al_xGa_{1-x}As$: material parameters for use in research and device applications, *J. Appl. Phys.*, Vol. 58, p. R1.

[10] Varshni, Y.P. 1967. Temperature dependence of the energy gap in semiconductors, *Physica*, Vol. 34, p. 149.

[11] Thurmond, C.D. 1975. The standard thermodynamic functions for the formation of electrons and holes in Ge, Si, GaAs and GaP, *J. Electrochem. Soc.*, Vol. 122, p. 1133.

[12] Sproul A.B. and Green, M.A. 1993. Intrinsic carrier concentration and minority-carrier mobility of silicon from 77-K to 300-K, *J. Appl. Phys.*, Vol. 73, pp. 1214–1225.

[13] Marshak A.H. and van Vliet, K.M. 1978. Electrical currents in solids with position dependent band structure, *Solid-State Electron.*, Vol. 21, p. 417.

[14] Smith, R.R. 1978. *Semiconductors* (2nd edition), Cambridge University Press, Cambridge.

[15] Caughey D.M. and Thomas, R.E. 1967. Carrier mobilities in silicon empirically related to doping and field, *Proc. IEEE*, Vol. 55, p. 2192.

[16] Klaassen, D.B.M. 1992. A unified mobility model for device simulation – I. Model equations and concentration dependence, *Solid-State Electron.*, Vol. 35, pp. 953–959.

[17] Arora, N.D., Hauser, T.R. and Roulston, D.J. 1982. Electron and hole mobilities in silicon as a function of concentration and temperature. *IEEE Trans. Electron Devices*, Vol. ED-29, p. 292.

[18] Swirhun, S.E., Kwark Y.-H. and Swanson, R.M. 1986. Measurement of electron lifetime, electron mobility and band-dap narrowing in heavily doped p-type silicon, *IEDM'86*, pp. 24–27.

[19] del Alamo, J., Swirhun, S. and Swanson, R.M. 1985. Simultaneous measurement of hole lifetime, hole mobility and band-gap narrowing in heavily doped n-type silicon, *IEDM'85*, pp. 290–293.

[20] Sze, S.M. 1981. *Physics of Semiconductor Devices* (2nd edition), John Wiley & Sons, New York.

[21] Lancefield, D. 1996. Electron mobility in GaAs: overview, in Brozel, M.R. and Stillman, G.E., Eds., *Properties of Gallium Arsenide* (3rd edition), IEE/INSPEC, Institution of Electrical Engineers, London, p. 41.

[22] Harmon, E.S., Lovejoy, M.L., Lundstrom M.S. and Melloch, M.R. 1996. Minority electron mobility in doped GaAs, in Brozel, M.R. and Stillman, G.E., Eds., *Properties of Gallium Arsenide* (3rd edition), IEE/INSPEC, Institution of Electrical Engineers, London, p. 81.

[23] Lovejoy, M.L., Melloch, M.R. and Lundstrom, M.S. 1996. Minority hole mobility in GaAs, in Brozel, M.R. and Stillman, G.E., Eds., *Properties of Gallium Arsenide* (3rd edition), IEE/INSPEC, Institution of Electrical Engineers, London, p. 123.

[24] Barnes, J.J., Lomax R.J. and Haddad, G.I. 1976. Finite element simulation of GaAs MESFET's with lateral doping profiles and submicron gates, *IEEE Trans. Electron Devices*, Vol. ED-23, p. 1042.

[25] Littlejohn, M.A., Hauser, J.R. and Glisson, T.H. 1977. Velocity-field characteristics of GaAs with $\Gamma_6^c - L_6^c - X_6^c$ ordering, *J. Appl. Phys.*, Vol. 48, p. 4587.

[26] Ahrenkiel, R.K. 2000. Minority carrier lifetime in InP, in T.P. Pearsall, Ed., *Properties, Processing and Applications of Indium Phosphide*, INSPEC/IEE, London.

[27] Palik, E.D., Ed., 1985. *Handbook of Optical Constants of Solids*, Academic Press Handbook Series, Orlando.

[28] Palik, E.D., Ed., 1991. *Handbook of Optical Constants of Solids II*, Academic Press, San Diego.

[29] Rajkanan, K., Singh, R., and Shewchun, J. 1979. Absorption coefficient of silicon for solar cell calculations, *Solid-State Electron.*, Vol. 22, p. 793.

[30] Schmid, P.E. 1981. Optical absorption in heavily doped silicon, *Phys. Rev.*, Vol. B23, p. 5531.

[31] Fan, H.Y. 1967. In R.K. Willardson and A.C. Beer, Eds., *Semiconductors and Semimetals*, Vol. 3, Academic Press, p. 409.

[32] Landsberg, P.T. 1991. *Recombination in Semiconductors*, Cambridge University Press.

[33] van Roosbroeck, W. and Shockley, W. 1954. Photon-radiative recombination of electrons and holes in germanium, *Phys. Rev.*, Vol. 94, p. 1558.

[34] Pilkuhn, M.H., Light emitting diodes, in Moss, T.S., Ed., Vol. 4, *Handbook of Semiconductors*, North Holland, p. 539.

[35] Levinstein, M., Rumyantsev, S. and Shur, M., Eds., 1996, 1999. *Handbook Series on Semiconductor Parameters*, Vols. 1 and 2, World Scientific, London. See also http://www.ioffe.rssi.ru/SVA/NSM/Semicond/.

[36] Shockley, W. and Read, W.T. 1952. Statistics of the recombination of holes and electrons, *Phys. Rev.*, Vol. 87, p. 835.

[37] Hall, R.N. 1952. Electron hole recombination in germanium, *Phys. Rev.*, Vol. 87, p. 387.

[38] Cuevas, A., Giroult-Matlakowski, G., Basore, P.A., du Bois C., and King, R. 1994. Extraction of the surface recombination velocity of passivated phosphorus doped emitters, *Proc. 1st World Conference on Photovoltaic Energy Conversion*, Hawaii, pp. 1446–1449.

[39] King, R.R., Sinton, R.A. and Swanson, R.M. 1990. Studies of diffused emitters: saturation current, surface recombination velocity and quantum efficiency, *IEEE Trans. Electron Devices*, Vol. ED-37, p. 365.

[40] Andreev, V.M., Grilikhes, V.A. and Rumyantsev, V.D. 1997. *Photovoltaic Conversion of Concentrated Sunlight*, Wiley, Chichester.

[41] Coutts, T.J. and Yamaguchi, M. 1988. Indium phosphide based solar cells: a critical review of their fabrication, performance and operation, in T.J. Coutts and J.D. Meakin, Eds., *Current Topics in Photovoltaics*, Vol. 3, p. 79.

[42] Klaassen, D.B.M. 1992. A unified mobility model for device simulation – II. Temperature dependence of carrier mobility and lifetime, *Solid-State Electron.*, Vol. 35, p. 961.

[43] Tada, H.Y., Carter, J.R., Anspaugh B.E. and Downing, R.G. 1982. *Solar-Cell Radiation Handbook*, JPL Publication 82-69, Jet Propulsion Laboratory, California Institute of Technology, Pasadena, CA.

[44] Anspaugh, B.E. 1996. *GaAs Solar Cell Radiation Handbook*, JPL Publication 96-9, Jet Propulsion Laboratory, California Institute of Technology, Pasadena, CA.

[45] Kinchin, G.H. and Pease, R.S. 1955. The displacement of atoms in solids by radiation, *Rep. Prog. Phys.*, Vol. 18, p. 1.

[46] Seitz, F. and Koehler, J.S. 1956. Displacement of atoms during irradiation, *Solid State Physics*, Vol. 2, p. 307.

[47] Hovel, H.J. 1975. Semiconductor solar cells, in R.K. Willardson and A.C. Beer, Eds., *Semiconductors and Semimetals*, Vol. 11, Academic Press, New York.

[48] Markvart, T. 1990. Radiation damage in solar cells, *J. Materials Science: Materials in Electronics*, Vol. 1, p. 1.
[49] Yamaguchi, M. and Ando, K. 1988. Mechanism for radiation resistance of InP solar cells, *J. Appl. Phys.*, Vol. 63, p. 5555.
[50] Smits, F.M. 1963. *IEEE Trans. Nucl. Sci.*, Vol. NS-10, p. 88.
[51] Meulenberg, A. and Treble, F.C. 1973. Damage in silicon solar cells from 2 to 155 MeV protons, *Proc. 10th IEEE Photovoltaic Specialists Conf.*, Palo Alto, p. 359.
[52] Rosenzweig, W. 1962. Diffusion length measurement by means of ionizing radiation, *Bell. Syst. Tech. J.*, Vol. 41, p. 1573–1588.
[53] Wilsey, N.D. 1972. *Proc. 9th IEEE Photovoltaic Specialists Conf.*, Silver Springs, p. 338.
[54] Minahan, J.A. and Green, M.J. 1985. *Proc. 18th IEEE Photovoltaic Specialists Conf.*, p. 350.
[55] Downing, R.G, Carter, J.R. Jr. and Denney, J.M. 1964. The energy dependence of electron damage in silicon, *Proc. 4th IEEE Photovoltaic Specialists Conf.*, Vol. 1, p. A-5-1.
[56] Rosenzweig, W., Smits, F.M., and Brown, W.L. 1964. Energy dependence of proton irradiation damage in silicon, *J. Appl. Phys.*, Vol. 35, p. 2707.
[57] Keyes, R.W. 1977. The energy gap of impure silicon, *Comm. Solid State Phys.*, Vol. 7(6), p. 149.
[58] Wagner, J. and delAlamo, J.A. 1988. Band-gap narrowing in heavily doped silicon: a comparison of optical and electrical data, *J. Appl. Phys.*, Vol. 63, p. 425.
[59] Jain, S.C. and Roulston, D.J. 1991. A simple expression for bandgap narrowing in heavily doped Si, Ge, GaAs and Ge_xSi_{1-x} strained layers, *Solid-State Electron.*, Vol. 34, p. 453.
[60] Jain, S.C., McGregor, J.M., Roulston D.J. and Balk, P. 1992. Modified simple expression for bandgap narrowing in n-type GaAs, *Solid-State Electron.*, Vol. 35, p. 639.
[61] Klaassen, D.B.M., Slotboom, J.W and de Graaf, H.C. 1992. Unified apparent bandgap narrowing in n and p-type silicon, *Solid-State Electron.*, Vol. 35, p. 125.
[62] Lundstrom, M.S., Harmon, E.S. and Melloch, M.R. 1996. Effective bandgap narrowing in doped GaAs, in Brozel, M.R. and Stillman, G.E., Eds., *Properties of Gallium Arsenide* (3rd edition), IEE/INSPEC, Institution of Electrical Engineers, London, p. 186.
[63] Tsang, C. and Street, R.A. 1979. *Phys. Rev.*, Vol. B19, p. 3027.
[64] Fritzsche, H., Ed. 1989. *Amorphous Silicon and Related Materials*. University of Chicago.
[65] Puigdollers, J. and Voz, C., personal communication.
[66] Street, R.A. 1991. *Hydrogenated Amorphous Silicon*. Cambridge University Press.

Ideal Efficiencies

Peter T. Landsberg, Faculty of Mathematical Studies,
University of Southampton, UK
Tom Markvart, School of Engineering Sciences,
University of Southampton, UK

1 Introduction

In this chapter we deal with the simplest ideas which have been used in the past to attain an understanding of solar cell efficiencies from a theoretical point of view. The first and most obvious attack on this problem is to use thermodynamics, and we offer four such estimates in Section 2. Only the first of these is the famous Carnot efficiency. The other three demonstrate that one has more possibilities even within the framework of thermodynamics. To make progress, however, one has to introduce at least one solid-state characteristic and the obvious one is the energy gap E_g. That this represents an advance in the direction of a more realistic model is obvious, but it is also indicated by the fact that the efficiency now calculated is lower than the (unrealistically high) thermodynamic efficiencies (Section 3). In order to get closer to reality we introduce in Section 4 the fact that the radiation is effectively reduced from the normal black-body value (Equation (6)) owing to the finite size of the solar disc. This still leaves important special design features such as the number of series-connected tandem cells and higher order impact ionisation, and these are noted in Section 5.

2 Thermodynamic Efficiencies

The formulae for ideal efficiencies of solar cells are simplest when based on purely thermodynamic arguments. We here offer four of these; they involve only (absolute) temperatures:

- T_a, temperature of the surroundings (or the ambient),
- T_s, temperature of the pump (i.e. the sun),
- T_c, temperature of the actual cell which converts the incoming radiation into electricity.

From these temperatures we form the following efficiencies [1]:

$$\eta_C \equiv 1 - T_a/T_s, \text{ the Carnot efficiency} \tag{1}$$

$$\eta_{CA} \equiv 1 - (T_a/T_s)^{\frac{1}{2}}, \text{ the Curzon–Ahlborn efficiency} \tag{2}$$

$$\eta_L \equiv 1 - (4/3)(T_a/T_s) + (1/3)(T_a/T_s)^4, \text{ the Landsberg efficiency} \tag{3}$$

$$\eta_{PT} = \left[1 - (T_c/T_s)^4\right]\,[1 - T_a/T_c], \text{ the photo-thermal efficiency due to Müser} \tag{4}$$

In the latter efficiency the cell temperature is determined by the quintic equation

$$4T_c^5 - 3T_aT_c^4 - T_aT_s^4 = 0 \tag{5}$$

The names associated with these efficiencies are not historically strictly correct: for example, in Equations (2) and (3) other authors have played a significant part.

Figure1 [1] shows curves of the four efficiencies which all start at unity, when $T_a/T_s \equiv 0$, and they all end at zero, when $T_a = T_s$. No efficiency ever beats the Carnot efficiency, of course, in accordance with the rules of thermodynamics. Values near T_s = 5760–5770 K seem to give the best agreement with the observed solar spectrum and the total energy received on Earth but a less accurate but more convenient value of T_s = 6000 K is also commonly used. Using the latter value of T_s and T_a = 300 K as the temperature for the Earth, one finds

$$\eta_C = 95\%, \quad \eta_{CA} = 77.6\%, \quad \eta_L = 93.3\%, \quad \eta_{PT} = 85\%$$

If $T_s = T_a = T_c$ one has in effect an equilibrium situation, so that the theoretical efficiencies are expected to vanish.

The above thermodynamic efficiencies utilise merely temperatures, and they lie well above experimental results. One needs an energy gap (E_g) as well to take us from pure thermodynamics to solid-state physics. Incident photons can excite electrons across this gap, thus enabling the solar cell to produce an electric current as the electrons drop back again. The thermodynamic results presented earlier, on the other hand, are obtained simply by considering energy and entropy fluxes.

3 Efficiencies in Terms of Energies

In order to proceed we need next an expression for the number of photons in black-body radiation with an energy in excess of the energy gap, E_g say, so that they can excite electrons across the gap. At black-body temperature T_s the number of photons incident on unit area in unit time is given by standard theory as an integral over the photon energy [2]:

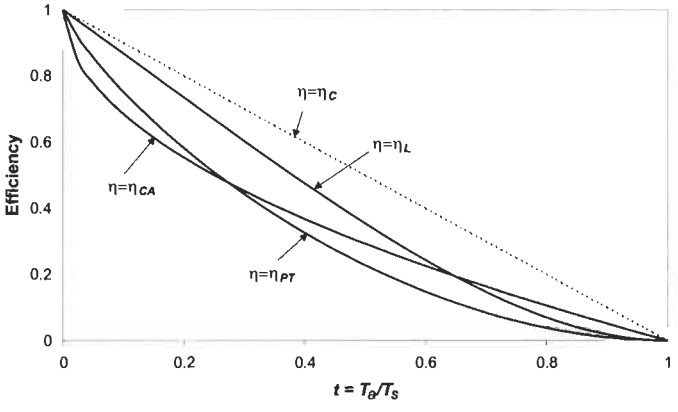

Figure 1 The efficiencies (1)–(4) as functions of T_a/T_s.

$$\Phi(E_g, T_s) = \frac{2\pi k^3}{h^3 c^2} T_s^3 \int_{E_g/kT_s}^{\infty} \frac{x^2 dx}{e^x - 1} \tag{6}$$

Now suppose that each of these photons contributes only an energy equal to the energy gap to the output of the device, i.e. a quantity proportional to

$$x_g \int_{x_g}^{\infty} \frac{x^2 dx}{e^x - 1} \quad (x_g \equiv E_g/kT_s) \tag{7}$$

To obtain the efficiency η of energy conversion we must divide this quantity by the whole energy which is in principle available from the radiation:

$$\eta = x_g \int_{x_G}^{\infty} \frac{x^2 dx}{e^x - 1} \Big/ \int_0^{\infty} \frac{x^3 dx}{e^x - 1} \tag{8}$$

Equation (8) gives the first of the Shockley–Queisser estimates for the limiting efficiency of a solar cell, the *ultimate efficiency* (see Figure 5). The argument neglects recombination in the semiconductor device, even radiative recombination which is always present (a substance which absorbs radiation can always emit it!). It is also based on the black-body photon flux (Equation (6)) rather than on a more realistic spectrum incident on the Earth.

We shall return to these points in Section 4, but first a brief discussion of Equation (8) is in order. There is a maximum value of η for some energy gap which may be seen by noting that $\eta = 0$ for both $x_g = 0$ and for x_g very large. So there is a maximum efficiency between these values. Differentiating η with respect to x_g and equating to zero, the condition for a maximum is

$x_g = x_{g\,opt} = 2.17$, corresponding to $\eta = 44\%$.

This is still higher than most experimental efficiencies, but the beauty of it is that it is a rather general result which assumes merely properties of black-body radiation.

Let $f(x)$ be a generalised photon distribution function; then a generalised efficiency can be defined by

$$\eta = \frac{x_g \int_{x_g}^{\infty} f(x)dx}{\int_0^{\infty} x f(x)dx}. \tag{9}$$

The maximum efficiency with respect to x_g is then given by

$$x_{gopt} f(x_{gopt}) = \int_{x_{gopt}}^{\infty} f(x)dx \tag{10}$$

This is rather general and will serve also when the photon distribution departs from the black-body forms, and even for radiation in different numbers of dimensions.

4 Efficiencies using the Shockley Solar Cell Equation

A further step in finding the appropriate efficiency limits for single-junction solar cells can be made by estimating the relevant terms in the Shockley ideal solar cell equation (Equation (1) in Chapter IIa-1). To this end, further remarks must be made about the solar spectrum and solar energy incident on the Earth's surface. The ultimate efficiency, discussed in Section 3, was based on the black-body photon flux (Equation (6)), a rigorous thermodynamic quantity but not a very good estimate of the solar spectrum as seen on Earth. By virtue of the large distance between the Sun and the Earth, the radiative energy incident on the Earth's surface is less than that of Equation (6), by a factor f_ω which describes the size of the solar disk (of solid angle ω_S) as perceived from the Earth:

$$f_\omega = \left(\frac{R_S}{R_{SE}}\right)^2 = \frac{\omega_S}{\pi} \tag{11}$$

where R_S is the radius of the Sun (696×10^3 km), and R_{SE} is the mean distance between the Sun and the Earth (149.6×10^6 km), giving $\omega_S = 6.85 \times 10^{-5}$ sterad and $f_\omega = 2.18 \times 10^{-5}$. The resulting spectrum is shown in Figure 2 alongside the standard terrestrial AM1.5 spectrum (a further discussion of the spectra that are used for solar cell measurements in practice can be found in Chapter IV-1 which also shows the extraterrestrial spectrum AM0).

The maximum value of the photogenerated current I_{ph} now follows if we assume that one absorbed photon contributes exactly one electron to the current in the external circuit:

$$I_{ph} = A\, q\, f_\omega \Phi(E_g, T_S) \tag{12}$$

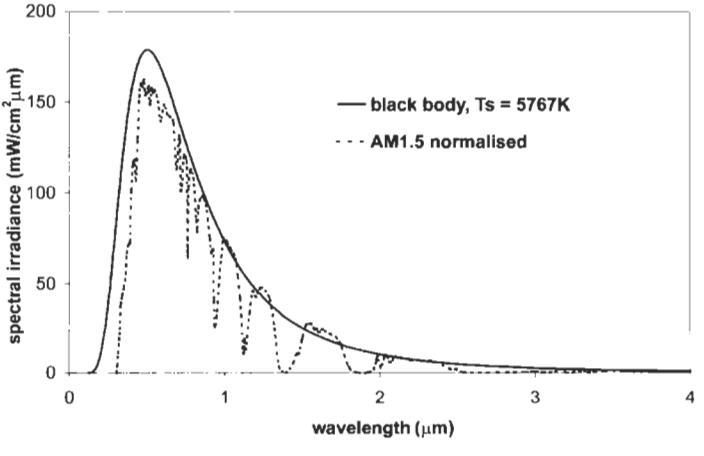

Figure 2 The black-body spectrum of solar radiation and the AM1.5 spectrum, normalised to total irradiance 1 kW/m², which is used for the calibration of terrestrial cells and modules.

where A is the illuminated area of the solar cell and q is the electron charge. The maximum photogenerated current density $J_{ph} = I_{ph}/A$ that can be produced by a solar cell with band gap E_g is shown in Figure 3. To allow a comparison with photocurrents measured in actual devices, Figure 3 is plotted for the AM1.5 solar spectrum which used for calibration of terrestrial solar cells, rather than for the black body spectrum used in Section 3.

The open circuit voltage V_{oc} can now be obtained using the photogenerated current I_{ph} (Equation (12)) and the (dark) saturation current I_o which appears in the ideal solar cell equation:

$$V_{oc} = \frac{kT}{q} \ln\left(1 + \frac{I_{ph}}{I_o}\right) \tag{13}$$

The current I_o can be obtained by a similar argument as the photogenerated current I_{ph} since, as argued by Shockley and Queisser, it can be equated to the black-body photon flux at the cell temperature T_c (in what follows, the cell temperature T_c will be assumed to be equal to the ambient temperature T_a):

$$I_0 = A\, q\, f_0 \Phi(E_g, T_a) \tag{14}$$

where the coefficient f_0 has been inserted to describe correctly the total area $f_0 A$ exposed to the ambient photon flux. Various values of f_0 (some dependent on the refractive index **n** of the cell material) can be found, appropriate for different device structures and geometries. The usual value is $f_0 = 2$, as suggested by Shockley and Queisser [2], since this radiation is incident through the two (front and rear) surfaces of the cell. A similar argument for a spherical solar cell yields an effective value $f_0 = 4$ [3]. Henry [4] gives $f_0 = 1 + \mathbf{n}^2$ for a cell grown on a semiconductor substrate but the value $f_0 = 1$ is also sometimes used (see, for

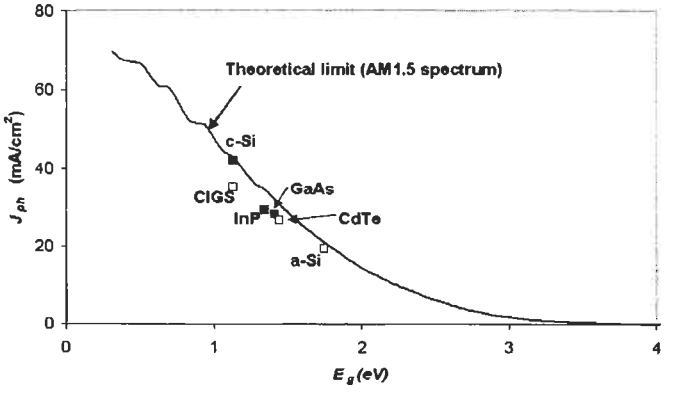

Figure 3. The theoretical limit on photogenerated current, compared with the best measured values. The curve is obtained by replacing the product $f_\omega \Phi(E_g, T_S)$ *in Equation (12) by the appropriate AM1.5 photon flux. Full symbols correspond to crystalline materials, open symbols to thin films.*

example, [5]). Green [6] gives a semi-empirical expression for the dark saturation current density $J_o = I_0/A$:

$$J_0 \text{ (in Amps/cm}^2) = 1.5 \times 10^5 \, exp\left(-\frac{E_g}{kT_a}\right) \tag{15}$$

An approximate analytical method for estimating V_{oc} can also be useful, particularly as it stresses the thermodynamic origin of V_{oc}. Indeed, it can be shown [7] that, near the open circuit, the solar cell behaves as an ideal thermodynamic engine with Carnot efficiency $(1 - T_c/T_s)$. Ruppel and Würfel [3] and Araùjo [8] show that V_{oc} can be approximated to a reasonable accuracy by the expression

$$V_{oc} = \frac{E_g}{q}\left(1 - \frac{T_c}{T_s}\right) + \frac{kT}{q}\ln\frac{f_\omega}{f_0} + \frac{kT_c}{q}\ln\frac{T_s}{T_c} \tag{16}$$

which depicts the dependence of V_{oc} on the band gap E_g and on the cell temperature T_c. Figure 4 compares this theoretical values for the open circuit voltage with data for the best solar cells to-date from different materials.

Using now an expression for the fill factor (defined by Equation (3) in Chapter IIa-1), one readily obtains a theoretical estimate for the efficiency. Slightly different results may be encountered, principally by virtue of the different ways one can estimate the current and the voltage. Figure 5 shows the best-known result, the celebrated Shockley–Queisser ideal efficiency limit [2]. Shockley and Queisser call this limit the *nominal efficiency*, to be compared with the *ultimate efficiency* which is discussed in Section 3. Figure 5 shows two such curves: one labelled 'one-sun' corresponds to the AM0 solar intensity, as observed outside the Earth's atmosphere. A second curve, labelled 'maximum concentration'

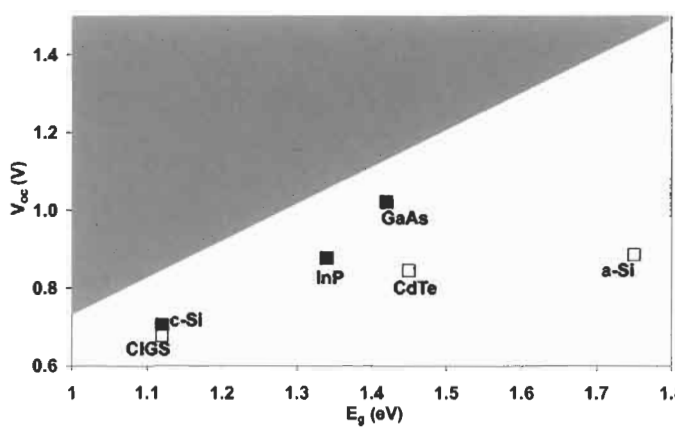

Figure 4 The theoretical Shockley–Queisser limit on open circuit voltage: values exceeding this limit lie in the shaded area of the graph. Line corresponding to Equation (16) appears as identical to within the accuracy of this graph. Full symbols correspond to crystalline materials, open symbols to thin films.

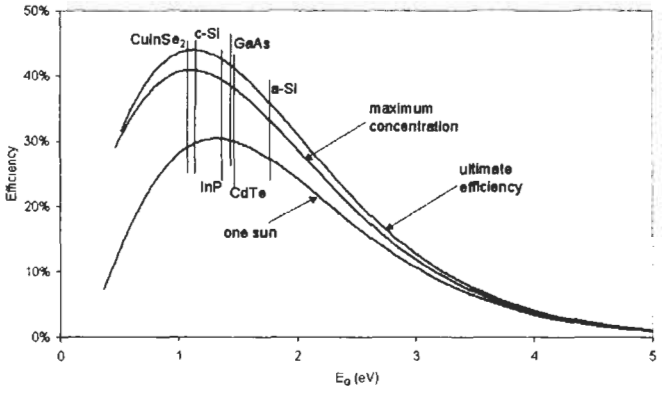

Figure 5 The 'ultimate' and two 'nominal' Shockley–Queisser efficiencies. Note that the black-body radiation with temperature $T_s = 6000$ K has been used here, in keeping with the Shockley–Queisser work [2].

corresponds to light focused on the cell, by a mirror or a lens, at the maximum concentration ratio of $1/f_\omega = 45{,}872$ [9].

The various unavoidable losses in photovoltaic energy conversion by single-junction solar cells can be depicted in a graph constructed by Henry [4] and analogous to Figure 6. There are two curves in this graph:

- The photogenerated current density J_{ph} from Equation (12) as a function of photon energy. J_{ph} is divided here by the total irradiance, making the area under this curve equal to unity by construction.
- The maximum voltage that can be extracted from the cell at the maximum power point. This curve is drawn in such a way that the ratio of lengths of the two arrows b/a is equal to V_m/E_g.

The three shaded areas then depict the three fundamental losses in a single junction solar cell (shown here for silicon with band gap E_g equal to 1.12 eV):

- Shaded area marked $h\nu < E_g$ is equal to the loss of current due to the inability of the semiconductor to absorb below-band-gap light.
- Shaded area marked $h\nu > E_g$ represents energy losses due to the thermalization of electron-hole pairs to the band gap energy.
- Hatched area marked $V < E_q$ corresponds to the combined thermodynamic losses due to V_{oc} being less than E_g, and losses represented by the fill factor FF.

The area of the blank rectangle then represents the maximum efficiency that can be obtained for a single junction cell made from a semiconductor with band gap E_g. The graph is drawn here for light with maximum possible concentration. A different 'voltage curve' would result if light with one-sun intensity were used.

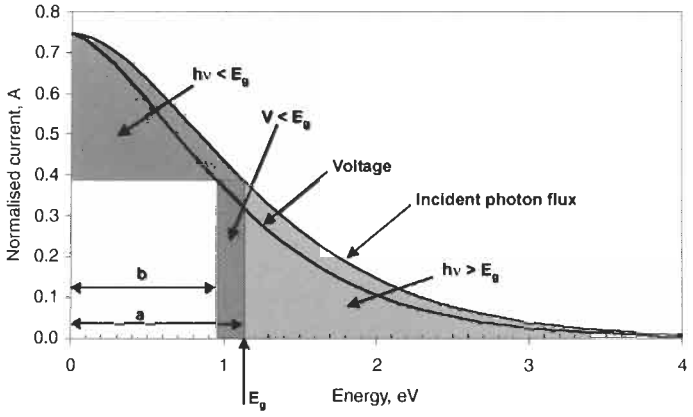

Figure 6 Henry's construction.

5 General Comments on Efficiencies

The ideal solar cell efficiencies discussed above refer to single-junction semiconductor devices. The limitations considered in the ultimate efficiency of Section 3 are due to the fact that the simplest semiconductor (i.e. one whose defects and impurities can be ignored) cannot absorb below band gap photons. Furthermore it is also due to the fact that the part of the energy of the absorbed photons in excess of the band gap is lost as heat. Radiative recombination at the necessary fundamental level was taken into account in the treatment of Section 4. It is sometimes argued that there are other 'unavoidable' losses, due to electronic energy transfer to other electrons by the Auger effect (electron–electron collisions) [10–12]. There is also the effect of band gap shrinkage, discussed in Chapter 2, and light trapping may also play a part [11]. None of these effects are discussed here, and the reader is referred to the relevant literature.

It is clear that it is most beneficial if one can improve the effect of a typical photon on the electron and hole density. This can be achieved, for example, if the photon is energetic enough to produce two or more electron–hole pairs. This is called impact ionisation and has been studied quite extensively. A very energetic photon can also project an electron high enough in to the conduction band so that it can, by collision, excite a second electron from the valence band. This also improves the performance of the cell. On the other hand, an electron can combine with a hole and the energy release can be used to excite a conduction band electron higher into the band. In this case energy is uselessly dissipated with a loss of useful carriers and hence of conversion efficiency. This is one type of Auger effect. For a survey of these and related effects, see [12]. These phenomena suggest a number of interesting design problems. For example, is there a way of limiting the deleterious results of Auger recombination [13]? One way is to try to 'tune' the split-off and the fundamental band-gaps appropriately. If one is dealing with parabolic bands, then the obvious way is to examine the

Table 1 The maximum efficiencies of tandem cells as a function of the number of cells in the stack, for different concentration ratios [17]. Note that de Vos [17] uses a slightly smaller value of f_ω than Shockley and Queisser, resulting in a marginally different maximum concentration ratio than used in Figure 5

Concentration ratio	Number of cells in the stack	Maximum efficiency (%)
1	1	31.0
	2	49.9
	3	49.3
	...	
	∞	68.2
46,300	1	40.8
	2	55.7
	3	63.9
	...	
	∞	86.8

Table 2 The currently best reported efficiencies of different types of solar cells [18]

	Efficiency (%)	J_{sc} (mA/cm^2)	V_{oc} (V)	FF (%)
Crystalline: single junction				
c-Si	24.7	42.2	0.706	82.8
GaAs	25.1	28.2	1.022	87.1
InP	21.9	29.3	0.878	85.4
Crystalline: multijunction				
GaInP/GaAs/Ge tandem	31.0	14.11	2.548	86.2
Thin-film: single junction				
CdTe	16.5	25.9	0.845	75.5
CIGS	18.9	34.8	0.696	78.0
Thin-film: multijunction				
a-Si/a-SiGe tandem	13.5	7.72	2.375	74.4
Photoelectrochemical				
Dye-sensitised TiO_2	11.0	19.4	0.795	71.0

threshold energies which an electron has to have in order to jump across the gap, and to make these large so as to make this jump difficult.

Then there is the possibility of placing impurities on the energy band scale in such a way as to help better use to be made of low-energy photons, so that they can now increase the density of electrons in the system. This is sometimes referred to as the impurity photovoltaic effect. So one can make use of it [14].

One can also utilise excitons to improve the efficiencies of solar cells. There may be as many as 10^{17} cm^{-3} excitons in silicon at room temperature. If they are split up in the field of a p-n junction, this will increase the concentration of current carriers and so increase the light generated current, which is of course beneficial.

We have here indicated some useful ideas for improving solar cells. There are of course many others, some of which are discussed in Chapters IIb-5, IId-1 and elsewhere [15]. Note, in particular, the idea of developing tandem cells in which photons hit a large band gap material first and then proceed gradually to smaller band gap materials. Tandem cells are now available with three of more stages. Solar cells with efficiency of order 20% are predicted to be produced on a large scale in the near future [16]. Table 2 shows the best laboratory efficiencies at the present time for different materials.

References

[1] Landsberg, P.T. and Badescu, V. 1998. Solar energy conversion: list of efficiencies and some theoretical considerations. *Prog. Quantum Electronics*, Vol. 22, pp. 211 and 231.

[2] Shockley, W. and Queisser, 1961. H. J. Detailed balance limit of efficiency of pn junction solar cells, *J. Appl. Phys.* Vol. 32, p. 510.

[3] Ruppel, W. and Würfel, P. 1980. Upper limit for the conversion of solar energy, *IEEE Trans. Electron Devices*, Vol. ED-27, p. 877.

[4] Henry, C.H. 1980. Limiting efficiencies of ideal single and multiple energy gap terrestrial solar cells, *J. Appl. Phys.* 51, p. 4494.

[5] Kiess, H. and Rehwald, W. 1995. On the ultimate efficiency of solar cells, *Solar Energy Materials and Solar Cells*, Vol. 38, pp. 45-55.

[6] Green, M.A. 1982 *Solar Cells*. Prentice Hall, New York.

[7] Baruch, P. and Parrott, J.E. 1990. A thermodynamic cycle for photovoltaic energy conversion, *J. Phys. D: Appl. Phys.* Vol. 23, p. 739.

[8] Araùjo, G.L. 1990. Limits to efficiency of single and multiple band gap solar cells, in Luque A. and Araùjo G.L., Eds., *Physical Limitations to Photovoltaic Energy Conversion*, Adam Hilger, Bristol, p. 106.

[9] Welford, W.T. and Winston, R. 1978. *The Physics of Non-imaging Concentrators*, Academic Press, New York, Chapter 1.

[10] Green, M.A. 1984. Limits on the open-circuit voltage and efficiency of silicon solar cells imposed by intrinsic Auger process, *IEEE Trans Electron Devices* Vol. ED-31, p. 671.

[11] Tiedje, T., Yablonovich, E., Cody, G.C. and Brooks, B.G. 1984. Limiting efficiency of silicon solar cells, *IEEE Trans Electron Devices*, Vol. ED-31, p.711.

[12] Landsberg, P.T. 1987. The band-band Auger effect in semiconductors, *Solid-State Electronics*, Vol. 30, p. 1107.

[13] Pidgeon, C.R., Ciesla, C.M. and Murdin, B.N. 1997. Suppression of non-radiative processes in semiconductor mid-infrared emitters and detectors, *Prog. Quantum Electron.* Vol. 21, p. 361.

[14] Kasai, H. and Matsumura, H. 1997. Study for improvement of solar cell efficiency by impurity photovoltaic effect, *Solar Energy Materials and Solar Cells*, Vol. 48, p. 93.

[15] Green, M.A. 2001. Third generation photovoltaics: Ultra high conversion efficiency at low cost, *Prog. Photovoltaics Res. Appl.*, Vol. 9, pp. 123–135.

[16] Wilcke, G.P. 2002. The Fraunhoffer ISE roadmap for crystalline silicon solar cell technology, *Proc. 29th IEEE Photovoltaic Specialists Conf.*, New Orleans.

[17] deVos, A. 1980. Detailed balance limit of the efficiency of tandem solar cells, *J. Phys. D: Appl. Phys.* Vol. 13, p. 839. See also deVos, A. 1992. Endoreversible *Thermodynamics of Solar Energy Conversion*, Oxford University Press.

[18] Green, M.S., Emery, K.L., King, D.L., Igari, S. and Warta, W. 2002. Solar cell efficiency tables (version 20), *Prog. Photovoltaics Res. Appl.*, Vol. 10, pp. 355–360.

Part IIb

Crystalline Silicon Solar Cells

Crystalline Silicon: Manufacture and Properties

Francesca Ferrazza, Eurosolare S.p.A, Nettuno, Italy

1 Introduction

The majority of silicon wafers used for solar cells are Czochralski (CZ) single crystalline and directional solidification, or cast, multicrystalline (mc) material. The split between the two types of wafer is presently about 55% mc-Si and 45% CZ-Si. Until 1995 CZ wafers represented 60% of the substrates used by industry and mc-Si wafers around 25%. The fast scale up of commercially available multicrystalline wafers changed the picture rapidly. The remainder of the silicon substrates used by the industry are non-wafered sheets or ribbons that are of different types and have recently gained significant production figures, following long development phases. Non-wafer silicon accounted for about 4% of the market in 2001, up from 1–2% in the mid-1990s [1, 2].

2 Characteristics of Silicon Wafers for Use in PV Manufacturing

2.1 Geometrical Specifications

Most of the wafer substrates used in production facilities have dimensions relating to the diameters of monocrystalline silicon cylinders for the semiconductor industry (essentially 5 and 6 inch) that, in turn, have influenced standards for wafer carriers, automation, packaging etc. However, in order to maximise the power density of the modules, wafers are square, or pseudo-square in the case of monocrystalline silicon, that is cylinders are shaped as squares with rounded off corners. This reduces the surface area of the wafers by between 2% and 5% compared with a full square of same dimensions.

In the case of mc-Si, ingot sizes are designed to be compatible with multiple numbers of each of the standard wafer dimensions, in order to maximise geometrical yield. Yield considerations limit the possible wafer sizes achievable for any given ingot dimension, as much as expensive wafer cassettes, automation and packaging do later in the process. Table 1 reports the different sizes for commercially available wafers, including typical tolerances.

A SEMI® (Semiconductor Equipment and Materials International) standard, M61000, was developed with the purpose of covering the requirements for silicon wafers for use in solar cell manufacturing [3], including dimensional specifications, defects and electronic properties. Most commercial suppliers sell their wafer products using specifications that are close to those described by

Table 1 Commercially available wafer sizes.

Nominal size	Dimension (mm)	Diagonal (multi) (mm ± 1)	Diameter (mono) (inch)
103	103 ± 0.5	146	5
125	125 ± 0.5	177	6
150	150 ± 0.5	212	–

M61000. However, smaller wafers are usually 103 mm rather than 100 mm as specified, and there are some notable exceptions to the specifications, e.g. dimensions of wafers produced in-house by some of the early players who have developed their own standard and do not usually buy wafers on the market. Another obvious exception is provided by non-wafer substrates, the dimensions of which are in general determined by the growth equipment and technique. Some manufacturers use rectangular wafers. Other requirements, besides the geometrical definitions of the wafers, are thickness uniformity and reduced levels of cracks and saw marks that could adversely affect later processing.

Typical specifications for commercially available wafers are described in Table 2.

The absolute value of the wafer thickness has dropped by about 100 μm in the last decade, as a consistent cost reduction measure [4, 5], and is expected to decrease further in the next years [2] as automation and cell processing become more sophisticated and can allow effective handling of thin wafers. Some wafer and cell producers already have less than 300 μm wafers in their production lines, although in general wafer sizes in such cases are limited to the 100 cm^2 range in order to maintain mechanical yields in the high 90s. Similarly to the case of the area dimensions, thickness in non-wafer substrates is determined by the process, and is in general less homogeneous, providing one of the major differences between wafer and non-wafer cell technologies. A great deal of effort was put in the last decade in developing automated thickness measurement tools for manufacturing plants, to inspect wafer thickness variations in lots, an extremely difficult task in manually inspected wafer fabrication sequences.

2.2 Physical Specifications

Wafers are generally classified in terms of resistivity, type, and oxygen and carbon content. These data are generally present in all commercial specifications related to single and multicrystalline wafers, and refer to ASTM or equivalent standards. However, the PV community has had to face the unavoidable departure from standard test conditions of all parameters when measuring the properties of the inherently inhomogeneous nature of multicrystalline wafers, which led to agreement on relatively broad ranges for resistivity or upper thresholds for oxygen and carbon contents. Early concerns, for instance, of the influence of grain boundaries on the determination of resistivity using the

Table 2 Other dimensional specifications for typical PV wafers

Parameter	Value
Thickness of a batch	330 ± 40 μm
Total Thickness Variation (TTV) of a wafer	50 μm
Cracks	< 1 mm
Saw marks	< 10 μm
Bow	< 50 μm

four-point probe method are now somewhat more relaxed, after significant statistical feedback has provided comfort in the values proposed. Still, in strict terms, standards related to the measurement of resistivity in multicrystalline wafers do not exist, which is true of course for non-wafer silicon technologies as well. This is also true for other kinds of measurements, and the effort to develop meaningful characterisation tools for lower or inhomogeneous quality materials as compared to the semiconductor industry is a clear indication of such a need (see Chapter IIb-4). Furthermore, the increasing volumes of wafers in the growing PV market has forced a second, big departure from semiconductor wafer characterisation standards, imposing fast, non-destructive test methods to optimise costs and yields. In most cases, for instance, resistivity and type are measured at block rather than at wafer level. Table 3 shows the typical values for physical parameters of commercially available wafers for industrial processing. These are either multicrystalline or monocrystalline Czochralski. Float zone wafers for PV may become commercial products, and will be discussed in a later paragraph.

2.3 Physical Specifications

Minority carrier lifetime characterisation of commercial silicon is worth a paragraph on its own. This is by far the most complicated parameter to measure and to effectively relate to subsequent processing quality and yield. It is also most influenced by the inhomogeneity of multicrystalline silicon, as well as by thermal treatments. It became immediately evident to all PV manufacturers at the very beginning of the expansion of the multicrystalline silicon market that the identification of an appropriate tool for analysing and understanding the properties of mc-Si would have been one of the keys for the commercial success of the material. A generous number of attempts were made to adapt the existing lifetime measurements – rigorously valid for high quality polished single crystalline wafers – to provide meaningful values for mc-Si and even CZ-Si for the PV community. Also, as mentioned before, any acceptable test would need to be fast, cost effective, and obviously non-destructive as the number of samples to inspect was bound to be large. This focussed effort led to the development of a number of automated lifetime analysers, which at the end of the development process had relatively low resemblance with the semiconductor industry

Table 3 Physical specifications of commercial silicon wafers

Parameter	Value
Type	P – boron doped
Resistivity	0.5–3 ohm cm
Oxygen (mc-Si)	$< 8 \times 10^{17}$ at/cm^3
Oxygen (CZ-Si)	$< 1 \times 10^{18}$ at/cm^3
Carbon (mc-Si)	$< 1 \times 10^{18}$ at/cm^3
Carbon (CZ-Si)	$< 2 \times 10^{17}$ at/cm^3

counterparts. Probably the most successful commercial methods are the microwave photoconductance decay method (μ-PCD) performed directly on silicon blocks, and the photoconductance decay or quasi-steady state method developed by Ron Sinton which is discussed in Chapter IIb-4.

For the purposes of the present chapter, we will focus on the μ-PCD characterisation of mc-Si blocks. This measurement technique is commercially available and its use is widespread, although strong debates on the validity of the results occurred for many years. The measurement is based on the detection of the amplitude of the microwave field reflected by the sample surface. This amplitude variation depends on the conductivity, and thus also on the number of minority carriers generated by a short laser pulse [6]. The time in which the system recovers the initial state is associated with the quality of the semiconductor material and with the recombination mechanisms in the bulk and at the surface. It is generally rather complicated to separate different contributions, and PV silicon has peculiar characteristics which enhance difficulties, such as relatively high doping, rough surfaces and short diffusion lengths for minority carriers. Furthermore, as mentioned before, the industry requirements are for fast non-destructive techniques which enable prediction of later behaviour of the material in the processing line, in order to minimise the costs of processing low quality material as early as possible. For this reason, the industry has pushed towards the use of fast non-invasive block scanners since the early 1990s, despite the inability of the measurement systems to conform to any of the existing standards. A certain effort has been directed until relatively recently towards developing uniform measurement systems and procedures, which has proven once more the difficulty of the problem [7] and finally led to generally accepted principles subject to bilateral confirmation in the case of commercial relationships between wafer vendors and cell producers.

The main problems with block scanners, besides separation of bulk and surface components, lie in the fact that the measurement is actually performed on a very thin portion of the block. This is due to the absorption of the laser pulse in silicon (usually in the near infrared range) and to the high reflectivity of microwaves which only allow the field to penetrate a skin depth of the sample under examination. Other difficulties lie in the unpredictable behaviour of the material in three dimensions, lateral distribution of carriers, trapping effects, unknown injection levels, and the macroscopic saw damage affecting the control of the distance of the measurement head from the sample. Microwave block-scanners are unable to handle these problems, which are better taken into account by the technique described in Chapter IIb-4. The experience of crystal growers and the feedback from cell processing lines, however, led to the establishment of a method for the analysis of silicon blocks which is able to reject low quality material at block level, and which allows the identification of the correct cropping position for the rejection of tops and tails.

A typical map, performed with a commercially available automated system [8], of a standard block of mc-Si grown by the directional solidification method is shown in Figure 1. The silicon is boron doped to a resistivity of about 1×10^{16} at/cm^3, and the measurement is performed with a microwave field in

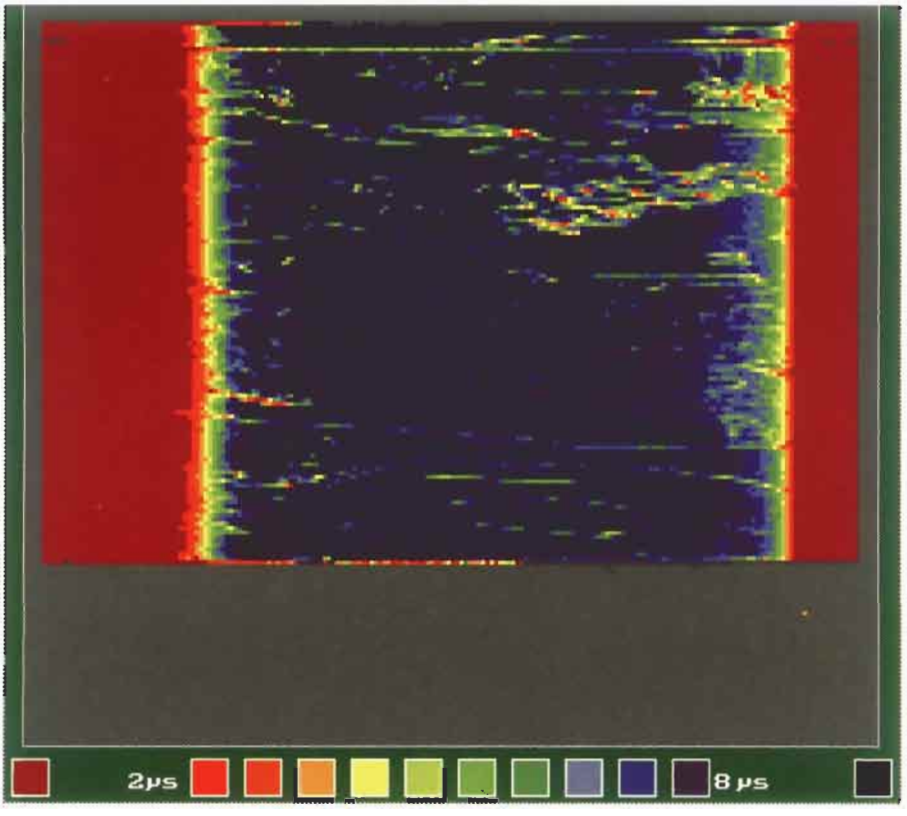

Figure 1 Lifetime map.

the GHz range coupled by an antenna for a sample irradiated by a laser diode pulse at 904 nm.

The absolute value of the minority carrier lifetime is surface limited, as the sample is measured 'as cut'. Normally, in fact, no impractical etching or passivation treatments are applied to the surface which therefore has a high recombination velocity. It is assumed that the surface is always in the same conditions, so any change in the relaxation time is associated with bulk properties. A map such as the one in Figure 1 takes a few minutes to be realised with a modern lifetime scanner such as the one in [8]. Early systems could take several hours to perform measurements with the same resolution. The low lifetime regions (in red) have different physical origins, and this is where the extensive material-to-cell correlation work performed over the years has been essential in comfortably introducing these instruments in the production environment [4, 5, 9]. The red zones at the top, in fact, are determined by the segregation of metals due to the refining process during solidification, and the wafers cannot effectively be used in cell processing, so they are rejected, and possibly remelted. The red zones at the bottom of the block are composed of a highly defected area – the initial crystal growth, highly dislocated and unusable

for solar cells within about 1 cm from the start – and the 2–3 cm region of oxygen rich material which, despite its low initial lifetime, recovers after the thermal treatments used in cell processing and normally produces good quality cells. Care must be taken, therefore, to exactly determine the cut off (by any means possible!) between good and low quality material at the bottom of the block, and this is probably the most difficult part of the quality control procedure at block level.

Figure 2 shows a typical correlation between the lifetime at block level and cell performance, being evidence of a good performance of initially low quality material as detected by the block scanner [9]. The central part of the block is instead relatively uniform and produces good quality cells, in the range 12–15% depending on the particular process used, the higher value provided by silicon nitride-based sequences.

Typical values in the central part of the blocks are around 5–10 μs, depending on the specific measurement system used. A fundamental assumption of this method is a relative uniformity of the material in any given region of the block (i.e. all central regions behave similarly in same conditions), which is also a result of extensive correlation work [5, 9].

μ-PCD testers are also used to inspect incoming wafers in production lines, and in this case as well, there has been important correlation work to be able to confidently accept material for subsequent processing. This applies to CZ-Si wafers, which are inspected for uniformity as well as for the acceptance threshold value (which varies from case to case).

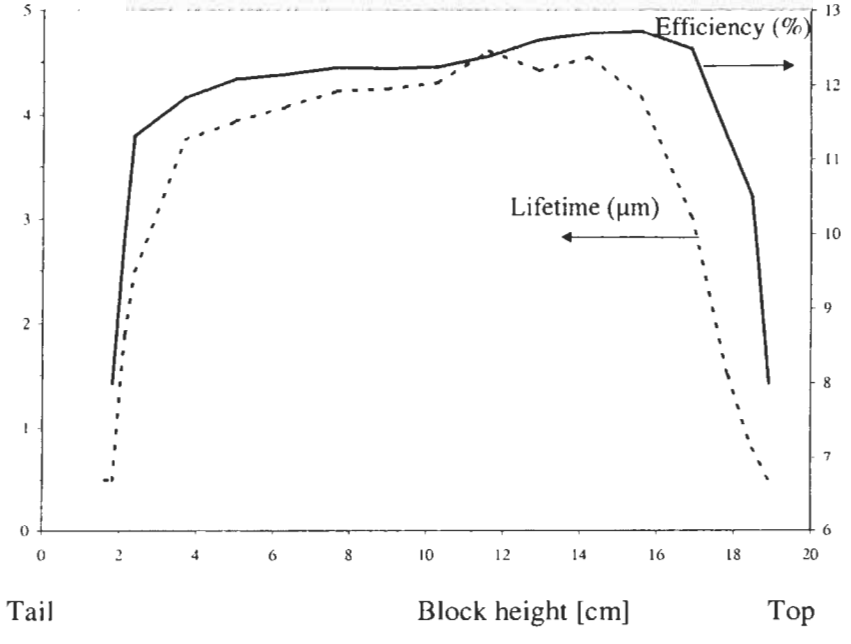

Figure 2 Correlation of lifetime with cell efficiency.

3 Feedstock Silicon

The commercial success of PV is driven critically by its cost. Silicon wafers account for about 50% of the total production cost of a module, a figure which has increased over the years, from the 33% of about 10 years ago, thanks to the constant improvements in technology which has allowed to identify the wafer as the ultimate cost limiting factor [10].

There is no source of silicon feedstock unique to the PV industry, so the issue of a possible feedstock shortage has been largely debated, and is still not concluded. About 10–15% of the silicon used by the microelectronics industry is available in various forms for PV use. This is in the range of 1800–2500 tons per year of higher quality scrap, and an extra 1500–2000 tons of lower quality material (e.g. pot scrap). Based on an effective usage rate of 10–15 tons per MWp produced, the amounts considered cannot feed the fast growing PV market for long. Whilst extensive research programmes have been conducted for many years to upgrade cheap metallurgical silicon to be an independent low cost silicon source for PV, none of the techniques proposed has reached commercial maturity [5]. The scare of a silicon shortage as early as the middle of the present decade has instead favoured several proposals for processes similar to those used for the production of polysilicon, but with looser specifications [11, 12].

From a practical point of view there is, in general, no constraint related to the geometrical specification of the starting material, so for the moment PV can enjoy low cost scrap such as silicon chips from the cutting processes of semiconductor manufacturing, popcorn silicon rods, tops and tails from crystal growth processes, etc. [13].

However, different crystallisation methods require different specifications. In general, monocrystalline and non-wafer technologies require high quality starting material, while the multicrystalline technology can allow a looser specification if some care is taken, due to its purifying characteristics – another point in its favour.

4 Crystal Preparation Methods

A number of techniques are available for the production of silicon wafers for the PV industry: CZ-Si and multicrystalline silicon (which have already been mentioned), magnetically confined multicrystalline silicon, float zone silicon and the non-wafer technologies (also already mentioned). In this paragraph we will briefly introduce the main features of each of them. The reader is encouraged to consult specific references for further details, as we will focus on the most relevant recent developments of the technologies under discussion.

4.1 Czochralski Silicon

The most common method for the growth of single crystalline ingots consists of pulling an oriented seed slowly out of the molten silicon contained in a pure

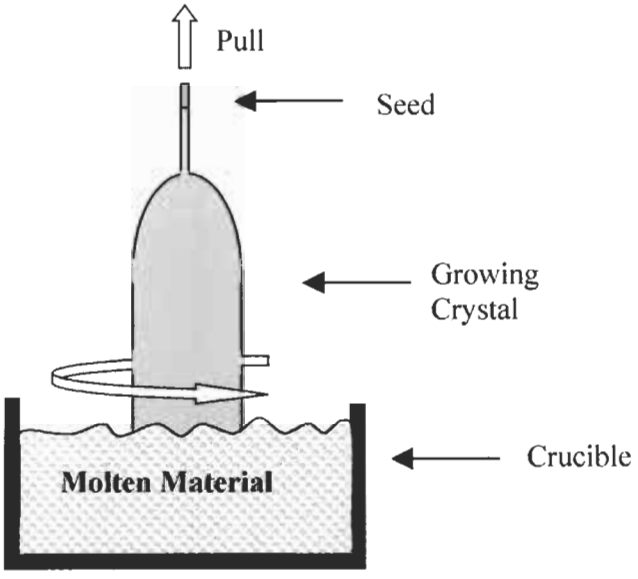

Figure 3 Schematic of CZ growth principle.

quartz crucible. The method is well known and extensively described in literature [10, 14].

What we will mention here is that a number of actions have been taken in the last 10 years to reduce the cost of CZ material, and regain competitiveness against multicrystalline silicon.

For instance, crystal growers now quite commonly use some kind of scrap silicon from the semiconductor industry as well as virgin poly as feedstock. Lower energy consumption, from the standard 100 kWh/kg figure to a promising 40 kWh/kg was recently reported due to improved furnace design, including heaters and gas distribution systems [15]. A crystallisation yield up to 70% from the standard 50% was also reported in the same study.

4.2 Multicrystalline Silicon

The realisation of multicrystalline silicon ingots is a relative simple process, and is based on controlling the extraction of heat from the melt in a quartz crucible in such a way that the interface between the growing solid and the ingot is as flat as possible. In this way, silicon grows in large columns of a few centimetres in section and as tall as 25 cm, and most detrimental impurities are segregated towards the top of the ingot. The critical steps to ensure a high quality and high yield process are in the design of the furnace for appropriate heat control, and in the quality of the quartz crucibles. A schematic of the general method is given in Figure 4.

Modern mc-Si furnaces are designed to minimise inhomogeneity, and maximise productivity [16, 17], and in the last few years a great deal of effort has

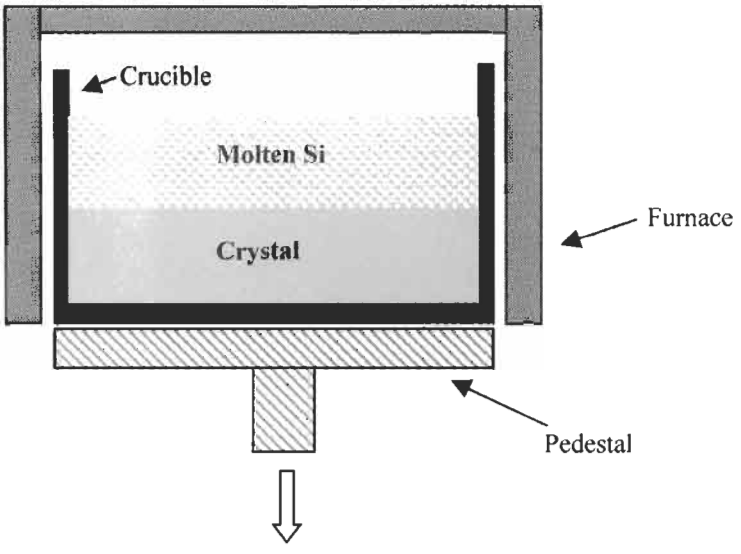

Figure 4 Schematic of mc-Si ingot growth.

been put in the study of appropriate models for growth control and optimisation [18]. Some of the distinctive features of mc-Si ingot growing are summarised in Tables 4 and 5.

As discussed in Section 2.3, the central part of the ingot enjoys a relatively uniform quality, and the purification ability of the process is witnessed by the following typical values for impurities other than O, C.

4.2.1 Charge Preparation

Ingots are normally doped at the level of about 1×10^{16} at/cm^3 of boron. This can be achieved with different mixtures of starting feedstock, and is a common practice in the PV industry which has to use feedstock form different sources and of different nature. For the range of resistivity values used in PV, no special requirements are needed for doping the ingot. If the feedstock is virgin poly or lowly doped silicon, highly doped silicon powder, available commercially with specifications of the B content, can be added to the charge. It is easy to control the final resistivity of an ingot given the starting characteristics of the material. A simple set of equations determines the amounts of each kind of feedstock to be added to the mix. The constraints are the weight of the ingot and the doping level, the latter given by the difference between donor and acceptor concentrations, assuming all impurities are ionised at room temperature. The relationship between resistivity and doping level is known from the literature [14] and a simple spreadsheet can be used to do the conversion.

4.2.2 Crucibles

Crucibles are one of the critical points of mc-Si technology. They are made of slip-cast silica, a technique known since the medieval age, which consists

Table 4 Typical features of DS mc-Si

Parameter	Typical value
Energy consumption	10 kWh/kg
Crystallisation yield	70–80%
Growth rate	5–10 mm/h
Ingot size	100–300 kg
Ingot base	Square, 66 cm × 66 cm
Ingot height	20–25 cm

Table 5 Impurity levels of a typical mc-Si ingot

Impurity	Typical value (ppma)
Fe	< 0.1
Al	0.5–2
Cu, Mn, Cr, Mg, Sr	< 0.1

of letting a plaster mould slowly absorb the quartz present in a water suspension. A layer of up to about 2 cm thick can be realised in this way, and the mould can have a double jacket to improve thickness uniformity. The crucible is then baked for mechanical resistance.

The crucibles currently used have been developed to withstand the high temperatures of a heavy silicon ingot growth process in order to avoid unwanted failures in the presence of liquid silicon. Crucibles are lined with a Si_3N_4-based coating to prevent liquid silicon sticking to the walls and subsequent cracking of the ingot due to the strong stress during solidification and cooling. However, only a limited number of companies manufacture crucibles worldwide, and the maximum size of a 'safe' crucible has probably already been reached (68 × 68 cm). This imposes a boundary condition on the design of future mc-Si furnaces [17].

4.3 Electromagnetic Continuous Casting

Electromagnetic continuous casting (EMC) uses an RF coil to induce currents in an appropriately designed circuit able to push the melt away from the walls, therefore making it unnecessary to use crucibles. A schematic of the furnace is shown in Figure 5 [19]. The process is carried out in an argon ambient at slight overpressure. The top end is open for the ingot to be pulled down while new feed material is added. The resulting ingot is a long bar of about 240 kg in weight. The idea behind this growth method is to completely avoid the use of any physical crucible by confining electromagnetically the charge. This gets rid, at one time, of two major issues of the DS techniques that have previously been described: expensive crucibles and related contamination. However, inhomogeneous nucleation occurs and grain size is also rather small, resulting in a low starting quality of the material [20], although a low oxygen content is reported. This kind

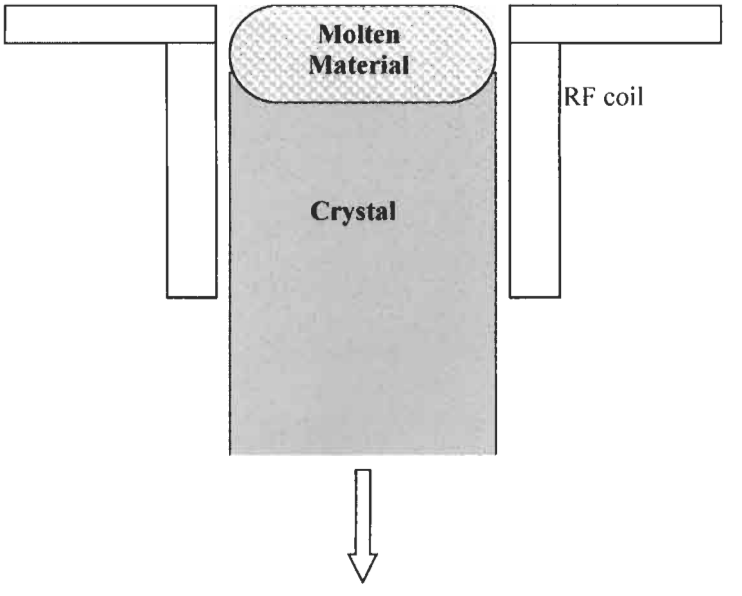

Figure 5 Schematic of EMC furnace.

of material is not commercially available yet, but there are announcements it could be shortly.

4.4 Float Zone Silicon

As float zone silicon typically is used for power electronic components and detectors, the advantage of using large diameter substrates has been limited and even today, the majority of all float zone crystals are only 100–125 mm in diameter, which is advantageous for the PV industry needs. Most product and process optimisation activities have been focused on achieving highly predictable yields when running many small series of different types, constantly varying with respect to crystalline orientation (or), diameter (25–150 mm), dopant type (n- or p-type), and resistivity range (0.01–100,000 Ω cm).

During the float zone growth method, a molten zone is passed along the silicon rod, eating up the raw polycrystalline silicon material and leaving behind a purified monocrystal. Modern FZ machines are now capable of accepting feedrods up to 2 m long with a weight between 60 and 100 kg. The bottom end of the feedrod is coned by a grinding operation, and during the process, the surface of this cone is heated to the melting temperature of silicon. This results in a thin layer of molten silicon continuously running down the feedrod bottom tip, and through the centre hole of the induction coil. The feedrod is heated by a skin current induced by an electromagnetic field. As the feedrod, the molten silicon and the finished crystal are freely suspended in the growth chamber; there is never direct physical contact between silicon and the surroundings, except for

the ambient gas, typically argon. Contamination is therefore very low, and the process also allows purification of impurities which segregate in the melt.

As the feed rates of the feedrod and finished crystal can be controlled independently, there is no constrains on the diameter of the monocrystal and the diameter of the feedrod. Typical growth rates of the monocrystal are between 2 and 3 mm/min.

Beside the physical dimension of the monocrystal, the fundamental parameter that must be controlled is the shape of the phase boundaries, i.e. the free surface of the melt and the melt-solid interface where the crystallisation takes place. Factors affecting the phase boundaries are the induction coil current, the pull velocities of the feedrod and monocrystal, the rotation rates, the eccentricity of the rod and monocrystal with respect to the coil centre and additional heat sources.

The monocrystalline perfection of the finished crystal is very high, as neither volume defects (precipitates or voids), planar defects (twins grain boundaries or stacking faults) or line defects dislocations) are present. The purity of the finished monocrystal is very high, with oxygen and carbon as the two impurities of highest concentrations (upper limit at 1.0 and 2.0×10^{16} cm^{-3}, respectively). Also due to the purity of the feedrod material, the concentration of other impurities is very low, and the total concentration of all metal atoms typically lies below 10^{13} at/ cm^3 [21, 22].

4.5 Non-wafer Technologies

The idea of lowering the wafer manufacturing costs by avoiding the wafer-cutting step with its silicon loss was the main motivation for the development of a number of silicon ribbon-growth technologies. The common feature to all

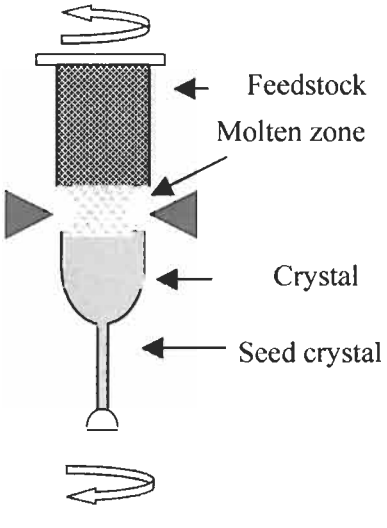

Figure 6 Schematic of FZ growth.

of them is the principle of a continuous production of a thin foil or sheet directly from the silicon melt, using different techniques to confine or stabilise the edges. From these different technologies, developed in R&D programmes such as the JPL Flat-plate solar module project [23], only few are used in commercial wafer production today. The most relevant to date are the edge-defined film fed growth (EFG) [24] (by far the most advanced in terms of industrial performance), the string ribbon (SR) [25] and the dendritic web [26] technology. A great deal of improvement was reported recently in all technologies, and in all cases industrial facilities are described or anticipated. In all cases tailored cell processing is needed to improve the starting quality of the material which is, in general, low. Also, in all cases the technologies appear to be capable of producing very thin sheets, in the 100 μm range. A promising technique from the point of view of productivity is the Ribbon-Growth on Substrate (RGS), originally developed by Bayer and now under development at ECN [27].

Other silicon ribbon technologies with the potential for high production rates by de-coupling ribbon production from crystal growth (such as the low angle silicon sheet (LASS) or the supporting web (S-Web)) are not yet developed to industrial production. Table 6 compares production speed and capacity of different silicon ribbon production technologies. The last column shows the number of furnaces for a 100 MWp production line. [27].

5 Shaping and Wafering

5.1 Shaping

The large, square-based mc-ingots are cut into smaller blocks using large blade or band machines. Blade machines are in general more robust and easy to use and maintain, but have the disadvantage of producing a relatively high kerf loss, up to 3–4 mm. Band saws, on the other hand, suffer from frequent band breakage and may produce waviness in the blocks, which will then need rectifying. However, modern band saws seem to have greatly improved from this point of view.

Monocrystalline silicon ingots instead are treated as the semiconductor counterpart for removing heads and tails, and are shaped to pseudo-square by removing parts of the rounded edges, a process which does not present particular problems, thanks to the relatively small dimension of the ingots.

Table 6 Comparison of different ribbon technologies

Material type	Pull rate (cm/min)	Throughput (m^2/h)	Furnaces per 100 MWp
EFG	1.7	1	100
SR	1–2	0.03–0.1	1200
RGS	600	45	2–3

In the case of mc-Si blocks, it is after the shaping step that blocks are inspected for minority carrier lifetime and resistivity, as described earlier, so finally tops and tails can be removed to leave the material ready to be wafered.

5.2 Wafering

Wafering of Si ingots for the PV industry is probably one of the only examples of technology successfully transferred to the semiconductor industry, which was originally developed for the PV industry. Cost constraints in PV in fact imposed the development of a slicing technique able to reduce kerf loss and increase productivity, as an alternative to slow, large kerf loss blade cutting techniques used until about 10 years ago [15]. On the other hand, the specifications for semiconductor grade wafers up to 300 mm diameter needed a totally new concept of machines for the control of taper, thickness variation and surface smoothness, so at the end both industries enjoy the development of wire saw technology.

Modern slicing technology is based on wire sawing, where a thin wire (160 μm diameter) web pushes an abrasive-based slurry into the silicon to be cut. In this way several wafers are cut at the same time, with high mechanical precision, and in a highly automated process.

The principle of wire sawing is shown in Figure 7. A spool of single bronze coated stainless steel wire up to several hundreds of kilometres long (!) is fed on high precision grooved wire guides. The feeding system, not detailed in the figure, is designed to allow high precision control of the wire tension, one of the critical parameters of the process, throughout the cut. The silicon block(s) is glued on a low cost glass support, which in turn is mounted on a motor-driven table which translates downwards through the web. The abrasive slurry is fed to the wire web through a nozzle, and allows the silicon to be cut. The abrasive is

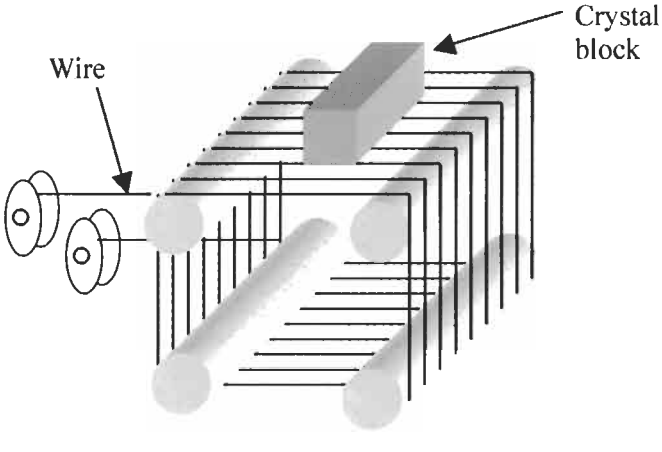

Figure 7 Principle of wire sawing.

Table 7 Typical wafering conditions for 350 μm thick, 125 mm square mc-Si wafers

Parameter	Value
Wire speed (m/s)	5–10
Table speed (μm/min)	300–400
Wire diameter (μm)	160–180
Wire guide pitch (μm)	550–570
SiC mesh	500–600
Slurry temperature (°C)	25 ± 5
Slurry mixture	1:1 (glycol based) 5:8 (oil based)
Viscosity (g/l)	1600
Wire tension (N)	23–25

fine mesh silicon carbide powder. The process is completed when the wires reach the glass, thus allowing the wafers to be separated without any damage, as they are attached to the support through a very thin layer of glue. Wire speed and tension, table speed, slurry viscosity and temperature and abrasive characteristics are the main parameters to control in order to produce wafers that match the specifications indicated in an earlier paragraph. As the conditions tend to change during the process, e.g. because of the increase of the temperature of the slurry or because of the contamination of the slurry by the silicon dust produced by the process, it is critical to be able to adjust the parameters to avoid waves or thickness variations. The slurry can be based on oil or on other fluids which are water washable and can improve subsequent cleaning and handling steps, although the waste treatment system tends to be more sophisticated and needs a COD control device than with oil-based technology.

Typical parameters for cutting 125 mm square wafers over a length of about 30 cm are given in Table 7.

Large wafer manufacturers have developed automated washing and handling equipment for the steps following the cutting one.

References

[1] *Photon International*, March 2002.

[2] Bruton, T., 2002. General trends about photovoltaics based on crystalline silicon. *Proc. E-MRS 2001 Spring Meeting, Symposium E on Crystalline Silicon Solar Cells, Sol. Energy Mater. Sol. Cells*, Vol. 72, pp. 3–10.

[3] SEMI ® Standard M61000 – SEMI ® International Standards www.semi.org.

[4] Ferrazza, F., 1995. New developments and industrial perspectives of crystalline silicon technologies for PV, *Proc. 13th European Photovoltaic Solar Energy Conf.*, Nice, p. 3.

[5] Ferrazza, F. et al., 1998. The status of crystalline silicon modules, *World Renewable Energy Conf.*, Florence.

[6] Kunst, H. and Beck, G.1986. The study of charge carrier kinetics in semiconductors by microwave conductivity measurements, *J. Appl Phys*, Vol. 60(10), p. 3558.

[7] Schonecker, A. et al., 1997. Results of five solar silicon wafer minority carrier lifetime round robins organised by the SEMI M6 Solar Silicon Standardisation Task Force, *Proc. 14th European Photovoltaic Solar Energy Conf.*, Barcelona, p. 666.

[8] Semilab homepage www.semilab.hu.

[9] Ferrazza, F. et al., 1998. Cost effective solar silicon technology, *Proc. 2nd World Conference on Photovoltaic Solar Energy Conversion*, Vienna, p. 1220.

[10] Endroes, A., 2002. Mono- and tri-crystalline Si for PV application, *Proc. E-MRS 2001 Spring Meeting, Symposium E on Crystalline Silicon Solar Cells, Sol. Energy Mater. Sol. Cells*, Vol. 72, pp. 109–124.

[11] Maurits, J., 1998. Policrystalline Silicon-World Demand and Supply, Eighth NREL Workshop on Crystalline Silicon Solar Cell Materials and Processes, Colorado, 1998.

[12] Woditsch, F. and Koch, W., 2002. Solar grade silicon feedstock supply for PV industry, *Proc. E-MRS 2001 Spring Meeting, Symposium E on Crystalline Silicon Solar Cells, Sol. Energy Mater. Sol. Cells* , vol. 72, 2002, pp. 11-26.

[13] Aulich, H. and Schulze, F., 2002. Crystalline silicon feedstock for solar cells, *Prog. Photovolt: Res. Appl.*, Vol. 10, pp. 141–147.

[14] O'Mara, W., Herring, R., and Hunt, L, Eds., 1990. *Handbook of Semiconductor Silicon Technology*, Noyes Publication, p. 395.

[15] Jester, T., 2002. Crystalline silicon manufacturing progress, *Prog. Photovolt: Res. Appl.*, Vol. 10, pp. 99–106.

[16] Ferrazza, F., 1995. Growth and Post growth Processes of multicrystalline silicon for photovoltaic use, in: Polycrystalline Semiconductors IV – Physics, Chemistry and Technology, S. Pizzini, H. P. Strunk and J. H. Werner, Eds., in *Solid State Phenomena*, Transtec, Switzerland, Vols 51–52, pp. 449–460.

[17] Ferrazza, F., 2002. Large size multicrystalline silicon ingots. *Proc. E-MRS 2001 Spring Meeting, Symposium E on Crystalline Silicon Solar Cells, Sol. Energy Mater. Sol. Cells*, Vol. 72, pp. 77–81.

[18] Franke, D. et al., 2002. Silicon ingot casting: process development by numerical simulations, *Proc. E-MRS 2001 Spring Meeting, Symposium E on Crystalline Silicon Solar Cells, Sol. Energy Mater. Sol. Cells*, Vol. 72, pp. 83–92.

[19] Durand, F., 2002. Electromagnetic continuous pulling process compared to current casting processes with respect to solidification characteristics, *Proc. of the E-MRS 2001 Spring Meeting, Symposium E on Crystalline Silicon Solar Cells, Sol. Energy Mater. Sol. Cells*, Vol. 72, pp. 125–132.

[20] Perichaud, I., Martinuzzi, S. and Durand, F., 2002. Multicrystalline silicon prepared by electromagnetic continuous pulling: recent results and comparison to directional solidification material, *Sol. Energy Mater. Sol. Cells*, Vol. 72, pp. 101–107.

[21] Dietze, W., Keller W. and Muhlbauer, A., 1981. Float-zone grown silicon, in *Crystals, Growth, Properties, and Applications*, Vol. 5, Silicon, Springer-Verlag, p. 1.

[22] Luedge, A., Riemann, H., Hallmann, B., Wawra, H., Jensen, L., Larsen T. L. and Nielsen, A., 2002. High-speed growth of FZ silicon for photovoltaics, *Proc. High Purity Silicon VII*, Electrochemical. Society, Philadelphia.

[23] Flat plate solar array project: Vol. III, Silicon sheet: wafers and ribbons, Report *DOE/JPL-1012-125*, 1986.

[24] Kaleis, J., 2002. Silicon ribbons and foils – state of the art, *Proc. E-MRS 2001 Spring Meeting, Symposium E on Crystalline Silicon Solar Cells, Sol. Energy Mater. Sol. Cells*, Vol. 72, pp. 139–153.

[25] Hanoka, J., 2002. PVMat contribution towards Evergreen Solar's new factory, *Proc. 29th IEEE Photovoltaic Specialists Conference*, New Orleans, p.66.

[26] Meyer, D.L. et al, 2002. Production of thin (70–100 mm) crystalline silicon cells for conformable modules, *Proc. 29th IEEE Photovoltaic Specialists Conference*, New Orleans, p.110.

[27] Schonecker, A. et al., 2002. Ribbon growth-on-substrate: progress in high speed crystalline silicon wafer manufacturing, *Proc. 29th IEEE Photovoltaic Specialists Conf.*, New Orleans, p. 316.

Low Cost Industrial Technologies of Crystalline Silicon Solar Cells☆

Jozef Szlufcik[1], S. Sivoththaman[2], Johan F. Nijs[1], Robert P. Mertens, and Roger Van Overstraeten*, Interuniversity Microelectronics Centre, Leuven, Belgium

[1] Now at Photovoltech, Brussels, Belgium.

[2] Now at University of Waterloo, Ontario, Canada.

1 Introduction

Although efficiency is important, the principal requirement for industry is low cost. Processing techniques and materials are selected for the maximal cost reduction while maintaining a relatively good efficiency. Industrial solar cells are fabricated in large volumes mainly on large area($\geqslant 100$ cm^2) Czochralski monocrystalline or multicrystalline silicon substrates.

Analysis indicates that the market price of the commercial PV modules lies in the range 3.5–4.5 \$/Wp. 40–50% of the PV module cost is due to ingot growth (including the polysilicon feedstock material), single crystal ingot formation and wafering. The tendency here is to develop a cheap, good quality solar grade polysilicon feedstock material, to increase the substrate size, to reduce the kerf loss in slicing and to decrease the thickness of the substrates below 200 μm. Cell fabrication and module assembly are each responsible for 25 to 30% of the final module cost.

Typical efficiency of commercially produced crystalline silicon solar cells lies in the range 13–16%. Because the efficiency of the cell influences the production cost at all production stages, substantial effort is directed towards efficiency improvement. The required future efficiency goals for industrial cells are 18–20% for monocrystalline and 16–18% for multicrystalline silicon. Based on laboratory scale achievements one can consider that production type cells able to fulfil the efficiency goal should will possess most of the following features (providing that they can be introduced in a cost effective way):

- front surface texturing,
- optimised emitter surface concentration and doping profile,
- effective front surface passivation,
- fine line front electrode,
- front electrode passivation:
  - point contact,
  - deep and highly doped emitter under the contact,
  - MIS contact,
- thin base, i.e. much smaller than the minority carrier diffusion length,
- back surface passivation:
  - oxide and/or nitride passivation + local BSF(PERL)
  - floating junction structure
- or back surface field,
- back electrode passivation:
  - point contact,
  - deep back-surface diffusion under the contact,
- back reflector,
- back surface texture,
- antireflection coating optimised for encapsulation.

The current status in the development of industrial type processing steps leading to an improved cell efficiency will be described in detail in the sections below.

2 Cell Processing

2.1 Substrates

Although the standard substrate size is still 10 × 10 cm^2, there is a clear tendency to larger sizes. Many solar cell manufacturers base their production lines on 12.5 × 12.5 cm^2 wafers. Efficient cells of 15 × 15 cm^2 and even 20 × 20 cm^2 [1] have been reported. The driving force towards these larger cell sizes results from the fact that the cell manufacturing and module assembly costs show little area dependence and, therefore, the cost per Wp decreases with increasing cell size. The optimum cell size, however, is limited by series resistance and by a limitation on the module size due to handling, wind loads, module transportation and system assembly. Therefore, cell sizes larger than 20 × 20 cm^2 appear to be excluded. Due to the successful developments in multiwire sawing, wafer thickness of 150 μm or thinner are becoming feasible, corresponding to a final cell thickness of 120 μm or lower [2]. This allows an important material saving and, at the same time, thinner cells correspond to the optimum thickness if efficient light trapping and surface passivation are possible. In spite of significant progress in slicing techniques, around 200 μm of high quality silicon per wafer is still lost in kerf waste.

Kerf loss can be completely avoided in the ribbon and sheet silicon technologies. Although many technologies have been tried on the laboratory or pilot scale [3–6] only the Edge-defined-Film-fed Growth (EFG) polysilicon sheets have been introduced into high volume production [5]. An individual crystal is grown in the form of hollow octagonal tube, with eight 10 cm wide faces and average tube wall thickness of 300 μm. A total tube length is usually 4.6 m. The faces are then separated and cut to lengths appropriate for cell processing.

2.2 Etching, Texturing and Optical Confinement

Silicon substrates used in commercial solar cell processes contain a near-surface saw-damaged layer which has to be removed at the beginning of the process. Thickness of the damage depends on the technique used in wafering of the ingot. A layer with thickness of 20 to 30 μm has to be etched from both sides of wafers cut by an inner-diameter (ID) blade saw, while only 10 to 20 μm is enough when a wire saw is used. The damage removal etch is typically based on 20–30 wt.% aqueous solution of NaOH or KOH heated to 80–90°C. The etching process has to be slightly modified when applied to multicrystalline substrates. Too fast or prolonged etching can produce steps at grain boundaries. This can lead to problems with interruptions of metal contacts. This problem can be avoided by an isotropic etching based on a mixture of nitric, acetic and hydrofluoric acids. However, a strong exothermic reaction makes this etching process difficult to control and toxicity of the solution creates safety and waste disposal problems.

The silicon surface after saw damage etching is shiny and reflects more than 35% of incident light. The reflection losses in commercial solar cells are reduced

mainly by random chemical texturing [7, 8]. Surface texturing reduces the optical reflection from the single crystalline silicon surface to less than 10% by allowing the reflected ray to be recoupled into the cell. Monocrystalline silicon substrates with a surface orientation $<100>$ can be textured by anisotropic etching at temperature of 70-80°C in a weak, usually 2 wt.%, solution of NaOH or KOH with addition of isopropanol. This etch produces randomly distributed upside pyramids [8]. However, this process brings often production problems of repeatability, lack of pyramid size control and the presence of untextured regions [7]. The important parameters are: adequate surface preparation, temperature control, mixing rate and isopropanol concentration [8]. The solution to this problem requires the use of appropriate additives which enhance the pyramid nucleation process [7]. When the process is under control, uniformly distributed pyramids with height of 3–5 μm are optimal for low reflection losses and later metallization process. Figure 1 shows the SEM micrograph of a randomly textured $<100>$ oriented silicon surface.

The random texturization process is not effective on multicrystalline substrates due to its anisotropic nature. Isotropic texturing methods based on photolithography and wet etching are not cost-effective. Many techniques such as defect etching, reactive ion etching or laser scribing have been tried by many groups [9–14]. The best results, from the optical point of view, have been obtained by mechanical texturing and by reactive ion etching [13]. Mechanical grooving is a method of forming V-grooves in Si wafer by mechanical abrasion, using a conventional dicing saw and bevelled blades [14]. The optical quality of the mechanically textured surface depends on the blade tip angle, groove depth and damage layer etching. An average reflection of 6.6% in the range 500–1000 nm was obtained with a minimum reflection of 5.6% at 950 nm on multi-Si grooved with a blade having tip angle of 35° [14]. Figure 2 shows the influence of

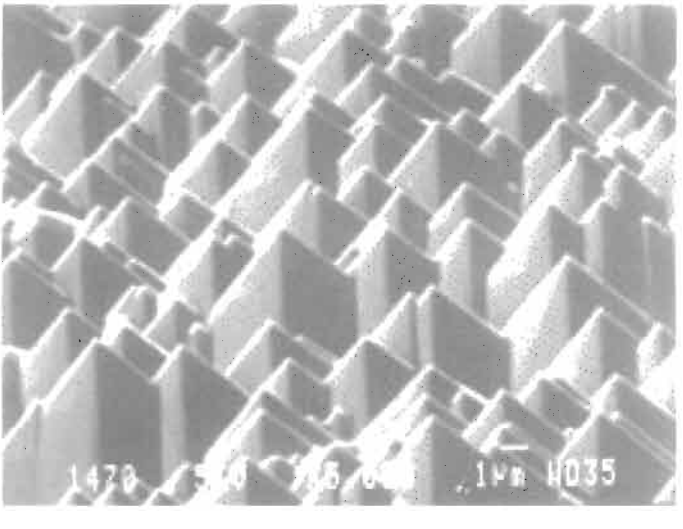

Figure 1 SEM micrograph of a randomly textured $<100>$ oriented silicon surface.

the groove depth on the reflectance. In addition to the reduced reflection, an improvement in internal quantum efficiency in the range 750–1000 nm has been observed in multicrystalline cells, indicating the effect of light trapping [15]. The light trapping effect is very important when thin silicon substrates ($< 200\ \mu m$) are used for material saving. Optimised grooving can bring as much as 0.5–1% absolute improvement in cell performance [16]. The efficiency of 17.2%, the highest ever reported for $10 \times 10\ cm^2$ multicrystalline cells, has been achieved by Sharp with mechanical grooving and screen printing [17]. The best results are obtained when a single blade bevelled saw is used. The main disadvantage of this approach is the low throughput of one wafer every two hours. A multiblade system can reduce the grooving process to a few seconds but the quality of the grooves are poorer than obtained with single blade grooving [18]. Lately a new technique of the mechanical surface structuring, wire grooving has been introduced [19]. This process has a much higher throughput than V-grooving with a bevelled blade and a dicing saw. A homogeneous web of stainless steel wires of about 180 μm in diameter and at a certain distance are guided by four grooved rollers as in the standard wafer cutting technique.

A very elegant technique of isotropic surface texturing of multicrystalline surface has been developed [20]. Here the proprietary acid solution gives isotropic surface structuring which, in combination with a TiOx antireflection coating, decreases the surface reflection to the value of monocrystalline randomly textured wafers.

2.3 Cleaning

In an industrial high-efficiency silicon solar cell process, wafers are typically cleaned after texturing and before surface passivation (oxide growth).

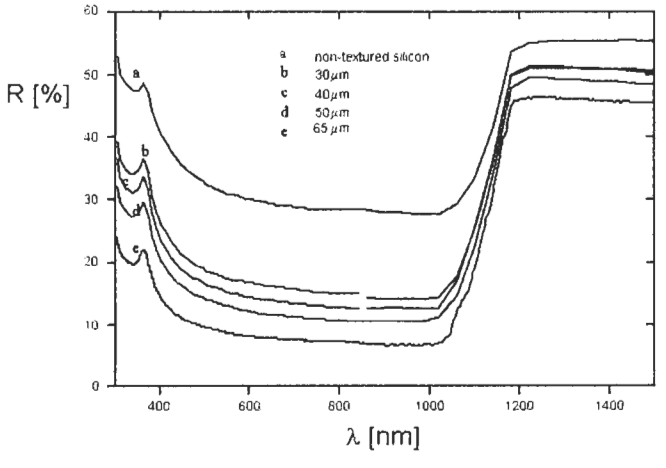

Figure 2 Reflectance curves of mechanically V-grooved multicrystalline silicon substrates. Influence of the groove depth is presented.

Traditionally RCA clean [21], originally developed for use in microelectronics, is the most widespread cleaning recipe in solar cell processing. Although not often discussed in the solar cell technical literature, cleaning is very important for solar cell performance. Long diffusion lengths of minority carriers, necessary for high efficiency cells, require low levels of metal contamination at the silicon surface before a high temperature treatment. Moreover, a growing concern in the photovoltaic community is the chemical waste produced during cell processing. The conventional RCA cleaning consists of two steps normally referred to as SC1 and SC2. The SC1 step consisting of a $NH_4OH/H_2O_2/H_2O$ mixture, aims at organic particle removal, whereas the SC2 step (an $HCl/H_2O_2/H_2O$ mixture) is used to remove metal contaminants. A more detailed analysis reveals that, because of their large feature size and the absence of photolithographic processes, organic particles are not an important issue and therefore the SC1 step is not essential for industrial solar cells. On the contrary, it is known that the metal contamination resulting from the SC1 step may be high and a one-to-one correlation between the metal concentration of the SC1 bath and the metal contamination of the silicon surface was found. This requires the use of sub ppb metal contamination specification of chemicals.

Recently, a new cleaning concept has been introduced [22] as a potential replacement for the standard RCA clean. This new 'IMEC-clean', which reveals a perfect removal of metallic particles, usually consists of H_2SO_4/H_2O_2 step, followed by a 1% diluted HF step. There are, however, processes developed already for surface cleaning which use ozonated mixtures as H_2SO_4/O_3, H_2O/O_3 and UV-O_3. Table 1 presents the metal contamination removal for RCA-clean and IMEC-clean.

If removal of metallic contamination is the only issue, a single cleaning step in 1% diluted HCl yields excellent results. This is especially important for the cleaning step performed after texturization. A further advantage is the low consumption of chemicals. This results not only in important cost savings but also in a considerable reduction of chemical waste products.

2.4 Junction Formation

It has been proved by many workers [23–26] that the optimum emitter doping profile should be relatively deep and moderately doped, or a shallow emitter should be formed with a high surface concentration. Both profiles combined with surface passivation by high quality thermal oxides show reduced surface

Table 1 Metal contamination removal (in 10^{10} at/cm^2 after IMEC vs. RCA+HF clean) [22]

Cleaning treatment	Ca	Fe	Cu	Zn
Starting level	15	1	2	1
IMEC	0.7	0.3	< 0.1	0.7
RCA + HF	2.5	0.8	0.5	4.9
5 × (IMEC) +HF	< 0.1	< 0.1	< 0.1	0.1
5 × (RCA) + HF	4.5	0.3	< 0.1	< 0.1

recombination losses and increased emitter collection efficiency. However, both industrial techniques used for front contact fabrication – i.e. screen printing of silver pastes and electroless plating of Ni – require a highly doped P surface concentration (above 10^{20} cm^{-3}) and a deep junction to obtain acceptable contact resistance and to avoid metallic impurity penetration towards the junction region. Typical emitter sheet resistance used in a screen printing metallization process is between 30 and 50 ohm/sq. This can be achieved by diffusion from liquid $POCl_3$ or solid P_2O_5 sources in open tube furnaces or, more industrially, from screen printed, sprayed- or spin-on P-sources followed by a conveyor belt furnace diffusion. Deep emitter and poor surface passivation lead to voltage loss and collection losses in the short light wavelengths. The perfect solution brings a selective emitter structure shown in Figure 3.

The heavy and deep diffusion under the contact fingers not only assures low contact resistance, giving good fill factor, but also reduces the contact contribution to front surface recombination losses. The emitter between fingers is optimised for high spectral response and high Voc thanks to relatively low surface concentration. The selective emitter structure is realised in practice by double diffusion [27] or single diffusion and etching back the active emitter region to the desired sheet resistance [28]. The high thermal budget of the emitter diffusion process can be significantly reduced by adapting rapid thermal processing RTP [29, 30] to the industrial cell process. Although this technology is at an early stage of development, the first trials bring promising results.

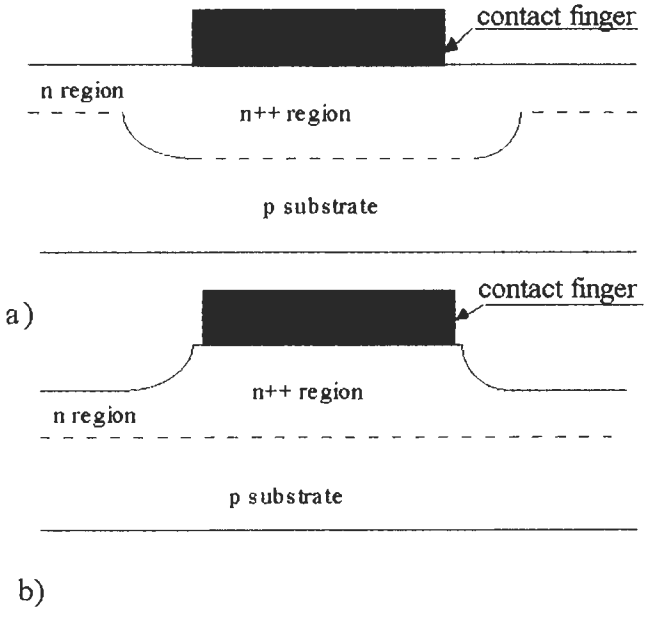

Figure 3 Schematic representation of a selective emitter fabricated by: (a) two diffusions, (b) one deep diffusion and selective etch-back.

An entirely different approach is presented by MIS inversion layer solar cell technology. Here, the emitter diffusion process is completely eliminated by inducing an n^+ inversion layer in the p-type silicon substrate. The inversion layer is induced by positive charge in the top silicon nitride antireflection coating layer. The high positive charge density is achieved by the incorporation of cesium [31].

2.5 Front Surface Passivation and Antireflection Coating

Surface recombination can be effectively decreased by many techniques. The most common one for the laboratory cells is to grow a thin thermal oxide and deposit a double antireflection coating by evaporating ZnS and MgF_2 layers [32], or by growing a thick thermal oxide up to 110 nm which serves, at the same time, as a passivating and anti-reflection coating (ARC) layer [33]. This gives a decreased surface recombination velocity at the Si-SiO_2 interface depending on the P surface concentration of the emitter and density of interface states. The interface quality is further improved by a low temperature anneal in forming gas. Such surface passivation is very effective especially with low emitter doping concentration, and regularly leads to an enhancement in the photogenerated current and open circuit voltage. Both approaches are excluded in industrial processes due to the high cost and low throughput of vacuum processes and long time needed to grow a thick thermal oxide The thickness of the passivating oxide in case of industrial cells is in the range 6–15 nm which is thin enough not to disturb the optical system in combination with antireflection coating and thick enough to ensure an effective surface passivation.

Industrial solar cells today widely use TiO_2 anti-reflection coating deposited mainly by atmospheric pressure chemical vapour deposition (APCVD) in a conveyor belt furnace, spin-on or spray-on techniques. An investigation revealed that perfect passivation for mono- as well as multicrystalline cells is obtained by a combination of a thin dry oxide and a plasma enhanced chemical vapour deposition (PECVD) silicon nitride [13, 34]. The thermal treatment of the PECVD SiNx layer during the contact firing through the SiNx layer is a crucial process to get good surface and bulk passivation. This process is particularly attractive for multicrystalline cells since it can eliminate lengthy Si-bulk passivation processes in atomic hydrogen ambient [34, 35].

2.6 Back-Surface-Field (BSF) and Back Side Passivation

Since the trend in industrial solar cell manufacturing is towards producing cells on thinner wafers, the role of back side recombination becomes important also in industrial mono- and multicrystalline solar cells. Currently, in most of the industrial cell structures, back side passivation is performed by alloying a screen printed aluminium paste with silicon. Aluminium forms an eutectic alloy with silicon at a temperature of 577°C. During the firing process, a liquid Al–Si phase is formed according to the Al–Si phase diagram. The molten Al–Si region acts as a sink for many impurities, giving a perfect gettering effect. During cooling

down, the silicon recrystallises and is doped with aluminium at its solubility limit of Al at given temperature, creating a p^+ Back Surface Field (BSF) layer (Figure 4(a)) [36, 37]. A sufficient thickness of Al is required to achieve a significant contribution of Si in the formation of the liquid phase. A very low back surface recombination velocity down to 200 cm/s can be achieved when a thick aluminium layer above 20 μm is printed and fired at a temperature above 800°C for a duration of 1 to 5 minutes [37, 38]. This process, however, causes significant wafer warping which can create a problem of low mechanical yield if thin substrates are used. The p^+ BSF can be created by evaporating an Al layer and sintering for a few hours at high temperature [39]. The wafer warping problem is significantly reduced but this process, however, is not able to achieve as low a surface recombination velocity as screen-printed Al BSF. A rear surface recombination velocity above 1000 cm/s at the p-p^+ interface has been measured [40, 41].

Another method which proved to be very effective is the so-called local BSF process (Figure 4(b)). In this case most of the back side surface is passivated with thermally grown oxide while the gridded back side electrode covers between 1 and 4% of the total back surface area [42]. An emerging and very promising process for back side passivation is the floating junction approach [43, 44] (Figure 4(c)). Here, a back side n^+ junction which is created during $POCl_3$ diffusion of the emitter, is at a floating and forward biased potential. In theory, this should give a very effective back side passivation not strongly dependent on the back surface recombination velocity. The back contact grid can be made by screen printing Ag/Al pastes [20, 45], mechanical of laser grooving, boron diffusion and plating [44].

2.7 Front Contact Formation

The process of front contact formation is one of the most important solar cell processing steps. The applied metallization technique determines the shadowing and series resistance losses, determines the emitter diffusion profile and surface doping concentration, and dictates the choice of certain surface passivation techniques. High efficiency, large area solar cells require front electrodes with low series resistance and a low area coverage. In order to meet these requirements, two basic techniques are implemented in solar cell mass production: laser grooved buried contact metallization and advanced screen printing processes.

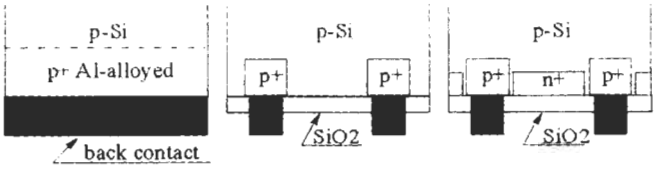

Figure 4 Schematic representations of different backside structures: (a) Al-alloyed BSF, (b) locally diffused BSF and (c) floating junction.

In the first method, plated metal contacts are formed in deep grooves cut by laser or mechanically into a lightly diffused and protected (by nitride or oxide) front surface. After etching and cleaning, the grooves are subjected to a second very heavy diffusion. The metallization is then obtained by a self-aligned plating process of nickel, copper and thin layer of silver [46]. The advantages of these cells have been described in the literature [40] and include the very large height-to-width ratio of the finger metallization and the fine line width (typically 20–25 μm, see Figure 5(a)). Based on this cell structure and using simplified processing, a cost effective production technology is now in operation, yielding average efficiencies between 16–17% and occasionally up to 18% on 100 cm^2 CZ pseudo-square cells [47].

The main problems related to this technology are the environmental issues. The external costs of meeting environmental specifications of developed countries with processes producing an enormous amount of rinse water containing nickel and copper must be taken into account [48, 49]. It can be a major issue for planning large-volume plants above 100 MW.

In the screen printing method, a stainless steel or polyester mesh screen stretched on a metal frame is covered by a photo-emulsion layer. Then openings, which define the front contact pattern, are photolithographically formed in the screen. Highly conductive silver paste is pushed by a squeegee through openings in the screen onto substrates with a well-defined adjustable pressure.

Screen printing is a traditional industrial solar cell technology, existing since the beginning of the 1970s. The advantages of screen-printing solar cells are the fact that the technology is well established and can be improved step by step without requiring large capital investment, the robustness of the production equipment and the low amount of chemical wastes. The first generation of photovoltaic devices made with this technology suffered from severe limitations:

- Screen printed contacts were typically 150–200 μm wide, giving rise to large shading losses,
- Fill factors were very low (below 75%) because of the high contact resistance and low metal conductivity of screen-printed contacts,
- Effective emitter surface passivation was difficult because a high emitter surface concentration and deep emitter are needed to limit the contact resistance and avoid junction shunting. This also resulted in a poor response to short wavelength light.

Due to all these factors the efficiency of screen printed cells was typically about 25 to 35% lower than the efficiency of buried-contact cells.

Since the early stages of this technology, an important effort has been made by several research groups and companies, mainly in Japan and Europe, to improve the screen printing process [13, 17, 35, 50]. It appears possible to reduce the finger width to values between 50 and 100 μm with a high aspect ratio. By optimising pastes and firing temperatures, fill factors between 78 and 79% for 100 cm^2 screen printed cells can be obtained [34]. Screen printed metallization can also be combined with effective surface passivation in selective emitter

structures. Figure 5 depicts the cross-section of buried and screen printed contacts drawn in the same scale.

Among other techniques for front contact formation, there are reports of direct pen writing, offset printing [51] and roller printing [18] The direct pen writing with a very high aspect ratio has been applied for a front contact metallization of EFG silicon sheets solar cells [52].

2.8 Substrate Material Improvement

Maintaining a high-enough bulk minority carrier lifetime is essential to improving the performance of crystalline Si solar cells. Unlike the high quality and expensive FZ Si, the 'solar-grade quality' CZ-Si and multicrystalline Si (mc-Si) substrates generally exhibit moderate bulk lifetimes depending on various factors that introduce generation-recombination (GR) centres within the band gap. The major sources of these centres include the oxygen and carbon content, metallic impurities, high densities of crystallographic defects, and the presence of grain and sub-grain boundaries. Many of these factors are not completely avoidable given the low-cost substrate requirement for silicon photovoltaics. Gettering is a technique which either reduces or eliminates metallic impurities in the substrates by localising and blocking them away from the device active regions, or by completely removing them from the substrate. The former is referred to as intrinsic gettering and the latter as extrinsic gettering. Gettering techniques are well-established in Si IC technology for various purposes. for example, to reduce the leakage currents induced by GR centres in CCD image sensors, CMOS devices etc. In solar cell fabrication, it is desirable that the gettering treatment remains part of the cell processing and does not considerably increase the production cost. Phosphorus diffusion and aluminium diffusion are the most efficient gettering schemes used in Si solar cell processing.

2.8.1 Gettering by Phosphorus Diffusion

Impurity migration towards gettering sites takes place as a consequence of a strong emission of Si interstitials due to the formation of SiP particles by heavy

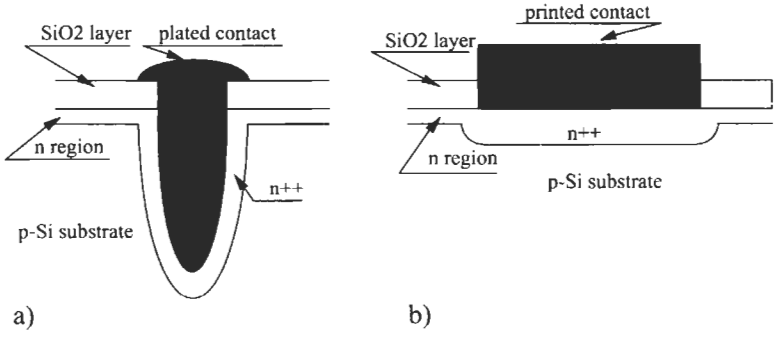

Figure 5 Cross-section of a laser grooved buried plated contact (a) in comparison with a fine line screen printed contact (b).

P-diffusion [53]. Enhanced solubility of metallic impurities in such heavily P-diffused regions, and impurity segregation at Si_3P_4 precipitates lead to efficient gettering [54]. In solar cell fabrication, P-diffusion can be performed prior to cell fabrication followed by the removal of the heavily diffused layers (pre-gettering) or as part of emitter formation, depending on the optimal gettering conditions required for the material and the costs involved. Certain selective emitter processes that involve two P-diffusions (see Section 2.4) benefit both from gettering and from the removal of heavily diffused layers with accumulated impurities. The gettering process is more complicated in mc-Si since, at high temperatures, the dissolution of impurities that are precipitated near bulk crystal defects is also initiated. Therefore, in mc-Si, high temperature gettering is not desirable due to the competition between the gettering rate and dissolution rate of the precipitated impurities [54]. Gettering efficiency depends also on certain material properties, for example, the interstitial oxygen $\{O_i\}$ content [55]. Some mc-Si wafers with lower $\{O_i\}$ reportedly showed a better improvement after pre-gettering compared to those with higher $\{O_i\}$ [56]. Diffusion length exceeding substrate thickness (200 μm) was obtained even on low resistivity mc-Si wafers after pre-gettering at low ($< 900°C$) temperatures [57]. However, the incorporation of an additional pre-gettering step in a production line adds to the production cost. An additional cost increment of 0.3 \$/wafer due to the pre-gettering step, based on a 5% relative efficiency improvement, has been reported [58]. Based on the same study, this additional cost can be halved by keeping the heavy P-diffused layer and etching back to the desired sheet resistance. Selective emitter structures, which can additionally lead to a better blue response and surface passivation, can therefore provide an acceptable solution.

2.8.2 Gettering by Aluminium Treatment

Formation of a p^+/p high/low junction at the rear side of the cell by regrowth from a 'fast-alloyed' Al-Si melt is the most commonly used process for creating BSF in industrial silicon cells (see Section 2.6). This treatment has an additional advantage of bulk gettering by prolonged firing or by a thermal anneal after the initial firing. At alloying times > 1 minute with screen printed Al, evidence of bulk impurity gettering has been noted at the grain boundaries of (100)/(111) CZ bi-crystals [59]. The effective grain boundary passivation obtained after Al diffusion has also been attributed to a much higher diffusion coefficient of Al along the grain boundaries [60]. Al-gettering effects have also been noted in single crystalline CZ-Si materials. From the relatively low temperatures generally used in Al gettering, it can be said that the gettered species are the fast moving interstitial impurities such as Cu, Fe, etc. Pilot line processes involving fast-alloying of screen printed Al-paste by firing, followed by removal of excess aluminium and a subsequent thermal anneal for up to 1h, resulted in considerable enhancement in bulk diffusion length in large area mc-Si wafers [61]. This process of fast firing also prevents impurities contained in the Al source from diffusing into Si. High performance, screen printed CZ-Si cells with Al-gettering have also been reported [50]. The thickness of the Al-layer

deposited on the rear side of the wafers is also of great importance in getting ideal pp^+ junctions for low-enough surface recombination velocity S_{eff} [36, 37, 62–65]. In ribbon materials such as EFG, efficiency enhancements of 1.4% absolute along with an increment of $> 60\ \mu m$ in diffusion length have been reported after an 850°C gettering treatment with evaporated aluminium [66]. Due to the large thickness requirement for the Al-source and for the cost effectiveness of the process, it appears that screen printing is the most efficient way for depositing the Al-source.

2.9 'Fast Processing' Techniques

In recent years, there has been an increased interest in the application of Rapid Thermal Processing (RTP) in solar cell fabrication. RTP is widely used in IC processing because of the low thermal budget for which it is essential to have a strict control over junction depth variation, lateral diffusion of dopants, etc. In RTP, which is based on annealing by radiation from incoherent light sources, the wafers are rapidly heated (50–150°C/s) and rapidly cooled. The process time is generally < 1 minute (Figure 6). A few examples of such RTP applications are

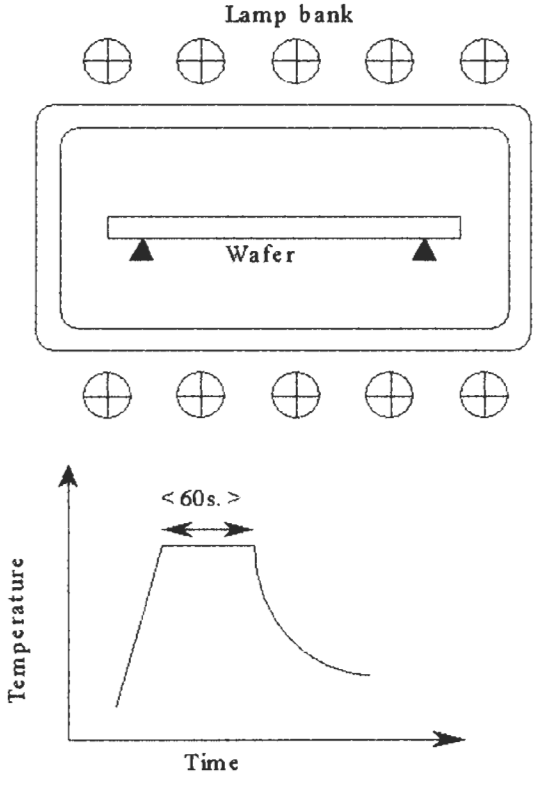

Figure 6 Cross-section of an RTP furnace and a typical RTP temperature cycle.

dopant activation after implantation, implantation damage anneal, silicidation, sintering, and oxide anneal.

A more recent application of RTP is the development of Si solar cells. RTP has been used in various cell processing steps such as junction formation, growth of high quality thin passivating oxides, annealing of Si/dielectric interface, and Si/metal contact firing. RTP differs from conventional furnace processing in that the wafer is optically heated by incoherent lamp radiation (tungsten–halogen or UV lamps) with much higher colour temperatures compared to conventional heating elements. Due to the availability of highly energetic, short wavelength, photons the electronically excited states influence and enhance diffusion, oxidation, and gettering phenomena [67].

In solar cell application, RTP looks attractive because of its reduced process time, reduced cross contamination (reactor parts are almost transparent to lamp spectrum), and the possibility to diffuse front and rear junctions together. Furthermore, extensive wafer cleaning steps can by avoided by, for example, UV cleaning. For junction formation, diffusion sources such as spin-on or spray-on P or B sources or APCVD-deposited SiO_2:P_2O_5 or SiO_2:B_2O_3 sources and evaporated or screen printed Al are used. In most cases, the emitter and BSF are formed simultaneously in a single cycle [68, 69]. The emitter junction depths are generally of the order of 0.15–0.25 μm. Although such shallow junctions yield an excellent blue response, it had been somewhat difficult to apply a cost-effective metallization scheme such as screen printing. However, successful application of screen printed front metallization to RTP emitters has recently been reported [29]. For surface passivation, either high quality, thin RT-grown oxides [68] or PECVD SiO_2/Si_3N_4 [69] followed by RT-anneal have been efficiently applied. Solar cells fabricated without involving any conventional furnace processes exhibit encouraging conversion efficiencies of 17% in 1 cm^2 FZ-Si [69] and 15.4% in 100 cm^2 CZ-Si [70]. MIS solar cells have also been fabricated with high quality, ultra-thin RT-oxides and oxynitrides [71]. Nevertheless, for the RTP technique to become a competitive alternative to existing conventional processing, the wafer yield of the process should be drastically increased. This can be achieved by building either continuous process systems with spectrum-engineered lamps or batch-process systems capable of handling large number of wafers. RTP system manufacturers and PV industry are presently working on this.

3 Industrial Solar Cell Technologies

Most of the commercially fabricated crystalline solar cells are still based on screen printing. The industrial production of more advanced solar cells technologies such as laser-grooved buried contact, MIS and EFG solar cells contribute less than 10% to the total commercial production. The way in which the high-efficiency solar cell features described above can be incorporated in the commercial processing sequence is outlined below.

3.1 Screen Printing Solar Cells

Screen printing is a well established, simple, robust, continuous and easily adaptable process. Fully automated screen printing solar cell production lines are offered by many companies. From all high efficiency features described in Section 2 (see also Chapter IIb-5), usually only the front surface texturing and Al-alloyed back-surface field are included in the screen printing solar cell process. This explains why the efficiency of some industrial crystalline solar cells still ranges from 13 to 15%. An important effort has been made by several research groups and companies, mainly in Japan and Europe, to improve the screen printing process [13, 17, 35, 50]. The main progress has been made in the paste formulation, fabrication of new type of fine line screens, and the development of modern screen printers.

The new type of silver pastes contains additives which permit a selective dissolving of silicon dioxide and ARC layers of TiOx or SiNx during the firing process while preventing deep penetration into bulk silicon. This gives the possibility of using a very simplified process with firing through passivating oxide and ARC. The improved screen-printability of new pastes and new types of metal screens [50] give the possibility to print narrower lines down to 50–60 μm with an improved aspect ratio. Therefore, spacing of the screen printed contact lines can be reduced, leading to more lightly doped emitters with improved short wavelength response. The problem of non-optimal surface passivation is tackled by the use of a selective emitter structure.

One applied process sequence for high efficiency screen printed solar cells is shown in Table 2 [72]. Figure 7 presents a cross section of such a processed cell.

Alignment of front contacts on top of a highly doped n^{++} region is done automatically by a new type screen printer equipped with digital cameras. The movement of the table and the squeegee is driven by linear motors controlled by a central computer.

The high efficiency features of these new screen printed solar cells are front surface texturing, deep diffusion under front metallization contacts, reduced total front surface shadowing losses down to 6%, shallow emitter with optimised profile and front surface passivation, Back Surface Field (BSF).

Table 2 Processing sequence of screen printing solar cell based on selective emitter and firing-through passivating oxide and ARC [72]

Step no.	Process description
1	Saw damage etching
2	Deep n^{++} diffusion over the whole front surface (15 ohm/sq.)
3	Selective texture etching of diffused layer between contact fingers
4	Second light n^{+} diffusion (80–120 ohm/sq.)
5	Growing of passivating dry thermal oxide
6	Edge junction isolation
7	ARC deposition (APCVD TiOx or PECVD SiNx)
8	Top and back contacts printing and drying
9	Co-firing of both contacts and firing through passivating oxide and ARC layer

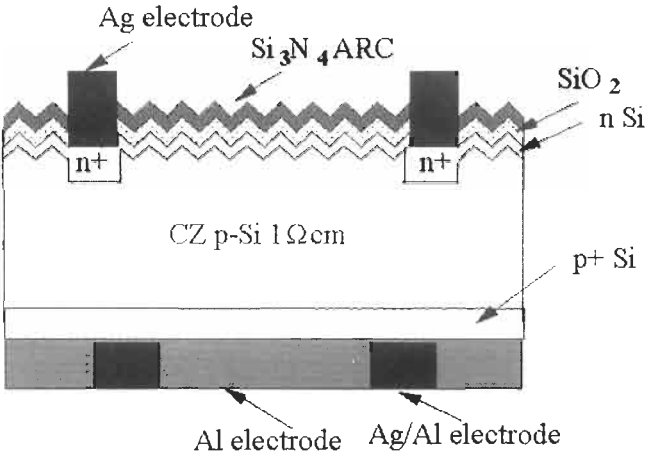

Figure 7. Cross-section of an advanced screen printed solar cell with selective emitter and Al-alloyed BSF [72].

Pilot line efficiencies of 16.6% for homogeneous emitter CZ large area solar cells have been obtained and independently measured [73]. The selective emitter process gives efficiencies close to 17.3% for CZ-Si [50] and 15.9% for large-area multicrystalline cells [73]. All processing steps can easily be transferred to large-volume production lines. A process that combines screen printing and grooving has demonstrated efficiencies above 17% on 100 cm^2 multicrystalline solar cells [17]. This is a record efficiency for a large area silicon multicrystalline solar cell fabricated by any type of technology. The screen printing process is also well suited for larger cell sizes: 15 × 15 cm^2 multicrystalline cells with efficiencies of 15.6% has also been demonstrated [74].

3.2 Buried Contact Solar Cells (BCSC)

The buried contact solar cell (BCSC) process has been developed at the University of New South Wales [46, 75]. Many aspects of the BCSC structure and its processing have been extensively described in the technical literature [39, 42, 44, 75, 76–79] (see also Chapter IIb-5). A laboratory efficiency as high as 21.3 % on small area FZ material has been reported [80]. Figure 10 in Chapter IIb-5 shows the structure of the buried contact solar cell. A conventional commercial BCSC processing sequence licensed to many solar cell manufactures is presented in Table 3.

The buried contact solar cell structure embodies almost all characteristic features of high efficiency laboratory cells described in Section 2: shallow emitter diffusion with a very good surface passivation by a thick thermal oxide, very fine metallization line width, front contact passivation by heavy diffusion in the contact area, BSF. One of the important processing steps is growing a very thick thermal oxide on the top surface which simultaneously acts as a diffusion mask,

Table 3 Conventional commercial process sequence of buried contact solar cell [78]

Step no.	Process description
1	Saw damage etching and random texturing
2	Light n^+ diffusion over the whole surface
3	Growing of thick thermal oxide
4	Mechanical or laser groove formation
5	Groove damage etching and cleaning
6	Second heavy diffusion in grooved areas only
7	Aluminium evaporation on a back side
8	High-temperature Al alloying
9	Electroless plating of nickel, sintering and etching
10	Electroless plating of copper and silver
11	Edge junction isolation by laser scribing

plating mask, and surface passivation layer. In some processing sequences, the thick oxide is replaced by silicon nitride which reduces the front surface reflection.

This process, however, has its disadvantages when commercial applications are considered: a large number of lengthy processing steps at high temperature (above 950°C for a total time of up to 16 hours), expensive equipment, many careful pre-cleaning steps that make the process complex and labour intensive [81]. Although the BCSC process has been licensed to many leading solar cell manufacturers, only one has succeeded introducing it into large-volume production by simplifying many processing steps [82]. Efficiencies close to 17% are rudimentarily obtained.

A simplified buried contact solar cell process has been proposed in reference [79]. The aim of this process simplification is to suit infrastructure and equipment existing already in many solar cell production plants based on screen printed contacts. The number of high temperature processing steps has been reduced to one, front surface passivation is achieved by retention of the diffusion oxide, and a sprayed-on TiO_2 layer acts as an ARC and plating mask. There are no data published about the cell performance achieved with this process.

3.3 Metal–Insulator–Semiconductor Inversion Layer (MIS-IL) Solar Cells

The commercial version of MIS-IL cells was developed in the 1980s [83]. Industrial production of 10×10 cm^2 cells was introduced in the early 1990s [84]. MIS-IL solar cells received much attention because of the elimination of high temperature steps, such as junction diffusion or thermal oxide passivation, from the cell processing sequence. The processing sequence of MIS is presented in Table 4. The diffused n-type front emitter is replaced by an inversion n-conducting layer at the front surface which is induced by a high-density fixed positive charge present in the transparent insulator film. Evaporated Al front contacts are separated from the silicon interface by a thin tunnel oxide that reduces surface recombination. An efficiency of 15.3% on 100 cm^2 CZ silicon has been measured and confirmed [73]. It appears that further improvement of the

MIS inversion layer requires the PECVD nitride deposition at 400°C prior to the MIS contact formation. This leads to several modifications of the first generation cell, for example, truncated pyramid or surface-grooved abrased-ridge-top MIS-IL cells [31]. The MIS-IL solar cells are especially suitable for a high quality material like FZ silicon since low temperature processing preserves a high initial lifetime. For industrial application, however, where low quality materials are used, an impurity gettering which accompanies the phosphorus diffusion or aluminium alloying are prerequisites for obtaining high efficiency.

The combination of p-n junction and MIS solar cells has been demonstrated in a MIS-contacted p–n junction solar cell (see Figure 8). Evaporated aluminium front contacts are separated from a phosphorus diffused p-n junction by a thin oxide layer. This process brings the advantages of phosphorus gettering, front contact passivation by tunnel oxide and front surface passivation by PECVD silicon nitride. An efficiency of 16.5% has been reported on a 98 cm^2 CZ-silicon substrate [73].

3.4 Solar Cells on EFG Silicon Sheets

EFG silicon sheets offer a significant cost advantage over traditional crystalline silicon technology like CZ pulling or casting multicrystalline blocks. The cost saving arises from elimination of the slicing process which is a significant cost contributor to CZ and multicrystalline wafers. However, the EFG material has high crystal defect density such as grain boundaries, twins and dislocations [5].

High mechanical stress and the uneven surface of EFG sheets make application of standard screen printing processes difficult because of high breakage. Several patented processing steps have been developed to passivate the highly defected EFG bulk material and to tackle the problem of contacting the uneven surface. A detailed description of the EFG solar cell process is not published but some information can be found in [85]. The process comprises several patented processing steps: spray-on of liquid P-source and diffusion in an IR-belt furnace, PECVD of silicon nitride antireflection coating preceded by ammonia plasma treatment in order to produce hydrogen implantation, 'pad printing' of solderable silver contacts on the back and drying, 'pad printing' of aluminium

Table 4 Processing sequence of MIS solar cells [84]

Step no.	Process description
1	Saw damage etching and surface texturing
2	Chemical texturing
3	Evaporation of 4 μm Al on the back side
4	Sintering of contacts at the back at 500°C and growth of 1.5 nm tunnel oxide on the front side
5	Front 6 μm Al grid evaporation through metal mask on the top of the tunnel oxide
6	Etch excess Al along the grid lines
7	Dip in CsCl solution to increased fixed positive charge density
8	Deposition of PECVD silicon nitride onto the entire front surface at 250°C for 5 min

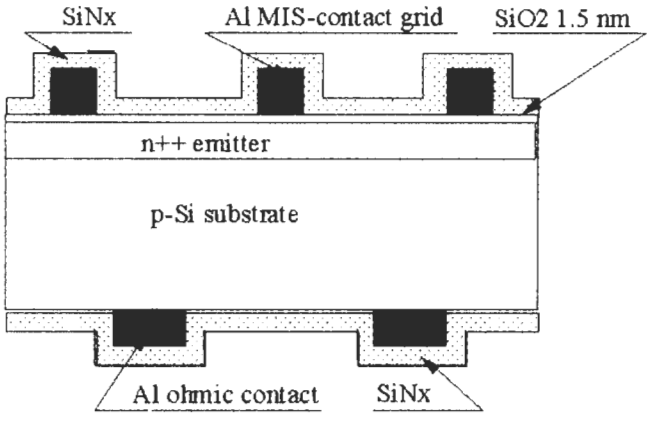

Figure 8 Cross-section of an MIS solar cell [31].

paste on the back and drying, direct writing of silver paste on the front, and drying and co-firing of all contacts in an IR-furnace

During the firing process the front contact paste penetrates through PECVD silicon nitride layer and forms a good ohmic contact. The aluminium paste creates a deep p^+ alloyed BSF region on the back and at the same time the heating process tends to release hydrogen from silicon nitride and drives it deeper into the substrate providing good bulk passivation. A record average efficiency of 14.3% on large-area EFG substrates has been reported [86].

3.5 Commercial Thin Film Crystalline Silicon Solar Cells

There is a growing interest in thin film silicon solar cells consisting of a thin (20–50 μm) silicon film deposited on potentially cheap substrates, as reviewed in detail Chapter IIb-3. Such thin structures offer the opportunity for silicon cells to use much less high-purity silicon than conventional ingot-type solar cells. When an effective light trapping scheme is utilised, efficiencies higher than for standard type thick cells are possible [87]. Potential substrates include metallurgical grade silicon, stainless steel, graphite, ceramics or even glass. Among the many deposition methods, the most common are chemical vapour deposition (CVD) or liquid phase epitaxial growth (LPE).

Although most of the development in this field is still in an early stage, the formation of continuous sheets of polycrystalline silicon on conductive ceramics, the so called Silicon-Film™ process has already been put in test production [88]. Since these sheets are fabricated at the desired thickness, ingot sawing is avoided, leading to a significant cost reduction. The cross section of a so-called product II Si-Film™ solar cell is shown in Figure 9.

The Silicon-Film™ is a proprietary process and only a very general process sequence has been published. The generic process consists of ceramic formation, metallurgical barrier formation, polycrystalline layer deposition, emitter

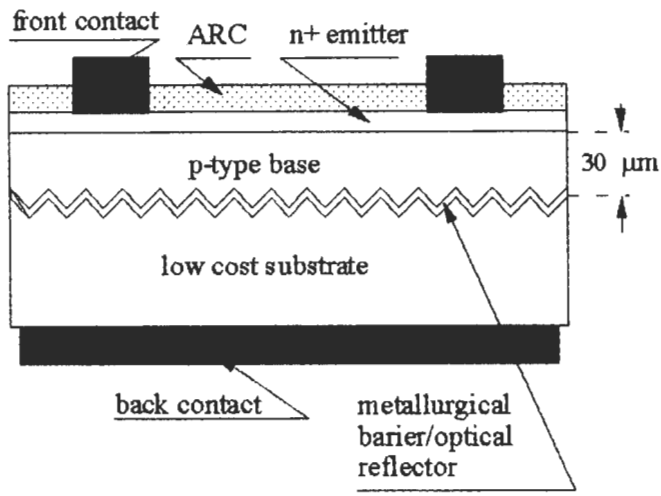

Figure 9 Cross-section of a Silicon Film™ solar cell [88].

diffusion and contact fabrication. The conductive ceramic substrate is fabricated from low-cost materials. The metallurgical barrier prevents substrate impurities from entering and contaminating the active thin silicon layer. The randomly textured and highly reflective metallurgical barrier layer improves the light trapping. A suitable p-type doped 30–100 μm active layer is deposited from a liquid solution. Phosphorus and aluminium impurity gettering are used for bulk quality improvement. The rest of the cell process is similar to a standard screen-printing solar-cell manufacturing sequence. Cells with large areas of 240, 300 and 700 cm^2 have been developed. A cell with an area of 675 cm^2 has demonstrated the record efficiency of 11.6% [89]. PV modules with Silicon Film™ cells are now in test production [6, 90]. A further discussion of this field can be found in Chapter IIb-3.

4 Cost of Commercial Photovoltaic Modules

A typical crystalline Si solar cell produces a voltage of 0.5 V around the maximum power point. In a module, the individual cells are usually connected in series to produce a voltage useful for practical application. Most industrial modules today comprise 36 series-connected cells in order to charge a 12 V battery. A cross section of a typical PV module is shown on Figure 10. The cells are placed in a sandwich structure glass/encapsulant sheet/cells/encapsulant sheet/back substrate. The cover glass normally has a low iron content to minimise light absorption and is generally either chemically or thermally tempered to increase the mechanical strength, especially against hailstorms. The encapsulant sheet is a transparent polymer that can be laminated onto glass.

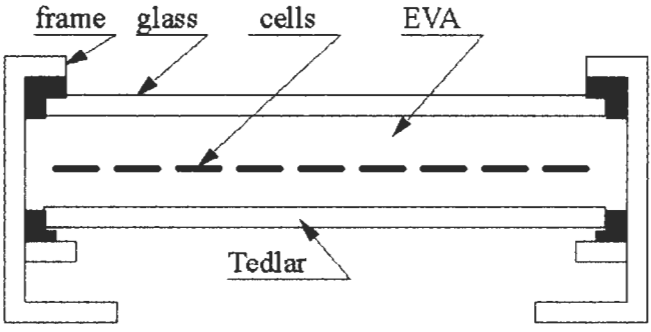

Figure 10 Cross-section of a photovoltaic module

The most commonly used encapsulants are polyvinyl butyral (PVB) or ethylene vinylacetate (EVA). For the back substrate, several materials are used, including anodised aluminium, glass or polymers such as Mylar or Tedlar.

The price of commercially available photovoltaic modules is 3.5–4.5 $/Wp. The average total cost breakdown from five cell manufacturers is shown in Table 5. Of the total module cost, the silicon wafer is responsible for 46%, cell fabrication 24% and module fabrication 30% . Sensitivity analysis of different cost elements, performed for a base-line screen printing process, shows that the cell efficiency is the most significant factor in the cost reduction [58, 91]. Cost reduction is a driving force for introducing efficiency enhancement techniques into commercial cell production. However, care must be taken that novel techniques do not bring significant cost from increased capital investment and lower yield associated with the higher complexity process [91]. The cost effectiveness of several efficiency enhancement techniques has been analysed [58] and has revealed that all techniques described in Section 2 are commercially viable. Processing sequences such as evaporated front contacts and selective emitter involving photolithography are not commercially applicable in their present form.

A study in the framework of the European project APAS RENA CT94 0008 [93] has demonstrated that practical implementation of new industrial processing schemes and increasing the market size towards 500 MWp/year will lead to drastic crystalline silicon photovoltaic module price reductions to 0.95–1.73 $/Wp depending on the wafer type and cell process. The different commercial technologies of mono- and multi-crystalline solar cells have been studied include screen printing, laser-grooved buried contact, MIS-contacted diffused emitter, and a proprietary cell process on EFG silicon sheets. The study assumptions and cost breakdown are presented in Table 6. These results demonstrate that cell fabrication based on EFG silicon sheets gives the lowest module cost mainly due to the avoidance of the costly wafering step. The well-known and established screen-printed cells on multicrystalline wafers fabricated by directional solidification shows the next lowest cost of 1.21 $/Wp. It is worth

Table 5 Average values for five manufacturers of total cost breakdown of crystalline silicon photovoltaic modules

Total cost ($/Wp)	Si feedstock	Crystallisation	Wafering	Cell fab.	Module fab.
4	0.38	0.73	0.73	0.96	1.2

Table 6 Manufacturing cost in $/Wp for different crystalline manufacturing scenarios at 500 MWp/year production. Case 1: EFG Si sheets, printed contacts = 15%; Case2: direct solidification multi-Si, screen printed contacts, η = 15% ; Case3: CZ mono-Si, LGBC, η = 18%; Case 4: CZ mono-Si, screen printed contacts, η = 16%; Case5: mono-Si, MIS contacted, η = 17%. Wafer size in all cases is 125 mm × 125 mm and thickness 250 μm [93]

Fabrication step	Case 1	Case 2	Case 3	Case 4	Case 5
Ingot growing	0.37	0.37	0.73	0.82	0.78
Wafering	0.00	0.29	0.24	0.28	0.28
Solar cell fab.	0.15	0.15	0.19	0.16	0.24
Module fab.	0.43	0.40	0.37	0.41	0.43
Factory cost	0.95	1.21	1.53	1.67	1.73

mentioning that efficiencies between 16 and 17%, higher than the 15.5% assumed by the model, have already been achieved on large-area screen-printed multicrystalline cells. All the processes based on CZ wafers show higher costs because of the costly mono-Si wafers.

References

[1] Watanabe, H., Shirasawa, K., Masuri, K., Okada, K., Takayama, M., Fukui, K. and Yamashita, H., 1990. Technical Progress on Large Area Multicrystalline Silicon Solar Cells and its Applications. *Optoelectronics – Devices and Technologies*, Vol. 5, pp. 223–238.

[2] De Villers, T. and Smekens, G.R., 1995. *Monochess II – Final Report*, JOU2-CT92-0140.

[3] Eyer, A., Schilinger, N., Rauber, A. and Grabmaier, J.G., 1989. Continuous Processing of Silicon Sheet Material by SSP-Method. *Proc. 9th European Photovoltaic Solar Energy Conf.*, Freiburg, pp.17–18.

[4] Vermeulen, T., Evrard, O., Laureys, W., Poortmans, J., Caymax, M., Nijs, J., Mertens, R., Vinckiers, C. and Hofs, H.U., 1995. Realisation of Thin Film Solar Cells in Epitaxial Layers Grown on Highly Doped RGS-Ribbons. *Proc. 13th European Photovoltaic Solar Energy Conf.*, Nice, pp.1501–1504.

[5] Kardauskas, M., 1996. Processing of Large-Area Silicon Substrates with High Defect Densities into Higher Efficiency Solar Cells. *Proc. 6th Workshop on the Role of Impurities and Defects in Silicon Device Processing*, pp.172–176.

[6] Ingram, A.E., Barnett, A.M., Cotter, J.E., Ford, D.H., Hall, R.B., Rand, J.A. and Thomas, C.J., 1996. 13% Silicon Film ® Solar Cells on Low Cost Barrier-Coated Substrates. *Proc. 25th IEEE Photovoltaic Specialists Conf.*, Washington DC, pp. 477–480.

[7] Gee, J. and Wenham, S., 1993. Advanced Processing of Silicon Solar Cells. *Tutorial Notebook of Proc. of 23rd. IEEE Photovoltaic Specialists Conf.*, Louisville.

[8] King, D.L. and Buck, M.E., 1991. Experimental Optimization of an Anisotropic Etching Process for Random Texturization of Silicon Solar Cells. *Proc. 22nd IEEE Photovoltaic Specialists Conf.*, Las Vegas, pp. 303–308.

[9] Grauvogl, M., Aberle, A. and Hezel, R., 1996. 17.1% Efficient Truncated-Pyramid Inversion -Layer Silicon Solar Cells. *Proc. 25th IEEE Photovoltaic Specialists Conf.*, Washington DC, pp. 433–436.

[10] Kaiser, U., Kaiser, M. and Schindler, R., 1990. Texture Etching of Multicrystalline Silicon. *Proc. 10th European Photovoltaic Solar Energy Conf.*, Lisbon, pp. 293–294.

[11] Narayanan, S., Zolper, J., Yung, F., Wenham, S., Sproul, A., Chong, C. and Green, M., 1990. 18% Efficient Polycrystalline Silicon Solar Cells. *Proc. 21st IEEE Photovoltaic Specialists Conf.*, Orlando, pp. 678–680.

[12] Pirozzi, L., Garozzo, M., Salza, E., Ginocchietti, G. and Margadona, D., 1994. The Laser Texturization in a Full Screen Printing Fabrication Process of Large Area Poy silicon Solar Cells. *Proc. 12th European Photovoltaic Solar Energy Conf.*, Amsterdam, pp.1025–1028.

[13] Shirasawa, K., Takahasashi, H., Inomata, Y., Fukui, K., Okada, K., Takayaka, M. and Watanabe, H., 1994. Large Area High Efficiency Multicrystalline Silicon Solar Cells. *Proc. 12th European Photovoltaic Solar Energy Conf.*, Amsterdam, pp. 757–760.

[14] Willeke, G., Nussbaumer, H., Bender, H. and Bucher, E., 1992. A simple and Effective Light Trapping Technique for Polycrystalline Silicon Solar Cells. *Sol. Energy Mat. and Sol. Cells*, Vol. 26, pp. 345–356.

[15] Bender, H., Szlufcik, J., Nussbaumer, H., Nijs, J., Mertens, R., Willeke, G. and Bucher, E., Polycrystalline Silicon Solar Cells with a Mechanically Formed Texturization. *Appl. Phys. Lett.*, Vol. 62, pp. 2941–2943.

[16] Szlufcik, J., Fath, P., Nijs, J., Mertens, R., Willeke, G. and Bucher, E., 1994. Screen Printed Multicrystalline Silicon Solar Cells with a Mechanically Prepared V-Groove Front Texturization. *Proc. 12th European Photovoltaic Solar Energy Conf.*, Amsterdam, pp.769–772.

[17] Nakaya, H., Nishida, M., Takeda, Y., Moriuchi, S., Tonegawa, T., Machida, T. and Nunoi, T., 1994. Polycrystalline Silicon Solar Cells with V-Grooved Surface. *Sol. Energy Mat. Sol. Cells*, Vol. 34, pp. 219–225.

[18] Fath, P., Marckmann, C., Bucher, E. and Willeke, G., 1995. Multicrystalline Silicon Solar Cells Using a New High Throughput Mechanical Texturization Technology and a Roller Printing Metallization Technique. *Proc. 13th European Photovoltaic Solar Energy Conf.*, Nice, pp. 29–32.

[19] Hezel, R., 1995. A Novel Approach to Cost Effective High Efficiency Solar Cells. *Proc. 13th European Photovoltaic Solar Energy Conf.*, Nice, pp.115–118.

[20] Sarti, D., Le, Q.N., Bastide, S., Goaer, G. and Ferry, D., 1995. Thin Industrial Multicrystaline Solar Cells and Improved Optical Absorption. *Proc. 13th European Photovoltaic Solar Energy Conf.*, Nice, pp.25–28.

[21] Kern, W. and Poutinen, D.A., 1970. Cleaning Solution Based on Hydrogen Peroxide for Use in Silicon Semiconductor Technology. *RCA Review*, pp. 187–206.

[22] Meuris, M., Mertens, P.W., Opdebeeck, A., Schmidt, H.F., Depas, M., Vereecke, G., Heyns, M.M. and Phillipossian, A., 1995. The IMEC Clean: A New Concept for Particle and Metal Removal on Si Surfaces. *Solid State Technology*, July 1995, pp.109–113.

[23] King, R.R., Sinton, R.A. and Swanson, R.M., 1990. Studies of Diffused Phosphorus Emitters: Saturation Current, Surface Recombination Velocity, and Quantum Efficiency. *IEEE Trans. Electron. Dev.* ED-37, pp. 365–371.

[24] Morales-Acevado, A., 1986. Optimization of Surface Impurity Concentration of Passivated Emitter Solar Cells. *J. Appl. Phys.*, Vol. 60, pp. 815–819.

[25] Wolf, M., 1986. The Influence of Heavy Doping Effects on Silicon Solar Cells Performance – I. *Solar Cells*, Vol.17, pp. 53–63.

[26] Morales-Acevado, A., 1991. Theoretical Study of Thin and Thick Emitter Silicon Solar Cells. *J. Appl. Phys.*, Vol.70, pp. 3345–3347.

[27] Wenham, S., 1993. Buried-Contact Solar Cells. *Progress in Photovoltaics*, Vol. 1, pp. 3–10.

[28] Szlufcik, J., Elgamel, H., Ghannam, M., Nijs, J. and Mertens, R., 1991. Simple Integral Screen Printing Process for Selective Emitter Polycrystaline Silicon Solar Cells. *Appl. Phys. Lett.*, Vol. 59, pp. 1583–1584.

[29] Doshi, P., Mejia, J., Tate, K., Kamra, S., Rohatgi, A., Narayanan, S. and Singh, R., 1996. High-Efficiency Silicon Solar Cells by Low-Cost Rapid Thermal Processing, Screen Printing and Plasma-Enhanced Chemical Vapour Deposition. *Proc. 25th IEEE Photovoltaic Specialists Conf.*, Washington DC, pp. 421–424.

[30] Sivoththaman, S., Laureys, W., De Schepper, P., Nijs, J. and Mertens, R., 1996. Rapid Thermal Processing of Conventionally and Electromagnetically Cast 100 cm2 Multicrystalline Silicon. *Proc. 25th IEEE Photovoltaic Specialists Conf.*, Washington DC, pp. 621–624.

[31] Hezel, R., 1996. A Review of Recent Advances in MIS Solar Cells. *Proc. 6th Workshop on the Role of Impurities and Defects in Silicon Device Processing*, pp. 139–153.

[32] Zhao, J. and Green, M., 1991. Optimized Antireflection Coatings for High-Efficiency Silicon Solar Cells. *IEEE Trans. Electron. Dev.*, Vol. 38, pp. 1925–1934.

[33] Aberle, A., Glunz, S., Warta, W., Knopp, J. and Knobloch, J., 1991. SiO_2-Passivated High Efficiency Silicon Solar Cells: Process Dependence of Si–

SiO_2 Interface Recombination. *Proc. 10th European Photovoltaic Solar Energy Conf.*, Lisbon, pp. 631–635.

[34] Szlufcik, J., De Clercq, K., De Schepper, P., Poortmans, J., Buczkowski, A., Nijs, J. and Mertens, R., 1994. Improvement in Multicrystalline Silicon Solar Cells After Thermal Treatment of PECVD Silicon Nitride AR Coating. *Proc. 12th European Photovoltaic Solar Energy Conf.*, Amsterdam, pp.1018–1021.

[35] Takayama, M., Yamashita, H., Fukui, K., Masuri, K., Shirasawa, K. and Watanabe, H., 1990. Large Area High Efficiency Multicrystalline Silicon Solar Cells. *Tech. Digest Int. PVSEC-5*, pp. 319–322.

[36] Cheeck, G.C., Mertens, R.P., Van Overstraeten, P. and Frisson, L., 1984. Thick Film Metallization for Silicon Solar Cells. *IEEE Trans. Electron Dev.* Vol. ED-31, pp. 602–609.

[37] Lolgen, P., Leguit, C., Eikelboom, J.A., Steeman, R.A., Sinke, W.C., Verhoef, L.A., Alkemande, P.F.A. and Algra, E., 1993. Aluminium Back-Surface Field Doping Profiles with Surface Recombination Velocities Below 200 cm/sec. *Proc. 23rd. IEEE Photovoltaic Specialists Conf.*, Louisville, p. 231.

[38] Amick, J.A., Battari, F.J. and Hanoka, J.I., 1994. The Effect of Aluminium Thickness on Solar Cell Performance. *J. Electroch. Soc.*, Vol. 141, pp.1577–1585.

[39] Chong, C.M., Wenham, S.R. and Green, M.A., 1988. High-Efficiency, Laser Grooved Buried Contact Silicon Solar Cells. *Appl. Phys. Lett.*, Vol. 52, pp. 407–409.

[40] Wenham, S., 1993. Buried-Contact Silicon Solar Cells. *Progress in Photovoltaics*, Vol. 1, pp. 3–10.

[41] Narasimha, S., Kamra, S., Rohatgi, A., Khattak, C.P. and Ruby, D., 1996. The Optimization and Fabrication of High Efficiency HEM Multicrystalline Silicon Solar Cells. *Proc. 25th. IEEE Photovoltaic Specialists Conf.*, Washington DC, pp. 449–452.

[42] Wenham, S.R., Honsberg, C.B. and Green, M.A., 1994. Buried Contact Solar Cells. *Sol. Energy Mat. Sol.* Cells, Vol. 34, pp. 101–110.

[43] Ghannam, M., Demesmaeker, E., Nijs, J., Mertens, R. and Van Overstraeten, R., 1992. Two Dimensional Study of Alternative Back Surface Passivation Methods for High Efficiency Silicon Solar Cells. *Proc. 11th European Photovoltaic Solar Energy Conf.*, Montreux, pp. 45–48.

[44] Honsberg, C.B., Yun, F., Ebong, A., Tauk, M., Wenham, S.R. and Green, M.A., 1994. 685 mV Open-Circuit Voltage Laser Grooved Silicon Solar Cell. *Sol. Energy Mat. Sol.* Cells, Vol. 34, pp. 117–123.

[45] Gutierrez, R., Jimeno, J.C., Hernanado, F., Recart, F. and Bueno, G., 1995. Evaluation of Standard Screen Printed Solar Cells. *Proc. 13th European Photovoltaic Solar Energy Conf.*, Nice, pp. 1508–1511.

[46] Wenham, S.R. and Green, M.A., 1988. Buried Contact Solar Cell. US Patent 4,726,850.

[47] Mason, N.B., Jordan, D. and Summers, J.G., 1991. A High Efficiency Silicon Solar Cell Production Technology. *Proc. 10th European Photovoltaic Solar Energy Conf.*, Lisbon, pp. 280–283.

[48] Munzer, A., 1996. *MONOCEPT 1st Progress Report EC project JOR 3-CT-95-0011.*

[49] Wald, F., 1991. EFG Crystal Growth Technology for Low Cost Terrestrial Photovoltaics: Review and Outlook. *Sol. Energy Mat. Sol.* Cells, Vol. 23, pp. 175–182.

[50] Nijs, J., Demesmaeker, E., Szlufcik, J., Poortmans, J., Frisson, L., De Clercq, K., Ghannam, M., Mertens, R. and Van Overstraeten, R., 1994. Latest Efficiency Results with the Screenprinting Technology and Comparison with the Buried Contact Structure. *Proc. First World Conf. on Photovoltaic Energy Conversion*, Hawaii, pp. 1242–1249.

[51] Dziedzic, A., Nijs, J. and Szlufcik, J., 1993. Thick-Film Fine-Line Fabrication Techniques – Application to Front Metallisation of Solar Cells. *Hybrid Circuits*, No. 30, pp. 18–22.

[52] Hanoka, J.I. and Danielson, S.E., 1992. Method for Forming Contacts. US Patent 5,151,377.

[53] Ourmazd, A. and Schroter, W., 1984. Phosphorus gettering and intrinsic gettering of nickel in silicon. *Appl. Phys. Lett.*, Vol. 45, p.781.

[54] Sopori, B., Jastrzebski, L. and Tan, T., 1996. A comparison of gettering in single and multicrystalline silicon for solar cells. *Proc. 25th IEEE Photovoltaic Specialists Conf.*, Washington DC, 1996, pp. 625–628.

[55] Gee, J., 1991. Phosphorus diffusions for gettering-induced improvement of lifetime in various silicon materials. *Proc. 22nd IEEE Photovoltaic Specialists Conf.*, Las Vegas, pp.118–123.

[56] Perichaud, I., Floret, F. and Martinuzzi, S., 1993. Limiting factors in phosphorus external gettering efficiency in multicrystalline silicon. *Proc. 23rd IEEE Photovoltaic Specialists Conf.*, Louisville, pp. 243–247.

[57] Sivoththaman, S., Rodot, M., Nam, L., Sarti, D., Ghannam, M. and Nijs, J., 1993. Spectral response and dark I–V characterization of polycrystalline silicon solar cells with conventional and selective emitters. *Proc. 23rd IEEE Photovoltaic Specialists Conf.*, Louisville, pp.335–339.

[58] Narayanan, S. and Wohlgemuth, J., 1994. Cost-benefit analysis of high efficiency cast polycrystalline silicon solar cell sequences. *Progress in Photovoltaics*, Vol. 2, pp.121–128.

[59] Orr, W. and Arienzo, M., 1982. Investigation of polycrystalline silicon BSF solar cells. *IEEE Trans. Electron Dev.*, Vol. ED-29, p.1151.

[60] Kazmerski, L., 1985. Polycrystalline silicon: Impurity incorporation and passivation. *Proc. 6th European Photovoltaic Solar Energy Conf.*, London, pp. 83–89.

[61] Verhoef, L., Roorda, S., Van Zolingen, R. and Sinke, W., 1988. Improved bulk and emitter quality by backside aluminum doping and annealing of polycrystalline silicon solar cells. *Proc. 20th IEEE Photovoltaic Specialists Conf.*, Las Vegas, pp.1551–1556.

[62] Mandelkorn, J. and Lamneck, J.H., 1990. Simplified Fabrication of Back Surface Electric Field Silicon Cells and Novel Characteristics of Such Cells. *Solar Cells*, pp. 121–130.

[63] Del Alamo, J., Eguren, J. and Luque, A., 1981. Operating Limits of Al-Alloyed High-Low Junctions for BSF Solar Cells. *Solid State Electronics*, Vol. 24, pp. 415–420.

[64] Lolgen, P., Sinke, W.C. and Verhoef, L.A., 1990. Bulk and Surface Contribution to Enhanced Solar-Cell Performance Induced by Aluminium Alloying. *Tech. Digest Int. PVSEC-5*, pp. 239–243.

[65] Amick, J.A., Battari, F.J. and Hanoka, J.I., 1994. The Effect of Aluminium Thickness on Solar Cell Performance. *J. Electrochem. Soc.*, Vol. 141, pp. 1577–1585.

[66] Sana, P., Rohatgi, A., Kalejs, J. and Bell, R., 1994. Gettering and hydrogen passivation of EFG multicrystalline silicon solar cells by aluminum diffusion and forming gas anneal. *Appl. Phys. Lett.*, Vol. 64, pp. 97–99.

[67] Singh, R., Radpour, F. and Chou, P., 1989. Comparative study of dielectric formation by furnace and rapid isothermal processing. *J. Vac. Sci. Technol.*, Vol. A7, pp.1456–1460.

[68] Sivoththaman, S., Laureys, W., Nijs, J. and Mertens, R., 1995. Fabrication of large area silicon solar cells by rapid thermal processing. *Appl. Phys. Lett.*, Vol. 67, pp. 2335–2337.

[69] Rohatgi, A., Chen, Z., Doshi, P., Pham, T. and Ruby, D., 1994. High efficiency solar cells by rapid thermal processing. *Appl. Phys. Lett.*, Vol. 65, pp. 2087–2089.

[70] Sivoththaman, S., Laureys, W., De Schepper, P., Nijs, J. and Mertens, R., 1995. Large area silicon solar cells fabricated by rapid thermal processing. *Proc. 13th European Photovoltaic Solar Energy Conf.*, Nice, pp. 1574–1577.

[71] Beyer, A., Ebest, G. and Reich, R., 1996. MIS solar cells with silicon oxynitride tunnel insulators by using rapid thermal processing. *Appl. Phys. Lett.*, Vol. 68, pp. 508–510.

[72] Szlufcik, J., Duerinckx, F., Van Kerschaver, E., Einhaus, R., Ziebakowski, A., Vazsonyi, E., De Clercq, K., Horzel, J., Frisson, L., Nijs, J. and Mertens, R., 1997. Simplified Industrial Type Processes for High Efficiency Crystalline Silicon Solar Cells. *Proc. 14th. European Photovoltaic Solar Energy Conf.*, Barcelona.

[73] ISE PV Chart, Fraunhofer Institute FhG-ISE, Freiburg, Germany, November 1996.

[74] Saitoh, T., Shimokawa, R. and Hayashi, Y., 1991. Recent Improvements of Crystalline Silicon Solar Cells in Japan. *Proc. 22nd IEEE Photovoltaic Specialists Conf.*, Las Vegas, pp. 1026–1029.

[75] Wenham, S.R. and Green, M.A., Laser Grooved Solar Cell, in US Patent 4,748,130.

[76] Green, M.A. and Wenham, S.R., 1991. Present Status of Buried Contact Solar Cells. *Proc. 22nd IEEE Photovoltaic Specialists Conf.*, Las Vegas, pp. 46–49.

[77] Green, M.A., Wenham, S.R., Honsberg, C.B. and Hogg, D., 1994. Transfer of Buried Contact Cell Laboratory Sequences into Commercial Production. *Sol. Energy Mat. Sol. Cells*, Vol. 34, pp. 83–89.

[78] Honsberg, C.B. and Wenham, S.R., 1995. New Insights Gained Through Pilot Production of High-Efficiency Silicon Solar Cells. *Progress in Photovoltaics*, Vol. 3, pp.79–87.

[79] Wenham, S.R. and Green, M.A., 1996. Silicon Solar Cells. *Progress in Photovoltaics*, Vol. 4, pp. 3–33.

[80] Green, M.A., Wenham, S.R. and Zhao, J., 1993. Progress in High Efficiency Silicon Solar Cells and Module Research. *Proc. 23rd IEEE Photovoltaic Specialists Conf.*, Louisville, pp. 8–13.

[81] Narayanan, S., Wohlgemuth, J.H., Creager, J.B., Roncin, S.P. and Perry, J.M., 1993. Buried Contact Solar Cells. *Proc. 23rd. IEEE Photovoltaic Specialists Conf.*, Louisville, pp. 277–280.

[82] Jordan, D. and Nagle, J.P., 1994. New Generation of High-Efficiency Solar Cells: Development, Processing and Marketing. *Progress in Photovoltaics*, Vol. 2, pp. 171–176.

[83] Hezel, R. and Schroner, 1981. Plasma Si Nitride – A Promising Dielectric to Achieve High-Quality Silicon MIS/IL Solar Cells. *J. Appl. Phys.*, Vol. 27, p. 3076.

[84] Hezel, R., Hoffmann, W. and Jager, K., 1991. Recent Advances in Silicon Inversion Layer Solar Cells and Their Transfer to Industrial Pilot Production. *Proc. 10th European Photovoltaic Solar Energy Conf.*, Lisbon, p. 511.

[85] Amick, J., Bottari, F.J. and Hanoka, J.I., 1994. Solar Cell and Method of Making Same. US Patent 5,320,684.

[86] Bell, R.O., Prince, M., Wald, F.V., Schmidt, W. and Rasch, K.D., 1996. A Comparison of the Behavior of Solar Silicon Material in Different Production Processes. *Sol. Energy Mat. Sol. Cells*, Vol. 33, pp. 71–86.

[87] Campbell, P. and Green, M.A., 1986. The Limiting Efficiency of Silicon Solar Cells under Concentrated Sunlight. *IEEE Trans. Electron Dev.*, Vol. ED-33, pp. 234–239.

[88] Barnett, A.M., Collins, S.R., Cotter, J.E., Ford, D.H., Hall, R.B. and Rand, J.A., 1994. Polycrystalline Silicon Film™ Solar Cells: Present and Future. *Progress in Photovoltaics*, Vol. 2, pp. 163–70.

[89] Ford, D.H., Barnett, A.M., Checchi, J.C., Collins, S.R., Hall, R.B., Kendall, C.L., Lampo, S.M. and Rand, J.A., 1996. 675-cm2 Silicon-Film™ Solar Cells. *Tech. Digest 9th Int. PVSEC*, pp. 247–248.

[90] Ford, D.H., Barnett, A.M., Hall, R.B., Kerndall, C.L. and Rand, J.A., 1996. High Power, Commercial Silicon Film™ Solar Cells. *Proc. 25th IEEE Photovoltaic Specialists Conf.*, Washington DC, pp. 601–604.

[91] Hogan, S., Darkazalli, D. and Wolfson, R., 1991. An Analysis of High Efficiency Si Cells Processing. *Proc. 10th European Photovoltaic Solar Energy Conf.*, Lisbon, pp. 276–279.

[92] Nijs, J., 1994. Photovoltaic Cells and Modules: Technical and Economic Outlook Towards the Year 2000. *Int. J. Solar Energy*, Vol. 15, pp. 91–122.

[93] Final Report of the EC project 'Multi-Megawatt Upscaling of Silicon and Thin Film Solar Cell and Module Manufacturing '*Music FM' – APAS RENA CT94*', in press.

IIb-3

Thin Silicon Solar Cells

Michael Mauk, Paul Sims, James Rand, and Allen Barnett[1],
AstroPower Inc., Solar Park, Newark, Delaware, USA

[1] For current address, see List of Contributors on page x

1 Introduction, Background and Scope of Review

Thin silicon solar cells are an important class of photovoltaics that are currently the subject of intense research, development, and commercialisation efforts. The potential cost reductions realised by manufacturing solar cells in a thin device configuration are highly compelling and have long been appreciated. However, most work on thin film approaches to solar cells has centred on materials other than crystalline silicon because it was believed that the optical properties of crystalline silicon would limit its usefulness as a thin-film solar cell, and for various reasons, crystalline silicon did not readily lend itself to the common thin-film deposition technologies. Several early experimental efforts on making thin film crystalline silicon solar cells seemed to confirm at least some of these perceived difficulties. Still, there were proponents of thin crystalline silicon solar cells including Redfield [1], Spitzer et al. [2] and Barnett [3], who advocated their potential advantages and articulated design principles of light trapping and high-open-circuit voltage needed to achieve high efficiencies. Starting in the late 1980s and gaining momentum in the 1990s, thin-film crystalline silicon solar cells emerged (or perhaps more aptly 're-emerged') as a promising approach. This was partly due to several device design and materials processing innovations proposed to overcome the difficulties and limitations in using crystalline silicon as a thin film solar cell material, and also partly due to the stubborn lack of progress in many competing photovoltaic technologies. Progress on thin crystalline silicon solar cells has now reached a level where they are positioned to capture a significant share of the photovoltaics market, and a thin silicon solar cell may well become the successor to the conventional (thick) silicon wafer solar cells that are presently the mainstay of the photovoltaics industry. This chapter reviews the issues and technical achievements that motivate the current interest in thin silicon solar cells, and surveys developments and technology options.

Thin silicon solar cells is actually an umbrella term describing a wide variety of silicon photovoltaic device structures utilising various forms of silicon (monocrystalline, multicrystalline, polycrystalline, microcrystalline, amorphous, and porous), and made with an almost incredibly diverse selection of deposition or crystal growth processes and fabrication techniques. Thin silicon solar cells are distinguished from traditional silicon solar cells that are comprised of $\sim$0.3 mm thick wafers or sheets of silicon. The common defining feature of a thin silicon solar cell is a relatively thin (< 0.1 mm) 'active' layer or film of silicon formed on, or attached to, a passive supporting substrate. Nevertheless, even this very general description may not subsume all the different variations of 'thin silicon solar cell' designs currently under investigation. One purpose of a review such as this is to provide some perspective and objective criteria with which to assess the merits and prospects of different approaches. However, such comparisons must be tempered with the realisation that the technology is still in a state of flux and relatively early development, and there are many disparate solar cell applications, each with a different emphasis on cost and performance. Thus, it is possible – if not probable – that no single solar cell technology will satisfy or otherwise be the best choice for every present or future application. For

example, a thin-film solar cell design for large-scale (~megawatt) utility grid-connected power applications may not be the best choice for a small (~1 watt) minimodule battery-charger for walk lights. Further, the projected economics of solar cells is based on complicated and sometimes speculative assumptions of materials costs, manufacturing throughput and scale-up issues, as well as balance of systems constraints and costs, and it would be imprudent at this stage to 'downselect' the most promising technical path for the solar industry. From this vantage, it is fortunate that there is such a diverse choice of technology options under development that should lead to thin silicon solar cells with a wide range of cost and performance characteristics.

Such considerations not withstanding, Bergmann [4] has categorised thin silicon solar cells into three groups, and this delineation serves as rational and useful framework to discuss and review the subject.

1. Thin-film solar cells based on small-grained (< 1 micron) nanocrystalline or microcrystalline silicon films (2–3 microns in thickness) deposited on glass substrates typically using technologies adapted from thin-film amorphous silicon solar cells. These types of cells are usually made as p–i–n structures, sometimes in combination with amorphous silicon layers in heterojunction or tandem cell designs.
2. Thick (~30 micron) silicon layers deposited on substrates that are compatible with recrystallisation of silicon to obtain millimeter size grains. A diffused p–n junction is the preferred device design. Also included in this category are epitaxial silicon solar cells on upgraded metallurgical silicon substrates.
3. Transfer techniques for films of silicon wherein an epitaxial monocrystalline silicon film is separated from the silicon substrate upon which it seeded and bonded to a glass superstrate. The anticipated cost reductions in this technology are based on reuse of the seeding substrate.

In this chapter we will concentrate on the second and third types of solar cells listed above. The first type is more properly considered as an extension or outgrowth of amorphous silicon technology, although much of the technology and design considerations are also relevant to other kinds of thin silicon solar cells. We will briefly survey device designs deposition technologies for making nanocrystalline and microcrystalline thin-film silicon solar cells, but not discuss materials and device physics of this type of solar cell. Amorphous silicon and related thin-film solar cells are considered in a separate chapter of this book. Bergman [4] has provided several penetrating reviews of thin-film microcrystalline and nanocrystalline silicon solar cells. Our emphasis will be on polycrystalline silicon solar cells formed on ceramics, because most of our experience is with this type of solar cell. The third type of solar cell listed above is of general interest as it provides the shortest route to making thin silicon devices in which device issues can be analysed independent of material properties issues. For instance, light trapping and surface passivation effects can be studied in thin device structures with and without grain boundaries.

The plan of the chapter is as follows. We first provide a general discussion of effects and features that are common to most thin silicon solar cells such as light trapping designs, modelling, and methods of analysis. We next discuss voltage enhancement issues including surface passivation, followed by a review of grain boundary effects in thin silicon solar cells. A survey of technologies for producing thin silicon solar cells is then presented. This will include descriptions of various silicon deposition techniques such as chemical vapour deposition, melt and solution growth, as well as substrate issues and post-deposition recrystallisation to enhance grain size and texture. Low-temperature CVD methods for microcrystalline silicon solar cells is also covered, as are techniques for wafer thinning and transfer of thin layers to surrogate substrates. Finally, we end with a tabulation summarising some of the prominent experimental results for thin silicon solar cells.

2 Light Trapping in Thin Silicon Solar Cells

Thin silicon solar cells can greatly benefit from light trapping effects, which can offset the relatively weak absorption near-bandgap energy photons by increasing the optical path length of light within the solar cell structure. The basic idea of light trapping in a thin solar cell is shown in Figure 1. The back side of the solar cell with a grooved, blazed, textured or otherwise roughened surface is made reflective by, for example, a change in refractive index or by coating with a reflective material such as a metal. In a free-standing solar cell, this surface is the backside of the solar cell itself, but in thin solar cell formed on a substrate, the reflective backside 'mirror' is situated at the interface between the silicon film and the substrate. This latter design for a solar cell made on a substrate is obviously more difficult to implement than with a solar cell formed as a free-standing wafer or sheet. As suggested by the schematic ray tracing of Figure 1, it appears in this case the light makes at least several passes of the silicon layers. Thus, the effective optical thickness is several times the actual silicon physical thickness, in which case a thin silicon solar cell with light trapping could reap the same absorption and carrier generation as a conventional solar cell (without light trapping) of much greater thickness.

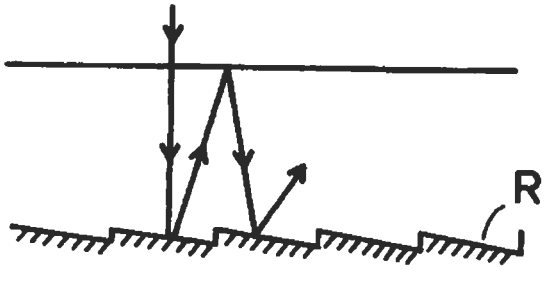

Figure 1 Illustration of the light-trapping concept [5].

Further, the generation of minority carriers would be relatively close to the p–n junction formed near the top surface of the solar cell, thus providing a high collection efficiency. To effect light trapping, it is necessary that at least one interface (front or back) deviates from planarity. If both front and back surfaces are smooth and parallel, a simple analysis shows that the first internal reflection at the front side will result in a large loss of the light due to transmission. This is especially true since the front surface of the solar cell will use an optical coating to reduce reflection (maximise transmission) of incident light. Since the transmission characteristics are symmetrical, the internal reflection from the front surface would be small. Instead, if the back surface is grooved, textured, or roughened as indicated in Figure 1, then light reflected from the back surface will in general be obliquely incident to the front surface, and if the angle of incidence exceeds a critical angle of about 16 degrees, then the light will be totally internally reflected as shown.

Nevertheless, in a real device with imperfect interfaces and diffuse components of light, a certain fraction of internally trapped light will eventually fall within the near-normal incidence angle for transmission, so some light leakage is inevitable and perfect confinement is impossible. An alternative approach is to texture or groove both the top and front surface, in which case, external reflection at the top surface is also reduced [5]. In theory, this is the best approach. In such cases, Yablonovitch and Cody [6] have predicted that for weakly absorbed light, the effective optical thickness a silicon solar cell with both surfaces textured to form Lambertian diffuse reflectors can be about 50 times greater than its actual thickness.

Enhancing the performance of thin crystalline silicon layers with light-trapping has been actively discussed in the literature since the 1970s [1, 2, 7]. In general, texturing one or both surfaces, and maximising the reflection at the back surface obtains optical path lengths greater than the thickness of the device. Texturing results in oblique paths for internally confined light and maximises total internal reflection at the illuminated device surface.

To quantify the effects of light trapping on device performance and optimisation, we define a parameter Z that indicates the ratio of effective optical thickness to actual thickness for weakly absorbed light. Z can thus be interpreted as the number of passes trapped light makes in the solar cell. Z can vary from 1 (no light trapping) to about 50, and is regarded as an adjustable parameter in the optimisation. Although this is an overly simplistic way to describe light trapping in a solar cell, it does not appear that the main conclusions of such and similar modelling depend on the details of the optical absorption and carrier generation due to light trapping phenomena. The main effect on solar cell efficiency is the total level of enhanced absorption and generation in the thin silicon active layers, rather than the microscopic details. However, such detailed modelling is necessary to optimise light trapping designs.

In Figure 2, an example result of the determination of optimal solar cell thickness as a function of light trapping (Z) is illustrated. In this analysis, the doping level was adjusted to yield a minority carrier diffusion length twice the layer thickness, thus insuring good collection efficiency. (We regarded this as

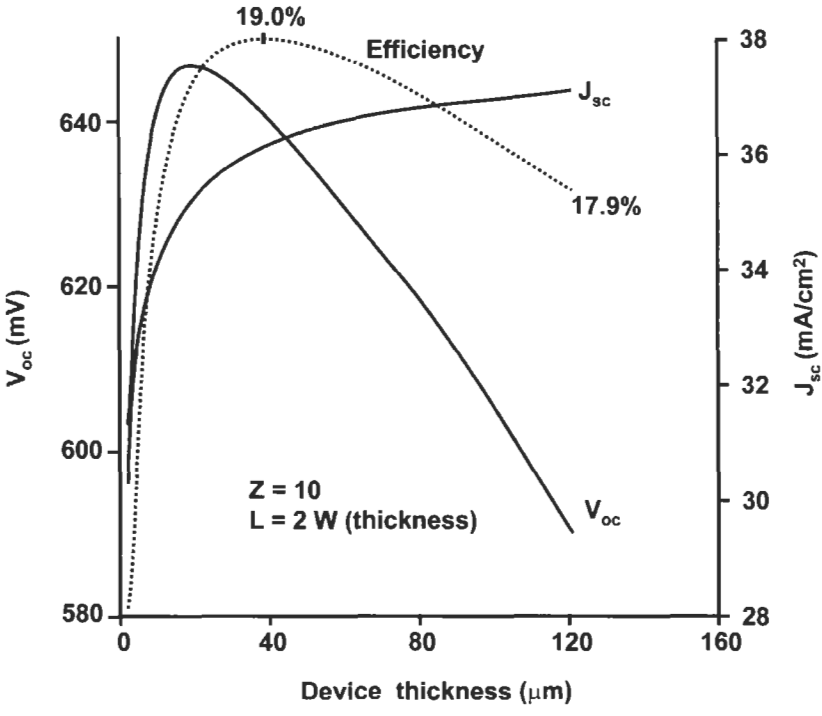

Figure 2 Thin silicon device performance predictions for the case where the optical thickness due to light trapping (Z) is ten times the device thickness and the diffusion length is twice the actual device thickness. The optimum silicon thickness using these assumptions is in the range of 30–40 microns [8].

a general design principle of thin silicon solar cells.) As a conservative estimate, the diffusion length for a given doping concentration was degraded by a factor of 5 from typical single-crystal values to account for the relatively inferior material quality generally expected for silicon deposited on a substrate. Modest surface passivation corresponding to front and back minority carrier surface recombination velocities of 1000 cm/s, a front surface solar-spectrum averaged reflection of 5%, and a series resistance of 0.1 ohm-cm were also assumed. The results of this analysis are shown in Figure 2 for a Z factor of 10. For this set of assumptions, the optimum efficiency occurs at silicon thicknesses between 30 and 40 microns.

2.1 Methods of Implementing Light Trapping

As might be imagined, there is ample opportunity for creative designs to effect light trapping in silicon solar cells, and light-trapping structures have been realised by many different methods. For purposes of review, three types of reflective surfaces can be distinguished – random texture, geometric or regular structuring, and the use of optical elements external to the silicon solar cell structure.

2.1.1 Random Texturing

Random texturing holds promise for two reasons: modelling predicts such random texturing can provide very reflective light trapping, and the perceived ease at which random texture can be experimentally realised. For Lambertian diffuse reflectors made by random surface or interface texturing, and where the angular distribution of reflected light follows a cosine law, Goetzberger [5] has shown that the fraction of light reflected by total internal reflection at the front surface is equal to $1 - 1/n^2$, where n is the refractive index of silicon (approximately 3.4). In this case, when weakly absorbed light is reflected from a diffuse back reflector, 92% will be internally reflected from the front surface. The 50-fold increase in optical path length suggested by Yablonovitch and Cody [6] is based on front and back surface texturing to effect Lambertian reflection. Unfortunately, the experimental realisation of a Lambertian reflector [9] has proved to be more difficult.

Random textures of varying effectiveness have been experimentally realised by the following methods:

- reactive ion etching [10–12]
- sand blasting [13]
- photolithography [14]
- natural lithography [15]
- porous etching [16]
- rapid thermal processing of an aluminium–silicon interface [17]
- random-textured ancillary dielectric layers such as ZnO or SnO_2 [18-21]

2.1.2 Geometrical or Regular Structuring

Surface structuring is relatively easy to realise in single-crystal silicon wafer surfaces by taking advantage of the anisotropic (crystal orientation-dependent) etch rates of alkaline solutions. This approach has been used to fabricate the majority of light-trapping structures demonstrated to date, a few examples of which are shown in Figure 3. Common structures include 54-degree pyramids, inverted pyramids, slats, and perpendicular slats. Regular patterns are achieved with photolithography in combination with anisotropic etching [22–24]. Random pyramids are formed with the use of anisotropic etchants on non-patterned surfaces [25, 26]. A similar result can be achieved in multicrystalline substrates (with much more effort) with the use of mechanical scribing, abrading or grinding or with laser ablation [27–32]. An option for very thin layers is conformal growth on a textured substrate [33] (Figure 3).

Modelling of geometrical textures is often carried out by computer-aided ray tracing techniques [35–38]. Ray tracing analysis makes no assumptions about the distribution of light within the absorber layer. Instead, the path of representative incident rays of light are plotted using geometric optics to follow the light path through as it is reflected and refracted at surfaces and interfaces. Attenuation of light due to optical absorption in bulk silicon is also incorporated in the model. This approach is useful for the analysis of regularly structured

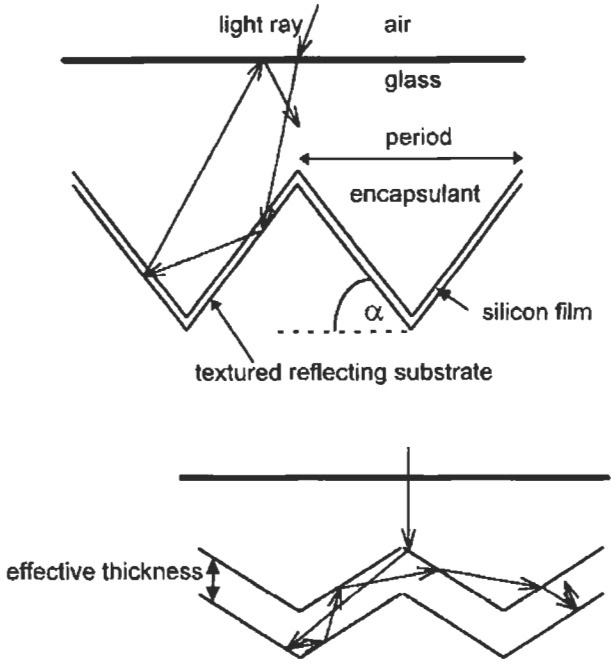

Figure 3 Examples of structured surfaces to effect light trapping in silicon solar cells [34].

surfaces [39] with complex geometries as well as unusual solar cell shapes such as the Spheral Solar™ Cell [40].

2.1.3 External Optical Elements

The solar cell can be overlayed with refractive optics elements such as prismatic cover slips (Figure 4) to effect a degree of light trapping. These optical elements were originally developed to ameliorate shading by the front contact grid metallisation, but they can also be used to redirect light back into the solar cell after it has escaped. External reflectors and optical cavities are two other examples of the use of external optical elements to implement light trapping. Miñiano et al. [41] have analysed light-confining cavities for concentrator solar cells.

2.2 Assessment of Light-Trapping Effects

Light trapping has been incorporated in structures with thickness ranging from less than 1 micron to 400 microns with varying degrees of success. The short-circuit current is the ultimate figure of merit for comparisons, as the objective of light trapping is to enhance absorption and contribute to minority carrier generation. Using short-current current to assess the effectiveness of light-trapping schemes is complicated by other losses, such as bulk recombination and front surface reflection. In laboratory settings spectral

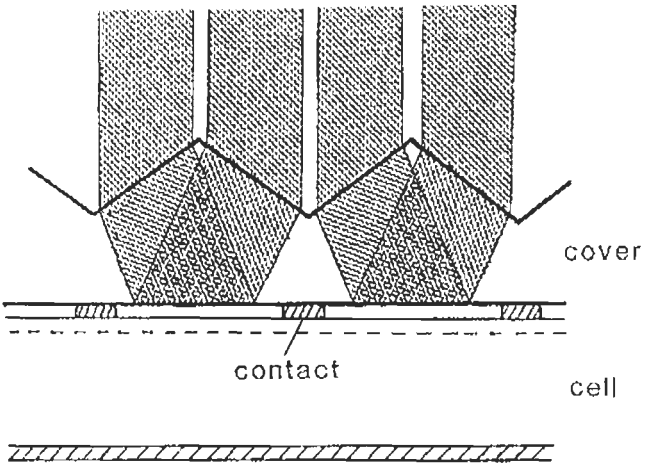

Figure 4 A prismatic cover slip can be used to effect light trapping in solar cells [42].

response and reflection data can be analysed to extract detailed information about light trapping; however, these techniques require assumptions that limit their usefulness in predicting final cell performance. Each analysis method is reviewed below.

2.2.1 Short-Circuit Current Analysis of Light Trapping

Modelling the current generated by a known thickness of silicon is straightforward when all absorbed photons contribute a charge carrier. A 'no light-trapping' scenario can be generated that has perfect anti-reflection properties (no front surface reflection), and only one pass of light through the device thickness (back surface is 100% absorbing with no contribution to current). To the extent an experimental result exceeds this model light trapping features are indicated. In real devices shading, imperfect AR, and parasitic absorption make the 'no light-trapping' model impossible to achieve [43]. Calibration of the light source is another source of error in this method.

Figure 5 shows modelling results and experimental data for short circuit current as a function of thickness. The effect of light trapping becomes more pronounced as the device thickness is reduced and the light not absorbed on the first pass through the device grows to a significant level. Theoretical analysis of Green [44] and Tiedje [45] are included in Figure 5 and serve as the 'best case' limit for perfect light trapping. The analysis of Green appears to predict perfect collection (J_{SC} = 44 mA/cm^2) independent of thickness. The method of Tiedje assumes random texture, Lambertian-type reflection, and more realistic modelling using a loss-cone analysis for front surface internal reflections. The baseline case with no light trapping was computed with PC-1D [46].

The experimental results shown in Figure 5 indicate that most laboratory and commercial devices have not produced a level of photogenerated current exceeding that which would be possible in a device of comparable thickness

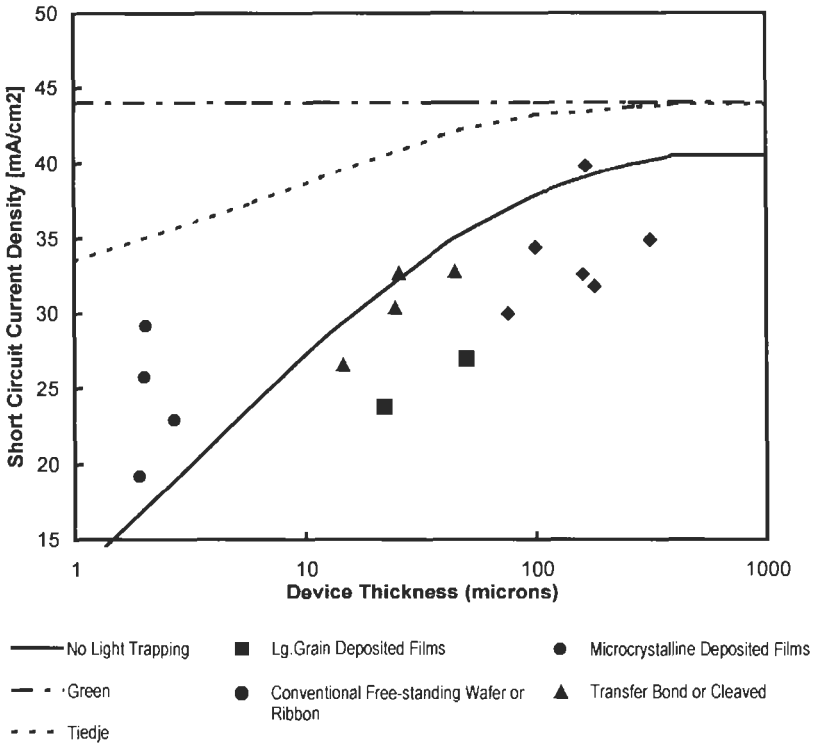

Figure 5 Summary of the last five years of published data on silicon layer thickness and short-circuit current. Theoretical analyses are shown as lines. Laboratory results are shown as solid symbols [47–68].

without light trapping. Thus, based solely on total current, it cannot be concluded that in these particular solar cells light trapping makes a significant contribution to solar cell performance. These devices may include some light-trapping enhancement of current, but additional losses due to imperfect anti-reflection coatings, bulk and surface recombination, possibly exacerbated by adding light trapping features to the solar cell, may have offset any gains from light trapping. This has prompted researchers to investigate other methods based on reflection and spectral response measurement to analyse light-trapping effects in ways that are not obscured by various losses [69].

2.2.2 'Sub-bandgap' Reflection Analysis of Light Trapping

The effectiveness of backside reflectors can be evaluated at long wavelengths ('sub-bandgap' energy photons), i.e., longer than about 1100 nm. The silicon layer is approximately transparent to light in this wavelength range. As shown in the inset of Figure 6, the measured total reflection for non-absorbed light at these wavelengths of a thin solar cell with a backside mirror is due to contributions of multiple internal reflections from the front and back surface. If absorption is negligible, the ratio between the measured reflection and the reflection expected of an infinitely thick slab of silicon gives an estimate of

the effective light trapping in a device. This technique does not measure light trapping *per se*, but instead provides an indicator of the effectiveness of the backside mirror and the level of optical confinement for near-bandgap, weakly absorbed photons. This analysis can be especially decisive if test structures, both *with* and *without* backside reflectors, are compared. In thin silicon structures, the effect of the buried reflector is shown as an enhancement of sub-bandgap (>1050 nm wavelength) reflection, which is attributed to unabsorbed light reflected at the backside mirror and transmitted through the front surface. This escaping light boosts the measured front surface reflection (Figure 6), and the increased reflectance permits an estimate of the internal reflections in the silicon layer.

2.2.3 Extended Spectral Response Analysis of Light Trapping

The extended spectral response method was developed by Basore [71] as a means to estimate an effective optical path length for near-bandgap light in a thin silicon solar cell, and is based on an analysis of the internal quantum efficiency of a solar cell as a function of wavelength.

The method utilises a plot of 1/IQE vs. $1/\alpha$ where α is the optical absorption coefficient for silicon and *IQE* is the internal quantum efficiency. Two representative examples of such plots are shown in Figure 7, for a thick silicon wafer-based solar cell and a thin (4 micron) silicon solar cell, both of which have textured surfaces to effect light trapping. The $1/\mathrm{IQE}(\lambda)$ vs. $1/\alpha$ curves show two linear regions, which appears to be a general feature of solar cells with light trapping.

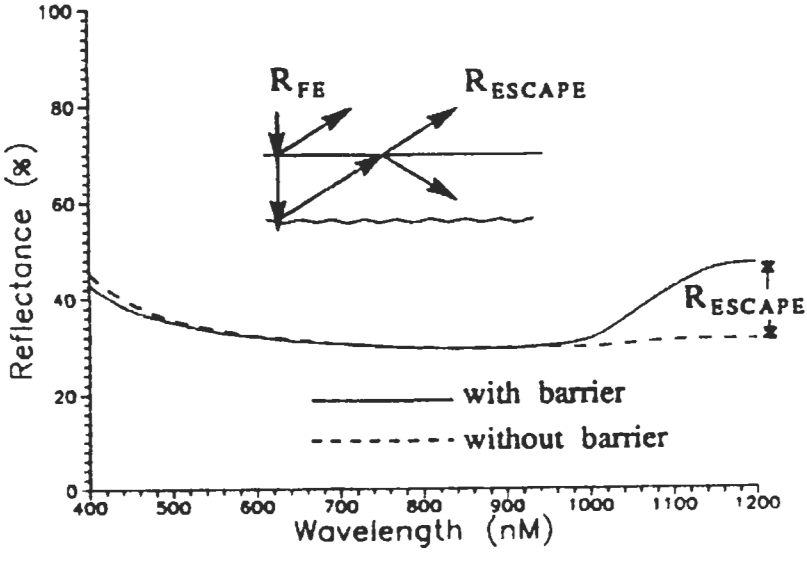

Figure 6 External reflection measurements in thin silicon structures with reflecting barrier layer between silicon layer and substrate [70].

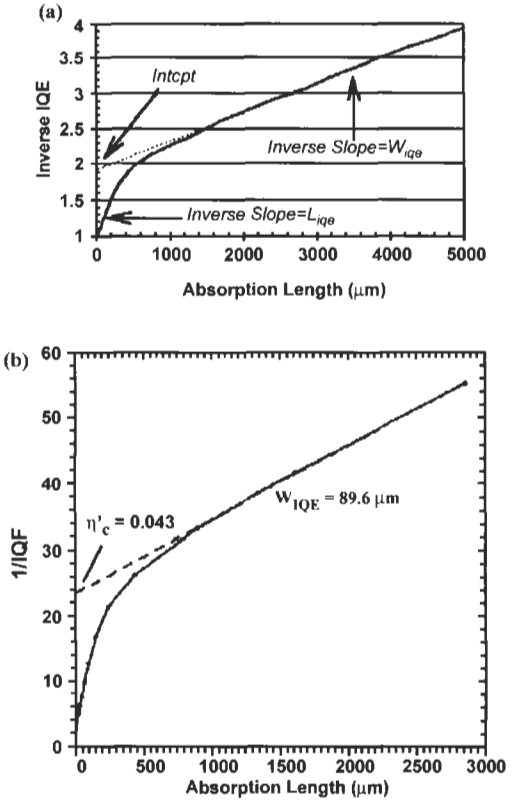

Figure 7 *(a) Plot of $1/\alpha$ vs. $1/IQE$ for a textured (thick) wafer-based silicon solar cell [71]; and (b) textured 4 micron thick silicon solar cell [72].*

We will not discuss the details of the somewhat involved analysis in which Basore shows that the slopes and intercepts of the linearised parts of these curves can be used to estimate the collection efficiency, the back reflectance, the back surface recombination velocity, and the effective minority carrier diffusion length. This extended spectral response analysis, although more complicated than other techniques, appears to be the most useful method for assessing light trapping in solar cells.

3 Voltage Enhancements in Thin Silicon Solar Cells

The factors that influence the open-circuit voltage of a silicon solar cell are the same whether the device is thin or thick. These include doping levels, the various bulk recombination mechanisms (defect-mediated Shockley–Read–Hall, radiative, and Auger), and surface recombination. The open-circuit voltage V_{OC} depends logarithmically on the dark diode current density J_0. The diode is analysed in terms of current components from the silicon layer (base) and a thin

emitter layer formed on the surface of the base, usually by impurity diffusion. J_0 can vary by orders of magnitude depending on device parameters and silicon properties. The dark current can be calculated as

$$J_0 = \frac{q \cdot n_i^2}{N_D} \frac{D}{L} \left[\frac{(SL/D)\cosh(W_b/L) + \sinh(W_b/L)}{\cosh(W_b/L) + (SL/D)\sinh(W_b/L)} \right]$$

where q is the electronic charge, n_i is the intrinsic carrier concentration of silicon, N_D is the base doping concentration, S is the back surface recombination velocity which characterises the extent of minority recombination at the silicon/substrate interface, L and D are the minority carrier diffusion length and diffusivity in the base, respectively, and are sensitive to doping levels and material quality, and W_b is the thickness of the base. Actually, the above equation represents only the base layer contribution to J_0. There is an analogous equation for emitter contribution to J_0, but in well-designed solar cells, normally the base component is the dominant contribution to J_0. At any rate, our purpose here is to simply highlight the factors that contribute to J_0 and indicate the design principles to reduce J_0. In a thin silicon solar cell, the diffusion length will normally be longer than the layer thickness, i.e., $W_b/L < 1$, in which case the above equation simplifies to

$$J_0 = \frac{q \cdot n_i^2 \cdot S}{N_D}$$

In such cases, the dark current does not depend on diffusion length, but is directly proportional to the surface recombination velocity, thus underscoring the importance of surface passivation in thin silicon devices. Higher doping concentrations N_D will decrease J_0, so long as the doping does not degrade L such that $L <$ W and bulk recombination becomes significant. Another consideration of high doping but which is not evident from the above equations are bandgap narrowing effects. As doping levels exceed about 10^{19} atoms/cm^3, the effective bandgap of silicon is reduced, leading to increased intrinsic carrier concentrations n_i, and correspondingly increased J_0. Thus increasing doping to increase V_{OC} becomes self-defeating after a certain point.

3.1 Minority Carrier Recombination Issues in Thin Silicon Solar Cells

As already pointed out, an important potential, although not completely experimentally verified, advantage of thin silicon solar cells is their decreased sensitivity to minority carrier recombination. This permits higher doping levels to enhance open-circuit voltage, and leads to better tolerance of impurities and defects. A sensitivity analysis of solar cell efficiency to device thickness and minority carrier lifetime is shown in Figure 8. Minority carrier lifetime τ and diffusion length L are related as

$$L = \sqrt{D \cdot \tau}$$

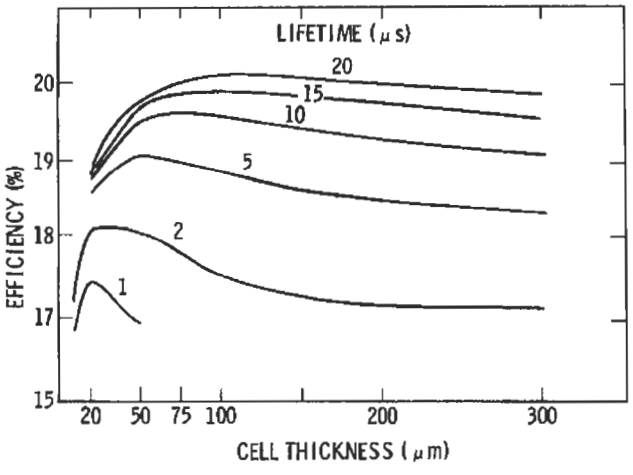

Figure 8 Sensitivity of solar cell efficiency to device thickness and minority carrier lifetime [74].

where D is the minority carrier diffusivity which is proportional to the minority carrier mobility. While D is not highly sensitive to impurity and defects, τ can easily vary by more than an order of magnitude in silicon of various purity and quality. The analysis summarised in Figure 11 shows the interesting result that for a given minority carrier lifetime there is an optimum thickness, and that for material with relative low minority carrier lifetimes the optimum thickness is less than 50 microns.

Films of silicon deposited on substrates will usually be polycrystalline, although not all thin silicon solar cells are necessarily polycrystalline; epitaxial films removed from a monocrystalline silicon substrate and bonded to a superstrate, as well as solar cells made by thinning monocrystalline silicon wafers need not have grain boundaries. In fact, these types of silicon solar cells provide an interesting control for exploring the effects of grain boundaries. Nevertheless, many low-cost approaches to thin silicon solar cells will produce material with varying grain sizes and textures. The effects of grain boundaries are complex and depend on the microstructure, film thickness, grain size distribution, junction depth, doping, etc. Diffused junctions can spike down grain boundaries, which may improve collection efficiency but also make the solar cell more prone to shunting effects (Figure 9). These issues are not unique to thin silicon solar cells, and in fact, polycrystalline cast silicon solar cells have been an established line of solar cells for many years. Grain boundaries act as surfaces for minority carrier recombination, and can be depleted or accumulated and exhibit space charge regions much as junctions and free surfaces. For single-crystal silicon solar cells, space-charge recombination is usually so small that it can be neglected, and the performance of the device, particularly open-circuit voltage, is controlled by bulk, surface, and shunt losses, but this may not be the case with multicrystalline solar cells. It was initially thought that polycrystalline silicon solar cells would suffer major short-circuit current and open-circuit voltage losses from grain-boundary recombination, which

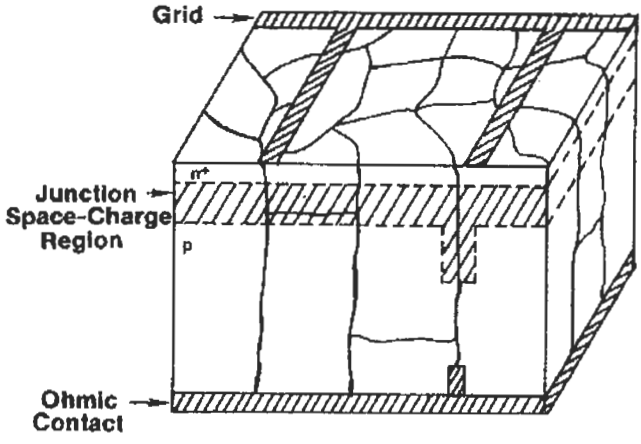

Figure 9 Geometry of grain boundaries in silicon solar cells [75].

would severely restrict the maximum light-generated current [73]. However, it has been shown that when the grain diameter is several times larger than the intra-grain (bulk) minority-carrier diffusion length, the short-circuit current is controlled not by grain-boundary recombination, but by the intra-grain diffusion length.

Other factors that may play a substantial role in determining the electrical performance of polycrystalline silicon solar cells are the presence of inclusions and tunnel junctions, both of which act as resistive shunts and degrade the open-circuit voltage and fill-factor locally. Although their impact on performance is fairly straightforward, it is not clear that either of these two possible defects is intrinsic to any polycrystalline silicon solar cell material or process. Accordingly, the analysis of the thin polycrystalline silicon solar cell is based on the relaxation of single crystal material and device properties due to the polycrystalline characteristics of the semiconductor.

As expected, increasing grain size results in better solar cell performance (Figure 10), but note the discontinuity between trends for p-i-n microcrystalline silicon solar cells and p-n multicrystalline silicon solar cells. The electric field in thin p-i-n cells is probably aiding collection efficiency and mediating the effect of grain boundary recombination. The grain structure in these thin microcrystalline silicon solar cells may also have a texture resulting in grain boundaries with less electrical activity (e.g., minority carrier recombination). Grain boundary effects are one of the most active areas for research in silicon solar cells and passivation techniques can be very effective in all types of multicrystalline silicon solar cells (Figure 11).

4 Silicon Deposition and Crystal Growth for Thin Solar Cells

In this section, we review some of the more important technologies used to realise thin silicon solar cells on supporting substrates (Figure 12). There is a

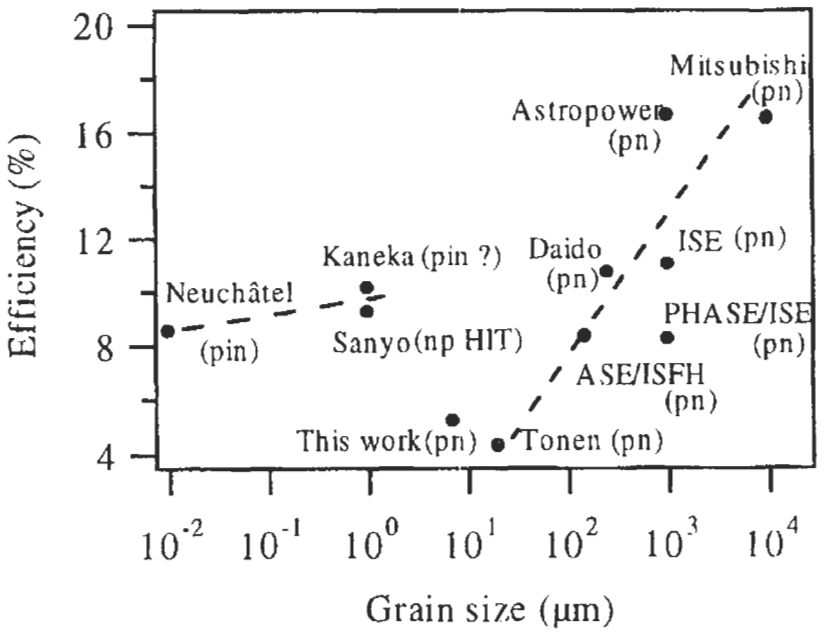

Figure 10 Effect of grain size on solar cell efficiency for pin microcrystalline silicon devices, and p–n multicrystalline thin silicon devices [76].

wide range of methods used to deposit semiconductor materials, virtually all of which have been applied to some extent or degree to the production of thin silicon solar cells. This section is offered as a survey of the diverse approaches; space limitations do not permit an in-depth review. Where possible, common issues and criteria and unifying design principles are noted.

4.1 Substrate Considerations

One of the key technological challenges to achieving a commercially viable thin-layer polycrystalline silicon solar cell technology is the development of a low-cost supporting substrate. The requirements for the substrate material are severe. Mechanical strength and thermal coefficient of expansion (TCE) matching are needed to prevent the film from breaking or deforming during handling and high-temperature processing. There are several good candidates for thermal expansion matched substrates including mullite, a compound of alumina and silica. The substrate must also provide good wetting and nucleation during the film growth process without contaminating the film. The substrate can be conducting or insulating, depending on device requirements. Finally, the substrate-silicon interface must provide a high degree of diffuse reflectivity and surface passivation.

The following substrates have been utilised to fabricate thin silicon solar cells:

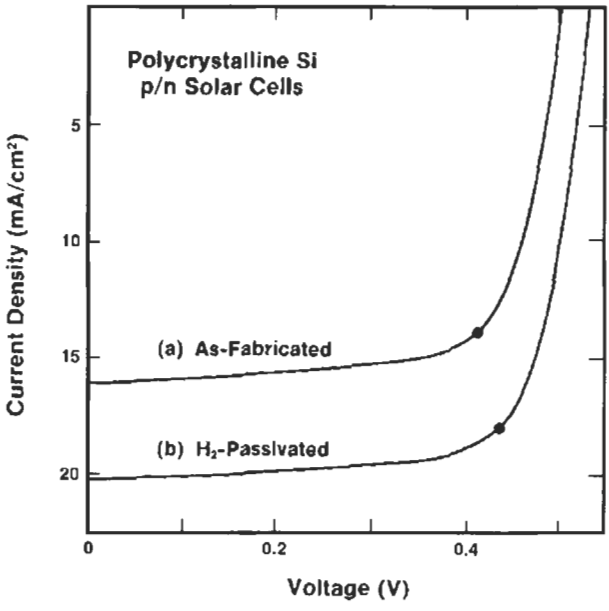

Figure 11 Hydrogen passivation of multicrystalline silicon solar cells showing improvement in current and voltage [77].

- glass [80–82]
- ceramics [83–90]
- steel [91–93]
- graphite [94–99]
- upgraded metallurgical silicon sheet or wafers [100–103]

4.2 High-Temperature Silicon Deposition Methods

It is useful to distinguish silicon deposition methods that employ high temperatures ($>1000°C$) from low-temperature deposition techniques. The high temperatures impose significant constraints on and limit the choice of substrates, especially if a post-deposition recrystallisation step is desired. High-temperature deposition methods are probably the only way to achieve high silicon deposition rates (e.g., 1–20 microns/min), and therefore if silicon layers of 10–50 microns thickness are required, such high-temperature steps may be the only viable option. High temperature deposition methods include:

- Melt growth or melt coating techniques where elemental silicon is melted and then deposited as a film or layer on a substrate.
- Chemical vapour deposition (CVD) where a silicon-containing gaseous precursor is thermally decomposed on a substrate.
- Liquid phase epitaxy (LPE) where silicon is precipitated from a molten metal solution.

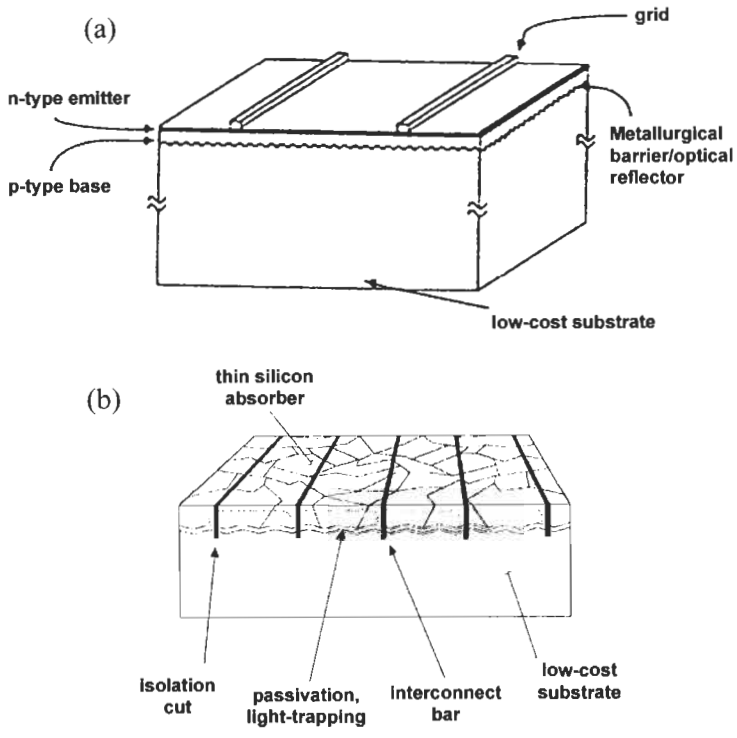

Figure 12 Generic polycrystalline thin-film silicon device structures: (a) the electrically active part of the device consists of a thin silicon layer on top on a passive mechanically supporting substrate [78]; (b) similar structure with interconnection achieved monolithically, a benefit unavailable to conventional wafer based devices [79].

4.2.1 Melt Growth Techniques

Melt growth processes characteristically have both high growth rates and good material quality [83, 84, 104]. An example melt coating process is shown in Figure 13. In these examples, a substrate is contacted with molten silicon, which wets the substrate and then solidifies as a silicon layer. In many cases, the substrate is drawn through a bath of molten silicon. Generally, such processes cannot produce layers much less than 100 microns in thickness.

4.2.2 Recrystallisation of Silicon

Related to melt growth are various recrystallisation techniques. These are generally not deposition processes per se, but instead are used to melt already-deposited silicon layers and recrystallise them in order to achieve a more favourable grain structure. In this case, the grain-structure of the as-deposited silicon layer is not critical, and the deposition process can be optimised for high-growth rates, large-areas and purity specifications. For instance, a plasma-enhanced CVD process such as shown in Figure 14 can be used to plate a silicon layer of desired thickness on a suitable substrate, such as a ceramic, which is compatible with a recrystallisation step.

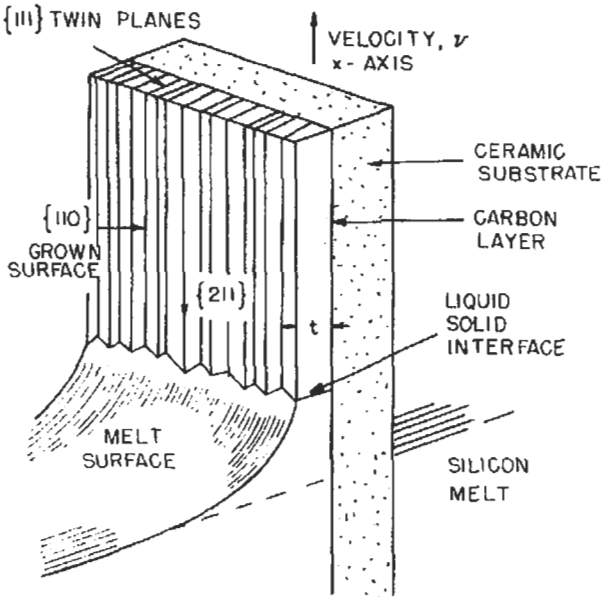

Figure 13 Honeywell silicon-on-ceramic dip coating process [83].

In the preferred techniques of recrystallisation, the deposited silicon layer is not usually simultaneously melted in its entirety. Instead, a zone-melting recrystallisation (ZMR) process is effected by localised heating to create a melted zone that moves or scans across the deposited silicon layer, melting the silicon at the leading edge and resolidifying a silicon layer at the trailing edge. Such ZMR techniques can yield millimetre to centimetre-sized grain structures. There are several ways to induce localised or zone melting of layers including moving point- or line-focused infrared lamps, travelling resistively heated strip heaters, and laser and electron beams. Figure 15 shows several of these zone melting recrystallisation techniques commonly used for silicon solar cell applications.

Much work has been done on optimising the quality of silicon layers produced by ZMR. For example, Figure 16 shows the effects of silicon layer thickness and zone melting scan speed on defect density of recrystallised silicon layers.

4.2.3 High-Temperature Silicon Chemical Vapour Deposition

Chemical vapour deposition or CVD is defined as the formation of a solid film on a substrate by reacting vapour-phase chemicals, or 'precursors', which contain the desired constituents [110]. For example, substrates can be coated with silicon layers by decomposition of gaseous silane (SiH_4) or trichlorosilane ($SiHCl_3$). In fact, many precursors are possible for silicon CVD, and silane or the chlorosilanes are probably the most commonly used, although for example, iodine and bromine compounds are also sometimes considered as silicon precursors. In general, Silicon CVD is a well-developed technology commonly used in integrated circuit fabrication, in which case it is often used for epitaxial

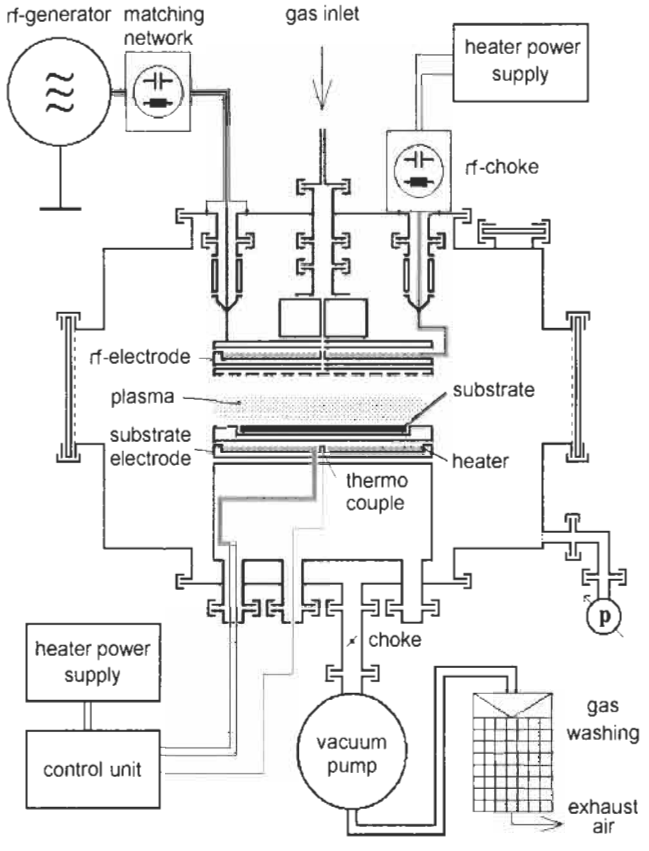

Figure 14 PECVD silicon deposition process [105].

growth of silicon layers on monocrystalline silicon substrates. For solar cell applications where CVD is used to deposit a 10–50 micron thick silicon layer for subsequent, post-deposition ZMR, the CVD is optimised for high precursor utilisation (i.e., the fraction of precursor converted to silicon), deposition efficiency (i.e., the fraction of deposited silicon that ends up on the substrate rather than the walls of the reactor chamber or the substrate susceptor), the deposition rate, the purity of the deposited silicon, areal uniformity, the potential to recover unreacted precursors or reaction product, and various safety and environmental issues.

For solar cell applications, three types of CVD are most used:

- atmospheric pressure chemical vapour deposition (APCVD)
- rapid thermal CVD (RTCVD)
- low-pressure CVD (LPCVD)

In all these types of CVD, a gaseous silicon precursor (e.g., SiH_4 or $SiHCl_3$), generally mixed with a dilution carrier gas such as hydrogen or nitrogen, is

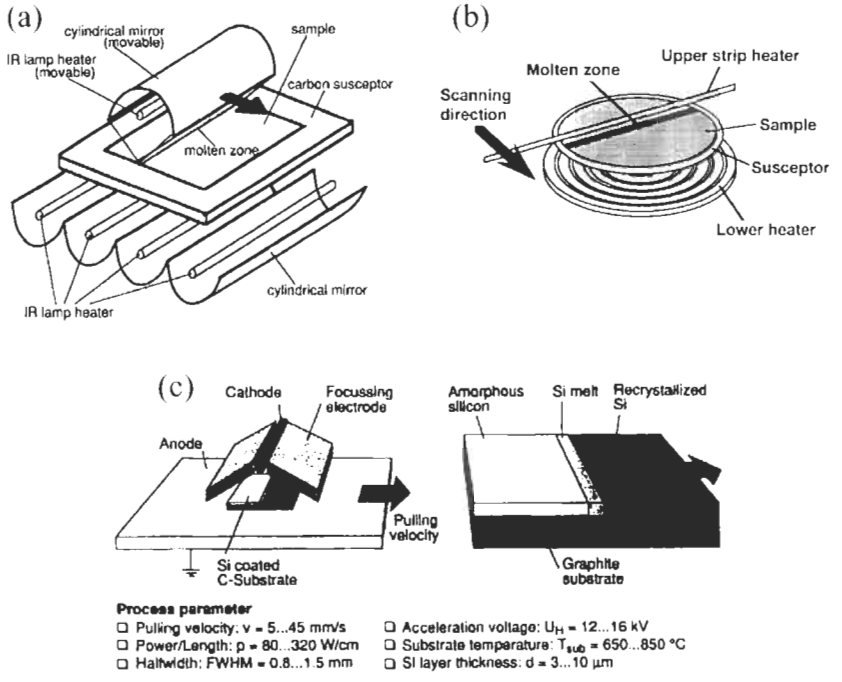

Figure 15 (a) Halogen IR lamp heating for ZMR [106]. (b) Travelling strip heaters for ZMR [107]. (c) Electron beam heating [108].

delivered into a reaction chamber. These gases move from the inlet to the outlet in a continuous stream to form the main gas flow region which bring the precursor into close proximity of the heated substrate. Some further description and details of the three main types of CVD processes used for thin silicon solar cells follows.

Atmospheric pressure CVD. APCVD systems were historically the first used for applications in the microelectronics industry [111, 112]. These systems are simple in design and are generally composed of three subsystems, a gas delivery system, a reactor, and an effluent abatement system. For the most part, APCVD is carried out at relatively high temperatures for silicon containing precursors (1100–1250°C). This allows for high deposition rates to be achieved. At these high temperatures, APCVD is in the mass-transport limited regime. This requires that a very uniform gas flow be achieved within the reactor to ensure that all areas of the heated substrate are exposed to equal amounts of precursor. This requirement is the primary concern during APCVD reactor geometry design and, to date, has limited this process to batch type processes with respect to CVD silicon.

Rapid thermal CVD. RTCVD is a variation of APCVD. It is based on the energy transfer between a radiant heat source and an object with very short processing times, of the order of seconds or minutes. This is typically from an optical heating system such as tungsten halogen lamps. The obvious benefit of this process is the

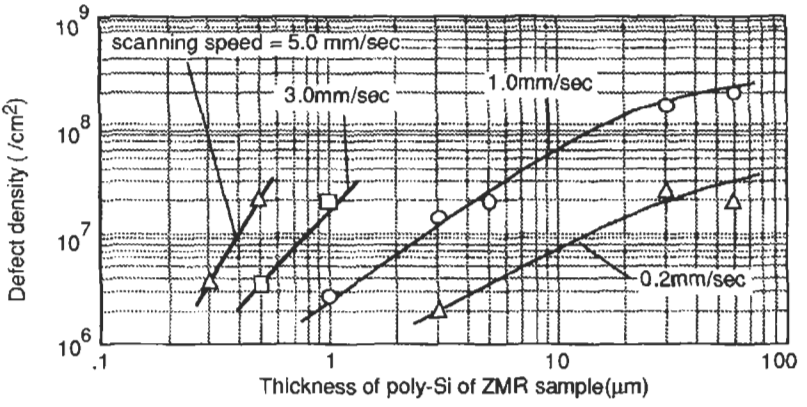

Figure 16 Relation between deposited silicon layer thickness, scan speed, and silicon defect density in ZMR [109].

fast cycle times for heating substrates to their required deposition temperature. A detailed explanation of this process along with its advantages and disadvantages can be found in Faller et al. [113].

Low-pressure CVD. LPCVD systems are inherently more complex than APCVD systems since they require robust vacuum systems that are capable of handling the often toxic corrosive precursor effluents. With respect to silicon deposition, LPCVD is generally conducted using vacuum pressures of 0.25–2.0 torr and temperatures of 550–700°C. At these pressures and temperatures LPCVD is in the surface rate-limited regime. It is important to note that at reduced pressures the diffusivity of the precursor is greatly enhanced. This allows for multiple wafers to be stacked very closely together, on the order of a few millimetres, and still achieve a highly uniform deposition. However in order to ensure this, very precise temperature control is necessary across the entire reactor, within 0.5–1°C is not uncommon. Since LPCVD is in the surface rate-limited regime it has the constraint of very low deposition rates. These low growth rates have limited its application in silicon solar cell fabrication.

A summary of silicon CVD growth rates for various precursors and deposition temperatures is given in Table 1.

4.2.4 Low-Temperature Chemical Vapour Deposition

Some low-temperature chemical vapour techniques can be distinguished from the high-temperature ($>1000°C$) CVD processes discussed above. These methods are employed with substrates such as glass which are not compatible with either a high-temperature deposition step nor a post-deposition recrystallisation step. The relatively slow growth rates inherent in a low-temperature deposition process necessitates thin device structures on the order of several microns thickness or less. The as-deposited silicon layers have average grain sizes of 1 micron or less and are characterised as microcrystalline. Hydrogenated microcrystalline silicon solar cells using a p–i–n structure which

is similar to the amorphous silicon solar cell structure, can achieve very respectable conversion efficiencies in excess of 10%. The benefits of such microcrystalline silicon solar cells over amorphous silicon solar cells are a greater stability to light-induced degradation processes. The deposition processes for microcrystalline silicon solar cells are typically adaptations of those used for amorphous silicon solar cells.

Liquid-phase epitaxy (LPE). Liquid-phase epitaxy is a metallic solution growth technique that can be used to grow semiconductor layers on substrates. Silicon can be precipitated from solutions of a number of molten metals in the temperature range 600–1200°C. This method has been used to grow thin silicon solar cells on low-cost metallurgical grade (MG) silicon substrates. In this case, the MG silicon substrate is too impure for direct use in photovoltaics. Instead, the substrate is used as a substrate for the growth of high-purity layers of silicon by either LPE or CVD. The MG silicon provides a thermal-expansion matched substrate for the thin silicon solar cell. The grain size of MG substrates is relatively large (several millimetres to centimetres in lateral dimension), and as the epitaxial layer will replicate the grain structure of the silicon substrate, this approach will yield thin silicon solar cells with large grain sizes. One issue with using a MG silicon substrate is contamination of the solar cell device by outdiffusing substrate impurities. Other favourable features of LPE are the high mobility of adatoms in the liquid phase (as compared to surface diffusion upon which vapour-phase techniques depend), and the near-equilibrium growth conditions which reduce point defects and dislocations originating from the substrate. A conventional slideboat LPE system, similar to that used for making compound semiconductor optoelectronics devices, and suitable for R&D of LPE thin silicon solar cells is shown in Figure 17. This type of LPE system employs a programmed transient cooling mode, and is essentially a batch process. Steady-state LPE processes (Figure 18) using an imposed temperature difference across the growth solution in conjunction with a solid silicon source to replenish the solution have been proposed and developed for high-throughput production.

5 Thin Silicon Solar Cells Based on Substrate Thinning

Figure 19 shows a solar cell made by thinning and grooving the backside of a silicon wafer. Such solar cells obviously have little cost advantage in that they

Table 1 Common silicon precursors

Silicon precursor	Deposition temperature (°C)	Growth rates (μm/min)
Silicon tetrachloride ($SiCl_4$)	1150–1250	0.4–1.5
Trichlorosilane ($SiCl_3H$)	1000–1150	0.4–4.0
Dichlorosilane (SiH_2Cl_2)	1020–1120	0.4–3.0
Silane (SiH_4)	650–900	0.2–0.3
Disilane (Si_2H_6)	400–600	< 0.1

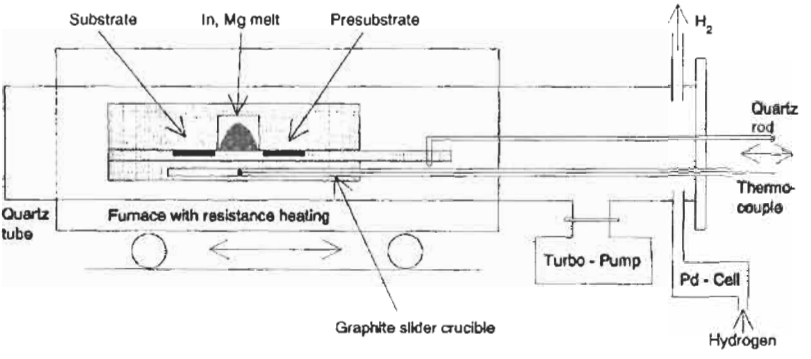

Figure 17 Small-scale LPE system [114].

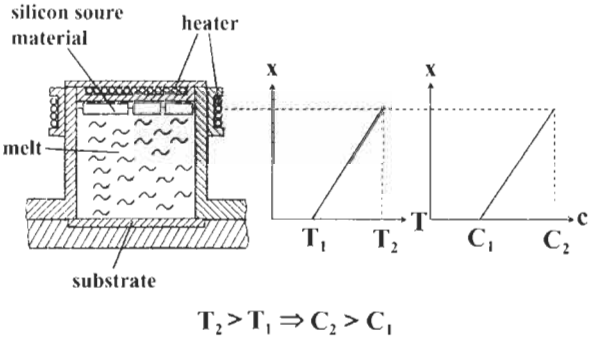

Figure 18 Principle of the temperature difference method [115].

utilise a high-quality silicon wafer and add considerable processing complexity. Because of the decreased sensitivity of performance to lifetime in such thin solar cells, they have application to space solar cells due to their potential radiation hardness. Further, these cells provide a means of studying basic effects such as light trapping and surface passivation in thin solar cell structures, without the complicating issues of material quality and grain boundaries. A similar type of thin solar cell is shown in Figure 20. This device structure permits a planar back mirror to be effected close to the front surface (Figure 20(a)). The dependence of short-circuit current on effective device thickness can be readily studied with this type of thin solar cell (Figure 20(b)).

Even thinner silicon solar cells can be made with silicon wafers using epitaxial growth, provided a superstrate is used for mechanical support. For instance, Figure 21 shows a thin silicon solar cell that made by layer transfer and wafer bonding techniques. An epitaxial silicon solar cell structure is grown on a monocrystalline silicon substrate. The structure is then bonded to a glass superstrate. The silicon substrate is then removed. Most simply, the removal of the silicon substrate can be effected by controlled etching, in which case the substrate is dissolved away. Various schemes have been proposed to separate the substrate from the epitaxial layer after bonding the solar cell structure to a

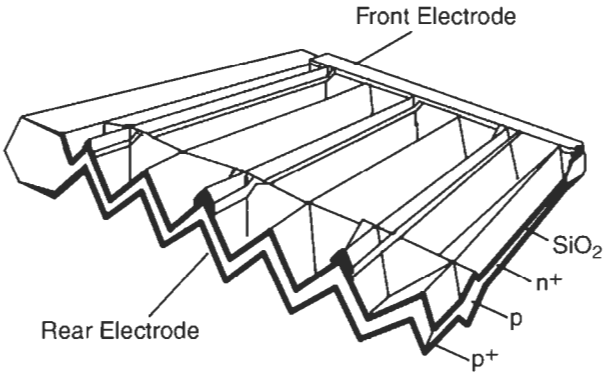

Figure 19 Thinned and grooved wafer-based silicon solar cell [116].

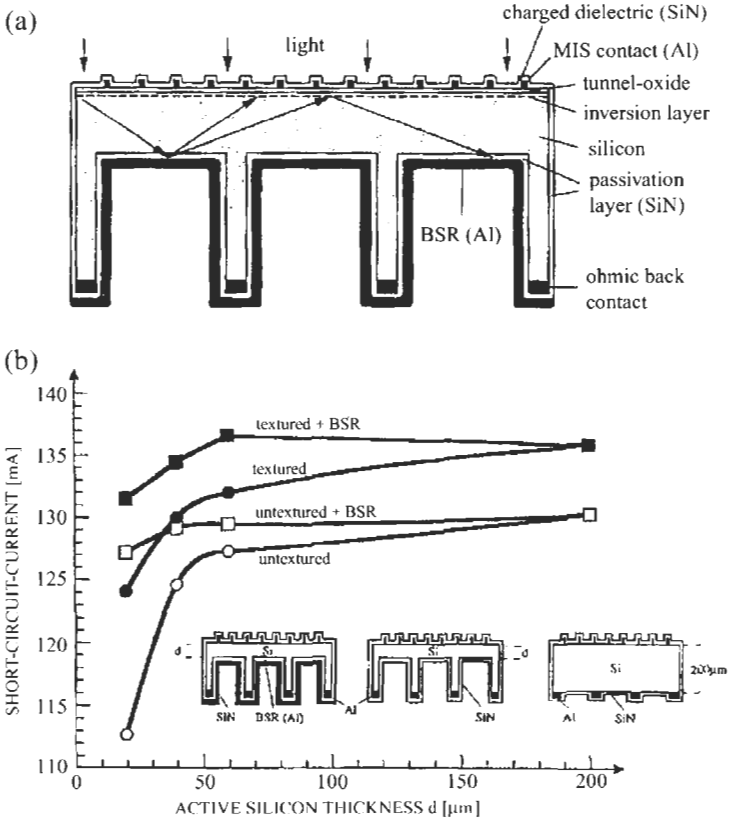

Figure 20 (a) Cross-section of ultra-thin, self-supporting MIS solar cell made by structuring a silicon wafer [117]. (b) Short-circuit current as a function of active layer silicon thickness for solar cell structures shown in inset [117].

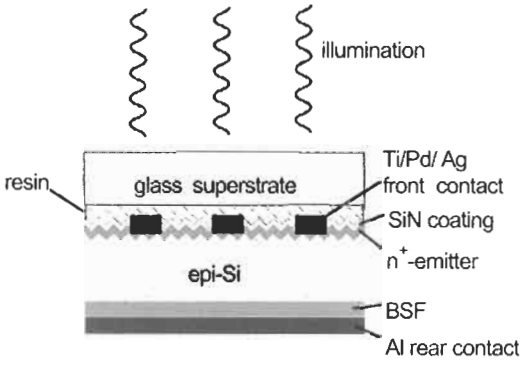

Figure 21 Monocrystalline silicon substrate made by layer transfer and bonding to a glass superstrate [119].

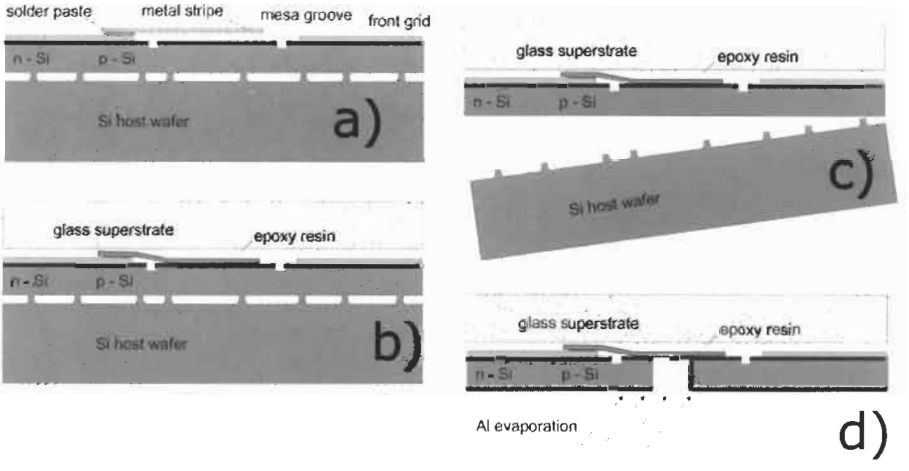

Figure 22 Schematic representation of series connection of thin-film Si transfer solar cells. (a) Two epitaxial thin-film silicon solar cells connected to the host wafer with the separation layer (columns). A metal stripe (Ag) is soldered to the front side grid of the left solar cell. Mesa grooves provide electrically isolation of the emitter in the interconnection area. (b) Epoxy resin fixes the superstrate glass to the surface of the cell. (c) Mechanical force removes the host wafer from the cell. (d) A groove structured via chip dicing sawing separates the two solar cells. Oblique deposition of aluminium creates the back contact of the solar cells and electrically connects the metal stripe that is in contact with the front side grid of the left solar cell with the back side contact of the right solar cell [120].

superstrate. One method of achieving this shown in detail in Figure 22. Some creative variations on this approach have been reported, as for example shown in Figure 23.

6 Summary of Device Results

We end this review by summarising results for thin silicon solar cells. Table 2 lists reports for thin silicon layers made by high-temperature growth methods, often

Pulsed Solar Simulator

Flasher and Measuring Systems

BERGER Lichttechnik has over 25 years of experience in designing and building flashers.

Our products are used worldwide in the photovoltaic industry for testing and qualification.

The Berger Pulsed Solar Simulator systems allows the high throughput for terrestrial solar cells and modules as well as the enormous accuracy required for satellites.

- Real class A simulator in accordance with IEC 904-9

The exact measurements of the electrical characteristics of solar cells up to large area panels are carried out by the computer controlled flasher, electrical load and data acquisition system.

- Measurements in accordance with DIN, EN, ISO, IEC and UL standards

Regarding the space application, the multi junction solar cells and the advanced scientific approach we work together with Dr. Ralf Adelhelm. He gained his background in one of a leading calibration laboratory and the space industry (www.photovoltaic-consultant.com).

BERGER Lichttechnik GmbH & Co. KG • Isarstrasse 2 • 82065 Baierbrunn, Germany
Phone ++49-89-793 55 266, Fax ++49-89-793 55 265
www.bergerlichttechnik.de

Table 2 High-temperature growth on foreign substrates (after Catchpole et al. [122])

Institution	Substrate	Deposition method	Grain size (μm)	Electrical	Reference
PHASE, ECN and CNRS-LMPM	Alumina	RTCVD	10	$\tau = 0.3\ \mu$s, $L = 10\ \mu$m	[123, 124]
PHASE, LPM and GEMPPM	Alumina	LPE with RTCVD seed	10		[125]
IMEC and PHASE	Alumina	RTCVD	5–10	$\tau = 0.5\ \mu$s	[126, 127]
ETL	Alumina	ECR-PCVD with EB-ZMR, diff. Barrier	10×200		[128]
ETL	Alumina	CVD with laser recryst., diff. Barrier		$\eta = 6.5\%$	[129]
TU-Berlin	Alumina	CVD	10	$L = 8\ \mu$m	[130]
PHASE and IMEC	Mullite	RTCVD	10–15	$\tau = 0.5\ \mu$s	[131]
MPI-F, MPI-M and LSG	Glassy carbon	LPE with RF plasma seed	10		[132]
MPI-F, Siemens and TU-Hamburg	Graphite	PECVD or sputtering + ZMR + CVD	100×1000		[133]
Fraunhofer ISE	Graphite	LPCVD, diff. Barrier, ZMR	mm × cm	$L = 30\ \mu$m, $\eta = 11.0\%$	[134]
Daido Hoxan	Graphite	LPE (temp diff) with diff. Barrier	100–300	$L = 30\ \mu$m	[135, 136]
PHASE, IMEC and Fraunhofer	Graphite	RTCVD with diff. Barrier	0.1–6	$L = 3\ \mu$m	[137]
ASE GmbH	Graphite	CVD with ZMR, diff. Barrier	100	$L = 10$–$15\ \mu$m	[138]
TU-Hamburg	Graphite	LPCVD with EB-ZMR	$100\ \mu$m × cm		[139]
ECN	Si/SiAlON	LPE with plasma-spray	10–100		[140]
UNSW	High-temperature glass	LPE with a-Si seed	50		[141]
UNSW	High-temperature glass	LPE	100		[142]
MPI-F, U Erlangen and U Stuttgart NTT	High-temperature glass	CVD with LPCVD and SPC seed	2	$L = 2\ \mu$m, $\eta = 2\%$	[143, 144]
AstroPower	Tape cast ceramic	APCVD + ZMR	mm × cm	9.18%, 543 mV	[145]

Table 3 Summary of thin silicon-on-silicon device results (after McCann et al. [146]).

Institution	Substrate	Deposition method	Electrical	Reference
Single-crystal substrates				
ANU	p-type sc-Si	LPE and substrate thinning	18%, 666 mV	[147]
UNSW	p^+ sc-S	CVD	17.6%, 664 mV	[148]
Fraunhofer ISE	p^+ sc-Si	RTCVD	17.6%	[149]
MPI-F	sc-Si	CVD	17.3%, 661 mV	[150]
ANU	p^+ sc-Si	LPE and substrate thinning	17%, 651 mV	[151]
UNSW	p^+ sc-Si	LPE	16.4%, 645 mV	[152]
ASE GmbH	p^+ sc-Si	CVD	15.4%, 623 mV	[153]
Imec	p^+ sc-Si	CVD	14.9%, 635 mV	[154]
MPI-F	p^+ sc-Si	LPE	14.7%, 659 mV	[155]
Beijing SERI	p^+ sc-Si	RTCVD	12.1%, 626 mV	[156]
Mc-Si, ribbon and MG-Si substrates				
ANU	p-type mc-Si	LPE	15.4%, 639 mV	[157]
ANU	p^+ mc-Si	LPE	15.2%, 639 mV	[157]
IMEC and KU	p^+ mc-Si	APCVD	13.3%, 615 mV	[158]
Fraunhofer ISE	p^+ mc-Si	RTCVD	13.2%, 614 mV	[149]
IMEC	p^+ mc-Si	CVD and industrial cell Process	12.1%	[159]
IMEC, KU Leuven and Bayer	RGS-ribbons	CVD	10.4%, 558 mV	[160]
Fraunhofer ISE	SSP ribbons	RTCVD	8.0%, 553 mV	[161]
IMEC and KU	SSP pre-ribbon	CVD	7.6%	[162]
Leuven 1 Kristallzuchtung	mc-Si	Temp. diff. LPE	$\tau = 5$–$10\ \mu m$	[163]
NREL	MG-Si	LPE	$L = 42\ \mu m$	[164, 165]
Substrates with diffusion barriers				
Mitsubishi Electric	SiO_2 on Si	ZMR and CVD	16.4%, 608 mV	[166]
Fraunhofer ISE	SiO_2 (perforated) on SSP-Si	RTCVD and large area heating	11.5%, 562 mV	[167]
IMEC and Fraunhofer ISE	SiO_2 on Si	ZMR and CVD	9.3%, 529 mV	[168]
Fraunhofer ISE	SiO_2 on Si	LPCVD and ZMR	6.1%	[169]
Delft UT	SiO_2 on Si	CVD	Grain size 1–2 μm	[170]

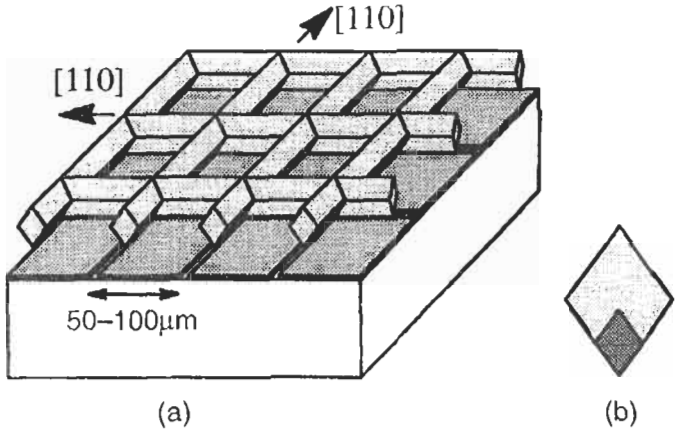

Figure 23 An example of the epitaxial lift-off process [121].

including a post-deposition recrystallisation (e.g., ZMR) step, on non-silicon substrates such as ceramics, graphite, and high-temperature glasses. Samples are characterised either by diffusion length or minority carrier lifetime, or in cases where a solar cell was made, by efficiency. Table 3 shows a similar summary of results for thin silicon solar cell structures on silicon-based substrates, which include oxidised silicon, MG silicon, and various types of silicon sheet.

References

[1] Redfield, D., 1975. Enhanced Photovoltaic Performance of Thin Silicon Films by Multiple Light Passes. *Proc. 11th IEEE Photovoltaic Specialists Conf.*, Scottsdale, pp. 431–432.

[2] Spitzer, M., Shewchun, J., Vera, E.S. and Loferski, J.J., 1980. Ultra High Efficiency Thin Silicon p–n Junction Solar Cells Using Reflecting Surfaces. *Proc. 14th IEEE Photovoltaic Specialists Conf.*, San Diego, pp. 375–380.

[3] Barnett, A.M., 1980. Thin Film Solar Cell Comparison Methodology. *Proc. 14th IEEE Photovoltaic Specialists Conf.*, San Diego, pp. 273–280.

[4] Werner, J.H. and Bergmann, R.B., 2001. Crystalline Silicon Thin Film Solar Cells. *Tech. Digest Int. PVSEC-12*, Jeju, pp. 69–72.

[5] Goetzberger, A., 1981. Optical Confinement in Thin Si-Solar Cells by Diffuse Back Reflectors. *Proc. 15th IEEE Photovoltaic Specialists Conf.*, Orlando, pp. 867–870.

[6] Yablonovitch, E. and Cody, G.D., 1982. Intensity Enhancement in Textured Optical Sheets for Solar Cells. *IEEE Trans. Electron Devices*, Vol. ED-29, pp. 300–305.

[7] Redfield, D., Multiple-Pass Thin-Film Silicon Solar Cell. *Applied Physics Letters*, Vol. 25(11), pp. 647–648.

[8] Barnett, A.M., Rand, J.A., Domian, F.A., Ford, D.H., Kendall, C.L., Rock, M.L. and Hall, R.B., 1988. Efficient Thin Silicon-Film Solar Cells on Low

Cost Substrates. *Proc. 8th European Photovoltaic Solar Energy Conf.*, Florence, Italy, pp. 149–155.

[9] Green, M.A. and Campbell, P., 1987. Light Trapping Properties of Pyramidally Textured and Grooved Surfaces. *Proc. 19th IEEE Photovoltaic Specialists Conf.*, New Orleans, pp. 912–917.

[10] Ruby, D.S., Yang, P., Zaidi, S. et al., 1998. Improved Performance of Self-aligned, Selective-emitter Silicon Solar Cells. *Proc. 2nd World Conf. on Photovoltaic Solar Energy Conversion*, Vienna, pp. 1460–1463.

[11] Schnell, M., Lüdemann, R. and Schaefer, S., 2000. Plasma Surface Texturization for Multicrystalline Silicon Solar Cells. *Proc. 28th IEEE Photovoltaic Specialists Conf.*, Anchorage, pp. 367–370.

[12] Wells, T., El-Gomati, M.M. and Wood, J., 1997. Low Temperature Reactive Ion Etching of Silicon with SF_6/O_2 Plasmas. *J. Vac. Sci. Technol. B*, Vol. 15, p. 397.

[13] Deckman, H.W., Roxlo, C.B., Wronski, C.R. and Yablonovitch, E., 1984. Optical Enhancement of Solar Cells. *Proc. 17th IEEE Photovoltaic Specialists Conf.*, pp. 955–960.

[14] Stocks, M.J., Carr, A.J. and Blakers, A.W., 1994. Texturing of Polycrystalline Silicon. *Proc. 24th IEEE Photovoltaic Specialists Conf.*, Hawaii, pp. 1551–1554.

[15] Deckman, H.W., Wronski, C.R., Witzke, H. and Yablonovitch, E., 1983. Optically Enhanced Amorphous Solar Cells. *Appl. Phys. Lett.*, Vol. 42(11), pp. 968–970.

[16] Tsuo, Y.S., Xiao, Y., Heben, M.J., Wu, X., Pern, F.J. and Deb, S.K., 1993. Potential Applications of Porous Silicon in Photovoltaics. *Proc. 23rd IEEE Photovoltaic Specialists Conf.*, Louisville, pp. 287–293.

[17] Cudzinovic, M. and Sopori, B., 1996. Control of Back Surface Reflectance from Aluminum Alloyed Contacts on Silicon Solar Cells. *Proc. 25th IEEE Photovoltaic Specialists Conf.*, Washington DC, pp. 501–503.

[18] Rothwarf, A., 1985. Enhanced Solar Cell Performance by Front Surface Light Scattering. *Proc. 18th IEEE Photovoltaic Specialists Conf.*, Las Vegas, pp. 809–812.

[19] Gee, J.M., King, R.R. and Mitchell, K.W., 1996. High-Efficiency Cell Structures and Processes Applied to Photovoltaic-Grade Czochralski Silicon. *Proc. 25th IEEE Photovoltaic Specialists Conf.*, Washington DC, pp. 409–412.

[20] Gee, J.M., Gordon, R. and Liang, H., 1996. Optimization of Textured-Dielectric Coatings for Crystalline-Silicon Solar Cells. *Proc. 25th IEEE Photovoltaic Specialists Conf.*, Washington DC, pp. 733–736.

[21] Hegedus, S.S. and Deng, X., 1996. Analysis of Optical Enhancement in a-Si n–i–p Solar Cells Using a Detachable Back Reflector. *Proc. 25th IEEE Photovoltaic Specialists Conf.*, Washington DC, pp. 1061–1064.

[22] Tobin, S.P., Keavney, C.J., Geoffroy, L.M. and Sanfacon, M.M., 1988. Experimental Comparison of Light-Trapping Structures for Silicon Solar Cells. *Proc. 20th IEEE Photovoltaic Specialists Conf.*, Las Vegas, pp. 545–548.

[23] Rand, J.A., Hall, R.B. and Barnett, A.M., 1990. Light Trapping in Thin Crystalline Silicon Solar Cells. *Proc. 21st IEEE Photovoltaic Specialists Conf.*, Orlando, pp. 263–268.

[24] Restrepo, F. and Backus, C.E., 1976. *IEEE Trans. Electron Devices*, Vol. 23, pp. 1195–1197.

[25] Campbell, P., Wenham, S.R. and Green, M.A., 1988. Light-Trapping and Reflection Control with Tilted Pyramids and Grooves. *Proc. 20th IEEE Photovoltaic Specialists Conf.*, Las Vegas, pp. 713–716.

[26] King, D.L. and Buck, M.E., 1991. Experimental Optimization of an Anisotropic Etching Process for Random Texturization of Silicon Solar Cells. Proc. *22nd IEEE Photovoltaic Specialists Conf.*, Las Vegas, pp. 303–308.

[27] Terheiden, B., Fath, P. and Bucher, E., 2000. The MECOR (Mechanically Corrugated) Silicon Solar Cell Concept. *Proc. 28th IEEE Photovoltaic Specialists Conf.*, Anchorage, pp. 399–402.

[28] Fath, P. et al., 1995. Multicrystalline Silicon Solar Cells Using a New High-Throughput Mechanical Texturization Technology and a Roller Printing Metallization Technique. *Proc. 13th European Photovoltaic Solar Energy Conf.*, Nice, pp. 29–32.

[29] Narayanan, S., Wenham, S.R. and Green, M.A., 1989, *Tech. Digest. Int. PVSEC-4*, Sydney, p. 1111.

[30] Kaiser, U., Kaiser, M. and Schindler, R., 1991. Texture Etching of Multicrystalline Silicon. *Proc. 10th European Photovoltaic Solar Energy Conf.*, Lisbon, pp. 293–294.

[31] Willeke, G., Nussbaumer, H., Bender, H. and Bucher, E., 1992. Mechanical Texturization of Multicrystalline Silicon Using a Conventional Dicing Saw and Bevelled Blades. *Proc. 11th European Photovoltaic Solar Energy Conf.*, Montreux, pp. 480–483.

[32] Stocks, M.J., Carr, J.J. and Blakers, A.W., 1994. Texturing of Polycrystalline Silicon. *Proc. First World Conf. on Photovoltaic Energy Conversion*, Hawaii, pp. 1551–1554.

[33] Campbell, P. and Keevers, M., 2000. Light Trapping and Reflection Control for Silicon Thin Films Deposited on Glass Substrates Textured by Embossing. *Proc. 28th IEEE Photovoltaic Specialists Conf.*, Anchorage, pp. 355–358.

[34] Thorp, D., Campbell, P. and Wenham, S.R., 1996. Absorption Enhancement in Conformally Textured Thin-Film Silicon Solar Cells. *Proc. 25th IEEE Photovoltaic Specialists Conf.*, Washington DC, pp. 705–708.

[35] Smith, A.W., Rohatgi, A. and Neel, S.C., 1990. Texture: A Ray-Tracing Program for the Photovoltaic Community. *Proc. 21st IEEE Photovoltaic Specialists Conf.*, Orlando, pp. 426–431.

[36] Sopori, B.L. and Marshall, T., 1993. Optical Confinement in Thin Silicon Films: A Comprehensive Ray Optical Theory. *Proc. 23rd IEEE Photovoltaic Specialists Conf.*, Louisville, pp. 127–132.

[37] Rau, U., Meyer, T., Goldbach, M., Brendel, R. and Werner, J.H., 1996. Numerical Simulation of Innovative Device Structures for Silicon Thin-Film Solar Cells. *Proc. 25th IEEE Photovoltaic Specialists Conf.*, Washington DC, pp. 469–472.

[38] Abouelsaood, A.A., Ghannam, M.Y., Poortmans, J. and Mertens, R.P., 1997. Accurate Modeling of Light Trapping in Thin Film Silicon Solar Cells. *Proc. 26th IEEE Photovoltaic Specialists Conf.*, pp. 183–186.

[39] Campbell, P. and Green, M.A., 1987. Light Trapping Properties of Pyramidally Textured Surfaces. *J. Appl. Physics*, July, pp. 243–249.

[40] Bisconti, R. and Ossenbrink, H.A., 1995. Light Trapping in Spheral Solar™ Cells. *Proc. 13th European Photovoltaic Solar Energy Conf.*, Nice, pp. 386–389.

[41] Minano, J.C., Luque, A. and Tobias, I., 1992. Light-Confining Cavities for Photovoltaic Applications Based on the Angular-Spatial Limitation of the Escaping Beam. *Applied Optics*, Vol. 31(16), pp. 3114–3122.

[42] Zhao, J., Wang, A., Blakers, A.W. and Green, M.A., 1988. High Efficiency Prismatic Cover Silicon Concentrator Solar Cells. *Proc. 20th IEEE Photovoltaic Specialists Conf.*, Las Vegas, pp. 529–531.

[43] Gee, J.M., 1988. The Effect of Parasitic Absorption Losses on Light Trapping in Thin Silicon Solar Cells. *Proc. 20th IEEE Photovoltaic Specialists Conf.*, Las Vegas, pp. 549–554.

[44] Green, M.A. et al., 1995. Enhanced Light-Trapping in 21.5% Efficient Thin Silicon Solar Cells. *Proc. 13th European Photovoltaic Solar Energy Conf.*, Nice, pp. 13–16.

[45] Tiedje, T., Yablonovitch, E., Cody, G.D. and Brooks, B.G., 1984. Limiting Efficiency of Silicon Solar Cells. *IEEE Trans. Electron Devices*, Vol. ED-3 1, pp. 711–716.

[46] Basore, P.A., 1990. Numerical Modeling of Textured Silicon Solar Cells Using PC-1D. *IEEE Trans. Electron Devices*, ED-37, p. 337.

[47] Zimmerman, W. and Eyer, A., 2000. Coarse-Grained Crystalline Silicon Thin Film Solar Cells On Laser Perforated SIO_2 Barrier Layers. *Proc. 28th IEEE Photovoltaic Specialists Conf.*, Anchorage, pp. 233–236.

[48] Bruton, T.M., Roberts, S., Heasman, K.C. and Russell, R., 2000. Prospects For High Efficiency Silicon Solar Cells In Thin Czochralski Wafers Using Industrial Processes. *Proc. 28th IEEE Photovoltaic Specialists Conf.*, Anchorage, pp. 180–183.

[49] Berge, C., Bergmann, R.B., Rinke, T.J. and Werner, J.H., 2001. Monocrystalline Silicon Thin Film Solar Cells By Layer Transfer. *17th European Photovoltaic Solar Energy Conf.*, Munich, pp. 1277–1281.

[50] Zimmerman, W., Bau, S., Eyer, A., Haas, F. and Oßwald, D., 2000. Crystalline Silicon Thin Film Solar Cells On Low Quality Silicon Substrates With And Without SiO_2 Intermediate Layer. *Proc. 16th European Photovoltaic Solar Energy Conf.*, Glasgow, pp. 1144–1147.

[51] Finck von Finckenstein, B., Horst, H., Spiegel, M., Fath, P. and Bucher, E., 2000. Thin MC SI Low Cost Solar Cells With 15% Efficiency. *Proc. 28th IEEE Photovoltaic Specialists Conf.*, Anchorage, pp. 198–200.

[52] Zahedi, C., Ferrazza, F., Eyer, A., Warta, W., Riemann, H., Abrosimov, N.V., Peter, K. and Hötzel, J., 2000. Thin Film Silicon Solar Cells On Low-Cost Metallurgical Silicon Substrates By Liquid Phase Epitaxy. *Proc. 16th European Photovoltaic Solar Energy Conf.*, Glasgow, pp. 1381–1384.

[53] Tanda, M., Wada, T., Yamamoto, H., Isomura, M., Kondo, M. and Matsuda, A., 1999. Key Technology for μc-Si Thin-Film Solar Cells Prepared at a High Deposition Rate. *Tech. Digest Int. PVSEC-11*, Sapporo, pp. 237–238.

[54] Hanoka, J.I., 1999. An Overview of Silicon Ribbon-Growth Technology. *Tech. Digest Int. PVSEC-11*, Sapporo, pp. 533–534.

[55] Brendel, R., Auer, R., Feldrapp, K., Scholten, D., Steinof, M., Hezel, R. and Schultz, M., 2002. Crystalline Thin-Film Si Cells From Layer Transfer Using Porous Si (PSI-Process). *Proc. 29th IEEE Photovoltaic Specialists Conf.*, New Orleans, pp. 86–89.

[56] Meier, D.L., Jessup, J.A., Hacke, P. and Granata, Jr., S.J., 2002. Production of Thin (70–100 μm) Crystalline Silicon Cells for Conformable Modules. *Proc. 29th IEEE Photovoltaic Specialists Conf.*, New Orleans, pp. 110–113.

[57] Cudzinovic, M.J. and McIntosh, K.R., 2002. Process Simplifications to the Pegasus Solar Cell – Sunpower's High-Efficiency Bifacial Silicon Solar Cell. *Proc. 29th IEEE Photovoltaic Specialists Conf.*, New Orleans, pp. 70–73.

[58] Schmidt, J., Oberbeck, L., Rinke, T.J., Berge, C. and Bergmann, R.B., 2001. Application of Plasma Silicon Nitride To Crystalline Thin-Film Silicon Solar Cells. *Proc. 17th European Photovoltaic Solar Energy Conf.*, Munich, pp. 1351–1354.

[59] Münzer, K.A., Eisenrith, K.H., Schlosser, R.E. and Winstel, M.G., 2001. 18% PEBSCO – Silicon Solar Cells For Manufacturing. *Proc. 17th European Photovoltaic Solar Energy Conf.*, Munich, pp. 1363–1366.

[60] Tayanaka, H., Nagasawa, A., Hiroshimaya, N., Sato, K., Haraguchi, Y. and Matsushita, T., 2001. Effects of Crystal Defects in Single-Crystalline Silicon Thin-Film Solar Cell. *Proc. 17th European Photovoltaic Solar Energy Conf.*, Munich, pp. 1400–1403.

[61] Terheiden, B., Fischer, B., Fath, P. and Bucher, E., 2001. Highly Efficient Mechanically V-Textured Silicon Solar Cells Applying A Novel Shallow Angle Contacting Scheme. *Proc. 17th European Photovoltaic Solar Energy Conf.*, Munich, pp. 1331–1334.

[62] Schneiderlöchner, E., Preu, R., Lüdemann, R., Glunz, S.W. and Willeke, G., 2001. Laser-Fired Contacts. *Proc. 17th European Photovoltaic Solar Energy Conf.*, Munich, pp. 1303–1306.

[63] Glunz, S.W., Dicker, J., Kray, D., Lee, J.Y., Preu, R., Rein, S., Schneiderlöchner, E., Sölter, J., Warta, W. and Willeke, G., 2001. High Efficiency Cell Structures For Medium-Quality Silicon. *Proc. 17th European Photovoltaic Solar Energy Conf.*, Munich, pp. 1286–1292.

[64] Yamamoto, K., Yoshimi, M., Suzuki, T., Okamoto, Y., Tawada, Y. and Nakajima, A., 1997. Thin Film Poly-Si Solar Cell With Star Structure on

Glass Substrate Fabricated at Low Temperature. *Proc. 26th IEEE Photovoltaic Specialists Conf.*, Anaheim, 1997, pp. 575–580.

[65] Yamamoto, K., Yoshimi, M., Tawada, Y., Okamoto, Y. and Nakajima, A., 1999. Cost Effective and High Performance Thin Film Si Solar Cell Towards the 21st Century. *Tech Digest Int. PVSEC-11*, Sapporo, pp. 225–228.

[66] Golay, S., Meier, J., Dubail, S., Faÿ, S., Kroll, U. and Shah, A., 2000. First pin/pin Micromorph Modules By Laser Patterning. *Proc. 28th IEEE Photovoltaic Specialists Conf.*, Anchorage, pp. 1456–1459.

[67] Meier, J., Vallat-Sauvain, E., Dubail, S., Kroll, U., Dubail, J., Golay, S., Feitknecht, L., Torres, P., Fischer, D. and Shah, A., 1999. Microcrystalline Silicon Thin-Film Solar Cells by the VHF-GD Technique. *Tech. Digest Int. PVSEC-11*, Sapporo, pp. 221–223.

[68] Shah, A., Meier, J., Torres, P., Kroll, U., Fischer, D., Beck, N., Wyrsch, N. and Keppner, H., 1997. Recent Progress On Microcrystalline Solar Cells. *Proc. 26th IEEE Photovoltaic Specialists Conf.*, Anaheim, pp. 569–574.

[69] Rand, J.A. and Basore, P.A., 1991. Light-Trapping Silicon Solar Cells Experimental Results and Analysis. *Proc. 22nd IEEE Photovoltaic Specialists Conf.*, Las Vegas, pp. 192–197.

[70] Rand, J.A., Ford, D.H., Bacon, C., Ingram, A.E., Ruffins, T.R., Hall, R.B. and Barnett, A.M., 1991. Silicon-Film Product II: Initial Light Trapping Results. *Proc. 10th European Photovoltaic Solar Energy Conf.*, Lisbon, pp. 306–309.

[71] Basore, P.A., 1993. Extended Spectral Analysis of Internal Quantum Efficiency. *Proc. 23rd IEEE Photovoltaic Specialists Conf.*, Louisville, pp. 147–152.

[72] Yamamoto, K., Suzuki, T., Yoshimi, M., and Nakajima, A., 1996. Low Temperature Fabrication of Thin Film Polycrystalline Si Solar Cell on the Glass Substrate and Its Application to the a-Si:H/Polycrystalline Si Tandem Solar Cell. *Proc. 25th IEEE Photovoltaic Specialists Conf.*, Washington DC, pp. 661–664.

[73] Rothwarf, A., 1976. Crystallite Size Considerations in Polycrystalline Solar Cells. *Proc. 12th IEEE Photovoltaic Specialists Conf.*, Baton Rouge, pp. 488–495.

[74] Mokashi, A.R., Daud, T. and Kachare, A.H., 1985. Simulation Analysis of a Novel High Efficiency Silicon Solar Cell. *Proc. 18th IEEE Photovoltaic Specialists Conf.*, Las Vegas, pp. 573–577.

[75] Milstein, J.B., Tsuo, Y.S., Hardy, R.W. and Surek, T., 1981. The Influence of Grain Boundaries on Solar Cell Performance. *Proc. 15th IEEE Photovoltaic Specialists Conf.*, Orlando, pp. 1399–1404.

[76] Beaucarne, G., Bourdais, S., Slaoui, A. and Poortmans, J., 2000. Carrier Collection in Fine-Grained p–n Junction Polysilicon Solar Cells. *Proc. 28th IEEE Photovoltaic Specialists Conf.*, Anchorage, pp. 128–133.

[77] Kazmerski, L.L., 1984. Silicon Grain Boundaries: Correlated Chemical and Electro-Optical Characterization. *Proc. 17th IEEE Photovoltaic Specialists Conf.*, Orlando, pp. 379–385.

[78] Barnett, A.M., Rand, J.A., Domian, F.A., Ford, D.H., Kendall, C.L., Rock, M.L. and Hall, R.B., 1988. Efficient Thin Silicon-Film Solar Cells on Low-Cost Substrate. *Proc. 8th European Photovoltaic Energy Conf.*, Florence, pp. 149–155.

[79] Ford, D.H., Rand, J.A., Barnett, A.M., DelleDonne, E.J., Ingram, A.E. and Hall, R.B., 1997. Development of Light-Trapped, Interconnected, Silicon-Film Modules. *Proc. 26th IEEE Photovoltaic Specialists Conf.*, Anaheim, pp. 631–634.

[80] Silier, M., Konuma, A., Gutjahr, E., Bauser, F., Banhart, C., Zizler, V., Schöllkopf, H. and Frey, H., 1996. High-Quality Polycrystalline Silicon Layers Grown on Dissimilar Substrates from Metallic Solution, I. *Proc. 25th IEEE Photovoltaic Specialists Conf.*, Washington, DC, pp. 681–684.

[81] Bergmann, R., Kühnle, J., Werner, J.H., Oelting, S., Albrecht, M., Strunk, H.P., Herz, K. and Powalla, M., 1994. Polycrystalline Silicon for Thin Film Solar Cells. *Proc. 24th IEEE Photovoltaic Specialists Conf.*, Hawaii, pp. 1398–1401.

[82] Andrä, G., Bergmann, J., Ose, E., Schmidt, M., Sinh, N.D. and Falk, F., 2002. Multicrystalline LLC-Silicon Thin Film Cells on Glass. *Proc. 29th IEEE Photovoltaic Specialists Conf.*, New Orleans, pp. 1306–1309.

[83] Zook, J.D., Shuldt, S.B., Maciolek, R.B. and Heaps, J.D., 1978. Growth, Evaluation and Modeling of Silicon-on-Ceramic Solar Cells. *Proc. 13th IEEE Photovoltaic Specialists Conf.*, Washington DC, pp. 472–478.

[84] Heaps, J.D., Schuldt, S.B., Grung, B.L., Zook, J.D. and Butter, C.D., 1980. Continuous Coating of Silicon-on-Ceramic. *Proc. 14th IEEE Photovoltaic Specialists Conf.*, San Diego, pp. 39–48.

[85] Minagawa, S., Saitoh, T., Warabisako, T., Nakamura, N., Itoh, H. and Tokuyama, T., 1976. Fabrication and Characterization of Solar Cells Using Dendritic Silicon Thin Films Grown on Alumina Ceramic. *Proc. 12th IEEE Photovoltaic Specialists Conf.*, Baton Rouge, pp. 77–81.

[86] Barnett, A.M., Fardig, D.A., Hall, R.B., Rand, J.A. and Ford, D.H., 1987. Development of Thin Silicon-Film Solar Cells on Low-Cost Substrates. *Proc. 19th IEEE Photovoltaics Specialists Conf.*, New Orleans, pp. 1266–1270.

[87] van Roosmalen, J.A.M., Tool, C.J.J., Huiberts, R.C., Beenen, R.J.G., Huijsmans, J.P.P., Sinke, W.C., 1996. Ceramic Substrates for Thin-Film Crystalline Silicon Solar Cells. *Proc. 25th IEEE Photovoltaic Specialists Conf.*, Washington DC, pp. 657–660.

[88] Shuldt, S.B., Heaps, J.D., Schmit, F.M., Zook, J.D. and Grung, B.L., 1981. Large Area Silicon-on-Ceramic Substrates for Low Cost Solar Cells. *Proc. 15th IEEE Photovoltaic Specialists Conf.*, Orlando, pp. 934–940.

[89] Slaoui, A., Rusu, M., Fosca, A., Torrecillas, R., Alvarez, E. and Gutjar, A., 2002. Investigation of Barrier Layers on Ceramics for Silicon Thin Film Solar Cells. *Proc. 29th IEEE Photovoltaic Specialists Conf.*, New Orleans, pp. 90–93.

[90] DelleDonne, E., Ingram, A., Jonczyk, R., Yaskoff, J., Sims, P., Rand, J. and Barnett, A., 2002. Thin Silicon-on-Ceramic Solar Cells. *Proc. 29th IEEE Photovoltaic Specialists Conf.*, New Orleans, pp. 82–85.

[91] Barnett, A.M., Mauk, M.G., Zolper, J.C., Hall, R.B. and McNeely, J.B., 1984. Thin-Film Silicon and GaAs Solar Cells on Metal and Glass Substrates. *Tech. Digest Int. PVSEC-1*, Kobe, pp. 241–244.

[92] Barnett, A.M., Mauk, M.G., Hall, R.B., Fardig, D.A. and McNeely, J.B., 1985. Design and Development of Efficient Thin-Film Crystalline Silicon Solar Cells on Steel Substrates. *Proc. 6th European Photovoltaic Solar Energy Conf.*, London, pp. 866–870.

[93] Barnett, A.M., Hall, R.B., Fardig, D.A. and Culik, J.S., 1985. Silicon-Film Solar Cells on Steel Substrates. *Proc. 18th IEEE Photovoltaics Specialists Conf.*, Las Vegas, pp. 1094–1099.

[94] Kunze, T., Hauttmann, S., Seekamp, J. and Müller, J., 1997. Recrystallized and Epitaxially Thickened Poly-Silicon Layers on Graphite Substrates. *Proc. 26th IEEE Photovoltaic Specialists Conf.*, Anaheim, pp. 735–738.

[95] Chu, T.L., Mollenkopf, H.C., Singh, K.N., Chu, S.S. and Wu, I.C., 1975. Polycrystalline Silicon Solar Cells for Terrestrial Applications. *Proc. 11th IEEE Photovoltaic Specialists Conf.*, Scottsdale, pp. 303–305.

[96] Merber, M., Bettini, M. and Gornik, E., 1984. Large Grain Polycrystalline Silicon Films on Graphite for Solar Cell Applications. *Proc. 17th IEEE Photovoltaic Specialists Conf.*, Orlando, pp. 275–280.

[97] Pauli, M., Reindl, T., Krühler, W., Homberg, F. and Müller, J., 1994. A New Fabrication Method for Multicrystalline Silicon Layers on Graphite Substrates Suited for Low-Cost Thin Film Solar Cells. *Proc. 24th IEEE Photovoltaic Specialists Conf.*, Hawaii, pp. 1387–1390

[98] Lin, A.Z., Fan, Z.Q., Sheng, H.Y. and Zhao, X.W., 1982. Thin-Film Polycrystalline Silicon Solar Cell. *Proc. 16th IEEE Photovoltaic Specialists Conf.*, San Diego, pp. 140–145.

[99] Lüdemann, R., Schaefer, S., Schüle, C. and Hebling, C., 1997. Dry Processing of mc-Silicon Thin-Film Solar Cells on Foreign Substrates Leading to 11% Efficiency. *Proc. 26th IEEE Photovoltaic Specialists Conf.*, Anaheim, p. 159

[100] Chu, T.L., Chu, S.S., Duh, K.Y. and Yoo, H.I., 1976. Silicon Solar Cells on Metallurgical Silicon Substrates. *Proc. 12th IEEE Photovoltaic Specialists Conf.*, Baton Rouge, pp. 74–78.

[101] Chu, T.L., Chu, S.S., Stokes, E.D., Lin, C.L. and Abderrassoul, R., 1978. Thin Film Polycrystalline Silicon Solar Cells. *Proc. 13th IEEE Photovoltaic Specialists Conf.*, Washington DC, pp. 1106–1110.

[102] Hötzel, J., Peter, K., Kopecek, R., Fath, P., Bucher, E. and Zahedi, C., 2000. Characterization of LPE Thin Film Silicon on Low Cost Silicon Substrates. *Proc. 28th IEEE Photovoltaic Specialists Conf.*, Anchorage, p. 225.

[103] Chu, T.L., Stokes, E.D., Chu, S.S. and Abderrassoul, R., 1980. Chemical and Structural Defects in Thin Film Polycrystalline Silicon Solar Cells. *Proc. 14th IEEE Photovoltaic Specialists Conf.*, San Diego, pp. 224–227.

[104] Belouet, C., Hervo, C., Mautref, M., Pages, C. and Hervo, J., 1982. Achievement and Properties of Self-Supporting Polysilicon Solar Cells Made From RAD Ribbons. *Proc. 16th IEEE Photovoltaic Specialists Conf.*, San Diego, pp. 80–85.

[105] Heemeier, J., Rostalsky, M., Gromball, F., Linke, N. and Müller, J., 2002. Thin Film Technology for Electron Beam Crystallized Silicon Solar Cells on Low Cost Substrates. *Proc. 29th IEEE Photovoltaic Specialists Conf.*, New Orleans, pp. 1310–1313.

[106] Deguchi, M., Morikawa, H., Itagaki, T., Ishihara, T., Namizaki, H., 1991. Large Grain Thin Film Polycrystalline Silicon Solar Cells Using Zone Melting Recrystallization. *Proc. 22nd IEEE Photovoltaic Specialists Conf.*, Las Vegas, pp. 986–991.

[107] Takami, A., Arimoto, S., Naomoto, H., Hamamoto, S., Ishihara, T., Kumabe, H. and Murotani, T., 1994. Thickness Dependence of Defect Density in Thin Film Polycrystalline Silicon Formed on Insulator By Zone-Melting Recrystallization. *Proc. 24th IEEE Photovoltaic Specialists Conf.*, Hawaii, pp. 1394–1397.

[108] Reindl, T., Krühler, W., Pauli, M. and Müller, J., 1994. Electrical and Structural Properties of the Si/C Interface in Poly-Si Thin Films on Graphite Substrates. *Proc. 24th IEEE Photovoltaic Specialists Conf.*, Hawaii, pp. 1406–1409.

[109] Kawama, Y., Takami, A., Naomoto, H., Hamamoto, S. and Ishihara, T., 1996. In-Situ Control in Zone-Melting Recrystallization Process for Formation of High-Quality Thin Film Polycrystalline Si. *Proc. 25th IEEE Photovoltaic Specialists Conf.*, Washington DC, pp. 481–484.

[110] Tauber, R.N. and Wolf, S., 2000. *Silicon Processing for the VLSI Era, Volume 1 – Process Technology* (2nd Edition), Lattice Press, Sunset Beach.

[111] Kern, W. and Ban, V., 1978. Chemical Vapor Deposition of Inorganic Thin Films. In: Vossen, J.L. and Kern, W., Eds., *Thin Film Processes*, Academic Press, New York, pp. 257–331.

[112] Hammond, M., 1979. Introduction to Chemical Vapor Deposition. *Solid State Technology*, December, p. 61.

[113] Faller, F.R., Henninger, V., Hurrle, A. and Schillinger, N., 1998. Optimization of the CVD Process for Low Cost Crystalline Silicon Thin Film Solar Cells. *Proc. 2nd World Conf. on Photovoltaic Solar Energy Conversion*, Vienna, pp. 1278–1283.

[114] Wagner, B.F. Schetter, Ch., Sulima, O.V. and Bett, A., 1993. 15.9% Efficiency for Si Thin Film Concentrator Solar Cell Grown by LPE. *Proc. 23rd IEEE Photovoltaic Specialists Conf.*, Louisville, pp. 356–359.

[115] Thomas, B., Müller, G., Wilde, P.-M. and Wawra, H., 1997. Properties of Silicon Thin Films Grown by the Temperature Difference Method (TDM). *Proc. 26th IEEE Photovoltaic Specialists Conf.*, Anaheim, pp. 771–774.

[116] Ida, M., Hane, K., Uematsu, T., Saitoh, T. and Hayashi, Y., 1989. A Novel Design for Very-Thin, High Efficiency Silicon Solar Cells with a New Light Trapping Structure. *Tech. Digest PVSEC-4*, Sydney, pp. 827–831.

[117] Hezel, R. and Ziegler, R., 1993. Ultrathin Self-Supporting Crystalline Silicon Solar Cells with Light Trapping. *Proc. 23rd IEEE Photovoltaic Specialists Conf.*, Louisville, pp. 260–264.

[118] Markvart, T., 2000. *Solar Electricity (2nd edition)*, John Wiley & Sons, Chichester.

[119] Schmidt, J., Oberbeck, L., Rinke, T.J., Berge, C. and Bergmann, R.B., 2001. Application of Plasma Silicon Nitride to Crystalline Thin-Film Silicon Solar Cells. *Proc. 17th European Photovoltaic Solar Energy Conf.*, Munich, p. 1351.

[120] Rinke, T.J., Hanna, G., Orgassa, K., Schock, H.W. and Werner, J.H., 2001. Novel Self-Aligning Series-Interconnection Technology for Thin Film Solar Modules. *Proc. 17th European Solar Energy Conf.*, Munich, p. 474.

[121] Weber, K.J., Catchpole, K., Stocks, M. and Blakers, A.W., 1997. Lift-Off of Silicon Epitaxial Layers for Solar Cell Applications. *Proc. 26th IEEE Photovoltaic Specialists Conf.*, Anaheim, p. 474.

[122] Catchpole, K.R., McCann, M.J., Weber, K.J. and Blakers, A.W., 2001. A Review of Thin-Film Crystalline Silicon for Solar Cell Applications. Part 2: Foreign Substrates. *Sol. Energy Mater. Sol. Cells*, Vol. 68, pp. 173–215.

[123] Angermeier, D., Monna, R., Slaoui, A., Muller, J.C,. Tool, C.J., Roosmalen, J.A., Acosta, S. and Ayral, A., 1997. Analysis of Silicon Thin Films on Dissimilar Substrates Deposited By RTCVD For Photovoltaic Application. *Proc. 14th European Photovoltaic Solar Energy Conf.*, Barcelona, p. 1452.

[124] Slaoui, A., Monna, R., Angermeier, D., Bourdias, S. and Muller, J.C., 1997. Polycrystalline Silicon Films on Foreign Substrates By a Rapid Thermal-CVD Technique. *Proc. 26th IEEE Photovoltaic Specialist Conf.*, Anaheim, p. 627.

[125] Bourdais, S., Monna, R., Angermeier, D., Slaoui, A., Rauf, N., Laugier, A., Mazel, F., Jorand, Y. and Fantozzi, G., 1998. Combination of RT-CVD and LPE for Thin Silicon-Film Formation on Alumina Substrates. *Proc. 2nd World Conf. on Photovoltaic Solar Energy Conversion*, Vienna, pp. 1774–1777.

[126] Beaucarne, G., Hebling, C., Scheer, R. and Poortmans, J., 1998. Thin Silicon Solar Cells Based on Re-Crystallized Layers on Insulating Substrates. *Proc. 2nd World Conf. on Photovoltaic Solar Energy Conversion*, Vienna, p. 1794.

[127] Beaucarne, G., Poortmans, J., Caymax, M., Nijs, J. and Mertens, R., 1997. CVD-Growth of Crystalline Si on Amorphous or Microcrystalline Substrates. *Proc. 14th European Photovoltaic Solar Energy Conf.*, Barcelona, p. 1007.

[128] Takahashi, T., Shimokawa, R., Matsumoto, Y., Ishii, K. and Sekigawa, T., 1997. *Sol. Energy Mater. Sol. Cells*, Vol. 48, p. 327.

[129] Shimokawa, R., Ishii, K., Nishikawa, H., Takahashi, T., Hayashi, Y., Saito, I., Nagamine, F. and Igari, S., 1994. *Sol. Energy Mater. Sol. Cells*, Vol. 34, p. 277.

[130] Nell, M.E., Braun, A., von Ehrenwell, B., Schmidt, C. and Elstner, L., 1999. Solar Cells From Thin Silicon Layers on Al_2O_3. *Tech. Digest Int. PVSEC-11*, Sapporo, p. 749–750.

[131] Angermeier, D., Monna, R., Bourdais, S., Slaoui, A., Muller, J.C., Beaucarne, G. and Poortmans, J., 1998. Thin Polysilicon Films on Mullite Substrates For Photovoltaic Cell Application. *Proc. 2nd World Conf. on Photovoltaic Solar Energy Conversion*, Vienna, p. 1778.

[132] Gutjahr, A., Silier, I., Cristiani, G., Konuma, M., Banhart, F., Schöllkopf, V. and Frey, H., 1997. Silicon Solar Cell Structure Grown By Liquid Epitaxy on Glass Carbon. *Proc. 14th European Photovoltaic Solar Energy Conf.*, Barcelona, p. 1460.

[133] Pauli, M., Reindl, T., Krühler, W., Homberg, F. and Müller, J., 1996. *Sol. Energy Mater. Sol. Cells*, Vol. 41/42, p. 119.

[134] Ludemann, R., Schaefer, S., Schule, C. and Hebling, C., 1997. Dry processing of mc-Silicon Thin-Film Solar Cells on Foreign Substrates Leading to 11% Efficiency. *Proc. 26th IEEE Photovoltaic Specialists Conf.*, Anaheim, p. 159.

[135] Mishima, T., Kitagawa, Y., Ito, S. and Yokoyama, T., 1998. Polycrystalline Silicon Films For Solar Cells By Liquid Phase Epitaxy. *Proc. 2nd World Conf. on Photovoltaic Solar Energy Conversion*, Vienna, p. 1724.

[136] Ito, S., Kitagawa, Y., Mishima, T. and Yokoyama, T., 1999. Direct-Grown Polycrystalline Si Film On Carbon Substrate By LPE. *Tech. Digest Int. PVSEC-11*, Sapporo, pp. 539–540.

[137] Monna, R., Angermeier, D., Slaoui, A., Muller, J.C., Beaucarne, G., Poortmans, J. and Hebling, C., 1997. Poly-Si Thin Films on Graphite Substrates By Rapid Thermal Chemical Vapor Deposition For Photovoltaic Application. *Proc. 14th European Photovoltaic Solar Energy Conf.*, Barcelona, p. 1456.

[138] Campe, H.V., Nikl, D., Schmidt, W. and Schomann, F., 1995. Crystalline Silicon Thin Film Solar Cells. *Proc. 13th European Photovoltaic Solar Energy Conf.*, Nice, p. 1489.

[139] Kunze, T., Hauttmann, S., Kramp, S. and Muller, J., 1997. Thin Recrystallized Silicon Seed Layers on Graphite Substrates. *Proc. 14th European Photovoltaic Solar Energy Conf.*, Barcelona, p. 1407.

[140] Schiermeier, S.E., Tool, C.J., van Roosmalen, J.A., Laas, L.J., von Keitz, A. and Sinke, W.C., 1998. LPE-Growth of Crystalline Silicon Layers on Ceramic Substrates. *Proc. 2nd World Conf. on Photovoltaic Solar Energy Conversion*, Vienna, p. 1673.

[141] Shi, A., Young, T.L., Zheng, G.F. and Green, M.A., 1993. *Sol. Energy Mater. Sol. Cells*, Vol. 31, p. 51.

[142] Shi, Z.,Young, T.L. and Green, M.A.., 1994. Solution Growth of Polycrystalline Silicon on Glass at Low Temperatures. *Proc. 1st World Conf. on Photovoltaic Energy Conversion*, Hawaii, p. 1579.

[143] Bergmann, R.B., Brendel, B., Wolf, M., Lölgen, P. and Werner, J.H., 1998. High Rate, Low Temperature Deposition of Crystalline Silicon Film Solar Cells on Glass. *Proc. 2nd World Conf. on Photovoltaic Solar Energy Conversion*, Vienna, pp. 1260–1265.

[144] Brendel, R., Bergmann, R.B., Fischer, B., Krinke, J., Plieninger, R., Rau, U., Reib, J., Strunk, H.P., Wanka, H. and Werner, J.H., 1997. Transport

Analysis For Polycrystalline Silicon Solar Cells on Glass Substrates. *Proc. 26th Photovoltaic Solar Conf.*, Anaheim, p. 635.

[145] DelleDonne, E., Ingram, A., Jonczyk, R., Yaskoff, J., Sims, P., Rand, J. and Barnett, A., 2002. Thin Silicon-on-Ceramic Solar Cells. *Proc. 29th IEEE Photovoltaic Specialists Conf.*, New Orleans, p. 82.

[146] McCann, M.J., Catchpole, K.R., Weber, K.J. and Blakers, A.W., 2001. A Review of Thin-Film Crystalline Silicon for Solar Cell Applications. Part 1: Native Substrates. *Sol. Energy Mater. Sol. Cells*, Vol. 68, pp. 135–171.

[147] Blakers, A.W., Weber, K.J., Stuckings, M.F., Armand, S., Matlakowski, G., Stocks, M.J. and Cuevas, A., 1995. 18% Efficient Thin Silicon Solar Cell By Liquid Phase Epitaxy. *Proc. 13th European Photovoltaic Solar Energy Conf.*, Nice, p. 33.

[148] Zheng, G.F., Wenham, S.R. and Green, M.A., 1996. *Prog. Photovoltaics*, Vol. 4, p. 369.

[149] Faller, F.R., Henninger, V., Hurrle, A. and Schillinger, N., 1998. Optimization of the CVD Process For Low-Cost Crystalline-Silicon Thin-Film Solar Cells. *Proc. 2nd World Conf. on Photovoltaic Solar Energy Conversion*, Vienna, p. 1278.

[150] Werner, J.H., Arch, J.K., Brendel, R., Langguth, G., Konuma, M., Bauser, E., Wagner, G., Steiner, B. and Appel, W., 1994. Crystalline Thin Film Silicon Solar Cells. *Proc. 12th European Photovoltaic Solar Energy Conf.*, Amsterdam, pp. 1823–1826.

[151] Blakers, A.W., Weber, K.J., Stuckings, M.F., Armand, S., Matlakowski, G., Carr, A.J., Stocks, M.J., Cuevas, A. and Brammer, T., 1995. *Prog. Photovoltaics*, Vol. 3, p. 193.

[152] Zheng, G.F., Zhang, W., Shi, Z., Gross, M., Sproul, A.B., Wenham, S.R. and Green, M.A., 1996. *Sol. Energy Mater. Sol. Cells*, Vol. 40, p. 231.

[153] Campe, H.V., Nikl, D., Schmidt, W. and Schomann, F., 1995. Crystalline Silicon Thin Film Solar Cells. *Proc. 13th European Photovoltaic Solar Energy Conf.*, Nice, p. 1489.

[154] Evrard, O., Demesmaeker, E., Vermeulen, T., Zagrebnov, M., Caymax, M., Laureys, W., Poortmans, J., Nijs, J. and Mertens, R., 1995. The Analysis of the Limiting Recombination Mechanisms on High Efficiency Thin Film Cells Grown With CVD Epitaxy. *Proc. 13th European Photovoltaic Solar Energy Conf.*, Nice, p. 440.

[155] Werner, J.H., Kolodinski, S., Rau, U., Arch, J.K. and Bauser, E., 1993. *Appl. Phys. Lett.*, Vol. 62, p. 2998.

[156] Wang, W., Zhao, Y., Xu, Y., Luo, X., Yu, M. and Yu, Y., 1998. The Polycrystalline Silicon Thin Film Solar Cells Deposited on SiO_2 and Si_3N_4 by RTCVD. *Proc. 2nd World Conf. on Photovoltaic Solar Energy Conversion*, Vienna, p. 1740.

[157] Ballhorn, G., Weber, K.J., Armand, S., Stocks, M.J. and Blakers, A.W., 1997. High Efficiency Thin Multicrystalline Silicon Solar Cells By Liquid Phase Epitaxy. *Proc. 14th European Photovoltaic Solar Energy Conf.*, Barcelona, p. 1011.

[158] Vermeulen, T., Poortmans, J., Caymax, M., Nijs, J., Mertens, R. and Vinckier, C., 1997. The Role of Hydrogen Passivation in 20 μm Thin-Film Solar Cells on p^+ Multicrystalline-Si Substrates. *Proc. 14th European Photovoltaic Solar Energy Conf.*, Barcelona, p. 728.

[159] Vermeulen, T., Deurinckx, F., DeClercq, K., Szlufcik, J., Poortmans, J., Laermans, P., Caymax, M., Nijs, J. and Mertens, R., 1997. Cost-Effective Thin Film Solar Cell Processing on Multicrystalline Silicon. *Proc. 26th IEEE Photovoltaic Specialists Conf.*, Anaheim, p. 267.

[160] Vermeulen, T., Evrard, O., Laureys, W., Poortmans, J., Caymax, M., Nijs, J., Mertens, R., Vinckier, C. and Hofs, H.-U., 1995. Realization of Thin Film Solar Cells in Epitaxial Layers Grown on Highly Doped RGS-Ribbons. *Proc. 13th European Photovoltaic Solar Energy Conf.*, Nice, p. 1501.

[161] Faller, F.R., Schillinger, N., Hurrle, A. and Schetter, C., 1997. Improvement and Characterization of Mi-Si Thin-Film Solar Cells on Low Cost SSP Ribbons. *Proc. 14th European Photovoltaic Solar Energy Conf.*, Barcelona, p. 784.

[162] Vermeulen, T., Poortmans, J., Said, K., Evrard, O., Laureys, W., Caymax, M., Nijs, J., Mertens, R. and Vinckier, C., 1996. Interaction between Bulk and Surface Passivation Mechanisms in Thin Film Solar Cells on Defected Silicon Substrates. *Proc. 25th IEEE Photovoltaic Specialists Conf.*, Washington, DC, p. 653.

[163] Thomas, B., Muller, G., Heidborn, P. and Wartra, H., 1997. Growth of Polycrystalline Silicon Thin Films Using the Temperature Difference Method. *Proc. 14th European Photovoltaic Solar Energy Conf.*, Barcelona, p. 1483.

[164] Wang, T.H., Ciszek, T.F., Schwerdtfeger, C.R., Moutinho, H. and Matson, R., 1996. *Sol. Energy Mater. Sol. Cells*, Vol. 41–42, p. 19.

[165] Ciszek, T.F. and Gee, J.M., 1997. Crystalline Silicon R&D at the US National Center for Photovoltaics. *Proc. 14th European Photovoltaic Solar Energy Conf.*, Barcelona, p. 53.

[166] Ishihara, T., Arimoto, S., Kumabe, H., Murotani, T., 1995. *Progr. Photovoltaics*, Vol. 3, p. 105.

[167] Zimmerman, W., Bau, S., Haas, F., Schmidt, K. and Eyer, A., 1998. Silicon Sheets From Powder as Low Cost Substrates For Crystalline Silicon Thin Film Solar Cells. *Proc. 2nd World Conf. on Photovoltaic Solar Energy Conversion*, Vienna, p. 1790.

[168] Beaucarne, G., Hebling, C., Scheer, R. and Poortmans, J., 1998. Thin Silicon Solar Cells Based on Recrystallized Layers on Insulating Substrates. *Proc. 2nd World Conf. on Photovoltaic Solar Energy Conversion*, Vienna, p. 1794.

[169] Hebling, C., Gaffke, R., Lanyi, P., Lautenschlager, H., Schetter, C., Wagner, B. and Lutz, F., 1996. Recrystallized Silicon on SiO_2-Layers for Thin-Film Solar Cells. *Proc. 25th IEEE Photovoltaic Specialists Conf.*, Washington, DC, p. 649.

[170] van Zutphen, A.J., Zeman, M., Tichelaar, F.D. and Metselaar, J.W., 1997. Deposition of Thin Film Silicon By Thermal CVD Processes For

IIb-4

Characterisation and Diagnosis of Silicon Wafers and Devices

Andrés Cuevas, Faculty of Engineering and IT,
Australian National University, Canberra, Australia
Ronald A. Sinton, Sinton Consulting Inc.,
Boulder, Colorado, USA

1 Introduction

Monitoring the fabrication process of a solar cell entails a number of different measurements, including mechanical, optical and electronic properties. This chapter focuses on the latter, the most important of which are described both for the silicon wafers and for solar cell precursors and finished devices. Emphasis is placed on measurements of the minority carrier lifetime and their interpretation to extract relevant information about the properties of the silicon material, the surface passivation and the emitter diffusions. The correlation between the effective lifetime measured at the various stages of fabrication and the final device characteristics is discussed. Direct measurements of the open-circuit voltage under variable illumination conditions are shown to provide most of the parameters needed by the process engineer to assess the ultimate potential efficiency of the solar cells, including diode saturation currents and ideality factors, shunting resistance, intrinsic fill factor and pseudo conversion efficiency (that is, excluding series resistance losses). These Illumination–V_{oc} techniques can be applied before the final cell metallisation, at steps back into the process as far as the junction formation, which makes them very attractive for process control and optimisation. The electrical characterisation of the finished devices is a necessary requirement in solar cell production, and the standard methods to measure the one-sun I–V curves are covered in Chapter IV-1.

2 Measurement of the Bulk Lifetime and Surface Passivation of Silicon Wafers

Once created within a semiconductor, photogenerated electrons and holes last, on average, a finite time called the *lifetime*. When carriers are continuously generated, as in a solar cell, the value of the lifetime determines the stable population of electrons and holes. This population should desirably be as high as possible because it determines the voltage produced by the device. A second, equally important aspect of the lifetime is that it is directly related to the *diffusion length*, which is the average distance that carriers can travel from the point of generation to the point of collection (the p–n junction). The relationship between L and τ is $L_n = \sqrt{D_n \tau_n}$, with a value for the diffusion coefficient of $D_n = 27\ \text{cm}^2/\text{s}$, for electrons (minority carriers) in 1 Ω cm p-type silicon. The diffusion length should be greater than the wafer thickness or the longest generation depth to ensure a high photogenerated current. Since the lifetime determines both the voltage and the current of the device, its characterization is of the utmost importance.

2.1 Lifetime Testing Methods

There are three basic approaches to measure the lifetime, depending on the way that an excess of carriers is created in the semiconductor. In the *transient decay method*, a photogeneration is terminated abruptly and the rate at which carriers disappear, dn/dt, is measured, together with the excess electron concentration,

Δn, itself (note that every photon generates one electron-hole pair, so that $\Delta n = \Delta p$). If no current is flowing from the device, then the rate of carrier density change is equal to the recombination rate:

$$\frac{d(\Delta n)}{dt} = -\frac{\Delta n}{\tau_{eff}} \tag{1}$$

This equation implies an exponential decay of the carrier density with time, which means that 37% of electrons are still present after one lifetime, decreasing to 5% after 3 lifetimes. This method, classically known as *Photoconductance decay*, or *PCD* [1], is quite robust, because it is based on the measurement of the relative change of Δn with time. It is, nevertheless, advisable to measure the absolute value of Δn at which the lifetime has been determined, since the lifetime is, in general, strongly dependent on the carrier injection level.

In the *steady-state method* [2] a constant generation rate of known value is maintained, and the effective lifetime (to be discussed more fully below and in Section 2.4) is determined from the balance between generation and recombination:

$$G = \frac{\Delta n}{\tau_{eff}} \tag{2}$$

This simple expression assumes a uniform generation rate across the thickness of the sample and also a uniform excess carrier density, Δn. Nevertheless, in cases where they may be non-uniform, Equation (2) is still applicable, with Δn representing an average value.

If the illumination varies slowly, quasi-steady-state conditions prevail within the semiconductor, leading to the *quasi-steady-state photoconductance method*, or *QSSPC* [3]:

$$\tau_{eff} = \frac{\Delta n(t)}{G(t) - \frac{\partial \Delta n}{\partial t}} \tag{3}$$

An absolute measurement of the excess carrier density, Δn, is required to determine the lifetime in the *steady-state* and *QSSPC* methods. In addition, the generation rate needs to be determined accurately as well. The latter is measured using a photodetector (for example a calibrated solar cell). The detector gives the total photon flux incident on the surface of the wafer. For the standard solar spectrum the number of photons per second and cm^2 with energy greater than the bandgap of silicon, 1.12 eV is $N_{ph} = 2.7 \times 10^{17}$ cm^{-2} s^{-1}. This flux is commonly referred to as *one sun* intensity and it gives, multiplied by the electronic charge, the upper limit of the current density for a silicon solar cell, 43.25 mA cm^{-2}. Silicon wafers absorb only a fraction of these photons, depending on the reflectivity of the front and back surfaces, possible faceting of those surfaces, and the thickness of the wafer. The value of the absorption fraction for a polished, bare silicon wafer is $f_{abs} \approx 0.6$. If the wafer has an

optimised antireflection coating, such as a 70 nm thick silicon nitride or titanium oxide layer, $f_{abs} \approx 0.9$, while a textured wafer with antireflection coating can approach $f_{abs} \approx 1$. The uncertainties associated with the determination of f_{abs} can be kept very small by using tables or graphs that can be calculated using optical models. The generation rate per unit volume G can then be evaluated from the incident photon flux and the wafer thickness:

$$G = \frac{N_{ph} f_{abs}}{W} \tag{4}$$

One of the strengths of the *QSSPC* method is the ease with which the carrier injection level can be scanned to give a full picture of recombination processes within the semiconductor. A steady-state condition can be maintained as long as the time constant for the changing illumination is long compared to the effective carrier lifetime being measured. Using flashlamps and attenuating filters, a range of illumination intensities from 10^{-5} to 1000 suns can be investigated without significant heating of the wafers. Some PCD methods, such as microwave PCD (μ-PCD), use a small signal excitation. For these methods, a scan of carrier injection level can be implemented by taking measurements at several different levels of steady-state bias light.

Note that the lifetime in Equations (1)–(3) has been labelled τ_{eff} to indicate that it is an effective parameter that may encompass several different recombination and transport mechanisms. It is, nevertheless, possible to discriminate between these various mechanisms, as discussed in the following sections. For all three testing methods, the excess electron concentration, Δn, needs to be measured. There are several techniques to do this based on different properties of semiconductor materials. The simplest and most common of them is to measure the conductance of the wafer and the way it changes with illumination and time. The excess photoconductance for a wafer of thickness W is given by

$$\Delta\sigma_L = qW(\mu_n + \mu_p)\Delta n \tag{5}$$

Typical mobility values for 1 Ω cm silicon in low injection are $\mu_n = 1100$ cm^2 V^{-1} s^{-1} for electrons and $\mu_p = 400$ cm^2 V^{-1} s^{-1} for holes. The electron and hole mobilities are functions of the dopant density and injection level.

The most straightforward apparatus to measure the photoconductance is based on applying electrical contacts to the silicon (typically an ingot or a wafer), forcing a flow of current through it and measuring the resulting voltage drop [4]. This can also be done in a contactless fashion by using an inductor that forms part of a radio-frequency circuit; this circuit produces a voltage that is proportional to the conductivity of the wafer, with the added advantage that the relationship between conductance and voltage is practically linear over a broad range [5]. The microwave-detected photoconductance decay systems are based on directing a microwave beam to the silicon wafer and measuring the reflected microwave power, which is proportional to the conductance of the wafer [6, 7]. The excess carrier density can also be directly determined by probing the sample

with infrared light and measuring the amount of free-carrier absorption [8, 9], or using an infrared camera to visualize the free-carrier infrared (IR) absorption for the entire wafer with a fine resolution [10]. Schroder [11] gives a comprehensive description of these methods, their theoretical background and practical implementation. Additional methods, also described in [11], such as the surface photovoltage (SPV) and the short-circuit current response, measure the minority carrier diffusion length. Both rely on the formation of a surface space charge region to collect minority carriers. The SPV approach achieves this by chemically treating the surface so that a surface charge is created that forms the space charge region. A transparent contact is used to measure the voltage associated with the collection of carriers by the space charge region. The latter is usually in the mV range to maintain linearity and simplify the analysis. When a real junction exists, as in a finished solar cell, it is preferable to measure the spectral response of the short-circuit current, an analysis of which can give information on the bulk diffusion length, surface recombination velocity and optical light trapping [12]. The formation of a liquid electrolyte-semiconductor junction that allows the extraction of the short-circuit current is also possible, and constitutes the basis for the Elymat technique [11]. Different applications of the above techniques are also described in a collection of papers published by the ASTM [13].

Depending on the specific details of their practical implementation, in particular the magnitude of the excitation used, lifetime testing methods can be broken down into two categories, large-signal and small signal methods. Many commercial systems, such as the microwave-PCD, use a modulated laser beam to create a relatively small number of carriers in the semiconductor. The resulting small signal is then separated from a background illumination provided by a bias light (and background noise) using electronic amplification and lock-in techniques. It should be kept in mind that the result of such measurement is, in general, different from the true recombination lifetime. Converting the small-signal lifetime into the actual lifetime requires measuring the former as a function of injection level, followed by integration [14, 15].

2.2 Variability of the Carrier Lifetime

The lifetime should not be assumed to be a constant, single value. It can vary considerably depending on the process history of the sample (including possible contamination and thermal degradation), measurement conditions (injection level and temperature), and it can degrade or recover when the sample is exposed to light or annealed at certain temperatures. The measured, apparent lifetime can also be affected by non-recombination mechanisms, such as carrier trapping. Figure 1 shows, as an example of variability, the lifetime measured over a broad range of carrier density injection levels for two FZ silicon wafers, one of which was purposely contaminated with iron. The behaviour of the lifetime can be understood in most cases with the assistance of the theoretical models that describe the most important physical mechanisms. It should be kept in mind that the measured lifetime, τ_{eff}, may include several of them simultaneously.

In practical silicon wafers, the most important recombination losses occur through crystallographic defects and impurities that create energy levels within the band gap. The effect of such recombination centres can be described by the Shockley–Read–Hall model, which predicts that the injection-level dependence of the lifetime, τ_{SRH}, is a function of the dopant density, N_A, recombination centre density N_{SRH}, defect energy level E_T and capture cross-sections:

$$\frac{1}{\tau_{SRH}} = \frac{N_A + \Delta n}{\tau_{p0}(n_1 + \Delta n) + \tau_{n0}(N_A + p_1 + \Delta n)} \tag{6}$$

In this expression, which applies to p-Si, $\Delta n = \Delta p$ is the excess carrier density (assuming negligible trapping), and τ_{n0} and τ_{p0} are the fundamental electron and hole lifetimes, which are related to the recombination centre density, the thermal velocity $v_{th} = 1.1 \times 10^7$ cm s^{-1}, and the capture cross-sections via $\tau_{n0} = 1/(v_{th}\sigma_n N_{SRH})$ and $\tau_{p0} = 1/(v_{th}\sigma_p N_{SRH})$. The magnitudes n_1 and p_1 are given by:

$$n_1 = \mathcal{N}_c \exp\left(\frac{E_T - E_C}{k_B T}\right) \qquad p_1 = \mathcal{N}_v \exp\left(\frac{E_C - E_G - E_T}{k_B T}\right) \tag{7}$$

The values for the effective densities of states at the conduction and valence band edges are $\mathcal{N}_c = 2.86 \times 10^{19}$ and $\mathcal{N}_v = 3.10 \times 10^{19}$ cm^{-3}. For recombination centres located near the middle of the energy gap, Equation (6), predicts an increased lifetime between very low and very high injection level from τ_{no} to $\tau_{no} + \tau_{po}$. Nevertheless, every recombination centre is characterised by a distinctive set of parameters E_T, τ_{n0} and τ_{p0}. This leads to different injection and temperature dependences of the lifetime, and can be used to identify the characteristic signature of each centre. The diversity of possible lifetime curves and the determination of E_T, τ_{n0} and τ_{p0} based on the injection level or temperature dependence of the lifetime are reviewed in [16]. Figure 1, which is part an injection-level study for the case of iron–boron pairs in silicon [17], shows a good fit of Equation (6) to the experimental data. The light-soaked results show a widely varying lifetime in the low-injection range of interest for solar cells.

The upper limit to lifetime that may be measured for an otherwise perfect silicon sample is determined by two intrinsic mechanisms, Coulomb-enhanced Auger and band to band recombination, with Auger being the most important of the two. Simple empirical expressions for the intrinsic lifetime for p-type and n-type silicon have recently been proposed [18]:

$$\frac{1}{\tau_{intrinsic}} = (\Delta n + N_A)\left(6 \times 10^{-25} N_A^{0.65} + 3 \times 10^{-27} \Delta n^{0.8} + 9.5 \times 10^{-15}\right) \tag{8}$$

$$\frac{1}{\tau_{intrinsic}} = (\Delta p + N_D)\left(1.8 \times 10^{-24} N_D^{0.65} + 3 \times 10^{-27} \Delta p^{0.8} + 9.5 \times 10^{-15}\right) \tag{9}$$

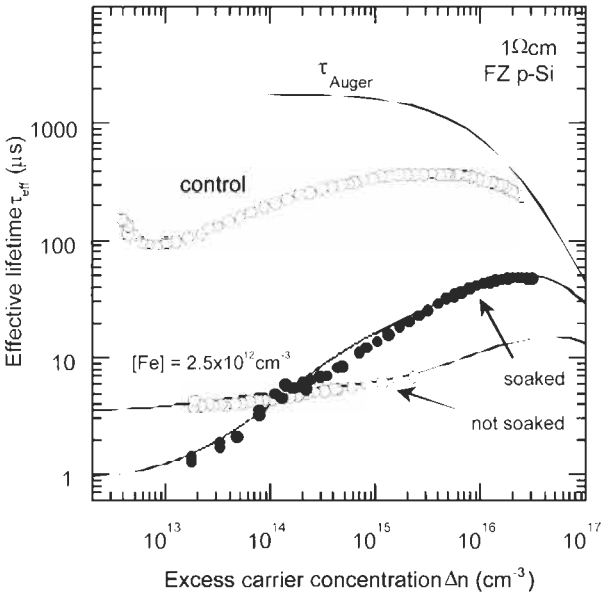

Figure 1 Measured effective carrier lifetime τ_{eff} as a function of the excess carrier concentration Δn for a 1 Ω cm boron-doped FZ silicon wafer contaminated with iron before and after light soaking. An uncontaminated control wafer is also shown. Both had the surfaces passivated with PECVD SiN.

For perspective, Equation (8) is plotted in Figure 1 for a 1 Ω cm boron-doped wafer. The intrinsic (Auger) lifetime is quite high, and will only impact very high efficiency or concentrator solar cells. However, it has a strong dependence on carrier density at high injection and should therefore be taken into account when using injection level dependence techniques to characterize and separate recombination mechanisms, as described in this section and those that follow.

2.3 Lifetime Instabilities

For p-type silicon solar cells, an important type of instability of the lifetime is a degradation induced by light. Two cases of such degradation have been documented extensively and are given here as examples: one is due to the presence of iron, the other to oxygen, both forming complexes or pairs with boron. While iron is avoidable, oxygen is innate to CZ grown silicon (except advanced CZ methods using magnetic confinement of the melt), which typically has an oxygen concentration in the vicinity of 7×10^{17} cm^{-3}. The effect only occurs when both boron and oxygen are present, and is more severe the higher the concentration of both is [19]. The conversion efficiency of 1 Ωcm CZ silicon cells has been reported to degrade by 4% relative after about 50 hours one sun illumination, while for 0.45 Ω cm the degradation is greater (about 7.5%) and for 10 Ω cm it is lower (1% or less). The lifetime of typical 1 Ω cm boron doped silicon degrades by more than a factor of ten after 5 hours exposure to one sun illumination, approaching a final lifetime of 10–20 μs [20].

Similar levels of efficiency degradation of 3–4% relative (about 0.5% absolute) after 30 minutes one-sun illumination have been attributed to the presence of iron [21]. In effect, iron is a well known lifetime killer and the change in lifetime upon exposure is an established method to determine its concentration in silicon. There are significant differences between Fe and Fe–B pairs and B–O complexes. (1) In the case of Fe, an anneal at 210°C degrades the lifetime (in much the same way as illumination) [22]. In the case of B–O complexes, the lifetime recovers after annealing at moderate temperatures. (2) The shape of the injection level dependent lifetime curve changes differently: the curves before and after degradation cross over in the case of Fe and Fe–B (see Figure 1), while they remain approximately parallel in the case of B–O. (3) An additional differentiating feature is that the lifetime of Fe contaminated silicon recovers after long-term storage in the dark.

2.4 Surface Component of the Effective Lifetime

The ability to separate out the different recombination mechanisms and identify where the major losses occur within the solar cell device is an essential part of the characterisation and diagnosis process. It is useful to express mathematically that the *effective lifetime*, τ_{eff}, is the net result of summing up all the recombination losses that occur within the different regions that constitute a given silicon wafer or a solar cell. The surfaces frequently have a significant impact on the measured effective lifetime. This is represented by the *surface recombination velocities*, S_{front} and S_{back}, at the front and back sides of the wafer as:

$$\frac{1}{\tau_{\text{eff}}} - \frac{1}{\tau_{\text{intrinsic}}} = \frac{1}{\tau_{\text{SRH}}} + \frac{S_{front} + S_{back}}{W} \tag{10}$$

where W, as in Section 2.3, is the thickness of the wafer. Surface recombination is commonly attributed to Shockley–Read–Hall processes and can, therefore be expected to vary with the carrier injection level, in much the same way as the bulk lifetime [23]. In addition, when a dielectric layer is used to passivate the surface, a space charge region may form. This effect has been documented for silicon dioxide [24] and SiN [25]. Since similar injection level dependencies can be due to either surface or bulk recombination, their separation is not trivial. The preferred method, applicable to both steady-state and transient methods, involves the preparation of several wafers with different thicknesses and identical bulk and surface properties [11]. Alternatively, by using wafers with a very high bulk lifetime, an upper bound for S can be determined by assuming $\tau_{SRH} = \infty$ in Equation (10).

Equation (10) is a simplified expression, and would predict a zero effective lifetime when the surface recombination velocity is very high. In reality there is a limit on how low the effective lifetime can be because electrons and holes have to travel towards the surfaces by diffusion in order to recombine, which is a relatively slow mechanism. It can be calculated that, for uniform steady-state photogeneration (produced by infrared light) or for a transient decay

measurement, the minimum effective lifetime is, respectively, given by the following expressions:

$$\tau_{\text{eff}(S=\infty)QSSPC} = \frac{W^2}{12D_n} \qquad \tau_{\text{eff}(S=\infty)PCD} = \frac{W^2}{\pi^2 D_n} \tag{11}$$

For a typical p-type 0.03 cm thick wafer and a diffusion coefficient for electrons $D_n = 27\ \text{cm}^2\ \text{s}^{-1}$, the lifetime that can be expected for a non-passivated surface is $\tau_{eff} = 2.8\ \mu\text{s}$ (3.4 μs for a transient decay measurement). Note that the steady-state surface-limited lifetime can be even lower if the source of light is not infrared, because the electrons that are photogenerated by short-wavelength light are very close to the surface and diffuse to it almost instantaneously.

The dependence of the measured effective lifetime on the surface recombination velocity is shown in Figure 2 for the example of a 300 μm thick, 1 Ω cm p-type wafer and four different values of the bulk lifetime. The graph indicates the lifetime that would be measured for this wafer with either 400 nm or 1000 nm light using a steady-state photoconductance method. The curves were calculated for minority-carrier densities in low injection conditions using PC1D computer simulation [26]. Transient methods, such as μ-PCD, will determine the lifetime approximately as shown by the 1000 nm curves, except that in the limit of high surface recombination the difference between the measured effective lifetime and the actual bulk lifetime is reduced by 22%, as follows from Equation (11). Note that the diffusion limitation on the measurable lifetime varies quadratically with the wafer thickness. Several main features can be identified on this plot.

1 The measured effective lifetime is equivalent to the actual bulk lifetime if the surfaces are well passivated, independent of the wavelength of illumination (lower part of Figure 2). The demands on surface passivation can, nevertheless, be relaxed when determining relatively low bulk lifetimes. For example, for 0.1 μs bulk lifetime surface recombination velocities up to 1000 cm/s can be tolerated. On the other hand, to accurately determining high bulk lifetimes requires very good passivation. For example, the surface recombination velocity should be less than 10 cm/s to determine $\tau_{\text{bulk}} > 100\ \mu\text{s}$.

2. If the surface recombination velocity is greater than 10^5 cm/s, typical of unpassivated silicon wafers, infrared light (for example 1000 nm) measurements are more indicative of the bulk lifetime. The sensitivity to τ_{bulk} is excellent if the latter is lower than 2 μs, and a one-to-one correspondence can be made between the IR measured effective lifetime and the actual bulk lifetime. The sensitivity is still reasonable to resolve bulk lifetimes up to 10 μs, but is poor for higher lifetimes. Importantly, however, a pass-fail test for τ_{bulk} up to 10 μs can be established for bare, unpassivated wafers by using infrared light. For example, a measured lifetime of 2 μs indicates an actual bulk lifetime greater than 10 μs.

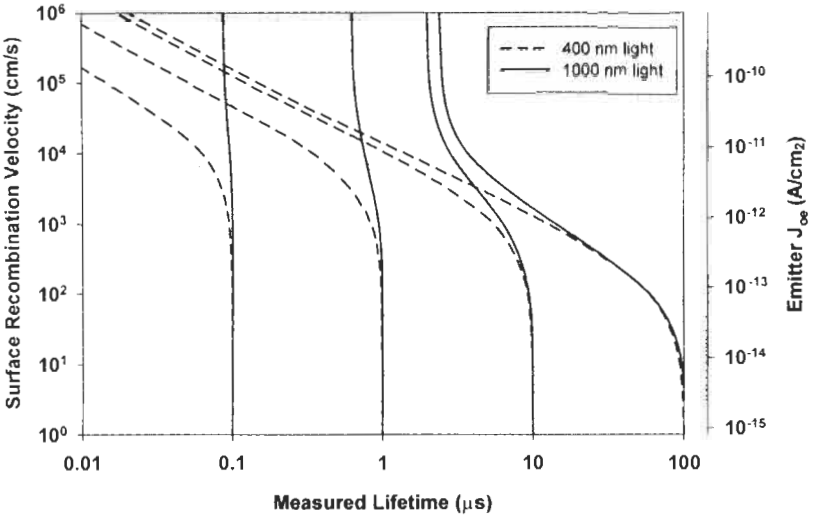

Figure 2 Effective lifetime for a 300 μm, 1 Ω cm p-type wafer as a function of the surface recombination velocity. The curves, modelled with PC1D for steady-state conditions, correspond to wafers with 0.1, 1, 10 and 100 μs bulk lifetimes. Two sets of curves are shown, for 400 nm and 1000 nm, monochromatic illumination, respectively.

3. When the surface recombination velocity is greater than 1000 cm/s (upper portion of Figure 2), the effective lifetime is significantly different for blue and IR light, and this allows the bulk lifetime and the surface recombination velocity to be uniquely determined by measuring with both wavelengths [27]. For example, from Figure 2, a wafer that measures 0.65 μs with 1000 nm light and 0.05 μs with 400 nm light has a bulk lifetime of 1 μs and a surface recombination velocity of 1×10^5 cm/s. This method exploits the fact that the photogeneration from blue light is very sensitive to the front surface recombination velocity, while the IR light penetrates deep into the bulk of the wafer. Note that the higher lifetime range (above 10 μs) cannot be discriminated even using this method, because the relatively high surface recombination velocity (SRV) above 1000 cm/s completely masks bulk recombination.

2.5 Emitter Component of the Effective Lifetime

Dopant-diffused, or *emitter* regions are commonly characterised through a *saturation current density*, J_{oe}. This parameter encompasses recombination within the bulk of the thin diffused region, which normally occurs through the Auger process, as well as the recombination at the heavily doped surface. If both sides of a p-type wafer are diffused, then the effective lifetime can be expressed as:

$$\frac{1}{\tau_{\text{eff}}} - \frac{1}{\tau_{\text{intrinsic}}} = \frac{1}{\tau_{\text{SRH}}} + [J_{\text{oe}(front)} + J_{\text{oe}(back)}]\frac{(N_A + \Delta n)}{qn_i^2 W} \tag{12}$$

In this expression, N_A is the dopant density of the wafer and $J_{oe(front)}$ and $J_{oe(back)}$ are the *saturation current densities* that characterise the front and back emitter regions, respectively. At 25°C, $qn_i^2 = 12\ C\ cm^{-6}$. The fact that the emitter recombination term has a different dependence on the carrier injection level than the bulk and surface recombination terms allows determination of the J_{oe} by examining the injection level dependence of the lifetime, particularly in the high injection regime.

It is straightforward to consider the case when one of the surfaces is diffused (hence characterised by an emitter saturation current) and the other is not (hence characterised by a surface recombination velocity) by combining Equations (10) and (12). In fact, both concepts are equivalent in low injection, $S_{eff} \approx J_o N_A / qn_i^2$. The scale on the right of Figure 2 shows the emitter-saturation current densities that correspond to the surface recombination velocities on the left axis, for a 1 Ω cm wafer. Equations (10) and (12) assume an approximately uniform carrier density across the wafer. The region of applicability of this assumption is visually displayed in Figure 2 as the region where the 400 nm curves and the 1000 nm curves overlap.

Figure 3 shows a family of curves for different values of emitter saturation current density and a bulk doping of $1.5 \times 10^{16}\ cm^{-3}$ (1 Ω cm). The data is plotted as inverse measured lifetime, following the form of Equation (12). This equation indicates that for measurements performed at minority carrier densities above the doping density, the emitter saturation current density will be given by the slope of the line for each curve in Figure 3. The variations in lifetime due to the SRH recombination in the $1/\tau_{bulk}$ term occur primarily at carrier densities

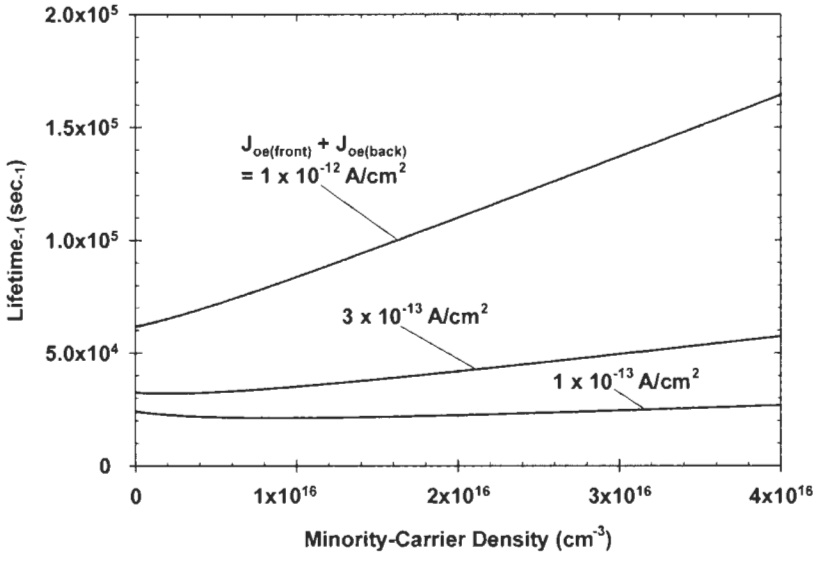

Figure 3 The inverse of the measured lifetime for a 1 Ω cm p-type wafer with three different emitters. Calculation from Equation (12) assuming a low injection lifetime of 50 μs and subtracting out the Auger contribution to the recombination.

less than the doping level, so that they do not significantly affect the slope of the data above the doping level.

There is a limited range for which the use of Equation (12) for extracting J_{oe} is valid. For very high-injection levels, the near-surface recombination due to the doped emitter becomes very high, and the effective lifetime decreases correspondingly. The limit imposed by the finite diffusivity of carriers towards the surface discussed above in Equation (11) applies also to the case of very high J_{oe} (in high injection conditions the ambipolar diffusivity, $D_A \approx 18$ cm^2 s^{-1}, substitutes the minority carrier one, D_n). Because of this, the highest J_{oe} that can be discriminated is, assuming equal front and back diffusions:

$$J_{oe} \ll \frac{6qn_i^2 D_A}{W[N_A + \Delta n]} \approx \frac{1300}{W[N_A + \Delta n]} \tag{13}$$

This indicates that lower substrate doping, thinner wafers, or both can be used to extend the range of J_{oe} values that can be determined and optimise the range of data that can be used. The thinner and more lightly doped the wafer, the wider the range of minority-carrier densities that can be fit to Equation (12).

For optimal measurements of silicon wafers after emitter diffusion, it is advisable to use wavelengths of light longer than 700 nm in order to have a relatively uniform generation within the wafer and minimize the fraction of light absorbed within the emitter. For a detailed discussion of the qualifications for this data analysis for various cell geometries, lifetimes, and J_{oe} values, see references [28, 29]. For wafers with high recombination on one or both surfaces, a measurement strategy can be devised using front illumination, back illumination, IR and blue light to determine the values for recombination at the surfaces and in the bulk [27, 30].

In addition to this analysis for lifetime and emitter saturation current density, an analysis comparing measurement with red and blue monochromatic light can be used in order to specifically characterize the internal quantum efficiency of the heavily-doped emitter region [31].

2.6 Carrier Trapping Effects

Some materials, in particular multicrystalline silicon, show abnormally high photoconductance and apparent lifetime at very low carrier densities. The phenomenon affects both transient-decay and steady-state photoconductance measurements. The conventional analysis of the data results in an apparent *increase* of the effective lifetime τ_{eff} as the carrier injection level *decreases*. The physical reason for this behaviour is, in most cases, the trapping of minority carriers (electrons in p-type material). The semiconductor under illumination has a certain number of excess free electrons Δn and of trapped electrons n_t. Charge neutrality requires that the number of excess holes equals the sum of trapped and free electrons, $\Delta p = \Delta n + n_t$. This results in an anomalously high excess photoconductance, with an extra term due to trapping compared to Equation (5):

$$\sigma_L = q(\mu_n + \mu_p)\Delta n + q\mu_p n_t \tag{14}$$

Therefore, the photoconductance is a poor indicator of the recombination of electron-hole pairs except at high light intensities, when $\Delta n \gg n_t$. This does not affect other lifetime testing methods such as those based on device voltage or current measurements. If the effect of trapping on the photoconductance is properly accounted for, it is frequently possible to accurately determine the lifetime from a photoconductance measurement at all but the lowest minority-carrier densities.

Figure 4 [32] shows data from multicrystalline silicon where the transition from the SRH lifetime, in a range 1–60 μs, shifts up by an order of magnitude or more at the lowest carrier densities. This high apparent lifetime that is approached at low carrier density corresponds to the lifetime for trapped electrons before being released back into the conduction band. This trapping effect has been studied with application of a more detailed model than Equation (14), the Hornbeck–Haynes model [33], to multicrystalline and contaminated FZ silicon [34, 35]. The trapping levels and lifetimes can be separated from the SRH effects in many cases as long as data is taken at very low photoconductance values, to establish the the behavior of the second term in Equation (14). Then the data at moderate carrier densities can be corrected, enabling accurate characterization of the SRH levels. Simple corrections using

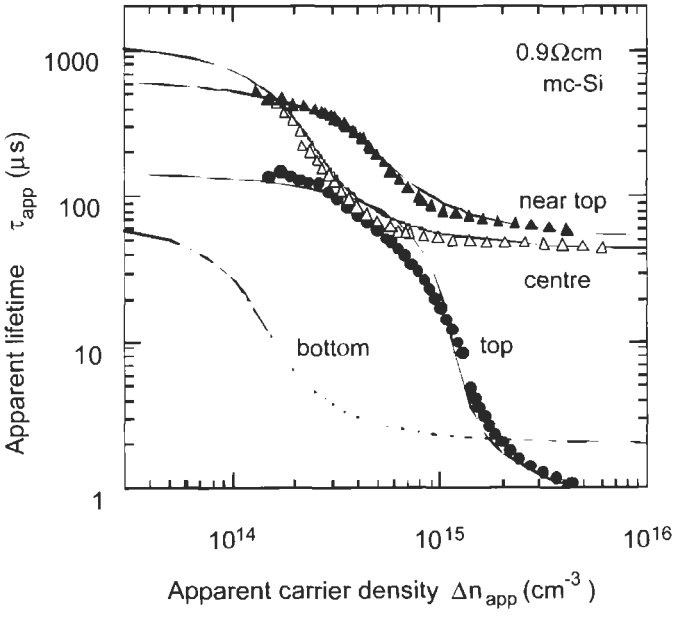

Figure 4 Multicrystalline silicon wafers from different regions of a cast ingot showing trapping effects.

bias light have been compared to the complete model and have been found to be adequate for many practical situations [36]. For some materials, particularly multicrystalline silicon, the trapping can obscure photoconductance data in the carrier-density range corresponding to the operating point for solar cells, generally between 1×10^{13} and 1×10^{15} cm^{-3}. In such cases the voltage characterisation techniques, described in the following section, can give less uncertainty in the lifetime determination.

3 Relationship Between Device Voltage and Carrier Lifetime

The output voltage of a solar cell is determined by the excess minority carrier density at the junction edge of the quasi-neutral base region, defined to be at the plane $x = 0$ in the following expression:

$$\Delta n(0)[N_A + \Delta n(0)] = n_i^2 \exp\left(\frac{V}{k_B T/q}\right) \tag{16}$$

In open-circuit conditions, this minority carrier density is the result of a balance between photogeneration and recombination. The conditions are identical to those of the steady-state method to measure the lifetime, described in Section 2. It is therefore possible to obtain Δn from a photoconductance measurement and determine an implicit, or expected voltage. Complete I–V characteristic curves can be obtained by plotting the implicit voltage as a function of the illumination, expressed in unit of *suns* (1 sun = 1 kW/m^2).

Direct measurements of the voltage are possible as soon as a junction exists in the wafer. By taking data at a range of illumination intensities, *Illumination–*V_{oc} curves can be constructed and analysed to obtain diode saturation currents, ideality factors, shunts and ideal efficiencies [37]. Applications of this are shown in Section 4. A generalised expression to obtain the I–V curves from voltage measurements under quasi-steady-state illumination or during a transient open-circuit decay (OCVD) has also been developed [38]. This formulation extends the validity for accurate measurement to the regime when the light varies at a rate comparable to the minority-carrier lifetime or is extinguished entirely (as in OCVD measurements).

In addition, solving for Δn as a function of voltage and substituting this value in Equations (1), (2) or (3) converts any voltage measurement into a lifetime measurement. Note that these equations for the lifetime use an average carrier density, which in some cases can be substantially lower than the value of $\Delta n(0)$ obtained from the voltage through Equation (16) [30]. Trapping effects have a negligible effect on the measured device voltage, and *Illumination–*V_{oc} data can be used to determine lifetimes at minority carrier densities less than 10^9 cm^{-3}. Note that temperature control, knowledge of the intrinsic carrier density n_i, and the dopant density are necessary to obtain the lifetime from a voltage

measurement, and vice-versa. In contrast, photoconductance lifetime measurements require knowledge of carrier mobilities and are relatively insensitive to temperature.

4 Applications to Process Monitoring and Control of Silicon Solar Cells

Although in-process monitoring of the electronic properties of the silicon wafer using minority-carrier measurements has been extensively used for high-efficiency solar cell optimisation at research laboratories, this has not been true in typical large-scale production of terrestrial cells. Several possible industrial process-control applications are detailed here for single- and multi-crystalline solar cells and illustrated with examples. The main electronic properties that can be measured during the fabrication process of typical commercial silicon solar cells include the resistance, carrier lifetime and device voltage. It is possible to measure the resistance of the substrate, doped layers, and metallisation at each stage in the process. The effective lifetime of minority carriers in the silicon can also be monitored at each stage using photoconductance measurements (these may require metal etching after the metallisation is applied to the cell). Finally, after phosphorus diffusion, measurements can be made of the junction voltage, which is a clear indicator of device performance.

4.1 Resistance Measurements

The resistivity of the silicon bulk material can be measured at the ingot or wafer levels using contacting or non-contacting arrangements [11]. Knowledge of the resistivity and, subsequently, the net doping density, is very important in the optimisation of the fabrication process and the interpretation of solar cell performance, since both the voltage and the current depend on it. The lifetime and diffusion length are also correlated to the resistivity of the substrate, with lower resistivities usually being accompanied by lower lifetimes. A higher resistivity, on the other hand, makes the device more dependent on the quality of the surfaces.

The sheet resistance of the emitter (usually phosphorus) diffusion is another essential control parameter. It is correlated to the dopant density profile, which determines the emitter saturation current density, the emitter quantum efficiency, the contact resistance properties, and the tolerance to shunt formation during firing. The sheet resistance can be measured by the 4-point-probe method [11], or by contactless inductive coupling [5] if the wafer bulk resistivity is subtracted. Resistance measurements can also be used to monitor the thickness of metal deposited at the rear of the wafers (an alternative is to measure the weight differential) and the resulting alloying of the aluminium to form a highly doped p-type back-surface field (BSF) layer.

Measuring the contact resistance between the metal and the semiconductor usually requires separate experiments and special test structures. The recently developed Corescan instrument [39] provides detailed information about the

contact resistance and the emitter sheet resistance on the finished solar cell. The technique, which is destructive, is based on scanning a probe directly on the silicon and the metal fingers to map the voltage drop vs. position across the illuminated solar cell. Such voltage maps can be used to optimise the front grid metallisation and diagnose metal contact problems [40].

The global series resistance of the device can be measured by a number of methods. It is important to emphasise that not all the methods provide the relevant value of series resistance. Methods based on measurements of the device under illumination are more realistic than methods in the dark [41]. The most robust method is based on a comparison between the open-circuit I–V curve and the photovoltaic I–V curve, as illustrated in Section 4.3.

4.2 Minority-Carrier Lifetime Measurements

In R&D laboratories, most of the fabrication steps are characterized in detail using lifetime measurements. Frequently, these detailed studies are done under ideal conditions to achieve unambiguous results. For example, studies of wafers vs. position in the original cast block have often tested the bulk lifetime after each process step by etching off the surface and subsequently applying a high-quality surface passivation, in order to determine the effect of each step on bulk lifetime without confounding effects of the surface [42, 43]. Alternatively, the surface can be etched back and passivated using a liquid, such as hydrofluoric acid [44] or iodine in ethanol [43, 45]. Satisfactory low-temperature passivation has also been obtained with corona-charged photoresist [46] and polymer films [47]. Many studies have also been performed on wafers with the surfaces as they exist after each step in the process [48, 49]. Such measurements do not require special wafer preparation and are ideal for industrial process control in production lines. Especially on multicrystalline material, high-resolution mapping of the wafer has been used to map the response of different grains and grain boundaries to gettering and hydrogenation [50]. These spatially resolved methods include microwave-PCD, modulated free carrier absorption, surface photovoltage, IR carrier density imaging, microwave phase-shift techniques and light beam induced current (LBIC) [51].

4.2.1 Measurements of Lifetime in a Boule or Block

At the level of the block or boule, the lifetime is often mapped to determine the region of potentially good wafers. The top and tail of a boule have low lifetimes and are discarded or recycled. Cast ingots have low lifetime at the top and bottom of the blocks, as well as near the edges of the crucible. Detailed two-dimensional high-resolution μ-PCD measurements are often used to characterise these blocks or boules using commercially available instruments. The initial lifetimes for as-grown material are, however, not perfectly correlated with final solar cell efficiency. It has been shown, for example, that some regions of cast blocks that might be discarded based on initial lifetime measurements recover lifetime during the high-temperature steps in cell processing due to gettering effects [49, 52]. Many of these low lifetime regions can also result in good solar cells after

hydrogen bulk passivation procedures. Despite these complexities, a better understanding of the initial silicon lifetime and the effects of the process on the various regions of boules and blocks is expected to result in better strategies for optimising the silicon growth and choosing the regions of silicon to submit to the expensive sawing, wafer cleaning, and cell fabrication processes. Rejecting material at this early stage has great value. Tight tolerances for incoming wafers at the beginning of cell fabrication will also permit better optimisation and control of the fabrication process.

4.2.2 Lifetime Measurements on Bare Wafers

In principle, measurements on bare wafers should not be necessary if the boule or block has been measured prior to sawing. In practice, a measurement at the wafer level can indicate if a sufficient thickness of silicon was removed at the saw-damage etch step. In addition, many silicon solar cell manufacturers do not fabricate the wafers, but purchase them, and it is of great interest for both the vendor and the manufacturer to have the capability to measure the minority-carrier lifetime of the individual bare wafers. This is not simple, since the measured effective lifetime of a wafer without surface passivation can be very low and poorly correlated to the bulk lifetime of the material.

For typical commercial solar cells, the efficiency is relatively constant for bulk lifetimes greater than 5 μs, corresponding to diffusion lengths greater than 116 μm. Therefore, the main point of a lifetime measurement at the stage of bare wafers is to determine if the wafer has a minimum required lifetime of 2–5 μs. Wafers with greater lifetime than this clearly 'pass' and wafers with lower lifetime 'fail'. This type of pass/fail test is possible even in the absence of surface passivation by using infrared light, as discussed in Section 2.4.

As seen in Figure 2, measurements on bare wafers will generally result in effective lifetimes in the range 0.1–2 μs. The low levels of photoconductance corresponding to these lifetimes makes it critically important to determine the lifetime with a data analysis that removes the artifacts that come from trapping, as discussed in Section 2.6. Due to the dependence of the lifetime on injection level discussed in Section 2.2, all measurements of lifetime should be performed at the same minority-carrier injection level. This injection level should preferably be chosen to be relevant to the maximum power operating point of the finished solar cell.

4.2.3 Effective Lifetime After Emitter Diffusion

After the emitter diffusion is an ideal point to measure the lifetime, since its value at this stage is often very predictive of the final solar cell efficiency. The front phosphorus diffusion and oxidation acts as a surface passivation. In normal operating conditions of low injection, a diffused region is seen from the base of the cell as a surface recombination velocity, whose value is determined by the emitter-saturation current density J_{oe} of the diffused region (see Section 2.5). This correspondence between SRV and J_{oe} is shown in Figure 2 for a 1 Ω cm p-type wafer. It can be noted that J_{oe} values below 10^{-12} A cm^{-2} provide a reasonable passivation (SRV < 1000 cm/s). Yet such $J_{oe} = 10^{-12}$ A cm^{-2}

would limit the measurable effective lifetime to approximately 12 μs in 1 Ω cm material, even if the bulk lifetime may be much higher. This surface-like role of the diffused regions applies to both aluminium alloyed BSF regions and to open-circuited phosphorus (or boron) diffused regions. Representative values for industrial phosphorus (n^+ region) and aluminium (p^+ region) diffusions are 8×10^{-13} A cm^{-2} and 5×10^{-13} A cm^{-2}, respectively. It should be noted that the measured lifetime limit imposed by a given value of J_{oe} is less restrictive for higher resistivity wafers.

The techniques discussed in Section 2.5 can be applied to determine both the bulk lifetime and the emitter saturation current density for the phosphorus diffusion. It is frequently advisable to use special test wafers with a lower substrate doping to optimise the range of carrier injection data that can be used for the analysis and extend the range of J_{oe} values that can be determined. Once J_{oe} is determined, its contribution to the low injection range can be subtracted. Therefore data taken in two minority-carrier density injection ranges allows both the bulk lifetime in the relevant range of cell operation and the emitter saturation current density to be uniquely determined. The exact analysis will depend on the technology used for the emitter diffusion, since this step may result on a diffused region at the front only, or at both surfaces. If emitter surface passivation is done in a subsequent, separate step, the same measurement methodology discussed above can be used to determine the bulk lifetime and the emitter saturation current density that results from that process step. This provides an ideal way to characterize the effectiveness of emitter passivation by, for example, oxidation or silicon nitride deposition.

4.3 Voltage Measurements for Characterisation of Process Steps After Junction Formation

Although measurements of device voltage have traditionally been reserved until the completion of its fabrication, an earlier voltage measurement is possible. This offers a powerful monitoring and process control tool complementary to the lifetime techniques described above. The most common, and frequently sole, characterisation used in industry consists of the final I–V curve testing of the solar cell under simulated one sun illumination. Whereas undeniably important and necessary, this test has limited usefulness as a diagnostic and control tool. Research laboratories have used I_{sc} V_{oc} measurements to gain further insight into the device. Very early in the history of solar cell development, it was realised that the I_{sc}–V_{oc} curve contained information about the fundamental diode characteristic free from series resistance effects [53]. Comparison of I_{sc}–V_{oc} data with the final I–V curve of the solar cell can then determine the series resistance very precisely. In a recent variation of the I_{sc}–V_{oc} method, the *Quasi-Steady-State open-circuit voltage*, or $QSSV_{oc}$ [54], the device is kept in open-circuit at all times, but its short-circuit current is not actually measured at every light intensity. Instead, the incident light intensity is measured with a calibrated reference solar cell. This illumination intensity can be converted to a measure of current by using as a scaling factor, either the short-circuit current of the cell (if already

known) or the modelled photogeneration in the test sample. It is often overlooked that such *Illumination–V_{oc}* data can be obtained and analysed as soon as a junction is formed in the solar cell fabrication. The *Illumination–V_{oc}* method only requires that the contacts to the p^+ and n^+ regions of the cell be better than the input impedance of the instrument used to measure the voltage. This very simple requirement means that, in many cases, the characteristic curve can be taken at any point in the process after the emitter diffusion by simply probing the appropriate areas of the silicon, giving valuable information in the middle stages of processing the wafers. Some care must be taken to ensure that the probed contacts are ohmic, rather than rectifying. The resistance between two probe contacts on the p-type region can be checked to verify that sufficiently good contact is made. Similarly, the n-type contacts can also be checked. This ensures that the subsequently measured voltage will be indicative of the junction voltage.

In the *QSSV_{oc}* technique, the light intensity can be swept with a 1/e time constant sufficiently long (for example 4 ms), such that the solar cell voltage is in quasi-steady-state with the light intensity for typical effective carrier lifetimes encountered in most silicon solar cells (usually well below 4 ms after the device is completed). The short overall duration of the illumination (typically 12 ms), means that the sample does not heat significantly even at high light intensities, which allows data acquisition over a wide range of illumination intensities. The main methods of analysing these data are described below.

4.3.1 Standard Diode Analysis of Illumination–V_{oc} Curves

An example of *Illumination–V_{oc}* data is shown in Figure 5 in the form of the standard semi-logarithmic diode characteristic curve [32]. In this case *Illumination–V_{oc}* data was taken after cell completion, and the measured short-circuit current was used to convert the illumination scale from suns to current density. A classical interpretation of these characteristics leads to the determination of saturation current densities and ideality factors. The data in Figure 5 can be fit with a double exponential diode model using $J_{o1} = 4 \times 10^{-13}$ A cm $^{-2}$ ($n = 1$ component), $J_{o2} = 3.7 \times 10^{-8}$ A cm^{-2} ($n = 2$ component), and a shunt resistance, $R_{shunt} = 2.4 \times 10^3$ Ω. It is important to realise that the saturation current densities obtained from this analysis are global parameters, encompassing recombination within the emitter and base regions, as well as at the surfaces and within any space charge regions. It is usually the case that J_{o1} is higher than the emitter saturation current J_{oe} discussed in preceding sections. Another important observation is that, whereas a satisfactory fit to the data is usually possible using the double exponential model, the transition from ideality 1 to ideality 2 (or greater) factors is often due to the variability of the bulk lifetime or the surface recombination velocity [55]. Process control using the analysis of Figure 5 should optimise the voltage at 0.05 to 0.1 suns, corresponding to the maximum power operating voltage of the solar cell.

Note that voltage can always be translated into lifetime, as described in Section 3. In some cases, a voltage measurement prior to metallisation is valuable and warranted, for example to check the p–n junction properties before

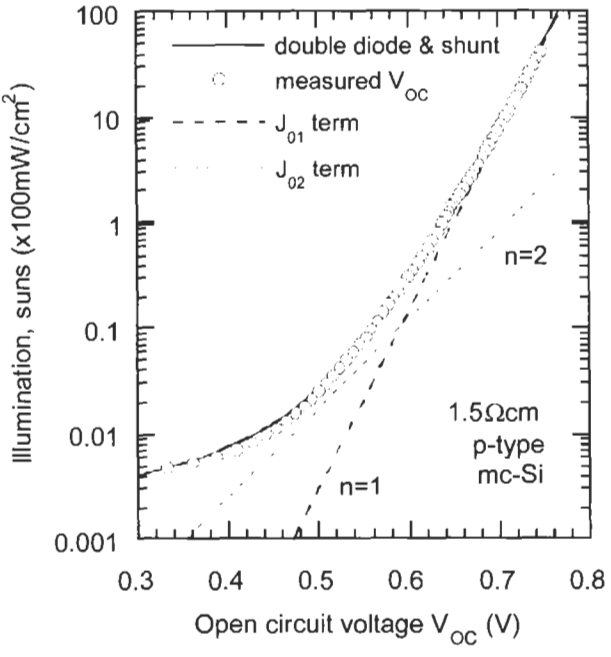

Figure 5 Illumination–V_{oc} *data plotted in a semi-logarithmic scale, with a double exponential diode curve fit. The experimental data was taken using the QSS*V_{oc} *technique for a 1.5 Ω cm multicrystalline silicon solar cell.*

metal sintering. Often though, the contactless lifetime measurements are easier and preferable at the stage of the fabrication process immediately after emitter diffusion. However, once the aluminium BSF is formed, voltage measurements become the preferred diagnostic technique, since the p-type contact can now be easily probed, while the alloyed Al layer with segregated metal at the surface presents a high conductance and must be etched before good photoconductance measurements can be made.

4.3.2 Voltage Monitoring of Contact Formation

Although not immediately obvious, data taken under open-circuit conditions can be valuable for monitoring the properties of the solar cell contacts. Metal contacts can be modelled as a Schottky potential barrier, which is formed by most metals on silicon, in parallel with some form of leakage current. The leakage might be from the metal locally doping or spiking the silicon or from thermally assisted tunnelling through the potential barrier. Under one-sun conditions, for a well-formed contact, the Schottky barrier is effectively shorted by the leakage. However, at a sufficiently high light intensity on a poorly formed contact, the Schottky diode will build up a voltage opposing the solar cell junction voltage by generating a current that the leakage is unable to fully shunt. An aluminium metallisation that has not sufficiently fired through a phosphorus diffusion on the back of the solar cell will also produce an opposing

voltage at high illumination intensities. Note that Schottky-type contacts usually result in low fill factors and efficiencies. This poor contact effect is indicated as an ideality factor less than unity, or even a voltage that decreases at high illumination intensity. By monitoring the open-circuit voltage at light intensities significantly higher than the operating conditions, this effect can be used to anticipate problems in the contact formation. Departures from ideal behaviour can often be seen before they result in a yield loss due to low efficiency. This method is both a good diagnostic and a process-control technique.

4.3.3 Photovoltaic I–V curves from Illumination–V_{oc} data

An alternative presentation of *Illumination*–V_{oc} (or I_{sc}–V_{oc}) data is shown in Figure 6. By using the superposition principle, an implied photovoltaic I–V curve can be constructed from the open-circuit voltage measurements of Figure 5. At each open-circuit voltage, the implied terminal current is given by:

$$J_{terminal} - J_{sc}(1 - \text{suns}) \tag{17}$$

This yields the familiar photovoltaic I–V curve format, permitting the customary interpretation of fill factor, efficiency and shunt. The parameters that matter most to solar cell performance are now visually obvious. For example, it can immediately be seen if the shunt is having a major effect on the maximum

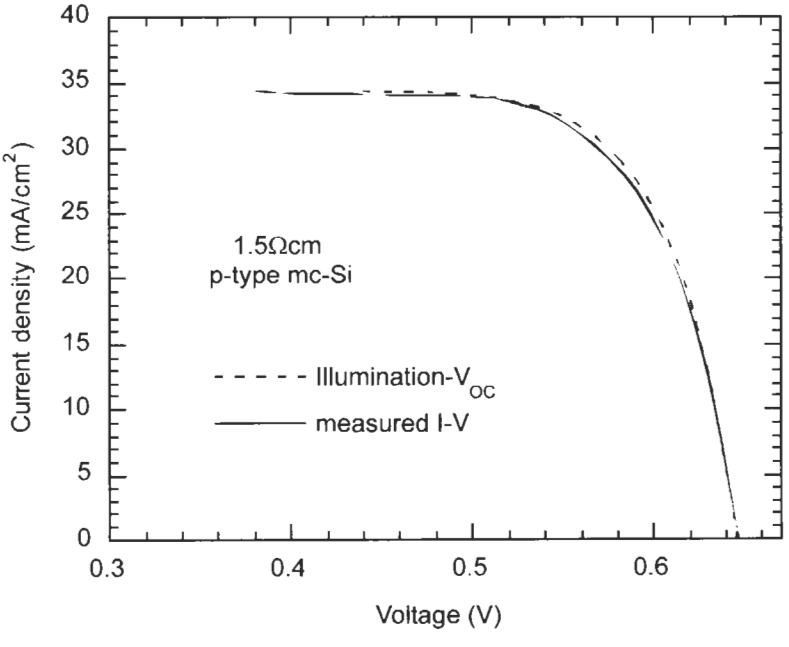

Figure 6 The same Illumination–V_{oc} *data as in Figure 5, plotted as a photovoltaic I–V curve and compared to the I–V curve taken on the finished cell.*

power point or not, and the upper bound on fill factor and efficiency (without series resistance effects) is clearly displayed. As discussed in the previous section, this 'pseudo' I–V curve can be measured very early in the process, by probing the silicon after junction formation. This allows the qualification of basic materials and device properties in terms of potential device performance, before the 'back end' processing may complicate the interpretation. The metallisation and sintering process steps can subsequently also be monitored for voltage loss and shunts using the $QssV_{oc}$ technique.

Eventually, by comparing the *Illumination–*V_{oc} curve with the actual output I–V curve of the finished solar cell, the series resistance can be determined with precision. Since the implied I–V curve from the open-circuit voltage has the shunt and ideality factors fully included, the differences between the two curves are clearly isolated to be due to series resistance. The latter is simply given by the voltage difference between the two curves at the knee, in the vicinity of the maximum power point, divided by the current. As an example, the same data in Figure 5 for a laboratory multicrystalline silicon cell is shown in Figure 6 [32]. The curves closely follow each other except near the maximum power point, where series resistance effects are greater. The measured output I-V curve gives an efficiency of 17.39%, with a fill factor of 0.785. The curve constructed from the *Illumination–*V_{oc} data indicates a pseudo-efficiency of 17.47%, with a fill factor of 0.790. This indicates that the series resistance is very small for this device and that the main limitation to voltage and fill factor is due to recombination losses within the solar cell.

Acknowledgement

We would like to thank M. Kerr and D. Macdonald for collaborations in developing expertise in this area of research and in discussions and preparation of this manuscript.

References

[1] Stevenson, D.T. and Keyes, R.J., 1995. Measurement of Carrier Lifetimes in Germanium and Silicon. *J. Appl. Phys.*, Vol. 26, pp. 190–195.

[2] Bube, R.H., 1960. *Photoconductivity of Solids*. Wiley, New York.

[3] Sinton, R.A. and Cuevas, A., 1996. Contactless determination of current–voltage characteristics and minority-carrier lifetimes in semiconductors from quasi-steady-state photoconductance data. *Appl. Phys. Lett.*, Vol. 69(17), pp. 2510–2512.

[4] ASTM, 1981. *Designation: F-28-75. Measuring the minority carrier lifetime in bulk germanium and silicon*. American Society for Testing of Materials.

[5] Miller, G.L., Robinson, D.A.H., and Wiley, J.D., 1976. Contactless measurement of semiconductor conductivity by radio frequency free carrier power absorption. *Rev. Sci. Instrum.*, Vol. 47(7), pp. 799–800.

[6] Deb, S. and Nag, B.R., 1962. Measurement of carriers in semiconductors through microwave reflection. *J. Appl. Phys.*, Vol. 33(4), p. 1604.

[7] Kunst, M. and Beck, G., 1986. The study of charge carrier kinetics in semiconductors by microwave conductivity measurements. *J. Appl. Phys.*, Vol 60(10), pp. 3558–3566.

[8] Harrick, N.J., 1956. Lifetime measurements of excess carrier kinetics in semiconductors. *J. Appl. Phys.*, Vol. 27(12), pp. 1439–1442.

[9] Glunz, S.W. and Warta, W., 1995. High resolution lifetime mapping using modulated free-carrier absorption. *J. Appl. Phys.*, Vol. 77(7), pp. 3243–3247.

[10] Brendel, R., Bail, M., and Bodman, B., 2002. Analysis of photoexcited charge carrier density profiles in Si wafers by using an infrared camera. *Appl. Phys. Lett.*, Vol. 80(3), pp. 437–439.

[11] Schroder, D.K., 1998. *Semiconductor Material and Device Characterization.* 2nd ed. John Wiley and Sons, New York.

[12] Basore, P.A., 1993. Extended spectral analysis of internal quantum efficiency. *Proc. 23rd IEEE Photovoltaic Specialists Conf.*, Louisville, pp. 147–152.

[13] ASTM, 1998. *Recombination lifetime measurements in silicon.* In: Gupta, D.C., Bacher, F.R. and Hughes, W.M. Eds., Vol. STP 1340, American Society for Testing of Materials.

[14] Brendel, R. and Wolf, M., 1995. Differential and actual surface recombination velocities. *Proc. 13th European Photovoltaic Solar Energy Conf.*, Nice, pp. 428–431.

[15] Schmidt, J., 1999. Measurement of differential and actual recombination parameters on crystalline silicon wafers. *IEEE Transactions on Electron Devices*, Vol. 46, 1999, pp. 2018–2025.

[16] Rein, S., Rehrl, T., Warta, W., and Glunz, S.W., 2002. Lifetime spectroscopy for defect characterization: Systematic analysis of the possibilities and restrictions. *J. Appl. Phys.*, Vol. 91(4), pp. 2059–2070.

[17] Macdonald, D., Cuevas, A., and Wong-Leung, J., 2001. Capture cross sections of the acceptor level of iron–boron pairs in p-type silicon by injection-level dependent lifetime measurements. *J. Appl. Phys.*, Vol 89(12), pp. 7932–7939.

[18] Kerr, M.J. and Cuevas, A., 2002. General parameterization of Auger recombination in crystalline silicon. *J. Appl. Phys.*, Vol. 91(4), pp. 2473–2480.

[19] Schmidt, J., Aberle, A.G., and Hezel, R., 1997. Investigation of carrier lifetime instabilities in Cz-grown silicon. *Proc. 26th IEEE Photovolt. Specialists Conf.*, Washington DC, pp. 13–17.

[20] Glunz, S.W., Rein, S., Warta, W., Knobloch, J. and Wettling, W., 1998. On the degradation of CZ-silicon solar cells. *Proc. 2nd World Conf. on Photovoltaic Energy Conversion*, Vienna, pp. 1343–1346.

[21] Reis, J.H., King, R.R. and Mitchell, K.W., 1996. Characterization of diffusion length degradation in Czochralski silicon solar cells. *Appl. Phys. Lett.*, Vol. 68(23), pp. 3302–3304.

[22] Zoth, G. and Bergholz, W., 1990. A fast, preparation-free method to detect iron in silicon. *J. Appl.. Phys.*, Vol. 67(11), pp. 6764–6771.

[23] Aberle, A.G., Robinson, S.J., Wang, A., Zhao, J., Wenham, S.R. and Green, M.A., 1993. High-efficiency silicon solar cells: fill factor limitations and non-ideal diode behaviour due to voltage-dependent rear surface recombination velocity. *Prog. Photovoltaics*, Vol. 1, pp. 133–143.

[24] Glunz, S.W., Biro, D., Rein, S. and Warta, W., 1999. Field-effect passivation of the SiO_2–Si interface. *J. Appl. Phys.*, Vol. 86, pp. 683–691.

[25] Kerr, M.J. and Cuevas, A., 2002. Comprehensive study of the doping and injection-level dependence of stoichiometric plasma silicon nitride passivation for silicon solar cells. *Proc. 29th IEEE Photovoltaic Specialists Conf.*, New Orleans, pp. 102–105.

[26] Basore, P.A. and Clugston, D.A., 1998. *PC1D V5.3*. University of New South Wales, Sydney, Australia.

[27] Bail, M. and Brendel, R., 2000. Separation of bulk and surface recombination by steady state photoconductance measurements. *Proc. 16th European Photovoltaic Solar Energy Conf.*, Glasgow, pp. 98–101.

[28] Kane, D.E. and Swanson, R.M., 1985. Measurement of the emitter saturation current by a contactless photoconductivity decay method. *Proc. 18th IEEE Photovoltaic Specialists Conf.*, Las Vegas, pp. 578–583.

[29] Cuevas, A., 1999. The effect of emitter recombination on the effective lifetime of silicon wafers. *Sol. Energy Mater. Sol. Cells*, Vol. 57, pp. 277–290.

[30] Cuevas, A. and Sinton, R.A., 1997. Prediction of the open-circuit voltage of solar cells from the steady-state photoconductance. *Prog. Photovoltaics*, Vol. 5, pp. 79–90.

[31] Cuevas, A., Sinton, R.A., Kerr, M., Macdonald, D. and Mackel, H., 2002. A contactless photoconductance technique to evaluate the quantum efficiency of solar cell emitters. *Sol. Energy Mater. Sol. Cells*, Vol. 71(3), pp. 295–312.

[32] Macdonald, D.H., 2001. *Recombination and Trapping in Multicrystalline Silicon Solar Cells*. PhD thesis, Australian National University, Canberra.

[33] Hornbeck, J.A. and Haynes, J.R., 1955. Trapping of minority carriers in silicon. I. p-type silicon. *Phys. Rev.*, Vol. 97(2), pp. 311–321.

[34] Macdonald, D. and Cuevas, A., 1999. Trapping of minority carriers in multicrystalline silicon. *Appl. Phys. Lett.*, Vol. 74(12), pp. 1710–1712.

[35] Macdonald, D. and Cuevas, A., 2000. Understanding carrier trapping in multicrystalline silicon. *Sol. Energy Mater. Sol. Cells*, Vol. 65(4), pp. 509–516.

[36] Macdonald, D., Sinton, R.A. and Cuevas, A., 2001. On the use of a bias-light correction for trapping effects in photoconductance-based lifetime measurements in silicon. *J. Appl. Phys.*, Vol. 89(5), pp. 2772–2778.

[37] Sinton, R.A. and Cuevas, A., 2000. A quasi-steady-state open-circuit voltage method for solar cell characterization. *Proc. 16th European Photovoltaic Solar Energy Conf.*, Glasgow, pp. 1152–1155.

[38] Kerr, M.J., Cuevas, A. and Sinton, R.A., 2001. Generalized analysis of quasi-steady-state and transient decay open circuit voltage measurements. *J. Appl. Phys.*, Vol. 91(1), pp. 399–404.

[39] van der Heide, A.S.H., Schonecker, A., Wyers, G.P. and Sinke, W.C., 2000. *Proc. 16th European Photovoltaic Solar Energy Conf.*, Glasgow, pp. 1438.

[40] van der Heide, A.S.H., Bultman, J.H., Hoornstra, J., Schonecker, A., Wyers, G.P. and Sinke, W.C., 2002. Optimizing the front side metallization process using the Corescan. *Proc. 29th IEEE Photovoltaic Specialists Conf.*, New Orleans, pp. 340–343.

[41] Araujo, G.L., Cuevas, A. and Ruiz, J.M., 1986. Effect of distributed series resistance on the dark and illuminated characteristics of solar cells. *IEEE Transactions on Electron Devices*, Vol. ED-33(3), pp. 391–401.

[42] Macdonald, D., Cuevas, A. and Ferrazza, F., 1999. Response to phosphorus gettering of different regions of cast multicrystalline silicon ingots. *Solid-State Electronics*, Vol. 43, pp. 575–581.

[43] Rohatgi, A., Yelundur, V., Jeong, J., Ebong, A., Meier, D., Gabor, A.M. and Rosenblum, M.D., 2000. Aluminium-enhanced PECVD SiN_x hydrogenation in silicon ribbons. *Proc. 16th European Photovoltaic Solar Energy Conf.*, Glasgow, pp. 1120–1123.

[44] Yablonovitch, E., Allara, D.L., Chang, C.C., Gmitter, T. and Bright, T.B., 1986. Unusually low surface-recombination velocity on silicon and germanium substrates. *Physical Review Letters*, Vol. 57, pp. 249–252.

[45] Horanyi, T.S., Pavelka, T. and Tutto, P., 1993. In situ bulk lifetime measurement on silicon with a chemically passivated surface. *Appl. Surf. Sci.*, Vol. 63, pp. 306–311.

[46] Schmidt, J. and Aberle, A.G., 1998. Easy-to-use surface passivation technique for bulk carrier lifetime measurements on silicon wafers. *Prog. Photovoltaics*, Vol. 6, pp. 259–263.

[47] Biro, D. and Warta, W., 2002. Low temperature passivation of silicon surfaces by polymer films. *Sol. Energy Mater. Sol. Cells*, Vol. 71, pp. 369–374.

[48] Stocks, M., Cuevas, A. and Blakers, A., 1997. Process monitoring of multicrystalline silicon solar cells with quasi-steady state photoconductance measurements. *Proc. 26th IEEE Photovoltaic Specialists Conf.*, Anaheim, pp. 123–126.

[49] Coletti, G., Iuliis, S.D. and Ferrazza, F., 2001. A new approach to measure multicrystalline silicon solar cells in a production process. *Proc. 17th European Photovoltaic Solar Energy Conf.*, Munich, pp. 1640–1642.

[50] Geiger, P., Kragler, G., Hahn, G., Fatch, P. and Bucher, E., 2002. Spatially resolved lifetimes in EFG and string ribbon silicon after gettering a hydrogenation steps. *Proc. 29th IEEE Photovoltaic Specialists Conf.*, New Orleans, pp. 186–189.

[51] Warta, W., 2002. Defect and impurity diagnostics and process monitoring. *Sol. Energy Mater. Sol. Cells*, Vol. 72, pp. 389–401.

[52] Cuevas, A., Macdonald, D., Kerr, M.J., Samundsett, C., Sloan, A., Leo, A., Mrcarica, M., Winderbaum, S. and Shea, S., 2000. Evidence of impurity gettering by industrial phosphorus diffusion. *Proc. 28th IEEE Photovoltaic Specialists Conf.*, Anchorage, pp. 108–111.

[53] Wolf, M. and Rauschenbach, H., 1963. *Advanced Energy Conversion*, Vol. 3, pp. 455–479.

[54] Sinton, R.A. and Cuevas, A., 2000. A quasi-steady open-circuit voltage method for solar cell characterisation. *Proc. 16th European Photovoltaic Solar Energy Conf.*, Glasgow, pp. 1152 1155.

[55] MacDonald, D. and Cuevas, A., 2000. Reduced fill factors in multicrystalline silicon solar cells due to injection-level dependent bulk recombination lifetimes. *Prog. Photovoltaics*, Vol. 8(4), pp. 363–375.

High-Efficiency Silicon Solar Cell Concepts

Martin A. Green, Centre for Advanced Silicon Photovoltaics and Photonics, University of New South Wales, Sydney, Australia

1 Introduction

The vast majority of solar cells sold up to 2003 used crystalline or multicrystalline silicon wafers in combination with a simple screen-printing approach to applying the metal contacts. This approach has the advantage of being well established with the ready availability of appropriate equipment, such as screen-printers and furnaces for drying and firing the screened metal patterns, since these already had been developed for the thick-film hybrid microelectronics area. This limited the capital requirements and risks involved in setting up cell manufacture in an era where the viability of the photovoltaics industry was marginal.

However, there are disadvantages with the simplicity of the screen-printing approach. One is the limited cell performance that results. Commercial solar cell modules based on this approach are limited to efficiencies in the 10–13% range [1], corresponding to cell efficiencies of 12–15%. Also, as wafers are thinned to reduce material costs, both performance and yield become more difficult to maintain, limiting the economic benefits of such thinning.

Now that the photovoltaic industry's future seems more assured, with rapidly growing markets and increasingly positive cash flows, it will become important to pay more attention to the full economics of cell manufacture. It is well known that the starting wafers account for about 50% of total module costs and encapsulants account for another large portion, with such material costs accounting for over 70% of finished module costs. The cost of processing wafers into cells is less than 20% of the total cost of the finished product.

Simple arithmetic based on these figures shows that doubling the cell processing costs would give a cheaper product if the resulting cells were 20% more efficient on a relative basis. The product additionally would have more value due to both the prestige associated with better performance and the reduced systems costs resulting from its use. The implications of this simple calculation often are not fully appreciated, with the notion that high efficiency automatically means high cost ingrained into the subconscious of many.

As the photovoltaic industry becomes more mature, it seems likely that such costing issues will be more closely examined than warranted in the 'hand-to-mouth' days of the past. It will become important to explore approaches that offer higher performance than possible with the screen-printing approach.

With this as the basic rationale, this chapter will explore approaches that offer the potential for higher silicon solar cell efficiency than seems possible from screen-printing. First, the recent history of high-efficiency laboratory cell development will be outlined, highlighting features improved in each successive generation. The features that limit screen-printed cells to the relatively modest performance levels previously mentioned will then be identified. Two commercial high-efficiency cell designs that overcome some of these limitations will then be described, followed by an exploration of other approaches that may have some potential.

2 High-Efficiency Laboratory Cells

2.1 Silicon Space Cell Development

The evolution of record silicon laboratory cell efficiency is shown in Figure 1, showing several stages in the evolution of cell design. After an initial period of rapid evolution in the 1950s, design stabilised for more than a decade on the conventional space cell of Figure 2(a). Key features include the use of 10 Ω cm p-type substrates to maximise radiation resistance, and the use of a nominally 40 Ω/square, 0.5 μm deep phosphorus diffusion. Although it was known that lighter diffusions gave better blue response, this value was chosen because it was found to be more resistant to shunting by the top contact metallisation during processing [2]. These cells remained the standard for space use for more than a decade and are even now still specified for some space missions. Energy conversion efficiency was 10–11% under space radiation, and 10–20% higher on a relative basis under terrestrial test conditions.

Towards the end of the 1960s, the benefits of a rear Al treatment became apparent, particularly for cells which were thinner than normal [3, 4]. The corresponding increase in space cell efficiency to 12.4% was attributed to the gettering action of the Al treatment [5].

More detailed work showed that it was the presence of a heavily doped region beneath the rear contact which gave rise to these beneficial effects [6]. These benefits were postulated to arise from spillage of majority carriers from the rear

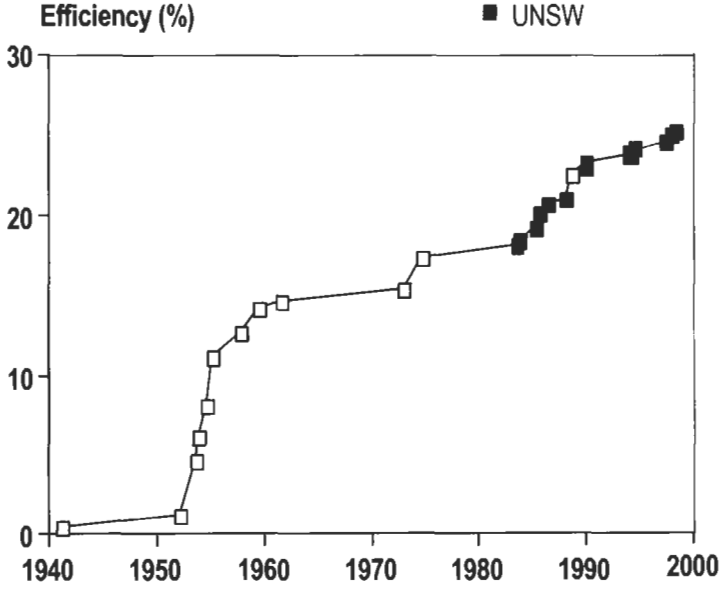

Figure 1 Evolution of silicon laboratory cell efficiency.

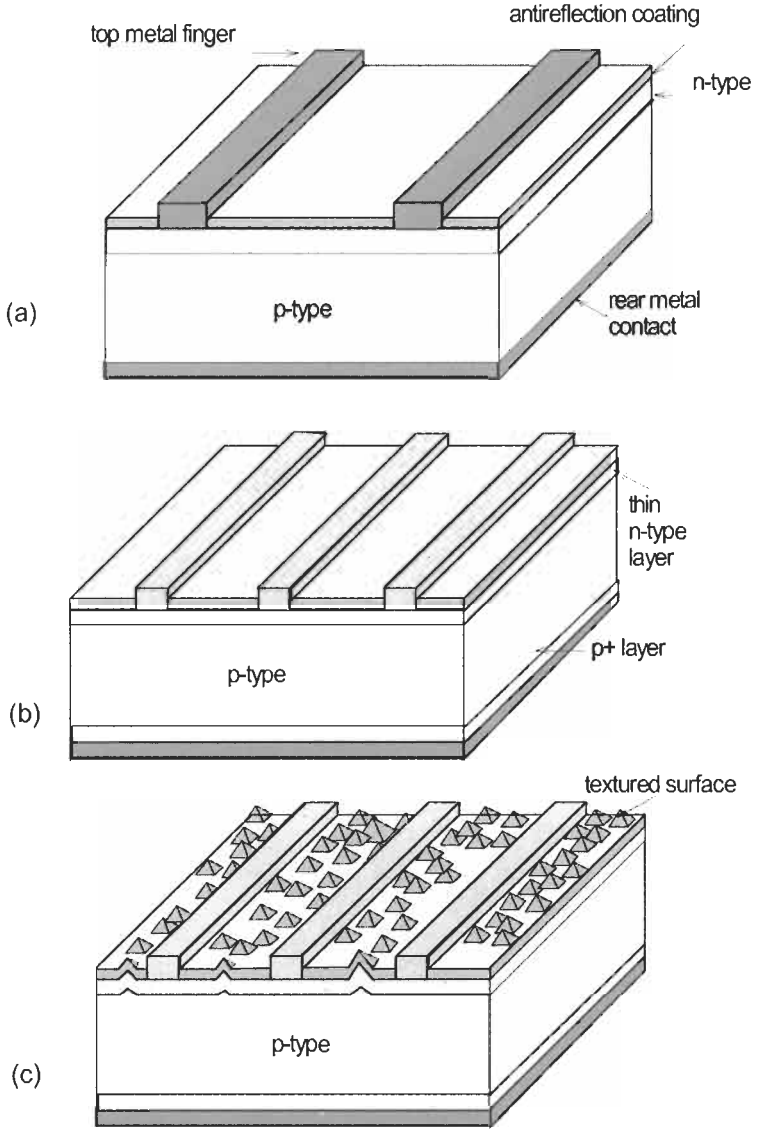

Figure 2 (a) Space silicon cell design developed in the early 1960s which became a standard design for over a decade; (b) shallow junction 'violet' cell; (c) chemically textured non-reflecting 'black' cell.

doped region into the bulk region of the cell, thus increasing the effective bulk concentration and hence the open-circuit voltage [6]. Although the correct explanation, in terms of a reduction in the effective rear surface recombination velocity, was soon forthcoming [7], the effect is still rather inappropriately, but almost universally, referred to as the back surface field (BSF) effect [6].

The conventional space cells had a relatively poor response to wavelengths which were shorter than 0.5 μm, due to the relatively heavy top junction

diffusion, as previously noted, and the use of an SiO AR coating which absorbs light below this wavelength. A marked improvement in performance was demonstrated in the early 1970s by replacing such junctions with much shallower (0.25 μm), higher sheet resistivity junctions, and redesigning the entire cell to accommodate this change, as shown in Figure 2(b).

To accommodate the increased sheet resistivity of the diffused layer, much finer metal finger patterns were also incorporated using photolithography to define their geometry. As a consequence, the cell resistance was actually lower than in conventional cells. Improved antireflection coatings, based upon TiO_2 and Ta_2O_5, were also incorporated. These were less absorbing than SiO, as well as providing a better optical match between the cells and the cover glass to which space cells are normally bonded. The thickness of these coatings was also selected so they would be effective at shorter wavelengths than were traditional coatings, thus giving the cells their characteristic violet appearance. (A subsequent development, made possible by the higher refractive index of the new AR coating materials, was the use of double layer AR coatings.)

The final design change in these 'violet' cells was the use of lower resistivity 2 Ω cm substrates. Since the improved output of the cells at blue wavelengths was quite tolerant to radiation exposure, the overall radiation tolerance remained at least equal to that of the conventional devices, while giving an improved voltage output. The combination of improved open-circuit voltage (due to the change in substrate resistivity), improved current output (due to the removal of 'dead layers', better antireflection coatings, and lower top contact coverage), and improved fill factor (due to the improved open-circuit voltage and decreased cell resistance) resulted in a massive increase of 30% in performance as compared to an average space cell of conventional design. Efficiencies of 13.5% were obtained under space radiation, with terrestrial efficiencies close to 16% being demonstrated [8].

Not long after the superior performance of the violet cell had been established, a further boost in performance was obtained by texturing the top surface of the cell [9]. The idea of mechanically forming pyramids on the top surface of the cell to reduce reflection had been suggested some time earlier [10]. In the black cell, a simpler approach was used which relied upon the random nucleation of selective etches to expose (111) crystallographic planes in a substrate originally of (100) surface orientation. The intersecting (111) planes so exposed formed small, square-based pyramids of random size which were distributed randomly over the cell surface.

This has two advantages for cell performance. One is that light striking the sides of the pyramids is reflected downwards and hence has at least one more chance of being coupled into the cell. A second advantage is that light coupled into the cell enters obliquely. Most light will be coupled in at the first point of incidence on the pyramids. This light is refracted in at an angle of about 48° to the original surface, resulting in an increase in the path length of weakly absorbed light by a factor of 1.35 compared to a non-textured cell. The effect is similar to that of an increase in the silicon absorption coefficient or in the bulk diffusion length by the same factor. A third feature of the texturing approach is

the high degree of trapping of light within the cell that is possible. For terrestrial cells, this is an advantage since it improves the long wavelength response of cells. However, for space cells, it is a disadvantage since it increases the absorption of sub-bandgap photons in the rear contact of the cell. This causes the cells to operate at a higher temperature in the space environment, largely negating the previous advantages. Combined with a greater potential for mechanical damage during array assembly by knocking peaks from pyramids, this has meant that textured cells have not been as widely used in space as their apparent performance advantage initially seemed to warrant.

These 'black' cells gave an energy conversion efficiency of 15.5% under AM0 radiation, corresponding to an energy conversion efficiency of about 17.2% under the current terrestrial standard (Global AM1.5, 100 mW/cm^2, 25°C). Such were the strengths of the texturing concept, when combined with the technological improvements incorporated into the violet cell, that it was almost a decade before any further significant improvement in cell performance was demonstrated. These improvements ultimately came about as a result of an increased open-circuit voltage due to the development of improved surface and contact passivation approaches.

2.2 High-Efficiency Terrestrial Cells

The simplicity of the surface passivation afforded by its thermal oxide is one of the key features of silicon technology which explains its present dominance in microelectronics. Unfortunately for photovoltaics, the refractive index of silicon dioxide is too low for its use as an effective antireflection coating in high-performance cells. In fact, if present in any reasonable thickness (greater than 20 nm) on the top surface of the cell, it will limit the ability to reduce reflection by the subsequent deposition of any number of compensating layers [11]. Hence, if oxide passivation is to be used on the cell surface exposed to light, the oxide layer has to be very thin.

The potential of such oxide passivation became clear around 1978 [12, 13]. All subsequent high efficiency silicon cells have taken advantage of the passivation provided by thin thermal oxide layers to maximise their open-circuit voltage and short-wavelength response.

Contacts made to the surface are generally regions of high recombination velocity. Best cell performance will be obtained when the electronic activity at such contacts is 'passivated'. The earliest approach was to passivate by isolating the contact from minority carriers by interposing a heavily doped region. As already discussed, rear-contact passivation via the 'back surface field' effect resulted in significant gains in cell performance. Heavily doped regions, localized to those areas where the top contact is made to the cell, are used in most recent high efficiency cell designs.

A second approach to reducing contact effects is to minimise the contact area [14,15]. The benefits were demonstrated by increased open-circuit voltages on low resistivity substrates [16]. Most recent high-efficiency cells employ this low contact area approach. A third approach is to employ a contacting scheme in

which the contact itself has an inherently low recombination velocity. The MINP (metal-insulator-NP junction) cell of Figure 3 was the first successfully to exploit this approach [17]. The thin surface passivating oxide is continued under the metal, thus reducing its effective recombination velocity. Polysilicon [18] and semi-insulating polysilicon (SIPOS) [19] contact passivation have also been demonstrated. It appears that a thin interfacial oxide layer may play an important role in both of these schemes [19, 20]. More recently, excellent surface passivation has been demonstrated by a combination of a very thin layer of lightly doped amorphous silicon followed by a layer of doped amorphous silicon [21].

As seen in Figure 1, the performance levels established by 'violet' and 'black' cells in the mid-1970s remained unchallenged for close to a decade. Cells successfully incorporating the above mentioned oxide and contact passivation approaches, along the top surface, were the first to exceed these levels.

The MINP cell (Figure 3), the first silicon cell to demonstrate 18% efficiency, employs top contact passivation by the use of a thin oxide layer underlying this contact, as well as top surface passivation by a slightly thicker oxide layer. This difference in thickness complicates processing but was found necessary to achieve maximum device performance. The top contact metallisation is a Ti/Pd/Ag multilayer. The use of a low work function metal such as Ti as the contact layer is essential with this approach. This is to produce an electrostatically induced accumulation layer in the underlying silicon, an important factor in reducing contact recombination. The cells used alloyed aluminium to give a heavily doped region near the rear contact and were fabricated on polished (100)-oriented 0.2 Ω cm substrates. Surface passivation is easier to achieve on polished rather than textured or 'as-lapped' surfaces. To minimise reflection losses, a double layer antireflection coating was used which

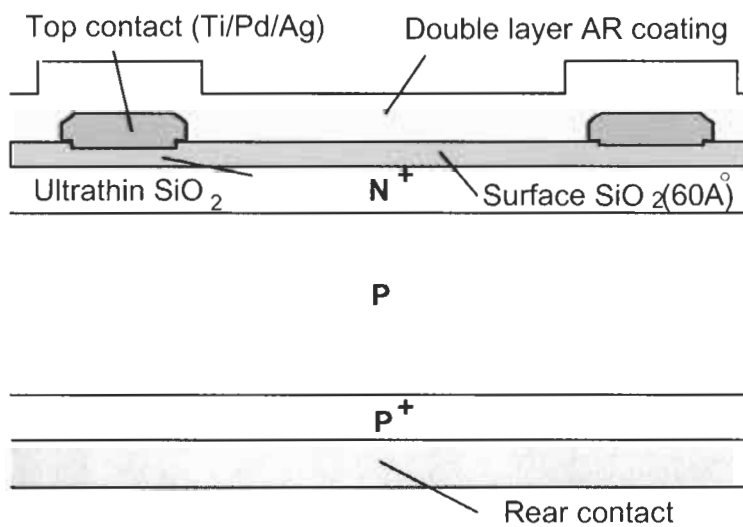

Figure 3 Metal–insulator–NP junction (MINP) solar cell.

consisted of approximately a quarter-wavelength of ZnS on top of the thin oxide, followed by a quarter-wavelength of MgF_2.

The PESC (Passivated Emitter Solar Cell) structure, shown in Figure 4, further improved cell efficiency. It is similar to the MINP cell structure, except that electrical contact is made directly through narrow slots in the thin oxide. In this case, contact passivation is obtained by minimising the contact area. In this case, surface texture is also used.

By combining the benefits of surface texture with the strengths of the PESC approach, the first non-concentrating silicon cells with an efficiency greater than 20% were fabricated in 1985 [22]. Rather than pyramidal texturing, the cells used microgrooving to achieve the same effect. The microgrooves were defined by using selective etches to expose crystal planes. Photolithographically designed oxide patterns were used to protect the surface against etching where this was not required, and so determine the final pattern of microgrooves. This approach was found to be easier to combine with fine line photolithography than was the normal pyramidal texturing.

The key characteristics of the PESC sequence are oxide surface passivation, self-aligned contacts through this oxide, high sheet resistivity top junction diffusion, alloyed aluminium rear surface passivation and antireflection control by texturing or double layer antireflection coating. The PESC sequence has proved to be very rugged and repeatable. Within one year of the initial 20% results, two groups had reported results approaching this figure (when referred to present calibrations) using almost identical structures [23, 24]. The sequence has since been reproduced in many laboratories, with commercial product now available for space and concentrator cells or for high value-added applications such as solar car racing.

The next major advance in cell performance came as a result of applying surface and contact passivation approaches to both top and rear surfaces.

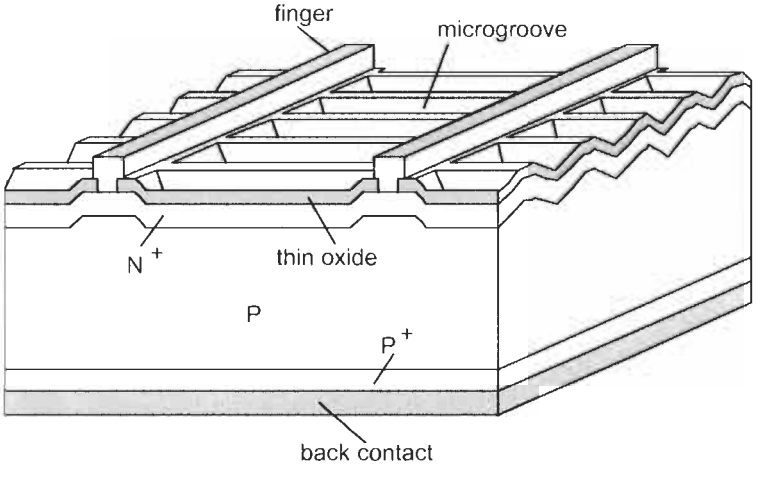

Figure 4 The microgrooved PESC cell, the first silicon cell to exceed 20% efficiency in 1985.

The rear point contact solar cell of Figure 5 achieved this landmark in cell design. Since both contacts are on the rear of the cell, the design places enormous pressure both upon the quality of surface passivation along both top and rear surfaces and upon post-processing carrier lifetimes. To achieve design objectives in these areas, full advantage had to be taken of 'state of the art' microelectronics technology.

Although originally developed for concentrator cells [25], the device design was modified for one-sun use by adding a phosphorus diffusion along the illuminated surface [26]. This produced the first one-sun silicon cells of efficiency above 22%.

Combining the earlier PESC sequence with similar double-sided surface passivation and chlorine based processing [27] produced an improved device, the PERL cell (Passivated Emitter, Rear Locally-diffused cell) shown in Figure 6. This took silicon cell efficiency to 23% by the end of the 1980s, an enormous improvement over the figure of 17%, the highest value only 7 years earlier. The PERL cell shares many features in common with the rear point contact cell, including almost complete enshroudment in a passivating oxide layer and small area contacts passivated by local heavy diffusions. However, it is a more robust design, being more tolerant of poor surface passivation and poor bulk lifetimes.

Since then, further improvements in PERL cells has taken their efficiency to close to 25%. Major improvements include the growth of much thinner oxide for top surface passivation which allows the direct application of a double layer antireflection coating to increase short-circuit current [11], the use of an annealing sequence for this top oxide and localised top contact points to increase

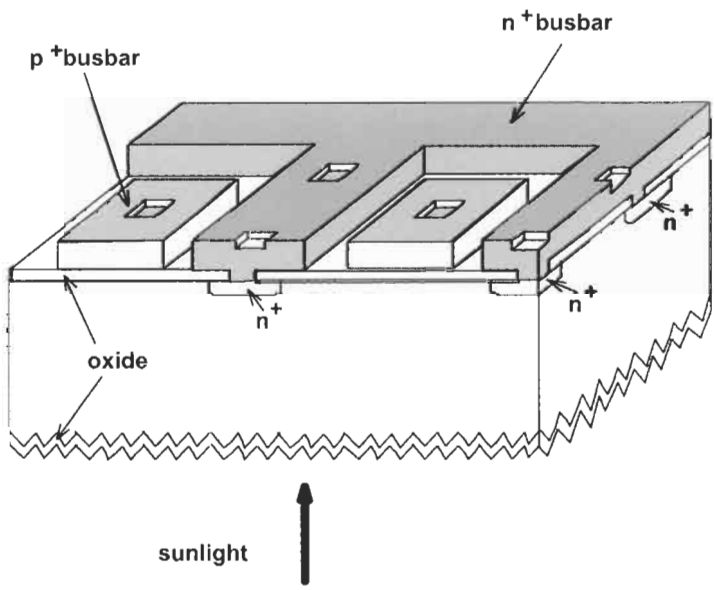

Figure 5 Rear point contact solar cell which demonstrated 22% efficiency in 1988 (cell rear shown uppermost).

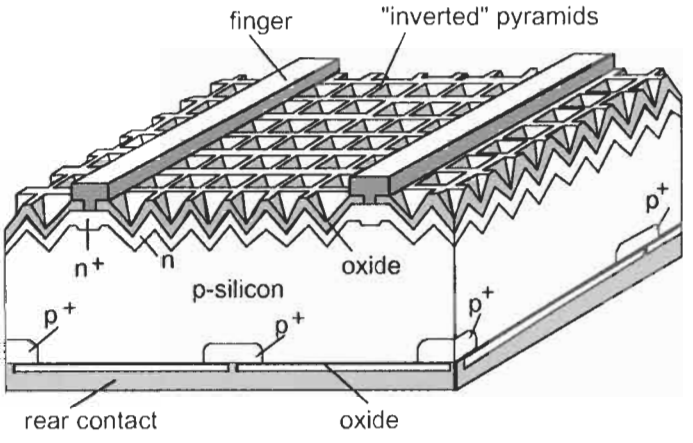

Figure 6 The PERL cell which took efficiency above 24% in the early 1990s.

open-circuit voltage and improved rear surface passivation and reduced metallisation resistance to improve fill factor.

2.3 *PERL Cell Design Features*

To maximise cell performance, as much light as possible of useful wavelengths should be coupled into and absorbed by the cell. Modern cell designs such as the PERL cell of Figure 6 incorporate several features of a primarily optical nature to achieve this result.

The inverted pyramids along the top surface serve primarily in such an optical role. Most light incident on this structure will hit one of the side walls of the pyramids at the first point of incidence with the majority of this light coupled into the cell. That reflected will be reflected downwards, ensuring that it has at least a second chance of entering into the cell. Some of the light incident near the bottom of the pyramids has three such chances. The pyramids are covered by an oxide layer of appropriate thickness to act as a quarter-wavelength antireflection coating. In more recent designs, this oxide is grown thin and a double layer antireflection coating applied [11].

Light coupled into the cell moves obliquely across the cell towards the rear surface with most absorbed on the way. Weakly absorbed light reaching the rear is reflected by the very efficient reflector formed by the combination of the rear oxide layer covered by an aluminium layer [28]. The reflectance from this combination depends upon the angle of incidence of the light and the thickness of the oxide layer, but is typically above 95% for angles of incidence close to the normal, decreasing to below 90% as the incidence angle approaches that for total internal reflection at the silicon/oxide interface (24.7°), and increasing to close to 100% once this angle is exceeded.

Light reflected from the rear then moves towards the top surface. Some reaching this surface strikes a face of a pyramid of opposite orientation to that

which coupled it into the cell. Most of this immediately escapes from the cell. Light striking other faces of the pyramid is totally internally reflected. This results in about half the light striking the top surface internally at this stage being reflected back across the cell towards the rear contact. The amount of light escaping after the first double pass depends on the precise geometry involved. It can be reduced by destroying some of the symmetries involved, for example by using tilted inverted pyramids or by using a 'tiler's pattern' [28]. The latter approach is currently used in PERL cell designs.

The combination of the inverted pyramids and the rear reflector therefore forms a very efficient light-trapping scheme, increasing the pathlength of weakly absorbed light within the cell. Effective pathlength enhancement factors [28] above 40 are measured. The light trapping boosts the infrared response of the cell. The external responsivity (amps per watt of incident light) of PERL cells peaks at longer wavelengths at higher values than previous silicon cells with values of 0.75 A/W measured at 1.02 μm wavelength. Energy conversion efficiency under monochromatic light peaks at the same wavelength with values above 45% measured [29]. Further improvements could push this figure to above 50% at 1.06 μm.

Other optical losses are due to reflection from, and absorption in, the top metal fingers of the cell. This can be minimised by making these lines as fine as possible with, ideally, as large an aspect ratio (height to width ratio) as possible. Alternatively, optical approaches can be used to steer incoming light away from these lines or to ensure that light reflected from them eventually finds its way to the cell surface [30, 31].

Present PERL cells lose about 5% of incoming light due to absorption or reflection loss associated with these metal fingers, when combined with reflection from the unmetallised top surface of the cell. They also lose 1–2% in performance from the use of a less than optimum light-trapping scheme and from less than 100% reflection of light from the rear surface of the cell. There is therefore some scope for small to moderate gains in performance by further improving the optical properties of these cells.

Although such advanced cell designs have been used for spacecraft and high value terrestrial applications such as solar car racing, the multiple photolithographic steps required in their fabrication make them too expensive for low cost terrestrial applications [32]. They do, however, provide a reference point for the discussion of the compromises involved in lower cost designs, as discussed in the following sections.

3 Screen Printed Cell Limitations

3.1 Structure

Figure 7 shows the structure of a typical crystalline screen-printed cell. The normal cell processing sequence would consist of [33]: saw damage removal

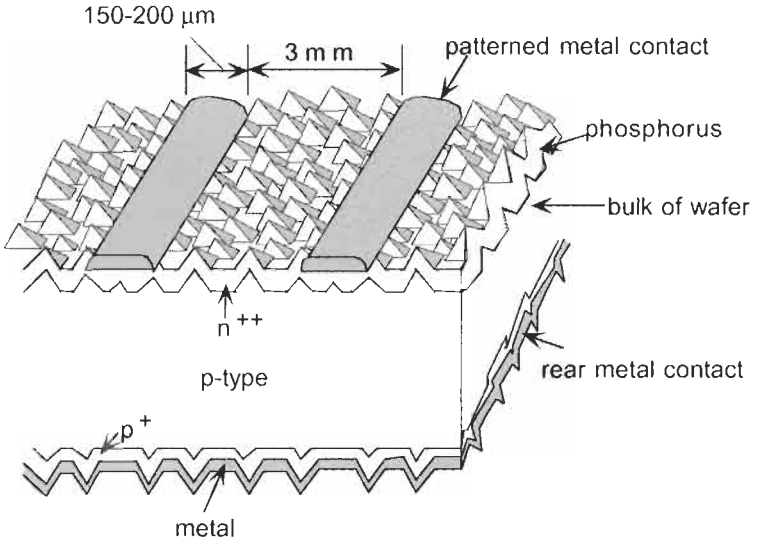

Figure 7 Screen printed crystalline silicon solar cell (not to scale).

from the starting wafer by etching; chemical texturing of the top surface, if a (100) crystalline wafer were the starting material; top surface diffusion to about 40 Ω/square; edge junction isolation normally by 'coin stacking' the cells and etching the edges in a plasma; etching to remove diffusion oxides; screening of front metal paste through a suitably patterned screen; drying and firing of the front surface metallisation; screening of the rear surface metal paste; drying and firing of rear metal contact; cell testing and sorting.

Using the normal boron-doped, 'solar grade' Czochralski silicon wafers of 0.5–5 Ω cm resistivity, the resulting cell efficiency is typically 12–15%. Application of a antireflection coating (usually TiO_2 or Si_3N_4) gives about 4% relative improvement.

For multicrystalline substrates, the use of an antireflection coating is mandatory due to the inability to reduce reflection substantially by texturing the multicrystalline wafer surface. This is due to the random orientations of the grains in the multicrystalline material which results in only a fraction being suitable for texturing. A recent development in this area has been the use of remote plasma enhanced chemical vapour deposited nitride coatings that are extremely beneficial for multicrystalline cells.

The major disadvantages of the screen printing approach relate to the cost of the metal pastes used in the process and the relatively low cell efficiency which results. The latter is due most fundamentally to the restricted line-width possible by screen printing. The relatively high contact resistance between the paste and the silicon is another constraint. The low aspect ratio (height/width) of the final lines due to paste thickness shrinkage during firing is another problem compounded by the low conductivity of the fired paste (about 3 times lower than that of pure silver).

There have been several investigations of the feasibility of screening pastes other than those based on silver. Nickel and copper have been investigated without success [34].

To reduce the linewidth, special fine screens can be used. However, the screens have been too frail for use in commercial production, although often used to produce a good research result [35].

The contact resistance between the paste and silicon can be a sensitive function of the precise firing environment and temperature. The glass frit (dispersed glass particles used in the paste as a binder) forms an oxide precipitate along the interface between the screened paste and the silicon surface. This contributes to the high contact resistance, although often, phosphorus is added to the paste to decrease the contact resistance to n-type material. Etching of the top surface with HF after firing is known to decrease the contact resistance, presumably by etching away some of the interfacial frit in this area. However, this is also considered to reduce the reliability of the cell in a moist environment.

The rear surface contact resistance is generally less of a problem. Even though contact is being made to more lightly doped material, a much larger contact area is available. Furthermore, the addition of aluminium to the silver paste or the use of an aluminium paste precursor can increase the doping level in the surface region by alloying. Under appropriate firing conditions, a significant 'back surface field' effect can be obtained by the use of such aluminium.

3.2 Typical Performance

Typically, the screen printing approach will produce cell open circuit voltages in the 580-620 mV range, depending on substrate resistivity, short circuit current densities in the 28–32 mA/cm^2 range, and fill factors for large area cells in the 70–75% range. For a large area cell, typically 10–15% of the top surface of the cell will be shaded by the screened metallization which, as indicated in Figure 7, typically consists of metal fingers of about 150–200 microns width, spaced about 2–3 mm apart. Due to the low conductivity of the paste, an interconnect busbar design, as indicated in Figure 8, is mandatory for large area cells. Although contributing to the large shading loss of this approach, this design also has the advantage of improving the cell tolerance to cracks. If scaling to large area cells, the number of busbar interconnections would have to be increased.

To maintain reasonable contact resistance, quite low sheet resistivities for the top surface diffusion are required. The 40 Ω/square typically used results in a significant loss in blue response of the cells due to dead layers along the surface. Higher sheet resistivities will improve the blue response but at the expense of cell fill factor. The heavy diffusion also limits the open-circuit voltage output of the cells. Oxide surface passivation is not of much benefit in improving performance due to this limitation. Using improved quality substrates such as floatzone silicon also generally does not result in any substantial performance improvement again due to this limitation.

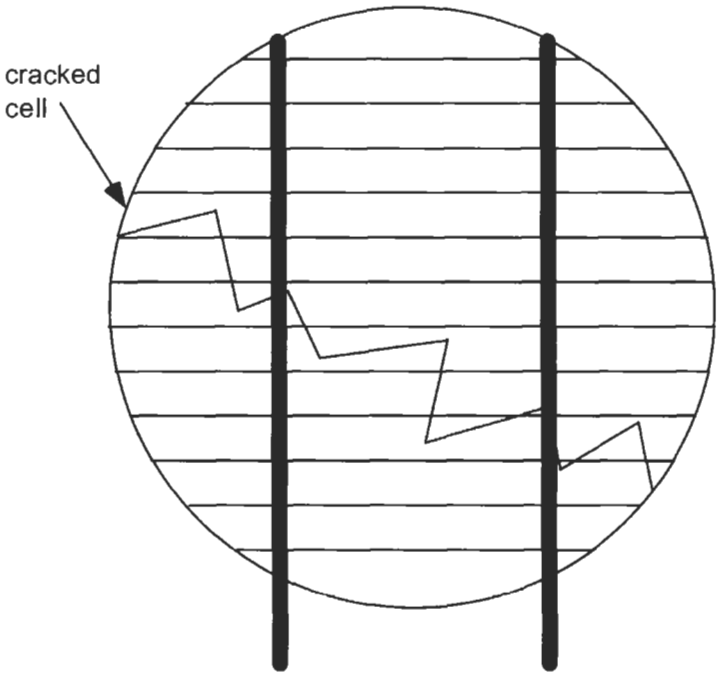

Figure 8 Cell design using the strip metal cell interconnects as busbars to reduce finger resistive losses and to improve tolerance to cracks.

3.3 Improved Technology

The limitations of the screen printing approach may not be fundamental to this approach but may be able to be overcome by introducing new ideas.

To reduce the linewidth, finer screens can be used although these require weaker material in their construction and have not been sufficiently durable for volume manufacturing. There are frequently alternative claims in this area [35], but commercial practice is a telling indicator of what is feasible here. Approaches for defining metal contacts, similar to ink jet printing approaches, have also been used in commercial production.

Some recent progress has been reported in improving the contact resistance obtainable by screen printing [35, 36]. Approaches similar to those shown in Figure 9 have also been suggested which rely on having different top layer sheet resistivities in contacted and non-contacted areas [37, 38]. A conductive antireflection coating such as formed by conducting metal oxides could be used in conjunction with this scheme to allow reasonable metal spacing [39].

However, it is doubtful that a high efficiency cell can ever be produced using the screen printed approach, with good screen printed laboratory cells only giving about 16.7% efficiency [11]. Even if both the linewidth and the contact resistance problems are successfully solved in production, there are still challenges due to conductivity and small aspect ratio.

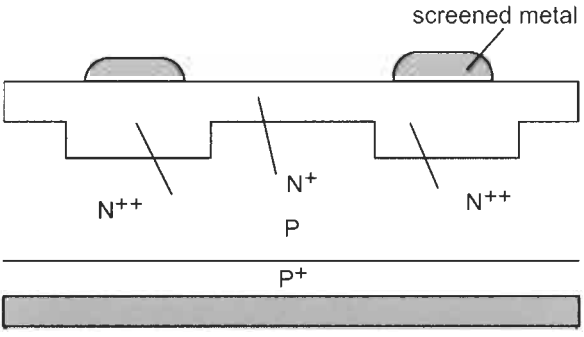

Figure 9 Ideal situation for fine linewidth screen printed metallisation with contact being made to selectively doped areas.

4 Buried Contact Cells

4.1 Structure

The buried contact solar cell of Figure 10 was developed to overcome the efficiency limitations of the screen printed cell approach previously described. The most distinctive feature of this approach is the use of grooves in the top surface to locate the cell metallisation. Although originally investigated using screen printed metallisation sequences (where the metal was forced into the groove during the screening operation), the most successful designs have used electrolessly plated metal contacts [40].

Cell processing bears some resemblance to the screen printing sequence previously described. After saw damage removal and texturing, the surface is lightly diffused and an oxide grown over the entire surface. This oxide serves multiple purposes during cell processing and is the key to the relative simplicity of the processing. Note that there is no need to remove the diffusion oxide as in the screen printed approach. Grooves are then cut into the top cell surface either using a laser scribing machine, mechanical cutting wheels, or other mechanical or chemical approaches.

After cleaning of the grooves by chemical etching, these are subject to a second phosphorus diffusion, much heavier than the first. This produces selective doping in the contact areas (previously discussed as desirable in connection with screen printed cells and as used in high efficiency silicon PERL cells). Aluminium is then deposited on the rear surface by evaporation, sputtering, screen printing or plasma deposition.

After firing of the aluminium and etching to remove oxides, cell metallisation is then completed by electroless plating of a nickel/copper/silver layer. A thin layer of nickel is first deposited. This is then fired and a substantial thickness of copper then deposited. Finally, the thin layer of silver is formed on the top surface by displacement plating. All these processes are electroless meaning that canisters containing the wafers are simply immersed in the plating solution.

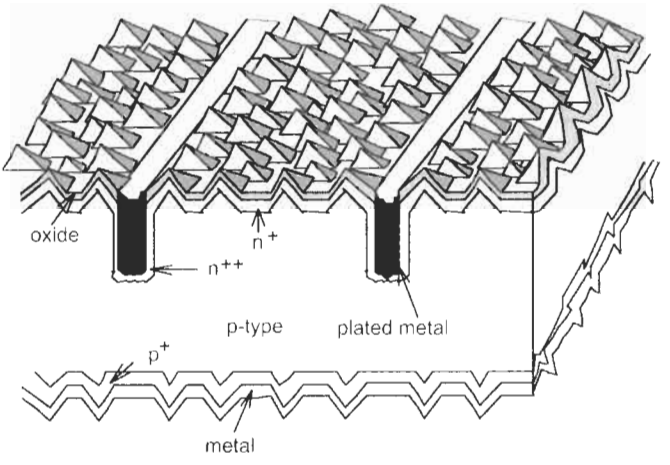

Figure 10 Buried contact solar cell.

An improved sequence uses Si_3N_4 in lieu of the oxide during the processing [41]. This layer withstands high temperature steps while giving better antireflection properties in the final cell. BP Solar have reported excellent results with this approach [41–43] as has the University of Konstanz where a record 17.5% efficiency has been demonstrated on large-area multicrystalline silicon substrates with this approach [44].

4.2 Performance Analysis

The buried contact cell gives substantial performance advantage over screen printed cells. Figure 11 shows the comparison reported by BP Solar, using identical starting substrate material. Approximately 30% performance advantage is reported in this case, although incremental improvements in screen printed cells have since reduced some of this gap. At the same time, BP Solar report that processing costs *per unit area* are virtually identical, within 4% of that of the screen printed cell [42]. This gives a much lower cost/watt, given the higher power output per unit area. Although capital costs are higher, the lower material costs compensate. A study involving representatives of several European manufacturers and research institutes reached essentially identical conclusions [32].

There are several reasons for this improved performance. The higher fill factor is due to the better conductance of the metallisation fingers and the lower contact resistance between these and the heavily doped grooved regions. The higher voltage is due to the high sheet resistivity; of the diffusion over the top surface, combined with the excellent surface passivation provided by the overlying oxide in these areas, and with the contact passivation provided by the heavy doping in the grooved areas. An open-circuit voltage approaching 700 mV has been demonstrated for this combination, close to the highest ever demonstrated for laboratory silicon cells [45].

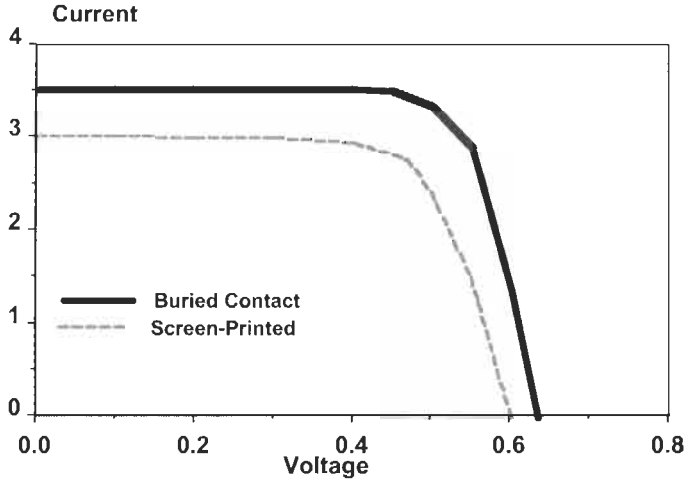

Figure 11 Output characteristics of buried contact cells compared to screen printed cells (after [43]).

The high current output is due to the relatively low top surface shading feasible with this approach even in large area cells. This is a result, most fundamentally, of the high aspect ratio possible with buried contacts. Aspect ratios as high as 5:1 have been demonstrated, although not essential in some metallisation design approaches. Low metallisation linewidths of 15–20 μm are feasible with laser grooving and linewidths of 40 μm are feasible with mechanical approaches. The low metallisation loss also makes the approach very well suited for the increasingly large size of commercial cells, an aspect hinted at, but not fully explored, in an earlier study [32]. The other contributor to the improved output current is the improved blue response resulting from the almost ideal surface properties in non-contacted areas.

The processing sequence has also shown itself capable of producing considerable gettering benefits during processing. The damage during the grooving process appears to be beneficial. Laser damage can produce effective gettering when applied to the rear of the wafers. Similarly, the laser grooves on the top surface might be expected to be effective gettering sites. One of the advantages of the buried contact sequence is that after grooving, the top surface is subjected to a heavy diffusion in the grooved areas. The phosphorus will diffuse preferentially in damaged areas and automatically passivate damage introduced by the grooves. Direct evidence for this effect has been observed [46]. Aluminium on the rear these cells provides another well established gettering strategy as does heavy phosphorus diffusion as used in the grooved areas [47].

4.3 Production Experience

Buried contact solar cell technology has been licensed to several major cell manufacturers, with pilot production experience reported by some. A

high-efficiency array was fabricated by Telefunken [48] for the Swiss car 'Spirit of Biel', which convincingly won the 1990 World Solar Challenge, the solar car race from Darwin to Adelaide. Array efficiency was 17%, then, the highest ever for silicon. The array gave 25% more power than that of the second placed car, which used enhanced screen printing technology [49].

BP Solar has reported on both manufacturing yields and process economics [41]. Using the same 'solar grade' CZ substrates as in their screen printing process, BP reports substantial efficiency improvement for the technology (~30%) and cell efficiencies of 17.5–18%. Economic analysis shows that the approach, as developed by BP with nitride antireflection coating, is well suited for polycrystalline material [41]. BP Solar supplied modules for the first reasonably sized installation using buried contact technology, a 20 kW system powering the Marzili furnicular railway in Berne. This was the most efficient flat-plate system of this size installed up to this time [50]. BP Solar also supplied 550 kW of these modules for the 1 MW Union Fenosa system near Toledo in Spain [51]. When it began operation in 1994, this was Europe's largest PV installation. In 1994, BP Solar launched the Saturn 585 module, an 85 W module based on 123 mm square buried contact solar cells as its 'top-of-the-line' commercial product [52], with module size more recently doubled to 170 W [1]. Production capacity at BP Solar was reported to be 10 MW/year in 1998, with an increase to 80 MW/year planned to be in place by 2004.

Solarex, since incorporated into BP Solar, has reported preliminary work using mechanical dicing wheels to form the grooves [53]. Experiments at UNSW with 35 ganged dicing blades have produced grooves of 2% depth uniformity over the wafer surface with a processing time of 3 s/cell. The attraction of this approach is lower equipment costs, although consumable costs are higher than with laser grooving. A small pilot production line operated by Unisearch Ltd in conjunction with UNSW has also given good yields of laser grooved cells with efficiencies of 19–20% demonstrated in production volumes of 10,000 cells per year [54].

The consensus of these pilot line and production studies is that the buried contact process, when transferred into production, can give efficiency margins of 20–30% over screen printing. Although more processing steps are involved than in the simplest screen printing approach, expensive silver pastes are eliminated so that processing costs per unit area are not greatly different, with costs per watt of product lower [32, 55]. Marketing experience has shown that higher selling prices are feasible for this product due to the lower balance of systems costs in installed systems and the perceived higher quality due to the superior performance.

5 HIT Cell

The HIT cell (heterojunction with intrinsic thin layer) combines both crystalline and amorphous silicon cell technology to produce cells with conversion efficiency in production similar to the buried contact cell and some of the highest

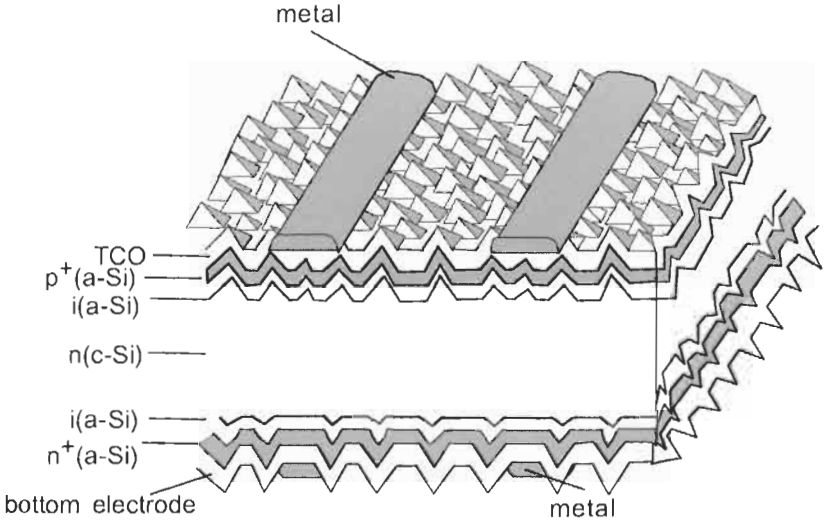

Figure 12 HIT cell structure using a textured n-type silicon wafer with amorphous silicon heterojunctions on both front and rear surfaces.

efficiency large area laboratory devices ever reported. The basic device structure is shown in Figure 12.

The starting substrate is an n-type silicon wafer, the opposite polarity from most other commercial product. This is a fortunate choice since such substrates are free from the light induced degradation effects that limit the performance of cells made on p-type, boron doped substrates, attributed to the formation of boron-oxygen complexes under illumination. After texturing, very thin layers of intrinsic hydrogenated and p-type amorphous silicon are deposited on the top surface and intrinsic and n-type on the rear surface. As is usual in amorphous silicon technology, these layers are contacted by transparent conducting oxide (TCO) layers, in turn contacted by screen printed metal contacts.

The low sheet resistivities possible with these TCO layers relax the constraints previously described on the screen printed metallisation parameters. However, these layers are quite absorbing and the underlying doped layers of amorphous silicon are inactive for photocurrent collection, resulting in poor blue response of the cell. About 10% of available current is lost by absorption in these layers. However, the bandgap of amorphous silicon is very much higher than in silicon and the quality of the interface between the amorphous and crystalline material is excellent. This good interface has produced some of the highest open-circuit voltages seen in silicon cells (710–720 mV).

This approach has produced record large-area laboratory cell performance of up to 21.0% [56, 57]. The differences between these laboratory devices and commercial devices are not clear. Commercial devices have more modest efficiencies but nonetheless result in a nominal module efficiency of 15.2% in Sanyo's 'top of the line' product, the highest value presently quoted [1]. Sanyo appears to have produced about 16 MW of HIT cell product during 2001 [58].

6 Nitride-Based Approaches

6.1 Remote Plasma Passivation

One limitation of the HIT cell structure arises from the absorption in the amorphous silicon layer and in the transparent conductor required on top of it to provide lateral conductivity. However, over the last decade, one development of note in silicon photovoltaics has been the use of remote plasma passivation, both of surfaces using silicon nitride [59] and of bulk regions using hydrogen [60].

The low temperatures associated with this passivation step give the potential for the relatively simple processing of high performance devices. It seems it should be possible to develop relatively simple high efficiency approaches based on this approach. Some of the work being conducted in this area is discussed in the following sections.

6.2 MIS-n^+p or MINP Approaches

The MINP cell structure of Figure 3 was important in the history of cell development since it produced the first 18% efficient cell, demonstrating the first improvement in silicon cell performance for close to a decade [17]. More recent work has sought to simplify the structure while incorporating the benefits of nitride surface passivation.

The challenge is to find a simple approach to obtaining the fine linewidths required for good performance. One approach uses a metal shadow masking process to produce the device structure of Figure 13 on multicrystalline wafers. The basic sequence is gettering of the starting wafer by a heavy phosphorus diffusion, removal of the gettering layer, diffusion of the n^+ emitter, evaporation of an Al grid on the cell rear, alloying at 850°C to form a local back surface field (LBSF), passivation of the rear by remote plasma nitride and evaporation of a rear Al contact/reflector over the entire rear surface, evaporation of the front Al contact onto a thin thermally grown tunnel oxide, also patterned using a shadow mask, followed by remote plasma nitride antireflection coating. An alternative sequence avoids the first patterned rear Al deposition step by instead patterning the nitride by mechanical abrasion.

A key result with this approach has been the demonstration of 18% cell efficiency on multicrystalline wafers [60], one of the highest values obtained for a cell larger than 1 cm^2 area, despite the relative simplicity of the approach. Problem areas are the use of shadow masks which are wasteful of deposited material, and rear shunting problems when the simpler technique above is used [60].

An alternative approach avoids the use of shadow masks by combining the mechanical abraded rear approach with obliquely evaporated contacts (OECO) onto a mechanically structured top surface. Using crystalline substrates with chemical texturing of the front surface (Figure 14) after larger scale mechanical structuring has resulted in large area cells of efficiency of 20%, using float-zoned substrates [61].

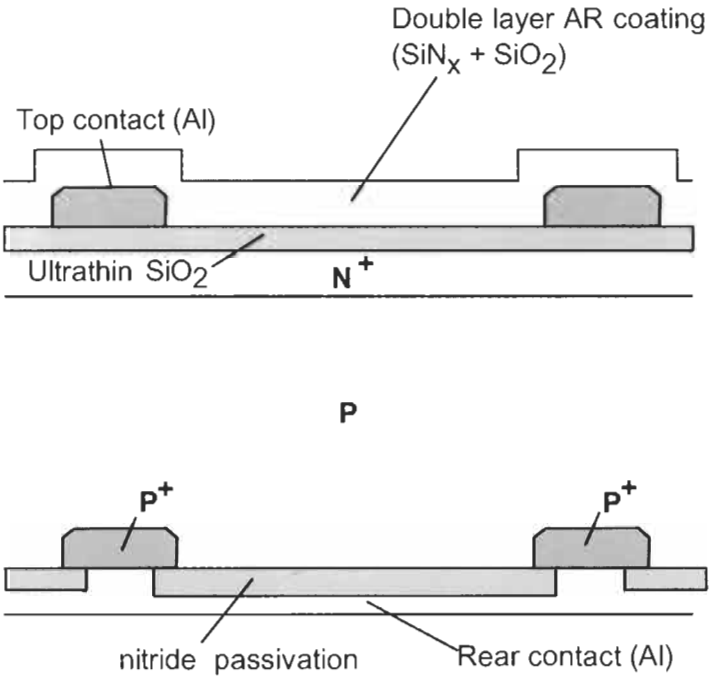

Figure 13 Simplified MINP cell fabricated using metal masks.

7 Conclusions

With the costs of present wafer-based silicon approaches dominated by material costs, particularly those of the wafers, encapsulants and low-iron tempered glass superstrates, increasing cell efficiency is an effective, if often counter-intuitive, approach to reducing the cost of the final product. Processing costs can be allowed to double if this results in a 20% improvement in cell performance. Work that stresses the trimming of processing costs at the expense of cell efficiency is not always as sensible as it might at first appear, in such a material-cost-dominated scenario.

Recent years have seen a diversification of manufacturing into higher efficiency approaches. Several manufacturers have realised the potential of plasma nitride based processing sequences to improve the performance of standard screen-printed cells on both multicrystalline and crystalline substrates, as first documented close to 20 years ago by Kyocera [62].

More revolutionary departures from the standard approach have been made by BP Solar, with its 'top of the line' Saturn processes, based on laser grooved, buried contacts, and Sanyo, with its crystalline/amorphous silicon hybrid HIT cells. These cells have demonstrated a clear advantage over standard cells in production, resulting in product with a clear performance margin.

In production, there is still the potential to capture more of the improvements in silicon cell performance that have been demonstrated in the laboratory. One

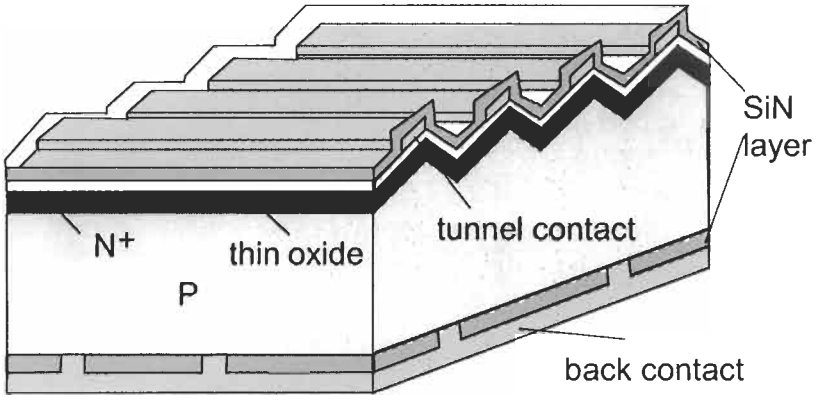

Figure 14 Possible implementation of a maskless MINP process on a mechanically textured wafer using oblique evaporation of top contact to eliminate this mask and mechanical abrasion to provide rear contact.

factor that has only quite recently been recognised as an impediment to this has been the tendency for boron-doped silicon to form an active boron-oxygen defect under illumination, restricting the quality of fielded material.

Several strategies, including the use of other dopants, have been suggested as a way of avoiding this problem. If successful, this gives rise to the possibility of material of much higher quality than currently used with only slight modification to the crystal growth economics. Such a development would increase the margin between the basic screen-printing and the more sophisticated approaches, giving real prospects for commercial cell efficiencies above 20%.

Acknowledgements

The author gratefully acknowledges an Australian Government Federation Fellowship. The Centre for Third Generation Photovoltaics is supported under the Australian Research Council Research Centre Scheme. The author thanks the Centre for Photovoltaic Engineering for its permission to reproduce material and figures from the text 'Silicon Solar Cells: Advanced Principles and Practice'.

References

[1] Schmela, M., 2003. Multicultural on the Roofs: Market Survey on Solar Modules, *Photon International*, February, pp. 32–41.

[2] Smith, K.D., Gummel, H.K., Bode, J.D., Cuttriss, D.B., Nielson, R.J. and Rosenzweig, W., 1963. The Solar Cells and their Mounting. *Bell Sys. Tech. J.*, Vol. 41, pp. 1765–1816.

[3] Iles, P.A., 1970. Increased Output from Silicon Solar Cells. *Proc. 8th IEEE Photovoltaic Specialists Conf.*, Seattle, pp. 345–352.

[4] Gereth, R., Fischer, H., Link, E., Mattes, S. and Pschunder, W., 1970. Silicon Solar Technology of the Seventies. *Proc. 8th IEEE Photovoltaic Specialists Conf.*, Seattle, p. 353.

[5] Gereth, R., Fischer, H., Link, E., Mattes, S. and Pschunder, W., 1972. *Solar Cell Technology Energy Conversion*, Vol. 12, pp. 103–107.

[6] Mandelkorn, J. and Lamneck, J.H., 1973. A New Electric Field Effect in Silicon Solar Cells. *J. Appl. Phys.*, Vol. 44, p. 4785.

[7] Godlewski, M.P., Baraona, C.R. and Brandhorst, H.W., 1973. Low-High Junction Theory Applied to Solar Cells. *Proc. 10th IEEE Photovoltaic Specialists Conf.*, Palo Alto, pp. 40–49.

[8] Lindmayer, J. and Allison, J., 1973. The Violet Cell: An Improved Silicon Solar Cell. *COMSAT Tech. Rev.*, Vol. 3, pp. 1–22.

[9] Haynos, J., Allison, J., Arndt, R. and Meulenberg, A., 1974. The Comsat Non-Reflective Silicon Solar Cell: A Second Generation Improved Cell. *Int. Conf. on Photovoltaic Power Generation*, Hamburg, p. 487.

[10] Rudenberg, H.G. and Dale, B., 1961. Radiant Energy Transducer, US Patent 3,150,999, filed 17 February 1961.

[11] Zhao, J. and Green, M.A., 1991. Optimized Antireflection Coatings for High Efficiency Silicon Solar Cells. *IEEE Trans. Electron Devices*, Vol. 38, pp. 1925–1934.

[12] Fossum, J.G. and Burgess, E.L., 1978. High Efficiency p^+ n n^+ Back-Surface-Field Silicon Solar Cells. *Applied Physics Letters*, Vol. 33, pp. 238–240.

[13] Godfrey, R.B. and Green, M.A., 1979. 655 mV Open Circuit Voltage, 17.6% Efficient Silicon MIS Solar Cells. *Applied Physics Letters*, Vol. 34, pp. 790 793.

[14] Green, M.A., 1975. Enhancement of Schottky Solar Cell Efficiency above its Semiempirical Limit. *Applied Physics Letters*, Vol. 28, pp. 287–268.

[15] Lindmayer, J. and Allison, J.F., 1976. Dotted Contact Fine Geometry Solar Cell. US Patent 3,982,964, September 1976.

[16] Arndt, R.A., Meulenberg, A. and Allison, J.F., 1981. Advances in High Output Voltage Silicon Solar Cells. *Proc. 15th IEEE Photovoltaic Specialists Conf.*, Orlando, pp. 92–96.

[17] Green, M.A., Blakers, A.W., Shi, J., Keller, E.M. and Wenham, S.R., 1984. High-Efficiency Silicon Solar Cells. *IEEE Trans. on Electron Devices*, Vol. ED-31, pp. 671–678.

[18] Lindholm, F.A., Neugroschel, A., Arienze M. and Iles, P.A., 1985. Heavily Doped Polysilicon Contact Solar Cells. *Electron Device Letters*, Vol. EDL-6, pp. 363–365.

[19] Yablonovitch, E., Gmitter, T., Swanson R.M. and Kwark, Y.H., 1985. A 720 mV Open Circuit Voltage, SiO_X:c-Si:SiO_X Double Heterostructure Solar Cell. *Applied Physics Letters*, Vol. 47, pp. 1211–1213.

[20] Van Halen, P. and Pulfrey, D.L., 1985. High-Gain Bipolar Transistors with Polysilicon Tunnel Junction Emitter Contacts. *IEEE Trans. on Electron Devices*, Vol. ED-32, p. 1307.

[21] Tanaka, M., Taguchi, M., Takahama, T., Sawada, T., Kuroda, S., Matsuyama, T., Tsuda, S., Takeoka, A., Nakano, S., Hanafusa, H. and Kuwano, Y., 1993. Development of a New Heterojunction Structure (ACJ-HIT) and its Application to Polycrystalline Silicon Solar Cells. *Progress in Photovoltaics*, Vol. 1, pp. 85–92.

[22] Blakers, A.W. and Green, M.A., 1986. 20% Efficiency Silicon Solar Cells. *Applied Physics Letters*, Vol. 48, pp. 215–217.

[23] Saitoh, T., Uematsu, T., Kida, T., Matsukuma, K. and Morita, K., 1987. Design and Fabrication of 20% Efficiency, Medium-Resistivity Silicon Solar Cells. *19th IEEE Photovoltaic Specialists Conf.*, New Orleans, pp. 1518–1519.

[24] Callaghan, W.T., 1986. Evening presentation on Jet Propulsion Lab. Photovoltaic activities. *Proc. 7th European. Photovoltaic Solar Energy Conf.*, Seville.

[25] Sinton, R.A., Kwark, Y., Gan, J.Y. and Swanson, R.M., 1986. 27.5% Si Concentrator Solar Cells. *Electron Device Letters*, Vol. EDL-7, p. 567.

[26] King, R.R., Sinton, R.A. and Swanson, R.M., 1988. Front and Back Surface Fields for Point-Contact Solar Cells. *Proc. 20th IEEE Photovoltaic Specialists Conf.*, Las Vegas, pp. 538–544.

[27] Blakers, A.W., Wang, A., Milne, A.M., Zhao, J., Dai, X. and Green, M.A., 1989. 22.6% Efficient Silicon Solar Cells. *Proc. 4th International Photovoltaic Science and Engineering Conf.*, Sydney, pp. 801–806.

[28] Green, M.A., 1995. *Silicon Solar Cells: Advanced Principles and Practice*. Bridge Printery, Sydney.

[29] Green, M.A., Zhao, J., Wang, A. and Wenham, S.R., 1992. 45% Efficient Silicon Photovoltaic Cell Under Monochromatic Light. *IEEE Electron Device Letters*, Vol. 13, pp. 317–318.

[30] Green, M.A., Zhao, J., Blakers, A.W., Taouk, M. and Narayanan, S., 1986. 25-Percent Efficient Low-Resistivity Silicon Concentrator Solar Cells. *IEEE Electron Device Letters*, Vol. EDL-7, pp. 583–585.

[31] Cuevas, A., Sinton, R.A. and Swanson, R.M., 1990. Point- and Planar-Junction P–I–N Silicon Solar Cells for Concentration Applications, Fabrication, Performance and Stability. *Proc. 21st IEEE Photovoltaic Specialists Conf.*, Kissimimee, pp. 327–332.

[32] Bruton, T., Luthardt, G., Rasch, K-D. Roy, K., Dorrity, I.A., Garrard, B., Teale, L., Alonso, J., Ugalde, U., Declerqu, K., Nijs, J., Szlufcik, J., Rauber, A., Wettling, W. and Vallera, A., 1997. A Study of the Manufacture at 500 MWp p.a. of Crystalline Silicon Photovoltaic Modules. *Proc. 14th European Photovoltaic Solar Energy Conf.*, Barcelona, pp. 11–26.

[33] Green, M.A. and Wenham, S.R., 1995. Silicon Cells: Single Junction, One Sun, Terrestrial, Single- & Multi-Crystalline. In: Partain, L., Ed., *Solar Cells and Their Applications*, Wiley, New York.

[34] Final Report, Flat Plate Solar Array Project, Vol. V, *Jet Propulsion Laboratory*, Publication 86-31, October 1986.

[35] Mertens, R., 1994. Silicon Solar Cells. *Proc. 12th European Photovoltaic Solar Energy Conf.*, Amsterdam, pp. 1–6.

[36] King, R.R., Mitchell, K.W. and Gee, J.M., 1994. Back Surface Cell Structures for Reducing Recombination in CZ Silicon Solar Cells. *Proc. First World Conf. on Photovoltaic Energy Conversion*, Hawaii.

[37] Wenham, S.R., Willison, M.R., Narayanan, S. and Green, M.A., 1985. Efficiency Improvement in Screen Printed Polycrystalline Silicon Solar Cells by Plasma Treatments. *Proc. 18th IEEE Photovoltaic Specialists Conf.*, Las Vegas, p. 1008.

[38] Szlufcik, J., Elgamel, H.E., Ghannam, M., Nijs, J. and Mertens, R., 1991. Simple Integral Screenprinting Process for Selective Emitter Polycrystalline Silicon Solar Cells. *Appl. Phys. Lett.*, Vol. 59, pp. 1583–1584.

[39] Mardesich, N., 1981. Solar Cell Efficiency Enhancement by Junction Etching and Conductive AR Coating Processes. *Proc. 15th IEEE Photovoltaic Specialists Conf.*, Kissimmee, pp. 446–449.

[40] Wenham, S.R., 1993. Buried-Contact Silicon Solar Cells. *Progress in Photovoltaics*, Vol. 1, pp. 3–10.

[41] Bruton, T.M., Mitchell, A. and Teale, L., 1991. Maximizing Minority Carrier Lifetime in High Efficiency Screen Printed Silicon BSF Cells. *Proc. 10th European Photovoltaic Solar Energy Conf.*, Lisbon, pp. 667–669.

[42] Bruton, T.M., Mason, N.B. and Summers, J.G., 1992. Towards Production of High Efficiency Terrestrial Solar Cells. *Proc. 6th International Photovoltaic Science and Engineering Conf.*, New Delhi, pp. 21–24.

[43] From data sheet, BP Saturn Solar Cells, 1991.

[44] Jooss, W., Fath, P., Bucher, E., Roberts, S. and Bruton, T., 2002. Large Area Multicrystalline Silicon Buried Contact Solar Cells with Bulk Passivation and Efficiency of 17.5%. *Proc. 29th IEEE Photovoltaic Specialists Conf.*, New Orleans, pp. 202–205.

[45] Honsberg, C.B., Yun, F., Ebong, A., Taouk, M., Wenham, S.R. and Green, M.A., 1994. 685 mV Open Circuit Voltage Laser Grooved Silicon Solar Cell. *Sol. Energy Mater. Sol. Cells*, Vol. 34, pp. 117–124.

[46] Chan, B.O., 1993. Defects in Silicon Solar Cell Materials. PhD Thesis, University of New South Wales.

[47] Sopori, B.L., Jastrzebski, L., Tan, T.Y. and Narayanan, S., 1994. Gettering Effects in Polycrystalline Silicon. *Proc. 12th European Photovoltaic Solar Energy Conf.*, Amsterdam, pp. 1003–1006.

[48] Boller, H.-W. and Ebner, W., 1989. Transfer of the BCSC-Concepts Into an Industrial Production Line. *Proc. 9th European Photovoltaic Solar Energy Conf.*, Freiburg, pp. 411–413.

[49] Kyle, C., 1991. Racing with the Sun: The 1990 World Solar Challenge. Engineering Society for Advancing Mobility: Land, Sea, Air and Space, SAE Order No. R-111.

[50] Knöpfel, H. and Nordmann, Th., 1992. 24 kW Photovoltaic Interconnected Network Installation to Power the Marzili Funicular Railway, Berne. *Proc. 11th European Photovoltaic Solar Energy Conf.*, Montreux, pp. 1475–1482.

[51] Alonso, M., Pottbrock, R., Voermans, R., Villa, J.J. and Yordi, B., 1994. 1 MW Photovoltaic Power Station Toledo/Spain – Plant Description and

Gained Experience during Construction – Toledo PV. *Proc. 12th European Photovoltaic Solar Energy Conf.*, Amsterdam, pp. 1163–1166.

[52] BP Saturn product sheet, April 1994.

[53] Wohlgemuth, J. and Narayanan, S., 1991. Buried Contact Concentrator Solar Cells. *Proc. 22nd IEEE Photovoltaic Specialists Conf.*, Las Vegas, pp. 273–277.

[54] Wenham, S.R., Wu, Y., Xiao, R.D., Taouk, M., Guelden, M., Green, M.A. and Hogg, D., 1992. Pilot Line Production of Laser Grooved Silicon Solar Cells. *Proc. 11th European. Photovoltaic Solar Energy Conf.*, Montreux, pp. 416–422.

[55] Bruton, T.M., 1994. Fabrication of Laser Grooved Buried Contact Si Solar Cells. *Proceedings 1st EU International Workshop on Crystalline Silicon Solar Cells*, Spain.

[56] Sakaata, H., Nakai, T., Baba, T., Taguchi, M., Tsuge, S., Uchihashi, K. and Kiyama, S., 2000. 20.7% Highest Efficiency Large Area (100.5 cm^2) HIT™ Cell. *Proc. 28th IEEE Photovoltaic Specialists Conf.*, Anchorage, p. 7.

[57] Green, M.A., Emery, K., King, D.L., Igari, S. and Warta, W., 2002. Solar Cell Efficiency Tables (Version 20). *Progress in Photovoltaics*, Vol. 10, pp. 355–360.

[58] Schmela, M., 2003. A Bullish PV Year: Market Survey on World Cell Production in 2001. *Photon International*, March, pp. 42–48.

[59] Aberle, A.G., 1999. *Crystalline Silicon Solar Cells*. University of New South Wales.

[60] Mittelstadt, L., Dauwe, S., Metz, A., Hezel, R. and Hassler, C., 2002. Front and Rear Silicon-Nitride-Passivated Multicrystalline Silicon Solar Cells with an Efficiency of 18.1%. *Progress in Photovoltaics*, pp. 35–39.

[61] Metz, A. and Hezel, R., 2001. Easy-to-Fabricate 20% Efficiency Large-Area Silicon Solar Cells. *Sol. En. Matls. Sol. Cells*, Vol. 65, pp. 325–330.

[62] Kimura, K., 1984. Recent Developments in Polycrystalline Silicon Solar Cell. *Technical Digest, 1st International Photovoltaic Science and Engineering Conf.*, Kobe, pp. 37–42.

Part IIc

Thin Film Technologies

Amorphous Silicon Solar Cells

David E. Carlson, BP Solar, Linthicum, Maryland, USA
Christopher R. Wronski, Center for Thin Film Devices, Pennsylvania State University, USA

1 Introduction

Significant progress has been made over the last two decades in improving the performance of amorphous silicon (a-Si) based solar cells and in ramping up the commercial production of a-Si photovoltaic (PV) modules, which is currently more than 40 peak megawatts (MW_p) per year. The progress in a-Si solar cell technology can be attributed to concurrent advances in the areas of new and improved materials, novel cell designs and in the development of large-area deposition techniques suitable for mass production. There are currently more than 40 research, development and engineering organisations at universities, companies and government laboratories around the world that are actively investigating a-Si PV technology.

The first investigation of amorphous silicon deposited from a silane discharge was performed by Chittik et al. in 1969 [1]. Subsequent work carried out on this material showed that it had a much lower density of defects than evaporated or sputtered amorphous silicon. The ability to dope this material both n- and p-type was independently discovered by Carlson [2] and Spear and LeComber [3]. Carlson and Wronski [4] showed that a-Si had useful optoelectronic properties when they reported the first results on a-Si solar cells with a conversion efficiency of 2% in 1976, and the efficiency was increased to 5% shortly afterwards [5]. These device results sparked a worldwide interest not only in a-Si solar cells but also in other applications. This heightened interest led to a wide range of fundamental studies on the a-Si alloys materials as well as a large effort to improve the performance of a-Si solar cells.

It soon became clear that hydrogen was playing an important role in determining the optoelectronic properties of these materials [6], and that discharge-deposited a-Si is actually an alloy of hydrogen and silicon or hydrogenated amorphous silicon (a-Si:H). Subsequently, many organisations started investigating the intrinsic optoelectronic and photovoltaic properties of a-Si:H alloys. In 1977, Staebler and Wronski [7] observed large changes in the photoconductivity and dark conductivity of a-Si:H when the material was exposed to sunlight. The metastable changes, commonly known as the Staebler-Wronski Effect (SWE), are perfectly reversible upon annealing at or above 150°C for a few hours [7]. These light-induced changes manifest themselves in both thin film materials and solar cells. The early discovery of the SWE had a critical effect on the development of a-Si solar cell technology by impacting the design of the devices and the optimisation of the a-Si:H alloys. Approaches were developed to minimise the effects of the SWE on the light-soaked (or stabilised) cell efficiencies, which rely on engineering the cells to have active layers as thin as possible [8].

The development of high-performance a-Si based solar cells and their technology advanced along several fronts. Continuous improvements were made in a-Si:H materials by investigating a wide range of deposition conditions for plasma-induced decomposition of silane, a process that is commonly referred to as plasma-enhanced chemical vapour deposition (PECVD). While the early deposition work was performed using primarily DC and RF PECVD [2],

subsequent studies showed that good quality a-Si alloys could be deposited using VHF [9] (~30–110 MHz) and microwave (~2.45 GHz) PECVD [10, 11]. These studies established the optimum decomposition conditions for a-Si:H and led to the development of commercial processes that allow a-Si solar cell structures to deposited on large-area substrates at relatively low substrate temperatures (~200–250°C) [12]. Other work established the highly beneficial effects of diluting the silane with hydrogen on the initial and stabilised properties of a-Si:H [13]. It is now recognised that hydrogen dilution leads to the growth of protocrystalline a-Si:H [14], which is now generally used in the fabrication of high-performance a-Si solar cells.

Another key advance in the development of a-Si:H alloys for solar cells was the discovery that the bandgap can be changed by varying the incorporation of hydrogen [15]. Moreover, as in the case of the crystalline materials, the bandgap of a-Si-based alloys can be varied by alloying with carbon or germanium. The development of wide bandgap p-type a-Si:C:H alloys has allowed the fabrication of heterojunction solar cells that exhibit very little absorption in the p-layer and also yield high built-in potentials [16]. The development of narrow bandgap a-Si:Ge:H alloys has led to the fabrication of both tandem and triple junction cells with relatively high efficiencies [17, 18]. While alloying with carbon or germanium does create additional defect states, relatively good optoelectronic properties can be obtained over bandgaps ranging from ~1.3 eV (~75 at.% Ge) to ~2.1 eV (~15 at.% C). This ability to tune the bandgap of a-Si based alloys has been an underlying factor in the improvement in the performance of a-Si based solar cells which has led to initial efficiencies as high as 15.2% [19]. The use of multijunction solar cell structures allows one to use relatively thin component cells, which in turn helps to reduce the degradation resulting from the SWE [8].

However, there are serious constraints imposed on the reduction in the thickness of the junctions since this leads to a decrease in the absorption of sunlight (and a corresponding decrease in short circuit currents) and also to an increase in shorts and shunts. The difficulty with low light absorption in thin cells was greatly reduced with the development of efficient optical enhancement obtained by introducing textured rather than smooth optical reflectors [20, 21]. Such optical enhancement, which was first successfully applied to a-Si based solar cells, is now extensively used in all types of thin film solar cells including thin film crystalline solar cells.

There has also been significant progress made over the last few decades in developing large-scale processing for a-Si based PV modules. All commercial a-Si based PV modules are fabricated using PECVD to deposit the a-Si alloy layers since excellent uniformity can be obtained over substrates more than 1 m^2 in area. In addition, early work at RCA Laboratories showed that most shorts and shunts could be cured by applying a reverse bias [22], and this curing process has allowed manufacturers to obtain relatively high yields in the production of large-area a-Si based PV modules [23]. Other work at RCA Laboratories led to the development of a laser scribing process that automatically patterned the a-Si on insulating substrates (such as glass) so that the resulting product was a large-area, monolithic PV module of a-Si solar cells connected in series [24].

2 Amorphous Silicon Alloys

The optoelectronic properties of amorphous silicon alloys vary over a wide range of parameters and are strongly influenced by the plasma deposition conditions used in PECVD reactors. In the this section, we will discuss the influence of the deposition conditions on the microstructure and optoelectronic properties, and also review the important aspects of doping and light-induced degradation.

2.1 Deposition Conditions and Microstructure

Although historically a variety of deposition methods has been used to deposit hydrogenated amorphous silicon, the most common method by far is PECVD, also known as glow-discharge deposition. The decomposition of the feedstock gases is carried out with plasmas that are generated over an extremely wide frequency range that includes DC, RF (13.56 MHz), VHF (30–110 MHz); and microwave (2.45 GHz) frequencies. A source gas such as silane (SiH_4) is decomposed by electron impact into a mixture of radical and ionic species that land on the substrate to produce the solid film. The PECVD process contains many variables that determine the quality of the materials produced: the substrate temperature, the pressure, the flow rate of the source gases, the plasma power, the frequency, the electrode spacing, and the source gases. In addition, the electronic properties of the a-Si alloys can be adversely affected by impurities such as oxygen, carbon and nitrogen [25, 26], which can be introduced by air leaks, residual water vapour and pump oil contamination.

The temperature of the substrate controls the reactions on the growing surface, and thus is a critical parameter in determining the quality of the materials. The gas pressure determines the mean free path for the collisions of the gas molecules and influences whether the reactions are at the growing surface or in the gas. The flow rate of the source gases is an important deposition parameter since it determines the residence time of the gas species in the plasma and hence affects the growth kinetics. The power controls the rate of dissociation of the gas and therefore also the film growth rate. The frequency used also affects the nature of the plasmas, and in particular the ion bombardment, which becomes less significant at VHF and microwave frequencies.

Finally, the nature of the plasmas and the growth processes also change with the introduction of the alloy forming gases, GeH_4 and CH_4, and with the addition of the n-type or p-type dopant gases. However, in all the types of depositions using PECVD, hydrogen plays a key role in reducing defects and improving the quality of the materials. The large number of variables are *interdependent* making PECVD a very complex process. This large number of variables, however, also makes the process and thus the material properties very flexible.

The a-Si alloy deposition process consists of four steps. First, the silane and hydrogen molecules are dissociated by electron impact into a reactive mixture of neutrals and radicals, which consists of a variety of radicals and ions of silane and hydrogen, unreacted silane, and higher silane species (such as disilane and trisilane). This mixture is then transported to the surface of the growing film via

gas diffusion, a process during which further chemical reactions of the different species can occur. The molecules arriving on the surface can then react with and adsorb to the growing film. Finally, the reaction byproducts, mainly hydrogen and unreacted silane radicals, desorb from or are etched off the surface by incoming reactive species, and are then pumped away. It has been established that high quality films with low defect densities are generally obtained with pure silane (or hydrogen-diluted silane), low RF power, and a substrate temperature of 200–300°C [27].

The low temperature PECVD process offers a number of technological advantages. Not only can it be readily scaled up to produce photovoltaic modules with very large areas, but this process also allows an extremely high degree of uniformity to be obtained over large areas. PECVD is also a deposition process that allows controlled changes in composition to be carried out during growth with very high precision.

The optoelectronic properties of the a-Si:H based materials depend very strongly on their microstructure and its evolution during growth. Because the hydrogen bonding is very sensitive to the deposition conditions, the presence of hydrogen in the plasma is closely related to the quality of material since it not only passivates dangling bonds, but it is also believed to be responsible for a reconstruction of the network [28, 29].

The beneficial effect of hydrogen available from the feedstock gases (such as SiH_4, GeH_4, CH_4, etc.) has been successfully augmented by diluting the feedstock gases with hydrogen gas (H_2) [30, 31], and this is being extensively utilised in the deposition of high-performance solar cells. The dilution with hydrogen has a large effect on the growth beginning with the nucleation and coalescence of the thin films and then in controlling the bulk as well as the growing surface [32]. With relatively low hydrogen dilution, for example $R = [H_2]/[SiH_4] = 10$, the growth of a-Si:H films not only becomes dependent on the nature of the substrate but the growth also changes so as to make the microstructure thickness dependent. As a result, during growth, the materials, which are initially amorphous, eventually become microcrystalline as the films become thicker.

Using in-situ real time spectroscopic ellipsometry [32], deposition phase diagrams have been developed that describe how the microstructure and phase evolve during the growth of Si:H films [33–36]. Such diagrams identify the thickness regime within which a-Si:H grows, the thickness regime which involves a transition to a mixed phase of amorphous and microcrystalline Si:H (μc-Si:H) and then the thickness at which the film becomes single-phase μc-Si:H. The hydrogen-dilution gas flow ratio is used most often as the key parameter in these phase diagrams since it provides the most direct control over the phase. However, the microstructure and phase can also be controlled by other parameters such as the substrate temperature, power and total gas pressure [37]. An example phase diagram is shown in Figure 1 for a-Si:H deposited as a function of the dilution gas flow ratio $R = [H_2]/[SiH_4]$ on a $R = 0$ amorphous silicon substrate (i.e., a-Si:H prepared without H_2-dilution).

The striking and key characteristic of the phase diagram in Figure 1 is how the hydrogen dilution affects the film thickness at which the transition from an

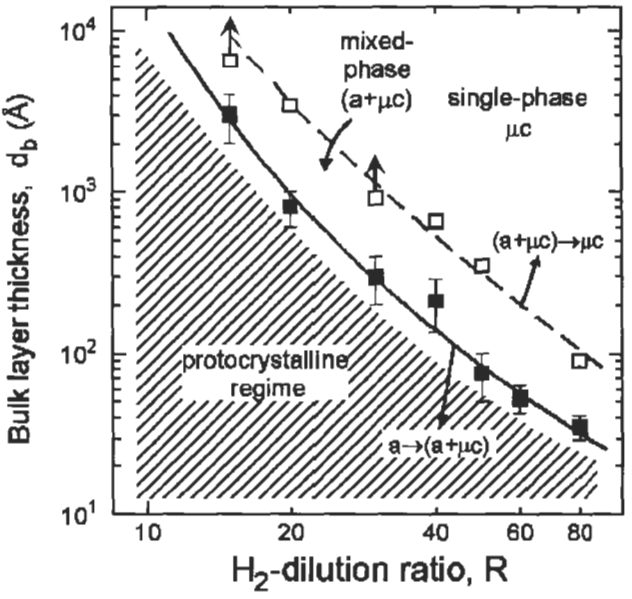

Figure 1 Film thickness, d_b, at which the different phase transitions occur during Si:H film growth plotted as a function of the hydrogen dilution ratio R.

amorphous to a mixed phase occurs. The rapid decrease in this thickness at high hydrogen dilutions has to be taken into account as it limits the thickness of the i-layers in cells that can be fabricated with purely a-Si:H. Such deposition phase diagrams have led to the concept of the *protocrystalline* Si:H growth regime, shaded in Figure 1 [14, 36].

Despite the evolutionary nature of the Si:H materials prepared with moderate hydrogen dilution, these materials exhibit uniform bulk properties over extended regions of thickness. In addition to the unique evolutionary growth behaviour exhibited under the protocrystalline Si:H growth conditions, the protocrystalline material itself exhibits unique optoelectronic properties. One of these is that the hydrogen incorporated into the protocrystalline Si:H with higher R increases its bandgap [38]. Consequently by taking into account the evolutionary nature it is possible to maximise the bandgap for different thickness layers while maintaining their excellent properties as protocrystalline a-Si:H [39, 40]. It also allows doped protocrystalline a-Si:H deposited with high R to be successfully applied in forming the p-contacts in n–i–p solar cells [41, 42]. Because these layers are very thin, the highest open-circuit voltages (V_{OC}) are obtained with protocrystalline p layers and not, *as has been extensively claimed* [43], with p-type microcrystalline Si:H, which actually results in low open-circuit voltages.

2.2 Optoelectronic Properties

The absence of long-range order broadens the distribution of states compared to crystalline Si, forming bandtails and a continuous distribution of localised states

in the gap that reduces the carrier scattering length to atomic distances. The localised states that lie in the bandgap are a result of the disorder and structural defects such as broken bonds [7, 44]. These gap states determine many of the electronic properties since they cause carrier trapping and act as recombination centres [45]. Amorphous silicon based alloys have a very high absorption coefficient due to the random nature of the atomic ordering so they behave like a direct bandgap semiconductor [46]. The electron densities of states are still a function of energy, but there is now a continuous distribution of localised states. The equivalent of the bandgap in crystalline silicon becomes a region of extended states in amorphous silicon where electrons and holes can move as free carriers. Both the strong light absorption and the values of the mobility gaps, which are adjustable by alloying, make a-Si:H attractive for solar cell technology since it offers the possibility of very thin cells as compared to crystalline silicon cells.

The bandgaps and optical absorption, α, of the a-Si:H based materials can be changed by the extent to which hydrogen, germanium and carbon are incorporated to form a-Si:H, a-SiGe:H and a-SiC:H alloys [15, 47, 48]. Incorporation of hydrogen into the a-Si:H network not only removes defects and their states in the gap, but also widens the gap. Using hydrogen dilution of silane, it is possible to obtain bandgaps of around 2 eV without deteriorating the microstructure and the electronic properties [38, 40]. However the rapid transition in the microstructure with high hydrogen dilution limits the protocrystalline a-SiH regimes to very thin layers, which does not allow them to be used as intrinsic absorber layers. As in the case of a-Si:H, hydrogen dilution allows one to deposit a-SiGe:H and a-SiC:H alloys with better microstructure, and hence lower defect densities. However, the electronic properties of a-SiGe:H and a-SiC:H alloys are not as good as a-Si:H, and their deterioration with the increase of either germanium or with carbon limits the range of bandgaps that can be used in efficient cells [30, 34, 49].

Both the bandgap and the densities of gap states can be changed by controlling the hydrogen content and the microstructure of a-Si:H. The densities of dangling bond defects is less than 10^{16} cm^{-3} in PECVD a-Si:H materials with a hydrogen content of $\sim$10 at.%, and the variation of the defect density with energy exhibits a rapid falloff in the vicinity of the tail states. The exponential regions of the optical absorption (α) between about 10^3 and 10 cm^{-1} arise from the absorption in valence band tail states, which are due to gap states introduced by the disorder [50]. The densities of the valence band tail states are significantly higher than those of the conduction band tails [51] even in the recently developed materials with a highly ordered network [52]. The absorption that is useful in creating free carriers in solar cells is at values of α greater than about 10^3 cm^{-1} which corresponds to photons with energies greater than the bandgap of the material. The phase transitions in protocrystalline a-Si:H set an upper limit of $\sim$1.9 eV for the bandgap of a-Si:H while the increase in defects with the incorporation of germanium set the lower limit at $\sim$1.3 eV for the bandgap of a-SiGe:H. These bandgaps, however, cover a sufficiently wide range to offer the flexibility required for constructing efficient single-junction, as well as multijunction solar cells.

A knowledge of the densities of states (DOS) and their energy distributions in the gap of a-Si:H is necessary for quantitative analysis that describes the role of both native and light-induced defects on the optoelectronic properties of the material. The determination of the complete density of states distribution for amorphous silicon is extremely difficult because there is no periodic structure and it is prepared under non-equilibrium conditions and is therefore metastable. Many models for the a-Si:H DOS have been proposed, all of which envisage conduction and valence band-tails. However, each model has distinctly different distributions of states near the middle of the gap. One distribution of densities of electronic states that is found useful in the self consistent interpretation of results of both a-Si:H films and cells is illustrated in Figure 2. The differences in the optical and electronic transport properties of amorphous silicon associated with such a DOS with those of its crystalline counterpart must be taken into account in the design of a-Si solar cells.

Deep lying gap states consist of neutral dangling-bond states (D^0) in the middle of the gap, negatively charged defect states (D^-) below the middle of the gap, and positively charged defect states (D^+) above the middle of the gap [53–55]. It is these deep lying states that are very important in determining the collection of photogenerated carriers in a-Si solar cells. Alloying with Ge has little effect on the tail states but a large effect on increasing the densities of the deep lying states.

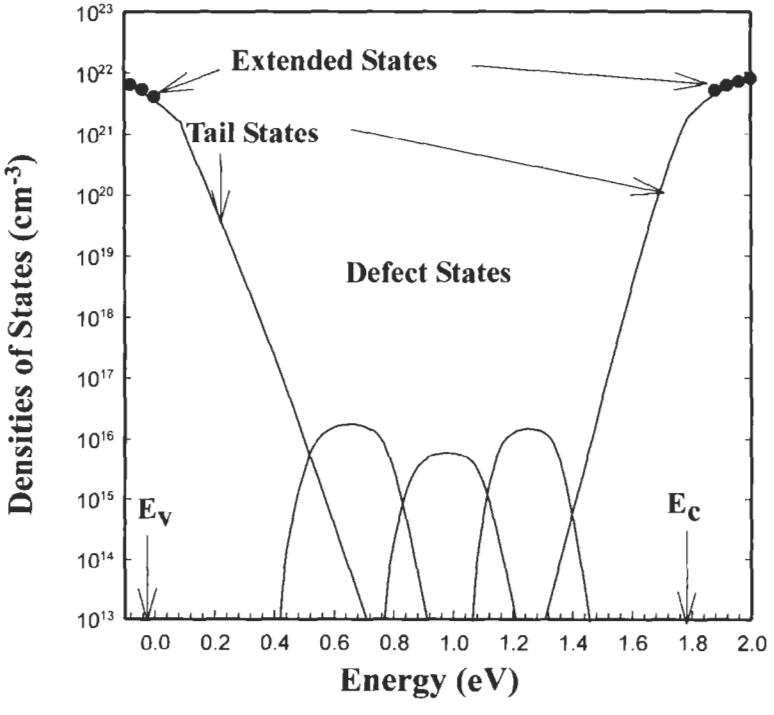

Figure 2 Schematic representation of the density of electronic state distribution in a-Si:H showing the conduction band edge (E_C), the valence band edge (E_V), the extended states, tail states, and defect states.

There is also little effect on the electronic properties of the materials with low levels of impurities such as O, N, C which are generally less than several times 10^{18} cm^{-3} [56]. The semiconductor properties and the stability of the a-Si:H based alloys, however, do depend on the growth processes, the incorporation of hydrogen and the resultant microstructure [13, 32, 57]. By optimising the growth conditions it has been possible to obtain a-Si:H materials with properties that are outstanding for an amorphous semiconductor. Intrinsic (undoped) materials have Fermi levels near the middle of the energy gap, and free carrier transport occurs in extended states with mobilities that are significantly lower than those in crystalline silicon, being only about 10 and 1 cm^2 V^{-1} s^{-1} for electrons and holes respectively [51].

The densities of the deep lying states, which are as low as 10^{15} to 10^{16} cm^{-3} in the a-Si:H based materials, are key to efficient solar cell operation. Consequently, the hole and electron lifetimes are in the range of 10^{-8} to 10^{-6} s, and the space charge densities in the junctions are low enough to allow the electric fields in the junctions to extend over the entire thickness of efficient solar cells [45]. The a-SiGe:H alloys retain good semiconductor properties with densities of midgap states around 10^{16} cm^{-3} even with about 60 at.% of germanium in the alloy. In the case of the a-SiC:H alloys, even a relatively low incorporation of carbon (< 10 at.%) has a large effect on the microstructure, and the resulting density of defects, especially after light soaking, is too high for use as an absorber layer in solar cells.

2.3 Doping

The undoped materials used in solar cells have the Fermi levels at or near midgap but are slightly n-type. Because the a-Si:H based materials have such low densities of midgap defects, they are the only amorphous materials that can be doped both n- and p-type. The introduction of donors or acceptors can readily move the Fermi level towards the conduction or the valence band, respectively. As in the case of crystalline silicon, n-type doping is achieved by incorporating phosphorous into the materials, and p-type doping by incorporating boron. The incorporation of high densities of these dopants however introduces defect states near midgap, which limit the doping efficiency and drastically reduce free carrier lifetimes [58]. As a result, doped materials cannot be used as active absorber layers in solar cells as is the case in p/n junction crystalline silicon solar cells.

Instead, thin films of either p-type a-SiC:H [59] or p-type protocrystalline Si:H [42] are used in p/i heterojunctions while n-type a-Si:H or n-type μc-Si:H layers are used as ohmic contacts. The p-type a-SiC:H and the p-type *protocrystalline*-Si:H materials result in excellent window contacts since their quasi Fermi levels are located about 0.4 eV and 50 meV from their respective valence bands. The n-type a-Si: H and n-type μc-Si:H provide excellent ohmic contacts to the i-layers since their Fermi levels are about 0.2 eV and 50 meV from their respective conduction bands. By incorporating such p-type and n-type materials into p-i–n and n–i–p cells, it is possible to obtain built-in voltages well over one volt [60]. The use of thin p-type and n-type contacts with absorber i

layers that have adjustable bandgaps and low densities of deep lying gap states offers great flexibility in efficiently absorbing and utilising different parts of the solar spectrum.

2.4 Light-Induced Degradation

Although hydrogenated amorphous silicon has many technologically attractive properties, there are several challenges regarding material properties that have yet to be overcome for further advances to be made in the technology. The most problematic of these is the Staebler–Wronski effect , which was discovered in 1977 [7]. It was found that not only did the illumination of glow-discharge deposited a-Si:H films with sunlight lower both the photoconductivity and dark conductivity, but even more striking was that these properties return to their as-deposited values after annealing at temperatures above ~150°C. The reversible changes that occur between the annealed, initial state and 'light-soaked' state have become one of the most investigated phenomena in a-Si:H based material and solar cells [61–64].

However, progress has been relatively slow in obtaining a definitive understanding and systematic control of the SWE and though advances have been made in the understanding of SWE, as of yet there is still no *general consensus* on *the exact nature* of the light-induced defects *or the mechanisms responsible for their creation*. This is in large part because unlike crystalline silicon there is no unique a-Si:H material, and a dependence not only of intrinsic but also of light-induced defects on the deposition conditions and resultant microstructure. However, there is general agreement that hydrogen, which is critical to the passivation of dangling bonds, also plays an important role in the SWE [55, 65–68].

This creation of defects by light severely limits the optoelectronic properties of the a-Si:H based materials since the metastable defects adversely affect not only the electron but also the hole transport, which results in a significant reduction of the performance of solar cells. Extensive studies have been carried out on thin film materials to characterise and understand the mechanisms responsible for the SWE [55, 61, 69, 70], and the results in the vast majority of these studies have been interpreted based on the creation of neutral dangling bonds. Strong evidence has been found in more recent studies carried out on *both* solar cells and corresponding intrinsic thin films that light-induced changes in the charged defects D^-, D^+ states are just as, if not more, important as the D^0 (neutral dangling bond) states [14, 71–74]. Significant progress has been made over the years not only in improving the initial properties of a-Si:H based material but also in reducing the light-induced degradation by optimising the growth conditions to improve the microstructure. The development of protocrystalline a-Si:H materials has resulted in solar cells that not only have higher initial efficiencies, but even more importantly better *end of life* performance [31, 75]. The significant improvements obtained with protocrystalline Si:H are illustrated in Figure 3, which shows the light-induced changes of the fill factor for a 4000 Å thick p–i–n solar cell with a

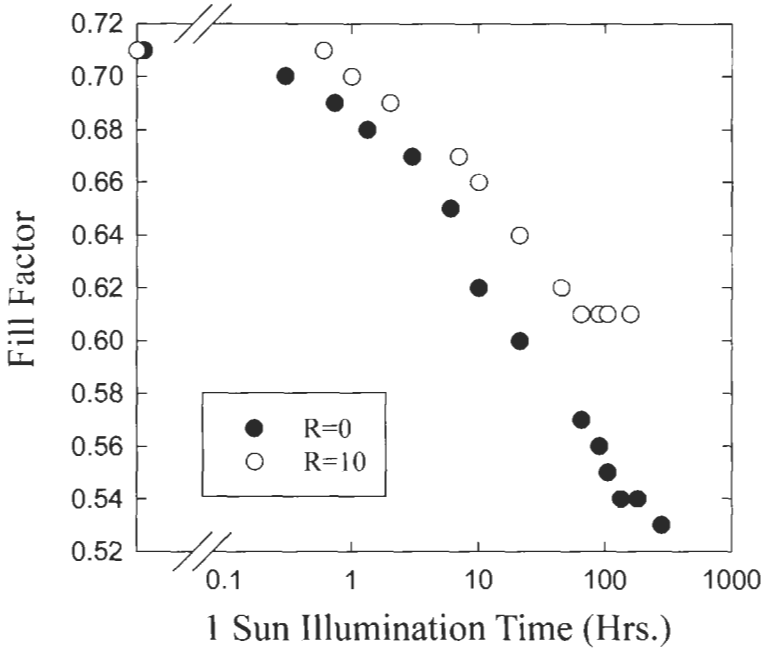

Figure 3 Degradation of the fill factor of a-Si:H p-i-n cells with undiluted (R=0) and protocrystalline (R=10) intrinsic layers under 1 sun illumination at 25°C.

protocrystalline (R = 10) a-Si:H i-layer and for a similar cell deposited under the same conditions with an undiluted (R = 0) intrinsic layer.

However, despite significant advances in improving the properties of a-Si:H based alloys, the fundamental understanding of the SWE *still remains a key issue* that has to be addressed and resolved to assure further improvements in the performance of solar cells based on a-Si:H alloys.

3 Amorphous Silicon Solar Cells

3.1 Physics of Operation

The operation of all solar cells is based on common physical principles. However, since efficient a-Si based solar cells rely on material properties distinctly different from those of crystalline silicon, the basic cell structures are somewhat different. In order to take advantage of the excellent properties of the intrinsic (undoped) a-i:H and a-SiGe:H materials, p–i–n and n–i–p heterojunction cell structures are used rather than the classic n/p junction structures in crystalline silicon. A schematic energy band diagram of an a-Si:H p–i–n structure generated by numerical simulation, using the distribution of defect states illustrated in Figure 2, is shown in Figure 4 under equilibrium conditions in the dark.

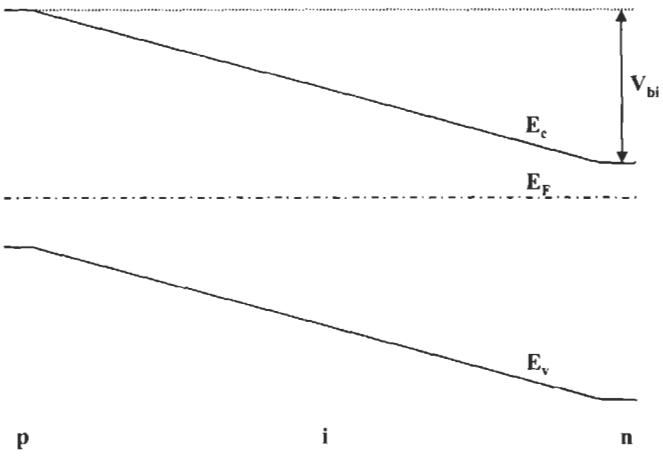

Figure 4 Energy band diagram of an a-Si p-i-n photovoltaic cell in thermodynamic equilibrium in the dark E_c and E_v are the conduction and valence band edges, E_F is the Fermi level and V_{bi} is the built in potential.

The p- and n-layers provide the built in potential of the junction in the device, however due to the short lifetime in the highly defective doped materials [58] the photogenerated carriers in the doped layers are not collected and do not contribute to the cell photocurrents. The fabrication of a p–i–n cell begins with the deposition of a p-type 'window layer' on the transparent conductive oxide (TCO). An a-Si:H intrinsic layer (i-layer) is deposited to form the bulk absorber region of the cell. The final step in forming the single-junction p–i–n cell is the n-layer deposition.

Important considerations for the choice of TCO materials are their optical transmission, conductivities and ability to form a good contact to the p-layers. The ideal TCO should have a low sheet resistance, high optical transparency in the wavelength range 400 to 1000 nm, and result in a small or ideally no potential barrier at the p/TCO interface. The band bending at the interface depends on the front contact material, the p-layer bandgap, doping and densities of states, as well as its thickness. In order to minimise optical absorption the p-type window layers used in high efficiency cells are thin (~10 nm), which increases the likelihood that they are fully depleted. In order to maximise the cell efficiency it is necessary to achieve a high V_{OC} using a very thin p-layer. If the p-layer is too thick the device performance will be adversely affected by the loss in the photocurrent due to the higher absorption in the thick p-layer.

Most of the important differences in the physics of a-Si based solar cells and crystalline silicon solar cells are a direct result of the most fundamental difference in the materials – the large density of localised gap states in a-Si:H. In a-Si solar cells, light that is absorbed in the i-layer will create electrons and holes, and the collection of these photogenerated carriers is assisted by the internal electric field. Due to the short carrier lifetimes associated with the localised gap states, the photogenerated carriers in a-Si based cells must be collected primarily as a drift current, not as a diffusion current as is the case in crystalline silicon

solar cells. These gap states have important ramifications on the cell performance since a large density of photogenerated carriers can become trapped in these states. The native and light-induced defects in a-Si p–i–n devices adversely affect the carrier collection in two ways – they act as recombination centres and also shield the electric field produced by the doped layers – which changes the electric field distribution in the i-layer. Under 1 sun illumination the carrier generation and recombination rates, the electric field distributions, and the carrier profiles in a-Si solar cells are highly non-uniform. The densities of native midgap defect states in a-Si solar cell materials are $\sim 10^{16}$ cm^{-3} in the as-deposited and annealed states. The effects of such a density of defects on the built-in field of an a-Si p–i–n solar cell is illustrated in Figure 5 where the magnitude of the field over the 0.4 μm thick i-layer, determined by the space charge density, is shown for both the equilibrium case of Figure 4 and for the open-circuit condition under 1 sun illumination. It can be seen in Figure 5 that under illumination the large number of excited carriers trapped in localised states exert a strong influence on the electric field distribution with a significant reduction in the field near the centre of the i-layer.

It should be noted that not only the i-layer but also the p/i interface region has a large influence on a-Si solar cell characteristics and the stability of the cells [39, 52, 76, 77]. 'Buffer layers' between the p- and i-layers are generally used to mitigate the detrimental effects of interface defects and thus improve solar cell

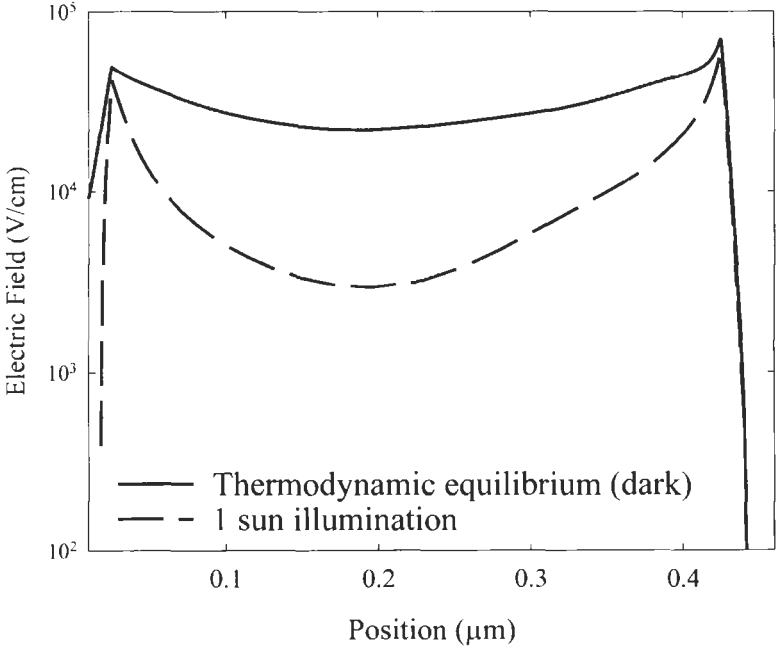

Figure 5 Electric field profile generated by a numerical simulation for a 4000Å thick single-junction a-Si p-i-n cell under thermodynamic equilibrium conditions and under 1 sun illumination at open-circuit conditions.

performance. Highly effective buffer layers have been obtained using protocrystalline Si:H materials fabricated with silane highly diluted with hydrogen [78, 79].

Open-circuit voltages in the amorphous cells just as in crystalline solar cells are determined by the quasi-Fermi level splitting, which depends on the density of photogenerated carriers and the bandgap (E_g); this in turn leads to the well-known dependence of V_{OC} on E_g [80]. Large values of the built-in potential (V_{bi}) are desirable not only in that they can limit the quasi-Fermi splitting but also because they determine the electric field across the i-layer, which is important in the collection of the photogenerated carriers. Over a large range of illumination intensities, the D^0, D^+ and D^- gap states determine the recombination and lifetimes, but at intensities approaching 1 sun illumination the quasi-Fermi level splitting is sufficiently large that the effect of the band tails has to be considered [81]. In addition, carrier recombination in the p/i interface regions can become more important than that in the bulk and can limit the open-circuit voltage under 1 sun illumination, particularly after the introduction of the light induced defects [82].

The short circuit current densities (J_{SC}) are determined by the collection of carriers photogenerated in the i-layer, which depends on its optical absorption and thickness as well as the ability to extract them from the cell. The amount of absorbed sunlight can be readily increased by making the i-layers thicker. However, field-assisted carrier collection is also sensitive to thickness, which results in a negative effect on carrier collection. This adversely affects not only J_{SC}, but generally has an even larger negative effect on the fill factor, since the internal fields are significantly reduced under load (forward bias). The challenge is not only to maximise the optical absorption, such as by increasing the thickness of the i-layer, but also at the same time retain the collection of carriers at a level necessary for high values of the fill factor. A major breakthrough in achieving this result is obtained with optical enhancement based on textured substrates and reflectors [20, 21]. This optical enhancement effect greatly increases the already high optical absorption at longer wavelengths so that significantly higher quantum efficiencies can be obtained at these wavelengths without any increase in the cell thickness. An example of improvements that can be obtained in the spectral response at long wavelengths using different reflectors on p–i–n cells is shown in Figure 6 for two (Cr, Ag) flat metal and two textured (detached, tuned) reflectors.

The fill factor is the cell parameter that is most sensitive to cell thickness as well as the nature and density of native and light-induced defect states in the gap [54, 55, 71, 83]. It is therefore not surprising that there is this strong dependence of the fill factors on the thickness of the i-layer. It should be noted that even though the p/i regions extend over a relatively thin region they can have a large effect on both carrier collection and the electric field distribution, which impacts not only V_{OC} but also the fill factor [40, 78]. The introduction of defects associated with the SWE reduces the free carrier lifetimes and increases the space charge [38, 72, 73]. Since the corresponding redistribution and lowering of the electric fields across the i-layers depend very strongly on their

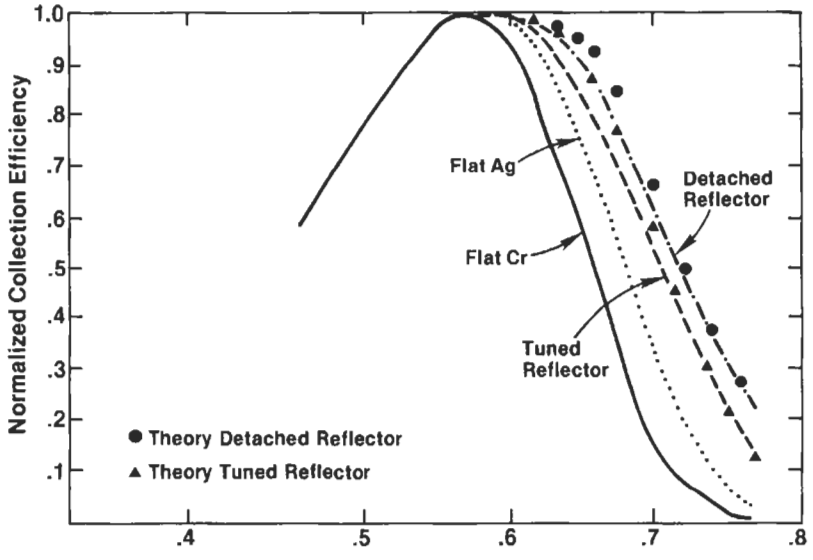

Figure 6 The experimental results for the collection efficiency as a function of wavelength for an a-Si p-i-n solar cell with flat Cr and Ag reflectors as well as a two different textured reflectors. The results are normalized to the peak quantum efficiency at 0.55 μm. Also shown as symbols are the theoretical results for tuned and detached reflectors.

thickness, the large effect on the fill factor is further amplified. This is the underlying reason for making the solar cells as thin as possible.

The development of tandem a-Si:H/a-SiGe:H and triple a-Si:H/a-SiGe:H/a-SiGe:H cell structures allows not only a larger fraction of the incident sunlight to be absorbed, but also allows this increased absorption to be achieved with thin intrinsic absorber layers. Since the optical enhancement is most efficient for the bottom absorber layer [19] and germanium alloying is used to increase the absorption in the bottom absorber layers, one is able to use relatively thin i-layers in the bottom cells. The thickness and optical absorption of each i-layer in a multijunction structure must be adjusted to assure that the same photocurrent is generated in each junction while under 1 sun illumination.

3.2 Device Structures

Amorphous silicon solar cells have been fabricated in the laboratory in a wide variety of different structures [84, 85], but most commercial products utilise p–i–n or n–i–p junction configurations in either single-, double- or triple-junction structures [86]. Most manufacturers offer multijunction structures since they generally exhibit higher stabilised conversion efficiencies.

The device structures used for a-Si based solar cells can also be categorised according to the substrate material. PV Manufacturers such as BP Solar, Energy Photovoltaics, Intersolar, Kaneka, Phototronics, Sanyo, and Sharp use commercial float glass as a substrate while Canon and United Solar Systems use

stainless steel foil. In addition, some companies such as Fuji Electric, Iowa Thin Films and Sanyo deposit a-Si solar cells on plastic substrates.

Generally, a p–i–n junction configuration is used with glass substrates so that the light is incident on the glass and passes first through the p-layer side of the cell (this is sometimes referred to a glass superstrate structure). An example of a glass superstrate cell structure is shown in Figure 7. This is a device structure used by BP Solar in the Toano, VA manufacturing plant and has the configuration: glass/textured tin oxide/p–i_1–n/p–i_2–n/zinc oxide/aluminum/EVA/glass where the i_1-layer is an a-Si:H alloy, the i_2-layer is an a-SiGe:H alloy and EVA is ethylene vinyl acetate.

BP Solar buys commercial tin oxide coated soda-lime-silicate glass and has another company seam the edges of the glass, apply a conductive frit and heat-strengthen the glass. The glass companies deposit a layer of silicon dioxide or a similar layer on the glass to obtain uniform nucleation of the textured tin oxide so as to assure a uniform appearance. The textured tin oxide has a surface roughness on the order of a few hundred nm, which scatters the light as it enters the cell leading to increased absorption of the longer-wavelength radiation.

The first junction is formed by depositing a thin p-layer (~10 nm of a boron-doped a-SiC:H alloy) on the tin oxide, followed by ~160 nm of an a-Si:H i-layer and then ~10 nm of phosphorus-doped microcrystalline Si:H. A tunnel or recombination junction is then formed by depositing ~10 nm of another a-SiC:H p-layer. The second i-layer consists of ~100 nm of an a-SiGe:H alloy where the Ge content is varied so that the band gap of the junction is graded. The second junction is completed by depositing ~20 nm of a phosphorus-doped a-Si:H layer. The back contact is made by first depositing about 100 nm of zinc oxide by low-pressure chemical vapour deposition (CVD) and then sputter depositing about 300 nm of aluminium. The PV modules are then encapsulated using EVA and another sheet of heat-strengthened glass.

An example of an a-Si based multijunction cell structure fabricated on a stainless steel foil is shown in Figure 8. This is a device structure used by United Solar Corporation, which is starting up a new manufacturing facility with an

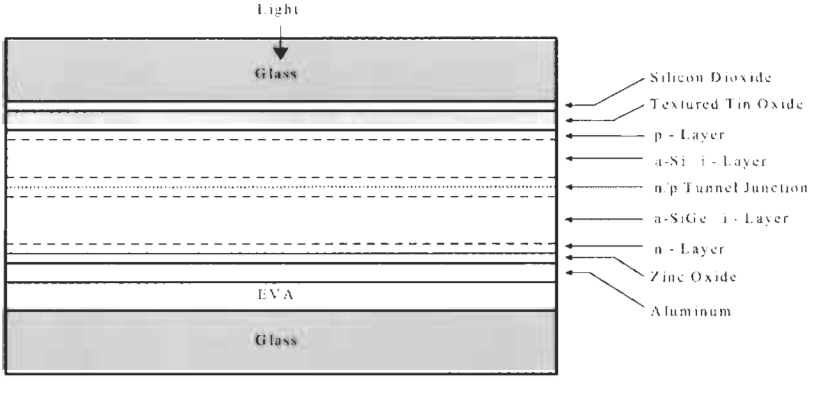

Figure 7 A schematic of an a-Si/a-SiGe tandem device structure fabricated on a glass substrate.

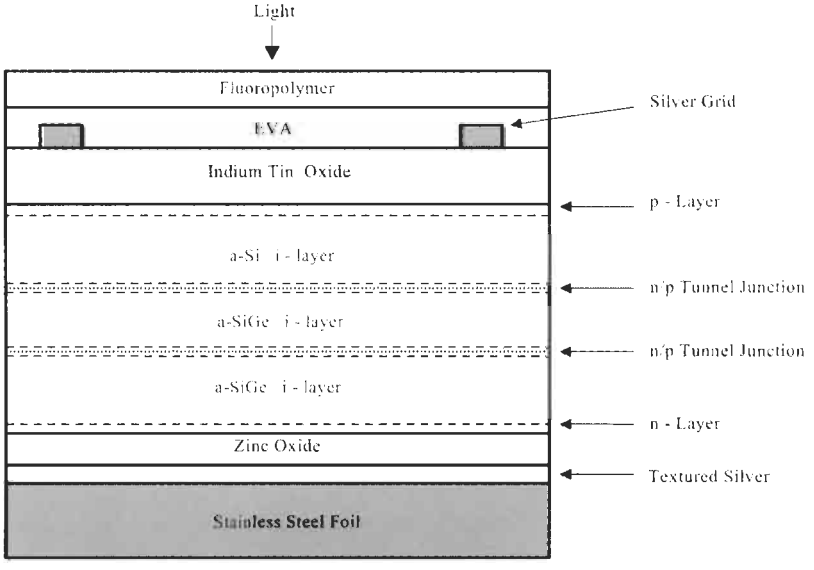

Figure 8 A schematic of a triple-junction device structure fabricated on a stainless steel substrate.

annual capacity of 30 MW_P. This type of device is constructed using an n–i–p configuration where the first a-Si layer deposited on the foil is an n-layer, and the triple-junction device has the configuration: stainless steel foil/textured silver/zinc oxide/n–i_3–p/n–i_2–p/n–i_1–p/ITO/EVA/fluoropolymer where both i_2 and i_3 are a-SiGe:H alloys, i_1 is an a-Si:H alloy, ITO is indium–tin–oxide and the fluoropolymer is typically Tefzel® (a fluoropolymer made by DuPont) [87].

This device structure is fabricated by forming a textured layer of silver or aluminium on the stainless steel foil and coating it with ~100 nm of zinc oxide before depositing the thin silicon semiconductor layers in a continuous process using a roll-to-roll, multi-chamber PECVD system [88]. The first semiconductor junction formed consists of ~20 nm of phosphorus-doped a-Si:H followed by ~130 nm of a graded a-SiGe:H i-layer (i_3) and then ~10 nm of boron-doped microcrystalline Si:H. The next junction is formed by depositing ~10 nm of phosphorus-doped a-S:H (which also forms a tunnel or recombination junction with the underlying p-layer), ~110 nm of another graded a-SiGe:H layer (i_2), which contains less Ge on average than the i_3-layer, and ~10 nm of boron-doped microcrystalline Si:H. The last junction is then formed by depositing ~10 nm of phosphorus-doped a-S:H (which forms another tunnel junction on the underlying p-layer), ~100 nm of a-Si:H (i_1) and ~10 nm of boron-doped protocrystalline Si:H. All the undoped layers (i-layers) are deposited using hydrogen dilution so that the films are close to becoming microcrystalline [88]. The top contact is formed by evaporating a conductive antireflection coating of indium–tin–oxide (ITO), and silver grids are then deposited to help collect the photocurrent. The device structure is completed by laminating the solar cell with EVA and Tefzel®.

Several companies are using other types of device structures that utilise amorphous silicon-based alloys. Phototronics and Energy Photovoltaics manufacture a-Si tandem PV modules on glass where both junctions consist of a-Si:H, and the i-layer thicknesses are adjusted so that they generate approximately the same photocurrent. Kaneka has been manufacturing single-junction a-Si PV modules on glass, and recently started production of a tandem module on glass that utilises a front junction of a-Si:H and a rear junction of microcrystalline silicon (~1–2 microns thick) [89]. Sanyo has developed a single-crystal silicon solar cell that utilises p/i and i/n a-Si:H heterojunction layers that are only 10–20 nm thick, and this type of device exhibits efficiencies as high as 21% in laboratory devices [90].

3.3 *Performance and Stability*

Present-day commercial a-Si based PV modules typically exhibit stabilised conversion efficiencies in the range of 6–8% while those based on single-crystal or polycrystalline silicon generally exhibit efficiencies in the range of 11–14%. The best stabilised efficiencies of a-Si based PV modules reported by a number of companies are listed in Table 1. In some cases, ranges of efficiencies are shown and were estimated from company product data.

For a small-area (0.25 cm^2) laboratory triple-junction cell, United Solar reported a stabilised conversion efficiency of 13.0% [87], which is the highest efficiency achieved to date in an a-Si based solar cell; the initial efficiency was 15.2%, which is also a record for an a-Si based solar cell.

Triple-junction cells typically exhibit light-induced degradation on the order of about 10–15% while tandem cells exhibit about 12–20% and single-junction cells about 18–30%, depending on a variety of factors such as the thickness of the i-layers and the deposition conditions. The light-induced degradation of a-Si based solar cells is strongly influenced by the thickness of the i-layer [8], and thus triple-junction cells which typically contain i-layers that are on the order of 100 nm thick usually exhibit less light-induced degradation than cell structures

Table 1 Stabilised efficiencies of a-Si-based PV modules

Company	Stabilised efficiency (%)/(aperture area)	Device configuration
BP Solar	8.1%/(0.36 m^2)	a-Si/a-SiGe tandem on glass
BP Solar	7.6%/(0.74 m^2)	a-Si/a-SiGe tandem on glass
Fuji Electric	9.0%/(0.32 m^2)	a-Si/a-SiGe tandem on plastic
Intersolar	~4.5–5.0%/(0.30 m^2)	Single junction on glass
Iowa Thin Films	~4.5–5.5%/(0.45 m^2)	Same gap tandem on plastic
Kaneka	8.1%/(0.41 m^2)	Single junction on glass
Kaneka	~10%/(0.37 m^2)	a-Si/μc-Si tandem on glass
Phototronics	~6.0–6.5%/(0.55 m^2)	Same gap tandem on glass
Sanyo	9.3%/(0.51 m^2)	a-Si/a-SiGe tandem on glass
United Solar	10.1%/(0.09 m^2)	Triple junction on steel foil
United Solar	7.9%/(0.45 m^2)	Triple junction on steel foil

with thicker i-layers (single-junction cells generally contain i-layers that are ~250–350 nm thick).

The effect of i-layer thickness and device structure on the light-induced degradation is shown in Figure 9. As shown in the figure, the tandem cell degraded about 12% after a few hundred hours of light soaking and then stabilised. The degradation of the single-junction cells varied from about 25% for a device with a 0.25 μm thick i-layer to about 50% for a device with a 0.60 μm thick i-layer. It is clear from the data in Figure 9 that most of the degradation occurred in the first week of exposure to simulated sunlight.

Outdoor testing of BP Solar tandem modules has shown that they stabilise in the first several months of outdoor exposure and then exhibit seasonal variations in performance associated with changes in the solar spectrum [91] and with changes in the ambient temperature [92]. Many of the a-Si PV arrays exhibit a sinusoidal variation in performance with a 1-year cycle time, which has been attributed to partial annealing of the light-induced degradation. However, as shown in Figure 10, some arrays such as the one at Montgomery College in Maryland exhibit a variation in performance (open circles) with a cycle time of six months. As also shown in the figure, this is the same cycle time exhibited by the plane of array irradiance (gray vertical lines) [91]. While the data collection at the Montgomery College array did not start until after the array had been exposed to sunlight for several months, it is evident from the figure that the output power of the array has remained essentially constant over the four-year period shown.

While the temperature behaviour of a-Si based solar cells can vary over a wide range depending on the device structure and material quality [93], the temperature coefficient of the output power of commercial a-Si PV modules is

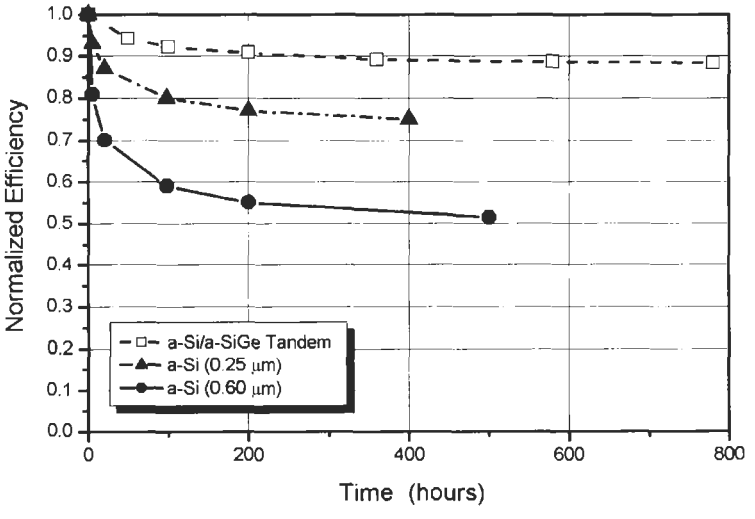

Figure 9 The conversion efficiency of different types of a-Si based solar cells as a function of exposure time to 1 sun illumination. (The initial efficiencies were in the 6 – 8% range.)

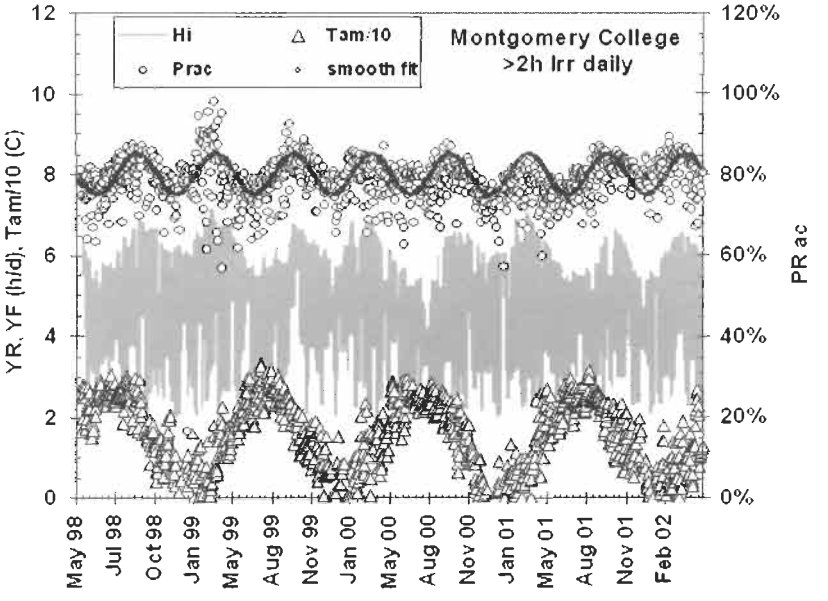

Figure 10 Performance of the BP Solar tandem module array at Montgomery College (Maryland) over a four-year period.

usually in the range of −0.2 to −0.3%/°C, which is about one half the value observed for crystalline silicon modules. However, some a-Si PV arrays have exhibited positive temperature coefficients [93, 94], which could be related to power conditioning effects or spectral effects [91]. Amorphous silicon solar cells that were light soaked and characterised at temperatures of 40 and 80°C in the laboratory exhibited relatively small temperature coefficients [93]. Thus while an a-Si PV module might exhibit a temperature coefficient for the power of about −0.25%/°C for short-term temperature excursions, the temperature dependence of stabilised a-Si PV arrays operating in a steady-state mode appears to be quite small due to annealing effects. However, the actual performance of a-Si PV arrays is also strongly influenced by other factors such as the solar spectrum and the power conditioning.

3.4 Reliability

While there is convincing field data that the latest generation of a-Si PV modules can operate reliably for periods of more than four years (see Figure 10), there are still concerns about the long-term reliability of thin-film modules. There are other factors besides light-induced degradation that can adversely influence the long-term performance of a-Si PV modules and arrays. The performance of all PV arrays can be adversely affected by a number of factors such as malfunctioning power conditioning equipment, failures associated with the wiring or interconnects between modules and damaged or degraded modules. One of the

major challenges for thin-film PV technologies is to assure good module reliability over operational periods of 20 years or more.

All PV modules are subjected to a battery of qualification tests, which have been developed to assure that the modules will meet all functional specifications after exposure to a variety of environmental conditions. The tests that simulate these exposures are specified in publications (IEC 1215, IEEE 1262 and UL 1703) issued by the International Electrotechnical Commission (IEC), the Institute of Electrical and Electronics Engineers (IEEE) and the Underwriters Laboratory (UL). The qualification procedure includes tests such as electrical performance, electrical isolation (dry and wet), visual inspection, thermal cycling between −40 and +85°C, light soaking, ultraviolet light exposure, humidity freeze cycling between −40 and +85°C (while maintaining a relative humidity of 85% for temperatures above room temperature), static and dynamic mechanical loading, hail impact tests, surface cut susceptibility, hot-spot endurance and outdoor exposure.

These qualification tests appear to work well for crystalline silicon modules since there have been many crystalline silicon PV arrays that have operated for over two decades or more in a variety of outdoor environments. However, other tests may need to be added to adequately qualify thin-film modules for reliable operation over 20 years of more in all outdoor environments. In general, thin-film PV modules appear to be more susceptible to moisture ingression problems than crystalline silicon modules since the contacting layers and semiconductor layers are very thin, and some of these layers can be delaminated or consumed by electrochemical corrosion [95, 96]. Thus, companies making thin-film PV modules are actively investigating ways to develop improved encapsulants that will not delaminate and that will minimise moisture ingression.

4 Production of Amorphous Silicon Solar Cells

The manufacturing process for a-Si solar cells can vary significantly depending on the type of substrate used to make PV modules. In this section, we will describe the manufacturing process used by BP Solar to make tandem modules on glass, the process used by United Solar to make triple-junction modules on stainless steel foil and the process used by Iowa Thin Films to make single-junction modules on plastic.

4.1 Manufacturing Process

The manufacturing process used by BP Solar to manufacture a-Si/a-SiGe tandem modules on glass is shown schematically in Figure 11. This plant has an annual capacity of 10 MW_P per year and produces PV modules on soda-lime-silicate float glass (each glass plate is 0.8 m^2 in area). BP Solar purchases glass that has been coated with textured tin oxide, conductive silver frit bus bars and has also been edge-seamed and heat strengthened before it is delivered to the plant. The production process starts with washing the glass plates and then transporting

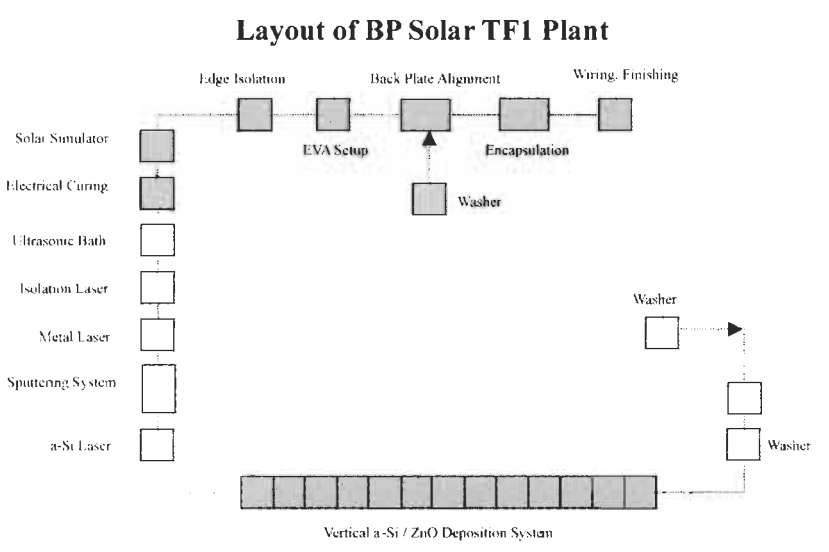

Figure 11 A diagram showing the layout of the BP Solar plant in Toano, VA.

them to a laser scribing station that segments the tin oxide layer and defines the operating characteristics (nominal voltage and current) of the module. The tin oxide is generally scribed into a series of parallel strips ~9 mm wide using a Nd:YAG laser that is frequency doubled to produce a green laser beam that is ~15 microns in diameter.

After the laser scribing process, the plates are washed and loaded in a multi-chamber PECVD system that deposits doped and undoped layers of amorphous silicon and microcrystalline silicon alloys to form an a-Si/a-SiGe tandem structure (see Figure 7). The last deposition chamber in this system uses low-pressure CVD to deposit a thin layer of ZnO. The a-Si and ZnO layers are then scribed using another Nd:YAG laser. After laser scribing, the plates are coated with a thin layer of aluminium using magnetron sputtering. The plates are then laser scribed again in close proximity to the earlier scribes to selectively remove all the layers other than the tin oxide. This laser-scribing step completes the series connection as shown in Figure 12 since the front contact of each strip cell is connected in series to the back contact of the next adjacent cell.

Next a final laser scribe is made at a relatively high power around the perimeter of the plates to ensure electrical isolation. The plates are then cleaned in an ultrasonic bath to remove all debris before passing to a bed-of-nails station that applies a reverse bias to electrically cure cells that are excessively leaky [22]. After electrical curing, the performance of the plates is determined using a solar simulator. Good electrical isolation is assured by using an abrasion wheel to remove all the thin films from the outside edge of the plate. The plates are then fabricated into modules by encapsulating a back plate of float glass to the front plate with ethylene vinyl acetate (EVA), attaching lead wires and mounting the module in a frame. The completed modules then undergo a final power test before they are shipped to customers.

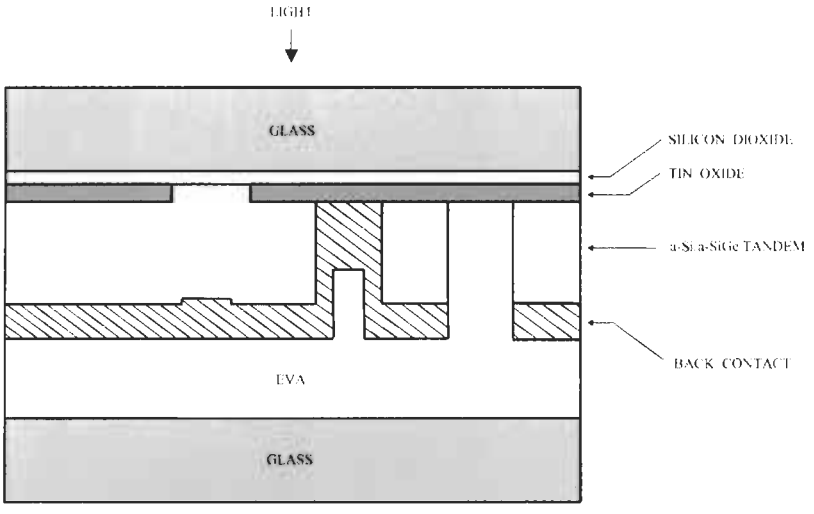

Figure 12 A schematic showing the interconnection region of a tandem module.

The distribution of the initial output power for a run of several thousand modules in the BP Solar TF1 facility is shown in Figure 13. When the light-induced degradation is taken into account, the stabilised power is about 14% less than that shown. The data in Figure 13 show that large-area a-Si PV modules can be produced with relatively high yields (greater than 80%).

Companies such as United Solar that use stainless steel foil as a substrate are using a roll-to-roll process to deposit an a-Si/a-SiGe/a-SiGe triple-junction structure [87]. United Solar has been operating a PV module manufacturing plant in Troy, Michigan since 1997 with an annual capacity of 5 MW_P. The starting substrate for this facility is a roll of flexible stainless steel foil that is about 0.8 km long and 35.6 cm wide on which they sequentially sputter-deposit aluminium and ZnO and then deposit nine a-Si alloy layers (see Figure 8) using a highly automated, multi-chamber PECVD system. They sputter ITO onto the a-Si structure to form a top-contacting layer, and they cut the foil into individual solar cells and apply a current-collecting metal grid onto the ITO. The cells are wired together, laminated with EVA and Tefzel®, fitted with electrical connectors or a junction box and framed to form an environmentally protected module. United Solar has also published data showing that their manufacturing process is capable of producing cells with yields greater than 80% [97].

United Solar is now starting up a new manufacturing plant in Auburn Hills, Michigan, with an annual capacity of 30 MW_P of triple-junction modules per year. This facility contains a multi-chamber PECVD system that is almost 100 m long and will process six rolls of stainless steel foil simultaneously, and each roll of steel foil is about 2.4 km long.

Companies such as Iowa Thin Films use a roll of polyimide plastic (0.05 mm thick) as a starting substrate in the production of another type of flexible a-Si PV module [98]. Each polyimide roll is about 33 cm wide and 0.73 km long. Iowa

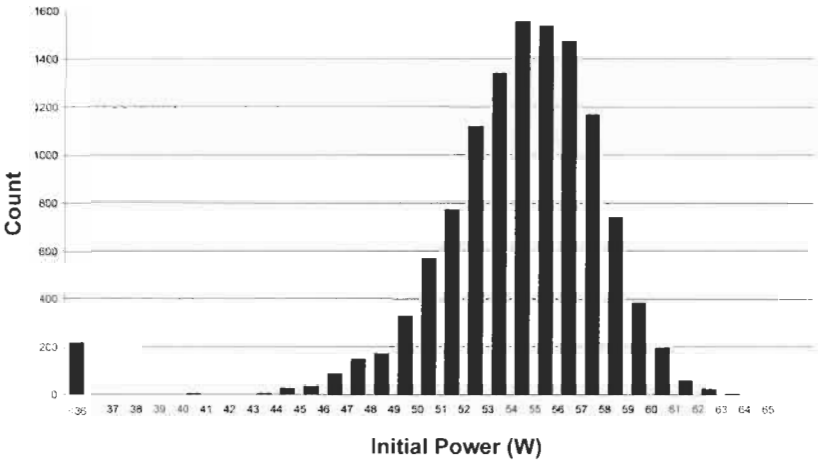

Figure 13 Distribution of the initial power of tandem modules produced at the BP Solar TF1 facility in Toano, VA.

Thin Films sputters aluminium onto the polyimide before depositing a p–i–n a-Si structure by PECVD. They use a laser to scribe through both the a-Si and aluminium layers, and screen-print an insulating ink in the interconnection region before sputter-depositing ZnO. They then screen-print a silver grid onto the ZnO before laser scribing the ZnO. A laser is used to interconnect the cells by fusing a section of the silver grid of one cell to the bottom aluminium contact of the adjacent cell. The coated substrates are laminated to a Tedlar sheet using a roll-based laminator and then cut into individual modules before being framed and wired.

4.2 Manufacturing Costs

A number of studies [99–101] have predicted that manufacturing costs should be on the order of $\$1/W_P$ or less when thin-film modules are produced at rates greater than about 10 MW_P per year. Most of these studies assume that the manufacturing plants would be highly automated and that the PV modules would be produced at high yields. The first generation thin-film PV manufacturing plants are costing about \$2–\$3 per W_P (of annual capacity) to construct, and this capital cost will probably drop to about $\$1/W_P$ as the size of the plants increase to 100 MW_P per year and larger. As the plants get larger, the material costs become the major cost component [100].

As shown in Figure 14 for a-Si/a-SiGe tandem modules, more than 60% of the material costs are associated with the glass, frames and packaging, while only 13.3% is associated with the silane, germane and doping gases used to deposit the a-Si alloy layers. Since the utilisation of silane and germane is only on the order of several % in most PECVD reactors, it may be possible to reduce the costs of the semiconductor layers to less than $\$0.02/W_P$. While it will be difficult to reduce most of the other material costs (such as glass), the cost of the modules

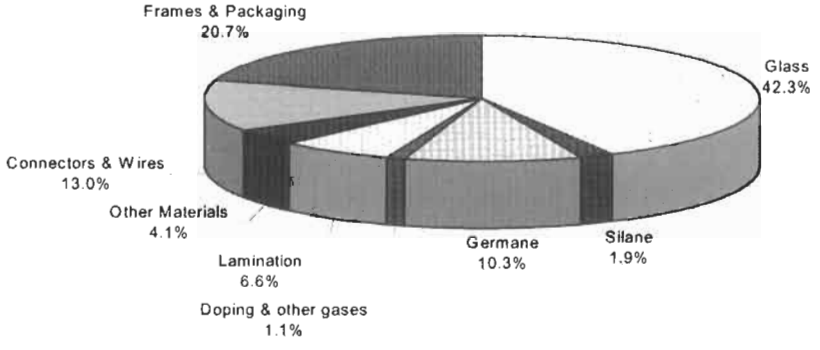

Figure 14 Material cost percentages for a-Si/a-SiGe tandem modules on glass. (The glass cost includes a front plate of tin oxide coated glass and a back plate.)

(in $\$/W_P$) can be reduced by increasing the efficiency of the modules. Increasing the module efficiency also helps to reduce the total cost of a PV system by reducing area-related balance of system costs (such as mounting structures and land).

Another way to significantly reduce the cost of PV systems is to integrate the thin-film PV structure into building materials such as roofs or windows. United Solar has developed a-Si PV modules that function as roofing shingles, standing seam metal roofs and PV laminates that can be installed directly onto metal roofs [102]. BP Solar has developed semi-transparent PV modules (called PowerView^{TM}) that are patterned by selective laser ablation so that they allow partial transmission of light (5–10%), and can also be patterned with signs or logos [103]. These PowerView^{TM} modules have been integrated into the canopy over automobile fueling stations and can now be found in over 300 BP service stations worldwide. Building-integrated PV (BIPV) applications reduce the cost of PV systems since the product has dual use. In the case of a PV window, the glass, frame, and installation are all similar to that associated with an architectural window. Thus, the incremental cost of a PV window system over architectural windows is that associated with the thin film PV structure, the wiring and power conditioning equipment.

4.3 Environmental Issues

While PV solar energy is widely viewed as an ideal way to produce electric power from a virtually inexhaustible source without noise or pollution, there are environmental issues that must be addressed. The entire process of mining and refining raw materials, manufacturing PV modules and disposing of obsolete modules must be developed not only for low cost, but must also be environmentally friendly.

If the PV module manufacturing processing requires the use of toxic materials, then systems and procedures must be established to minimise the risk to employees. BP Solar uses toxic doping gases such as diborane and phosphine only in a diluted form (~1–20 vol.% in silane) in the production of a-Si/a-SiGe

tandem modules. Trimethylboron (~ 1–5% in silane), which is less toxic than diborane is also used as a p-type dopant source. Since silane is pyrophoric, a leak will cause the silane to ignite, and the dopant gas will be oxidised in the flame. The resulting silicate glass powder is non-toxic.

The silane and germane feedstock gases at the BP Solar TF1 plant in Virginia are stored in an outdoor holding area, and are fed into the facility through stainless steel pipes. All exhaust gases are passed through a burn box and the powder is collected in a bag house for disposal. The powder consists mainly of silicon dioxide fused with small amounts of oxides of germanium, boron and phosphorus.

The process used by BP Solar to manufacture a-Si modules does not use any solvents, acids or other wet chemicals (except for detergents in water for cleaning substrates). As described in Section 4.1, all module patterning and interconnections are performed using lasers, so there are no harmful waste products or effluents produced in the manufacturing process. In addition, since a-Si PV modules do not contain any toxic materials, there are no environmental risks associated with module breakage, fires or long-term disposal in landfills.

5 Future Trends

While the overall market for PV has grown by about 15–20% over the last 20 years (and even more rapidly in the last few years), the market for a-Si solar cells has experienced a different growth pattern. Amorphous silicon solar cells were first introduced commercially by Sanyo in 1980 for use in solar-powered calculators, and shipments increased rapidly to 3.5 MW_P by 1985 (representing about 19% of the total PV market that year). Shipments of a-Si PV modules reached ~40 MW_P in 2001, but this represented only about 11% of the total PV market. This apparent loss of market share is due to the saturation of the low-light consumer application market and the relatively slow acceptance of a-Si PV modules in the terrestrial PV market.

The key drivers behind the terrestrial PV market are module efficiency, selling price and reliability. The conversion efficiencies of crystalline silicon PV modules are generally in the range of 11–14% while the stabilised efficiencies of a-Si PV modules are typically in the range 6–8%. Crystalline silicon PV modules currently sell for about \$3.00–\$3.30 per W for large-quantity purchases, and a-Si PV modules sell for about 10–20% less on a $/$W_P$ basis. However, the total price of many PV systems (in $/$W_P$) is less with crystalline silicon modules due to the costs associated with the balance of system (the cost of the area-related components are reduced with higher efficiency cells). Crystalline silicon PV modules have exhibited good long-term reliability with many arrays still in operation after more than two decades. Many first generation thin-film modules exhibited reliability problems in outdoor testing, and the reliability of more recent thin-film product has not yet been demonstrated since the product has only been in the field for a few years.

Thus, the future of a-Si PV modules will depend critically on the ability to further increase the stabilised efficiency, lower the manufacturing cost and improve the long-term reliability. The major factor limiting the performance of a-Si PV modules is the light-induced degradation. While a-Si/a-SiGe tandem modules degrade about 12–20% before reaching a steady state, elimination of the light-induced degradation would allow a much larger increase in performance since both junctions could then be made thicker leading to significantly higher photocurrents. At this juncture, it is not clear that the light-induced degradation can be completely eliminated since most investigators believe that the metastable defects are intrinsic to the a-Si alloys. Nonetheless, there is a large R&D effort to develop a better understanding of the light-induced degradation in a-Si alloys and to reduce the degradation. Considering the large potential payoff, this effort is likely to continue for the near future.

One approach that is being aggressively pursued by a number of organisations is to develop new types of solar cells based on microcrystalline silicon (μc-Si) or multijunction structures involving both a-Si and μc-Si [104, 105]. Recently stabilised efficiencies of the order of 10% have been demonstrated for large-area (0.41 m^2) a-Si/μc-Si tandem modules [106].

As mentioned in Section 4.2, the cost of thin-film PV modules and systems can be reduced by integrating thin-film PV into building materials, but this approach requires both large-scale production of suitably sized BIPV products and the integration of the products into the building industry infrastructure. In addition, BIPV products must be designed to be cosmetically appealing since they should not detract from the appearance of the building. The successful implementation of BIPV on a large scale will require a cooperative effort involving PV manufacturers, building materials companies, construction companies, electric utilities and government agencies.

Another factor that affects the cost of a-Si PV modules is the relatively high capital cost of the manufacturing equipment and facilities. This cost can be reduced by increasing the throughput of the production equipment. At the present time, the production bottleneck and major equipment cost are usually associated with the a-Si alloy deposition process where the deposition rate is typically on the order of 0.1–0.2 nm/s. Thus, a number of organisations are engaged in research and development programs to increase the deposition rates for both a-Si and μc-Si alloys.

The reliability of a-Si PV modules has improved over the last 20 years with the development of new processes for electrically isolating and encapsulating the modules. However, more research and development is required to assure that all thin-film PV modules can survive for extended periods (> 20 years) in hostile environments such as high-voltage arrays operating in hot humid climates.

In summary, while a-Si photovoltaics has become a $100 million dollar business, further research, development and engineering will be required to increase the performance, lower the manufacturing costs and improve the reliability in order to assure that a-Si PV will play a major role in future world energy production.

References

[1] Chittik, R.C., Alexander, J.H. and Sterling, H.E., 1969. The preparation and properties of amorphous silicon. *J. Electrochem. Soc.*, Vol. 116, pp. 77–81.

[2] Carlson, D.E., 1977. Semiconductor device having a body of amorphous silicon. US Patent 4,064,521.

[3] Spear, W.E. and LeComber, P.G., 1975. Substitutional doping of amorphous silicon. *Solid State Communications*, Vol. 17, pp.1193–1196.

[4] Carlson, D.E. and Wronski, C.R., 1976. Amorphous silicon solar cells. *Appl. Phys. Lett.*, Vol. 28, pp. 671–673.

[5] Carlson, D.E., Wronski, C.R., Triano, A. and Daniel, R.E., 1976. Solar cells using Schottky barriers on amorphous silicon. *Proc. 12th IEEE Photovoltaic Specialists Conf.*, Baton Rouge, pp. 893–895.

[6] Brodsky, M.H., Frisch, M.A., Ziegler, J.F. and Lanfard, W.A., 1977. Quantitative analysis of hydrogen in glow discharge amorphous silicon. *Appl. Phys. Lett.*, Vol. 30, pp. 561–563.

[7] Staebler, D.L. and Wronski, C.R., 1977. Reversible conductivity change in discharge produced amorphous silicon. *Appl. Phys. Lett.*, Vol. 31, pp. 292–294.

[8] Hanak, J. and Korsun, V., 1982. Optical stability studies of a-Si solar cells. *Proc. 16th IEEE Photovoltaic Specialists Conf.*, San Diego, pp. 1381–1383.

[9] Kroll, U., Meier, J., Keppner, H., Shah, A., Littlewood, S.D., Kelly, I E. and Giannoules, P., 1995. Origins of atmospheric contamination in amorphous silicon prepared by very high frequency (70 MHz) glow discharge. *J. Vac. Sci. Technol.* Vol. A 13(6), pp. 2742–2746.

[10] Watanabe, T., Azuma, K., Nakatani, M., Suzuki, K., Sonobe, T. and Shimada, T., 1986. Chemical vapor deposition of a-Si:H films utilising a microwave excited Ar plasma stream. *Jpn. J. of Applied Physics*, Vol. 25(12), pp. 1805–1810.

[11] Saito, K., Sano, M., Ogawa, K. and Kajita, I., 1993. High efficiency a-Si:H alloy cell deposited at high deposition rate. *J. Non-Cryst. Solids*, Vols. 164–166, pp. 689–692.

[12] Carlson, D.E., Rajan, K., Arya, R.R., Willing, F. and Yang, L., 1998. Advances in amorphous silicon photovoltaic technology. *J. Materials Research*, Vol. 13(10), pp. 2754–2762.

[13] Tanaka, K. and Matsuda, A., 1987. Glow-discharge amorphous silicon: growth process and structure. *Materials Science Report*, Vol. 2, pp. 139–184.

[14] Wronski, C.R., Pearce, J.M., Koval, R.J., Niu, X., Ferlauto, A.S., Koh, J. and Collins, R.W., 2002. Light induced defect creation kinetics in thin film protocrystalline silicon materials and their solar cells. *Mat. Res. Soc. Proc.*, Vol. 715, p. A13.4.

[15] Zanzucchi, P., Wronski, C.R. and Carlson, D.E., 1977. Optical and photoconductivity properties of discharge produced a-Si. *J. Appl. Phys.*, Vol. 48, pp. 5227–5236.

[16] Tawada, Y., Okamoto, H. and Hamakawa, Y., 1981. a-SiC:H/a-Si:H heterojunction solar cell having more than 7.1% conversion efficiency. *Appl. Phys. Lett.*, Vol. 39(3), pp. 237–239.

[17] Nakamura, G., Sato, K., Ishihara, T., Usui, M., Okaniwa, K. and Yukimoto, Y., 1983. Tandem type amorphous solar cells. *J. Non-Cryst. Solids*, Vol. 59–60, pp. 1111–1114.

[18] Ishihara, T., Terazono, S., Sasaki, H., Kawabata, K., Itagaki, T., Morikawa, H., Deguchi, M., Sato, K., Usui, M, Okaniwa, K., Aiga, M., Otsubo, M. and Fujikawa, K., 1987. High efficiency triple-junction amorphous solar cells. *Proc. 19th IEEE Photovoltaic Specialists Conf.*, New Orleans, pp. 749–755.

[19] Yang, J., Banerjee, A., Lord, K. and Guha, S., 1998. Correlation of component cells with high efficiency amorphous silicon alloy triple-junction solar cells and modules. *Proc. 2nd World Conf. on Photovoltaic Solar Energy Conversion*, Vienna, pp. 387–390.

[20] Yablonovitch, E., and Cody, G.D., 1982. Intensity enhancement in textured optical sheets for solar cells. *IEEE Trans. Electron Dev.*, Vol. 29, pp. 300–305.

[21] Deckman, H., Wronski, C.R., and Yablonovitch, E., 1984. Optical enhancement of solar cells. *Proc. 17th IEEE Photovoltaic Specialists Conf.*, Kissimmee, pp. 955–960.

[22] Nostrand, G. E. and Hanak, J., 1979. Method of removing the effects of electrical shorts and shunts created during the fabrication process of a solar cell. US Patent 4,166,918.

[23] Ayra, R.R. and Carlson, D.E., 2002. Amorphous silicon PV module manufacturing at BP Solar. *Progress in Photovoltaics*, Vol. 10, pp. 69–76.

[24] Hanak, J.J., 1981. Laser processing technique for fabricating series-connected and tandem junction series-connected solar cells into a solar battery. US Patent 4,292,092.

[25] Carlson, D.E., Gleaton, M. and Ganguly, G., 2000. Effects of oil and dopant contaminants on the performance of amorphous silicon solar cells. *Proc. 16th European Photovoltaic Solar Energy Conf.*, Glasgow.

[26] Kinoshita, T., Isomura, M., Hishikawa, Y. and Tsuda, S., 1996. Influence of oxygen and nitrogen in the intrinsic layer of a-Si solar cells. *Jpn. J. Appl. Phys.*, Vol. 35, pp. 3819–3824.

[27] Tsai, C.C., Knights, J.C., Chang, G. and Wacker, B., 1986. Film formation mechanisms in the plasma deposition of hydrogenated amorphous silicon. *J. Appl. Phys.*, Vol. 59, pp. 2998–3001.

[28] Street, R.A., 1991. *Hydrogenated Amorphous Silicon*. Cambridge University Press, New York.

[29] Shimizu, T., Zhang, Q., Nishino, T., Takashima, H. and Kumeda, M., 1996. Influence of hydrogen content and Si-H bond structure on photocreated dangling bonds in hydrogenated amorphous silicon films. *Jpn. J. Appl. Phys.*, Vol. 35, pp. 4409–4412.

[30] Ganguly, G. and Matsuda, A., 1996. Role of hydrogen dilution in improvement of a-SiGe:H alloys. *J. Non-Cryst. Solids*, Vols. 559–562, pp. 98–200.

[31] Lee, Y., Jiao, L., Liu, H., Lu, Z., Collins, R. W. and Wronski, C. R., 1996. Stability of a-Si solar cells and corresponding intrinsic materials fabricated using hydrogen diluted silane. *Proc. 25th IEEE Photovoltaic Specialists Conf.*, Washington, DC, pp. 1165–1168.

[32] Collins, R.W., 1994. Real time spectroscopic ellipsometry studies of the nucleation, growth and optical functions of thin films, Part 1: tetrahedrally bonded materials. In: *Physics of Thin Films*, Academic Press, New York, pp. 49–125.

[33] Koh, J., Ferlauto, A.S., Rovira, P.I. Wronski, C.R. and Collins, R.W., 1999. Evolutionary phase diagrams for plasma-enhanced chemical vapor deposition of silicon thin films from hydrogen diluted silane. *Appl. Phys. Lett.*, Vol. 75, pp. 2286–2288.

[34] Lu, Y., Kim, S., Gunes, M., Lee, Y., Wronski, C.R. and Collins, R.W., 1994. Process-property relationships for a-$Si_{1-x}C_x$:H deposition: excursions in parameters space guided by real time spectroellipsometry. *Mat. Res. Soc. Symp. Proc.*, Vol. 336, pp. 595–600.

[35] Collins, R.W., Koh, J., Ferlauto, A.S., Rovira, P.I., Lee, Y., Koval, R.J. and Wronski, C.R., 2000. Real Time Analysis of Amorphous and Microcrystalline Silicon Film Growth by Multichannel Ellipsometry. *Thin Solid Films*, Vol. 364, pp. 129–137.

[36] Ferlauto, A.S., Ferreira, G.M., Koval, R.J., Pearce, J.M., Wronski, C.R., Collins, R.W., Al-Jassim, M.M. and Jones, K.M., 2002. Thickness Evolution of the Microstructural and Optical Properties of Si:H Films in the Amorphous-to-Microcrystalline Phase Transition Region. *Proc 29th IEEE Photovoltaic Specialists Conf.*, New Orleans, pp. 1076–1081.

[37] Ferlauto, A.S., Rovira, P.I., Koval, R.J., Wronski, C.R. and Collins, R.W., 2000. Effects of H_2-Dilution and Plasma Power in Amorphous Silicon Deposition: Comparison of Microstructural Evolution and Solar Cell Performance. *Proc. 28th IEEE Photovoltaics Specialists Conf.*, Anchorage, pp. 713–716.

[38] Koval, R.J., Koh, J., Lu, Z., Jiao, L., Wronski, C.R. and Collins, R.W., 1999. Performance and Stability of Si:H *p–i–n* Solar Cells with i-Layers Prepared at the Thickness-Dependent Amorphous-to-Microcrystalline Phase Boundary. *Appl. Phys. Lett.*, Vol. 75, pp. 1553–1555.

[39] Koval, R.J., Pearce, J.M., Ferlauto, A.S., Rovira, P.I., Collins, R.W. and Wronski, C.R., 2000. The Role of Phase Transitions in Protocrystalline Si:H on the Performance their of Solar Cells. *Proc. 28th IEEE Photovoltaic Specialists Conf.*, Anchorage, pp. 750–753.

[40] Koval, R.J., Pearce, J.M., Ferlauto, A.S., Collins, R.W. and Wronski, C.R., 2001. Evolution of the Mobility Gap with Thickness in Hydrogen-Diluted Intrinsic Si:H Materials in the Phase Transition Region and Its Effect on *pi–n* Solar Cell Characteristics. *Mat. Res. Soc. Proc.*, Vol. 664, p. A16.4.

[41] Koval, R.J. Chen, C. Ferreira, G.M., Ferlauto, A.S., Pearce, J.M., Rovira, P.I., Wronski, C. R. and Collins, R.W., 2001. Protocrystalline Si:H p-type Layers for Maximization of the Open Circuit Voltage of a-Si:H *n–i–p* Solar Cells. *Mat. Res. Soc. Proc.*, Vol. 715, p. A6.1.

[42] Koval, R.J., Pearce, J.M., Chen, C., Ferreira, G.M., Ferlauto, A.S., Collins, R.W. and Wronski, C.R., 2002. Microstructurally Engineered p-layers for Obtaining High Open-Circuit Voltages in a-Si:H *n–i–p* Solar Cells. *Proc. 29th IEEE Photovoltaic Specialists Conf.*, New Orleans, pp. 1090–1093.

[43] Guha, S., Yang, J., Nath, P. and Hack, M., 1986. Enhancement of open circuit voltage in high efficiency amorphous silicon alloy solar cells. *App. Phys. Lett.*, Vol. 49, pp. 218–219.

[44] Dersch, H., Stuke, J. and Beichler, J., 1981. Light induced dangling bonds in hydrogenated amorphous silicon. *Appl. Phys. Lett.*, Vol. 38, pp. 456–458.

[45] Carlson, D.E. and Wronski, C.R., 1979. Amorphous silicon solar cells, in Topics. In: Brodsky, M.H. Ed., *Applied Physics*, Spring-Verlag, Berlin, pp. 289–329.

[46] Collins, R.W. and Vedam, K., 1995. Optical properties of solids. In: Trigg G.L., Ed., *Encyclopedia of Applied Physics*, VCH Publishers, New York, pp. 285–336.

[47] Luft, W., 1988. Characteristics of hydrogenated amorphous silicon-germanium alloys. *Proc. 20th IEEE Photovoltaic Specialists Conf.*, Vol. 1, Las Vegas, pp. 218–223.

[48] Nevin, W.A., Yamagishi, H., Asaoka, K. and Tawada, Y., 1992. Wide-bandgap hydrogenated amorphous silicon carbide prepared from an aromatic carbon source, *Proc. 22nd IEEE Photovoltaic Specialists Conf.*, Vol. 2, Las Vegas, pp. 1347–1351.

[49] Dawson, R.M., Li, Y., Gunes, M., Nag, S., Collins, R.W., Bennett, M. and Wronski, C.R., 1992. Optical properties of the component materials in multijunction hydrogenated amorphous silicon based solar cells. *Proc. 11th European Photovoltaic Solar Energy Conf.*, Montreux, pp. 680–683.

[50] Roxlo, C., Wronski, C.R., Abeles, B., Cody, G.D., 1983. Comment on optical absorption edge in a-Si:H_x. *Solid State Communications*, Vol. 47, pp. 985–987.

[51] Tiedje, T., 1984. Information about band-tail states from time-of-flight experiments. In: Pankove J.I., Ed., *Semiconductors and Semimetals*, Academic Press, Orlando, Vol. 21C, pp. 207–238.

[52] Koh, J., Lee, Y., Fujiwara, H., Wronski, C.R., and Collins, R.W., 1998. Optimization of hydrogenated amorphous silicon *p–i–n* solar cells with two-step i layers guided by real-time spectroscopic ellipsometry. *Appl. Phys. Lett.*, Vol. 73, pp. 1526–1528.

[53] Branz, H.M. and Silver, M., 1990. Potential fluctuation due to inhomogeneity in hydrogenated amorphous silicon and the resulting charged dangling bond defects. *Phys. Rev. B.*, Vol. 42, pp. 7420–7428.

[54] Jiao, L., Liu, H., Semoushikina, S., Lee, Y. and Wronski, C. R., 1996. Initial, rapid light induced changes in hydrogenated amorphous silicon

materials and solar cell structures: the effect of charged defects. *Appl. Phys. Lett.*, Vol. 69, pp. 3713–3715.

[55] Gunes, M. and Wronski, C.R., 1997. Differences in the densities of charged defect states and kinetics of Staebler–Wronski in undoped (non-intrinsic) hydrogenated amorphous silicon. *J. Appl. Phys.*, Vol. 81, pp. 3526–3536.

[56] Kamei, T., Hata, N., Matsuda, A., Uchiyama, T., Amano, S., Tsukamoto, K., Yoshioa, Y. and Hirao, T., 1996. Deposition and extensive light soaking of highly pure hydrogenated amorphous silicon. *Appl. Phys. Lett.*, Vol. 68, pp. 2380–2382.

[57] Collins, R.W. and Fujiwara, H., 1997. Growth of hydrogenated amorphous and its alloys. *Current Opinion in Solid State & Material Science*. Vol. 2, pp. 417–424.

[58] Wronski, C.R., Abeles, B., Tiedje, T. and Cody, G.D., 1982. Recombination centers in phosphorous doped hydrogenated amorphous silicon. *Solid State Communications*, Vol. 44, pp. 1423–1426.

[59] Tawada, Y., Okamoto, H., and Hamakawa, Y., 1997. a-SiC:H/a-Si:H heterojunction solar cell having more than 7.1% conversion efficiency. *Appl. Phys. Lett.*, Vol. 39, pp. 237–239.

[60] Lee, Y., Ferlauto, A. and Wronski, C.R., 1997. Contributions of bulk, interface and build-in potential to the open circuit voltage of a-Si solar cells. *Proc. 26th IEEE Photovoltaic Specialists Conf.*, Anaheim, pp. 683–686.

[61] Wronski, C.R., 1984. The Staebler–Wronski Effect. *Semiconductors and Semimetals*, Vol. 21C, pp. 347–373.

[62] Fritzsche, H., 1997. Search for explaining the Staebler–Wronski effect. *Mat. Res. Soc. Symp. Proc.*, Vol. 467, pp. 19–31.

[63] Stutzmann, M., 1997.Microscopic aspects of the Staebler–Wronski effect. *Mat. Res. Soc. Symp. Proc.*, Vol. 467, pp. 37–48.

[64] Wronski, C.R., 1997. The light-induced changes in a-Si:H materials and solar cells – Where we are now. *Mat. Res. Soc. Symp. Proc.*, Vol. 467, pp. 7–17.

[65] Yang, L. and Chen, L., 1993. Fast and slow metastable defects in hydrogenated amorphous silicon. *Appl. Phys. Lett.*, Vol. 63, pp. 400–402.

[66] Von Roedern, B., 1993. Shortfall of defect models for amorphous silicon solar cells. *Appl. Phys. Lett.*, Vol. 62, pp.1368–1369.

[67] Sakata, I., Yamanaka, M., Namase, S. and Hayashi, Y., 1992. Deep defect states in hydrogenated amorphous silicon studied by a constant photocurrent method. *J. Appl. Phys.*, Vol. 71, pp. 4344–4353.

[68] Carlson, D.E. and Rajan, K., 1998. Evidence for Proton Motion in the Field-Induced Recovery of Light-Induced Degradation in Amorphous Silicon Solar Cells. *J. Appl. Phys.*, Vol. 83, pp. 1726–1729.

[69] Stutzmann, M., Jackson, W.B. and Tsai, C.C., 1985. Light induced metastable defects in hydrogenated amorphous silicon: a systematic study. *Phys. Rev. B*, Vol. 32(1), pp. 23–47.

[70] Wronski, C.R., Gunes, M. and McMahon, T.J. 1994. Charged defect states in intrinsic hydrogenated amorphous silicon. *J. Appl. Phys.*, Vol. 76(4), pp. 2260–2263.

[71] Lu, Z., Jiao, H., Koval, R., Collins, R.W. and Wronski, C.R., 1999. Characteristics of different thickness a-Si:H/metal Schottky barrier cell structures – results and analysis. *Mat. Res. Soc. Symp. Proc.*, Vol. 557, pp. 785–790.

[72] Koval, R., Niu, X. Jiao, L., Pearce, J., Ganguly, G., Yang, J., Guha, S., Collins, R.W. and Wronski, C.R., 2000. Kinetics of Light Induced Changes in Protocrystalline Thin Film Materials and Solar Cells. *Mat. Res. Soc. Proc.*, Vol. 609, p. A15.5.

[73] Pearce, J., Niu, X., Koval, R., Ganguly, G., Carlson, D., Collins, R.W. and Wronski, C.R., 2001. Contributions of D^0 and non-D^0 gap states to the kinetics of light induced degradation of amorphous silicon under 1 sun illumination. *Mat. Res. Soc. Proc.*, Vol. 664, p. A12.3.

[74] Wronski, C.R., Pearce, J.M., Koval, R.M. and Collins, R.W., 2001. Metastability in Hydrogenated Amorphous Based Materials and Solar Cells. *Technical Digest of the 12th International Photovoltaic Science and Engineering Conf.*, Jeju, Korea, pp. 33–36.

[75] Yang, L. and Chen, L.F., 1994. The effect of hydrogen dilution on the stability of a-Si:H based solar cells. *Mat. Res. Soc. Proc.*, Vol. 336, pp. 669–674.

[76] Sakai, H., Yoshida, T., Fujikake, S., Hama, T. and Ichikawa, Y., 1990. Effect of p/i interface layer on dark J–V characteristics and Voc in *p–i–n* a-Si solar cells. *J. Appl. Phys.*, Vol. 67, pp. 3494–3499.

[77] Hack, M. and Shur, M., 1986. Limitations to the open circuit voltage of amorphous silicon solar cells. *Appl. Phys. Lett.*, Vol. 49, pp. 1432–1434.

[78] Lee, Y., Ferlauto, A.S., Lu, Z., Koh, J., Fujiwara, H., Collins, R.W. and Wronski, C.R., 1998. Enhancement of stable open circuit voltage in a-Si:H *P–I–N* solar cell by hydrogen dilution of P/I interface regions. *Proc. 2nd World Conf. on Photovoltaic Solar Energy Conversion*, Vienna, pp. 940–943.

[79] Pearce, J.M., Koval, R.J., Ferlauto, A.S., Collins, R.W., Wronski, C.R., Yang, J. and Guha, S., 2000. Dependence of open circuit voltage in protocrystalline Si:H solar cells on carrier recombination in p/i interface and bulk regions. *Appl. Phys. Lett.*, Vol. 77, pp. 3093–3095.

[80] Crandall, R. and Schiff, E.A., 1985. The correlation of Open Circuit Voltage with Bandgap in Amorphous Silicon-based *P–i–n* Solar Cells. *AIP Conference Proceedings*, Tempe, AZ, pp. 481–486.

[81] Schiff, E.A., 2002. Thermionic emission model for interface effects on the open-circuit voltage of amorphous silicon based solar cells. *Proc. 29th IEEE Photovoltaic Specialists Conf.*, New Orleans, in press.

[82] Pearce, J.M., Koval, R.J., Ferlauto, A.S., Collins, R.W. and Wronski, C.R., 2001. Limitations of Bulk Generation-Recombination on Open Circuit Voltage under 1 Sun Illumination in Amorphous Silicon Solar Cells. *Technical Digest of the 12th International Photovoltaic Science and Engineering Conf.*, Jeju, Korea, pp. 251–252.

[83] Wronski, C.R., Lu, Z., Jiao, L. and Lee, Y., 1997. An approach to self consistent analysis of a-Si:H material and *p–i–n* solar cell properties. *Proc. 26th IEEE Photovoltaic Specialists Conf.*, Anaheim, pp. 587–590.

[84] Carlson, D.E., 1977. Amorphous Silicon Solar Cells. *IEEE Trans. Electron Devices*, ED-24(4), pp. 449–453.

[85] Carlson, D.E., 1984. Solar Energy Conversion. In: Joanopoulos, J.D. and Lucovsky, G., Eds., *Topics in Applied Physics*, Springer-Verlag, Berlin, Heidelberg, Vol. 55, pp. 203–244.

[86] Wronski, C.R. and Carlson, D., 2001. Amorphous Silicon Solar Cells. In: *Photoconversion of Solar Energy*, Vol. 3: Clean Electricity from Photovoltaics. Imperial College Press.

[87] Guha, S., Yang, J., Banerjee, A., Hoffman, K. and Call, J., 1999. Manufacturing issues for large volume production of amorphous silicon alloy photovoltaic modules. *AIP Conf. Proc.*, Vol. 462, pp. 88–93.

[88] Guha, S. and Yang, J., 2002. Amorphous Silicon Technology. *Proc. 29th IEEE Photovoltaic Specialists Conf.*, New Orleans, pp. 1070–1075

[89] Yamamoto, K., Nakajima, A., Yoshimi, M., Sawada, T., Fukuda, S., Hayashi, K., Suezaki, T., Ichikawa, M., Koi, Y., Goto, M., Takata, H. and Tawada, Y., 2002. High efficiency thin film silicon cell and module, *Proc. 29th IEEE Photovoltaic Specialists Conf.*, New Orleans, pp. 1110–1113.

[90] Kawamoto, K., Nakai, T., Baba, T., Taguchi, M., Sakata, H., Tsuge, S., Uchihashi, K., Tanaka, M. and Kiyama, S., 2001. A high-efficiency HIT™ Solar Cell (21.0% – 100 cm^2) with excellent interface properties. *Proc. 12th Photovoltaic Science and Engineering Conf.*, Cheju Island, Korea.

[91] Ransome, S., and Wohlgemuth, J., 2002. Performance of BP Solar Tandem Junction Amorphous Silicon Modules. *Proc. 29th IEEE Photovoltaic Specialists Conf.*, New Orleans, pp. 1420–1423.

[92] King, D., Kratochvil, J. and Boyson, W., 2000. Stabilization and Performance Characteristics of Commercial Amorphous Silicon PV Modules. *Proc. 28th IEEE Photovoltaic Specialists Conf.*, Anchorage, pp. 1446–1449.

[93] Carlson, D.E., Lin, G. and Ganguly, G., 2000. Temperature dependence of amorphous silicon solar cell PV parameters. *Proc. 28th IEEE Photovoltaic Specialists Conf.*, Anchorage, pp. 707–712.

[94] Gottschalg, R., Infield, D.G. and Kearney, M.J., 2002. Experimental Investigation of Spectral Effects on Amorphous Silicon Solar Cells in Outdoor Operation. *Proc. 29th IEEE Photovoltaic Specialists Conf.*, New Orleans, pp. 1138–1141.

[95] Fagnan, D.A., D'Aiello, R.V. and Mongon, J., 1987. Solarex/Philadelphia Electric Amorphous Silicon PV Test Site. *Proc. 19th IEEE Photovoltaic Specialists Conf.*, New Orleans, pp. 1508–1509.

[96] Osterwald, C.R., McMahon, T.J. and del Cueto, J.A., 2002. Electrochemical corrosion of SnO_2:F transparent conducting layers in thin film photovoltaic modules. *Solar Energy Materials and Solar Cells*, in press.

[97] Guha, S., Yang, J., Banerjee, A., Hoffman, K., Sugiyama, S. and Call, J., 1997. Triple-Junction Amorphous Silicon Alloy PV Manufacturing Plant

of 5 MW Annual Capacity. *Proc. 26th IEEE Photovoltaic Specialists Conf.*, Anaheim, pp. 607–610.

[98] Braymen, S., Grimmer, D., Jeffrey, F., Martens, S., Noack, M., Scandrett, B. and Thomas, M., 1999. Monolithic amorphous silicon modules on continuous polymer substrates'. *AIP Conf. Proc.*, Vol. 462, pp. 737–740.

[99] Carlson, D.E., 1989. Low-cost power from thin film photovoltaics. In: Johansson, T.B., Bodlund, B. and Williams, R.H., Eds., *Electricity*, Lund University Press, Lund, Sweden, pp. 595–626.

[100] Woodcock, J.M., Schade, H., Maurus, H., Dimmler, B., Springer, J. and Ricaud, A., 1997. A study of the upscaling of thin film solar cell manufacture towards 500 MW_P per annum. *Proc.14th European Photovoltaic Solar Energy Conf.*, Barcelona, pp. 857–860.

[101] Sabisky, E., Kiss, Z., Ellis, F., Eser, E., Gau, S., Kampas, F., VanDine, J., Weakliem, H. and Varvar, T., 1989. "Eureka" – a 10 MW_P a-Si:H Module Processing Line. *Proc. 9th European Photovoltaic Solar Energy Conf.*, Freiburg, 1989, p. 27.

[102] Nath, P., Vogeli, C., Jones, K., Singh, A., Garcia, I. and Guha, S., 2000. Field-installed peal and stick PV laminates for metal roofs. *Proc. 28th IEEE Photovoltaic Specialists Conf.*, Anchorage, pp. 1543–1544.

[103] Ayra, R.R. and Carlson, D.E., 2002. Amorphous Silicon PV Module Manufacturing at BP Solar. *Progress in Photovoltaics*, Vol. 10, pp. 69–76.

[104] Meier, J., Sptiznagel, J., Fay, S., Bucher, C., Graf, U., Kroll, U., Dubail, S., Shah, A., 2002. Enhanced light-trapping for micromorph tandem solar cells by LP-CVD ZnO. *Proc. 29th IEEE Photovoltaic Specialists Conf.*, New Orleans, pp. 1118–1121.

[105] Yamamoto, K., Yoshimi, M., Suzuki, T., Nakata, T., Sawada, T., Nakajimi, A. and Hayashi, K., 2000. Large-area and high efficiency a-Si/poly-Si stacked solar cell submodule. *Proc. 28th IEEE Photovoltaic Specialists Conf.*, Anchorage, pp. 1428–1432.

[106] Yamamoto, K., Nakajimi, A., Yoshimi, M., Sawada, T., Fukuda, S., Hayashi, K., Suezaki, T., Ichikawa, M., Koi, Y., Goto, M., Takata, H. and Tawada, Y., 2002. High Efficiency Thin Film Silicon Solar Cell and Module. *Proc. 29th IEEE Photovoltaic Specialists Conf.*, New Orleans, pp. 1110–1113.

IIc-2

Microcrystalline Silicon Solar Cells

Kenji Yamamoto, Kaneka Corporation, Otsu, Shiga, Japan

1 Introduction

With raw materials for crystalline solar cells in increasingly short supply, renewed efforts are being made in the study of ways to make practical thin-film solar cells for use in tomorrow's large-scale solar cell installations. In particular, since thin-film polycrystalline silicon solar cells are made of the same materials as frequently used, bulk silicon solar cells, they are being enthusiastically studied at laboratories worldwide due to the abundance of raw materials for such devices, their stability, and the characteristics they are expected to possess as silicon devices. Part of the motivation behind these studies comes from the theoretical finding that if these devices can be constructed so that they trap sufficient light, it should ideally be possible to achieve photoelectric conversion efficiencies in excess of 20%, even with solar cells in which the photoelectric layer is just a few micrometres thick [1].

Historically, the silicon thin-film photo absorbed layers in such devices have been produced by high-temperature processes, chiefly chemical vapour deposition (CVD) [2], liquid-phase epitaxy (LPE) [3], and zone melt recrystallisation (ZMR) [4].

However, it has become apparent that the properties of the underlying substrate are the key to obtaining high-performance silicon thin-film solar cells. That is, a high-quality silicon thin-film photoelectric layer can be obtained by suppressing the diffusion of impurities from below and using epitaxial deposition that exploits the characteristics of the underlying material, and evidently single-crystal silicon has become the optimal material for the substrate. Accordingly, this research has shifted toward recycling single-crystal silicon, and at present research is being actively performed into single-crystal silicon thin-film solar cells, primarily focusing on porous silicon delamination techniques [5].

In a somewhat different direction, attention has recently been focused on thin-film solar cells made with crystalline silicon with a small grain size. These are formed by plasma CVD using inexpensive substrate materials such as glass and by using low temperatures regardless of the type of substrate instead of these high-temperature processes [6–11].

Figure 1 shows the relationship between grain size and V_{oc} (open circuit voltage) as summarised by Werner [12]. Here, V_{oc} can be regarded as a parameter reflecting the cell characteristics and crystalline properties. As Figure 1 shows, superior characteristics are obtained with a grain size of 100 μm, but the characteristics are worse with a grain size of a few tens of μm. Conversely, favourable characteristics have been obtained experimentally both at Neuchâtel University and at Kaneka Corporation's PV Research Division by using thin-film polycrystalline silicon formed at low temperatures by plasma CVD with a submicron grain size (this is generally referred to as microcrystalline silicon due to the small grain size). This is an interesting discovery that has caused recent research to shift toward both extremes.

This chapter discusses these thin-film polycrystalline silicon solar cells with very small grain size formed at low temperatures (referred to as microcrystalline silicon solar cells) that have been the subject of studies conducted by the

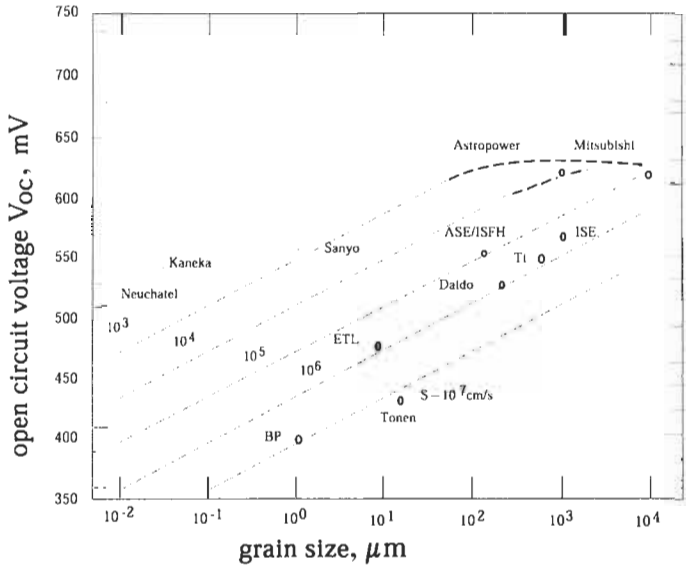

Figure 1 The relationship between grain size and open circuit voltage (V_{oc}) in solar cells. V_{oc} is correlated with the carrier lifetime (diffusion length). In this chapter, microcrystalline silicon cells correspond to a grain size of 0.1 μm or less. S indicates the recombination velocity at the grain boundaries, and Ti, BP, ASE and ISE are abbreviations of the research facilities from which the associated data came.

Kaneka PV Research Division. It will also introduce the results of the research and development of silicon hybrid solar cells with a tandem structure comprising these solar cells and amorphous solar cells, which were put to practical use for the first time in 2001.

2 Thin-Film Polycrystalline (Microcrystalline) Silicon Solar Cells

2.1 Microcrystalline Silicon Thin-Film Solar Cells Formed at Low Temperature

Microcrystalline silicon solar cells formed by plasma CVD at low temperatures are assumed to have a shorter lifetime than single-crystal cells, and it is common to employ a p–i–n structure including an internal electric field in the same way as in amorphous solar cell. A p–i–n type microcrystalline silicon solar cell is formed by a process fairly similar to that of an amorphous solar cell. Strictly speaking, these cells can be divided into p–i–n and n–i–p types according to the film deposition order, although the window layer of the solar cell is the p-type layer in both cases.

The characteristics of a cell having a p–i–n structure were first reported by workers at Neuchâtel University [6, 7]. Unlike an amorphous solar cell, this cell does not deteriorate when exposed to light. The very first reports on the characteristics of an n–i–p cell were made by the Kaneka PV Research

Division using the light trapping structure described below. These cells had an intrinsic conversion efficiency of 10.7% and an apparent efficiency of 10.1% for a film thickness of 2 μm (surface area 1 cm^2, measured by the Japan Quality Assurance Organization (JQA)) (Figure 2) [8–11]. Also, by subjecting the silicon film in the photoelectric layer of this cell to X-ray diffraction (XRD) measurements, it was found to have a preferential (110) orientation. The p–i–n and n–i–p cells have different characteristics due to their different fabrication sequences. A large difference is that the underlying layer of a p–i–n cell is the transparent electrode, whereas the underlying layer of a n–i–p cell is the back electrode.

As a general rule, transparent electrodes are made of oxides, and since there is a risk of these oxides being reduced by the hydrogen atoms that are needed to form microcrystalline cells, there is a smaller process window in the cell formation conditions for the p–i–n type. From the viewpoint of the ease with which integrated structures can be formed, which is a characteristic of thin-film solar cells, an advantage of p–i–n cells is that they can be formed as superstrate modules using integration techniques similar to those used for amorphous silicon as described below. Furthermore, it should be possible to make integrated structures of n–i–p cells by methods equivalent to those used for Cu(InGa)Se_2-based solar cells [13]. At the present time, it is difficult to determine which is better, but it should become possible to arrive at a conclusion in terms of cost, performance and applications through the production of sub-modules in the future.

2.2 Carrier Transport in Microcrystalline Silicon Thin-Film Solar Cells

To improve the efficiency of these solar cells in the future, it is absolutely essential to gain some understanding of the relationship between the crystalline

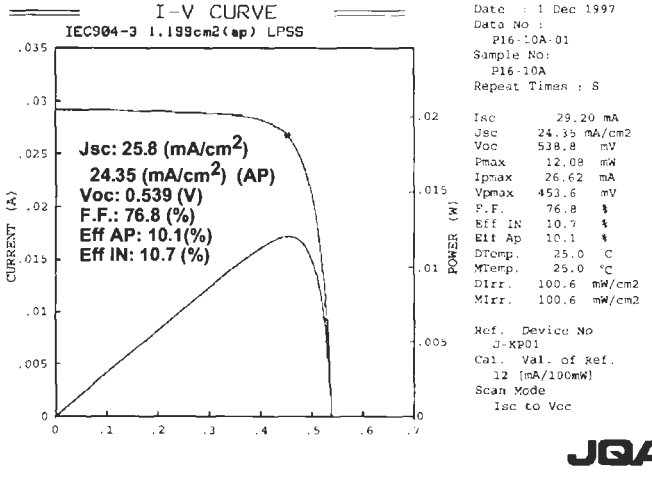

Figure 2 Current–voltage characteristics of an n–i–p type microcrystalline silicon cell (film thickness 2 μm, area 1 cm^2, measured by JQA). Eff_{AP} *is the characteristic for the area including the grid electrode, and* Eff_{IN} *is the characteristic of the effective area not including the grid.*

microstructure including grain boundaries and the carrier transport process. In particular, the carrier lifetime (diffusion length) that determines the solar cell characteristics and the recombination velocity at grain boundaries. However, in a microcrystalline silicon cell, the general non-uniformity that is typical of its grain structure has a direct and complex effect on carrier transport, and thus there have been no conclusive reports relating to these physical properties by direct measurement and analysis. Rather, the efficiency of these solar cells has only recently come to light, so only the first steps have been made in the research of their fundamental properties.

A report by Werner et al. [12] discussed why the very small crystals produced at low temperature (as discussed in the introduction) exhibit relatively favourable cell characteristics. Although the cell characteristics are the product of current, voltage and fill factor, the open circuit voltage is directly related to the cell's lifetime and is used here as a guide to the overall cell characteristics. This is because the current is related to light trapping effects and the cell film thickness as discussed below.

According to Werner et al., the reason why a microcrystalline silicon cell exhibits a characteristic of 10% or more regardless of its small grain size is because of the very low recombination speed at its grain boundaries. This low recombination speed originates from the small barrier height at the grain boundaries, which is guaranteed by (a) the passivation of hydrogen at grain boundary defects, (b) uncharged intrinsic grains (low oxygen density), and (c) the (110) orientation of the crystal grains.

In Figure 1, as can be seen from the relationship between the open circuit voltage, the grain size and the recombination speed already summarised by Werner et al., further improvement of the lifetime of the crystalline silicon layer (i.e., improvement of V_{oc}) in order to make substantial efficiency improvements may require not only a substantially larger grain size but also a lower recombination velocity at the grain boundaries (e.g., 100 cm/s). Or, to put it another way, however much the grain size is increased as shown in Figure 1, the conversion efficiency decreases when the recombination velocity at the grain boundaries increases (corresponding to a film produced at high temperature).

The actual crystalline structure of a microcrystalline silicon solar cell has been investigated by transmission electron microscopy (TEM) and atomic force microscopy (AFM). For example, Meier et al. [14], at Neuchâtel University, have classified the crystalline structures. Of course the microstructures differ depending on the production process and conditions. It has also been reported that diffusion transport mechanisms are dominant within the grains whereas drift transport is more prominent at the grain boundaries [14]. These grain boundaries exhibit amorphous characteristics which give rise to a passivation effect, and it has been pointed out that this may reduce the boundary recombination velocity.

At the Julich Research Laboratory, Rech et al. evaluated the cell characteristics as a function of the silane concentration with respect to the hydrogen dilution [15] and showed that the peak cell performance (where the maximum value of V_{oc} is achieved for the crystal) occurs at the boundary

where the resulting film changes from amorphous to crystalline. It is hoped that a more precise analysis of the microstructure and a deeper understanding of its relationship with the boundary recombination velocity will be possible in the future.

To understand the phenomena behind carrier transport, the Kaneka PV Research Division is at the initial stages of a study into the relationship between V_{oc} and film thickness [10, 11]. Figure 3 shows the dependence of V_{oc} on film thickness for a microcrystalline silicon device we produced. The maximum value of V_{oc} we obtained was about 550 mV. As the film thickness decreases, V_{oc} increases slightly. This is thought to be because as the film thickness decreases, the overall number of defects decreases and V_{oc} increases. We thus obtained a result that agrees with the theory stated at the beginning that V_{oc} improves with a thinner film.

Figure 3 also shows the results of simulation by the one-dimensional computer program PCID [16]. For a given carrier lifetime (for the case of diffusion length), V_{oc} can be increased by further increasing the carrier concentration. However, according to Werner's findings, this causes the grain boundaries in microcrystalline layers to become weakly n-type, resulting in a higher recombination velocity. This has the effect of causing V_{oc} to decrease, so it is also essential to control the grain boundaries.

In any case, compared with the V_{oc} of highly efficient single-crystal solar cells (about 700 mV), the V_{oc} of microcrystalline silicon solar cells is at least 20% lower, and the key to improving the cell efficiency is to increase V_{oc} – i.e., to improve their lifetime.

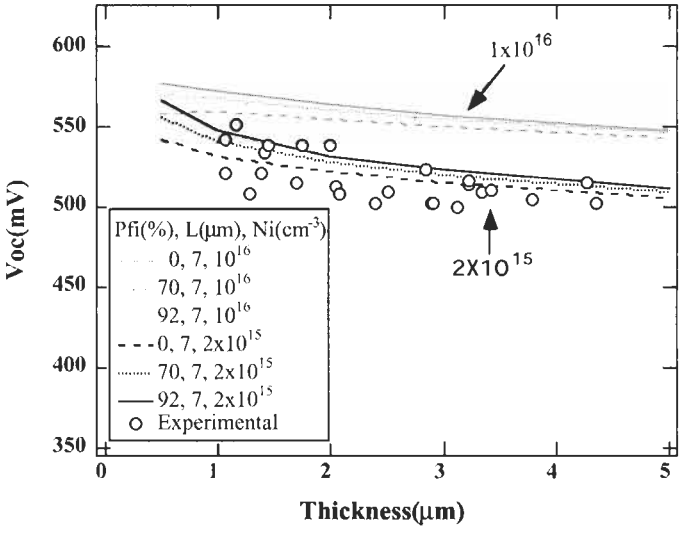

Figure 3 The variation of V_{oc} with film thickness. The open circles represent experimental data, P_{fi}(%) represents the confinement factor (0%, 70% or 92%), L represents the diffusion length, and N_i represents the carrier concentration. A simulation was also performed using PCID. The simulated results agree well with the experimental data at a carrier concentration of $2 \times 10^{15}/cm^3$.

2.3 High-Speed Fabrication of Microcrystalline Silicon Films

To consider the fabrication speed of microcrystalline silicon films, it is essential to understand the film fabrication mechanisms involved. A detailed description of these mechanisms can be found in a report published by Kondo et al. [17].

Based on the large amount of experimental data gained by the Kaneka PV Research Division, the guidelines for forming high-quality microcrystalline silicon by plasma CVD are very simple – as long as it is possible to supply a sufficient quantity of hydrogen atoms to the substrate during crystallisation without causing any damage (most of it is ion damage), then the film fabrication speed can be improved without deteriorating the cell characteristics. Throughput is another important consideration for mass-production, and it is, therefore, essential to develop ways of depositing films at high speed over large areas. At the Kaneka PV Research Division, as stated below, we have devised a technique for fabricating high quality, uniform thin films of microcrystalline silicon at a film deposition rate of 1.1 nm/s on metre-size substrates.

2.4 The Light-Trapping Effect of Microcrystalline Silicon Cells

Light-trapping techniques are a way of increasing the performance of microcrystalline solar cells. This is a core technique for cells made from microcrystalline silicon because – unlike amorphous silicon – it is essentially an indirect absorber with a low absorption coefficient. That is, the thickness of the Si film that forms the active layer in a microcrystalline silicon solar cell is just a few micrometres, so it is not able to absorb enough incident light compared with solar cells using ordinary crystalline substrates. As a result, it is difficult to obtain a high photoelectric current. Light-trapping technology provides a means of extending the optical path of the incident light inside the solar cell by causing multiple reflections, thereby improving the light absorption in the active layer.

Light trapping can be achieved in two ways: (i) by introducing a highly reflective layer at the back surface to reflect the incident light without absorption loss, and (ii) by introducing a textured structure at the back surface of the thin-film Si solar cell. Of course, the carrier lifetime is also important, and it goes without saying that the diffusion length must be at least as long as the film thickness.

At the initial stages, we focused on the light trapping effects of textured structures formed on the silicon surface [8]. We then improved the solar cell characteristics by reducing the film fabrication temperature (although as the film fabrication temperature decreases, the degree of surface texturing also decreases). A solar cell with a textured surface and a back reflective layer for increasing absorption is said to have a STAR (naturally Surface Texture and enhanced Absorption with a back Reflector) structure.

At present, two types of light trapping structure are in use. Figure 4(a) shows a cell that uses a flat highly reflective layer at the back surface, and Figure 4(b) shows a cell that uses a textured type of highly reflective layer. This highly

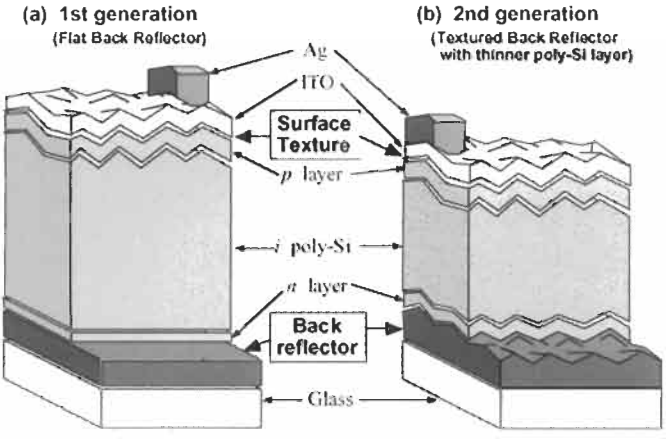

Figure 4 Cross-sections through light-trapping microcrystalline silicon solar cell devices. (a) First generation (flat back reflector); (b) second generation (textured back reflector, thinner polycrystalline silicon layer).

reflective back layer also acts as the solar cell's back electrode. Thin-film polycrystalline silicon forms naturally with a textured structure on its surface, and the size of this texture is strongly dependent on the film thickness. When the film is relatively thick (4 μm or more), the surface texture is suitable for light trapping, but when the film is relatively thin (1.5 μm or less), an adequate surface texture does not form [8–11]. It is thus necessary to use a textured reflective layer at the back surface. Of course, to be precise the texture characteristics depend on the fabrication conditions as well as on the film thickness.

Cells of this sort are fabricated as follows. First, after a back reflector layer has been formed on a glass substrate, a layer of n-type silicon is deposited on it by plasma CVD. Next, the active layer, which is a thin film of intrinsic polycrystalline silicon, is formed by plasma CVD. Finally, a p-type silicon film and an indium tin oxide (ITO) film are deposited in turn, and then a comb grid electrode is formed on top.

Now consider the light trapping effect of a thin film polycrystalline silicon layer with a thickness of 1.5 μm. Figure 5(a) shows the reflection spectra of samples corresponding to two types of 1.5 μm thick cell (one with a flat back reflector and one with a textured back reflector), and Figure 5(b) shows the corresponding collection efficiency spectra.

In Figure 5(a) the minimum that appears in the spectra at around 550 nm arises because the ITO film was deposited under non-reflective conditions. The oscillation seen at wavelengths above 600 nm is caused by interference with the silicon film in the active layer. The reflectivity of the sample with the textured back surface is significantly lower in the infrared region. Figure 5(b) shows the spectral sensitivity spectra corresponding to the flat and textured samples. In the case of the textured sample, it can be seen that the sensitivity is higher at

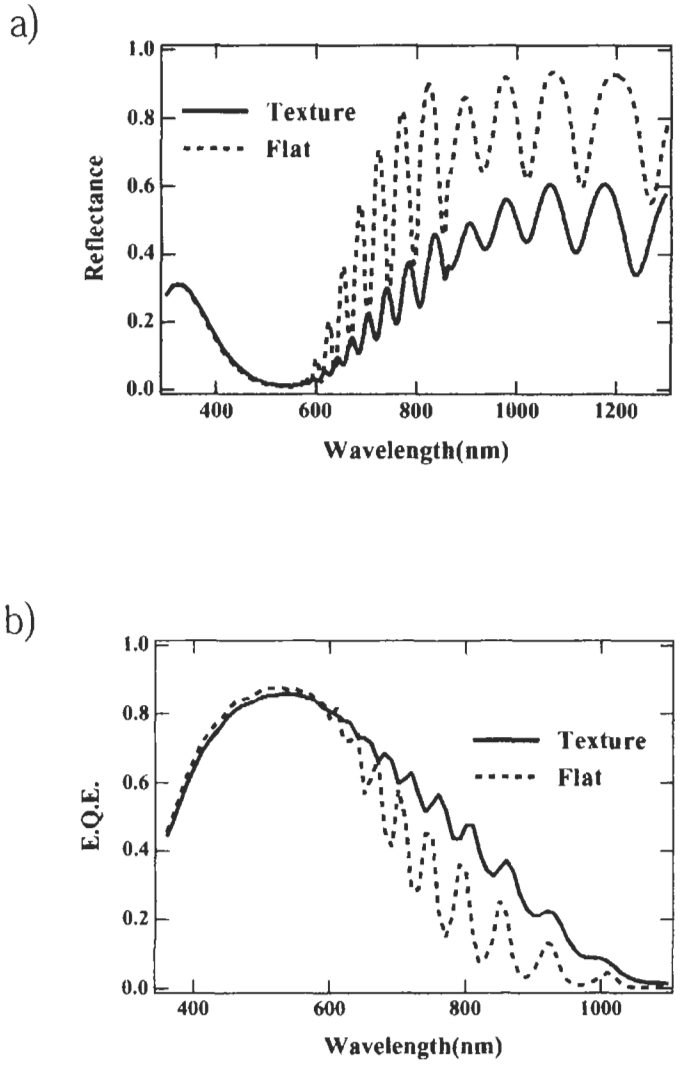

Figure 5 The characteristics of microcrystalline solar cells on glass substrates having flat and textured back reflectors: (a) reflectivity and (b) collection efficiency characteristics (quantum efficiency).

wavelengths above 600 nm, which corresponds to the reduction of the reflectivity spectrum at longer wavelengths.

This result provides experimental verification of the contribution made by the minute textured structures to light trapping. In the future, it will be necessary to aim at increasing the efficiency by obtaining larger currents in the thin film through the formation of better light trapping structures by controlling the profile of the microcrystalline silicon surface and the underlying reflective layer.

3 Application to Stacked (Hybrid) Type Solar Cells

3.1 Silicon Hybrid Solar Cells

Although the microcrystalline silicon cells formed at low temperature as described above have a potential for high efficiency, their efficiency in single-cell structures is currently only about 10%, which is much lower than that of bulk polycrystalline cells. To achieve a substantial improvement of efficiency there needs to be some kind of breakthrough, such as a substantial reduction in the abovementioned grain boundary recombination or the establishment of more advanced light trapping techniques. In an attempt to achieve this, we have investigated the use of two- and three-stacked (hybrid) structures in which multiple cells with different light absorption characteristics are stacked together. This approach allows better characteristics to be obtained with existing materials and processes. The advantages of using a layered structure include the following: (i) it is possible to receive light by partitioning it over a wider spectral region, thereby using the light more effectively; (ii) it is possible to obtain a higher open-circuit voltage; and (iii) it is possible to suppress, to some extent, the rate of reduction in cell performances caused by optical degradation phenomena that are observed when using amorphous silicon based materials.

At the Kaneka PV Research Division, we have recently made further progress with the investigation of stacked (tandem) cells in which the abovementioned amorphous silicon cells are combined with microcrystalline silicon cells. We have been studying structures in which a transparent intermediate layer is provided between the amorphous silicon layer of the top cell ad the microcrystalline silicon layer of the bottom cell (next-generation hybrid solar cell).

Figure 6(a) illustrates the structure of such a device. Compared with a conventional hybrid cell, the presence of a transparent intermediate layer, by its nature, causes some of the light that reaches the microcrystalline silicon layer of the bottom cell by passing through the amorphous silicon layer of the top cell to be reflected back into the top cell (amorphous silicon). As a result, the effective light sensitivity of the top cell is higher than that of a top cell with the same thickness in a conventional hybrid structure, so it is possible to expect an improvement in the short-circuit current J_{sc} of the overall hybrid cell. Figure 6(b) shows how the sensitivity spectrum of the hybrid cell is affected in practice by the addition of a transparent intermediate layer. Even if the amorphous silicon and microcrystalline silicon layers have the same thickness, the cell with a transparent intermediate layer is more sensitive at shorter wavelengths (top cell).

This result seems to suggest the possibility of controlling the respective light sensitivities of the top and bottom cells by introducing a suitable transparent intermediate layer. From the results of Figure 6(b) it can be inferred that by controlling the thickness of the transparent intermediate layer it is possible to reduce the thickness of the top cell needed to obtain the same current compared with a conventional hybrid cell. As a result, it should be possible to

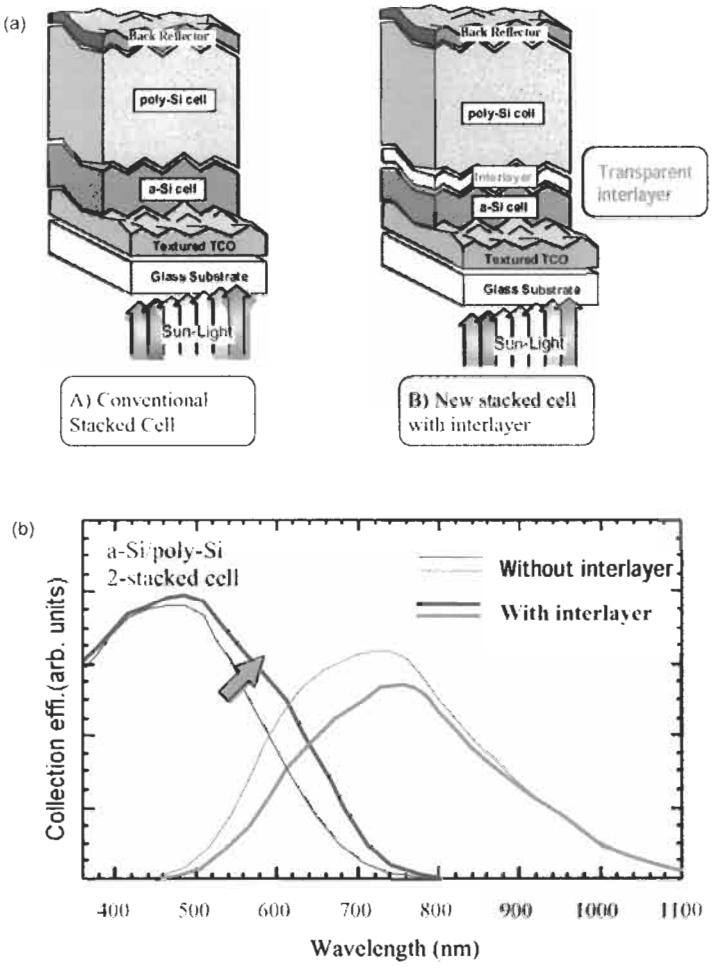

Figure 6 A next-generation tandem model. (a) Device cross-section of an amorphous–microcrystalline silicon layered next-generation tandem cell having a transparent intermediate layer (next-generation silicon hybrid cell). (b) Spectral sensitivity characteristics of the hybrid cell including the intermediate layer (absorption efficiency). An arrow indicates the enhancement of spectral response of top cell by the insertion of intermediate layer.

obtain roughly the same short circuit current J_{sc} even when the amorphous silicon film thickness is reduced. If the thickness of the amorphous silicon film in the top cell can be reduced, then it should also be possible to reduce the photo-degradation of cell.

This structure (amorphous silicon–transparent intermediate layer–microcrystalline silicon) makes it possible to improve not only J_{sc}, but also the cell characteristics compared with a conventional hybrid cell with no transparent intermediate layer without reducing V_{oc} or the fill factor (FF). As Figure 7 shows,

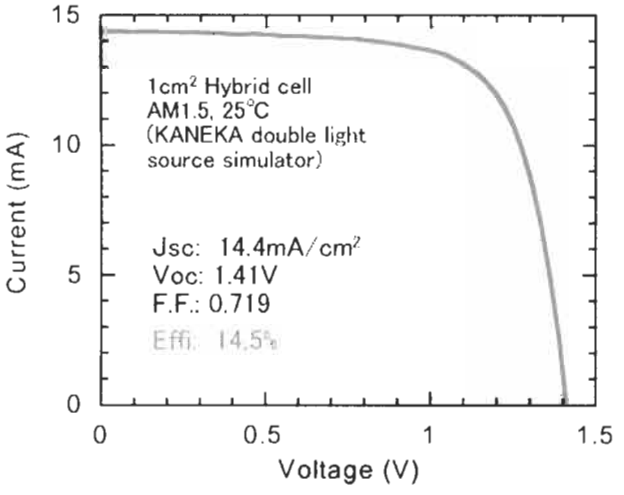

Figure 7 Current-voltage characteristic of an amorphous–microcrystalline silicon stacked next-generation hybrid cell with a transparent intermediate layer (initial efficiency; area 1 cm²).

an initial conversion efficiency of 14.5% has been achieved with a 1 cm square small area cell of this type [18].

3.2 Large-Area Thin-Film Silicon Hybrid Modules

At the Kaneka PV Research Division, we have begun developing techniques for depositing microcrystalline silicon films on large area substrates, and for the production of silicon hybrid modules based on tandem cells of amorphous silicon and microcrystalline silicon [19, 20]. We have also been developing mass production techniques that were put into commercial operation in 2001. These hybrid modules employ a superstrate structure in which light is incident through a glass substrate on which a transparent electrode is formed, and are integrated by laser scribe processing (Figure 8(a)). By adding a microcrystalline silicon film deposition process, the amorphous silicon module production process can be used to fabricate silicon hybrid modules.

As a result of improving the efficiency of a large area hybrid module measuring 910 × 455 mm, we have achieved an initial efficiency of 12.3% and a peak output power of 47.1 W as shown in Figure 8(b). We have also achieved the goal of a film deposition speed of 1.1 nm/s on metro-size large area substrates. The efficiency of these cells is somewhat lower (11.2%), but still of practical use [21]. Some of these modules are shown in Figure 9.

4 Conclusion

It has been demonstrated that microcrystalline silicon with a very small grain size formed at low temperature by plasma CVD is a promising material for use in

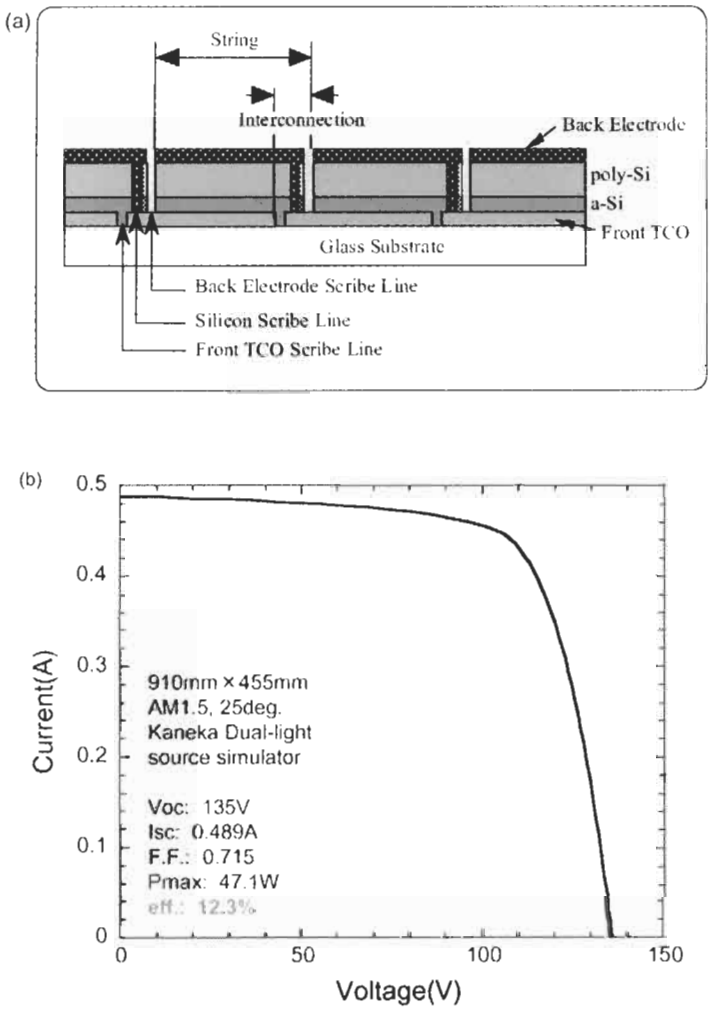

Figure 8. A silicon hybrid cell. (a) Cross-sectional structure of the silicon hybrid module (amorphous–microcrystalline silicon tandem solar cell module; series-connected). (b) Current–voltage characteristics of a large area (910 × 455 mm) silicon hybrid module (initial efficiency).

solar cells. Amorphous solar cells and stacked silicon (hybrid) solar cells have already been put to practical use in power modules. Further study is needed to ascertain and control the relationship between recombination at grain boundaries and the grain boundary microstructure, which is a non-uniform system. This should make it possible to improve the inherent performance of microcrystalline silicon solar cells. There is also a need for the development of crystal deposition methods that allow some degree of control over the texture structure of the silicon surface to allow a suitable level of light trapping to be implemented.

Figure 9 Appearance of the hybrid modules.

References

[1] Spitzer, M., Schewchun, J., Vera, E.S. and Lofersky, J.J., 1980. *Proc. 14th IEEE Photovoltaic Specialists Conf.*, San Diego, p. 375.

[2] Reif, R., 1984. *J. Electrochem. Soc.*, Vol. 131, p. 2430.

[3] Nishida, S., Nakagawa, K., Iwane, M., Iwasaki, Y., Ukiyo, N., Mizutani, M. and Shoji, T., 2001. Si-film growth using liquid phase epitaxy method and its application to thin-film crystalline Si solar cell. *Sol. Energy Mater. Sol. Cells*, Vol. 65, p. 525.

[4] Morikawa, S., Kawama, Y., Matsuno, Y., Hamamoto, S., Imada, K., Ishihara, T., Kojima, K. and Ogama, T., 2001. Development of high-efficiency thin-film Si solar cells using zone-melting recrystallization. *Sol. Energy Mater. Sol. Cells*, Vol. 65, p. 261.

[5] Bergmann, R., Rinke, T., Wagner, T. and Werner, J., 2001. Thin film solar cells on glass based on the transfer of monocrystalline Si films. *Sol. Energy Mater. Sol. Cells*, Vol. 65, p. 355.

[6] Meier, J., Flueckiger, R., Keppner, H. and Shah, A., 1994. Complete microcrystalline *p–i–n* solar cell – Crystalline or amorphous cell behavior? *Appl. Phys. Lett.*, Vol. 65, p. 860.

[7] Meier, J., Torres, P., Platz, R., Dubail, S., Kroll, U., Anna Selvan, J.A., Pellaton Vaucher, N., Hof, Ch., Fischer, D., Keppner, H., Shah, A., Ufert, K.-D., Giannoules, P. and Koehler, J., 1996. *MRS Spring Meeting*, San Francisco, Vol. 131, p. 507.

[8] Yamamoto, K., Nakajima, A., Suzuki, T., Yoshimi, M., Nishio, H. and Izumina, M., 1994. *Jpn. J. Appl. Phys.* Vol. 33, p. L1751.

[9] Yamamoto, K., Yoshimi, M., Suzuki, T., Tawada, Y., Okamoto, Y. and Nakajima, A., 1998. Below 5 μm thin film poly-Si solar cell on glass substrate fabricated at low temperature. *Proc. 2nd World Conf. on Photovoltaic Solar Energy Conversion*, Vienna, p. 1284.

[10] Yamamoto, K., Yoshimi, M., Suzuki, T., Tawada, Y., Okamoto, Y. and Nakajima, A., 1999. Thin-film poly-Si solar cells on glass substrate fabricated at low temperature. *Appl. Phys.* Vol. A69, p. 179.

[11] Yamamoto, K., 1999. Very thin film crystalline silicon solar cells on glass substrate fabricated at low temperature. *IEEE Trans. Electron Devices*, Vol. ED-46, p. 2041.

[12] Werner, J. and Bergmann, R., 1999. *Technical Digest 12th Int. Photovoltaic Science and Engineering Conf.*, Sapporo, p. 2041.

[13] Wieting, R., Delaney, D., Dietrich, M., Fredric, C., Jensen, C. and Willett, D., 1995. Progress in CIS-based photovoltaics through statistical process control, *Proc. 13th European Photovoltaic Solar Energy Conf.*, Nice, p. 1627.

[14] Vallat-Sauvain, E., Kroll, U., Meier, J., Wyrsch, N. and Shah, A., 2000. Microstructure and surface roughness of microcrystalline silicon prepared by very high frequency-glow discharge using hydrogen dilution. *J. Non-Cryst. Solids*, Vol. 125, pp. 266–269.

[15] Repmann, T., Appenzeller, W., Roschek, T., Rech, B. and Wagner, H., 2000. *Proc. 28th IEEE Photovoltaic Specialists Conf.*, Anchorage, p. 912.

[16] Basore, A., 1990. Numerical modeling of textured silicon solar cells using PC-1D, *IEEE Trans. Electron Devices* Vol. ED-37, p. 337.

[17] Kondo, M., Fukawa, M., Guo, L. and Matsuda, A., 2000. *J. Non-Cryst. Solids*, Vol. 84, pp. 226–269.

[18] Fukuda, S., 2002. 49th Spring Meeting of the JSAP and Related Societies, p. 930.

[19] Yamamoto, K., Yoshimi, M., Suzuki, T., Nakata, T., Sawada, T., Nakajima, A. and Hayashi, K., 2000. *Proc. 28th IEEE Photovoltaic Specialists Conf.*, Anchorage, p. 1428.

[20] Yamamoto, K., Yoshimi, M., Sawada, T., Nakajima, A., Hayashi, K., Suezaki, T., Takata, H. and Tawada, Y., 2001. *Tech. Digest 12th Photovoltaic Science and Engineering Conf.*, Jeju, p. 547.

[21] Suezaki, T., 2002. 49th Spring Meeting of the JSAP and Related Societies, p. 931.

CdTe Thin-Film PV Modules

Dieter Bonnet[1], ANTEC Solar GmbH, Arnstadt, Germany

[1] For current address, see List of Contributors on page x

1 Introduction

CdTe is very well suited for use as active material in thin-film solar cells due to four special properties [1]:

- CdTe has an energy gap of 1.45 eV, and therefore is well adapted to the spectrum of solar radiation.
- The energy gap of CdTe is 'direct', leading to very strong light absorption.
- CdTe has a strong tendency to grow as an essentially highly stoichiometric, but p-type semiconductor film and can form an p–n heterojunction with CdS. (CdS has a rather wide energy gap of 2.4 eV and grows n-type material under usual film deposition techniques.)
- Simple deposition techniques have been developed suited for low-cost production.

Current densities of up to 27 mA cm^{-2} and open-circuit voltages of 880 mV, leading to AM 1.5 efficiencies of 18%, can be expected for CdTe cells made under a mature technology.

Figure 1 shows the typical film sequence of this cell. In the preferred arrangement, first a transparent conducting film (typically In_2O_3 or SnO_2 or a combination of both) is deposited onto glass-plate used as transparent substrate. Then an n-CdS film is deposited, followed by the active p-conducting CdTe film. A special treatment improves the p–n junction between CdS and CdTe ('activation'). Finally a low-resistance contact is deposited onto the CdTe, which can be opaque.

Light enters the cell through the glass-substrate. Photons transverse the TCO and CdS layers. These films are not active in the photovoltaic charge generation process although leading to some – unwanted – absorption. The CdTe film is the active absorber of the solar cell. Electron–hole pairs are generated close to the junction. The electrons are driven by the built-in field through the interface into the n-CdS film. The holes remain in the CdTe and join the pool of the holes promoting the p-conduction of this material and finally have to leave the cell via

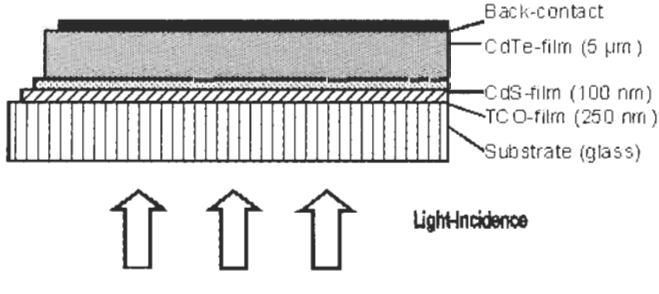

Figure 1 Film sequence of the CdTe thin-film solar cell.

the back contact. Electric power is drawn by metallic contacts attached to the TCO film and the back contact.

Due to the strong light absorption in CdTe of about 10^5 cm^{-1} for light having a wavelength below 800 nm, a film thickness of a few micrometres would be sufficient for complete light absorption. For practical reasons a thickness of about 3–7 μm is often preferred.

Intensive research has shown that this junction can be mastered so that the following basic criteria for solar cells can be fulfilled under conditions of industrial production:

- Effective generation of mobile minority charge carriers in the CdTe film.
- Efficient separation of charge carriers by means of the internal electric field of the p-n junction between n-CdS and p-CdTe.
- Low loss-extraction of the photocurrent by means of ohmic contacts to the TCO and back-contact films.
- Simple fabrication technologies for low-cost, high-volume production.

Solar cells of efficiencies above 16% have been made in research laboratories and industrial efforts have led to the recent start-up of industrial production units at three private companies in the USA and Germany each aiming at large scale production of 100,000 m^2 per annum or more. First large area modules have recently surpassed the 10% efficiency mark.

2 Steps for Making Thin-Film CdTe Solar Cells

2.1 Film Deposition

2.1.1 CdTe

Most techniques to deposit CdTe films rely on one or both of the following properties:

- CdTe, if heated in vacuum up to temperatures above 600°C, sublimes congruently liberating Cd and Te in equal amounts, the residue remaining stoichiometric CdTe.
- In CdTe films condensing on substrates kept above 400°C (or heated up to this temperature after deposition) the stoichiometric compound is the stable solid phase. The constituting elements have a significantly higher vapour pressure than the compound.

These properties make it relatively easy to produce CdTe films suited for thin-film solar cells: No excessive care has to be taken to provide for stoichiometry, as long as the substrate temperature is sufficiently high. CdTe or Cd + Te or decomposable compounds of Cd and Te can be used as starting material. Upon

arrival of Cd and Te on the substrate even in a non 1:1 ratio, CdTe condenses (nearly) stoichiometrically as long as the substrate is heated at 400–500°C or higher during or after the actual deposition. The film quality increases with temperature up to 600°C. At higher temperatures the sticking coefficient decreases (re-sublimation). A p-doping effect is achieved due to a small natural nonstoichiometry, in the form of Cd deficiencies, probably vacancies. No additional doping is used. Typical doping levels are around 10^{15} cm^{-3}. These values are somewhat low, but can be tolerated in thin-film cells. If films are deposited at lower temperatures and therefore not necessarily at stoichiometric ratio, they can be heated to create the stoichiometric compound. This allows numerous film deposition technologies to be applied. The only requirement is absence of disturbing impurities, which might jeopardise the native p-doping and charge carrier lifetime. High purity (up to 99.999%) of the elements and the compound can be achieved on an industrial scale as the elements – Cd and Te – can be easily purified by standard metallurgical procedures.

Numerous film deposition processes have been studied in the past and all have led to good cells exhibiting efficiencies above 10%. Only a few processes have properties suited to large-scale production, though. They have been developed by industrial units, as discussed in the following.

Vacuum Deposition – Sublimation/Condensation. Solid CdTe material in form of powder or granulate is sublimed in vacuum and condenses on the substrate maintained at elevated temperatures between 450 and 600°C, using the basic thermodynamic properties of CdTe already mentioned. Commercial processes of different kind have been developed, which can achieve very high deposition rates (> 10 μm/min) and can be applied to continuous-flow in-line processes, using low-cost, rugged vacuum systems. The processes do have high materials yield as the material is forced to condense only on the substrate either by close space between source and substrate (close-spaced sublimation = CSS) or by prevention of deposition on the walls kept at elevated temperatures above 600°C. Two factories using sublimation processes have been built in Germany and the USA. Production and sale of modules has started in both facilities.

Electrodeposition. CdTe films are formed from aqueous solutions of $CdSO_4$ and Te_2O_3 at temperatures of around 90°C. An n-type film of low electronic quality is formed. The basic reaction is as follows:

$$Cd^{2+}_{(aq)} + HTeO^{+}_{2\,(aq)} + 3H^{+}_{(aq)} + 6e^{-} \rightarrow CdTe_{(s)} + 2H_2O_{(liq)}$$

Grain-size enhancement, doping conversion into p-type and improvement of electronic transport properties are achieved by thermal post-annealing under the influence of Cl-based compounds. The driving electric potential is applied to the transparent conductive film on the substrate and has to be very homogeneous over the whole surface to be coated. This requires low deposition current density, resulting in low deposition rates. This can be compensated for high throughput by coating a large number of substrates in parallel. A

production plant has been built in the USA and presently is ramped-up to production quantities.

Chemical Spraying. An aerosol of water droplets containing heat-decomposable compounds of Cd and Te is sprayed onto a heated substrate, forming CdTe from the liberated elements. Processes have been developed, which do not require vacuum and can be applied easily in inline systems by using linear nozzle arrays. A first pilot plant has been built in the USA by an industrial venture, which subsequently has been put for sale and finally was abandoned.

Screen Printing. Slurries containing Cd and Te are screen printed onto the substrate and transformed into CdTe by thermal reaction under the influence of added $CdCl_2$. Due to some porosity of the films, comparatively thick layers are required for good operation of the cells. This technology is presently employed on a commercial scale with production capacity of ~1 MW_p/year. Small modules are manufactured and used in consumer applications. There are some doubts on the suitability of this process for large-scale production of high-efficiency, low-cost modules.

2.1.2 CdS

Like CdTe, CdS has the same strong tendency to form stoichiometric films, but unlike CdTe, CdS films are natively n-doped by a slight non-stoichiometry. CdS films can be deposited by the same processes as CdTe as its basic properties are quite similar to those of CdTe, e.g. its tendency to sublime and condense congruently. The following processes have been studied more intensely in view of production:

- Sublimation/condensation, like close-spaced sublimation and hot-wall sublimation
- Electrodeposition
- Screen printing

Another process is especially suited for CdS: chemical bath deposition (CBD). In this process a metastable solution containing Cd and S leads to spontaneous formation of thin CdS films on surfaces of substrates immersed into the solution at temperatures around 80°C. The chemical reaction basically is as follows:

$$Cd^{2+}(complex)_{(aq)} + (NH_2)CS_{(aq)} + 2OH^-_{(aq)} \rightarrow CdS_{(s)} + H_2O_{(liq)}$$

The CdS films so formed are tightly adherent and very homogeneous even at low thickness.

A potential disadvantage on forming abrupt junctions of high photoelectronic quality between CdTe and CdS is that CdS has a significant lattice mismatch to CdTe. Fortunately post-deposition treatments, described below, allow the amelioration of the junction.

2.1.3 TCO Films

In TCO films a compromise is achieved between high electronic conduction required for low series resistance in cells and high optical transmission for high light input and ensuing high photocurrent. Several materials are presently in use and under development for industrial application:

SnO_2. SnO_2 films can be produced by a spraying process at ambient pressure. $SnCl_4$ is dissolved in water and sprayed onto a heated substrate in air. $SnCl_4$ decomposes under reaction with oxygen forming SnO_2 films and yielding HCl, which is led away. Substrates of this kind are made on a commercial basis and are presently used by several industrial solar cell manufacturers. The films typically have area resistivities of 10 Ω/square and transmission values of around 70–80%. Alternative deposition techniques are cathode sputtering of metallic Sn targets in an oxidising ambient. Although more expensive than spraying, better quality films are achieved.

ITO. In, Sn mixed oxide films have higher performance, when sputtered from an oxide target (either better conductivity or optical transmission than pure SnO_2 films). They are more expensive due to the use of In. As indium may diffuse into the CdS/CdTe film packet and lead to unwanted n-doping of CdTe during high-temperature processing, usually a thin pure SnO_2 film is deposited onto the ITO as diffusion barrier for In.

$CdSnO_4$. This compound can be deposited by co-sputtering of oxides of Cd and Sn. It requires annealing processes at elevated temperatures, which are not suited for use of cheap soda-lime glass. Future process improvements may overcome this setback. The films show better performance than ITO, i.e. higher transmission at equal resistivity or lower resistivity at equal transmission, making them an interesting option for industrial production.

ZnO:Al. This material is routinely used as transparent contact for CIS-based thin-film solar cells. It can easily be fabricated in thin-film form by sputtering of a heterogeneous target containing ZnO and Al. Al acts as donor in ZnO. Unfortunately the film looses its doping during thermal stress ($> 500°C$) at deposition of CdTe. There is hope that more stable films can be made eventually, as the material is more cost efficient than ITO.

2.1.4 Substrates

The most common transparent substrate to be used is glass. The cheapest glass – soda-lime glass or windowpane glass – is suitable. It exhibits, if made by the float glass process, a very flat surface well suited to thin-film deposition. It is limited in processing-temperature at 520°C or somewhat higher, if suitably suspended. It is sufficiently cheap ($< 10\$/m^2$), and can be bought cut and edge treated in virtually unlimited quantities. It is indeed used by the three production facilities, which have recently become operative.

If higher temperature (which may lead to better quality films) is desired, the second option is borosilicate glass, which can be heated to temperatures above 600°C without softening. The higher cost of this material presently prevents its industrial use. Research groups have made cells of up to 16.2% efficiency on such glass.

2.2 Improvement of Critical Regions of the CdTe Solar Cell

Figure 2 shows an image obtained by scanning electron microscopy of the broken edge of a CdTe solar cell in which the CdTe film has been made by close-spaced sublimation. Figure 3 shows the critical regions, i.e. the CdTe/CdS junction and the back-contact region, which have proven to be the most critical parts of the cell, on which efficiency depends strongly.

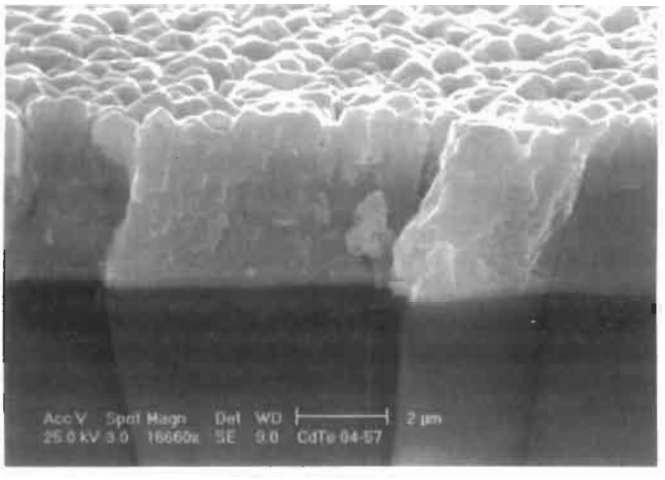

Figure 2 SEM image of the cross-section of a CdTe solar cell.

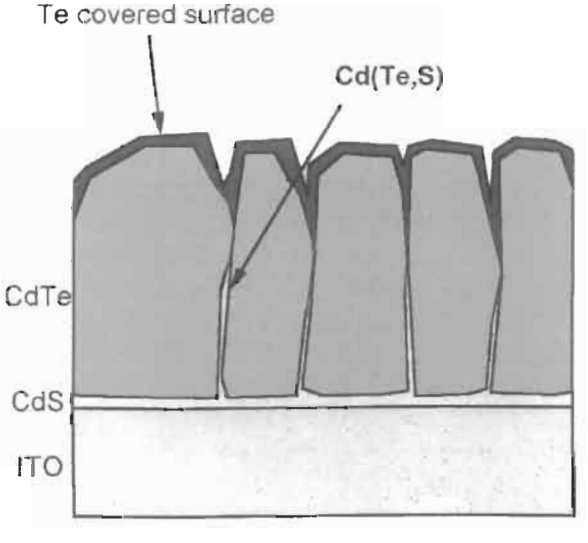

Figure 3 Schematic illustration of the key features of the CdTe solar cell.

2.2.1 The p–n Heterojunction – Improvement by Activation

Although both materials forming the junction are II–VI compounds and have a close chemical relationship, their lattice constants differ by about 5%. This leads to a significant density of interface states which can be expected to result in strong charge carrier recombination. Junctions 'as made' indeed show low charge carrier collection efficiency and thereby low power efficiency of around 2%. Annealing of the system at temperatures of around 400°C leads to some improvement, but only the still not completely understood 'activation' changes the junction so far that efficiencies of up to 16% have been observed. In this activation step, the junction is annealed at temperatures of 400–500°C in the presence of Cl-containing species, generally $CdCl_2$, which is deposited onto the film stack or admitted in vapour form for a time of around a few minutes. Figure 4 shows the strong improvement of the quality of the I–V curves under this treatment [2]. This procedure in the first instance has been developed quite empirically, although based on historic processes for manufacture of CdS photoconductive films [3]. Only recently has light been shed on the basic processes which take place during activation. Three essential effects go hand-in-hand.

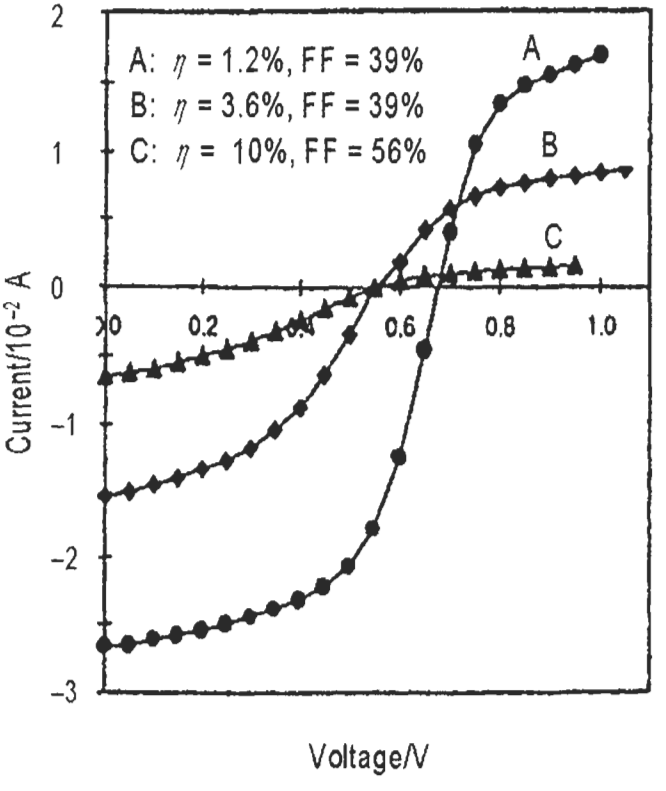

Figure 4 I–V curves of cells showing improvement by thermal treatment processes (from [2]).

Recrystallisation – Grain Growth. Generally for polycrystalline materials in which grain growth may occur there is a limiting grain size in which the driving force is balanced by a retarding force. The net driving force decreases as the grain radius increases. Generally smaller grain sizes are observed for films grown at lower substrate temperatures due to lower mobility of atoms during growth. Upon annealing and activation small grains can start to grow, but only to a certain limit. If on the other hand larger grains are formed already upon film deposition at higher deposition temperatures, such grains will grow less, as they are already closer to the final equilibrium. This has been observed experimentally: Grain size in films deposited at 500°C does not increase upon activation. Figure 5 shows that the grain diameter grows with distance from the junction – at which location nucleation of the films occurs – to an average size of 2 μm [4]. (The film has been deposited by CSS at 500°C.) It does not change even under extended treatment times with $CdCl_2$ species at 400°C. This means that for these samples the grains were at equilibrium directly after material deposition, a satisfying situation. Figure 6 shows a TEM cross-section of a CdS/CdTe film stack deposited at a substrate temperature of 525°C, indicating the typical morphology of such a system, clearly showing the high density and three dimensional distribution of planar defects, mainly stacking faults and twins [5]. The density, however, varies from one grain to the other.

For films deposited at significantly lower temperatures (< 400°C) the films show smaller grain sizes directly after deposition, together with strong orientation with the 111-axis perpendicular to the substrate. This orientation is lost upon recrystallisation during $CdCl_2$ activation [6]. Figure7, obtained by AFM (atomic force microscopy), shows directly three steps in the process of recrystallisation: During annealing under $CdCl_2$ new small grains form on the highly oriented films and grow into the final unoriented phase, indicating close

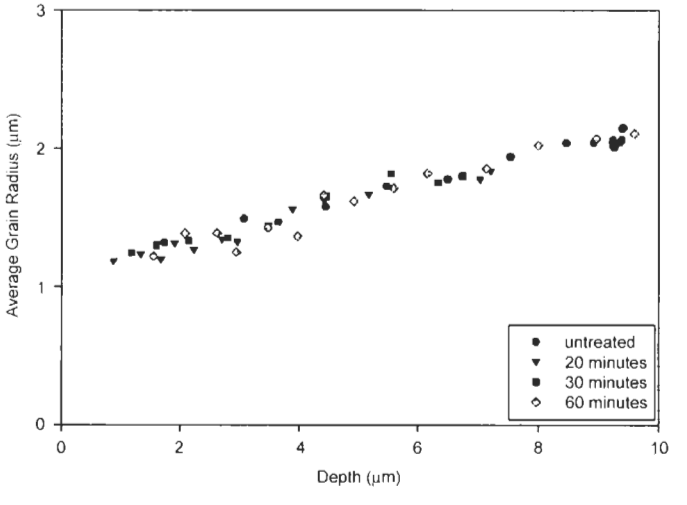

Figure 5 Grain size distribution of a CdTe film as function of the distance from the junction after different thermal treatments [4].

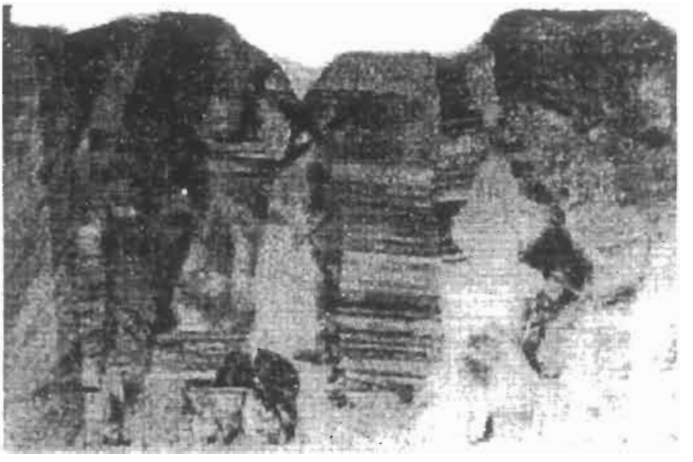

Figure 6 X-ray transmission image of a CdTe film [5]. (Reproduced with permission from IEEE.)

packing. The reference film deposited at 590°C does not grow. The loss of preferential orientation upon annealing of this low temperature film is strikingly illustrated in Figure 8 by X-ray pole diagrams by the same author [7]. The author attributes the grain growth and recrystallisation to lattice strain energy present in the films, which drives the process. In high-temperature-deposited films no strain is present, leading to no significant recrystallisation. This strain present in low-temperature films is clearly illustrated by the author from an effective decrease of lattice constant: After (low-temperature) deposition the lattice constant for a is 6.498 Å, which is reduced on activation to 6.481 Å, the published equilibrium value for crystalline powder.

In another study (Figure 9) grain size distributions were measured [8] for films deposited at relative low temperatures directly after deposition (at 340°C) and after annealing (at 580°C) and alternatively after activation (at 430°C). The final grain size distribution has a maximum at 1 μm.

Immediately at the junction, where the film nucleates, some grain growth has been observed for high-temperature films also [9]. This region is difficult to access. More detailed knowledge may be crucial for an efficiency increase.

Interdiffusion – Intermixing. CdS and CdTe in thermal equilibrium may form mixed compounds CdS_xTe_{1-x} only for quite limited regions close to the single compounds, leaving a miscibility gap between $x = 0.16$ and $x = 0.86$ at 650°C [10]. At lower temperatures the gap widens. In the Te-rich region the material shows a lower band gap than pure CdTe, an interesting feature in some II–VI compounds containing Te.

It is to be expected that CdS and CdTe intermix upon deposition at elevated temperatures to a certain degree. Intermixing at the interface can be expected to reduce the effects of lattice mismatch between CdS and CdTe. This can be analysed by SIMS-depth profiling: SIMS analyses allow the elements to be determined quantitatively at the surface, while it is removed layer by layer, e.g.

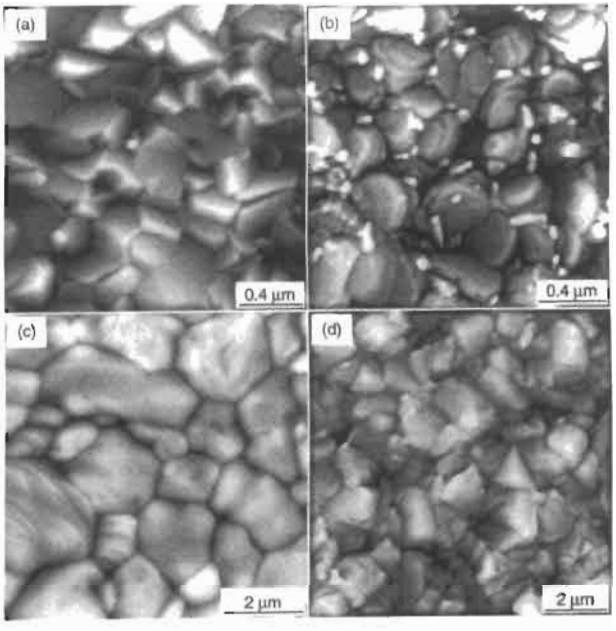

Figure 7 Grain reconstruction in a CdTe film made at low temperature during activation (a, b, c) and unchanged film made by high-temperature CSS (d) [6]. (© American Institute of Physics.)

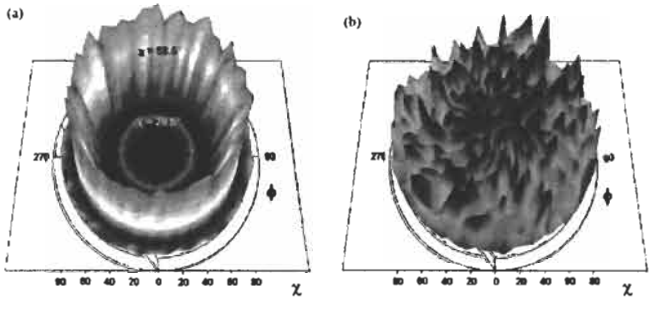

Figure 8 X-ray pole diagrams of 311 planes in a CdTe film: (a) before and (b) after activation at 400°C V. (© American Institute of Physics.)

by sputtering ('depth-profiling'). Such experiments have shown that intermixing of CdS and CdTe is a function of substrate temperature and post-deposition $CdCl_2$ activation. The degree of intermixing indeed has been observed to increase with increase of substrate temperature. Further increase is induced by activation. Excessive interdiffusion leads to deterioration of the device performance. Spectral response curves for devices made from CdTe films deposited at 610°C and activated for different times are shown in Figure 10 [11]. Indeed the intermixing is manifest by a longer wavelength response due to the lower bandgap material

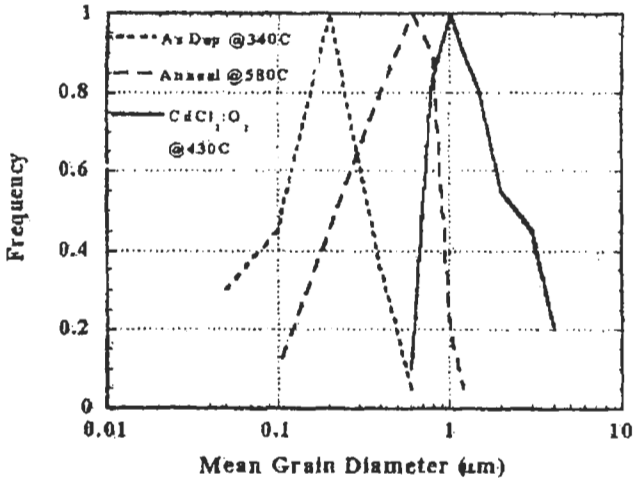

Figure 9 Grain size distribution of a CdTe film directly after deposition, after annealing and after activation [8]. (Reproduced with kind permission of James & James Publ.)

for small values of x, the Te rich mixture. This goes hand in hand with increased total photocurrent. Significant amounts of sulphur (probably CdS_xTe_{1-x}) can be detected both at grain boundaries and within heavily faulted grains (as opposed to grains with low defect density) for films deposited at temperatures between 500 and 600°C [5]. Model calculation yielded three-dimensional distributions of S and Te which have led to isocompositional contour plots of diffused regions [12] (Figure 11). In the case shown for two adjacent grains after activation the different grain sizes result in a different alloy profile. For the narrower grain, no pure CdTe remains at all, while the wider grain exhibits the entire range of alloy composition. The evolution of mixed regions and their progression have been followed by X-ray diffraction studies, impressively showing the emergence of lines corresponding to mixed material. Figure 12 shows initially the line of pure CdTe and after 10, 20 and 40 minutes of activation the emergence and growth of alloy lines. Modelling of these results yielded diffusion coefficients, which have been used to obtain the above three-dimensional profiles of Figure 11. Similar results have been obtained by measuring the lattice constant of films before and after activation [6]. The value for lattice constant a before annealing – as mentioned above – has a value of 6.498 Å (indicating stress in the CdTe film) and changes into two distinct values of 6.481 (relaxed CdTe) and 6.468 Å. The latter value does not occur for films deposited onto ITO film without any CdS. These results can only be explained by the occurrence of a CdS_xTe_{1-x} species with $x = 0.2$, corresponding to 6.468 Å.

The presence of oxygen traces during CdTe film deposition usually is considered harmless, a fact which eases the requirements on vacuum equipment. Recently [13] it has been observed that oxygen leads to a reduced CdTe/CdS interdiffusion during activation, a fact which may reduce the danger of shunting of cells by CdS-enhanced grain boundaries, as illustrated in Figure 11.

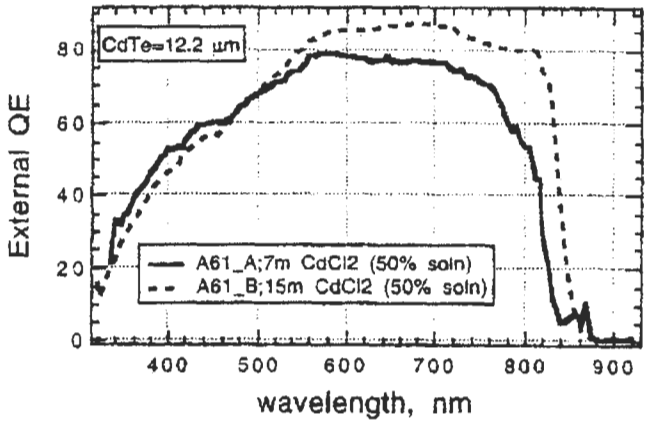

Figure 10 Illustration of intermixing of CdTe and CdS, by long wavelength extension of sensitivity due to lower bandgap mixed compound [11]. (Reproduced with kind permission of the Material Research Society.)

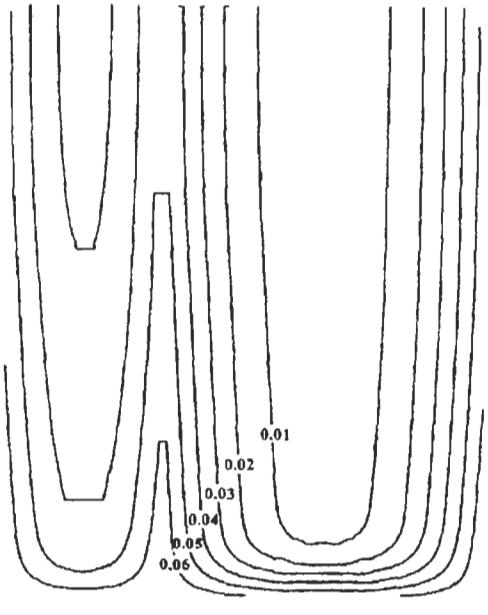

Figure 11 Simulated isocomposition lines of two grains in a CdTe/CdS film. Parameter = x in $CdTe_xS_{1-x}$ [8]. (© American Institute of Physics.)

Increase of Charge-Carrier Lifetime. Electrons generated as minority carriers in the CdTe films have to reach (by diffusion) the field region at the junction and transverse the junction (by drift). Even under low lifetime conditions, electrons generated directly at the junction can transverse the field region: The 'Schubweg' for an electron of 10 cm^2/Vs mobility and a lifetime of 1 ns in an

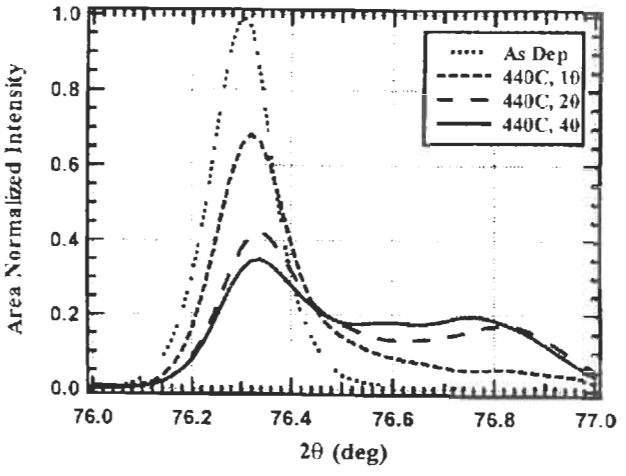

Figure 12 Emergence of mixed CdTe/CdS material after increased thermal stressing identified by X-ray diffraction [8]. (© American Institute of Physics.)

internal field of 10^4 V/cm of 1 μm with at a potential difference of 1 V i: $\mu\tau E = 10^{-4}$ cm. If diffusion in the field-free region is required – for carriers created further away from the junction by red light – lifetime becomes more important. Moutinho et al. [14] have shown that CdTe films of good cells (11%) can show 2 ns lifetime. They have plotted efficiency of cells made similarly as function of lifetime (Figure 13) allowing the conclusion that in CdTe solar cells diffusion of minority carriers also plays an important role for achieving high efficiency.

Conclusions on Activation. All these results indicate that major structural effects in CdTe solar cells occur upon the 'magic' activation process, namely grain growth and interdiffusion, which are stronger for low-temperature deposited films than for films deposited at temperatures of 500°C or more. These ('high-temperature') films directly lead to a stable structure with less recrystallisation and grain grow required.

The main effect of activation on efficiency of the devices, although, is an electronic improvement not so much by morphological effects but by improvement of the crystalline and electronic quality of grains immediately at the junction. Evidently the lifetime of minority carriers in CdTe (electrons) determines the charge carrier collection efficiency of the device.

2.2.2 The Back Contact

It is well-known from semiconductor physics that it is not easy to contact a low-doped p-type semiconductor of relatively high energy gap. There are two general principles for making ohmic contacts to p-type semiconductors:

1 Use of a metal of work function higher than the electron affinity + energy gap of the semiconductor in order to align the top of the valence band

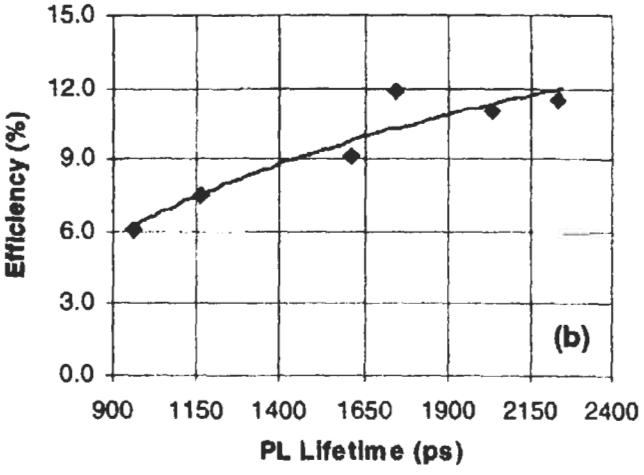

Figure 13 Increase of efficiency of a cell by increase of minority carrier lifetime [14]. (Reproduced with permission from IEEE.)

with the Fermi level of the metal. The electron affinity + energy gap of CdTe is > 6 eV. There is no metal of work function of > 6 eV. This means that all metals lead to a blocking contact, as is illustrated in Figure 14, showing the band diagram of this situation.

2 Generation of a highly doped back-surface layer in the semiconductor. The unavoidable Schottky barrier created by the back-contact metal in the semiconductor will then be thin enough for holes to tunnel through efficiently. Figure 15 shows the band diagram for the second option, a highly p-doped surface region. Consequently it remains to find practical solutions for this.

Efforts for high p-doping in CdTe usually fail due to a strong tendency for self-compensation of acceptors by formation of donors at elevated temperatures as are used here. Furthermore acceptors cannot be introduced by diffusion of atoms or ions from the surface, as diffusion preferentially proceeds along grain boundaries, leading to shunting of the cell by conducting grain boundaries before sufficient doping levels are achieved within the grains. In many cases copper (an acceptor in CdTe) has been added, e.g. in graphite contacts still used for experimental contacting, which upon annealing can diffuse into the CdTe film. Its diffusion coefficient along grain boundaries is 100 times that in bulk CdTe [15]. If Cu reaches the junction, it first reduces the junction width, and then it compensates donors in the CdS layer. Recently, more stable contacts using Cu have been made by depositing Te/Cu double films, which can react to produce Cu_2Te compound films upon annealing, some of the Cu diffusing into the CdTe film, leading to a minute surface doping. [16].

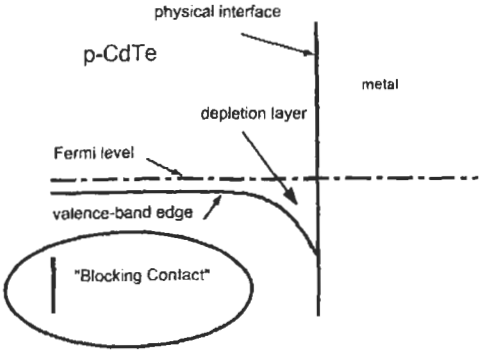

Figure 14 Energy band scheme of the metal–CdTe interface of a CdTe solar cell illustrating blocking contact.

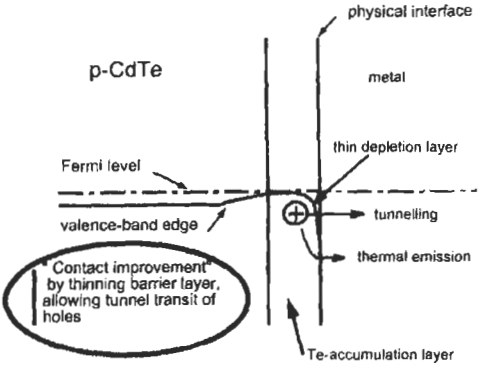

Figure 15 Energy band scheme of a metal contact to CdTe after generation of a p^+ surface by Te enhancement leading to a thin barrier.

Alternative efforts in the past have been directed primarily towards three semiconductors HgTe, ZnTe:Cu, Te and Cu_2Te [17, 18]. All of them have led to unstable contacts.

It has become obvious in the course of recent work [4] that a stable back contact cannot consist simply of a metal film. A new contact system has been developed, consisting of a triple procedure [4]:

- Generation of an *accumulation layer*, e.g. by suitable etching of CdTe a Te-enhanced surface layer can be generated.
- Deposition of a p-type narrow-bandgap, chemically inert semiconductor or semimetal ('*buffer layer*').
- Deposition a metal film for low resistance current collection ('*metal contact*').

The role of the buffer layer essentially consists of protecting the (chemically sensitive) p-type accumulation layer from being corroded by the (reactive) metallic current-collection film. All three components had to be individually

optimised and mutually adjusted. Such a triple structure can be highly stable and made by using techniques suited to large-scale production.

The etching process used proceeds into the grain boundaries, leading to 'Te-caps' covering the grains as illustrated in Figure 3. This has been strikingly visualised experimentally [17] by sputter-etching away the first 30 nm of the film and analysing the new surface by scanning Auger analysis. Figure 16 clearly shows grain boundaries having excess Te in the form of lighter coloured regions.

2.3 Stability Issues

Due to the material's strong ionicity (72%) the energy of the bond between Cd and Te is quite high (5.75 eV) [18]. The energy of any photon in the solar spectrum is lower than the binding energy in CdTe or CdS, so that breaking of bonds must not be considered. The strong bonding leads to an extremely high chemical and thermal stability, reducing the risk of degradation of performance or any liberation of Cd to a very low level. No degradation intrinsic to the material can be expected.

The stability risks of back contacts has been virtually eliminated by the triple structure described in Section 2.2.2. Nevertheless careful process development has to be performed to avoid stability risks from other processing steps, like influences of additives in the lamination material. Only dedicated tests of products can yield to assured stability of the product.

2.4 Best Performance of Cells

Using the most advanced techniques, record efficiencies have been achieved by a few groups, indicating the potential of the CdTe thin-film solar cell. In 1984 the magic limit of 10% efficiency was surpassed by a group at Kodak laboratories, using close spaced sublimation [19]. In 1993 an efficiency of 15.8% was achieved [20] by using again CSS for formation of CdTe films on borosilicate

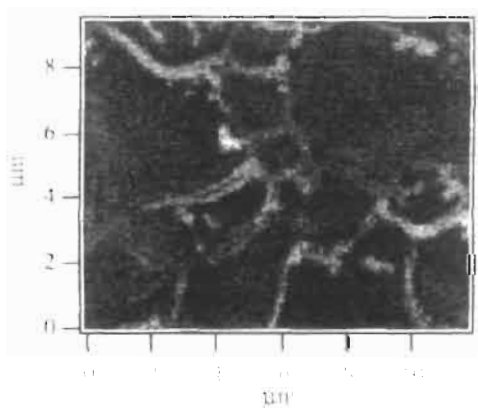

Figure 16 Te-capped CdTe grains by scanning EDX analysis of an ion milled back surface (light areas are Te-enhanced) [17]. (Reproduced with permission from IEEE.)

glass, at temperatures of around 600°C by a group from the University of South Florida. Fine-tuning has been achieved using CdS films made by chemical bath deposition and finally applying an antireflection coating onto the glass surface positioned towards the sun. This value could be surpassed only 7 years later by a group from NREL, which achieved 16.5% efficiency [21]. The important advance in this work has been the use of $CdSnO_4$ deposited onto borosilicate glass.

In both recent cases the higher deposition temperature allowed by use of (expensive) borosilicate glass has been a central issue. For industrial production this type of glass is presently considered too expensive. Therefore in industrial production, low-cost soda-lime glass is used, which is limited in temperature endurance.

3 Making of Integrated Modules

3.1 Interconnection of Cells

Semiconductor solar cells are devices delivering open circuit voltages of less than 1 V. As electric power for commercial applications requires higher voltages, it has proven advantageous to connect a multitude of cells in series in 'modules'. Whereas in the case of silicon solar cells, individual cells have to be series connected by conductors welded onto both sides of wafers, thin-film cells have a strong advantage to allow integrated series connection of numerous cells, which are at the same time defined in area and interconnected. If the different layers of the cells – TCO, p–n film stack and back contact-are individually separated (scribed) into parallel stripes, which overlap asymmetrically the series-connection of one distinct cell with its neighbour can be achieved periodically for all cells so generated, as illustrated in Figure 17. After deposition of the TCO film, a first set of separation scribing lines at a periodic distance of about 1 cm is applied, typically by laser ablation. Subsequently the p-n film sandwich is deposited and separated at the same periodicity, so that this scribing line opens the TCO beneath for the back contact, which is deposited subsequently. If the back contact now is separated by a similar set of lines at a small distance from its contact line to the TCO, the interconnection is achieved. Figure 17 shows the principle for a set of three cells.

In some cases, such as electrodeposition, it is not permissible to separate the TCO film before depositing the semiconductor film. Here a variation in the procedure allows the scribing of the first two lines after the deposition of the semiconductor film [22]. An insulating fill-up of the first scribing line is required in this process, illustrated in Figure 18.

Evidently, using these techniques, the cell width can be adjusted according to technical needs and/or commercial requirements: On the one hand, more interconnection triple scribes lead to higher loss in active area. (Typically a scribing system requires between 0.2 and 0.3 mm.) On the other hand wider cells will lead to increased series resistance (lower fill-factor), as the current density

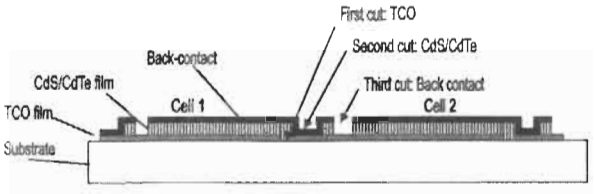

Figure 17 Interconnection principle.

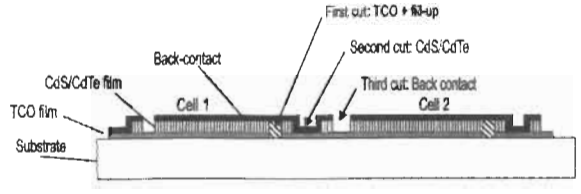

Figure 18 Modified interconnection principle.

being conducted through the TCO film will be higher, leading to higher voltage drop. For CdTe a cell width of 9–10 mm seems to be an optimum value for TCO films of 8–10 Ω per square resistivity. (For CIS cells, due to higher current density and lower voltage of the individual cell, smaller cells – about 6 mm wide – are appropriate; for amorphous silicon conversely wider cells are optimal.)

3.2 Contacting

The photocurrent of a module transverses all series connected cells and is extracted by contacts to the first and last cell, and all individual cell voltages add to the total voltage. Usually metallic conductors are attached to the free contact area of the first and last cell by conducting adhesive and further connected by contact bands towards the point of the module, where it is to transverse the back sealing, typically glass. Usually the contact bands are Sn-plated Cu ribbons. Figure 19 indicates the topology of the contacting conductors. Care has to be taken to avoid shunting at any place.

3.3 Lamination

After contact bus attachment the module needs sealing and protection against external influences. This usually is achieved by laminating a second glass plate to the module-carrying side of the first glass plate. It is required to remove all films at a boundary region of 1–2 cm of the module to provide the required electric insulation of the module. This is usually achieved before contacting by sand blasting or laser ablation.

For historical reasons, in many cases the technology used for silicon modules is also used for CdTe modules, namely sealing by EVA (ethyl-vinyl-acetate),

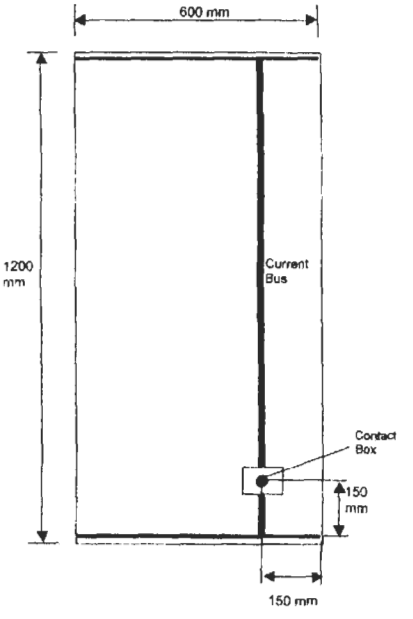

Figure 19 Topology of contact bus system, as seen from the back of the module.

which is used as a monomer, applied as a sheet and polymerised by a thermal annealing step under vacuum. Commercial EVA is readily available. It is 'overqualified' for CdTe, as intense development work has been invested into the commercial product to stabilise it against degradation in the sunlight impinging onto silicon modules. In the case of CdTe this special quality is not required, as sunlight directly enters the junction after having passed the glass and the lamination material is positioned below the second glass and therefore oriented away from the sun.

The cover glass so laminated to the module has a hole, through which the contact bands are guided into a contact box, which is attached to the glass (cf. Figure 19). Two stable current guides with plugs are attached to the box and will be used for connecting the modules so generated to the user-circuit. Evidently all connections and contacts must be extremely well protected against water and water vapour for achieving the expected lifetime of the module.

4 Production of CdTe Thin-Film Modules

4.1 Generalised Production Sequence

The different steps to make cells and modules, described in Sections 2 and 3 can be arranged into a sequence to make ready-to-use modules as a product:

1. Selection of substrate glass, soda-lime glass ('floatglass') as substrate.
2. Deposition of the transparent conductive coating (SnO_2, ITO, etc.).
3. Scribing of the TCO film into parallel bands, defining and separating the cells. For some processes this scribing can be done later, after deposition of the semiconductor films.
4. Deposition of CdS films of lowest possible thickness, typically around 100 nm.
5. Deposition of CdTe by the process of choice for the particular product.
6. Activation of the film stack by influence of $CdCl_2$ at temperatures of around 400°C.
7. Application of the second scribing step, which opens the semiconductor stack for contacting the TCO film. Optionally step 3 can be applied in parallel, the scribing line afterwards has to be filled up for electrical insulation.
8. Application of the back-contact structure, consisting of a set of steps, e.g. etching to achieve a Te accumulation, application of a buffer layer, application of the metallic back contact.
9. Separation cut to separate the back contacts of the neighbouring cells.
10. Attachment of the contact bus structure.
11. Lamination with a second glass (or plastic) using a suitable plastic, such as EVA or a thermoplastic film, the contacts protruding through a hole in the cover glass plate for the next step.
12. Contact box attachment, in which the fragile contact bands from the module are connected to stable cables with suitable plugs for commercial application.
13. Measurement of each module's efficiency using a solar simulator.

This sequence – with some modifications – is the basis of the following industrial efforts into production.

4.3 Industrial Production of Modules

A commercial product can only be manufactured with expectation of cost-covering revenues, if a factory above a certain capacity is built, using the dimensions of scale. It is generally accepted today that a capacity of around 100,000 m^2 per annum is presently appropriate. All units of significantly lower capacity should be called pilot plant as they will require more funds than any return can provide. At around 600,000 m^2 per annum a cost potential of 0.6 / W_p has been estimated by a group of experts [23].

Presently three industrial units are known to actively pursue the target of large-scale production. They basically differ by the deposition technique for CdS and CdTe.

4.3.1 BP Solar Inc. (Fairfield, California, USA)

Work at BP Solar has started in Great Britain in 1984, when British Petroleum took over a galvanic deposition process for CdTe thin-film solar cells from

Monosolar Inc. in the USA. BP Solar continued development of the basic electrodeposition process for CdTe [24]. Upscaling work resulted in a factory, which has been built in the USA. Due to low deposition rates, parallel deposition is used: A large number (40 to 100) plates is immersed into a tank containing a recirculation system for the continuously replenished electrolyte. A constant potential is applied to the plates via the TCO films, already covered by CdS. (The CdS film is deposited by the chemical bath deposition technique, also in parallel onto a larger number of TCO-coated glasses.) The total charge applied to the plates is a measure for film thickness. A charge of about 12000 Cb/m^2 leads to approximately 1.6 μm of CdTe film. Post annealing leads to strain relief, change of conduction polarity from n to p and activation by means of a Cl-compound added to the bath. The grain size grows from 0.1 to 0.2μm to about 0.4 μm during this procedure.

Great care has to be taken to avoid lateral voltage drop over the plate surface during CdTe deposition. Te- or Cd-rich compounds can form upon deviation from this condition. To achieve good quality films, lowest possible surface resistivity of the TCO has to be chosen. The cell-defining and module-generating scribe application follows the principle shown in Figure 18. In order to keep the TCO film intact as long as possible, the TCO scribing lines are applied after CdTe deposition, necessitating a fill-up procedure. Module sizes are around 1 m^2, yielding a power of around 72 W under simulated terrestrial solar light are reported [25]. More than 150,000 m^2 of glass substrates can be processes per annum. The line can produce 0.55 m^2 and 0.94 m^2 modules. The deposition system consists of 8 identical deposition tanks. Each tank is able to simultaneously coat 40 0.55 m^2 or 24 0.94 m^2 substrates. Recently (2002) BP Solar has manufactured the first large area CdTe module of > 10% efficiency[2].

4.3.2 First Solar LLC (Toledo, Ohio, USA)

This company has started work within the scope of a predecessor called Solar Cells Inc. around 1991 in Toledo by a senior shareholder of Glasstech Inc. In 1999 a joint venture with a finance group from Arizona, USA, has been formed, which led to the new name First Solar LLC [26]. The basic process for generating CdS/CdTe junctions relies on the sublimation/condensation properties of CdS and CdTe described above. Substrates coated by SnO_2 films by Libbey Owens Ford using a spray process, enter a vacuum system through a loadlock and move – lying on a roller system, to avoid warping – into a chamber heated to temperatures around 560°C. Vapour sources are positioned above the substrates out of which CdS and CdTe vapours emerge, are directed towards the substrates and condense sequentially on the substrates. The CdS and CdTe material is continuously fed into the evaporators. Module interconnection of cells is performed ex-post, i.e. first and second scribing lines are applied after semiconductor deposition, requiring filling of scribing line 1 (cf. Figure 18).

[2] In 2002 the management of BP Solar decided to terminate its CdTe development and production efforts after 18 years of investment and closed down the factory.

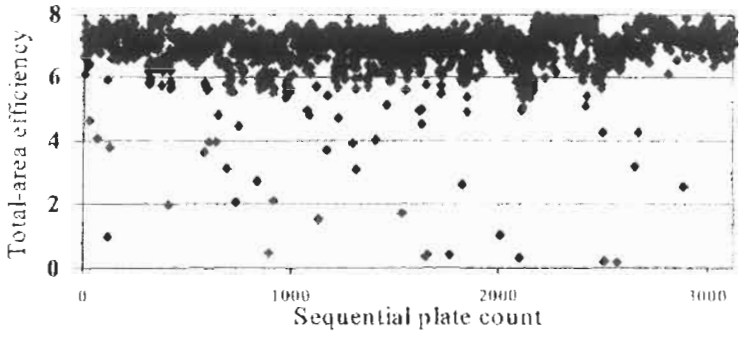

Figure 20 Total-area efficiency for 3128 sequentially deposited modules from First Solar LLC (from [27]).

The standard module size of First Solar is 60 × 120 cm^2 = 0.72 m^2 [27]. Efficiencies of 6–8% can be routinely achieved. Figure 20 shows area efficiency vs. sequential plate count for 3128 sequentially deposited modules.

4.3.3 ANTEC Solar GmbH (Arnstadt, Germany)

The technology used at ANTEC Solar is essentially based on the development started at Battelle Institut around 1970 [28]. After closure of Battelle Institut the know how has been transferred to ANTEC GmbH, a management buy-out from Battelle and developed into a manufacturing technology. ANTEC Solar has been founded in 1996 in order to start production of CdTe thin-film PV modules. A fully automated production plant has been built in Arnstadt (Germany) and production has started in 2001. The basic process used for deposition of CdTe is close spaced sublimation. Glass-substrates carrying scribed TCO films are transported in vacuum above crucibles containing CdS and CdTe at temperatures of 700°C. The semiconductor materials condense at temperatures of 500°C and form the n–p diode structure, which is activated in a $CdCl_2$ atmosphere. Module size is 60 × 120 cm^2, presently efficiencies of modules is about 7%, increase up to 8% is expected to be achieved in 2002. In contrast to BP Solar and First Solar the TCO is also made in the plant in the online system. Definition of interconnected cells is achieved according to Figure 17, i.e. at three different stages of the plant by laser ablation (first scribe) and mechanical ablation (second end third scribe)[3].

Figure 21 shows the total area efficiency of 2000 modules manufactured in one production run. The production plant presently employs 100 persons.

4.4 A 10 MW Production Line

In the following, by means of an example, the production line of ANTEC Solar GmbH is described and illustrated.

[3] Because of financial problems, ANTEC Solar had to declare insolvency in 2002. In 2003 the plant has been taken-over by a new owner, who successfully restarted production.

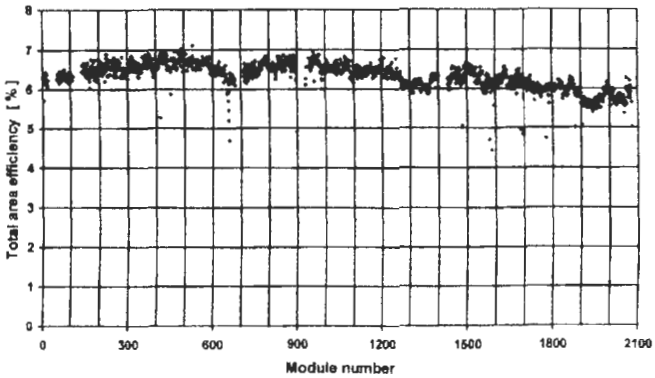

Figure 21 Total area efficiency for 2000 sequentially deposited modules from ANTEC Solar GmbH.

The deposition line was conceived as a two-step production line, consisting of a fully automated deposition line for integrated modules on glass substrates of 60 × 120 cm^2 and a semi-automatic module line, for hermetical sealing, contacting, measuring and customising of the modules into a marketable product.

The fully automatic in-line deposition procedure consists of nine steps:

1. Cleaning of the substrate (float glass).
2. Deposition of the transparent contact (ITO + SnO_2) at around 250°C.
3. Scribing of the TCO film for cell definition and interconnection).
4. Deposition of CdS and CdTe by Close-Spaced Sublimation (CSS) at around 500°C.
5. Activation (improvement of junction by annealing in Cl-containing atmosphere at around 400°C).
6. Wet-chemical etching for contact preparation (Te accumulation).
7. Scribing by mechanical tools for interconnection of cells.
8. Deposition of two-layer back contact by sputtering.
9. Scribing by mechanical tools for separation and interconnection of cells.

Most of these positions are connected by heating or cooling segments in order to present the plates to the deposition steps at the adequate temperatures They take a large part of the equipment length. The highest temperature (500°C) is reached during deposition of the semiconductor films, compatible with glass stability. The total length of the automated deposition line is 165 m. Glass plates (to become modules) are transported by automated conveyor systems and are not touched by human hands during the processes. They are collected in boxes in sets of 30 and transferred to the module line in an adjacent hall.

In the module line the substrates with sets of interconnected cells (often called 'submodules') are contacted and sealed for convenient use in energy generating systems. This part of the factory consists of the following procedures:

1. Cleaning of the cover glass (float glass).
2. Deposition of the contact buses onto the modules.
3. PV function testing to identify substandard modules, which can be excluded from further processing.
4. Cutting of EVA sheet to size.
5. Joining of module, EVA sheet and cover glass.
6. Lamination (sets of 6 modules).
7. Fill-in of contact hole in cover glass.
8. Attachment of contact box.
9. Quantitative measurement of PV performance (sets of 3 modules).
10. Type-tag attachment.
11. Classification, selection and packaging for dispatch.

The module line requires some manual handling and adjustments, due to the heterogeneity of the processes. Figure 22 shows the geometrical arrangement of the different processes. Each line has been installed in a separate hall. Both halls are connected by an aisle for transfer of modules. Buffer stations allow the removal of partly completed modules in case of an incident in the down-line stations without crashes in the up line stations. The overall primary parameter for the deposition line and also the module line has been the production speed defined at 120,000 modules per annum, which leads to an average linear transportation speed of approximately 1 m/min in the production line.

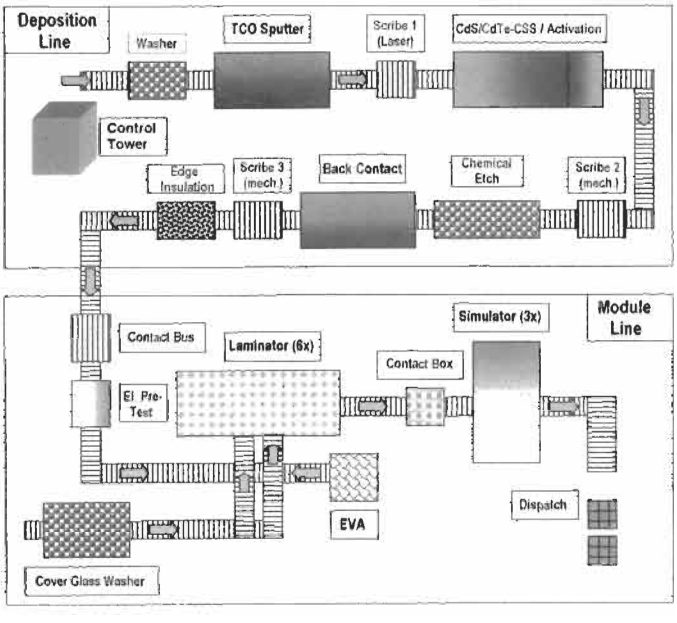

Figure 22 Schematic of the components of the plant.

The procedures described above contain (a) state-of-the-art procedures, (b) new, but simple procedures, and (c) new developed procedures.

Standard procedures are sputter-deposition of ITO, SnO_2, metals. Dedicated equipment has been constructed by experienced equipment manufacturers. In some cases (e.g. ITO deposition) multiple sputtering targets are needed in order to achieve the required film thickness at the given transport-speed of the substrates (around 1 m/min). The final steps of contacting and lamination are also using state-of-the-art techniques. Equipment can be bought custom-made on the market. An unforeseen effort in the set-up and initial operation of the plant had to be dedicated to the transport of the substrate sheets through heating and cooling stages without breakage due to excessive thermal gradients. After some significant modifications breakage under thermal stress could be virtually eliminated.

Simple, but new processes are essentially the core processes for the active semiconductors, namely CSS-deposition of CdS, CdTe, and – if required – back contact buffer-semiconductors. It has been shown, that CdTe can be deposited onto stationary substrates at rates of 10 μm/min and more. For achieving the required production speed, three crucibles containing a week's supply of starting material of CdTe are used. For CdS, due to its low thickness only one crucible is used. As mentioned, the vacuum requirements are rather low, so that no high-vacuum equipment is needed. (For CdTe oxygen-incorporation to some extent indeed is considered advantageous by some researchers.) Laser scribing of the TCO film does not require basic new technologies. Equipment can be built by industry and processing data have to be developed and adjusted. In spite of these arguments, some problems have been incurred by thermal stress conditions of crucibles and substrates. Fast heating invariably leads to breakage of glass substrates.

More involved *new processes* are activation of the junction CdS/CdTe and etching of the CdTe surface as contact preparation procedure. Etching requires the wetting of the substrates carrying the activated CdS/CdTe film stacks by nitric/phosphoric acid plus water solutions ('NP'-etch), rinsing and drying. Although being essentially simple, procedures equipment had to be developed to incorporate these processes under tightly controlled parameters into the production line allowing the target speed to be achieved. Activation requires exposition of the substrates carrying the TCO-CdS-CdTe film-stack to, e.g.$CdCl_2$ at elevated temperatures. Fortunately traces of oxygen do not play a detrimental role. (The activation step in the laboratory can even be executed in air.) Furthermore, $CdCl_2$ at room temperature has extremely low vapour pressure. Some special chemical engineering skill has been needed to conceive an in-line activation stage fitting into the production line. Mechanical scribing has turned out to be more involved, due to the requirement that the production line should have only one service interval per week. Scribing tools have to survive one week under tough tolerances. New solutions had to be found for recognising and identifying the first laser cuts below the CdTe film for precise positioning of the second and third scribing lines. Implementation of automatic image recognition of previously scribed lines in the TCO films for precise positioning of subsequent scribing lines has been a non-trivial task

Figure 23 View of the total deposition line.

After the plant had been built and assembled in 1999 and first functional tests had been passed early 2000, de-bugging and process optimisation has required extensive tests and equipment-modifications by the hardware and software manufacturers. Production has started in 2001. Figure 23 shows the deposition line in its entirety.

4.5 Environmental and Health Aspects

The production of polycrystalline thin-film CdTe solar modules basically employs techniques common in chemical and microelectronic industry. The substances involved are easily manageable by standard processes. Production is possible under existing safety laws without putting into risk health of staff. It is technically and economically possible to design and operate a factory with zero emission. Workers in a production environment have been tested regarding Cd uptake and shown Cd content in blood and urine far below the threshold concern level under periodic medical scrutiny [29]. Smokers have shown a somewhat higher Cd level than non-smokers, but still below any threshold for concern.

A number of studies from third parties [30–33] show negligible risk under use of CdTe solar modules for the environment and humans even under irregular conditions. In case of exposure to fire, the substrate- and cover-glass will melt long before the CdTe decomposes, thereby including the semiconductor into the re-solidifying glass. Incineration experiments conducted by BP Solar in cooperation with a fire research institution using typical household inventory plus CdTe modules have not led to detectable emissions of Cd compounds [30].

During use a CdTe module can be compared to laminated glass similar to that used in cars. Thus modules will not easily break and release their content. At their end of life, modules can be recycled by crushing the whole modules and

either returning the debris to the smelters, which can inject the material into their processes without significant additional cost, or dissolving the films by liquid or gaseous etchants.

The system's company debis (a subsidiary of Daimler-Chrysler AG) has established a life cycle inventory for CTS thin-film solar modules of ANTEC Solar GmbH guided by ISO 14040 and 14041. To achieve this aim, the total energy and material flow for the module's life cycle has been accounted with help of the CUMPAN® software system. This allows, for example, for the raw materials the determination of the total energy required for their production and processing.

- The manufacture of one square metre of CTS-module uses 126 kg raw material and primary energy carrier and 70 kWh electric energy.
- Under the climatic conditions of Germany, the generation of 1000 kWh of electricity per annum at a module lifetime of 30 years saves 16,244 kg of carbon dioxide and further undesired materials, such as sulphuric dioxide and nitrogenic oxides.
- The production plant is built not to emit any material. Water is reprocessed and re-used. (Waste heat at this time is emitted to the environment, though.)
- A recycling process is envisaged for spent and reject modules. In view of environmental safety, economical retrieval of valuable raw materials, and securing of hazardous materials, this process can be considered satisfying.
- Compared with alternative thin-film modules (a-Si, CIS), emissions and waste during production amount to similar values.
- The emission of cadmium can be judged as low in comparison to other emission sources (coal-fired power plants, phosphate fertiliser). Even in case of accidents (e.g. fire), by reason of the small quantities of (thermally stable) material per square metre of module area, no environmentally critical emission must be contemplated.
- The total energy used for fabricating a module will be retrieved by the module within 15 months using the actual energy uptake of the ANTEC factory. From then on the module operates in an environmentally benign way.

4.6 Material Resources

More than 99% of the weight of a CdTe modules consist of float glass, EVS and metal connectors, readily available in virtual unlimited quantities. TCO films made of SnO_2 are not considered to by limited by available Sn supplies. In used in ITO films is a more rare resource at an annual production of 120 t [34]. Furthermore it is also used for ITO films in liquid crystal displays and the $CuInSe_2$-based thin-film solar cell. ITO can be substituted by SnO_2 and – possibly – ZnO, Sn and Zn being abundant metals. CdTe and CdS warrant a closer consideration. Presently CdTe (and CdS) are offered in the required purity by 5 industrial enterprises. Cd is presently produced as a by-product of Zn at 20,000 t per year [34]. Te, due to low demand is presently produced at 300 t per year as a by-product of Cu [34]. Growing future demand according to an expert in the field [35] can be satisfied by more efficient extraction from the anodic slurries in Cu

Figure 24 View of a CdTe thin-film PV module.

electrorefining on the one hand and also by exploiting Te-rich ores in South America not yet exploited. S finally is an abundant element.

In summary, no critical material bottleneck is expected for an expanding production. The CdTe thin-film solar cell will be able to take a share in ameliorating future energy shortages and the climate change expected from burning fossil fuels.

5 The Product and Its Application

The photovoltaic modules manufactured in a factory are ready-to-use in a suitable PV installation. CdTe modules by any one manufacturer are mass products made on large scale (100,000 per year or more). Typically the modules are sized about 0.6×1.2 m^2. A module 60 cm wide can easily be carried under the arm by one person. Glass-glass laminates, as manufactured, e.g., by First Solar and ANTEC Solar have a weight of 16 kg. A contact box furnishes two cables carrying plugs (male and female for easy series connection), which are long-term stable. Figure 24 shows an ATF module from ANTEC Solar. A very homogeneous appearance of most thin-film modules helps organic and visually pleasing installation.

5.1 Product Qualification

A PV module is a product made for long time deployment in a harsh environment and therefore must be furnished with a warranty for approximately 20 years of useful life. In order to provide such assurance, the international standards agencies (IEC = International Electrotechnic Commission) have designed

international norms which are valid worldwide. The norm pertaining to thin-film modules is IEC 61646, 'Thin film terrestrial photovoltaic modules – Design qualification and type approval'. This norm has been published in 1996 and originally has been designed with amorphous silicon modules in mind.

Modules to be classified as fulfilling IEC 61646 have to undergo an extensive set of tests defined in detail in the text of this norm. Briefly these are 4 sets, for which 8 modules have to be provided, typical for the production discussed:

A. Performance tests

- Power output at standard test condition (25°C, 1 sun)
- Power output at nominal operating conditions
- Power output at low sunlight intensity (20%)

B. Endurance tests

- Long-term outdoor exposure
- Light soaking
- Temperature shock tests
- Damp-heat test

C. Mechanical tests

- Mechanical load
- Twist test
- Hail-test

Figure 25 Installation of CdTe modules from First Solar LLC on an office building.

Figure 26 Installation of CdTe modules from ANTEC Solar on the wall of a public administration building.

Figure 27 Installation of CdTe modules on a private residence roof.

D. Electric tests

- Insulation test
- Water immersion test

5.2 Examples of Installation of CdTe Modules

Thin-film modules can show a highly homogeneous surface appearance and very little variation from module to module. This allows the assembly of large,

Figure 28 Close-up of mounting system on metal rafters for roof installation.

highly homogeneous panels on rooftop, facade or on the ground. Figures 25–27 show examples of such installations. Modules in form of glass/glass laminates can be mounted on special structures, which can be invisible and nonetheless watertight. Figure 28 shows how modules can be mounted on metal rafters, which allow water drainage and also seal the interior of the roof by rubber lips.

6 The Future

After more than 20 years of development in various industrial and academic laboratories, the CdTe thin-film solar module has entered the production stage and first experience is gained in this process. This will definitively lead to the next generation of plant at capacities around 1,000,000 m^2 per year. It is expected that the 'learning curve' will be transgressed quite fast which will lead to a mature low-cost product.

References

[1] Zanio, K., 1978. Cadmium Telluride: Materials Preparation, Physics, Defects, Applications. *Semiconductors and Semimetals*, Vol. 13.

[2] Bonnet, D. et al., 1995. The CdTe Thin Film Solar Cell – EUROCAD. Final Report to the Commission of the European Communities, Project No. JOU2-CT92-0243, 1995. Referenced data later also published in: Al Allak, H.M. et al., 1995. The Effect of Processing Conditions on the Electrical and Structural Properties of CdS/CdTe Solar Cells. *Proc. 13th European Photovoltaic Solar Energy Conference*, Nice, pp. 2135–2138.

[3] Bube, R., 1960. *Photoconductivity of Solids*. Wiley, New York, London, p. 94.
[4] Bonnet, D. et al., 2002. CADBACK: The CdTe Thin Film Solar Cell – Improved Back contact. *Final Report to the European Commission*, Contract No. JOR3-CT98-0218.
[5] Dhere, R. et al., 1997. Influence of CdS/CdTe Interface Properties on the Device Properties. *Proc. 26th IEEE Photovoltaic Specialists Conference*, Anaheim, pp. 435–437.
[6] Moutinho R.H. et al., 1998. Effects of $CdCl_2$-treatment on the recrystallization and electro-optical properties of CdTe films. *J. Vac. Sci. Technol.*, Vol. A16, pp. 1251–1257.
[7] Moutinho H.R. et al., 2000. Alternative procedure for the fabrication of close-spaced sublimated CdTe solar cells. *J. Vac. Sci. Technol.*, Vol. A18, pp.1599–1603.
[8] McCandless, B. and Birkmire, R., 2000. Diffusion in CdS/CdTe Thin-Film Couples. *Proc. 16th European Photovoltaic Solar Energy Conf.*, Glasgow, pp. 349–352.
[9] Durose, K., private communication.
[10] Nunoue, Sh., Hemmi, T. and Kato, E., 1990. Mass Spectrometric Study of the Phase Boundaries of the CdS/CdTe System. *J. Electrochem. Soc.*, Vol. 137, pp.1248–1251.
[11] Dhere, R.G. et al., 1966. Intermixing at the CdS/CdTe interface and its Effect on Device Performance. *Mat. Res. Soc. Symp. Proc.*, Vol. 426, pp. 361–366.
[12] McCandless, B., Engelman, M.G and Birkmire, R.W., 2001. Interdiffusion of CdS/CdTe Thin Films: Modelling X-Ray Diffraction Line Profiles. *J. Appl. Phys.*, Vol. 89, pp. 988–994.
[13] Yan, Y., Albin, D.S. and Al-Jassim, M.M., 2001. The effect of oxygen on junction properties in CdS/CdTe solar cells. *Proc. NCPV Program Meeting*, pp. 51–52.
[14] Moutinho, H.R. et al., 2000. Study of CdTe/CdS solar cells using CSS CdTe deposited at low temperature. *Proc. 28th IEEE Photovoltaic Specialists Conf.*, Anchorage, pp. 646–649.
[15] Hegedus, S.S., McCandless, B.E. and Birkmire, R.W., 2000. Analysis of stress-induced degradation in CdS/CdTe solar cells. *Proc. 28th IEEE Photovoltaic Specialists Conf.*, Anchorage, pp. 535–538.
[16] Hegedus, S.S., McCandless, B.E. and Birkmire, R.W., 2001. Initial and Stressed Performance of CdTe Solar Cells: Effect of Contact Processing. *Proc. NCPV Program Review Meeting*, pp. 119–120.
[17] Levi, D.H. et al., 1997. Back contact effects on junction photoluminescence in CdTe/CdS solar cells. *Proc. 26th IEEE Photovoltaic Specialists Conf.*, Anaheim, pp. 351–354.
[18] Hartmann, H., Mach, R. and Selle, B., 1981. Wide gap II–VI compounds as electronic materials. In: Kaldis, E., Ed., *Current Topics in Materials Science*, Amsterdam, pp. 1–414.

[19] Tyan, Y.-S. and Perez-Albuerne, E.A., 1982. Efficient Thin Film CdS/CdTe Solar Cells. *Proc. 16th IEEE Photovoltaic Specialists Conf.*, San Diego, pp. 794–800.

[20] Britt, J. and Ferekides, C., 1993. Thin film CdS/CdTe solar cell with 15.8% efficiency. *Appl. Phys. Lett.*, Vol. 62, pp. 2851–2852.

[21] Wu, X. et al., 2001. 16.5% efficient CdS/CdTe polycrystalline thin film solar cell. *Proc. 17th European Photovoltaic Solar Energy Conf.*, Munich, pp. 995–1000.

[22] Rose, D. et al., 2000. R&D of CdTe-absorber photovoltaic cells, modules and manufacturing equipment: Plan and progress to 100 MW/yr. *Proc. 28th IEEE Photovoltaic Specialists Conf.*, Anchorage, pp. 428–431.

[23] Woodcock, J.M. et al., 1997. A study on the upscaling of thin film solar cell manufacture towards 500 MWp per annum. *Proc. 14th European Photovoltaic Solar Energy Conf.*, Barcelona, pp. 857–860.

[24] Cunningham, D.W. et al., 2000. Advances in Large Area Apollo Module Development. *NCPV Program Review Meeting*, pp. 261–262.

[25] Cunningham, D.W. et al., 2000. Large Area Appollo Thin Film Module Development. *Proc. 16th European Photovoltaic Solar Energy Conf.*, Glasgow, pp. 281–285.

[26] McMaster, A. et al., 2000. PVMat Advances in CdTe Product Manufacturing. *NCPV Program Review Meeting*, pp. 101–102.

[27] Rose, D., Powell, R., 2001. Research and Progress in High-Throughput Manufacture of Efficient, Thin-Film Photovoltaics. *NCPV Program Review Meeting*, pp. 209–210.

[28] Bonnet, D. and Rabenhorst, H., 1972. New Results on the Development of a Thin Film p-CdTe–n-CdS Heterojunction Solar Cell. *Proc. 9th IEEE Photovoltaic Specialists Conf.*, Silver Springs, pp.129–131.

[29] Bohland, J.R. and Smigielski, K., 2000. First Solar's Module Manufacturing Experience; Environmental, Health and Safety Results. *Proc. 28th IEEE Photovoltaic Specialists Conf.*, Anchorage, pp. 575–578.

[30] Alsema, E.A. and van Engelenburg, B.C.W., 1992. Environmental Risks of CdTe and CIS Solar Cell Modules. *Proc. 11th European Photovoltaic Solar Energy Conf.*, Montreux, pp. 995–998.

[31] Patterson, M.H., Turner, A.K., Sadeghi, M. and Marshall, R.J., 1994. Health, Safety and Environmental Aspects of the Production and Use of CdTe Thin Film Photovoltaic Modules. *Proc. 12th European Photovoltaic Solar Energy Conf.*, Amsterdam, pp. 951–953.

[32] Moskowitz, P.D., Steinberger, H. and Thumm, W., 1994. Health and Environmental Hazards of CdTe Photovoltaic Module Production, Use and Decommissioning. *Proc. First World Conf. on Photovoltaic Energy Conversion*, Hawaii, pp. 115–118.

[33] Steinberger, H., 1998. Health and Environmental Risks from the Operation of CdTe- and CIS Thin Film Modules. *Proc. 2nd World Conf. on Photovoltaic Solar Energy Conversion*, Vienna, pp. 2276–2278.

[34] US Bureau of Mines, 1992. Mineral Commodity Summary.

[35] Daub, G., PPM Pure Metals GmbH., personal communication.

Cu(In,Ga)Se_2 Thin-Film Solar Cells

U. Rau and H. W. Schock, Institut für Physikalische Elektronik (IPE), Universität Stuttgart, Germany

1 Introduction

With a power conversion efficiency of 18.8% on a 0.5 cm^2 laboratory cell [1] and 16.6% for mini-modules with an area of around 20 cm^2 [2] $Cu(In,Ga)Se_2$ is today by far the most efficient thin-film solar cell technology. The start of production at several places provides a new challenge for research on this material. However, these recent achievements are based on a long history of research and technological development.

$CuInSe_2$ was synthesised for the first time by Hahn in 1953 [3]. In 1974, this material was proposed as a photovoltaic material [4] with a power conversion efficiency of 12% for a single-crystal solar cell. In the years 1983–84, Boeing Corp. reported efficiencies in excess of 10% from thin polycrystalline films obtained from a three-source co-evaporation process [5]. In 1987 Arco Solar achieved a long-standing record efficiency for a thin-film cell of 14.1% [6]. It took a further ten years, before Arco Solar, at that time Siemens Solar Industries (now Shell Solar), entered the stage of production. In 1998, the first commercial $Cu(In,Ga)Se_2$ solar modules were available [7]. In parallel, a process which avoids the use of H_2Se is being developed by Shell Solar in Germany [8] (see also Chapter V-1). Other companies in the USA, Global Solar and ISET, plan to commercialise modules prepared on other than glass substrates. In Europe, the long-term development efforts of the EUROCIS consortium on the co-evaporation process resulted in the activity of Würth Solar with pilot production envisaged in 2003 [9, 10]. In Japan, two lines for film preparation are planned by Showa Shell (selenisation by H_2Se) [11] and Matshushita (co-evaporation) [12].

In this chapter, we give a short overview on the present knowledge of $Cu(In,Ga)Se_2$-based heterojunction thin film solar cells. We focus on four points: (i) The description of the basic material properties such as crystal properties, phase diagram, and defect physics. (ii) Description of the cell technology starting from the growth of the polycrystalline $Cu(In,Ga)Se_2$ absorber up to device finishing by heterojunction formation and window layer deposition. This section

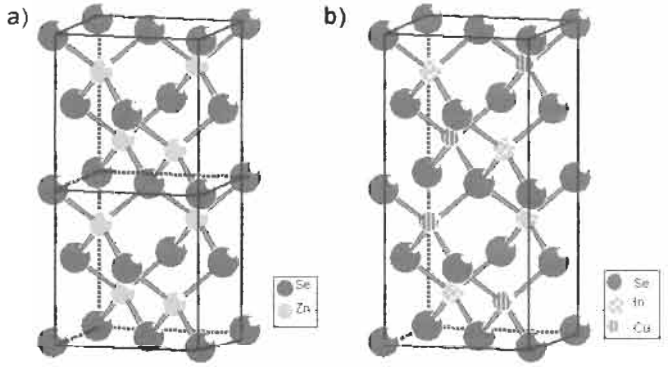

Figure 1 Unit cells of chalcogenide compounds. (a) Sphalerite or zinc blende structure of ZnSe (two unit cells); (b) chalcopyrite structure of CuInSe2. The metal sites in the two unit cells of the sphalerite structure of ZnSe are alternately occupied by Cu and In in the chalcopyrite structure.

also discusses basic technologies for module production. (iii) The electronic properties of the finished heterostructure. (iv) Finally, Section 5 discusses the photovoltaic potential of wide-gap chalcopyrites, namely $CuGaSe_2$ and $CuInS_2$, as well as that of the pentenary alloy system $Cu(In,Ga)(S,Se)_2$ and the possibility of building graded-gap structures with these alloys.

This chapter can only briefly cover those scientific issues that are relevant for photovoltaic applications. More detailed information can be found in two recent review articles by the present authors [13, 14] as well as in references [15–19].

2 Material Properties

2.1 Chalcopyrite Lattice

$CuInSe_2$ and $CuGaSe_2$, the materials that form the alloy $Cu(In,Ga)Se_2$, belong to the semiconducting I–III–VI_2 materials family that crystallise in the tetragonal chalcopyrite structure. The chalcopyrite structure of, for example, $CuInSe_2$ is obtained from the cubic zinc blende structure of II–VI materials like ZnSe by occupying the Zn sites alternately with Cu and In atoms. Figure 1 compares the two unit cells of the cubic zinc blende structure with the chalcopyrite unit cell. Each I (Cu) or III (In) atom has four bonds to the VI atom (Se). In turn each Se atom has two bonds to Cu and two to In. Because the strengths of the I–VI and III–VI bonds are in general different, the ratio of the lattice constants c/a is not exactly two. Instead, the quantity $2 - c/a$ (which is -0.01 in $CuInSe_2$, $+0.04$ in $CuGaSe_2$) is a measure of the tetragonal distortion in chalcopyrite materials.

2.2 Band Gap Energies

The system of copper chalcopyrites $Cu(In,Ga,Al)(Se,S)_2$ includes a wide range of band-gap energies E_g from 1.04 eV in $CuInSe_2$ up to 2.4 eV in $CuGaS_2$, and even 2.7 eV in $CuAlS_2$, thus, covering most of the visible spectrum. All these compounds have a direct band gap making them suitable for thin film photovoltaic absorber materials. Figure 2 summarises lattice constants a and band-gap energies E_g of this system. Any desired alloys between these compounds can be produced as no miscibility gap occurs in the entire system. We will discuss the status and prospects of this system in Section 5 in more detail.

2.3 The Phase Diagram

Compared with all other materials used for thin-film photovoltaics, $Cu(In,Ga)Se_2$ has by far the most complicated phase diagram. Figure 3 shows the phase diagram of $CuInSe_2$ given by Haalboom et al. [20]. This investigation had a special focus on temperatures and compositions relevant for the preparation of thin-films. The phase diagram in Figure 3 shows the four different phases which

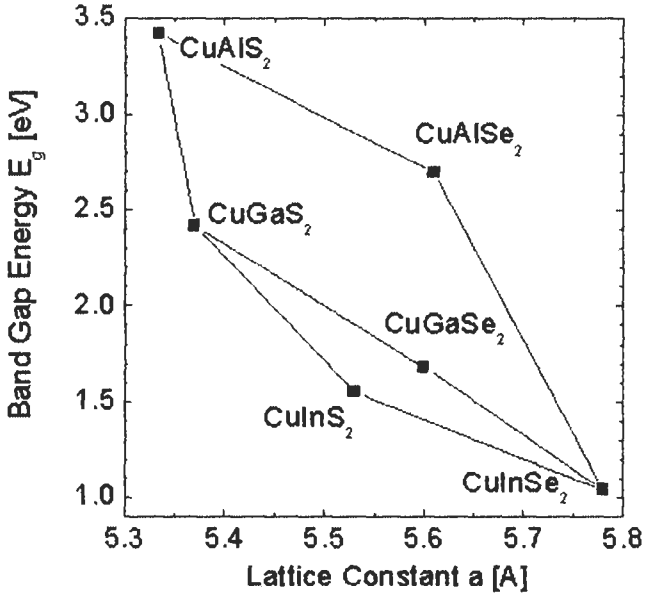

Figure 2 Band-gap energies Eg *vs. the lattice constant a of the Cu(In,Ga,Al)(S,Se)$_2$ alloy system.*

have been found to be relevant in this range: the α-phase ($CuInSe_2$), the β-phase ($CuIn_3Se_5$), the δ-phase (the high-temperature sphalerite phase) and Cu_ySe. An interesting point is that all neighbouring phases to the α-phase have a similar structure. The β-phase is actually a defect chalcopyrite phase built by ordered arrays of defect pairs (Cu vacancies V_{Cu} and In–Cu antisites In_{Cu}). Similarly, Cu_ySe can be viewed as constructed from the chalcopyrite by using Cu–In antisites Cu_{In} and Cu interstitials Cu_i. The transition to the sphalerite phase arises from disordering the cation (Cu, In) sub-lattice, and leads back to the zinc blende structure (cf. Figure 1(a)).

The existence range of the α-phase in pure $CuInSe_2$ on the quasi-binary tie line Cu_2Se-In_2Se_3 extends from a Cu content of 24 to 24.5 at.%. Thus, the existence range of single-phase $CuInSe_2$ is relatively small and does not even include the stoichiometric composition of 25 at.% Cu. The Cu content of absorbers for thin-film solar cells varies typically between 22 and 24 at.% Cu. At the growth temperature this compositional range lies within the single-phase region of the α-phase. However, at room temperature it lies in the two-phase $\alpha + \beta$ region of the equilibrium phase diagram [20]. Hence one would expect a tendency for phase separation in photovoltaic-grade $CuInSe_2$ after deposition. Fortunately, it turns out that partial replacement of In with Ga, as well as the use of Na-containing substrates, considerably widens the single-phase region in terms of (In + Ga)/(In + Ga + Cu) ratios [21]. Thus, the phase diagram hints at the substantial improvements actually achieved in recent years by the use of Na-containing substrates, as well as by the use of $Cu(In,Ga)Se_2$ alloys.

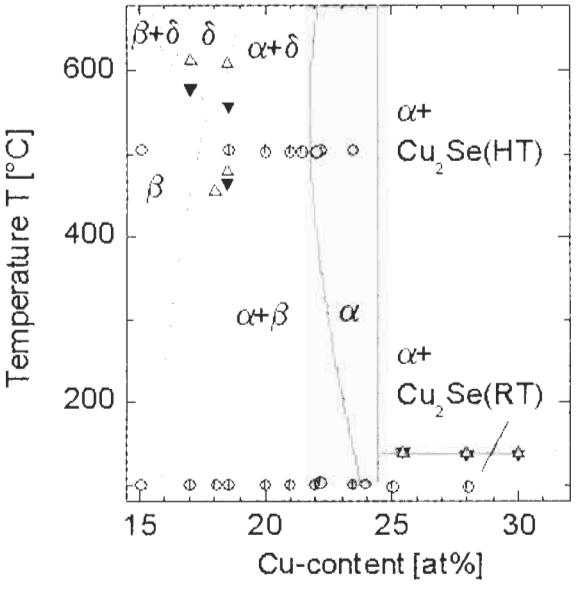

Figure 3 Quasi-binary phase diagram of $CuInSe_2$ along the tie-line that connects the binary compounds In_2Se_3 and Cu_2Se established by Differential Thermal Analysis (DTA) and microscopic phase analysis (After Haalboom et al. [20]). Note that at 25 at. % Cu no single phase exists.

2.4 Defect Physics of Cu(In,Ga)Se_2

The defect structure of the ternary compounds $CuInSe_2$, $CuGaSe_2$, $CuInS_2$, and their alloys, is of special importance because of the large number of possible intrinsic defects and the role of deep recombination centres for the performance of the solar cells. The features that are somewhat special to the Cu-chalcopyrite compounds are the ability to dope these compounds with native defects, their tolerance to large off-stoichiometries, and the electrically neutral nature of structural defects in these materials. It is obvious that the explanation of these effects significantly contributes to the explanation of the photovoltaic performance of these compounds. Doping of $CuInSe_2$ is controlled by intrinsic defects. Samples with p-type conductivity are grown if the material is Cu-poor and annealed under high Se vapour pressure, whereas Cu-rich material with Se deficiency tends to be n-type [22, 23]. Thus, the Se vacancy V_{Se} is considered to be the dominant donor in n-type material (and also the compensating donor in p-type material), and the Cu vacancy V_{Cu} the dominant acceptor in Cu-poor p-type material.

By calculating the metal-related defects in $CuInSe_2$ and $CuGaSe_2$, Zhang et al. [24] found that the defect formation energies for some intrinsic defects are so low that they can be heavily influenced by the chemical potential of the components (i.e., by the composition of the material) as well as by the electrochemical potential of the electrons. For V_{Cu} in Cu-poor and stoichiometric material, a

negative formation energy is even calculated. This would imply the spontaneous formation of large numbers of these defects under equilibrium conditions. Low (but positive) formation energies are also found for the antisite Cu_{In} in Cu-rich material (this defect is a shallow acceptor which could be responsible for the p-type conductivity of Cu-rich, non-Se-deficient $CuInSe_2$). The dependence of the defect formation energies on the electron Fermi level could explain the strong tendency of $CuInSe_2$ to self-compensation and the difficulties of achieving extrinsic doping. The results of Zhang et al. [24] provide a good theoretical model of defect formation energies and defect transition energies, which exhibits good agreement with experimentally obtained data. Table 1 summarises the ionisation energies and the defect formation energies of the 12 intrinsic defects in $CuInSe_2$. The energies (bold values in Table 1) for V_{Cu}, V_{In}, Cu_i, Cu_{In}, In_{Cu}, are obtained from a first principle calculation [24] whereas the formation energies in italics (Table 1) and for the other defects are calculated from the macroscopic cavity model [25]. The ionisation energies used in Table 1 are either taken from Zhang et al. [24] or from the data compiled in reference [26]. Note that the data given in references [25, 26] for the cation defects differ significantly from those computed in reference [24].

Further important results in reference [24] are the formation energies of *defect complexes* such as $(2V_{Cu},In_{Cu})$, (Cu_{In},In_{Cu}) and $(2Cu_i,Cu_{In})$, where Cu_i is an interstitial Cu atom. These formation energies are even lower than those of the corresponding isolated defects. Interestingly, the $(2V_{Cu},In_{Cu})$ complex does not exhibit an electronic transition within the forbidden gap, in contrast to the isolated In_{Cu}-anti-site, which is a deep recombination centre. As the $(2V_{Cu},In_{Cu})$ complex is most likely to occur in In-rich material, it can accommodate a large amount of excess In (or likewise deficient Cu) and, at same time, maintain the

Table 1 Electronic transition energies and formation energies ΔU of the 12 intrinsic defects in $CuInSe_2$. Source: the ionisation energies in italics are derived from reference [26], and the formation energies in italics are from reference [25]. All the numbers in bold type are from reference [24]

Transition	Defect transition energies[a] and formation energies[b] (eV)											
	V_{Cu}	V_{In}	V_{Se}	Cu_i	In_i	Se_i	In_{Cu}	Cu_{In}	Se_{Cu}	Cu_{Se}	Se_{In}	In_{Se}
(−/0)	**0.03**	**0.17**						**0.29**				
	0.03	*0.04*	*0.04*[c]			*0.07*		*0.05*		*0.13*	*0.08*	
(−/2−)		**0.41**						**0.58**				
(2−/3−)		**0.67**										
(0/+)				**0.2**			**0.25**					
			0.11[d]	*0.08*	*0.07*		*0.04*		*0.06*			*0.09*
(+/2+)							**0.44**					
ΔU/ eV	**0.60**	**3.04**		**2.88**			**3.34**	**1.54**				
	2.9	*2.8*	*2.6*	*4.4*	*9.1*	*22.4*	*1.4*	*1.5*	*7.5*	*7.5*	*5.5*	*5.0*

[a] Difference between the valence/conduction band energy for acceptor/donor states.
[b] Formation energy ΔU of the neutral defect in the stoichiometric material.
[c] Covalent.
[d] Ionic.

electrical performance of the material. Furthermore, ordered arrays of this complex can be thought as the building blocks of a series of Cu-poor Cu–In–Se compounds such as $CuIn_3Se_5$ and $CuIn_5Se_8$ [24].

Let us now concentrate on the defects experimentally detected in photovoltaic grade (and thus In-rich) polycrystalline films. In-rich $Cu(In,Ga)Se_2$ is in general highly compensated, with a net acceptor concentration of the order of 10^{16} cm^{-3}. The shallow acceptor level V_{Cu} (which lies about 30 meV above the valence band) is assumed to be the main dopant in this material. As compensating donors, the Se-vacancy V_{Se} as well as the double donor In_{Cu} are considered. The most prominent defect is an acceptor level at about 270–300 meV above the valence band, which is reported by several groups from deep-level transient spectroscopy [27] and admittance spectroscopy [28, 29]. This defect is also present in single crystals [30]. The importance of this transition results from the fact that its concentration is related to the open-circuit voltage of the device [31–33,]. Upon investigating defect energies in the entire $Cu(In,Ga)(Se,S)_2$ alloy system, Turcu et al. [34] found that the energy distance between this defect and the valence band maximum remains constant when alloying $CuInSe_2$ with Ga, whereas the energy distance increases under S/Se alloying. Assuming that the defect energy is independent from the energy position of the band edges, like the defect energies of transition metal impurities in III–V and II–IV semiconductor alloys [35, 36], the authors of reference [34] extrapolate the valence band offsets $\Delta E_v = -0.23$ eV for the combination $CuInSe_2/CuInS_2$ and $\Delta E_v = 0.04$ eV for $CuInSe_2/CuGaSe_2$. Recently, transient photocapacitance studies by Heath et al. [37] unveiled an additional defect state in $Cu(In,Ga)Se_2$ at about 0.8 eV from the valence band. Again, the defect energy is independent of the Ga content in the alloy. Figure 4 summarises the energy positions of bulk defects in the $Cu(In_{1-x}Ga_x)Se_2$ and the $CuIn(Se_{1-y}S_y)_2$ alloy system with the defect energy of the bulk acceptor used as a reference energy to align the valence and conduction band energy [38]. Additionally, Figure 4 shows the activation energy of an interface donor. This energy corresponds to the energy difference ΔE_{Fn} between the Fermi energy and the conduction band minimum at the buffer absorber interface [39]. Notably this energy difference remains small upon alloying $CuInSe_2$ with Ga, whereas ΔE_{Fn} increases when alloying with S.

3 Cell and Module Technology

3.1 Structure of the Heterojunction Solar Cell

The complete layer sequence of a $ZnO/CdS/Cu(In,Ga)Se_2$ heterojunction solar cell is shown in Figure 5. The device consists of a typically 1 μm thick Mo layer deposited on a soda-lime glass substrate and serving as the back contact for the solar cell. The $Cu(In,Ga)Se_2$ is deposited on top of the Mo back electrode as the photovoltaic absorber material. This absorber layer has a thickness of 1–2 μm. The heterojunction is then completed by chemical bath deposition (CBD) of CdS

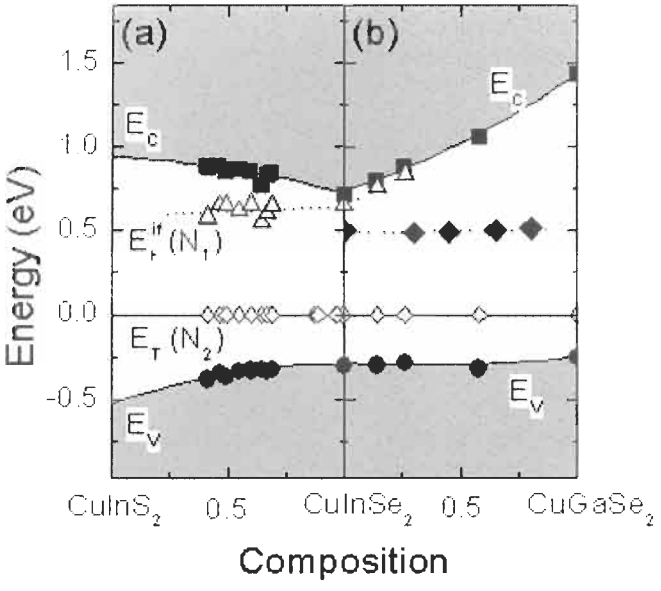

Figure 4 Band gap evolution diagram of the $CuIn(Se,S)_2$ (a) and the $Cu(In,Ga)Se_2$ (b) alloy system with the trap energy $E_T(N_2$, open diamonds) taken as an internal reference to align the conduction band and the valence band energies E_c and E_v. The energy position of an additional defect state in $Cu(In,Ga)Se_2$ (full diamonds) as well as that of an interface donor (open triangles) in $Cu(In,Ga)(Se,S)_2$ is also indicated.

(typically 50 nm thick) and by the sputter deposition of a nominally undoped (intrinsic) *i*-ZnO layer (usually of thickness 50–70 nm) and then a heavily doped ZnO layer. As ZnO has a band-gap energy of 3.2 eV it is transparent for the main part of the solar spectrum and therefore is denoted as the window layer of the solar cell.

3.2 Key Elements for High-Efficiency $Cu(In,Ga)Se_2$ Solar Cells

We first mention four important technological innovations which, during the decade 1990–2000, have led to a considerable improvement of the efficiencies and finally to the record efficiency of 18.8% [1]. These steps are the key elements of the present $Cu(In,Ga)Se_2$ technology:

- The film quality has been substantially improved by the crystallisation mechanism induced by the presence of Cu_ySe ($y < 2$). This process is further supported by a substrate temperature close to the softening point of the glass substrate [40].
- The glass substrate has been changed from Na-free glass to Na-containing soda-lime glass [40, 41]. The incorporation of Na, either from the glass substrate or from Na-containing precursors, has led to an enormous improvement of the efficiency and reliability of the solar cells, as well as to a larger process tolerance.

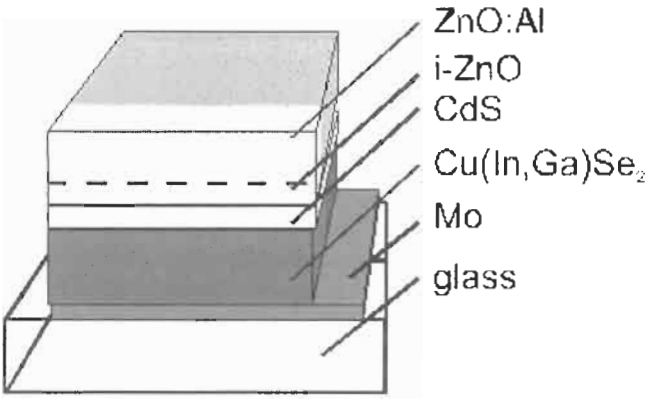

Figure 5 Schematic layer sequence of a standard ZnO/CdS/Cu(In,Ga)Se_2 thin-film solar cell.

- Early absorbers consisted of pure $CuInSe_2$. The partial replacement of In with Ga [42] is a further noticeable improvement, which has increased the band gap of the absorber from 1.04 eV to 1.1–1.2 eV for the high-efficiency devices. The benefit of 20–30% Ga incorporation stems not only from the better band gap match to the solar spectrum but also from the improved electronic quality of $Cu(In,Ga)Se_2$ with respect to pure $CuInSe_2$ [21, 32].
- The counter electrode for the $CuInSe_2$ absorber of the earlier cells was a 2 μm thick CdS layer deposited by Physical Vapour Deposition (PVD). This has been replaced by a combination of a 50 nm thin CdS buffer layer laid down by chemical bath deposition [43, 44] and a highly conductive ZnO window layer.

3.3 Absorber Preparation Techniques

3.3.1 Basics

The preparation of $Cu(In,Ga)Se_2$-based solar cells starts with the deposition of the absorber material on a Mo-coated glass substrate (preferably soda-lime glass). The properties of the Mo film and the choice of the glass substrate are of primary importance for the final device quality, because of the importance of Na, which diffuses from the glass through the Mo film into the growing absorber material. In the past, some processes used blocking layers such as SiN_x, SiO_2 or Cr between the glass substrate and the Mo film to prevent the out-diffusion of Na. Instead, Na-containing precursors like NaF [45], Na_2Se [46] or Na_2S [47] are then deposited prior to absorber growth to provide a controlled, more homogeneous, incorporation of Na into the film. The control of Na incorporation in the film from precursor layers allows the use of other substrates like metal or polymer foils. The most obvious effects of Na incorporation are better film morphology and higher conductivity of the films [48]. Furthermore, the incorporation of Na induces beneficial changes in the defect distribution of the absorber films [49, 50].

The explanations for the beneficial impact of Na are manifold, and it is most likely that the incorporation of Na in fact results in a *variety* of consequences. During film growth, the incorporation of Na leads to the formation of $NaSe_x$ compounds. This slows down the growth of $CuInSe_2$ and could at same time facilitate the incorporation of Se into the film [51]. Also the widening of the existence range of the α-($CuInSe_2$) phase in the phase diagram, discussed above, as well as the reported larger tolerance to the Cu/(In + Ga) ratio of Na-containing thin films, could be explained in this picture. Furthermore, the higher conductivity of Na-containing films could result from the diminished number of compensating V_{se} donors.

During absorber deposition, a $MoSe_2$ film forms at the Mo surface [52, 53]. $MoSe_2$ is a layered semiconductor with p-type conduction, a band gap of 1.3 eV and weak van der Waals bonding along the *c*-axis. The *c*-axis is found to be in parallel with, and the van der Waals planes thus perpendicular to, the interface [53]. Because of the larger band gap of the $MoSe_2$ compared with that of standard $Cu(In,Ga)Se_2$ films, the $MoSe_2$ layer provides a low-recombinative back surface for the photogenerated minority carriers (electrons) in the $Cu(In,Ga)Se_2$ absorber and at the same time provides a low-resistance contact for the majority carries (holes).

Photovoltaic-grade $Cu(In,Ga)Se_2$ films have a slightly In-rich overall composition. The allowed stoichiometry deviations are astonishingly large, yielding a wide process window with respect to composition. Devices with efficiencies above 14% are obtained from absorbers with (In + Ga)/(In + Ga + Cu) ratios between 52 and 64% if the sample contains Na [48]. Cu-rich $Cu(In,Ga)Se_2$ shows the segregation of a secondary Cu_ySe phase preferentially at the surface of the absorber film. The metallic nature of this phase does not allow the formation of efficient heterojunctions. Even after *removal* of the secondary phase from the surface by etching the absorber in KCN, the utility of this material for photovoltaic applications is limited. However, the importance of the Cu-rich composition is given by its role during film growth. Cu-rich films have grain sizes in excess of 1 μm whereas In-rich films have much smaller grains. A model for the film growth under Cu-rich compositions comprises the role of Cu_ySe as a flux agent during the growth process of co-evaporated films [54]. For $Cu(In,Ga)Se_2$ prepared by selenisation, the role of Cu_ySe is similar [55].Therefore, growth processes for high quality material have to go through a copper-rich stage but have to end up with an indium-rich overall composition.

3.3.2 Co-evaporation Processes

The absorber material yielding the highest efficiencies is $Cu(In,Ga)Se_2$ with a Ga/(Ga + In) ratio of 20–30%, prepared by co-evaporation from elemental sources. Figure 6 sketches a co-evaporation set-up as used for the preparation of laboratory-scale solar cells and mini-modules. The process requires a maximum substrate temperature of about 550°C for a certain time during film growth, preferably towards the end of growth. One advantage of the evaporation route is that material deposition and film formation are performed during the same processing step. A feedback loop based on a quadrupole mass spectrometer or an

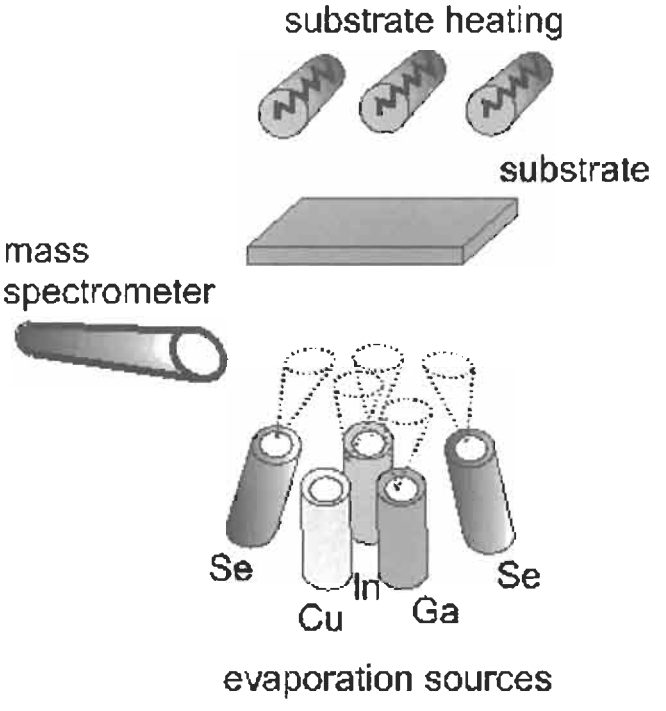

Figure 6 Arrangement for the deposition of Cu(In,Ga)Se_2 films on the laboratory scale by co-evaporation on a heated substrate. The rates of the sources are controlled by mass spectrometry.

atomic absorption spectrometer controls the rates of each source. The composition of the deposited material with regard to the metals corresponds to their evaporation rates, whereas Se is always evaporated in excess. This precise control over the deposition rates allows for a wide range of variations and optimisations with different sub-steps or stages for film deposition and growth. These sequences are defined by the evaporation rates of the different sources and the substrate temperature during the course of deposition.

Advanced preparation sequences always include a Cu-rich stage during the growth process and end up with an In-rich overall composition in order to combine the large grains of the Cu-rich stage with the otherwise more favourable electronic properties of the In-rich composition. The first example of this kind of procedure is the so called Boeing or *bilayer process* [5], which starts with the deposition of Cu-rich Cu(In,Ga)Se_2 and ends with an excess In rate. The most successful co-evaporation process is the so-called *three-stage process* [56]. This process starts with the deposition of In,Ga, and Se at relatively low temperatures, then uses a Cu-rich growth stage by evaporating Cu in excess at elevated temperature, and at the end again deposits only In, Ga, and Se to ensure the overall In-rich composition of the film. The three-stage process currently leads to the Cu(In,Ga)Se_2 solar cells with the highest efficiencies.

3.3.3 Selenisation Processes

The second class of absorber preparation routes is based on the separation of deposition and compound formation into two different processing steps. High efficiencies are obtained from absorber prepared by selenisation of metal precursors in H_2Se [57–59] and by rapid thermal processing of stacked elemental layers in a Se atmosphere [60]. These sequential processes have the advantage that approved large-area deposition techniques like sputtering can be used for the deposition of the materials. The $Cu(In,Ga)Se_2$ film formation then requires a second step, the selenisation.

The very first large-area modules were prepared by the selenisation of metal precursors in the presence of H_2Se more than ten years ago [6]. Today, a modification of this process yields the first commercially available $Cu(In,Ga)Se_2$ solar cells manufactured by Shell Solar Industries. This process is schematically illustrated in Figure 7. First, a stacked layer of Cu, In and Ga is sputter-deposited on the Mo-coated glass substrate. Then selenisation takes place under H_2Se. To improve the device performance, a second thermal process under H_2S is added, resulting in an absorber that is $Cu(In,Ga)(S,Se)_2$ rather than $Cu(In,Ga)Se_2$.

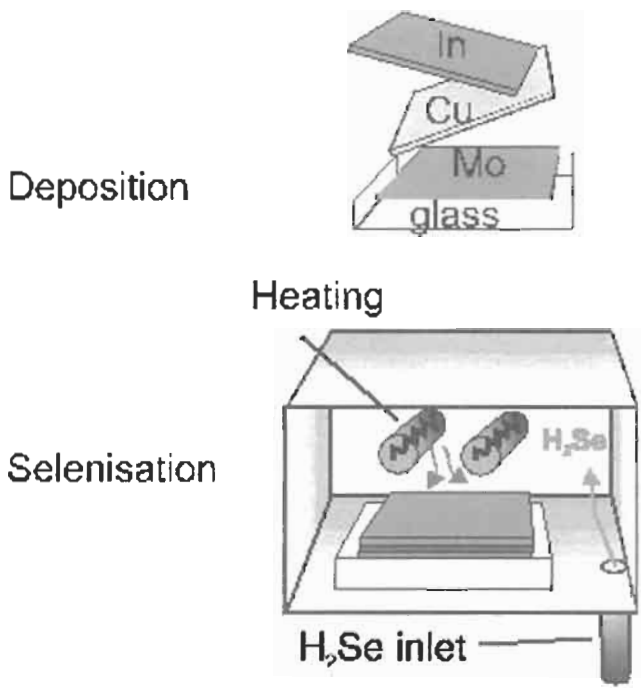

Figure 7 Illustration of the sequential process. First a stack of metal (Cu,In,Ga) layers deposited by sputtering onto a Mo-coated glass. In the second step, this stack is selenised in H_2Se atmosphere and converted into $CuInSe_2$.

A variation of the method that avoids the use of the toxic H_2Se during selenisation is the rapid thermal processing of stacked elemental layers [60]. Here the precursor includes a layer of evaporated elemental Se. The stack is then selenised by a rapid thermal process (RTP) in either an inert or a Se atmosphere. The highest efficiencies are obtained if the RTP is performed in an S-containing atmosphere (either pure S or H_2S).

On the laboratory scale, the efficiencies of cells made by these preparation routes are smaller by about 3% (absolute) as compared with the record values. However, on the module level, co-evaporated and sequentially prepared absorbers have about the same efficiency. Sequential processes need two or even three stages for absorber completion. These additional processing steps may counterbalance the advantage of easier element deposition by sputtering.

3.3.4 Other Absorber Deposition Processes

Besides selenisation and co-evaporation, other deposition methods have been studied, either to obtain films with very high quality or to reduce the cost of film deposition on large areas. Methods that are used to grow epitaxial III–V compound films, such as molecular beam epitaxy (MBE) [61] or metal organic chemical vapour deposition (MOCVD) [62] have revealed interesting features for fundamental studies like phase segregation and defect formation, but could not be used to form the absorber material for high-efficiency solar cells.

Attempts to develop so-called low-cost processes include electrodeposition [63–66], screen printing and particle deposition [67, 68]. Electrodeposition can be done either in one or two steps. The crucial step is the final film formation in a high-temperature annealing process. The recrystallisation process competes with the decomposition of the material. Therefore, process optimisation is quite difficult. Cells with high efficiencies were obtained by electrodeposition of a Cu-rich $CuInSe_2$ film and subsequent conditioning by a vacuum evaporation step of In(Se) [69]. Particle deposition by printing of suitable inks and subsequent annealing lead to absorber layers with good quality enabling the fabrication of solar cells with efficiencies over 13% [70].

3.3.5 Post-deposition Air Anneal

Air annealing has been an important process step, crucial for the efficiency especially of the early solar cells based on $CuInSe_2$. Though often not mentioned explicitly, an oxygenation step is still used for most of the present-day high-efficiency devices. The beneficial effect of oxygen was explained within the defect chemical model of Cahen and Noufi [71]. In this model, the surface defects at grain boundaries are positively charged Se vacancies V_{Se}. During air annealing, these sites are passivated by O atoms. Because of the decreased charge at the grain boundary, the band bending as well as the recombination probability for photogenerated electrons is reduced. The surface donors and their neutralisation by oxygen are important for the free $Cu(In,Ga)Se_2$ surface as well as for the formation of the $CdS/Cu(In,Ga)Se_2$ interface [72, 73].

3.4 Heterojunction Formation

3.4.1 The Free $Cu(In,Ga)Se_2$ Surface

The surface properties of $Cu(In,Ga)Se_2$ thin films are especially important as this surface becomes the active interface of the completed solar cell. However, the band diagram of the $ZnO/CdS/Cu(In,Ga)Se_2$ heterojunction, especially the detailed structure close to the $CdS/Cu(In,Ga)Se_2$ interface, is still under debate (for recent reviews see references [74, 75]).

The free surfaces of as-grown $Cu(In,Ga)Se_2$ films exhibit two prominent features:

(i) The valence band-edge energy E_V lies below the Fermi level E_F by about 1.1 eV for $CuInSe_2$ films [76]. This energy is larger than the band-gap energy E_g^{bulk} of the bulk of the absorber material. This finding was taken as an indication for a *widening of band gap* at the surface of the film. A recent direct measurement of the surface band gap of polycrystalline $CuInSe_2$ by Morkel et al. [77] proved that the band gap energy E_g^{surf} at the surface of the film is about 1.4 eV, i.e., more than 0.3 eV larger than $E_g^{bulk} \approx 1.04$ eV. In $Cu(In_{1-x},Ga_x)Se_2$ alloys the distance $E_F - E_V$ was found to be 0.8 eV (almost independently of the Ga content if $x > 0$) [78].

(ii) The surface composition of Cu-poor $CuInSe_2$, as well as that of $Cu(In,Ga)Se_2$ films, corresponds to a surface composition of (Ga + In)/(Ga + In + Cu) of about 0.75 for a range of bulk compositions of $0.5 < (Ga + In)/(Ga + In + Cu) < 0.75$ [76].

Both observations (i) and (ii) have led to the assumption that a phase segregation of $Cu(In,Ga)_3Se_5$, the so-called Ordered Defect Compound (ODC), occurs at the surface of the films. From the fact that bulk $Cu(In,Ga)_3Se_5$ exhibits n-type conductivity [79] it was argued that Cu-poor $Cu(In,Ga)Se_2$ thin films automatically generate a rectifying, buried junction. However, the existence of a separate phase on top of standard $Cu(In,Ga)Se_2$ thin films has not yet been confirmed by structural methods such as X-ray diffraction, high resolution transmission electron microscopy or electron diffraction. Furthermore, if the surface phase exhibited the weak n-type conductivity of bulk $Cu(In,Ga)_3Se_5$, simple charge neutrality estimations [21] show that this would not be sufficient to achieve type inversion.

Based on these arguments, another picture of the surface of $Cu(In,Ga)Se_2$ thin films and of junction formation has emerged [21, 80]. Within the classical Bardeen model [81] of Fermi level pinning by electronic states at semiconductor surfaces, a density of surface states of about 10^{12} cm^{-2} eV^{-1} is sufficient to pin the Fermi level at the neutrality level of the free semiconductor surfaces. Positively charged surface donors are expected in the metal terminated (112) surface of $CuInSe_2$ owing to the dangling bond to the missing Se [71]. Thus, these surface states, rather than a distinct n-type surface phase determines the type inversion of the surface.

Surface states play also an important role in the completed heterostructure, where they become *interface states* at the absorber/buffer interface. *The defect layer model* [21, 80] takes into account a modification of the band structure due to the Cu deficiency of the surface *as well as* the presence of positively charged surface states due to the missing surface Se. However, the defect layer model considers the surface layer not as n-type bulk material (as does the ODC model) but as a p^+-layer. Furthermore, the defect layer is viewed *not as the origin but rather as the consequence* of the natural surface type inversion [21, 80]. Surface states are responsible for the surface band bending that leads to the liberation of Cu from its lattice sites and to Cu migration towards the neutral part of the film. The remaining copper vacancies V_{Cu}^- close to the surface result in a high density of acceptor states, i.e., the p^+-defect layer at the film surface. Recent photoelectron spectroscopy experiments of Klein and Jaegermann [82] suggest that the band bending occurring during junction formation leads to a loss of Cu atoms from the surface of $CuInSe_2$ and $CuGaSe_2$, whereas a similar effect was not observed in $CuInS_2$.

3.4.2 Buffer Layer Deposition

Surface passivation and junction formation is most easily achieved by the CBD deposition of a thin CdS film from a chemical solution containing Cd ions and thiourea [83]. The benefit of the CdS layer is manifold:

- CBD deposition of CdS provides complete coverage of the rough polycrystalline absorber surface at a film thickness of only 10 nm [84].
- The layer provides protection against damage and chemical reactions resulting from the subsequent ZnO deposition process.
- The chemical bath removes the natural oxide from the film surface [83] and thus re-establishes positively charged surface states and, as a consequence, the natural type inversion at the CdS/Cu(In,Ga)Se_2 interface.
- The Cd ions, reacting first with the absorber surface, remove elemental Se, possibly by the formation of CdSe.
- The Cd ions also diffuse to a certain extent into the Cu-poor surface layer of the absorber material [85, 86], where they possibly form Cd_{Cu} donors, thus providing additional positive charges enhancing the type inversion of the buffer/absorber interface.
- Open-circuit voltage limitations imposed by interface recombination can be overcome by a low surface recombination velocity in addition to the type inversion of the absorber surface. Thus one might conclude that interface states (except those shallow surface donors responsible for the type inversion) are also passivated by the chemical bath.

Due to the favourable properties of CdS as a heterojunction partner and the chemistry of the CBD process it is difficult to find a replacement. Avoiding CdS and the chemical bath step would be advantageous from the production point of view. On the one hand, a toxic material such as CdS requires additional safety regulation; on the other hand, the chemical bath deposition does not comply

with the vacuum deposition steps of an in-line module fabrication. Therefore, research and development in this area relates to two issues: (i) the search for alternative materials for a chemical deposition, and (ii) the development of ways to deposit the front electrode without an intermediate step in a chemical bath.

Promising materials to replace CdS are In(OH,S) [78], Zn(OH,S) [88, 89], ZnS [90, 91] and ZnSe [92–94]. However, all these materials require additional precautions to be taken for the preparation of the absorber surface or front electrode deposition.

3.4.3 Window Layer Deposition

The most commonly used material for the preparation of the front electrode is ZnO doped with B or Al. The first large-area modules produced by ARCO Solar (later Siemens Solar Industries, now Shell Solar Industries) had a ZnO:B window layer deposited by chemical vapour deposition (CVD). Later production facilities at Boeing and EUROCIS use sputtering processes. Present pilot production lines also favour sputtering. As mentioned above, an undoped *i*-ZnO layer with a thickness of about 50–100 nm is needed at the heterojunction in order to achieve optimum performance.

3.5 Module Production and Commercialisation

3.5.1 Monolithic Interconnections

One inherent advantage of thin-film technology for photovoltaics is the possibility of using monolithic integration for series connection of individual cells within a module. In contrast, bulk Si solar cells must be provided with a front metal grid, and each of these front contacts has to be connected to the back contact of the next cell for series connection. The interconnect scheme, shown in Figure 8, has to warrant that the front ZnO layer of one cell is connected to the back Mo contact of the next one. In order to obtain this connection, three different patterning steps are necessary. The first one separates the Mo back contact by a series of periodical scribes and thus defines the width of the cells, which is of the order of 0.5–1 cm. For Mo patterning, a laser is normally used. The second patterning step is performed after absorber and buffer deposition, and the final one after window deposition (cf. Figure 8). Scribing of the semiconductor layer is done by mechanical scribing or laser scribing. The total width of the interconnect depends not only on the scribing tools, but also on the reproducibility of the scribing lines along the entire module. The length of the cells and, accordingly, that of the scribes can be more than 1 m. The typical interconnect width is of the order of 300 μm. Thus, about 3–5% of the cell area must be sacrificed to the interconnects.

3.5.2 Module Fabrication

The technologies for absorber, buffer and window deposition used for module production are the same as those discussed above for the production of small laboratory cells. However, the challenge of producing modules is to transform

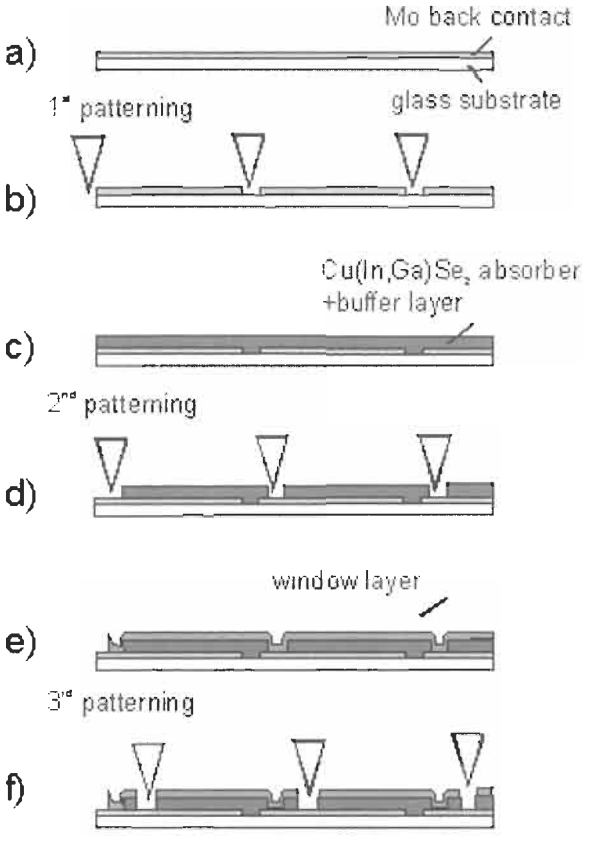

Figure 8 Deposition and patterning sequence to obtain an integrated interconnect scheme for Cu(In,Ga)Se_2 thin-film modules.

the laboratory-scale technologies to much larger areas. The *selenisation* process uses as much off-the-shelf equipment and processing as possible (e.g., sputtering of the metal precursors) for fabricating Cu(In,Ga)Se_2 films. For *co-evaporation* on large areas, the Centre for Solar Energy and Hydrogen Research in Stuttgart (ZSW) has designed its own equipment, schematically shown in Figure 9, for an in-line co-evaporation process. Line-shaped evaporation sources allow continuous deposition of large-area, high-quality Cu(In,Ga)Se_2 films. The relatively high substrate temperatures that are necessary for high-quality material impose problems in handling very large area glass sheets. Future process optimisation therefore implies reduction of the substrate temperature.

A bottleneck for the production is the deposition of the buffer layer in a chemical bath. On the one hand, it is not straightforward to integrate this process in a line consisting mainly of dry physical vapour deposition processes, on the other, it would be favourable for environmental reasons to replace the currently used CdS layer by a Cd-free alternative.

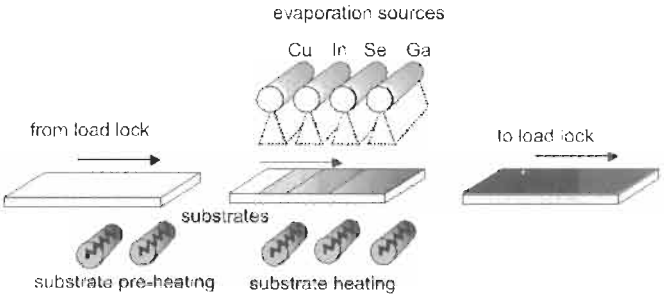

Figure 9 Sketch of an in-line deposition system for co-evaporation of $Cu(In,Ga)Se_2$ absorber films from line-sources.

The ZnO transparent front electrode is put down either by CVD or sputtering. Each method has its specific advantages with respect to process tolerance, throughput, cost and film properties. The widths of the cells within the module – and therefore the relative losses from the patterning – mainly depend on the sheet resistance of the ZnO.

Module encapsulation is an important issue because module stability depends on proper protection against humidity. Low-iron cover glasses provide good protection against ambient influences. Hermetic sealing of the edges is mandatory to obtain stable modules (see below).

3.5.3 Up-Scaling Achievements

$Cu(In,Ga)Se_2$ has the best potential to reach more than 15% module efficiency in the near future. Mini-modules ranging in area from 20 to 90 cm^2 that use the process sequence anticipated for larger area commercial modules have already reached efficiencies around 14–15%. Recently, Siemens Solar Industries fabricated a 1 ft × 4 ft power module (~44 watts) with an independently verified efficiency of 12.1%. Using a totally different approach to the deposition of the absorber layer, the ZSW fabricated a 30 cm × 30 cm module with a verified efficiency of 12.7%. Based on the same co-evaporation process, Würth Solar GmbH, Stuttgart, reported an efficiency of 12.5% for a module of aperture area 5932 cm^2 [95]. More results of the different processes are summarised in Table 2. Note that, because of the promising results from the laboratory scale and the first approaches of up-scaling, several companies other than those mentioned in Table 2 now plan commercial production.

A further challenge is to develop CIGS cells on flexible substrates and hence to extend their area of applications. There are ongoing efforts to produce cells on various kinds of substrates like stainless steel, polymide and at the same time to retain the performance achieved with devices on soda-lime glass [96]. For space applications it is important to reduce the weight by depositing the cells on lightweight foil substrates. Highest small area efficiencies on polymide films formed by spin coating on a glass substrate reach 12.8% [97]. Roll to roll coating on metal foils [98] and polymer films [99, 100] has already reached the stage of pilot production.

Table 2 Comparison of efficiencies η and areas A of laboratory cells, mini-modules, and commercial-size modules achieved with Cu(In,Ga)Se_2 thin films based on the co-evaporation and the selenisation process. NREL denotes the National Renewable Energy Laboratories (USA), ZSW is the Center for Solar Energy and Hydrogen Research (Germany), EPV is Energy Photovoltaics (USA), ASC is the Angstrom Solar Centre (Sweden)

Process	Laboratory cell		Mini-module		Module		Laboratory/company
	η (%)	A (cm^2)	η (%)	A (cm^2)	η (%)	A (cm^2)	
Co-evap.	18.8	0.45					NREL [1]
	16.1	0.5	13.9	90	12.7	800	ZSW
					12.3	5932	Würth Solar [95]
			9.6	135			EPV
	11.5	0.5	5.6	240			Global Solar[a]
			16.6	20			ASC [2]
Selenis.	> 16	0.5	14.7	18	12.1	3600	Shell Solar
			14.2	50	11.6	864	Showa, Japan

[a] Flexible cells.

3.5.4 Stability

The long-term stability is a critical issue of any solar cell technology because the module lifetime contributes as much to the ratio between produced energy and invested cost as does the initial efficiency. Cu(In,Ga)Se_2 modules fabricated by Shell Solar Industries more than 10 years ago show until today very good stability during outdoor operation [101, 102]. However, intense accelerated lifetime testing is made for the now commercially available Cu(In,Ga)Se_2 modules. Careful sealing and encapsulation appears mandatory, especially because of the sensitivity of Cu(In,Ga)Se_2 to humidity. For non-encapsulated modules, corrosion of the molybdenum contact and the degradation of zinc oxide were found to be the dominating degradation mechanisms [103] during the so-called damp heat test (1000 hours in hot (85°C) and humid (85% humidity) atmosphere). Investigations of non-encapsulated cells [104–106] unveiled further a humidity induced degradation of the Cu(In,Ga)Se_2 absorber material. Despite of the sensibility of Cu(In,Ga)Se_2 with respect to humidity, well encapsulated modules pass the damp heat test [107].

Recent work of Guillemoles et al. [108, 109] investigates the chemical and electronic stability of Cu(In,Ga)Se_2 based solar cells and possible fundamental instabilities of the material system, namely, interface reactions, defect metastability, and constituent element (Cu) mobility. Guillemoles et al. conclude that all reasonably anticipated detrimental interface reactions at the Mo/Cu(In,Ga)Se_2, the Cu(In,Ga)Se_2 /CdS, or the CdS/ZnO interface are either thermodynamically or kinetically limited. Furthermore, Cu mobility does not contradict long-term stability [108, 109].

3.5.5 Radiation Hardness and Space Applications

One important prospective application for Cu(In,Ga)Se_2 cells is in space, where the main power source is photovoltaics. Satellites in low-earth orbits for communication systems require solar cells with high end-of-life efficiencies,

despite the high flux of high-energy electrons and protons in that ambient. The radiation hardness of $Cu(In,Ga)Se_2$ has been recognized as early as 1984/85 [110, 111], but only recently have systematic investigations on the radiation response of $Cu(In,Ga)Se_2$ solar cells been undergone using high enough electron and proton fluences to allow quantitative conclusions regarding the defect generation rates [112]. The radiation resistance of $Cu(In,Ga)Se_2$ against high-energy (0.3–3 MeV) electrons turns out to be far better than that of any other photovoltaic material [112]. The radiation hardness of $Cu(In,Ga)Se_2$ against high-energy (0.4–10 MeV) protons is also high, though the difference from other materials is not as high as in case of electron irradiation. Walters et al. [113] have analysed $Cu(In,Ga)Se_2$ in the frame of the so-called damage dose model and found that the damage coefficients for $Cu(In,Ga)Se_2$ are comparable to those of InP and considerably smaller than those of Si and GaAs.

The high mobility of Cu in the $Cu(In,Ga)Se_2$ lattice was proposed to be one important ingredient for a defect healing mechanism that could explain the high radiation resistance of $Cu(In,Ga)Se_2$ [108, 114]. Recent thermal annealing experiments of electron-irradiated [115] and proton-irradiated [116] $Cu(In,Ga)Se_2$ solar cells unveiled a thermally activated healing process with an activation energy of around 1 eV leading to a complete recovery of the device performance. Illumination of the solar cell enhances this annealing process further [116, 117].

The challenge for developing CIGS space cells is to reduce the weight by depositing the cells on foil substrates, and at the same time to retain the performance achieved with devices on soda-lime glass. Recently, Tuttle et al. [118] reported a $Cu(In,Ga)Se_2$ solar cell on lightweight metal foil with a power conversion efficiency of 15.2% (under AM0 illumination) and a specific power of 1235 W/kg. Other approaches to flexible and lightweight $Cu(In,Ga)Se_2$ solar cells embrace $Cu(In,Ga)Se_2$ deposited on plastic foil such as polyimide [119] or the use of a lift-off technique to remove the absorber from the glass substrate after device fabrication [120].

4 Device Physics

4.1 The Band Diagram

The band diagram of the ZnO/CdS/$Cu(In,Ga)Se_2$ heterostructure in Figure 10 shows the conduction and valence band energies E_c and E_v of the $Cu(In,Ga)Se_2$ absorber, the CdS buffer layer and the ZnO window. Note that the latter consists of a highly Al-doped (ZnO:Al) and an undoped (i-ZnO) layer. For the moment, we neglect the polycrystalline nature of the semiconductor materials, which in principle requires a two- or three-dimensional band diagram. Even in the one-dimensional model, important details of the band diagram are still not perfectly clear. The diagram in Figure 10 concentrates on the heterojunction and does not show the contact between the Mo and $Cu(In,Ga)Se_2$ at the back side of the absorber.

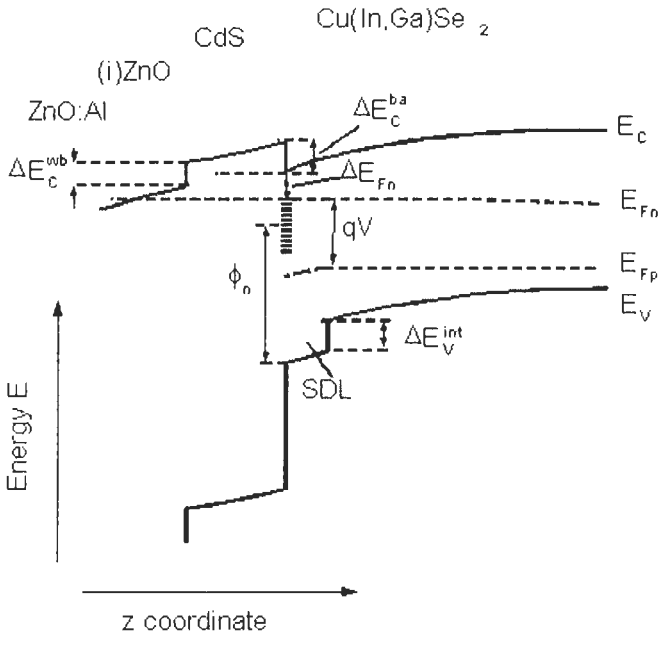

Figure 10 Band diagram of the ZnO/CdS/Cu(In,Ga)Se_2 heterojunction under bias voltage showing the conduction and valence band-edge energies ΔE_c and E_v. The quantities $\Delta E_c^{wb/ba}$ denote the conduction band offsets at the window/buffer and buffer/absorber interfaces, respectively. An internal valence band offset ΔE_v^{int} exists between the bulk Cu(In,Ga)Se_2 and a surface defect layer (SDL) on top of the Cu(In,Ga)Se_2 absorber film. The quantity ΔE_{Fn} denotes the energy distance between the electron Fermi level E_{Fn} and the conduction band at the CdS buffer/Cu(In,Ga)Se_2 absorber interface, and ϕ_n denotes the neutrality level of interface states at this heterointerface.

An important feature in Figure 10 is the 10–30 nm thick surface defect layer (SDL) on top of the Cu(In,Ga)Se_2 absorber, already discussed in Section 3.4. The physical nature of this SDL is still under debate. However, the fact that the band gap at the surface of Cu(In,Ga)Se_2 thin films (as long as they are prepared with a slightly Cu-poor final composition) exceeds the band gap energy of the bulk material [76, 77], has important implications for the contribution of interface recombination to the overall performance of the solar cell. A simplified approach to the mathematical description of the ZnO/CdS/Cu(In,Ga)Se_2 heterojunction including the consequence of the surface band gap widening is given in reference [121].

The most important quantities to be considered in the band diagram are the band discontinuities between the different heterojunction partners. Band discontinuities in terms of valence band offsets ΔE_v^{ab} between semiconductor *a* and *b* are usually determined by photoelectron spectroscopy (for a discussion with respect to Cu-chalcopyrite surfaces and interfaces, see [74]). The valence band offset between a (011)-oriented Cu(In,Ga)Se_2 single crystal and CdS deposited by PVD at room temperature is determined as [122, 123] $\Delta E_v^{ab} = -0.8$ (± 0.2) eV (and, therefore, $\Delta E_c^{ab} = E_g^{CdS} - E_g^{CIS} + \Delta E_v^{ab} \approx 0.55$ eV, with the band

gaps $E_g^{CdS} \approx 2.4$ eV and $E_g^{CIS} \approx 1.05$ eV of CdS and $CuInSe_2$, respectively). Several authors have investigated the band discontinuity between polycrystalline Cu(In,Ga)Se_2 films and CdS, and found values between −0.6 and −1.3 eV with a clear centre of mass around −0.9 eV, corresponding to a conduction band offset of 0.45 eV [74]. Wei and Zunger [124] calculated a theoretical value of $\Delta E_v^{ab} = -1.03$ eV, which would lead to $\Delta E_C^{ab} \approx 0.3$ eV. Recently, Morkel et al. [77] found a valence band offset between the surface of polycrystalline, Cu-poor prepared $CuInSe_2$ and chemical bath deposited CdS of $\Delta E_v^{ab} = -0.8$ eV. By combining their photoelectron spectroscopy results with measured surface band gap energies of CdS and $CuInSe_2$ from inverse photoemission spectroscopy, the authors of reference [77] conclude that the conduction band offset ΔE_c^{ab} is actually zero. This is because the deposited CdS has $E_g = 2.2$ eV due to S/Se intermixing and the $CuInSe_2$ film exhibits a surface band gap of 1.4 eV, thus $\Delta E_c^{ab} = E_g[\mathrm{Cd(Se,S)}] - E_g^{surf}[CuInSe_2] + \Delta E_V^{ab} \approx 0$.

The band alignment of polycrystalline $CuInSe_2$ and Cu(In,Ga)Se_2 alloys was examined by Schmid et al. [76, 78] who found that the valence band offset is almost independent of the Ga content. In turn, the increase of the absorber band gap leads to a change of ΔE_C^{ab} from positive to negative values. The conduction band offset between the CdS buffer and the ZnO window layer was determined by Ruckh et al. to be 0.4 eV [125].

4.2 Short-Circuit Current

The short circuit current density J_{sc} that can be obtained from the standard 100 mW cm^{-2} solar spectrum (AM1.5) is determined, on the one hand, by *optical losses*, that is, by the fact that photons from a part of the spectrum are either not absorbed in the solar cell or are absorbed *without* generation of electron-hole pairs. On the other hand, not all photogenerated electron-hole pairs contribute to J_{sc} because they recombine before they are collected. We denote these latter limitations as *recombination losses*. Figure 11 illustrates how much from an incoming photon flux from the terrestrial solar spectrum contributes to the final J_{sc} of a highly efficient Cu(In,Ga)Se_2 solar cell [126] and where the remainder gets lost. The incoming light, i.e., that part of the solar spectrum with photon energy $h\nu$ larger than the band gap energy $E_g = 1.155$ eV of the specific absorber would correspond to a (maximum possible) J_{sc} of 41.7 mA cm^{-2}. By reflection at the surface and at the three interfaces between the MgF_2 anti-reflective coating, the ZnO window, the CdS buffer, and the Cu(In,Ga)Se_2 absorber layer we loose already 0.6 mA cm^{-2}. A further reflection loss of 0.1 mA cm^{-2} is due to those low-energy photons that are reflected at the metallic back and leave the solar cell after having traversed the absorber twice. Due to the high absorption coefficient of Cu(In,Ga)Se_2 for $h\nu > E_g$, this portion is very small. More important are parasitic absorption losses by free carrier absorption in the highly doped part of the ZnO window layer (0.9 mA cm^{-2}) and at the absorber/Mo interface (0.5 mA cm^{-2}). Thus, the sum of all *optical losses* amounts to 2.1 mA cm^{-2}. Note that in solar cells and modules there are additional optical losses due to the grid shadowing or interconnect areas, respectively. These losses are not discussed here.

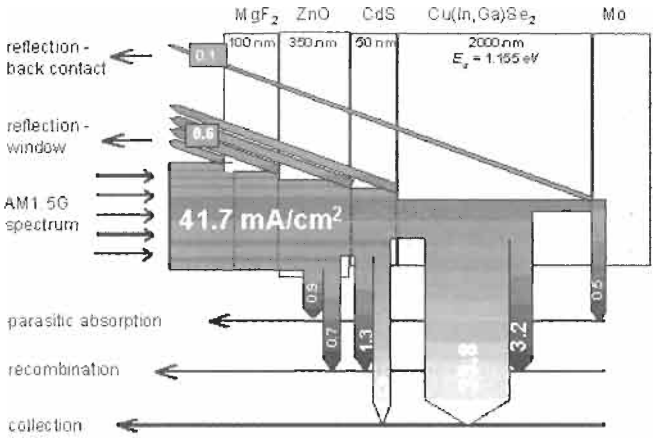

Figure 11 Optical and electronic losses of the short circuit current density J_{sc} of a high-efficiency ZnO/CdS/Cu(In,Ga)Se_2 heterojunction solar cell. The incident current density of 41.7 mA/cm² corresponds to the range of the AM 1.5 solar spectrum that has a photon energy larger than the band gap energy $E_g = 1.155$ eV of the Cu(In,Ga)Se_2 absorber. Optical losses consist of reflection losses at the ambient/window, at the window/buffer, the buffer/absorber, and at the absorber/back contact interface as well as of parasitic absorption in the ZnO window layer (free carrier absorption) and at the Mo back contact. Electronic losses are recombination losses in the window, buffer, and in the absorber layer. The finally measured J_{sc} of 34.6 mA/cm² of the cell stems almost exclusively from the Cu(In,Ga)Se_2 absorber and only to a small extend from the CdS buffer layer.

Next, we have to consider that electron hole pairs photogenerated in the ZnO window layer are not separated. Therefore, this loss affecting photon energies $h\nu > E_g(\text{ZnO}) = 3.2$ eV contributes to the *recombination losses*. As shown in Figure 11, this loss of high-energy photons costs about 0.7 mA cm^{-2}. Another portion of the solar light is absorbed in the CdS buffer layer (E_g (CdS) $\approx$ 2.4 eV). However, a part of the photons in the energy range 3.2 eV $> h\nu >$ 2.4 eV contributes to J_{sc} because the thin CdS layer does not absorb all those photons and a part of the electron-hole pairs created in the buffer layer still contributes to the photocurrent [127]. In the present example 1.3 mA cm^{-2}, get lost by recombination and 0.8 mA cm^{-2} are collected. However, the major part of J_{sc} (33.8 mA cm^{-2}) stems from electron hole pairs photogenerated in the absorber. Finally, the collection losses in the absorber amount to 3.2 mA cm^{-2}.

The above analysis shows that, accepting the restrictions that are given by the window and the buffer layer, this type of solar cell makes extremely good use of the solar spectrum. There is however still some scope for improving J_{sc} by optimising carrier collection in the absorber and/or by replacing the CdS buffer layer by an alternative material with a higher E_g.

4.3 Open-Circuit Voltage

At open circuit no current flows across the device, and all photogenerated charge carriers have to recombine within the solar cell. The possible recombination

paths for the photogenerated charge carriers in the Cu(In,Ga)Se_2 absorber are indicated in the band diagram of Figure 12. Here we have considered recombination at the back surface of the absorber (A′) and in the neutral bulk (A), recombination in the space-charge region (B), and recombination at the buffer/absorber interface (C). Note that due to the presence of high electrical fields in the junction region, the latter two mechanism may be enhanced by tunnelling.

The *basic* equations for the recombination processes (A–C) can be found, for example, in [128]. Notably, all recombination current densities J_R can be written in the form of a diode law

$$J_R = J_0\left\{\exp\left(\frac{qV}{n_{id}k_BT}\right) - 1\right\} \tag{1}$$

where V is the applied voltage, n_{id} the diode ideality factor, and k_BT/q the thermal voltage. The saturation current density J_0 in general is a thermally activated quantity and may be written in the form

$$J_0 = J_{00}\exp\left(\frac{-E_a}{n_{id}k_BT}\right) \tag{2}$$

where E_a is the activation energy and the prefactor J_{00} is only weakly temperature dependent.

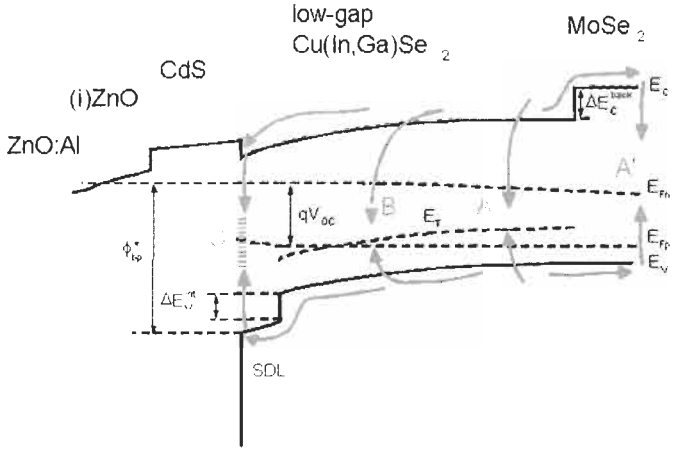

Figure 12 Recombination paths in a ZnO/CdS/(low-gap) Cu(In,Ga)Se2 junction at open circuit. The paths A represent recombination in the neutral volume, A′ recombination at the back contact, B recombination in the space-charge region, and C recombination at the interface between the Cu(In,Ga)Se2 absorber and the CdS buffer layer. Back contact recombination is reduced by the conduction band offset ΔE_c^{back} between the Cu(In,Ga)Se_2 absorber and the MoSe2 layer that forms during absorber preparation on top of the metallic Mo back contact. Interface recombination (C) is reduced by the internal valence band offset ΔE_v^{int} between the bulk of the Cu(In,Ga)Se2 absorber and the Cu-poor surface layer. The quantity ϕ_{bp}^* denotes the energy barrier at the CdS/absorber interface and E_T indicates the the energy of a recombination centre in the bulk of the Cu(In,Ga)Se_2.

The activation energy E_a for recombination at the back surface, in the neutral zone, and in the space charge recombination is the absorber band gap energy E_g, whereas in case of interface recombination E_a equals the barrier ϕ_{bp} that hinders the holes from the absorber to come to the buffer/absorber interface (cf. Figure 12). In the simplest cases, the diode ideality factor n_{id} is unity for back surface and neutral zone recombination as well as for recombination at the buffer/absorber interface, whereas for space charge recombination $n_{id} = 2$. Equalising the short circuit current density J_{sc} and the recombination current density J_R in Equation (1) for the open circuit voltage situation (i.e., $V = V_{oc}$ in Equation (1)) we obtain with the help of Equation (2)

$$V_{oc} = \frac{E_a}{q} - \frac{n_{id}k_BT}{q}\ln\left(\frac{J_{00}}{J_{sc}}\right) \tag{3}$$

Note that Equation (3) yields the open circuit voltage in a situation where there is single mechanism clearly dominating the recombination in the specific device. Note that Equation (3) is often used for the analysis of the dominant recombination path. After measuring V_{oc} at various temperatures T, the extrapolation of the experimental $V_{oc}(T)$ curve to $T = 0$ yields the activation energy of the dominant recombination process, e.g. $V_{oc}(0) = E_g/q$ in case of bulk recombination or $V_{oc}(0) = \phi_{bp}/q$ in case of interface recombination.

We emphasise that, in practice, measured ideality factors considerably deviate from that textbook scheme and require more refined theories (see e.g. [14] and references therein). However, for a basic understanding of the recombination losses in thin-film solar cells, a restriction to those textbook examples is sufficient.

The band diagram in Figure 12 contains two important features that appear important for the minimisation of recombination losses in Cu(In,Ga)Se_2 solar cells. The first one is the presence of a considerably widened band gap at the surface of the Cu(In,Ga)Se_2 absorber film. This surface band gap widening implies a valence band offset ΔE_v^{int} at the internal interface between the absorber and the surface defect layer (discussed in Section 4.1). This internal offset directly increases the recombination barrier ϕ_{bp} to an effective value

$$\phi_{bp}^{*} = \phi_{bp} + \Delta E_v^{\text{int}} \tag{4}$$

Substituting Equation (4) in Equation (3) we obtain

$$V_{oc} = \frac{\phi_{bp}}{q} + \frac{\Delta E_v^{\text{int}}}{q} - \frac{n_{id}k_BT}{q}\ln\left(\frac{J_{00}}{J_{sc}}\right) \tag{5}$$

It is seen that the internal band offset directly adds to the open circuit voltage that is achievable in situations where only interface recombination is present. However, the open circuit voltage of most devices that have this surface band gap widening (those having an absorber with a final Cu-poor composition) is then limited by bulk recombination.

The second important feature in Figure 12 is the conduction band offset ΔE_c^{back} between the Cu(In,Ga)Se_2 absorber and the thin $MoSe_2$ film. The back surface recombination velocity at the metallic Mo back contact is reduced from the value S_b (without the $MoSe_2$) to a value $S_b^* = S_b \exp(-\Delta E_c/k_B T)$.

4.4 Fill Factor

The fill factor FF of a solar cell can be expressed in a simple way as long as the solar cell is well described by a diode law. Green [129] gives the following phenomenological expression for the fill factor

$$FF_0 = \frac{v_{oc} - \ln(v_{oc} + 0.72)}{v_{oc} + 1} \tag{6}$$

It is seen that, through the dimensionless quantity $v_{oc} = qV_{oc}/n_{id}k_B T$, the fill factor depends on the temperature T as well as on the ideality factor n_{id} of the diode (see also Chapter IIa-1). The fill factor FF_0 results solely from the diode law form of Equation (1). In addition, effects from series resistance R_s and shunt resistance R_p add to the fill factor losses. A good approximation is then given by

$$FF = FF_0(1 - r_S)\left[1 - \frac{(v_{oc} + 0.7)}{v_{oc}}\frac{FF_0(1 - r_S)}{r_P}\right] \tag{7}$$

with the normalised series and parallel resistances given by $r_s = R_s J_{sc}/V_{oc}$ and $r_p = R_P J_{sc}/V_{oc}$, respectively. The description of Cu(In,Ga)Se_2 solar cells in terms of Equations (6) and (7) works reasonably well, e.g., the world record cell [1] has a fill factor of 78.6% and the value calculated from Equations (6) and (7) is 78.0% (V_{oc} = 678 mV, J_{sc} = 35.2 mA cm^{-2}, R_s = 0.2 Ω cm^2, $R_p = 10^4$ Ω cm^2, n_{id} = 1.5).

Factors that can further affect the fill factor are (i) the voltage bias dependence of current collection [130], leading to a dependence of $J_{sc}(V)$ on voltage V in Equation (1), (ii) recombination properties that are spatially inhomogeneous [131], or (iii) unfavourable band offset conditions at the heterointerface [132].

4.5 Electronic Metastabilities

The long time increase (measured in hours and days) of the open circuit voltage V_{OC} of Cu(In,Ga)Se_2 based solar cells during illumination is commonly observed phenomenon [133, 134]. In some cases it is not only V_{oc} but also the fill factor that improves during such a light soaking procedure. Consequently, light soaking treatments are systematically used to re-establish the cell efficiency after thermal treatments [107, 135].

For the present day ZnO/CdS/Cu(In,Ga)Se_2 heterojunctions it appears established that there exist at least three types of metastablities with completely different fingerprints [136, 137].

Type I: A continuous increase of the open circuit voltage during illumination and the simultaneous increase of the junction capacitance. Both phenomena are satisfactorily explained as a consequence of persistent photoconductivity in the Cu(In,Ga)Se_2 absorber material [138, 139], i.e., the persistent capture of photogenerated electrons in traps that exhibit large lattice relaxations like the well-known DX centre in (Al,Ga)As [140]. This type of metastability affects exclusively the open circuit voltage and can vary from few mV up to 50 mV, especially if the sample has been stored in the dark at elevated temperatures.

Type II: A decrease of the fill factor after the cell has been exposed to reverse voltage bias. In extreme cases, this type of metastability leads to a hysteresis in the IV characteristics, e.g., the fill factor of an illuminated IV curve becomes dependent on whether the characteristic has been measured from negative voltages towards positive ones or vice versa. The application of reverse bias also leads to a metastable increase of the junction capacitance and to significant changes of space charge profiles as determined from capacitance vs. voltage measurements [136, 137]. The type II metastability is especially important for devices with non-standard buffer/window combinations (e.g., Cd-free buffer layers) [141, 142].

Type III: An increase of the fill factor upon illumination with light that is absorbed in the buffer layer or in the extreme surface region of the Cu(In,Ga)Se_2 absorber, i.e., the blue part of the solar spectrum. This type of instability counterbalances, to a certain extend, the consequences of reverse bias, i.e., it restores the value of the fill factor after it has been degraded by application of reverse bias.

Our overall understanding of metastabilities, especially of type II and III, is still incomplete. Fortunately, all metastabilities observed in Cu(In,Ga)Se_2 so far, tend to improve the photovoltaic properties as soon as the device is brought under operating conditions.

5 Wide-Gap Chalcopyrites

5.1 Basics

The alloy system Cu(In,Ga,Al)(S,Se)$_2$ provides the possibility of building alloys with a wide range of band-gap energies E_g between 1.04 eV for $CuInSe_2$ up to 3.45 eV for $CuAlS_2$ (cf. Figure 2). The highest efficiency within the chalcopyrite system is achieved with the relatively low-band-gap energy E_g of 1.12 eV, and attempts to maintain this high efficiency level at $E_g > 1.3$ eV have so far failed (for a recent review, see [143]). Practical approaches to wide-gap Cu-chalcopyrites comprise (i) alloying of $CuInSe_2$ with Ga up to pure $CuGaSe_2$ with $E_g \approx 1.68$ eV, (ii) Cu(In,Al)Se_2 alloys with solar cells realised up to an Al/(Al + In) ratio of 0.6 and $E_g \approx 1.8$ eV [144], (iii) CuIn(Se,S)$_2$ [145] and Cu(In,Ga)(Se,S)$_2$ [146] alloys with a S/(Se + S) ratio up to 0.5, and (iv) $CuInS_2$ [147] and Cu(In,Ga)S_2 [148] alloys. Note that the approaches (i)–(iii) are realised with a

final film composition that is slightly Cu-poor, whereas approach (iv) uses films that are Cu-rich. In the latter case, CuS segregates preferably at the film surface. This secondary phase has to be removed prior to heterojunction formation.

The advantage of higher voltages of the individual cells by increasing the band gap of the absorber material is important for thin-film modules. An ideal range for the band gap energy would be between 1.4 and 1.6 eV because the increased open circuit voltage and the reduced short circuit current density would reduce the number of necessary scribes used for monolithic integration of the cells into a module. Also, the thickness of front and back electrodes can be reduced because of the reduced current density.

Table 3 compares the solar cell output parameters of the best chalcopyrite-based solar cells. This compilation clearly shows the superiority of $Cu(In,Ga)Se_2$ with a relatively low Ga content which leads to the actual world champion device. The fact that the best $CuInSe_2$ device has an efficiency of 3 % below that of the best $Cu(In,Ga)Se_2$ device is due not only to the less favourable band-gap energy but also to the lack of the beneficial effect of small amounts of Ga on the growth and on the electronic quality of the thin film, as discussed above.

The difficulty of obtaining wide-gap devices with high efficiencies is also illustrated by plotting the absorber band gap energies of a series of chalcopyrite alloys vs. the attained open-circuit voltages. Figure 13 shows that below $E_g = 1.3$ eV, the V_{OC} data follow a straight line, indicating the proportional gain of $V_{oc} = E_g/q - 0.5$V, whereas at $E_g > 1.3$ eV the gain is much more moderate. At the high band-gap end of the scale the differences of the band-gap energies and the open-circuit voltages of $CuInS_2$ and $CuGaSe_2$ amount to 840 mV and 820 mV, respectively, whereas $E_g - qV_{oc}$ is only 434 eV in the record $Cu(In,Ga)Se_2$ device.

One reason for these large differences $E_g - qV_{oc}$ in wide-gap devices is the less favourable band offset constellation at the absorber/CdS-buffer interface. Figure 14 shows the band diagram of a wide-gap Cu chalcopyrite-based heterojunction with (Figure 14(a)) and without (Figure 14(b)) the surface defect layer. As the increase of band gap in going from $CuInSe_2$ to $CuGaSe_2$ takes place almost exclusively by an increase of the conduction band energy E_c, the positive or zero band offset ΔE_c^{ab} between the absorber and the buffer of a low-gap device (cf.

Table 3 Absorber band-gap energy E_g, efficiency η, open-circuit voltage V_{oc}, short-circuit current density J_{sc}, fill factor FF, and area A of the best $Cu(In,Ga)Se_2$, $CuInSe_2$, $CuGaSe_2$, $Cu(In,Al)Se_2$, $CuInS_2$, $Cu(In,Ga)S_2$, and $Cu(In,Ga)(S,Se)_2$ solar cells

Material	E_g (eV)	η (%)	V_{oc} (mV)	J_{sc} (mA cm^{-2})	FF (%)	A (cm^2)	Ref.
$Cu(In,Ga)Se_2$	1.12	18.8	678	35.2	78.6	0.45	[1][a]
$CuInSe_2$	1.04	15.4	515	41.2	72.6	0.38	[40][b]
$CuGaSe_2$	1.68	8.3	861	14.2	67.9	0.47	[151][a]
$Cu(In,Al)Se_2$	1.16	16.6	621	36.0	75.5	?	[157][a]
$Cu(In,Ga)(S,Se)_2$	1.36	13.9	775	24.3	74.0	0.5	[146][b]
$CuInS_2$	1.5	11.4	729	21.8	72.0	0.5	[159][a]
$Cu(In,Ga)S_2$	1.53	12.3	774	21.6	73.7	0.5	[148][a]

[a] Confirmed total area values.

[b] Effective area values (not confirmed).

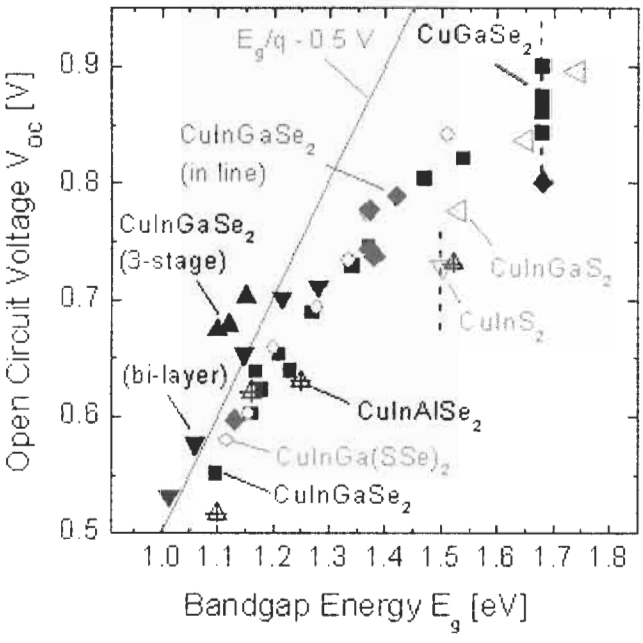

Figure 13 Open-circuit voltages of different Cu-chalcopyrite based solar cells with various band-gap energies of the absorber layers. Full symbols correspond to Cu(In,Ga)Se_2 alloys prepared by a simple single layer process (squares), a bi-layer process (triangles down), and the three-stage process (triangles up). Cu(In,Ga)Se_2 cells derived from an in-line process as sketched in Fig. 9 are denoted by diamonds. Open triangles relate to Cu(In,Ga)S_2, open circles to Cu(In,Ga)(S,Se)$_2$, and the crossed triangles to Cu(In,Al)Se_2 cells.

Figure 12) turns into a negative one in Figure 14. This effect should be weaker for $CuInS_2$ and $CuAlSe_2$ as the increase of E_g in these cases is due to an upwards shift of E_c *and* a downwards shift of E_v. However, *any* increase of E_c implies that the barrier ϕ_{bp} that hinders the holes from the absorber from recombination at the heterointerface does not increase proportionally with the increase of the band-gap energy. Thus in wide-gap absorbers, the importance of interface recombination (determined by the barrier ϕ_{bp}) grows considerably relative to that of bulk recombination (determined by E_g of the absorber) [149]. Using the same arguments with respect to the $MoSe_2$/absorber, the back-surface field provided by this type of heterojunction back contact, as shown in Figure 12, vanishes when the conduction-band energy of the absorber is increased.

Up to now, all arguments for explaining the relatively low performance of wide-gap chalcopyrite alloys deal with the changes in the band diagram. However, recent work focuses on the differences in the electronic quality of the absorber materials. Here, it was found that the concentration of recombination active defects increases when increasing the Ga content in Cu(In,Ga)Se_2 above a Ga/(Ga + In) ratio of about 0.3 [32] and the S content in Cu(In,Ga)(Se,S)$_2$ alloys over a S/(Se+S) ratio of 0.3 [34]. Moreover, a recent systematic investigation of

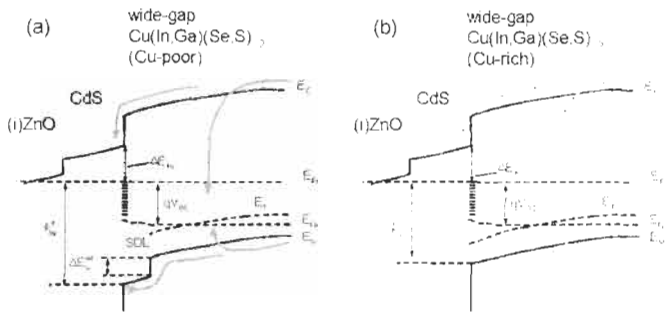

Figure 14: Energy band diagram of a ZnO/CdS/(wide-gap) Cu(In,Ga)(Se,S)2 heterojunction. The band diagram (a) that includes the surface defect layer (SDL) of a Cu-poor prepared film shows that the interface recombination barrier $\phi^*_{bp} = \phi_{bp} + \Delta E_v^{int}$ is larger than the barrier ϕ_{bp} in the device that was prepared Cu-rich (b). The difference is the internal valence band offset ΔE_v^{int} between the SDL and the bulk of the absorber. The larger value of ϕ^*_{bp} reduces interface recombination.

the dominant recombination mechanism in large series of $Cu(In,Ga)(Se,S)_2$ based solar cells with different compositions [150] suggests that bulk recombination prevails in all devices that were prepared with a Cu-poor final film composition. Only devices that had a Cu-rich composition (before removing Cu-rich secondary phases) showed signatures of interface recombination. The absence of interface recombination in Cu-poor devices could be a result of the presence of the Cu-poor surface defect layer in these devices. Comparison of Figures 14(a) and (b) illustrates that interface recombination is much more likely to dominate those devices that lack this feature.

5.2 $CuGaSe_2$

$CuGaSe_2$ has a band gap of 1.68 eV and therefore would represent an ideal partner for $CuInSe_2$ in an all-chalcopyrite tandem structure. However, a reasonable efficiency for the top cell of any tandem structure is about 15%, far higher than has been reached by the present polycrystalline $CuGaSe_2$ technology. The record efficiency of $CuGaSe_2$ thin-film solar cells is only 8.3% (9.3% active area) [151] despite of the fact that the electronic properties of $CuGaSe_2$ are not so far from those of $CuInSe_2$. However, in detail, all the differences quantitatively point in a less favourable direction. In general, the net doping density N_A in $CuGaSe_2$ appears too high [152]. Together with the charge of deeper defects, the high doping density leads to an electrical field in the space-charge region, which enhances recombination by tunnelling [153]. The high defect density in $CuGaSe_2$ thin films absorbers additionally leads to a low diffusion length and, in consequence, to a dependence of the collected short circuit current density J_{sc} on the bias voltage V. Because of the decreasing width of the space charge region, $J_{sc}(V)$ decreases with increasing V affecting significantly the fill factor of the solar cell [130]. Note that, on top of the limitation by the unfavourable bulk properties, interface recombination also plays a certain role in $CuGaSe_2$ [154] because of the unfavourable band diagram

shown in Figure 14. Therefore, substantial improvement of the performance requires simultaneous optimisation of bulk *and* interface properties. Notably, $CuGaSe_2$ is the only Cu-chalcopyrite material where the record efficiency of cells based on bulk crystals (with $\eta = 9.4\%$, total area) [155] exceeds that of thin-film devices.

5.3 Cu(In,Al)Se$_2$

As can be seen in Figure 2, the bandgap change within the Cu(In,Al)Se_2 alloy system is significant even if a small amount of Al is added to $CuInSe_2$ [144]. This fact allows to grow graded structures with only small changes in the lattice constant. Al–Se compounds tend to react with water vapour to form oxides and H_2Se. Furthermore, there is a tendency to phase segregations [144]. However, cells with very good performance have been achieved by a co-evaporation process of absorbers in a band gap range between 1.09 and 1.57 eV, corresponding to Al/(In + Al) ratio x between 0.09 and 0.59 [144, 156]. The highest confirmed efficiency of a Cu(In,Al)Se_2 solar cell is 16.9% [157] (see also Table 3). This device has about the same band gap energy as the record Cu(In,Ga)Se_2 device [1].

5.4 CuInS$_2$ and Cu(In,Ga)S$_2$

The major difference between $CuInS_2$ and Cu(In,Ga)Se_2 is that the former cannot be prepared with an overall Cu-poor composition. Cu-poor $CuInS_2$ displays an extremely low conductivity, making it almost unusable as a photovoltaic absorber material [145]. Even at small deviations from stoichiometry on the In-rich side, segregation of the spinel phase is observed [158]. Instead, the material of choice is Cu-rich $CuInS_2$. As in the case of $CuInSe_2$, a Cu-rich preparation route implies the removal of the unavoidable secondary Cu–S binary phase by etching the absorber in KCN solution [147]. Such an etch may involve some damage of the absorber surface as well as the introduction of shunt paths between the front and the back electrode. However, as shown in Table 3, the best $CuInS_2$ device [159] has an efficiency above 11%. This record efficiency for $CuInS_2$ is achieved by a sulphurisation process rather than by co-evaporation.

As we have discussed above, interface recombination dominates the open circuit voltage V_{oc} of Cu(In,Ga)(Se,S)$_2$ devices that are prepared with a Cu-rich absorber composition (prior to the KCN etch), like the $CuInS_2$ and Cu(In,Ga)S_2 devices discussed here. It was found recently, that alloying $CuInSe_2$ with moderate amounts of Ga enhances the open circuit voltage V_{oc} [160]. This increase of V_{oc} can counterbalance the loss of short circuit current density J_{sc} resulting from the increased band gap. Apparently, addition of Ga to $CuInS_2$ reduces interface recombination by increasing the interfacial barrier ϕ_{bp}(cf. Figure 14(b)) [150]. However, for Cu(In,Ga)S_2 devices prepared by the sulphurisation route, the benefit of Ga alloying is limited, because, during preparation, most of the Ga added to the precursor ends up confined to the rear part of the absorber layer and, therefore, remains ineffective at the absorber

surface [160]. In contrast, when preparing $Cu(In,Ga)S_2$ with co-evaporation, Ga is homogeneously distributed through the depth of the absorber and the Ga content at the film surface is well controlled. Recent work of Kaigawa et al. [148] represents a major progress in wide-gap Cu-chalcopyrites with the preparation of $Cu(In,Ga)S_2$ solar cells with a confirmed efficiency of 12.3% at a band gap energy E_g = 1.53 eV. In the same publication [148] an efficiency of 10.1% is reported for a device with E_g = 1.65 eV. The open circuit voltage V_{oc} of this device is 831 mV, i.e., only slightly lower than V_{oc} of the best $CuGaSe_2$ cell having an efficiency of 8.3%.

5.5 $Cu(In,Ga)(Se,S)_2$

One possible way of overcoming the disadvantages of the ternary wide-gap materials $CuInS_2$ and $CuGaSe_2$ is to use the full pentenary alloy system $Cu(In_{1-x}Ga_x)(Se_{1-y}S_y)_2$ [146]. Among the materials listed in Table 3, the pentenary system is the only one with an open-circuit voltage larger than 750 mV and an efficiency above 13%, outperforming $CuInS_2$ in both these respects. The advantage of $Cu(In,Ga)(Se,S)_2$ could be due to the mutual compensation of the drawbacks of $CuGaSe_2$ (too high charge density) and that of (Cu-poor) $CuInS_2$ (too low conductivity, if prepared with a Cu-poor film composition).

5.6 Graded-Gap Devices

An interesting property of the $Cu(In,Ga,Al)(S,Se)_2$ alloy system is the possibility of designing graded-gap structures in order to optimise the electronic properties of the final device [161–164]. Such band-gap gradings are achieved during co-evaporation by the control of the elemental sources, but selenisation/sulphurisation processes also lead to beneficial compositional gradings. The art of designing optimum band-gap gradings is to push back charge carriers from critical regions, i.e., regions with high recombination probability within the device. Such critical regions are (i) the interface between the back contact and the absorber layer and (ii) the heterojunction interface between the absorber and the buffer material. Figure 15 shows a band diagram of a graded structure that fulfils the requirements for minimising recombination losses.

(i) To keep the back contact region clear from electrons, one can use a Ga/In grading. The increase of the Ga/(Ga + In) ratio causes a movement of the conduction band minimum upward with respect to its position in a non-graded $CuInSe_2$ device. Thus, back surface grading leads to a gradual increase of the conduction-band energy, as illustrated in Figure 15, and therefore drives photogenerated electrons away from the metallic back contact into the direction of the buffer/absorber junction.

(ii) The minimisation of junction recombination, both at the point of equal capture rates of holes and electrons in the space charge region (recombination path B in Figure 15) as well as at the absorber/buffer interface (path C), requires an increased band gap towards the absorber

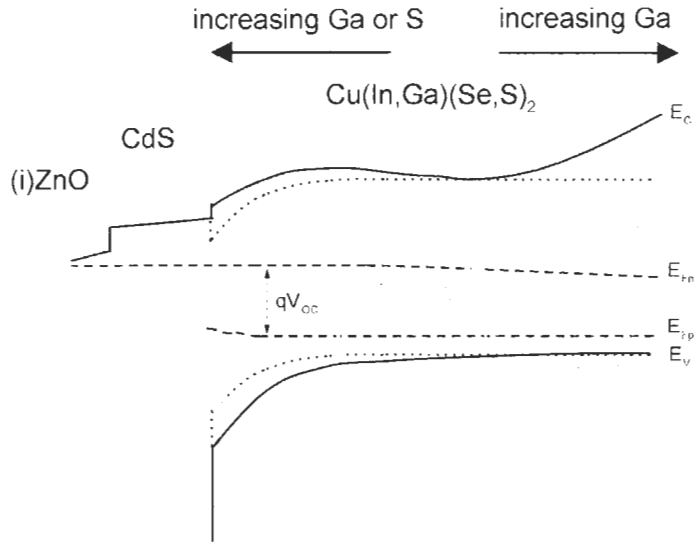

Figure 15 Band diagram of a ZnO/CdS/Cu(In,Ga)(Se,S)$_2$ heterojunction with a graded-gap absorber. The minimum band gap energy is in the quasi neutral part of the absorber. An increasing Ga/In ratio towards the back surface and an increasing Ga/In or S/Se-ratio towards the front minimise recombination in critical regions at the back contact (recombination path A'), in the space charge region (path B), and at the heterointerface (path C). The dotted lines correspond to the conduction and valence band edge energies of a non-graded device.

surface. If one had the choice, one would clearly favour a decrease of the valence-band energy, as shown in Figure 15, over an increase of the conduction band energy. This favours a grading with the help of S/Se alloying, as at least a part of the increasing band-gap energy is accommodated by a decrease of the energy of the valence-band edge that should minimise interface recombination.

6 Conclusions

The objective of this chapter is the description of the recent achievements on Cu(In,Ga)Se$_2$-based solar cells as well as an account of our present understanding of the physical properties of the materials involved and the electronic behaviour of the devices. Cu(In,Ga)Se$_2$ is in a leading position among polycrystalline thin-film solar cell materials because of the benign, forgiving nature of the bulk materials and interfaces. Nevertheless, we want to guide the attention of the reader also in the direction of the work that has still to be done.

Three of the four cornerstones 1–4 for the recent achievements mentioned in Section 3.2 concern the *growth of the films*: the optimised deposition conditions, and the incorporation of Na and Ga. However, no detailed model is available to describe the growth of Cu(In,Ga)Se$_2$, and especially the impact of Na which,

in our opinion, is the most important of the different ingredients available to tune the electronic properties of the absorber. A clearer understanding of Cu(In,Ga)Se_2 growth would allow us to find optimised conditions in the wide parameter space available, and thus to reduce the number of recombination centres and compensating donors and optimise the number of shallow acceptors.

The deposition of the buffer layer, or more generally speaking, the formation of the heterojunction, is another critical issue. The surface chemistry taking place during heterojunction formation, and also during post-deposition treatments, is decisive for the final device performance. Both processes greatly affect not only the surface defects (i.e., recombination *and* charge), and therefore the charge distribution in the device, but also the defects in the bulk of the absorber. Concentrated effort and major progress in these tasks would not only allow us to push the best efficiencies further towards 20%, but would also provide a sound knowledge base for the various attempts at the commercialisation of Cu(In,Ga)Se_2 solar cells.

Acknowledgements

The authors thank all our colleagues at the IPE for various discussions and fruitful collaboration. We are especially grateful to J. H. Werner for his continuous support of the Cu(In,Ga)Se_2 research at the *ipe*. We are grateful to M. Turcu for a critical reading of the manuscript. Support of our work during many years by the German Ministry of Research, Technology, and Education (BMBF), by the Ministry of Economics, and by the European Commission is especially acknowledged.

References

[1] Contreras, M., Egaas, B., Ramanathan, K., Hiltner, J., Swartzlander, A., Hasoon, F. and Noufi, R., 1999. Progress toward 20% efficiency in Cu(In,Ga)Se_2 polycrystalline thin-film solar cells. *Prog. Photovolt. Res. Appl.* Vol. 7, p. 311.

[2] Kessler, J., Bodegard, M., Hedström, J. and Stolt, L., 2000. New world record Cu(In,Ga)Se_2 based mini-module: 16.6%. *Proc.16th European Photovoltaic Solar Energy Conf.*, Glasgow, p. 2057.

[3] Hahn, H., Frank, G., Klingler, W., Meyer, A. and Störger, G., 1953. über einige ternäre Chalkogenide mit Chalkopyritstruktur. *Z. Anorg. u. Allg. Chemie*, Vol. 271, p.153.

[4] Wagner, S., Shay, J.L., Migliorato, P. and Kasper, H.M., 1974. $CuInSe_2$/CdS heterojunction photovoltaic detectors. *Appl. Phys. Lett.* Vol. 25, p. 434.

[5] Mickelsen, R.A. and Chen, W.S., 1980. High photocurrent polycrystalline thin-film CdS/$CuInSe_2$ solar cell. *Appl. Phys. Lett.* Vol. 36, p. 371.

[6] Mitchell, K.C., Ermer, J. and Pier, D., 1988. Single and tandem junction $CuInSe_2$ cell and module technology. *Proc. 20th IEEE Photovoltaic Specialists Conf.*, Las Vegas, p. 1384.

[7] Wieting, R.D., 2002. CIS Manufacturing at the Megawatt Scale. *Proc. 29th IEEE Photovoltaic Specialists Conf.*, New Orleans, p. 480.

[8] Probst, V., Stetter, W., Riedl, W., Vogt, H., Wendl, M., Calwer, H., Zweigart, S., Ufert, K.D., Freienstein, B., Cerva, H. and Karg, F.H., 2001. Rapid CIS-process for high efficiency PV-modules: development towards large area processing. *Thin Solid Films*, Vol. 387, p. 262.

[9] Dimmler, B., Powalla, M. and Schock, H.W., 2002. CIS-based thin-film photovoltaic modules: potential and prospects. *Prog. Photovolt. Res. Appl.* Vol. 10, p.149.

[10] Powalla, M., Lotter, E., Waechter, R., Spiering, S., Oertel, M. and Dimmler, B., 2002. Pilot Line Production of CIGS Modules: First Experience in Processing and Further Developments. *Proc. 29th IEEE Photovoltaic Specialists Conf.*, New Orleans, p. 571.

[11] Kushiya, K., 2001. Improvement of electrical yield in the fabrication of CIGS-based thin-film modules. *Thin Solid Films*, Vol. 387, p. 257.

[12] Negami, T., Satoh, T., Hashimoto, Y., Nishiwaki, S., Shimakawa, S. and Hayashi, S., 2001. Large-area CIGS absorbers prepared by physical vapor deposition. *Solar Energy Mat. Solar Cells*, Vol. 67, p. 1.

[13] Rau, U. and Schock, H.W., 1999. Electronic properties of $Cu(In,Ga)Se_2$ heterojunction solar cells- recent achievements, current understanding, and future challenges. *Appl. Phys. A*, Vol. 69, p. 191.

[14] Rau, U. and Schock, H.W., 2001. $Cu(In,Ga)Se_2$ Solar Cells. In: Archer, M.D. and Hill, R., Eds., *Clean Electricity from Photovoltaics*, Imperial College Press, London, p. 270.

[15] Shay, J.L. and Wernick, J.H., 1975. *Ternary Chalcopyrite Semiconductors: Growth, Electronic Properties, and Applications*, Pergamon Press, Oxford.

[16] Kazmerski, L.L. and Wagner, S., 1985. Cu-ternary chalcopyrite solar cells. In: Coutts, T.J. and Meakin, J.D., Eds., *Current Topics in Photovoltaics*, Academic Press, Orlando, p. 41.

[17] Coutts, T.J., Kazmerski, L.L. and Wagner, S., 1986. *Ternary Chalcopyrite Semiconductors: Growth, Electronic Properties, and Applications*, Elsevier, Amsterdam.

[18] Rockett, A. and Birkmire, R.W., 1991. $CuInSe_2$ for photovoltaic applications. *J. Appl. Phys.* Vol. 70, p. 81.

[19] Stanbery, B.J., 2002. Copper indium selenides and related materials for photovoltaic devices. *Crit. Rev. Solid State*, Vol. 27, p. 73.

[20] Haalboom, T., Gödecke, T., Ernst, F., Rühle, M., Herberholz, R., Schock, H.W., Beilharz, C. and Benz, K.W., 1997. Phase relations and microstructure in bulk materials and thin films of the ternary system Cu-In-Se. *Inst. Phys. Conf. Ser.*, Vol. 152E, p. 249.

[21] Herberholz, R., Rau, U., Schock, H.W., Haalboom, T., Gödecke, T., Ernst, F., Beilharz, C., Benz, K.W., and Cahen, D., 1999. Phase segregation, Cu

migration and junction formation in Cu(In,Ga)Se_2. *Eur. Phys. J. Appl. Phys.*, Vol. 6, p. 131.

[22] Migliorato, P., Shay, J.L., Kasper, H.M. and Wagner, S., 1975. Analysis of the electrical and luminescent properties of $CuInSe_2$. *J. Appl. Phys.* Vol. 46, p. 1777.

[23] Noufi, R., Axton, R., Herrington, C. and Deb, S.K., 1984. Electronic properties versus composition of thin films of $CuInSe_2$. *Appl. Phys. Lett.*, Vol. 45, p. 668.

[24] Zhang, S.B., Wei, S.H., Zunger, A. and Katayama-Yoshida, H., 1998. Defect physics of the $CuInSe_2$ chalcopyrite semiconductor. *Phys. Rev B*, Vol. 57, p. 9642.

[25] Neumann, H., 1983. Vacancy formation in $A^{I}B^{III}C_2^{VI}$ chalcopyrite semiconductors. *Cryst. Res. Technol.* Vol. 18, p. 901.

[26] Abou-Elfotouh, F.A., Moutinho, H., Bakry, A., Coutts, T.J. and Kazmerski, L.L., 1991. Characterization of the defect levels in copper indium diselenide. *Solar Cells*, Vol. 30, p. 151.

[27] Igalson, M. and Schock, H.W., 1996. The metastable changes of the trap spectra of $CuInSe_2$-based photovoltaic devices. *J. Appl. Phys.*, Vol. 80, p. 5765.

[28] Schmitt, M., Rau, U. and Parisi, J., 1995. Investigation of deep trap levels in $CuInSe_2$ solar cells by temperature dependent admittance measurements. *Proc. 13th European Photovoltaic Solar Energy Conf.*, Nice, p. 1969.

[29] Walter, T., Herberholz, R., Müller, C. and Schock, H.W., 1996. Determination of defect distributions from admittance measurements and application to Cu(In,Ga)Se_2 based heterojunctions. *J. Appl. Phys.*, Vol. 80, p. 4411.

[30] Igalson, M., Bacewicz, R. and Schock, H.W., 1995. 'Dangling bonds' in CuInSe2 and related compounds. *Proc. 13th. European Photovoltaic Solar Energy Conf.*, Nice, p. 2076.

[31] Herberholz, R., Nadenau, V., Rühle, U., Köble, C., Schock, H.W. and Dimmler, B., 1997. Prospects of wide-gap chalcopyrites for thin film photovoltaic modules. *Solar Energy Mater. Solar Cells*, Vol. 49, p. 227.

[32] Hanna, G., Jasenek, A., Rau, U. and Schock, H.W., 2000. Open circuit voltage limitations in $CuIn_{1-x}Ga_xSe_2$ thin- film solar cells – dependence on alloy composition. *Phys. Stat. Sol. A*, Vol. 179, p. R7.

[33] Rau, U., Schmidt, M., Jasenek, A., Hanna, G. and Schock, H.W., 2001. Electrical characterization of Cu(In,Ga)Se_2 thin-film solar cells and the role of defects for the device performance. *Solar Energy Mater. Solar Cells*, Vol. 67, p.137.

[34] Turcu, M., Kötschau, I.M. and Rau, U., 2002. Composition dependence of defect energies and band alignments in the $Cu(In_{1-x}Ga_x)(Se_{1-y}S_y)_2$ alloy system. *J. Appl. Phys.*, Vol. 91, p.1391.

[35] Caldas, M., Fazzio, A. and Zunger, A., 1984. A universal trend in the binding energies of deep impurities in semiconductors. *Appl. Phys. Lett.*, Vol. 45, p. 67.

[36] Langer, J.M. and Heinrich, H., 1985. Deep-level impurities: a possible guide to prediction of band-edge discontinuities in semiconductor heterojunctions. *Phys. Rev. Lett.*, Vol. 55, p.1414.

[37] Heath, J.T., Cohen, J.D., Shafarman, W.N., Liao, D.X. and Rockett, A.A., 2002. Effect of Ga content on defect states in $CuIn_{1-x}Ga_xSe_2$ photovoltaic devices. *Appl. Phys. Lett.*, Vol. 80, p. 4540.

[38] Turcu, M. and Rau, U., 2003. Compositional trends of defect energies, band alignments, and recombination mechanisms in the $Cu(In,Ga)(Se,S)_2$ alloy system. *Thin Solid Films*, Vol. 431–432, p. 158.

[39] Herberholz, R., Igalson, M. and Schock, H.W., 1998. Distinction between bulk and interface states in $CuInSe_2$/CdS/ZnO by space charge spectroscopy. *J. Appl. Phys.*, Vol. 83, p. 318.

[40] Stolt, L., Hedström, J., Kessler, J., Ruckh, M., Velthaus, K.O. and Schock, H.W., 1993. ZnO/CdS/$CuInSe_2$ thin-film solar cells with improved performance. *Appl. Phys. Lett.*, Vol. 62, p. 597.

[41] Hedström, J., Ohlsen, H., Bodegard, M., Kylner, A., Stolt, L., Hariskos, D., Ruckh, M. and Schock, H.W., 1993. ZnO/CdS/Cu(In,Ga)Se/sub 2/ thin film solar cells with improved performance. *Proc. 23rd IEEE Photovoltaic Specialists Conf.*, Lousville, p. 364.

[42] Devaney, W.E., Chen, W.S., Steward, J.M. and Mickelson, R.A., 1990. Structure and properties of high efficiency ZnO/CdZnS/$CuInGaSe_2$ solar cells. *IEEE Trans. Electron Devices*, Vol. ED-37, p. 428.

[43] Potter, R.R., Eberspacher, C. and Fabick, L.B., 1985. Device analysis of $CuInSe_2$ /(Cd,Zn)S solar cells. *Proc. 18th IEEE Photovoltaic Specialists Conf.*, Las Vegas, p. 1659.

[44] Birkmire, R.W., McCandless, B.E., Shafarman, W.N. and Varrin, R.D., 1989. Approaches for high efficiency $CuInSe_2$ solar cells. *Proc. 9th. European Photovoltaic Solar Energy Conf.*, Freiburg, p.134.

[45] Contreras, M.A., Egaas, B., Dippo, P., Webb, J., Granata, J., Ramanathan, K., Asher, S., Swartzlander, A. and Noufi, R., 1997. On the role of Na and modifications to Cu(In,Ga)Se absorber materials using thin-MF (M = Na, K, Cs) precursor layers. *Proc. 26th IEEE Photovoltaic Specialists Conf.*, Anaheim, p. 359.

[46] Holz, J., Karg, F. and Phillipsborn, H.V., 1994. The effect of substrate impurities on the electronic conductivity in CIGS thin films. *Proc. 12th. European Photovoltaic Solar Energy Conf.*, Amsterdam, p. 1592.

[47] Nakada, T., Mise, T., Kume, T. and Kunioka, A., 1998. Superstrate type $Cu(In,Ga)Se_2$ thin film solar cells with ZnO buffer layers - a novel approach to 10% efficiency. *Proc. 2nd. World Conf. on Photovoltaic Solar Energy Conversion*, Vienna, p. 413.

[48] Ruckh, M., Schmid, D., Kaiser, M., Schäffler, R., Walter, T. and Schock, H.W., 1994. Influence of substrates on the electrical properties of $Cu(In,Ga)Se_2$ thin films. *Proc. First World Conf. on Photovoltaic Solar Energy Conversion*, Hawaii, p. 156.

[49] Keyes, B.M., Hasoon, F., Dippo, P., Balcioglu, A. and Abouelfotouh, F., 1997. Influence of Na on the elctro-optical properties of Cu(In,Ga)Se_2. *Proc. 26th. IEEE Photovoltaic Specialists Conf.*, Anaheim, p. 479.

[50] Rau, U., Schmitt, M., Engelhardt, F., Seifert, O., Parisi, J., Riedl, W., Rimmasch, J. and Karg, F., 1998. Impact of Na and S incorporation on the electronic transport mechanisms of Cu(In,Ga)Se_2 solar cells. *Solid State Commun.*, Vol. 107, p. 59.

[51] Braunger, D., Hariskos, D., Bilger, G., Rau, U. and Schock, H.W., 2000. Influence of sodium on the growth of polycrystalline Cu(In.Ga)Se_2 thin films. *Thin Solid Films*, Vol. 361, p. 161.

[52] Takei, R., Tanino, H., Chichibu, S. and Nakanishi, H., 1996. Depth profiles of spatially resolved Raman spectra of a $CuInSe_2$- based thin-film solar cell. *J. Appl. Phys.*, Vol. 79, p. 2793.

[53] Wada, T., Kohara, N., Negami, T. and Nishitani, M., 1996. Chemical and structural characterization of Cu(In,Ga)Se_2/Mo interface in Cu(In,Ga)Se_2 solar cells. *Jpn. J. Appl. Phys.*, Vol. 35, p. 1253.

[54] Klenk, R., Walter, T., Schock, H.W. and Cahen, D., 1993. A model for the successful growth of polycrystalline films of $CuInSe_2$ by multisource physical vacuum evaporation. *Adv. Mat.*, Vol. 5, p. 114.

[55] Probst, V., Rimmasch, J., Stetter, W., Harms, H., Riedl, W., Holz, J. and Karg, F., 1995. Improved CIS thin film solar cells through novel impurity control techniques. *Proc. 13th European Photovoltaic Solar Energy Conf.*, Nice, p. 2123.

[56] Gabor, A.M., Tuttle, J.R., Albin, D.S., Contreras, M.A., Noufi, R. and Hermann, A.M., 1994. High-efficiency $CuIn_xGa_{1-x}Se_2$ solar cells from $(In_x,Ga_{1-x})_2Se_3$ precursors. *Appl. Phys. Lett.*, Vol. 65, p. 198.

[57] Binsma, J.J.M. and Van der Linden, H.A., 1982. Preparation of thin $CuInS_2$ films via a two-stage process. *Thin Solid Films*, Vol. 97, p. 237.

[58] Chu, T.L., Chu, S.C., Lin, S.C. and Yue, J., 1984. Large grain copper indium diselenide films. *J. Electrochem. Soc.*, Vol. 131, p. 2182.

[59] Kapur, V.K., Basol, B.M. and Tseng, E.S., 1987. Low-cost methods for the production of semiconductor films for $CuInSe_2$/CdS solar cells. *Solar Cells*, Vol. 21, p. 65.

[60] Probst, V., Karg, F., Rimmasch, J., Riedl, W., Stetter, W., Harms, H. and Eibl, O., 1996. Advanced stacked elemental layer progress for Cu(InGa)Se_2 thin film photovoltaic devices. *Mat. Res. Soc. Symp. Proc.*, Vol. 426, p. 165.

[61] Niki, S., Fons, P.J., Yamada, A., Suzuki, R., Ohdaira, T., Ishibashi, S. and Oyanagai, H., 1994. High quality $CuInSe_2$ epitaxial films – molecular beam epitaxial growth and intrinsic properties. *Inst. Phys Conf. Ser.*, Vol. 152E, p. 221.

[62] Gallon, P.N., Orsal, G., Artaud, M.C. and Duchemin, S., 1998. Studies of CuInSe2 and $CuGaSe_2$ thin films grown by MOCVD from three organometallic sources. *Proc. 2nd World Conf. on Photovoltaic Solar Energy Conversion*, Vienna, p. 515.

[63] Guillemoles, J.-F., Cowache, P., Lusson, A., Fezzaa, K., Boisivon, F., Vedel, J. and Lincot, D., 1996. High quality $CuInSe_2$ epitaxial films – molecular beam epitaxial growth and intrinsic properties. *J. Appl. Phys.*, Vol. 79, p. 7293.

[64] Abken, A., Heinemann, F., Kampmann, A., Leinkühler, G., Rechid, J., Sittinger, V., Wietler, T. and Reineke-Koch, R., 1998. Large area electrodeposition of $Cu(In,Ga)Se_2$ precursors for the fabrication of thin film solar cells. *Proc. 2nd World Conf. on Photovoltaic Solar Energy Conversion*, Vienna, p.1133.

[65] Lincot, D., Guillemoles, J.-F., Cowache, P., Marlot, A., Lepiller, C., Canava, B., Yousfi, F.B. and Vedel, J., 1998. Solution deposition technologies for thin film solar cells: status and perspectives. *Proc. 2nd World Conf. on Photovoltaic Solar Energy Conversion*, Vienna, p. 440.

[66] Guimard, D, Grand, P.P., Boderau, N., Cowache, P., Guillemoles, J.-F., Lincot, D., Taunier, S., Farah, M. B., and Mogensen, P. 2002. Copper indium diselenide solar cells prepared by electrodeposition, *Proc. 29th IEEE Photovoltaic Specialists Conf.*, New Orleans, p. 692.

[67] Eberspacher, C., Pauls, K.L. and Fredric, C.V., 1998. Improved processes for forming $CuInSe_2$ films. *Proc. 2nd World Conf. on Photovoltaic Solar Energy Conversion*, Vienna, p. 303.

[68] Eberspacher, C., Pauls, K. and Serra, J., 2002. Non-vacuum processing of CIGS solar cells. *Proc. 29th IEEE Photovoltaic Specialists Conf.*, New Orleans, p. 684.

[69] Ramanathan, K., Bhattacharya, R.N., Granata, J., Webb, J., Niles, D., Contreras, M.A., Wiesner, H., Haason, F.S. and Noufi, R., 1998. Advances in the CIS research at NREL, *Proc. 26th IEEE Photovoltaic Specialists Conf.*, Anaheim, p. 319.

[70] Kapur, V.K., Bansal, A., Le, P., and Asensio, O. I. 2002. Non-vacuum printing process for CIGS Solar cells on rigid and flexible substrates. *Proc. 29th IEEE Photovoltaic Specialists Conf.*, New Orleans, p. 688.

[71] Cahen, D. and Noufi, R., 1989. Defect chemical explanation for the effect of air anneal on $CdS/CuInSe_2$ solar cell performance. *Appl. Phys. Lett.*, Vol. 54, p. 558.

[72] Rau, U., Braunger, D., Herberholz, R., Schock, H.W., Guillemoles, J.-F., Kronik, L. and Cahen, D., 1999. Oxygenation and air-annealing effects on the electronic properties of $Cu(In,Ga)Se_2$ films and devices. *J. Appl. Phys.*, Vol. 86, p. 497.

[73] Kronik, L., Rau, U., Guillemoles, J.-F., Braunger, D., Schock, H.W. and Cahen, D., 2000. Interface redox engineering of $Cu(In,Ga)Se_2$-based solar cells: oxygen, sodium, and chemical bath effects. *Thin Solid Films*, Vols. 361–362, p. 353.

[74] Scheer, R., 1997. Surface and interface properties of Cu-chalcopyrite semiconductors and devices. *Research Trends in Vacuum Sci. Technol.*, Vol. 2, p. 77.

[75] Rau, U., 2000. Role of defects and defect metastabilities for the performance and stability of $Cu(In,Ga)Se_2$ based solar cells. *Jpn. J. Appl. Phys.*, Vol. 39 (Suppl. 39-1), p. 389.

[76] Schmid, D., Ruckh, M., Grunwald, F. and Schock, H.W., 1993. Chalcopyrite/defect chalcopyrite heterojunctions on the basis of $CuInSe_2$. *J. Appl. Phys.*, Vol. 73, p. 2902.

[77] Morkel, M., Weinhardt, L., Lohmüller, B., Heske, C., Umbach, E., Riedl, W., Zweigart, S. and Karg, F., 2001. Flat conduction-band alignment at the $CdS/CuInSe_2$ thin-film solar-cell heterojunction. *Appl. Phys. Lett.*, Vol. 79, p. 4482.

[78] Schmid, D., Ruckh, M., and Schock, H.W., 1996. A comprehensive characterization of the interfaces in Mo/CIS/CdS/ZnO solar cell structures. *Solar Energy Mater. Solar Cells*, Vol. 41, p. 281.

[79] Contreras, M.A., Wiesner, H., Niles, D., Ramanathan, K., Matson, R., Tuttle, J., Keane, J. and Noufi, R., 1996. Defect chalcopyrite $Cu(In_{1-x}Ga_x)_3Se_5$ materials and high Ga-content $Cu(In,Ga)Se_2$-based solar cells. *Proc. 25th IEEE Photovoltaic Specialists*, Washington, DC, p. 809.

[80] Niemeegers, A., Burgelman, M., Herberholz, R., Rau, U., Hariskos, D. and Schock, H.W., 1998. Model for electronic transport in $Cu(In,Ga)Se_2$ solar cells. *Prog. Photovolt. Res. Appl.*, Vol. 6, p. 407.

[81] Bardeen, J., 1947. Surface states and rectification at a metal semiconductor contact. *Phys. Rev.*, Vol. 71, p. 717.

[82] Klein, A. and Jaegermann, W., 1999. Fermi-level-dependent defect formation in Cu-chalcopyrite semiconductors. *Appl. Phys. Lett.*, Vol. 74, p. 2283.

[83] Kessler, J., Velthaus, K.O., Ruckh, M., Laichinger, R., Schock, H.W., Lincot, D., Ortega, R. and Vedel, J., 1992. Chemical bath deposition of CdS on $CuInSe_2$, etching effects and growth kinetics. *Proc. 6th. Int. Photovoltaic Solar Energy Conf.*, New Delhi, India, p. 1005.

[84] Friedlmeier, T.M., Braunger, D., Hariskos, D., Kaiser, M., Wanka, H.N. and Schock, H.W., 1996. Nucleation and growth of the CdS buffer layer on $Cu(In,Ga)Se_2$ thin films. *Proc. 25th IEEE Photovoltaic Specialists Conf.*, Washington DC, p. 845.

[85] Ramanathan, K., Wiesner, H., Asher, S., Niles, D., Bhattacharya, R.N., Keane, J., Contreras, M.A. and Noufi, R., 1998. High efficiency $Cu(In,Ga)Se_2$ thin film solar cells without intermediate buffer layers. *Proc. 2nd World Conf. on Photovoltaic Solar Energy Conversion*, Vienna, p. 477.

[86] Wada, T., Hayashi, S., Hashimoto, Y., Nishiwaki, S., Sato, T. and Nishitina, M., 1998. High efficiency $Cu(In,Ga)Se_2$ (CIGS) solar cells with improved CIGS surface. *Proc. 2nd World Conf. on Photovoltaic Solar Energy Conversion*, Vienna, p. 403.

[87] Hariskos, D., Ruckh, M., Rühle, U., Walter, T., Schock, H.W., Hedström, J. and Stolt, L., 1996. A novel cadmium free buffer layer for $Cu(In,Ga)Se_2$ based solar cells. *Solar Energy Mat. Solar Cells*, Vols. 41/42, p. 345.

[88] Kushiya, K., Nii, T., Sugiyama, I., Sato, Y., Inamori, Y., Takeshita, H., 1996. Application of Zn-compound buffer layer for polycrystalline $CuInSe_2$-based thin-film solar cells. *Jpn. J. Appl. Phys.*, Vol. 35, p. 4383.

[89] Kushiya, K., Tachiyuki, M., Kase, T., Nagoya, Y., Miura, T., Okumura, D., Satoh, M., Sugiyama, and I., Yamase, O., 1997. Improved FF of CIGS

thin-film mini-modules with $Zn(O,S,OH)_x$ buffer by post-depostion light soaking. *Proc. 26th IEEE Photovoltaic Specialists Conf.*, Anaheim, p. 327.

[90] Nakada, T., Furumi, K. and Kunioka, A., 1999. High-efficiency cadmium-free Cu(In,Ga)Se-2 thin-film solar cells with chemically deposited ZnS buffer layers. *IEEE Trans. Electron. Devices*, Vol. ED-46, p. 2093.

[91] Nakada, T. and Mizutani, M., 2002. 18% efficiency Cd-free $Cu(In, Ga)Se_2$ thin-film solar cells fabricated using chemical bath deposition (CBD)-ZnS buffer layers. *Jpn. J. Appl. Phys.*, Vol. 41, p. L165.

[92] Ohtake, Y., Kushiya, K., Ichikawa, M., Yamada, A. and Konagai, M., 1995. Polycrystalline $Cu(InGa)Se_2$ thin-film solar cells with ZnSe buffer layers. *Jpn. J. Appl. Phys.*, Vol. 34, p. 5949.

[93] Ohtake, Y., Ichikawa, M., Yamada, A. and Konagai, M., 1995. Cadmium free buffer layers for polycrystalline $Cu(In,Ga)Se_2$ thin film solar cells. *Proc. 13th European Photovoltaic Solar Energy Conf.*, Nice, p. 2088.

[94] Konagai, M., Ohtake, Y. and Okamoto, T., 1996. Development of $Cu(InGa)Se_2$ thin film solar cells with Cd-free buffer layers, *Mat. Res. Soc. Symp. Proc.*, Vol. 426, p.153.

[95] Powalla, M., Lotter, E., Waechter, R., Spiering, S., Oertel, M., Dimmler, B., 2002. Pilot line production of CIGS modules: first experience in processing and further developments. *Proc. 29th IEEE Photovoltaic Specialists Conf.*, New Orleans, p. 571.

[96] Hartmann, M., Schmidt, M., Jasenek, A., Schock, H.W., Kessler, F., Herz, K. and Powalla, M., 2000. Flexible and light weight substrates for $Cu(In,Ga)Se_2$ solar cells and modules. *Proc. 28th IEEE Photovoltaic Specialists Conf.*, Anchorage, p. 638.

[97] Tiwari, A.N., Krejci, M., Haug, F.-J. and Zogg, H., 1999. 12.8% Efficiency $Cu(In,Ga)Se_2$ solar cell on a flexible polymer sheet. *Prog. Photovolt.*, Vol. 7, p. 393.

[98] Wiedemann, S., Beck, M.E., Butcher, R., Repins, I., Gomez, N., Joshi, B., Wendt, R.G. and Britt, J.S., 2002. *Proc. 29th IEEE Photovoltaic Specialists Conf.*, New Orleans, p. 575.

[99] Fabick, L.B., Jehle, A., Scott, S., Crume, B., Jensen, G., and Armstrong, J., 2002. A new thin-film space PV module technology. *Proc. 29th IEEE Photovoltaic Specialists Conf.*, New Orleans, p. 971.

[100] Hanket, G.M., Singh, U.P., Eser, E., Shafarman, W.N. and Birkmire, R.W., 2002. Pilot-scale manufacture of $Cu(InGa)Se_2$ films on a flexible polymer substrate. *Proc. 29th IEEE Photovoltaic Specialists Conf.*, New Orleans, p. 567.

[101] Gay, R.R., 1997. Status and prospects for CIS-based photovoltaics. *Solar Energy Mater. Solar Cells*, Vol. 47, p. 19.

[102] Karg, F., Kohake, D., Nierhoff, T., Kühne, B., Grosser, S. and Lux-Steiner, M.C., 2002. Performance of grid-coupled PV arrays based on CIS solar modules. *Proc. 17th European Photovoltaic Solar Energy Conf.*, Munich, p. 391.

[103] Powalla, M. and Dimmler, B., 2001. Process development of high performance CIGS modules for mass production. *Thin Solid Films*, Vol. 387, p. 251.

[104] Schmidt, M., Braunger, D., Schäffler, R., Schock, H.W. and Rau, U., 2001. Influence of damp heat on the electrical properties of $Cu(In,Ga)Se_2$ solar cells. *Thin Solid Films*, Vols. 361–362, p. 283.

[105] Igalson, M., Wimbor, M. and Wennerberg, J., 2002. The change of the electronic properties of CIGS devices induced by the 'damp heat' treatment. *Thin Solid Films*, Vols. 403–404, p. 320.

[106] Deibel, C., Dyakonov, V., Parisi, J., Palm, J., Zweigart, S. and Karg, F., 2002. Electrical characterisation of damp-heat trated $Cu(In,Ga)(S,Se)_2$ solar cells. *Proc. 17th European Photovoltaic Solar Energy Conf.*, Munich, p. 1229.

[107] Karg, F., Calwer, H., Rimmasch, J., Probst, V., Riedl, W., Stetter, W., Vogt, H. and Lampert, M., 1998. Development of stable thin film solar modules based on $CuInSe_2$, *Inst. Phys. Conf. Ser.*, Vol. 152E, p. 909.

[108] Guillemoles, J.-F., Kronik, L., Cahen, D., Rau, U., Jasenek, A. and Schock, H.W., 2000. Stability issues of $Cu(In,Ga)Se_2$-based solar cells. *J. Phys. Chem. B*, Vol. 104, p. 4849.

[109] Guillemoles, J.F., 2002. The puzzle of $Cu(In,Ga)Se_2$ (CIGS) solar cells stability. *Thin Solid Films*, Vols. 403–404, p. 405.

[110] Gay, C.F., Potter, R.R., Tanner, D.P. and Anspaugh, B.E., 1984. Radiation effects on thin film solar cells, *Proc. 17th IEEE Photovoltaic Specialists Conf.*, Kissimmee, p. 151.

[111] Mickelsen, R.A., Chen, W.S., Stanbery, B.J., Dursch, H., Stewart, J.M., Hsiao, Y.R. and Devaney, W., 1985. Development of $CuInSe_2$ cells for space applications, *Proc. 18th IEEE Photovoltaic Specialists Conf.*, Las Vegas, p. 1069.

[112] Jasenek, A. and Rau, U., 2001. Defect generation in $Cu(In,Ga)Se_2$ heterojunction solar cells by high-energy electron and proton irradiation. *J. Appl. Phys.*, Vol. 90, p. 650.

[113] Walters, R.J., Summers, G.P., Messenger, S.R., Jasenek, A., Schock, H.W., Rau, U., Nocerino, J., Tringe, J. and Reinhardt, K., 2002. Displacement damage dose analysis of proton irradadiated CIGS solar cells on flexible substrates. *Proc. 17th European Photovoltaic Solar Energy Conf.*, Munich, p. 2191.

[114] Guillemoles, J.-F., Rau, U., Kronik, L., Schock, H.W. and Cahen, D., 1999. $Cu(In,Ga)Se_2$ solar cells: device stability based on chemical flexibility. *Adv. Mat.*, Vol. 8, p. 111.

[115] Jasenek, A., Schock, H.W., Werner, J.H. and Rau, U., 2001. Defect annealing in $Cu(In,Ga)Se_2$ heterojunction solar cells after high-energy electron irradiation. *Appl. Phys. Lett.*, Vol. 79, p. 2922.

[116] Kawakita, S., Imaizumi, M., Yamaguchi, M., Kushia, K., Ohshima, T., Itoh, H. and Matsuda, S., 2002. Annealing enhancement effect by light illumination on proton irradiated $Cu(In,Ga)Se_2$ thin-film solar cells. *Jpn. J. Appl. Phys.*, Vol. 41(2), p. L797.

[117] Jasenek, A., Rau, U., Weinert, K., Schock, H.W. and Werner, J.H., 2002. Illumination-enhanced annealing of electron irradiated $Cu(In,Ga)Se_2$ solar cells. *Proc. 29th IEEE Photovoltaic Specialists Conf.*, New Orleans, p. 872.

[118] Tuttle, J.R., Szalaj, A. and Keane, J., 2000. A 15.2% AMO/1433 W/kg thin-film Cu(In,Ga)Se_2 solar cell for space applications. *Proc. 28th IEEE Photovoltaic Specialists Conf.*, Anchorage, p. 1042.

[119] Hartmann, M., Schmidt, M., Jasenek, A., Schock, H.W., Kessler, F., Herz, K. and Powalla, M., 2000. Flexible and light weight substrates for Cu(In,Ga)Se_2 solar cells and modules. *Proc. 28th IEEE Photovoltaic Specialists Conf.*, Anchorage, p. 838.

[120] Tiwari, A.N., Krejci, M., Haug, F.J. and Zogg, H., 1999. 12.8% Efficiency Cu(In,Ga)Se_2 solar cell on a flexible polymer sheet. *Prog. Photov.*, Vol. 7, p. 393.

[121] Turcu, M. and Rau, U., 2003. Fermi level pinning at CdS/Cu(In,Ga)$(Se,S)_2$ interfaces: effect of chalcopyrite alloy composition, *J. Phys. Chem. Solids*, Vol. 64, p. xxx.

[122] Nelson, A.J., Schwerdtfeger, C.R., Wei, S.-H., Zunger, A., Rioux, D., Patel, R., and Höchst, H., 1993. Theoretical and experimental studies of the ZnSe/$CuInSe_2$ heterojunction band offset, *Appl. Phys. Lett.*, Vol. 62, p. 2557.

[123] Löher, T., Jaegermann, W. and Pettenkofer, C., 1995. Formation and electronic properties of the CdS/$CuInSe_2$ (011) heterointerface studied by synchrotron-induced photoemission. *J. Appl. Phys.*, Vol. 77, p. 731.

[124] Wei, S.-H. and Zunger, A., 1993. Band offsets at the CdS/$CuInSe_2$ heterojunction. *Appl. Phys. Lett.*, Vol. 63, p. 2549.

[125] Ruckh, M., Schmid, D., and Schock, H.W., 1994. Photoemission studies of the ZnO/CdS interface. *J. Appl. Phys.*, Vol. 76, p. 5945.

[126] Orgassa, K., Nguyen, Q., Kötschau, I.M., Rau, U., Schock, H.W. and Werner, J.H., 2002. Optimized reflection of CdS/ZnO window layers in Cu(In,Ga)Se2 thin film solar cells. *Proc. 17th European Photov. Solar Energy Conf.*, Munich, p. 1039.

[127] Engelhardt, F., Bornemann, L., Köntges, M., Meyer, Th., Parisi, J., Pschorr-Schoberer, E., Hahn, B., Gebhardt, W., Riedl, W. and Rau, U., 1999. Cu(In,Ga)Se_2 solar cells with a ZnSe buffer layer: interface characterization by quantum efficiency measurements. *Prog. Photovolt. Res. Appl.*, Vol. 7, p. 423.

[128] Bube, R.H., 1992. *Photolectronic Properties of Semiconductors*, Cambridge University Press, Cambridge, UK.

[129] Green, M.A., 1986. *Solar Cells*, University of New South Wales, Sydney, Australia, p. 96.

[130] Shafarman, W.N., Klenk, R. and McCandless, B.E., 1996. Device and material characterization of Cu(InGa)Se_2 solar cells with increasing band gap. *J. Appl. Phys.*, Vol. 79, p. 7324.

[131] Rau, U. and Schmidt, M., 2001. Electronic properties of ZnO/CdS/Cu(In,Ga)Se_2 solar cells – aspects of heterojunction formation. *Thin Solid Films*, Vol. 387, p. 141.

[132] Niemegeers, A., Burgelman, M. and De Vos, A., 1995. On the CdS/$CuInSe_2$ conduction band discontinuity. *Appl. Phys. Lett.*, Vol. 67, p. 843.

[133] Ruberto, M.N. and Rothwarf, A., 1987. Time-dependent open-circuit voltage in $CuInSe_2$/CdS solar cells: Theory and experiment. *J. Appl. Phys.*, Vol. 61, p. 4662.

[134] Sasala, R.A. and Sites, J.R., 1993. Time dependent voltage in $CuInSe_2$ and CdTe solar cells. *Proc. 23rd IEEE Photovoltaic Specialists Conf.*, Louisville, p. 543.

[135] Kushia, K., Tachiyuki, M., Kase, T., Sugiyama, I., Nagoya, Y., Okumura, D., Sato, M., Yamase, O., and Takeshita, H. 1997. Fabrication of graded band-gap Cu(InGa)Se_2 thin-film mini-modules with a $Zn(O,S,OH)_x$ buffer layer, *Solar Energy Mat. Solar Cells*, Vol. 49, p. 277.

[136] Rau, U., Jasenek, A., Herberholz, R., Schock, H.W., Guillemoles, J.-F., Lincot, D. and Kronik, L., 1998. The inherent stability of Cu(In,Ga)Se_2-based solar cells. *Proc. 2nd World Conf. on Photovoltaic Energy Conversion*, Vienna, p. 428.

[137] Zabierowski, P., Rau, U., and Igalson, M., 2001. Classification of metastabilities in the electrical characteristics of ZnO/CdS/Cu(In,Ga)Se_2 solar cells, *Thin Solid Films*, Vol. 387, p. 147.

[138] Rau, U., Schmitt, M., Parisi, J., Riedl, W. and Karg, F., 1998. Persistent photoconductivity in Cu(In,Ga)Se_2 heterojunctions and thin films prepared by sequential deposition. *Appl. Phys. Lett.*, Vol. 73, p. 223.

[139] Meyer, Th., Schmidt, M., Engelhardt, F., Parisi, J. and Rau, U., 1999. A model for the open circuit voltage relaxation in Cu(In,Ga)Se_2 heterojunction solar cells. *Eur. Phys. J. App. Phys.*, Vol. 8, p. 43.

[140] Lang, D.V. and Logan, R.A., 1977. Large-lattice-relaxation model for persistent photoconductivity in compound semiconductors, *Phys. Rev. Lett.*, Vol. 39, p. 635.

[141] Delahoy, A.E., Ruppert, A. and Contreras, M., 2000. Charging and discharging of defect states in CIGS/ZnO junctions. *Thin Solid Films*, Vols. 161–162, p. 140.

[142] Rau, U., Weinert, K., Nguyen, Q., Mamor, M., Hanna, G., Jasenek, A. and Schock, H.W., 2001. *Mat. Res. Soc. Symp. Proc.*, Vol. 668, p. H9.1.1.

[143] Siebentritt, S., 2002. Wide gap chalcopyrites: material properties and solar cells. *Thin Solid Films*, Vols. 403–404, p. 1.

[144] Paulson, P.D., Haimbodi, M.W., Marsillac, S., Birkmire, R.W. and Shafarman, W.N., 2002. $CuIn_{1-x}Al_xSe_2$ thin films and solar cells. *J. Appl. Phys.*, Vol. 91, p. 10153.

[145] Walter, T., Content, A., Velthaus, K.O. and Schock, H.W., 1992. Solar-cells based on $CuIn(Se,S)_2$. *Sol. Energy Mater. Sol. Cells*, Vol. 26, p. 357.

[146] Friedlmeier, T.M. and Schock, H.W., 1998. Improved voltages and efficiencies in Cu(In,Ga)(S,Se)2 solar cells. *Proc. 2nd. World Conf. on Photovoltaic Solar Energy Conversion*, Vienna, p. 1117.

[147] Scheer, R., Walter, T., Schock, H.W., Fearhailey, M.L. and Lewerenz, H.J., 1993. $CuInS_2$ based thin film solar cell with 10.2% efficiency. *Appl. Phys. Lett.*, Vol. 63, p. 3294.

[148] Kaigawa, R., Neisser, A., Klenk, R., Lux-Steiner, M.-Ch., 2002. Improved performance of thin film solar cells based on Cu(In,Ga)S_2. *Thin Solid Films*, Vol. 415, p. 266.

[149] Klenk, R., 2001. Characterisation and modelling of chalcopyrite solar cells. *Thin Solid Films*, Vol. 387, p. 135.

[150] Turcu, M., Pakma, O. and Rau, U., 2002. Interdependence of absorber composition and recombination mechanism in Cu(In,Ga)(Se,S)$_2$ heterojunction solar cells. *Appl. Phys. Lett.*, Vol. 80, p. 2598.

[151] Nadenau, V., Hariskos, D. and Schock, H.W., 1977. $CuGaSe_2$ based thin-film solar cells with improved performance. *Proc. 14th European Photovoltaic Solar Energy Conf.*, Barcelona, p. 1250.

[152] Jasenek, A., Rau, U., Nadenau, V. and Schock, H.W., 2000. Electronic properties of $CuGaSe_2$-based heterojunction solar cells. Part II. Defect spectroscopy. *J. Appl. Phys.*, Vol. 87, p. 594.

[153] Nadenau, V., Rau, U., Jasenek, A. and Schock, H.W., 2000. Electronic properties of $CuGaSe_2$-based heterojunction solar cells. Part I. Transport analysis. *J. Appl. Phys.*, Vol. 87, p. 584.

[154] Reiß, J., Malmström, J., Werner, A., Hengel, I., Klenk, R. and Lux-Steiner, M.Ch., 2001. Current Transport in $CuInS_2$ solar cells depending on absorber preparation, *Mat. Res. Soc. Symp. Proc.*, Vol. 668, p. H9.4.1.

[155] Schön, J.H., Klenk, M., Schenker, O. and Bucher, E., 2000. Photovoltaic properties of $CuGaSe_2$ homodiodes. *Appl. Phys. Lett.*, Vol. 77, p. 3657.

[156] Shafarman, W.N., Marsillac, S., Paulson, P.D., Haimbodi, M.W. and Birkmire, R.W., 2002. Material and device characterization of thin film Cu(InAl)Se_2 solar cells. *Proc. 29th IEEE Photovoltaic Specialists Conf.*, New Orleans, p. 519.

[157] Marsillac, S., Paulson, P.S., Haimbodi, M.W., Birkmire, R.W. and Shafarman, W.N., 2002. High-efficiency solar cells based on Cu(InAl)Se_2 thin films. *Appl. Phys. Lett.*, Vol. 81, p. 1350.

[158] Walter, T. and Schock, H.W., 1993. Structural and electrical investigations of the anion-exchange in polycrystalline CuIn(S,Se)2 thin-films. *Jpn. J. Appl. Phys.*, Vol. 32(3), p. 116.

[159] Siemer, K., Klaer, J., Luck, I., Bruns, J., Klenk, R., Bräunig, D., 2001. Efficient $CuInS_2$ solar cells from a rapid thermal process (RTP). *Solar Energy Mat. Solar Cells*, Vol. 67, p. 159.

[160] Hengel, I., Neisser, A., Klenk, R. and Lux-Steiner, M.C., 2000. Current transport in $CuInS_2$:Ga/Cds/ZnO – solar cells. *Thin Solid Films*, Vols. 361–362, p. 458.

[161] Gray, J.L. and Lee, Y.J., 1994. Numerical modeling of graded band gap CIGS solar cells. *Proc. First World Conf. on Photovoltaic Solar Energy Conversion*, Hawaii, p. 123.

[162] Dhingra, A. and Rothwarf, A., 1996. Computer simulation and modeling of graded bandgap CuInSe2/CdS based solar cells. *IEEE Trans. Electron Devices*, Vol. ED-43, p. 613.

[163] Gabor, A.M., Tuttle, J.R., Bode, M.H., Franz, A., Tennant, A.L., Contreras, M.A., Noufi, R., Jensen, D.G. and Hermann, A.M., 1996. Band-gap engineering in $Cu(In,Ga)Se_2$ thin films grown from $(In,Ga)_2Se_3$ precursors. *Solar Energy Mater. Solar Cells*, Vol. 41, p. 247.

[164] Dullweber, T., Rau, U., Contreras, M., Noufi, R. and Schock, H.W., 2000. Photogeneration and carrier recombination in graded gap $Cu(In, Ga)Se_2$ solar cells. *IEEE Trans. Electron. Dev.*, Vol. ED-47, p. 2249.

Part IId

Space and Concentrator Cells

GaAs and High-Efficiency Space Cells

V. M. Andreev, Ioffe Physico-Technical Institute,
St. Petersburg, Russia

1 Historical Review of III–V Solar Cells

Since the first solar-powered satellites Vanguard-1 and Sputnik-3 were launched in the spring of 1958, solar cells had become the main source of energy on the spacecrafts. The first space arrays were based on single crystal silicon solar cells with an efficiency of about 10%. During the 1960 and 1970s, the improvements in the Si cell design and technology, such as fabrication of 'violet' cells with an increased short-wavelength photosensitivity, back surface field formation, application of photolithography to make optimal front grid fingers, reduction of optical losses owing to front surface texturing and improvement of the anti-reflection coating, allowed an increase of efficiency of up to 14% (1 sun, AM0). In the last two decades, the Si space cell efficiencies were increased by up to 18%. These advanced Si cells are used for space missions that do not strictly require III–V cells with both higher efficiency and better radiation stability [1, 2].

At the beginning of the 1960s, it was found that GaAs-based solar cells with the Zn-diffused p–n junction ensured the better temperature stability and higher radiation resistance. One of the first scaled applications of the temperature-stable GaAs solar cells took place on the Russian spacecrafts Venera-2 and Venera-3 launched in November 1965 to the 'hot' planet Venus. The area of each GaAs solar array constructed by the Russian Enterprise KVANT for these spacecrafts was 2 m^2. Then the Russian moon-cars were launched in 1970 (Lunokhod-1) and in 1972 (Lunokhod-2) with GaAs 4 m^2 solar arrays in each. The operating temperature of these arrays on the illuminated surface of the Moon was about 130°C. Therefore, silicon-based solar cells could not operate effectively in these conditions. GaAs solar arrays have shown efficiency of 11% and have provided the energy supply during the lifetime of these moon-cars.

The first AlGaAs/GaAs solar cells with passivating wide bandgap window were created in 1970 [3,4]. In the following decades, by means of the liquid-phase-epitaxy (LPE) of AlGaAs/GaAs heterostructures [4–12], their AM0 efficiency was increased up to 18–19% [10–14] owing to the intensive investigations in the fields of physics and technology of space solar cells [15- 18]. These investigations were stimulated and supported by ambitious space programmes in the former USSR and in the USA [1, 2, 18]. Owing to the high efficiency and improved radiation hardness of the AlGaAs/GaAs solar cells, the LPE technology was utilised in the high scale production of AlGaAs/GaAs space arrays for the spacecrafts launched in the 1970s and 1980s. For example, an AlGaAs/GaAs solar array with a total area of 70 m^2 was installed in the Russian space station MIR launched in 1986. During 15 years in orbit, the array degradation appeared to be lower than 30%, despite being under severe conditions such as appreciable shadowing, effects of numerous docking and the ambient environment of the station. At that time, it was the most large-scale demonstration of the AlGaAs/GaAs solar cell advantages for space applications. The further improvement of the LPE technology [19, 20] led to increased efficiencies of 24.6% (AM0, 100 suns) on the base of the heterostructures with an ultra thin window AlGaAs layer and a back surface field layer.

Since the late 1970s, AlGaAs/GaAs heterostructures were also produced by the metal organic chemical vapour deposition (MOCVD) technique using metal organic compounds of Group III elements and hydrides of Group V elements [21, 22]. The advantage of MOCVD is a possibility to fabricate multilayer structures in high-yield reactors with layers of a specified composition and a precise thickness varying from 1 to 10 nm to several microns. AlGaAs/GaAs heterostructures with an ultra thin (0.03 μm) top window layer and with a back surface wide-bandgap barrier were fabricated by MOCVD for space cells. AlGaAs/GaAs 4 cm^2 1 sun space solar cells with efficiencies of 21% [23] and 21.7% [24] were fabricated on the base of these structures.

Enhanced light absorption was provided in the cells with an internal Bragg reflector [25–27]. This dielectric mirror increases the effective absorption length of sunlight within the long-wavelength part of photoresponse spectrum and allows the base layer to be made thinner. In this case, the cell efficiency is more tolerant to a reduction of the carrier diffusion length, and, as a result, these cells are more radiation resistant [27].

Owing to the fact that MOCVD is capable of producing single crystal layers on silicon and germanium substrates, it has a potential for fabrication of low-cost, high efficiency III–V solar cells on these substrates. Growing GaAs on Si of a sufficient quality is not possible as a result of the mismatch of 4% between Si and GaAs. However, there is progress in improving the GaAs/Si structure quality by using special structures and growth techniques: strained superlattice, thermo cyclic growth and cyclic structure annealing.

Ge is a quite good lattice match to the GaAs material. Therefore, epitaxial growth of GaAs with a high quality was realised by MOCVD and this is now the basic technique for growth of multilayer AlGaAs/GaAs/Ge single-junction and GaInP/GaAs/Ge multi-junction solar cells. This method provides a good crystal quality of epitaxial structures on Ge substrates, high productivity and reproducibility.

Among other single junction cells, the InP-based cells are rather promising for space applications owing to that fact that InP has a higher radiation resistance [2, 28] than GaAs. However, there are some obstacles for the scaled application of InP-based cells in space arrays. Firstly, there is no lattice-matched wide bandgap window for InP to make stable passivation of the front surface. Secondly, it is difficult to grow this material to a high quality on the Ge and Si substrates due to lattice-mismatches that are as high as 8% between InP and Si and 4% between InP and Ge. Thirdly, InP is a quite expensive material. In spite of these obstacles there are some possible applications of InP cells in the arrays for satellites expected to be launched towards the intermediate orbits, high Earth orbits or orbit-transfer, which are characterised by very high radiation fluencies.

Multi-junction (cascade) cells ensured the further increase of III–V solar cell efficiencies. Despite a large number of theoretical studies of cascade solar cells [1, 29–32], their efficiencies remained low enough for a long time, since the ohmic and optical losses in available designs were unacceptably large. Monolithic and mechanically stacked tandem cells with increased efficiencies were developed in the beginning of the 1990s. In mechanically stacked tandems with GaAs top

cells and GaSb (or InGaAs) bottom cells [33–35, 38, 41–43], efficiencies of about 30% were achieved under the concentrated AM0 sunlight. Monolithic cascade cells have been developed and fabricated by MOCVD on the structures GaInAs/InP [40], Si/AlGaAs [44, 64], AlGaAs/GaAs [45, 42], GaAs/Ge [47–51], GaInP/GaAs [36, 52, 53] GaInP/GaAs/Ge [54–60], GaInP/GaInAs [61] and GaInP/GaInAs/Ge [57, 62, 63] heterostructures. Table 1 presents the best reported efficiencies of the cells based on the different structures under one sun and concentrated AM0 sunlight illumination.

2 Single-Junction III–V Space Solar Cells

2.1 Solar Cells Based on AlGaAs/GaAs Structures

Among different investigated heterostructures based on III–V heterojunctions appropriate for fabrication of single junction solar cells, AlGaAs/GaAs heterostructures have found the first application due to the well-matched lattice parameters of GaAs and AlAs, and because GaAs has an optimal bandgap for effective sunlight conversion. In the first solar cells based on AlGaAs/GaAs heterojunctions [3, 4], the basic narrow bandgap material was GaAs. A wide bandgap window was made of AlGaAs close in the composition to AlAs, which is almost completely transparent to sunlight, making solar cells very sensitive in the short wavelength range of the sun spectrum. Such a cell is illuminated through the window, and the light with photon energy exceeding the bandgap value of GaAs is absorbed in it, while the generated minority carriers are separated by the p–n junction field located in GaAs. Because of the close lattice parameters of the contacting materials, the interface in AlGaAs/GaAs

Table 1 Reported efficiencies for III–V space solar cells under AM0 conditions at $T = 25–28°C$

Cell material	Cell type	Sunlight concentration	Area, cm^2	Eff., %	Ref.
AlGaAs/GaAs	single junction	No concentration	4	21.7	[24]
GaAs/Si	single junction		4	18.3	[64]
InP	single junction		4	19.9	[2]
AlGaAs/GaAs	monolithic 2-junction		0.5	23.0	[2]
GaInP/GaAs	monolithic 2-junction		4	27.2	[56]
GaInP/GaAs/Ge	monolithic 3-junction		4	29.3	[56]
GaInP/GaInAs/Ge	monolithic 3-junction		4	29.7	[57]
GaInP/GaAs/Ge	monolithic 3-junction		26.6	29.0	[56]
AlGaAs/GaAs	single junction	100×	0.07	24.6	[41]
GaAs/GaSb	mechanical stack 2-junction	100×	0.05	30.5	[2]
GaAs/Ge	monolithic 2-junction	9×	0.136	23.4	[50]
GaInP/GaInAs/Ge	monolithic, 3-junction	7.6×	4.1	31.1	[58]
GaInP/GaAs/GaSb	monolithic/mechanical stack 3-junction	15×	circuit	34.0	[65]

heterojunctions is characterised by a low density of surface states, providing a highly effective accumulation of carriers.

The composition n-GaAs/p-GaAs/p-AlGaAs (Figure 1(a)) was the first mostly used heterostructure. The structures were grown by LPE [3–14] or by MOCVD [21, 22]. For example, a 0.5 μm thick p-GaAs layer is either grown epitaxially (MOCVD) or formed by zinc or beryllium diffusion during the growth (LPE) of the $Al_xGa_{1-x}As$ solid solution doped with one of these impurities. The diffusion produces a quasi-electric field that arises as a result of the acceptor concentration gradient (Figure 1(a)) which enhances the effective diffusion length of electrons generated by light in the p-GaAs layer. Using the LPE technique, the highest conversion efficiencies of about 19% (1 sun; AM0) have been obtained in the structures with the wide-bandgap layer of smaller thickness [10–14]. A way of enhancing the short-wavelength photosensitivity is to use in the front layer a solid solution of graded composition with the bandgap (Figure 1(b)) increasing towards the illuminated surface [10]. The strong built-in electric field significantly enhances the value of the effective electron diffusion length and suppresses the surface recombination of the electron–hole pairs generated near the surface by short-wavelength light.

Introduction of a potential barrier at the back surface of the cell photoactive region assists the collection of minority carriers generated in the base. This barrier is made either by growing a buffer layer (Figure 1(d)) of n^+-GaAs, doped to a level exceeding that in the active layer, or by growing an n-AlGaAs layer (Figure 1(c)). The one-sun AM0 efficiency of 21.7% and the concentrator AM0 efficiency of 24.5% at 170 suns have been measured [24] in the cells based on these structures grown by MOCVD with the n-$Al_xGa_{1-x}As$ layer as the back surface barrier. Similar results have been obtained during development of a low-temperature LPE modification for the growth of AlGaAs/GaAs structures [19]

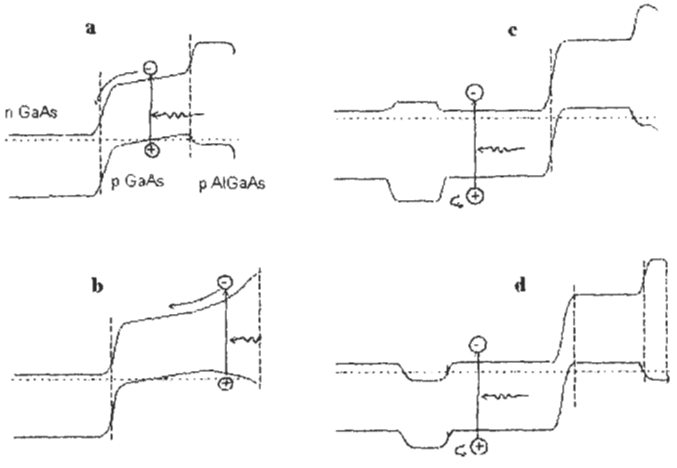

Figure 1 Band diagrams of AlGaAs/GaAs heterostructures developed for space solar cells: (a) p-AlGaAs/p-GaAs/n-GaAs; (b) structure with a graded p-AlGaAs front layer; (c, d) structures with a back-surface field, made of n-AlGaAs (c) and n^+GaAs (d).

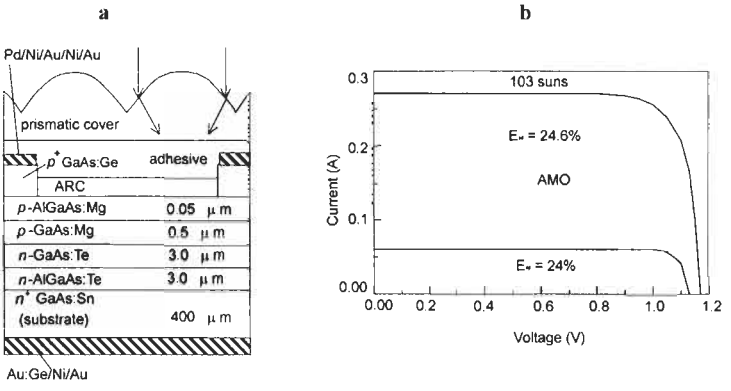

Figure 2 Schematic diagram (a) and illuminated I–V curves (b) of the LPE grown single junction AlGaAs/GaAs concentrator solar cell with a prismatic cover [19]. The cell area is 0.07 cm².

that resulted in fabrication of high efficiency solar cells with a structure shown in Figure 2(a). Silicone prismatic covers optically eliminate the grid line obscuration losses in concentrator cells. Owing to the high crystal quality of the LPE material and optimised optical parameters, a high quantum yield is obtainable in a wide spectral range. The AM0 efficiency of these cells with a prismatic cover was 24.6% (Figure 2(b)) under 103 suns at 25°C.

2.2 Solar Cells With Internal Bragg Reflector

The Bragg reflector (BR) made of semiconductor layers is widely used in lasers and other optical devices. By using a multiple layer composed of two materials with different refractive indices, nearly 100% reflectance can be achieved over a restricted wavelength range. The thickness of each of the two materials is chosen for quarter-wavelength reflection for the given wavelength. These multilayer dielectric stacks selectively reflect a part of the unabsorbed photons providing a second pass through the photoactive region, thereby increasing the photocurrent.

Epitaxial (MOCVD) Bragg reflectors in solar cells [25–27] were based (Figure 3(a)) on the pairs of $Al_xGa_{1-x}As$ and GaAs layers. By increasing the number (N) of pairs, the BR reflectance increases, asymptotically tending to unity and reaches 96% at $N = 12$ [26, 27]. A reflector of this type allows us to increase the effective absorption within the long-wavelength part of the photosensitivity spectrum and to make the base layer thinner. The cell efficiency in this case becomes more tolerant to decreasing the diffusion lengths caused by the high-energy particle irradiation. The solar cell structure with a Bragg reflector (Figure 3(a)) was grown [26, 27] by MOCVD using equipment with a low-pressure horizontal reactor. BR was optimised for reflectance in the 750–900 nm spectral region and consisted of 12 pairs of AlAs and GaAs layers with a thickness of 72 nm for AlAs layers and 59 nm for GaAs. The photocurrent density of 32.7 mA/cm² (AM0, 1 sun, 25°C) and the efficiency of 23.4% (AM0, 18 suns, 25°C) were

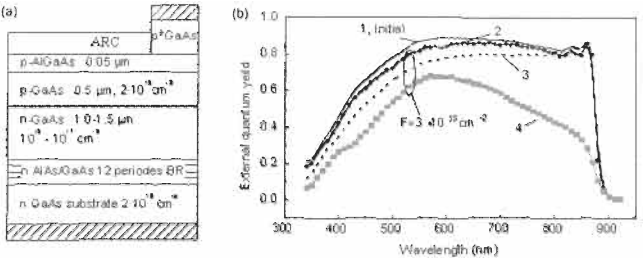

Figure 3 Schematic cross-section of a AlGaAs/GaAs solar cell with internal Bragg reflector (BR) (a) and spectral responses (b), which are shown for the cells with BR (1–3) and without BR (4) before (1) and after (2, 3, 4) irradiation by 3.75 MeV electrons with fluence of 3×10^{15} *cm*$^{-2}$.

registered for this cell. These values are fairly good, taking into account the smaller thickness of the n-GaAs base layer. The long-wavelength response of the cell with a 1.5 μm n-GaAs layer is nearly the same as for the cell with a 3 μm n-GaAs layer without BR. Reduction of the base thickness improves the cell radiation resistance. Figure 3(b) shows spectral responses of the cells with BR (curves 1–3) and without BR (4). Base thickness in the cells with BR was reduced to 1.1 μm (curves 1, 2) and to 1.3 μm (3), and the base doping level was reduced to 10^{15} cm^{-3} (curves 1, 2) and to 7×10^{15} cm^{-3} (curve 3). The base thickness of 3.5 μm and the base doping level of 10^{17} cm^{-3} were in the cell without BR (curve 4). It is seen from Figure 3(b) that reduction of the base thickness and the base doping level in the cells with a Bragg reflector allowed an increase in the radiation resistance. The remaining power factor was 0.84–0.86 in these cells after 1 MeV electron irradiation with a fluence of 10^{15} cm^{-2}.

2.3 GaAs-Based Cells on Ge Substrates

Intensive investigations of single and dual junction GaAs-based heterostructures MOCVD grown on Ge substrates were carried out [47–50]. Ge is less expensive and more mechanically strong than GaAs. Therefore, Ge substrates can be thinned down to 100–150 μm, and cells can be made larger reducing the weight and cost of space arrays. Owing to a good lattice matching between Ge and GaAs, the structures based on GaAs can be grown with a good crystal quality. An increase of the output voltage was observed in GaAs/Ge cells with a photoactive Ge/GaAs interface. A disadvantage of this photoactive Ge results from mismatching of the photocurrents generated in Ge and in GaAs active regions. Usually, the photocurrent from a Ge-sub cell was lower. Therefore, the I–V curve of these cells was 'kinked' with reduced FF and efficiency [48, 49, 51]. Reproducible growth conditions were developed to form GaAs cells on Ge substrates with an inactive interface [49, 51]. MOCVD equipment produced by EMCORE (USA) and AIXTRON (Germany) provides the GaAs-based solar cell structures on Ge-substrates with high productivity (up to 0.2 m^2 per run in AIX-3000 reactor) and with excellent uniformity and reproducibility of the cell performance. AlGaAs/GaAs structure production on

the 4-inch Ge wafers allows fabricating the large area (up to 36 cm^2) cells with an average efficiency of 19% (1 sun, AM0, 25°C).

3 Multi-junction Space Solar Cells

3.1 Mechanically Stacked Cells

Optimum bandgaps for multi-junction solar cells were calculated in a number of works [1, 2, 29–40]. Figure 4 illustrates the bandgaps and lattice constants for III–V compounds and their solid solutions. The hatched areas represent the theoretical optimum E_g values for the current matched bottom and top cells: E_{g1} = 1.65–1.8 eV for the top cells and E_{g2} = 1.0–1.15 eV for the bottom cells. The theoretical 1 sun AM0 efficiency for tandem solar cells with these bandgap values is about 32.5% (Figure 5, curve 1).

Mechanical stacks ensure more possibilities for the material choice than monolithic tandems owing to the use of lattice- and current-mismatched combinations of semiconductors. An obstacle for high-scale applications of stacks in space is a more complicated design. It is one reason why stacks are only used in concentrator array applications. In spite of the higher equilibrium temperature in the cells operating under concentrated sunlight, theoretical efficiencies of multi-junction, mechanically stacked cells under 10–100 suns at temperatures of 70–80°C are higher by 2–4% than 1-sun solar cells at 25°C. The use of sunlight concentration for space arrays offers additional advantages: better cell shielding from space radiation, and a potentially low cost of concentrator arrays owing to the low semiconductor material consumption.

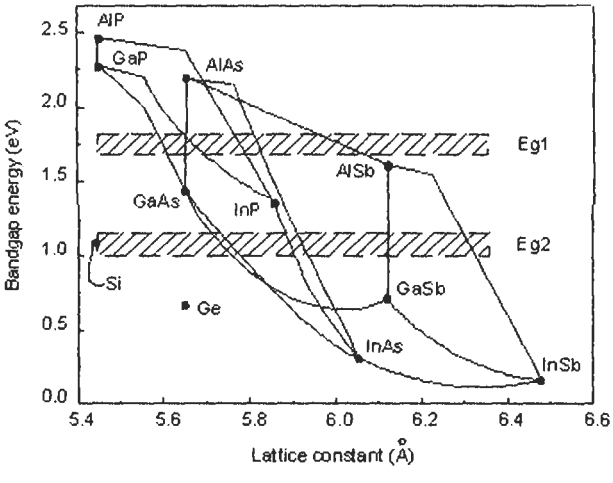

Figure 4 Energy bandgap versus lattice constant for Ge, Si, III–V compounds and ternary solid solutions. Hatched boxes correspond to the highest efficiency current-matched two-junction solar cells.

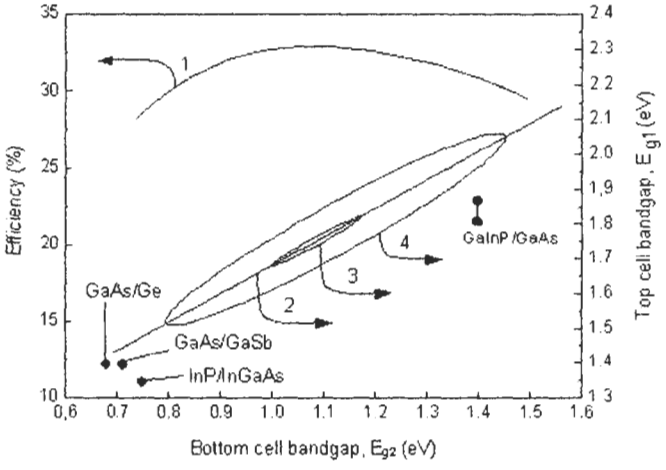

Figure 5 Curve 1: one sun AM0 efficiency (curve 1) for two-junction, two-terminal solar cells as a function of E_{g2} under conditions of matched photocurrents in the top and bottom cells. Line 2: relationship between E_{g1} and E_{g2} values, for which the condition of matched photocurrents is fulfilled. Curve 3: iso-efficiency contour ensuring the highest AM0 efficiencies of about 32.5%. Curve 4: iso-efficiency contour, for which efficiency decreases down to 30%. The bold points show the bandgaps E_{g1} and E_{g2} of GaAs/Ge, GaAs/GaSb, InP/InGaAs and GaInP/GaAs tandems.

The first high efficiency, mechanically stacked tandems consisted of AlGaAs/GaAs infrared transparent top cells and GaSb infrared sensitive bottom cells were fabricated [35]. GaAs-based cells were made transparent to the infrared part ($\lambda > 0.9$ μm) of sunlight in these stacked cells as n-GaAs substrate doping level was reduced to 10^{17} cm^{-3}. GaSb cells for stacks were fabricated mainly using Zn-diffusion. Maximum photocurrent densities in GaSb cells for the AM0-spectrum were about 30 mA/cm^2 behind a GaAs filter, and efficiencies of about 6% (AM0, 100x) were achieved behind a transparent GaAs cell. The best efficiencies of 29–30% (AM0, 100x) were obtained in two-junction stacks based on AlGaAs/GaAs top and GaSb (or InGaAs) bottom cells [35, 41], which have promise for use in space concentrator arrays [66, 67].

The further efficiency increase up to 34% (AM0, 25°C, 15 suns) was obtained in the triple junction, mechanically stacked voltage-matched circuits based on the monolithic GaInP/GaAs two-junction top cell and the GaSb bottom cell [65]. The efficiencies of 27.5% in the GaInP/GaAs top cell and of 6.5% in the bottom cell were obtained at 15 suns AM0 concentration. To obtain two-terminal circuits, seven GaSb cells were connected in series ensuring output voltage (V_{mp}) of 7×0.375 V = 2.63 V slightly exceeding V_{mp} of 2.4 V for the InGaP/GaAs two-junction cells which were connected in parallel.

Efficiency of 30% is expected in the mini-modules based on these stacks in the ultralight stretched lens array [66], characterised by overall efficiency of 26% and array power density of 350 W/m^2. The further efficiency increase is expected

in four-junction stacks based on the monolithic two-junction GaInP/GaAs top cells and the monolithic two-junction AlGaAsSb/GaSb bottom cells (or with another type of the cascade bottom cells).

3.2 Monolithic Multi-junction Solar Cells

In monolithic AlGaAs/GaAs tandems consisting of an $Al_{0.37}Ga_{0.63}As$ (E_g = 1.93 eV) upper cell and a GaAs lower cell were grown by MOCVD [45]. The component cells were electrically connected by a metal contact fabricated during the post-growth processing. The efficiency of 25.2% measured under AM0 one-sun illumination was achieved in AlGaAs/GaAs/InGaAsP three-junction cells consisted of a monolithic AlGaAs/GaAs tandem mechanically stacked with InGaAsP (E_g = 0.95 eV) single-junction cell.

Monolithic two-terminal GaAs/Ge tandem space concentrator cells with efficiency of 23.4% (9 suns AM0, 25°C) were developed [50]. MOCVD growth of n-GaAs formed a bottom cell in Ge owing to simultaneous diffusion of As and Ga into Ge. Series resistance of the n^+GaAs–p^+Ge tunnel junction formed on the interface limited the effective operation of these tandem cells to 10 suns only.

As is seen in Figures 4 and 5, silicon is a material with an optimum bandgap for the fabrication of bottom cells for two-junction cells with a theoretical efficiency exceeding 30%. Wide bandgap cells in these tandems, however, can be made only from such materials as AlGaAs, GaInP, and GaPAs, which are not lattice-matched to silicon. A considerable advance was realised in the fabrication of GaAs-based epitaxial layers on Si substrates [44, 64]. The results obtained hold a promise for high efficiency monolithic cascade cells on Si substrates, costing less than those on Ge substrates.

Cascade cells based on GaInP/GaAs heterostructures were at first proposed and fabricated at NREL [52, 53]. Then this technology was successfully applied for high-scale production of space arrays based on dual and triple junction GaInP/GaAs/Ge in Spectrolab [54–58], Tecstar [59] and Emcore [60]. Figure 6 shows two of the developed triple junction cell structures, consisting of a (Al)GaInP top cell connected in series by tunnel junction to a GaAs (Figure 6(a)) or InGaAs (Figure 6(b)) middle cell, connected in turn by tunnel junction with a bottom Ge cell. A 1 sun AM0 efficiency as high as 29.3% was achieved in Spectrolab [56] in a three-junction GaInP/GaAs/Ge cell. Large area (26.6 cm^2) three-junction cells have reached 29% AM0 efficiency. The high efficiencies of these cells are compatible with the high radiation hardness. The power remaining factor P/P_0 = 0.83 at 10^{15} e^-/cm^2 was measured in typical GaInP/GaAs/Ge cells, ensured mainly by the high radiation resistance of the top GaInP cell.

As mentioned above, the sub cells with E_g = 1–1.15 eV ensure a higher theoretical efficiency in cascade cells. Suitable Ge substrates can only be employed for the growth of lattice-mismatched GaInAs epilayers of an optimal composition. GaInAs layers on GaAs or Ge substrates of a satisfactory quality were grown and used for a subsequent epitaxial growth of GaInP/GaInAs cascade structures [61–63]. Efficiency of 27.3% (1 sun AM0, 28°C) was measured [63] in the triple junction $Ga_{0.43}In_{0.57}P/Ga_{0.92}In_{0.08}As$/Ge cells with

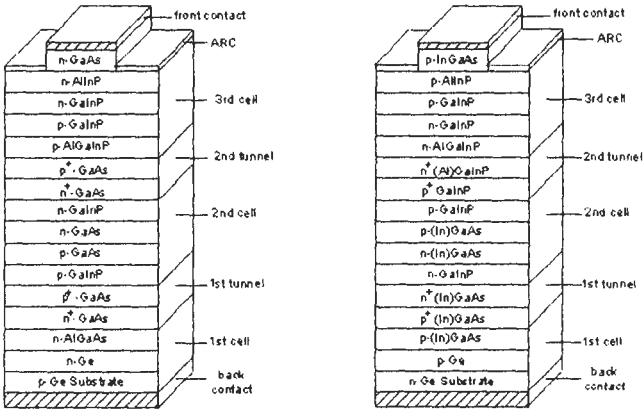

Figure 6 Cross-section of the developed triple junction solar cells: (a) (Al)GaInP/GaAs/Ge cascade cell (n-on-p) with GaAs-based first and second tunnel junctions and second cell; (b) (Al)GaInP/(In)GaAs/Ge cascade cell (p-on-n) with InGaAs-based first tunnel junction and second cell, and (Al)GaInP-based second tunnel junction.

the 0.5% lattice-mismatch to Ge substrate, similar to high-efficiency conventional lattice-matched GaInP/GaAs/Ge cells. The record efficiency of 29.7% [57] at 1 sun AM0 was achieved in a triple junction cell based on the GaInP/GaInAs/Ge structure with improved bandgap control: the bandgap of the GaInP top cell and tunnel junction layers, the bandgap of the GaInAs structure and simultaneous reduction of dislocation density in the structure. Owing largely to this very high efficiency at the start of life, the prototype cells have demonstrated end-of-life AM0 efficiency over 24.4% after irradiation with 1-MeV electrons at fluence of 1×10^{15} e$^-$/cm^2.

The next step for the efficiency increase was proposed in [36]: the development of monolithic four-junction (Al)GaInP/GaAs/GaInNAs/Ge cells, which contain a 1 eV GaInNAs sub cell lattice-matched to GaAs between the Ge and GaAs sub cells. However, GaInNAs layer has not been obtained with parameters acceptable for incorporation in such a four-junction cells until now, in spite of the intensive investigations of this material. The further efficiency increase was predicted for monolithic five-junction cells based on the (Al)GaInP/GaInP/GaAs/GaInAs/Ge structures with the lattice-mismatched GaInAs layers in a second (from Ge substrate) cell [62].

Recently, new III–V low-dimensional structures based on supperlattice and multi-quantum wells [68, 69], as well as metallic and quantum dot intermediate bands [70, 71] were proposed for solar cells. The main idea in these works is to use low-dimensional heterostructures in order to extend the sunlight absorption to longer wavelengths, but to conserve the high output voltage corresponding to the wide bandgap bulk semiconductor. It was predicted that these structures could obtain higher theoretical efficiencies than the multi-junction solar cells reviewed above. However, new materials, new technologies, and, maybe, new approaches should be developed to realise these predictions.

Acknowledgements

The author expresses his thanks to colleagues from the Photovoltaics Laboratory of the Ioffe Physico-Technical Institute for the help and valuable discussions, Zh. I. Alferov for the continuous interest and support and to all researchers for the permissions to use the copyright material.

References

[1] Flood, D. and Brandhorst, H., 1987. Space solar cells. In: *Current Topics in Photovoltaics*, Coutts, T.J., Meakin, J.D., Eds, Vol. 2, Academic Press, New York, London, pp.143–202.

[2] Bailey, S.G. and Flood, D.J., 1998. Space Photovoltaics. *Prog. Photovolt: Res. Appl.*, Vol. 6(1), pp. 1–14.

[3] Andreev,V.M., Grilikhes,V.A. and Rumyantsev,V.D., 1997. *Photovoltaic Conversion of Concentrated Sunlight*. John Wiley & Sons Ltd.

[4] Alferov, Zh.I., Andreev, V.M., Kagan, M.B./ Protasov, I.I. and Trofim, V.G., 1970. Solar cells based on heterojunction p-AlGaAs–n-GaAs. *Sov. Phys. Semicond.*, Vol. 4(12).

[5] Hovel, H.J. and Woodall, J.M., 1972. High-efficiency AlGaAs-GaAs solar cells. *Appl. Phys. Lett.*, Vol. 21, pp. 379–381.

[6] Andreev, V.M., Golovner, T.M., Kagan, M.B., Koroleva, N.S., Lubochevskaya, T.A., Nuller, T.A. and Tret'yakov, D.N., 1973. Investigation of high efficiency AlGaAs–GaAs solar cells. *Sov. Phys. Semicond.*, Vol. 7(12).

[7] Andreev,V.M., Kagan,M.B., Luboshevskaia,T.I.., Nuller,T.A. and Tret'yakov, D.N., 1974. Comparison of different heterophotoconverters for achievement of highest efficiency. *Sov. Phys. Semicond.*, Vol. 8(7).

[8] Alferov, Zh.I., Andreev, V.M., Daletskii, G.S., Kagan, M.B., Lidorenko, N.S. and Tuchkevich, V.M., 1977. Investigation of high efficiency AlAs–GaAs heteroconverters. *Proc. World Electrotechn. Congress*, Moscow, Section 5A, report 04.

[9] Hovel, H.J., 1975. Solar cells. In: *Semiconductors and Semimetals*. Vol. 11, Willardson, R.K. and Beer, A.C., Eds, Academic Press, New York, London.

[10] Woodall, J.M. and Hovel, H.J., 1977. An isothermal etchback–regrowth method for high efficiency $Ga_{1-x}Al_xAs$–GaAs solar cells. *Appl. Phys. Lett.*, Vol. 30, pp. 492–493.

[11] Andreev, V.M., Larionov, V.R., Rumyantsev, V.D., Fedorova, O.M. and Shamukhamedov, Sh.Sh., 1983. P-AlGaAs–pGaAs–nGaAs solar cells with efficiencies of 19% at AM0 and 24% at AM1.5. *Sov. Tech. Phys. Lett.*, Vol. 9(10), pp. 537–538.

[12] Hovel,H.J., 1978. Novel materials and devices for sunlight concentrating systems. *IBM Journal of Research and Development*, Vol. 22, pp. 112–121.

[13] Fanetti, E., Flores, C., Guarini, G., Paletta, F. and Passoni, D., 1981. High efficiency 1.43 and 1.69 eV band gap $Ga_{1-x}Al_xAs$–GaAs solar cells for multicolor applications. *Solar Cells*, Vol. 3, pp. 187–194.

[14] Knechtly, R.C., Loo, R.Y. and Kamath, G.S., 1984. High-efficiency GaAs solar cells. *IEEE Trans. Electron Dev.*, ED-31 (5), pp. 577–588.

[15] Rauschenbach, H.S., 1980. *Solar Cell Array Design Handbook. The Principles and Technology of Photovoltaic Energy Conversion*. Litton Educational Publishing, Inc., New York.

[16] Luque, A., 1989. *Solar Cells and Optics for Photovoltaic Concentration*. Adam Hilger, Bristol, Philadelphia.

[17] Partain, L.D. Ed., 1995. *Solar Cells and Their Application*, John Wiley & Sons.

[18] Iles, P.A., 2000. Future of Photovoltaics for space applications. *Prog. Photovolt: Res. Appl.*, Vol. 8, pp. 39–51.

[19] Andreev, V.M., Kazantsev, A.B., Khvostikov, V.P., Paleeva, E.V., Rumyantsev, V.D. and Shvarts, M.Z., 1994. High-efficiency (24.6%, AM0) LPE Grown AlGaAs/GaAs Concentrator Solar Cells and Modules. *Proc. First World Conf. on Photovoltaic Energy Conversion*, Hawaii, pp. 2096–2099.

[20] Andreev, V.M. and Rumyantsev, V.D, 1996. A^3B^5 based solar cells and concentrating optical elements for space PV modules. *Sol. Energy Mater. Sol. Cells*, Vol. 44, pp. 319–332.

[21] Dupuis, R.D., Dapkus, P.D., Vingling, R.D. and Moundy, L.A., 1977. High-efficiency GaAlAs/GaAs heterostructure solar cells grown by metalorganic chemical vapor deposition. *Appl. Phys. Lett.*, Vol. 31, pp. 201–203.

[22] Nelson, N.J., Jonson, K.K., Moon, R.L., Vander Plas, H.A. and James, L.W., 1978. Organometallic- sourced VPE AlGaAs/GaAs concentrator solar cells having conversion efficiencies of 19%. *Appl. Phys. Lett.*, Vol. 33, pp. 26–27.

[23] Werthen, J.G., Virshup, G.F., Ford, C.W., Lewis, C.R. and Hamaker, H.C., 1986. 21% (one sun, air mass zero) 4 cm^2 GaAs space solar cells. *Appl. Phys. Lett.*, Vol. 48, pp. 74–75.

[24] Tobin, S.P., Vernon, S.M., Woitczuk, S.J., Baigar, C., Sanfacon, M.M. and Dixon, T.M., 1990. Advanced in high-efficiency GaAs solar cells. *Proc. 21st IEEE Photovoltaic Specialists Conf.*, pp.158–162.

[25] Tobin, S.P., Vernon, S.M., Sanfacon, M.M. and Mastrovito, A., 1991. Enhanced light absorption in GaAs solar cells with internal Bragg reflector. *Proc. 22nd IEEE Photovoltaic Specialists Conf.*, pp.147–152.

[26] Andreev, V.M., Komin, V.V., Kochnev, I.V., Lantratov, V.M. and Shvarts, M.Z., 1994. High-efficiency AlGaAs–GaAs Solar Cells with Internal Bragg Reflector. *Proc. First World Conf. on Photovoltaic Energy Conversion*, Hawaii, pp.1894–1897.

[27] Shvarts, M.Z., Chosta, O.I., Kochnev, I.V., Lantratov, V.M. and Andreev, V.M., 2001. Radiation resistant AlGaAs/GaAs concentrator solar cells with internal Bragg reflector. *Sol. Energy Mater. Sol. Cells*, Vol. 68, pp. 105–122.

[28] Yamaguchi, M., Space solar cell R&D activities in Japan. 1997. *Proc. 15th Space Photovoltaic Research and Technology Conf.*, pp. 1–10.

[29] Fan, C.C., Tsaur, B.-Y. and Palm, B.J., 1982. Optimal design of high-efficiency tandem cells. *Proc. 16th IEEE Photovoltaic Specialists Conf.*, San Diego, pp. 692–698.

[30] Green, M.A., 1982. *Solar Cells*. Prentice-Hall Inc., New Jersey.

[31] Lamorte, M.F. and Abbott, D.H., 1980. Computer modeling of a two-junction, monolithic cascade solar cell. *IEEE Trans. Electron. Dev.*, ED-27, pp. 231–249.

[32] Spitzer, M.B. and Fan, C.C., 1990. Multijunction cells for space applications. *Solar Cells*, Vol. 29, pp. 183–203.

[33] Fraas, L.M., 1995. High-efficiency III–V multijunction solar cells. In: *Solar Cells and Their Applications*. Partain, L.D., Ed., John Wiley & Sons, pp.143–162.

[34] Jain, R.K. and Flood, D.J., 1993. Monolithic and mechanical multijunction space solar cells. *Journal of Solar Energy Engineering*, Vol. 115, pp. 106–111.

[35] Fraas, L.M., Avery, J.E., Martin, J., Sundaram, V.S., Giard, G., Dinh, V.T., Davenport, T.M., Yerkes, J.W. and O'Neil, M.J., 1990. Over 35-percent efficient GaAs/GaSb tandem solar cells. *IEEE Trans. Electron. Dev.*, Vol. ED-37, pp. 443–449.

[36] Kurtz, S.R., Myers, D. and Olson, J.M., 1997. Projected performance of three- and four-junction devices using GaAs and GaInP. *Proc. 26th IEEE Photovoltaic Specialists Conf.*, Anaheim, pp. 875–878.

[37] Yamaguchi, M., 2001. Multi-junction solar cells: present and future. *Technical Digest 12th Int. Photovoltaic Solar Energy Conf.* pp. 291–294.

[38] Bett, A.W., Dimroth, F., Stollwerk, G. and Sulima, 1999. O.V., III–V compounds for solar cell applications. *Appl. Phys.*, A69, pp. 119–129.

[39] Yamaguchi, M. and Luque, A., 1999. High efficiency and high concentration in photovoltaics. *IEEE Trans. Electron Devices*, Vol. ED-46(10), pp. 41–46.

[40] Wanlass, M.W., Ward, J.S., Emery, K.A., Gessert, T.A., Osterwald, C.R. and Coutts, T.J., 1991. High performance concentrator tandem solar cells based on IR-sensitive bottom cells. *Solar Cells*, Vol. 30, pp. 363–371.

[41] Andreev, V.M., Karlina, L.B., Kazantsev, A.B., Khvostikov, V.P., Rumyantsev, V.D., Sorokina, S.V. and Shvarts, M.Z., 1994. Concentrator Tandem Solar Cells Based on AlGaAs/GaAs–InP/InGaAs (or GaSb) Structures. *Proc. First World Conf. on Photovoltaic Energy Conversion*, Hawaii, pp. 1721–1724.

[42] Andreev, V.M., Khvostikov, V.P., Paleeva, E.V., Rumyantsev, V.D., Sorokina, S.V., Shvarts, M.Z. and Vasil'ev, V.I., 1996. Tandem solar cells based on AlGaAs/GaAs and GaSb structures. *Proc. 23d Int. Symposium on Compound Semiconductors*, pp. 425–428.

[43] Andreev, V.M., 1999. R&D of III–V compound solar cells in Russia. *Technical Digest 11th Int. Photovoltaic Solar Energy Conf.* pp. 589–592.

[44] Umeno, M., Kato, T., Yang, M., Azuma, Y., Soga, T. and Jimbo, T. 1994. High efficiency AlGaAs/Si tandem solar cell over 20%. *Proc. First World Conf. on Photovoltaic Energy Conversion*, Hawaii, pp.1679–1684.

[45] Chung, B.-C., Virshup, G.F., Ristow, M. Ladle, Wanlass, M.W., 1991. 25.2%-efficiency (1-sun, air mass 0) AlGaAs/GaAs/InGaAsP three-junction, two-terminal solar cells, *Proc. 22nd IEEE Photovoltaic Specialists Conf.*, Las Vegas, pp. 54–57.

[46] Andreev,V.M., Khvostikov, V.P., Rumyantsev, V.D., Paleeva, E.V., Shvarts, M.Z., Monolithic two-junction AlGaAs/GaAs solar cells. 1997. *Proc. 26th IEEE Photovoltaic Specialists Conf.*, Anaheim, pp. 927–930.

[47] Timmons, M.L., Hutchley, J.A., Wagner, D.K. and Tracy, J.M., 1988. Monolithic AlGaAs/Ge cascade cell. *Proc. 21st IEEE Photovoltaic Specialists Conf.*, Kissimmee, pp. 602–606.

[48] Tobin, S.P., Vernon, S.M., Bajgar, C., Haven, V.E., Geoffroy, L.M., Sanfacon, M.M., Lillington, D.R., Hart, R.E., Emery, K.A. and Matson, R.L., 1988. High efficiency GaAs/Ge monolithic tandem solar cells. *Proc. 20th IEEE Photovoltaic Specialists Conf.*, Las Vegas, pp. 405–410.

[49] Iles, P.A., Yeh, Y.-C.M., Ho, F.N., Chu, C.L. and Cheng, C., 1990. High-efficiency (> 20% AM0) GaAs solar cells grown on inactive Ge substrates. *IEEE Electron Device Letters*, Vol. 11(4), pp. 140–142.

[50] Wojtczuk, S., Tobin, S., Sanfacon, M., Haven, V., Geoffroy, L. and Vernon, S., 1991. Monolithic two-terminal GaAs/Ge tandem space concentrator cells. *Proc. 22nd IEEE Photovoltaic Specialists Conf.*, Las Vegas, pp. 73–79.

[51] Iles, P.A. and Yeh, Y.-C.M., 1995. Silicon, gallium arsenide and indium phosphide cells: single junction, one sun space. In: *Solar Cells and Their Applications*, Partain, L.D., Ed., John Wiley & Sons, pp. 99–121.

[52] Olson, J.M., Kurtz, S.R., Kibbler, A.E. and Faine, P., 1990. Recent advances in high efficiency $GaInP_2$/GaAs tandem solar cells. *Proc. 21st IEEE Photovoltaic Specialists Conf.*, Kissimmee, pp. 24–29.

[53] Bertness, K.A., Kurtz, S.R., Friedman, D.J., Kibbler, A.E., Kramer, C. and Olson, J.M., 1994. High-efficiency GaInP/GaAs tandem solar cells for space and terrestrial applications. *Proc. First World Conf. on Photovoltaic Energy Conversion*, Hawaii, pp.1671–1678.

[54] Chiang, P.K., Krut, D.D., Cavicchi, B.T., Bertness, K.A., Kurtz, S.R. and Olson, J.M., 1994. Large area GaInP/GaAs/Ge multijunction solar cells for space application. *Proc. First World Conf. on Photovoltaic Energy Conversion*, Hawaii, pp. 2120–2123.

[55] Chiang, P.K., Ermer, J.H., Niskikawa, W.T., Krut, D.D., Joslin, D.E., Eldredge, J.W. and Cavicchi, B.T., 1996. Experimental results of $GaInP_2$/GaAs/Ge triple junction cell development for space power systems. *Proc. 25th IEEE Photovoltaic Specialists Conf.*, Washington, D.C., pp. 183–186.

[56] King, R.R., Karam, N.H., Ermer, J.H., Haddad, M., Colter, P., Isshiki, T., Yoon, H., Cotal, H.L., Joslin, D.E., Krut, D.D., Sudharsanan, R., Edmondson, K., Cavicchi, B.T. and Lillington, D.R., 2000. Next-generation, high-efficiency III–V multijunction solar cells. *Proc. 28th IEEE Photovoltaic Specialists Conf.*, Anchorage, pp. 998–1005.

[57] King, R.R., Fetzer, C.M., Colter, P.C., Edmondson, K.M., Ermer, J.H., Cotal, H.L., Yoon, H., Stavrides, A.P., Kinsey, G., Krut, D.D. and Karam, N.H., 2002. High-efficiency space and terrestrial multijunction solar cells trough bandgap control in cell structures. *Proc. 29th IEEE Photovoltaic Specialists Conf.*, New Orleans, pp. 776–781.

[58] Stavrides, A., King, R.R., Colter, P., Kinsey, G., McDanal, A.J., O'Neill, M.J. and Karam, N.H., 2002. Fabrication of high efficiency, III–V multi-junction solar cells for space concentrators. *Proc. 29th IEEE Photovoltaic Specialists Conf.*, New Orleans, pp. 920–922.

[59] Chiang, P.K., Chu, C.L., Yeh, Y.C.M., Iles, P., Chen, G., Wei, J., Tsung, P., Olbinski, J., Krogen, J., Halbe, S. and Khemthong, S. 2000. Achieving 26% triple junction cascade solar cell production. 2000. *Proc. 28th IEEE Photovoltaic Specialists Conf.*, Anchorage, pp.1002–1005.

[60] Hou, H.Q., Sharps, P.R., Fatemi, N.S., Li, N., Stan, M.A., Martin, P.A., Hammons, B.E. and Spadafora, F., 2000. Very high efficiency InGaP/GaAs dual-junction solar cell manufacturing at Emcore Photovoltaics. *Proc. 28th IEEE Photovoltaic Specialists Conf.*, Anchorage, pp.1173–1176.

[61] Bett, A.W., Dimroth, F., Lange, G., Meusel, M., Beckert, R., Hein, M., Riesen, S.V. and Schubert, U., 2000. 30% monolithic tandem concentrator solar cells for concentrations exceeding 1000 suns. *Proc. 28th IEEE Photovoltaic Specialists Conf.*, Anchorage, pp. 961–964.

[62] Dimroth, F., Schubert, U., Bett, A.W., Hilgarth, J., Nell, M., Strobl, G., Bogus, K. and Signorini, C., 2001. Next generation GaInP/GaInAs/Ge multijunction space solar cells. *Proc. 17th European Photovoltaic Solar Energy Conf.*, Munich, pp. 2150–2154.

[63] King, R.R., Haddad, M., Isshiki, T., Colter, P., Ermer, J., Yoon, H., Joslin, D.E. and Karam, N.H., 2000. Metamorphic GaInP/GaInAs/Ge solar cells. *Proc. 28th IEEE Photovoltaic Specialists Conf.*, Anchorage, pp. 982–985.

[64] Yamaguchi, M., Ohmachi, Y., O'Hara, T., Kadota, Y., Imaizumi, M. and Matsuda, S., 2000. GaAs-on-Si solar cells for space use. *Proc. 28th IEEE Photovoltaic Specialists Conf.*, Anchorage, pp. 1012–1015.

[65] Fraas, L.M., Daniels, W.E., Huang, H.X., Minkin, L.E., Avery, J.E., O'Neill, M.J., Mc.Danal, A.J. and Piszczor, M.F., 2001. 34% efficient InGaP/GaAs/GaSb cell-interconnected-circuit for line-focus concentrator arrays. *Proc. 17th European Photovoltaic Solar Energy Conf.*, Munich, pp. 2300–2303.

[66] O'Neill, M.J., McDanal, A.J., George, P.J., Piszczor, M.F., Edwards, D.L., Hoppe, D.T., Eskenazi, M.I., Botke, M.M., Jaster, P.A. and Brandhorst, H.W., 2002. Development of the ultra-light stretched lens array. *Proc. 29th IEEE Photovoltaic Specialists Conf.*, New Orleans, pp. 916–919.

[67] Andreev, V.M., Larionov, V.R., Lantratov, V.M., Grilikhes, V.A., Khvostikov, V.P., Rumyantsev, V.D., Sorokina, S.V. and Shvarts, M.Z., 2000. Space concentrator module based on short focus linear Fresnel lenses and GaAs/GaSb tandem stacks. *Proc. 28th IEEE Photovoltaic Specialists Conf.*, Anchorage, pp.1157–1160.

[68] Green, M.A., 2000. Prospects for photovoltaic efficiency enhancement using low-dimensional structures. *Nanotechnology*, Vol. 11, pp. 401–405.

[69] Ekins-Daukes, N.J., Barnes, J.M., Barnham, K.W.J., Connolly, J.P., Mazzer, M., Clark, J.C., Grey, R., Hill, G., Pate, M.A. and Roberts, J.S., 2001. Strained and strain-balanced quantum well devices for high-efficiency tandem solar cells, *Sol. Energy Mater. Sol. Cells* , Vol. 68, pp. 71–87.

[70] Luque, A. and Marti, A., 2001. A metallic intermediate band high efficiency solar cell. *Prog. Photovolt: Res. Appl.*, Vol. 9, pp. 73–86.

[71] Marti, A. Cuadra, L. and Luque, A., 2001. Partial filling of a quantum dot intermediate band for solar cells. *IEEE Trans. Electron Devices*. Vol. ED-48(10), pp. 2394–2399.

High-Efficiency Concentrator Silicon Solar Cells

Pierre J. Verlinden, Origin Energy, Adelaide, Australia

1 Introduction

Concentrating sunlight for photovoltaic conversion has always been a very attractive solution. Since one can easily acknowledge that the cost of photovoltaic energy conversion is driven by the fabrication cost of the solar cells, and particularly the cost of the semiconductor material, it becomes obvious that much less expensive concentrating lenses or mirrors can replace the expensive solar cells area. The concentration ratio can be increased several hundred fold, to the point where the cost of fabricating the solar cells becomes insignificant in the overall PV system cost. However, this benefit does not come without cost. Concentrating PV systems need solar trackers with a tracking precision that increases with the concentration ratio, and a more expensive module design with a well-engineered and low-cost cooling system for the solar cells.

Concentration not only increases the energy productivity of the solar cell material and device, but also increases its efficiency, since both current and voltage increase with the light intensity. However, in order to compare efficiencies of concentrator PV systems with flat plate PV systems, we have to remember that concentrator systems only use direct sunlight, about 85% of the incident power density on a clear sunny day. Therefore, a 20% efficient concentrator system would produce about the same amount of energy as a 17% efficient flat plate system, if they are both mounted on the same tracking system.

The series resistance of the cell limits the concentration ratio to which the solar cells can be used and the efficiency advantage of concentration systems over flat plates. To collect a current that is, for example at 500× concentration, almost 20 A/cm^2 from a solar cell that has an open-circuit voltage of 0.800 V requires a series resistance that is less than 0.001 Ω cm^2. To achieve such low series resistance, the concentrator solar cell requires a well-engineered double-level, solderable metallisation scheme [4, 5] (see Figure 1).

The carrier recombination in commercial one-sun solar cells for flat-plate application is usually dominated by bulk Shockley-Read-Hall (SRH) or surface recombination. In high-efficiency (> 18%) solar cells or when medium-concentration (< 100×) is applied, the carrier recombination is usually

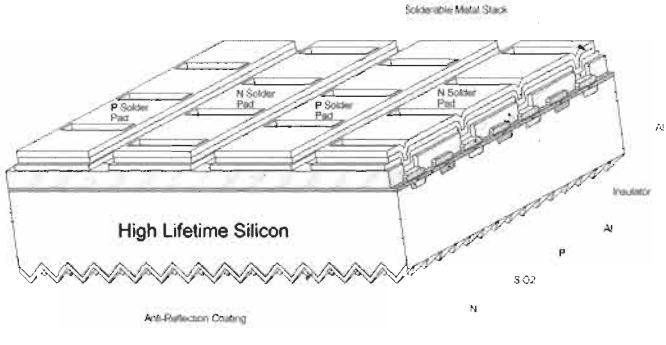

Figure 1 Structure of IBC silicon solar cell.

dominated by junction recombination. Auger recombination usually dominates in high-concentration silicon solar cells. Auger recombination occurs when an electron from the conduction band recombines with a hole from the valence band giving its energy to another electron. This is the opposite mechanism of impact ionisation. The Auger recombination rate increases as the cube of the carrier density, and is generally the dominant recombination mechanism when the carrier concentration exceeds 10^{17} cm^{-3}. In order to reduce the Auger recombination rate, concentrator solar cells must be as thin as possible (typically 120 μm or less) and, therefore, require a good light trapping.

Because the solar cell cost represents only around 10% of the total concentrator PV system cost, a high efficiency solar cell provides a great leverage for reducing the cost of solar electricity; the higher the concentration ratio the greater the leverage. The most efficient silicon solar cell, both for laboratory cells and for production scale, is currently the interdigitated back contact (IBC) and, in particular, the point-contact (PC) solar cell [5–9]. The structure of such a cell is shown in Figure 1. It has attained a conversion efficiency of 28.3% [2, 3] in the laboratory, and 26.8% at 100× (AM1.5D, 10 W/cm^2, 25°C) at the production scale [1]. It is, at the present time, the only high-intensity silicon solar cell commercially available. Figures 2 and 3 show examples of concentrator silicon solar cells manufactured by SunPower Corporation of Sunnyvale, California. Two examples of a reflective concentrator dish, built by Solar Systems Pty Ltd of Hawthorn, Australia and using high-efficiency concentrator silicon solar cells, are shown in Figures 4 and 5. The 20 m^2 concentrator system represented in Figure 5 was the first silicon-based concentrator system to reach an overall system efficiency of 20% under normal operating conditions [6]. Figure 6 shows a picture of the receiver of such concentrator system in operation.

2 The Family of Backside Contact Silicon Solar Cells

2.1 IBC Solar Cells

Schwartz et al. [7, 8] introduced the IBC design in 1975. The main reason that the IBC solar cell design is particularly suitable for high concentration is that both metal contacts are made on the backside of the cell (Figure 1). Therefore, there is no shadowing effect on the front side. The trade-off between the shadowing effect and the series resistance is eliminated, which is particularly interesting for concentration applications. Furthermore, the design of the front side (optical side) and the backside (electrical side) can easily be optimised separately. In a conventional solar cell, the doping of the front side emitter is a trade-off between series resistance and efficiency: a lighter doped front side emitter would improve the quantum efficiency and reduce the emitter saturation current density, but it would increase the series resistance of the cell. On the other hand, in IBC solar cells, the front side could be optimised for maximum

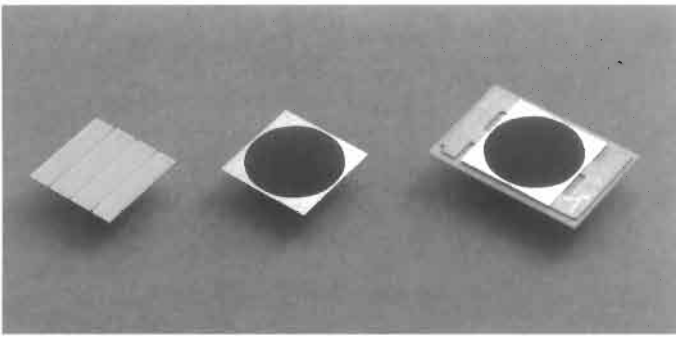

Figure 2 A point-contact silicon solar cell for Fresnel concentrator application. (Courtesy of SunPower Corporation.)

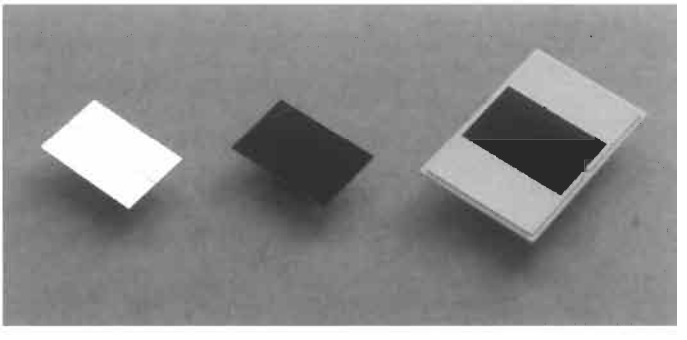

Figure 3 A point-contact silicon solar cell for dense array concentrator application. (Courtesy of SunPower Corporation.)

quantum efficiency, reduced recombination and reduced sub-linearity, without compromising the series resistance of the cell.

The main requirements for obtaining a high efficiency with IBC cells are:

- Long recombination lifetime in the bulk. After the solar cell fabrication the diffusion length must be at least 5 times longer than the solar cell thickness. For this reason, Float-Zone (FZ), high-resistivity, n-type substrates with carrier lifetime greater than 1 ms are generally preferred. The typical solar cell thickness is 100–150 μm.
- Low front surface recombination velocity. The front surface must be passivated with a thin, thermally grown, silicon dioxide layer, grown in a very clean environment.

2.2 Front-Surface-Field, Tandem-Junction and Point-Contact Solar Cells

Over the years, several variants in the IBC design have been introduced. The front-surface-field (FSF) solar cell has a high-low (n+/n or p+/p) junction on the

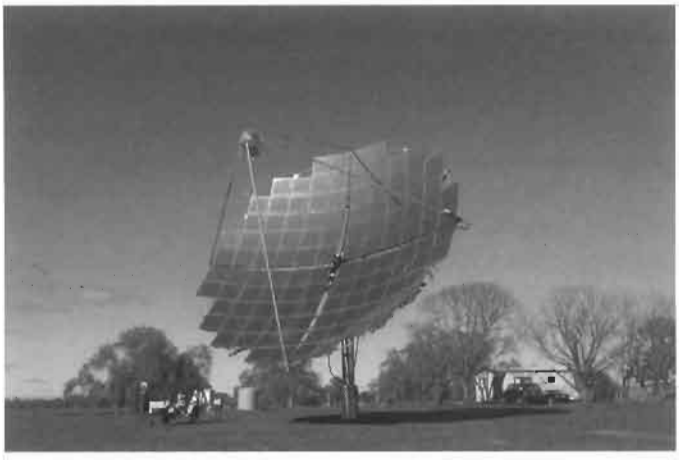

Figure 4 Picture of a 2.5 kW dish concentrating PV system with point-contact silicon solar cells. (Courtesy of Solar Systems Pty Ltd.)

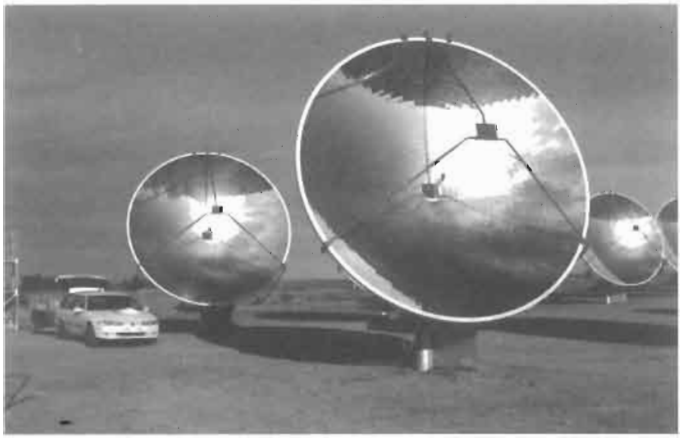

Figure 5 A dish concentrating PV system with point-contact silicon solar cells. This PV system, installed in White Cliff, Australia, demonstrated 20% overall efficiency under normal operating conditions [6]. (Courtesy of Solar Systems Pty Ltd.)

front side of the IBC solar cell (Figure 7(a)). The function of the front surface field is to reduce the effective front-surface recombination velocity for the carriers in the bulk of the device. It behaves the same way as a back surface field (BSF) in a conventional n+/p/p+ solar cell. However, since the high-low junction is now applied on the front side of the cell and since the solar cell is operating under high injection, the effective recombination velocity increases as the injection level increases and the effect of the FSF decreases. In high injection, the front-surface recombination current density, $J_{fs,rec}$, can be expressed as a function of the

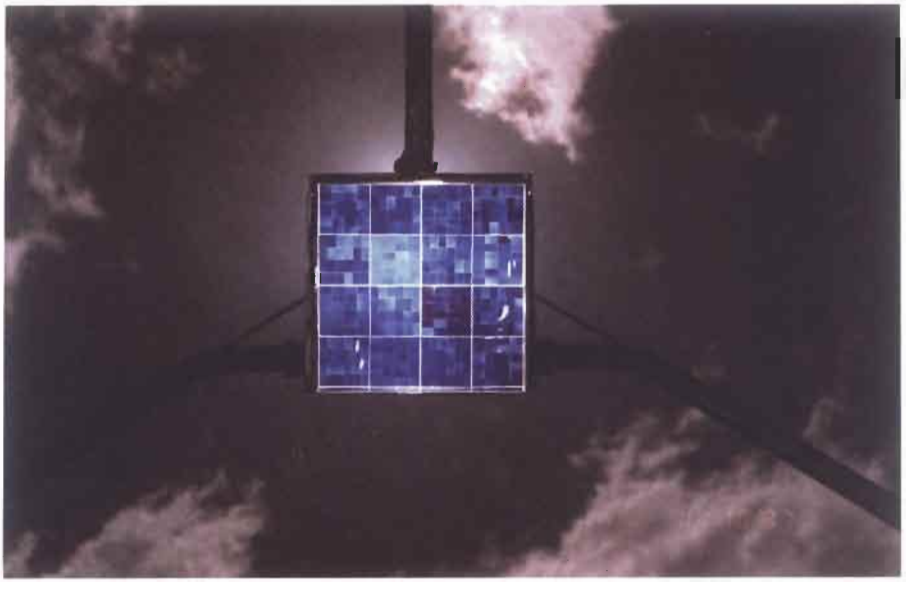

Figure 6 A dense array receiver with point-contact silicon solar cells. (Courtesy of Solar Systems Ltd Pty.)

saturation current density of the high-low junction, J_{0+}, or as a function of an effective surface recombination velocity, S_{eff}:

$$J_{fs,rec} = \frac{n^2}{n_i^2} J_{0+} = qnS_{eff} \tag{1}$$

where n is the carrier concentration (note that, in high-injection, the electron and hole concentrations are equal, $n = p$) at the front surface of the cell and n_i is the intrinsic carrier concentration.

Tandem-junction (TJ) solar cells are identical to FSF solar cell, except that a floating p-n junction replaces the high-low junction at the front side of the cell (Figure 7b). The front surface recombination current density, $J_{fs,rec}$, is determined by Equation (1) in the same way as in the FSF solar cell, and there is practically no difference between a TJ and a FSF solar cell (the only difference resides in the space charge recombination current at a very low intensity). The designer choice between a TJ and a FSF solar cell is fully determined by the ability to make a front side emitter with the lowest emitter saturation current density, J_{0+}, as possible. For this reason, n-type (phosphorous doped) emitters are usually preferred.

As we can see from Equation (1), the front surface recombination current increases as n^2 and the effective surface recombination velocity increases as the injection level increases:

$$S_{eff} = \frac{n}{qn_i^2} J_{0+} \tag{2}$$

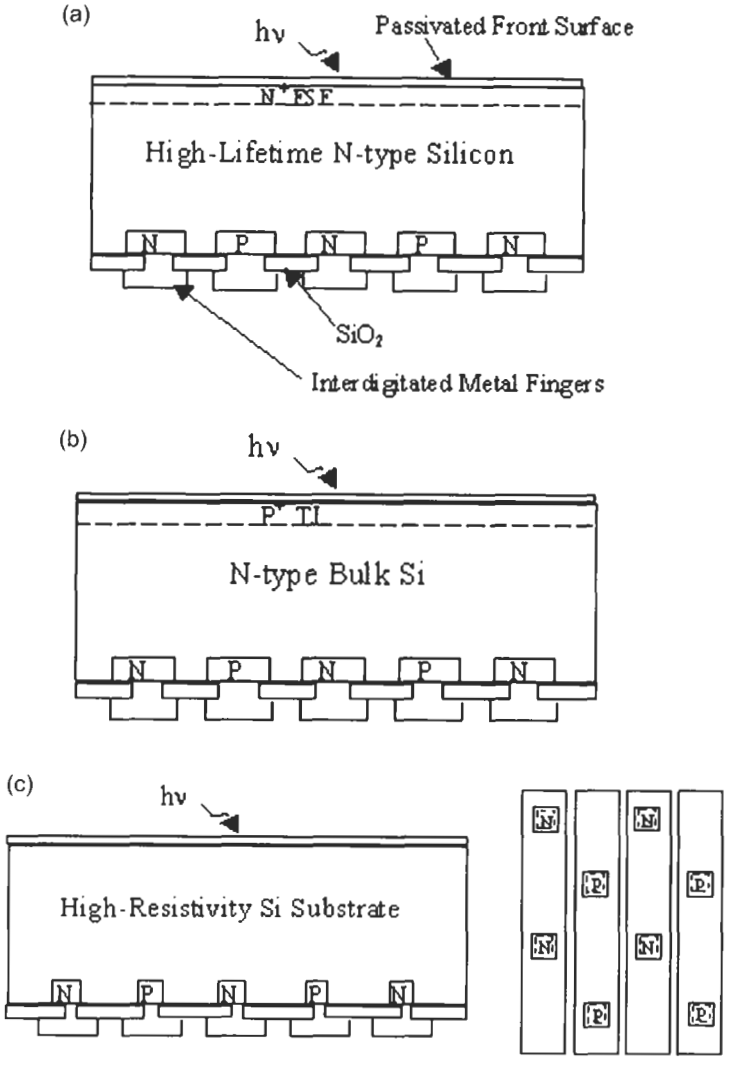

Figure 7 (a) Structure of a front-surface-field silicon solar cell. (b) Structure of a tandem junction silicon solar cell. (c) Structure of a point-contact silicon solar cell.

These characteristics result in a significant sub-linearity of the responsivity of the cell. The responsivity of a solar cell is, for a given spectrum, the total photo-generated current per unit of incident power. The responsivity has the dimension of amp/watt. The typical value of responsivity for high-efficiency concentrator solar cells is 0.395 A/W. If it varies with the concentration ratio, the solar cell is called sub-linear or super-linear. Therefore, a doped front side surface (TJ or FSF) is usually reserved to low-concentration applications ($< 10\times$).

Point-contact solar cells are IBC cells with a reduced emitter area and reduced metal contact area on the backside of the cell (Figure 7(c)) in order to decrease as

much as possible the emitter recombination. For one-sun or low-concentration applications ($< 5\times$), the backside emitter coverage fraction could be kept at almost 100% since the dominant recombination mechanisms are SRH and surface recombinations, and a simple IBC design is preferred. However, the metal contact area is kept very low, typically less than 1%, depending on the metal-Si contact resistance. For concentration ratios between $5\times$ and $200\times$, the backside emitter coverage fraction could be reduced to typically around 10%, whereas the metal contact area is typically 5% of the backside of the cell.

3 Modelling of Backside Contact Solar Cells

The simplest way to model IBC solar cells is to consider the integral approach as proposed by R.M. Swanson [9, 10] and, for a precise simulation of an IBC or PC solar cell, we refer the reader to the model developed in these papers which includes 3D effects close to the backside contacts. However, we will give below a simple formulation.

The current, I, at the terminals of a solar cell can be written in the form:

$$I = I_{ph} - I_{b,rec} - I_{s,rec} - I_{em,rec} \tag{3}$$

where I_{ph} is the photogenerated current (the maximum photogenerated current within the silicon material with a defined thickness, including reflection losses and light trapping), $I_{b,rec}$ is the sum of all the bulk recombination currents (including SRH and Auger recombination), $I_{s,rec}$ is the sum of all the surface recombination currents (including front side, backside and edge surface recombination) and $I_{em,rec}$ is the sum of all the emitter recombination currents (including backside emitters, the front TJ or FSF emitter if it exists, and also including recombination at the contacts). The recombination currents increase as the carrier concentration increases and, therefore, increase as the terminal voltage increases. Eventually, at the open-circuit condition, the sum of all the recombination currents will be equal to the photocurrent, I_{ph}, and the terminal current will be equal to zero. Therefore, at V_{oc}

$$I_{ph} = I_{b,rec} + I_{s,rec} + I_{em,rec} \tag{4}$$

Calculating the different components of the recombination current is the most interesting and the most powerful approach to simulate, optimise or analyse the performance of solar cells. Table 1 gives a summary of the different relevant recombination mechanisms in silicon, their controlling parameters, typical values in high-efficiency concentrator silicon solar cells and the corresponding recombination currents under high-level injection.

If an IBC solar cell is to be modelled, in a simple manner, as a backside illuminated conventional solar cell, one has to realise that:

- in most of the device, the electron and holes are flowing in the same direction, from the front side of the cell toward the backside where the collecting n-type and p-type junctions are;

Table 1 Recombination mechanism and the corresponding recombination current in highly injected silicon solar cells.

Carrier recombination mechanism	Controlling parameter	Unit	Typical values	Recombination current density (A/cm^2)
Bulk (SRH, trap assisted)	τ_B	s	1–10 ms	$\frac{qnW}{\tau_B}$
Surface (trap assisted)	S	cm/s	1–4 cm/s	qnS
Emitter	J_o	A/cm^2	50–200 fA/cm^2	$\frac{n^2}{n_i^2}J_o$
Auger	C_A	cm^6/s	1.66×10^{-30}	qn^3C_AW

The ambipolar Auger coefficient value is from Sinton [11, 12]. In this chapter, τ_B represents the bulk lifetime and, since we are considering high-injection conditions only, we have assumed that $\tau_n = \tau_p = \tau_B$, where τ_n and τ_p are the electron and hole lifetimes.

- since the cell is under high injection, and to maintain electrical neutrality in the device, the electron and hole concentrations are equal throughout the device;
- for the same reasons as above, electrons and holes are flowing with the same ambipolar diffusion constant, $D_a = 2D_nD_p/(D_n + D_p)$, where D_n and D_p are the electron and hole diffusion constants;
- in most of the device, from the front-side to very close to the emitter area where 3D current flow starts to appear, the current flow is almost unidirectional, perpendicular to the surface:

$$J_n = -J_p = qD_a\frac{dn}{dx} = qD_a\frac{dp}{dx} \tag{5}$$

where J_n and J_p are the electron and hole current densities, and, therefore, the total current along the wafer J_T is negligible:

$$J_T \approx 0 \tag{6}$$

Since the backside carrier concentration is determined by the terminal voltage of the solar cell

$$n_{back} = n_i \exp\left(\frac{qV}{2k_BT}\right) \tag{7}$$

we can use Equation (3) and the expression of recombination currents in Table 1 to calculate the cell current at any bias voltage. We can take, as a simple example, a high-efficiency IBC or PC solar cell under high injection, with long carrier lifetime ($\tau_n = \tau_p \gg W^2/D_a$, where W is the thickness of the cell) and low surface recombination velocity ($S_0 \ll D_a/W$, where S_0 is the surface recombination velocity at the front surface).

In short-circuit condition, we can consider that, in the first approximation:

- $n_{back} = 0$,

- the emitter and surface recombination currents at the back of the cell can be neglected, as well as Auger recombination,
- the electron and hole concentrations linearly decrease from front to back.

Equation (3) then becomes:

$$J_{sc} = J_{ph} - \frac{qn_0 W}{2\tau_B} - qn_0 S_0 = qD_a \frac{n_0}{W} \tag{8}$$

where J_{sc} is the short circuit current density, n_0 is the front-surface electron concentration and currents were replaced by current densities in view of the effectively planar geometry of the cell as a result of the perpendicular direction of the current. A few iterations are necessary to determine the short-circuit current and the front-surface carrier concentration.

It becomes immediately apparent that, if the thickness of the cell, W, increases, the front-surface carrier concentration, n_0, increases, which, in turn, results in an increased bulk and front-surface recombination current.

In open-circuit condition, we can consider that the electron and hole concentrations are constant throughout the device. The open-circuit voltage is given by:

$$V_{oc} = 2\frac{k_B T}{q}\ln\left(\frac{n}{n_i}\right) \tag{9}$$

after solving the following equation:

$$J_{ph} = \frac{qnW}{\tau_B} + qn^3 C_a W + qnS_0 + qnS_{back}(1 - A_n - A_p) + \frac{n^2}{n_i^2}(A_n J_{0n} + A_p J_{0p}) \tag{10}$$

where J_{on} and J_{op} are the saturation current densities at the n and p junctions, A_n and A_p are the n-type and p-type emitter coverage fractions respectively, and S_{back} is the backside surface recombination velocity.

The maximum power point and efficiency of the solar cell can be determined the same way, considering that the backside carrier concentration is given by Equation (7) and that the carrier concentration is still linearly distributed from front to back. Equation (3) becomes:

$$\begin{aligned} J_{mp} = J_{ph} - \frac{qn_{avg}W}{\tau_B} - q\int_0^W n(x)^3 C_a dx - qn_0 S_0 \\ - qn_{back}S_{back}(1 - A_n - A_p) - \frac{n_{back}^2}{n_i^2}(A_n J_{0p} + A_p J_{0p}) = qD_a \frac{n_0 - n_{back}}{W} \end{aligned} \tag{11}$$

where $n_{avg} = (n_0 + n_{back})/2$ is the average carrier concentration and

$$n(x) = n_{back} + (n_0 - n_{back})\left(1 - \frac{x}{W}\right) \tag{12}$$

Several iterations are necessary to reach the solution.

This is a very simple way to analyse the IBC or PC solar cells. It allows a quick determination of the carrier concentration in the device and an analysis of the different recombination mechanisms. Note that Equation (1) must be used for the front-side recombination current expression in FSF or TJ solar cells. For a more precise modelling, including 3D effects at the backside of the solar cell, the reader is referred to the Swanson model [9, 10].

4 Perimeter and Edge Recombination

So far, we have not considered the edge recombination. It has been recently demonstrated that, in most high-efficiency silicon solar cells, the dominant recombination mechanism is a recombination current at the unpassivated surface at the edge of the silicon die [13]. Two cases need to be considered here:

- aperture illuminated solar cells (e.g. cells for Fresnel lens modules, Figure 2).
- totally illuminated solar cells (e.g. cells for dense array receivers, dish and thermo-photovoltaic (TPV) applications, Figure 3).

In order to reduced the edge recombination, the aperture illuminated IBC solar cells must have its active area as far as possible from the edge of the silicon die, in theory at a distance of least three times the ambipolar diffusion length at the considered carrier concentration. In practice, economical considerations prevent manufacturers to increase this distance too much and a typical distance between the edge of the silicon die and the nearest emitter at the backside of the cell is 500 μm. For totally illuminated solar cells, there is an optimal distance that can be calculated as explained in [13]. The width of the border region is optimal when the illuminated border region generates just enough current to supply the recombination current at the edge of the silicon die. A wider or narrower border region than the optimal width would result in a lower efficiency. If d is the width of the border region, P the cell perimeter, and n the average carrier density at the middle of the cell, at the maximum power point (V_m, I_m) and at the considered concentration ration, the current generated by the border region is:

$$I_{border} = dPJ_{sc}$$

and the edge recombination current is:

$$I_{edge} = qPWD_a n/d$$

The border width is optimal when:

$$I_{border} = I_{edge}$$

and

$$d = \sqrt{\frac{qWD_a n}{J_{sc}}} \tag{13}$$

For a fixed geometry and cell thickness, the carrier concentration and short-circuit current are more or less proportional to the concentration ratio. Therefore, the optimal border width is generally independent of the concentration ratio. However, since the average carrier concentration increases with the thickness of the cell, the optimal border width is roughly proportional to the thickness of the cell. For a typical IBC solar cell for dense array application at 400× and with a thickness of 100 μm ($n \approx 10^{17}\text{cm}^{-3}$), the optimal border width is about 135 μm.

Equation (13) is valid if the edge is unpassivated such as in silicon solar cells diced with a dicing saw. New techniques to passivate the edges of solar cells are needed but, so far, there has been no satisfactory development in low-temperature passivation of silicon surfaces.

5 Manufacturing Process for Backside Contact Solar Cells

The typical process flow to manufacture IBC solar cells is presented in Figure 8 although actual processes may significantly differ in practice. A typical process requires 6 photolithography steps. Additional photolithography steps are required for:

- inverted pyramid texturisation instead of random texture,
- local thinning instead of uniform wafer thinning.

6 Stability of Backside Contact Cells

In the same way as many other high-efficiency silicon solar cells, the IBC cells are subject to efficiency degradation. If float-zone (FZ) wafers are used, the degradation is limited to the silicon-silicon dioxide interface [1, 14–16]. The degradation of the interface could be due to the loss of hydrogen atoms passivating the dangling bonds at the silicon-silicon dioxide interface, or the creation of new interface states. The degradation of the interface is manifested by:

- an increase of the surface recombination velocity, which, in turn, results in a reduction of the short-circuit current over the entire range of concentration ratio or,
- by an increase of the front emitter current Jo which results in an increase of the sub-linearity (the cell responsivity decreases as the concentration ratio increases) if the front surface is lightly doped or inverted due to charges in the dielectric layer.

Both mechanisms will result in a significant decrease in efficiency. The degradation has been observed so far due to the following individual or combined conditions:

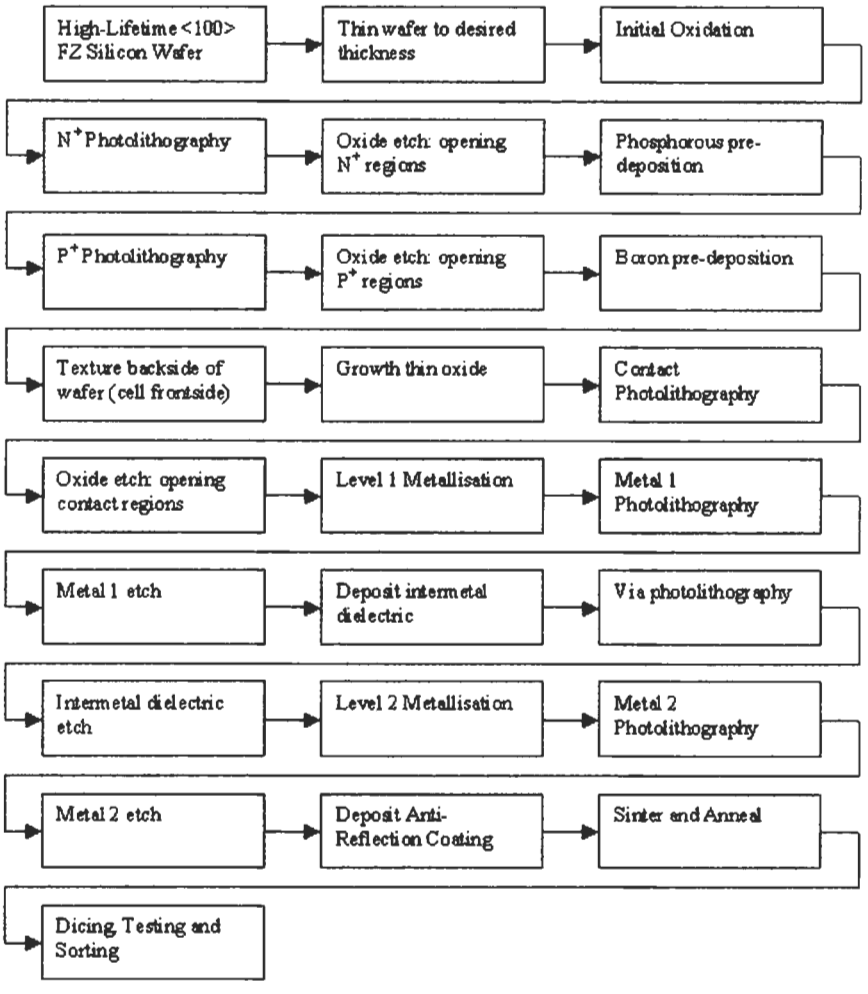

Figure 8 Process flow of manufacturing IBC solar cells.

- UV light, which creates hot electrons that can overcome the potential barrier at the silicon-silicon dioxide interface and create new interface states,
- elevated temperature (> 100°C), which allows hydrogen atoms to escape from the interface,
- mechanical stress.

It is also assumed that the following conditions enhance the degradation:

- highly concentrated sunlight which creates a large concentration of carriers at the surface of the solar cell;

- the presence of moisture;
- the presence of atomic hydrogen which could break an existing Si-H bond to form a hydrogen molecule H_2.

There is still much research to be done to understand the degradation mechanisms and to find a solution to this issue.

The easiest way to prevent the strong influence of the degradation of the surface recombination velocity to solar cell efficiency is to isolate the surface from the rest of the cell with FSF or a floating tandem junction. Unfortunately, although it makes the cell more stable, the front side emitter has a significant impact on the sub-linearity of the solar cell [1, 15], which makes this solution unsuitable for concentration application. In any case, the front emitter must be lightly doped in such way that the front emitter J_o is kept as low as possible. Indeed, we can see from Equation (1) that the greater the front emitter J_o, the more significant the sub-linearity of the solar cell will be.

There are other ways to ensure stability of the IBC solar cells:

- It is very important that, during the solar cell fabrication, the front passivating oxide layer is grown with the smallest interface state density. 1,1,1-Trichloroethane (TCA), dichloroethane (DCA), trichloroethylene (TCE) or HCl oxide growth, as well as an aluminium anneal, should be avoided as they have been recognised as giving very unstable Si–SiO_2 interfaces [16, 17].
- UV light with wavelength below 400 nm should be filtered from the solar spectrum, either at the solar cell level or at the concentrator module level. For example, the anti-reflection coating (ARC) can include a UV filter such as TiO_2 or a very thin polysilicon layer [14, 16].
- The front surface of the solar cell should be coated with a thin layer of silicon nitride (as part of the ARC), or another material, hopefully compatible with the ARC, forming a great hydrogen and moisture diffusion barrier (for example, a very thin amorphous silicon or polysilicon layer) [16].

7 Toward 30% Efficiency Silicon Cells

In 1985, Gray and Schwartz presented a paper entitled 'Why don't we have a 30% efficient silicon solar cell?' [18]. At that time, the highest reported efficiency for silicon solar cell was 22% under concentrated sunlight. In that paper, the authors concluded that 30% efficiency would be attainable with a silicon solar cell if:

- good light trapping was developed which does not degrade the open-circuit voltage of the solar cell,
- the contact and grid series resistance could be reduced enough to allow for high concentration ratio,
- the current crowding effects are reduced by a judicious design,

- a novel heterojunction or heteroface contact with small contact resistance and low emitter saturation current was developed.

A few years later, the first three steps to attain the 30% efficiency target had been addressed and resolved: the PC solar cell with a thin substrate and long carrier lifetime, with a textured and passivated front surface, proved to be the best design for high efficiency concentrator solar cell [19, 20]. In 1989, the highest reported efficiency for silicon PC solar cell was 28.3% [21]. The same year, Swanson responded to Gray's paper in a publication entitled "Why we will have a 30% efficient silicon solar cell" [22] where he demonstrates that all the pieces are now in place to fabricate a 30% efficient silicon solar cell. The last milestone to reach the 30% breakthrough, namely the development of polysilicon emitters with a low contact resistance, and low emitter saturation currents had just been demonstrated at Stanford [23, 24]. Swanson announced: Within one year, cells will be reported with efficiency in excess of 30% [22].

We believe that 30% efficient silicon solar cells are possible in a manufacturing environment. In order to achieve this goal, polysilicon or heterojunction emitter technology needs to be implemented, along with several other improvements to the existing technology (thinner cells, improved light trapping, and reduced dimension geometries).

8 How to Improve the Efficiency of Backside Contact Solar Cells

Campbell and Green [25] discussed the efficiency limit of silicon solar cells under concentrated sunlight. They showed that the limit of efficiency for a silicon cell is between 30 and 35%. These very high efficiencies have never been demonstrated so far with a single-junction silicon solar cell. Commercially available PC concentrator cells have efficiencies around 26.5%. In order to reach such high efficiencies, the recombination mechanisms such as trap-assisted SRH recombination, in the bulk or at the surface, and emitter recombination must be negligible compared to Auger recombination. The Auger recombination is intrinsic to the material and, for example, cannot be improved by using a purer starting material or a cleaner fabrication process. Therefore, the only way to

Table 2 Strategy for 30% efficient backside contact solar cells.

Step	Parameter	Target value	Acceptable value	Unit
1	Emitter J_o	3×10^{-14}	5×10^{-14}	A/cm^2
2	Emitter contact resistance	10^{-6}	10^{-4}	Ω cm^2
3	Cell thickness with manufacturable yield	30	80	μm
4	Light trapping: number of passes for long wavelengths	50	35	passes
5	Unit cell geometry	25	40	μm
6	Total series resistance	5×10^{-4}	10^{-3}	Ω cm^2

reduce the Auger recombination rate inside the cell is to reduce its thickness. However, using a very thin silicon solar cell requires the use of a very effective scheme for light trapping. For example, Campbell and Green [25] suggest that the optimum cell would be less than 1 μm thick and could reach 36–37% under concentration.

By comparison, the recombination in the PC solar cell at 250× (25 W/cm^2) is almost equally dominated by emitter (40%) and Auger (40%) recombination. The surface and bulk SRH recombination represents less than 20% of the overall recombination rate. In the PC design, the emitter coverage fraction has already been reduced to the minimum acceptable, and the only way to further reduce the emitter recombination rate is to reduce the emitter saturation current density Jo. Therefore, in order to reach 30% or greater efficiency, the following strategy needs to be used:

1. Reduce the emitter recombination by reducing the emitter saturation current density from 2×10^{-13} to 5×10^{-14} A/cm^2. Polysilicon heterojunction emitters with less than 5×10^{-14} A/cm^2 as saturation current density have already been demonstrated [23, 24].
2. Demonstrate low contact resistance between the bulk and the emitters. A desired value for the contact resistance between bulk and emitter is less than $10^{-5}\,\Omega\,\text{cm}^2$.
3. Reduce the cell thickness in order to reduce the Auger recombination rate. For a practical concentrator for which the angle of incidence of the light to the cell is between 0 and 30 degrees, the optimal thickness is about 30 μm [25]. This is very difficult to achieve in a manufacturing environment. Manufacturing techniques, such as local thinning, need to be implemented.
4. Improve light trapping by designing new textured surfaces on both sides of the cell.
5. Reduce the unit cell geometry down to a dimension equal or smaller than the thickness of the cell.
6. Reduce the external series resistance (metal and interconnect).

8.1 Reduce Emitter Saturation Current Density

The saturation current density of an emitter J_o represents the sum of all the recombination mechanisms inside the emitter. It includes the SRH, surface, contact and Auger recombination mechanisms, as well as heavy doping effects such as band gap narrowing. The best diffused emitter J_o that can be achieved is around 2×10^{-14} A/cm^2. However, such an emitter is very transparent which means that, if a metal contacts it, its saturation current density dramatically increases about 100 fold. For contacting PC solar cell, the emitter must be opaque and the best saturation current density of such emitter is around 2×10^{-13} A/cm^2.

An ideal emitter for silicon should be transparent to majority carriers and a mirror for minority carriers. Therefore, it should have a wide band gap such that

an additional potential barrier will appear in the minority band when it is doped (see Figure 9). Although there are many semiconductors with a larger band gap than silicon, so far none of the large band gap materials have proven to be ideal for contacting silicon. Indeed, the potential barrier at the emitter heterojunction blocks the minority carriers, they still can recombine at the interface due to the presence of interface traps.

There are only two materials that were reported to have low J_o: polysilicon emitters and semi-insulating polysilicon emitters (SIPOS), both used with an interfacial thin oxide layer [23, 24, 26, 27]. However, some very promising results have recently been reported on non-concentrator solar cells with amorphous silicon emitters [28] that do not require an interfacial thin oxide to block the minority carriers.

8.2 Demonstrate Low Contact Resistance

The growth of a thin (10 to 20 Å) interfacial layer of silicon dioxide is critical to obtain low emitter saturation current density with polysilicon. However, in order to achieve a low contact resistance, it is necessary to anneal the polysilicon emitter to break up the oxide layer on about 1% of the contact area [23]. The trade-off between J_o and a high contact resistance is highly dependent on the oxide thickness and the anneal (or breakup) step.

8.3 Reduce the Cell Thickness

Once the emitter recombination mechanism has been reduced, it is possible to reduce the Auger recombination rate by using a thinner substrate for the solar cell. Solar cells made on 100 μm thick wafers are can be manufactured in large volumes but thinner cells present a real challenge for manufacturing. Since both sides of the cells must be processed for texturing, passivation and anti-reflection coating, the thinning of the wafers cannot just be done by lapping the wafers at the end of the process. Solar cells of 30–80 μm thickness must be fabricated on locally thinned substrates.

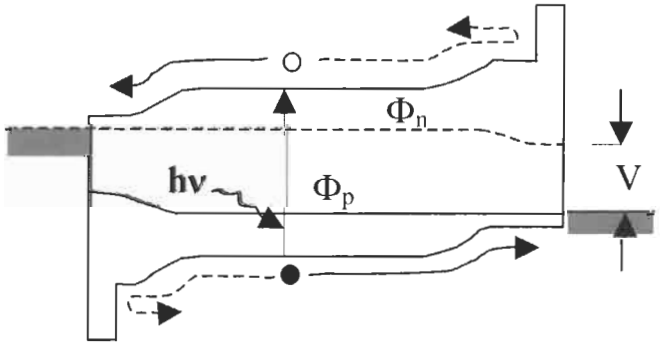

Figure 9 Band diagram of a p–i–n solar cell with heterojunction emitters.

8.4 Improve Light Trapping

When very thin silicon solar cells are designed, the light trapping property of the cells becomes a significant factor for the efficiency. Present cells have only one-side texturisation. Unfortunately, this is not enough for cells thinner than 100 μm. In this case, a double side texturisation or perpendicular grooving must be designed in order to insure good light trapping. In current PC solar cells, the analysis of the internal quantum efficiency near the edge of the band gap shows that the effective number of passes for long wavelength light is greater than 30 [1]. The light trapping can be improved with double side texture, perpendicular slats, or parquet grooves in order to attain up to 50 passes of the light.

8.5 Shrink Geometries

The present PC solar cells have a significant current crowding loss and large internal series resistance accounting for about 0.002 Ω cm^2 which represents about 3% power loss at 25 W/cm^2 or 250×. The unit cell dimension should be reduced from the current 140 μm to 40 μm, and if possible to 25 μm. The metallisation and inter-metal dielectric technology usually prevents the shrinking of the unit cell. In order to be able to shrink the unit-cell dimension to 40 or even 25 μm, a state-of-the-art plasma etching process for the metal, as well as a plasma-enhanced chemical vapour deposition (PECVD) SiO_2-based dielectric as inter-metal dielectric layer must be adopted.

8.6 Reduce Series Resistance

Shrinking the geometries of the unit cell in order to reduce the internal series resistance may have a negative effect on the external series resistance. This problem is due to the fact that, if the gap between metal lines is kept constant, the metal coverage fraction decreases with decreasing the dimensions of the unit cell. A new metallisation design, similar to what has been proposed in previous papers [4, 5], must be implemented in order to reduce the series resistance. As in step 8.5, the new metal design requires a plasma etching process for metal and a SiO_2-based dielectric layer. The target is to reduce the total series resistance to less than 0.001 Ω cm^2, or about a 2.5% power loss at 500× concentration.

Table 3 Comparison of performance of a commercial PC solar cell (HECO335 from SunPower Corporation) cell with the projected new high-performance cell at 100× and 275× (AM1.5D, 10 and 27.5 W/cm^2, T_c = 25°C). The values at 275× concentration are in brackets.

Parameter	Commercially available PC solar cell	New high-performance cell	Unit
Responsivity	0.403 (0.379)	0.416 (0.416)	A/W
Open-circuit voltage	807 (825)	826 (845)	mV
Fill factor	82.6 (79)	87 (85.9)	%
Efficiency	26.8 (24.7)	29.9 (30.2)	%

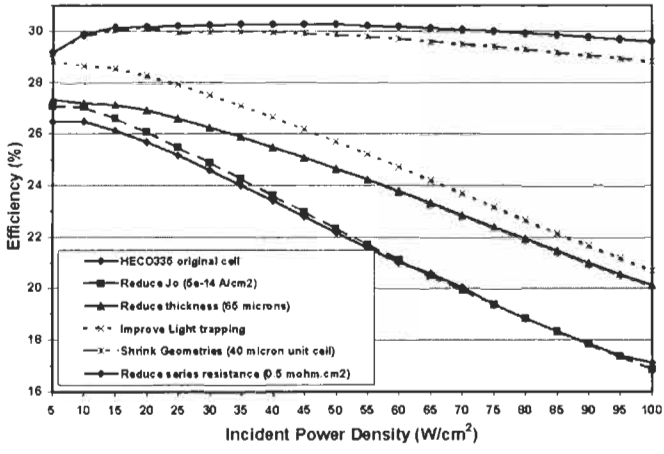

Figure 10 Efficiency (AM1.5D, 25°C) of the point-contact silicon solar cell vs. incident power density after each step of this strategy.

8.7 Target Performance

Table 3 shows the target performance of a 30% efficient silicon solar cell compared to the commercially available point-contact solar cells. Figure 10 shows the improvement in efficiency based on the above strategy. Of course, the full benefit of the polysilicon emitter with low J_o is observed when all the other improvements (thinner cells, improved light trapping and shrunk geometries) are in place.

9 Conclusions

Interdigitated back contact and point-contact silicon solar cells have demonstrated to be the most efficient and the most suitable silicon solar cells for high-concentration applications. Commercially available PC solar cells have demonstrated efficiencies up to 26.8% (at 10 W/cm^2, AM1.5D, 25°C) in large volume production. This chapter has described the structure of IBC, FSF, TJ and PC cells, as well as the process to fabricate them. A simple model for the simulation, optimisation and analysis of the different recombination mechanisms in concentrator IBC cells has been presented. Finally, we have presented a plan for the development of 30% efficiency concentrator cells.

Acknowledgements

The author would like to thank A. Terao and S. Daroczi of SunPower Corporation, and J. Lasich of Solar Systems Pty Ltd for supplying pictures of the point-contact solar cells and the concentrator PV systems.

References

[1] Verlinden, P.J., Swanson, R.M., Crane, R.A., Wickham K. and Perkins, J. 1995. A 26.8% Efficient Concentrator, Point-Contact Solar Cell, *Proc. 13th European Photovoltaic Solar Energy Conf.*, Nice, pp. 1582–1585.

[2] Sinton R.A. and Swanson, R.M. 1992. Development Efforts on Silicon Solar Cells, Final Report, Electric Power Research Institute, Palo Alto, CA, February, pp. 2–44

[3] Swanson, R.M., Sinton, R.A., Midkiff, N. and Kane, D.E. 1988. Simplified Designs for High-Efficiency Concentrator Solar Cells, *Sandia Report, SAND88-0522*, Sandia National Laboratories, Albuquerque, NM, July.

[4] Verlinden, P.J., Swanson, R.M., Sinton, R.A. and Kane, D.E. 1988. Multilevel Metallization for Large Area Point-Contact Solar Cells, *Proc. 20th IEEE Photovoltaic Specialists Conf.*, Las Vegas, pp. 532–537.

[5] Verlinden, P.J., Sinton, R.A. and Swanson, R.M. 1988. High-Efficiency Large-Area Back Contact Concentrator Solar Cells with a Multilevel Interconnection, *Int. Journal of Solar Energy*, Vol. 6, pp. 347–365.

[6] Verlinden, P.J., Terao, A., Smith, D.D., McIntosh, K., Swanson, R.M., Ganakas, G. and Lasich, J. 2001. Will We Have a 20%-efficient (PTC) Photovoltaic System?, *Proc. 17th European Photovoltaic Solar Energy Conf.*, Munich, pp. 385–390.

[7] Schwartz, R.J. and Lammert, M.D. 1975. *IEEE International Electron Devices Meeting*, Washington DC, pp.350–351.

[8] Lammert, M.D. and Schwartz, R.J. 1977. *IEEE Trans. Electron Devices*, Vol. ED-24(4), pp.337–342.

[9] Swanson, R.M. 1985 Point Contact Silicon Solar Cells, Theory and Modeling, *Proc. 18th IEEE Photovoltaic Specialist Conf.*, Las Vegas, pp. 604–610.

[10] Swanson, R.M. 1988. Point Contact Solar Cells, Modeling and Experiment, *Solar Cells*, Vol. 7(1), pp.85–118.

[11] Sinton, R.A. 1987. Device Physics and Characterization of Silicon Point-Contact Solar Cells, Ph.D. Thesis, Stanford University, Stanford, CA.

[12] Sinton, R.A. and Swanson, R.M. 1987. Recombination in Highly Injected Silicon, *IEEE Trans. Electron Devices*, ED-34(6), p. 1380.

[13] Sinton, R.A., Verlinden, P.J., Swanson, R.M., Crane, R.A., Wickham K. and Perkins, J. 1995. Improvements in Silicon Backside-Contact Solar Cells for High-Value One-Sun Applications, *Proc. 13th European Photovoltaic Solar Energy Conf.*, Nice, pp.1586–1589.

[14] Gruenbaum, P.E., Gan, J.Y., King, R.R. and Swanson, R.M. 1990. Stable Passivations for High-Efficiency Silicon Solar Cells, *Proc. 21st IEEE Photovoltaic Specialists Conf.*, Kissimmee, pp. 317–322.

[15] Verlinden, P.J., Swanson, R.M., Sinton, R.A., Crane, R.A., Tilford, C., Perkins, J. and Garrison, G. 1993. High-Efficiency Point-Contact Silicon Solar Cells for Fresnel Lens Concentrator Modules, *Proc. 23rd IEEE Photovoltaic Specialists Conf.*, Louisville, pp. 58–64.

[16] Gruenbaum, P.E. 1990. Photoinjected Hot-Electron Damage at the Silicon/Silicon Dioxide Interface in Point-Contact Solar Cells, Stanford University, Stanford.

[17] Cudzinovic, M., Pass, T., Terao, A., Verlinden, P.J. and Swanson, R.M. 2000. Degradation of Surface Quality due to Anti-Reflection Coating Deposition on Silicon Solar Cells, *Proc. 28th IEEE Photovoltaic Specialists Conf.*, Anchorage, pp. 295–298.

[18] Gray, J.L. and Schwartz, R.J. 1985. Why don't we have a 30% efficient Silicon Solar Cell?, *Proc. 18th IEEE Photovoltaic Specialists Conf.*, Las Vegas, pp. 568–572.

[19] Verlinden, P., Van de Wiele, F., Stehelin, G. and David, J.P. 1986. An Interdigitated Back Contact Solar Cell with High Efficiency under Concentrated Sunlight, *Proc. 7th European Photovoltaic Solar Energy Conf.*, Seville, pp. 885–889.

[20] Sinton, R.A. et al., 1986. 27.5 Percent Silicon Concentrator Solar Cells, *IEEE Electron Device Letters*, Vol. EDL-7(10), pp. 567–569.

[21] Sinton, R.A. and Swanson, R.M. 1987. An Optimization study of Si Point-Contact Concentrator Solar Cells, *Proc. 19th IEEE Photovoltaic Specialists Conf.*, New Orleans, pp. 1201–1208.

[22] Swanson, R.M. 1989. Why we will have a 30% efficient Silicon Solar Cell, *Proc. 4th International Photovoltaic Science and Engineering Conf.*, Sydney, pp. 573–580.

[23] Gan, J.Y. 1990. Polysilicon Emitters for Silicon Concentrator Solar Cells, Ph.D. Thesis, Stanford University, Stanford.

[24] Gan, J.Y. and Swanson, R.M. 1990. Polysilicon Emitters for Silicon Concentrator Solar Cells, *Proc. 21st IEEE Photovoltaic Specialists Conf.*, Kissimmee, pp. 245–250.

[25] Campbell, P. and Green, M. 1986. The Limiting Efficiency of Silicon Solar Cells under Concentrated Sunlight, *IEEE Trans. Electron Devices*, Vol. ED-33(2), pp. 234–239.

[26] Christel, L.A. 1987. Polysilicon-Contacted P+ Emitter for Silicon Solar Cell Applications, *Sandia National Laboratories Report SAND87-7021*.

[27] Kwark, Y.H. and Swanson, R.M. 1985. SIPOS Heterojunction Contacts to Silicon, *Sandia National Laboratories Report SAND85-7022*.

[28] Sakata, H., Kawamoto, K., Taguchi, M., Baba, T., Tsuge, S., Uchihashi, K., Nakamura, N. and Kiyama, S. 2000. 20.1% Highest Efficiency Large Area (101 cm^2) HIT Cell, *Proc. 28th IEEE Photovoltaic Specialists Conf.*, Anchorage, pp. 7–12.

Part IIe

Organic and Dye Sensitised Cells

Photoelectrochemical Solar Cells

A. J. McEvoy, Institute for Molecular and Biological Chemistry, Faculty of Basic Sciences, Ecole Polytechnique Fédérale de Lausanne, Switzerland

1 Origins of Photoelectrochemistry

It has already been made evident in previous chapters that the photovoltaic effect results from a non-ohmic contact between two phases with different conduction mechanisms, typically a metal and a semiconductor to provide a Schottky barrier, or two semiconductors of opposite carrier polarity for a p–n junction device. In each case the excitation of the charge carrier pair, a conduction band electron and the positive hole in the valence band, is consequent on the absorption of a photon by the semiconductor, the energy of the photon being greater than the bandgap. The contact then serves to separate the photoexcited charge carriers, the electrons and holes, so that a potential difference can be maintained across it under illumination and a current can flow in an external circuit. In all of these cases, the materials are solids and the conduction is by electronic processes, the mobility of holes or electrons. These solid-state semiconductor-based devices dominate photovoltaic science and technology. However, it should be remembered that the first observation of the photovoltaic effect by Becquerel almost 200 years ago [1] was of the asymmetry of behaviour of two identical electrodes, one illuminated, both immersed in an a liquid electrolyte. We can now recognise the material he used, a silver halide, as a semiconductor, and the Becquerel device would at present be classified as a photoelectrochemical cell. The contact of the semiconductor with the electrolyte, in which the conduction mechanism is the mobility of ions rather than of electrons or holes, therefore forms a photoactive junction functionally equivalent to those later discovered for solid-state photovoltaic devices. There has been the suggestion, therefore, given the ease of formation of semiconductor–electrolyte junctions, that they would offer a low-cost practical alternative in the field of solar energy conversion.

In the conventional solid-state cell the Fermi levels of the two materials forming the junction equilibrate in darkness, this being associated with a displacement of majority carriers within the semiconductor and the establishment of a depletion layer near the interface. Where the contacting phase is a redox electrolyte in a photoelectrochemical system, there is an analogy with the Fermi level of a Schottky contact metal. The redox electrolyte is so named because ions of the same species but different oxidation states are present, the more reduced (red-) being convertible to an oxidised state (-ox) by the acquisition of a positive charge, at an anodic electrode for example. The process is reversible at a cathode. The potential at which no current passes at a reversible electrode, able to donate or acquire charge in contact with a given redox system, is the redox potential, at which electrode and both ionic components are at equilibrium. In the photoelectrochemical system it is the redox potential of the ions in the electrolyte which is functionally equivalent to the Fermi level of the photovoltaic junction materials. The range of potential associated with the oxidised component, more positively charged and therefore depleted in electrons, corresponds to the conduction band of a semiconductor, while the filled electron states of the valence band find their analogue in potential distribution of the reduced component. As with the permitted electron energy levels in condensed

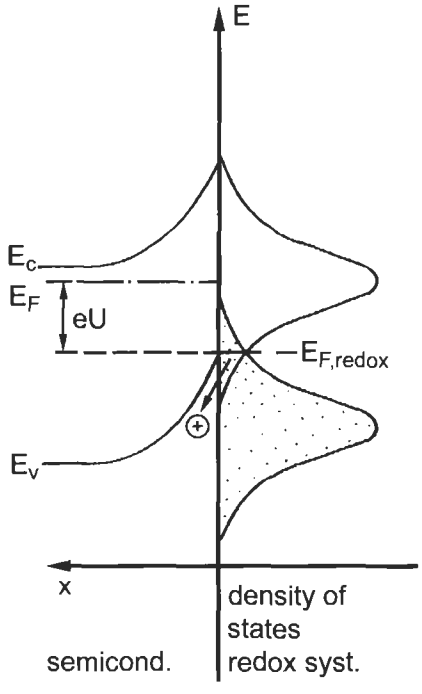

Figure 1 In darkness the Fermi level of the semiconductor equilibrates with the redox level of the electrolyte: under illumination the electron quasi-Fermi level is raised, giving rise to a photovoltage.

matter, these ionic species also form bands and with the ionic levels dispersed due to effects such as solvation, their interaction with the electrolyte environment gives rise to a reorientation energy which may be of the order of 1 eV.

Under illumination, as in the case of a solid state junction, photons of energy greater than the bandgap of the semiconductor are absorbed, their energy then serving to excite an electron to the conduction band, leaving a mobile positive hole in the valence band. The gradient of the bands then orients the separation of the charge carrier pairs, the hole being directed towards the electrolyte interface in the case of an n-type semiconductor, where it is available to oxidise an ion in the reduced state of the redox system. The electrode, here functioning as a photoanode since an oxidation reaction takes place on its surface, then delivers the accumulated electrons through an ohmic contact to an external circuit, whence they are returned to the electrochemical system though a counterelectrode, normally metallic and therefore photoinert. On the counterelectrode, the cathode surface in the present example, a reduction reaction takes place, thereby regenerating the electrolyte whose overall redox composition remains unaltered. The photogeneration of the charge carriers of course splits the Fermi level into quasi-Fermi levels representative of the occupation of states by holes and electrons respectively, the extent of the splitting representing the generation of a photovoltage between the electrolyte redox level (and the counterelectrode) and

the ohmic collector contact to the photoanode. The parallel between the photovoltaic device and photoelectrochemical energy conversion by a regenerative cell is therefore complete, the system remaining invariant while a part of the radiant energy of the absorbed incident light appears as electrical energy in the external circuit. Figure 1 shows schematically the relationship on the energy scale of the factors relevant to the photoelectrochemical process, based on this model as developed by Gerischer [2]. A 'mirror image' process can also be presented for a regenerative cell with a p-type semiconductor photocathode operated with a metal anode as oxidising counterelectrode.

2 Photoelectrolysis

Since in a photoelectrochemical cell a photoactive electrode is effectively integrated into an electrolytic cell, it is not a requirement that a reversible redox process constitute the electrochemical activity. Otherwise stated, the cathodic reaction is not necessarily the reverse reduction of the oxidation taking place at the anode. The electrochemistry can therefore also give rise to a photoelectrolytic or a photosynthetic effect. For example, the redox system of hydrogen oxidation to water in an acid environment is commonly accepted as the reference level in the electrochemical scale, with respect to which the electrolytic evolution of oxygen from water takes place at +1.23 V. If the valence band edge is more positive than this level, the photogenerated holes (h^+) may transfer directly to an aqueous electrolyte for the reaction:

$$2H_2O + 4h^+ \Longleftrightarrow O_2 + 4H^+ \tag{1}$$

With a sufficiently wide band-gap, the selected semiconductor can also deliver electrons via the external circuit to the metal cathode, whose Fermi level can then lie negative of the hydrogen evolution potential, and which can then sustain the reaction:

$$2H^+ + 2e^- \Longleftrightarrow H_2 \tag{2}$$

An efficient photoelectrolytic system of this type as been the 'philosopher's stone' of electrochemists since the first report of photoassisted water splitting into its component elements by Fujishima and Honda some 30 years ago [3] using a titania electrode. The necessity of such a wide bandgap semiconductor to obtain photoelectrolysis points up the two major problems in photoelectrochemical materials selection, namely efficiency and stability. The band gap of titania is over 3 eV, so the material generates charge carrier pairs only by the absorption of ultraviolet light, being insensitive in the visible spectrum. The efficiency of solar energy conversion is therefore low, since as is already known, the optimum spectral matching bandgap is 1.4 eV. As Memming [4] pointed out also, it is relatively easy to obtain the hydrogen evolution reaction at a chosen electrocatalytic counterelectrode; the oxygen evolution process however, as is

evident from Equation (1) is a multistep process for which the photoanode surfaces seldom offer a catalytic reaction route with correspondingly fast kinetics. For those semiconductors more favourable catalytically to oxygen evolution, such as tungsten trioxide, an external bias voltage may be required to displace the Fermi level negative of the hydrogen evolution potential, a voltage which may be supplied by an auxiliary photovoltaic device [5].

Given the overpotentials involved, it is not surprising that alternative hole consumption processes are offered, the most significant of which is the anodic photocorrosion of the semiconductor itself. A typical example is a cadmium chalcogenide, which would otherwise offer appropriate valence and conduction band edge levels to sustain photoelectrolysis. For instance, cadmium sulfide with a badgap of 2.2 eV is not ideal but could still be relatively efficient (Figure 2). Instead in its photoanodic reaction cadmium ions dissolve in the electrolyte and the surface becomes sulphur coated:

$$CdS + 2h^{+} \Longleftrightarrow Cd^{2+} + S \tag{3}$$

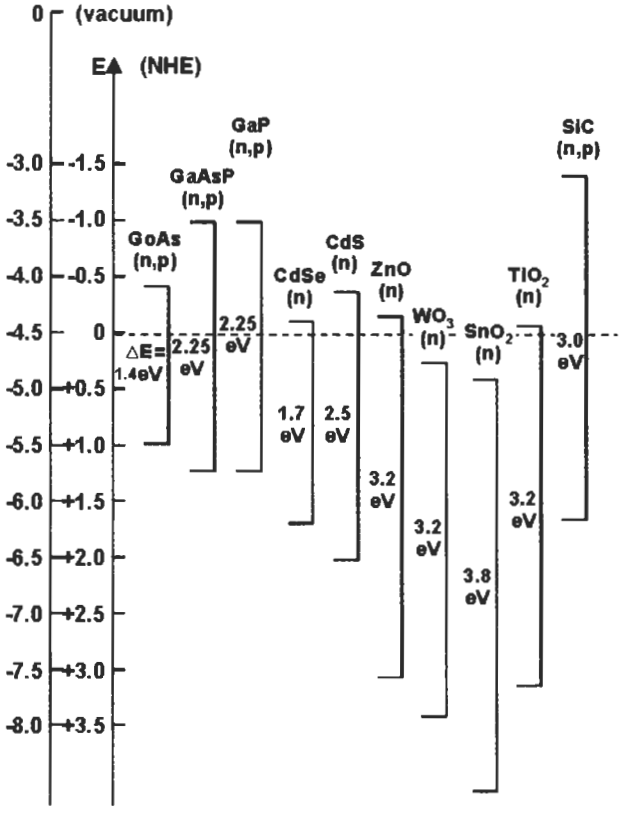

Figure 2 Bandgaps and band edge energies of compound semiconductors for photoelectrochemical applications. E_c^s is the conduction band edge at the semiconductor–electrolyte interface

The chemical stability of a compound against an oxidative photoprocess is therefore related to its bandgap, a reaction similar to Equation (3) being promoted for the narrower-bandgap materials. This is a process in competition even with the redox reaction in regenerative cells, so that while a redox mechanism may relatively stabilise a narrow-gap semiconductor, it is never totally inert against photocorrosion. Intensive research over the past three decades has led to an inescapable conclusion: stability is attained only at the cost of a wide band gap with insensitivity to the greater part of the solar spectrum and therefore low energy conversion efficiency. This recalcitrant problem has impeded the establishment of a credible electrochemical photovoltaic energy conversion system over this period; the resolution of this dilemma lies in the separation of light absorption from the charge separation function of the semiconductor, by sub-bandgap sensitisation to visible light of a wide bandgap stable material through visible light absorption in an electroactive dye.

3 Photoelectrochemistry, Photography and Sensitisation

The choice of a silver halide as the electrode material in Becquerel's experiments reflects the rapid growth in knowledge of photochemical effects at that time. Biot [6] was aware of the use of paper sensitised by silver chloride, being contemporary with the introduction of photography by Daguerre and Fox-Talbot. Although the art of formulating photographic emulsions only became a science a century later with the theoretical analysis of the process by Gurney and Mott in 1938 [7], there was constant empirical progress in extending the overall sensitivity of photographic emulsions, which had been particularly deficient for mid-spectral visible light and towards the red. The early 'orthochromic' materials had limited capability to register scenes observed in colour realistically on a grey scale due to the semiconductor nature of the silver halides with their band gaps between 2.7 and 3.2 eV and for which the photoresponse is negligible for wavelengths longer than 460 nm. It was noted, for example, that the origin of the gelatin used as the support medium for the alkali halide grains significantly modified the film spectral sensitivity. Only in the twentieth century was it demonstrated that an organosulphur compound present in calf skin gelatin was responsible [8], and which is now known to have its effect by inducing a superficial nanostructure of silver sulphide on each grain. This can now be recognised as the first sensitisation at a semiconductor heterojunction, silver sulphide to halide. Even more significant was the work of Vogel, professor of 'photochemistry, spectroscopy and photography' in Berlin. In 1873 [9] he established empirically that silver halide emulsions could be sensitised to red and even infrared light by suitably chosen dyes, thereby making possible the modern 'panchromatic' broad-spectrum black and white film, and more recently with the use of spectrally-selective dyes, colour photography.

The concept of dye enhancement was carried over already by 1887 from photography to the photoelectric effect by Moser [10] using the dye erythrosine, again on silver halide electrodes, and confirmed by Rigollot in 1893 [11]. (It

is, incidentally, curious to note that Moser, writing before the formulation of the Einstein theory of the photoelectric effect, records his observations of dye enhancement in terms of potential (volts) rather than the more fundamental current (amps), despite referring in his title to a 'strengthened photoelectric *current* through optical sensitising'.) This parallel between sensitisation in photography and in photoelectrochemistry, both of which are charge transfer processes, still seems to come as a surprise to successive generations of chemists [12]. It continues to apply to such recent observations as two-electron sensitisation [13] where the photoexcited dye after transferring one electron to the halide, reacts in turn with a reducing agent in the emulsion producing a second charge-transfer step; such current-enhancement reactions have been investigated in photoelectrochemistry since 1984 [14].

That the same dyes were particularly effective for both processes was recognised among others by Namba and Hishiki [15] at the 1964 International Conference on Photosensitisation in Solids in Chicago, a seminal event in the history of dyes in the photosciences. It was also recognised there that the dye should be adsorbed on the semiconductor surface in a closely packed monolayer for maximum sensitisation efficiency [16]. On that occasion the theoretical understanding of the processes was clarified, since until then it was still disputed

Notiz über Verstärkung photoelektrischer Ströme durch optische Sensibilisirung.[1]

Von Dr. James Moser.

(Aus dem physikalisch-chemischen Laboratorium der Wiener Universität.

(Vorgelegt in der Sitzung am 23. Juni 1887.)

Ich erlaube mir mitzutheilen, dass ich die von Herrn E. Becquerel entdeckten photoelektrischen Ströme erheblich dadurch verstärken konnte, dass ich die beiden chlorirten, jodirten oder bromirten Silberplatten in einer Farbstofflösung, z. B. Erythrosin, badete.

Beispielsweise war zwischen zwei chlorirten Silberplatten die elektromotorische Kraft im Sonnenlicht 0·02, zwischen zwei anderen in gleicher Weise behandelten, aber gebadeten Platten 0·04 Volt.

Bisher sind nur an jodirten Platten von Herrn Egoroff elektromotorische Kräfte beobachtet, und zwar bis $^1/_{15}$ Volt. Ich konnte bei jodirten und bromirten Platten durch Baden in Erythrosin $^1/_4$ Volt erreichen.

Ich halte es für meine Pflicht, schon an dieser Stelle Herrn Max Reiner, der mir bei diesen Versuchen assistirt, meinen verbindlichsten Dank auszusprechen.

[1] Akadem. Anzeiger Nr. XVI.

Figure 3 Report of the first dye-sensitised photoeffect observed on an illuminated semiconductor – Moser, Vienna, 1887.

whether the mechanism was a charge-transfer or an Auger-like energy-coupling process, as illustrated in Figure 4, taken from the proceedings of the Conference [17]. With the subsequent work of Gerischer and Tributsch [18, 19] on ZnO, there could be no further doubt about the mechanism, nor about the significance for photoelectrochemistry of the dye-sensitisation phenomenon, finally rendering compatible effective wideband visible spectral absorption with stability of a semiconductor substrate. It is now evident that the process involved the excitation of the dye from its charge-neutral ground state to an excited state by the absorption of the energy of a photon.

The chemical bond results from the interaction of the valence electrons associated with the atoms of a molecule. As in the semiconductor, the lowest-lying permitted energy levels are first filled, up to the highest occupied molecular level, the HOMO. Excitation, for example by the absorption of the energy of a photon, can promote an electron to the lowest unoccupied molecular level, the LUMO. Therefore as far as absorption of light is concerned, the HOMO–LUMO gap of a molecule is fully analogous to the band gap of a semiconductor. It defines the response to incident light and consequently the optical absorption spectrum. At the same time the absolute energy level of the LUMO can determine the energetics of the permitted relaxation processes of the excited molecule. When it lies above the conduction band edge of a semiconductor substrate, relaxation may take the form of emission of an electron from the dye into the semiconductor, leaving that molecule in a positively charged cationic state. In the photographic process the injected electron reduces a silver ion, and thereby establishes the latent image. In a photoelectrochemical cell, injected electrons provide a current in an external circuit, returning to the redox electrolyte through a cathode in contact with it. The uncharged ground state of the dye is then restored by electron transfer from the redox system, completing the circuit

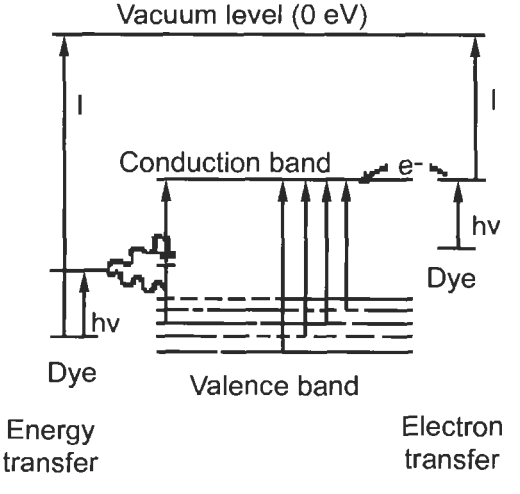

Figure 4 Disputed mechanism for sensitisation in photographic semiconductor colloid particles – here silver bromide – as presented by Bourdon in 1964 [17].

centrotherm
thermal dynamics

Solar Cell Production

Turn-key Solutions and Single Equipment

40 MW Solar Cell
Factory-Layout

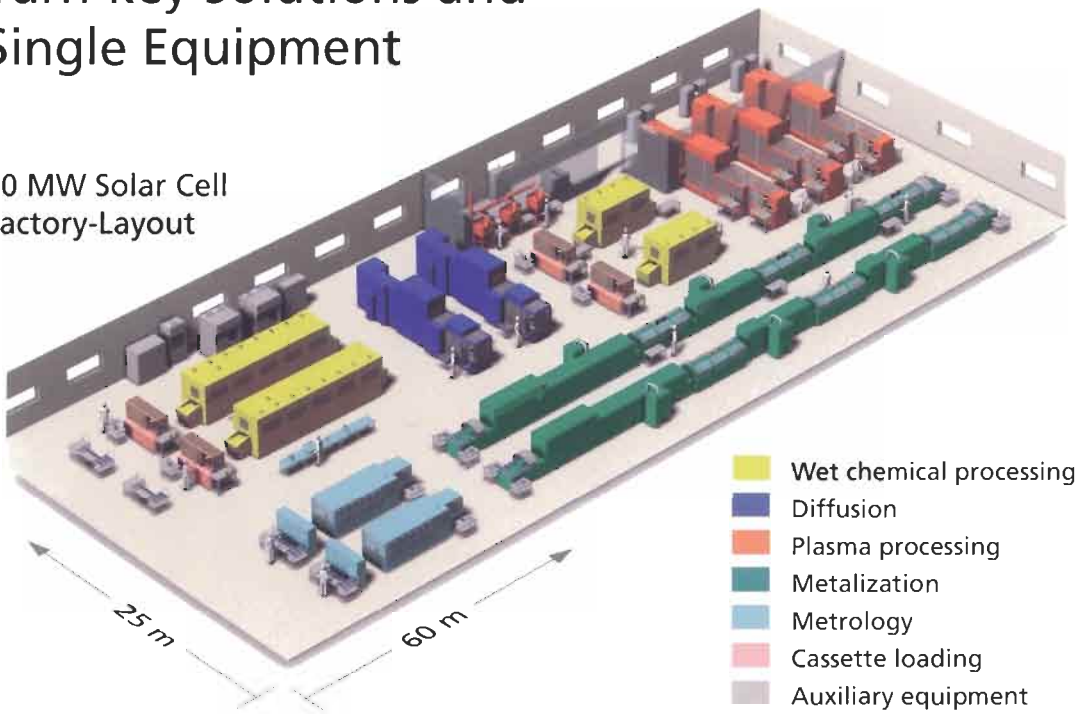

- Wet chemical processing
- Diffusion
- Plasma processing
- Metalization
- Metrology
- Cassette loading
- Auxiliary equipment

Diffusion

• Batch diffusion

• Inline diffusion

Plasma Processing

• Automatic wafer handling

Metalization

• View into the furnace

Our in-house technology and manufacturing departments provide solar cell production facilities as a unified whole. Full service for tooling design, thermal process equipment manufacturing, facility construction and start-up engineering ensure our leading position as a supplier of turn-key solutions. Our experts ensure full support from the first ideas to start up of production.

• centrotherm • Elektrische Anlagen GmbH+Co.KG • 89143 Blaubeuren, Germany • Ph. +49-7344-951-0 · Fax +49-7344-951-333 • www.centrotherm.info

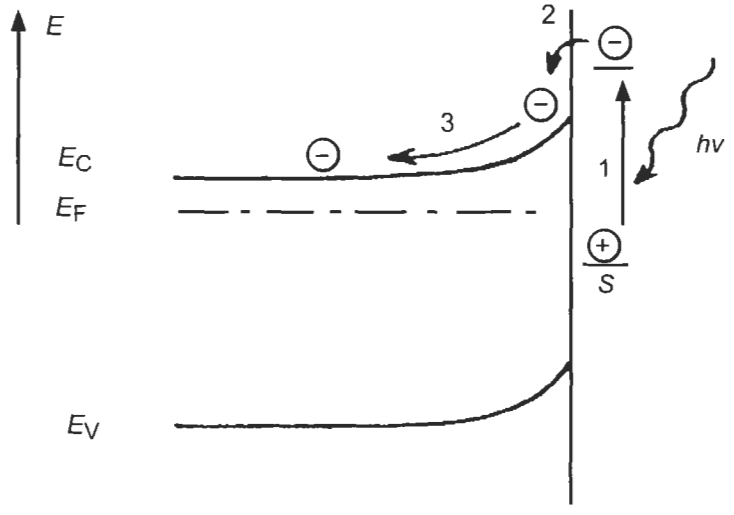

Figure 5 Definitive photosensitisation mechanism for a ZnO semiconductor as presented by Gerischer and Tributsch in 1968 [18].

and providing a regenerative cycle functionally comparable with other photovoltaic devices, as presented in Figure 6. It was also recognised that the major loss mechanism associated with semiconductors in photovoltaics, the recombination of the photoexcited charge carriers in the crystalline lattice, is strongly inhibited at a dye-sensitised photoelectrode [20]. Conventional photovoltaic junctions are essentially minority carrier devices, holes being generated in the n-type material, electrons in the p-type material, then transported to the interface. During this process carriers of each polarity can be lost due to recombination with the local majority carriers, the losses being minimised by attention to the bulk crystallinity and surface quality of the semiconductor. In the dye-sensitisation case, in contrast, no specific action is necessary, as the electron injected from the photoexcited dye finds itself within the semiconductor, already separated spatially, in a different phase, and by a potential barrier from the oxidised dye species and from the electrolyte (Figure 6). It is a majority carrier device, no holes being found in the n-type semiconductor valence band. Electron escape from the semiconductor and recapture by the dye cations or the redox electrolyte is therefore significantly suppressed, as will be seen later. This relieves the restrictions placed in the solid-state case by the requirement for low bulk and surface recombination velocities on the morphology, impurity content and crystallinity of the semiconductor. A rough and porous surface is therefore permissible, so that the dye is no longer a single monolayer on a plane area, with consequently weak optical absorption; on the rough surface with a greatly enhanced area, the optical density is such that the photoelectrode is opaque and incident light is efficiently absorbed [21].

The dye-sensitised photoelectrochemical cell integrates all these considerations, the molecular engineering of a suitable dye, its adsorption as a monomolecular

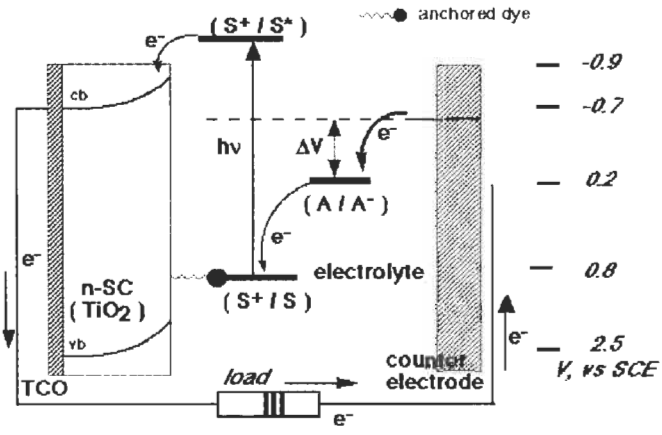

Figure 6 The regeneration cycle in a dye-sensitised solar cell. After relaxation of the photoexcited state of the dye by electron loss to the semiconductor substrate, the positive charge remaining is neutralised by the electrolyte, which in turn recovers the electron through the external circuit and the metallic cathode. A^- = redox anion, S = sensitising dye.

film on a rough wide bandgap stable semiconductor to obtain adequate optical absorption, an ohmic contact to deliver the resulting current to an external circuit, and finally establishment of a suitable regenerative system through a cathodic counterelectrode and redox electrolyte, in a single device [21]. The established semiconductor choice for this application is titanium dioxide, TiO_2, with a bandgap of 3.1 eV. It has many advantages for sensitised photochemistry and photoelectrochemistry, being a low cost, widely available, non-toxic and biocompatible material, and as such it is even used in health care products as well as in domestic applications such as paint pigmentation. Since light must enter the cell to photoexcite the dye- semiconductor composite, the ohmic contact is usually made to a transparent conducting oxide (TCO) such as an indium-tin oxide or zinc oxide supported on glass or a suitable polymer. Most research has used the iodine/iodide ($3I^- \Longleftrightarrow I_3^- + 2e^-$) redox system, with others, including transition metal complexes, now under development. Progress of the sensitised electrochemical photovoltaic device since 1991, with a conversion efficiency at that time of 7.1% under solar illumination, has been incremental, by optimising the synergy of structure, substrate roughness, dye photochemistry, counter-electrode kinetics and electrolyte redox chemistry. That evolution has continued progressively since then, with certified efficiency now over 10% (Figure 8).

4 Molecular Engineering of Electroactive Dyes

The constraints determining the dye selection have already been indicated, and the production of a suitable formulation is a demanding exercise in synthetic chemistry. Firstly and evidently there is the matter of an optical absorption

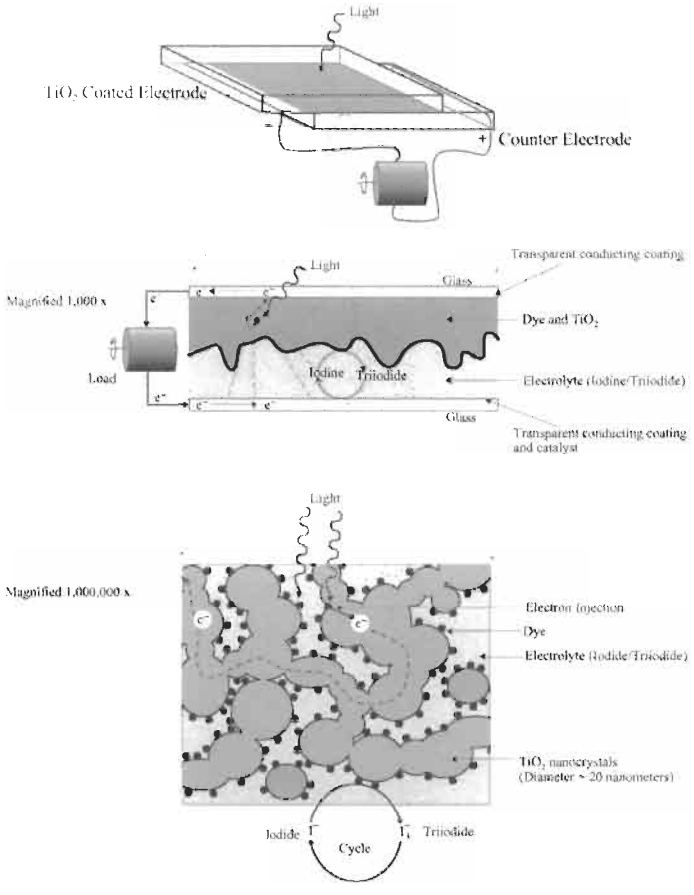

Figure 7 Structure of a dye-sensitised photoelectrochemical cell on different scales. Top: a complete cell (centimetric scale). Centre: electrodes and electrolyte, micron scale. Bottom: nanocrystalline semiconductor interconnected porous layer, with adsorbed monolayer of dye and entrained electrolyte (nanometric scale).

spectrum closely matched to the application of the photovoltaic device, whether it be to the solar spectrum for energy conversion or to artificial light sources for indoor use. With a high optical absorption coefficient across the visible spectrum, the excitation process should be rapid but subsequent relaxation slow, as already explained. For attachment to the semiconductor surface the molecule should adsorb strongly, by preference through a specific chemical bond, to the substrate, but avoid aggregation so that a monolayer coverage forms spontaneously on contact between the semiconductor and the dye in solution. The dye structures selected for intensive development arose originally from biomimetic considerations, given the role of photosynthesis in the natural world. The prototype energy-converting dye provided by nature is of course chlorophyll, a molecule consisting of a central magnesium atom surrounded by a nitrogen-containing porphyrin ring. Variations are due to minor modifications of certain side groups. Chlorophyll is in turn similar in structure to haemoglobin,

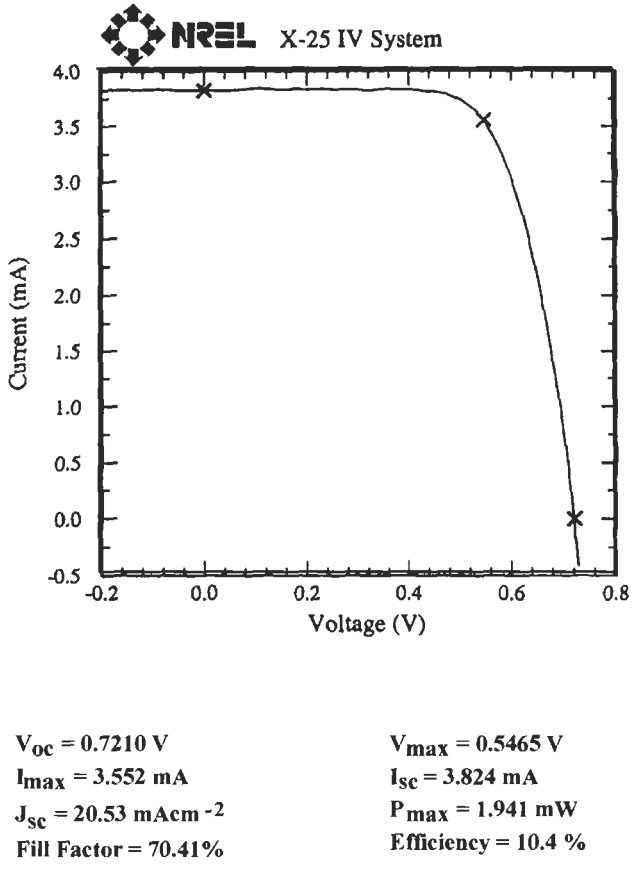

Figure 8 Certified I–V characteristic under simulated sunlight, of a dye-sensitised photoelectrochemical cell, showing a conversion efficiency > 10%.

the oxygen-carrying iron-based pigment found in blood. Given that the development of the dye-sensitised cell was associated with an interest in artificial photosynthesis, the adoption of porphyrin-like organometallic dyes as sensitisers was logical. However, whereas plant photosynthetic processes rely on chlorophyll the synthetic chemist can select from the whole range of complex-forming metals to design an appropriate metal ligand charge transfer structure.

Typical is the use of ruthenium pyridyl complexes. Clark and Suttin had already used a tripyridyl ruthenium complex in 1977 to sensitise titanium dioxide to sub-bandgap illumination [22], but in solution only. Charge transfer could only occur only after diffusion of the photoexcited molecule to the semiconductor so the efficiency of the sensitisation was very low. By 1980 the idea of chemisorption of the dye, through an acid carboxylate group bonding to the metal oxide surface had already emerged [23] so that the sensitiser was immobilised and formed a monomolecular film on the semiconductor substrate, thereby facilitating charge transfer by electron injection. The carboxylated trisbipyridyl dye ('RuL_3') therefore became the prototype sensitiser for this type of electrochemical cell. The objective at that time was to photoelectrolyse water using sensitised electrodes. Although other compounds have since been assessed as sensitisers, such as zinc porphyrins and even Prussian blue analogues [24], the most suitable dyes today are still modifications of the ruthenium-based pyridyl complexes. The objective had also evolved to become a photovoltaic device, rather than photosynthesis.

The first priority for any PV cell is of course efficient conversion of incident radiation, requiring the spectral match of the optically absorbant component to the incident light, and in this regard the early dyes were inadequate. Development of dye molecules for extension of sensitivity, ultimately into the infrared, is dramatically illustrated in Figure 10. The progress in extension of the absorption spectrum of ruthenium complexes from the early tris-bipyridyl ('RuL_3') molecule, absorbent only in the blue region and therefore appearing red, to the present-day wide-spectrum material ('$RuL'(NCS)_3$'), panchromatic, absorbing right across the visible range and therefore presenting itself as a 'black' dye, has been a key step in cell development. The strategy has been to

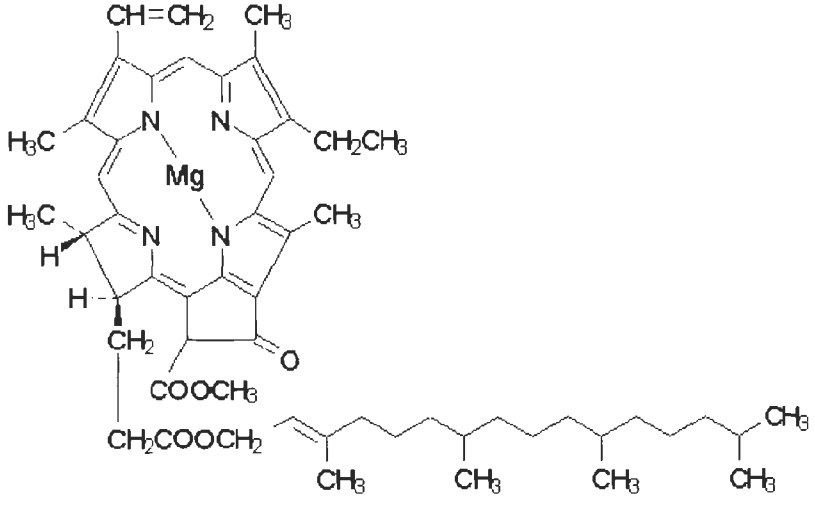

Figure 9 Structure of one of the principal variants of chlorophyll, the natural pigment converting solar energy in the photosynthetic process in plants.

retain ruthenium as the metallic component, with structural modification of the ligands to tune the energetics of the molecule. The LUMO level to which the photoexcited electron in promoted must remain above the conduction band edge of the semiconductor substrate if electron injection is to occur. Extension of the spectral sensitivity is then accomplished by raising the HOMO of the molecule, as in Figure 11. This molecular engineering process is of particular interest to physicists, as there is a close analogy to band gap modification in compound semiconductors.

A trimer structure, consisting of three ruthenium bis-biphridyl entities, cyanide bridged, and chemisorbed through carboxylate groups to the titania surface, gave the first significant extension of absorption spectrum, on the principle that an antenna structure with consequent charge transfer could be appropriate. However monomer structures are inherently simpler, and modification of pyridyl complexes by nucleophilic groups provided a more promising route. By thiocyanate substitution, this gave rise to the dye $RuL_2(NCS)_2$, (L = bipyridyl), for several years our standard chromophore and the basis for most of the system development work. Under the product name N3 it is now probably the best-understood photosensitisation molecule, particularly for its charge exchange kinetics [25]. In HOMO the metal ion is in oxidation state (II), but on excitation it loses a further electron to the organic ligand structure, a metal-to-ligand charge transfer. Injection of the electron through the bridging carboxylate to the semiconductor substrate occurs within picoseconds, faster than other relaxation processes and explaining the high quantum efficiency of the system sensitised with this dye.

Isomerism of the dye molecule can permit the identification of structures with variant optical properties. For example the standard N3 is a *cis*-isomer (both NCS thiocyanate groups on the same side of the molecule); the corresponding trans-isomer has an extended sensitivity into the infrared, but over time it tends to revert to the *cis*-structure. A *trans*-type configuration can be stabilised by replacing the L_2, bis-bipyridyl ligand system by a single tetrapyridyl coordination [26]. This example illustrates the sensitive dependence of the orbitals and their energetics on molecular structure. Addition of a third thiocyanate group, with the necessary reduction of pyridyl complexation from bis-bi- or tetra- to ter-pyridyl (L′) gives the structure of the state-of the art black dye, $RuL'(NCS)_3$, whose spectral sensitivity extends throughout the visible and into the infrared, approaching the ideal absorption edge position (1.4 eV) for optimal solar energy conversion. It can be expected that this type of molecular engineering will make available suitable dye formulations for a variety of applications, such as infra-red sensitive dyes with lower visible absorptivity, useful for 'transparent' cells, or dyes with selective absorption, the resulting colour presentation being determined for example by architectural options for building-integrated PV.

The interaction between the dye molecule and the adsorbant surface also influences the energetics of the dye and the kinetics of its chemical reactions. For example it is known that on adsorption of a carboxylated dye, a titania surface becomes positively charged, due to the deprotonation of the acid dye. The

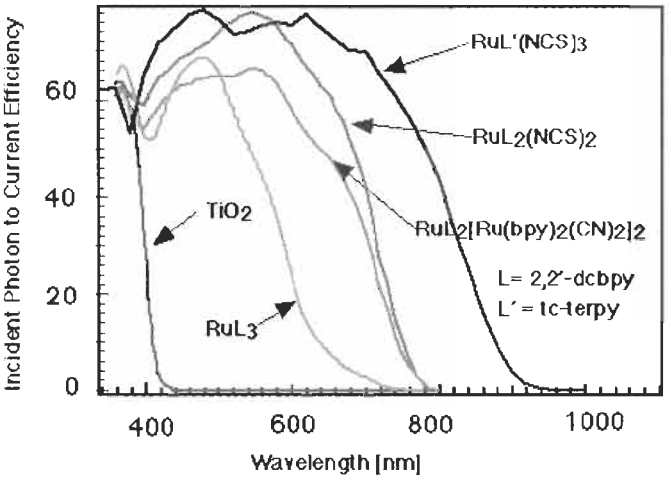

Figure 10 The photocurrent action spectrum of a cell containing various sensitisers, where the incident photon to current conversion efficiency is plotted as a function of wavelength.

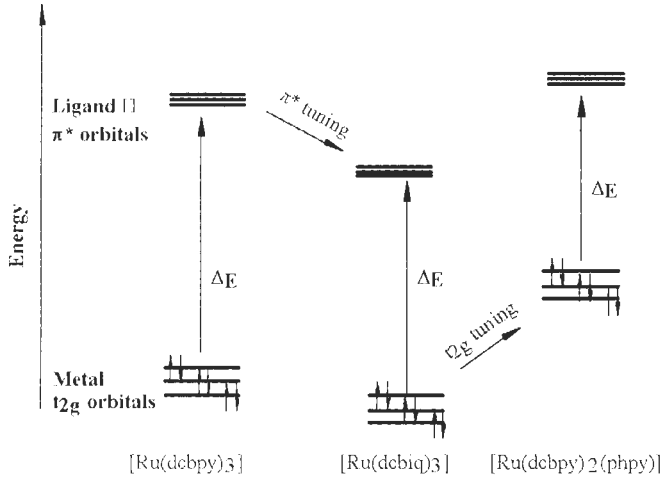

Figure 11 Tuning of HOMO (t_{2g}) and LUMO (π^*) orbital energy in various ruthenium complexes. (a) $Ru(dcbpy)_3$ = ruthenium tris(dicarboxyl bipyridyl) or RuL_3. (b) (dcbiq) = dicarboxybiquinoline. (c) $Ru(dcbpy)_2(phpy)$ is a modified RuL_2 where phpy = phenylpyridine. In all cases the ruthenium atom is 6-fold coordinated with cyclic pyridyl-type ligands.

consequent interface potential gradient obviously enhances electron injection efficiency, leading to a higher photocurrent. However efficiency does not proportionately rise, since the positive shift of band edge is associated with a lower open-circuit voltage. Optimisation of the cell efficiency also requires a control of protonation of the dye. With this in mind several salts of N3 with organic cations such as tetrabutylammonium and imidazolium have been

investigated [26]. These salts are also more soluble, facilitating purification by recrystallisation and thereafter adsorption to the semiconductor from the more concentrated solution. The thermal dehydration behaviour shows the association of only 1.5 molecules of water per Ru ion, for the optimum di-tetrabutylammonium salt, with a thermal stability thereafter to 190°C; at that point the organic cation tends to dissociate. When adsorbed on the semiconductor the dye stability is further enhanced, decarboxylation requiring over 300°C. This remarkable rise is attributed to the strength of the Ti ion to carboxylate bond between the semiconductor surface and the chemisorbed molecule. This confirmation of the thermal stability of the surface-bonded dye therefore opens the prospect of a very wide temperature window for processing the sensitised semiconductor during any manufacturing routine, simplifying bonding and sealing processes by permitting thermal treatment and curing of sealants even after the dye has been admitted to the cell.

Modification of the surface of the semiconductor to optimise adsorption and charge transfer behaviour of the dye is a further option. Several years ago, deposition of an outer intrinsic titania [27] or a solid solution layer [28] on each semiconductor grain was investigated in order to control the interface properties after dye adsorption. Evidently a nanostructure emulating the oxide or insulator layer in MOS or MIS solid state Schottky devices has a similar effect in defining the band edge characteristics in the photoelectrochemical case.

5 Semiconductor Layer Characteristics

If molecular design and engineering has underpinned the evolution of efficient stable sensitiser dyes, for the semiconductor substrate it is a matter of the materials science of nanoporous ceramic films. The nanoporous structure permits the specific surface concentration of the sensitising dye to be sufficiently high for total absorption of the incident light, necessary for efficient solar energy conversion, since the area of the monomolecular distribution of adsorbate is 2–3 orders of magnitude higher than the geometric area of the substrate. As already noted, this high roughness does not promote charge carrier loss by recombination, since the electron and the positive charge find themselves within picoseconds on opposite sides of the liquid-solid interface, much faster than any possible electron escape and redox or cation capture process. The original semiconductor structure used for early photosensitisation experiments was a fractal derived by hydrolysis of an organo-titanium compound. Later, suspensions of commercially available anatase titania powders were found to be equally effective. At present however hydrothermal techniques are employed for the synthesis of an optimised nanoparticulate anatase TiO_2 powder which is then used in suspension in a liquid medium [29].

A specific advantage of the hydrothermal technique is the ease of control of the particle size, and hence of the nanostructure and porosity of the resultant semiconductor substrate. The microstructure of the semiconductor is of course a compromise, to achieve an optimal optical absorption and photovoltaic

performance. Nanosize grains give the greatest surface area, but pores must remain sufficiently large that the mobility of the charge carriers in the electrolyte, the redox ions, is not unduly inhibited. Also some degree of optical scattering by larger particles in the semiconductor film is also desirable, particularly for devices which function under indirect illumination such as vertical building facades. Processing parameters such as precursor chemistry, hydrothermal growth temperature for the titania powder, and sintering conditions are varied in the optimisation procedure. A flowsheet for hydrothermal processing is presented in Table 1 as an example of the required development work. Figure 12 shows the control of porosity of the final film which results from it, as determined by a nitrogen adsorption method. The procedure involves the hydrolysis of the titanium alkoxide precursor in an aqueous medium to produce a sol which is then subjected to the hydrothermal Ostwald ripening in an autoclave. The temperature of the hydrothermal treatment is decisive for the ultimate particle size. A standard sol, treated for 12 hours at 230°C has a mean particle diameter of the order of 10 nm. The colloidal suspension can be applied to the TCO support by one of several standard coating processes – tape casting, spraying or screen printing. A firing protocol to dry the film, then pyrolyse binders and organics ensures a coherence and low-resistance ohmic contact to the conducting underlayer. Figure 13 shows a micrograph of a semiconductor film suitable for sensitisation. Other oxide semiconductors which have been studied in the context of dye-sensitised photovoltaics include ZnO, SnO_2, Nb_2O_5, and $SrTiO_3$ [30–34].

For cell assembly, the anode as described is photosensitised by chemisorption of the dye from solution. The cathode or counter-electrode is usually a similar TCO supported on glass, treated to electrocatalyse the redox electrolyte

Table 1 Flow diagram for the preparation of TiO_2 colloids and mesoporous films (after Brooks et al. [29]).

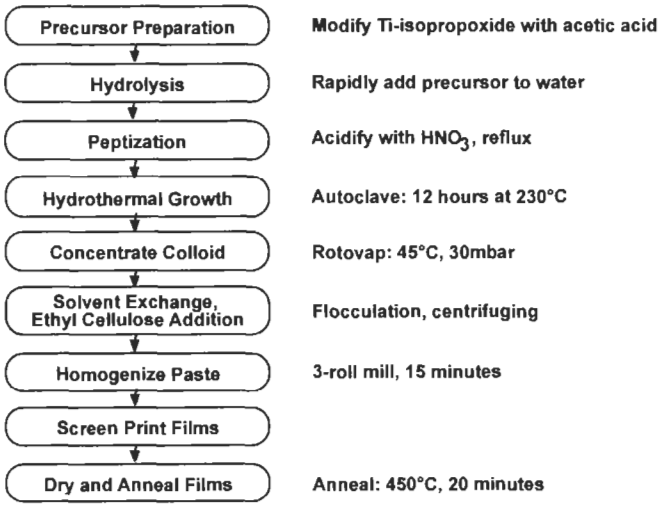

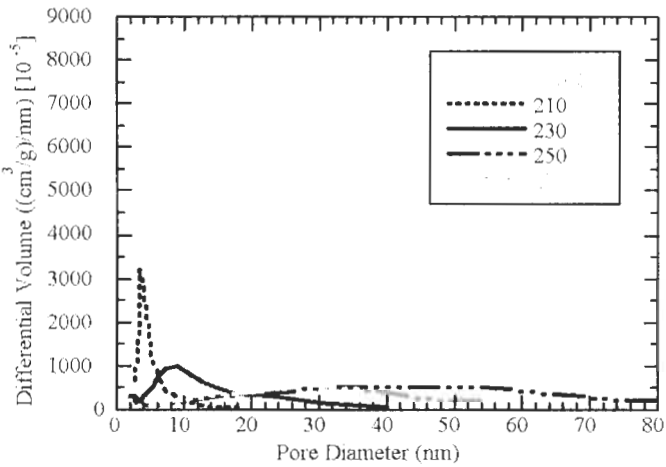

Figure 12 Control of semiconductor substrate porosity by temperature of hydrothermal processing.

regeneration, for example with highly dispersed platinum. The cell is completed with an edge seal to contain the electrolyte, usually a liquid, although gel or solid variants are also possible.

6 Dye Sensitisation in Heterojunctions

Given that a dye at the interface in a photoelectrochemical cell can sensitise the system to photons of lower energy that would not otherwise be absorbed by the semiconductor, the possibility presents itself that the effect is not restricted to the electrochemical device. Both conductors may in principle be in the solid state. Here we are not considering the special cases of gel or polymer electrolytes [35], because in these media charge transport is ionic, by the same mechanism as in a conventional liquid electrolyte. The key distinction is that a heterojunction is essentially a solid-state device, a contact between two chemically different semiconductors, organic or inorganic; they also differ in the conduction mechanism, for example with an n-type electron-conducting TiO_2 contacted by a p-type hole-conducting organic species. In an electrochemical device on the other hand the phase contacting the semiconductor substrate, as already stated, is an electrolyte with an ionic conduction mechanism. The difference is essentially in the nature of the mobile carrier, although the devices may be functionally the same. Since the sensitiser provides charge separation but not charge transport, and is distributed at an interface in the form of an immobilised molecular monolayer, it is evident that for charge transfer each dye molecule must bridge both conducting phases. This applies in the first instance to the wide bandgap porous semiconductor substrate into which the photoexcited chemisorbed molecules inject electrons. It is also evident that in the photoelectrochemical format of the sensitised cell the liquid electrolyte penetrates

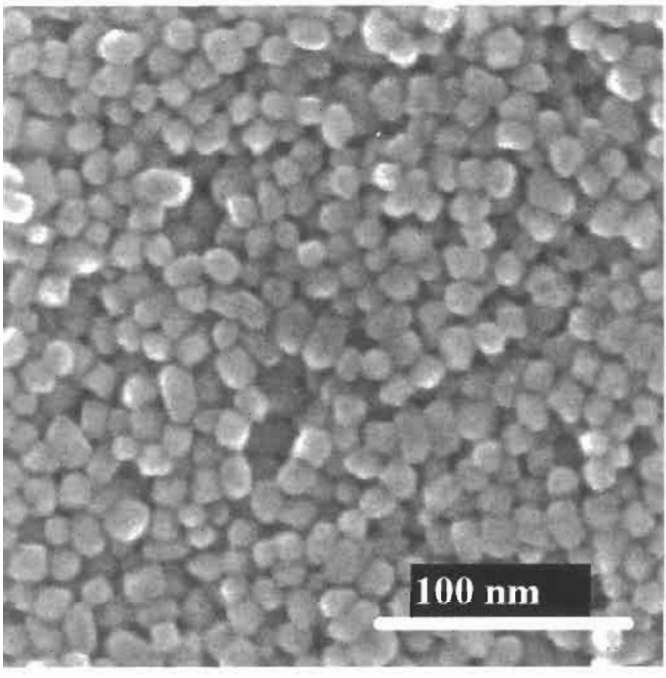

Figure 13 SEM image of the surface of a mesoporous film prepared from the hydrothermal TiO_2 colloid.

into the porosity, thereby permitting the required intimate contact with the charged dye molecule necessary for charge neutralisation after the electron loss by exchange with the redox system in solution. It is not immediately evident that an interpenetrating network of two conducting inorganic solids can be established so effectively that an immobilised molecule at their interface can exchange charge carriers with both. This is a particular obstacle to the realisation of a sensitised nanostructured metal–semiconductor Schottky junction. However use of transparent organic semiconductors is a possibility, and initial results [36, 37] are promising. The materials science, fabrication procedures and photovoltaic performance of systems incorporating organic conductors are presented in a separate chapter. These heterojunction devices can now be expected to follow a similar learning curve to the electrochemical concept, which has significantly increased in efficiency since the initiation of its development [21], and as noted, the improvements in efficiency and stability are not the consequence of any radical breakthrough, but rather of gradual evolution.

7 Commercial Prospects

The status of the dye-sensitised device as the only verified alternative to solid-state junction devices has already been mentioned. However it must be recognised that the solid-state devices, particularly the silicon p-n junction cells,

benefit from over 40 years of industrial and development experience, the technology transfer from the silicon-based electronics industry, and even the widespread availability of high quality silicon at low cost resulting from the expansion of that industry. The procedures for high-yield fabrication of silicon devices, both crystalline and amorphous, are well understood, with costing precisely established, based on decades of solid industrial experience. For the dye-sensitised cell, in contrast, fabrication procedures require development and costing is based on estimates of the requirements of chemical processes rather than those of the silicon metallurgy with its elevated temperatures and vacuum technology as required for conventional cells. This may in fact turn to the advantage of some variants of the dye-sensitised concept. Equally it is well known that the substitution of an established technology by an upcoming alternative requires that the new concept has definite advantages and no clear disadvantages. It is therefore noted with some satisfaction that several companies in Europe, Japan and Australia have taken up the challenge and are currently engaged under license in the venture of industrialisation and commercialisation of dye-sensitised PV cells. More, the existence of a credible challenger is a stimulus to the solid-state photovoltaic industry to improve its existing products and to remain open to new concepts.

8 Conclusions

The development of reproducible and stable photovoltaic devices adapted for manufacturing processes has proceeded in evolutionary steps, with each component optimised and verified for compatibility with system requirements. The dye-sensitised nanocrystalline solar cell, either the electrochemical device, or the closely related sensitised heterojunction, provides a scientifically verified photovoltaic option, challenging the conventional semiconductor junction solid-state cell. Time and the market will tell if it can compete successfully.

Acknowledgements

The team at EPFL greatly appreciates the vote of confidence represented by the licences taken up by industry for this type of solar cell. In the present work, the initiative and innovative spirit of the research team members, past and present, in the areas of dye synthesis, catalysis and electrochemistry, and semiconductor thin film fabrication are acknowledged.

References

[1] Becquerel, A.E., 1839. Memoire sur les effets électriques produits sous l'influence des rayons solaires. *C. R. Acad. Sci. Paris*, Vol. 9, pp. 561–567.

[2] Gerischer, H., 1969. Role of electrons and holes in surface reactions on semiconductors. *Surface Science*, Vol. 13, pp. 265–278.

[3] Fujishima, A. and Honda, K., 1972. Electrochemical photolysis of water on a semiconductor electrode. *Nature*, Vol. 238, pp. 37–38.

[4] Memming, R., 1988. Photoelectrochemical solar energy conversion. *Topics Current Chem.*, Vol. 143, pp. 79–112.

[5] Grätzel, M. and Augustynski, J., 2000. Tandem cell for water cleavage by visible light. *Int. Patent Appl.* PCT/EP00/06350.

[6] Biot, J.B., 1839. Memoires et communications. *C. R. Acad. Sci. Paris*, Vol. 9, pp. 169–173.

[7] Gurney, R.W. and Mott, N.F., 1938. Theory of photolysis of silver bromide and the photographic latent image. *Proc. Roy. Soc.*, Vol. A164, pp. 151–167.

[8] James, T.H., 1977. *The Theory of the Photographic Process*. 4th. Ed., Macmillan, New York, USA.

[9] West, W., 1974. First hundred years of spectral sensitisation. *Photogr. Sci. Eng.*, Vol. 18, pp. 35–48.

[10] Moser, J., 1887. Notiz über Verstärkung photoelektrischer Ströme durch optischer Sensibilierung. *Monatsh.Chem.*, Vol. 8, p. 373.

[11] Rigollot, H., 1893. Memoires et communications. *C. R. Acad. Sci. Paris*, Vol. 116, p. 873.

[12] Spitler, M.T., 1983. Dye photo-oxidation of semiconductor electrodes: a corollary to spectral sensitization in photography. *J. Chem. Ed.*, Vol. 60, pp. 330–332.

[13] Gould, I.R., Lenhard, J.R., Münter, A.A., Godelski, S.A. and Farid, S., 2000. Two-electron sensitisation: a new concept for silver halide photography. *J. Am. Chem. Soc.*, Vol. 122, pp. 11934–11943.

[14] Kato, T., Maekawa, E., Fujishima, A. and Honda, K., 1984. Current doubling effect generated by formate on the cadmium sulfide photoanode and characterisation of the photo-electrochemical cell. *Nippon Kagaku Kaishi*, pp. 233–238.

[15] Namba, S. and Hishiki, Y., 1965. Color sensitisation of zinc oxide with cyanine dyes. *J. Phys. Chem.*, Vol. 69, pp. 774–779.

[16] Nelson, R.C., 1965. Minority carrier trapping and dye sensitisation. *J. Phys. Chem.*, Vol. 69, pp. 714–718.

[17] Bourdon, J., 1965. Spectral sensitisation of chemical effects in solids. *J. Phys. Chem.*, Vol. 69, pp. 705–713.

[18] Gerischer, H. and Tributsch, H., 1968. Electrochemical studies on the spectral sensitisation of zinc oxide single crystals. *Ber. Bunsenges. Phys.Chem.*, Vol. 72, pp. 437–445.

[19] Tributsch, H., 1968. Ph.D. thesis, Techn. Hochschule München, Germany.

[20] McEvoy, A.J., 1988. Functional components for solar energy chemical photoconversion systems. In: Bloss, W.H. and Pfisterer, F., Eds., *Advances in Solar Energy*, Pergamon, Oxford, UK, pp. 2921–2926.

[21] O'Regan, B. and Grätzel, M., 1991. A low-cost high effiiciency solar cell based on dye-sensitised colloidal titanium dioxide films. *Nature*, Vol. 335, pp. 737–739.

[22] Clark, W.D.K. and Suttin, N., 1977. Spectral sensitisation of n-type titanium dioxide by polypyridine-ruthenium complexes. *J. Amer. Chem. Soc.*, Vol. 99, pp. 4676–4682.

[23] Dare-Edwards, M.P., Goodenough, J.B., Hamnett, A., Seddon, K.R. and Wright, R.D., 1980. Sensitisation of semiconductor electrodes with ruthenium-based dyes. *Faraday Discuss. Chem. Soc.*, Vol. 70, pp. 285–298.

[24] Vlachopoulos, N., Liska, P., McEvoy, A.J. and Grätzel, M., 1988. Efficient sensitisation of TiO_2 electrodes using transition metal charge transfer complexes. In: Bloss, W.H. and Pfisterer, P., Eds., *Advances in Solar Energy*, Pergamon, Oxford, UK, pp. 3003–3009.

[25] Haque, S.A., Tachibana, Y., Willis, R.L., Moser, J.E., Grätzel, M., Klug, D.R. and Durrant, J.A., 2000. Parameters influencing charge recombination kinetics in dye-sensitised nanocrystalline titanium dioxide films. *J. Phys. Chem. B*, Vol. 104, pp. 538–547.

[26] Nazeeruddin, M.K., Zakeeruddin, S.M., Humphrey-Baker, R., Jirouzek, M., Liska, P., Vlachopoulos, N., Shklover, V., Fischer, C.-H. and Grätzel, M., 1999. Acid–base equilibria of (2,2'-bipyridyl-4,4'-dicarboxylic acid)ruthenium(II) complexes and the effect of protonation on charge-transfer sensitisation of nanocrystalline titania. *Inorg. Chem.*, Vol. 38, pp. 6298–6305.

[27] Kay, A., O'Regan, B. and Grätzel, M., 1996. Method for the manufacture of a photo-electrochemical cell and a cell made by this method. US patent 5525440.

[28] O'Regan, B., Grätzel, M. and Nazeeruddin, M.K., 1994. Photovoltaic cells, US patent 5350644.

[29] Brooks, K.G., Burnside, S.D., Shklover, V., Comte, P., Arendse, F., McEvoy, A.J. and Grätzel, M., 1999. Mesoporous nanocrystalline thin films for electrochemical applications. *Proc. Am. Ceram. Soc.*, Indianapolis, USA, pp. 115–122.

[30] Bedja, I., Hotchandani, S., Kamat, P.V., 1994. Preparation and photoelectrochemical characterization of thin SnO_2 nanocrystalline semiconductor films and their sensitisation with bis(2,2'-bipyridine)(2,2'-bipyridine-4,4'-dicarboxylic acid)ruthenium(II) complex. *J. Phys. Chem.*, Vol. 98, pp. 4133–4140.

[31] Sayama, K., Sugihara, H. and Arakawa, H., 1998. Photoelectrochemical properties of a porous Nb_2O_5 electrode sensitised by a ruthenium dye. *Chem. Mater.* Vol. 10, pp. 3825–3832.

[32] O'Regan, B. and Schwartz, D.T., 1996. Efficient dye-sensitised charge separation in a wide-band-gap p-n heterojunction. *J. Appl. Phys.*, Vol. 80, pp. 4749–4754.

[33] Rensmo, H., Keis, K., Lindstrom, H., Sodergren, S., Solbrand, A., Hagfeldt, A., Lindquist, S.E., Wang, L.N. and Muhammed, M., 1997.

High light-to-energy conversion efficiencies for solar cells based on nanostructured ZnO electrodes. *J. Phys. Chem. B*, Vol. 101, pp. 2598–2601.

[34] Dabestani, R., Bard, A.J., Campion, A., Fox, M.A., Mallouk, T.E., Webber, S.E. and White, J.M., 1988. Sensitization of titanium dioxide and strontium titanate electrodes by ruthenium(II) tris(2,2'-bipyridine-4.4'-dicarboxylic acid) and zinc tetrakis(4-carboxyphenyl)porphorin: an evaluation of sensitisation efficiency for component photoelectrodes in a multipanel device. *J. Phys. Chem.*, Vol. 92, pp. 1872–1878.

[35] Mikoshiba, S., Sumino, H., Yonetsu, M. and Hayase, S., 2000. Highly efficient photo-electrochemical cell with novel polymer gel electrolytes. *Proc. 16th European Photovoltaic Solar Energy Conf.*, Glasgow, pp. 47–50.

[36] Bach, U., Lupo, D., Comte, P., Moser, J.-E., Weissörtel, F., Salbeck, J., Spreitzer, H. and Grätzel, M., 1998. Solid-state dye-sensitised mesoporous TiO_2 solar cells with high photon-to-electron conversion efficiencies. *Nature*, Vol. 395, pp. 583–585.

[37] Halls, J.J.M., Walsh, C.A., Greenham, N.C., Marseglia, E.A., Friend, R.H., Moratti, S.C. and Holmes, A.B., 1995. Efficient photodiodes from interpenetrating polymer networks. *Nature*, Vol. 376, pp. 498–500.

Organic and Plastic Solar Cells

Jenny Nelson, Centre for Electronic Materials and Devices, Department of Physics, Imperial College London, UK

1 Introduction

The last three years have seen an unprecedented growth of interest in solar cells made from organic electronic materials. This is due partly to the rapid growth of the photovoltaic market, which has stimulated research into longer term, more innovative photovoltaic technologies, and partly to the development of organic electronic materials for display applications. Rapid progress in optoelectronic molecular materials has introduced a range of potential new photovoltaic materials, as well as an improved understanding of the capabilities of such materials and confidence in their application. For a review see [1].

Organic materials are attractive for photovoltaics primarily through the prospect of high throughput manufacture using processes such as reel-to-reel deposition. Additional attractive features are the possibilities for ultra thin, flexible devices which may be integrated into appliances or building materials, and tuning of colour through chemical structure. The field has made impressive progress since the late 1990s. At the time of writing, solar power conversion efficiencies of over 3% have been reported for four distinct classes of organic solar cell, a growing range of new photovoltaic materials have been studied and increasing numbers of research groups and companies have declared an interest in 'soft' solar cells [2–4].

Unlike other photovoltaic technologies featured in this handbook, organic or 'plastic' solar cells are far from commercialisation. It is not known which, if any, of several different materials systems and cell designs will prevail and there is no experience in module production. In this chapter, we will discuss the principles of organic electronic materials and the ways in which they differ from inorganic photovoltaic materials, the range of device concepts, the most efficient device designs and the main challenges in increasing efficiency. Possible production and processing technologies are discussed, but the practical details are largely speculative.

2 Organic Photovoltaic Materials

Organic electronic materials are conjugated solids where both optical absorption and charge transport are dominated by partly delocalised π and π^* orbitals. Candidates for photovoltaic applications include crystalline or polycrystalline films of 'small molecules' (conjugated molecules of molecular weight of a few 100), amorphous films of small molecules prepared by vacuum deposition or solution processing, films of conjugated polymers or oligomers processed from solution, and combinations of any of these either with other organic solids or with inorganic materials. A comprehensive discussion of the development of organic solids for photovoltaic applications is given by Halls [4].

Organic photovoltaic materials differ from inorganic semiconductors in the following important respects.

- Photogenerated excitations ('excitons') are strongly bound and do not spontaneously dissociate into charge pairs. (Dissociation requires an input

of energy of ~100 meV compared to a few meV for a crystalline semiconductor.) This means that charge carrier separation generation does not necessarily result from the absorption of light.

- Charge transport proceeds by *hopping* between localised states, rather than transport within a band, which results in low mobilities.
- The spectral range of optical absorption is relatively narrow compared to the solar spectrum.
- Absorption coefficients are high ($\sim 10^5$ cm $^{-1}$) so that high optical densities can be achieved, at peak wavelength, with films less than 100 nm thick.
- Many organic materials are susceptible to degradation in the presence of oxygen or water.
- As one-dimensional semiconductors, their electronic and optical properties can be highly anisotropic. This is potentially useful for device design.

The first two features are due to the fact that the intermolecular van der Waals forces in organic solids are weak compared to bonds in inorganic crystals and much weaker than the intramolecular bonds. As a consequence all electronic states are localised on single molecules and do not form bands. Low mobility is aggravated by the high degree of disorder present in many organic solids. The optical excitations accessible to visible photons are usually π to π^* transitions. Most conjugated solids absorb in the blue or green; absorption in the red or infrared is harder to achieve. However, the absorption bandwidth depends on the degree of conjugation and wider spectral sensitivity can be achieved in highly conjugated dye molecules.

These properties impose some constraints on organic photovoltaic devices:

- A strong driving force should be present to break up the photogenerated excitons.
- Low charge carrier mobilities limit the useful thickness of devices.
- Limited light absorption across the solar spectrum limits the photocurrent.
- Very thin devices mean interference effects can be important.
- Photocurrent may be sensitive to temperature through hopping transport and thermal dissociation of excitons.

3 Principles of Operation and Device Concepts

3.1 Homojunctions

The simplest device structure is a layer of organic material sandwiched between two different conducting contacts, typically indium tin oxide (ITO) and a low work function metal such as Al, Ca or Mg (Figure 1). The difference in work function provides an electric field which drives separated charge carriers towards the respective contacts (in rough analogy to a p–i–n junction in

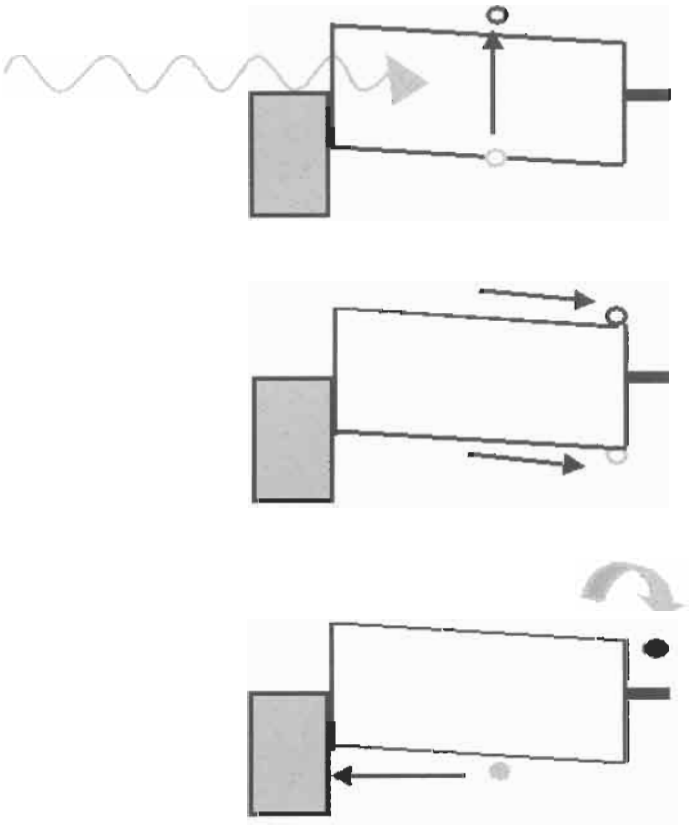

Figure 1 Schematic energy-band diagram of a simple device consisting of a single organic layer between two metal contacts. An electric field results from the difference in work functions of the contacts. Absorbed photons generate excitons which diffuse towards one or other contact where they may dissociate to yield charge pairs. Only the layer of organic material which lies within an exciton diffusion length of a contact can contribute to the photocurrent.

amorphous silicon). This electric field is seldom sufficient to break up the photogenerated exciton. Instead the exciton diffuses within the organic layer until it reaches a contact, where it may be broken up to supply separate charges, or recombine. Since exciton diffusion lengths are short, typically 1–10 nm, exciton diffusion limits charge carrier generation in such a device. Photocarrier generation is therefore a function not only of bulk optical absorption, but also of available mechanisms for exciton dissociation. Other loss factors are non-radiative recombination at the interfaces and non-geminate recombination at impurities or trapped charges.

Single layer solar cells of this type typically deliver quantum efficiencies (QE) of less than 1% and power conversion efficiencies of less than 0.1%. (QE is the ratio of electrons delivered to the external circuit per incident photon of a given wavelength, and is the figure of merit in organic photovoltaics. High QE is a necessary, though not sufficient, condition for high photovoltaic efficiency. In

organic devices the value is still far from the values of 80–90% typical in inorganic solar cells.)

3.2 Heterojunctions

Most of the developments that have improved performance of organic photovoltaic devices are based on donor–acceptor heterojunctions. At the interface between two different materials, electrostatic forces result from the differences in electron affinity and ionisation potential. If both electron affinity and ionisation potential are greater in one material (the electron acceptor) than the other (the electron donor) then the interfacial electric field drives charge separation (Figure 2). These local electric fields are strong and may break up photogenerated excitons provided that the differences in potential energy are larger than the exciton binding energy. In a planar heterojunction, or 'bi-layer' device, the organic donor–acceptor interface separates excitons much more efficiently than the organic–metal interfaces in a single layer device and with very high purity materials, photovoltaic devices with high QE may be made.

3.3 Dispersed Heterojunctions

A revolutionary development in organic photovoltaics (and photodetectors) came in the mid 1990s with the introduction of a *dispersed* heterojunction, where an electron accepting and an electron donating material are blended

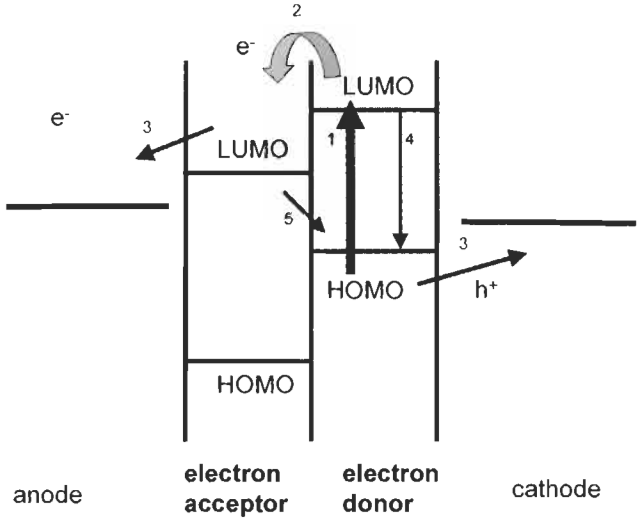

Figure 2 Schematic energy-band diagram of a donor-acceptor heterojunction. If both the excited state (LUMO) and ground state (HOMO) of the donor material lie at energies sufficiently higher than those of the acceptor material, then it is energetically favourable for an exciton reaching the interface to dissociate, leaving a positive polaron on the acceptor and a negative polaron on the donor. For efficient photocurrent generation, charge separation (2) should compete successfully with geminate recombination (4) after a photon absorption event (1), and transfer to contacts (3) should compete with interfacial recombination (5).

together. If the domain size in either material is similar to the exciton diffusion length, then wherever an exciton is photogenerated in that material, it is likely to diffuse to an interface and break up. If continuous paths exist in each material from the interface to the respective electrodes, then the separated charge carriers may travel to the contacts and deliver current to the external circuit (Figure 3(a)). This effect was reported independently by several groups [5–7] for a blend of two conjugated polymers. The blend improved QE to around 6–8% from less than 1% for either polymer alone. Around the same time, Yu and co-workers reported a QE of 29% for a blend of the hole transporter, poly-phenylene vinylene (PPV), with a derivative of C_{60} [8], where the C_{60} acts as the electron transporting component (Figure 3(b)).

This was followed by observations of enhanced QE in heterojunctions made from conjugated polymers with inorganic nanocrystals [9,10] and organic dye crystals [11]. The demonstration of improved QE with dispersed heterojunctions represents a departure from the device physics of conventional solar cells and has led to new device and materials designs. The principles of operation are shared by dye sensitised solar cells which are discussed in reference [12] and Chapter IIc-1.

4 Leading Device Designs

The early 2000s have seen developments in the synthesis of new photovoltaic materials; the combination of materials into new device architectures; studies of the effect of processing conditions and other factors on morphology and performance; and manipulation of materials at a molecular level, exploiting molecular self assembly and modification of interfaces. During this period power conversion efficiencies of over 3% have been reported in four distinct classes of device and QEs of over 20% achieved in several others. Several studies of issues relating to production, field performance and stability have been reported. Progress has been made with the understanding of photocurrent generation and charge separation, and the first approaches to developing a device physics for organic solar cells, have been made.

At time of writing, organic solar cell technology is young and the field is still wide open. Several very different device designs are competing as front runners and it is too early to guess which, if any, of these will emerge as a serious contender for commercialisation. Below we summarise the main features of the most promising options.

Power conversion efficiencies of over 3% have now been achieved in the three classes of device listed below and in Table 1. (High power conversion efficiencies have been reported [13,14] for a fourth class, a Schottky barrier device made from a doped molecular crystal in contact with an n-type a metal or n-type oxide layer, but these results are still unconfirmed.)

(1) Planar heterojunction devices made by vacuum deposition of thin films of small molecules have been studied by several groups, for application to LEDs as well as solar cells. An impressive result has been achieved at Princeton with a

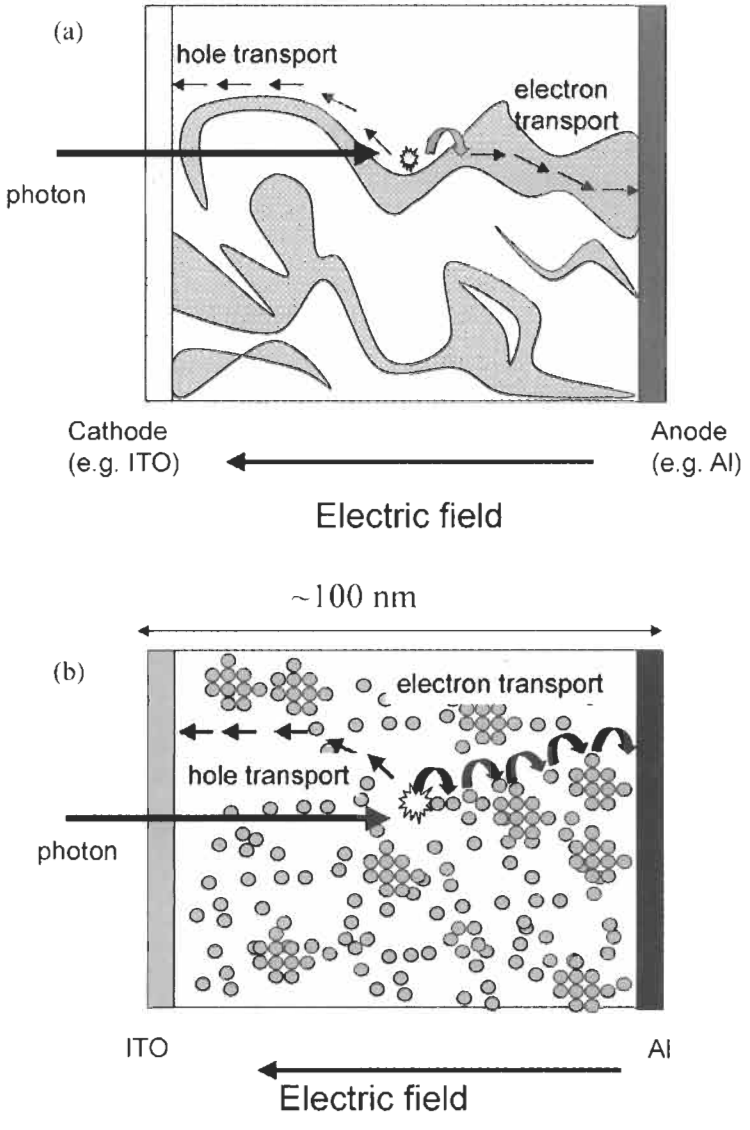

Figure 3 Donor and acceptor materials may be blended together to yield a dispersed heterojunction. If the domain size in the blend is similar to the exciton diffusion length, then the probability that an exciton will reach the interface and dissociate is high. For efficient photocurrent collection, each material must provide a continuous path for the transport of separated charge to the contacts. Isolated domains can trap charges, causing recombination. (a) A blend of two polymers. (b) A blend of one polymer with electron accepting nanoparticles or fullerenes. The concentration of nanoparticles should be sufficient to allow percolation.

four layer heterojunction, containing wide band gap hole transporting and electron transporting 'window' layers [15, 16]. These buffer layers function to block excitons from lossy metal contacts and to enhance optical field strength in photoactive layers via interference effects. Subsequent research on the same

materials system has shown that greatly increased voltages can be achieved using tandem structures with tunnel junctions made from nanoparticulate silver. [17].

(2) Blends of polyphenylenevinylene derivatives and methanofullerenes are a well studied combination and are under intense development at Linz [3]. Photon absorption in the polymer is followed by electron transfer to the fullerene on a sub ps time scale. Current collection depends on charge percolation through the fullerene network and the polymer matrix and is therefore critically dependent upon the blend ratio and the degree of phase separation. The combination of poly(2-methoxy-5-(3',7'-dimethyloctyloxy)-1-4-phenylene vinylene), (MDMO-PPV) with 1-(3-methoxycarbonyl)-propyl-1-phenyl-(6,6)C_{61} (PCBM) appears to be a promising materials system. A breakthrough was achieved in 2001 by using chlorobenzene as a solvent in place of toluene, leading to QE of over 50% and power conversion efficiency of 2.5% [18]. The much improved performance is attributed to improved phase separation with chlorobenzene. Further development led to increased open circuit voltages by using LiF interfacial layers, leading to power conversion efficiencies exceeding 3% at 50°C [19].

(3) Solid-state dye-sensitised solar cells (DSSC) are the most promising amongst organic-inorganic composite devices to date. In the DSSC three active materials are used: an organic dye as light absorber, a nanocrystalline metal oxide film as electron transporter and liquid or organic hole transporting material (HTM) [12]. The original design used a redox active liquid electrolyte for hole transport, but a non volatile HTM is desirable for commercialisation. The ideal material should regenerate the photo-oxidised dye quickly and transport holes with high mobility. Candidates for solid state HTMs include doped arylamine based small molecules (OMeTAD) [20] and polythiophenes [21]. A power conversion efficiency of 2.5% using OMeTAD was reported by the EPFL group in 2001 [22], greatly improving on earlier studies of that material. The improvement is attributed to the suppression of electron–hole recombination at the metal oxide surface using adsorbed pyridine. The efficiency of this system was raised to over 3% by using silver ions to increase the density of adsorbed dye molecules on the TiO_2 surface, so increasing both J_{sc} and V_{oc} through increased photocurrent generation [23].

A number of other device types have achieved QE comparable with the devices in Table 1, though lower power conversion efficiencies. These include donor–acceptor polymer blend devices with well controlled morphology [24, 25], three layer donor–sensitiser–acceptor structures [26], inorganic–organic heterojunctions [27]; and liquid crystal–crystalline dye devices [28], all discussed below.

5 Challenges in Materials and Device Design

Table 1 shows that whilst organic solar cells produce quite respectable open-circuit voltages, the short circuit photocurrent and fill factor are much lower than those available from inorganic devices. The lower photocurrent is due to poorer light absorption as well as photocurrent generation and transport;

Table 1 The key performance characteristics for these cells as well as the peak QE. For comparison, the characteristics of the best amorphous and monocrystalline silicon solar cells are listed.

Material system	J_{sc} (ma cm^{-2})	V_{oc} (V)	Fill Factor	Efficiency (%)	Peak QE and wavelength (nm)	Reference
Cu phthalocyanine/C_{60} bi-layer cell	13[a]	0.53	0.52	3.6	18% at 620 nm; 35% at 400 nm	[16]
MDMO-PPV-PCBM	5.25	0.83	0.61	2.5; 3.3[b]	50% at 470 nm	[18], [19]
Dye-sensitised solar cell with OMeTAD	4.6	0.93	0.71	3.2	38% at 520 nm	[23]
Amorphous silicon	19.4	0.887	0.74	12.7	~90%	http://www.pv.unsw.edu.au/eff
Monocrystalline silicon	42.2	0.706	0.83	24.7	>90%	http://www.pv.unsw.edu.au/eff

[a] Estimated.
[b] Calculated, at 50°C.

the fill factor is due to poor transport and recombination. Most current research on organic photovoltaic materials and devices is therefore focussed on the following goals:

- Improving light harvesting.
- Improving photocurrent generation.
- Improving charge transport.
- Understanding device function and limits to performance.

Approaches to processing technology and stability are discussed in Sections 7 and 8.

5.1 Light Harvesting

A preferred strategy is to replace conducting polymers in devices with others which absorb further into the red. In the polymer-fullerene cell, lower optical gap replacements for the PPV derivatives, include polythiophene derivatives [29], polypyrrole/thiazadole copolymers [30] and thiophene/naphthene copolymers [31]. (Polythiophenes are of general interest as the hole transporting component in a blend, on account of both their red absorption and good hole mobilities when aligned.) Special red absorbing polymers may be developed for photovoltaic applications, including copolymers with mixed properties, such as a hole transporting backbone with red absorbing side groups.

Another approach is to replace the electron transporting polymer in a blend with conjugated crystalline dyes, such as anthracene or perylene, with wider absorption bands [32]. Extended red absorption can also be achieved using red absorbing *inorganic* semiconductor nanoparticles. Cadmium selenide nano-rods extend absorption to 700 nm [33]. Copper indium diselenide is particularly attractive on account of its very low band gap ($\sim$1 eV in the bulk) and is now being used in polymer-nanoparticle blends [34].

Dye sensitisation is a different strategy where a monolayer of a third material, usually an organic dye, is introduced between donor and acceptor to function as light absorber. Since light absorption and charge transport are carried out by different materials, the light absorber does not need to be a good bulk transporter of charge. Efforts to improve light harvesting in DSSCs include development of alternative dyes and combinations of dyes. A similar concept, of an all-organic donor-absorber-acceptor structure was proposed by Yoshino [6].

A different approach is to maximise the absorption of incident photons in the organic layers. From the perspective of light absorption, organic photovoltaic films are different from inorganic structures in the following important respects:

- Films are sufficiently thin that interference occurs within the layered device, allowing for the design of *light trapping* structures.
- Films are optically anisotropic.

Light trapping structures improve the capture of photons in the active layers through constructive interference. They allow thinner photovoltaic films to be used, and this improves the efficiency of charge transport and collection. The possibilities for light trapping for organic solar cells are discussed by Inganas [35]. Some of these have been investigated using embossed polymer layers for light trapping [36, 37] and exploiting interference effects inside cavities made from photoactive and optically transmitting organic layers [15, 38]. Embossed polymer light trapping structures are already used in thin film silicon solar cells.

Optical anisotropy is important for illumination at large angles, and is relevant to the use of plastic solar cells in diffuse light conditions. In the case of spin cast polymers, the conjugated backbone is likely to be lying in the plane of the film [39] with the result that light incident at large angles is less likely to be absorbed than in an isotropic material. For columnar structures such as discotic liquid crystals, anisotropy *enhances* absorption of light incident at wide angles.

Both effects need to be considered when designing organic photovoltaic devices. Calculation of optical absorption is non-trivial, and relies on good data for the optical functions of the films, usually provided by optical ellipsometry. Figure 4 shows how absorption of light in a thin organic film can be affected by interference.

5.2 Improving Charge Transport

Charge transport is limited by the low intrinsic mobilities of organic solids, and by the charge trapping effects of impurities and defects. In several recent studies, higher mobility polymers such as fluorene-triarylamine and thiophene copolymers have been used to replace MEH-PPV in blend devices [40, 41]. Materials with ordered phases offer high, though anisotropic, mobilities and in this respect liquid crystals [28, 42] and polymers with liquid crystal phases, such as polythiophenes [43], are interesting.

Because organic electron mobilities are generally very poor, an inorganic electron transporting component may be preferred. Thin film [27, 44, 45] and dispersed nanocrystalline [10] TiO_2 has been used in several approaches. TiO_2 is particularly interesting as a cheap and non-toxic material which is stable in oxygen, can be prepared as rigid nanostructured templates, can be used in light trapping structures, and benefits from a wide experience base due to dye sensitised solar cell research. Efficient charge transfer to TiO_2 from various polymers has been reported (MEH-PPV [10, 46], phenyl-amino-PPV [27], polythiophene [21]) and the sensitisation of other oxides such as SnO_2 with polymers has been demonstrated [47].

Elongated crystalline components are attractive as electron transporters if crystal size and orientation can be controlled. Blend devices using needle-like crystalline dyes [32, 48], CdSe nano-rods [33] and carbon nanotubes [49, 50] have been studied. Meanwhile, organic electron transporters with improved mobility and stability are being developed.

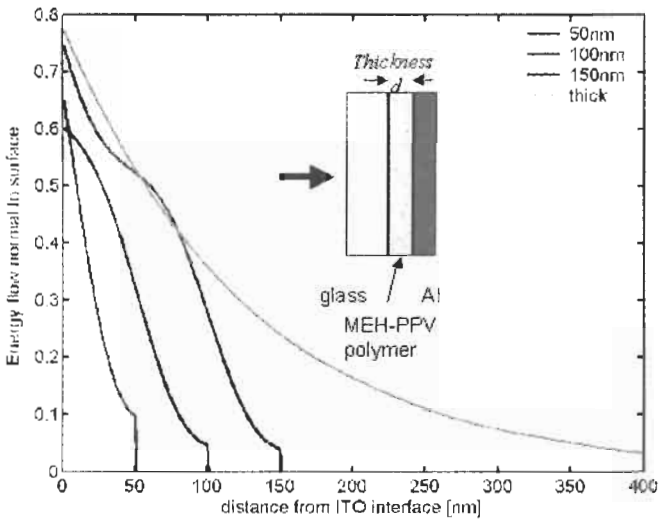

Figure 4 Interference effects influence light harvesting in layered structures. Shown is the fraction of 500 nm light absorbed in a layer of MEH-PPV of thickness d, *sandwiched between glass and aluminium contacts. Interference effects are clear in the shape of the attenuation curve for films of less than 200 nm thick. Notice that a film of 50nm is able to absorb 55% of the light, whilst if interference were neglected 200 nm of material would be needed to absorb the same fraction of the light.*

5.3 Control of Morphology

In a dispersed heterojunction device, both photocurrent generation and charge transport are functions of morphology. Photocurrent generation requires blending on the scale of the exciton diffusion length while transport requires continuous paths from interface to contacts. In polymer-nanocrystal or polymer-fullerene blends, the concentration of the particulate component should be sufficient for charge percolation [9, 51]. One attractive hypothetical configuration is a set of interdigitated electron and hole transporting channels, directed perpendicular to the contacts (this is one motivation for the study of rod-like nanocrystals). Another is a compositionally graded blend with an excess of donor type material on one side and acceptor type on the other. This concept has been demonstrated by Yoshino using vacuum deposited layers [6], and by Granstrom for a laminated assembly [24]. The concept was taken further by Takahashi and co-workers who reported QE of 49% for a three layer structure where electron and hole transporting layers are separated by a heterodimer light absorbing layer [26]. The absorbing layer is polarised upon light absorption to drive the charges towards the appropriate transport layers. This is essentially an all-organic version of the dye-sensitised solar cell. Some different morphologies are illustrated in Figure 5.

In practice many materials tend to segregate when blended, and much attention has focussed on ways of controlling the morphology of blends. Routes include:

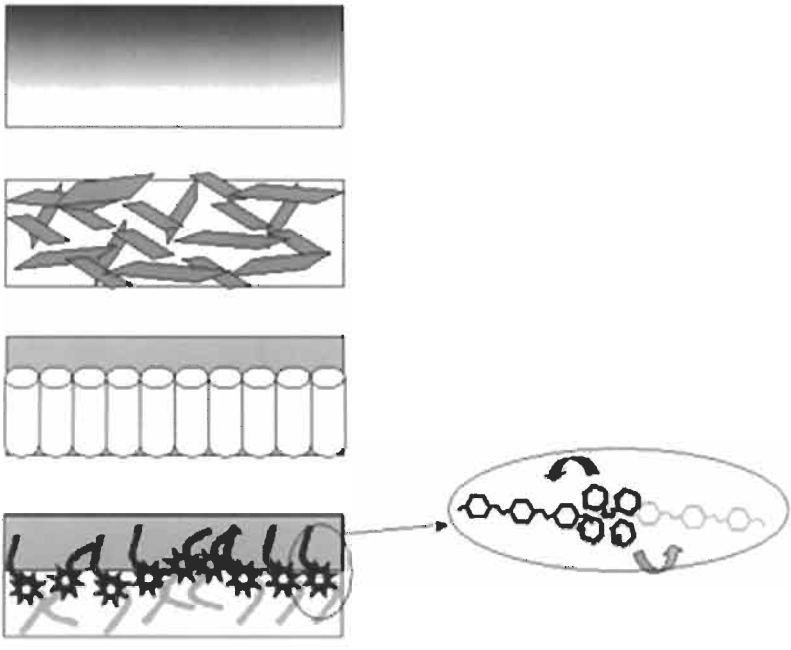

Figure 5 Some approaches to improved charge separation and collection in organic solar cells. In each figure the direction of photocurrent generation is from top to bottom and the electron accepting component is shaded. (a) A compositionally graded blend improves the collection of positive and negative charges near the respective contacts [6, 24]. (b) Elongated electron acceptors such as nano-rods or dye crystals can improve electron transport [32, 33], but for efficient collection they should be directed perpendicular to the contacts. (c) Self-organising discotic liquid crystals are one way of achieving preferential charge transport perpendicular to the contacts [28]. (d) A light absorbing dimer designed to drive positive and negative charges apart after photoexcitation can help to channel respective charges towards electron transporting and hole transporting layers [26].

- Control of blend morphology through processing conditions. Choice of solvent, atmosphere and substrate temperature strongly influence the morphology of polymer blends [40, 41]. Choice of solvent appears to influence segregation of fullerenes in MDMO-PPV [18].
- Self organisation. Self assembly by discotic liquid crystals [28], and by ionically or electrostatically interacting monolayers [52, 53] have been used to construct structured heterojunctions. Self-assembled monolayers can also be used to modify substrate surfaces to control the segregation of blend components [25].
- Synthesis of donor (D)–acceptor (A) copolymers (such as polymer with pendant fullerene groups [54]) and block copolymers. Positioning D and A groups on the same polymer backbone can ensure effective photoinduced D → A electron transfer under all conditions and avoids the problems of phase segregation. D–A copolymers may be designed to absorb longer wavelength photons than single polymers, so improving light harvesting, but charge extraction may be more difficult.

- Use of porous organic or inorganic films as templates (for example, [55]).
- Cosublimation of small molecules to form graded D–A heterostructures [56, 57].

Novel characterisation techniques have been developed to study blend morphology, including spatially resolved fluorescence [40] and confocal Raman spectroscopy [58] as well as AFM and SEM imaging techniques.

5.4 Understanding Function

Understanding of the device physics of organic solar cells is still at a primitive stage, compared to inorganic solar cells. As a basis for device physics, consider the steady-state continuity equation which describes the charge carrier population in any photonic device:

$$\frac{1}{q}\nabla.J_p + G - U = 0 \tag{1}$$

where p is the density of carriers of charge q, J_p the current density, G the volume generation rate and U the recombination rate. For crystalline inorganic p–n junction devices, G can be equated with the local photon absorption rate, and minority carrier recombination and current terms are linear in the carrier density. In organic devices, the description of all three terms is more complicated.

Charge carrier generation, G, can be related to exciton generation if the exciton lifetimes and diffusion lengths, and exciton dissociation efficiencies at interfaces, are known. In planar structures, charge carriers are effectively generated only at the interface (Figure 6) and photocurrent generation can be interpreted in terms of a filter effect [59]. This effect may cause higher photocurrents to result from thinner films, in contradiction to the usual case. In blends, photocurrent generation is a function of interface morphology. In the ideal blend, all photogenerated excitons are dissociated by nearby interfaces, and charge carrier generation is equivalent to light absorption. (Ultrafast transient spectroscopy has been used to demonstrate the fast (sub ps) rate and high yield of charge separation in well dispersed blends, such as polymer-fullerene structures [3].) In all cases interference should be accounted for in calculating the exciton generation profile.

Because organic materials are seldom heavily doped, charge recombination, U, is a bimolecular process. However the kinetics may be influenced by the trapping of charge at defects in the disordered material or competing recombination and transport pathways, and need to be measured for each new material system. Transient optical spectroscopy has proved useful for monitoring the rate of charge recombination in dye sensitised devices [60] and polymer-fullerene structures [61], as has electron spin resonance [62]. In the case of MDMO-PPV/PCBM structures under solar illumination, recombination appears

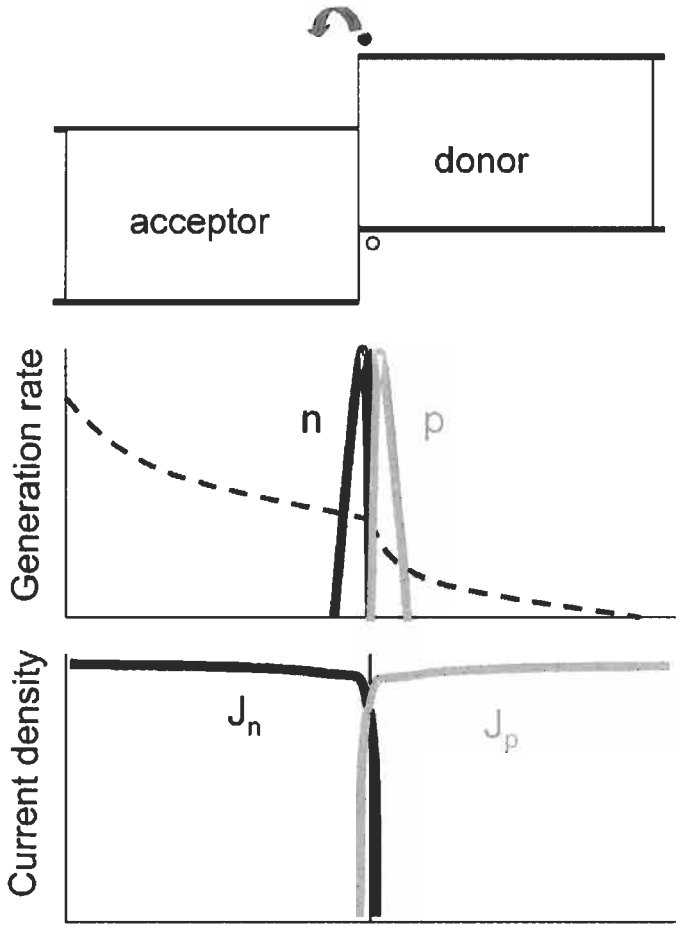

Figure 6 Schematic exciton generation, charge generation and current density profiles for bi-layer structure. Exciton generation follows the absorption of light in the two materials (dashed line). Charge carrier generation occurs only at the interface, leading to delta function profiles for negative charge generation in the acceptor material (black line) and positive charge generation in the donor material (grey line). These narrow charge generation region lead to constant, unipolar currents in the respective materials, and a bimolecular recombination zone located at the interface. The amplitude of the charge generation and therefore the current depends upon the exciton diffusion length and thickness of the front (acceptor) layer. For short exciton diffusion lengths, thinner layers result in higher photocurrents.

to be dominated by the release of positive polarons from trap states and U is a superlinear function of the polaron density.

The current term, J, depends upon the relative contributions of drift and diffusive currents and charge trapping, as well as upon the morphology of donor–acceptor heterostructures. Many organic conductors exhibit dispersive charge transport characteristics, so that both diffusive and drift currents are non-linear functions of carrier density. In blends, charge carrier mobilities are also dependent upon blend composition [63]. The relative importance of drift

and diffusive currents at photovoltaic operating conditions is not well known, but recent work [64, 65] indicates that in planar heterojunctions the driving force due to charge carrier generation at the interface may dominate over the electrostatic driving force due to difference in work function of the contacts, and may dominate the open circuit voltage (Figure 6). This is in contrast with single layer devices where photovoltage is limited by the difference in work functions of the electrode materials, but in agreement with experimental studies of polymer-fullerene blends which show that the photovoltage depends upon the electron affinity of the acceptor rather than the work function of the cathode [66]. This indicates that photocurrent collection in donor-acceptor blends does not require a macroscopic electric field, a situation which is largely agreed to apply to dye sensitised solar cells [67]. Charge trapping further influences current through its influence on the electric field distribution.

On the whole, the device physics of organic solar cells is complicated by uncertainties in material parameters, the effects of heterojunctions and interfaces on materials, and the effects of light, bias and ageing. Further understanding and the development of appropriate models will require further fundamental experimental studies on model systems.

6 Organic Photovoltaic Modules

Plastic solar cells are first likely to be commercialised for low-power, consumer applications, which currently take up about 10% of the market. In this they will compete (most directly) with amorphous silicon (a-Si), and to a lesser extent with emerging thin film technologies. Plastic solar cells may offer advantages over a-Si, in lower production cost, in ease of deposition onto flexible substrates or as conformal coatings on to building materials, or in colour, and these may open up new areas in the consumer photovoltaics market.

Examples of applications might be power supplies for displays and monitors, control electronics, mobile communications, battery chargers, thermoelectric coolers, various consumer products, and photovoltaic windows and other architectural materials. The modules could be integrated into appliances or building materials. In such applications the module would be designed for the specific power output required and would consist of a small number of cells in series, depending on the operating voltage required. Note that since organic solar cells deliver relatively high voltages, any given operating voltage may be achieved with fewer cells than for inorganic materials. Whether cells need to be connected in parallel depends upon the current output required. The high series resistance of ITO coated flexible substrates (10–100 Ω cm^2) place a limit on the useful cell area before unacceptable power loss to series resistance. With a short circuit current density of 10 mA cm^{-2} at one sun (a reasonable goal for organic photovoltaics), this limit might be a few tens of cm^2. However, initial applications for plastic solar cells are likely to be designed for low light levels, such as indoors. The lower illumination levels (indoor illumination is typically less than one tenth of AM1.5 intensity) lead to lower current densities and lower

series resistance penalties, and may avoid the need for parallel connections for current ratings of less than, say, 100 mA.

Modules would be produced directly during cell production (discussed below) whether a batch or a continuous process. Cell interconnects can be integrated into the modules by etching the conductive substrate, scribing the photoactive layers and pattering the top contacts during production, much as is done for inorganic thin films. After metallisation the cell material must be encapsulated in a barrier coating to protect against moisture and oxygen, and in an outer coating appropriate to the intended environment. Outer plastic encapsulants may be used as passive optical concentrators to enhance the amount of light absorbed in the thin active layers the cell. In the case of building integrated modules such as windows or roofing tiles, the deposition of contacts, photoactive layers and cell interconnections could be integrated into the production process for that component. Again, cell sizing and connections will be a function of the expected current output and power requirements.

Although there is as yet no commercial production of organic solar cells, prototype plastic solar modules have been produced at the University of Linz, consisting of several cells in series, with a cell area of a few tens of cm^2. Studies of the effects of increasing cell area [68] show that polymer-fullerene cells can be scaled up to 150cm^2 without large losses in performance.

Production of standard 12 or 24 V dc modules for power generation using plastic photovoltaic materials is still remote. The low efficiency of organic solar cells leads to larger area requirements for power generation, and higher relative costs for the balance of system components. The lower lifetime expectations also increase the cost per kWh. For these reasons organic solar cells are not foreseen to be competitive with inorganic materials for high power applications at least until the obstacles to efficiency and lifetime are overcome.

7 Production Issues

The main driver for organic solar cell development has been the prospect of fabricating large area devices at low cost using production techniques developed for conventional plastics. However, there is as yet no experience in large scale organic cell production, and the following discussion is largely speculative. We discuss below established organic device production technologies which could be applied to photovoltaics, several other approaches which have been explored only in the laboratory, and hypothetical production schemes which are so far untested.

7.1 General Issues

Issues for organic solar cell production are:

- *Flexible substrates.* Conductivity, transmissivity and impermeability to oxygen and water are required. The most widely used material is ITO coated poly(ethylene terephthalate) (PET) which is already used as a

substrate for flexible amorphous silicon solar cells. ITO is limited by a transmissivity of around 80–90% in the visible and a relatively high resistivity (typically 10–50 Ω cm^2) which leads to series resistance limitations, as mentioned above. Film forming properties and electrical contact are improved by coating the ITO with a layer of the doped conducting polymer PEDOT:PSS, though this introduces an additional processing stage. New organic transparent conducting coatings are being studied, but do not yet compete with ITO.

- *Ease of deposition.* In principle, deposition of films from solution is easier and cheaper than that from the gas phase, therefore solution processible materials are preferred. 'One pot, one shot' approaches to deposition of donor-acceptor blend films, where both components are deposited from a single solution, are attractive and enable much easier processing than the sequential deposition of separate layers. In such approaches the use of self assembling materials such as discotic liquid crystals [28] or solvent controlled blend segregation (e.g. [25]) can help control the resulting blend morphology.
- *Chemical stability.* Many conjugated organic solids are unstable in the presence of oxygen and light, and may also be sensitive to water. Devices for research are preferentially fabricated in an inert and dry atmosphere, but maintaining such conditions for large-scale production is costly. Costs could be reduced by finding materials which are sufficiently stable so that devices can be prepared in ambient conditions before encapsulation.
- *Encapsulation.* Coatings are needed which are sufficiently impermeable to moisture and oxygen. This is a problem with organic substrates such as PET which are intrinsically permeable. Recent progress in development of barrier coatings for flexible OLEDs, usually using multiple deposition of organic and inorganic layers to achieve the required combination of flexibility and impermeability [69], has enabled plastic OLED lifetimes approaching 4000 hours [70]. Such coatings may be used for plastic photovoltaic devices.
- *Processing temperature.* High temperature processing stages are costly and damaging to organic films. This may be an issue for solid state dye sensitised solar cells, where electrical contact must be achieved within the metal oxide film without the usual high temperature sintering stage.

The production technology depends upon the materials system used. For dry deposition of photoactive layers, a batch process similar to that used for organic light emitting diodes (OLEDs) could be used. For deposition from solution, batch or continuous processes are in principle possible, although there is as yet no industrial experience in this.

7.2 Production Processes for Molecular Films

Batch or semi-batch processes are already routinely employed for production of OLEDs. The organic materials used are layers of 'small molecules' which can be

evaporated on to the conducting glass substrate, followed by top metal electrodes. The devices are encapsulated in a stainless steel can using an epoxy resin before separation into individual devices. In this process the most expensive stage is the vacuum evaporation, since many expensive vacuum components are required in order to maintain high vacuum ($\sim 10^{-6}$ torr). Batches of area $\sim 370 \times 470$ mm^2 are processed this way. Solar cells or modules could be produced by the same techniques. The process for solar cells should be much simpler since (a) the device unit area (pixel) is much larger and the fine interconnections needed to address OLEDs are not needed, and (b) the number of molecular layers needed is lower (for a colour OLED, more than three electroactive materials are needed as well as contact layers). Nevertheless the process would still be expensive for solar cell production, on account of the high capital and maintenance costs of the vacuum chamber.

A typical batch process for deposition on glass is summarised below in Table 2. The procedures on plastic substrates would be different, and include additional encapsulation stages.

An alternative to vacuum deposition for small molecules is organic vapour-phase deposition (OVPD). Molecules are carried in a flowing gas at high temperature (~ 300°C) and condense on to a cool substrate. Compared to vacuum deposition, the technique does not require high vacuum nor high maintenance costs, it can enable large area coating and it may be compatible with continuous processing. Films of a few tens to hundreds of nm can be produced and surface roughness can be minimised by controlling the flow rate. The applicability of the technique to multilayer OLED fabrication has been demonstrated [71].

7.3 Batch Production Processes for Polymer Films

When the active materials are available in solution, new deposition techniques are available which may greatly reduce costs. Deposition from solution is more viable for solar cells than for LEDs because of the larger device unit area and facile interconnections.

Table 2 Steps in a typical batch process for organic LED deposition on glass.

Pre process	– Clean substrate
	– Etching of bottom contact patterns
	– Building of passivation layer and cathode separator by photolithography
Post process	– Evaporation of molecular layers
	– Evaporation of top contacts
Encapsulation process	– Attachment of desiccant film
	– Alignment of stainless steel casing.
	– Bonding of can to substrate.
Module process	– Scribing into individual devices
	– Connection to flexible printed circuit board
	– Reliability test

For research devices, spin coating is commonly used, but this is uneconomical for large areas because of the material waste. Some of the following production techniques have been considered:

- Doctor blading or 'wire' blading. A rod is drawn over a line of the polymer solution, to spread it out into a thin sheet. This process works well for films of 1 μm thickness, but for thicknesses of a few 100 nm, uniform thicknesses are harder to achieve. Thinner films may be achieved using a rod loosely wrapped with wire of a given thickness. The wire supports the rod and determines the thickness of the resulting polymer film. These approaches are being investigated at Linz.
- Screen printing. A fine mesh screen loaded with polymer solution is brought into temporary contact with the substrate and polymer solution flows across. This technique has been applied to (small area) organic solar cells made from polymer-fullerene blends, producing thin and uniform films (active layer thickness of 40 nm with a roughness of about 2 nm) [72]. The screen printing technique is readily applied to large areas and is widely used in conventional photovoltaic cell production for contact printing. It is also being studied for depositing the metal oxide paste in dye-sensitised solar cells. However, for large area thin films, the mesh is likely to introduce thickness variations.
- Inkjet printing. A fine jet of polymer solution is sprayed on to the substrate in a required pattern. The technique has huge potential for organic electronic devices where fine circuit structures are required, and has been used successfully for organic thin-film transistors [73]. It offers precise contact definition and an easy way to deposit multiple layers. The technique could be applied to organic photovoltaic devices, although processes to achieve uniform film thickness over large areas will need to be developed (the polymer solution needs to wet the substrate surface rather than bead up). A simpler approach is printing polymer and contact materials using an embossed stamp [74]. This may be compatible with reel-to-reel processing.

Some of these techniques are illustrated in Figure 7.

7.4 Continuous Production Processes for Polymer Films

Since the device structure and contact designs for organic solar cells and modules are relatively simple, the modules could be produced from solution by a continuous reel-to-reel process similar to the processes currently used to produce plastic sheeting. Such a process is particularly appropriate for solar cell applications (compared to LEDs) because large areas are required yet the contact patterns and device structures are simple. In principle, well understood production technologies can be adapted and existing plant may be redeployed to the new purpose as a way of reducing production costs. However, reel-to-reel processing has not yet been attempted for any application of organic electronic materials and experience is extremely limited.

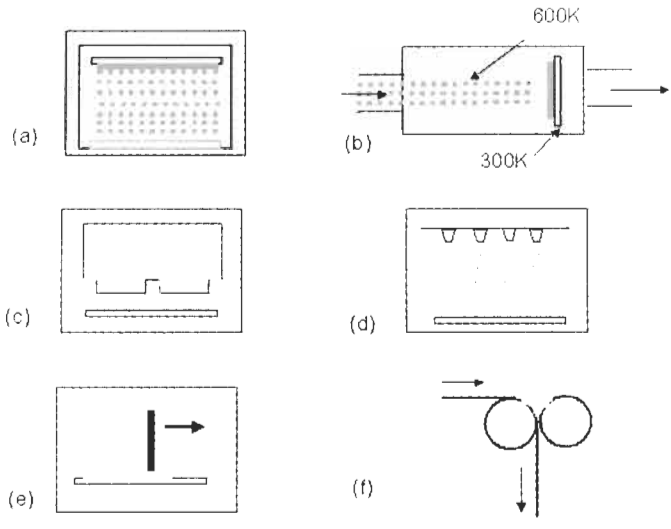

Figure 7 Several possible techniques for deposition of organic photovoltaic films. (a) Molecular deposition in high vacuum. (b) Organic vapour phase deposition. Molecules carried in a heated gas are condensed on to cooled substrates. (c) Printing. Patterned stamps can be used to print polymer films of defined area. (d) Inkjet printing. This allows very fine contact definition. (e) Doctor blading. (f) Compression between rollers.

The stages involved could be as follows (see also Figure 8):

- patterned conducting coating on flexible substrate,
- scribe the conducting coating,
- deposit active layers of 100–200 nm thickness,
- scribe the active layers,
- deposit metal contacts by in-line sputtering at low pressure,
- low-temperature annealing,
- add the encapsulating layer by reel-to reel contact,
- dry and cut.

The key stage in such a process is the deposition of the active layers. The material could be deposited as a blend from a single dispenser, or from a second roller. Dispersed donor acceptor blends can be deposited from a single solution, or laminated donor–acceptor 'bi-layer' structures could be deposited by contact between rollers. As yet these processes are untried. Achieving uniform film thicknesses to within 10 nm over areas of hundreds of cm^2 represents a major challenge.

An important consideration is the sensitivity of the materials to air and moisture whilst in solution. For sensitive materials the entire process could be carried out in a dry and inert atmosphere, but this adds to the cost of the plant.

A number of other industrial techniques are relevant to the development and production of organic photovoltaics. An example is the use of combinatorial techniques to screen different materials combinations and select the best ones [44].

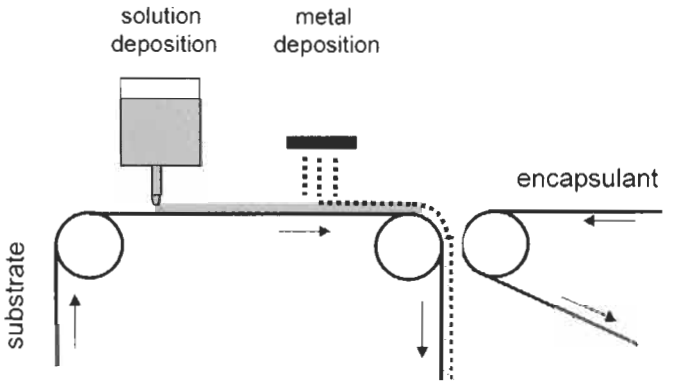

Figure 8 A hypothetical reel-to-reel process. A thin layer of polymer solution is deposited on a conducting substrate, followed by deposition of top metal contacts by a process such as in-line sputtering. Barrier coatings can be applied by a second roller. Scribing of layers to interconnect cells into modules can be integrated into the process (not shown).

8 Stability and Performance

Organic solar cells suffer from instability in two main respects. First, many conjugated materials are unstable in the presence of oxygen and light. The photogenerated exciton is capable of reducing oxygen, generating reactive products (such as superoxide) which react with the molecular material and chemically degrade it. The second is the mechanical instability of donor–acceptor blends. On casting the components are frozen into a non-equilibrium configuration. Over time, the components may segregate, reducing the degree of blending and the effectiveness of charge separation. The latter is a particular problem with polymer-fullerene blends, where the fullerenes tend to cluster.

As yet there is no general solution to the problem of the photostability of conjugated solids. One option is to develop or to use more stable components. Some conjugated dye molecules, liquid crystals and inorganic nanocrystals offer better stability. Until more air stable materials can be developed, devices need to be encapsulated using barrier coatings, as discussed above. An alternative approach is to incorporate sacrificial oxygen scavenging components into the device, such as TiO_2 or other metal oxides. The TiO_2 in solid-state dye-sensitised cells may help to protect the organic components from degradation. Another lesson from dye sensitised solar cell research is that the photoactive components in a solar cell do not have to be extremely stable in isolation. The ruthenium based dye which is used in DSSCs is more stable in the cell configuration than in isolation [75]. This can be attributed to the very short lifetimes of the reactive photogenerated excited state and cation state when in the cell configuration. A similar effect is observed in polymer/fullerene blends, where the photodegradation of the polymer is slowed down by blending with fuilevenes, and again can be attributed to the removal of the reactive exciton by rapid charge separation [76].

The most detailed stability and performance studies of organic solar cells have been carried out on polymer/fullerene systems. These indicate that under normal operation unprotected cells degrade after a few hours, encapsulated cells maintain over 50% of their initial performance for several months [76], degradation is accelerated by high temperatures both in the laboratory [77] and in the field in hot ambient conditions [78]. However, these devices exhibit improved performance with increasing temperature, an advantage over inorganic devices which is attributed to temperature dependent mobility, [79] and shared by polymer blend devices [39] and DSSCs.

Structural instability due to phase segregation in donor-acceptor blends is a function of materials, temperature and time. To some extent segregation may be minimised by choice of solvent and control of interfacial forces (as discussed in Section 5). The problem can be avoided by the use of rigidly connected porous templates such as inorganic semiconductor or metal oxide nanostructures.

A common problem with new device designs of degradation of QE with increasing light intensity, so that cells perform well only under low illumination. Such behaviour is a signature of recombination mechanisms which may be due to impurities, and must be eliminated for the cells to be useful in solar conditions.

Finally it is worth commenting on the measurement and characterisation of organic solar cells. On account of their poor spectral range and poor performance under high light intensities, organic photovoltaic device performance is often reported at a single wavelength and low light intensity. For new materials combinations, the figure of merit is often the QE at peak wavelength rather than the power conversion efficiency. Since wavelength and light intensity vary between reported measurements, as well as ambient conditions (vacuum or air), the comparison of device performance is difficult.

Since organic solar cells are likely to be used in quite different contexts to conventional photovoltaics, for instance, under low or diffuse light levels, or in windows where partial transparency is required, the standard test condition may not be the most relevant. There is a case for establishing new measurement standards more relevant for organic solar cell measurement and calibration.

9 Conclusions

Progress with organic photovoltaic materials and devices in recent years has been impressive. Power conversion efficiencies over 3% have been achieved in at least three different device structures, varying from high quality, vacuum deposited multilayer molecular films to dispersed heterojunctions in spin cast soluble polymers. All are based on the concept of a donor–acceptor system where photogenerated excitons are split by forces at the donor–acceptor interface. Higher efficiency requires improvements in absorption of red light, in charge transport and in material stability. Recent research focuses on the synthesis and testing of new photovoltaic materials in established device structures, and the development of new structures where morphology is controlled through self-assembly and processing conditions. Experience with commercial scale

devices is still limited, as is the theoretical understanding of device function. Based on current trends, efficiencies of 5–10% appear to be within reach, although stability remains an obstacle.

Acknowledgements

The author is grateful to Youngkyoo Kim, Stephen Forrest, Ralph Gottschalg and James Durrant for helpful discussions, and to Felix Braun for help with Figure 4. The support of the Engineering and Physical Sciences Research Council and the Greenpeace Environmental Trust is acknowledged.

References

[1] Heeger, A.J., 2001. Semiconducting and metallic polymers: The fourth generation of polymeric materials. *J. Physical Chemistry B*, Vol. 105(36), pp. 8475–8491.

[2] Wallace, G.G. et al., 2000. Conjugated polymers: New materials for photovoltaics. *Chemical Innovation*, Vol. 30 (4), pp. 15–22.

[3] Brabec, C.J., Sariciftci, N.S. and Hummelen, J.C., 2001. Plastic solar cells. *Advanced Functional Materials*, Vol. 11(1), pp. 15–26.

[4] Halls, J.J.M. and Friend, R.H., 2001. Organic Photovoltaic Devices. In: Archer, M.D. and Hill, R.D., Eds., *Clean Electricity from Photovoltaics*, Imperial College Press, London, pp. 377–445.

[5] Yu, G. and Heeger, A.J., 1995. Charge Separation and Photovoltaic Conversion in Polymer Composites with Internal Donor–Acceptor Heterojunctions. *J. Appl. Phys.* Vol. 78(7), pp. 4510–4515.

[6] Yoshino, K. et al., 1997. Novel photovoltaic devices based on donor–acceptor molecular and conducting polymer systems. *IEEE Transactions on Electron Devices*, Vol. ED-44(8), pp. 1315–1324.

[7] Halls, J.J.M. et al., 1995. Efficient Photodiodes from Interpenetrating Polymer Networks. *Nature*, Vol. 376(6540), pp. 498–500.

[8] Yu, G. et al., 1995. Polymer Photovoltaic Cells – Enhanced Efficiencies Via a Network of Internal Donor–Acceptor Heterojunctions. *Science*, Vol. 270(5243), pp. 1789–1791.

[9] Greenham, N.C., Peng, X.G. and Alivisatos, A.P., 1996. Charge separation and transport in conjugated polymer/semiconductor-nanocrystal composites studied by photoluminescence quenching and photoconductivity. *Physical Review B*, Vol. 54(24), pp. 17628–17637.

[10] Salafsky, J.S., 1999. Exciton dissociation, charge transport, and recombination in ultrathin, conjugated polymer-TiO2 nanocrystal intermixed composites. *Physical Review B*, Vol. 59(16), pp. 10885–10894.

[11] Petritsch, K. et al., 2000. Dye-based donor/acceptor solar cells. *Solar Energy Materials and Solar Cells*, Vol. 61(1), pp. 63–72.

[12] Hagfeldt, A. and Gratzel, M., 2000. Molecular photovoltaics. *Accounts of Chemical Research*, Vol. 33(5), pp. 269–277.

[13] Schon, J.H. et al., 2000. Efficient organic photovoltaic diodes based on doped pentacene. *Nature*, Vol. 403(6768), pp. 408–410.

[14] Schon, J.H., Kloc, C. and Batlogg, B., 2001. Pentacene based photovoltaic devices. *Synthetic Metals*, Vol. 124(1), pp. 95–97.

[15] Peumans, P., Bulovic, V. and Forrest, S.R., 2000. Efficient photon harvesting at high optical intensities in ultrathin organic double-heterostructure photovoltaic diodes. *Applied Physics Letters*, Vol. 76(19), pp. 2650–2652.

[16] Peumans, P. and Forrest, S.R., 2001. Very-high-efficiency double-heterostructure copper phthalocyanine/C-60 photovoltaic cells. *Applied Physics Letters*, Vol. 79(1), pp. 126–128.

[17] Yakimov, A. and Forrest, S.R., 2002. High photovoltage multiple-heterojunction organic solar cells incorporating interfacial metallic nanoclusters. *Applied Physics Letters*, Vol. 80(9), pp. 1667–1669.

[18] Shaheen, S.E. et al., 2001. 2.5% efficient organic plastic solar cells. *Applied Physics Letters*, Vol. 78(6), pp. 841–843.

[19] Brabec, C.J. et al., 2002. Effect of LiF/metal electrodes on the performance of plastic solar cells. *Applied Physics Letters*, Vol. 80(7), pp. 1288–1290.

[20] Bach, U. et al., 1998. Solid-state dye-sensitized mesoporous TiO2 solar cells with high photon-to-electron conversion efficiencies. *Nature*, Vol. 395(6702), pp. 583–585.

[21] Spiekermann, S. et al., 2001. Poly(4-undecyl-2,2'-bithiophene) as a hole conductor in solid state dye sensitized titanium dioxide solar cells. *Synthetic Metals*, Vol. 121(1–3), pp. 1603–1604.

[22] Kruger, J. et al., 2001. High efficiency solid-state photovoltaic device due to inhibition of interface charge recombination. *Applied Physics Letters*, Vol. 79(13), pp. 2085–2087.

[23] Kruger, J. et al., 2002. Improvement of the photovoltaic performance of solid-state dye- sensitized device by silver complexation of the sensitizer cis-bis(4,4'-dicarboxy-2,2'-bipyridine)-bis(isothiocyanato) ruthenium(II). *Applied Physics Letters*, Vol. 81(2), pp. 367–369.

[24] Granstrom, M. et al., 1998. Laminated fabrication of polymeric photovoltaic diodes. *Nature*, Vol. 395(6699), pp. 257–260.

[25] Arias, A.C. et al., 2002. Vertically segregated polymer blend photovoltaic thin film structures through surface mediated solution processing. *Applied Physics Letters*, in press.

[26] Takahashi, K. et al., 2000. Three-layer organic solar cell with high-power conversion efficiency of 3.5%. *Sol. Energy Mater. Sol. Cells*, Vol. 61(4), pp. 403–416.

[27] Arango, A.C. et al., 2000. Efficient titanium oxide/conjugated polymer photovoltaics for solar energy conversion. *Advanced Materials*, Vol. 12(22), p. 1689.

[28] Schmidt-Mende, L. et al., 2001. Self-organized discotic liquid crystals for high-efficiency organic photovoltaics. *Science*, Vol. 293(5532), pp. 1119–1122.

[29] Brabec, C.J. et al., 2001. Influence of disorder on the photoinduced excitations in phenyl substituted polythiophenes. *Journal of Chemical Physics*, Vol. 115(15), pp. 7235–7244.

[30] Dhanabalan, A. et al., 2001. Synthesis and characterization of a low bandgap conjugated polymer for bulk heterojunction photovoltaic cells. *Advanced Functional Materials*, Vol. 11(4), pp. 255–262.

[31] Shaheen, S.E. et al., 2001. Low band-gap polymeric photovoltaic devices. *Synthetic Metals*, Vol. 121(1–3), pp. 1583–1584.

[32] Dittmer, J.J., Marseglia, E.A. and Friend, R.H., 2000. Electron trapping in dye/polymer blend photovoltaic cells. *Advanced Materials*, Vol. 12(17), 2000, p. 1270.

[33] Huynh, W.U., Dittmer, J.J. and Alivisatos, A.P., 2002. Hybrid nanorod-polymer solar cells. *Science*, Vol. 295(5564), pp. 2425–2427.

[34] Arici, E. et al., 2001. CIS Plastic Solar Cells. *Proc. 17th European Photovoltaic Solar Energy Conf.*

[35] Inganas, O. et al., 2001. Recent progress in thin film organic photodiodes. *Synthetic Metals*, Vol. 121(1–3), pp. 1525–1528.

[36] Niggemann, M. et al., 2001. Trapping Light in Organic Plastic Solar Cells with integrated Diffraction Gratings. *Proc. 17th European Photovoltaic Solar Energy Conf.*

[37] Roman, L.S. et al., 2000. Trapping light in polymer photodiodes with soft embossed gratings. *Advanced Materials*, Vol. 12(3), p. 189.

[38] Rostalski, J. and Meissner, D., 2000. Photocurrent spectroscopy for the investigation of charge carrier generation and transport mechanisms in organic p/n junction solar cells. *Sol. Energy Mater. Sol. Cells*, Vol. 63(1), pp. 37–47.

[39] Ramsdale, C.M. and Greenham, N.C., 2002. Ellipsometric determination of anisotropic optical constants in electroluminescent conjugated polymers. *Advanced Materials*, Vol. 14(3), p. 212.

[40] Halls, J.J.M. et al., 2000. Photodiodes based on polyfluorene composites: Influence of morphology. *Advanced Materials*, Vol. 12(7), p. 498.

[41] Arias, A.C. et al., 2001. Photovoltaic performance and morphology of polyfluorene blends: A combined microscopic and photovoltaic investigation. *Macromolecules*, Vol. 34(17), pp. 6005–6013.

[42] Struijk, C.W. et al., 2000. Liquid crystalline perylene diimides: Architecture and charge carrier mobilities. *Journal of the American Chemical Society*, Vol. 122(45), pp. 11057–11066.

[43] Videlot, C., El Kassmi, A. and Fichou, D., 2000. Photovoltaic properties of octithiophene-based Schottky and p/n junction cells: Influence of molecular orientation. *Sol. Energy Mater. Sol. Cells*, Vol. 63(1), pp. 69–82.

[44] Thelakkat, M., Schmitz, C. and Schmidt, H.W., 2002. Fully vapor-deposited thin-layer titanium dioxide solar cells. *Advanced Materials*, Vol. 14(8), pp. 577–581.

[45] Fan, Q. et al., 2001. A solid state solar cell using sol-gel processed material and a polymer. *Chemical Physics Letters*, Vol. 347(4–6), pp. 325–330.

[46] Savenije, T.J., Warman, J.M. and Goossens, A., 1998. Visible light sensitisation of titanium dioxide using a phenylene vinylene polymer. *Chemical Physics Letters*, Vol. 287(1–2), pp. 148–153.

[47] Anderson, N.A. et al., 2002. Subpicosecond photoinduced electron transfer from a conjugated polymer to SnO_2 semiconductor nanocrystals. *Physica E*, Vol. 14, pp. 215–218.

[48] Cabanillas-Gonzales, J. et al., 2003. Effect of aggregation on photocurrent generation in polyfluorene doped with violanthrone. *Synthetic Metals*, Vol. 137, pp. 1471–1472.

[49] Ago, H. et al., 1999. Composites of carbon nanotubes and conjugated polymers for photovoltaic devices. *Advanced Materials*, Vol. 11(5), pp. 1281.

[50] Lee, S.B. et al., 2001. Electrical and optical properties of conducting polymer-C-60 carbon nanotube system. *Synthetic Metals*, Vol. 121(1–3), pp. 1591–1592.

[51] Brabec, C.J. et al., 1999. Photovoltaic properties of conjugated polymer/methanofullerene composites embedded in a polystyrene matrix. *J. Appl. Phys.*, Vol. 85(9), pp. 6866–6872.

[52] Baur, J.W. et al., 2001. Photovoltaic interface modification via electrostatic self- assembly. *Synthetic Metals*, Vol. 121(1–3), pp. 1547–1548.

[53] Schroeder, R. et al., 2001. Control of excited state dynamics in ionically self-assembled monolayers of conjugated molecules. *Synthetic Metals*, Vol. 121(3), pp. 1521–1524.

[54] Ramos, A.M. et al., 2001. Photoinduced electron transfer and photovoltaic devices of a conjugated polymer with pendant fullerenes. *Journal of the American Chemical Society*, Vol. 123(27), pp. 6714–6715.

[55] de Boer, B. et al., 2001. Synthesis and self-organization of PPV-based block copolymers for photonic applications. *Synthetic Metals*, Vol. 121(1–3), pp. 1541–1542.

[56] Murgia, M. et al., 2001. Intedigitated p–n junction: a route to improve the efficiency in organic photovoltaic cells. *Synthetic Metals*, Vol. 121(1–3), pp. 1533–1534.

[57] Pfeiffer, M., et al., 2000. Controlled p-doping of pigment layers by cosublimation: Basic mechanisms and implications for their use in organic photovoltaic cells. *Sol. Energy Mater. Sol. Cells*, Vol. 63(1), pp. 83–99.

[58] Stevenson, R., et al., 2001. Raman microscopy determination of phase composition in polyfluorene composites. *Applied Physics Letters*, Vol. 79(14), pp. 2178–2180.

[59] Harrison, M.G., Gruner, J. and Spencer, G.C.W., 1997. Analysis of the photocurrent action spectra of MEH-PPV polymer photodiodes.*Physical Review B*, Vol. 55(12), pp. 7831–7849.

[60] Nogueira, A.F. et al., 2001. Electron transfer dynamics in dye sensitized nanocrystalline solar cells using a polymer electrolyte. *Journal of Physical Chemistry B*, Vol. 105(31), pp. 7517–7524.

[61] Montanari, I. et al., 2002. Transient optical studies of charge recombination dynamics in a polymer/fullerene composite at room temperature. *Applied Physics Letters*, Vol. 81(16), pp. 3001–3003.

[62] Dyakonov, V. et al., 2001. Spectroscopy on polymer-fullerene composites and photovoltaic cells. *Synthetic Metals*, Vol. 121(1–3), pp. 1529–1532.

[63] Pacios, R. et al., 2003. Efficient polyfluorene based solar cells. *Synthetic Metals*, Vol. 137, pp. 1469–1470.

[64] Ramsdale, C.M. et al., 2002. The origin of the open-circuit voltage in polyfluorene-based photovoltaic devices. *Journal of Applied Physics*, Vol. 92(8), pp. 4266–4270.

[65] Gregg, B.A. and Hanna, M.C., 2003. Comparing organic to inorganic photovoltaic cells: Theory, experiment and simulation. *Journal of Applied Physics*, Vol. 93, pp. 3605–3614.

[66] Brabec, C.J. et al., 2001. Origin of the open circuit voltage of plastic solar cells. *Advanced Functional Materials*, Vol. 11(5), pp. 374–380.

[67] Cahen, D. et al., 2000. Nature of photovoltaic action in dye-sensitized solar cells. *Journal of Physical Chemistry B*, Vol. 104(9), pp. 2053–2059.

[68] Padinger, F. et al., 2000. Fabrication of large area photovoltaic devices containing various blends of polymer and fullerene derivatives by using the doctor blade technique. *Opto-Electronics Review*, Vol. 8(4), pp. 280–283.

[69] Burrows, P.E. et al., 2001. Ultra barrier flexible substrates for flat panel displays. *Displays*, Vol. 22(2), pp. 65–69.

[70] Weaver, M.S. et al., 2002. Organic light-emitting devices with extended operating lifetimes on plastic substrates. *Applied Physics Letters*, Vol. 81(16), pp. 2929–2931.

[71] Shtein, M. et al., 2001. Material transport regimes and mechanisms for growth of molecular organic thin films using low-pressure organic vapor phase deposition. *J. Appl. Phys.*, Vol. 89(2), pp. 1470–1476.

[72] Shaheen, S.E. et al., 2001. Fabrication of bulk heterojunction plastic solar cells by screen printing. *Applied Physics Letters*, Vol. 79(18), pp. 2996–2998.

[73] Sirringhaus, H. et al., 2000. High-resolution inkjet printing of all-polymer transistor circuits. *Science*, Vol. 290, pp. 2123–2126.

[74] Kim, C., Shtein, M. and Forrest, S.R., 2002. Nanolithography based on patterned metal transfer and its application to organic electronic devices. *Applied Physics Letters*, Vol. 80(21), pp. 4051–4053.

[75] Nazeeruddin, M.K. et al., 1993. Conversion of Light to Electricity by Cis-X2bis(2,2'-Bipyridyl-4,4'-Dicarboxylate) Ruthenium(II) Charge-Transfer Sensitizers (X = Cl^-, Br^-, I^-, Cn^-, and Scn^-) on Nanocrystalline TiO_2 Electrodes. *Journal of the American Chemical Society*, Vol. 115(14), pp. 6382–6390.

[76] Neugebauer, H. et al., 2000. Stability and photodegradation mechanisms of conjugated polymer/fullerene plastic solar cells. *Sol. Energy Mater. Sol. Cells*, Vol. 61(1), pp. 35–42.

[77] Padinger, F. et al., 2001. Degradation of bulk heterojunction solar cells operated in an inert gas atmosphere: a systematic study. *Synthetic Metals*, Vol. 121(1–3), pp. 1605–1606.

[78] Tuladhar, S.M. et al., 2001. Out-door photovoltaic characterization of plastic solar cells. Presented at the *International Workshop on Nanostructures in Photovoltaics*, Dresden, unpublished.

[79] Katz, E.A. et al., 2001. Temperature dependence for the photovoltaic device parameters of polymer-fullerene solar cells under operating conditions. *J. Appl. Phys.*, Vol. 90(10), pp. 5343–5350.

Part III

Photovoltaic Systems

Part IIIa

Introduction

Energy Production by a PV Array

Luis Castañer and Sandra Bermejo, Universidad Politecnica de Catalunya, Barcelona, Spain
Tom Markvart and Katerina Fragaki, School of Engineering Sciences, University of Southampton, UK

1 Annual Energy Production

The power produced by a PV system depends on a range of factors which need to be examined when the system is designed; it is also useful to assess the accuracy of simplified treatments where these factors are ignored or neglected. Such analysis is conveniently carried out by looking at the total annual energy produced by the system. A recent comprehensive study has identified seven factors influencing the annual performance of PV modules [1] and a brief summary of the main conclusions follows.

- *Cumulative solar irradiance.* Long-term irradiance profiles depend on surface orientation and possibly tracking. This factor depends on the location and varies between a reduction by about 25% for a vertical surface to over 30% increase for two axis tracking, in comparison with a latitude-tilt fixed system. The effect of module orientation is considered further in Section 5, and is analysed in detail in Part I.
- *Module power rating at standard test conditions.* Analysis of several PV technologies has shown that for the same power rating all technologies were equivalent in terms of the expected annual energy production within 5% calculation error.
- *Operating temperature.* Analysis of various technologies and sites shows that the annual production can be reduced due to the operating temperature by a factor between 2 and 10%, depending on the module design, wind speed, mounting technique and ambient temperature. The effect of operating temperature is discussed quantitatively in Section 4.
- *Maximum power point voltage dependence on irradiance level.* a-Si and CdTe modules tend to have a value of the maximum power point voltage larger at low irradiance levels than at the standard 1 sun conditions. This fact can result in an additional 10% increase in annual energy production.
- *Soiling.* Soiling may account for up to a 10% of reduction of the annual energy production.
- *Variation in solar spectrum.* It is found that the effects of the hourly variation of the solar spectrum almost cancel out in a yearly basis. Amorphous silicon technology has the highest sensitivity to this effect, but the observed changes usually remain under 3%.
- *Optical losses when the sun is at a high angle of incidence (AOI).* The optical losses are due to the increased reflectance of the cover glass of the PV modules for AOI greater than approximately 60°. However, the effect on a long term basis is relatively small (typically under 5%) although it may have larger effect on a seasonal basis (close to 10% for a vertical inclination).

2 Peak Solar Hours: Concept, Definition and Illustration

The initial approximate analysis and design of a PV system is usually based on Peak Solar Hours (PSH): a convenient definition of the equivalent of one day.

This concept is particularly useful for the first-order sizing of flat-plate (non-concentrating) arrays which operate under global radiation (see IIIa-3). The magnitude of Peak Solar Hours is equal to the length of an equivalent day with a constant irradiance equal to the 1 sun intensity (1 kW/m^2), resulting in the same value of the daily radiation. This parameter has units of time and when given in hours, it has the same numerical value as the total daily radiation in kWh/m^2-day. Accordingly, the total generation of a PV array exposed to solar radiation a whole year can be estimated as,

$$E_A = \sum_{i=1}^{365} (PSH)_i P_0 \tag{1}$$

where $(PSH)_i$ is the value of the parameter PSH for day i and P_0 is the nominal array power under standard or reference conditions.

For arrays operating at the maximum power point, the normalised instantaneous power output P_A/P_{max} depends on temperature and irradiance, and Equation (1) is therefore only an approximation. A better estimate of the annual generation can be obtained by a model which uses actual values of the ambient temperature, and estimates the cell operating temperature using the *NOCT* concept (see Section 4) [3] and the cell efficiency temperature coefficient [2]. Figure 1 shows the error involved in the use of Equation (1) rather than by taking into account the full temperature and irradiance dependence of the array power output. As can be seen, the average annual errors lie between −2% and −15%, similar to the experimentally observed values discussed in Section 1. Clearly, the error is larger in locations where the yearly radiation and average temperature are higher.

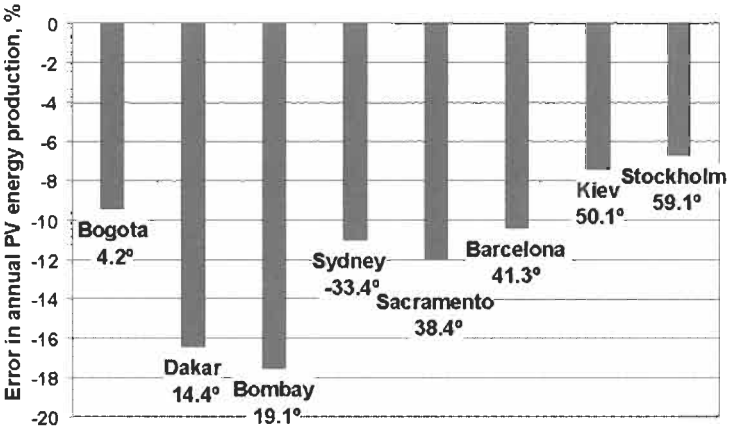

Figure 1 Error involved in the use of Equation (1) to calculate the annual energy output by a PV array at several locations worldwide. Numbers by locations indicate the latitude. Source of the radiation and temperature data: Meteonorm program [11].

3 Nominal Array Power

Results in Figure 1 are specific for arrays operating at the maximum power point This usually includes all systems with an inverter and larger DC systems, with power rating in excess of 1 kW or so. In these systems, the voltage is controlled by the maximum power point tracker (MPPT) to follow the optimum maximum power point voltage V_m.

The situation is somewhat different in smaller stand alone systems where the array voltage is controlled by the load typically consisting of a charge regulator and a battery (Figure 2). Here, the array delivers power at a voltage close to the battery voltage V_{bat} and the reduction in array output shown in Figure 1 is compensated by a lower nominal array power instead of P_{max}. The design of a standard PV module consisting of 36 crystalline silicon cells has evolved from the need to charge a 12 V battery. In practical usage, the module then operates in the linear part of its I–V characteristic and supplies approximately the same current I_{sc} as at short circuit. The power P_A delivered by the array to the battery and load in parallel connection is then

$$P_A \cong V_{bat} I_{sc} \tag{2}$$

which takes into account the actual bias point of the module and the instantaneous value V_{bat} of the battery voltage. The voltage drop at the blocking diode which is not included in Equation (2) is discussed in more detail in Section 7. Losses in the charge regulator can often be neglected as most modern regulators have switches in place of diodes and hence the voltage drop is small.

The average value of P_A – the effective module power rating – is often approximated by nominally setting V_{bat} equal to 12 V:

$$P_{eff} = \langle P_A \rangle \cong 12 I_{sc} \tag{3}$$

Equation (3) – *valid for a system without maximum power point tracking* – is a useful approximation for the analysis of the long-term energy balance in stand alone systems, and for the development of sizing procedures, as discussed in Chapters IIIa-2 and -3. The accuracy of Equation (2) in a specific application can be verified for the actual daily load profile with the help of detailed system models.

As a practical example, BP Solar module with manufacturers rating of 85 W_p, I_{sc} = 5 A and maximum power point values V_m = 18 V, I_m = 4.72 A produces P_{eff} = 12 × 5 = 60 W which is a reduction of about 29% on P_{max} at STC.

4 Temperature Dependence of Array Power Output

The principal effect of temperature on the PV array output comes from the temperature dependence of the open-circuit voltage (see Figure 4) which can be described by

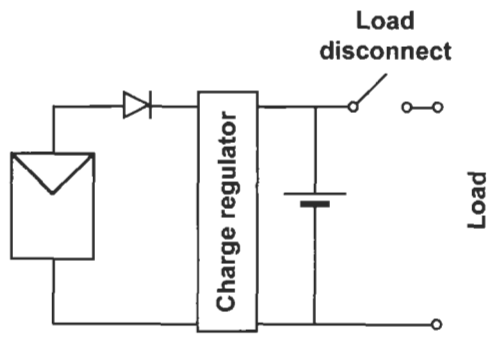

Figure 2 A typical configuration of a stand-alone photovoltaic system. The load disconnect is usually incorporated in the charge regulator.

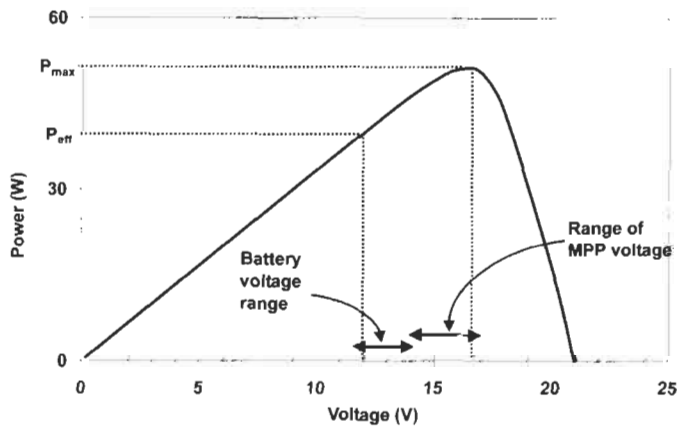

Figure 3 The power output from a typical crystalline silicon PV module, showing two characteristic power levels: P_{max}, the power at the maximum power point, and P_{eff}, the effective power output at the nominal battery voltage.

$$V_{oc}(T_c) = V_{oc}(STC) + \frac{dV_{oc}}{dT}(T_c - 25) \tag{4}$$

where T_c is the cell temperature and dV_{oc}/dT is the temperature coefficient. If an accurate measured value is not known, the following theoretical expression

$$\frac{dV_{oc}}{dT} = \frac{V_{oc} - E_{g0} - \gamma k_B T_c}{T_c} \times \textit{number of cells in the module} \tag{5}$$

can be used, where the energy gap E_{g0} (extrapolated linearly to 0 K) and the thermal energy $k_B T_c$ are given in electronvolts, and $\gamma = 3$ for silicon [2]. For a typical module of 36 crystalline silicon cells, Equation (4) gives a temperature coefficient of approximately -80 mV/°C. The cell temperature T_c can be estimated from the ambient temperature T_a and the irradiance G with the use of a parameter called the Nominal Operating Cell Temperature (*NOCT*)

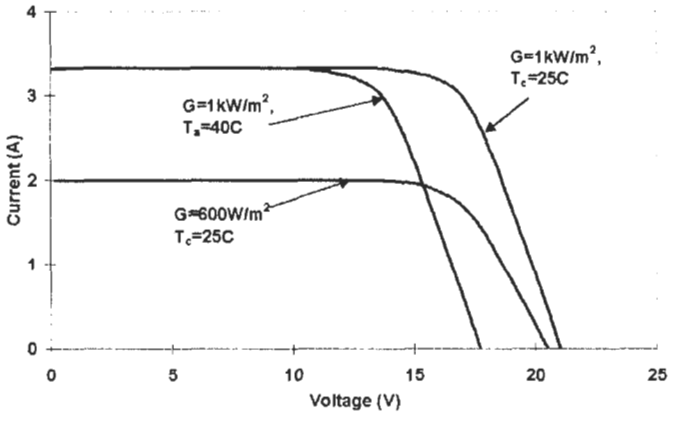

Figure 4 The IV characteristic of a typical crystalline silicon PV module as a function of irradiance G and temperature. T_a denotes the ambient temperature, and T_c the is temperature of the solar cells.

$$T_c = T_a + \frac{NOCT - 20}{800} G \tag{6}$$

where *NOCT* is expressed in °C and the irradiance *G* in W/m² [3]. If *NOCT* is not known, 48°C is recommended as a reasonable value which describes well most of the commonly used PV modules.

Under most circumstances, the temperature dependence of the short-circuit current can be neglected (for example, the temperature coefficient of the BP585 module is equal to 0.065%/°C).

The measurement of the temperature coefficient of PV modules is discussed in Chapters IV-1 and -3. A theoretical discussion of the temperature dependence of solar cell parameters including other materials can be found in [4]. A scheme that can be used to calculate the temperature dependence of the power output at maximum power is discussed by Lorenzo [5] A simplified version which uses the assumption on temperature-independent fill factor is given in [6]. At maximum power, for example, BP Solar give the value of −0.5%/°C for the module BP585.

5 Module Orientation

5.1 Fixed Tilt Arrays

The output from the PV generator depends on solar radiation incident on the inclined panels of the PV array. Methods to analyse solar radiation data are discussed extensively in Part I; software packages which were developed for PV applications are reviewed in Chapter IIIa-3. In some applications, the array orientation will be constrained by the nature of the support system: for example, the orientation of a building-integrated array will normally be dictated

by the orientation of the roof or facade where the array is to be installed. For a free-standing PV array, the most important consideration in deciding the array orientation is to maximise the energy collection by the inclined PV panels. This will frequently depend on the seasonal nature of the load. The typical examples include:

- Some applications require energy only during the summer months. This may be the case, for example, for many irrigation systems.
- If load is to be powered over the entire year, energy supply during the winter months is likely to be key to satisfactory operation, and the panel orientation should ensure optimum energy capture during the month with the lowest daily radiation. In the Northern hemisphere, this is usually be the month of December.
- The annual average is sometimes used in locations with little variation of daily solar radiation during the year. The PV system battery is then used partly as a seasonal energy storage, and care should be exercised to choose an appropriate type of battery for this purpose (see Chapter IIIb-2).

Practical 'rules-of-thumb' for panel inclination are summarised in Table 1 [7]. The use of the recommended values in Table 1 is normally justified by the simplicity and by the fact that the energy produced by the array is not very sensitive to the precise angle of inclination. For best results, however, one of the software packages discussed in Chapter IIIa-3 and Part I should be consulted.

5.2 Arrays with Tracking

PV arrays which track the sun can collect a higher amount of energy than those installed at a fixed tilt. The use of tracking is common for concentrator arrays which – at least for appreciable concentration ratios – collect only the direct (beam) radiation. The relationship between the annual solar radiation captured by a tracking system and a fixed tilt panel inclined at the angle of latitude for a number of locations across the world is illustrated in Figure 5 [8]. It is seen that, on a yearly basis, the energy capture by a tracking flat-plate system is increased by more than 30% over a fixed array at latitude inclination. At the same time we note, however, that a tracking concentrator system will collect more energy than a flat-plate system only in locations with predominantly clear skies. Practical methods of estimating the solar energy available to concentrator systems are discussed further in Chapter IIId-1.

Table 1

Season	Optimum angle of inclination
Summer	Latitude −15°
Winter	Latitude +15°
Year average	Latitude

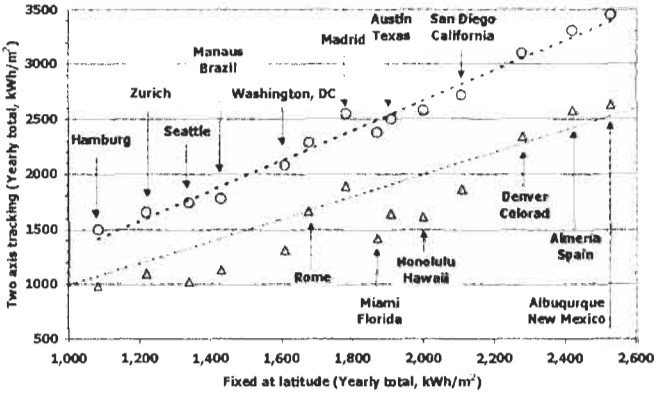

Figure 5 Comparison of energy collected by a panel at a fixed tilt equal to the angle of latitude, with two axis tracking. Circles are measured values of global radiation, triangles correspond to direct beam. The dashed line is a fit to the global radiation points, corresponding to an increase of 33.5%. The dash-dot line shows solar radiation on the fixed tilt plane at latitude inclination (adapted from reference [8]).

6 Statistical Analysis of the Energy Production

In a number of situations – for example, when considering the rating of an inverter in grid-connected systems (see Chapter IIIa-3) – it is useful to know the statistical distribution of power produced by the array. To this end, let us consider the (average) number of hours that solar irradiance on the array falls in a small interval δG between G and $G + \delta G$. This number of hours is proportional to δG and will be denoted $h_I(G)\delta G$. Clearly

$$\int_0^\infty h_I(G)dG = H \tag{7}$$

where H is the total number of hours in a year which can be taken equal to 8760. The integral of the incident energy $Gh_I(G)\delta G$, expressed in kWh, is then equal to the sum of Peak Solar Hours over the whole year:

$$\int_0^\infty Gh_I(G)dG = \sum_{i=1}^{365} PSH_i \tag{8}$$

The statistics of power generation by the array can be analysed in a similar fashion. If $h_P(P)\delta P$ denotes the number of hours the array generates power between P and $P + \delta P$, the energy produced in this interval is equal to $Ph_P(P)\delta P$. The integral of this function is the total energy produced in a year E_A:

$$\int_0^\infty Ph_I(P)dP = E_A \tag{9}$$

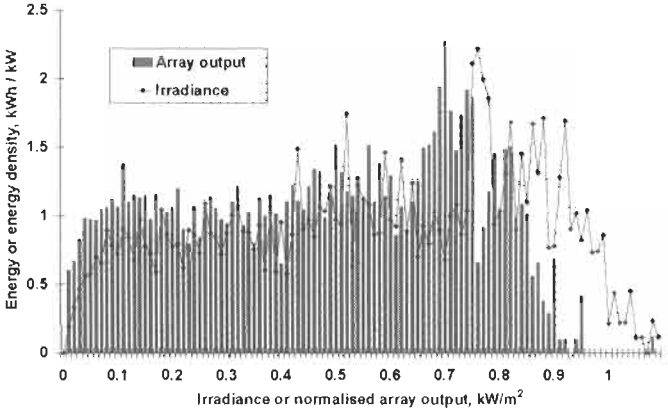

Figure 6 The array output energy $\mathrm{Ph_P(P)}$ *and solar radiation* $\mathrm{Gh_I(G)}$ *as functions of the ratio* $\mathrm{P_{max}/P_{max}(STC)}$ *and G, respectively. Source of data: STaR Facility, University of Southampton.*

The energy E_A was already discussed in Sections 1 and 2 which also analysed the validity of approximating E_A by the sum (1).

The functions $Gh_I(G)$ and $Ph_P(P)$ are important for the sizing of inverters and will be discussed further in Chapter IIIa-3, Section 4. In practice, these functions can be obtained from a representative sample of solar radiation and array power output data by sorting the results in classes and counting the energy generated in the whole year when the irradiance or power output belongs to each class. This values can also be plotted in absolute values [1] or as a percentage [3]. A detailed statistical analysis of the irradiance for different parts of the world can be found in Part I.

For comparison purposes, it is usual to consider the array output function $Ph_P(P)$ as a function of the ratio $P_{max}/P_{max}(STC)$, where $P_{max}(STC)$ is the peak power rating of the array at STC, as illustrated in Figure 6 using observed data in the northern Europe. The function $Gh_I(G)$ is also shown. At lower latitudes, the peak of both graphs is shifted towards higher values at the expense of energy output at lower power levels.

7 Mismatch Losses and Blocking/Bypass Diodes

A number of issues arises in an array consisting of several series or parallel connected modules. Mismatch losses may occur, for example, due to non-uniform illumination of the array or because different modules in the array have different parameters. As a result, the output power from the array will be less than the sum of the power outputs corresponding to the constituent modules. Worse still, some cells may get damaged by the resulting excess power dissipation by what is called a *hot spot formation*.

The PV array in the dark behaves as a diode under forward bias and, when directly connected to a battery, will provide a discharge path for the battery.

These reverse currents are traditionally avoided by the use of blocking (or string) diodes (Figure 7). Blocking diodes also play a role in preventing excess currents in parallel connected strings.

The mismatch losses which result from shading a part of a series string are illustrated in Figure 8 which shows the I–V characteristics of five series connected solar cells. When one cell is shaded, the current output from the string is determined by the current from the shaded cell. At or near the short circuit, the shaded cell dissipates the power generated by the illuminated cells in the string; if the number of cells is substantial, the resulting heating may damage the glass, the encapsulant or the cell. This problem can be alleviated by the use of bypass diodes. It should be noted, however, that the resulting I–V characteristic now has two local maxima, an effect that may affect adversely the maximum power point tracking.

The use of blocking diodes has been subject of some discussion and their use should be evaluated in each specific situation, focusing on the trade off between the power losses due to voltage drops across the diode, and the losses through reverse currents in the dark if the diodes are omitted. With the use of modern charge regulators and inverters which disconnect the array in the dark, the blocking diodes may become redundant in any case.

As an illustration, Figure 9 compares the losses incurred with and without the use of blocking diodes, in an array shown in Figure 9(a) of a stand-alone system with a battery, without a maximum power point tracker. If no diodes are connected and one of the strings is in dark and the other is illuminated with the irradiance in Figure 9(d), the total power dissipated in the dark string is shown in Figure 9(b). It can be seen that the power dissipated by the dark string never reaches more than some 200 mW, which is less that 0.1% of the nominal peak power of the array. When a blocking diode is included to avoid dissipation in

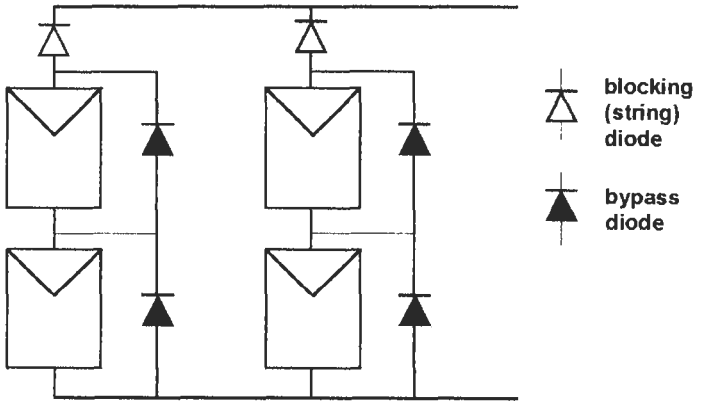

Figure 7 An array consisting of two strings, each with a blocking diode. Each module is furnished with a bypass diode. In practice, it recommended that bypass diode are used for every series connection of 10–15 cells [2].

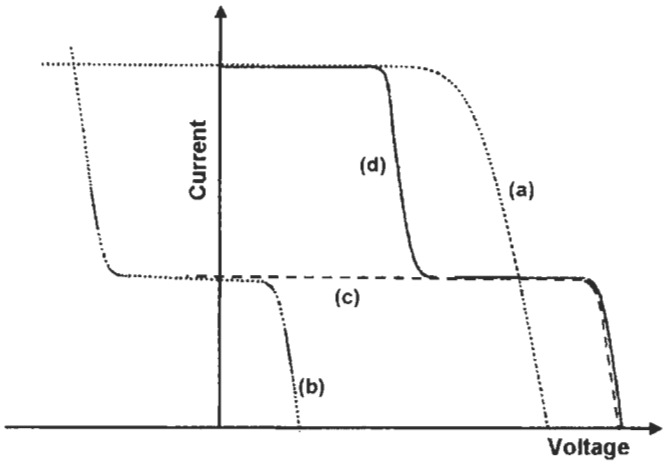

Figure 8 The I–V characteristic of a series string, with four illuminated and one shaded cell. (a) Four illuminated cells. (b) One shaded cell with a bypass diode. (c) Four illuminated cells and one shaded cell, no diode. (d) Four illuminated cells and one shaded cell, with a bypass diode across the shaded cell.

the dark string, the power dissipated is reduced to the level of tenths of milliwatts. The power dissipated by the diode itself, however, is much higher and reaches several watts, as shown in Figure 9(c).

This has different implications for grid connected and stand alone systems. Grid connected systems normally have MPPT features and the power lost in the diode reduces the available power generation, thus reducing the overall system efficiency. In a stand-alone system without MPPT, the operating point at the load is set by the battery voltage and – unless the diode connection brings the operating point beyond the maximum power point – the energy supplied to the load remains the same. The energy dissipated in the diode comes from the additional energy produced by the PV array.

In low-voltage applications there are, however, concerns about potential safety hazards if no fuses or blocking diodes are used [9], especially under fault or other unusual operating conditions. These issues have been addressed by simulation and experimental work which conclude that fuses may not be the best solution to the problem, and that blocking diodes may be more reliable.

Recommendations as to the installation of blocking diodes in grid connected systems for a number of countries in the Task 5 of the International Energy Agency can be found in reference [10].

Acknowledgement

We are grateful to Santiago Silvestre for help with modelling and useful comments.

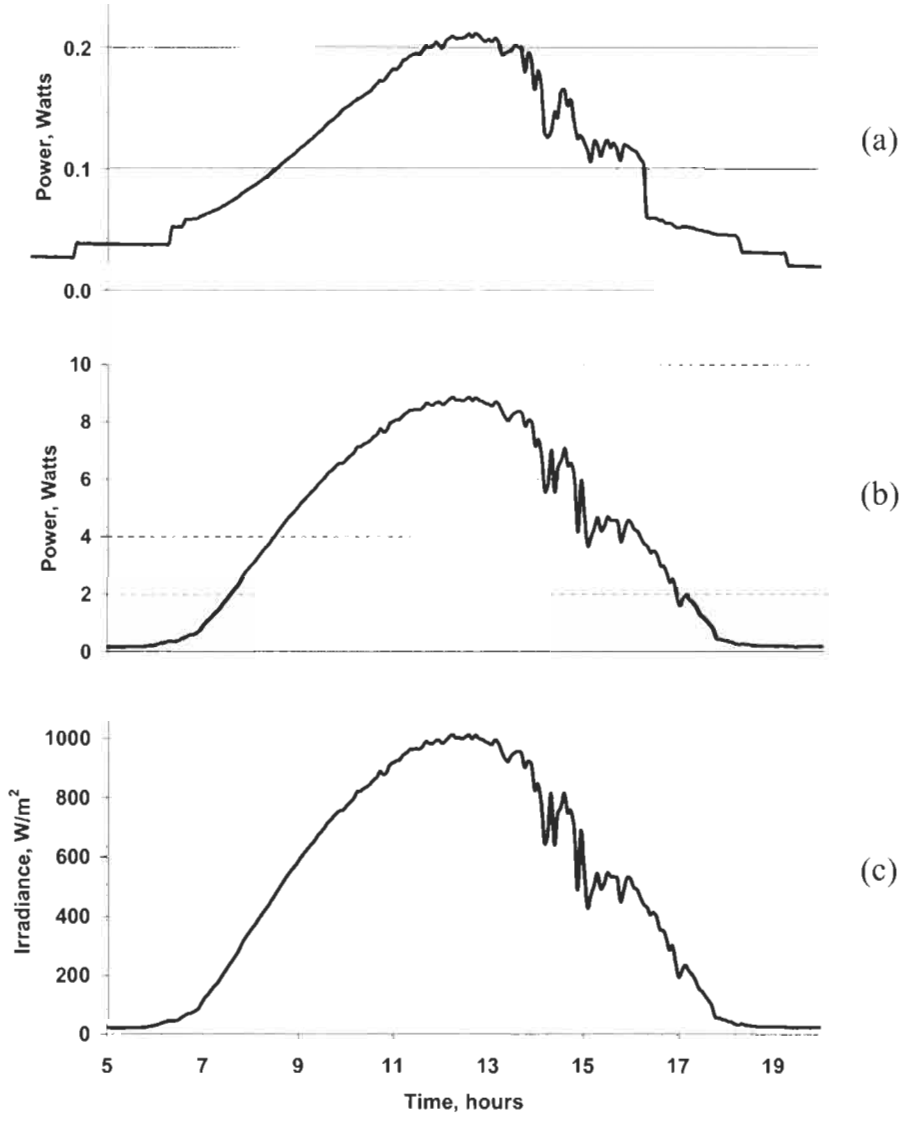

Figure 9 The power losses during one day in one of the strings of array in (a) resulting from reverse currents through the string in the dark (shaded) if the blocking diode is omitted (b). The power dissipated in the blocking diode of one string (c). (d) shows the irradiance used in the modelling. Each module of the array (a) consists of 32 cells in series with nominal power of 45.55 Wp under standard AM1.5, 1 kW/m² irradiance.

References

[1] King, D.L., Boyson, W.E. and Kratochvil, J.A. 2002. Analysis of factors influencing the annual energy production of photovoltaic systems, *Proc. 29th IEEE Photovoltaic Specialist Conf.*, New Orleans, pp. 1356–1361.

[2] Wenham, S.R., Green M.A. and Watt, M.E., *Applied Photovoltaics*, Centre for Photovoltaic Devices and Systems, UNSW.

[3] Ross, R.G. and Smockler, M.I. 1986. *Flat-plate solar array project*, Jet Propulsion Laboratories Publ. No. 86-31.

[4] Fan, J.C.C., 1986. Theoretical temperature dependence of solar cell parameters, *Solar Cells*, Vol. 17, pp. 309–315.

[5] Lorenzo, E. 1994. *Solar Electricity*, Progensa, Seville.

[6] Castaner, L. 2000. Photovoltaic systems engineering, in: Markvart, T. Ed., *Solar Electricity* (2nd edition), John Wiley & Sons, Chichester, Chapter 4.

[7] Markvart, T. Ed., 2000. *Solar Electricity* (2nd edition), John Wiley & Sons, Chichester, Chapter 2.

[8] Boes, E.C. and Luque, A., 1993. Photovoltaic concentrator technology, in: Johansson, T.B et al., Eds. *Renewable Energy: Sources of Fuel and Electricity*, Earthscan, London, p. 361.

[9] Wiles, J.C. and King, D.L. 1997. Blocking diodes and fuses in low-voltage PV systems, *Proc. 26th IEEE Photovoltaic Specialist Conf.* Anaheim, pp. 1105–1108.

[10] PV System Installation and Grid-Interconnection Guidelines in Selected IEA Countries. International Energy Agency Report IEA PVPS T5-04-2001.

[11] METEONORM version 4.0, Meteotest, Switzerland, http://www.meteonorm.com

Energy Balance in Stand-Alone Systems

Luis Castañer and Sandra Bermejo, Universidad Politecnica de Catalunya, Barcelona, Spain
Tom Markvart and Katerina Fragaki, School of Engineering Sciences, University of Southampton, UK

1 Introduction

An important part of stand-alone PV system design is concerned with the balance between energy produced by the PV array and energy consumed by the load. Any short-term mismatch between these two energy flows is compensated by energy storage, usually in the form of a rechargeable battery. Other types of storage – for example, water pumped into a tank – may also be encountered in certain applications. Considerations of energy balance cover a number of characteristic time scales, and can be discussed in terms of the energy stored in the battery (in other words, the battery state of charge), shown schematically in Figure 1.

The energy balance displays various cycles which occur with different degree of regularity [2]. In the daily cycle, the battery is charged during the day and discharged by the night-time load, or indeed at any time when the energy

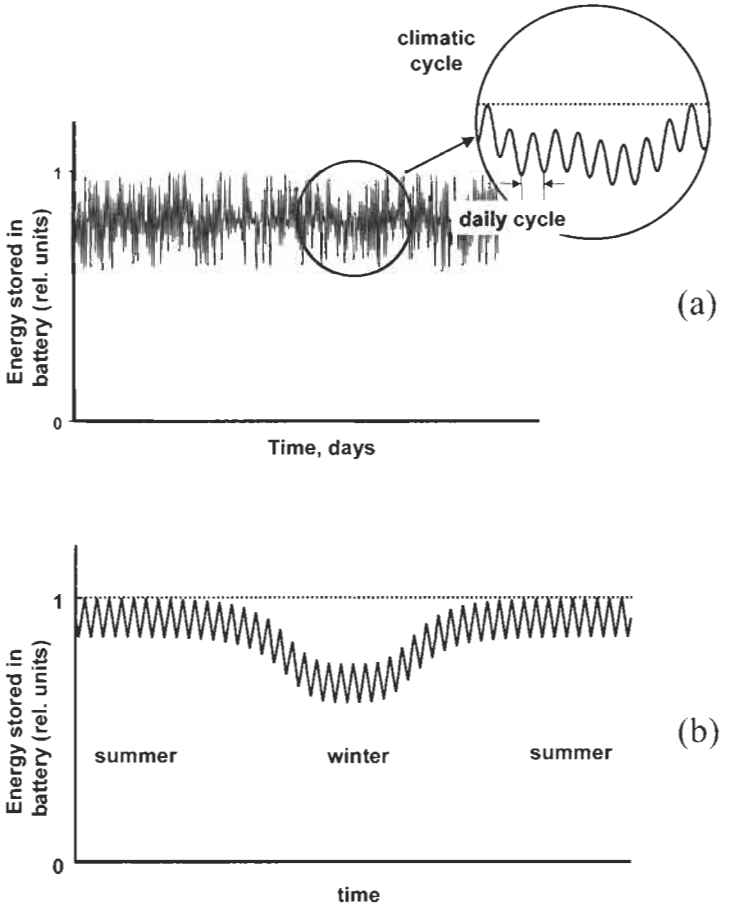

Figure 1 A schematic diagram of the characteristic times scales of energy balance in stand-alone PV systems, as indicated by the energy stored in the battery. (a) The daily and climatic cycles. (b) The seasonal cycle (adapted from [2]).

consumption exceeds supply (see Section 2.2). The depth of discharge in the daily cycle varies from application to application but, for systems without a back-up generator, it is always fairly shallow.

Superimposed on the daily cycle is a climatic cycle which is due to variable climatic conditions. The climatic cycle occurs when the daily load exceeds the average design value of the daily energy supply from the PV generator. In some systems (usually in applications where reliability is not paramount), the battery may act as seasonal energy storage, and the climatic cycle then extends over a substantial part of the season.

Figure 2 illustrates these phenomena by plotting the battery voltage (a measure of the state of charge) and the energy flow in and out of the battery, as measured by the charge (integrated current) removed from the battery. The data correspond to an 11-day climatic cycle observed during the operation of an experimental PV system in the south of England in December 2002 [1] The system parameters are plotted alongside the solar irradiance in the plane of the array. The system voltages, and the battery current and charge during one day of this cycle, are shown in more detail in Figure 3.

For a regular daily load, the daily and long-term energy balance become effectively decoupled and can be discussed separately. The daily energy balance and the calculation of the mismatch between solar radiation and the load that needs to be covered by the battery are discussed in Section 2. The long-term aspects of energy balance can be analysed using the time series of daily solar radiation (measured or synthetic, see Part I), to produce a statistical picture of the energy supply by the system as a function of its configuration. This aspect of PV system design is related to sizing and is discussed in detail in Chapter IIIa-3. An example of the seasonal cycle in battery operation and its relationship to system design is discussed briefly in Section 3.

2 Load Description

Stand-alone systems can only be sized effectively for predictable loads, and random load patterns are likely to result in uncertain reliability of supply by the PV system. We should note, however, that the load coverage will be improved if there is a possibility of adjusting or disconnecting non-essential loads.

Load description is recognised in the international standards (see, for example, [3, 4]) which describe accurate procedures for load determination. For example, the standard [4] contains the following recommendations:

1. Describe all loads by a voltage and current with a starting and finishing time for a period of 24 hours
2. Describe the AC loads separately and combine with the inverter efficiency
3. The following types of load data are considered:

    - Momentary current: a current lasting less than one minute, associated with the starting or surge of certain loads

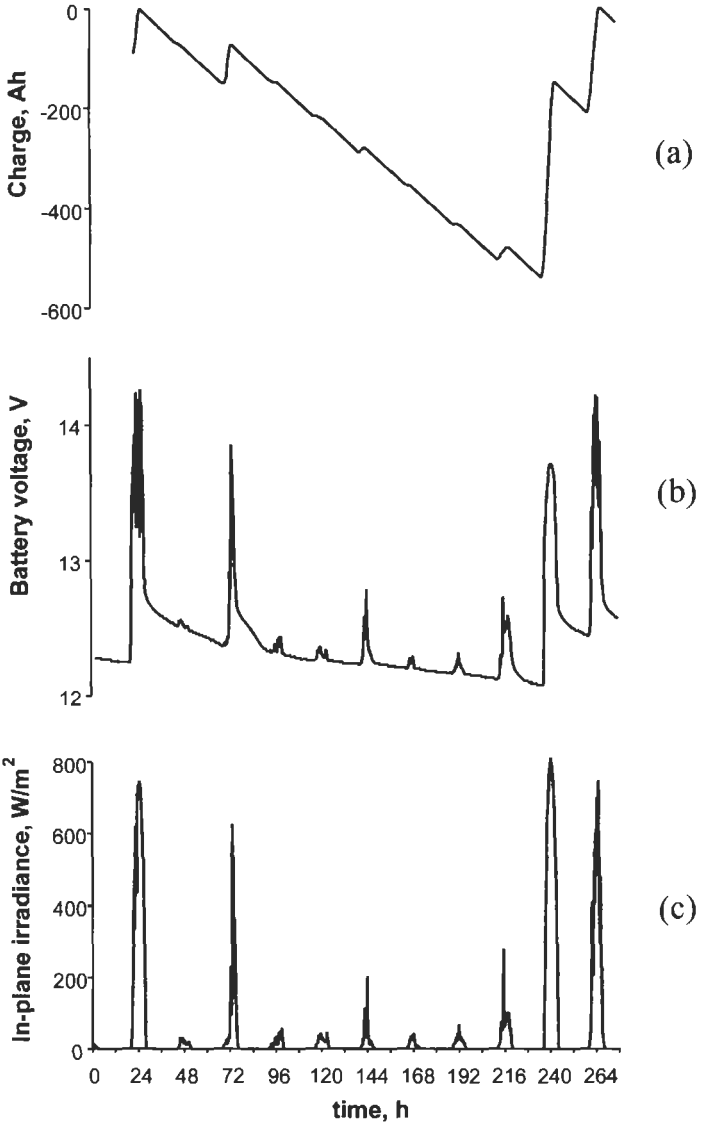

Figure 2 (a) The charge removed from the battery, and (b) the battery voltage in a stand-alone PV system during a 'climatic cycle'. The in-plane irradiance is shown in (c). Each point corresponds to a 5 minute average of measured data [1].

- Running current: a current drawn by the load once the initial transient has come to an end
- Parasitic currents
- Load duration
- Load coincidence: simultaneous occurrence of loads
- Load voltage: range of maximum and minimum voltage.

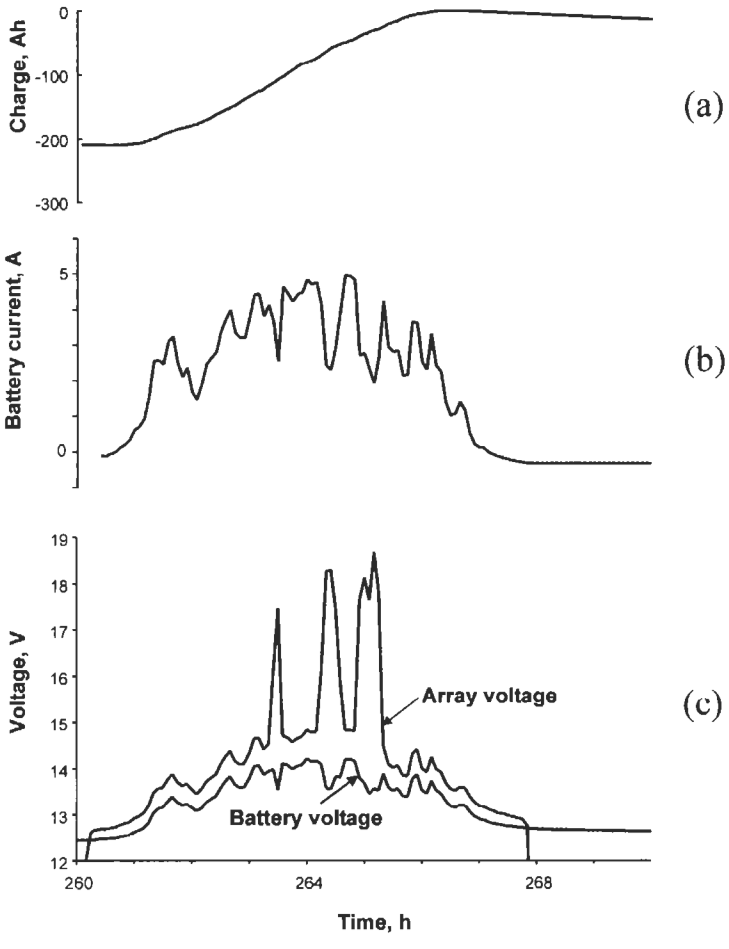

Figure 3 (a) The charge removed from the battery, (b) battery current, and (c) the battery and array voltage during the last day of the climatic cycle in Figure 2. Intervals where the array is disconnected by the series regulator as the battery approaches full charge are clearly visible [1].

The meaning of some of these parameters is illustrated in Figure 4.

It is seen that there may be loads having a momentary current of duration less than one minute and a running current of known duration. There may be several occurrences per day, as shown in Figure 4(a), or conventional loads having only a running rated current and a run time as shown in Figure 4(b). The loads may be coincident or non-coincident in time (see Figures 4(c) and (d), respectively). There may also be load profiles requiring a longer period of time than 24 hours which need to be described; in this case, an average and a maximum daily load should be given.

This information allows the derivation of the load profile, or at least the typical load profile for a 24 hour period load. This is performed by multiplying each load current by the duration and then adding all the products to find the daily

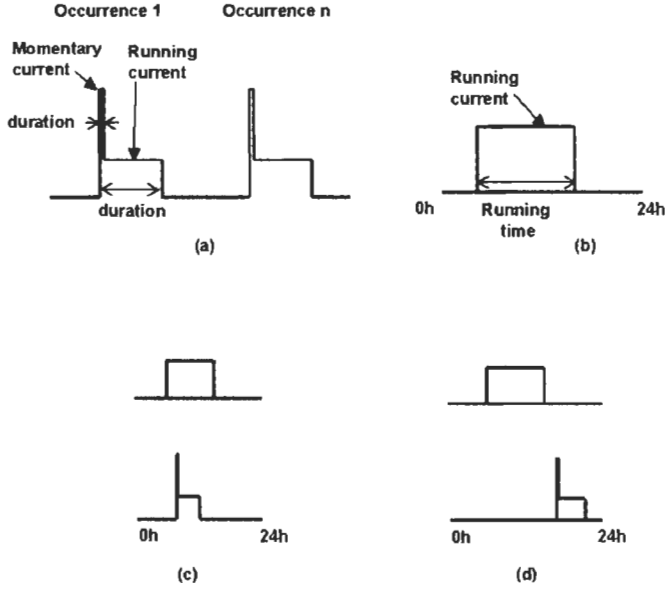

Figure 4 (a) Individual load having a momentary and running currents and a number n *of occurrences. (b) Load used a number of hours per day. (c) Coincident loads. (d) Non-coincident loads. Elaborated from IEEE standard 1144-1996.*

ampere-hour load. If the duration of the momentary load is not known one minute should be taken as recommended in reference [3]. The load profile also provides the necessary information about the maximum discharge rates which need to be sustained by the battery.

2.1 Electricity Consumption by Lighting and Electrical Appliances

Table 1 gives a summary of the load values for the main domestic appliances. The principal results on energy consumption for lighting in the residential sector can be found in references [5–9]. Most of these studies conclude that 50–150 W incandescent lamps that are on for at least 3 hours a day can be cost- effectively replaced by compact fluorescent lamps. This affects the results shown in Table 1 as an incandescent lamp can be substituted by a fluorescent lamps of approximately a factor 2.8 to 3.9 lower rating (i.e. a 60 W incandescent lamp can be substituted by a 20 W compact fluorescent lamp; more details can be found in Table 4-1 of reference [8]). The average total consumption per household in the USA used for lighting is about 1800 kWh/year [8]. About one third less energy is used during months with high solar radiation, and this lighting consumption does not appear to depend on the population demographics. More information about typical values of the power of common appliances can be found in reference [10].

There are, however, indications that the owners of off-grid houses have a tendency to adapt their pattern of energy use, leading to a clear reduction in

Table 1 Values of typical energy consumption. Source of data: lighting [6]; other appliances [5]. (Asterisk indicates estimated value.)

Appliance	Average rated power (W)	Average usage (h/day)	Annual energy consumption (kWh/year)
Lighting			
Bedroom	94	1.0	36
Closet	66	1.3	31
Dining room	165	2.3	136
Hall	78	1.7	49
Family room	106	2.0	77
Garage	103	1.9	71
Kitchen	95	3.2	109
Living room	124	2.4	109
Master bedroom	93	1.2	41
Outdoor	110	2.9	116
Utility room	84	2.4	74
Bathroom	138	1.9	96
Other	103	1.5	55
All	105	2.0	78
Other Appliances			
Refrigerator			649
Freezer			465
Washing machine	0.375 (kWh/load)	4 loads per week*	78
Dish washer	0.78 (kWh/load)	One load per day*	283
Electric oven	2300	0.25*	209
Coffee machine (drip)			301
Microwave			120
Toaster			50
Vacuum cleaner			14
Audio equipment			36
TV	100	5*	182
PC			25
Printer (inkjet)			28
Satellite dish			96
VCR			158
Video games			49
Clothes iron			53
Hair drier			40

comparison with baseline load figures [11] which are in the range of 25% for the larger systems that have been analysed. Most of the studies of the performance of PV systems agree that an adequate estimation of the load is essential to reach reasonable values of the performance ratio.

2.2 Daily Energy Balance Dynamics

Power has to be supplied to the load according to the consumption patterns of the application, and energy may be required at different times than when it is

generated by the PV array. This creates a mismatch in the energy flow between the PV system and the load.

The daily energy balance between PV energy supply and a typical domestic load is illustrated in Figure 5 on the example of a PV system operating in Sacramento, USA. Figures 5(a) and (b) show the ambient temperature and solar radiation data for a typical day of the year, with PV array at latitude tilt. These data have been generated statistically by the METEONORM software [12].

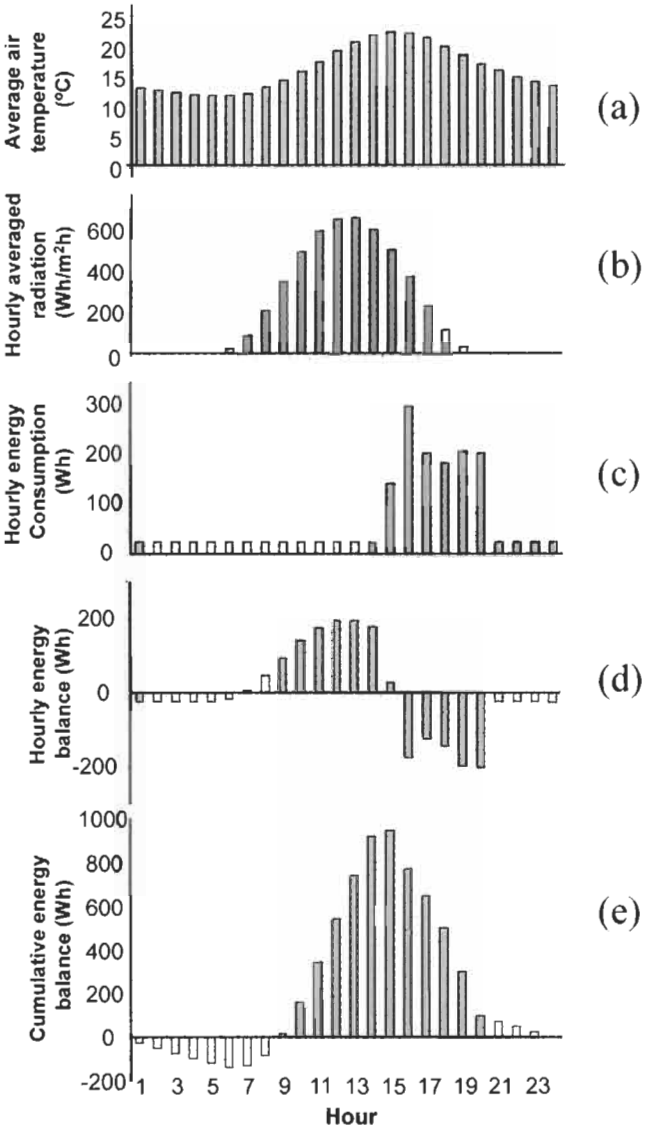

Figure 5 (a) The hourly temperature profile and (b) solar radiation for a typical day in a year in Sacramento, USA. (c) A typical hourly load profile. (d) The hourly energy balance. (e) The cumulative energy balance.

Figure 5(c) shows the profile of energy consumption in a typical household, obtained as described in the IEEE standard [3]. If the array size is chosen so that the total energy produced by the array is equal to the energy consumed by the load, the resulting hourly energy balance (energy produced minus energy consumed) is shown in Figure 5(d). The cumulative energy balance (integral of (d) from 0 to time t) is shown in Figure 5(e).

This result shows that, although there is complete energy balance at the end of the day, there is considerable imbalance between the energy supply and the load for a number of hours during the day when the load consumes more energy than supplied by the PV generator. If this situation is encountered in a stand-alone system this mismatch has to be supplied by energy storage or a back-up generator. This is the daily energy storage which was introduced in Section 1.

3 Seasonal Energy Balance

Considerations regarding the seasonal energy balance are key to the design of stand alone systems, and depend critically on the latitude where the system is installed. The gently varying profile of daily solar radiation during the year in a tropical location near the equator should be contrasted with the wide differences between summer and winter at high latitudes (see Section 2 in Part I). The seasonal mismatch between the PV energy supply and demand is potentially much larger than commonly encountered in the daily energy balance, and a careful analysis is needed to determine the principal parameters of the system – the size of the array and the battery capacity. These parameters, in turn, affect the likely reliability of energy supply by the PV system. This analysis is the principal aim of sizing which is discussed in some detail in Chapter IIIa-3.

In conclusion to this chapter we take up an issue which was introduced in Section 1 and consider the profile of energy stored in the battery during the seasonal energy cycle. This analysis illustrates the intimate relationship between the configuration of a stand-alone PV system and the behaviour of battery state of charge over prolonged periods of time which may have a considerable impact on the battery lifetime. By way of example, Figure 6 shows the battery state of charge during the year for two PV systems operating in the south of England. The results, obtained by modelling, refer to high-reliability systems with a similar reliability of supply; detailed system configurations can be found in Chapter IIIa-3. For clarity, the daily charge and discharge cycle has been omitted from the graphs which show the maximum state of charge reached by the battery in each particular day.

The system in Figure 6(a) has 16 days of autonomy; this is a large battery but not uncommon in remote industrial systems at these latitudes. Figure 6(b) corresponds to a system with an array 60% larger than the system in Figure 6(a) but with only 7.2 days of autonomy. Although the minimum depth of discharge is similar, there are important differences in the detailed battery behaviour. We note, in particular, that the duration of the longest climatic cycle for the system in Figure 6(b) is approximately half the duration

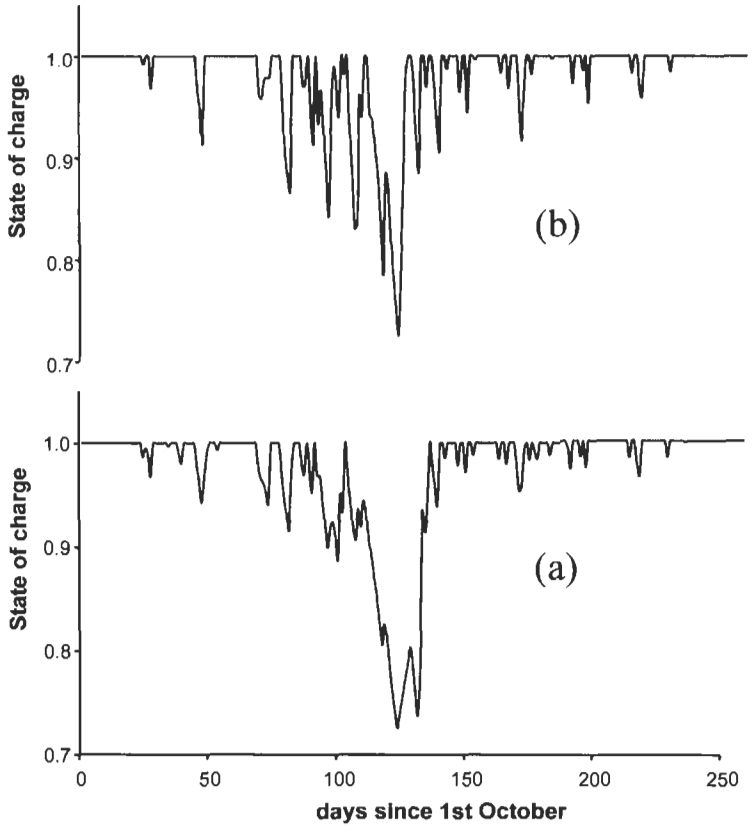

Figure 6 The battery state of charge during the winter months for two stand-alone PV systems operating in the south of England with different system configurations but a similar reliability of energy supply.

observed for the system in Figure 6(a). The implications of these profiles for the optimal type of battery and for the battery life can be significant, and are considered in Chapter IIIb-2.

References

[1] Fragaki, K. 2003. Advanced Photovoltaic System Design. MPhil Thesis, University of Southampton, unpublished.

[2] Markvart, T. Ed., 2000. *Solar Electricity* (2nd edition), John Wiley and Sons, Chichester, Section 4.4.2.

[3] IEEE standard 1013-2000: IEEE Recommended practice for sizing lead-acid batteries for Photovoltaic Systems, IEEE.

[4] IEEE standard 1144-1996: IEEE Recommended practice for sizing nickel-cadmium batteries for stand-alone PV systems, IEEE.

[5] http://hes.lbl.gov/hes/aboutapps.html.

[6] From Table 1 in http://homeenergysaver.lbl.gov/hes/aboutltg.html.

[7] Sanchez, M.C. 1997. Miscellaneous electricity use in US residences, MS thesis, University of California, Berkeley.

[8] Tribwell, L.S. and Lerman, D.I. 1996. Baseline residential lighting energy use study, *Final report, Tacoma Public Utilities*, Tacoma, Washington, May 29 (http://www. Nwcouncil.org/comments/documents/CFUselighting.doc).

[9] Wenzel, T.P, Koomey, J.G., Rosenquist, G.J., Sanchez, M. and Handford, J.W. 1997. Energy data sourcebook for the US residential sector. *Report LBNL-40297*, September 1997 (available at http://www.osti.gov/gpo/servlets as pdf document nr. 585030.

[10] Energy use of some typical home appliances. Energy efficiency and renewable energy network of the US Department of Energy (in http://www.eren.doe.gov/consumerinfo/refbriefs/ec7.html).

[11] Energy use patterns in off-grid houses, *Canadian Housing Information Center, Technical Series 01-103* (http://www.cmhc-schl.gc.ca/publications/en/rh-pr/tech/01-103-e.html).

[12] METEONORM version 4.0, Meteotest, Switzerland, http://www.meteonorm.com.

Review of System Design and Sizing Tools

Santiago Silvestre, Universidad Politecnica de Catalunya, Barcelona, Spain

1 Introduction

System modelling forms a key part of the photovoltaic system design. It can provide answers to a number of important issues such as the overall array size, orientation and the electrical configuration; it can also determine the size of various subsystems such as the battery and/or the inverter (see the standard [1] for a detailed discussion of the relevant terminology used to described PV systems). The design criteria will vary depending on the nature of the application. In stand-alone systems, the consideration of energy production to meet the load is paramount; the reliability of supply and economic considerations may also be important. A critical aspects of stand-alone system design is sizing which is discussed in Section 2.

The applications of grid-connected systems vary from small building integrated systems to PV power stations. Modelling tools are available to provide solar radiation data, assess possible shading effects (which may be particularly important at an urban site), and produce the resulting electrical layout of the array. Further considerations will include the restrictions imposed by the connection to the local utility, discussed in Chapter IIIc-1. Economic aspects may include an investigation of financial support mechanisms (discussed in Chapter V-4) and of the economic impact of local electricity generation, including possible revenue for electricity exported to the utility (see, for example, [2]).

2 Stand-Alone PV Systems Sizing

Sizing is one of the most important tasks during the design of a stand-alone PV system. The sizing procedure will determine the power rating of the PV array and the battery storage capacity needed to power the required load; the electrical configuration of the array may also be considered at this stage. More sophisticated sizing procedures will ensure that the reliability of power delivered to the load is appropriate for a given application and optimise the cost of the system. Sections 2.1 and 2.2 outline the two most frequently used sizing methods: by using energy balance, and a more complex procedure which invokes the reliability of supply [3–6]. An example of sizing a water pumping systems is discussed in Section 2.3.

2.1 Sizing Based on Energy Balance

The essential features of photovoltaic system sizing can be understood in terms of the daily energy balance between the daily load and the energy delivered by the array which is considered in some detail in Chapter IIIa-2. The input side of this balance – the expected energy production by the PV array – is determined principally by the solar radiation at the site, and can be conveniently discussed using the concept of Peak Solar Hours (*PSH*, see Chapter IIIa-1). Depending on the application, the appropriate value of *PSH* to use may be an average over the entire year, or a part of the year.

Typical examples were considered in Section 5.1 of Chapter IIIa-1. The appropriate value of PSH should correspond to the critical period of the system operation, be it the month with the lowest solar radiation or the month with the highest load. A similar consideration governs also the array inclination. The annual average value of *PSH* is sometimes used when daily solar radiation does not vary a great deal throughout the year, and the battery can be used partly as a seasonal buffer.

The second fundamental parameter is the typical daily load demand. Detailed aspects of the load, including the analysis of the daily energy balance, are considered in Chapter IIIa-2. Here we shall only need the total amount of energy consumed in one day, to be denoted by L.

The values of *PSH* and L determine the (average) daily balance between the energy supply and the required nominal power rating of the PV array:

$$P_0 = \frac{L}{PSH} \tag{1}$$

which, in turn, gives the total number of PV modules N:

$$N = \frac{P_0}{P_{\text{mod}}} \tag{2}$$

where P_{mod} is the power produced by one module under standard conditions, equal to P_{max} or P_{eff} for systems with and without a maximum power point tracker, respectively (see Chapter IIIa-1).

Once the operating DC voltage has been specified, this sizing procedure gives the array configuration in terms of the number of modules to be connected in series and in parallel (Figure 1). This argument applies for systems without maximum power point tracking, where the nominal battery voltage V_{bat} is usually set equal to 12 V, as discussed in Chapter IIIa-1. The security (sizing) factor *SF* is inserted to allow for additional losses, such as the accumulation of dirt on the modules, or to increase the system performance. It plays a similar role as the dimensionless array size C_A which will be introduced in Section 2.2.

A separate argument is used to size the battery. The critical parameter is the number of 'days of autonomy' (denoted by C_S) that the system is required to operate without any energy generation. C_S is related to the battery capacity C_n (in energy units, i.e., the battery capacity in Ah multiplied by the voltage) by

$$C_n = C_S \frac{L}{DOD_{\text{max}}} \tag{3}$$

where DOD_{max} is the maximum allowed depth of discharge of the battery. If appropriate, seasonal storage can be added to the battery capacity C_n, but is not included in Equation (3). In the energy balance method, the number of autonomy days is determined from experience in the field rather than by a

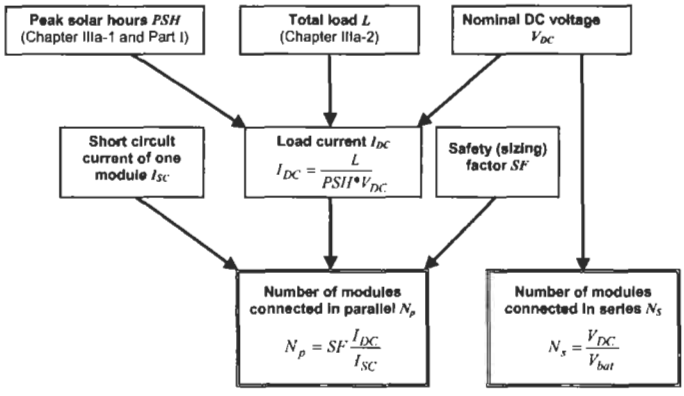

Figure 1 Sizing based on energy balance.

rigorous theoretical argument. BP Solar [7], for example, recommend the values shown in Table 1. A more rigorous method for the battery size is offered by sizing procedures based on the reliability of supply which are discussed in Section 2.2.

The determination of battery size completes the sizing of the system. One of the software packages discussed in Section 4 can be now used to analyse the system performance in more detail. This recommended particularly for 'professional' (or remote industrial) systems where strict requirements on system performance may be imposed by the nature of the application.

2.2 Sizing Based on the Reliability of Supply

The reliability of electricity supply is an important factor in PV system design, and this is also reflected in some sizing procedures. One way to quantify the reliability of supply is by a parameter known as the Loss-of-Load Probability (LLP), defined as the ratio between the estimated energy deficit and the energy demand over the total operation time of the installation. Other names for the same concept have also been used: Load Coverage Rate (LCR) [8], Loss of Power Probability (LOPP) [9], or Loss of Power Supply Probability (LPSP) [10]. The recommended values of LLP for various applications are shown in Table 2 [11]. Reviews of the methods based on reliability of supply can be found in [5, 6, 11, 12]; an elegant analytical method which uses the random walk methodology was developed by Bucciarelli [13, 14].

Sizing methods of this type are frequently used in applications where high reliability is required. To be statistically significant, long time series of solar radiation data are required which can usually be obtained only in the form of synthetic solar radiation data [5]. A more pragmatic approach in such circumstances may be to determine system configurations which would be expected to deliver energy to load without interruption over a certain specified period of time; such configurations can be determined with the help of system modelling [15]. Despite the apparent differences, this methodology and the methods based on LLP result in a similar formalism.

Table 1

Latitude of site	Days of autonomy
0–30°	5–6
30–50°	10–12
50–60°	15

Table 2

Application	Recommended LLP
Domestic	
Illumination	10^{-2}
Appliances	10^{-1}
Telecommunications	10^{-4}

The results of sizing based on system reliability are often displayed in a graphical form. To this end, the expected daily energy produced by the PV generator is expressed in a dimensionless form [6]:

$$C_A = \frac{P_0 PSH}{L} \tag{4}$$

where P_0 is the nominal power of the array and the value of PSH, corresponding to in-plane daily radiation, is usually taken for the 'worst month' of the year (see Section 2.1). The array size C_A (4) and the number of autonomy days C_S (3) are then considered as coordinates in a Cartesian coordinate system and the required system configurations displayed as a locus of points in the C_S–C_A plane.

It turns out (see, for example [11, 12, 15]) that all system configurations (C_S, C_A) which deliver energy with a given reliability of supply lie on a line called the sizing curve (Figure 2; the term 'isoreliability line' is also used [11]); all configurations with a higher reliability lie in the shaded region in the graph bounded by the sizing curve. A different reliability of supply (a different value of LLP or a different period of time required for expected operation without shedding load) will yield a different sizing curve.

A further bonus of this method is that it allows an insight into the system economics. Indeed, it can be shown that the least cost system is determined by a point on the sizing curve where the tangent has a slope equal to the ratio of unit battery cost to the unit array cost. It should be emphasised, however, that this calculation is based solely on capital costs, as it only takes into account components which are installed at the start of the system operation but later replacements are not included. This concerns, in particular, the batteries which have to be replaced several times during the lifetime of PV modules.

Egido and Lorenzo [5] developed a comprehensive library of data which allows the determination of LLP for a wide range of locations over the Iberian peninsula. A sizing curve based on measured solar radiation data is illustrated in Figure 3

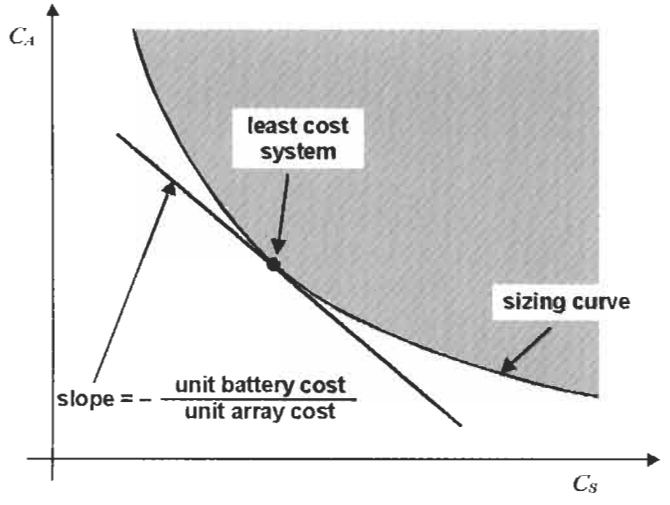

Figure 2 The sizing curve, showing also the system with minimum initial outlay cost.

for a PV system operating in the south of England for 10 years without shedding load. Once the load is specified, this universal curve provides an immediate description of all high-reliability PV system configurations by converting the dimensionless coordinates C_S and C_A into battery capacity and array size with the use of Equations (3) and (4). It is seen that taking the array size as predicted by the energy balance method and C_A ($=S_F$) = 1, the sizing curve in Figure 3 gives16 days of autonomy, quite close to the BP recommended value of 15 days. If the array size is increased by 15% (in other words, we take $C_A = S_F = 1.15$), the battery can be reduced to 13 days of autonomy without affecting the supply reliability; a larger array increase would give a more substantial battery reduction.

The consideration of different system configurations has implications for the system cost, and affects also another important feature of PV system operation: the pattern of seasonal battery charge and discharge cycles which may affect battery life. This point has already been touched upon and is illustrated in Figure 6 of Chapter IIIa-2. This figure illustrates that although all points on the sizing curve correspond to systems with identical reliability of supply, the pattern of battery charge and discharge cycles will be different along the curve. The two system configurations on the sizing curve marked by 1 and 2 in Figure 3 correspond to graphs (a) and (b) in Figure 6 of Chapter IIIa-2, respectively. Thus, it is seen that increasing the array size along the sizing curve shortens the duration of the climatic cycles, and helps reduce possible degradation of the battery. A full discussion of battery life can be found in Chapter IIIb-2 and in the standards [16, 17].

2.3 Sizing of Solar Pumping Systems

Water pumping for irrigation and water supply for rural communities represents an important area of stand-alone PV systems, These systems usually consist of a

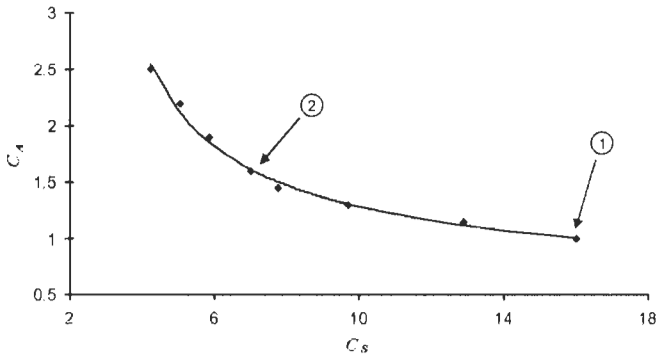

Figure 3 Example of a sizing curve using solar radiation data for Bracknell, near London. Panel inclination: 65 degrees; period of data: 1981–1990; source of data: reference [58]. Points are results obtained by modelling; line is a fit to the points with the expression

$$C_A = \frac{1}{0.4514 \ln C_S - 0.2601}.$$

photovoltaic generator, source of water, a water storage tank, and a DC pump. The role of batteries is here played by the water storage tank and the electric power load demand L in now replaced by daily water demand. If expressed in Wh/day, this represents the energy needed to pump the required volume of water demanded by the user into the storage tank. These considerations show that PV pumping systems can be sized in a similar way than PV systems with other applications [18, 19].

In particular, the PV system sizing method based on Loss-of-Load Probability can be also used to design PV pumping systems [18]; LLP now corresponds to the ratio of energy deficit and energy demand, as water pumped volume, over the system's working period. To introduce the LLP sizing method into water pumping applications, Equation (2) can used to calculate the PV generator capacity C_A. In this case the energy load demand L represents the daily load or water demand. Equation (3) can then be rewritten as Equation (5) below [18] to estimate the storage capacity C_s that represents the necessary volume of the water storage tank:

$$C_S = \frac{C_U}{L} \tag{5}$$

where C_U (in units of energy per day) is the energy required to pump the entire tank full of water.

Using the desired values of LLP for the PV pumping system, it is possible to obtain sizing curves which give the required pairs of C_A and C_s values to determine the sizes of the water tank and PV generator which represent the best compromise between cost and reliability, in the same way as for the system sizing methods considered in Section 2.2.

3 Grid-Connected PV Systems

The array architecture in grid connected systems should be considered alongside the DC characteristics of the inverter, including the maximum input current, the nominal and minimum input voltage and the maximum power tracking range. Sizing of grid-connected systems is considered, for example, in [20, 57]. This analysis can be carried out by analogy with the energy balance arguments that were used in Section 2.1 to develop a sizing procedure for stand alone PV systems. The AC energy E_{AC} produced by the PV system in one day, say, can be estimated by using an equation similar to (1):

$$E_{AC} = \eta_I P_0 PSH \tag{6}$$

where P_0 is the nominal power of the array at STC, PSH is the average value of Peak Solar Hours at the specific location, and η_I is the inverter efficiency which, in general, depends on the output power. This dependence can be expressed in terms of the inverter self consumption and load-dependent losses as [59, 60]:

$$\eta_I = \frac{p_{out}}{p_{out} + k_0 + k_1 p_{out} + k_2 p_{out}^2} \tag{7}$$

where

$$p_{out} = \frac{P_{AC}}{P_I}$$

is the instantaneous AC output power P_{AC} normalised to the nominal AC output power of the inverter P_I. The parameter k_0 represents the self-consumption factor which is independent of the output power. The linear and quadratic terms in the denominator take into account losses which are linear in the load power such as voltage drops whereas the ohmic losses are taken into account by the quadratic term. Experimentally measured inverter efficiency curves can be easily fitted to this equation and parameter values can be extracted (see, for example, [61]). This procedure allows a comparison between different inverters and to gain insight into the origin of the dominant losses by modelling [62]. A typical form of the functional dependence of the inverter efficiency of the output power is shown in Figure 4.

The reduction of inverter efficiency at low power should be allowed for in the choice of the power rating of the inverter. It is generally recognised that advantage can be gained by choosing the power rating of the inverter P_I smaller than the nominal power P_0 of the array. Based on inverter efficiency this represents, in fact, a trade-off between the self-consumption and inverter losses which scale down as the inverter is rated smaller, and the energy lost at the upper limit of PV generation close to the STC conditions. Thus, the choice of optimum inverter size depends on the statistics of the array output which is related to the latitude of the site as discussed in Section 6 of Chapter IIIa-1. For example, the recommended value of the ratio P_I/P_0 is between 0.65 and 0.8 for countries in

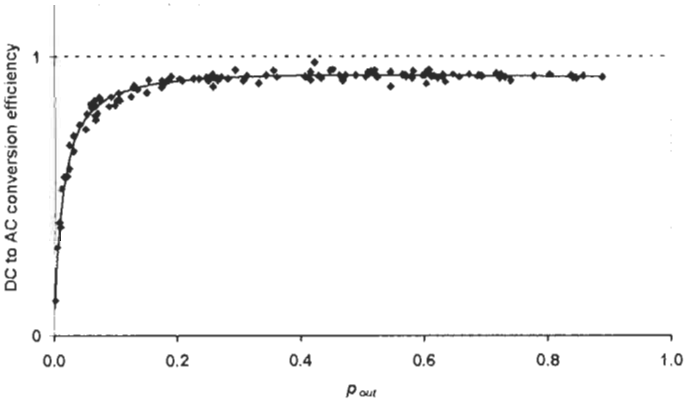

Figure 4 Typical inverter efficiency during operation in a grid-connected PV system as a function of the output power. Data: STaR Facility, University of Southampton. Line is a fit using Equation (7) with $k_0 = 0.013$; $k_1 = 0.02$; $k_2 = 0.05$.

northern Europe and 0.75 to 0.9 is more suitable in mid-European latitudes. In southern Europe, the suggested figure is 0.85 to 1 [60, 21].

Whilst system efficiency is important, care should be taken to avoid long periods of inverter operation under overload conditions. Nofuentes and Almonacid [21] suggest a size that exceeds the DC power supply to the inverter for 99% of the time (Figure 5). The inverter power rating determined using this '99% criterion' is usually somewhat larger than the value based on the efficiency argument.

4 PV System Design and Sizing Tools

A wide variety of software tools now exist for the analysis, simulation and sizing of photovoltaic systems. These tools present different degrees of complexity and accuracy depending on the specific tasks that each tool has been developed for. This chapter presents an overview of the available software tools. The list of software tools described below is not exhaustive due to the large numbers that exist but can help PV system designers and installers to examine the available PV system design and analyse the options from different points of view. It is usual to distinguish between sizing tools (which determine the component size and possibly also configuration) and simulation/modelling tools which analyse the system output and performance once its specifications are known.

Examples of these sizing and simulation tools are given in Sections 4.1 and 4.2 below, accompanied by a brief description of each program and the source from which it can be procured. The source indicated in the references should be contacted for more detailed information on specific capabilities, operating environment requirements, report functions, technical support, and licensing/user restrictions.

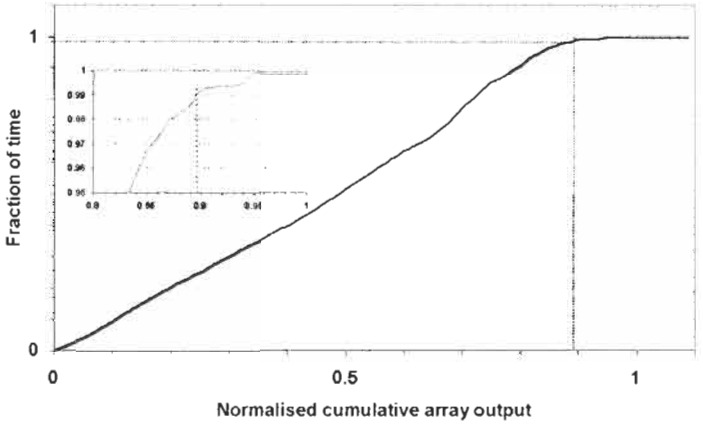

Figure 5 The cumulative array output obtained by integrating the graph of $Gh_1(G)$ *in Figure 6 of Chapter IIIa-1, illustrating inverter sizing by the '99% criterion'.*

4.1 Sizing Tools

Sizing tools allows dimensioning photovoltaic systems, taking into account energy requirements, site location, and system costs (Table 3). Most of these software tools are relatively simple and help users to automatically solve energy balance calculations considering different combination of PV system components, including batteries, modules and loads. These tools are usually implemented using spreadsheets at different level of complexity and offer a first approach for the evaluation of specific PV system applications. In their basic form, these tools are easy to use and some solar cell manufacturers and vendors of PV system components offer this kind of tools to potential customers (often via Internet) to enable the customer to adapt the PV system components to their products. Similar sizing tools are also available which focus at specific studies for complete sets of modules, batteries, inverters, electronic power conditioning components and loads from the principal manufacturers in the photovoltaic market.

More sophisticated sizing tools are also available in the market offering, in some cases, the possibility of optimising the size of each PV system component. More detailed analysis can then be carried out of the energy flows in the PV system and the determination of critical periods along the year. Of particular interest is often the deficit of energy associated with these periods of time, or to minimise the final cost of the system for a specific application.

4.2 Simulation Tools

More specialised simulation tools are available on the market which offer, in addition to sizing, also the chance to model PV system components or to carry out accurate simulations of the PV system behaviour and a more accurate design. A selection of such simulation/modelling tools is given in Table 4.

Table 3 System sizing programs

Program	Source	Description
Design Your System	Helyos Technology [22]	On-line sizing estimation of stand-alone systems using the energy balance method. The program gives information about the necessary number of modules and batteries, from a predefined set of products, to cover a user defined power load demand profile.
Estimating Stand-Alone System Size	BP Solar [7]	Provides a good estimate of the PV system size required to support a given electrical load at a specific site. Includes BP Solar's World Design Insolation map, and an Excel workbook which helps users to calculate their average daily electrical load.
FATE2-P	NREL and Princeton Economic Research Inc. [23]	Financial Analysis Tool for Electric Energy Projects, FATE2-P is a power plant project finance model for calculating cost of energy or internal rate of return for alternative energy projects.
Hybrid designer	Energy & Development Research Center of Cape Town University, South Africa [24]	This software application provides help with the design of component sizing configuration and with the choice of appropriate control settings. The application also runs a sensitivity analysis to indicate critical areas of the system, and provides a good approach to the life-cycle cost.
HOMER	NREL [25].	HOMER (Hybrid Optimisation Model for Electric Renewable) is a computer model that simulates and optimises stand-alone electric hybrid power systems. It can consider any combination of wind turbines, PV panels, small hydropower, generators, and batteries. The design optimisation model determines the configuration, dispatch, and load management strategy that minimises life-cycle costs for a particular site and application.
ILSE	Technical University of Berlin [26, 27].	ILSE allows some online calculations and simulations including sun orbit diagrams, a simple model of solar cell characteristics, and the temperature effect on silicon solar cells.

(Table continued on next page)

Table 3 (*continued*)

Program	Source	Description
NSol	Orion Energy Corporation [28]	NSol is a computer-assisted sizing tool for stand-alone battery-based PV systems. The program uses probabilistic sizing algorithms and produces different proposal-quality reports. The input system data are: site information, radiation, definition of batteries and PV modules, and up to five separate loads, including a choice of load profiles.
PVcad	ISET [29]	Computer program for the planning of PV facades (grid-coupled systems). PVcad offers interfaces to civil engineering CAD systems (DXF-Import) as well as extensive databases for weather data at many different locations, modules and inverters. Allows the calculation of the electrical energy yield. Shading of the modules is calculated, for direct and diffuse light, and thermal proprieties of the modules taken into account.
PVWATTS	NREL [30]	An internet accessible tool that calculates the electrical energy produced by a grid-connected PV system for locations within the USA and its territories.
RETScreen	CANMET Energy Diversification Research Laboratory [31]	RETScreen International is a renewable energy decision-support and capacity building tool. Each RETScreen renewable energy technology model, including hybrid PV systems, is developed within an individual Microsoft Excel spreadsheet 'Workbook' file. The Workbook file is in-turn composed of a series of worksheets. These worksheets have a common format and follow a standard approach for all RETScreen models. In addition to the software, the tool includes product, weather and cost databases, an online manual, a Website, project case studies, and a training course. See also Part I of this book.

Table 3 (*continued*)

Program	Source	Description
Solar Sizer	CREST and SEI with funding by US DoE [32]	Solar Sizer adds up the electrical requirements of predefined appliances and provides help with the selection of the appropriate components, such as PV modules, inverters, controllers and batteries. The program includes solar radiation data for 240 sites in North America and 50 round the world. Information about energy usage, storage and life-cycle cost can also be obtained.
System Applications and Design Considerations	Sandia [33]	This web site describes general sizing instructions, and a set of worksheets to design PV systems is also available. Some of these worksheets have been developed to give the size of the PV array and battery, others to determine the size of wires, fuses, switches, etc.

Abbreviations: NREL = National Renewable Energy Laboratory, USA; CREST = Centre for Renewable Energy and Sustainable Technology; SEI = Solar Energy International; ISET = Institut für Solare Energieversorgungstechnik.

Table 4 PV system simulation software

ASHLING	A consortium of NMRC (Ireland), ARMINES (France), ICI (Romania) and IMIO (Poland) [34]	Ashling 7.0 is a simulation and modelling software developed for PV systems, both stand alone and grid connected. Main functionality includes the design, analysis, simulation and cost evaluation of the PV system.
Hybrid2	NREL and University of Massachusetts [35]	Hybrid2 allows a detailed long-term performance and economic analysis of a wide variety of hybrid power systems: wind/PV/diesel hybrid systems.
EnergyPlus	[36]	Energy simulation program for modelling building heating, cooling, lighting, ventilating, and other energy flows; it includes simulation capabilities such as time steps of less than an hour, modular systems and plant integrated with heat balance-based zone simulation, multizone air flow, thermal comfort, and PV systems.
PV F-CHART	University of Wisconsin Solar Energy Laboratory [37]	A PV system analysis and design program. The program provides monthly averaged performance estimates for each hour of the day. System types: utility interface systems, battery storage and stand-alone systems, tracking options are also included. Main features: Weather data for over 300 locations (can also be added), hourly load power demand profiles for each month, statistical load variation, buy/sell cost differences, time-of-day rates for buy/sell, and life-cycle economics.
PVSOL	Valentin Energy Software [38]	A program for the design, planning and simulation of PV systems. The calculations are based on an hourly data balance and results can be presented in graphic form, in a detailed project report or in a results summary. Program features include: grid-connected and stand-alone systems, any number of panels set up at varying angles, shading from the horizon and other objects, use of different makes of PV modules and inverters within the system, module, string and system inverters, manufacturer and weather databases, determination of electricity consumption through profiles, full flexibility in inputting charge rates for electricity use and supply to utility detailed information on power production/consumption, and costs calculation.
PVSYST	CUEPE [39]	PVSYST is a PC software package for the study, sizing, simulation and data analysis of complete PV systems. It is suitable for grid-connected, stand-alone and DC-grid (public transport) systems, and offers an extensive meteorological and PV-components database.

Table 4 (*continued*)

RAPSIM	MUERI in a project funded by ACRE [40]	The 'Remote Area Power Supply Simulator' (RAPSIM) is a computer modelling program designed for simulation of PV, wind and diesel stand-alone hybrid systems.
SOMES	Utrecht University [41]	This tool allows one to simulate the performance of renewable energy systems. The energy system can comprise renewable energy sources (PV array and wind turbines), a motor generator, a grid, battery storage, and several types of converters. An analysis of the results gives information about energy flows, technical and economic performance of the system and the reliability of the electricity supply.
SolSim	Institut für Angewandte Forschung, Schwerpunkt Energiewandlung in Solar Systemen [42, 43]	SolSim is a software tool developed for simulation of PV solar/hybrid systems.
SolarPro	Laplace System Co. Ltd [44]	This software creates and supports virtual simulations for PV systems, allowing one to compute solar power over module arrays. It also computes shadowing effects on the PV generator. Results of calculation of electric power can be obtained on a daily, monthly and annual basis.
TRNSYS	Solar Energy Laboratory, University of Wisconsin-Madison [45]	TRNSYS was first written in 1975 to study a building with passive solar heating. It is currently developed by a joint US–European team of engineers and computer scientists. PV arrays, batteries, charge controllers and inverters are also available in its libraries from 2001.
PV-DesignPro-S	[46]	PV-DesignPro is a suite of Windows 95, 98, and NT software designed to simulate photovoltaic energy system operation on an hourly basis for one year, based on a user selected climate and system design. Three versions of the PV-DesignPro program are included on the CD-ROM: 'PV-DesignPro-S' for stand-alone systems with battery storage, 'PV-DesignPro-G' for grid-connected systems with no battery storage, and 'PV-DesignPro-P' for water pumping systems.

Abbreviations: CUEPE = Centre universitaire d'Etude des problèmes de l'énergie de l'Université de Genève; MUERI = Murdoch University Energy Research Institute; ACRE = Australian Cooperative Research Centre for Renewable Energy.

Apart from these specialised simulation tools, the possibility of modelling and simulation of PV systems and components using programs such as Matlab [47] or Pspice [48] should be given a serious consideration. Most electrical and electronic engineers today will be familiar with these open architecture research tools that include advanced mathematical manipulation toolboxes which can be helpful in the accurate simulation of PV systems.

Pspice is one of the most popular standard programs for analogue and mixed-signal simulation. The possibilities of modelling the different components of a PV system (including solar cells, PV modules and batteries) has been discussed in the literature [20, 49–51]. Furthermore, experimental measurements have been successfully compared with Spice simulations [49–51. Long-term simulation of PV systems using PSPICE has also been demonstrated [20]. System designers are generally interested in these long-term simulations provided that they are fast enough to allow easy interaction, such as changes of parameter values, to refine the adjustment of the system size at the design stage.

Matlab is a powerfull technical computing environment that can be complemented by a wide set of associated toolboxes offered by Mathworks, the developer of Matlab. Matlab can also be combined with the Simulink interface, a friendly modular graphical environment of simulation, resulting in a very powerful modelling and simulation platform. As in the case of Pspice, models developed in the Matlab/Simulink environment are available for main components of PV systems, and very accurate simulations of the PV system behaviour can be carried out [52–54]. The output data can be easily manipulated to extract further realistic values of the model parameters of PV system components. Matlab capabilities can help PV system designers to gain deep understanding of the PV system behaviour under realistic circumstances of system operation.

Finally, general purpose programming languages, for example C, Fortran or Pascal, have been also used for PV system simulation and modelling. Some computer models and calculation algorithms, specially developed for the simulation of PV systems have been presented by many authors [55, 56]. These tools offer total freedom of programming to create an accurate model of a specific PV system and its components in return, however, for substantial efforts in the development and implementation of these tools.

References

[1] ANSI/IEEE Standard 928-1986: IEEE Recommended Criteria for Terrestrial Photovoltaic Power Systems, Institute of Electrical and Electronics Engineers, New York, USA.

[2] Hernández, J.C., Vidal, P.G. and Almonacid, G., 1998. Modelling of the optimal size of a PV generator on a grid-connected building. *Proc. 2nd World Conf. Photovoltaic Solar Energy Conversion*, Vienna, pp. 2640–2643.

[3] Markvart, T., Castañer, L. and Egido, M.A., 1994. Sizing and reliability of stand-alone PV systems. *Proc. 12th European Photovoltaic Solar Energy Conf.*, Amsterdam, pp. 1722–1724.

[4] Castañer, L., 1994. Photovoltaic Engineering. In: Markvart, T., Ed., *Solar Electricity*, John Wiley and Sons, Chichester, pp. 74–114.

[5] Egido, M.A. and Lorenzo, E., 1992. The sizing of stand alone PV-systems. A review and a proposed new method. *Sol. Energy Mat. Sol. Cells*, Vol. 26, pp. 51–69.

[6] Lorenzo, E. and Narvate, L., 2000. On the usefulness of stand-alone PV sizing methods. *Progress in Photovoltaics: Research and Applications*, Vol. 8, pp. 391–409.

[7] http://www.bpsolar.com/.

[8] Negro, E., 1995. On PV simulation tools and sizing techniques: a comparative analysis towards a reference procedure. *Proc. 13th European PV Solar Energy Conf.*, Nice, pp. 687–690.

[9] Cowan, W., 1994. A performance test and prediction method for stand-alone/battery systems- looking for quality assurance. *Proc. 12th European Solar Energy Conf.*, Amsterdam, pp. 403–407.

[10] Abouzahr, I. and Ramakumar, R., 1991. Loss of power supply probability of stand-alone photovoltaic systems: a closed form solution approach. *IEEE Transactions on Energy Conversion*, Vol. EC-6, pp. 1–11.

[11] Lorenzo, E., 1994. *Solar Electricity. Engineering of Photovoltaic Systems*, Progensa, Seville.

[12] Gordon, J.P., 1987. Optimal sizing of stand-alone photovoltaic power systems. *Solar Energy*, Vol. 20, p. 295.

[13] Bucciarelli, L.L., 1984. Estimating loss-of-power probabilities of stand-alone photovoltaic conversion systems. *Solar Energy*, Vol. 32, p. 205.

[14] Bucciarelli, L.L., 1986. The effect of day-to-day correlation in solar radiation on the probability of-loss of power in a stand-alone photovoltaic energy systems. *Solar Energy*, Vol. 36, p. 11.

[15] Markvart, T., He, W., Ross, J.N., Ruddell, A., Haliday, J., Rodwell, B., Wannell, M. and Benney, A., 2001. Battery charge management for minimum-cost photovoltaic systems. *Proc. 16th European Photovoltaic Solar Energy Conf.*, Munich, pp. 2549–2552.

[16] IEEE Standard 1013-2000: IEEE Recommended practice for sizing lead-acid batteries for photovoltaic systems, Institute of Electrical and Electronics Engineers, New York.

[17] IEEE Standard 1144-1996: IEEE Recommended practice for sizing nickel-cadmium batteries for stand-alone PV systems, Institute of Electrical and Electronics Engineers, New York.

[18] Díaz, P. and Egido, M.A. 1998. Sizing PV pumping systems method based on loss of load probability. *Proc. 2nd World Conf. on Photovoltaic Solar Energy Conversion*, Vienna, pp. 3246–3249.

[19] Vilela, O.C. and Fraidenraich, N., 2001. A Methodology for the design of photovoltaic water supply systems. *Progress in Photovoltaics: Research and Applications*, Vol. 9, pp. 349–361.

[20] Castañer, L. and Silvestre, S., 2002. *Modelling Photovoltaic Systems Using Pspice*, John Wiley and Sons, Chichester.
[21] Nofuentes, G. and Almonacid, G., 1999. Design tools for the electrical configuration of architecturally integrated PV in buildings. *Progress in Photovoltaics: Research and Applications*, Vol. 7, pp. 475–488.
[22] http://www.heliostechnology.com/design.asp.
[23] http://www.nrel.gov/international/tools/fate-2p.html.
[24] http://www.edrc.uct.ac.za/hybrid-designer/.
[25] http://www.nrel.gov/international/tools/homer/homer.html.
[26] http://emsolar.ee.tu-berlin.de/.
[27] Quaschning, V., Hanitsch, R., Zehner, M. and Becker, G., 2000. PV simulation and calculation in the internet – the ILSE toolbook. *Proc. 16th European Photovoltaic Solar Energy Conf.*, Glasgow, pp. 2497–2500.
[28] http://www.orionenergy.com/Nsol/nsolhome.html.
[29] www.iset.uni-kassel.de/abt/w3-a/pvcad/pvcad12setup.exe.
[30] http://rredc.nrel.gov/solar/codes.algs/PVWATTS/.
[31] http://retscreen.gc.ca/.
[32] http://www.oikos.com/esb/54/solarsizer.html.
[33] http://www.sandia.gov/pv/sd.htm.
[34] http://www.ici.ro/ici/portfoliu/ashling/ASHLING1.htm.
[35] http://www.nrel.gov/international/tools/hybrid2.html.
[36] http://www.eren.doe.gov/buildings/energy.tools/energyplus/.
[37] http://www.fchart.com/pvfchart/pvfchart.shtml.
[38] http://www.valentin.de./englisch/startseite-e.htm.
[39] http://www.pvsyst.com/.
[40] http://wwwphys.murdoch.edu.au/.
[41] http://www.chem.uu.nl/nws/www/research/e&e/somes/somes.htm.
[42] http://ewis.fh-konstanz.de/solsim.htm.
[43] Schaffrin, C. and Knoblich, I., 2000. SolSim – A software tool for simulation of solar hybrid systems. *Proc. 16th European Photovoltaic Solar Energy Conf.*, Glasgow, pp. 2440–2444.
[44] http://www.lapsys.co.jp/english/eframe/eframepro.html.
[45] http://www.trnsys.com/.
[46] http://www.mauisolarsoftware.com/.
[47] http://www.mathworks.com/.
[48] http://www.pspice.com/.
[49] Castañer, L., Carles, D., Aloy, R. and Silvestre, S., 1995. SPICE simulation of PV systems. *Proc. 13th European Photovoltaic Solar Energy Conf.*, Nice, pp. 950–952.
[50] Moreno, A., Silvestre, S., Julve, J. and Castañer, L., 1998. Detailed simulation methodology for PV Systems. *Proc. 2nd World Conf. on Photovoltaic Energy Conversion*, Vienna, pp. 3215–3218.
[51] Moreno, A., Julve, J., Silvestre, S. and Castañer, L., 2000. SPICE Macromodeling of Photovoltaic Systems. *Progress in Photovoltaics: Research and Applications*, Vol. 8, pp. 293–306.

[52] Silvestre, S., Guasch, D., Moreno, A., Julve, J. and Castañer, L., 1999. A comparison on modelling and simulation of PV systems using Matlab and Spice. *Technical Digest of 11th International Photovoltaic Science and Engineering Conf.*, Hokkaido, Japan, pp. 901–902.

[53] Silvestre, S., Guasch, D., Goethe, U. and Castañer, L., 2001. Improved PV battery modelling using Matlab. *Proc. 17th European Photovoltaic Solar Energy Conf.*, Munich, pp. 507–509.

[54] Silvestre, S., Guasch, D., Moreno, A., Julve, J. and Castañer, L., 1999. Characteristics of solar cells simulated using Matlab. *Proc. CDE-99*, Madrid, Spain, pp. 275–278.

[55] Wakao, S., Onuki, T., Ono, K., Hirakawa, R., Kadokura, T. and Wada, J., 1998. The analysis of PV power systems by computational simulation. *Proc. 2nd World Conf. on Photovoltaic Solar Energy Conversion*, Vienna, pp. 3262–3265.

[56] Hamzeh, A., 1998. Computer aided sizing of stand-alone photovoltaic systems considering markedly variations of solar insolation over the year. *Proc. 2nd World Conf. on Photovoltaic Solar Energy Conversion*, Vienna, pp. 3250–3253.

[57] Messenger, R. and Ventre, J., 2000. *Photovoltaic Systems Engineering*, CRC Press LLC.

[58] *European Solar Radiation Atlas*, 4th Edition, 2000. Scharmer, K. and Grief, J., co-ordinators. Les Presses de l'Œcole des Mines de Paris, Paris.

[59] Laukamp, H., 1989. Wechselrichter in Photovoltaik-Anlagen, *Proc. 4th Symp. on Photovoltaic Energy Conversion*, Staffelstein.

[60] Jantsch, M., Schmidt, H. and Schmid, J. 1992. Results of the concerted action on power conditioning and control' *Proc. 11th Photovoltaic Solar Energy Conf.*, Montreux, pp. 1589–1593.

[61] Schmidt, H and Sauer, D.U., 1996. Wechselrichter-Wirkungsgrade: Praxisgerechte Modeliering und Absschätzung, *Sonnenenergie*, No. 4, p. 43.

[62] Schilla, T., 2003. Development of a Network Model of a PV Array and Electrical System for Grid Connected Applications, PhD Thesis, University of Northumbria.

[63] http://www.sunnyboy.com, 'Finding the optimal design of a utility interactive PV plant', Sunnyboy info September 2001.

Part IIIb

Balance of System Components

System Electronics

J. Neil Ross, Department of Electronics and Computer Science, University of Southampton, UK

1 Introduction

The very simplest PV system requires no electronic control or power conditioning. A PV array with a suitably chosen number of cells in series charges a battery. The battery sustains supply when there is insufficient solar energy, but it also helps to maintain the supply voltage within limits. Such an approach has the merit of simplicity but has severe limitations. There is no control to limit the charge supplied to the battery, other than that imposed by the battery voltage and the open circuit voltage of the PV array, and there is no means of limiting the depth of discharge of the battery. The power supplied to the load will be direct current (DC), and the voltage may fluctuate substantially according to the state of charge. Also, there is no way of controlling the voltage across the PV array to ensure that it is providing its maximum power.

In order to overcome these limitations power electronic circuits are used to control the battery charging current, transform the voltage (DC to DC conversion) and to convert the direct current to alternating current, AC (inversion). In this chapter some of the techniques of DC to DC conversion and power inversion will be described briefly and then their use within stand-alone and grid connected PV systems will be considered. In Section 5 the types of charge controllers and power conditioners available commercially are reviewed briefly.

2 DC to DC Power Conversion

For electronic power conversion it is essential that high efficiency be maintained, both to avoid wasting power and to avoid excessive heat dissipation in the electronic components. For this reason all practical power conversion circuits are built around energy storage components (inductors and capacitors) and power switches. The power switches used depend on the level of power to be converted or controlled. MOSFETs (metal oxide field effect transistors) are usually used at relatively low power (up to a few kW) or IGBTs (insulated gate bipolar transistors) at higher powers. At one time the use of thyristors was common, but these have been generally superseded, except at the very highest power levels.

There are three basic circuit topologies for DC to DC converters, the buck, or forward, converter, the boost converter, and the buck boost, or flyback, converter. More complex circuits exist but these are sufficient to illustrate the principles involved. Many good texts on power electronics have been written. Good wide-ranging books, which cover the basic principles of power conversion and some applications, are Mohan et al. [1] and Rashid [2].

2.1 The Buck Converter

The buck converter, in its basic form, is shown in Figure 1. The key components are the inductor, L, the switch, S, and the diode, D. The capacitor, C, stores charge and maintains a smooth output voltage as the switch is cycled on and off.

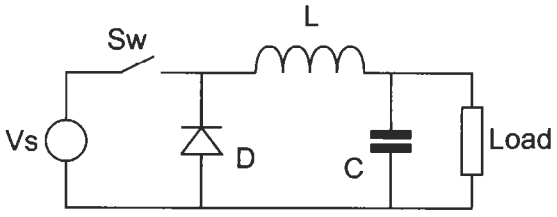

Figure 1 Basic circuit of the buck converter.

The switch may be a MOSFET or an IGBT which can be turned on or off rapidly. The source voltage, V_s, must be greater than the load voltage V_l.

While the switch is on the current in the inductor the current in the inductor will increase at a rate given by

$$\frac{dI}{dt} = \frac{V_s - V_l}{L}$$

When the switch is turned off the current in the inductor will still flow but it will be diverted from the switch to the diode, a process referred to as commutation. The polarity of the voltage across the inductor is now reversed and the current in the inductor will decay. Neglecting the voltage drop across the diode the rate of change of current is given by

$$\frac{dI}{dt} = -\frac{V_l}{L}$$

The switch is turned on and off cyclically with a period T and the current builds up and decays. If the current in the inductor does not decay to zero before the switch turns on again the converter is said to be operating in *continuous current* mode, as illustrated in Figure 2. In this case the load voltage depends only on the source voltage and the duty ratio, D:

$$V_l = DV_s$$

When operating in continuous current mode the current flowing from the inductor to the load is also continuous. This reduces the ripple current in the capacitor, enabling the use of a smaller value capacitor. However the current drawn from the supply is discontinuous.

In *discontinuous current* mode the inductor current falls to zero between switching cycles. In this case the load voltage depends in a more complex way on duty ratio and load current. Figure 3 shows how the load voltage varies with load current, at fixed duty ratio. At high load current the inductor current is continuous and the load voltage constant (for an ideal loss-less converter). When the converter moves to discontinuous mode at low load current the voltage rises. Continuous conduction mode is generally preferred, as it is more efficient.

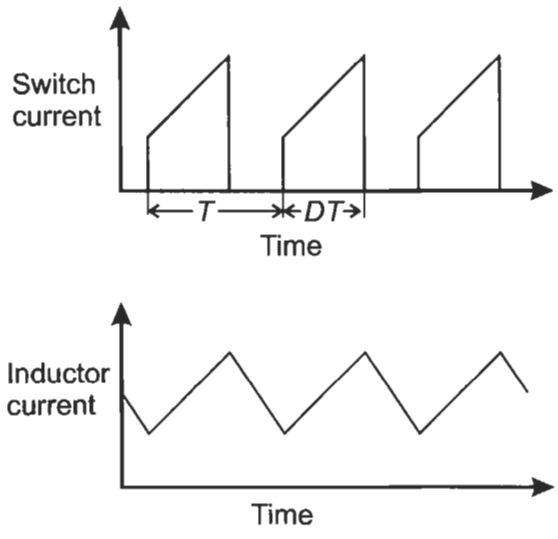

Figure 2 The currents in the switch and the inductor for a buck converter in continuous current.

In either continuous or discontinuous operation the load voltage may be controlled at any value less than the source voltage by varying the duty ratio D. Usually the operating frequency is kept constant and the pulse width (switch on time) varied. This is referred to as pulse width modulation (PWM). An alternative, used occasionally, is to hold the switch on time constant and vary the frequency (pulse frequency modulation, or PFM). At zero load current the voltage will rise to the source voltage even at very low duty ratio, hence most switching converters specify a minimum operating current at which proper voltage control can be maintained.

The switching frequency depends on the type and speed of the switch used. For MOSFET switches a switching frequency of greater than 100 kHz would be common. For IGBT switches, which are much slower to turn off, the frequency might be around 25 kHz.

The efficiency of this type of circuit may be high, typically the load power will be 90%, or more, of the power drawn from the source. Power is dissipated in the switch when it is on, but provided it has a low on resistance this power will be small. Power is also dissipated when the switch changes state (at this time both the voltage across the switch and the current through it may be substantial). These switching losses become more important as the system voltage rises, but are minimised by ensuring that the switching transition is as fast as possible. Similar considerations also apply to the diode.

It is important to note that a practical converter will require a suitable electrical filter at the input, between the array and the converter. This is necessary to make the current drawn from the PV array reasonably constant. This not only avoids problems of radiated interference from the converter but also is necessary to store energy and ensure that the array is supplying power continuously.

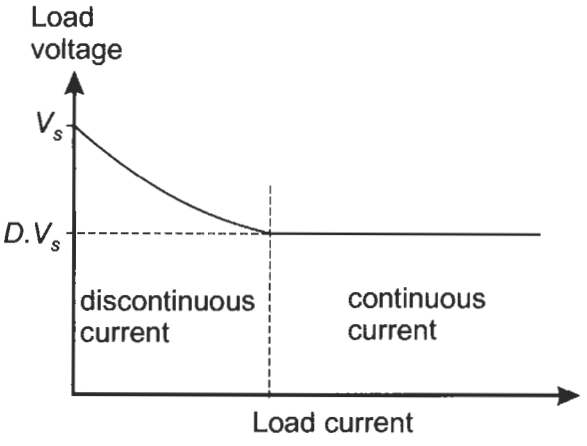

Figure 3 The variation of load voltage with load current for a buck converter at constant duty ratio.

2.2 The Boost Converter

The buck converter reduces the voltage, a circuit topology that increases the voltage, the boost converter, is shown in Figure 4. Again, the transistor is turned on and off in a cyclic manner. While it is on the current in the inductor builds up, then when the switch opens the voltage across the inductor changes sign and the current flows through the diode to the load. Again a capacitor is used to keep the load voltage constant.

As with the buck converter PWM is used to control the transformation ratio. The load voltage, in continuous current operation is given is given by

$$V_l = \frac{1}{1-D} V_s$$

The boost converter in continuous conduction draws a continuous source current, but the load current will be discontinuous. This continuous source current may be advantageous for PV applications as it reduces the filtering required between the PV array and the converter.

Again the converter may be operated in discontinuous mode, when the load voltage will depend on both duty ratio and switching current. With the boost (or buck-boost) converter the voltage may rise to a very high value if there is no load current, unless active measures are taken to prevent this happening.

2.3 The Buck-Boost or Flyback Converter

The third basic topology is shown in Figure 5. This converter has the feature that the voltage may be increased or decreased, depending on the switching duty ratio. The output voltage is however of opposite sign to the input voltage. While the switch is on the current in the inductor increases and energy is stored. When the switch turns off the voltage across the inductor is reversed and the

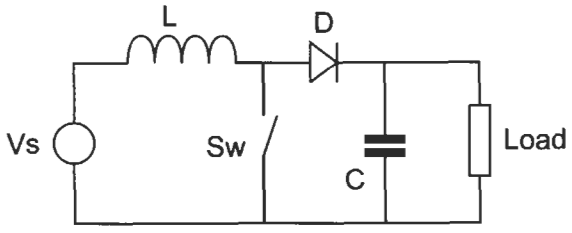

Figure4 The boost converter.

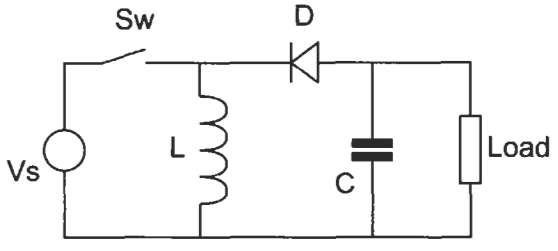

Figure 5 The buck-boost converter.

energy transferred to the load via the diode. In this case, for continuous inductor current, the load voltage is given by

$$V_l = \frac{-D}{1-D}$$

In this case, even in continuous current mode, both source and load currents are discontinuous.

2.4 More Advanced Topologies for DC to DC Converters

The basic converters described above have a number of limitations. The load is not electrically isolated from the source, which may be a serious limitation in higher voltage applications. Also efficient operation requires very rapid switching. This is because during the transition from ON to OFF or OFF to ON, in all the above circuits the switch may experience both large voltages and large currents. This implies that significant losses may occur during switching. A variety of *resonant converters* have been developed to reduce these losses (see, for example, references [1] or [2]).

Isolation of source from load may be achieved using a high frequency transformer. Both the buck converter and the flyback converter may be isolated in this way. A common circuit for a moderate power, isolated converter is shown in Figure 6. This is in fact a derivative of the buck converter with a transformer and diodes between the power switch and the inductor. The transformer may be made small and light by using a high switching frequency, typically of order 100 kHz at power levels around 1 kW. The transformer may also be used to vary

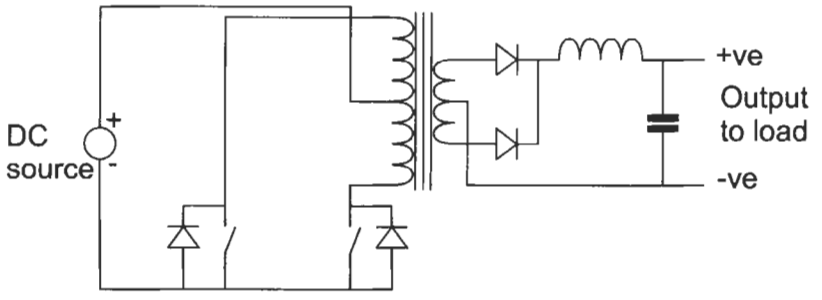

Figure 6 An example of an isolated DC to DC power converter.

the voltage ratio (in addition to the PWM) and hence this buck-derived converter, usually called a forward converter, may step the voltage up or down.

3 DC to AC Power Conversion (Inversion)

3.1 Single-Phase Inverters

In essence a single-phase inverter is just a switching circuit which reverses the polarity of the supply on a cyclic basis. There are two basic configurations, the half-bridge and the full-bridge, which are shown in Figure 7. The switching devices shown here as simple switches will, at low or medium power levels, be MOSFETs, IGBTs or bipolar transistors, depending on the voltage and power. The diodes across the switches are necessary to allow for reactive loads where the current will continue to flow even if all the switches are open, or try to flow through the switch in the reverse direction, which, the electronic switch may not permit.

The switches of the inverter may simply be switched alternately at the required frequency for the AC to obtain a *squarewave* (S1 and S4 ON, then S2 and S3 ON) as shown in Figure 8(a). This simple switching scheme has the merit of simplicity, but no control of load voltage is possible and the resulting waveform will have a high harmonic content. *Modified squarewave* inverters adjust the switching scheme so that the two pairs of switches do not operate simultaneously, but there is a phase shift between them. The consequence is that there are intervals when both sides of the bridge are high or low and the net waveform is as shown in Figure 8(b). The equivalent sine wave has the same r.m.s. value as the modified square wave. This is sometimes referred to as single pulse width modulation. It may be used to reduce and control the r.m.s. load voltage, or it may be used to reduce the harmonic distortion, by making the waveform somewhat closer to a sine wave [2]. These modified square wave inverters are usually, rather misleadingly, called *modified sinewave* by the manufacturers.

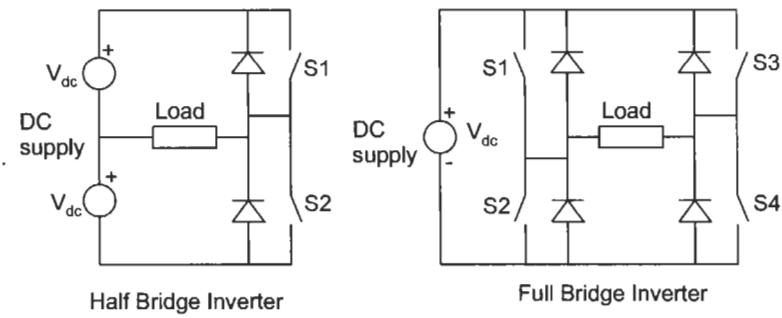

Figure 7 Single phase inverter circuits.

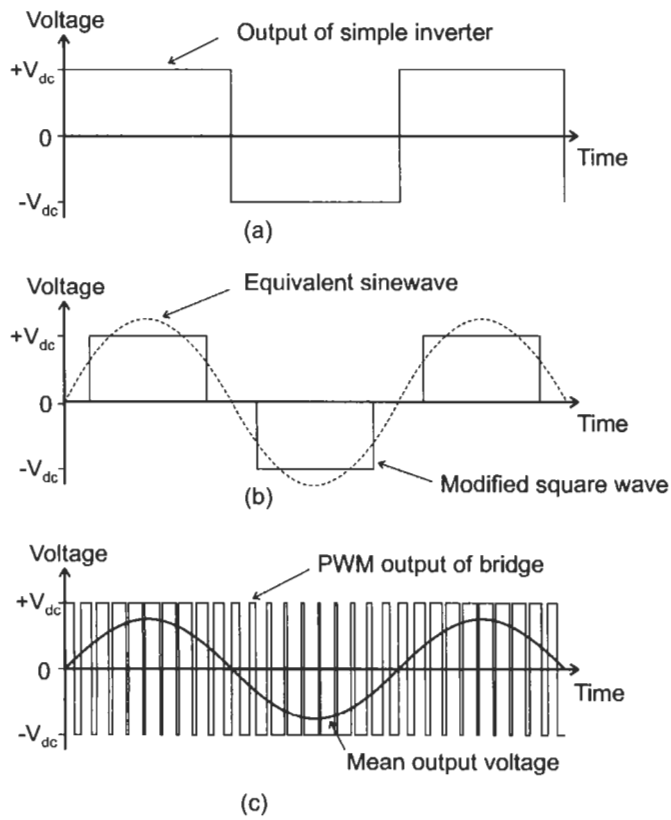

Figure 8 Output of single phase inverter with (a) simple square wave switching and (b) a PWM, quasi-sinusoidal output.

To reduce harmonic distortion and control the load voltage many modern inverters for PV and similar applications use high frequency pulse width modulation to synthesis a sinusoidal output. A variety of PWM schemes may be used; only one will be described to illustrate the principle.

The switches are operated in pairs to alternately provide a positive or negative voltage as in Figure 8(a), but at a much higher frequency than the desired AC output. By varying the duty ratio the mean output voltage may be positive or negative. By modulating the duty ratio in an appropriate way, as illustrated in Figure 8(c), the output voltage averaged over the switching period may be made to vary sinusoidal manner. The modulation frequency has been reduced in Figure 8(c), relative to the fundamental output frequency, for clarity. With a high modulation frequency, and using a suitable filter, the modulation frequency components may be removed, leaving a power frequency output with low harmonic distortion. Varying the maximum and minimum duty ratio the amplitude of the power frequency output may be controlled.

The inverters considered so far are voltage source inverters, that is the DC source is at a constant voltage. Such an inverter will act as an alternating voltage source on the AC side. It is also possible to have a current source inverter in which the DC voltage source is replaced by a constant direct current source. The inverter bridge must be modified slightly as shown in Figure 9, and the switches must be operated so that current flowing from the source has a suitable path. Zero output current is obtained by having both switches in a leg in the ON state to divert current from the load. The current source inverter approximates an ideal alternating current source. In practice the constant DC current source is supplied by a large inductance, which keeps the current constant on a short time scale. On a longer time scale a control system matches the source voltage to the load voltage to keep the current in the inductor constant.

If the inverter is to supply power independently of any other source then the inverter must control the load voltage and a voltage source inverter is the obvious choice. However, if the power is to be fed into a local power network where the voltage is controlled by other, more substantial sources of power then a current source inverter may be more appropriate.

An alternative to the current source converter is to use a voltage source inverter with PWM and with a fast control loop determining the current supplied to the load. In this case only a small value inductive filter is necessary at the output side of the inverter to keep the current approximately constant over the switching period and give the control loop time to respond. This approach

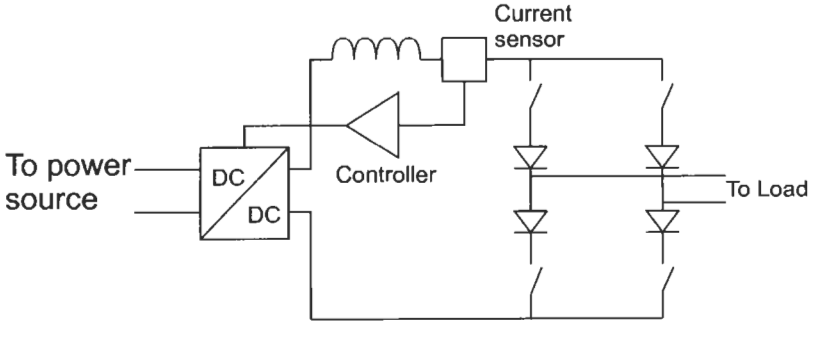

Figure 9 A current source converter.

is much more appropriate to small inverters as it avoids the large and heavy inductance.

A PV array acts as a source, which is neither an ideal current source, nor an ideal voltage source. It approximates a current source if the voltage is well below the open-circuit voltage and a voltage source if the voltage is close to the open-circuit voltage. In order to provide a stable output voltage, or current, feedback control is necessary. Also required is energy storage to keep the source voltage (or current stable during the power frequency cycle, as the load current, and source current vary. This may be achieved with a battery or capacitor for a voltage fed inverter or a series inductor for a current fed inverter.

If the load is not a pure resistance, but has a reactive component so that the load voltage and current are not in phase, or if the load is non-linear and generates harmonics, then the instantaneous power will flow through the inverter in both directions. (The reversal of power flow implies a reversal of the current on the DC side of the inverter.) This is not a problem for a stand-alone system with battery storage, however, if no battery storage is used a large value capacitor across the input is required to absorb the cyclic return of current through the inverter if the reactive power is non-zero.

3.2 Three-Phase Inverters

At higher power levels it is usual to generate and distribute power using three phases. A three-phase inverter is usually based on the circuit of Figure 10. The three pairs of switches are switched in a cyclic manner with a phase shift of 120° between each pair. Using a simple square-wave switching scheme the corresponding waveforms are as in Figure 11, which shows the voltages at each phase with respect to the negative end of the DC source, and one of the inter-phase voltages. The other inter-phase voltages look the same but with a phase shifts of 120° and 240°. As with a single-phase inverter PWM may be used to produce a quasi-sinusoidal output and/or control the output voltage or current.

For high power applications the preferred switches may be thyristors or gate turn-off thyristors (GTOs) since these devices are able to operate at high voltage

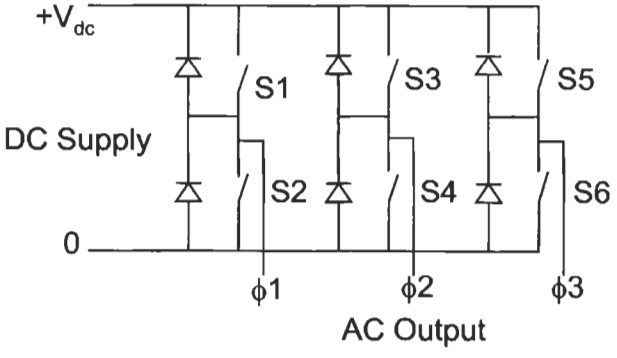

Figure 10 The basic circuit of a 3 phase inverter.

and very high current. Circuits based on these devices are considered in many textbooks on power electronics [2, 3].

3.3 Isolation

Generally it will be necessary to have electrical isolation between the PV array and the load, especially where the load side of the inverter is connected to the local electricity supply. This can be done simply with a power frequency transformer between the inverter and the load. The disadvantage of this approach is that power frequency transformers are relatively large heavy and expensive. An alternative approach is to provide isolation between the array and the inverter with a DC to DC converter isolated using a high frequency transformer (as in Figure 6). The high-frequency transformer approach has the advantages of small size and weight, at the expense of increased complexity.

4 Stand-Alone PV Systems

4.1 Battery Charge Control

Small stand-alone PV systems generally use battery back up and the roles of the system electronics are to control the charging of the battery and if necessary to change the voltage or to convert the DC to AC for the load. The most widely used batteries are lead–acid batteries in one of their various forms. This is because they are relatively cheap, have relatively good energy storage density and can be robust and reliable. Their disadvantage is that they do need some care in controlling the charging and discharging if good life and a large number of charge/discharge cycles is to be obtained.

A typical, simple, ideal, charging cycle for a lead–acid battery is as illustrated in Figure 12. Initially the battery is charged at constant current (the bulk charge phase) until the voltage reaches some predefined value then the voltage is held constant while the charging current decays (tapered charge phase). After a suitable time the charging voltage is reduced, or removed completely to avoid excessive gassing and loss of electrolyte. This ideal charging sequence can never be achieved with a PV system where the available power is constantly changing. The best the controller can do is to limit the peak charging current if necessary during the bulk charge phase, limit the voltage during the tapered charge phase and cut off the charge if the battery is deemed fully charged. Some charging schemes, rather than cutting off the charge altogether reduce the charging voltage by 5–10% to provide a trickle charge with a voltage low enough to avoid significant gassing. With some types of lead–acid cell it is also desirable to overcharge the battery occasionally to promote gassing and stir up the electrolyte.

With a PV array there are two basic methods by which the voltage or current may be controlled [4]. A series regulator introduces resistance in series with the

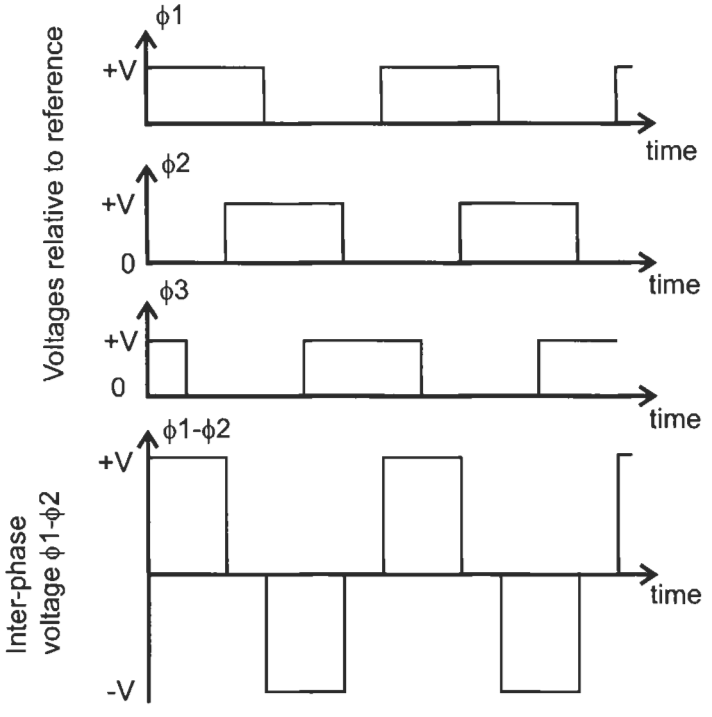

Figure 11 The voltage waveforms at ϕ1, ϕ2 and ϕ3 for simple square wave switching and one of the inter-phase voltages, ϕ1-ϕ2.

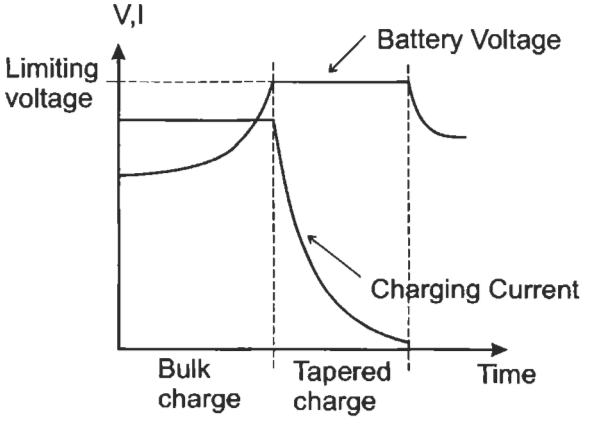

Figure 12 The typical ideal charging cycle for a lead acid battery.

array (Figure 13(a)), reducing the load current but allowing the array voltage to rise towards its open circuit value, and a shunt regulator which dumps current from the array pulling down both load and array voltage (Figure 13(b)). The diodes are necessary to avoid the battery being discharged either through

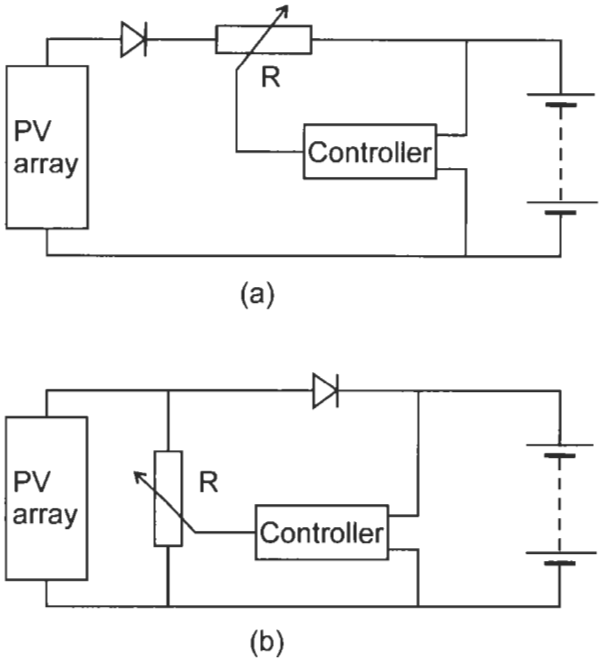

Figure 13 (a) Series regulation of battery charge current (b) Shunt regulation.

the array, or through the shunt regulator. Such regulators may be implemented using transistors as variable resistance elements. This approach requires the transistors to dissipate a large amount of power and is not generally used. The much more popular approach is to use the transistors as switches which turn on and off in such a way as to reduce the mean current flowing to the battery (Figure 14). Again either series (a) or shunt connection is possible (b). In the series switching regulator the switch makes and breaks the current to the battery. The mean switch current depends on the fraction of the time for which the switch is on. If the switching is rapid the voltage across the battery will be almost constant as the battery voltage responds quite slowly to changes in current. The excess power from the PV array is dissipated in the cells of the array. The shunt switching regulator operates in a similar manner. The diode prevents the battery discharging through the switch and effectively acts as a series switch which is off when the controlled switch is on. Again excess power is dissipated within the PV array.

Provision should also be made for cutting off the supply to the load if the state of charge of the battery falls below an acceptable level otherwise permanent damage to the battery may result. This requires some method of measuring or estimating the state of charge of the battery. This information is important to know when to shed load, it is also needed to establish when to discontinue charge. The state of charge is frequently deduced from the terminal voltage, either off load or with a known load. However this method is not very reliable as the voltage depends on many factors such as temperature and the recent

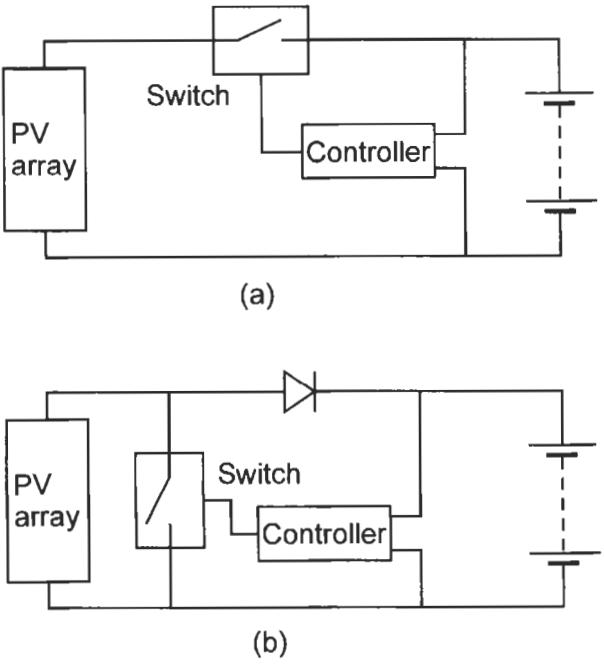

Figure 14 (a) Series switching regulator (b) Shunt switching regulator.

charge/discharge history of the battery. For flooded lead–acid cells the electrolyte specific gravity may be used, but this is not easy to measure using electronic techniques and may be modified by stratification of the electrolyte or loss of water due to excessive gassing. To try and overcome this ampere hour counting may be used to establish how much charge has been removed or added to the battery and hence deduce the state of charge. This method will drift, but may be recalibrated if there are times when the battery is known to be fully charged.

4.2 Maximum Power Point Tracking

The power supplied by a PV array varies with load voltage as shown in Figure 15. The voltage for optimum power transfer varies quite strongly with array temperature and more slowly with intensity of illumination. To ensure the optimum power transfer a DC to DC converter may be located between the array and the battery and used to optimise the power transfer. Any of the DC to DC converters described above may be used, depending on the array and battery voltages. The boost converter is probably the preferred configuration as it can draw current continuously at the input side, minimising the need for filtering and energy storage on the array side of the converter.

In order to ensure that the power converter is operating at the optimum voltage transformation ratio some form of feedback control is required. This

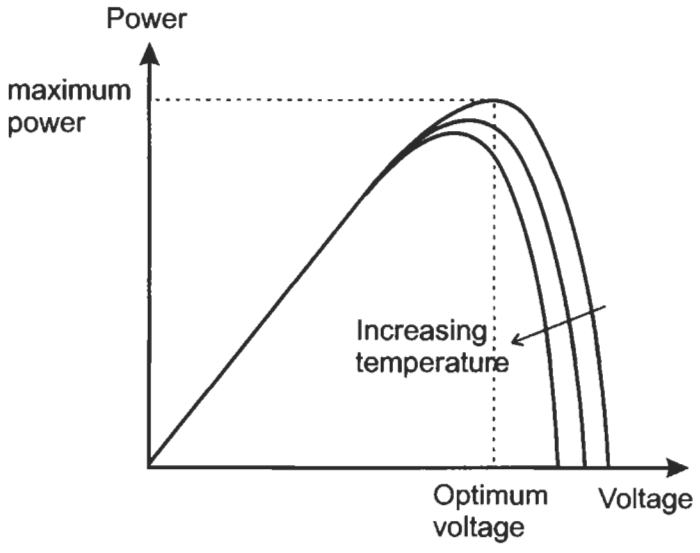

Figure 15 Power supplied by PV array as function of voltage, at constant illumination.

requires a method of identifying the voltage at which maximum power is obtained from the array and a controller on the power converter to maintain the array voltage at, or close, to this value. There are several approaches to estimating the optimum operating condition. The most general is to sweep the array current, measure the array voltage and current and deduce the maximum power point. Such an approach is however of little value if the array illumination and temperature are varying.

A more practical approach is to vary the array current and deduce if increasing the current increases or decreases the power delivered, and then deduce how the converter control must be changed so as to move the operating point in the direction of the maximum power point. A wide range of these hill climbing algorithms have been proposed. Possibly the simplest is the perturb and observe (P&O) algorithm [5]. Periodically a small variation is made to the operating point of the power controller. If this results in increased power the next perturbation will be in the same direction, if not the direction will be reversed. Another hill climbing scheme is to periodically vary the load current while measuring the instantaneous power and hence deduce the local gradient of the P-I curve. It is worth noting that the source current will be modulated by the input ripple current of the converter, and this modulation may be used [6] as the stimulus. The control algorithm moves the operating point to set this gradient to zero.

An approach to maximum power point tracking which requires minimal control electronics has been described by Boehringer [7]. This technique avoids the need to measure the power; only the current and voltage are needed. The scheme was originally proposed for use in a space on a small satellite. The scheme is simple and elegant but may be more appropriate to space applications

where the system is not required to operate with large changes of illumination (see, however, [8] for a discussion of an application of this technique to grid connected systems).

A simple approach to finding the maximum power point is to use the property of silicon solar cells that the optimum power point is always about 70–80% of their open circuit voltage [9]. By simply disconnecting the array periodically for a few milliseconds and measuring the open circuit voltage, the optimum array voltage may be found by multiplying the open circuit voltage by a factor k of about 0.75. A small error in the choice of k is relatively unimportant since power varies slowly with voltage near the turning point. (A similar approach is also possible using the short-circuit current.) A similar concept uses a monitor cell to deduce the open circuit voltage.

There has also been interest in the use of neural networks [10]. In this case a monitoring cell is used to deduce the open circuit voltage, as above, but the converter is controlled using a neural network which has been trained so that it can predict the optimum voltage of the installed array.

A recent comparison of various schemes [5] showed that the 'perturb and observe' scheme was simple to implement and could achieve high efficiency even under conditions of fluctuating illumination.

4.3 Power Inversion

Where the stand-alone PV system is to deliver AC for electrical appliances an inverter must be used. The appropriate type of converter for this type of application is voltage fed, with the battery controlling the input voltage to the converter. The inverter control system must maintain the supply voltage and frequency within acceptable limits. It must also cut the supply if battery charge falls to an unacceptably low value. Simple square wave inverters are now rarely used. Modified sine wave (really modified square wave, as described in Section 3.2) or sine wave converters are preferred because their better voltage waveform is required by many types of load and the cost difference is small. Modified sine wave converters still generate significant harmonics and are unsuitable for certain types of load, for example some types of electronic equipment. For this reason sine wave converters may be preferred. The main disadvantages of sine wave inverters are their somewhat higher cost and they may provide lower efficiency when compared with modified sine wave inverters (because of increased switching frequency, and hence, switching losses). However, these differences are being significantly reduced.

5 PV Systems Connected to the Local Electricity Utility

When a PV system is connected to the electrical utility the inverter must be operated synchronously with the utility, the voltage frequency and phase of the generation must match that of the utility. Inverters for this application are likely to be controlled so as to appear at the utility interconnection as a current source

with a sinusoidal waveform synchronous with the utility voltage. This may be achieved using a current fed inverter, but, as noted above, would in practice be achieved using a suitable PWM feedback control system to ensure that the load current is sinusoidal and to control its value. Control is quite complex. The utility voltage fixes the load voltage of the inverter, but the inverter must implement maximum power point tracking to ensure that the input voltage from the array is at the optimum value. This criterion determines the optimum r.m.s. value for the load current.

For medium size PV systems there seems to be a movement towards the use of multiple inverters, each connected to its own segment of the array, rather than a single larger inverter. Such an approach could lead to better reliability because of the redundancy. It may also reduce wiring costs if the AC voltage is much higher than the DC source voltage, as is usually the case, by reducing the need to carry large DC currents over significant distances.

There are two key issues that arise as the result of connecting small power generators to the public utility supply. These are power quality and safety. As far as power quality is concerned there are a number of points to consider. The power supplied must be sinusoidal with minimal harmonic distortion, there must be minimal injection of high-frequency switching components and the net power factor of the local generation and load should be as close as possible to unity. Good inverter design should ensure that the frequency spectrum of the injected power is acceptable and that the output from the inverter has no DC content, since small a direct current may cause saturation of the distribution transformer. The issue of power factor is more complex. If the inverter is controlled so as to generate the sinusoidal current in phase with the voltage it will not generate reactive power. Thus while the inverter will supply some or all the power needed by the load, the reactive current for the load will be drawn from the utility. Hence the local generation will degrade the power factor seen by the utility.

A particular safety issue raised by the connection of local generation to the utility is what happens when there is a loss of supply from the utility. If the loss of connection is not detected, and the inverter shut down, the local network may remain energised. If the inverter is able to supply sufficient power to match the load this situation may continue for some time. This is referred to as islanding. Islanding presents a potential safety hazard to utility and other personnel and also potential problems if the connection is remade while the inverter is supplying power. Basic protection measures such as shutting down operation if the voltage or frequency lie outside normal values will usually be sufficient to ensure that islanding is detected and the inverter shut down. However there are circumstances where such measures are inadequate, notably with multiple inverters, a matched resonant load or rotating machine. Other measures that may be taken to improve the prevention of islanding include monitoring the frequency for rapid changes, and measuring the impedance of the network by injecting a suitable current impulse.

A detailed overview of islanding and other issues which arise when a PV generator is connected to the utility supply can be found in Chapter IIIc-1.

6 Available Products and Practical Considerations

6.1 Charge Controllers

The role of the charge controller is to ensure that the battery is not overcharged. There is a bewildering array of commercial devices from a large number of manufacturers, with current ratings from a few amps up to hundreds of amps, and operating voltages generally in multiples of 12 V up to 48 V (nominal battery voltage).

Most commercially available charge controllers for PV applications use a switched series regulator to control the charging current Figure 14(a). The most common control scheme is pulse width modulation. The power to the battery is switched on and off at a constant frequency, with the duty ratio varied, to control either the mean current to the battery, or the charging voltage of the battery. This scheme is similar to a buck converter, but with a PV power source the current is limited, so a series inductor to limit the peak current is unnecessary, and the load voltage is smoothed by the battery. The control algorithm depends on the type of battery and most charge controllers provide a number of settings to accommodate different voltages and types of lead–acid battery. A typical control scheme would allow continuous current until the battery reaches a predetermined voltage and then the duty ratio of the PWM is reduced to limit the battery voltage. Some controllers use a three stage charging algorithm with a *bulk charge phase*, where the charging current is the maximum available, a *taper phase* where the voltage is held constant, and a *float phase* where the battery voltage is held constant at a reduced value. Many controllers will have control algorithms that will allow different control regimes and/or settings to accommodate different battery types.

A few controllers use switched shunt regulation. In this case a transistor switch bypasses the current from the PV array (Figure 14(b)). Again PWM may be used to control the mean load current. A variant on the shunt controller uses switches to divert power from charging the battery to a diversion load, again using PWM. The diversion load might be a water heater or similar. This enables the energy not used for charging the battery to be used usefully, rather than dissipated as heat in the PV panel. It is not clear that either series or shunt regulation is to be preferred. Both can achieve high overall efficiency.

In both series and shunt controllers the switches used are Field Effect Transistors (FETs) with an ON state resistance of only a few mΩ. Thus the voltage drop across the switch when it is on is usually small, avoiding unnecessary power dissipation, and in the case of a series regulator ensuring that overall efficiency is high. Control schemes other than PWM are possible and are used by some suppliers. One proprietary scheme, Flexcharge™, uses the way in which the battery voltage rises and falls as the current is switched ON and OFF to control the switching. The switch supplies current to charge the battery until the battery voltage reaches a desired upper limit. The current is then switched off until the voltage has fallen to a lower limit. This procedure charges the battery

with pulses of current which become shorter and less frequent as the battery approaches full charge.

Charge controllers incorporating maximum power point tracking are available, but much less common than simple charge controllers. To be useful a maximum power point tracker must have an efficiency of greater than 90%, this calls for careful design and the cost of such systems is significantly greater than for a basic charge controller. The gain in system efficiency however may be significant; gains of up to 30% are claimed. Such large gains will only be achieved when the battery is in a low state of charge (low voltage) and the PV array is cold (high voltage). Average efficiency gains are however likely to be significantly less (of the order of 10%). The cost of the maximum power point tracker must be weighed against the cost of extra array area.

6.2 Inverters

Inverters can broadly be split into two groups: those for stand-alone systems where the inverter controls the voltage and frequency of the AC, sometimes referred to as *off grid* and those intended for use to feed power into an AC supply which is connected to the power utility often referred to as *grid tied* or *grid connected*. The difference between the two groups is largely in the control algorithm which is generally implemented using a microprocessor. A significant number of dual application systems are available where the controller can implement either voltage control for stand-alone operation or current control for operation connected to the public utility or other generators.

Inverters available for stand-alone applications are readily available from as low as about 60 W up to several kW. They fall into two categories, modified sine wave or sine wave. Modified sine wave inverters generate a modified square wave as discussed in Section 3.1 and illustrated in Figure 8(b). This waveform may have relatively low total harmonic distortion and is adequate for many applications. The advantage of modified sine wave inverters is lower cost than true sine wave inverters, however some types of load will not function correctly with this type of waveform (e.g. thyristor or triac controllers may experience problems due to the ill-defined zero crossing point).

Sine wave inverters produce a waveform much closer to the ideal sinusoidal waveform. Typically the total harmonic distortion will be less than 3%. The waveform is much smoother than for modified sine wave and is suitable for all types of load. The only disadvantages are potentially lower efficiency because of the high switching frequency and risk of the emission electromagnetic interference (again due to the high switching frequency). This latter problem may be avoided with good design and adequate filtering. In practice the efficiencies claimed by manufacturers for sine wave inverters are not significantly less than for the simpler type.

Grid-connected inverters are rather more constrained than those used in stand-alone systems. Because they are connected to the public utility network they must meet all the safety and other criteria imposed by the local electricity utility. Thus they will be expected to generate low levels of harmonics and low levels of high

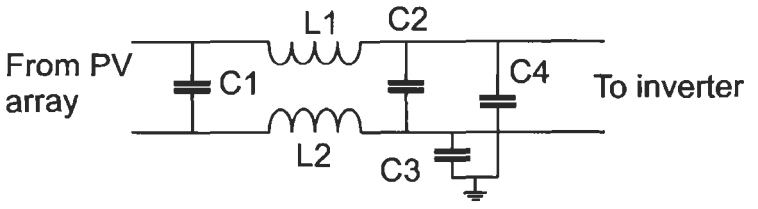

Figure 16 Example of filter to reduce the transmission of electromagnetic interference along power lines.

frequency noise due to the switching. In addition, as discussed earlier, they must be able to detect the loss of power from the utility and shut down. This islanding protection is required to ensure safety under the condition of loss of supply from the utility. Commercially available inverters use a variety of schemes to detect loss of utility connection (a detailed review of this topic can be found in Chapter IIIc-1). It is not usual to supply battery storage for grid-connected systems.

Inverters are available that will operate with either current control or voltage control. With suitable storage such a system can provide both utility connected and stand-alone operation. However, if the system is used to provide back-up power in the event of loss of utility supply, islanding protection is still required. Following loss of supply the inverter must be shut down and the local network isolated from the utility before the inverter may be restarted in voltage control mode.

7 Electromagnetic Compatibility

Converters and inverters using PWM are sources of electromagnetic interference because of the rapidly changing voltages and currents. Measures must be taken to limit the emissions from such systems in order to meet regulatory requirements and to avoid interference with other electronic equipment [11]. To minimise radiation care is necessary with the internal layout to minimise the area of loops with large, or rapidly changing, circulating currents. In addition a carefully designed screened enclosure will reduce radiated emissions further. Interference may also be conducted up the power leads into and out of the converter or inverter. This is minimised by the use of filters, a typical example of a filter for the out input of an inverter is shown in Figure 16. Careful design of the filters is necessary to obtain low levels of interference. It is also essential to ensure that the earthing arrangements do not provide loops around which the unwanted high frequency currents may circulate.

References

[1] Mohan, N., Undeland, T.M. and Robbins, W.P. 1995. *Power Electronics, Converters, Applications and Design* (2nd Edition), John Wiley & Sons, New York.

[2] Rashid, M.H. 1993. *Power Electronics, Circuits, Devices and Applications* (2nd Edition), Prentice Hall.

[3] Lander C.W. 1993. *Power Electronics* (3rd Edition), McGraw-Hill, London.

[4] Lasnier, F. and Ang, T.G. 1990. *Photovoltaic Engineering Handbook*, Adam Hilger, Bristol.

[5] Hohm, D.P. and Ropp, M.E. 2003. Comparative study of maximum power point tracking algorithms, *Prog. Photovolt: Res. Appl*, Vol. 11, pp. 47–62.

[6] Midya, P., Krein, P.T., Turnbull R.J., Reppa, R. and Kimball, J. 1996. Dynamic Maximum Power Point Tracker for Photovoltaic Applications 1996, *Proc. IEEE Annual Power Electronic Specialists Conference (PESC)*, pp. 1710–1716.

[7] Boehringer, A.F. 1968. Self-adapting dc converter for solar spacecraft power supply. *IEEE Trans. Aerospace Electronic Systems*, Vol. 4, pp. 102–111.

[8] Schilla, T. 2003. Development of a Network Model of a PV Array and Electrical System for Grid Connected Applications, PhD Thesis, University of Northumbria.

[9] Enslin, J.H.R., Wolf, M.S., Snyman, D.B. and Swiegers, W. 1997. Integrated Photovoltaic Maximum Power Point Converter, *IEEE Trans. Ind. Electron.*, Vol. 44, pp. 769–773.

[10] Hiyama, T., Kouzuma, S., Imakubo, T. and Ortmeyer, T.H. 1995. Evaluation of Neural Network Based Real Time Maximum Power Tracking Controller for PV System, *IEEE Trans. Energy Conversion*, Vol. 10, pp. 543–548.

[11] Keiser, B.E. 1985. *Principles of Electromagnetic Compatibility* (5th edition), Artech House Inc, MA, USA.

Batteries in PV Systems

David Spiers, Naps Systems, Naps-UK, Abingdon, UK

1 Introduction

Batteries are used in most stand-alone PV systems, and are in many cases the least understood and the most vulnerable component of the system. Most design faults (e.g. undersizing the PV array or specifying the wrong type of controller) and operating faults (e.g. use of more daily electrical energy than was designed for or simply some breakdown in the PV array or charge controller) will lead to ill-health, if not permanent failure, of the battery. In these cases, the battery is then often blamed for the failure of the system to deliver the promised regular amount of electrical energy, and the type of battery used in such a failed system can acquire, quite unfairly, a bad reputation as a 'PV battery'.

The aim of this chapter is to present the reader with enough information to understand how important it is to specify an appropriate type of battery, and with sufficient capacity, for satisfactory use in a PV system. We start by considering the battery as a 'black box' with certain properties, and for many purposes this is sufficient to design a satisfactory PV system as long as we understand that these 'black box' properties can change according to certain external conditions. To understand why these properties change the way they do, it is necessary to appreciate some general principles of how batteries are made and how they work, and this material forms the second part of this chapter. Finally, some guidelines are given on how to specify a battery correctly for a PV system and how to look after it properly.

2 What Is a Battery?

To some people, a battery is a small object that you insert into a radio or personal music system to provide some electrical energy. When it has run out of energy, it is thrown away (often irresponsibly). This is perhaps the best-known example of a non-rechargeable, or primary, battery. Many of these are in the form of cylindrical cells, and you need to put 2, 3, 4 or more of them into your device to make it work. This illustrates another essential feature of batteries: like PV cells, they are essentially low-voltage devices and you have to connect several in series to get a useful voltage (which is often 4.5, 6 or 9 V for small portable electrical consumer products). Even if a primary battery is supplied as a single package (for example, the familiar small 9 V battery with snap-on connectors), it nearly always consists of more than one cell inside.

To other people, a battery is the device in their mobile phone, laptop computer, cordless drill, electric toothbrush, etc that needs recharging from time to time, often at the most inconvenient moment. These are examples of rechargeable, or secondary, batteries, which in earlier times were often referred to as accumulators. In these types of devices, the batteries are often used until they have run out of energy to deliver, but instead of being thrown away are 're-filled' with electricity by connecting them to a mains charger. After several of these 'cycles', the battery will start to show signs of wearing out, and eventually it will not provide a satisfactory interval between recharges and will have to be replaced.

Most people prefer to forget that there is a battery inside their car, until of course it goes wrong – which often means that the car refuses to start, typically on the first cold morning of the winter. Actually, there is a 12 V rechargeable battery in every car that provides the electrical power for starting the engine and is recharged quite quickly by a generator that is driven by the car engine. This battery also powers the lights when needed, providing a more constant voltage than if the lights were powered from an engine-driven generator alone (so the lights do not change intensity as the engine speed varies). It also provides electrical power when the engine is not running. In many ways, this is quite similar to how a rechargeable battery is used in a PV system – it provides electricity when there is no power from the PV array (i.e. at night), it is recharged when power from the PV array is available (i.e. during the day) and it stabilises the voltage when there is power from the PV array. In several other ways, these two types of duty are quite different.

Few people realise just how widespread batteries are depended upon in other aspects of daily life. In offices, building plant rooms and power stations, etc., batteries are constantly waiting in 'stand-by' mode to provide emergency electrical power if there is a power cut. They are kept at full charge by a small charging current (called float charge) and they only undergo a discharge (and recharge) in the event of emergency power being required. In contrast, electric fork lift trucks and other electric vehicles have a large rechargeable battery that is discharged almost fully every working day and recharged every night.

3 Why Use a Battery in PV Systems?

There are three main functions that a battery performs in a PV system:

- *It acts as a buffer store to eliminate the mismatch between power available from the PV array and power demand from the load.* The power that a PV module or array produces at any time varies according to the amount of light falling on it (and is zero at night time). Most electrical loads need a constant amount of power to be delivered. The battery provides power when the PV array produces nothing at night or less than the electrical load requires during the day time. It also absorbs excess power from the PV array when it is producing more power than the load requires.
- *The battery provides a reserve of energy (system autonomy)* that can be used during a few days of very cloudy weather or, in an emergency, if some part of the PV system fails.
- *The battery prevents large, possibly damaging, voltage fluctuations.* A PV array can deliver power at any point between short circuit and open circuit, depending on the characteristics of the load it is connected to. In a nominal 12 V system, for example, this means anything between 0V and around 20V is possible from the PV array. Many loads cannot operate over such a wide range of voltages. Placing a battery between the PV array and the load ensures that the load will not see anything outside the range of voltages that

the battery can experience – in the case of a 12V system from around 9.5 V under deep discharge to around 16 V under extreme charging conditions.

These functions are needed in most PV applications. It is, for example, difficult to think of a viable PV lighting system that does not contain a battery. Perhaps it is easier to list those PV systems where a battery is not commonly used:

- *In grid-connected systems*, where the PV array produces AC electricity that is either used inside the building or exported to the main electricity supply network when there is an excess. Note that this only works at present without disturbing the grid because the amount of PV electricity produced is so small compared to the grid's capacity. If grid-connected PV becomes extremely widespread, some form of electrical storage will be needed to accommodate it.
- *In water pumping systems*, where a PV array is connected directly to an electric pump of suitable characteristics. The pump speed varies with amount of power available from the PV array at any time, and the mismatch between water supply and demand is smoothed out by storing water in a tank. This is a cheaper way to store energy than in batteries.
- *In other cases of directly-driven motor loads*, such as fans and sometimes compressors in refrigeration units. As with the PV driven pumps, the speed varies with the PV array output (and is zero at night).

4 Battery Duty Cycle in PV Systems

PV systems demand that batteries are used in a different way to any other type of battery application.

4.1 How Are Rechargeable Batteries Normally Used?

As we have seen above, batteries are mostly used in one of three modes:

- Regular deep cycling (as in electric vehicles and consumer devices)
- Standby use (kept at full charge in case of an emergency)
- Starting, lighting, ignition (SLI) for road vehicles. Starting requires a very high current for a short time, but the depth of discharge is small.

In all of the above normal duty cycles, the battery is given a full charge after discharging. Full charging means that some adequate 'overcharge' is given, often over quite a long period of time.

4.2 How Does This Differ from PV Systems?

The first difference to note in PV systems is that there is a limited (and variable) amount of charging energy available from the PV array and it is by no means guaranteed that the battery will be fully charged at the end of each day.

If the load is used every day, then the battery will undergo a daily cycle of discharge and recharge, but this is often a shallow cycle compared to normal cycling duty. Most stand-alone PV systems are specified to have a certain number of days of autonomy reserve in the battery – depending on the reliability required and the weather pattern, this can be anything from 3 to 20 days, and it is normal to specify that there is some charge left in the battery after this autonomy reserve has been used (often 20%). So, simplistically, we can estimate the range of daily cycling as follows:

- For 3 days autonomy, the battery needs a storage capacity equal to (3/0.8) = 3.75 times the daily load. The maximum daily cycle is then (1/3.75) = 26.7% (if the load is all consumed at night).
- For 20 days autonomy, the same reasoning leads to a battery capacity of (20/0.8) = 25 times the daily load and a maximum daily cycle of (1/25) = 4%.

If the load is continuous throughout the 24 hour period, these average daily depths of discharge will be less, as for some of the time the battery will be charging when the load is being powered. We can therefore say that the typical range of daily cycling is of the order of 2–30% per day.

One exception to this is when a PV array is coupled with a diesel generator and the diesel generator provides the back-up autonomy reserve instead of the battery. In these cases the batteries can indeed perform a deep cycle every day, and they are unlikely to give more than 2–3 years' service (1 year in such a duty cycle requires 365 deep cycles, 2 years 730 deep cycles and 3 years 1095 deep cycles).

In addition to shallow daily cycles, the battery may be required to provide seasonal storage during winter or some rainy season like a monsoon. This is basically a deeper and much longer cycle superimposed on the daily cycling pattern. The battery may be in a lower state of charge than normal for several weeks.

Similarly, after a deep discharge to supply system autonomy in an emergency, the battery may take several weeks to recover its full charge – there may only be a small excess of daily energy available from the PV array to restore this charge that has been withdrawn.

Figure 1 illustrates these various aspects of cycle duty in PV systems.

5 The Battery as a 'Black Box'

It is very convenient (and tempting) to treat a rechargeable battery as a 'black box', or perhaps, more graphically, a 'black bucket' into which electricity can be filled and withdrawn as needed. Like a bucket, a battery has a certain storage capacity, and when it is full, there is no point in trying to fill it further. Also like a bucket, when it is empty, there is no point in trying to empty it further. If you want to store more water in a bucket, or electricity in a battery, you have to use either a larger capacity bucket or battery, or more than one of the same size.

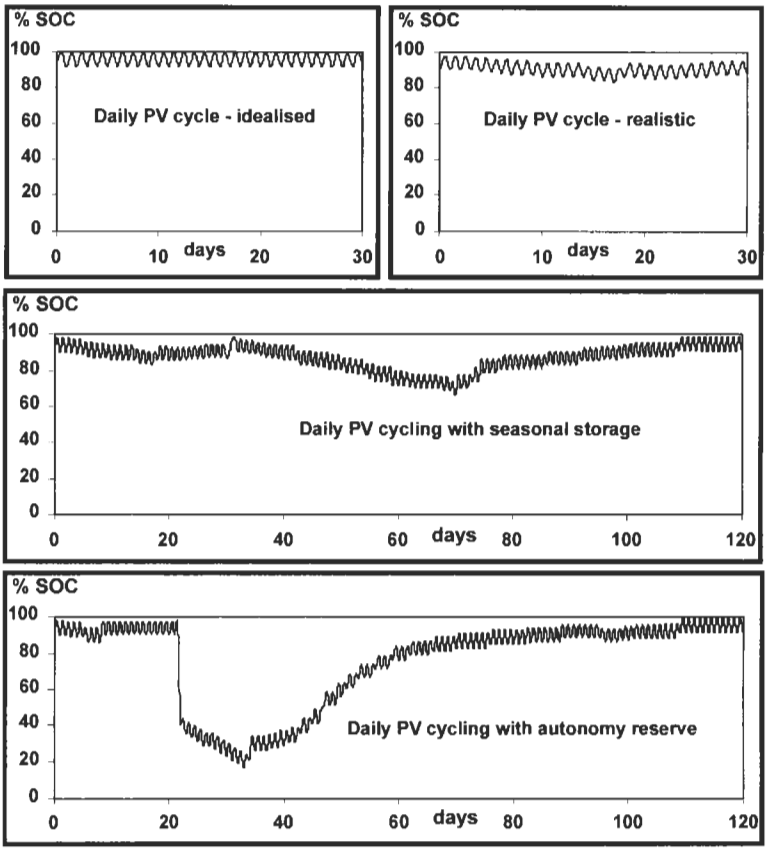

Figure 1 Illustration of PV duty cycles.

If you use ampere-hours (Ah) as the unit of electricity being stored, then as a first approximation, you can use the 'black box' or 'black bucket' approach. So if you want to store enough reserve electricity to power a 1 A load continuously for 5 days (120 hours), you are going to need a storage capacity of 120 ampere-hours (120 Ah). To determine whether that means using a battery with 120 Ah written on the label requires either understanding batteries in more detail, or simply learning a set of rather strange empirical rules about this black box that stores electricity.

If you want to just follow 'black box rules' for specifying batteries for PV systems, then the following are the main ones to be aware of. It soon becomes clear that the idea of a bucket into which electricity can be filled and withdrawn is a little simplistic.

- You must choose a battery of the appropriate voltage. Simply specifying that this is a 120 Ah battery does not tell you whether it should be 6, 12, 24, 48 V, etc. In most PV systems, to get the voltage you require means connecting 2, 6 or 12 V units of the required capacity in series.

- The storage capacity of a battery is not fixed. It depends mainly on how fast you try to extract it (i.e. the discharge current) and the temperature. How this varies depends on the exact battery type and you need to consult a data sheet.
- It is not a good idea to try to extract the full capacity of the battery, even under worst case conditions. Under most circumstances, you should aim not to extract more than 80% of the available capacity at any time.
- The more capacity you try to extract from a battery every day, the more quickly it will wear out. Just how quickly depends on the type of battery and its cycle life. For a given daily load, the smaller the battery capacity, the shorter its life will be, unless something else causes it to fail earlier than the wearing out due to this charge and discharge cycling.
- The battery voltage on charging depends to some extent on how fast you are charging it. If the current is particularly high, the voltage may rise more than the charge controller is expecting to find for a fully charged battery. It may disconnect the PV charge current (or reduce it) before the battery is fully charged.
- If you operate a battery at high temperatures (in this case, 'high' means more than about 20°C on average), it can wear out much faster than anything stated on a data sheet, or indeed much faster than the daily cycling and cycle life might predict.
- In general, the longer you wish a battery to last in a PV system, the more expensive it will be. But it is not always the case that the most expensive battery you can think of will give the longest life.

5.1 Battery Performance Definitions and Summary

If we consider a battery to be simply a 'black box' that stores electricity, there are various properties that we need to define in order to describe its performance.

5.1.1 Definitions of Capacity, Efficiency and Overcharge

- The amount of electrical energy stored is measured in watt-hours (Wh) or kilowatt-hours (kWh). The energy efficiency of a rechargeable battery is:

$$\frac{\text{energy in Wh discharged}}{\text{energy in Wh required for complete recharge}}$$

  and is usually around 70–80%.
- Battery capacity is measured in ampere-hours (Ah). The charge efficiency or Ah efficiency is:

$$\frac{\text{Ah discharged}}{\text{Ah required for complete recharge}}$$

  and is around 95% for a lead–acid battery, somewhat lower for a nickel–cadmium battery.

The energy efficiency of a battery is lower than the Ah efficiency because batteries discharge at a lower voltage than they charge at. Since the Ah efficiency is close to 1, it is considerably more convenient to work in Ah when balancing how much charging is required to replace a certain amount of discharge in PV (and indeed other) calculations. However, since the Ah efficiency for a full recharge is always at least slightly less than 1, somewhat more Ah have to be delivered to the battery than are consumed in the actual charging process. This additional charge, or overcharge, is consumed by other, unwanted, chemical reactions within the battery. In lead–acid and nickel–cadmium batteries, these are normally the production of oxygen gas from water at the positive electrode, and, in open batteries, the production of hydrogen gas from water at the negative electrode too.

5.1.2 Discharge Rate and Charge Rate

Discharge and charge rates are convenient scales to compare currents at which batteries are charged, independent of battery capacity. They are expressed as a number of hours, e.g. the 10 hour rate, the 240 hour rate, etc. The current to which they correspond is the appropriate total discharge capacity divided by the number of hours:

$$\text{Rate} = \frac{\text{Capacity (Ah)}}{\text{Time (h)}}$$

For example, C/10 (10 hour rate) is a current equal to the rated capacity in Ah divided by 10.

5.1.3 Battery Capacity Is Not Fixed

Unfortunately, the capacity of a battery is not constant, and we have to be very careful to understand the way it varies.

The Nominal or Rated capacity of a battery (in Ah) is defined as the maximum Ah a fully charged battery can deliver under certain specified conditions. These conditions include:

- the voltage to which the battery is discharged (the end voltage)
- the current (or rate) at which the discharge is carried out
- the battery temperature.

In particular, the discharge rate has to be carefully stated along with any capacity, since, for example, a battery rated at 100 Ah at the 10 hour rate will give 10 hours discharge at 10 A, but normally less than 1 hour discharge at 100 A and normally more than 100 hours discharge at 1 A. Capacity increases at lower discharge currents (longer discharge rates) and decreases at higher discharge currents (shorter discharge rates).

At low temperatures, capacities of all batteries are reduced. If the PV system requires a certain amount of autonomy back-up in a month when the battery

will experience a low temperature, then allowance for this has to be made in specifying the nominal battery capacity.

The end voltage obviously affects the amount of capacity that can be delivered. If a battery is discharged down to a lower voltage, it will of course give more capacity.

These capacity variations are illustrated in more detail later on in the chapter when the different types of batteries used in PV systems have been described. The exact variation of capacity depends on the type of battery, although the above trends are always true.

5.1.4 Depth of Discharge and State of Charge

Depth of Discharge (DOD) is the fraction or percentage of the capacity which has been removed from the fully charged battery. Conversely, the State of Charge (SOC) is the fraction or percentage of the capacity is still available in the battery. It is similar to considering whether a bucket (or drinking glass) is half empty or half full.

The following table shows the simple relationship between these two scales:

SOC	DOD
100%	0%
75%	25%
50%	50%
25%	75%
0%	100%

However, these state of charge/depth of discharge scales are normally referred to the nominal capacity (e.g. the capacity at the 10 hour rate). For lower discharge currents you may see references to a DOD of more than 100%. This simply means that the battery can produce more than 100% of its nominal capacity at discharge rates lower than the nominal rate.

5.1.5 Self-Discharge Rate

Self-discharge is the loss of charge of a battery if left at open circuit for an appreciable time. For example, a primary battery that has been sitting on the shelf of a shop for some years will not have its full capacity remaining (if any). For rechargeable batteries, the self-discharge rate is normally quoted as a percentage of capacity lost per month when starting with a fully charged battery, but it must be stated along with a battery temperature. In many cases it will double for each 10°C rise in battery temperature. In most calculations for PV batteries, the self-discharge rate of the preferred battery types is low (between 1 and 4% per month at 20–25°C) and self-discharge requires so little additional charging compared to the load (or even the control electronics) that it can be neglected.

5.1.6 Cycle Life

Cycling describes the repeated discharging and recharging process that a battery undergoes in service. One cycle equals one discharge followed by one recharge. Cycle life is a measure of how many cycles a battery can deliver over its useful life. It is normally quoted as the number of discharge cycles to a specified DOD that a

battery can deliver before its available capacity is reduced to a certain fraction (normally 80%) of the initial capacity.

The cycle life depends very much on the depth of each cycle, and this is described in more detail in the section on battery lifetimes. However, it can be mentioned here that if cycle life is experimentally measured at a high DOD, at lower DODs the product of (number of cycles x the DOD) is approximately constant, i.e. the 'capacity turnover' is about the same for lower DODs.

Care should be taken when analysing cycle life that is published by battery manufacturers. It is normally measured at relatively high currents (short discharge times) and the DOD quoted often refers to the capacity available at that short discharge time. As a concrete example, one manufacturer quotes a cycle life of 400 cycles of 50% DOD for their product. Closer inspection of the details shows that this was done at the 5 hour rate of discharge, and that the DOD quoted refers to the capacity at this rate. The rated capacity of this battery is quoted at the 20 hour rate, and the 5 hour rate capacity is 85% of the rated capacity. Although the capacity turnover is $400 \times 50\% = 200$ for the 5 hour rate figures, in terms of actual Ah turnover it is only $400 \times 50\% \times 85\% = 170$ relative to the rated (20 hour) capacity. That means that one might reasonably expect only 340 cycles at 50% DOD relative to the rated 20 hour capacity, not 400.

In cycle life tests, batteries are given a full recharge after each discharge. In PV systems, the recharging is not so thorough. As a safety factor, it is therefore prudent to derate the cycle life somewhat when using it to estimate lifetimes in PV systems. A figure of 80% of the tested cycle life is often used. Thus our above example battery which started at 400 cycles at '50% DOD' and was reduced to 340 cycles at 'true 50% DOD' would now be counted on to give only 272 such cycles under PV conditions.

In the early days of PV system design, the 'quick fix' for increasing battery life when these were found to be disappointingly low in some cases was to look for a battery with an increased cycle life. Unfortunately, cycle life is not the only factor that determines the lifetime of batteries in PV systems, and in some cases this change actually led to an even shorter lifetime.

5.1.7 Maximum Lifetime

Batteries that are used in standby ('float') applications are not cycled regularly. Using cycle life to estimate their lifetime is not at all useful. Instead the float service lifetime is stated as a certain number of years (at given temperature and float voltage) before the available capacity of a standby battery drops to 80% of its initial value. The float service life approximately halves for every 10°C rise in temperature above the stated value, because it is most often determined by internal corrosion processes that follow such a temperature dependence. The lifetime of a shallow cycling PV battery will often be similar to that in float service under the same conditions, and this gives an upper limit to the expected lifetime if the cycle life data predicts a longer (and perhaps unbelievable) value. Because the battery is not kept in such a precisely fully charged condition as on float or standby duty, it is again prudent to derate its maximum lifetime for PV life estimation purposes (again 80% is often used).

5.2 Example of Simple 'Black Box' Battery Calculations

In practice, you need to know the detailed characteristics of the battery type you are considering in order to work out accurately the size of battery required for a given PV system, and also its possible lifetime. You do not actually need to know why these characteristics vary the way they do for different battery types, but it does help if you appreciate something about the general principles of how battery properties depend on how they are made. These are summarised in the rest of this chapter. However, here is a hypothetical example to show how the battery properties influence the size and selection, and also the basic way to determine the battery size from the PV system characteristics.

5.2.1 Basic Data

A PV system has to run a daily load of 40 Ah per day at 24 V nominal. The load is lighting, and so is all consumed during night time.

- The PV array produces a maximum current of 9 A charging current under full sun conditions (1 kW/m^2 solar irradiance).
- The battery should provide at least 4 days of autonomy (i.e. run the load for 4 days if the PV system fails).
- The annual average temperature of the battery can be assumed to be around 20°C in this location.

Two types of lead–acid batteries can be considered:

- Type A: Available as 12 V, 100 Ah nominal only. Cycle life: 200 deep (80%) cycles. Expected maximum life: 5 years at 20°C.
- Type B: Available as 12 V, 50, 100, 150, 200 Ah nominal. Cycle life: 1200 deep (60%) cycles. Expected maximum life: 12 years at 20°C.

Type A is typical of a 'good' flat plate battery and Type B is typical of an industrial tubular plate battery. Per kWh, type B is about 3 times more expensive than type A.

5.2.2 Calculations

For explanations of many of these steps, you will need to read the later parts of this Chapter. Remember that the details will change for other battery types, and even between manufacturers for the same battery type.

Autonomy Requirement

- 4 days × 40 Ah/day = 160 Ah storage needed.
- If we specify this to extract no more than 80% of the battery capacity, we actually require (160/0.8) = 200 Ah actual capacity.

- This is extracted at a low rate of discharge (4 days to 80% capacity is equivalent to 5 days or 120 hours to extract 100% of the capacity). From their data sheets, battery type A will give 1.1× more than its rated capacity at this low rate, and battery type B 1.4×. Therefore the minimum rated capacity needed will be: Type A: (200/1.1) = 182 Ah; Type B: (200/1.4) = 143 Ah. We do not need to correct these capacities for other operating temperatures, since the annual average temperature of the battery is around 20°C. Particularly if this operating temperature was lower, we would need to correct for the capacity variation with temperature.
- Batteries do not come in such precise capacities as the above. The nearest actual sizes are 200 Ah for type A (actually 2 × 100Ah batteries in parallel) and 150 Ah for type B.

Lifetime Limit. Since the annual average temperature of the battery is around 20°C, if the batteries were operated as standby batteries, the highest lifetime expected would be 5 years for type A and 12 years for type B. However, in PV use we derate this to about 80% of these values, giving maximum expected daily lifetimes of 4 years and about 10 years (actually 9.6) respectively. If the expected battery temperature would be higher than 20°C, then we would need to reduce these lifetime limits.

Now we check the daily cycling. Since it is all at night, the batteries will be discharged by 40Ah each night. This is equivalent to (40/200) = 20% of the nominal capacity for type A and (40/150) = 26.7% for type B.

If the load was continuous, or at least did not all occur at night time, the daily cycling would be less than the above, since, for some of the time, the battery would not be discharging whilst the load was being delivered.

- Battery type A gives a maximum 'capacity turnover' of 200 × 80% = 160 times its nominal capacity. Scaling this to the 20% of nominal capacity it will cycle every day gives (160/0.2) = 800 cycles. At one cycle per day, this is (800/365) =2.2 years. If we are not happy with this short battery lifetime, and want to increase it to the maximum value of 4 years, then we have to increase the capacity, such that the daily cycling over 4 years is no more than 160 times the nominal capacity, i.e. so that it is no more than (160 / (4 × 365)) or about 11%. For a 40 Ah daily load, this means a minimum of (40 / (160 / (4 × 365))), which actually comes to 365 Ah. As the battery only comes in 100 Ah units, this means we have to specify 400 Ah of nominal capacity to achieve a 4 year life (i.e. 4 × 100Ah in parallel).
- Battery type B gives a maximum 'capacity turnover' of 1200 × 60% = 720 times its nominal capacity. Scaling this to the 26.7% of nominal capacity it will cycle every day gives (720/0.267) = 2700 cycles. At one cycle per day, this is (2700/365) = 7.4 years. If we wanted to get the maximum lifetime of this battery (9.6 years), then we would need to increase the capacity somewhat (by 9.6/7.4), but the lifetime due to the cycle limit is probably sufficient in this case.

Check the Maximum Charge Rate. For proper controller function, it is a good idea that the maximum charge current is no more than the 10 hour rate for open batteries such as these. The maximum charging current from the PV array is 9 A.

- For the type A 200 Ah battery, the maximum charge rate is (200/9) = 22.2 hours.
- For the type A 400 Ah battery, the maximum charge rate is (400/9) = 44.4 hours.
- For the type B 150 Ah battery, the maximum charge rate is (150/9) = 16.7 hours.

All of these are acceptable, and there is no need to increase the battery capacity to satisfy this condition.

Remember to Specify the Voltage!. The system (PV array and load) is 24 V nominal. If we are using 12 V batteries, we need two in series. If we are using more than one battery in parallel, each parallel group must be two 12 V units in series.

Examine the Options, and Bear the Cost in Mind. Our three possible options for this example are then:

- Option 1: 24 V, 200 Ah type A battery (two parallel strings of two 12 V, 100 Ah batteries in series). Expected lifetime: a little over 2 years. The lowest cost option.
- Option 2: 24 V, 400 Ah type A battery (four parallel strings of two 12 V, 100 Ah batteries in series). Expected lifetime: 4 years. Cost relative to option 1: double.
- Option 3: 24 V, 150 Ah type B battery (two 12 V, 150 Ah batteries in series). Expected lifetime: 7–8 years. Cost relative to option 1: 2.25 times (3 times the cost per kWh and 75% of the actual kWh of option 1).

Unfortunately, it is tempting to specify the first option, either to produce just the lowest cost quotation, or perhaps out of ignorance of any better option. However, the user is likely to be disappointed with the actual battery lifetime, and may not be able to afford a replacement battery after 2 years (especially if, like many real cases, this is an overseas aid project which has assumed that there are no recurring costs).

If the other two alternatives are compared, then option 3 (paying 2.25 the lowest battery price and getting around 3.5 times the battery life) is better than option 2 (paying twice the lowest battery price and getting a little less than twice the battery life).

6 The Battery as a Complex Electrochemical System

Electrochemistry can be described very generally as the study of what happens when electrical conductors are placed in an electrolyte (which is a material that

conducts electricity via ions, not electrons). Electrolytes are commonly thought of as liquids, and common examples that come to mind are sulphuric acid, brine (or salt solution) and more complex solutions such as sea water or blood. However, they do not have to be water-based solutions, they may be a solution of something dissolved in a non-aqueous solvent, or a pure liquid (or melted solid) or even a special type of solid. If two conductors (now we will call them electrodes) are placed in the same electrolyte, they may develop a voltage difference that can be measured, or they may have a current forced through them, or they may simply be short-circuited together. All these cases are covered by the realms of electrochemistry, and the most familiar practical examples include corrosion processes, electrolysis, electroplating and battery and fuel cell technology. At their most basic levels:

- Corrosion occurs when two dissimilar materials in the same electrolyte are connected electronically and reactions occur at each material.
- Electrolysis is what happens when two electrodes in the same electrolyte have a current passed through them. One of the most familiar examples is the production of hydrogen and oxygen gas when current is passed through a water-based electrolyte (but not through pure water which is a very poor conductor of ions). Electroplating is a special form of electrolysis where a metal is deposited smoothly at one of the electrodes.

In a battery, two dissimilar materials in the same electrolyte can produce a voltage and current that can drive an electrical circuit or load. It can be thought of as the reverse of electrolysis. A fuel cell works on the same principle, except that the dissimilar materials are gases, normally hydrogen and oxygen, which are fed to the electrodes and produce electrical energy. The principle here can be thought of as the reverse of water electrolysis.

One common feature of all electrochemical processes is that chemical reactions take place at both electrodes. At one electrode, electrons are removed from the active material, which is a reaction that chemists call oxidation, and injected into the electrical circuit. At the other electrode, electrons from the electrical circuit are added to the active material, a reaction that chemists call reduction. If the process is a 'driven' one, such as electrolysis, the oxidation occurs at the electrode that is made electrically positive and reduction occurs at the negative electrode. However, if the process is a 'driving' one, such as a battery discharging, oxidation occurs at the electrode which becomes electrically negative and reduction occurs at the positive electrode.

Whilst the basic bulk properties of different material determine what may or may not occur in theory in an electrochemical process, the actual events that take place in electrochemistry happen at surfaces and interfaces and follow special rules of their own. Small amounts of other substances at these surfaces and interfaces can affect the electrochemical behaviour in a totally disproportionate way, either beneficially or detrimentally. Even today, some of these effects are imperfectly understood theoretically, and although practical electrochemists know what works and what does not, they may not be sure

exactly why. There is still an element of art in all the main electrochemical disciplines, including battery technology.

A practical battery basically consists of the following items:

- Positive and negative electrodes. Often called plates, these hold the different active material on some form of conducting support.
- An electrolyte (normally a liquid).
- Separators to stop the electrodes touching.
- A container.
- Positive and negative connections to the external circuit.

On discharge, the active material in the electrodes is chemically changed and electrical energy released, the positive active material being reduced and the negative active material being oxidised. The voltage of the battery reflects the different 'chemical potentials' of the two active materials when they react with the electrolyte – simplistically speaking, the more reactive the two materials, the higher will be the voltage of a battery they comprise. Of course, when we say 'reactive' here, what we really mean is 'reactive when the battery circuit is completed, but otherwise totally unreactive towards the electrolyte, or towards the conducting supports, or towards anything like air or other gases that may be present inside the battery'. If these unwanted reactions go on when the battery is not being used, the battery will self discharge and will not be a very good electrical storage device.

We may be lucky enough to find a pair of active materials and an electrolyte that give us the required combination of high reactivity when we want it (meaning a good working voltage) and a lack of unwanted reactivity towards the surroundings (meaning a low rate of self discharge). This alone, however, does not guarantee that we have viable battery system. During the oxidation and reduction reactions, the active materials change into different chemical forms, and to be sure that our desired reactions continue to consume the active materials as we desire, certain properties of the products that are formed have to be right. They must not, for instance, be too low in density, since this could cause the active material to swell too much and block any further contact between the remaining active material and the electrolyte. Nor must they form an electrically insulating 'crust' on the surface of the remaining active material or at the point where the remaining active material is in contact with the electrically conducting support. If any of these occurs at either electrode, the battery discharge will quickly come to a halt with little of the active material consumed (i.e. there will be little capacity delivered).

It may be apparent from the above that even getting the right mix of material properties to make a primary, or non-rechargeable, battery is not that easy. An even larger combination of special materials properties are required to make a rechargeable system, since, on charging, the active material in the electrodes has to be chemically changed back to the original state using electrical energy. That means not just back to the same chemical form, but that the same basic shape (or morphology) must be maintained so that electrolyte access is possible to make

the reactions happen. And it also means that active material must not be lost from the electrodes, nor must it become insulated from the main conductors which carry the current in and out of the battery electrodes. It is, in fact, these last two processes that largely control what the cycle life of the battery will be.

7 Types of Battery Used in PV Systems

The above should explain why there are very few rechargeable battery systems compared to primary (non-rechargeable) types. Examples of rechargeable battery systems are:

- Lead–acid
- Nickel–cadmium
- Nickel–iron
- Nickel–hydride
- Rechargeable lithium of various types

Only lead–acid and to a small extent nickel–cadmium batteries are used in PV systems. Nickel–iron batteries are rarely used in any application, and suffer from a particularly high self-discharge rate that makes them unsuitable for most PV applications. Nickel–hydride and rechargeable lithium batteries are relatively modern developments whose main applications today are in high value electronic goods such as mobile phones and laptop computers. They are not widely available, if at all, in the large capacities (say hundreds or even thousands of Ah) that are required for large PV systems. They are considerably more expensive today per kWh than lead–acid batteries, and often need some rather sophisticated protection in their charging circuitry which is not easy to adapt to the changing nature of PV charge currents. There are other rechargeable battery types under development for such future battery applications as electric vehicles or load levelling. These are not commercially available yet, except in some limited cases. There is nothing yet to suggest that any of these would have the required properties or price to be competitive in PV systems, but we can always hope.

8 Lead–Acid Batteries

8.1 Basics of Lead–Acid Batteries

A lead–acid battery or cell in the charged state has positive plates with lead dioxide (PbO_2) as active material, negative plates with high surface area (spongy) lead as active material, and an electrolyte of sulphuric acid solution in water (about 400–480 g/l, density 1.24–1.28 kg/l). On discharge, the lead dioxide of the positive plate and the spongy lead of the negative plate are both converted to lead sulphate.

The basic reactions are:
Overall:

$$\underset{\text{charged}}{PbO_2 + Pb + 2H_2SO_4} \Leftrightarrow \underset{\text{discharged}}{2PbSO_4 + 2H_2O}$$

At the positive plate:

$$\underset{\text{charged}}{PbO_2 + 3H^+ + HSO_4^- + 2e^-} \Leftrightarrow \underset{\text{discharged}}{PBSO_4 + 2H_2O}$$

At the negative plate:

$$\underset{\text{charged}}{Pb + HSO_4^-} \Leftrightarrow \underset{\text{discharged}}{PbSO_4 + H^+ + 2e^-}$$

Note that the electrolyte (sulphuric acid) takes part in these basic charge and discharge reactions, being consumed during discharge and regenerated during charge. This means that the acid concentration (or density) will change between charge and discharge. It also means that an adequate supply of acid is needed at both plates when the battery is discharging in order to obtain the full capacity.

The lead–acid battery system has a nominal voltage of 2.0 V/cell. The typical end voltage for discharge in PV systems is 1.8 V/cell, and the typical end voltage for charging in PV systems varies between 2.3 and 2.5 V/cell, depending on battery, controller and system type. The relation of open circuit voltage to SOC is variable but somewhat proportional. However, if charging or discharging is interrupted to measure the open-circuit voltage, it can take a long time (many hours) for the battery voltage to stabilise enough to give a meaningful value.

8.2 Types of Lead–Acid Battery

Many different types of lead–acid battery are manufactured for different uses. The PV market today is not large enough to warrant the manufacture of a radically different lead–acid battery design from the standard products that are made in higher volumes for other uses, although some slightly modified 'solar' battery types are available. We can basically classify lead–acid batteries in two ways:

- Open or 'sealed' construction
- Mass-produced or 'industrial' types

There is a wide range of lead–acid battery types to choose from when designing a PV system, and there is always a trade-off between battery cost and expected lifetime. In order to understand the differences between the various types of lead–acid battery available, it is necessary to understand a little about how they differ in construction.

8.3 Construction of Lead–Acid Batteries

8.3.1 Plate Type

Lead–acid batteries for PV systems have one of the following types of plate.

- Pasted flat plates. The most common form of lead–acid battery plate is the flat plate or grid. It can be mass produced by casting or it can be wrought. This is what is in car batteries. The active material is applied to the grids by pasting and drying.
- Tubular plates. These are used in the positive plates of some larger industrial lead–acid batteries. Cycle life is longer because the active material is more firmly retained in woven tubes. The spines which carry the current are more protected against corrosion. So-called positive plate batteries actually have a tubular positive plate and flat negative plate.

Figure 2 illustrates these two plate types.

8.3.2 Grid Alloy

This is vitally important to achieve a satisfactory battery life. Pure lead is too weak to use as a conventional grid material except in special battery constructions. Alloy additives (antimony or calcium) are mainly used to strengthen the grid, but these primary additives can have bad effects on cycling, corrosion or water consumption, so secondary additives are used also.

- High antimony alloys (5–11%) give high water consumption as the battery ages but give good cycle life. Their use these days is mostly restricted to traction batteries.

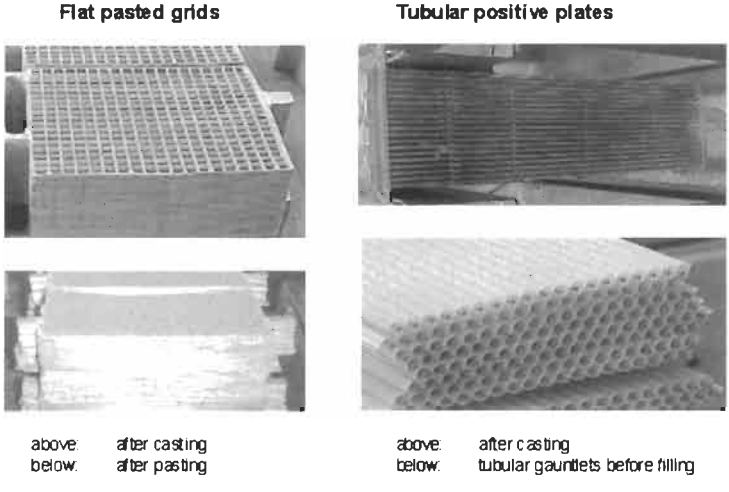

Figure 2 Flat plates and tubular plates.

- Low antimony alloys (1–3%) plus other elements such as selenium or arsenic are widely used in open lead-batteries, but cannot be used in 'sealed' batteries because a small amount of hydrogen gas is always produced.
- Calcium alloys (0.06–0.9%) are used for sealed batteries but pure lead-calcium alloys give poor cycle life and poor recovery from a deep discharge. The addition of tin to the alloy corrects this.
- Other alloys are used by some manufacturers but have similar properties to low antimony or lead–calcium–tin alloys.

It is important to check that the grid alloys are suitable for a battery selected for PV use.

8.3.3 Grid Thickness

Especially for the positive grid where corrosion mostly happens, the thicker the grid, the longer the battery life in most cases. However, the thicker the grid, the more expensive the battery is likely to be. For tubular plates, the same applies to the spine thickness.

8.4 Sealed Lead–Acid Batteries

There is a fundamental difference between open (vented) or 'sealed' (valve-regulated) lead–acid batteries. In open batteries, overcharge results in the conversion of water into hydrogen and oxygen gases, which are lost to the atmosphere. Water has to be added to these batteries from time to time to make up this loss. In valve-regulated batteries, overcharge results in oxygen gas production at the positive plate, but because the space between the plates is not completely filled with acid, the oxygen gas can reach the negative plate, where it is re-converted back to water. This recombination of oxygen gas can only proceed at a certain rate. If the charging current is too high, then oxygen gas pressure will build up inside the cell, and eventually the safety valve will release oxygen (and some acid spray) into the atmosphere. This will result in permanent loss of water.

There are two types of 'sealed' (more correctly, valve-regulated) lead–acid battery, the so-called AGM and gel types.

8.4.1 AGM Type

This type of battery uses an absorbent glass mat (AGM) between tightly-packed flat plates. All the acid is absorbed in the glass mat separator, but the pores of the glass mat are not completely filled. The empty (or part-empty) pores provide a pathway for oxygen gas, formed at the positive plate during charging, to move to the negative plate for recombination. AGM batteries were mainly developed for a good high current (short discharge time) performance. They contain very little acid, which means that they are very susceptible to water losses which especially occur at high temperatures. In contrast, they have a good resistance to being frozen solid, since there is space for expansion within the AGM.

8.4.2 Gel Type

In lead–acid gel batteries, the sulphuric acid is mixed with finely-divided silica which forms a thick paste or gel. The freshly mixed gel is poured into the cell container before it sets. As the gel dries, microscopic cracks form which allow the passage of gas between the positive and negative plates required for the recombination process. This formation of cracks may occur during the early part of a gel battery's service life, so both hydrogen and oxygen can be given off from a new battery through the safety valve. Attention should be paid to the manufacturer's instructions concerning this, especially regarding ventilation requirements.

Unlike AGM batteries, gel batteries can be made with either flat or tubular positive plates. The gel provides a better means of heat conduction from the plates to the cell walls than in AGM batteries, so heat produced on overcharge is lost more efficiently. The sustained high current capability (both charge and discharge) is not as good for gel batteries as for AGM batteries, but this is not normally a problem for PV use. At high operating temperatures, they will suffer to some extent from water loss, but since there is more acid that in an equivalent AGM battery, the lifetime reduction will not be so severe.

8.5 Mass-Produced and Industrial Batteries

The mass-produced lead–acid batteries are basically of the type used in cars for starting, lighting and ignition (SLI) use. They have relatively thin flat plates that are optimised for producing the high currents needed to start a vehicle engine. Conversely, the thin plates do not lead to a long lifetime in any other application which involves either cycling or operation at elevated temperatures. Most SLI batteries are of the open type. For trucks and boats, batteries with thicker plates are produced, and with some modification these may make a reasonable PV battery for light duty (infrequent or shallow cycling, no high temperature operation). Sealed types with moderately thick flat plates are made for such uses as golf carts, invalid carriages and general leisure uses. Although not strictly speaking mass-produced on the scale that SLI batteries are produced, they are capable of being made in reasonably large volumes and at relatively low cost.

Industrial batteries are made for two general applications: float (or standby) duty and deep cycling (especially traction batteries for fork lift trucks, etc). In Europe especially, the tubular plate construction is often used for both types. The tubular plate standby battery type, whether open or gelled, is often the battery of choice for larger PV systems where the highest possible lead–acid battery lifetime is required. The tubular plate battery is also available in deep cycling or 'solar' versions from some manufacturers. Unfortunately the techniques used to increase the cycle life nearly always reduce the standby life at the same time, and this generally means that they give a lower PV service lifetime unless the cycling requirement is unusually deep.

Industrial lead–acid batteries with very thick flat plates are also made, especially for standby use. They are available as open, gelled or AGM types. The thickness of their flat plates determines their maximum lifetime on standby duty.

and it is common to see such industrial batteries described by the manufacturer as 5 year design life, 10 year design life or even 20 year design life. These of course refer to the design life under optimum operating conditions, not those in PV systems.

Higher capacity industrial lead–acid batteries are mostly available only as 2 V single cells. These are assembled into batteries of the required voltage. Lower capacity industrial lead–acid batteries are normally available as 12 or 6 V units, known as blocks or monoblocks.

8.6 How the Capacity Varies

In this section graphs are used to show typical variations of capacity for different battery types. Manufacturers' data has been used to draw these graphs. It is not recommended that the figures in these graphs are used for actual PV system design, rather that similar information is requested from the intended battery supplier and that specific data is used.

8.6.1 Capacity Depends on the Discharge Rate

Lead–acid batteries with a lot of free acid and thicker plates gain more capacity at low discharge rates. The reason is that, at high rates, fresh acid cannot get inside the plates fast enough and the capacity is limited by the amount of acid available. At lower rates, acid can diffuse to the plates during the discharge and maintain a more adequate supply of acid to the discharge reactions.

The AGM type of sealed batteries have considerably less free acid than open or gel batteries, and therefore do not show much capacity increase at low discharge rates. The same is true for other types of flat plate battery in which there is not much free acid. In nickel–cadmium batteries, the electrolyte does not participate in the reaction, and there is not the same low rate capacity increase.

Figure 3 illustrates the typical increase at low rates for different battery types used in PV systems. Please note that these are average figures for selected ranges of commercially available batteries and that the actual variation for a particular type of battery of a specified capacity should be used in accurate calculations.

8.6.2 Capacity Reduces at Low Temperatures

The capacity (to a given end voltage) of all lead–acid batteries decreases at low temperatures. This is due to a combination of factors, including increased resistance and decreased diffusion rates in the electrolyte. The latter effect means that lead–acid batteries with a large reserve of acid tend lose more capacity at low temperatures than those with a smaller acid volume.

Rated capacities are normally stated for 20°C operating temperature. If a battery is required to provide an autonomy reserve capacity at a lower operating temperature, it is normal practice to increase the specified rated capacity to take into account the reduced capacity at the worst case temperature.

Capacities increase slightly at operating temperatures above 20°C, but it is not normal to reduce the specified battery capacity on account of this.

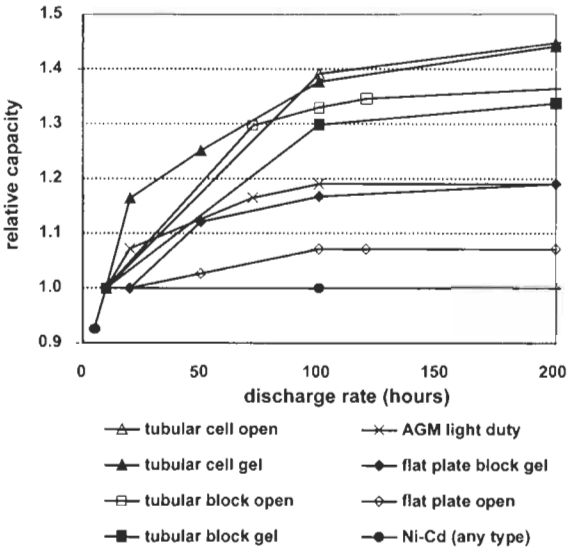

Figure 3 Capacity variation with discharge rate.

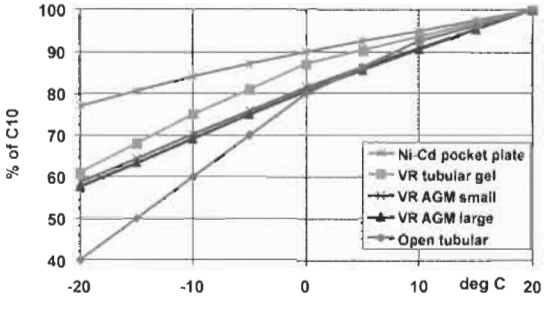

Figure 4 Capacity (10 h) reduction at low temperatures.

8.6.3 Capacity Depends on the End Voltage

Capacities stated in manufacturers' data sheets should specify the end voltage to which that capacity applies. For batteries used in PV systems, this is often between 1.75 and 1.85 V per cell. When comparing two different batteries, ensure that capacities to the same end voltage are compared. Obviously, the lower the end voltage, the greater will be the available capacity.

8.7 Acid Density

The concentration (or 'strength') of acid is normally conveniently measured by its density (kg/l), or, more precisely, by its density at 20°C. Specific gravity (SG) is a measure of density relative to that of water. It is the same as the value in kg/l, but without the units (i.e. 1.24–1.28). In some cases, the specific gravity is quoted as a number 1000 times the true value (e.g. 1240 instead of 1.24).

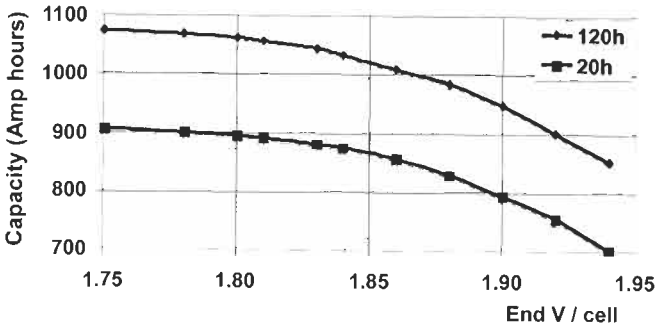

Figure 5 Capacity variation with end voltage. Typical values for large AGM type.

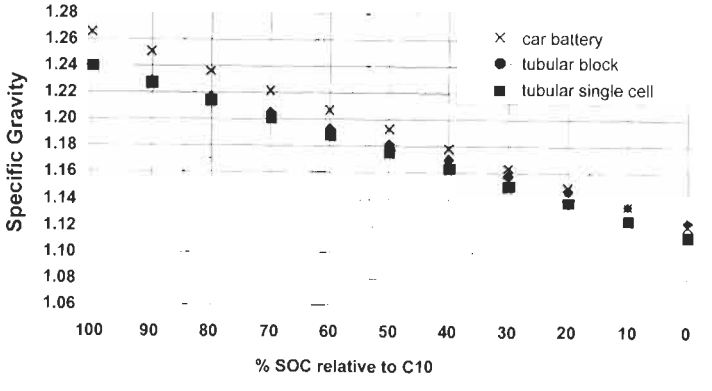

Figure 6 Typical specific gravity (20°C) change on discharge.

Most batteries used in temperate climates are supplied with acid of around 1.24 SG. For cold climates, and particularly for starter batteries, a higher acid SG of 1.26–1.28 is often used. Among other things, this provides a greater resistance to freezing. Batteries for hot climates may be supplied with somewhat lower SG acid than the usual 1.24. Lower SG starting acid means lower internal corrosion rates, but it also means slightly lower capacity.

Batteries with gelled electrolyte normally have the same acid starting SG as their open counterparts. Sealed AGM type batteries generally have a much higher acid starting SG of around 1.30.

8.7.1 Acid Density Falls During Discharge

Note the use of the term 'starting SG' in the above paragraphs. This means the SG of the acid which is supplied with a new, fully-charged battery. Because sulphuric acid is consumed in the discharge reactions, and regenerated in the charging reactions, the acid density falls as the battery is discharged. A fully discharged lead–acid battery will have an average SG of around 1.05–1.15, depending on the battery type and the rate of discharge. Note that we have to use the term 'average SG' now, since there is no guarantee that the acid will be completely mixed. As shown in the next section, the acid will have areas of

higher and lower than average density in different parts of the battery and at different points in the discharge and recharge cycle.

8.8 Acid Stratification

Stratification describes the tendency of the acid in lead–acid batteries to form layers of different density on cycling. Denser acid tends to form at the bottom of the battery, especially in the space below the plates. This can cause increased corrosion. A layer of less dense acid tends to form at the top of the battery, especially in the area above the plates. Batteries that are regularly deep discharged and then fully recharged, e.g. as in fork lift trucks, tend to suffer most from the build-up of lower density acid at the bottom. In contrast, batteries in PV systems that only experience regular shallow cycling and which are not 100% recharged every time tend to suffer more from the build-up of a less dense acid layer at the top. Figure 7 gives a simplified picture of how stratification develops in a lead–acid battery.

Stratification of an open battery in a PV system can be largely eliminated by stirring up the acid quite thoroughly by giving from time to time more overcharge than normal ('boost charging'). This produces gas bubbles that tend to carry the denser acid at the bottom of the battery upwards.

In AGM batteries, the acid is present as a liquid absorbed in a glass mat. Stratification will occur in these, although not to such a large extent as in an open battery since the denser acid experiences more resistance to downwards flow. However, because gassing to stir up the acid is not possible with such batteries, once stratification has occurred, it is difficult to remove. For this reason, larger (and especially taller) AGM batteries are often operated in the horizontal position to minimise the build-up of stratification.

In gel batteries, the denser acid has a much higher resistance to downwards flow, and stratification is not so pronounced as in open batteries. It does, however, occur to a small extent, and as with AGM batteries, cannot be reversed by periodic boost charging.

Stratification in open batteries can give misleading hydrometer readings of acid density when the acid is withdrawn from the top of a cell. Figure 8 shows some actual measurements on a battery discharged to 80% of its capacity and then recharged. Until the battery is more or less 100% recharged, the acid density reading taken at the top of a cell gives a quite false reading, suggesting that the battery is not as charged as it actually is. For this reason, a low hydrometer reading should not be taken to indicate a fault in a PV system, as it does not necessarily mean that the battery is in a low state of charge. In contrast, if one can be sure that the battery has received a full charge, then a suitably high hydrometer reading can confirm this.

8.9 Freezing

Since the acid in a lead–acid battery becomes more 'watery' as the battery is discharged, we can expect the freezing point to be raised. This can become dangerous if the battery is operated in sub-zero temperatures.

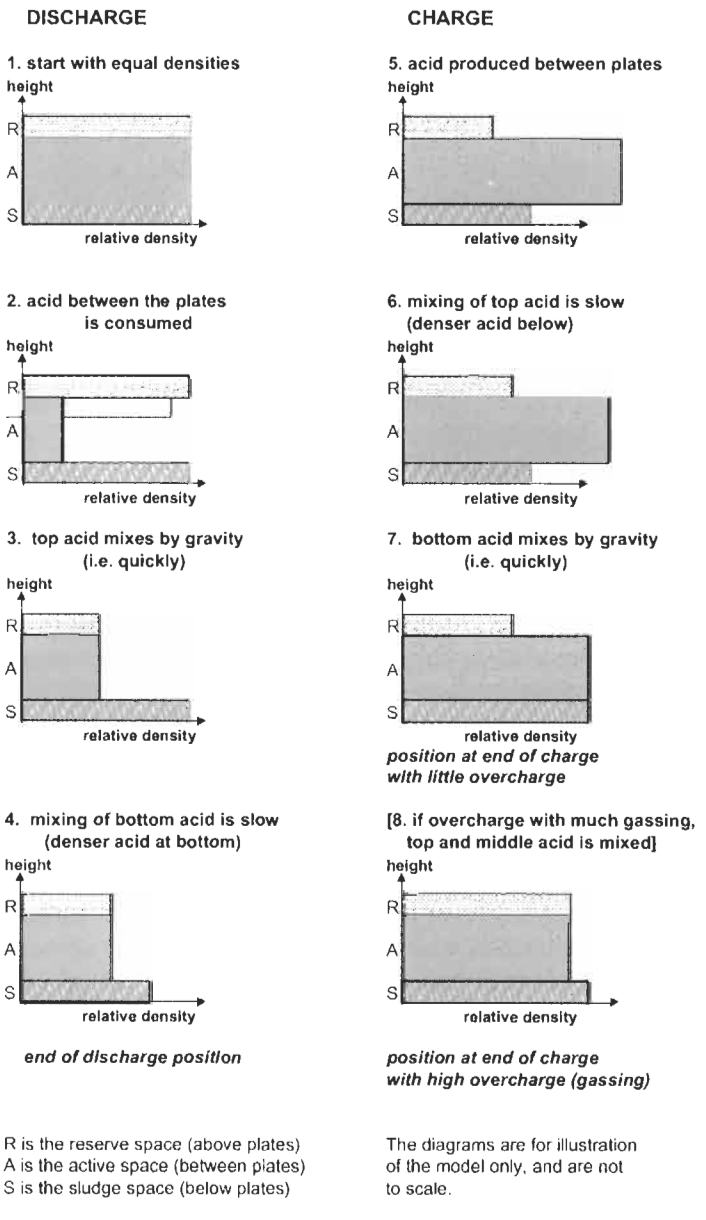

Figure 7 Principle of stratification. R denotes the reserve space (above plates), A is the active space (between plates) and S is the sludge space (below plates). The diagrams are for illustration of the model only, and are not to scale.

8.9.1 Acid Freezing Point

Figure 9 shows the freezing point of sulphuric acid of different SGs. We can see from this that the freezing point of 'normal starting SG acid' (1.24) is around −45°C, and if higher SG acid is used for colder climates (1.26–1.28) the freezing

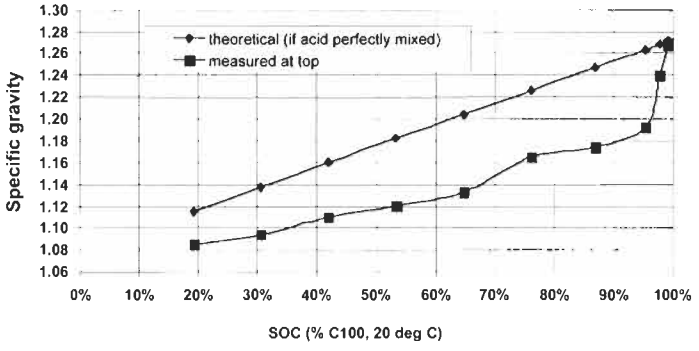

Figure 8 Illustration of stratification: acid density measured at the top of a flat-plate battery during recharging.

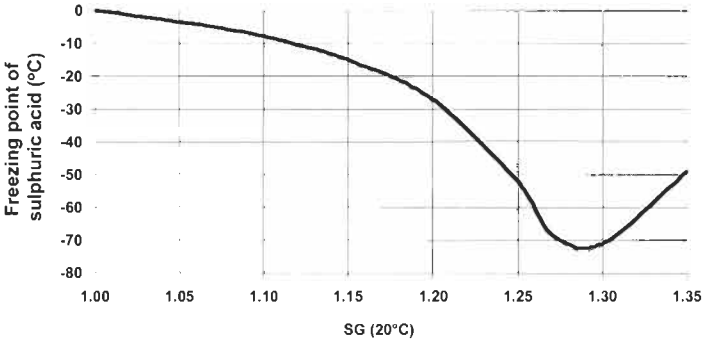

Figure 9 Freezing point of sulphuric acid.

point is lowered to between −60 and −70°C. The acid in a fully discharged battery (SG 1.10–1.15 say) has a much higher freezing point of −10 to −15°C.

8.9.2 Battery Freezing Points

Obviously, a discharged battery with low acid density will be more at risk of freezing than a fully charged one. However, since available capacity falls at low temperatures, the average acid density of a battery discharged at low temperatures will probably not fall to such low levels as 1.1–1.15. The most dangerous freezing risk is for a battery that has been discharged at normal temperatures (giving its full capacity, and so having a low acid density), and then left uncharged as the temperature falls to below zero.

Stratification can raise the freezing point of the acid above the plates. The 'theoretical' and 'local' freezing points for the stratified battery in Figure 8 are shown in Figure 10. Calculation of the freezing point of the battery from theoretical acid densities that assume the acid is completely mixed can be misleading for a partly recharged battery, since the weaker acid at the top has a much higher freezing point than the rest.

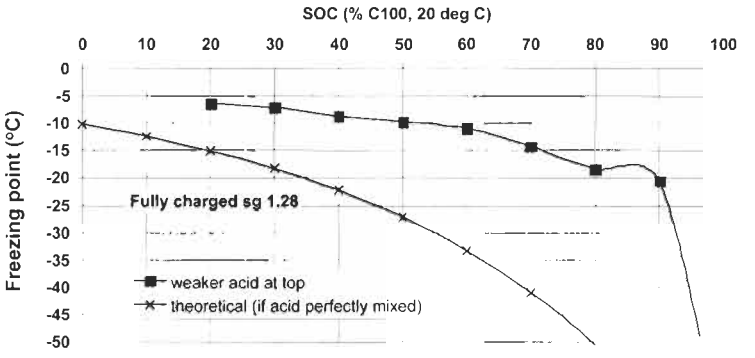

Figure 10 Freezing point of acid at the top of a deeply discharged stratified flat-plate battery during discharge.

8.10 Sulphation and Deep Discharge

Sulphation is a process which can reduce the capacity of lead–acid batteries permanently if they are kept at a low SOC for prolonged periods without recharging. Small lead sulphate crystals initially formed during discharge may recrystallise on standing into larger pieces which are not easy to recharge. The reason for this recrystallisation is that as the acid concentration falls to a low level, the lead sulphate becomes slightly soluble in the acid. Another consequence of this slight solubility of lead sulphate in the weaker acid is that some fine and 'whiskery' lead crystals (dendrites) can be electroplated back on the negative plate on recharging, and in extreme cases these can cause a disastrous short circuit to the positive plate. On deep discharge a thin layer of an electrically insulating type of lead sulphate can also form on the grid material (passivation). Just how serious a problem this is depends on the exact nature of the grid alloy.

The ability of lead–acid batteries to recover from a very deep discharge is something that depends on the exact nature of the battery, as grid alloy type, additives, etc will affect all the above problems of sulphation, dendrites and passivation. Careful selection of the battery type and the recharging conditions in a PV system, can give more or less full recovery of a lead–acid battery from a deep discharge, even if the battery has been in a deeply discharged condition for some weeks [2]. However, use of an inappropriate battery type, or an inappropriate means of PV recharging from such a condition, can result in total battery failure.

In view of the above, it is normal to restrict the maximum depth of discharge of a lead–acid battery in a PV system to around 80%, in order that the worst problems arising from deep discharge are not encountered.

9 Nickel–Cadmium Batteries

Nickel–cadmium (Ni-Cd) batteries in the charged state have positive plates with nickel oxy-hydroxide (NiOOH) as active material, negative plates with

finely-divided cadmium metal as active material, and an electrolyte of potassium hydroxide (KOH) in water (20–35% by weight). On discharge, the NiOOH of the positive plate is converted to $Ni(OH)_2$ and the cadmium metal of the negative plate is converted to $Cd(OH)_2$.

The basic reactions are:

Overall:

$$\underset{\text{charged}}{2NiOOH + Cd + 2H_2O} \Leftrightarrow \underset{\text{discharged}}{2NI(OH)_2 + Cd(OH)_2}$$

At the positive plate:

$$\underset{\text{charged}}{NiOOH + H_2O + e^-} \Leftrightarrow \underset{\text{discharged}}{Ni(OH)_2 + OH^-}$$

At the negative plate:

$$\underset{\text{charged}}{Cd + 2OH^-} \Leftrightarrow \underset{\text{discharged}}{Cd(OH)_2 + 2e^-}$$

Note that in the nickel–cadmium battery, there is no involvement of the KOH electrolyte in the charge or discharge reactions. This means that the electrolyte concentration does not change on charging and discharging, and nor does the discharge reaction need to have an adequate supply of ions from the electrolyte to ensure that full capacity is reached. Both of these are in contrast to the behaviour of the lead–acid battery.

The nickel–cadmium battery system has a nominal voltage of 1.2 V/cell. The typical end voltage for discharge in PV systems is 0.9–1.0 V/cell, and the typical end voltage for charging in PV systems varies between 1.45 and 1.6 V/cell, depending on battery, controller and system type. There is no relationship between open circuit voltage and SOC.

In PV systems, nickel–cadmium batteries are usually only selected in preference to lead–acid batteries when operation is at very low (sub-zero) or very high (over 40°C) temperatures, where lead–acid acid batteries may suffer from freezing or a much reduced lifetime respectively. Industrial open type nickel–cadmium batteries are typically 3–4 times more expensive per kWh of energy stored than industrial open types of lead–acid batteries.

Although a single nickel–cadmium cell can be discharged fully (to 0 V) without harm, it is not advisable to allow a complete battery to discharge to very low voltages. This is because some cells will inevitably have less capacity than others, and if the battery discharge exceeds their capacity limit, the low capacity cells can be driven into reverse polarity (i.e. will have a voltage less than 0 V), which can shorten their life. It is therefore usual to specify that a nickel–cadmium battery in a PV system has a maximum DOD of 90%.

Industrial nickel–cadmium batteries used in PV systems are normally of the open type designed for standby use at low discharge rates. They may be of the pocket plate or fibre plate type. There is pressure to ban nickel–cadmium batteries because of the toxic waste problem, and this is likely to happen for

small consumer type sealed batteries, for which alternative battery types are available. However, for large batteries, there is no alternative system at present with similar properties and it is difficult to see how these can be banned before such an alternative system is available. It should be borne in mind that any nickel–cadmium battery specified for a PV system has to be disposed of correctly at the end of life (by returning to the manufacturer for recycling).

Most industrial nickel–cadmium standby batteries are supplied with 20% KOH electrolyte as standard. The freezing point of this is −25°C. If the reason for choosing a nickel–cadmium battery rather than lead–acid is to prevent freezing problems, this freezing point may not be sufficiently low, and it may be necessary to use 30% KOH electrolyte, which has a freezing point of −58°C.

10 How Long Will the Battery Last in a PV System?

This rather simple question has been the subject of much confusion within the PV industry, especially in the early years. The author has been fortunate to have been able to work with an able team of battery researchers for several years to investigate the really important factors that affect battery life, and for more details of this work the reader is directed to the original published papers [2–4].

10.1 Factors Affecting Battery Life and Performance in PV Systems

In order to obtain the fullest possible life of a battery in a PV system, we first have to avoid the following:

Disasters, such as:

- Manufacturing faults
- User abuse
- Accidents

Among other things, this needs attention to such things as:

- Choosing a reliable and trusted battery manufacturer.
- Providing proper documentation and supervision or training for commissioning, operation and maintenance.
- Being careful (try to avoid dropping a metal spanner across the battery terminals).
- Being lucky!

Next we need to be sure that we design the PV system so that the following possible problems are avoided:

- Sulphation
- Stratification
- Freezing

These we can do by ensuring a full charge (at least periodically), restricting the maximum depth of discharge to an appropriate level and providing as rapid a recharge as possible following a deep discharge. Much of this is done by choosing an appropriate battery, sizing it properly and providing an appropriate method of charge control. Buying individual PV system components and putting them together without proper system design is probably the best way to ensure that one of the above will be a problem.

If we do all the above, we should be in a position to get the maximum service life of the battery in our PV system, and that should now be controlled by one of these two main characteristics:

- Cycle life
- Grid corrosion (temperature dependent)

Just which one this will be depends on the exact circumstances. It is not always the cycle life.

10.2 Cycle Life Can Be Misleading

Let us take for example a battery that is stated to give a thousand 80% cycles. This is equivalent to 'turning over' 800 times the capacity in cycling over the life of the battery. For lower depths of discharge, we can, to a good and conservative approximation, scale this figure [3, 4]. So, scaling this for one cycle per day predicts a battery life of:

Daily DOD	Cycles	Years
80%	1000	2.7
40%	2000	5.5
20%	4000	11
10%	8000	22
5%	16,000	44
2%	40,000	110
1%	80,000	219

Whilst we may believe the first few lines of this table, we start to predict some pretty unbelievable lifetimes for very shallow cycling. Something else must cause the end of the battery life before it wears out due to cycling here. The most logical case to look at here is the limiting case of a battery that does no cycles at all, i.e. is used on standby (or float charge) duty.

10.3 Battery Float Lifetime

Batteries that are used for non-cycling, non-PV duty (standby batteries) are continuously 'float-charged', only being discharged when a mains power failure occurs. For lead–acid batteries in this case, the life-limiting process is

the corrosion of the positive plate which occurs slowly during charging. This corrosion rate approximately doubles for each 10°C rise in temperature. Correspondingly, the lifetime on float charging approximately halves for each 10°C rise in temperature.

Expected lifetimes in such float or standby applications can be 5, 10 or even 20 years, so accelerated tests to establish such figures are the only practical option. These involve measuring the float charge lifetime at one or more elevated temperatures and extrapolating to a lower standard temperature.

A shallow cycling PV battery does not experience a constant charging voltage, although the voltage averaged over a day does not differ very much from a typical float charge voltage. Therefore, to a first approximation, we can take the limit to the battery lifetime in a PV system to be no more than what one would expect on float charging at the same temperature. If the cycle life predicts a longer lifetime than this, we can expect the temperature-dependent corrosion process to be the life-determining process.

10.4 Sealed Battery Lifetimes

There can be additional life-limiting factors for sealed lead–acid batteries, especially at high operating temperatures, of which the most common are:

- Water or acid loss, caused by one of three main processes:
  - (i) Less than 100% recombination (some oxygen from the positive plate is not reduced back to water at the negative plate on overcharge, and the gas may be vented)
  - (ii) Positive grid corrosion (which converts the lead grid to an oxide)
  - (iii) Water vapour loss through case
- Negative capacity loss

Self-discharge of the negative plate is a chemical, rather than electrochemical process, and can only be balanced in the battery by some positive grid corrosion current or recombination which is less than 100% efficient. Both of these processes consume water, so if you avoid the gradual discharging of the negative plate, it may be at the expense of losing water. Fortunately, the self-discharge of the negative plate is very slow unless there are some undesirable impurities present in the battery.

For more details of these additional factors for sealed lead–acid batteries, the reader is directed to reference [4] and the references cited therein.

Water loss is less of a problem in gel batteries than in the AGM type, simply because there is more acid to start with. For the AGM type of battery, the capacity is often limited by the amount of acid, and any loss of water or acid in these batteries will reduce the available capacity. In the gel batteries, especially the industrial types with tubular plates, there is the same volume of acid as in the corresponding open type of battery, and it will at least take much longer for any loss of water or acid to affect the capacity in a gel battery than an AGM type.

For this reason, gel batteries are preferred to the AGM type in PV systems where high operating temperatures are expected.

There is no simple method (yet) of predicting the effect of water and acid loss on the expected lifetime of an AGM type of sealed battery. For the gel batteries, the indication from actual field lifetimes in PV systems is that the lifetime can be predicted quite well from the cycle life or float life, as for open batteries.

10.5 Examples of Predicted Battery Lifetimes

The depth of daily cycling varies considerably between different types of PV system. In systems with a large autonomy reserve, such as in telecommunications, the cycling will be quite shallow, whereas in systems with less autonomy, such as lighting systems, the daily cycling will be higher. As shown, earlier, the typical range of daily cycling is of the order of 2–30%, except in some hybrid PV–diesel systems, where it can be much deeper. Similarly, there can be quite a wide range of operating temperatures experienced by batteries in PV systems, depending on the climate at the site and also the nature of the battery enclosure. For predicting the lifetime limit due to corrosion, the annual average battery temperature should be considered, and in a well-designed system this should be close to (probably a few degrees above) the average annual ambient temperature.

Figure 11 illustrates the different limits for typical PV systems of different types. We plot the corrosion-limited lifetime against battery temperature, and also display the cycle limit for different numbers of days of autonomy on the same graph.

The upper graph shows the situation in a 'professional' PV system with a continuous load and tubular plate batteries, typical of a remote telecommunications or cathodic protection PV system. The number of days of autonomy required for such systems is normally at least 5, and is often much higher. The combination of the shallow cycling and the good cycle life of the tubular plate battery means that the cycle life hardly ever limits the battery life at operating temperatures above 20°C. Instead, the corrosion limit of 12 years at 20°C, 6 years at 30°C or 3 years at 40°C is what normally applies for the battery life in such systems.

The middle graph illustrates a much different case, typical of many rural lighting PV systems. For reasons of cost, a flat plate battery is often specified. A good but low cost flat plate battery may give around 200 deep (80%) cycles, and this is what is illustrated in this graph. Daily cycling is considerably deeper in such a system than in the first example, not just because less days of autonomy are usually specified for such systems (2–5 is typical), but also because all the discharge occurs at night. Now we see that the predicted battery life is around 1 year for 2 days autonomy, whatever the temperature, around 2 years for 3–4 days autonomy at temperatures below about 32°C and around 3 years for 5 days autonomy at temperatures below about 30°C. Above these temperature limits, the corrosion limit applies, giving an even shorter life. If a normal car battery is used in such a PV system, it will give even less life than shown in the graph, due a shorter cycle life than the example battery. The message here is quite clear – relatively cheap batteries with a short cycle life can give a very disappointing life

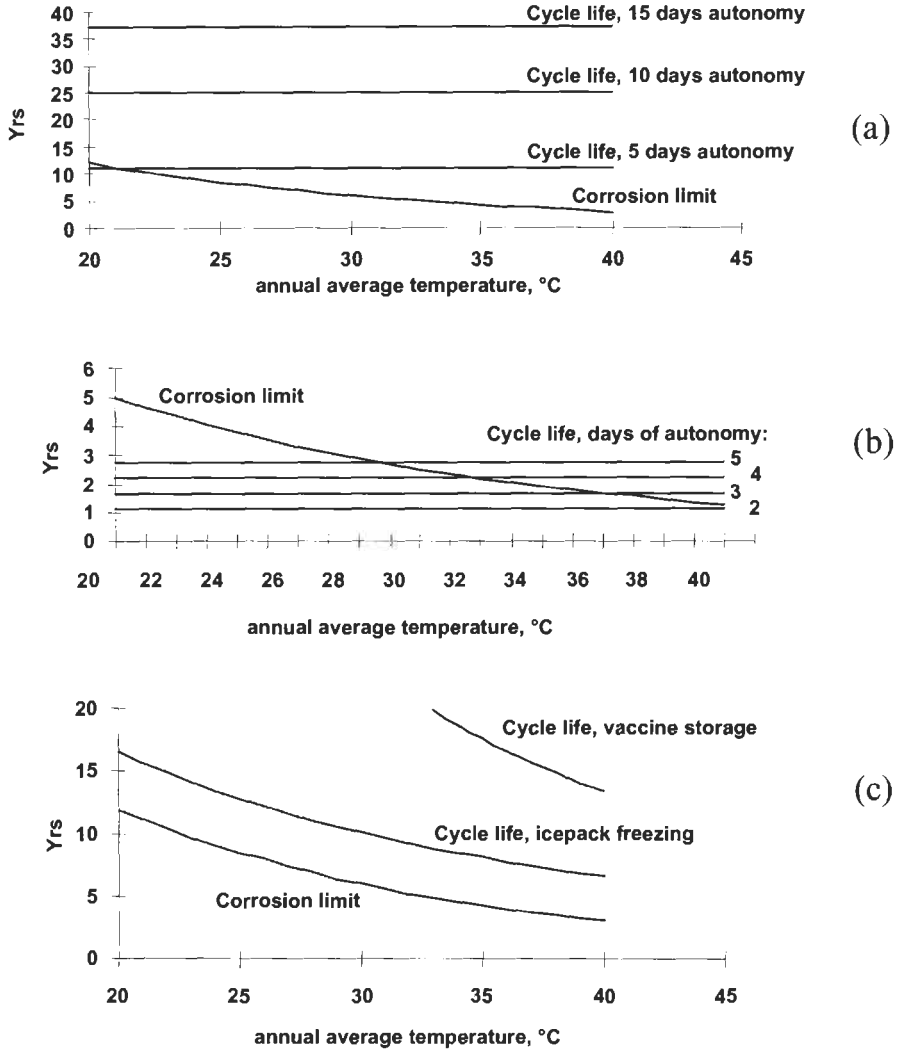

Figure 11 Predicted corrosion and cycle life limits in different types of PV system. (a) Professional PV system with continuous load, tubular batteries. (b) PV rural lighting system with flat plate batteries. (c) Vaccine Refrigerator CFS, tubular batteries

in PV lighting systems, especially if a low capacity (3 days autonomy or less) is also specified.

The lower graph shows the interesting case of a PV vaccine refrigerator system with tubular plate batteries. Here the daily load, and thus the daily depth of discharge, will vary with the ambient temperature (the refrigerator consumes more electrical energy if it is working in a hot location), and will also vary according to how it is used (e.g. if icepacks are frozen regularly, it will consume more than if it is just storing vaccine. Early examples of PV vaccine refrigerator

systems were often installed in some very hot locations, and the resulting battery life was disappointing (less than 5 years), even though good quality tubular plate batteries were used. The initial reaction was to look for batteries with a better cycle life, e.g. traction batteries, but the graph clearly shows that it is not the cycle life but the temperature-dependent corrosion which is causing the short battery life at high operating temperatures. Siting the battery in a cooler location is the answer to obtaining a longer battery life in this case.

10.6 Comparison of Predicted Battery Lifetime and Field Data

So far, all the above reasoning is theoretical. Checking such calculations against actual field data is not easy, especially when PV systems are often in extremely remote places. However, we have published what data is available from PV systems that we have supplied over a period that goes back to the early 1980s [3, 4], and in general there is quite good agreement between those battery lifetimes we have managed to establish, and what we have predicted.

Tables 1 and 2 are taken from [4] and show the situation in 1999 when the PV systems were last checked.

Table 1 shows results from relatively large single installations. Only three of the batteries in this table have been reported as having been replaced because they had failed, and their lifetimes were more or less in agreement with the predicted value. Of the remaining 10 entries, 4 had equalled or exceeded the predicted lifetime, and 1 was definitely still operating at present within its predicted lifetime. For the remaining 5, which had not failed inside their predicted lifetime in 1995, there was unfortunately no firm updated data, although if these unattended and very remote systems were not still working then we would probably have been notified.

In Table 2, all the entries except for Bolivia refer to several vaccine refrigerator systems (ranging from 15 to 150 in a particular country), so these are better

Table 1 Battery lifetimes: single PV systems with open tubular plate batteries.

Location	Type	Autonomy	Installed	Battery replacement	Last reported working	Service life (years)	Predicted years
Argentina	telecom	5 days	1984	–	1995	> 11	10–12
Saudi Arabia	telecom	10 days	1984	–	1995	> 11	8
Djibouti	ac system	? 4 days	1985	1994		9	6
Jordan	telecom	20 days	1987	–	1995	> 8	8–10
Oman	telecom	10 days	1987	1994		7	7–8
Oman	telecom	5 days	1987	–	1995	> 8	7–8
Venezuela	telecom	10 days	1988	–	1995	> 7	10–11
Uganda	lighting	6 days	1989	–	1999	> 10	10
Kenya	demo	8 days	1990	–	1999	> 9	11
Uganda	freezer	4 days	1990	1998		8	9
Guinea	telecom	5 days	1992	–	?1999	> 7	7–8
Chad	telecom	3 days	1993	–	?1999	> 6	4–6
Vietnam	telecom	5 days	1993	–	?1999	> 6	6–8

Table 2 Battery lifetimes: PV-powered vaccine refrigerators.

Location	Fridge type	Installed	Capacity (Ah)	Battery replacement	Last reported working	Service life (years)	Predicted years
Ghana	1	1986	360	1993		7	5–6
Maldives	1	1987	360	–	1995	> 8	5
Bolivia	2	1989	200	–	1998	> 10	12
Tanzania	1	1991	300	1996–98		5–7	6–8
Ethiopia	2	1992	200		1999	> 7	9–11
Ethiopia	2	1992	200		1999	> 7	5–7

statistical cases than the single systems in Table 1. Of the two locations where batteries had needed replacement at the time of reporting, this was within 1 year of the predicted lifetime.

All the entries in Tables 1 and 2 are for open tubular plate lead–acid batteries. It is less easy to track the lifetime of flat plate batteries that are more commonly used in domestic PV systems. However, evidence from the Nordic country cottage market for PV systems indicates that the lifetime model works for those too.

10.7 Battery Lifetimes Summary

We can summarise the above as follows:

- In most industrial PV systems positive grid corrosion rather than cycle life limits the battery lifetime when tubular plate batteries are used.
- If flat plate batteries are used in Solar Home Systems (mostly PV lighting), the cycle life often does limit the battery lifetime, especially when a low battery capacity (low autonomy) is specified.
- It is sometimes less easy to predict the lifetime of sealed batteries due to 'dry out' and negative capacity loss, especially for the AGM type.

It is necessary to know both the cycle life at some deep discharge depth and the life on standby duty at some reference temperature for a particular battery type in order to make an accurate estimate of the lifetime in a particular PV system. Such information should be obtained from the battery supplier and suitable derating factors applied to them for PV system use. Specific PV system details required for the battery lifetime calculation are the average daily depth of discharge and the average battery temperature. These can only be estimated accurately after the PV system has been specified in some detail.

11 Selecting the Best Battery for a PV Application

There is a wide range of lead–acid battery types to choose from when designing a PV system and there is always a trade-off between cost and expected lifetime.

The above examples of lifetime calculations show that if the daily cycling is relatively deep (i.e. less than 5 days autonomy), an open flat plate battery with a cycle life equivalent to 200 deep (75–80%) cycles can give a disappointingly short life of about 1–2 years. A car battery, with even shorter cycle life, will give even an even shorter and more disappointing service life in such a PV system. For a lifetime of 5 years or more in such relatively deep cycling conditions, there are only two real alternatives: specify a much larger battery capacity (i.e. increase the autonomy) to reduce the daily depth of discharge, or specify a battery with a longer cycle life, such as one with tubular plates.

In contrast, if the daily cycling is very shallow (i.e. autonomy more than 5 days for a 'day and night' load), the battery life is likely to be limited by the internal corrosion processes, and this is highly temperature-dependent. At high annual average operating temperatures, this is almost certain to limit the ultimate lifetime of a battery in such a PV system. Here the selection of a battery with at least 10 years design lifetime on standby duty at 20°C is recommended, which basically means an 'industrial' battery. A tubular plate lead–acid battery is suitable for most of the annual average operating temperatures that might be experienced in hot climates in a well-designed system. If the operating temperature is extremely high (say averaging close to 40°C) and a battery life of more than 5 years is required, then the two alternatives are really only either to reduce the annual average operating temperature somehow (e.g. better shelter or battery box design) or to use a nickel–cadmium battery.

Provision of purified water (distilled or deionised) for regular topping up of batteries may be problematical in very remote areas. In these cases, 'sealed' lead–acid batteries are often specified. For high operating temperatures, the gel type is preferable as it is less likely to suffer from 'dry-out'.

In small PV systems, where the battery capacity required may be only 40 Ah or less, the full range of battery types is not available. Often, small AGM-type sealed lead–acid batteries are used for these, especially those that have an enhanced cycle life or float life (depending on the daily depth of cycling of the system). It should be noted that normal methods of PV charge control are not possible for sealed nickel–cadmium, nickel–hydride or lithium batteries and these are rarely specified for smaller PV systems.

If the battery is expected to experience very low temperatures, such that there is a danger of freezing of a lead–acid battery, this must be taken into account at the battery specification stage. Unless there is a chance of a battery being very deeply discharged at normal temperatures and then subjected to sub-zero temperatures, the position is not quite as bad as may first be thought. If the battery undergoes discharge at sub-zero temperatures, its capacity is reduced and its freezing point will not be so high as if it had been discharged more fully. Often, the specification of higher acid density than normal, plus some additional oversizing of the capacity, is enough to avoid freezing problems in cold climates. Most AGM types of sealed lead–acid battery have a higher starting acid density (around 1.30 SG) than others, and these therefore will have a generally lower freezing point. However, if really low temperatures (say below −30°C) are expected when the battery will be discharged to any great extent, then a

nickel–cadmium battery is the safest (but most expensive) choice. If this is specified, it must be supplied with the correct electrolyte (30% KOH) to avoid freezing problems.

12 Calculating Battery Size for a PV System

Earlier, some rough calculations of required battery capacity were presented. We now list the full process of correctly calculating the capacity required for a particular battery type in a specific PV system.

Select the Appropriate Voltage. This is defined by the load (and PV array) nominal voltage unless some dc/dc converter is present in the system. This sets the number of cells or blocks that must be connected in series.

Define Maximum Depths of Discharge (DOD). These must be defined for each battery type according to the mode of operation.

- The maximum DOD for autonomy reserve is normally set at 80% for a lead–acid battery, although somewhat less may be specified for lead–acid batteries which are known to be particularly susceptible to sulphation problems.
- The maximum daily depth of discharge may either be set arbitrarily (e.g. a figure of 20–30% is common) or it may be worked out from the known daily cycle, the cycle life of the battery in question and the required lifetime (if cycling is the limiting factor).
- For seasonal storage (if used) a maximum depth of discharge needs to be set. If a lead–acid battery is not to be fully charged for some weeks, it is inadvisable to discharge it to more than about 30% DOD, for example.

Define Maximum Charge Rate

- For open batteries in most PV systems, a charge rate faster than the 10 hour rate is not recommended, as the voltage will rise very quickly towards the end of charge and most types of PV charge controller will interpret this as a sign of full charge being reached when in fact it has not.
- For sealed batteries, another consideration is the highest overcharge current that can be sustained with efficient gas recombination, and this is temperature-dependent. A guideline maximum charge rate of 20 hours is often used for sealed lead–acid batteries at normal operating temperatures, but a lower limit may be specified for very low temperatures.

We Now Calculate Four Capacities. For seasonal storage (if used), the amount of storage required to make up for the shortfall in PV array production in certain months is the 'seasonal Ah' requirement:

$$C1 = \frac{\text{seasonal Ah}}{\text{maximum seasonal DoD}}$$

(If there is no seasonal storage requirement, C1 = 0.)

For autonomy storage, we need to specify a certain number of days for which we wish the battery to supply the load under emergency conditions. Strictly speaking, the worst time this could occur is when the seasonal storage (if any) has just been used. If the site could encounter sub-zero conditions, we may wish to modify the normal DOD limit here to avoid battery freezing problems:

$$C2 = \frac{\text{Average daily load Ah} \times \text{days of autonomy} + \text{seasonal Ah}}{\text{maximum DoD (adjusted to prevent freezing if necessary)}}$$

For the capacity required to fulfil the daily cycling requirement, we need to know if the load is required only at night, only during the day, continuously for 24 hours, or some other combination. Night-time only loads mean that the daily Ah discharged will be equal to the total daily load. For other cases, the daily Ah discharged will be less than the daily load and some correction factor is needed. For continuous loads, we can expect the battery to be undergoing charging for 6–8 hours in a typical day, so the daily Ah of discharge would be daily load in Ah multiplied by a factor of between (16/24) to (18/24):

$$C3 = \frac{\text{daily Ah discharged}}{\text{maximum daily DoD}}$$

Finally we need to ensure that the maximum charging rate is not exceeded. For this, we need to know the maximum current that the PV array will produce under maximum sunlight conditions:

$$C4 = \frac{\text{battery maximum C rate (in hours)}}{\text{maximum array current in A}}$$

The required battery capacity, before any corrections are made, is whichever is the highest of C1 to C4.

We Now Correct the Chosen Capacity for Temperature and Discharge Rate

- If the battery will experience average daily temperatures below 20°C in any month, then a correction should be made for the reduced capacity available at such temperatures. This means increasing the actual capacity specified.
- If, as is normal, the load will be delivered at a lower discharge rate than the normal 10 or 20 hour rate at which the standard capacity is specified, the capacity available at this rate is higher than the rated capacity. The 'datasheet' capacity we require can then be somewhat less than the capacity calculated above.

- The battery manufacturer may be able to supply data to correct for low temperature and low discharge rates at the same time, but do not use such data unless it specifically refers to the particular battery model. If manufacturer's specific data is not available, then an approximation is to make both corrections using the deviations from the standard capacity given at a standard discharge rate and a temperature close to 20°C.

Final Specification of the Battery. Having arrived at a calculated battery capacity, we now have see which is the closest battery model with the desired capacity. Often two or more parallel batteries are used to improve system reliability, especially in larger systems, and if parallel batteries are used, the capacity per parallel string is the total capacity calculated divided by the number of strings. Finally, we need to remember the number of cells or blocks that are needed in series. If parallel strings are used, each string must contain this number of series cells or blocks.

13 Looking After the Battery Properly

Maintenance is vitally important for obtaining the maximum lifetime from a battery, but even the highest quality maintenance will not produce the maximum benefit if the battery is operating under the best possible conditions. Therefore the first thing to ensure is that the PV system has been designed with the battery's good health in mind.

13.1 System Design Considerations

13.1.1 Charge Control

Solar electricity is expensive and variable, and conventional charging methods that ensure 100% recharge are not possible. In most cases, the full available current from the PV array is transferred to the battery until the voltage level rises to a certain level, indicating that full charge is almost achieved. Then the PV array current is either cut off or reduced. This action is called charge regulation or more correctly voltage regulation. We need to ensure that the battery is as fully charged as practically possible, but on the other hand we do not want to cause problems from excessive overcharging.

Overcharge. Overcharge is the excess Ah delivered to recharge the battery. Some overcharge is necessary to achieve full charge and to prevent sulphation.

- In PV systems, 1–4% overcharge is common
- In conventional non-PV cycling systems, at least 10% overcharge is common

The energy delivered as overcharge causes gassing. In open batteries this results in water loss. In sealed batteries, overcharge results in heat being generated inside the battery. Gassing starts before full charge is reached, and

increases as charging progresses. Some gassing is needed in open batteries to stir up the acid and reduce stratification, but not such an excessive amount that would consume too much water.

Water Loss. In an open battery, each Ah of overcharge causes a loss of approximately 0.3 ml of water from each battery cell. We can estimate the time it takes to consume the 'acid reserve' above the plates from this factor, as in this example calculation: A 1500 Ah (C10) / 2265 Ah (C100) tubular plate single cell (2 V) in a typical telecom system, when new, is filled with 28.8 litres of 1.24 SG acid and the acid volume over the plates is 4.68 litres (16% of the acid volume). The number of days to lose this amount of water (i.e. to when the acid level falls to the top of plates) is:

- At 2% overcharge per day: 464 days
- At 3% overcharge per day: 309 days

The average acid SG increases to 1.28 if the level falls to the top of the plates.

A maximum 1 year interval between water additions is appropriate at overcharge levels below 3% in this case.

13.1.2 Internal Heating

All batteries produce significant amounts of heat on overcharge. In contrast, heat generation during charge and discharge is relatively low in lead–acid batteries at the low rates of charge and discharge encountered in most PV systems. In a sealed battery on overcharge, no net chemical changes occur, and all the input overcharge energy is turned into heat. In an open battery on overcharge, we can think of the 'excess' energy due to overvoltage of the gas-producing reactions being turned into heat. In practice, this means any voltage in excess of 1.4 V/cell.

Example calculations of the internal heating produced by 24 V (12 cell) batteries at 2.4 V/cell at the end of charge, being charged at an average current of 10 A:

- Open battery: $12 \times (2.4 - 1.4) \times 10 = 120$ W internal heating produced
- Sealed battery: $12 \times 2.4 \times 10 = 288$ W internal heating produced

13.1.3 Battery Environment

Ventilation. Ventilation is needed, not just to get rid of gases, but to lose heat, especially the internal heat produced on overcharge. Sealed batteries in tightly enclosed surroundings will, in particular, overheat, often disastrously.

On charge, open batteries will produce hydrogen and oxygen gases. Hydrogen will concentrate at the top of the battery enclosure if adequate ventilation is not given. If the concentration of hydrogen in air exceeds 4%, there is an explosion hazard, and the ventilation of open batteries should be designed to prevent this happening.

Sealed lead–acid batteries produce small amounts of hydrogen due to internal corrosion and some sealed batteries (especially gel batteries) produce normal amounts of gas at the beginning of their life. Sealed batteries also require some

ventilation, although the amount required is more dependent on cooling needs than the removal of hydrogen.

Temperature Control. The battery in a PV system may need protection from high temperatures or low temperatures, or both. This has to be done without consuming significant amounts of extra energy (which would lead to a larger PV system being needed). Some key guidelines for battery environments in different climates are as follows:

For a very hot climate

- Avoid direct sunlight on the battery enclosure, by shading it if necessary.
- Use light coloured enclosures if possible.
- Allow plenty of air circulation by providing sufficient air space and ventilation.
- Do not use a heavily-insulated enclosure – this retains internal heating.
- Do not be afraid to use an 'over-size' shelter. This will allow more air volume inside and have a higher surface area for heat losses.

For a very cold climate

- Reverse the above guidelines, but be careful of summer temperatures.
- Use a highly insulated enclosure.
- Use as little air space as possible around the battery (but do not restrict necessary ventilation).
- Use any available heat source (e.g. waste heat from a back-up generator), and even consider using passive solar techniques.

The most difficult type of climate to design a battery enclosure for is one that has hot summers and sub-zero winter temperatures. In some cases, the only real option here is to arrange for some changes to the battery's thermal environment between winter and summer.

13.2 Commissioning

Some batteries supplied for PV systems will only give their full capacity and lifetime if they are commissioned correctly. This particularly applies to dry-charged batteries, where acid of the correct purity needs to be added carefully to each cell and a proper commissioning charge given. This is a longer charge than normal and the load should not be switched on until the battery has reached full charge. Dry-charged batteries should not be stored for too long, nor in excessive heat or humidity, before they are commissioned.

When batteries of any type are supplied for PV use in very remote areas, it is often inevitable that they will have been stored for some time. Even if they are not supplied dry charged, they should be given a thorough charge (from the PV array) before use.

13.3 Maintenance, Replacement and Disposal

There is no such thing as a truly 'maintenance-free' battery. Even sealed batteries, which do not need water additions, should be regularly inspected and have their terminals cleaned and, if necessary, tightened.

For open batteries, the main maintenance requirement is to add distilled or demineralised water periodically. For an estimate of how to judge the safe period between water additions, see the section on water loss above. As mentioned in an earlier section, a low specific gravity reading does not mean that the battery or cell is necessarily undercharged – it may simply be due to stratification. However, if one cell does give a quite different reading to the others, especially if the battery is more or less fully charged, then that may indeed be taken as signifying a faulty cell. Similarly, a considerably different voltage to that of other cells or blocks in the same series connected circuit can also indicate a fault condition, as can one cell being considerably hotter than the rest.

Therefore, periodic maintenance procedures for all batteries should attempt to identify faulty cells or blocks. This may be done by specific gravity measurement (not possible for sealed batteries), voltage checks or case temperature checks.

If really defective cells or blocks are detected (e.g. those with internal short circuits or zero capacity), they should be replaced whenever practical. However, it is not recommended to mix aged and new cells or blocks in one series string. If replacement of some cells or blocks is contemplated, it is best to renew all the elements in one series group. If the battery consists of more than one parallel group, there is scope to reconfigure the cells or blocks so that those of similar aged characteristics are in the same series string. If any cells or blocks are replaced, the new elements should be clearly marked. If a series–parallel battery arrangement is changed, all the parallel strings should be fully charged separately before making the parallel connection.

Dead batteries should be disposed of responsibly, and not left lying around where they can be a source of pollution. Lead–acid and nickel–cadmium batteries can be recycled and have some scrap value, and if possible their return to the local battery company or the original supplier should be arranged. Indeed, recycling of industrial nickel–cadmium batteries is now mandatory in many countries.

14 Summary and Conclusions

The rechargeable batteries used in PV systems are required to perform under conditions which are different to the more conventional battery applications for which they are designed. In particular, the charging and discharging they undergo is not entirely regular or predictable, being subject to variations in the weather. Different types of PV system require different amounts of daily discharging, but in most cases this cycling is relatively shallow. The cycling capability of a battery is an important factor in determining its PV system

lifetime, but it is not the only one. The operating temperature, and the battery's resistance to internal corrosion, is equally important.

The main property of a battery – its capacity – is not fixed, but varies with temperature, discharge current and other factors. To specify the battery capacity correctly, the above system-specific factors must be known as well as the maximum fraction of the capacity that can be extracted safely under different conditions.

Rechargeable batteries are complex electrochemical devices that depend on a large number of material properties being 'just right' to function correctly. There are therefore not that many basic types in general use, and even fewer of these used regularly in PV systems. The majority of batteries used in PV systems are lead–acid, but there are several distinct types of these, each with their own set of properties. Perhaps the most obvious classification is into 'sealed' and 'open' types, but within each of these categories there are also many variations. The chemistry of the lead–acid battery means that there are certain specific problems to be avoided, such as stratification, freezing and sulphation. However, the relatively low cost and general availability of lead–acid batteries means that they are used in all but the most demanding PV system environments.

It is often the case that choosing a more expensive lead–acid battery will result in longer PV service life than if a 'cheap' one is used, but it is not always the most expensive battery that gives the longest PV system life. Use of low capacity, low cost, flat plate lead–acid batteries similar to truck starter batteries can result in a disappointingly short lifetime in many solar lighting systems in hot climates. In general, the best PV service lifetime is given by a tubular plate industrial lead–acid battery, although they are not available in the very low capacities required for small PV systems.

Whatever type of battery is chosen for a particular PV system, it must be sized correctly, placed in the best possible environment and maintained correctly if it is to have a good chance of reaching its predicted service lifetime.

It is impossible to present anything but an outline of the required information in a Chapter of this size. For more comprehensive information, the reader is directed to [1] and to the recommended literature for further reading.

Acknowledgements

The author would like to thank:

- Naps Systems, for permission to publish various battery test results and conclusions.
- Colleagues at Naps Systems and the former Neste Corporate R&D for many hours of painstaking battery tests and interpretation, plus stimulating discussions about what the results might mean.
- Many major battery companies for answering detailed technical questions with patience, and for allowing the author to photograph parts of the their production process, including the photographs shown in Figure 2.

References

[1] Spiers, D.J. and Royer J., 1998. *Guidelines for the Use of Batteries in Photovoltaic Systems*. Joint publication, NAPS, Vantaa, Finland and CANMET, Varennes, Canada.

[2] Spiers, D.J. and Rasinkoski, A.A., 1995. Predicting the Service Lifetime of Lead/Acid Batteries in Photovoltaic Systems. *J. Power Sources*, Vol. 53, pp. 245–253.

[3] Spiers, D.J. and Rasinkoski, A.A., 1996. Limits to battery lifetime in photovoltaic applications. *Solar Energy*, Vol. 58, pp. 147–154.

[4] Spiers, D.J., 2000. Understanding the factors that limit battery life in PV systems. *Proc. of World Renewable Energy Congress VI (WREC2000)*, Elsevier Science Ltd., Vol. II, pp. 718–723.

Further Reading

Barak, M., 1980. Lead-acid batteries, Chapter 4 in: *Electrochemical Power Sources*, M. Barak, Ed. Institute of Electrical Engineers, UK.

Bechtel National Inc., 1979. *Handbook for Battery Energy Storage in Photovoltaic Power Systems*, Department of Energy, USA.

Bode H., 1977. *Lead–Acid Batteries*, John Wiley & Sons, New York, USA.

Crompton, T., 1990. *Battery Reference Book*, Butterworths, UK.

Donepudi, V.S., Pell, W., Royer, J. W., 1993. Storage Module Survey of the IEA-SHCP Task 16; PV in Buildings, Canadian Solar Industry Association, Ottawa, Ont. Canada.

Falk, U., 1980 Alkaline storage batteries, Chapter 5 in: *Electrochemical Power Sources*, Barak, M. Ed. Institute of Electrical Engineers, UK.

Foster, R., Harrington, S., Durand, S., 1994. *Battery and Charge Controller Workshop for Photovoltaic Systems*, PV Design Assistance Center, Sandia National Laboratories, Albuquerque, NM, USA.

Hill M. and Mc Carthy, S., 1992. *PV Battery Handbook*, Hyperion Energy Systems Ltd., Ireland.

PV Design Assistance Center, 1990. *Stand-Alone Photovoltaic Systems. A Handbook of Recommended Design Practices*, Sandia National Laboratories, Albuquerque, NM, USA.

Roberts, S., 1991. *Solar Electricity; A Practical Guide to Designing and Installing Small Photovoltaic Systems*, Prentice Hall, New Jersey.

Strong, S., 1987. *The Solar Electric House: A Design Manual for Home-Scale Photovoltaic Power Systems*, Rodale Press, Emmaus, PA, USA.

Part IIIc

Grid-connected Systems

Grid Connection of PV Generators: Technical and Regulatory Issues

Jim Thornycroft, Halcrow Group Ltd, Burderop Park, Swindon, UK
Tom Markvart, School of Engineering Sciences,
University of Southampton, UK

With acknowledgement to IEA PV-PS Task 5.

1 Introduction

The "grid connection" of PV systems is a fast growing area, with a vast potential for domestic and industrial locations. A grid-connected PV system provides an individual or business with the means to be their own power producer, as well as contributing to an environmentally friendly agenda. The key to grid-connected systems is that they work in parallel with the already established Electricity Supply Network, and a number of their features are determined by this connection to the utility supply.

Traditionally, the connection of generators into the supply system has been done at high voltage (HV), in the kV range. Due to the restricted numbers, extensive experience and interconnected nature of the HV system, such generators can be accommodated into the distribution network using one-off assessments, and are large enough to justify the cost of the assessment and reinforcement measures. Photovoltaic generators on domestic roofs generally connect to the utility supply at low voltage (LV). Together with other generators which are connected to the low-voltage network, they are classed as distributed generation (often called 'embedded generation' in the UK). Such connections present new issues for the distribution network operators which have traditionally distributed power 'downwards' from a relatively few generators connected at high voltage (Figure 1).

One possible way of integrating the PV generator within a domestic installation is shown in Figure 2. In this scheme, the PV electricity is used to supply the consumer demand and any excess is metered and exported to the utility network. Other schemes are possible where, for example, the PV generator (after DC/AC conversion and the export meter) is connected directly to the incoming service cable. All the generated electricity is thus exported to

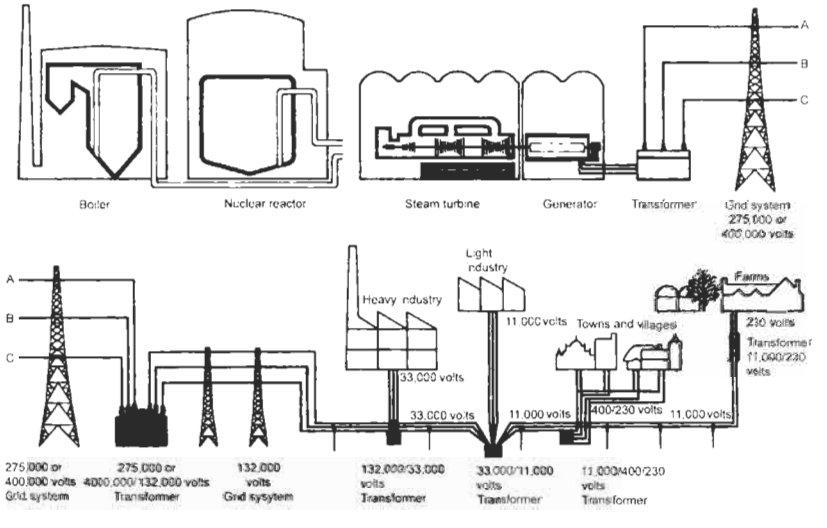

Figure 1 A typical electricity transmission and distributions system, illustrated on the example of the UK public electricity supply (adapted from R. Cochrane, Power to the People, CEGB/Newness Books, 1985). All but the largest PV generators are usually connected at 400/230 V.

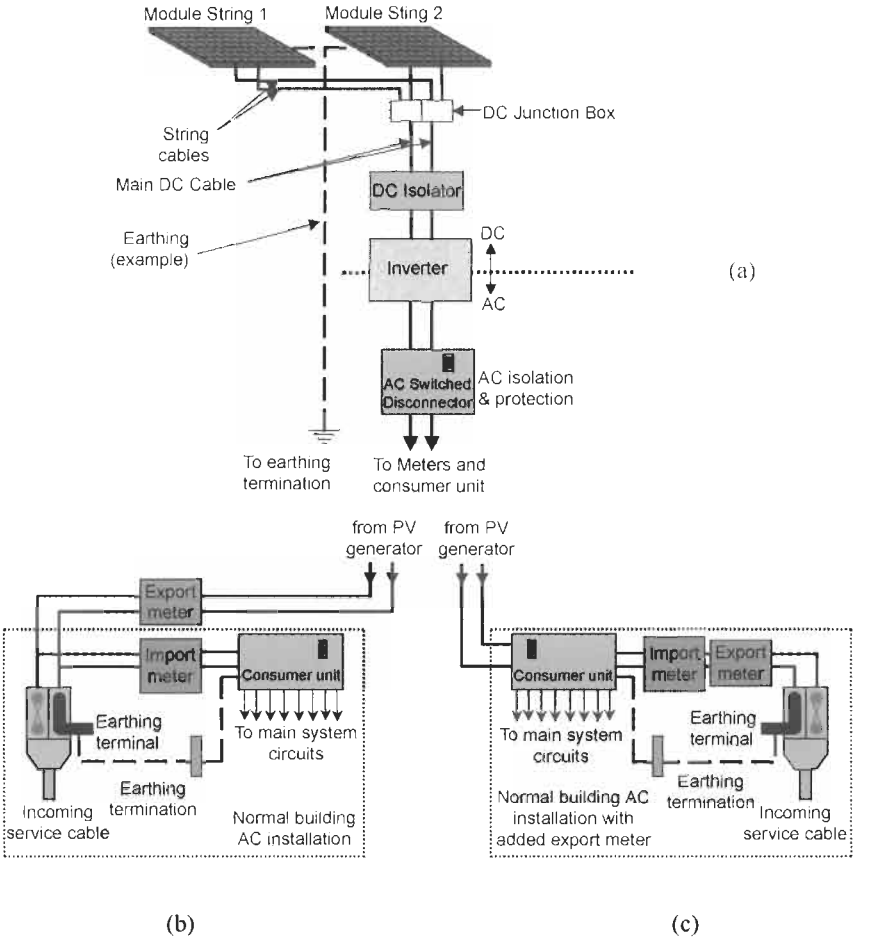

Figure 2 Typical layout of a domestic PV installation. (a) The PV generator. (b) Connection scheme of the meters and consumer units suitable for countries (notably Spain) where all PV power is exported to the network. (c) Connection scheme for countries (for example, UK) where only the excess power not used on-site is exported to the network. In the case (c), a PV generation meter is often installed on the AC side of the inverter. Combined export/import meters are now also available as a "dual register" unit.

the network, and the consumer unit is connected by a separate line through the import meter in the usual manner. This scheme is beneficial to the consumer if the utility price for PV electricity is higher than the usual domestic tariff.

For PV systems, a significant issue is the grid connect inverter used as part of the PV system. The inverter converts the DC power produced by the PV generators to alternating current (AC) in order that the generator may be connected and synchronised to the utility network. Previous regulations and recommendations for the connection of generators were not written with small inverter interfaces in mind, and so a new framework is emerging which will allow the PV generators to connect to the utility network safely but without undue complexity and cost.

Although there are differences in the grid-connection procedures which are at present applied in different countries and by different utility companies, these procedures share a number of common attributes. The network operator will generally require that the connection of a PV generator conforms to the relevant codes of practice and engineering recommendations, particularly with respect to safety. There must be adequate protection for both the supply network and the inverter. The power quality will also have to be sufficient not to affect adversely the utility equipment and other users connected to the network.

This chapter gives an overview of the principal grid connection issues and the existing codes of practice and engineering recommendations, drawing on the work of the Task 5 of the Photovoltaic Power Systems (PVPS) Programme of the International Energy Agency. Further details can be found on their website (http://www.iea-pvps.org) with copies of reports downloadable from www.oja-services.nl/iea-pvps/products/home.htm.

2 Principal Integration Issues

The integration of PV systems to electricity networks is covered at the top level in the standard [1] which groups the issues into two main categories: safety and power quality. DC injection and radio frequency suppression are also important considerations.

2.1 Safety

Safety of personnel and protection of equipment are the most important issues concerning a grid-connected PV generator. When the source of power is disconnected from the network section to which the inverter is connected, the inverter is required to shut down automatically within a given time. An inverter that remains generating into such a network is termed to be in *island operation*. Such operation could critically affect the safety of electricity supply staff and the public, as well as the operation and integrity of other equipment connected to the network [2]. The risks involved depend on the type of network and how it is operated.

With the advent of distributed PV generation, islanding has become one of the central issues of concern for the utility supply industry. For this reason, it forms the principal subject of this chapter, and is discussed in detail in Section 4.

2.2 Power Quality

Any generator or load connected to the 'mains' network may affect the quality of the waveform. Alterations to the voltage or frequency, or variations which affect the 'shape' of the sinewave, such as harmonics and flicker, are all important. Power factor and fault current contribution are also relevant considerations. Fortunately, with inverter connected PV systems, neither of these is a particular

problem. Most modern inverters can adjust their power factor to suit the network. Fault level contributions are low as there is little stored energy in an inverter in contrast with the rotation energy of a spinning generator.

2.3 DC Injection

Another aspect of inverter generators is the possibility of DC injection into the network. The network operators will not allow the presence of DC current in any significant amount and impose a limit close to zero on the DC current produced by the inverter. An inverter with an isolation transformer at the output to the utility is designed not to produce any DC current but this issue may arise for inverters with high frequency transformers which are now beginning to appear on the market.

2.4 Radio Frequency Suppression

Inverters now generally operate at switching frequencies of 20 kHz or higher, and may cause some interference in the RF region. This is usually avoided by the use of appropriate filtering and shielding.

3 Inverter Structure and Operating Principles

Inverters are discussed in detail in Chapter IIIb-1, and only a brief review of the relevant aspects will be given here. Inverters for utility connection can be broadly classified into two types: single-phase inverters, and three-phase inverters. Detection of islanding is much easier in a three-phase than a single-phase inverter, although inverters that are rated at a power below 5 kW are mostly connected to single-phase networks.

Most modern grid-connect PV inverters use self-controlled power switches (e.g., MOSFET, IGBT) and generally use pulse width modulation (PWM) control signals for producing an AC output. Previous thyristor based systems were turned off using the 'zero crossing' of alternating current from the mains. In either case, inverters need to synchronise with the utility network, and switch off on islanding.

Figure 3 shows a schematic structure of a typical PV inverter. The input DC power enters the maximum power point tracker aiming to keep the DC power input extracted from the array as high as possible. This DC power is converted to output AC power by the DC/AC converter. The basic function of the control circuit is to control the DC/AC converter to produce a sine-wave output (voltage or current) which is synchronised with the grid and has a low distortion. In order to reduce the weight and the price, some more recent PV inverters use a high frequency transformer. Here, the DC/DC converter converts the input DC voltage to a higher DC level to meet the voltage requirement of the DC/AC converter which is directly connected to the grid. Resonant technology can be used in this structure for higher efficiency.

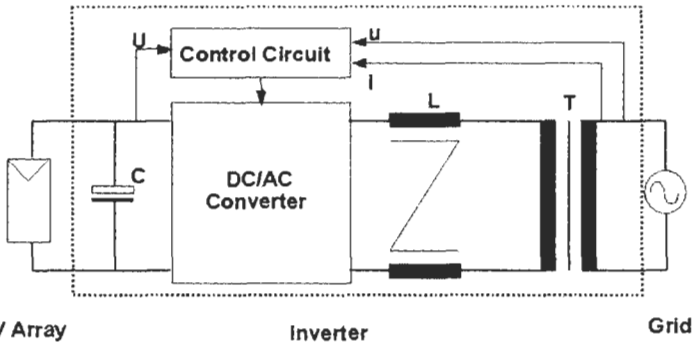

Figure 3 Schematic diagram of a typical PV inverter with low-frequency isolation.

4 Islanding

The main technical issue for utilities has been the issue of 'islanding' where the power to a local area of the electricity network could potentially be maintained live by a distributed generator, even where the main power station supply is switched off or lost in a fault. Alternatively, islanding can be considered as the condition in which a portion of the utility system, which contains both load and generation, is isolated from the remainder of the utility system and continues to operate.

Island operation is potentially undesirable both from the safety point of view – where a circuit may be assumed to be 'dead' when it is not, and from the point of view of power quality – where the standards normally guaranteed to customers may not be met. The risks of islanding has been researched in some detail under IEA Task 5 and the results are available in several IEA reports [2–4].

Traditionally, the problem would have been solved by providing an accessible lockable switch for each generator, but clearly this is impracticable once numbers rise above a very few. As a result, the functionality of the accessible switch has now normally been replaced by automatic anti-islanding protection circuits within each inverter [2].

Various methods of anti islanding detection and prevention have been developed and adopted across different countries, as described in Table 1. In general, there is a move not to be prescriptive on how islanding is detected leaving the choice of the islanding detection method to the inverter manufacturer. Instead, a standardised method of the testing of these devices is being produced through international standards [5]. Some differences may, however, remain to take into account the differences in electricity distribution networks in different countries.

In the countries participating in the IEA PVPS, for instance, anti-islanding requirements have been evolving for many years and today they still vary considerably from country to country. Some countries such as the Netherlands require only the out of frequency and out of voltage windows. Other countries such as Germany and Austria require a specific method based on sudden

Table 1

Methods	Characteristics
Passive methods	
Over Voltage	Switches off when voltage rises above a preprogrammed 'window' limit – very common
Under Voltage	As above but when value falls below preprogrammed limit – very common
Over Frequency	As above but for frequency – very common
Under Frequency	As above but for frequency – very common
Frequency Variation Rate	ROCOF (rate of change of frequency) – a more sophisticated method that is triggered by unusual changes in frequency – common
Voltage Phase Jump	Also known as power factor detection – monitors phase difference between inverter output voltage and current for sudden change
Third Harmonic Voltage Detection	Harmonics will typically increase if the low impedance of the grid is lost
Active methods	
Frequency Shift	A method of ensuring that if the mains is lost the inverter trips on its frequency limit. Various methods have been designed to achieve this
Impedance Measurement	One method injects a pulse into the network to detect if it is present – some difficulties in multi-inverter situations and with power quality degradation
Harmonic Impedance Measurement	Where a harmonic frequency is deliberately injected to detect response
Utility methods	
Utility Communications	Requires continuous signal from utility to keep generator connected (either power line or other communications)

impedance changes and described as ENS or MSD. Standards are also sometimes adopted that require inverters to detect and shut down within a variable amount of time that is determined by the out of tolerance condition that exists on the island or even on the utility grid.

However, a growing trend is to require that utility-interactive inverters be type tested for the purpose using a standard test circuit and test method that has been determined to be a worst-case condition. This allows a single inverter to be tested rather than requiring multiple inverter tests. There is a move to standardise the test, as far as possible, under IEC.

A general overview of the possible range of islanding detection techniques is given in Table 1. Some of these techniques (for example, those that are implemented by the utility) are outside the scope of the present book. We shall therefore focus on detection methods integrated within the PV system (e.g. inside or close to the inverter). These techniques can be further divided into active and passive measures depending on the type of monitoring, as discussed below. Further detail can be found in the comprehensive IEA report [6].

4.1 Passive Methods

Passive islanding detection methods detect the characteristic features of the islanding mode, and the operation of the inverter is stopped. Typical measured values are voltage, frequency and phase. This method is suitable for integration into the inverter. Passive techniques do not by themselves alter the operation of the power system in any way; they detect loss of grid by deducing it from measurements of system parameters. Passive techniques are suitable for all types of generators.

4.1.1 Voltage and Frequency Detection

The simplest way to achieve loss of mains protection is to use standard voltage and frequency protection to identify the islanding condition. This method works in most cases except where the load exactly matches the output from the generator. Voltage and frequency detection is implemented as basic protection on most inverters. Other methods can be added to this such as ROCOF below.

4.1.2 ROCOF Technique or Phase Jump Detection

A technique known as ROCOF [6] measures the rate of change frequency to determine whether the connection to the mains has been lost. Sometimes it is also referred as phase jump detection. The relay monitors the system frequency and is arranged to ignore the slow changes in frequency, which normally occur on the grid system, but respond to the relatively rapid changes of frequency when the grid is disconnected.

4.2 Active Methods

Active methods for detecting the island introduce deliberate changes or disturbances to the connected circuit and then monitor the response to determine if the utility grid with its stable frequency, voltage and impedance is still connected. If the small perturbation is able to affect the parameters of the load connected within prescribed limits, the active circuit causes the inverter to shut down.

4.2.1 Variation of Frequency

This is sometimes referred to as frequency shift. The output frequency of the inverter when the utility is lost is made to diverge, by giving bias to the inverter free running frequency (making it increase or decrease). Islanding is then detected when the frequency veers outside the allowed frequency band. This is a very efficient way to detect islanding in a single generator. Its effectiveness is being evaluated in situations when several generators work together. The effect of the technique on the mains when large numbers of these generators are connected is also subject to further research.

4.2.2 The Measurement of Impedance

In one implementation of this method, current is injected into the utility to determine the impedance of the utility line. The circuit is designed to detect

significant changes in impedance over a short period of time such as would occur if the utility were disconnected. This has been adopted in the ENS or MSD systems, but the effect on power quality and the effect when there are multiple units is still being evaluated. An example of waveform generated by an inverter using the ENS impedance measuring technique is shown in Figure 4.

4.2.3 Variation of Power and Reactive Power

Islanding can also be detected from the frequency change on islanding as a result of continuous variation of inverter reactive power output. Alternatively, islanding can be detected by monitoring the voltage change in response to a continuous variation of inverter active power output.

5 Regulatory Issues

To facilitate the installation of photovoltaic generators (particularly small domestic installations), regulations are being developed and are in place in a number of countries that relate to connection of PV generators. The technical, legal and commercial aspects of these regulations in various countries are discussed below. We shall also touch upon the associated procedures for the type approval of inverters and/or the allied interfacing equipment.

5.1 Technical Connection Guidelines

The grid-connection of PV systems is covered at the top level in the standard [1]. This document is in the process of being revised to include developments since its introduction several years ago. Although the main features are likely to remain in place, the precise values of the parameters are specific to each country, and a copy of the latest national regulations should therefore be obtained through the local electricity company. Current detailed information and contacts are given in the IEA report [7] and summarized here in Tables 2 and 3.

Until relatively recently, only a minority of countries had PV-specific standards but today most that are looking to implement PV systems have

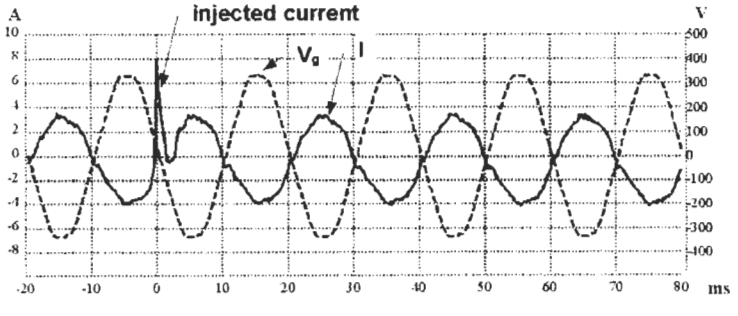

Figure 4 A typical waveform produced by an inverter using the impedance measuring technique of islanding detection.

developed guidelines for the grid interconnection of PV inverter systems. PV systems using static inverters are technically different from rotating generators and this fact has been generally recognised in these new guidelines.

Whilst it is evident that most countries now have specific PV standards, these standards differ from country to country and a harmonisation is intended as the next step. Activities at the IEC level have started work in this direction, with the main focal point IEC TC82 Working Groups WG3 and WG6. The output of the work from Task 5 to IEC TC82 has been essential for some of the present activities in these groups, and several members of Task 5 are also working as IEC experts. At the same time, it is clear that due to differing technical boundary conditions in different countries (earthing philosophy, layout of the grid, etc.) it will be difficult to achieve total harmonisation.

The status of this regulatory process in a number of countries that took part on the Task 5 of the Photovoltaic Power System Programme of the International Energy Agency is shown in Table 2.

5.2 Type Testing

The large number and relatively small size of many grid connected PV systems will impact on current network operator procedures. Through the pressure of numbers, each system cannot be considered on a 'one-off' basis. Projects also cannot be required to bear a connection cost (charge levied by a network operator) that is out of proportion to the cost of the systems themselves. This has lead to the concept of 'type verification' where a representative test is carried out on a sample of a product, and then this does not have to be repeated for every new installation. The situation on Type Testing is shown for various countries in Table 3.

5.2.1 Draft IEC Standard 62116

It has already been mentioned that international tests for inverter anti-islanding are being developed in the International Electrotechnical Commission Technical Committee 82 – Solar Photovoltaic Energy Systems, to be entitled 'Testing Procedure of Islanding Prevention Measures for Grid Connected Photovoltaic Power Systems' [5]. An example test circuit which is being discussed is shown in Figure 5.

The circuit has a resonant load to model the situation of multiple inverters. In preparation for the test, the resistive part of the load and the impedance of the resonant circuit are changed to match the active and reactive power produced by the inverter. The switch to the utility supply is then opened and the duration of inverter operation before shutting down is recorded. Depending on the regulations, the tests may be repeated at several values of the resistive load. The main item for debate between countries is the 'Q' factor of the resonant load which determines how sensitive the circuit is to the disruption, and also whether motors or similar loads should be included as part of the local load.

On issuing of a Type Test certificate (or 'listing' in the USA), simplified procedures and checks can be adopted by the utility companies when requests for connection of these type tested units are made.

Table 2 Guidelines for selected countries. Data from [7] and [9].

Country	Authorisation procedure
Australia	Installations are authorised by the local electricity utility. Usually required: – a copy of inverter conformance certificates – a licensed electrician to connect the PV system to the grid Commissioning tests include visual inspection and tests of the anti-islanding measures.
Austria	Installations are authorised by the local electric utility. Usually required: – a copy of the declaration of CE conformity of the inverter – a copy of the type-testing of the built-in anti-islanding measure ENS Only a licensed electrician may connect the PV system to the grid Commissioning tests include visual inspection and tests of the anti-islanding measures.
Germany	Approval by the grid operator is required. Installation work may be performed only by an authorised (skilled and licensed) installer. The grid operator usually demands single phase circuit diagram of installation – a copy of the declaration of CE conformity of the inverter – a copy of the type test approval of the anti-islanding ENS – protocol of commissioning by installer Tests are not regulated. Generally simple functional tests of inverter and ENS are conducted. Documentation of commissioning procedure is requested.
Italy	Installations are authorised by the local electric utility. Usually required: – a copy of the declaration of CE conformity of the inverter – a copy of the type-testing of the built-in anti-islanding measure ENS Only a licensed electrician may connect the PV system to the grid Commissioning tests include visual inspection and tests of the anti-islanding measures.
Japan	Installations are authorised by the local electric utility. Usually required: – a copy of electrical layout of the system – a copy of the declaration of confirmation of the requirements for grid interconnection guideline – a copy of the type-testing certification by JET Only a licensed electrician may connect the PV system to the grid Commissioning tests include visual inspection and insulation tests.
Netherlands	The connection of a generator to the power network has to be approved by the network operator. However, this requirement does not apply when dealing with small and medium sized PV systems on dwellings. Permission is asked for all large PV systems. By law, the network operator cannot refuse the connection of a PV system (or any other renewable energy source. All PV systems have to comply with regular and special standards described in more detail in the IEA report. Official procedures for commissioning are not available. Specialised consultancy firms often assist owners of large and/or special PV system in authorisation and acceptance testing.
Portugal	The licensing of an Independent Power Producer (IPP) plant requires the following documents to be submitted to the Government's Directorate General of Energy (DGE): 1. Normalised formal request to the Ministry of Economy (Energy) 2. Liability term, by which the installation conforms to the regulations in force.

(Table continued on next page)

Table 2 (*continued*)

Country	Authorisation procedure
	3. Technical information provided by the utility (grid company) regarding: – Interconnection point – Maximum and minimum short circuit power at the interconnection point – Type of neutral connection – Automatic reclosing devices available or to be installed 4. Detailed design of the whole system (generators, transformers, protective devices, connection line, local grid, etc.). The final decision (approval) is from the Minister of Economy or the Director General of Energy (DGE), depending on the system installed power (P > 1MVA or P < 1MVA, respectively). Before starting its regular operation, the power plant must be inspected by the DGE (P > 10 MVA) or the Ministry's Regional Delegation (P < 10 MVA), which will deliver an 'Operating Licence'.
Switzerland	All installations have to be authorised by the local electric utility. Usually required: – description of the inverter and the solar modules – form for grid connection of the electric power utility Only a licensed electrician may connect the PV system to the grid.Commissioning tests include visual inspection and tests of the anti-islanding measures. If an installation exceeds 3.3 kVA on one phase or 10 kVA on three phase an approval of the Eidgenossische Starkstrominspektorat (ESTI) is required. Usually required: – description of the inverter and the solar modules – form for grid connection of the ESTI Commissioning tests include visual inspection of the lightning protection and the grid connection. Tests of the anti-islanding measures.
United Kingdom	Installations need to be agreed with the local Distribution Network Operator (DNO). For larger units the DNO may require on-site commissioning tests and may also want the opportunity to witness the commissioning tests. However, the use of a type approved inverter for smaller units greatly simplifies the process. A connection (operating) agreement also needs to be in place with the local DNO and an appropriate supply (tariff) agreement with an electricity supplier if any export settlement is required.
Spain	For P < 100 kVA, the local electric utility requires : – Data concerning ownership and location of PV system – Single phase circuit layout of the installation – Proposal for the interconnection point to the grid – Technical characteristics of the main components of the installation : Nominal PV power, inverter characteristics, description of protection devices and connection elements A contract must be formalised between the local electric utility and the PV system owner, fixing economical and technical relationships as can be the interconnection point to the grid and the interconnection conditions. An authorized installer must inspect and test the system before it is connected to the grid.
USA	Permits for installation are required. Drawings, specifications, equipment lists and layout are normal. The local authority having jurisdiction (AHJ) inspects installations. Utility-interactive systems are required to use listed hardware and components. Generally, only a licensed electrician may wire and connect the PV system to the grid. Some states now certify PV installers. Inspections include visual checks before interconnection is approved.

Table 3 The accepted standardised islanding test and institutions authorised to perform the type approval tests in selected countries. Data from [7] and [9].

Country	Guideline/standard	Scope	Protection Settings
Australia	Australian Guidelines for grid connection of energy systems via inverters[a]	All energy sources that are connected to the electricity system via inverters 0–10kVA phase to neutral 0–30kVA 3 phase.	• Over Voltage (2 s) • Under Voltage (2 s) • Over frequency (2 s) • Under Frequency (2 s) • At least one active method of detecting AC disruptions
Austria	ÖVE/Önorm E2750[b]	PV systems – both stand alone and grid connected. Without specific approval the maximum power is limited to 5 kWp DC (4.6 kVA) per phase for small installations.	ENS (impedance measurement method): if grid impedance is $> 1.75\ \Omega$ OR grid impedance jump $> 0.5\ \Omega$ is detected then inverter must disconnect within 5 seconds.[c]
Germany	DIN VDE 0126 (draft) VdEW guideline of the Association of Electric Power Companies	No general limit for power generation capacity; up to 4.6 kVA (inverter) or 5 kWp (PV generator) single phase connection is permitted (VdEW Guideline). Above 5 kWp three-phase connection is requested. All systems need approval by local grid operator.	Islanding prevention device ENS (also called MSD) has become the de-facto standard for new systems. It monitors grid voltage, grid frequency, grid impedance and ground leakage current and disconnects the inverter, if one parameter is out of bounds.[c]
Italy	CEI 11-20[d]	All types including photovoltaic systems. The standard gives an indication of 50 kVA for LV systems and 8 MVA for MV systems (HV systems are not covered by this standard).	Voltage and frequency window.

(Table continued on next page)

Table 3 (*continued*)

Country	Guideline/standard	Scope	Protection Settings
Japan	See note [e]	All generating sources (Different grid-interconnection requirements for utility frequency rotating generators and DC sources utilising inverter for grid-interconnection).	Both active and passive methods should be installed. Any kind of active method and passive method is acceptable, e.g.: *Active methods:* Frequency shift, power variation, load variation. *Passive methods:* voltage phase jump, frequency variation rate, third harmonic voltage detection.
Netherlands	1: Supplementary conditions for decentralized generators low-voltage level 2: Guidelines for the electrical installation of grid connected photo-voltaic (PV) systems[f]	1: Covers all types of generators connected to the LV network. Simple protection is required for generators below 5 kVA. This class is intended for small generators in residential applications, e.g. PV systems and micro CHP. 2: This standard is intended for grid connected PV systems only. Clauses referring to the AC side may also be used for other small types of generators like micro CHP.	Required protection: ● Overvoltage ● Undervoltage ● Overfrequency ● Underfrequency ● Overload protection or maximum current
Portugal	No specific standard for grid connected PV systems. Law 168/99[g]	When the connection to the grid is made at the low voltage level (up to 1kV), the power cannot exceed 4% of the minimum short-circuit power at the interconnection point, with an upper limit of 100 kW. [h]	No reference is made (in the IPP law) to this phenomenon. The co-ordination between the IPP and the electrical grid must consider situations of grid disconnection, for maintenance and repair, in order to ensure the necessary safety conditions.
Switzerland	ESTI Nr. 233.0690; VSE Sonderdruck Abschnitt 12[i]	PV systems – both stand alone and grid connected. PV installations up to 3.3 kVA on one phase or up to 10 kVA on 3 phase do not require an approval of the ESTI.	Recommended: measurement of network voltage (one phase) and shutdown in case of frequency shift (e.g. in the US, Japan and Holland)[j]

Table 3 (*continued*)

Country	Guideline/standard	Scope	Protection Settings
United Kingdom	G77/1 (2002)[k]	PV inverters for grid connected systems. Up to 5 kVA, for a single installation.	● Over Voltage ● Under Voltage ● Over frequency ● Under Frequency ● A recognised loss of mains technique, such as vector shift or frequency shift. Active techniques that distort the waveform beyond harmonic limits or that inject current pulses are not allowed. Disconnection time 5 sec
Spain	No specific standard for grid connected PV systems. Law 17599, Real Decreto (RD) 1663/2000	Nominal power < 100 kVA and low voltage level. Connection Voltage to the grid < 1kV 3 phase inverter is required for interconnection to the grid of systems with power rating > 5 kW	– Manual line breaker – Automatic disconnection and reconnection to the grid – Overfrequency – Underfrequency – Overvoltage – Undervoltage

(*Table continued on next page*)

Table 3 (*continued*)

Country	Guideline/standard	Scope	Protection Settings
USA	NFPA 70; IEEE 929-2000; UL1741[l]	IEEE929 covers interconnection requirements when connected to the utility, and defines small systems as up to 10 kW. Some utilities still use their internally generated distributed generation interconnection requirements.	Requirements for allowable islanding are given in IEEE929 and UL1741. Methods are not specified.

Abbreviations: LV = low voltage; MV = Medium Voltage; HV = High Voltage; CHP = combined heat and power.

[a] Available from http://ee.unsw.edu.au/~std_mon/html_pages/inverter_passed.html.

[b] ÖVE/Önorm E 2750 Photovoltaische Energieerzeugungsanlagen – Sicherheits-anforderungen (Photovoltaic power generating systems – safety requirements).

[c] Older requirement for single phase inverters (still possible as alternative to ENS): 3 phase undervoltage relay and single phase overvoltage relay required.

[d] CEI 11-20 – Impianti di produzione di energia elettrica e gruppi di continuità collegati a reti di I e II categoria (Power production plants and uninterruptable power systems connected to 1st and 2nd grids). Available form Comitato Elettrotecnico Italiano CEI; Viale Monza, 261; 20126 Milano; e-mail: cei@ceiuni.it.

[e] Technical Guidelines for the Grid Interconnection of Dispersed Power Generating Systems (only available in Japanese). Available from for grid-interconnection guideline: http://www.energy-forum.co.jp/index.htm. For photovoltaic generation system standard: JIS (Japan Industry Standard). Japanese Standards Association, 4-1-24 Akasaka, Minato-ku, Tokyo 107-8440; see also the English page of JSA web site http://www.jsa.or.jp/eng/index.htm

[f] Available from EnergieNed; Utrechtseweg 310; P.O. Box 9042; 6800 Arnhem; tel +31 26 3 56 94 44; fax +31 26 4 46 01 46.

[g] Law 168/99 (last revision of all the legal and technical framework to IPP), first introduced in 1988.

[h] For higher voltage levels, see the IEA report.

[i] ESTI Nr. 233.0690 'Photovoltaische Energieerzeugungsanlagen – Provisorische Sicherheitsvorschriften' (Photovoltaic power generating systems – safety requirements draft); VSE Sonderdruck Abschnitt 12; 'Werkvorschriften über die Erstellung von elektr. Installation' Elektrische Energieerzeugungsanlagen ; Completes VSE 2.8d-95; available from: Eidgn. Starkstrominspektorat ESTI; Luppmenstr. 1; 8320 Fehraltorf.
Verband Schweizerischer Elektrizitätswerke VSE; Gerbergasse 5; Postfach 6140; 8023 Zürich.

[j] Methods used but not recommended include ENS (impedance measurement method) and the measurement of phase-to-phase and phase-to-neutral voltage for single phase inverters feeding into three phase networks.

[k] G77/1 (2002) – Recommendations for the Connection of Inverter-Connected Single-Phase Photovoltaic (PV) Generators up to 5kVA to Public Distribution Networks. Available from Electricity Association, Millbank, London. Work is underway on G83/1(2003) which it is planned will supersede G77/1 when published.

[l] NFPA 70 – National Electrical Code; IEEE 929-2000 Recommended Practice for Utility-interface of Photovoltaic Systems. UL1741 UL Standard for Static Inverters and Charge Controllers for Use in Photovoltaic Power Systems.

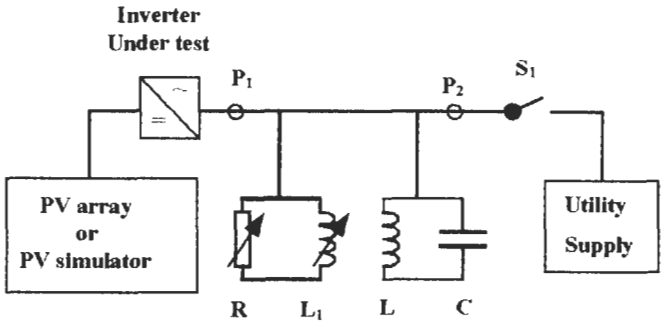

Figure 5 The test circuit for islanding detection.

5.3 Parallel Connection Agreement

A Parallel Connection Agreement is generally necessary for connection and operation even if export of power to the main network is not required. This covers the legal aspects and liability of connection. Requirements in selected countries are shown in Table 4.

5.4 Tariff Agreement

The Tariff Agreement embodies the commercial terms for payment for exported energy and varies from country to country and electricity company to electricity company. Examples of arrangements for metering and 'profiling' for PV electricity in various countries are summarised in Table 5. In a number of countries (for example, Germany, Spain and Switzerland) the utilities are obliged by law to pay a premium price for PV electricity. Further information on year by year changes is available from an annual survey report published by IEA Task 1 [8]. In some countries this benefit is enhanced further by the fact that all the PV generated power is exported direct to the utility (as mentioned in Section 1).

5.5 Post- or Pre-notification

The administration of processing a large number of network connections is also of issue to network operators. Once a Type Verification process is in place, there is no need for on-site tests, and hence the installer is responsible for correct connection. A system requiring pre installation or post installation notification can then be established.

Acknowledgements

The authors are grateful to the International Energy Agency for permission to publish sections of IEA Reports and, in particular, the work of Bas Verhoeven, Christoph Panhuber and Ward Bower. We also thank Rod Hacker, Martin

Table 4 The connection procedures in selected countries. Data from [7] and [9]

Country	Accepted standardised Islanding test	Authority/institute authorised to perform such a test and issue a certificate
Australia	Australian Guidelines for grid connection of energy systems via inverters. Appendix B	Not specified.
Austria	The ENS (impedance measurement) test method is nationally accepted.	Berufsgenossenschaft für Feinmechanik und Elektrotechnik, Cologne, Germany Bundesforschungs- und Prüfzentrum Arsenal, Vienna, Austria
Germany	The ENS (impedance measurement) test method as defined in VDE 0126 is empowered and nationally accepted.	Authorisation is not regulated, theoretically each laboratory could conduct the type approval test. In fact type tests are performed by: Berufsgenossenschaft für Feinmechanik und Elektrotechnik, Koln, Germany, hv@bgfe.de and by: TÜV Rheinland, Koln, Germany, mail@dc.tuv.com
Japan	Japanese Standard	Japan Electrical Safety & Environment Technology Laboratories 5-14-12 Yoyogi, Shibuya-ku, Tokyo, Japan
Netherlands	Correct function of the protection and proper settings have to be guaranteed by the manufacturer. For AC Modules a special KEMA-KEUR (K1 50) safety certification is required. The functioning and settings of the protections are included.	KEMA Registered Quality P.O. Box 9035 6800 ET Arnhem The Netherlands
Switzerland	The ENS (impedance measurement) test method is nationally not accepted.	Berufsgenossenschaft für Feinmechanik und Elektrotechnik, Cologne, Germany TÜV Rheinland, Cologne, Germany Bundesforschungs- und Prüfzentrum Arsenal, Vienna, Austria
United Kingdom	Part of the G77/1 Type Approval tests in G77/1 Appendix.	Manufacturers themselves, or STaR Facility, SES, University of Southampton, Southampton SO17 1BJ.
USA	IEEE929 and UL1741 contain test set-up and requirements for listing and utility interconnection recommended practices. The procedure was written so tests conducted on single inverters would apply to multiple inverters connected together.	Qualified electrical testing laboratories that are recognised as having the facilities to test as required by the NEC.

Table 5 Legal and tariff situation for electricity exported to the network by small grid-connected PV generators in member countries of IEA PVPS Task V. Data from [7] and [9]

Country	Legal and tariff situation
Australia	Utilities are not obliged to buy electricity produced by PV systems. Tariffs paid for electricity fed into the grid vary with Utility.
Austria	Utilities are obliged to buy electricity produced by PV systems. Tariffs paid for electricity fed into the grid vary locally; a recent change in law has generally raised the rates in most parts of Austria. Rates are between 0.04 and 0.55 Euro/kWh.
Denmark	Utilities are obliged to buy electricity produced by PV systems. Experimentally, for a 4-year period, normal households may use meters that can run in both directions. This means that they buy and sell electricity at the same price. Over one year there must not be a negative consumption. Companies and similar have to use separate meter for energy fed into the grid.
Germany	Utilities are obliged to buy electricity produced by PV systems (Law of Privilege for Renewable Energies). Tariffs are defined in this law. They are fixed for 20 years and depend on the year of installation. Price for systems built in 2001 is 0.99DM/kWh. Metering is not regulated, it depends on local grid operator. Usually energy fed to the grid is measured using a separate meter. The meter belongs to the grid operator and is rented for some 20 to 50 Euro annually to the Independent Power Producer.
Japan	Utilities are voluntarily buying electricity produced by PV systems. It is not legally regulated. Tariffs paid for electricity fed into the grid vary locally, however the rate is almost the same as electricity from the utility. Rates are around 23 Yen/kWh for a low voltage customer. A separate meter for energy fed into the grid is required.
Netherlands	Utilities normally accept decentralised generators in their networks. The new Dutch legislation on electrical energy requires a zero-obstruction policy from network operators towards renewable energy. Pay back rates and the necessity of a net-export kWh-meter are subject to the contract between the network operator and the owner of the PV-system.
Portugal	Utilities are obliged to buy electricity produced by PV systems and all the other IPP systems according to the Law 168/99, providing the technical conditions are met. Tariffs paid for electricity fed into the grid are specified in the Law 168/99: Rates are between 0.055 and 0.065 Euro/kWh. Different meters for the energy supplied by the IPP and for the energy consumed from the utility grid are mandatory.
Switzerland	Utilities are obliged to buy electricity produced by PV systems. Tariffs paid for electricity fed into the grid vary locally; the minimum rate for the electricity produced is 0.15 SFr./kWh (around 0.10Euro/kWh). Separate meter is used in most installations. Over 100 power utilities in Switzerland offer their clients the possibility to buy solar power. If a PV plant is installed within a green pricing model, tariffs are paid from 0.80 to 1.20 SFr/kWh (around 0.50–0.75 Euro/kWh). A separate net meter is mandatory.

(Table continued on next page)

Table 5 (*continued*)

Country	Legal and tariff situation
United Kingdom	Electricity suppliers are not obliged to buy electricity produced by PV systems. Tariffs paid for electricity fed into the grid vary with supplier, however the rate is normally less than that for imported units. Some suppliers now offer the same price. A separate meter for energy fed into the grid is required.
Spain	Utilities are obliged to buy electricity produced by PV systems at the rate of approximately 2.5 times the selling price.
USA	Utilities are obliged to buy electricity produced by PV systems but net metering laws are only recently providing guidelines for protection equipment required by the utilities, insurance requirements imposed on the PV owner, etc. Tariffs paid for electricity fed into the grid vary widely and depend on state laws and utility. Various net metering laws apply that vary from state to state.

Cotterell, Ian Butterss, Ray Arnold, Weidong He and Santiago Silvestre for useful input and discussions.

References

[1] IEC Standard 61727:1995. Photovoltaic Systems – Characteristics of the Utility Interface.

[2] Utility Aspects of Grid Connected Photovoltaic Power Systems, IEA Report PVPS T5-01:1998, International Energy Agency, 1998.

[3] Probability of Islanding in Utility Networks Due to Grid Connected Photovoltaic Power Systems, IEA Report PVPS T5-07:2002, International Energy Agency, 2002.

[4] Risk Analysis of Islanding of PV Power Systems Within Low Voltage Distribution Networks, IEA Report PVPS T5-08:2002, International Energy Agency, 2002.

[5] Draft IEC Standard 62116. Testing Procedure of Islanding Prevention Measures for Grid Connected Photovoltaic Power Generating Systems.

[6] Evaluation of Islanding Detection Methods for Photovoltaic Utility-Interactive Power Systems, IEA Report PVPS T5-09:2002, International Energy Agency, 2002.

[7] PV System Installation and Grid Connection Guidelines in Selected IEA Countries, Report PVPS T5-04:2001, International Energy Agency, 2001.

[8] Trends in Photovoltaic Applications in Selected IEA Countries between 1992 and 2000, IEA Report PVPS T1-10:2001, International Energy Agency, 2001.

[9] Santiago Silvestre, personal communication. An overview of the Spanish legal framework for the grid connection of photovoltaic generators including contract forms can be found at http://www.solarweb.net/fotovoltaica.php

IIIc-2

Installation Guidelines: Construction

Bruce Cross, PV Systems Ltd, Cardiff, UK

1 Roofs

1.1 Roof Types

1.1.1 Integral

An integral roof has the potential advantage of saving of material of the roof envelope that has been replaced. However, there are arduous requirements for water-tightness of roofs, which must be met. This can be achieved with regard to traditional roofing practice (which is country specific) and realistic engineering design (see Figure 1). A general overview of this field as well as examples of projects can be found in references [1–5].

The solutions that have been proven fall into the following categories:

- Interlocking panel systems, which either use panels that mimic roofing tiles with the PV element embedded in the surface or have a frame bonded to the PV panel which provides the sealing interlock.
- Adaptations of standard face-sealed sloping glazing systems, where the PV may be built into a double-glazed sealed unit. These are particularly suitable to buildings where the PV is visible from the inside, and must also provide a degree of transparency for internal lighting needs.
- Internally drained, secondarily sealed systems, where the high cost of a face sealed system cannot be justified.

Figure 1 Corncroft development, Nottingham, UK.

1.1.2 Over-Roof

The over-roof mounting of PV panels has been the normal practice in early installations. It is simple in concept, and has been proven provided that the attachment through the traditional roof is performed well. A range of standard frame systems have been tried, and provided that durable materials (hot dip galvanised steel, aluminium, or stainless steel) are used, have been successful. The time taken to install these varies greatly, and has the largest impact on the final cost of the mounting. The mounting brackets are generally most successful when they are standard roofing products, rather than 'special PV' made items, and should be rigid engineered mounts rather than the flexible strap type of fixing sometimes used for solar thermal collector mountings (Figure 2).

1.1.3 Tiles

PV roof tiles have been manufactured in several countries. The advantage of using a traditional roof product is that normal building trade practice can be used, and there is little resistance to the concept from the naturally conservative building trade. However tiles are small components and a large number are required for an installation – this implies are large number of interconnections, and also a mix of building trades is needed (e.g. electricians must work on a roof, or roofers must perform an electrical function). The use of tiles or slates frequently requires special tiles for edges, angled valleys, chimney joins, ridges, etc., and slates are generally cut to shape on site, and nail holes made to suit. This implies that the PV tile must link seamlessly into the standard roofing material (Figure 3).

1.2 Substructure

Most types of roof have been used for a PV system at some time. The overall construction must be capable of taking the additional load of the PV (or indeed

Figure 2 Domestic PV systems for Mr. Treble, Farnborough, UK.

Figure 3 Electraslate PV slate system.

survive the additional uplift when the PV replaces a much heavier roof surface such as concrete tiles). A more arduous requirement may be the local loads of a frame mounted system that has relatively few attachment points. The structure must also be able to accommodate any fixed, or temporary, access structures for maintenance or repair. A transparent or semi-transparent roof has a different set of requirements as it has to provide all the elements of the roof within a single system. This will also have to meet any aesthetic requirements from below as well as from outside. Thus an integral wiring pathway within the mounting system is an advantage (Figure 4).

1.3 New-Build vs. Retrofit

In a niche market such as PV at present, there is a need to be able to fit PV to both new and existing houses. In many countries the building stock is old and not being replaced, so the mechanisms for retrofitting PV are necessarily being developed. The costs of fitting PV to new buildings is significantly lower than for a retrofit due to access and adaptation at design stage being zero cost and the one-off costs being absorbed in the larger building project costs (Figure 5).

1.4 Mechanical Strength

The PV elements of the roof have to fulfil the requirements of wind loading, snow loading, fire resistance and possible traffic for maintenance. This means that a PV panel made for ground mounting may not always be suitable for a BIPV application. The grab zone of a standard PV laminate is small, and the glass thickness may also be inadequate. A purpose designed laminate or alternatively, a mounting system designed to transform the standard laminate into a building component may often be required to meet local codes.

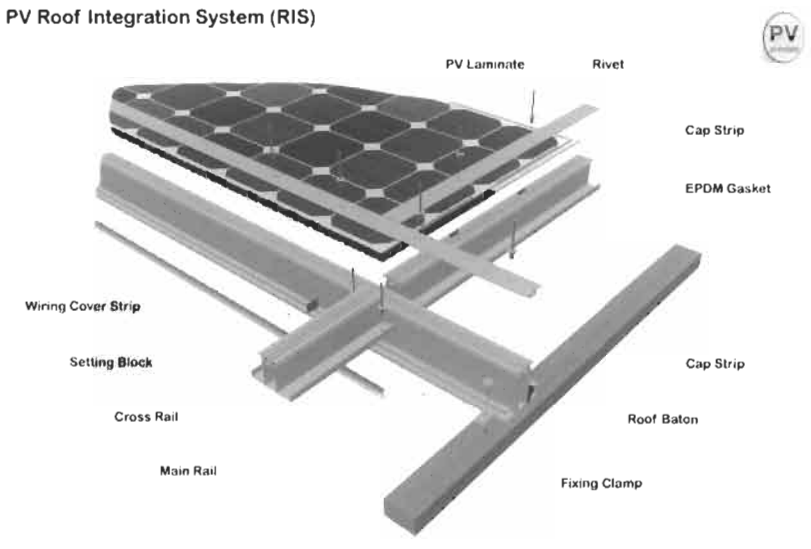

Figure 4 RIS PV roof integration system.

Figure 5 PV retrofits for New Progress Housing, UK.

1.5 Loading

Many standard PV laminates are fairly lightweight in roofing terms. The panels themselves may only weigh 5 kg/m^2, and say another 5 kg/m^2 for an aluminium mounting structure. However, a double glazed panel with a double glass front PV in a structural roofing system may add up to 40 kg/m^2.

1.6 Fixing Systems

Traditional roofs are fitted together with nails and screws. High technology fixings are rare in roofing, and PV systems that require precision fitting with specialist components will be expensive compared to those that are adapted for the trades already in use on site.

1.7 Weatherproofing

The requirement for the roof is to resist the ingress of water, and also to resist the loss of heat from the building, and to provide the degree of protection against fire for the type of building in which it is used. The external surface will have to resist degradation from UV, wind and rain for 30–60 years. This can be achieved for roofs with traditional materials, but is hard to demonstrate for new materials. Hence most PV on roofs has a glass external surface.

1.7.1 Sub-layer Membranes

Traditional interleaving roof coverings, such as tiles, slates, etc., have a need for a secondary membrane to stop water penetration in times of extreme weather. This requirement remains where PV equivalents are used. The high value of such roofs makes it a good investment to use high specification membranes, for additional security.

1.8 Interfaces with Traditional Roof Types

The join between the specialist PV part of a roof, and the traditional area of a roof, is an area for greatest care. Here a complete engineered system meets with a system developed over centuries and implemented by a craftsman. If the

Figure 6 Flashing detail.

understanding between these two is not clear, there is potential for the project to fail (Figure 6).

1.9 Standards

There are requirements for all building components to meet certain standards. For new products these take time to develop, and these are not yet in place for PV products. There are IEC standards that cover the operation of a PV product in itself, but not yet one that covers its operation in a building. Early moves have been made to establish a European test standard against which products can be tested in order to receive a CE mark, but this goal is still several years away [6]. The USA has several UL tests against which products can be tested (Figure 7).

2 Facades

2.1 Facade Types

2.1.1 Rain Screen

The simplest type of facade integration is the rain screen. Here the object is to keep the direct impact of the rain from the waterproofing layer, which is some distance behind. The intermediate space is ventilated with the ambient air and allowance is made for moisture to drain out from the space. Rain screen panels are generally a simple sheet product within a frame that hooks onto the lattice substructure. PV has been successfully embedded into such frames using the PV laminate to replace the sheet material (Figure 8).

2.1.2 Curtain Wall

In a curtain wall the external surface is the waterproof layer, and hence all parts of the structure behind are considered dry. This is not to say that there is no chance of moisture, as condensation must still be considered. Normal practice would be to allow a small amount of air movement behind the outer skin, but in the case of PV it should be increased, if possible, to provide some cooling from the rear surface of the PV. The advantage of the curtain wall is that it allows a continuous skin incorporating all the facade elements – windows, PV and blank panels within a proven design. These systems are complex and expensive without the PV and so the additional cost may be more readily absorbed into such a facade (Figure 9). It should be noted that the use of terms 'rain screen' and 'curtain wall' varies internationally.

2.2 Substructure

The substructure for a facade may use any type of normal construction material. The extra requirements caused by having PV as the external skin are that

Figure 7 Shell PV roof undergoing 'Prescript' test in Solar Simulator at Cardiff, UK.

Figure 8 Bowater House PV facade, Birmingham, UK.

temperatures may be higher (larger expansion may occur) and that a path must be found for the cabling and access provided to any connections or marshalling boxes within the building envelope. These cable paths must be accessible for maintenance, and must not provide a path for moisture ingress into the building fabric.

2.3 New-Build vs. Retrofit

A retrofit facade has more potential areas of risk than a new-build. The uncertainties of dimensions may require significant site work, and the locations

Figure 9 William Jefferson Clinton Peace Centre PV facade, Enniskillen, Northern Ireland, UK.

for cabling and electrical plant may have to be defined late in the project, when the old materials are removed. In a new-build facade there is likely to be a long time delay between fitting the PV elements as part of the external envelope, and installation and wiring of the electrical plant. The design of the system must ensure that these operations can be separated (e.g. external stringing may not be accessible for checking at the time the system is finally commissioned).

2.4 Mechanical Strength

Building designs often require the use of large glazing elements. This has the effect of increasing the glass thickness, which, in a PV panel, reduces output. In many areas the facade must withstand impact from foot traffic, and may have to provide a degree of security also. Standard laminates rarely have sufficient

thickness, so more expensive custom made panels are needed. In general BIPV facade panels are 50–80% more expensive than standard modules (Figure 10).

2.5 Weatherproofing

The PV is just one element of a facade system and this total system must provide the weatherproofing. Care is required that the cabling and the increased expansion allowance, do not compromise the performance of the mounting system.

2.6 Cooling

The output of a PV panel decreases with rising temperature. It is therefore advantageous to provide for the flow of air over the rear surface of the PV if at all possible. For rain screen systems there are usually ventilation slots around the periphery of each panel, so these need only to be checked for adequate passage of air. However, for curtain walls, it will be necessary to allow an entry for air at the

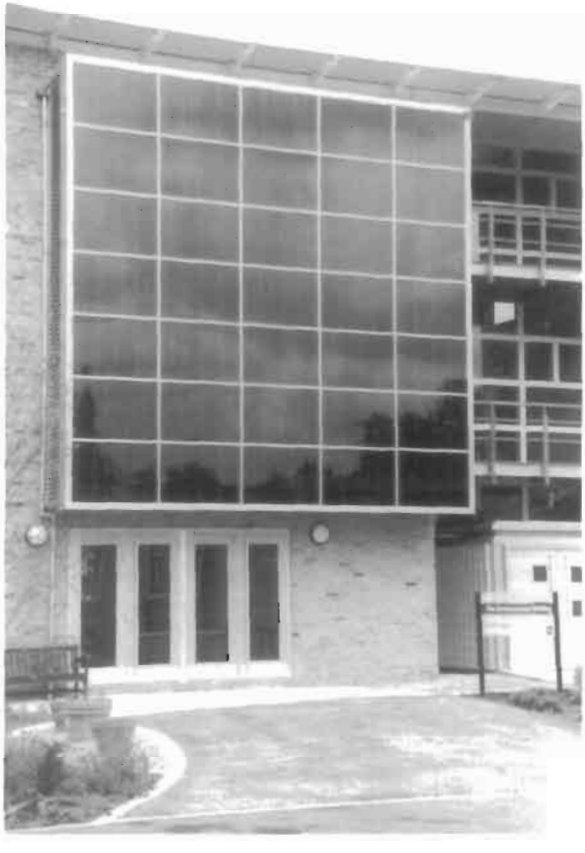

Figure 10 Office of the Future PV facade, Building Research Establishment, UK.

lowest part of the facade, and to allow the exit of air from the top, if the maximum output is to be achieved. This design requires care if the waterproofing of the system is not to be compromised. An EU project to assist this design process is underway (pvcool-build.com). When a fully face sealed double glazed transparent facade utilises PV, there is frequently no opportunity to ventilate the rear, and so the loss of performance (5–10%) must be accepted.

2.7 Maintenance

An important part of the design of the building is its future maintainability. Physical cleaning is not any more arduous for PV than for glass panels in general. Access should be provided for inspection and testing to any cable marshalling box, and a system should be in place to allow the testing, and possible replacement of any PV module in the system. In a large facade this may require simultaneous access externally, and internally to test, and to identify a fault.

2.8 Site Testing

There are standards for site testing the water-tightness of facade systems. These have been developed by the centre for window and cladding technology [7]. A

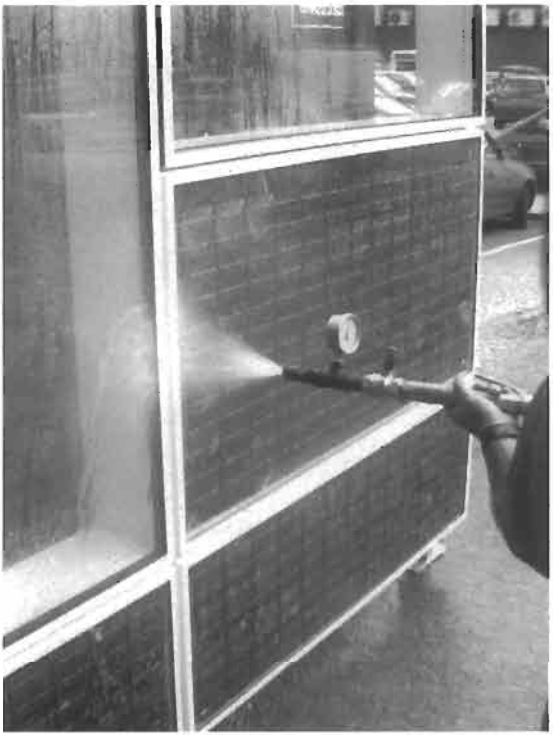

Figure 11 Pluswall PV facade, UK.

high-pressure water jet is used at susceptible joints and the system is inspected for water penetration. An addition to this test is to perform a high voltage isolation test immediately after, in order to evaluate whether any water has compromised the DC cabling or the PV modules (Figure 11).

3 Ground-Mounted Systems

When PV is mounted directly on a frame, pole, or concrete block, the requirements are to provide a rigid attachment that will resist gravitational, wind or impact forces, while protecting the PV from undue twisting or deflection. A typical frame uses standard sections which are assembled on site.

Since such systems are not usually part of a building and perform no weather protection function, there are few constraints on their design. However, car parking shelters, and entrance canopies are favoured locations for PV and often fall into the scope of building codes by association.

References

[1] Roaf, S. 2001. *Ecohouse – A Design Guide*, Architectural Press, Elsevier Science, Oxford.

[2] Sick, F. and Erge, T. 1996. *PVs in Buildings – A Design Handbook for Architects and Engineers*, International Energy Agency, Solar Heating and Cooling Programme, Task 16.

[3] Imamura, M.S., Helm, P. and Palz, W. Eds. 1992. *Photovoltaic System Technology: A European Handbook*, H.S. Stephens & Associates, Bedford.

[4] Max Fordham & Partners in association with Feilden Clegg Architects. 1999. *Photovoltaics in Buildings. A Design Guide*, Report ETSU S/P2/00282/REP, Department of Trade and Industry, UK.

[5] Studio E Architects. 2000. *Photovoltaics in Buildings. BIPV Projects.* Report ETSU S/P2/00328/REP, Department of Trade and Industry, UK.

[6] Prescript, *Final Report on EU Project.* JOR3-CT97-0132, European Commission, Brussels, 2000.

[7] *Test Methods for Curtain Walling* (2nd edition), Centre for Window and Cladding Technology, Bath University, 1996.

IIIc-3

Installation Guidelines: Electrical

Martin Cotterell, SunDog Energy, Penrith, UK

1 Introduction

Much of the electrical design and component specification work required to properly design and specify a PV system can be achieved by following the guidance in existing local and international electrical codes (see, for example, [1]). Such information is non-PV specific, though much will apply to the design of a PV system. A new section to IEC60364 – section 712 – is to be released shortly, which addresses some parts of PV system design [1].

PV specific regulations and guidance is available in some countries, either from stand-alone documents such as *Guide to the Installation of PV Systems* in the UK [2], or as a special section within the existing national code such as *Article 690 – Solar Photovoltaic Systems* in the US National Electrical Code [3]. The National Guidelines which address many aspects of this chapter are described in a recent report of the International Energy Agency [4].

This chapter covers some of the key issues particular to PV installations, that are contained within these PV specific codes and guidance documents. The chapter does not address the more general design issues, selection and rating of components that is well covered in the wider codes and electrical design handbooks. Three main areas are addressed:

- A PV array does not have a fixed voltage and current output – rather one that varies considerably under different operating conditions. It is important to determine the expected current and voltage maxima that may be generated by the PV array, in order to select suitably rated system components.
- A PV module is a current limiting device – PV arrays require a slightly different approach when designing suitable fault protection.
- PV modules cannot be switched off and, due to the current limiting nature, faults may not be detected or cleared. Precautions need to be taken to mitigate shock/fire hazards during installation, operation or maintenance. This includes careful consideration of earthing of the PV system.

2 DC Ratings (Array Voltage and Current Maxima)

When considering the voltage/current carrying requirements of the DC system, the maximum operational values that could occur need to be assessed. For a system without a battery, the maximum values originate from the two key PV module ratings: the open circuit voltage (V_{oc}) and the short circuit current (I_{sc}).

The values of V_{oc} and I_{sc} provided by the module manufacturer are those at standard test conditions (STC) – irradiance of 1000 W/m^2, air mass 1.5 and cell temperature of 25°C. As described in Chapter IIIa-1 the operation of a module outside of standard test conditions affects the values of V_{oc} and I_{sc} and these variations must be taken into consideration when specifying the voltage/current rating of all components of the DC system.

Cell temperatures are affected by ambient air temperatures; absorbed heat from the sun; cooling from the wind; the degree of ventilation and air movement behind the modules. Temperatures both well in excess of and well below the STC value of 25°C can be expected.

Irradiance can also vary considerably from the STC value of 1000 W/m^2. Of particular note are occasions when the irradiance rises above this level. A clear atmosphere and cloud enhancement effects can raise the irradiance above the STC value.

2.1 Maximum Voltage

The maximum voltage V_{oc} of a PV array occurs when the modules are open circuit. This voltage is increased above the rated STC value as the cell temperature drops below the STC temperature of 25°C. The amount of variation with respect to temperature depends upon the module type and cell material.

For example, a module with a temperature coefficient of 80 mV/°C, would see an increase in V_{oc} of 2 V at 0°C. For a series string of 10 such modules, this would result in an increased string voltage of 20 V.

2.2 Maximum Current

The maximum current I_{sc} generated by a PV array occurs under short circuit conditions. This current is affected most significantly by irradiance fluctuations and to a lesser extent by temperature changes.

Irradiance may increase above the STC value of 1000 W/m^2, taking the I_{sc} current above the rated value. This can occur around midday when the sun is at its highest, in very clear atmospheric conditions, and from enhancement from cloud or snow reflections.

2.3 Multiplication Factors

The standard approach to accommodating such increases in voltage and current is to apply a multiplication factor to the V_{oc}/I_{sc} quoted by the module manufacturer. *The resultant string/array voltage and current ratings are a minimum requirement for all parts of the DC system.*

2.3.1 Voltage Multiplication Factor – Mono/Multi Crystalline Silicon Modules

A multiplication factor of 1.15 is commonly used [1, 2, 5] but multiplication factors above this are used in some national codes. A range of multiplication factors, up to 1.25, is provided in the US code to accommodate regions with varying climatic conditions [3].

2.3.2 Current Multiplication Factor – Mono/Multi Crystalline Silicon Modules

A multiplication factor of 1.25 is stated in reference [1] and is commonly used in many national codes. However, multiplication factors above this value are also sometimes used.

2.3.3 Multiplication Factors – Other Modules

As discussed in Part IIc, some types of PV modules have temperature coefficients considerably different to those constructed of crystalline silicon cells. The effects of increased irradiance may also be more pronounced. In such cases the multiplication factors used for crystalline silicon modules may not cover the possible increase in voltage or current. In addition, some module types have an electrical output that is significantly elevated during the first weeks of operation. This increase is additional to that produced by temperature/irradiance variation. Typically, operation during this period will take V_{oc} and I_{sc} (and the output power P_{mmp}) well above any value calculated using a standard multiplication factor.

In such cases, specific calculations of worst case V_{oc} and I_{sc} must be performed. These must allow for the worst case temperature range and an irradiance of at least 1250 W/m^2. Calculations must also include a calculation of any increase in V_{oc} or I_{sc} over the initial period of operation.

2.4 Device Ratings

The calculations in Section 2.3 enable a system designer to assess the voltage and current maxima that may occur under normal, non faulted conditions. Following these calculations the designer will then ensure:

- Module maximum operating voltage is not exceeded (i.e. number of modules in string is selected to ensure string voltage will not exceed rating of modules within the string).
- Electronic components such as inverters are within operating range (e.g. string open circuit voltage will not exceed inverter maximum DC rating).
- All cables have suitable voltage and current ratings (after any de-rating factors applied).
- All switchgear is rated for DC operation at voltage and current maxima.
- All fuses are suitably rated.
- Any plugs/sockets or disconnecting means are suitably rated.
- Any other parts in DC system are suitably rated.

It is important to note that the DC voltage and current ratings of array components, particularly overcurrent protection devices and switchgear, must be checked. Devices will typically have DC ratings lower than their AC ratings, as a DC arc is more difficult to extinguish than one of AC (since the DC current does not pass through zero as with an AC current).

It should be noted that splitting an array into a number of smaller sub arrays to reduce the maximum shock voltage is sometimes considered at this stage. Such a reduction in voltage also enables the use of lower rated system components.

3 Array Fault Protection

The following analysis is directed towards faults arising where the PV array provides the only source of fault current, such as in a typical grid connected

system with no battery. For a system with a battery or other source of fault current see also Section 3.6.

The conventional means of automatic disconnection of supply under fault conditions is to rely upon a circuit protective device such as a fuse to clear the fault current. However, the current limiting nature of a PV circuit means that conventional protection measures are difficult to apply. The short circuit current of a module is little more than the operating current, so a circuit fuse would simply not operate to clear a short circuit fault.

3.1 Fault Scenarios

3.1.1 Earth Faults

Earth faults may occur due to a number of reasons. For example, faults can arise in cabling from a stray wire touching an earthed framework, cable insulation damaged during installation, corrosion, impact or abrasion damage. Earth faults may also develop within PV modules – for example through deteriorating sealant, faulty insulation on a metal backed roofing laminate, impact damage, or from water ingress and corrosion within a junction box.

In an ungrounded system (where none of the PV array cables have been intentionally earthed), two earth faults are required to create a fault current. Such an occurrence may be rare and can be minimised by good system design and installation practice. However, such faults can be difficult to detect and may develop over time.

3.1.2 Line Faults

While generally less likely, other fault circuits can develop. Such faults are often classed as line-line faults where string or array output cables become shorted. Such faults may occur as a result of cable insulation failure (from impact, abrasion or installation damage) or from faults developing in the DC junction box, DC disconnect or inverter (through mechanical damage, water ingress and corrosion).

3.1.3 Variations in String Voltages

Significant differences between the voltages on parallel strings, particularly at a time when the inverter or load is switched off can cause reverse currents to flow in an affected string. This can be caused by factors such as damaged or faulty modules, and complete or partial covering of a string, such as by a fall of snow.

3.2 Fault Analysis

For the purposes of looking at fault conditions, an example of an earth fault is considered. Such a fault provides a case with both cable overloading and module reverse currents. Figure 1 depicts a PV system consisting of three parallel connected strings, with the PV string cables commoned in separate DC junction

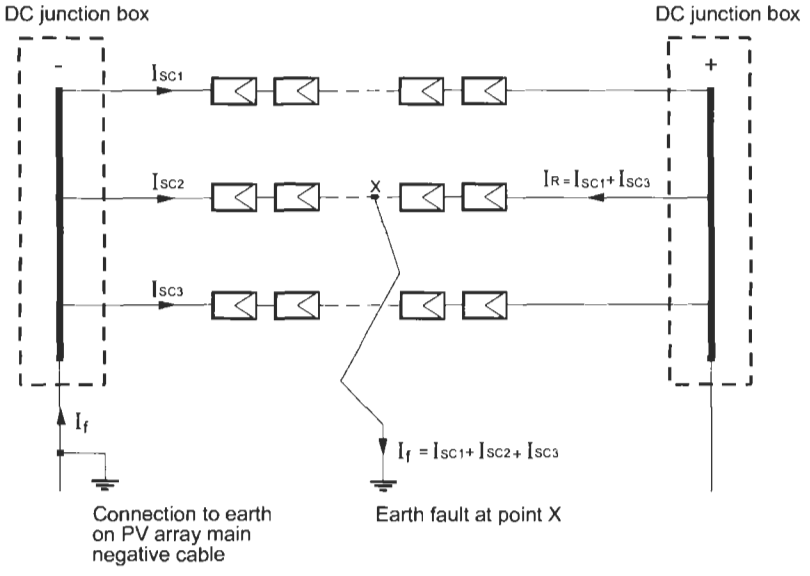

Figure 1 Schematic diagram of a PV system with three parallel strings.

boxes. Under normal conditions, the maximum current in each string cable is equal to I_{sc} of the modules used in the string.

In this floating system with no reference to earth, two earth faults are required to create a fault current. For example, if a long-standing earth fault in the PV array main negative cable is combined with a new fault at a point along a PV string (marked 'X' on the diagram) then fault currents will flow.

3.2.1 Maximum String Cable Fault Current

The maximum fault through any of the string cabling in the system of Figure 1 is that of I_R flowing to point X from the two non-faulty strings. I_R is the sum of the short circuit current flowing in these strings. In a system with nominally identical modules this fault current is then $2 \times I_{sc}$. For a system of n strings, this fault current is $(n - 1) \times I_{sc}$.

For a system without string fuses to clear the fault, this fault current may exceed the current carrying capabilities of the string cable and present a fire risk.

3.2.2 Maximum Fault Current

The only point in the fault circuit illustrated, where fault currents exceed those in the string cables, is I_f in the PV array main negative cable (see Figure 1). Under all circumstances, this fault current cannot exceed that of $3 \times I_{sc}(max)$, for an array of 3 strings, or $n \times I_{sc}(max)$ for an array of n strings, where $I_{sc}(max)$ is the maximum value of short circuit current, calculated after applying the appropriate multiplication factor as discussed in Section 2. As the PV array main cables should be sized for $I_{sc}(max)$ for the entire array, these cables will not be overloaded under fault conditions.

3.2.3 PV Module Reverse Currents

In the illustration given, a number of the PV modules in the faulty string have a reverse current flowing through them. The magnitude of this current is the same as that flowing through the string cable: $I_R = (n - 1) \times I_{sc}$ (see Figure 1).

Module reverse currents can cause heat build up, damage to the affected modules and may present a fire risk. Very high temperatures, melted encapsulant and module delamination have all been observed under significant reverse current events.

3.3 String Cable Protection

From the fault analysis above it can be seen that for a system of n parallel connected strings, with each formed of m series connected modules, string cables need to be rated at a minimum of:

$$\text{Voltage} = V_{oc}(max) \times m$$

$$\text{Current} = I_{sc}(max) \times (n - 1)$$

where $V_{oc}(max)$ is the maximum voltage at open circuit as calculated in Section 2.

Such cable oversizing provides a method of overload protection for the string cables by ensuring that the maximum potential fault current can be safely accommodated. This method does not clear the fault; it simply prevents a fire risk from overloaded string cables.

3.4 Module Reverse Current Protection (String Fuses)

Reverse current protection measures need to be adopted where the number of strings in the array means that the maximum rated module reverse current (as provided by the manufacturer) could be exceeded under fault conditions.

It is seen that the maximum module reverse current to be experienced under fault conditions $I_R = (n - 1) \times I_{sc}(max)$ (see Figure 1). Typical crystalline silicon modules are rated for reverse currents of at least $2 \times I_{sc}(max)$. Hence, a fault in an array formed of 4 or more strings could lead to reverse currents greater than the maximum reverse current rating of such modules.

In the case of standard crystalline silicon modules, it is a common practice to specify string fuses for all arrays of 4 or more strings and to rely on cable oversizing for fault protection in arrays of 3 or fewer strings.

With other module types, the reverse current rating provided by the manufacturer may permit more than 3 strings to be installed without string fuses. In such cases, the number of strings that may be connected without the use of fuses is calculated by ensuring $I_{mr} > I_{sc}(max) \times (n - 1)$, where I_{mr} is the maximum permitted reverse current quoted by the module manufacturer and $I_{sc}(max)$, as before, is the calculated worst case short circuit current.

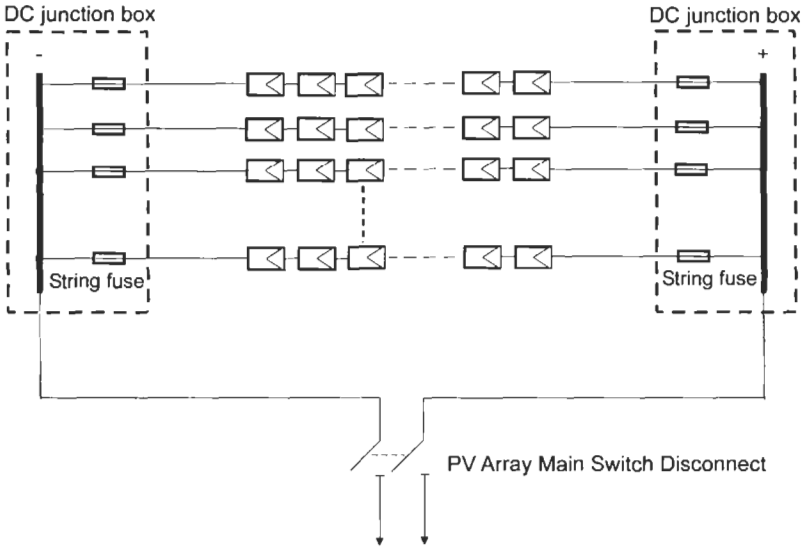

Figure 2 Typical array schematic with multiple strings.

In Figure 2 a string fuse in the positive leg of the string cabling would be required to clear the fault. However, if the earth fault at X were combined instead with an earth fault in the main positive cable (rather than in the negative cable as shown), this could only be cleared by a fuse in the negative leg.

Key requirements when selecting a string fuse are as follows:

- String fuses are required in both the positive and negative legs of the string cabling.
- The string fuse must be rated for operation at DC.
- The string fuse must be rated for operation at $V_{oc}(max) \times m$.
- The string fuse must have a tripping current which is less than the module reverse current rating.

Recommended switching and fusing practices in PV systems can be found in reference [3]. The use of circuit breakers may also be acceptable provided they meet the above criteria and are rated for operation with currents in either direction.

3.5 Blocking Diodes

Blocking diodes are sometimes specified in a PV array to prevent reverse currents, though should not be seen as a substitute for an overcurrent protective device. One application is to prevent losses in a battery system at night, however most modern charge controllers usually prevent such reverse currents in any case. Chapter IIIa-1 should be consulted for a further discussion of this topic.

3.6 Fault Protection with an Additional Source of Fault Current

Systems with any other source of fault current will need additional fault protection to that outlined above. With PV systems a typical fault current source will be that of a battery, however other fault current sources may also be present - for example, some grid-connect inverters. Most system designs assume these inverters not to be capable of any backfeed fault; however, some inverter designs may be capable of such faults.

Standard circuit design is to be applied for fault protection of other fault current sources. With a battery system it is important to ensure that any fuse or circuit breaker is rated to interrupt the very high fault currents that a battery can generate under short circuit conditions. Standard AC fuses are sometimes used on battery systems – not only are these fuses very often not DC rated, they may also not be capable of interrupting the high battery fault currents.

4 Earthing Issues

Earthing practice varies considerably and the local code must be applied when designing a PV electrical system. Earthing of electrical installations is performed to minimise electrical shock hazards and the risk of fire from faulted systems (see Table 1). It is also performed to provide a degree of surge protection and to reduce the effects of EMI.

The earthing of a PV system needs special consideration because, as discussed above, fault currents may not be detected or cleared using conventional circuit protection measures.

In the PV system, two items need consideration:

1. Earthing of exposed conductive parts which are not energised during normal operation – e.g. earthing of an array frame. This is often referred to as *equipment earthing*.
2. Earthing of the PV DC circuit (an intentional connection to earth at some point of one of the current carrying conductors in the PV system). This is often referred to as *system earthing*.

4.1 Equipment Earthing

The intention of equipment earthing is twofold: to provide protection against indirect contact and to provide the system with a degree of surge/EMI protection. The typical equipment earth decision is whether the PV array frame needs to be connected to earth.

Most international codes specify that equipment conductive parts must be bonded together and connected to earth to minimise electric shock hazard. Equipment earthing is not required where the equipment is of class II construction.

Table 1

	System earth	No system earth
Earth fault	Single fault will result in a fault current	A single fault to earth will not cause a fault current
	System will not operate as normal	Fault may not be detected and system may operate as normal
Fire hazard	Single earth fault results in fault current	Best protection as two faults are required for a fault current to flow
	Higher probability of fire	
Shock hazard	System referenced to ground, so high risk of shock from contact with a live part	With no reference to ground (in ideal case) contact with a live part cannot generate a shock current
	Shock risk may be reduced by use of nonconductive enclosures, etc	In real conditions, leakage paths/capacitive coupling may provide a shock current

In most circumstances the requirement for equipment earthing is clear. However in some circumstances, the extension of the equipotential zone that is a result of such a decision must be carefully considered.

4.2 System Earthing

This is the practice of bonding one part of the DC current conductors to earth (e.g. earth connection at mid point of PV string or earthed DC negative). System earthing practices and regulations vary considerably.

In most cases the decision to provide system earthing will be determined by the local code. Products such as grid connect inverters are designed to work when installed to the local code – care must be taken when considering the use of such items to ensure that they are will work if installed with a different system earthing arrangement.

5 Protection by Design

Prevention of faults by good design and the appropriate selection of system components, coupled with careful installation, provides the best means of fault prevention.

The DC wiring of an array should be specified so as to minimise the risk of faults occurring. This can be achieved, for example, by either the use single core insulated and sheathed cables (sometimes referred to as double insulated cable, Figure 3); single core basic insulated cable with an earthed armour or screen (Figure 4); or the use of insulated cable where the cables of opposite poles are laid in separate ducts or conduits (Figure 5).

Array cables should also be selected to ensure that they are properly rated for the environment in which they will be installed. For example, module interconnect cables must have sufficient UV and temperature ratings.

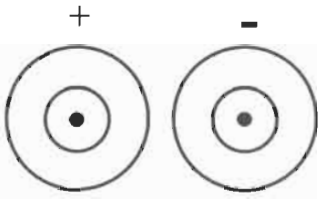

Figure 3 Single core insulated and sheathed cables.

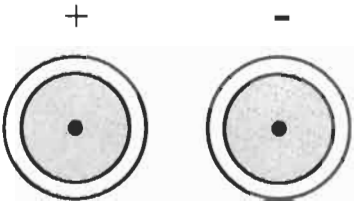

Figure 4 Single core basic insulated cable with an earthed armour or screen.

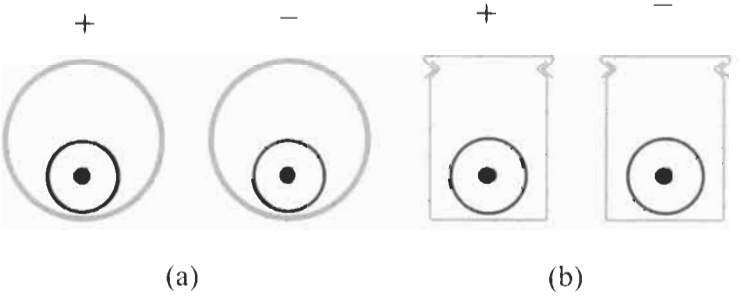

Figure 5 Insulated cable where the cables of opposite poles are laid in separate ducts (a) or conduits (b).

The short circuit protection afforded by double insulated cables also needs to be maintained in the construction and makeup of DC junction boxes and switch assemblies. Short circuit protection may be provided by:

- Fabrication of the enclosure from non conductive material.
- Positive and negative buses adequately separated within the enclosure and/or by a suitably sized insulating plate, or separate positive and negative junction boxes.
- Cable and terminal layout such that short circuits during installation and subsequent maintenance are extremely difficult.

6 Labelling

A PV array circuit cannot be turned off – terminals will remain live at all times during daylight hours. It is important to ensure that anyone opening any enclosure within the DC system is fully aware of this.

It is good practice to ensure that all parts of the system are suitably labelled to warn of this hazard, e.g. '*Danger, contains live parts during daylight*'. All labels should be clear, easily visible and constructed to last and remain legible as long as the enclosure.

References

[1] IEC standard 60364 – Part 7-712. Electrical Installations of Buildings. Special Installations or locations – Solar photovoltaic (PV) power supply systems.

[2] *Photovoltaics in Buildings. Guide to the Installation of PV Systems*, 2002. DTI/Pub URN 02/788, UK.

[3] NFPA 70. National Electrical Code (NEC), 1999. National Fire Protection Association, Quincy, MA 02269, USA.

[4] PV System Installation and Grid-Interconnection Guidelines in Selected IEA Countries. International Energy Agency Report IEA PVPS T5-04-2001.

[5] *Guidelines for the Electrical Installation of Grid Connected Photovoltaic (PV) Systems*. EnergieNed and NOVEM, The Netherlands.

Part IIId

Space and Concentrator Systems

Concentrator Systems

Gabriel Sala, Instituto de Energia Solar,
Universidad Politecnica de Madrid, Spain

1 Objectives of PV Concentration

The aim of combining solar cells with concentration systems is an attempt to reduce the cost of the electrical energy produced. Once this principal goal has been stated several aspects of this statement can be discussed in more detail.

On the one hand, PV concentrators reduce the fraction of the cell's cost in the total system cost, by substituting the area of expensive cells by less expensive collectors. This has been historically the first step in the development of concentrators, using mainly silicon concentrator solar cells (Figure 1).

On the other hand, concentration has more recently been seen as the only way to accept, into the commercial sphere, new generations of highly sophisticated solar cells. At he same time, these are very efficient, but also very expensive. Without the adoption of concentration as the operating mode these extremely expensive cells cannot be utilised. But by increasing the densities of light (irradiance or W/m^2) in excess of 1000 times over the standard one-sun solar radiation, the cell cost per unit of output power becomes acceptable. The higher efficiency then compensates for the cell cost achieving an overall cost reduction of the system.

Since cost reduction is the prime objective of PV concentration, let us examine a simple expression for the cost of energy produced by a concentrator system [1, 2]:

$$C_{kWh}\left(\frac{\$}{kWh}\right) = \frac{Array + \frac{Cell}{X}}{Collected\ energy.\eta_{op}.\eta_{cell}.PR} Return\ rate \qquad (1)$$

where: *Array* is the cost of the optics, the tracking structure, the heat sink, and of the driving control system, per m^2, *Cell* is the cost per unit area of the cells, per $/m^2$, X is the geometrical concentration (i.e. the ratio of the area of the collector

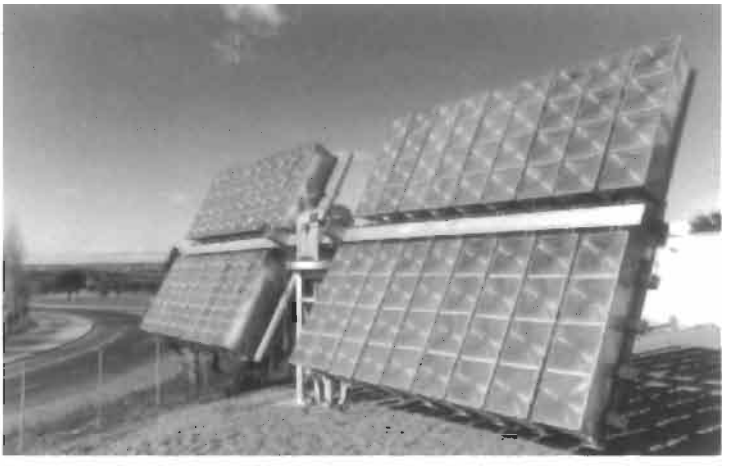

Figure 1 The Ramón Areces array (Madrid, 1980). One of the first 2 axis tracking European PV concentrators made following the ideas of the early Sandia I and II (USA, 1978). It uses patented hybrid glass-silicone Fresnel lenses and 50 mm diameter Si cells at 38×.

to the area of the solar cells). *Collected energy* is the direct radiation incident on the collector optics (depends on tracking strategy), in kWh/m^2 per year, η_{op} is the optical efficiency of the collector (i.e. the ratio of power incident on the receiver divided by the power incident on the collector), η_{cell} is the efficiency of the cell at standard test conditions (STC), *PR* is the performance ratio. This accounts for the losses at operating conditions of the cells over the losses at STC. Typically, PR is 0.70, including all balance-of-system (BOS) loses. A discussion of the balance of system components is deferred to Section 3. *Return rate* is the annuity over 20 years of the total capital invested (usually taken as 6% per year in Europe).

From this expression we understand that the cell cost contribution becomes less significant as the concentration level increases. It is also clear that the efficiencies are the key figures for cost reduction because they affect all components of the generator including the land needed to deploy the collectors. Typical figures for each term in Equation (1) are shown in Table 1 for different systems.

2 Physical Principles of PV Concentration

Solar cells generate a current (in A) proportional to the total power of light absorbed (in W). Assuming that the spectrum of light is kept the same, the electrical current supplied by the cell exactly at short circuit will follow a linear law up to a very high incident light power, i.e. up to several thousand times the normal sunlight [3, 4].

The intensity of light incident on a surface is commonly expressed by the value of the *irradiance* (W/m^2), that is, the power received per unit of area normal to the light rays. The effective concentration level, *C*, is usually defined as the ratio of the averaged irradiance on the PV receiver divided by the direct irradiance on the collector optics, and is measured as:

$$C = \frac{I_{sc}(\textit{under concentration})(A)}{I_{sc}(@1000W/m^2)(A)} = \frac{I_{sc}(C)}{I_{sc}(1)} \tag{2}$$

where I_{sc} is the short circuit current of the receiver cell under concentrated light or under the standard irradiance of 1000 W/m^2, as indicated in brackets. The irradiance of 1000 W/m^2 is usually referred to as '1 sun'.

Table 1 Typical values of PV concentrator cost components [1, 2, 11]

System concentration level	Solar cell type	Collector (euros/m^2)	Cell cost (euros/m^2)	X	η_{opt} (%)	η_{cell} (%) at STC
Low concentration	Silicon	150	200–500	10–40	80	20
High concentration	Silicon	200	15,000	300	80	26
Very high concentration	III–V single-junction	300–400	40,000	1000	80	28
Very high concentration	III–V multi-junction	300–400	80,000	> 2000	80	35

We can now define the optical efficiency, η_{op} as:

$$C = \eta_{op} X \tag{3}$$

For single junction cells (for example, cells made from crystalline silicon or III–V semiconductors) the variation of the spectral composition of natural sunlight can cause variations in the cell current of about 3% – a value which is insignificant for practical purposes.

In contrast, the output voltage increases as a result of the larger current relative to 1 sun conditions as:

$$\Delta V = \frac{kT}{q} \ln C = \frac{kT}{q} \frac{I_{sc}(C)}{I_{sc}(1)} \tag{4}$$

where ΔV is the increase of voltage, kT/q is the thermal voltage ~0.026 V at 25°C, lnC is the natural (Napier) logarithm of the effective concentration, $Isc(C)$ and $Ics(1)$ are the short-circuit currents at C and 1 sun, respectively.

Combining Equations (2) and (4) we deduce that the efficiency of a cell should be higher under concentration than at 1 sun. However, the unavoidable series resistance of solar cells dissipates power according to the expression:

$$P_{loss}(C) = I_{mp}^2(C) R_s = C^2 I_{mp}^2(1).Rs = C^2.P_{loss}(1) \tag{5}$$

In other words, for 10× concentration, the losses due to R_s are 100 times larger than at 1 sun. For this reason, special contact grid patterns must be designed to reduce the series resistance of C cells at least C times to maintain the same ratio of power losses to the power generated. The series resistance is the main physical parameter that prevents the use of cells designed for flat modules to operate efficiently under concentration.

The curve of Figure 2 provides a simple method for the determination of the series resistance of a cell, receiver or array, by measuring the negative slope of the curve at high concentration levels. The series resistance is given approximately by:

$$R_s \cong \frac{\eta(C_2) - \eta(C_1)}{C_1 - C_2} \cdot \frac{I_{mp}^2(1)}{A_r E(1)} \tag{6}$$

where $\eta(C_1)$ and $\eta(C_2)$ are two values of efficiency of the curve to the right of the maximum, C_1 and C_2 are the abscissas of these points, A_r is the area of the receiving cell, $E(1)$ is the average irradiance at 1 sun (= 0.1 W/cm^2), and I_{mp} is the cell current at the maximum power point at 1 sun ($I_{mp} = 0.95\ I_{sc}$).

Figure 3 shows a set of I–V curves for a C-cell under concentration. Figure 4 compares the I–V curves for a conventional cell under 1 sun and under concentration.

An implicit drawback of concentration is that the density of power which has to be dissipated as heat increases proportionally with C while the surface area of

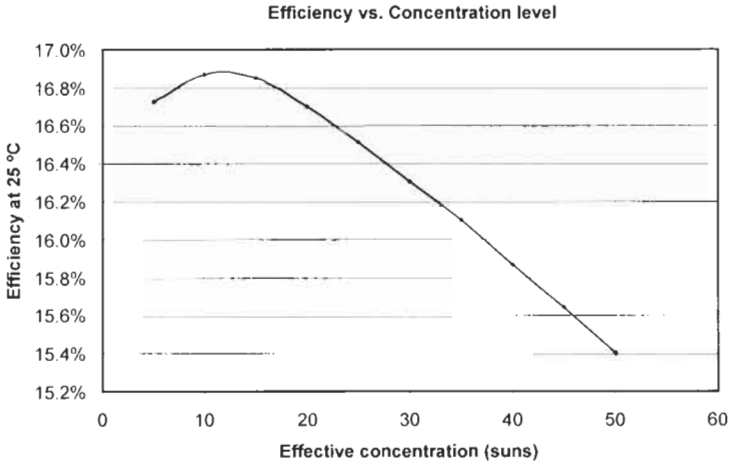

Figure 2 Variation of cell efficiency as a function of the concentration level. The maximum is obtained for 15 suns. The continuous drop after the maximum is caused by series resistance losses [4]. (Obtained by the author on a rejected Euclides-Tenerife cell.)

the receiver which is available to exchange the heat with the surrounding air is fixed. Special heat sinks are therefore required to hold the cell temperatures sufficiently low to maintain an acceptable value of the efficiency. Figure 5 shows the heat sink of the Madrid EUCLIDES prototype.

The series resistance constitutes the most serious limit to concentration for classical silicon n^+pp^+ structures because the base cannot be made sufficiently thin, and this resistance term cannot be reduced with any grid design. However, this limitation does not apply to the silicon Back Point Contact solar cells which maintain effective operation up to 400× (see Chapter IId-2). In contrast, recent III–V cells have been operated at concentrations up to 5900× and many experiments in the range 500× to 2000× are currently under way.

The secret to withstanding such intensities without series resistance problems nor thermal limitations is to use very small solar cells, of area in the range 1–2 mm^2 (Figure 6).

3 Description of a Typical Concentrator: Components and Operation

A PV concentrator consists of two principal elements: the optical collector and the cell receiver (Figure 7).The collector can be a mirror, a lens or a combination of both. The cells must be designed for the irradiance level which will be received by the focus from the collector, and they must be thermally bonded to a heat sink in order to remove the energy not converted into electricity. The wires must also be of sufficient thickness to carry the large currents generated. The thermal bond to heat sink must be compatible with a good electrical insulation which is sometimes a difficult compromise.

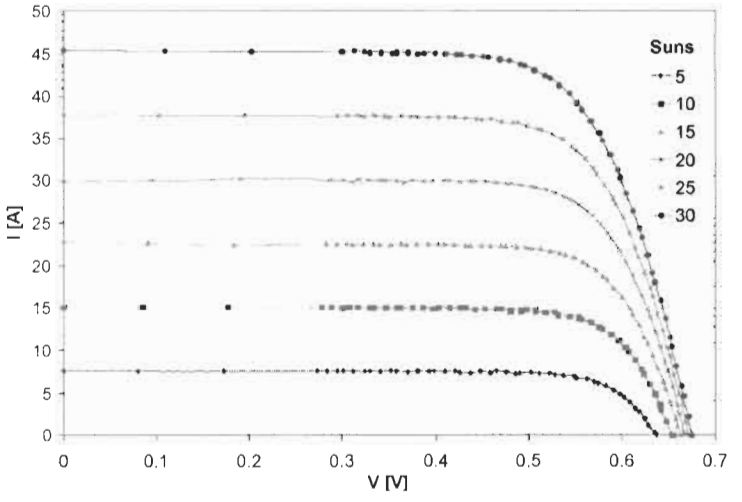

Figure 3 I–V curves of the EUCLIDES cells at several concentrations obtained with a multiflash test [11]. Note the increase of V_{oc} with concentration and the linearity of I_{sc} as a function of the concentration level (expressed in suns).

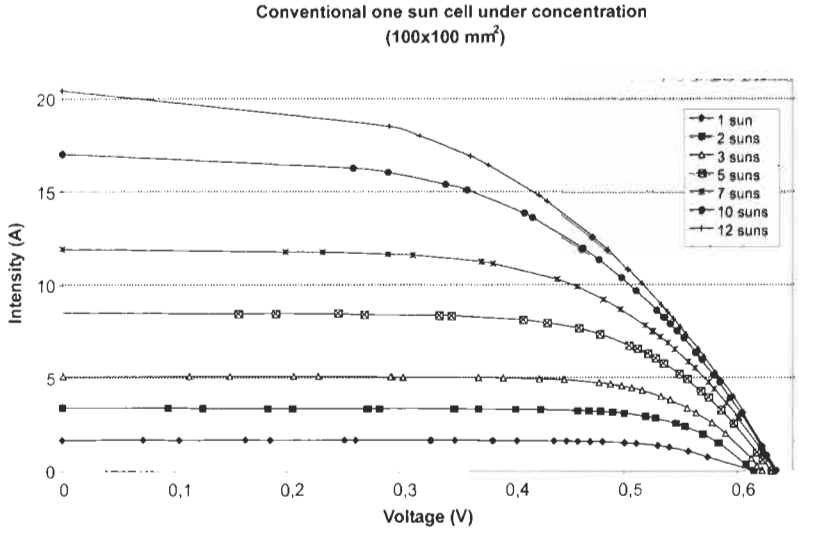

Figure 4 The efficiency of 1 sun cells drops dramatically when used under concentration due to series resistance: the efficiency of 14.6% at 1 sun becomes 10.3% at 12 suns.

The collector, receiver and heat sink as a whole are commonly known as the 'concentrator module'. This is the smallest part of the system that includes all direct current generating components. The rest of the C-system components are called the Balance of System (BOS).

The module must, in general, be directed towards the sun in order to cast the focussed direct light beam on the receiver. As a result, the C-systems require a

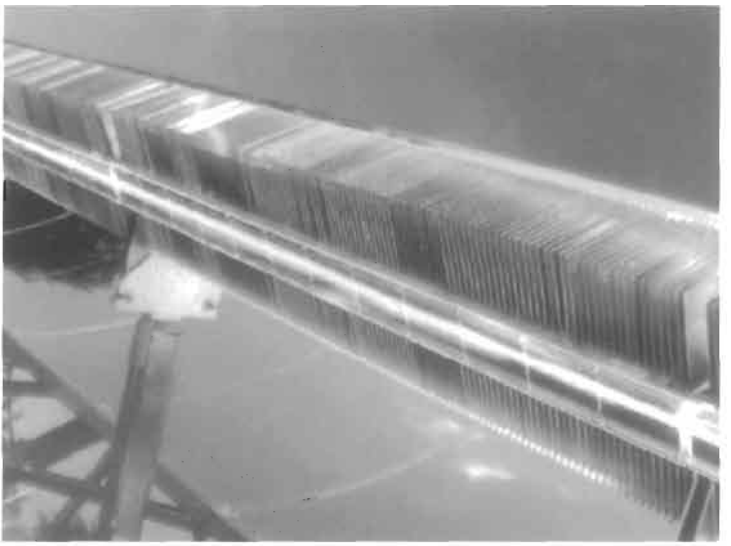

Figure 5 Close view of the EUCLIDES receiver (Madrid). You can see the focused light on a module glued to an optimal thin fins heat sink made of aluminium.

mobile structure to point them continuously towards the sun. Concentrator systems, except those with a high acceptance angle, cannot collect diffuse radiation, but this drawback is compensated for by the orientation of the collector towards the sun at all times.

As an example of a concentrator PV System, Figures 8–10 illustrate the principles of the single-axis tracking parabolic trough concentrator, and show the main components.

4 Classification of Concentrator Systems

The classification of concentrator systems is a complex task because of the number of different criteria according to which this can be done: the concentration level, the optical component (lenses or mirror), the shape of the optics (point focus, linear, etc.), the cell material or the cell structure (silicon, III–V semiconductors, single-junction, multi-junction), or the tracking strategy (two axis, single axis, stationary, quasi-stationary, etc.).

Among the large variety of concentrator systems that have been developed for research and demonstration, five specific combinations are sufficient to represent the tendencies and prototypes which are of interest today. These are listed in Table 2, and a picture of each is shown in Figures 10–14. The typical combinations of materials, concentration levels, cells tracking, etc. used for each type are presented in Table 2.

The experience during the last 20 years has not been sufficient in determining the level of concentration or which collector or tracking driver might be best.

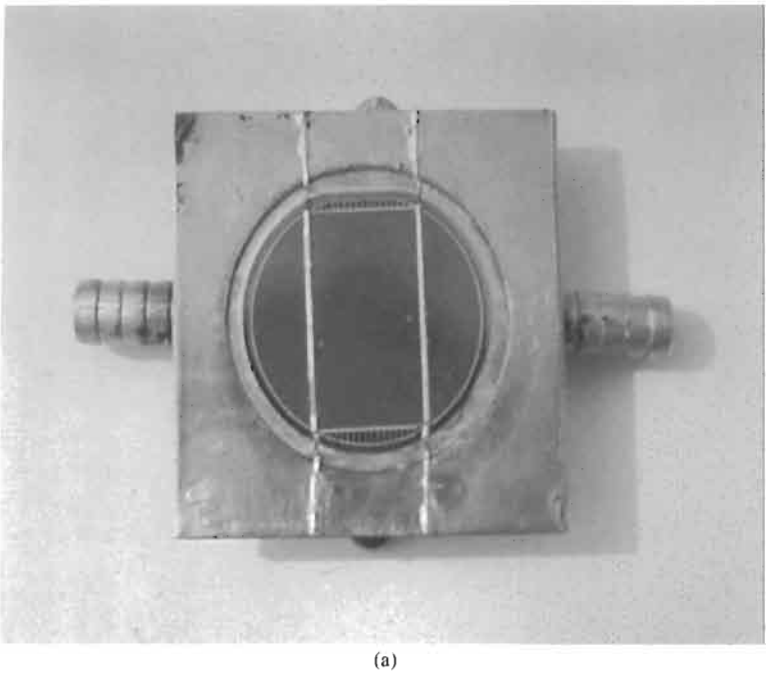

(a)

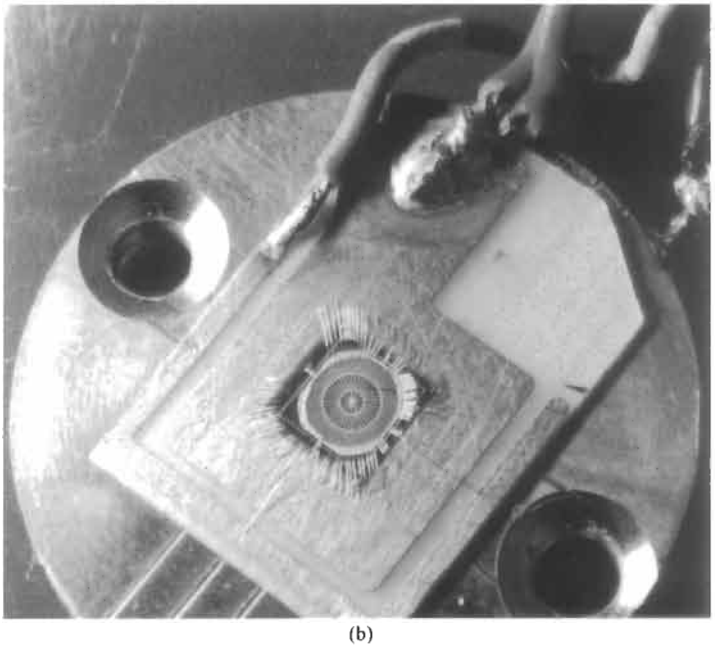

(b)

Figure 6 (a) Silicon concentrator cell, sized 5 cm diameter able to operate at 50×. This cell was actively cooled for testing purposes. Project MINER (Madrid, 1982). (b) GaAs solar cell with AlGaAs window made at IES (Madrid, 1995). This device demonstrates that operation over 1000× can be achieved without thermal problems if the cell is sufficiently small (0.1 cm^2, operating at 1290 suns, 23% efficiency).

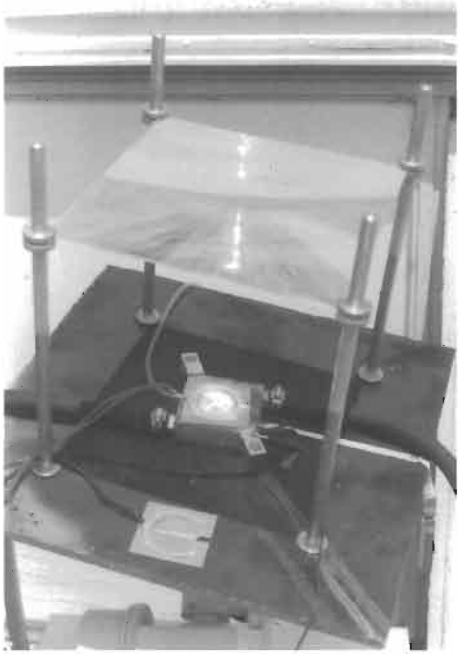

Figure 7 Concentrator test setup showing the principal sub-systems: lens, cell and heat sink (here actively cooled with water). Note that the cell requires suitable thermal and electrical connectors. (IES, 1978).

This lack of conclusion is probably due to the scarcity and diversity of experiments that have been carried out. However, the road to achieving competitiveness with the conventional energy sources should be based on a high overall system efficiency in which the cell cost share is below 15% of the total system cost.

The low and medium level concentration systems (from 2× to 40×) can reach probably this cost objective with inexpensive 20% efficient cells (crystalline silicon cells). The new multijunction and other third generation cells can reach these goals at over 1000× concentration, if the cell cost remains, as before, below 15% of total system cost. Currently, there are 34% efficient cells, operating at 400×, but suitable for concentrations up to 2000×. However, their cost is still too high and there is limited experience with outdoor systems. Notwithstanding, the mini-concentrators which are used in these very high concentration cells allow the genuine modularity of PV systems. This can be the key to the market penetration of concentrators as they need not compete with the conventional energy generators in the same way as the larger C systems do.

5 Tracking Control Strategies

PV concentrators converts only the light which comes directly from the solar disc because only the incident set of rays within a limited solid angle can reach

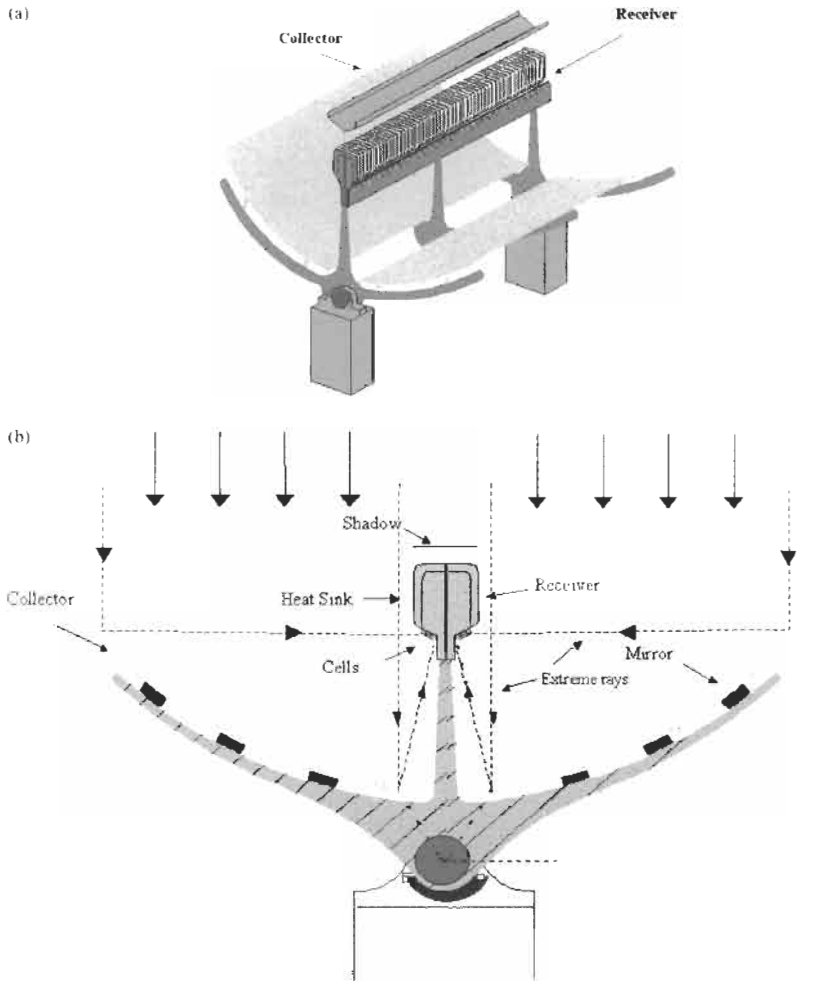

Figure 8 (a) Example of one C-array composed by two C-modules as used in EUCLIDES System. The collector is a line-focus parabolic mirror. The receiver consists of a heat sink and a linear cell assembly. (b) Frontal view of the EUCLIDES array showing the sun rays reflecting in the collector and striking the receiver.

the receiver. The laws of thermodynamics state that the maximum achievable concentration level is linked to the acceptance angle of a concentrator by [5]:

$$C \leqslant \frac{n^2}{\sin^2 \theta} \quad \text{for point focus C-system} \tag{4}$$

$$C \leqslant \frac{n}{\sin \theta} \quad \text{for linear C-system} \tag{5}$$

where θ is the half-acceptance angle and n the index of refraction of the transparent material surrounding the solar cell. The actual limits, however, are several times lower for many practical concentrators.

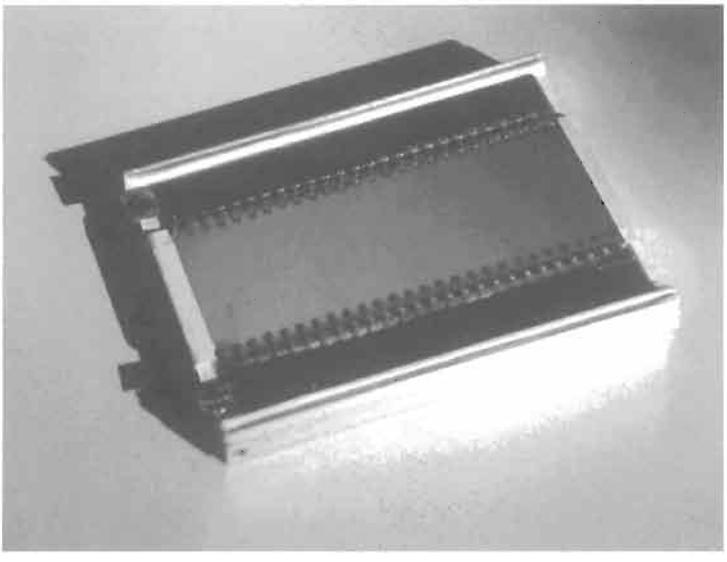

Figure 9 The picture shows a section of a EUCLIDES receiving module before final encapsulation and sealing. (Courtesy of BP Solar Ltd.)

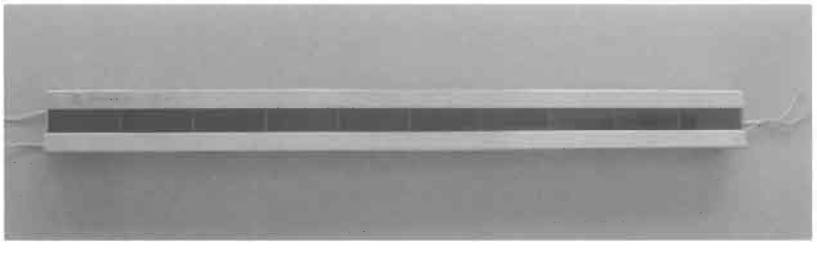

Figure 10 A complete EUCLIDES Module. Output wires emerge from the back side allowing continuity at the receiver plane. (Courtesy of BP Solar Ltd.)

The limited acceptance angle of concentrators requires that the collector is oriented towards the solar disc. According to Equations (4) and (5), the accuracy of such orientation is related to the concentration level and the optical design. As a result, the concentrators must be built on mechanically driven structures which are able to turn the collector to face the sun (Figure 15).

If the collector surface must be normal to the sun, 'two-axis' tracking is required. As an alternative, single axis strategies achieve good performance with linear reflective concentrators or with low gain linear lenses (Figure 16).

Table 3 shows the energy collected by tracking systems and by a static flat panel tilted at the angle of latitude towards the equator.

Another subject of interest concerns the strategies which can be employed so that the mobile mechanical structure tracks the sun every moment of the day with a given accuracy (for example, under $\pm 0.2°$). Two principal methods are commonly adopted:

Table 2

Reference concentrator type	Optics	Cell assembly	Cell type	Concentration ratio	Cooling	Tracking
Point focus on a single solar cell	Fresnel lens	One single cell or several cells with spectral beam splitting	Uni-junction silicon or uni-junction III–V or multi-junction	$50 < Xg < 500$ for silicon cells. > 500 for all other cells	Passive[a]	Two axis
Large area point focus systems	Big or medium size parabolic dish or central tower power plant	Parquet of cells	Uni-junction silicon or uni-junction III–V or multi-junction	$150 < Xg < 500$	Active	Two axis
Linear systems	Linear lens or parabolic trough	Linear array of cells	Silicon	$15 < Xg < 60$	Passive	One axis for parabolic troughs. Two axis for lenses
Static systems	Non imaging device	Usually linear array of cells	Silicon	$1.5 < Xg < 10$	Passive	No tracking
Compact mini point focus systems	Small lens or small parabolic dish or RXI[b] device	One single cell	Uni-junction silicon or uni-junction III–V or multi-junction	$Xg > 800$	Passive	Two axis

[a] Active cooling cannot be discarded in systems with high concentration ratio.
[b] RXI: refractive and reflective with total internal reflection.

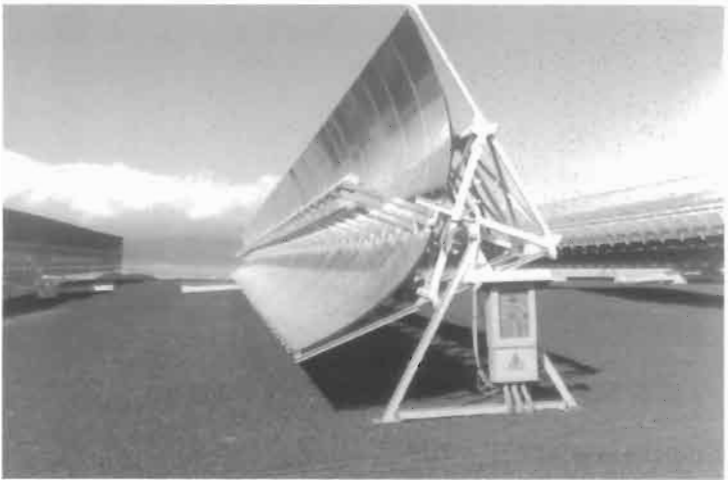

Figure 11 Example of a single axis tracking linear concentrator with a reflective collector. The trough is oriented north to south. EUCLIDES Plant (Tenerife, 1998).

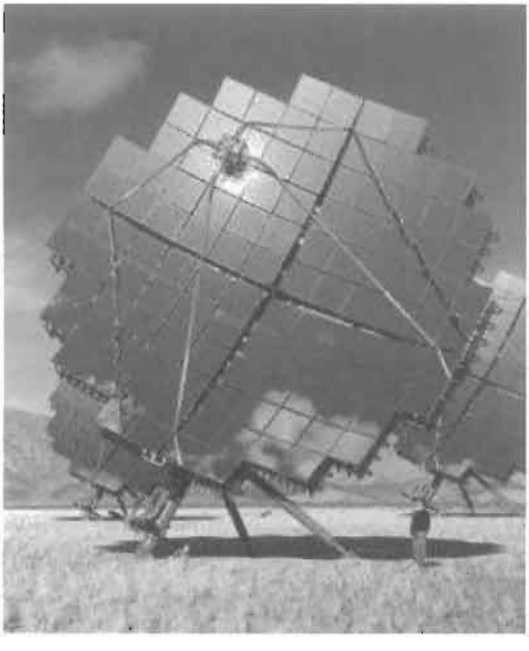

Figure 12 Prototypes of large-area point-focus parabolic dishes. A plant based on this concept will be built in Australia by Solar Systems PTY Ltd, 2002. (Courtesy of Solar Systems Pty Ltd.)

- Control system based on direct detection of the sun position.
- Control system based on the theoretical position of the sun according to astronomical equations and time.

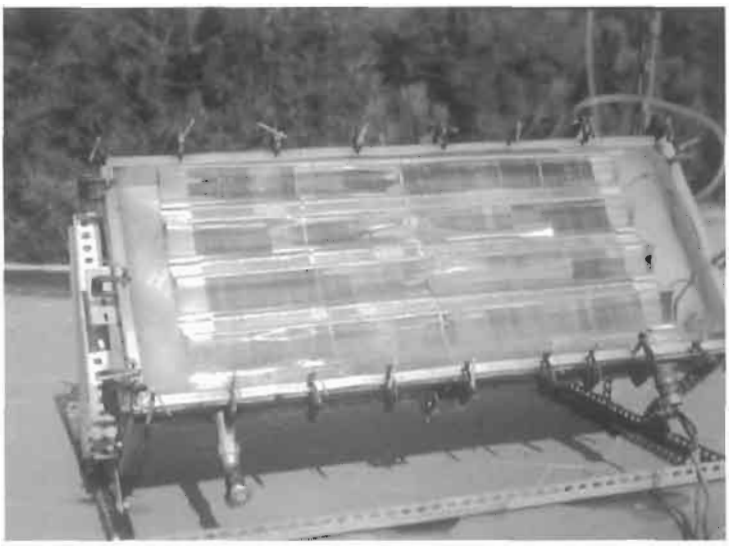

Figure 13 An early prototype of a static concentrator using bifacial cells. The acceptance angle is ± 23°, thus allowing collection of the sun light along its path for the entire year. Bifacial cells provide twice the concentration level for the same acceptance angle than the monofacial cell (IES, 1978).

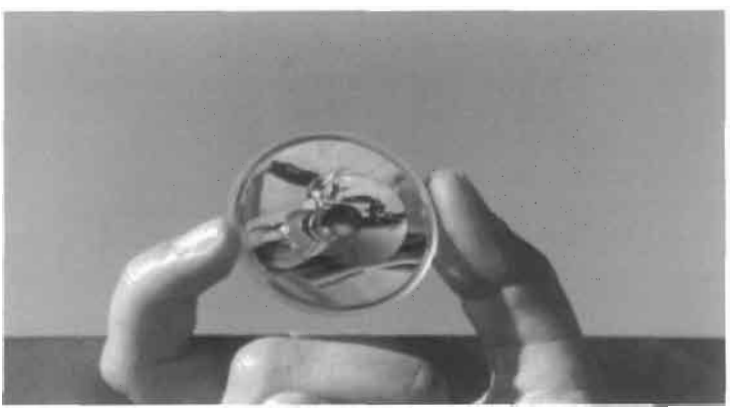

Figure 14 XRI concentrator allowing 1000+x geometric concentration with ± 1.5° acceptance angle. It is envisaged that such compact mini-concentrators will provide adequate optics for high-efficiency third generation micro-cells (IES, 1994).

The direct method is based on sensors that can generate a null signal when pointing directly towards the sun, and some proportional error signal in case of misorientation. [6, 7] A classical servomechanism circuit drives the motors to correct the array position continuously or by steps. Problems with these systems are encountered on cloudy days, and additional circuits are required to turn back the array during the night and to correct the possible miscalibration of the sensors.

Figure 15 A close-up view of a large tracking driver for a single-axis tracking system. The mechanism can carry up to 2000 N and provide a position accuracy of ± 0.05°. The accuracy of the driver is derated by the mechanical deformation of the structure, allowing only ± 0.2° (EUCLIDES-THERMIE Plant, Tenerife, 1998).

The other principal method is based on the astronomical equations [8, 9] and requires just a good clock signal which can currently be supplied by a GPS connection. Another requirement is an accurate zero reference for each axis, and a precise orientation of the axis.

The most onerous requirements of both methods can be eliminated if the electric power output of the system is used as a feedback to adjust and optimise the sun tracking. With such correcting capability the control unit becomes an adaptive system. In this case the concentration array is able to self-learn the sun path, change the values of the circuit variables, and correct errors.

A proposed third tracking method used for very low concentration (2–10×) consists of a thermo-driving mechanism that is at the same time a sensor and a driver. It consists of two metallic cylinders painted black which are located at the extremes of the array. When the array is not normal to sun the cylinders are at different temperature because one of them collects more light, generating a hydraulic force that corrects the orientation until both cylinders are at same temperature. This family of trackers are called 'passive', and those using driving motors are called 'active' trackers.

At present, the solar tracking control circuits and tracking structures are being developed and built principally by prototype makers. However, some companies (INSPIRA, SOLARTRACK, etc.) produce general purpose tracking control systems and mechanisms. [7, 10].

Tracking is considered as a drawback by contractors because:

(a) It adds cost.
(b) It reduces system reliability.
(c) It limits the applications (in houses, on roofs, for example).

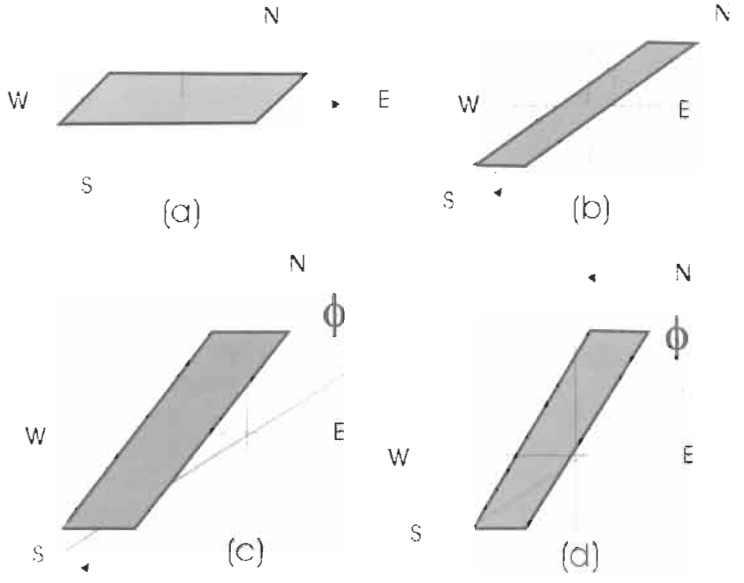

Figure 16 Single-axis tracking strategies: Single axis tracking is only compatible with mirrors, but lenses can be used if geometric concentration is well below 10×.

Table 3 Daily energy collected by an array in Madrid (yearly averages)

Radiation (kWh/m^2 year)	Static tilted 30° to noon[a]	1 axis E/W tracking	1 axis N/S tracking	Polar axis tracking	Two axis tracking
Global	5.20	5.61	6.24	6.87	7.08
Direct (beam)	–	3.48	4.46	4.90	5.15

[a] Due south in the northern hemisphere and north in the southern hemisphere.

However, points (a) and (b) will probably become negligible when experience is gained and quality control is applied to these subsystems.

6 Applications of C-systems

The low (or even non-existent) penetration of C-systems in the market 25 years after the demonstration of the first modern prototype shows that concentrator systems are not suitable for the current applications of photovoltaics, i.e. isolated professional applications, rural electrification, grid-connected home systems, etc. (see Part V for further examples).

The cost reduction achieved with early concentrators was due to their use in medium and large plants (between 100 and 2000 kW_p). These figures are today considered as very large in terms of PV solar electricity production, and can only be realised in grid-connected plants that must compete with the conventional sources of electricity.

However, the demonstrated cost in the range of 3 euros/W_p which are in line with the government incentives can change this situation in the short term. In many developing countries, the energy cost is high enough to make PV concentrators (with price in the range of 3 euros/W_p) competitive in comparison with diesel generators because of their lower maintenance and the price stability. Concentrators are often welcome in developing countries because more than 50% of the total cost is a direct local cost, but simplicity and reliability must be assured.

A new set of applications are beginning to appear based on the new high efficiency concentrator systems which use multi-junction solar cells operating at efficiencies of 30% or more. These arrays are as thin as a conventional flat module, with the same physical aspect and weight. The only drawback is the tracking, but since the 'panels' are so light the systems can easily enter the current modular market of few hundreds watts if reliable and very cheap trackers become available.

Figures 17 and 18 shows the largest and most representative PV concentrators PV Plants deployed in the world.

7 Rating and Specification of PV Systems

There are no standards and testing methods to rate concentrator cells, receivers, modules and arrays which are generally accepted at present. However, several methods have been adopted and widely used during the last 20 years.

The rating of concentrator solar cells requires that the cell is connected by thick wires and plates which are able to carry the high currents that flow under

Figure 17 Example of a concentrator array field. Seven of the fourteen parabolic troughs constituting the EUCLIDES demonstration plant installed in Tenerife are shown in this picture (480 kW_p). The plant includes a monitoring station and seven inverters, one for each pair of arrays. The project is supported by the JOULE-THERMIE Programme.

Figure 18 Example of an array field: 100 kW system at CSW Solar Park in Texas made by ENTECH Inc. The plant is composed of four arrays. Each array comprises 72 refractive Concentrator Modules with 220 m^2 total aperture. (Courtesy of Entech Inc.)

concentrated light. At the same time, a heat sink is required to avoid any damage to the cell, and to maintain as closely as possible the reference temperature during the test.

The objective of the rating is to obtain the I–V curve of the cell under reference conditions at the nominal or other concentration levels.

To plot the I–V curve under illumination requires a powerful light source, but the sources of uniform, high intensity illumination are scarce and very expensive. The most frequently recommended light source for concentrator cell measurement is a flash bulb. With a high power flash lamp (3000–6000 W) it is possible to illuminate 1 m^2 at 30× or 1 cm^2 at 2500× with an uniformity better than 2%. The lamp spectrum and its linear evolution along its life can be determined. It allows an interpolation of the actual spectrum between the spectra at the beginning of life and at the end of life.

To plot the complete I-V curve, one point per each flash discharge must be recorded. In addition, several I-V pairs can be obtained during the decay of each flash (lasting several milliseconds), and a complete set of curves at different concentration levels can thus be acquired within a single run. The use of a flash instead of continuous light makes the control of cell temperature much easier, and does not required additional precautions.

Such measurements were used to obtain the plots in Figures 2 and 3. These plots should be compulsory to specify any solar cell for C applications.

The test of single junction cells for practical use is not highly sensitive to the precise details of the light spectrum. The error in the figures obtained with natural sunlight or with a flash instead of a correct reference spectrum (whatever this may be) is always under 3%. Furthermore, if one assumes the linearity of the short circuit current as a function of the total power incident on

the cell, the concentration level of any measured I–V curve is given simply and accurately by the ratio $C = I_{sc}(C)/I_{sc}(1)$.

On the other hand, the rating of multi-junction cells requires a careful knowledge of the light spectrum impinging on the cell (note that optical elements modify the incoming spectrum), and also the spectral response of each cell in the stack. The calibration of multi-junction cells thus requires specialised laboratories.

7.1 Rating of C-modules

The C-modules include the optical collector, the receiving cells and the heat sink. Except in the case of very small modules (for example, mini-concentrators or micro-cells), the amount of uniform light necessary to illuminate the whole collector requires outdoor testing, and consequently sun tracking. The test should be carried out with the collector normal to sun on a clear day with a direct irradiance higher that 750 W/m^2. (If this condition is fulfilled but there are thin clouds in the sky do not test during such days: you will waste your time!)

Once the module is installed onto a two axis tracker, the following parameters must be measured and calculated for the correct and complete characterisation of the module (see Table 4(a)–(c)):

The calibration of an array is identical to the calibration of a module except that the array cannot point to the sun if the system does not have two-axis tracking, as in the case of a horizontal parabolic trough or a static concentrator. In these cases, Table 4 remains valid if we substitute for B (W/cm^2) the quantity:

$$B_{eff} = B.cos\ \gamma \tag{6}$$

where γ is the angle between the actual direct beam and the normal to the collector surface.

The efficiency of linear or static concentrator arrays can be different due to the different performance of the optical elements under different angles of incidence of sunrays. As a result, any comparative measurements must be carried out at an identical angle of incidence of the light.

Table 4(a) Parameters to measure

Symbol	Name and units	Testing equipment
B	Direct irradiance (W/m^2)	Pyrheliometer
T_{amb}	Ambient temperature (°C)	Thermometer
T_{cell}	Cell temperature in operation (°C)	Thermocouple[a]
$I_{sc}(C)$	Short circuit current under concentration C at 1 sun (A)	Ammeter
$V_{oc}(C)$	Open-circuit voltage under concentration C at T_{cell} (V)	Voltmeter
I–$V(C)$ curve	Complete I–V curve under concentration C at T_{cell} (I,V) pairs	I–V curve tracer (transient or continuous)

[a] Cell temperature can be deduced from V_{oc} if you have information of V_{oc} and dV/dT at given cell irradiance and temperature.

Table 4(b) Parameters calculated from measurement. Parameters required prior to concentrator measurements

Calculated parameter	Measured data and calculating formulas	Measurement conditions
$P_{max}(C)$	Maximum power at T_{cell}	At B and T_{cell}
η = module overall efficiency	$P_{max}(C)/(B \times A_c)$	At B and T_{cell}
η_{op} = optical efficiency	$I_{sc}(C)/(X \times I_{sc}(1))$	At B
η_{rec} = receiver efficiency	Overall efficiency/optical efficiency = η/η_{op}	At B and T_{cell}

Table 4(c) Parameters required previously to concentrator measurements

Symbol	Name and units	Test conditions
Ac	Collector area (cm^2)	–
$I_{sc}(1)$	Receiver short circuit current at 1 sun (A)	At B
$V_{oc}(1, T_{ref})$	Open circuit voltage at known cell temperature and illumination (V)	At B and T_{cell}
R_{th}	Thermal resistance dependence vs. wind (provided by the manufacturer or measured indoors) ($°C\,W^{-1}\,cm^2$)	At B and T_{cell}
R_s	Cell series resistance (Ω)	At B and T_{cell}

Furthermore, due to possible deformation of the structure supporting the modules, the efficiency can vary with array orientation. This fact must also be taken into account if a complete picture of the system performance under all real operating conditions is required, rather than only with the system 'centred at noon'.

The effect of structure deformation on the optical elements decreases the current at the maximum power point of the I-V curve. This effect is known as an 'optical mismatch' and is caused by the unequal illumination of the cells in a series connection, or by the dispersion of the I–V characteristics of the receiver.

7.2 Specifications That Must Be Required From C-systems

A PV concentrator is a complex system made of very different components: optical materials, a mechanical structure, control circuits, cells, receivers, heat sinks, insulators, wires, connectors, etc. Each component requires a set of specifications, but an approved and accepted list of minimum required specifications does not yet exist. The same can be said about the qualification of C-modules, systems and sub-systems.

Currently, the IEEE has approved a qualification procedure for receivers and concentration modules (IEEE P1513) that will be probably adopted by IEC (future IEC 62108). In Europe, a project (entitled C-RATING) with support from the European Commission aims to prepare a draft on specifications, testing methods and modelling for cells, modules and systems (see www.ies-def.upm.es/c-rating/). In addition, an initiative to develop qualification procedures for

tracking control units and tracking drivers is about to start. However, it will take about four years before any qualification method can be accepted worldwide.

In the meantime, standards, specifications and qualification tests approved for flat modules, with suitable modifications, are being used as a compromise.

8 Energy Produced by a C-system

The prediction of the energy produced by a concentrator should, in principle, be easier than for a flat panel because the irradiance distribution during the day for a concentrator is more uniform because of sun tracking. However, concentrators use only the direct sunlight, and the availability of historical data for direct beam irradiance (W/m^2) and radiation (kWh/m^2 day) is limited. There are computer codes and models that generate direct irradiance data based on global radiation, hourly average global irradiance, etc. Other data come from an analysis of meteorological satellite images. All these models are complicated to use and have not been verified.

One approximation that gives good results is based on the knowledge of two numbers: $\langle W_{day} \rangle$, the monthly averaged direct daily radiation on a tracking array (two-axis, single axis north/south, etc.) in kWh/m^2 day; and $\langle S \rangle$, averaged number of sunshine hours (as recorded with a Campbell–Stokes sunshine recorder).

A simple and effective model can then be obtained by assuming that the concentrator receives a uniform and constant irradiance equal to:

$$B_{eff} = \frac{Total\ direct\ daily\ radiation}{Sun\ hours - 2} = \frac{\langle W_{day} \rangle}{\langle S \rangle - 2} \tag{7}$$

during the $\langle S \rangle - 2$ hours around the solar noon.

Another simple method consists of assuming that the beam irradiance normal to the sun is always $800 W/m^2$. The operating time is then given by:

$$S(hours) = \frac{Total\ direct\ daily\ radiation}{0.8 kW/m^2} = \frac{\langle W_{day} \rangle}{0.8 kW/m^2} \tag{8}$$

which is also centred around noon.

Regarding ambient temperature, it can be assumed that it follows a daily oscillatory variation related to the horizontal solar radiation but delayed by 2 hours relative to noon. As a result, the average daylight ambient temperature is given by:

$$\langle T_{amb} \rangle = \langle T_{av} \rangle + 2 \frac{\langle T_{\max} \rangle - \langle T_{av} \rangle}{\pi} \tag{9}$$

where $\langle T_{max} \rangle$ and $\langle T_{av} \rangle$ are the maximum and average daily temperatures.

Using such site data and the system specifications outlined in Table 4, one can calculate the expected daily averaged I–V curve of the array for any day from the

I–V curve at reference conditions by using the following formulas. The average cell temperature for each day is:

$$\langle T_{cell} \rangle = \langle T_{amb} \rangle + R_{th} \cdot B_{eff} \cdot \eta_{op} \cdot (1 - \eta_{rec}) \tag{10}$$

$$I_{day}(\text{model}) = I(ref) \cdot \frac{C(\text{model})}{C(ref)} \tag{11}$$

$$\begin{aligned} V(\text{model}) = V(ref) + (E_G - V(ref))\left(1 - \frac{T_{\text{model}}}{T_{ref}}\right) \\ + \frac{kT_{ref}}{q} \ln \frac{C(\text{model})}{C(ref)} - R_s(I(\text{model}) - I(ref)) \end{aligned} \tag{12}$$

where E_g is the band gap of the cell material, q the electronic charge and η_{rec} the receiver efficiency.

Once the corrected I–V curve is known, the power output of the array can be calculated for any moment of time. The energy produced in a day is then:

$$P_{day}\left(\frac{kWh}{m^2 day}\right) = P_{\max}(\text{model}) \cdot (\langle S \rangle - 2) \tag{13}$$

Figure 19 shows a table of measured reference data and model results for a set of given site values. The measured and corrected I–V curves are shown (courtesy of Project C-RATING, EC Thermie Programme).

9 The Future of Concentrators

High conversion efficiency of PV systems is the key to low cost. It is currently accepted that the progress of technology based on the learning curve of conventional cell technology cannot reach the goal of 0.1 euros per kWh. Thus, innovative effort is necessary to increase the cell efficiency.

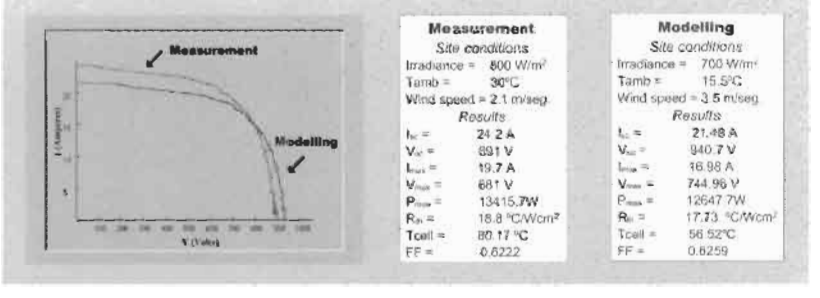

Figure 19 The I–V values, measured for given site conditions, can be used to deduce the I–V curve for any other set of conditions, by using Equations (9) and (11). (Results obtained by the code for modelling concentration systems within the project C-RATING, EC 5th FV Programme.)

In recent years, third generation cells are being mentioned with the promise of conversion efficiencies in the range of 40%; efficiencies of 34% have already been demonstrated experimentally. The required efficiency can therefore be reached, but the use of such highly expensive cells requires operation under high concentration levels, in excess of 1000×. This can be compared with demonstrated efficiencies of 24 and 20% which have been accomplished using the second generation cells (usually based on silicon) and systems, respectively. The total cost, including BOS, is then in the range of 3 euros/W_p, and compatible with the energy cost objectives.

In summary, two scenarios of PV progress have been outlined, based on the use of concentrators. It is not certain, however, what arrangement will be better for large-scale applications, or if one single type of concentrator is optimal for all applications and climatic regions.

References

[1] Boes, E.C. and Luque, A. 1993. Photovoltaic Concentrator Technology. In Johansson, T.B., Kelly, H., Reddy, A.K.N. and Williams, R.H., Eds., *Renewable Energy: Sources for Fuel and Electricity*, Earthscan, London.

[2] Sala, G. 2002. PV concentrator alternatives towards low energy costs, *Proc. PV in Europe: From PV technology to energy solutions*, Rome.

[3] Zirkle, E.T., Dondero, R.C., Backus, C.E. and Schorder, D.V. 1986. The superlinear behaviour of short-circuit current in silicon concentrator cells at concentrations up to 1400 suns. *Proc. 7th European Photovoltaic Solar Energy Conf.*, Seville.

[4] Araújo, G.L. and Ruiz, J.M. 1989. Variable injection analysis of solar cells. In: Luque, A. Ed., *Solar Cells and Optics for Photovoltaic Concentration*, Adam Hilger, Bristol and Philadelphia, pp. 32–74.

[5] Welford W.T. and Winston. R. 1978. *The optics of non-imaging concentrators*, Academic Press, New York.

[6] Castle, J.A. and Ronney, F. 1978. 10kW_p photovoltaic concentrator system design, *Proc. 13th IEEE Photovoltaic Specialists Conf.*, Washington DC, pp. 1131–1138.

[7] Luque, A., Sala, G., Alonso, A., Ruiz, J.M., Fraile, J., Araújo, G.L., Sangrador, J., Agost, M.G., Eguren, J., Sanz, J. and Lorenzo, E. 1978. Project of the "Ramón Areces" concentrated photovoltaic power station, *Proc. 13th IEEE Photovoltaic Specialists Conf.*, Washington DC, pp. 1139–1146.

[8] Maish, A.B., O'Neill, M., West, R. and Shugar, D.S. 1996. Solartrack controller developments for today's application, *Proc. 25th IEEE Photovoltaic Specialist Conf.*, Washington DC, pp. 1211–1214.

[9] Arboiro, J.C. and Sala, G. 1997. A constant self-learning scheme for tracking system, *Proc. 14th European Photovoltaic Solar Energy Conf.*, Barcelona, pp. 332–335.

[10] Sala, G., Antón, I., Arboiro, J.C., Luque, A., Camblor, E., Mera, E., Gasson, M.P., Cendagorta, M., Valera, P., Friend, M.P., Monedero, J. Gonzalez, S.

and Dobon, F. 2000. The 480 kW_p EUCLIDES®-THERMIE power plant: Installation, set-up and first results. *Proc. 16th European Photovoltaic Solar Energy Conf.*, Glasgow pp. 2072–2077.

[11] Anton, I., Solar, R., Sala, G. and Pachón, D. 2001. IV testing of concentration modules and cells with nonuniform light patterns, *Proc. 17th European Photovoltaic Solar Energy Conf.*, Munich, pp. 611–614.

[12] Yamaguchi, M. and Luque, A. 1999. High efficiency and high concentration in photovoltaics, *IEEE Transactions on Electron Devices*, ED-46 (10).

Operation of Solar Cells in a Space Environment

Sheila Bailey, Photovoltaic and Space Environments Branch, NASA Glenn Research Center, USA
Ryne Raffaelle, Physics Department, Rochester Institute of Technology, USA

1 Introduction

The beginning of the Space Age brought about a perfect application for the silicon solar cell developed at Bell laboratory in 1953. Sputnik was battery powered and remained active only a little over a week. The US launched the first successful solar powered satellite, Vanguard 1, seen in Figure 1, on March 17, 1958 [1]. The solar powered transmitter lasted six years before it is believed that the transmitter circuitry failed.

Vanguard I had eight small panels with six p on n silicon solar cells, each 2 cm × 0.4 cm, connected in series. Each panel output was approximately 50 mW with a cell efficiency of ~8%. This can be contrasted with the International Space Station (ISS), see Figure 2, which will have, when the power system is complete in 2004, the largest photovoltaic power system ever present in space. It will be powered by 262,400 n on p silicon solar cells, each 8 cm × 8 cm, with an average efficiency of 14.2% on 8 US solar arrays (each ~34 m × 12 m) [2]. This will generate about 110 kW of average power, which after battery charging, life support, and distribution, will supply 46 kW of continuous power for research experiments on ISS.

Figure 1 3/12/1957, Senator Lyndon B. Johnson, chairman of the US Senate Preparedness subcommittee, holds the tiny 6.5-inch American test satellite.

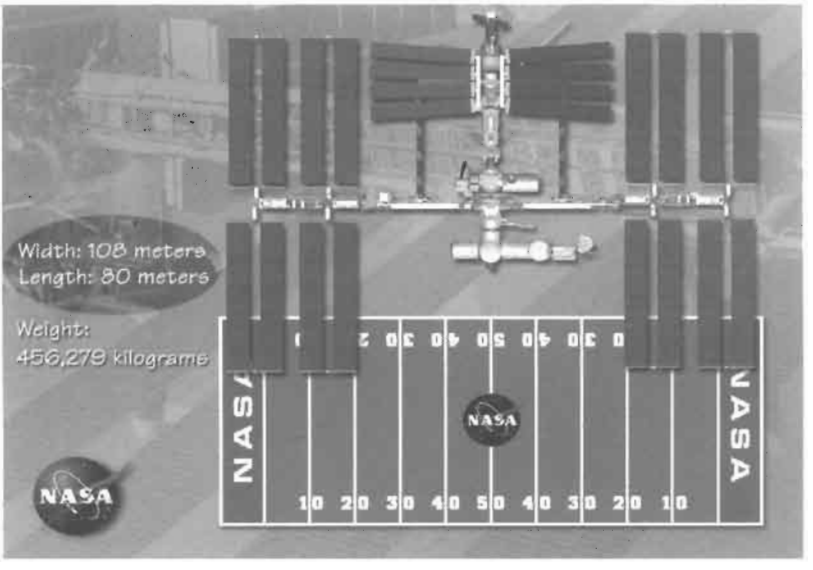

Figure 2 The International Space Station (football field indicating relative size).

2 Space Missions and their Environments

Space missions are defined by their trajectories. For Earth orbiting missions these are roughly classified as low Earth orbit (LEO), 300–900 km, mid-Earth orbit (MEO), and geosynchronous (GEO), 35,780 km. The orbit's size, defined by the semimajor axis, shape, defined by the eccentricity, and orientation, defined by the orbital plane in space (inclination and right ascension of the ascending node) and the orbit within the plane, defined by the argument of perigee, determine the space environment the spacecraft will encounter. NASA missions also involve interplanetary flight both toward and away from the Sun, planetary fly-bys, and orbiting other planets, each with their own unique set of environments. In addition both the moon and Mars may be sites for future human visits and have their own individual conditions for surface power.

At the heart of our solar system is the Sun which is both the source of the solar irradiance which a solar cell converts to electricity and the solar wind which is primarily a stream of protons and electrons moving with a mean velocity by Earth of ~400–500 km/s with a mean density of approximately 5/cm^3. In addition, the Sun is a dynamic body exhibiting facula, plages, spicules, prominences, sunspots, and flares over time. The only other source of radiation is galactic cosmic rays which emanate from beyond our solar system. These consist of about 85% protons, about 14% alpha particles, and about 1% heavier nuclei [3]. The differential energy spectra of the cosmic rays near the Earth tend to peak around 1 GeV/nucleon and the total flux of particles seen outside the magnetosphere at the distance of the Earth from the Sun (i.e., 1 AU) is approximately 4 per square centimetre per second.

2.1 The Air Mass Zero Spectrum

The spectral illumination that is available in space is not filtered by our atmosphere and thus is quite different from what is incident on Earth's surface (see Figure 3). Space solar cells are designed and tested under an Air Mass Zero (AM0) spectrum. This is in contrast to an Air Mass 1.5 or one and a half times the spectral absorbance of the Earth's atmosphere, which is the standard condition for testing terrestrial solar cells. Thus, cells intended for use in space will be optimised for a somewhat different spectrum. The change in spectral distribution will typically result in a decrease in overall cell efficiency, even though the intensity of light is somewhat higher (i.e., 1367 W/m^2 in space as compared to 1000 W/m^2 on Earth). A 12% efficient silicon solar cell as measured under AM1.5 condition on Earth would translate into an approximately 10% cell as measured under AM0.

As seen below the Sun resembles a black-body with a surface temperature of 5800 K with a peak of spectrally emitted energy at 480 nm. Approximately 77% of the emitted energy lies in the band from 300 to 1200 nm. The total energy

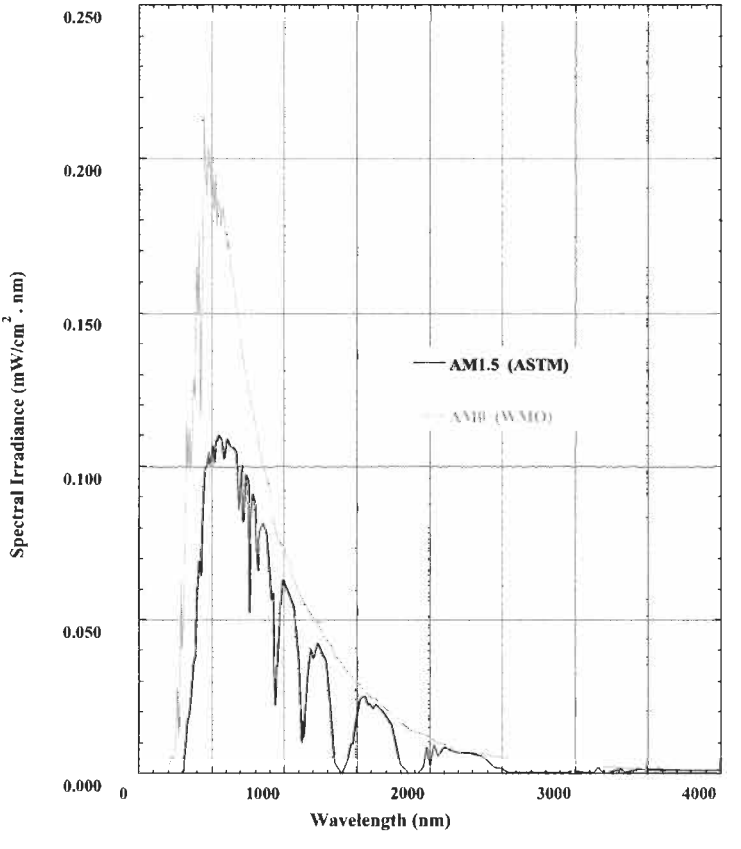

Figure 3 The Air Mass Zero (AM0) spectrum (WMO) and the Air Mass 1.5 (ASTM) spectrum.

received from the Sun per unit area perpendicular to the Sun's rays at the mean Earth–Sun distance (1 AU) is called the solar constant. The current accepted value of the solar constant is 1367 W/m^2. The solar intensity of course varies in time. However since space solar cells are calibrated in near-space, the variation in the value of the solar constant primarily affects the predicted solar cell operational temperature in orbit.

2.2 The Trapped Radiation Environment

The solar wind, solar flares and galactic cosmic rays all consist of charged particles, (electrons, protons and ions). These interact with a planetary magnetic field. Some planets have a very weak magnetic field or no magnetic field. Jupiter has a very large magnetic field. Jupiter, Saturn, and Uranus have trapped radiation belts. The Earth's magnetic field is 0.3 gauss at the surface on the equator and does change over time even reversing polarity every 10,000 years. The Earth's magnetic poles do not coincide with the poles determined by the axis of rotation, with approximately an eleven degree difference. The total magnetic field of the magnetosphere is determined by the internal magnetic field of the planet and the external field generated by the solar wind. These interact with each other and provide a complex asymmetric pattern of the geomagnetic cavity. Charged particles gyrate around and bounce along magnetic field lines, and are reflected back and forth between pairs of conjugate mirror points in opposite hemispheres. At the same time electrons drift eastward around the Earth while protons and heavy ions drift westward. These regions of trapped charged particles are called the Van Allen belts. An illustration of the regions of trapped particles can be seen in Figure 4, where L is a dimensionless ratio of the Earth's radius equal to the radial distance divided by the cos 2Λ, where Λ is the invariant latitude.

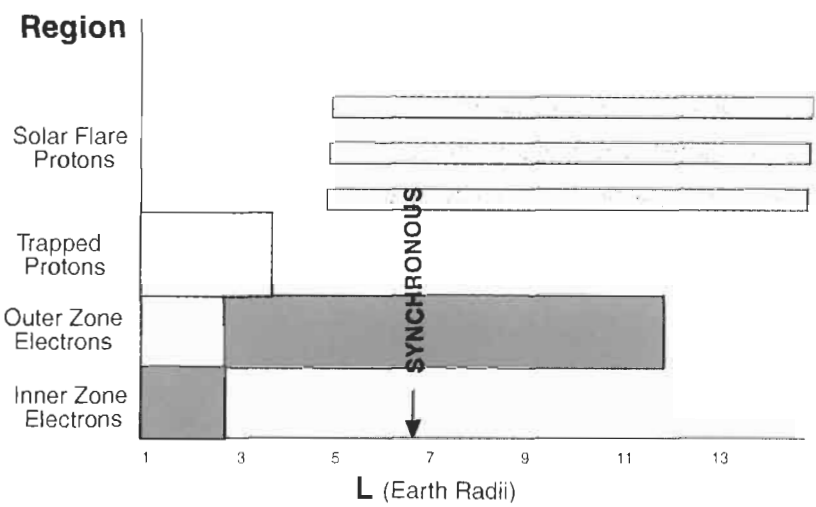

Figure 4 Regions of trapped particles as a function of distance in Earth radii from the Earth's centre

An example of the number of trapped particles as a function of energy from both Earth and Jupiter can be seen in Figure 5 [4]. The Jupiter data was provided by Pioneers 10 and 11 and Voyagers 1 and 2 during their encounters with the planet.

The models that are used for the trapped electron and proton environment at Earth were developed by the US National Space Science Data Center at NASA's Goddard Space Flight Center from available radiation measurements from space. The most recent models in use, AP8 for protons [5] and AE8 for electrons [6], permit long-term average predictions of trapped particle fluxes encountered in any orbit and currently constitute the best estimates for the trapped radiation belts, although they have been noted to overestimate the radiation in certain low Earth orbits.

2.3 Solar Flares

Solar activity, as measured by the number of sunspots, follows an 11-year cycle between maxima. The cycle has an active 7-year period during which solar flare events are probable and a quiescent 4-year period during which solar flare events are rare. The last peak in activity occurred in 2000. The most recent model, JPL 91, allows the spacecraft designer to predict the proton integral fluence as a function of confidence level and exposure time [7]. The exposure time must be correlated to the solar maxima. The calculated integral fluence is at 1 AU from the Sun. For missions at other radial distances from the Sun the fluence should be modified by $1/R^2$ to produce the most probable estimate. These solar flare proton events are associated with coronal mass ejections on the Sun. They occur at highly localized places on the Sun and rotate with the Sun.

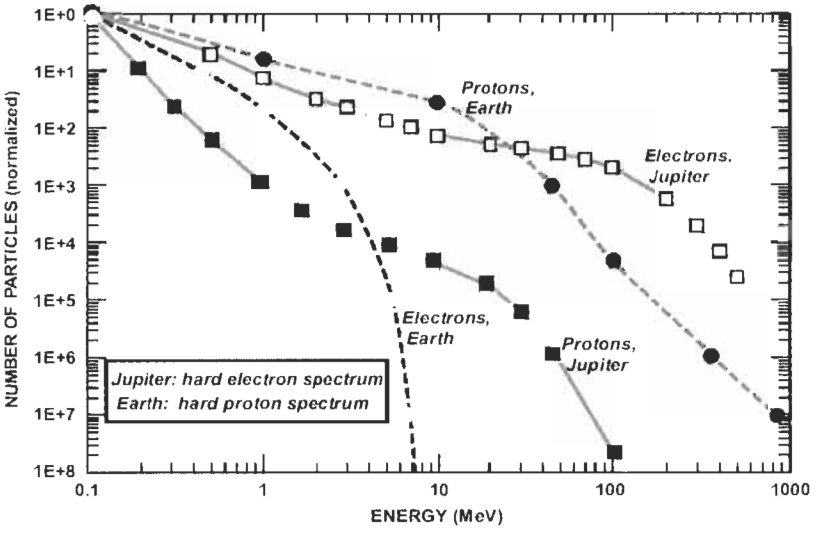

Figure 5 Normalised energy spectrum of trapped electron and proton radiation environment at Jupiter, compared to Earth.

Because they follow the field lines of the interplanetary magnetic field, only when the ejection occurs along the line from the Sun that intersects the Earth will the protons propagate immediately to the Earth, arriving approximately an hour after the flare. These protons are highly anisotropic and therefore variations in proton flux can be as large as 100 from the same flare at different points of the orbit. Protons can also reach Earth when ejection occurs away from a field line but then the protons must diffuse through the solar corona before they propagate to Earth. This takes longer, up to 10 hours, and the flux tends to become isotropic. The trapped proton population is also significantly effected by solar activity, particularly in lower Earth orbits. The increased energy output of the Sun expands the atmosphere and increases proton densities. There is a region of trapped particles close to the surface of the Earth called the South Atlantic Anomaly. For low altitude, low inclination orbits the South Atlantic Anomaly may be the most significant source of radiation.

The electron environment is also influenced by the solar cycle. Magnetic solar storms can raise the electron flux in the outer orbits by an order of magnitude over a short time period. This short-term variation in electron flux is usually more significant for spacecraft charging effects in GEO. AP8 and AE8 mentioned above have data for both solar maximum and solar minimum. A more recent model based on the CRRES spacecraft launched in July 1990 found differences between the AP8 and AE8 predictions to be as high as a factor of 3 orders of magnitude particularly at low altitudes due to the highly variable proton belts [8]. At high altitudes AE8 predictions are typically higher than CRRES predictions.

2.4 The Neutral Environment

The density, composition, pressure, and temperature change dramatically as a function of altitude. Orbits lower than 200 km are generally not stable due to atmospheric drag. At 300 km only 23% of the sea level molecular nitrogen remains and only 10% of molecular oxygen. 80% of the atmosphere at 300 km is highly reactive atomic oxygen. Atomic oxygen erodes polymers and composites that might be used in array substrates and also silver interconnects between solar cells [9]. The atmospheric density is very small above 800 km.

2.5 The Particulate Environment

The particulate environment is composed of both naturally occurring meteoroids and man-made space debris. The particles of most concern to space arrays are between 10^{-3} and 10^{-6} g, since those below 10^{-6} g do not have sufficient energy to cause significant damage and those above 10^{-3} are less frequently encountered [10]. Meteoroids, whose origin is either asteroids or comets, have an average velocity of 20 km/s and their density varies with the Earth's position around the Sun. Debris has of course become more problematical as the number of launched spacecraft and their relative time in orbit has increased. The relative damage of orbital debris, except for very large

objects, is less due to the reduced difference in orbital velocities for the debris that was created in that orbit. The flux of meteoroids and orbital debris has been observed for a variety of orbits [11]. Damage to the solar arrays of Mir and the Hubble Space Telescope were noted in primarily the erosion and cracking of the cover glass on the array and the erosion of the substrate rear surface thermal control coating.

2.6 Thermal Environment

The temperature of a solar cell in space is largely determined by the intensity and duration of its illumination [12]. In the case of the US array on the ISS, the operating temperature of the silicon solar cells is as high as 55°C while under illumination, and as low as −80°C when in eclipse. Similarly, as spacecraft venture further away from the Sun their average temperatures will decrease. Likewise, as they move closer to the Sun their average temperatures will rise. The average illuminated temperature at the orbit of Jupiter is −125°C, whereas at the average orbit of Mercury the temperature is 140°C.

The orbital characteristics of a space mission are also a major source of thermal variation for the associated photovoltaic arrays. The relative amount of illumination versus eclipse time and the rate of change in the temperature vary dramatically will the orbital path. The orbital path will also affect the fraction of incident solar radiation returned from a planet or albedo. The average albedo from the Earth is 0.34, but can range anywhere from 0.03 (over forests) to 0.8 (over clouds) [7].

The available power generated by a solar cell is directly related to its operating temperature. An increase in temperature will result in a reduction in output power. Although there will be a slight increase in the short-circuit current with increasing temperature, it will be overshadowed by the decrease in the open-circuit voltage. A GaAs solar cell will experience about a decrease of 0.05 mW/cm^2 per °C.

The degradation of solar cell performance as a function of temperature is expressed in terms of temperature coefficients. There are several different temperature coefficients used to describe the thermal behaviour of solar cells. They are based in terms of the change in a characteristic cell measurement parameter (i.e., I_{sc}, V_{oc}, I_{mp}, V_{mp}, or η) as a function of the change in temperature. The difference in the measured value at the desired temperature and a reference temperature is used to determine the coefficient. The International Space Organisation (ISO) standard reference measurement is taken at 25°C. For most space solar cells, the change in output is fairly linear from −100 to 100°C.

Temperature coefficients are often expressed as a normalised number. For example, if the case of the efficiency temperature coefficient the normalised value would be expressed as

$$\beta = \frac{1}{\eta}\frac{d\eta}{dT} \tag{1}$$

or the fractional change in efficiency with temperature. Representative temperature coefficients for the various types of cells used in space are given in Table 1. The temperature coefficient is inversely related to bandgap and negative for the majority of space solar types.

3 Space Solar Cells

The first 30 years of space solar cell development focused on the of silicon solar cells, although it was known even in the early days that better materials existed [13]. The concept of a tandem cell was also proposed in the early days to enhance the overall efficiency. An optimised three-cell stack was soon to follow with a theoretical optimum efficiency of 37% [14]. However it was 40 years later before a multi-junction solar cell flew in space. Today silicon cells still fly in space but the cell of choice is a multi-junction solar cell. Table 2 shows some of the best efficiencies for small area cells and the comparison to an AM0 efficiency.

A variety of cell types are listed in Table 2 because, while commercial satellites use silicon or dual or triple junction GaInP/GaAs/Ge, there is a marked interest in military applications of thin film cells. NASA also has planned missions in which a large specific power (kW/kg) and lower cost would be beneficial. The advantages of thin film solar cells are their large specific power when deposited on a flexible, lightweight substrate with a suitably lightweight support structure. Thin film solar cells are currently lower in efficiency and require a larger area for the same power levels, however, trade studies have identified several potential applications [19].

3.1 Radiation Damage in Space Solar Cells

Radiation degradation in space is a complex issue. The degradation is dependent on the type of particle, energy and fluence, shielding and cell design (layer thickness, number of junctions, etc.). In addition ground based radiation measurements use monoenergetic, unidirectional beams of particles (electrons or protons) and the simulation of the space solar environment, especially for

Table 1 Measured temperature coefficients for various types of solar cells used in space [26]

Cell Type	Temp (°C)	η (28 °C)	$1/\eta\, d\eta/dT$ ($\times 10^{-3}$ °C^{-1})
Si	28–60	0.148	−4.60
Ge	20–80	0.090	−10.1
GaAs/Ge	20–120	0.174	−1.60
2-j GaAs/Ge	35–100	0.194	−2.85
InP	0–150	0.195	−1.59
a-Si	0–40	0.066	−1.11(non-linear)
$CuInSe_2$	−40–80	0.087	−6.52

Table 2 Measured Global AM1.5 and measured or *estimated AM0 efficiencies for small area cells. These are based on cells measured under standard conditions, courtesy of Keith Emery, NREL. The calculated efficiency uses the ASTM E490-2000 reference spectrum and assumes that the fill factor does not change for the increased photocurrent. Quantum efficiencies corresponding to the table entries were used in the calculations.

Cells	Efficiency (%)	Efficiency (%)	Ratio	Area (cm2)	Manufacturer
	Global AM1.5	AM0	AM0/AM1.5		
c-Si	22.3	21.1	0.95	21.45	Sunpower [15]
Poly-Si	18.6	17.1*	0.92	1.0	Georgia Tech/HEM [16]
c-Si film	16.6	14.8*	0.89	0.98	Astropower [17]
GaAs	25.1	22.1*	0.88	3.91	Kopin [17]
InP	21.9	19.3*	0.88	4.02	Spire [17]
GaInP (1.88ev)	14.7	13.5	0.92	1.0	ISE [18]
GaInP/GaAs/Ge	31.0	29.3	0.95	0.25	Spectrolab [18]
$Cu(Ga,In)Se_2$	18.8	16.4*	0.87	1.04	NREL [15]
CdTe	16.4	14.7*	0.90	1.131	NREL [15]
a-Si/a-Si/a-SiGe	13.5	12.0	0.89	0.27	USSC [15]
Dye-sensitized	10.6	9.8*	0.92	0.25	EPFL [15]

multi-junction cells, is difficult. Historically the Jet Propulsion Laboratory (JPL) has provided the format for determining radiation damage in silicon and gallium arsenide space solar cells [20, 21]. The elements needed to perform degradation calculations are degradation data under normal 1 MeV electron irradiation, the effective relative damage coefficients for omnidirectional space electrons and protons of various energies with various coverglass thickness, and the space radiation data for the orbit of interest. As discussed in the section on the trapped radiation environment, AP8 and AE8 are current NASA models for trapped radiation. The models were based on observations from 43 satellites from 1958 to 1970 for AP8 and from 1958 to 1978 for AE8. They can return an integral or differential omnidirectional flux for a set of energies. The integral flux is the number of particles with energy greater than or equal to the input energy. The models calculate a numerical derivative of the integral flux to obtain the differential flux. For AP8 the energy range is 0.1 to 400 MeV with McIlwain L number ranging from 1.1 to 6.6. For AE8 the energy range is 0.04 to 7 MeV with an L number from 1.1 to 11. The models calculate a numerical derivative of the integral flux to obtain the differential flux. As mentioned in the section on solar flares the models permit a choice of solar maximum or solar minimum. AP8 and AE8 provide the largest coverage for Earth orbiting spacecraft and are internationally available. Other models exist with narrower coverage: the US Air Force model from the CRRES data, an ESA model based on the SAMPEX spacecraft and a Boeing model based on TIROS/NOAA satellites.

In recent years the Naval Research Lab (NRL) has developed a model of displacement damage dose based on the non-ionising energy loss (NIEL) [22]. The NIEL gives the energy dependence of the relative damage coefficients, and because the NIEL is a calculated quantity, the NRL method enables the analysis

of a solar cell response to irradiation by a spectrum of particle energies, as encountered in space, based on only one or two ground measurements. The Solar Array Verification and Analysis Tool (SAVANT) [23, 24] computer program being developed at NASA Glenn Research Center combines the NRL method with the NASA space environment models to produce a user-friendly space solar array analysis tool. Equator-S and COMETS satellite data have been analysed using SAVANT. In the Equator-S mission, the model was successful in predicting the onboard degradation of both GaAs/Ge and $CuInSe_2$ solar cells. This is the first time that the model has been applied to a thin film technology. SAVANT and the onboard measurements agreed to within a few percent over the entire mission. The COMETS mission used GaAs/Ge solar cells as its main power source, and SAVANT accurately modelled the power output of the arrays for the bulk of the mission lifetime [25]. SAVANT is not currently available to the public.

Normalised power as a function of altitude for solar cells in a 60° orbit for 10 years with 75 μm coverglass can be seen in Figure 6. Note that by using normalised power the higher radiation resistance of $CuInSe_2$ can be seen. Also, the larger particle flux can be noted for MEO orbits.

4 Small Power Systems

There has been considerable development over the last several years in the development of small spacecraft. Many so-called microsats or satellites whose

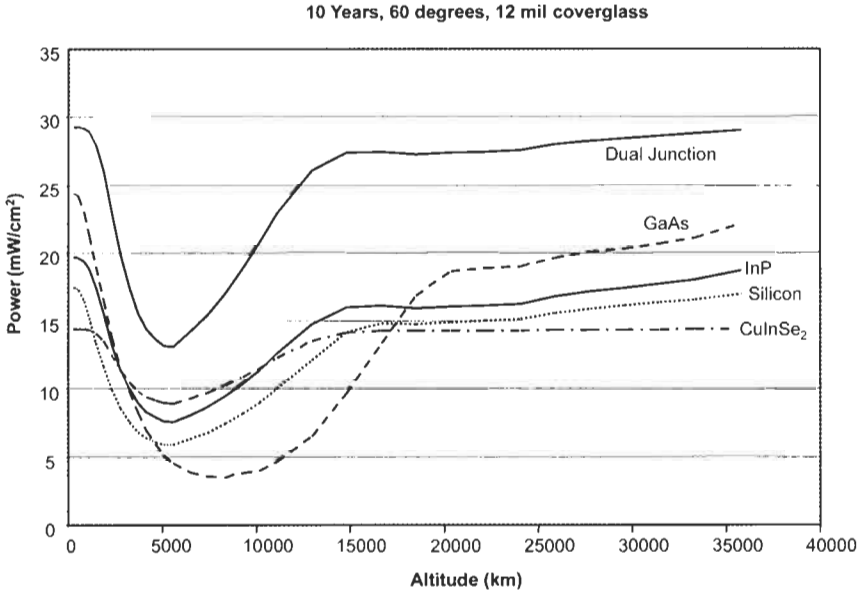

Figure 6 Normalised power versus altitude for a 60° orbit for 10 years with 75 μm coverglass. (Graph courtesy of Tom Morton, Ohio Aerospace Institute.)

total mass is less than 100 kg have been deployed. In fact, satellites whose total mass is less than 10 kg (i.e., nanosats) and even satellites weighing less that 1 kg (i.e., picosat) have already been tested in the space environment (see Figure 7). Consequently, the demands on the space power community to develop appropriately sized power systems for these new classes of satellites have arisen.

It is true that a premium has always been placed on the efficiency of space power systems and specifically the photovoltaic arrays. Specific power (W/kg) or power per mass is one of the most important figures of merit in judging a power system. The higher the specific power the less the spacecraft mass that has to be dedicated to the power system and the more that can be used for the scientific

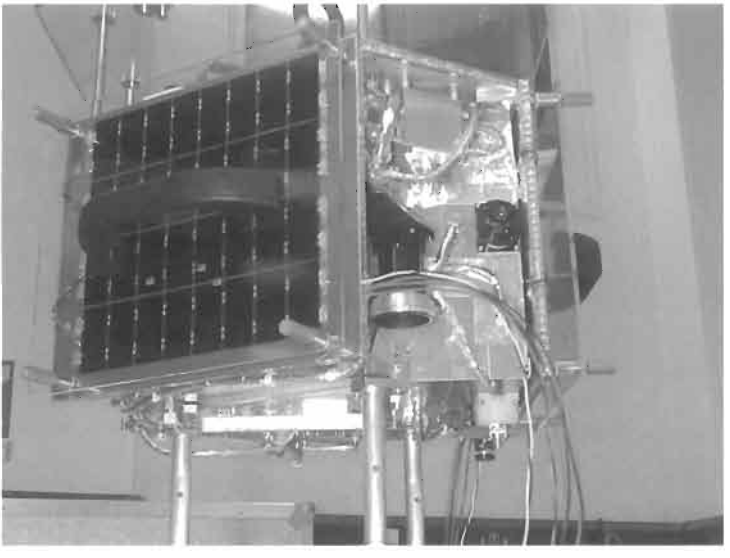

Figure 7 The SNAP-1 Surrey Nanosatellite Applications Platform was a 6 kg satellite with imager and propulsion. (Picture courtesy of NASA and Surrey Satellite Technology Ltd.)

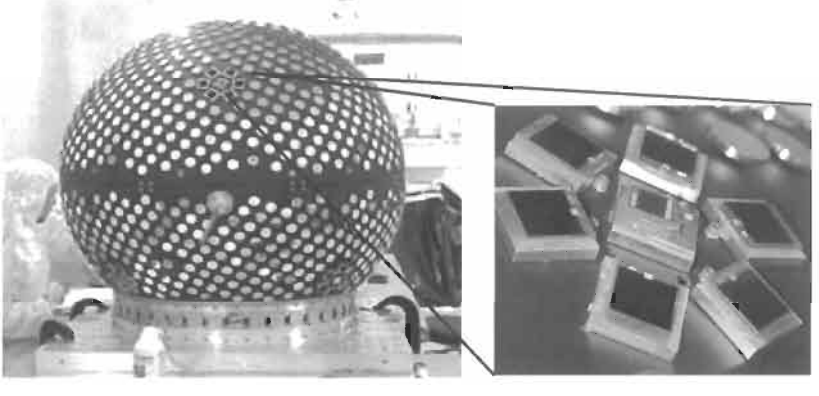

Figure 8 Photograph of Starshine 3 satellite with a magnified region of the integrated power supply.

mission. This is especially true in the case of a small power system. There is an economy of scale savings that can sometimes be recouped on a larger satellite. As power components are reduced in size, so too is there capacity. In the case of a solar cell this translates into their ability to gather light.

A number of approaches have been used to meet the demands of small satellites. One such approach is the development of integrated power supplies. These supplies combine both power generation and storage into single devices. In fact, NASA, the Naval Research Labs, and others are working to develop monolithically grown devices that combine monolithically interconnect module (MIM) solar cells or micro-sized solar arrays with lithium ion energy storage. A first demonstration of this concept, although not truly monolithic, was flown on the Starshine 3 satellite in 2002 (see Figure 8) [26].

Another approach is to integrate the photovoltaics to the satellite is such a way as to ensure light absorption. One method of this approach is to have photovoltaics incorporated to the skin of the spacecraft. This return to body mounted panels is very similar to the way the first small satellites where powered back in the space programs infancy. Another method is to tether a spherical array to the small spacecraft. The primary example of this approach is the so-called power sphere concept being developed by Aerospace Corporation in collaborations with ILC Dover and others (see Figure 9).

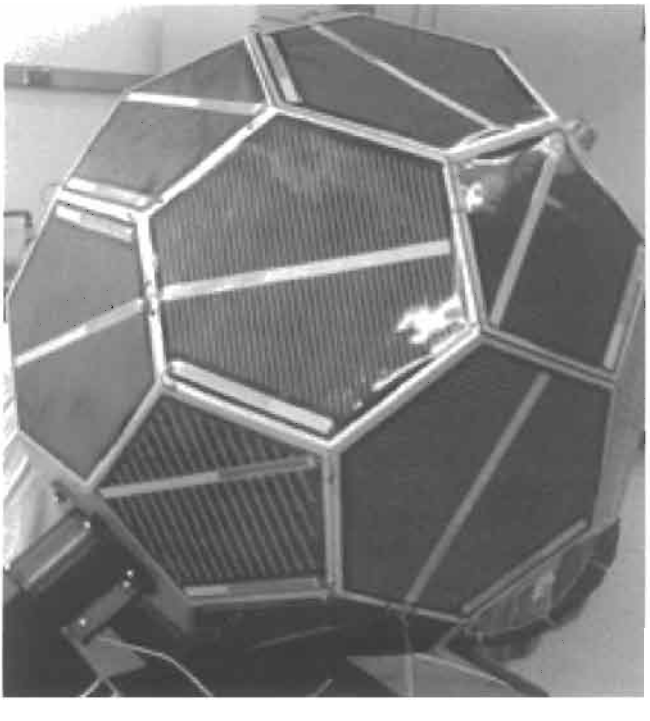

Figure 9 Aerospace Corporation PowerSphere nanosatellite. (Picture courtesy of the Aerospace Corporation.)

5 Large Power Systems

On the other end of the spectrum from nanosats in terms of the size of photovoltaic arrays used is the proposed development of Space Solar Power (SSP) systems. The intent is to develop systems that are capable of generating up to

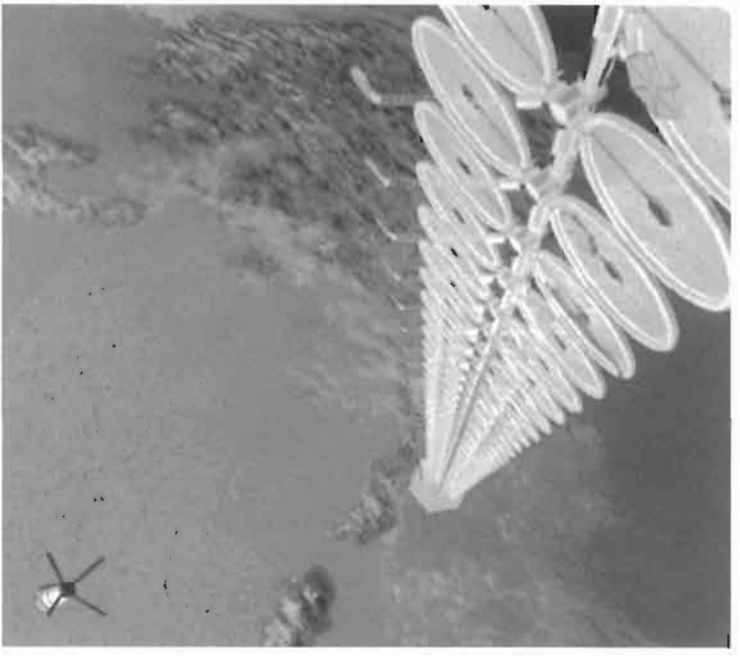

Figure 10 Sun tower. (Picture courtesy of NASA.)

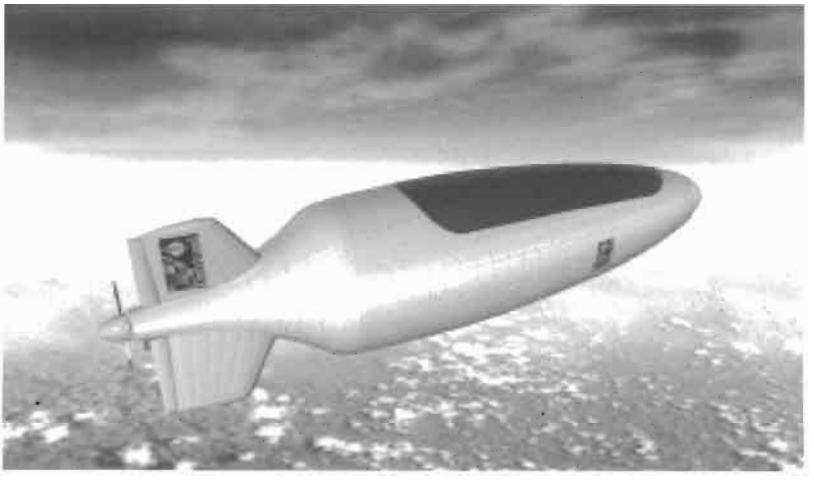

Figure 11 An artist's conception of the Linstrand Balloons Ltd proposed high altitude airship. (Picture courtesy of Linstrand Balloons Ltd.)

gigawatts of power. The proposed uses of these systems have been such things as beaming power to the Earth, Moon, or Mars or even to serve as an interplanetary refuelling station. These type of large power systems my play a key role in future manned missions to Mars. Several different concepts have been proposed, but they all have the common element of an incredibly large area of solar cells. The proposed systems employ solar arrays which have a total area in the neighbourhood of several football fields. One such SSP concept is the NASA Sun Tower shown in Figure 10.

The largest space solar array that has been deployed to date is the United State Solar Array which is being used to power the International Space Station (ISS) (see Figure 2). When completed the ISS will be powered by 262,400 (8 cm × 8 cm) silicon solar cells with an average efficiency of 14.2% on 8 US solar arrays (each ~34 m × 12 m) [2]. This will generate about 110 kW of average power. An additional 20 kW of solar power is also scheduled to be provided by arrays developed by Russia.

Another example of large solar power systems which although are not truly in space but share many of the same requirement are high altitude airships and aerostats. Lockheed Martin with ITN Energy Systems, Linstrand Balloons Ltd. and others are developing high altitude airships that incorporate large array solar arrays to produce power (see Figure 11). An airship with a surface area on the order of 10,000 m^2 would only need a small portion of its surface to be covered by solar cells to achieve a daytime power production over 100 kW.

References

[1] Easton, R.L. and Votaw, M.J. 1959. Vanguard I IGY Satellite (1958 Beta), *Rev. Scientific Instruments*, Vol. 30(2), pp. 70–75.

[2] Hague, L, Metcalf, J., Shannon, G., Hill, R. and Lu, C. 1996. Performance of International Space Station electric power system during station assembly, *Proc. 31st Intersociety Energy Conversion Engineering Conference*, pp. 154–159.

[3] Stassinopoulos, E. and Raymond, J. 1988. The space radiation environment for electronics, *Proc. IEEE*, Vol. 76(11), pp. 1423–1442.

[4] Kayali, S. Space radiation effects on microelectronics, *NASA Jet Propulsion Laboratories Course*. See material on JPL web site at: http://nppp.jpl.nasa.gov/docs/RadcrsFinal2.pdf.

[5] Sawyer, D.M. and Vette, J.I. 1976. AP8 trapped proton environment for solar maximum and solar minimum, *Report NSSDA 76-06*, National Space Science Data Center, Greenbelt, MD.

[6] Vette, J.I. 1991. AE8 trapped electron model, *NSSDC/WDC-A-R&S 91-24*, National Space Science Data Center, Greenbelt, MD.

[7] Feynman, J., Spitale, G., Wang, J. and Gabriel, S. 1993. Interplanetary Proton Fluence Model: JPL 1991, *J. Geophysical Research*, Vol. 98(A8), p. 13281.

[8] Garrett, H.B. and Hastings, D. 1994. The Space Radiation Models, Paper No. 94-0590, *32nd AIAA Aerospace Sciences Meeting*, Reno, Nevada.

[9] Tennyson, R.C. 1993. Atomic Oxygen and Its Effect on Materials, In: *The Behaviour of Systems in the Space Environment*, Kluwer Academic, pp. 233–257.

[10] *Solar Array Design Handbook*, Vol. 1, JPL, 1976.

[11] *TRW Space Data*, N. Barter, Ed., TRW Space & Technology Group, Fourth Edition, 1996.

[12] Fahrenbruch, A.L. and Bube, R.H. 1983. *Fundamentals of Solar Cells*, Chapter 2, Academic Press, Boston.

[13] Loferski, J.J. 1956. Theoretical considerations governing the choice of the optimum semi-conductor for the photovoltaic solar energy conversion. *J. Appl. Phys.*, Vol. 27, p. 777.

[14] Jackson, E.D. 1955. Areas for improvement of the semiconductor solar energy converter. *Trans. Conf. On the Use of Solar Energy*, Tucson, Arizona, Vol. 5, p. 122.

[15] Bücher, K. and Kunzelmann, S. 1998. The Fraunhofer ISE PV Charts: Assessment of PV Device Performance, Report EUR 18656 EN, Joint Research Center, pp. 2329–2333.

[16] Green, M., Emery, K., Bücher, K., King, D. and Igari, S. 1998. Solar Cell Efficiency Tables (version 11), *Progress in Photovoltaics: Research and Applications*, Vol. 6, pp. 35–42.

[17] Green, M., Emery, K., King, D., Igari, S. and Warta, W. 2001. Solar Cell Efficiency Tables (version 18), *Progress in Photovoltaics: Research and Applications*, Vol. 9, pp. 87–293.

[18] King, R., Haddad, M., Isshiki, T., Colter, P., Ermer, J., Yoon, H., Joslin, D. and Karam, N. 2000. Metamorphic GaInP/GaInAs/Ge Solar Cells, *Proc. 28th IEEE Photovoltaic Specialist Conf.*, Anchorage, pp. 982–985.

[19] Murphy, D., Eskenazi, M., White, S. and Spence, B. 2000. Thin-Film and Crystalline Solar Cell Array System Performance Comparisons, *Proc. 29th IEEE Photovoltaic Specialists Conf.*, Anchorage, pp. 782–787.

[20] Tada, H., Carter, J., Anspaugh, B. and Downing, R. 1982. *Solar Cell Radiation Handbook* (3rd edition), JPL Publication 82-69.

[21] Anspaugh, B. 1996. *GaAs Solar Cell Radiation Handbook*, JPL Publication 96-9.

[22] Summers, G.P., Burke, E.A. and Xapsos, M.A. 1995. Displacement Damage Analogs to Ionizing Radiation Effects, *Radiation Measurements*, Vol. 24(1), pp.1–8.

[23] Bailey, S., Long, K., Curtis, H., Gardner, B., Davis, V., Messenger, S. and Walters, R. 1998. *Proc. 2nd World Conf. on Photovoltaic Solar Energy Conversion*, Vienna, pp. 3650–3653.

[24] Morton, T., Chock, R., Long, K., Bailey, S., Messenger, S., Walters, R. and Summers, G. 1999. *Tech. Digest 11th Intl. Photovoltaic Science and Engineering Conf.*, Hokkaido, pp. 815–816.

[25] Messenger, S., Walters, R., Summers, G., Morton, T., La Roche, G., Signorini, C., Anzawa, O. and Matsuda, S. 2000. A Displacement Damage Dose Analysis of the COMETS and Equator-S Space Solar Cell Flight Experiments, *Proc. 16th European Photovoltaic Solar Energy Conference*, Glasgow, pp. 974–977.

[26] Jenkins, P., Kerslake, T., Scheiman, D., Wilt, D., Button, R., Miller, T., Piszczor, M. and Curtis, H. 2002. First Results from the Starshine 3 Power Technology Experiment, *Proc. 29th IEEE Photovoltaic Specialists Conference*, New Orleans, pp. 788–791.

Part IIIe

Case Studies

Architectural Integration of Solar Cells

Rafael Serra i Florensa, ETSAB, Universitat Politècnica de Catalunya, Barcelona, Spain
Rogelio Leal Cueva, GESP, Parc Cientific de Barcelona, Spain

1 Introduction

Architecture may be defined as a complex whole of interrelated systems that produce satisfactory spaces for human activity. The architectural conception of buildings is commonly made from matter and geometry; where energy usually plays a secondary role for architects who tend to interpret buildings by what can easily be represented in drawings or photographs. Energy in architecture is difficult to represent and, therefore, briefly studied in architectural projects. Only when the existence of energy is revealed in visual elements and components will the issue become important for architects.

The integration of energy-related systems in architecture tends to be roughly simplified, and unfortunately, often considered as components that should be hidden from view. Furthermore, as so often happens in the history of architecture, the incorporation of new technologies is realised in a shameful way, hidden as if they were an offence to good taste.

This is particularly evident in the integration of natural energy collector technologies in buildings, especially solar photovoltaic technology. When integration is considered, it is often thought of as covering up the presence of the collector surfaces, hiding them behind the railings of flat surfaces or putting them on top of inclined roofs with the same inclination as the roofs.

The final result is aesthetically inadequate, the camouflage tends not to be absolute and in many cases the added elements are visible with a dreadful appearance. The pre-existing constrictions frequently force collector surfaces to be badly oriented or to be partially shaded at a certain period of the day or year. This is one more example of the existing difficulty in architecture to integrate new technologies.

It would make sense to consider photovoltaic systems as one more element in the building that is being designed. Choosing a proper location, not only from the technical point of view, but also from the aesthetic point of view; ensuring that the module and its supports have the maximum quality. They should be interpreted as one more element in architecture that contributes to the formal quality of the whole.

2 Architectural Possibilities for PV Technology

Architecture allows for solar energy to be used when it is incident in its outer coatings. The impact of this energy may be positive or negative in buildings, depending on the climatic characteristics of the site and the time of the year. Therefore, the use of solar energy to generate electricity should be done in a way that the building may absorb heat during cold weather, and be protected from it during hot weather.

On the other hand, buildings are vast energy consumers, that use it for a varied range of applications. This energy is normally generated in complex, expensive and polluting systems. The collection of solar energy *in situ* results in a tempting alternative to the powerful supply grids that are

compulsory, allowing us to reduce the external supply or even eliminating it in many cases.

Making a comparison with natural ecosystems, buildings in our urban ecosystems must carry out a similar function as trees in the woods. This way, buildings would collect energy in its outer surface, and be able to conveniently transform and accumulate it to be used for its own needs. This way of approaching the issue would reduce dependence on external energies; the urban grids would be minor, functioning more like a balance of energy than a supplier.

2.1 Architectural PV Energy System

The city of today is a complex ecosystem, crossed by intense flows of matter, energy and information. A great part of the load that these ecosystems carry upon the planet is the result of deficient management of these flows, and in particular, the energy flows.

Solar energy, collected by photovoltaic systems, is actually one of today's most promising energy sources. Its integration in buildings located in urban areas play an important role when analysing its use on a large scale.

The quantity of solar radiation that is incident on buildings in cities represent a huge volume of energy that is only used in a minor proportion, partially due to it being ignored. Also, high density building in cities has turned solar-exposed urban structures into compact building forms, where buildings shade mutually.

There is an emerging awareness about the possibilities of using natural energies in architecture, but there is very little awareness about how urban building forms may contribute to this happening. A determined action in this sense would not only reduce fossil fuel consumption, but would also considerably improve the quality of the urban environment.

It is especially important to consider the most favourable strategies to obtain an efficient use of solar energy that is often being wasted. It is particularly

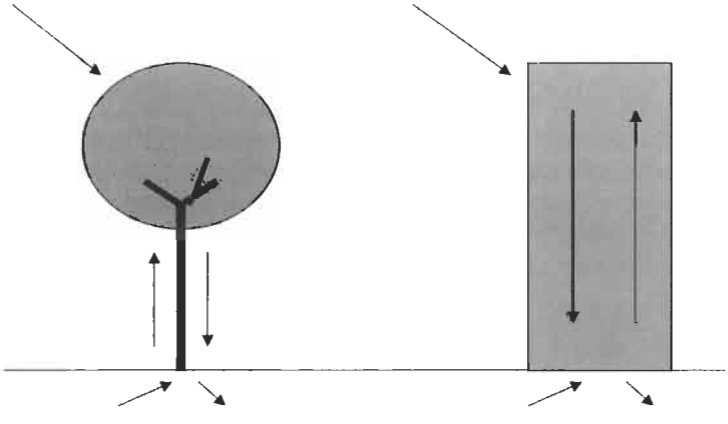

Figure 1 Urban and natural ecosystems

important to develop and use collector surfaces that may be integrated in buildings, using them to improve their functionality and aesthetics.

Buildings could be considered to be open ecosystems since various types of energy penetrate them. Some are natural energy, as solar radiation. Others are artificial energy, as electricity, gas conduction, etc. The thermal equilibrium of the building depends on the input and output (losses) flows of energy. Among artificial energy, electrical energy is more and more important every day. It is a high quality type of energy, offers great flexibility and is used in multiple types of applications even though it causes high environmental damage in its origin. In order to improve the architectural energy performance and the environment in general, we should reduce electricity consumption from artificial sources. Photovoltaic technology allows us to integrate solar collectors in buildings that will reduce consumption drastically while producing clean electrical energy.

2.2 Surface Availability in Buildings

There are four main possibilities to locate solar energy collectors in architectural projects (see Figure 3).

A. Flat roof. A common solution for PVs on buildings is on rooftops. Usually locating the collector surface on existing rooftops on additional structures.

B. Sloped surface. Collector surfaces may be linked to external inclined surfaces in buildings. This may result in a correct, aesthetic and functional solution if the inclined surface is well oriented and has the appropriate inclination.

There is, however, the danger of generating these roof tops 'artificially', without corresponding to spaces appropriate to the building, having a negative aesthetic effect and meaning unjustifiable supplementary economic costs. In this case, it could be a better solution to design a support structure for the collectors, integrating it to the forms of the building, but not trying to pretend to that functional spaces are being covered.

C. Facade. Photovoltaic modules may be located on the facade of buildings, replacing or complementing a part of the outer coating.

In this case, the main problem is the verticality of the facades. The annual efficiency of a 90° inclination surface would be around 35% below optimal in

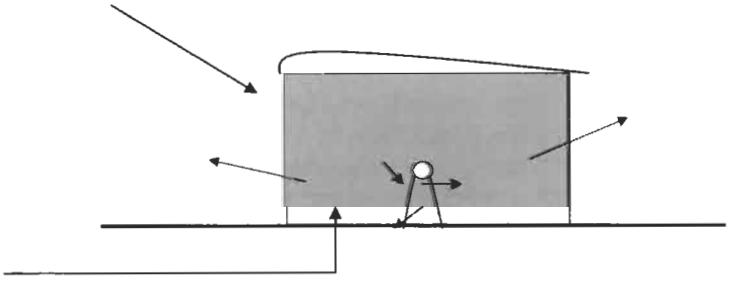

Figure 2 Architectural energy system.

A: flat roofs
B: sloped surface
C: vertical facade
D: independent structures

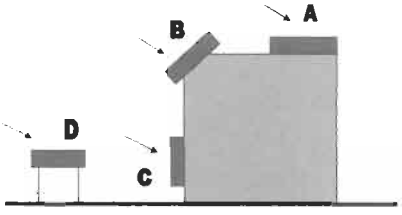

Figure 3 Surface availability.

Figure 4 Flat PV roof at Gouda. (© BEAR Architecten. Reprinted with permission).

southern European countries and around 20% for northern European countries (see Figure 8). However, losses during the winter would be lower than during the summer. The advantages that may result from facade integration, including the protection to the building from excessive solar radiation that modules may offer, make this solution advisable in certain cases.

In other occasions, collector surfaces form auxiliary facade elements, as blinds, railings, and others. In these cases, the inclination of the modules may be optimised, and even be able adapt to the solar path during different times of the year.

D. Independent structures. It is possible to incorporate collector surfaces to independent structures, as gazebos, shadings, and others, as part of the architectural whole of a project. In this case, mayor freedom of shape and situation may improve the orientation of the surfaces. Also, the independence

Figure 5 Sloped PV roofs at Amersfoort.

from the building may improve the formal impact of the whole, as long as the design of the element is adequate.

2.3 Solar Energy Availability in Buildings

The amount of solar energy that is incident to the external coating in buildings is related to several factors. These are basically: shadings, orientation and meteorological conditions. Figure 8 shows the incident solar energy on a collector surface in southern Europe, compared to the optimum according to its orientation. The collector surfaces in buildings must be free of shading from elements such as trees, chimneys, light posts, neighbouring buildings and others.

3 Building Integrated Photovoltaics (BIPVs)

Photovoltaic modules may become part of external coatings in buildings not only as energy generators, but also as external building elements capable of reducing energy consumption. To up-grade photovoltaic modules from energy generators to aesthetic and functional building elements, it requires the collaboration of a multidisciplinary team and the introduction of additional design concepts. Full awareness of the functionality of PV systems and of architectural quality is very important in order to create a multifunctional PV element that complies simultaneously with practical and aesthetic needs in buildings. Creativity will be a determinant factor when combining disciplines to

Figure 6 *PV facade at Sonnepark Dornbirn, Austria. Source: IEA Task VII PV Database. © stromaufwärts. Reprinted with permission.*

achieve an appealing result. Both multifunctionality and aesthetics are the most important factors in BIPVs.

3.1 Multifunctionality of PV Modules

A key property of BIPVs is that they perform various tasks simultaneously. They are active components that maximise energy production and they are passive external building elements that contribute to minimising energy consumption. Thus, sharing a number of functions in one same element forming a crucial part of the energy strategy in buildings.

It is possible to use conventional PV modules to achieve multifunctionality, but then, the architectural possibilities are limited and the aesthetics are compromised. More convenient are multifunctional PV modules, which are designed to comply with mechanical, aesthetic and functional requirements in buildings. There is a wide range of multifunctional PV modules in the market. Also, modules with special requirements may be custom-made by certain

Figure 7 An independent PV structure: the giant solar cube in southern California. Photo courtesy of Steven Strong, Solar Design Associates, Harvard, MA, USA.

manufacturers. All BIPV should comply with local building regulations (see also Chapter IIIc-2) [1].

3.2 PV Mounting Techniques

There are various ways of mounting PV modules to buildings. They vary according to the location of the PV array in the building, the size of the array and the additional functions the PV modules must carry out for the energy strategy of the building.

A. Flat roofs. A typical solution for installing PV modules in flat roofs is to fix the modules to a mounting system that is heavy enough to be able to stay in place

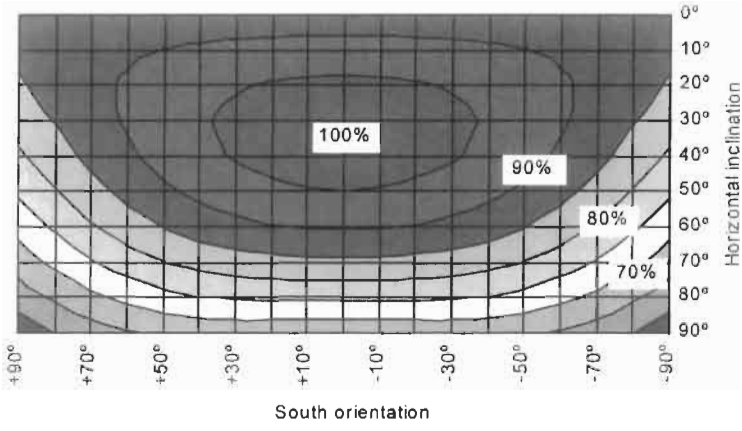

Figure 8 Solar energy availability in southern Europe. Source: Teulades i Façanes Multifuncionals.

without having to be fixed by bolts and nuts to the building, avoiding perforation. This mounting system is usually made of concrete, or there are solutions where a lightweight, easy to transport case may be filled-in at site with any heavy material such as stones (Figure 9).

B. Sloped roofs. Aluminium sections are often mounted to the roof to provide a primary structure to which the PV modules may be attached. Another common solution for mounting PVs in a sloped roof is as PV tiles. In this type of solution, the PV cells are encapsulated in modules that act as traditional tiles (Figure 10).

C. Facade. In facades, as on rooftops, when the system is large, it is convenient to pre-assemble the modules so that they may be mounted in groups. This way, time and money is saved. On the other hand, PV modules installed as louvres, have a special mounting system that usually offers a variety of sizes, fixing possibilities, solar cell types and densities (Figure 11).

D. Independent structures. Photovoltaics in independent structures are normally mounted in a conventional way. If they are to be integrated to the architectural whole of the building, as part of a landscape, then special attention should be paid to the aesthetic qualities of the mounting structure (Figure 12).

4 Aesthetics in PV Technology

The aesthetic properties of PV technology is crucial for its acceptance and implementation in the built environment. It is therefore important to harmonise the visual impact of PVs with the architectural language in buildings. There are various factors that determine the visual impact of PV technology. Mainly, these factors are the elements that compose the PV modules and their configuration. It is essential to explore the aesthetic potential these factors have in order to enhance the visual value of PV systems.

Table 1 Multifunctionality of BIPVs.

PVs as:	Multifunctionality	Figure	Explanation
Active components	Hybrid PV–thermal system	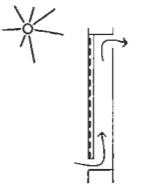	The produced heat in the PV modules may be transported in a heat transfer medium (air or water) to be used for minimising energy consumption for heating during winter. During summer, the heat may be discharged to the atmosphere, cooling the PV cells and increasing their efficiency.
Passive Components	Natural daylight	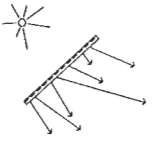	Semi-transparent PV modules produce electricity whilst allowing natural daylight into the building. Energy consumption is reduced in artificial lighting. The heat introduced to the building by daylight, should be controlled during hot weather.
	Shading	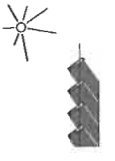	PV modules may produce electricity whilst protecting the building from excessive solar radiation. The cooling energy loads are reduced in hot weather by reducing solar incidence on the building.
	Natural ventilation	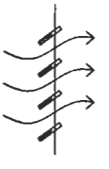	Natural ventilation, if well planned, may be used to cool the building reducing cooling energy loads during hot weather. Natural ventilation cools the PV modules increasing their performance.

It is in the manufacturing process that opportunities are found to transform the visual impact of the PV modules. A few of the properties that may be modified are shape, size, colour, texture and translucency (Table 2) [2].

4.1 Shape

The possibility to achieve various shapes of PV cells and modules increases the chances of adapting this technology onto architectural projects where there are various types of external surfaces not necessarily flat nor square. There are certain buildings in which the specific shapes of PV modules is the most convenient solution for fitting the system properly in place.

There are basically two factors that determine the shape of PV modules:

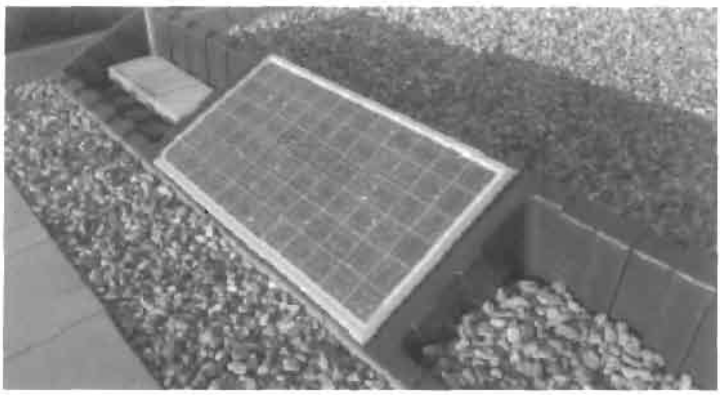

Figure 9 PV rooftop mounting system. © Econergy International. Reprinted with permission.

Figure 10 Installing a sloped PV roof. Source: IEA Task VII PV Database. © MSK Corporation. Reprinted with permission.

1. The photovoltaic wafers.
2. The front and back cover of the module.

Conventional crystalline-silicon wafers are square in shape if they are multi-crystalline and circular if they are single-crystalline. Single-crystalline circular wafers are often trimmed to semi-squares so that space is optimised in the module. During the manufacturing process, it is possible to obtain other forms of wafers as triangles, hexagons and others. Various shapes of thin-film PV modules may also be achieved by depositing the semiconductor material to a glass substrate with any type of shape.

The shape of the module where the wafers are encapsulated may be any shape the glass industry may offer. Aesthetically, most architects would prefer self-similitude where the shape of the PV module is the same shape as the cells (i.e. triangular modules with triangular cells, hexagonal cells in hexagonal modules, etc.) [3].

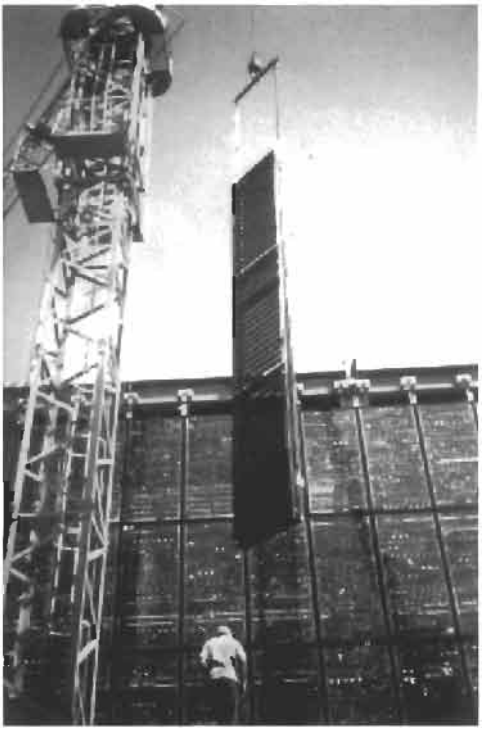

Figure 11 Installing PV facade. © Teulades i Façanes Multifuncionals. Reprinted with permission.

4.2 Size

Photovoltaic technology is characterised for being modular. A wide range of nominal power may be achieved in modules by interconnecting solar cells in series and/or in parallel. The nominal power for building integrated PV modules is normally between 50 and 200 W, but this may vary according to the specific project. The size of a crystalline silicon PV module is mostly determined by the amount of solar cells that are encapsulated in it. Amorphous silicon PV modules require more area per Wp than crystalline silicon PV modules.

4.3 Colour

The colour of crystalline-silicon solar cells is determined by the width of the antireflective coating, a thin layer of silicon nitride that prevents reflection of solar energy from the cells. The colours we normally see in solar cells (i.e. dark grey for single-crystalline, dark blue for multi-crystalline) are produced by the antireflective coating width that allows the highest efficiencies. By varying the width of the antireflective coating, we achieve new colours that add to the aesthetic possibilities of PV technology, but compromising the efficiency of the cells.

Figure 12 Installing an independent PV structure. © Teulades i Façanes Multifuncionals. Reprinted with permission.

Table 2 Visual determinants in PV technology

Property	Determined by:
Shape	Semi-conductor material, Front and back covers
Size	Number of cells Gap between the cells
Colour	Antireflective coating (front side) Back cover (back side)
Texture	Semiconductor material Gap between cells Contact grid
Translucency	Semiconductor material Gap between cells Front and back covers

4.4 Texture and Patterns

The texture of the solar cells is determined by the type of technology from which the solar cell is made of. Single crystalline solar cells have a homogenous texture; the texture of multi-crystalline solar cells is characterised by multi-faceted reflections. Amorphous silicon has a different texture from crystalline silicon cells as a result of the thin film manufacturing process.

Patterns in solar cells are determined by the contact grid, which extend through the cell in order to collect the produced electricity. It is necessary to

Table 3 Typical sizes for multi-crystalline silicon PV modules

Nominal Power (W):	Area (m^2):	H*W*T (mm):	No. of cells:
50	0.5	940*500*50	36
120	1.10	1100*990*50	72

Table 4 Typical sizes for amorphous silicon PV modules. Source: Photon Magazine

Nominal Power (W):	Area (m^2):	H*W*T (mm):	No. of cells:
50	0.8	1200*650*50	71
128	2.6	5800*450*30	22

(a) (b) (c) (d)

Figure 13 PV shapes. (a–c) Modules demonstrated in the EU BIMODE Project [4]. © BP Solar. Reprinted with permission. (d) The triangular module developed by one of the authors (R.L.C.) at the University of Southampton, UK.

consider the minimum obstruction possible on the front side in order to allow the maximum solar energy to reach the semiconductor material. Although most creative designs of contact grid are on a experimental stage, some may be found in the market. The designs shown in Figure 16 are an alternative to the standard H-grid pattern shown in Figure 15.

4.5 Translucency

The translucency of PV modules may be achieved in various ways. The front and back covers play an important role. The front cover is always transparent in order to allow the maximum solar energy through to the cells. The back cover may be opaque, translucent or transparent, depending on the natural lighting needs of the building. The gap between the cells may determine the semi-transparency of the modules by letting light through. Further so, crystalline silicon solar cells may be micro-perforated to achieve translucency. Thin-film PV modules made of amorphous silicon can also be used to produce semi-transparent or translucent cells [7].

4.6 Point of View

The distance and the angle from where the PVs are seen from is a determinant factor for the visual impact they produce. PV modules differ in appearance from

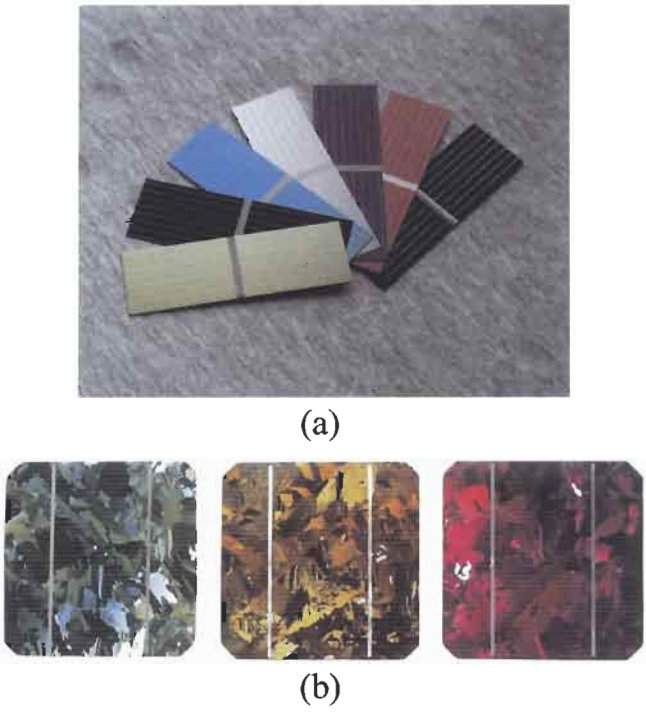

Figure 14 Coloured monocrystalline (a) and multicrystalline (b) silicon solar cells manufactured by Solartec. The efficiency of monocrystalline cells ranges from 11.8% (silver) to 15.8% (dark blue, standard).

the front and from the back. The front cover, seen from the outside of the building, shows the semiconductor material with an antireflexive coating and the contact grid. The back side, on the other hand, is seen from the interior of the building. There is also a difference whether it is seen from near or from far, as the following images show.

5 Built Examples

The following projects show how building integrated photovoltaics enrich the architectural value of buildings, applying new concepts of sustainability to the urban landscape.

5.1 Case Study 1: The British Pavilion, Expo '92 [8]

Location: Seville, Spain.
Date of construction: 1992.
Description: An example of bio-climatic architecture in a hot-dry climate that combines traditional cooling strategies with high-tech PVs.

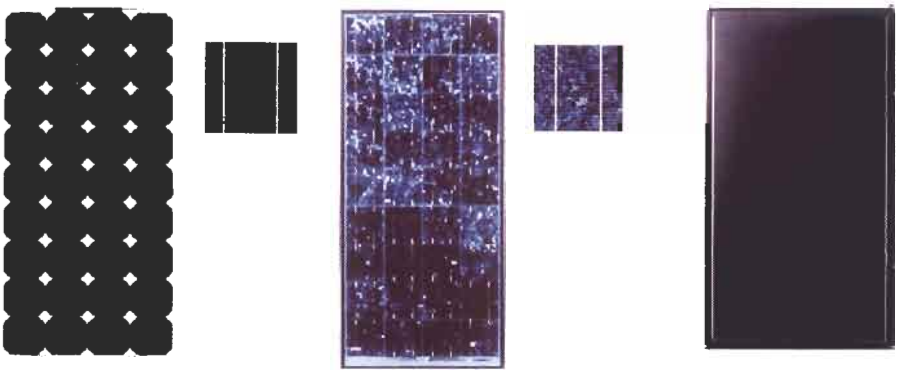

(a) (b) (c) (d) (e)

Figure 15 Texture in photovoltaics. 1: Single-crystal modules (a) and solar cells (b). The pseudo-square shape in (a) is more usual for the single crystal than the true square in (c). 2: Multicrystalline modules (c) and solar cells (d). 3: Amorphous modules (e). © *BP Solar. Reprinted with permission.*

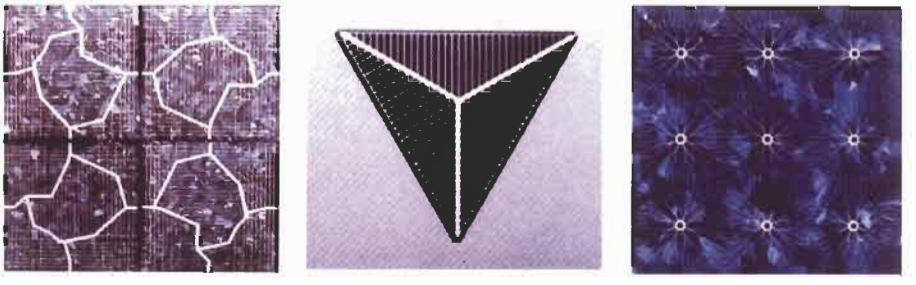

(a) (b) (c)

Figure 16 Patterns in photovoltaics. (a) One of the patterns developed by the Atomic Institute Vienna [5, 6]. © *Photon magazine. Reprinted with permission. (b) The triangular cell developed by one of the authors (R.L.C.) at University of Southampton, UK. (c) ECN Pin-up. (Source: ECN homepage.)*

PV system:

- Nominal power: 46 kWp
- Electricity generated: 70 MWh/year (estimated)
- Multifunctionality: PV elements shade the building whilst supplying energy for the cooling system.

Architectural energy system: A large water wall applies traditional cooling principles. Apart from giving the glass a translucent quality, the water limits the glass temperature to around 24 degrees, providing a cooler internal

Figure 17 Translucency in PVs. © Teulades i Façanes Multifuncionals. Reprinted with permission.

environment. The energy for the water pumps is supplied by the photovoltaic modules integrated to the sun sails on the flat roof.

5.2 Case Study 2: ECN, Buildings 31 and 42 [9]

Location: Netherlands Energy Research Foundation, Petten, the Netherlands.
Date of Construction: 2000–2001.
Description: PV technology is architecturally integrated in buildings 31 and 42 of the ECN, showing the proper integration of this technology into both new and existing buildings.

Building 31
PV system:

- Nominal power: 72 kWp
- Electricity generated: 57.60 MWh/year
- Multifunctionality: PV blinds that allow natural daylight and solar gains whilst shading.

Architectural energy system: An existing building is covered in PV sunshades that prevent the building from overheating during summertime whilst diffusing natural daylight to the interior. The renovation of the building is expected to reduce the primary energy demand by 75%.

Figure 18 PV back and front, far and close. (a) Source: IEA Task VII PV Database.(© Energie-Forum Innovation. (b) © *Teulades i Façanes Multifuncionals. Reprinted with permission.*

Figure 19 The British Pavilion, Expo '92. © BP Solar. Reprinted with permission.

Building 42
PV system:

- Nominal power: 43 kWp
- Electricity generated: 34.40 MWh/year
- Multifunctionality: Glass–glass PV modules that allow natural daylight and solar gains whilst shading.

Architectural energy system: A PV-covered conservatory, which is the connecting space between the two buildings, shades the building preventing overheating in summer at the same time that allows natural ventilation and a maximum use of daylight.

5.3 Case Study 3: Pompeu Fabra Public Library [10]

Location: Mataró, Spain.
Date of Construction: 1993.
Description: A pioneer demonstration project where a hybrid PV–thermal multifunctional system was installed in the facade and rooftop.

Figure 20 ECN, Buildings 31 and 42. © BEAR Architecten.

Figure 21 Pompeu Fabra Public Library. © Teulades i Façanes Multifuncionals.

PV system:

- Nominal power: 53 kWp
- Electricity generated: 45 MWh/year
- Multifunctionality: An air chamber in the PV modules acts as a thermal collector system whilst allowing natural daylight, solar gains and shading.

Architectural energy system: The south-facing vertical facade of the building and the skylights are equipped with a multifunctional hybrid PV–thermal system.

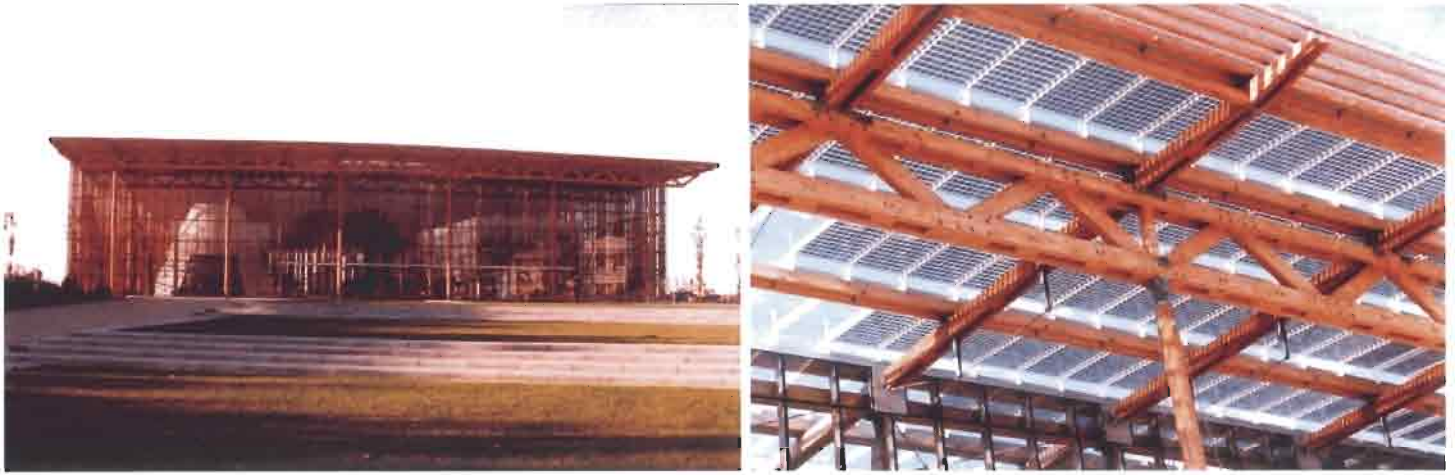

(a) (b)

Figure 22 The Mont Cenis Conference Centre in Herne Sondingen. (a) The front elevation. (b) The non-uniformly spaced solar cells in the roof modules resemble clouded sky.

The produced electricity is exported to the electric grid. The produced thermal energy is dissipated to the surroundings in summer, and used by the heating system during winter, thus reducing cooling and heating loads, respectively. Natural daylight is introduced to the building through the PV skylights and south facade, reducing artificial lighting in the building.

5.4 Case Study 4: Mont Cenis Conference Centre [11]

Location: Herne Sondingen, Germany.
Date of Construction: 1999.
Description: The old coal mining site of Mont Cenis, in Herne-Sodingen has now been developed into an energy and environmentally conscious conference centre. The buildings are protected by a carefully designed membrane containing photovoltaic modules that resemble clouds in the sky and create a Mediterranean climate in the site.
PV system:

- Nominal power: 1000 kWp
- Electricity generated: 750 MWh/year
- Multifunctionality: PV modules in the external membrane shade the buildings whilst allowing solar gains, natural daylight and natural ventilation to the conference centre area.

Architectural energy system: A series of architectural sustainability concepts have been applied to this project. There is plenty of vegetation, openings in the membrane allow for natural ventilation, and the translucent PV modules create a comfortable natural lighting effect. Rain water is collected and the building has an efficient water use system. The structure is made from wood grown near the site reducing the energy content in energy and materials.

During winter, the heat received by solar irradiation in the building is used, reducing heating loads. During the summer, natural ventilation is backed up by a mechanical system creating a breeze that maintains the site in a comfortable atmosphere.

References

[1] Markvart, T., Ed. 2000. *Solar Electricity*, John Wiley & Sons, p. 194.
[2] Sick, F. and Erge, T. 1996. *Photovoltaics in Buildings- A Design Handbook for Architects and Engineers*, International Energy Agency, Solar Heating and Cooling Programme, Task 16, pp. 87 and 88.
[3] Pearsall, N. 1997. Results of European wide consultation of architects, In: *Architecture and Photovoltaics – The Art of Merging*, January 28, 1997, Leuven, Belgium EUREC Agency.
[4] Schneider, A., Claus, J., Janka, J.P., Costard, H., Bruton, T.M., Noble, R., Radike, M, Summhammer, J., Hilcox, D., Aceves, O., Anzizu, O., Koch, W.,

Tobias, L., Luque, A. 2000. Development of Coloured Solar Modules for Artistic Expression with Solar Facade Designs Within the 'BIMODE' Project. *Proc. 16th European Photovoltaic Solar Energy Conf.*, Glasgow.

[5] Radike, M., Summhammer, J., Breymesser, A. and Sclosser, V. 1998. Optimization of artistic contact patterns on mSi solar cells. *Proc. 2nd World Conf. on Photovoltaic Solar Energy Conversion*, Vienna, p. 1603.

[6] Radike, M. and Summhammer, J. 1999. Electrical and Shading Power Losses of Decorative PV Front Contact Patterns. *Prog. Photovolt. Res. Appl.* Vol. 7, pp. 399–407.

[7] Hänel, A. 1999. *State of the Art in Building Integrated Photovoltaics*, European Directory of Sustainable and Energy Efficient Building, pp. 80–87.

[8] Humm, O. and Toggweiler, P. 1993. *Photovoltaics in Architecture*, Birkhaüser Verlag, Basel.

[9] Reijenga, T. *PV – Integration in solar shading (renovation) and PV – Integration in atrium glazing (New Building), ECN 31 and 42*, Petten (NL).

[10] Lloret, A. 1996. *The Little Story of the Pompeu Fabra Library of Mataró*, Editoreal Mediterranea; Lloret, A. 1996. *Móduls Fotovoltaics Multifuncionals a la Biblioteca de Mataró*. Eficiencia Energetica no. 137, April/June.

[11] *Entwicklungsgesellschaft Mont-Cenis* (Brochure with description of the project) Stadt Herne/Montan Grustuckgesselschaft, 1998; Energieland NRW, *Model Project: Mont-Cenis Energy Park*, Future Energies.

Further Reading

A Thermie Programme Action, 1998. *Integration of Solar Components in Buildings.*

Greenpeace, 1995. *Unlocking the Power of our Cities – Solar Power and Commercial Buildings.*

Greenpeace, 1996. *Building Homes with Solar Power*, London.

Hänel, A. 1999. *State of the Art in Building Integrated Photovoltaics*, European Directory of Sustainable and Energy Efficient Building.

Lloyd Jones, D. 1999. *The Solar Office: A Solar Powered Building With a Comprehensive Energy Strategy*, European Directory of Sustainable and Energy Efficient Building.

Max Fordham & Partners in association with Feilden Clegg Architects, 1999. *Photovoltaics in Buildings – A Design Guide*, Report No ETSU S/P2/00282/REP, Department of Trade and Industry, UK.

National Renewable Energy Laboratory, 1996. *Solar Electric Buildings – An Overview of Today's Applications*, DOE/GO-10096-253US, Department of Energy, Washington, USA.

Niephaus, D. and Mosko N. 1997. The polyfacial PV power plant concept based on triangle solar cells and bypass support modules. *Proc. 14th European Photovoltaic Solar Energy Conf.*, Barcelona, pp. 1589–1592.

Photovoltaic Solar Energy – Best Practice Stories, European Commission, Directorate General XVII Energy, 1997.
Shaar-Gabriel, E. 1999. *Berlin Turns to the Sun. Solar Projects in the German Capital*, European Directory of Sustainable and Energy Efficient Building.
Strong, S.J. 1996. Power Windows-Building Integrated Photovoltaics, *IEEE Spectrum*, October.
Studio E Architects, 2000. *Photovoltaics in Buildings – BIPV Projects*, Report ETSU S/P2/00328/REP, Department of Trade and Industry, London.
Ten Hagen & Stam, 1995. *Building with Photovoltaics*, International Energy Agency, the Netherlands, ISBN 9071 694372.
Toggweiler, P. 1998. *Integration of Photovoltaic Systems in Roofs, Facades and the Built Environment*, European Directory of Sustainable and Energy Efficient Building, pp. 42–45.
van Zee, E. 1998. Building Power Stations – Will new Residential areas be the power stations of the 21st century? *Renewable Energy World*, July.

IIIe-2

Performance, Reliability and User Experience

Ulrike Jahn, Institut für Solarenergieforschung GmbH Hameln/Emmerthal (ISFH), Germany

1 Operational Performance Results

1.1 Overview of Performance Indicators

This section focuses on the evaluation of the technical performance of photovoltaic (PV) systems. To a great extent existing evaluation procedures are based on the European Guidelines and the IEC Standard 61724. In addition, there are recommendations on guidelines at national level, aiming to harmonise procedures on data collection, data processing and presentation of data. The increasing awareness of the importance of the PV technology and its potential has resulted in a worldwide acceptance of impressive research and investment programmes.

The *European Guidelines for the Assessment of Photovoltaic Plants* had been prepared by the European Solar Test Installation of the Joint Research Centre (JRC) in Ispra resulting in Document A [1], Document B [2] and Document C [3]. These guidelines have played an important role in the preparation and realisation of the IEC Standard 61724 [4]. The Standard titled 'Photovoltaic system performance monitoring – Guidelines for measurement, data exchange and analysis', first published in April 1998, expresses an international consensus on the subject of PV system performance monitoring and analysis. The document has the form of guidelines for international use published in the form of standards and is accepted by national committees.

Various derived parameters related to the system's energy balance and performance can be calculated from the recorded monitoring data using sums, averages and ratios over reporting periods τ such as days, months or years. The irradiation quantities H_I are calculated from the recorded irradiance G_I. The electrical energy quantities are calculated from their corresponding measured power parameters over the reporting period τ, whereas E_A is the energy from the PV array, E_{II} the DC energy input to the inverter and E_{IO} the AC energy output from the inverter. Key parameters for PV system performance evaluation are given in Table 1.

For the comparison of PV systems, normalised performance indicators are used: e.g. energy yields (normalised to nominal power of the array P_O), efficiencies (normalised to PV array area A_a) and performance ratio (normalised to in-plane irradiation H_I). The most appropriate performance indicators of a PV system are:

- The final PV system yield Y_f is the total system output energy $E_{use,\tau}$ delivered to the load per day and kilowatt peak of installed PV array. The reference yield Y_r is based on the in-plane irradiation H_I and represents the theoretically available energy per kilowatt peak of installed PV per day.
- The performance ratio PR is the ratio of PV energy actually used to the energy theoretically available (i.e. Y_f/Y_r). It is independent of location and system size and indicates the overall effect of losses on the array's nominal power due to module temperature, incomplete utilisation of irradiance and system component inefficiencies or failures.

Table 1 Derived parameters for performance evaluation according to Standard IEC 61724

Parameter	Symbol	Equation	Unit
Global irradiation, in plane of array	H_I	$\int G_I dt$	kWh/m²
Array yield	Y_A	E_A/P_0	kWh/(kWp*day)
Final yield	Y_f	$E_{use,\tau}/P_0$	kWh/(kWp*day)
Reference yield	Y_r	$\int G_I dt/G_{STC}$	kWh/(kWp*day)
Array capture losses	L_c	$Y_r - Y_A$	kWh/(kWp*day)
System losses	L_S	$Y_A - Y_f$	kWh/(kWp*day)
Mean array efficiency	η_{Amean}	$E_A/\int_\tau G_I \cdot A_a dt$	%
Efficiency of the inverter	η_I	E_{IO}/E_{II}	%
Overall PV plant efficiency	η_{tot}	$E_{use,\tau}/\int_\tau G_I \cdot A_a dt$	%
Performance Ratio	PR	Y_f/Y_r	–

The normalised losses are calculated by subtracting yields (see Table 1) and also have units of [kWh/kWp*day]. The array capture losses L_c are caused by operating cell temperatures higher than 25°C (thermal losses) [5] and by miscellaneous causes such as:

- low irradiance
- wiring losses, string diode losses
- partial shading, contamination, snow covering, non-homogenous irradiance
- maximum power point tracking errors
- reduction of array power caused by inverter failures or by fully charged accumulators
- spectral losses, losses caused by glass reflections.

System losses L_s are gained from inverter conversion losses in grid-connected PV systems and from accumulator storage losses in stand-alone PV systems.

Figure 1 shows exemplarily the annual performance indices of a large grid-connected PV power system operating in Southern Italy since 1995. This standard presentation of energy yields and losses allows us to deduce malfunctions of PV systems. High capture losses and low final yields occurred in the first year of operation in 1995, corresponding to a low performance ratio of smaller 0.5 and low system availability as shown in Figure 2 for the same system and monitoring period. Both figures are related by the equation: $PR = Y_f/Y_r = Y_f/(Y_f + L_c + L_s)$.

Because of the given definition of L_c and L_s (see Table 1), a malfunction or inverter failure in grid-connected PV plants will result in a remarkable rise of capture losses L_c. This quantity is a very good indicator for system problems occurring in grid-connected PV plants. If the grid-connected system fails completely, the values of Y_A, Y_f and PR will drop to zero, while capture losses will rise towards Y_r and system losses become negligible. In the case of PV plant Serre during the first half of 1995, the inverters had to be adjusted to make them compatible with the frequent disturbances of the local medium voltage grid [6].

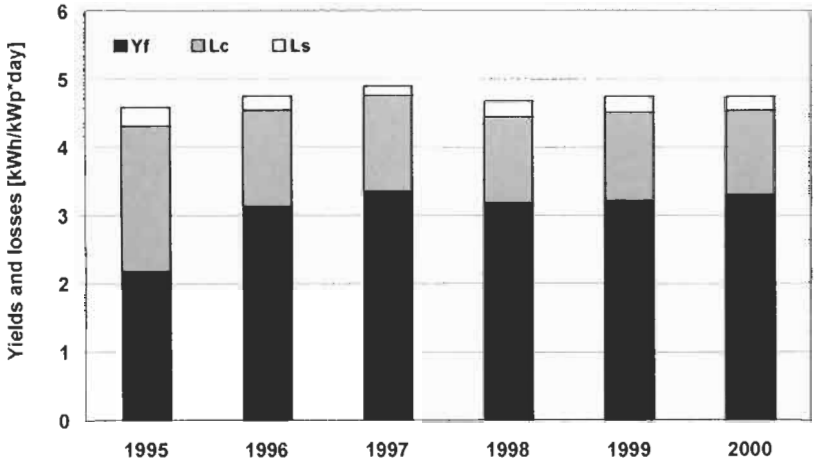

Figure 1 Annual performance results of 3.3 MWp PV system in Serre, Italy, in terms of final energy yield (Y_f), capture losses (L_c) and system losses (L_s).

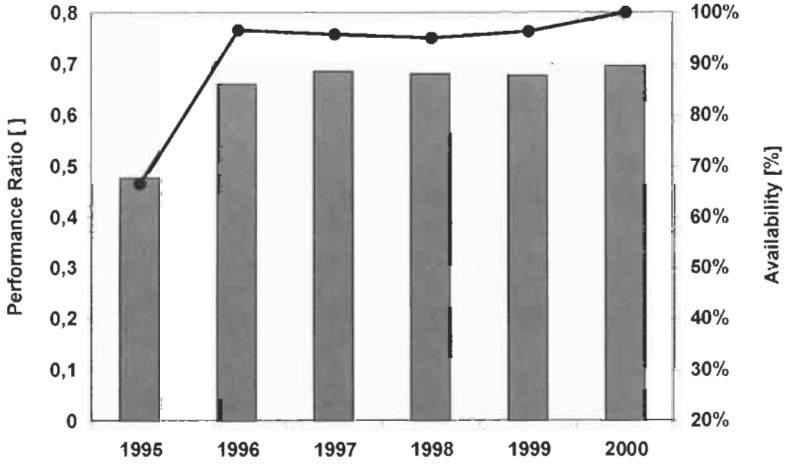

Figure 2 Annual performance results of 3.3 MWp PV system in Serre, Italy, in terms of performance ratio (PR) and system availability.

Thus unreliable inverters and complete system breakdowns were responsible for high capture losses and relatively low system losses in 1995 as shown in Figure 1.

The higher the PR, the better the system uses its potential. A low PR value means production losses due to technical or design problems. For the performance assessment of stand-alone PV systems, a high PR value does not always mean that the system is operating in the best conditions. If the system is under sized for the considered application, the PV system will show very high value of PR, but the user will not be supplied with electricity. For stand-alone systems (SAS), the value of PR is user consumption dependent. If the

consumption level is not correlated to the potential of the PV array, the PR will reach low values due to high capture losses. It has been shown that the PR, widely used for grid-connected PV systems, cannot be used alone to describe the quality of operation of SAS [7]. Different attempts have been made to introduce new parameters for the performance assessment of SAS [8, 9].

In this chapter, all results, experiences and lessons learnt are gained from the analysis of grid-connected PV systems. The investigated PV systems have an installed capacity between 1 kWp and 3 MWp adapted to various applications and located worldwide. The article aims at illustrating the operational behaviour of different grid-connected PV systems and at presenting the summary results in standard quantities allowing cross-comparison between the systems.

1.2 Summary Performance Results

From the performance analysis of 260 grid-connected PV systems supplied by the Performance Database of the International Energy Agency [10] (see Appendix), it was learnt that the average annual yield (Y_f) fluctuates only slightly from one year to another and has typical average values for one country (700 kWh/kWp for the Netherlands, 730 kWh/kWp for Germany, 790 kWh/kWp for Switzerland and up to $Y_f = 1\,470$ kWh/kWp for Israel). However, there is a considerable scattering around these average values for individual systems ranging from 400 kWh/kWp to 1030 kWh/kWp in Germany and from 450 kWh/kWp to 1400 kWh/kWp for plants in Switzerland [11].

Table 2 shows the annual final yields in terms of average, minimum and maximum values for PV systems in six different countries. While the different value of average final yield in each country can generally be explained by the difference in mean irradiation, the broad range of annual yields of factor two to three is quite significant and has system specific reasons.

High energy yields are due to:

- well-operating systems
- high component efficiencies
- optimum orientations of PV arrays
- well-maintained PV systems

Table 2. Annual final energy yields in different countries for comparison

Country	Systems analysed	Range of final yield in kWh/(kWp*year)	Average final yield in kWh/(kWp*year)	Reference
Netherlands	10	400–900	700	[12]
Germany	88	400–1030	730	[13]
Switzerland	51	450–1400	790	[14]
Italy	7	450–1250	864	[15]
Japan	85	490–1230	990	[16]
Israel	7	740–2010	1470	[17]

Reduced energy yields are caused by:

- failures of system or components
- shading of PV arrays
- frequent inverter problems
- long repair times
- bad orientations of PV arrays (e.g. facades)
- high module temperatures

The performance and yield of a PV system depend on all 'gain' and 'loss' factors and to which extend the loss factors can be avoided during project planning, plant installation and operation.

Figure 3 shows the distribution of annual performance ratios calculated from 993 annual datasets of 309 grid-connected PV systems operating in 14 different countries during 1989 and 2002 (for data used see Appendix). The annual performance ratio (PR) differs significantly from plant to plant and ranges between 0.4 and 0.85 with an average value of 0.67 for all 309 PV systems.

The broad range of performance ratios was also found for other research programmes, such as the Thermie programme of the European Commission [18, 19], the German 1000-Roofs-PV-Programme [20–22], the Japanese residential PV monitoring programme [23] and the PV programmes of the International Energy Agency [24, 25].

Former investigations on annual PR have shown that for well operating grid-connected PV systems during 1990 to 1999, a PR value between 0.6 and 0.8 can be expected [26]. It was found that well maintained PV systems show PR values of typically 0.75 at an availability of higher 98%. Taking into account realistic efficiency values of the improved inverter types of today, optimum

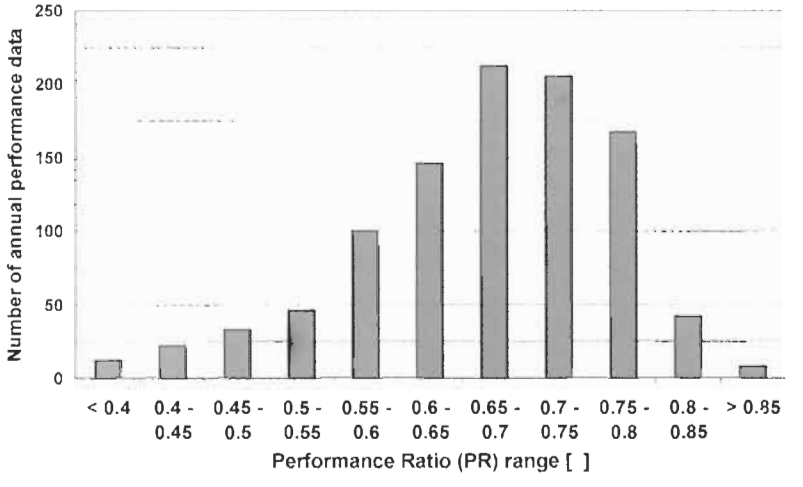

Figure 3 Distribution of annual performance ratios of 309 grid-connected PV systems (993 annual datasets) operating in 14 countries from 1989 to 2002.

values of annual PR between 0.81 and 0.84 may be achieved [27]. A tendency of increasing annual PR values during the past five years has been observed.

1.3 *Results from* 'Low Yield Analysis'

Within the German 1000-Roofs-Photovoltaic-Programme more than 2000 grid-connected PV residential systems of 1 to 5 kWp were installed during 1991 and 1995. This programme was accompanied by a monitoring and evaluation programme, which delivered remarkable results and experiences [28].

The low yield analysis was carried out at 17 selected PV systems to find the quantified reasons of reduced yields, which cannot be explained by system losses and tolerances due to system components. The selection criteria for the systems under investigation were the performance ratio (annual value lower than 0.60) and the final energy yield (75% less than the average value in that region) in addition to practical considerations, which allow technical inspections and four to six weeks monitoring campaigns at the selected sites. The detailed investigations of this project resulted in four additional reasons for very low yields and performances of grid-connected PV systems:

- Deviation from manufacturer's module specifications
- Shading due to trees, buildings or walls
- Defects of DC installation
- Inverter problems

1.3.1 Deviation from PV Module Specifications

During the 1000-Roofs-PV-Programme it became clear that various types of PV modules show significant differences in their performance [29, 30]. On one hand, there is a typical variance due to large-scale series production. On the other hand, a specific deviation of the PV module nominal power from the quoted rating was found depending on the manufacturer. This deviation of real measured power from the rated power was varying from manufacturer to manufacturer and generally appeared to be negative (typical value: −10%). During the investigations of the 17 selected PV systems, the differences of the monitored and to Standard Test Conditions (STC) converted module power and the power rating according to the manufacturer's module specifications ranged from −5% to −26% [31].

As a consequence, module manufacturers learned the lessons by declaring their PV modules for a quality check according to performance measurements. Additionally, standards organisations aimed at reduced measurement tolerances as well as at harmonisation of test equipment used by different manufacturers and authorised institutions.

1.3.2 Shading

Partial shading of the PV array leads to a significant reduction of the energy yield of a PV system [32]. The quantity of the reduction of the system yield is depending on the geometry of the shading object and that of the PV array. If

shading of one or more PV strings occurs during a clear and sunny day, the string currents of the shaded strings will be heavily reduced. During the annual course, the winter months are much more influenced by shading effects.

Out of the 17 PV plants under investigation, 10 PV systems were shaded to a higher or lower degree. Simulation calculations on the effect of PV array shading were carried out in order to gain quantitative figures [31]:

- Case 1: Partial shading of five of the six strings during morning hours by a tall (18 meters) leaf tree resulted in a reduced yield of 4%.
- Case 2: Partial shading of PV array by roof of neighbouring building as well as by surrounding trees lead to a reduced yield up to 10%.
- Case 3: Significant shading of the array by multiple trees located close to the house and exceeding the PV rooftop resulted in an annual reduction loss of higher 20%.

The analysis of the measured data and the calculations of the simulation programmes lead to the following results:

- Shading has reduced the annual energy yield up to 25% for an individual PV plant.
- Each plant has to be investigated individually as there are no typical shading conditions.
- From the very beginning of the project planning and concept making, the selection of shading free sites and optimum design of PV strings should be taken care of in order to avoid or minimise losses due to shading.

1.3.3 Defects of DC Installations

It is useful to perform technical inspections right after commissioning the PV system to detect and dissolve problems. During system operation failures due to bad installation techniques may occur, which often remain unnoticed. This may affect all components of the DC system. For the 17 PV systems under investigation, the following problems were found [31]:

- Defect clamp of a switch caused a loose contact and thus a partial failure of the string current.
- Defective screwed contacts inside the PV junction box caused the relevant strings to malfunction.
- Defect string diodes were caused by lightning.
- Cracked PV modules due to bubbles inside the laminate were observed and results in a reduced string current of about 60%.
- Defect connectors for PV roof tiles caused failures of strings.
- Defect monitoring equipment was responsible for failing string currents.
- Defect string fuses were registered in many plants.

The problems and defects encountered mainly caused failures of one string, in some cases that of several strings. For a PV system of five strings, the reduced

yield of one failing string is −20%, for example. It is advisable to check the strings currents and open circuit voltage on a regular basis (e.g. yearly maintenance). For the concept of new and improved PV systems, the use of switching elements and string fuses should be avoided and the installation technique should be as simple as possible.

1.3.4 Inverter Problems

The following inverter problems were identified:

- Partial or complete failure of the inverter due to hardware and software problems.
- Non-optimum maximum power point (MPP) tracking due to the permanent MPP tracking process of the inverter caused by fluctuations of irradiation and by partial shading of the PV array.
- Bad power regulation of inverters that operate with power/current limitation in case of limitation level being far below the rated power of the inverter.
- Fixed voltage operation may evolve adaptation losses, if an unsuitable level of inverter voltage is chosen.

It was found that the user of the PV system often discovers the problems related to inverters, but he is unable to estimate the significance of a particular failure. Except for complete inverter failures, the energy losses due to non-optimum operating inverters were found to be below 10%.

2 Trends in Long-Term Performance and Reliability

For the wide dissemination of PV technology, the results of long-term performance and reliability of PV systems are important. Financing schemes for PV such as fed-in tariffs require sound figures about real energy yields and performance data. This section deals with the questions:

- What is the technical performance of grid-connected PV systems in different countries?
- What are the significant differences?
- What is the long-term operational behaviour of PV systems?
- Does the average performance of PV systems increase for new installations?
- What is the reliability of PV systems and their components?
- Does the number of failures decrease?
- What are the trends in the technical performance of PV systems?

Performance data from 309 grid-connected PV systems in 14 countries are exported from the Performance Database of IEA (see Appendix) and 993 annual performance data are presented for operational years between 1989 and 2002.

Monthly input data come from different research and demonstration programmes in each of the countries, whereas the quality of the collected data depends on the level of monitoring (analytical or global), the kind of data acquisition system used, availability of the data, conditions of the programme and reliability of the data source.

For the interpretation of the results and the comparison between different countries, the amount of available data has to be considered: e.g. Germany is presented by 326 annual datasets, Switzerland by 244 and Italy by 81 annual datasets.

2.1 Trends from German 1000-Roofs-PV-Programme

The 48 PV systems under investigation are part of the 1000-roofs-PV-project in northern Germany and were installed between 1991 and 1993. These residential roof top systems have an installed capacity between 1 and 5 kWp (average 2.3 kWp) and operate since more than ten years. Global monitoring data are available from the standard monitoring and evaluation programme for the years 1993 to 2000. All PV rooftops are equipped with a calibrated silicon sensor (NES Si161) to measure the in-plane irradiation at the site of the PV array.

Figure 4 shows the annual performance ratios of 48 PV systems operating since the early 1990s. The annual PR differs significantly from plant to plant and shows a broad range for all operating years (e.g. in 1993: PR = 0.44 to 0.82). The average annual PR of 0.67 (48 plants) in 1993 drops to an average value of 0.62 (12 plants) in 2000. The average performance values show negative tendency and energy yields have been reduced by 8% between 1993 and 2000, although some defect inverters were replaced against new types with higher efficiencies.

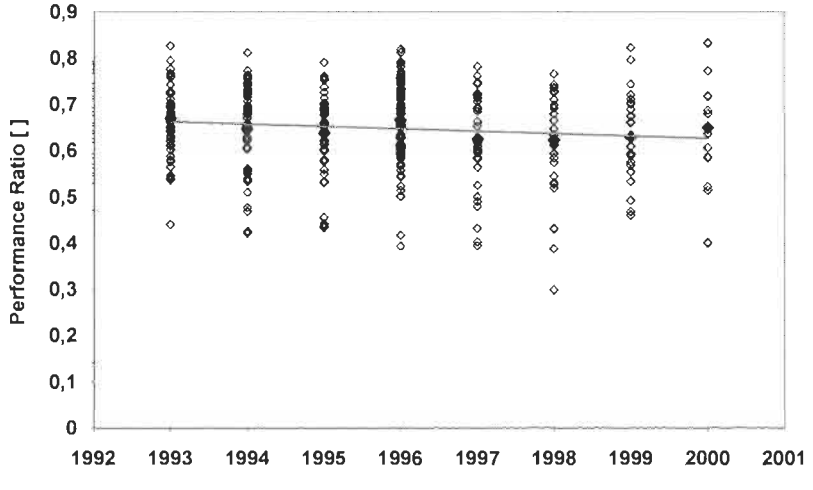

Figure 4 Trend of annual performance ratios of 48 residential PV systems in northern Germany installed between 1991 and 1993.

The registered failures at 21 PV systems during 10 years of operation show that defects and problems were first decreasing (1992 to 1995), but started to increase during last years (1999 and 2000). Considering a total number of 47 failures in 210 operational years, a statistical failure will occur every 4.5 years per plant. Inverters are contributing with 63%, PV modules with 15% and other system components with 23% to the total failures.

It can be concluded that a negative tendency in terms of performance and yields was observed for these early installations (1991–1993) from the rooftop programme during eight years of operation. Although the installers provided maintenance, some PV plants were facing severe failures of inverters and other components, which led to significant reductions of the annual energy yields. New PV installations (after 2000) in Germany revealed that they reach higher component efficiencies (e.g. inverter) and high performance ratios (> 0.80), but further investigations are required to confirm the increased quality of the newer systems in Germany.

2.2 Trends from Demonstration Projects in Switzerland

The 51 grid-connected demonstration plants in Switzerland are characterised by a broad range of applications (power plant, building integrated PV, roof top, sound barrier, freestanding) and by analytical monitoring campaigns. PV systems of 1 to 560 kWp installed power were continuously installed between 1989 and 1999 and monitored during 1991 and 2001. Due to online monitoring data availabilities of higher 95% were achieved. The average annual yield of 51 plants and 244 operational years result in 790 kWh/kWp and the average PR is 0.68.

Figure 5 shows the distribution of performance ratios between 1993 and 2001, which indicates a negative tendency of performance ratios. The range of

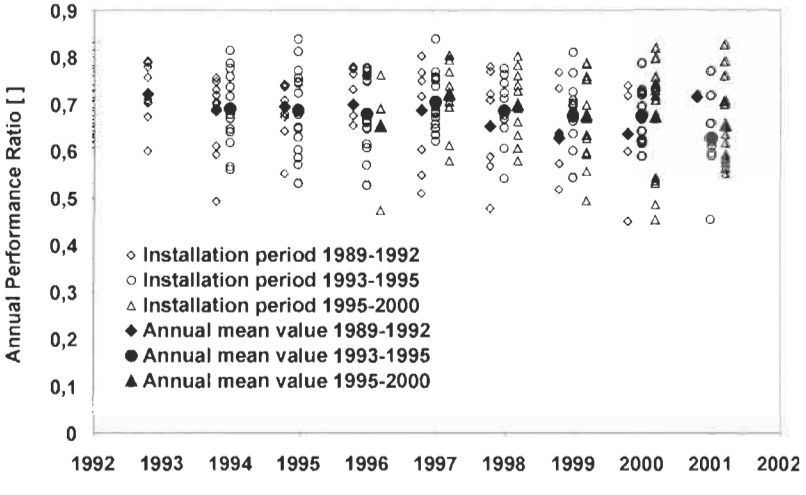

Figure 5 Trend of annual performance ratios of 51 grid-connected PV systems in Switzerland grouped in three parts according to their installation years.

PR values per year is rather high, e.g. in 2001 the plants take up PR values between 0.45 and 0.82. Well performing plants have reach annual 0.82 in conjunction with annual inverter efficiency of higher than 97%.

In Figure 5 the 244 annual PR values are grouped in three parts according to the period of plant installation:

1. The performance of early installations (1989 to 1992, presented by a square) has decreased between 1993 (PR = 0.72) and 2000 (PR = 0.64) due to failures of components and system. During their first operational years, they have performed well. It is assumed that the design criteria were high yields and favourable orientation conditions, which led to in optimum power plants and often free-standing PV systems.
2. PV plants installed between 1993 and 1995 (presented by a circle) show less decrease of average PR during eight operational years. They have lower PR values in the beginning (1994: PR = 0.69) and drop down to 0.63 in 2001. In this group of installations, many building integrated plants (BIPV) and facades are in operation, which reach lower PR values although they apply improved components (inverter).
3. The PV systems installed after 1995 (presented by a triangle) show low average PR values (1996: PR = 0.66), but this value of annual PR keeps nearly constant. The range of annual PR in 2001 is still very broad. During this period, PV design criteria were focussed on building requirements and architectural design criteria, which has led to lower yields and performances compared to the plants of the first group (primarily technical design criteria).

From this example, reduced performance factors are identified:

- System and component failures are the main factors for reduced PR values.
- High module temperatures of BIPV and facades have a negative impact on yields and PR (energy losses of 0% up to 10% [33]).
- Partial shading of the PV array is consciously accepted.
- Unfavourable array orientations given by the building structure play a negative role for the energy yield.

The overall performance of PR = 0.68 for the 51 Swiss PV systems remains below the expectations and efforts to build well-integrated *and* well-performing PV systems. BIPV substituting the building skin has a double value and must fulfil the compromise between architectural building aspects and technical performance of the system.

2.3 Trends from PV Programmes in Italy

Large PV power systems were installed since 1983 with capacities between 100 kWp and 3.3 MWp and deliver long-term performance data to 2002.

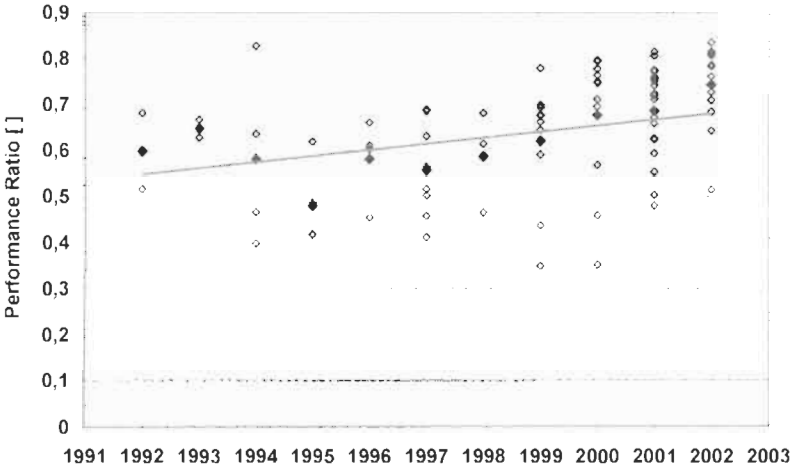

Figure 6 Trend of annual performance ratios of 29 grid-connected PV systems in Italy installed between 1983 and 2002.

New PV systems from the Italian PV-Roof-Top-programme were built since 2000 and monitoring data are available for two years (2001–2002).

Figure 6 shows the annual PR of 29 systems and 81 datasets from both programmes and a positive tendency of PR development between 1992 (average 0.60) and 2002 (average 0.74). The very low PR values of the early plants, which were designed as experimental and demonstration plants, can be explained by experimental activities and measurement campaigns as well as by frequent failures and long repair times for replacement of inverters and DC components [15].

The performance results of very large, but later installed plants (e.g. Serre, Figure 2) show good PR values and system availability (in 2000: PR = 0.7 and 100% availability) confirming their design values. The new PV systems from the Italian roof-top programme reach high performance values due to improved components and know-how. The Italian programme is accompanied by intensive PV training courses for designer and installers. The outcome of these efforts can be seen in the positive learning curve of long-term PV plant operation in Italy.

2.4 Rise in PV System Performance

Will the overall performance of new installations automatically increase as a consequence of higher efficiencies of PV modules and inverters available at the PV market? The 51 examples with a high proportion of BIPV in Switzerland showed that this is not a must if other design criteria will be applied and technical performance is not the only goal for a PV system.

Considering the 298 grid-connected PV plants in 14 countries from the Performance Database, a clear answer is given in Figure 7. It shows the distribution of 962 annual PR values, which are grouped into two

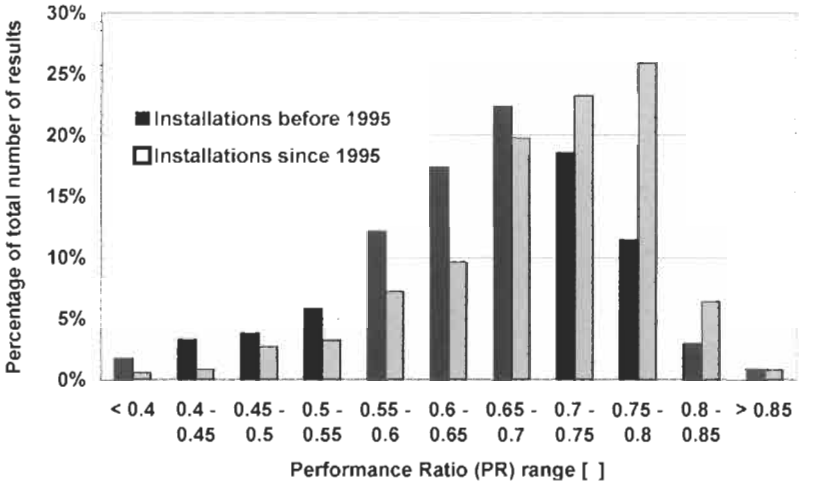

Figure 7 Distribution of annual performance ratios of 298 grid-connected PV systems (962 annual datasets) in 14 countries for two installation periods: (a) The average annual PR of PV plants installed before 1995 is 0.65. (b) The average annual PR of PV plants installed since 1995 is 0.70.

installation periods: all PV systems installed before 1995 have their maximum in the PR range of 0.65 to 0.7 and an average PR of 0.65 for 587 annual performance data.

The newer installations since 1995 have their maximum in the range 0.75–0.8 with an average value of PR = 0.70 for 375 annual datasets. This is a significant rise in PV system performance and reliability gained in these 14 countries during the past seven years of installation.

Using the same system data, it was observed:

- Measured inverter efficiencies also tend to have higher values.
- Measured array efficiency has slightly improved.
- System availability seems to improve with the years.

3 User Experience

3.1 Small Residential PV System in Germany

Long-term performance results for a 3.6 kWp PV rooftop system in northern Germany are presented in Figure 8. The monthly PR values during nine years of operation are shown in Figure 8. In its first years, the PV system obtains good annual PR values of 0.67 in 1992 and 0.71 in 1993, while the values continuously drop down in the following years to end up with to 0.54 in 2000.

The sudden decrease of monthly PR is well correlated with the frequent exchange of the inverter: seven exchanged inverters in nine years! And the

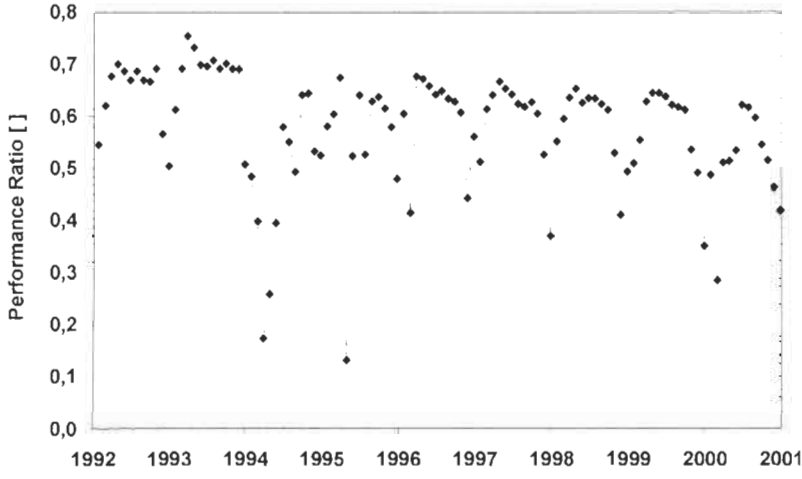

Figure 8 Monthly performance results of 3.6 kWp residential PV system in northern Germany installed in 1991.

installer checked the complete system after each replacement. The overall decline of performance of this system can be explained by:

- frequent inverter failures
- very long repair times (1–3 months for each replacement)
- bad adaptation of the inverter to the given PV array

The user did not notice how low the annual energy yields were during the past years due to a lack of information and data for comparison. He actively reduced the energy consumption of his household (four to six persons) and succeeded in obtaining a solar fraction of 60–70% per year independent of the continuously reduced yields.

3.2 PV Sound Barrier in Switzerland

The pilot and demonstration project of 104 kWp was built as the first PV sound barrier in 1989 and is analytically monitored for 13 years. The large PV plant along a Swiss motorway is regularly inspected and maintained. As shown in Figure 9, the PV system performs well over 10 years (annual PR = 0.73 to 0.80) except for the first year, when PV modules had to be replaced [34]. Severe operational losses in 2000 and 2001 are due to component failure of the inverter and the delays in the replacements of these components.

Climbing plants had to be removed from the PV array surfaces to avoid losses due to shading. In total, 33 modules had to be replaced (21 damaged, 12 stolen). The glass surfaces of the PV modules have never been cleaned and no significant decrease in array efficiency (η_A = 8.8%) was observed [34].

This successful project achieves an average annual PR of 0.68 and an average energy yield of 950 kWh/kWp for 13 years of operation.

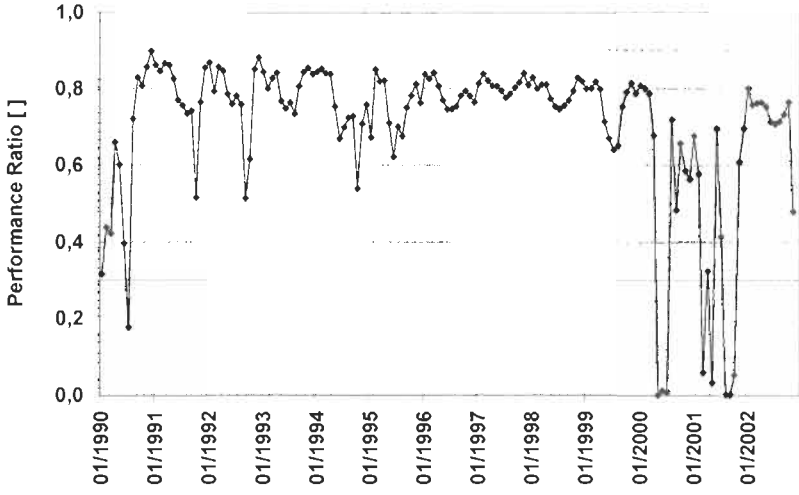

Figure 9 Monthly performance results of 104 kWp PV sound barrier in Switzerland installed in 1989.

3.3 PV Power Plant in Italy

The 100 kWp PV system is retrofitted on the flat roof of a parking shelter belonging to a research centre in Southern Italy and is monitored and inspected since 1991 [35]. The first prototype system shows low performance over 11 years (average PR of 0.57) and has performance constraints due to frequent failures. Between 1992 and 2002 about 40 outage events have been recorded corresponding to an average plant availability of 87%. Figure 10 shows the annual PR and availability for 1992 to 2002.

In 1997 and 1998, performance losses were caused by array partial shutdown due to junction box's serious failure. The replacement of the AC switchgear was responsible for the total shutdown of the system during summer months. [36]

The plant does not perform according to specifications and expectations except for the years 1999 and 2001 with high annual PR and availabilities: significant energy losses during the eleven years of operation were caused by [36]:

- inverter failures in summer months
- long repair times for replacement
- prototype nature of the inverter
- DC circuits' poor sizing

The PV plant produces about 0.5% of the electricity demand of the research centre.

3.4 Lessons Learnt

While many PV systems perform according to plan, a common performance experience was that in terms of final energy yield, the system did not meet the

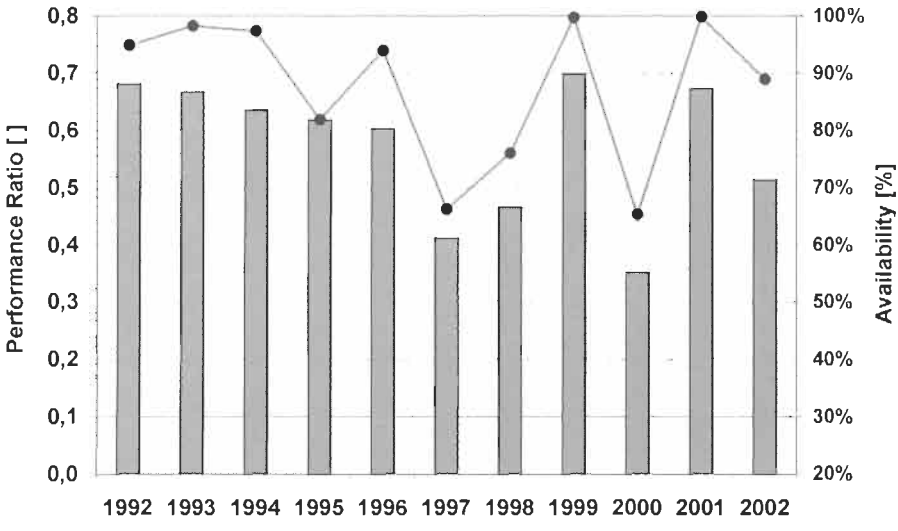

Figure 10 Annual performance ratios and availability of 100 kWp PV system in Italy installed in 1991.

expectations. Dominating performance constraints were the poor reliability of inverters, long repair times and shading problems.

From PV systems that provided well-documented failure reports, it was learnt that the power conditioner units often caused problems over the first year of installation. After problems of the utility interactive inverters had been solved, the system operated well for many years. A second high failure rate period of inverters was observed after 8–10 years of system operation. The replacement of 'old' power conditioner units caused long repair times and thus high operational losses. Good contacts between system user, installer and manufacturer of the system components helped to reduce delays in the replacement of the faulty parts. Step by step, the reliability will improve as the inverter technology matures. It has been suggested as an interim solution to design PV systems that allow for quick replacement of the inverter [37].

The energy losses due to partial shading by nature (e.g. trees) and by parts of the building structure are generally underestimated and cannot be eliminated after installation has been completed. In the planning stage partial shading can be avoided or reduced by the PV system designer in cooperation with the architect or project planner. The negative impact of unavoidable shading can be minimised by suitable electrical wiring configuration. Keeping shaded modules in one electrical string in the array will reduce shading losses.

It was further observed that some inverters deliver low energy output because the inverter is not well adapted to the PV array, the arrays are partly shaded or PV arrays with different orientations are connected to one central inverter. Under these conditions, the MPP unit of the inverter will not function properly and leads to energy losses, which are a matter of poor system design rather than one of poor DC/AC power conversion.

The following is recommended in the planning stage to improve PV system performance:

- Avoid shading and shading losses. Use suitable electrical wiring configuration of the PV array to minimise unavoidable losses.
- Optimise the orientations of PV arrays and avoid that PV arrays of different orientations are connected to one central inverter.
- Make DC installation technique as simple as possible: avoid switching elements and string fuses.
- Consider the reliability of the power conditioner units: Ensure that repair parts are available from the manufacturer in 10 years time and allow for easy replacement of faulty units.
- Optimise the efficiency of the inverter performance by suitable sizing of the PV array and adapting to operating conditions.
- Give realistic figures of expected energy yields to the PV system user by understanding and explaining the factors that influence the performance (e.g. reflection losses, module temperature, PV array coverage of snow or dirt, module mismatch, DC installation losses, inverter efficiency).

The summary of lessons learnt might give rise to the wrong impression of frequent negative results of PV system performance. The reason of focussing and presenting examples of low performance is that one learns how to improve from the negative examples. For the overall performance assessment, long-term performance results have shown a positive learning curve in terms of improved system energy yields and reliability of components. Many PV systems have demonstrated excellent performance and are meeting the expectations of their users and designers.

Acknowledgements

Special thanks go to my colleague Mr Wolfgang Nasse for his support and for preparing the figures of this chapter. The data and information on the Swiss and Italian case studies provided by Mr Luzi Clavadetscher, TNC Consulting, and by Mr Salvatore Castello, ENEA, are greatly appreciated. Thanks are due to all colleagues of IEA PVPS Task 2 who contributed their PV system data to the Performance Database.

Appendix. Specifications of Performance Database of IEA PVPS

IEA International Energy Agency

Photovoltaic Power Systems Programme

Performance Database

The Performance Database of Task 2 of the Photovoltaic Power Systems Programme (PVPS) of the International Energy Agency (IEA) is designed to provide experts, industry, utilities, manufacturers, system designers, installers and schools with suitable information on the operational performance, reliability and design of photovoltaic (PV) systems and components. The benefit of the Performance Database lies in sharing technical information focusing on long-term performance and reliability of PV systems and providing tools for practical and educational purposes.

Database programme

- CD-ROM at price of 20 EUR
- Internet download for free at www.task2.org (47 MB)
- English language
- First release in July 2001
- Last Update in May 2003
- Financed by the German Federal Ministry of Economy and Technology (BMWi)

Database contents

- Information on 372 photovoltaic systems in IEA countries worldwide
- Grid-connected, off-grid and hybrid photovoltaic systems of 1 kWp up to 3 MWp
- General system information (size, system type, mounting, location, cost, photo)
- System configuration and component data
- Monitoring data (values of monthly energies, irradiation and temperature)
- Calculated data (monthly and annual values of performance indicators)

Programme specifications

- PC of 64 MB RAM, 100 MB hard disk space
- Windows 95/98, NT4.0, 2000, XP
- Excel 97/2000 for reports and data exports
- Filter, selection and easy navigation through the database
- Import and export tools

Information and CD-ROM are available from:

Reinhard Dahl (Operating Agent)
Projekttraeger Juelich - PTJ ERG
Forschungszentrum Juelich GmbH
D-52425 Juelich
Germany
Fax: +49 (0) 24 61 - 61 28 40
Email: r.dahl@fz-juelich.de
Website: www.task2.org

Task 2 **Operational performance, maintenance and sizing of photovoltaic power systems and subsystems**

References

[1] Commission of the European Communities, *Guidelines for the Assessment of Photovoltaic Plants, Document A, Photovoltaic system monitoring, issue 4.2*, Joint Research Centre, 1993.

[2] Commission of the European Communities, *Guidelines for the Assessment of Photovoltaic Plants, Document B, Analysis and presentation of monitoring data*, issue 4.3, Joint Research Centre, 1997.

[3] Commission of the European Communities, *Guidelines for the Assessment of Photovoltaic Plants, Document C, Initial and periodic tests on photovoltaic plants*, Joint Research Centre, 1997.

[4] International Standard IEC 61724: *Photovoltaic system performance monitoring – Guidelines for measurement, data exchange and analysis. First edition*, International Electrotechnical Commission (IEC), Geneva, April 1998.

[5] Haeberlin, H. and Beutler, C. 1995. Normalized representation of energy and power for analysis of performance and online error detection in PV systems. *Proc. 13th European PV Solar Energy Conference*, Nice, pp. 934–937.

[6] Castello, S. 2002. *IEA PVPS Task 2 case study on PV plant Serre*, written communication, Italy.

[7] Mayer, D. 2000. PV stand-alone systems in France. In: *Report IEA-PVPS T2-01:2000, Analysis of photovoltaic systems*, pp. 52–58.

[8] Sobirey, A., Riess, H. and Sprau, P. 1998. Matching factor – a new tool for the assessment of stand-alone systems. *Proc. 2nd World Conf. on Photovoltaic Solar Energy Conversion*, Vienna.

[9] Mayer, D. 2002. Performance assessment for PV stand-alone systems. In: *Report IEA-PVPS T2-03:2002, Operational performance, reliability and promotion of photovoltaic systems*, pp. 39–42.

[10] Nasse, W. 2002. Performance Database of PVPS Task 2. In: *Report IEA-PVPS T2-03:2002, Operational performance, reliability and promotion of photovoltaic systems*, pp. 7–10.

[11] Jahn, U., Mayer, D. et al. 2000. International Energy Agency PVPS Task 2 – Analysis of the operational performance of the IEA database PV systems. *Proc. 16th European Photovoltaic Solar Energy Conf.*, Glasgow,pp. 2673–2677.

[12] Otterdijk, K.V. 2000. PV systems in the Netherlands. In: *Report IEA-PVPS T2-01:2000, Analysis of photovoltaic systems*, pp. 92–100.

[13] Jahn, U. 2000. PV systems in Germany. In: *Report IEA-PVPS T2-01:2000, Analysis of photovoltaic systems*, pp. 59–72.

[14] Clavadetscher, L. 2002. Experiences from long-term PV monitoring in Switzerland. In: *Report IEA-PVPS T2-03:2002, Operational performance, reliability and promotion of photovoltaic systems*, pp. 23–28.

[15] Castello, S., Guastella, S. and Guerra, M. 2002. Operational performance know-how and results of PV system analysis in Italy. In: *Report IEA-PVPS*

T2-03:2002, Operational performance, reliability and promotion of photovoltaic systems, pp. 11–15.

[16] Sakuta, K. and Sugiura, T. 2002. Results and future plans for monitoring residential PV systems in Japan. In: *Report IEA-PVPS T2-03:2002, Operational performance, reliability and promotion of photovoltaic systems*, pp. 17–21.

[17] Faiman, D. 2000. PV systems in Israel. In: *Report IEA-PVPS T2-01:2000, Analysis of photovoltaic systems*, pp. 73–76.

[18] Gillett, W.B., Kaut, W., Munro, D.K., Blaesser, G. and Riesch, G. 1992. Review of recent results and experience from CEC PV demonstration and THERMIE programmes. *Proc. 11th European Photovoltaic Solar Energy Conf.*, Montreux, pp. 1579–1582.

[19] Blaesser, G., Riesch, G., Munro, D.K. and Gillett, W.B. 1994. Operating experience with PV system components from the THERMIE programme. *Proc. 12th European Photovoltaic Solar Energy Conf.* Amsterdam, pp. 1159–1162.

[20] Jahn, U., Grochowski, J., Tegtmeyer, D., Rindelhardt, U. and Teichmann, G. 1994. Detailed monitoring results and operating experiences from 250 grid-connected PV systems in Germany. *Proc. 12th European Photovoltaic Solar Energy Conf.*, Amsterdam, pp. 919–922.

[21] Kiefer, K., Koerkel, T., Reinders, A., Roessler, E. and Wiemken, E. 1995. 2050 Roofs in Germany – Operating results from intensified monitoring and analysis through numerical modelling. *Proc 13th European Photovoltaic Solar Energy Conference*, Nice, pp. 575–579.

[22] Decker, B. and Jahn, U. 1997. Performance of 170 grid-connected PV plants in Northern Germany – Analysis of Yields and optimisation potentials. *Solar Energy*, Vol. 59(4–6), pp. 127–133.

[23] Otani, K. 2001. Year 2000 report book for PV systems. *Journal of Japanese Institute of Energy*, Vol. 80(3), pp. 116–122 (in Japanese).

[24] Schalkwijk, M.V., Schoen, T., Schmidt, H. and Toggweiler, P. 1995. Overview and results of IEA-SHCP Task 16 demonstration buildings. *Proc. 13th European Photovoltaic Solar Energy Conf.*, Nice, pp. 2141–2144.

[25] Jahn, U. 2000. Results of performance analysis. In: *Report IEA-PVPS T2-01:2000, Analysis of photovoltaic systems*, pp. 5–7.

[26] Jahn, U., Nasse, W. et al. 2000. Analysis of the Operational Performance of the IEA Database PV systems. *Proc. 16th European Photovoltaic Solar Energy Conf.*, Glasgow, pp. 2673–2677.

[27] Rindelhardt, U. 2001. *Photovoltaische Stromversorgung*. Teubner Verlag.

[28] Erge, T., et al. 1998. The German 1000-Roofs-PV Programme – a resume of 5 years pioneer project for small grid-connected PV systems. *Proc. 2nd World Conf. on Photovoltaic Solar Energy Conversion*, Vienna.

[29] Ossenbrink, H.A. 1994. Comparison of PV modules – data sheet specifications and reality. *Proc. 9th Symposium PV Solarenergie*, pp. 419–425 (in German).

[30] Jahn, U., Tegtmeyer, D. and Grochowski, J. 1995. Results from the 1000-Roofs-PV-Programme – Measurements of PV arrays. *Proc. 10th Symposium PV Solarenergie*,pp. 69–77 (in German).

[31] Grochowski, J. and Decker, B. 1998. Reasons for low energy yields. In: *Report 1000-Daecher-Mess- und Auswerteprogramm*, Fraunhofer Institute for Solar Energy Systems, Germany, pp. 30–42 (in German).

[32] Grochowski, J., Jahn, U., Decker, B. and Offensand, J. 1995. First results from the Low Yield Analysis and optimization potentials – a project within the 1000-Roofs-PV-programme. *Proc. 13th European Photovoltaic Solar Energy Conf.*, Nice, pp. 356–359.

[33] Nordmann, T. Clavadetscher, L., 2003. Understanding temperature effects on PV system performance. *Proc. 3rd World Conf. on Photovoltaic Energy Conversion*, Osaka.

[34] Clavadetscher, L. 2002. IEA PVPS Task 2 case study on PV plant Domat, written communication, Switzerland.

[35] Barra, L., Castello, S. and Messana, C. 1991. Design and development of a standard 100 kW PV plant. *Proc. 10th European Photovoltaic Solar Energy Conf.*, Lisbon.

[36] Castello, S. 2002. IEA PVPS Task 2 case study on PV plant Cassacia, written communication, Italy.

[37] Drewes, P. 2002. Electrical design issues. In: *Report IEA-PVPS Task 7:2002, Building with Solar Power*, October 2002.

Solar-Powered Products

Philip R. Wolfe, WolfeWare Limited, UK

1 The Genesis of Solar-Powered Products

Solar cells have two great advantages that other energy sources cannot offer:

- They can be used anywhere on the face of the planet – the only requirement is incoming light.
- They can generate power at any scale from milliwatts to gigawatts.

This is why the development of photovoltaics 'broke the mould' of traditional energy technology. For the first time power generation can be built into products at a practical level.

1.1 First Steps

Solar cells have been used for applications on earth since the 1970s. Most early applications used solar systems of discrete components as described in Part IV. However it soon became apparent that PV offers unique benefits in integrating the power generation into the very product, which it is powering.

It is hard to say which came first, but by the mid-1980s, quite a range of products incorporated integrated solar generation. Marine buoys had been developed with solar cells around the edges to power a flashing light on the top. Solar battery chargers were available, and soon solar powered calculators entered the mass market.

The advent of thin film solar cells made it easier to incorporate photovoltaics into a wider range of products and the applications mushroomed. Selections of the most common are described further in this chapter.

1.2 Integration of PV in Products

A huge proportion of the products we use today involve some form of electricity consumption. Traditionally this was provided by internal batteries, which needed to be replaced or recharged, or by connection to an external power supply, such as the grid.

The advent of the solar cell made it possible for the first time to build power generation into products, making them permanently independent of external energy sources. This is particularly beneficial in remote locations (including outer space, of course), but even in more accessible places it can save time, money and inconvenience.

Solar cells generate power only when exposed to light, so power storage must be included when the product needs power at other times. In many cases, however, this is not necessary. Many solar calculators are designed so that, as long as there is enough light to see the display, there is enough to power the device. Some solar ventilators operate on the basis that they are needed only when it is hot and this is normally when plenty of sunlight is available. Many solar pumps also are only needed when the sun is shining, or they can pump into a reservoir during the day to use the water at any time.

The solar cells generate the power necessary to operate the product, both in terms of current and voltage. In general the current is related to the size of the solar cell array, while the voltage is related to the number of cells used. This is further described in Section 5.1, which shows how the size of the solar cell can be matched to the power required by the product. For this reason solar cells are best suited to products with low power consumption. Recent advances in energy efficiency of a wide range of appliances have therefore brought ever more products into the realms, which suit 'solarisation'.

1.3 Thin Film Cells

The development of thin film solar cells gave great new impetus to the solar products business. Firstly thin film cells are less expensive, because they use less material of substantially lower cost. More importantly, however, they allow connections between cells to be made within the manufacturing process in an arrangement known as monolithic interconnection. As detailed in Part II, this means that the series connections needed to obtain higher voltages are compact and cheap, compared to crystalline solar cells, where series connections need further manufacturing operations to solder or weld neighbouring cells together (see Figure 1).

Solar products typically operate at voltages between 2 and 48 V, requiring therefore at least four and up to over one hundred series connections. Thin film cells have made this easy. They are therefore increasing the range of products, which can practically be solarised.

2 Stand-Alone Consumer Products

The major benefit of solar products is that they do not need a separate power source, so many of today's solar products are designed to operate independently of other electricity supplies. This is commonly known as 'stand-alone' operation.

2.1 Indoor Products

Several products have been designed for use in interior light levels, as described below. Many other products also operate 'indoors' while the solar cell is exposed to external daylight such as those described in Sections 2.3 and 3.

Thin film solar cells perform better than their crystalline counterparts at low light levels, and can be tailored to optimise the output under the typical indoor light spectrum, which is different from sunlight. For this reason, almost all indoor products use thin film solar cells, usually of amorphous silicon.

2.1.1 Calculators

Millions of solar calculators have been produced, probably accommodating more individual photovoltaic generators than any other single application. Many

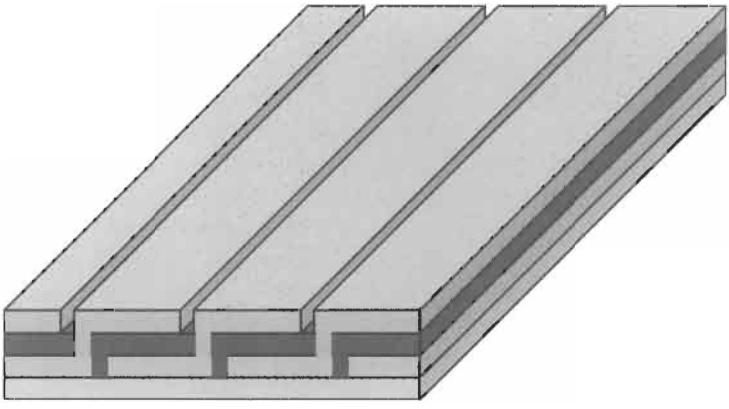

Figure 1 Monolithic interconnection of thin film solar cells on an insulating substrate. The front contact of one cell connects to the rear contact of the neighbouring cell.

adults and most schoolchildren are so familiar with solar calculators that the 'eternal energy source' is taken for granted.

The solar cell array looks like a small black panel, typically less than 1 × 4 cm, and is enough to power the calculator even under dim internal lighting. It comprises typically 4 monolithically interconnected amorphous silicon cells, many of which are produced in factories in Japan and Taiwan.

2.1.2 Watches and Clocks

Solar watches have also been mass-produced and are widely available. The solar array may be a small rectangle, but many designs also use a circular cell, which can be incorporated within the watch face (Figure 2).

Again, amorphous silicon is usually used in clocks and watches, because of its performance in interior lighting levels.

2.1.3 Chargers

Any parent knows how expensive it is to replace batteries in the plethora of portable music centres and game consoles to which children seem to be permanently attached!

The usage and disposal of primary batteries can, of course, be avoided by the use of rechargeable equivalents. Many suppliers have now developed solar chargers for maintaining this type of battery, with the added advantage that it can be used anywhere, without connection to a mains power socket. Ideally these chargers are placed on windowsills to maximise the light level and reduce the recharge time.

2.1.4 Other Indoor Products

Any electrical or battery powered product can be solar powered, by incorporating solar cells into it.

In addition to those mentioned above, there are many which have been designed with internal use in mind. A few examples are:

Figure 2 Solar watch incorporating a round array of four amorphous silicon solar cells.

- Digital weighing scales for domestic and industrial use
- Other solar powered meters
- A huge number of kits and toys
- Air-fresheners and essence dispensers
- Smoke alarms
- Desk-top gadgets and executive toys
- Units for rotating plants, and shop window displays
- I have even seen a solar powered food whisk.

The number of such products is doubtless increasing even as I write.

2.2 Garden and Stand-Alone Consumer Products

Where solar products are designed for external use, the major market is for garden products, especially lighting and aquatic items.

2.2.1 Lighting and Markers

Lighting technology has developed rapidly in recent years, particularly in terms of the power efficiency of the light source. New high intensity LEDs in particular give high light output, yet consume very little power.

Solar garden lights are now increasingly available in most major retailers as an alternative to mains powered garden lighting. The major benefit of having a built-in power source is that there is no need to dig up the garden to provide

electric cabling to the units. Solar lights, of course, incorporate a rechargeable battery so that the power can be stored during the day and used at night. Many also have a circuit which automatically turns the light on at nightfall either using a separate photocell or simply measuring the solar cell output and, when this falls to zero, switching the light on.

Solar lighting products first came to prominence in the mid- 1980s with offerings from Siemens and Brinkmann, amongst others. Probably the first thin film powered light at that time was the Chronar WalkLite range, which despite some initial technical problems achieved significant sales. A bewildering range of lights is now available, mainly in four distinct groups:

- Area illumination. These lights are solar equivalents of the mains-powered lighting, which has been available for years. The lights are designed to illuminate a patio, feature or area of the garden.
- Decorative accent lighting. Typically less bright than the area lights, accent lighting is used to provide a point of interest and to cast a glow in the immediate vicinity. Often several lights will be used to create an overall effect (Figure 3).

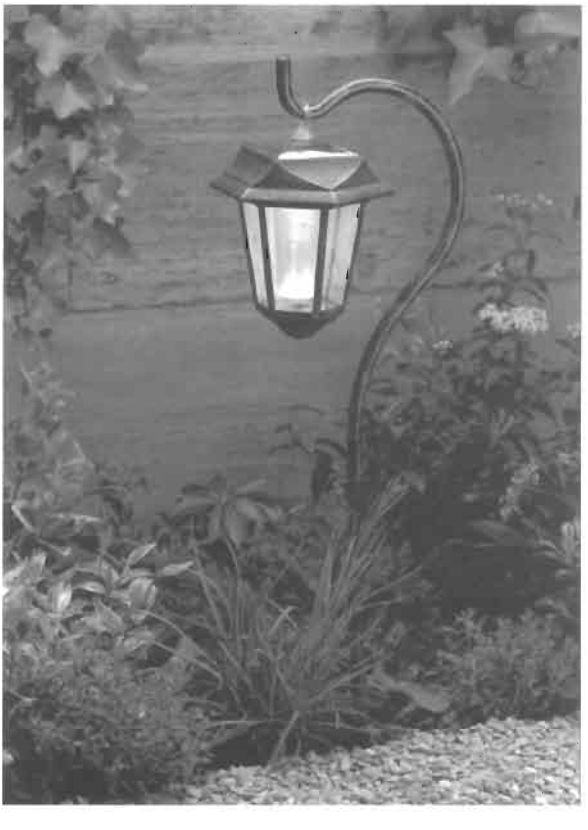

Figure 3 Solar garden light.

- Marker lights. Solar markers, usually with LEDs as the light source, are used to mark steps, paths and obstacles.
- Security lighting. Again these are a direct equivalent to mains-powered devices. A sensor circuit is typically used to turn the lights on when someone passes, for example. As the operational period is quite small, since the light switches off again after several seconds, the overall power consumption is low despite the brightness of the light.

2.2.2 Aquatic Products

Solar products for pools and garden water features have enjoyed tremendous growth in popularity over recent years. Many of these products particularly suit solarisation because they are required to operate only when the sun is out. This means that solar fountains, for example, do not need batteries, but can be directly driven from the solar panel. I now find that I hear the water droplets as the fountain outside my window starts up, and think 'Oh the sun must have come out!'

Most products in this category are pumps and derivatives thereof. There are many solar-driven pumps for waterfalls, fountains and a wide range of other aquatic applications. 'Jug and bowl' features are particularly popular as these give all the attraction and sound of moving water, while being sufficiently compact to use on patios and balconies.

An innovation in the late 1990s first promoted by Solar Trend, was a floating fountain system. Because this had the solar panel built in to the product, it needed no external wires and was therefore free to float around in ponds and pools (Figure 4).

Again the range of products in this sub-sector has expanded with the increasing acceptance of photovoltaic power. The principle that anything electrical can be solar-powered has extended to include pond aeration systems and several swimming pool accessories including a floating solar ioniser.

The ability of PV to make power available, where it would not otherwise be possible has led to several new concepts, too. In particular there are now a wide range of floating solar lights on the market, taking advantage of the independence of a built-in power source (Figure 5).

2.2.3 Deterrents and Other Products

The ability of PV to make power available where it would otherwise be too difficult or too expensive has given rise to several new products outside the aquatics sector. The Solar Company, for example has developed a mole deterrent operating by the emission of ultrasonic vibrations powered by a built in solar cell. A range of other similar deterrent products is expected.

Solar power is now one of the primary accepted ways of powering electric fences, which are mainly used for agricultural purposes but also in larger gardens. And to keep the lawn tidy without effort, Husqvarna has developed an automatic lawnmower also featuring a built-in solar cell array.

Solar products are now widely used in greenhouses and garden sheds. As most are derivatives of products used in household applications, these are described in the following section.

Figure 4 The integral solar cells power this fountain, which is therefore free to float around the pool.

2.3 Household Products

There is an increasing range of discrete household products now powered by solar cells, and some are described below. An important new trend is the development of architectural products incorporating solar cells, which generate power to feed into the building's traditional electricity distribution system, and these are described further in Section 3.

2.3.1 Ventilation and Air Conditioning

Ventilation is another application particularly well suited to solar power because the need is highest when the sunshine is strongest (Figure 6).

When Intersolar Group first acquired the SolarVent, originally developed for use on boats (see Section 2.4.1), they soon adapted it for household use in conservatories and greenhouses. As an extension to the concept the company has now patented a range of building ventilation designs incorporating solar power.

Solar-powered air conditioning is something of a 'Holy Grail' for the PV industry as the match between supply and demand is so good. However this is an application, which has not yet been widely exploited, mainly because of the high power consumption of traditional air-conditioning systems. Systems

Figure 5 Floating solar light from the Solar Company.

based on evaporative coolers have been offered in the market, but these require an abundant water supply, and I am not aware that the take-up has been strong.

The development of a more power efficient air-conditioner system, coupled with a solar power supply, will one day make someone very rich!

2.3.2 Lighting and Other Products

PV's main advantage is its ability to act as an independent power source without the need to replace batteries or wire into an established supply. An electricity supply is available throughout most houses in the developed world, and so the benefits of solar power are less marked. It is most widely used, therefore, in more remote rooms and outhouses, without a ring main.

Similarly, in the developing world where an estimated 2 billion people do not have access to a grid network, solar power is often the primary source of electricity. These areas have championed a wide range of products and applications for PV, especially:

- Lighting, particularly using low power fluorescent technology and increasingly high intensity LEDs. Various solar lanterns and stand-alone products have been developed, while the more advanced distributors in many countries offer package systems.
- Solar powered refrigeration both for domestic and medical uses.
- Televisions powered by solar panels, for educational and for recreational usage.

Solar products to feed into existing household electricity distribution are described further in Section 3.

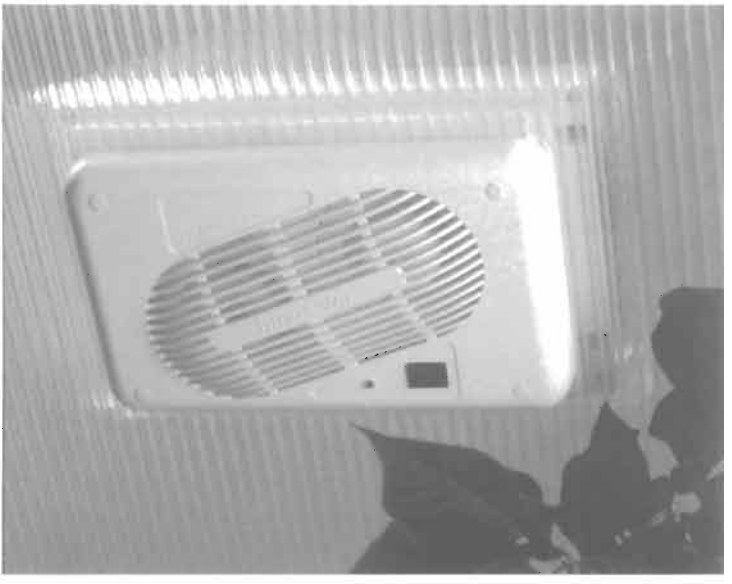

Figure 6 The SolarVent Turbo designed to fit into conservatory roofs, as seen from inside.

2.4 Portable and Transportable Products

The independence of solar power makes it ideal for transportable products. Because there is already such a bewildering selection, I will highlight here only the most widely adopted or interesting products.

2.4.1 Products for Vehicles

Probably the first outdoor solar consumer product was the SolarVent, first developed by Solar Ventilation Ltd in the UK. This comprises a round mono-crystalline solar cell cut into sections, which are then soldered together in series, to achieve the required voltage to direct drive a DC motor. A fan is attached to the motor and passes air through the unit whenever sufficient daylight falls on the cell.

The acquisition of this product in 1986 launched Intersolar into the solar products business and started what is probably now the most diverse range of PV products in the world. The SolarVent has subsequently been redesigned to offer many improvements and new features, but still uses crystalline cells and is a recognisable offspring of its predecessor (Figure 7).

The SolarVent was originally designed for use in boats, and has subsequently been developed for other transport uses such as caravans, in addition to the household applications already mentioned.

A massively successful follow-on product is the AutoVent first developed by Intersolar in 1987 and subsequently patented. This applies the solar ventilation principle to parked cars, without any modification to the vehicle itself. The AutoVent is designed to fit securely into the window of the vehicle and is

Figure 7 A marine SolarVent with schematic of the airflow.

calculated to change the air inside about every fifteen minutes. More than two million AutoVents have now been sold, with North America, Japan and Australasia being the major markets (Figure 8).

Vehicle applications naturally lend themselves to solar power because they need to be independent of a fixed electricity source. Boats, caravans and cars all include electrical devices and many are conveniently solar powered, especially for use when the vehicle in unattended and therefore the engine (its main power provider) is off.

Amongst the many applications are alarms and deterrents (including gas alarms for boats), lights, coolers and pumps. Solar panels are often used, too for topping up the vehicle's primary battery and a wide range of chargers is available for cars, caravans, RV's and boats.

2.4.2 Personal Products

Their need for independent power makes hand-held personal products particularly suited to solar energy. Again the range is almost endless and I will highlight just a selection:

- Lanterns and torches especially key-chain versions
- Laptop computers and computer game systems
- Mobile phones (mainly through the use of solar chargers as described below)

Figure 8 An AutoVent Turbo fitted in the front window of a parked car. The thin film solar cell array inside the window powers a fan, which exhausts stale air out over the top of the window glass.

- Hats incorporating solar fans seemed like a gimmick at first, but have now spawned many variants
- Radios and other portable music appliances (Figure 9).

Of course most portable electronic and electrical products are battery powered. A wide range of solar chargers also exists to replenish rechargeable batteries, which can be used in any such product. Some of these chargers also include integral batteries so that they can be used as a primary power source for mobile phones and hand-held game stations in particular.

3 Solar Products for Grid Connection

Most of the solar products described so far incorporate the solar cell array directly in the product being powered. An exciting recent development is the incorporation of solar cells in other products in such a way that they can then be connected to contribute to the overall electricity supply of buildings, for example.

Most such systems operate in conjunction with a traditional grid supply. The system draws a proportion of power from the grid, when the solar generation is less than the local consumption and can feed power back into the grid when there is a surplus, as described in Chapter IIIc-1.

Originally such architectural solar systems were individually designed for each building, or standard solar systems retrofitted to existing buildings, as described in Chapters IIIc-1 and -2. Recently, however, products have been specially designed for building use to include a solar cell array.

Figure 9 The Freeplay range of radios was originally developed to utilise the wind-up technology developed by Trevor Baylis, but many now incorporate solar cells too. Photo courtesy of the Freeplay Group.

3.1 Roofing Products

The most obvious approach is to incorporate solar cells into roofing products, and it is now possible to obtain solar tiles, slates, shingles and even pantiles. Initially solar tiles of standard sizes had low operating voltages of 6 V and under, so required specialist installation due to the series/parallel connection arrangement to achieve the required DC voltage, typically in the range 24–120 V.

A further breakthrough came with the use of monolithically interconnected thin film cells in solar roofing products. These make a high voltage per unit area viable and therefore enabled each product to operate at the designated system voltage. Then only parallel connections are needed, and it became possible to achieve this through simple inter-connections, which require no specialist electrical expertise and can be undertaken by established roofing contractors (Figure 10).

An example of such a product is the Electra-Slate, which looks virtually identical in size, weight, shape and colour to natural or synthetic slate, but generates power at up to 70 V. The unit incorporates a plug-socket device, which automatically interconnects with the neighbouring slates as each is fixed on the roof.

3.2 Cladding and Facade Products

A similar approach has been adopted for other products used in building envelopes, such as cladding panels and facade elements for use on vertical walls (Figure 11).

Figure 10 The uniform appearance of the thin film solar cells means that the four rows of Electra-slates being installed in Cardiff are almost indistinguishable from the rows of standard synthetic slate above and below them. The glass section at the top incorporates the interconnections and is covered by the row above when installation is complete.

3.3 Packaged Systems for Buildings

A combination of the approach used in several of the products described above is now leading to the development of packaged systems suitable for fitting to an existing building and providing a contribution to its power consumption.

One such package under the development name Kyoto Pack is designed to plug into an existing power socket in a house to provide an outlet where a freezer, for example, can be plugged in. The Kyoto Pack would provide a significant proportion of the power used, while the grid remains available for back-up when needed (Figure 12).

4 Non-consumer Products

I have attempted in this chapter to focus primarily on solar products, for which individuals may have a use. There are many applications of PV in other areas, such as those described in Part IV. Many of these, too, have led to the design of integrated solar products. Some of the main ones are described briefly below.

4.1 Commercial Applications

Many of the products described above are used, or have industrial equivalents used, in commercial situations such as hotels, parks, shops and public buildings.

Figure 11 The facade panels used at the first floor level of this building in the Department of the Built Environment at Nottingham University each incorporate about 1 m^2 of thin film solar cells, but look almost identical to standard glazing panels.

Additionally several solar products have been designed specifically for commercial applications, particularly for displays in shops and for roadside advertising.

4.2 Transportation

Solar powered navigational aids are now commonplace in our ports, rivers and inshore waters and will be familiar to any sailor. Solar aircraft warning lights are often used on towers, masts and high buildings on land too.

Road and rail transport have given rise to many solar products especially signals, track circuits, streetlights, parking meters, bus shelters and the ubiquitous roadside emergency telephones. Solar products in commercial vehicles are increasingly common, including solar roofs to power refrigerated trucks and ventilation of delivery vans.

This led coincidentally to the invention of the AutoVent. During a trip to Japan, where we were selling SolarVents to Nippon Fruehauf for use in produce delivery vans, Simon Pidgeon and I were sweltering in the traffic, when I idly suggested: 'If only we could fit a SolarVent to this taxi.' And bingo!

4.3 Other Industrial Applications

Wireless telecommunications is a natural application for a wireless source of electricity such as PV. In addition to the emergency telephones mentioned above, there are now too many solar powered telecommunications products to mention here.

The range also extends to telemetry products such as Scada devices, remote meteorological and hydrology systems, used particularly in the oil and gas and utility industries.

FRONIUS IG

The new inverter generation

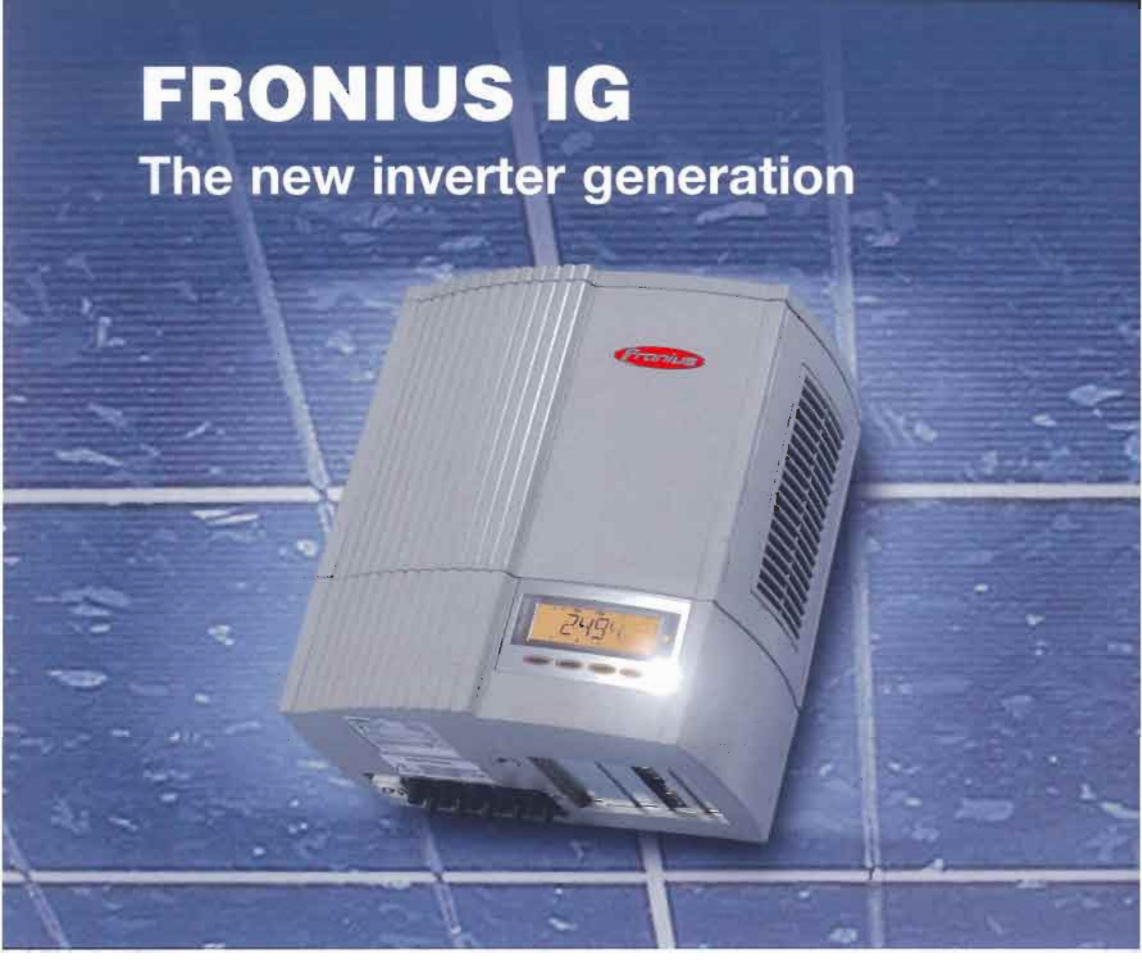

The value of high technology and innovation is shown by the series of grid connected inverters, the FRONIUS IG.

Energy efficiency is maximized not only due to the HF-technology but also by the energy saving Phase-Shift procedure and the high speed processors.

Flexibility for all photovoltaic systems is provided by the wide input voltage range and proven MPPT accuracy of the inverters.

Due to the high-tech communication centre of the FRONIUS IG, it is even more than a current transformer. On the graphic display you can view more than 20 critical system parameters. FRONIUS IG data communication gives you even more insight in your PV-system.

Moreover, the FRONIUS IG will convince you with its light weight of only 9 kg and a quick and easy installation.

FRONIUS INTERNATIONAL GMBH
A 4600 Wels-Thalheim, Günter Fronius-Strasse 1
E-Mail: PV@fronius.com
www.fronius.com

Figure 12 Schematic of the Kyoto Pack concept.

5 Designing PV for Products

The PV industry is relatively young, and there is still plenty of evidence that it is still learning about solar product design. I see too many products where the solar cell looks as if it has been stuck on as an afterthought, or where a PV manufacturer seems to have said: 'What else can I do with my solar panels?' In many cases the solar array is too intrusive or incongruous.

This is primarily a design issue, though marketing clearly has a part to play as some products cannot possibly have been conceived with any sane consumer in mind. In my view a good photovoltaic product would not look substantially different from the non-solar version, unless there is a good reason to highlight the PV aspect.

Thin films have made such holistic design easier, as the cells are largely uniform in appearance and without the shiny contact grids and tabs used in most crystalline cells. However there are some instances where, for example, the mottled appearance of multi-crystalline cells can be used to good visual effect.

5.1 Electrical Characteristics

Operationally the solar cell array is there to fulfil a defined electrical function. This can usually be reduced to a specified operating voltage and an expected peak, daily or annual current output. Where the solar cell is used as a trigger to

switch the product on in the dark (as described in Section 2.2.1) the electrical characteristic at low light level is also important.

The voltage is proportional to the number of series-connected cells, while the current is related to the cell area. In monolithically interconnected thin film arrays these factors can bear a direct relationship to the dimensions of the solar cell array (Figure 13).

5.2 Product Dimensions

Ideally the solar array size should be defined by the product, and not the other way round, though in many cases some compromise is necessary. Where space is limited, more efficient cells will need to be used.

The electrical characteristics may be a first determinant of the size of a thin film cell array as indicated above. Existing multi-junction amorphous silicon cells, for example, give about 50 V per metre of width and about 1 A per metre of length.

5.3 Mechanical and Structural Considerations

The most important feature of solar product design is the environmental protection of the solar cell. PV devices are highly reliable solid-state semiconductors. Their operating life is extremely long. The eventual failure of the device is more likely to relate to the connections or moisture induced degradation than the photovoltaic element itself.

All cells are susceptible to moisture in particular and should be packaged for weather resistance. In most designs protection is applied to the solar cell first, by spraying, adhering or printing a protective film, or by lamination. The product

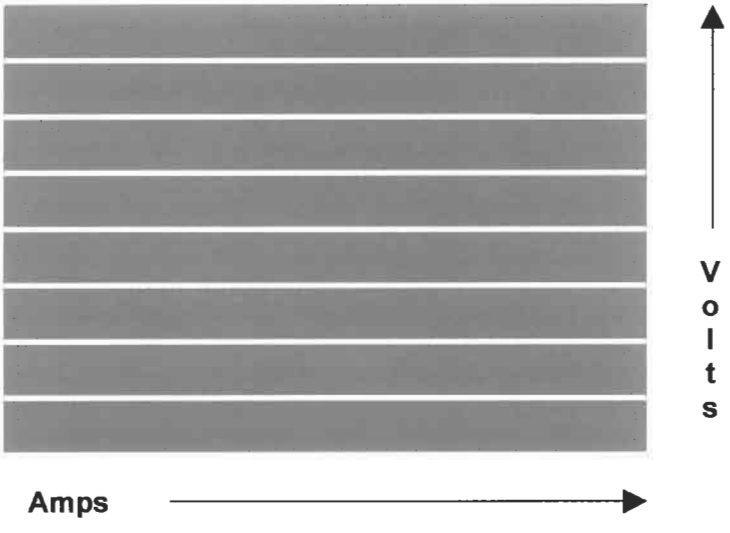

Figure 13 Monolithically interconnected thin film plate. The voltage is proportional to the number of series cells, and therefore the width. The current is proportional to the cell area and therefore the length.

design should then provide secondary protection, especially if the product is to be used outdoors.

These aspects of design are a science in themselves, and there is a gulf separating good solar products from some of the cheap replicas, which inevitably follow the success of a rapidly growing market.

6 Solar Products of the Future

This has given a flavour of the massive range of solar product applications, which have already been introduced. As I said at the start, anything which is, or could be, electrically operated can be solar powered. The eventual range is limitless.

The genesis of new solar products is expected to accelerate in the future, driven primarily by ever lower solar cell costs, but also by new advances in solar cell technology and by more power efficient products generally. Improvements in high efficiency LED technology have stimulated the solar lighting market tremendously. I expect continuing advances in consumer electronics to make this a major growth area for PV products in the medium-term future.

What of the long term? The key issue will become that of storage. Without reliable low cost power storage, it will still be necessary to operate in conjunction with other generation sources, and it is therefore likely that grid-connected products will lead the way. I hope an efficient, cheap, and preferably thin film battery will be developed. Imagine a credit card sized unit with solar cells on one face, a battery in the middle and display on the other face as a fully self-contained personal computer, television and communications system.

The applications, as many have said before, are limited only by our imagination.

Acknowledgements

The author thanks ICP Solar Technology UK Ltd for permission to feature some of their products and developments.

Part IV

Testing, Monitoring and Calibration

IV-1

Standards, Calibration and Testing of PV Modules and Solar Cells

Carl R. Osterwald, National Renewable Energy Laboratory, Golden, Colorado, USA

1 PV Performance Measurements

1.1 Introduction

When referring to the performance of a PV cell or module, the most important parameter is, of course, the maximum power point P_{max}, which is usually determined by varying the forward bias voltage across the device under test while illuminated. The light I–V curve is then recorded by measuring the current and voltage. Unfortunately, determination of P_{max} is complicated because it is a function of the total and spectral irradiance incident upon the device, the spatial and temporal uniformity of the irradiance, and the temperature of the device. It can even be a function of the voltage sweep rate and direction, as well as the voltage biasing history. Another important parameter, the power conversion efficiency η, defined as the power out divided by the power in, is proportional to P_{max}, and also to radiometric (the total incident irradiance, G) and physical (the device area, A) quantities: $\eta = P_{max}/AG$. Accurate determination of PV performance requires knowledge of the potential measurement problems and how these problems are influenced by the specific device to be tested. This section covers common PV measurement techniques and show how potential problems and sources of error are minimised.

Because the first solar cell applications were for satellite power systems, it was important for designers to know how much power could be expected from an individual solar cell in Earth orbit (i.e., when illuminated by the extraterrestrial solar irradiance). This could not be determined exactly for two reasons: (1) the precise nature of the extraterrestrial irradiance could only be estimated, and (2) sunlight at the Earth's surface is filtered by the atmosphere. Therefore, space solar cell performance could not be measured in a laboratory. By the early 1970s, a similar situation existed for terrestrial applications, but for a different reason – the total and spectral irradiance vary continuously due to the effects of the Earth's atmosphere. Thus, in both cases, it was essentially impossible to independently verify the efficiency measurements made by any laboratory [1].

1.2 Radiometry

The problems with measurement comparisons led to the concept of standard reporting conditions (SRC, also referred to as standard test conditions, STC), which consist of the device temperature, the total irradiance, and the spectral irradiance under which PV performance measurements are made or corrected to [1, 2]. Using SRC allows performance comparisons to be made within the error uncertainty limits of the measurements involved [2]. Table 1 lists the SRCs for space and terrestrial applications, and Figure1 is a plot of the extraterrestrial and global spectral irradiances, which are the result of measurements made by solar resource satellites, high-altitude balloons, and aircraft, combined with ground measurements and atmospheric models [4–11].

Table 1 Standard Reporting Conditions (SRC)

Application	Reference spectral irradiance	Total irradiance (W/m^2)	Temperature (°C)
Low-Earth orbit	ASTM E 490 [1]	1366.1	28
Terrestrial global (non-concentrator)	IEC 60904-3 [3] or ASTM G 159 [2]	1000	25

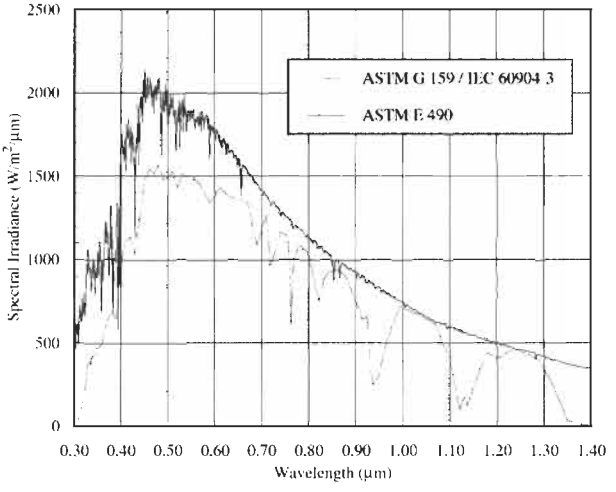

Figure 1 Reference spectral irradiances for Air Mass 0 (AM0) and Air Mass 1.5 hemispherical (global) [1–3].

For space applications, it is easy to identify a reference spectral irradiance, which is the extraterrestrial solar irradiance at a distance of one astronomical unit from the sun. Identification of a reference spectral irradiance for terrestrial applications is a much more difficult subject because of the effects of the atmosphere on sunlight, which are a function of the path length through the atmosphere [7]. A way of describing an atmospheric path is called the relative optical path length, which is commonly simplified to air mass (AM). To a first approximation, the air mass is the secant of the solar zenith angle. Thus, AM1 indicates the sun is directly overhead, and AM1.41 is a 45° zenith angle. Because air mass is actually a relative path length referenced to sea level, it can be less than one as the altitude increases above sea level. The extraterrestrial irradiance is commonly called air mass zero (AM0) because at the top of the atmosphere, the path length is zero.

Because solar cells convert light to electricity, radiometry is a very important facet of PV metrology. Radiometric measurements have the potential to introduce large errors in any given PV performance measurement because radiometric instrumentation and detectors can have total errors of up to 5% even with careful calibration [12, 13]. Other errors can be introduced through means as subtle as misunderstanding the objective of a particular measurement or its

potential limitations. Broadband radiometers, such as pyranometers and pyrhelimeters, can be difficult to use in PV measurements because of the large spectral response differences. The calibration and use of radiometric instruments such as pyrheliometers, spectroradiometers, and pyranometers is a subject that is beyond the scope of this chapter, but these instruments are important for PV measurements. A number of standards for radiometric instrumentation are available [14–19].

It should be emphasised that the standardised spectral irradiances in Figure 1 cannot be reproduced exactly in the laboratory. In addition, although light sources such as xenon arc lamps can approximate these curves (i.e. solar simulators), a method of setting the total irradiance is needed. These limitations have been overcome by the so-called reference cell method. Using this method, an unknown device is tested in a solar simulator for which the total irradiance has been set with a calibrated reference cell that has the same or similar spectral response as the test device. The output level of the simulator is adjusted until the short-circuit current, I_{sc}, of the reference cell is equal to its calibration. With the total irradiance established, the reference cell is replaced with the device to be tested and the performance measurement can then be made [20–22].

When considering the reference cell method, another problem becomes immediately obvious: How can it be used to test an unknown cell if a matched reference cell is not available? This problem was solved by calculating the error in a measurement of I_{sc} caused by spectral response differences between the reference and unknown devices, and by spectral irradiance differences of the solar simulator from the desired standard spectrum [23–25]; this error is now called the spectral mismatch error, M. It is important to note that once M is known, it can be used to correct PV current measurements for spectral error by dividing by M. The PV performance standards mentioned above all rely on the reference cell method with spectral mismatch corrections [20–22].

The measurement problem is then reduced to obtaining calibrated reference cells. Historically, reference cells calibrated in sunlight have been called primary cells, and cells calibrated in solar simulators are called secondary cells. Historically, for space applications, primary reference cell calibrations have relied on I_{sc} measurements under spectral conditions as close to AM0 as possible with locations such as high-altitude balloons and aircraft, and manned spacecraft [26–28]. Primary terrestrial calibrations require stable, clear sky conditions with total irradiances measured with an absolute cavity radiometer [29, 30]. Other primary terrestrial calibration methods are used by national laboratories worldwide [31]. Reference [32] is a standard for secondary reference cell calibrations, and referenec [33] describes calibrations and use of reference modules.

1.3 Instrumentation and Solar Simulation

Figure 2 is an electrical block diagram that illustrates how PV current-voltage measurements are made. A four-wire (or Kelvin) connection to the device under test allows the voltage across the device to be measured by avoiding voltage

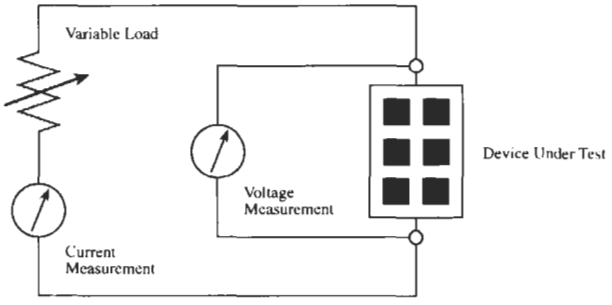

Figure 2 Block diagram of the four-wire Kelvin technique for I–V curve measurements of PV devices.

drops along the wiring in the current measurement loop. The device under test is illuminated, the load is varied, and the operating point of the device under test changes, which allows the current and voltage points to be captured along the I–V curve [3]. Typically, the entire measurement process is computer controlled.

There are two factors that greatly influence the design choices of an I–V measurement system: the type of the devices to be tested and the illumination source. For example, it is much easier to design a variable load if all test devices are similar in size and output, such as testing modules at the end of a production line. On the other hand, if a measurement system will be required to handle a wide variety of module sizes and outputs, or individual solar cells, the instrumentation must have the necessary voltage and current ranges. The need to test multijunction devices can greatly complicate the problems that must be solved in a measurement system design.

Any light source used (i.e. a solar simulator or natural sunlight) will have spatial non-uniformities, temporal instabilities, drift of its spectral irradiance, and an illumination time [34]. Outdoor measurements normally have uniform illumination in the test plane (less than 1% spatial variation) and stable irradiance for time periods up to several minutes. A Xe long-arc flash solar simulator can also achieve good spatial uniformities, but these lamps can have measurement times in the 1–20 ms range. Other flash simulators use a continuously pulsing source and measure one point on the I–V curve at each pulse. Continuous Xe simulators are commercially available for a wide range of sample sizes, from 50 mm square up to as much as 2 m square. Solar simulators with longer measurement times typically have poorer spatial uniformity, from several percent up to as much as 10 or 20%. Two standards have been developed that quantify the performance of solar simulators and can be used as aids in selection and use [35, 36].

Using these constraints, the equipment needed for I–V measurements in Figure 2 can be considered [3]. Voltage measurements are easily obtained with commercial voltmeters or high-speed analogue-to-digital (A/D) conversion cards. These same instruments can be connected across the sense leads of a four-wire resistor intended for current measurements. In high-current situations, such as source strings in an array, magnetic current probes are very convenient. The variable load can be as simple as a variable resistor, but such

loads cannot be used to trace the I–V curve outside of the power quadrant. Computer programmable DC power supplies, on the other hand, can be obtained in nearly any voltage and current range needed, and bipolar supplies can operate a PV device in reverse bias or beyond open-circuit voltage (V_{oc}).

In higher power applications, such as larger modules or whole arrays, a popular load for I–V measurements is a capacitor. The capacitor is initially uncharged and connected in series with the PV device to be tested, and any current produced by the device is stored in the capacitor. When the device is illuminated, the voltage across the device is close to zero. As the capacitor charges, the capacitor voltage and the device voltage both increase, thereby sweeping through the I–V curve. The charging stops when the current goes to zero at V_{oc}. Although it cannot operate the device outside of the power quadrant, this technique has the advantage of not dissipating large amounts of power, and it can sweep at high rates. Commercial capacitive sweep systems are available that are portable and can be used to obtain I–V curves of arrays or array segments up to about 100 kW in size.

1.4 Temperature

The I–V curve of a PV device under illumination is a strong function of temperature, which must be accounted for in performance measurements [37]. Typically, I_{sc} has the smallest temperature dependence, caused by the semiconductor bandgap shifting to longer wavelengths with higher temperatures. V_{oc} and P_{max}, on the other hand, degrade rapidly with increasing temperature [38, 39]. These strong dependencies are the reason a fixed temperature is used for SRC.

Temperature measurements of PV devices can be difficult. In general, measured temperatures should be those of the actual semiconductor junctions, but usually the only temperature that can be measured is at the rear surface of a cell. For modules, it not possible to contact individual cells and one is forced to apply temperature sensors to the rear surfaces. This leads to an error because the rear surface will normally be cooler than the cells laminated inside. Reference [40] states that at 1000 W/m^2, this error is an average of 2.5°C for typical crystalline Si modules. It is possible to correct I–V measurements to a reference temperature if temperature coefficients are known [41]. Another problem with modules is that the temperature can vary from cell to cell, requiring some sort of average if a single value is needed. The same problem is exacerbated in an array, where larger variations can be expected [42]. Temperature coefficients can also be difficult to apply correctly because they can be functions of irradiance and other factors [43].

1.5 Multijunction Devices

A multijunction PV device consists of several individual semiconductor junctions stacked together (also called subcells) and connected in series to obtain higher performance. With two subcells, a multijunction solar cell is commonly

referred to as a tandem cell. In such devices, however, both the I_{sc} and the fill factor (FF) are functions of the incident spectral irradiance, greatly complicating the determination of device performance at SRC [1]. Because all subcells are in series, the same current must flow through each, and the output current is usually limited by the junction generating the smallest current (called the limiting subcell). A special case occurs when all subcells generate the same amount of current, which is termed current matched. The reason the FF can be a function of the spectral irradiance is that the current generated by a limiting subcell can cause a different subcell to operate in reverse bias and result in a stepped I–V curve in forward bias [1, 44–46].

The only way to avoid measuring the wrong I_{sc} and FF is to ensure the currents generated in each subcell under the test light source are equal to those that would be generated under the desired reference spectral irradiance. In general, this can only be accomplished if the spectral response for each subcell is known and if the spectral irradiance of the test light source can be adjusted [1, 44, 45]. Such a simulator suitable for standard multijunction performance is called a spectrally adjustable solar simulator. There are a number of ways an adjustable simulator can be realised, including multiple independently adjustable light sources and selective filtering [44]. A number of procedures can be used to perform spectral matching in adjustable simulators. One procedure is an extension of the reference cell method with spectral mismatch corrections. An iterative process is used in which the spectral mismatch M for each subcell in the test is obtained, following a measurement of the simulator spectral irradiance. Based on these results, the simulator spectral irradiance is adjusted and the process is repeated. When all values of M are within an acceptable tolerance of one (usually 2–3%), the process is stopped and the I–V measurements are made [44, 45, 47]. This procedure will be standardised in the near future [48]. Another procedure relies on a multiple source simulator in which each source can be adjusted independently without changing its spectral distribution. A system of linear equations is then used to obtain the current outputs of one or more reference cells that indicate when the simulator is correctly adjusted [49].

It should be noted that the spectral adjustment of the simulator does not reproduce the reference spectral irradiance; instead, it sets the simulator spectral irradiance so that the test device is operating as if it were illuminated by the reference spectrum.

1.6 Other Performance Ratings

Although performance at SRC is an important parameter that allows measurement comparisons between different laboratories and different PV devices, it is not a realistic indication of the performance that can be expected outdoors, where devices see a range of irradiance conditions and almost never operate at 25°C when the irradiance is greater than 900 W/m^2. Another performance rating method is called Performance Test Conditions (PTC), the conditions for which are listed in Table 2 [50, 51]. This method is usually used to produce a rating for a system over a period of time (typically one month) when

Table 2 Performance Test Conditions (PTC)

Application	Irradiance (W/m^2)	Ambient temperature (°C)	Wind speed (m/s)
Flat-plate fixed tilt	1000 (global)	20	1
Concentrators	850 (direct normal)	20	1

conditions are close to the rating conditions. Data filtering and a regression fit to a linear equation are then used to obtain the performance at PTC. These ratings can be used to monitor the performance of a system over time, and it can be used for DC as well as AC ratings if the system is grid-connected. Another system rating uses translations to SRC based on a number of parameters measured outdoors on individual modules [52]. This method employs an empirical air mass versus irradiance correction factor that was called a measure of 'the systematic influence of solar spectrum' [53], but it should be noted that this factor is not a spectral correction to the reference spectral irradiance and is site specific [54].

There has also been interest in rating modules based on energy production, rather than output power at a single fixed condition [55]. A proposed energy rating establishes five reference days of hourly weather and irradiance data: hot-sunny, cold-sunny, hot-cloudy, cold-cloudy, and nice. Hourly module power outputs for each of the five days are obtained and then integrated to obtain the energy output for each condition [56]. Module energy ratings have been obtained from laboratory measurements as well as outdoor performance data [57–60].

1.7 Potential Problems and Measurement Uncertainty

Measurement uncertainty analysis is a formal process of identifying and quantifying possible errors, and combining the results to obtain an estimate of the total uncertainty of a measurement [61]. An inherent part of this process is understanding the potential problems that can affect the results of any given PV performance measurement. Although an exhaustive discussion of such problems cannot be included here, there are a number of common problems and pitfalls that can be identified. Many of these result from the instrumentation and apparatus used, the characteristics of the device to be tested, or both.

The voltage bias rate and direction can have profound effects on measured I–V data [62–64]. Test samples can exhibit hysteresis when swept toward forward bias and toward reverse bias, resulting in two different values of FF. Note that many I–V measurement systems are unable to sweep in both directions; especially capacitive loads, which can completely hide hysteresis problems. Thin-film devices such as $CuInSe_2$ and CdTe have mid-bandgap states that make them especially vulnerable to errors caused by fast sweep rates and prior light and voltage bias conditions [62]. Electronic loads used with flash simulators can greatly improve or degrade measurement results [65]. Mundane subjects such as area measurements, temperature measurements, and contacts and wiring

cannot be ignored [66]. Amorphous Si modules exhibit a dependence of the FF on the incident spectral irradiance, which can affect the results of outdoor performance measurements [67].

A number of uncertainty analyses of PV measurements have been published for general I–V measurements [68, 69], spectral corrections [70], and reference cell calibrations [29, 71]. Reference [70] concluded that the magnitude of uncertainty in spectral corrections is directly proportional to the size of the spectral mismatch factor.

2 Diagnostic Measurements

A number of diagnostic measurements are widely used in photovoltaic research and development. Two of these date to the earliest days of PV devices: dark I–V and spectral response (also called quantum efficiency). Dark I–V shows how a device operates as a p–n junction and can be used to obtain series resistance, shunt resistance, and diode quality factor [38, 39]. Although complicated by multiple individual cells connected in series, dark I–V can also be useful for module diagnostics [72]. Many of the same parameters can be derived from light I–V measurements as well [73, 74], and with careful design the same measurement system illustrated in Figure 1 can be used for both light and dark I–V measurements. Shunt resistance of individual cells is an important factor for the performance of monolithic thin-film modules such as a-Si, and reference [75] describes a technique for measuring individual shunt resistances in modules.

Spectral response is a fundamental property of solar cells, and it can provide information about optical losses such as reflection, and give insights into carrier recombination losses [39]. As previously stated, it is an important parameter for performance measurements because it is used as the basis for spectral mismatch corrections [24, 25]. Because of this importance, two standards for spectral response measurements have been developed [76, 77]. A wide variety of measurement schemes have been used for spectral response measurements [78–81]. Reference [82] discusses several sources of error that are commonly encountered. Note that special light- and voltage-biasing techniques are required to measure the spectral response of series-connected multijunction devices [47, 48, 83].

A very useful diagnostic for cells and modules is known as Laser (or Light) Beam Induced Current (LBIC), which produces a map of a device's response by rastering a laser spot across the front surface and measuring the resultant current [84, 85]. These maps can easily identify locations of reduced output, which can greatly simplify diagnostic investigations, such as looking for cracks in polycrystalline Si cells. LBIC can be used to measure photocurrents and shunt resistances of individual cells in crystalline Si modules [84]. When used with monolithic thin-film modules, LBIC will show regions of reduced photocurrent that might be caused by deposition non-uniformities.

Another technique that has become increasingly popular in recent years is thermal mapping using commercial infrared imaging cameras [86]. These

cameras easily measure temperature variations across the surfaces of both modules and arrays, and they are especially useful for locating hot spots, which can be caused by a number of conditions. A localised shunt path within a crystalline Si cell can produce small 20°C hot spots when a module is operated in reverse bias. In PV arrays, it is not uncommon for individual cells or a single module to be forced into reverse bias (thereby absorbing rather than generating power) if its output current has been reduced for some reason and the array design does not have adequate bypass diodes. These conditions will result in hot spots, 20–40°C higher than the surrounding cells or modules, which are easily detected in an infrared image.

Ultrasonic imaging is a non-destructive test that can identify voids and delamination in encapsulants. It is useful for studying the condition of solder joints in crystalline Si modules [87].

3 Commercial Equipment

There are a number of companies worldwide that market PV instrumentation, solar simulators, and complete PV measurement systems. Products are available for testing everything from small individual cells to large modules and small-sized arrays, for both space and terrestrial applications. These companies include:

- Berger Lichttechnik, Baierbrunn, Germany
- Beval S.A. (Pasan), Valangin, Switzerland
- Daystar, Inc., Las Cruces, NM, USA
- EKO Instruments Trading Co., Ltd, Tokyo, Japan
- Energy Equipment Testing Service Ltd, Cardiff, UK
- The Eppley Laboratory, Inc., Newport, RI, USA
- h.a.l.m elektronik GmbH, Frankfurt/Main, Germany
- Kipp & Zonen B.V., Delft, The Netherlands
- K.H. Steuernagel Lichttechnik, Morfelden-Walldorf, Germany
- LI-COR Environmental Research and Analysis, Lincoln, NE, USA
- NewSun, Nepean, ON, Canada
- NPC Inc., Tokyo, Japan
- Optosolar GmbH, Merdingen, Germany
- Photo Emission Tech., Inc., Newbury Park, CA, USA
- PV Measurements, Boulder, CO, USA
- Shanghai Jiaoda GoFly Green Energy Co., Ltd, Shanghai, China
- Spectrolab, Inc., Sylmar, CA, USA
- Spire Corp., Bedford, MA, USA
- Telecom-STV Co., Ltd, Moscow, Russia
- Thermo Oriel, Stratford, CT, USA
- Thermosenorik GmbH, Erlangen, Germany
- Vortek Industries, Ltd, Vancouver, BC, Canada
- Wacom Electric Co., Ltd, Tokyo, Japan

4 Module Reliability and Qualification Testing

4.1 Purpose and History

The 'holy grail' of module reliability that many people ask for is a single test, which if passed, indicates that a certain module design will last x number of years in use (typically 20 or 30 years). No such test exists, nor can it be developed [88]. The reason for this is that every possible failure mechanism has to be known and quantified. This condition is impossible to meet because some failures may not show themselves for many years and because manufacturers continually introduce new module designs and revise old designs.

Instead of a search for a single test, module reliability testing aims to identify unknown failure mechanisms and determine whether modules are susceptible to known failure mechanisms. Accelerated testing is an important facet of reliability testing, but accelerated tests need to be performed in parallel with real-time tests to show that a certain failure is not caused by the acceleration factor and will never appear in actual use. Qualification tests are accelerated tests, usually of short duration, that are known to produce known failure mechanisms, such as delamination. Thus, passing a qualification test is not a guarantee of a certain lifetime, although extending the duration of a qualification can provide added confidence that a module design is robust and durable [89].

The first PV module qualification tests were developed by the Jet Propulsion Laboratory (JPL) as part of the Low-Cost Solar Array program funded by the US Department of Energy [90–93]. Elements of the Block V qualification sequence included:

- Temperature cycling
- Humidity-freeze cycling
- Cyclic pressure loading
- Ice ball impact
- Electrical isolation (hi-pot)
- Hot-spot endurance
- Twisted-mounting surface test

Following the qualification sequences, test modules were compared with baseline electrical performance tests and visual inspection results to determine whether the design passed or failed. These tests have served as the starting point for all the qualification sequences that have been developed since.

The next development in module qualification was the adoption of the European CEC 502 sequence [94], which was significantly different from Block V and added several new tests:

- UV irradiation
- High-temperature storage

- High-temperature and high-humidity storage
- Mechanical loading

Another significant difference was that CEC 502 lacked humidity-freeze cycling. At the same time, Underwriters Laboratories (UL) developed the UL 1703 safety standard, which has become a requirement for all modules in the USA [95]. It incorporated the humidity-freeze, thermal cycling, and hi-pot tests from Block V, plus a large number of other safety-related tests. Note that as a safety standard, UL 1703 does not require a module to retain its performance at a certain level; rather, it simply must not become hazardous as a result of the test sequences.

With the development of commercially available a-Si modules, an investigation into the applicability of Block V to these devices resulted in publication of the so-called Interim Qualification Tests (IQT) [96]. The IQT were similar to the JPL tests but added two tests from UL 1703: surface cut susceptibility and ground continuity. A wet insulation resistance test was included as a check for electrochemical corrosion susceptibility.

Again building on prior work, Technical Committee 82 (TC-82) of the International Electrotechnical Commission (IEC) produced an international standard for qualification of crystalline Si modules, IEC 1215 (the designation was later changed to 61215), that included elements of all the prior tests [97]. It followed the sequences of JPL's Block V but added many of the new elements in CEC 502. Probably the most significant addition was the 1000-h damp heat test that replaced the high-temperature and high-humidity storage tests in CEC 502. Before IEC 61215 became a standard, a nearly identical draft version was adopted in Europe as CEC 503 [98]. Since its adoption, IEC 61215 has been a major influence on the reputation of excellent reliability that crystalline Si modules currently have. It has proven to be an invaluable tool for discovering poor module designs before they are sold on the open market [99].

In the USA, another significant development was that of IEEE 1262 [100], which was motivated by the lack of a US qualification standard. In 1989, IEC 61215 was only a draft standard that was several years away from adoption. Also, the IEC document was not suitable for a-Si modules because the UV and outdoor exposures resulted in the initial light-induced degradation inherent in these devices, which makes determination of performance losses due to the qualification sequences very difficult. Therefore, the goal was a document that was applicable to both technologies, which was accomplished with the addition of short thermal annealing steps to remove the light-induced degradation. IEEE 1262 includes a wet hi-pot test that is nearly impossible to pass if a module has insulation holes or flaws. Otherwise, IEEE 1262 is very similar to IEC 61215. TC-82 solved the problem of a-Si degradation by issuing a separate standard specifically for a-Si modules, IEC 61646 [101]. Rather than thermal annealing, however, IEC 61646 uses light soaking to condition the test modules prior to the qualification testing. In practice, light soaking has been shown to be lengthy and expensive for testing, so it is likely that light soaking will be replaced with thermal annealing in a future version.

4.2 Module Qualification Tests

TC-82 has been working on a revision of IEC 61215 for module qualification that is due to proceed to the Committee Draft for Voting (CDV) stage at the time of this writing [102]. This is an important document for the PV industry, so a brief description of the main test sequences is included below.

The new draft includes a wet insulation test, adopted from IEEE 1262, that all test modules must pass prior to and following the test sequences. A module is immersed in a surfactant solution and the insulation resistance between the solution and the shorted module leads is measured at 500 V. This test reveals insulation flaws that could be safety hazards in use, and also exposes possible paths of moisture intrusion that might result in performance degradation.

4.2.1 Thermal Cycling Sequence

One thermal cycle consists of a −40°C freeze for a minimum of 10 min, followed by an excursion to +85°C, again with a 10 min hold. The rate of change of module temperature must not exceed 100°C/h, and a complete cycle should not last longer than 6 h. This sequence is repeated until 200 cycles are completed.

According to reference [89], thermal cycling 'is intended to accelerate thermal differential-expansion stress effects so that design weaknesses associated with encapsulant system, cells, interconnects, and bonding materials can be detected as a direct result of the test'. An important change from the previous version of IEC 61215 is the added requirement that a forward-bias current equal to the output current at SRC P_{max} be passed through the test modules when the temperature is above 25°C. Current bias simulates the stresses that solder joints experience in actual use, and the biasing has been shown to reveal poor soldering [103].

4.2.2 Damp Heat Sequence

This sequence begins with the standard damp heat, which is 1000 h of exposure to 85% relative humidity (RH) at 85°C. Damp heat is followed by the 25 mm ice ball impact and 2400 Pa mechanical loading tests. Operating conditions as severe as 85% RH and 85°C never occur in actual use, but damp heat stresses the encapsulation and can result in delamination. Note that because these extremes, it is conceivable that damp heat could produce failures that would not be seen in the field.

4.2.3 UV Exposure, Thermal Cycling, and Humidity-Freeze Sequence

Prior to any stress tests, a short UV exposure of 60 MJ/m^2 (15 kWh/m^2) preconditions the modules. The UV exposure is followed by 50 thermal cycles and then 10 humidity-freeze cycles. Module designs that have tapes inside the encapsulation will typically delaminate during the subsequent thermal or humidity-freeze cycles. This sequence concludes with a robustness of termination test.

4.3 Reliability Testing

As noted previously, qualification testing uses accelerated tests, but it should not be considered reliability testing. However, this does not mean the specific tests that are part of a standard qualification sequence cannot be used for reliability testing. An example is extending the duration of the standard thermal cycle test by increasing the total number of cycles, or until failure of the module. Another is combining a qualification test with an added stress, such as damp heat with high voltage bias [103]. If possible, accelerated tests should be combined with real time tests. Reference [104] is a standard for solar weathering that uses techniques adapted from the materials industry. This standard uses total UV exposure doses to quantify both real-time and accelerated tests.

4.4 Module Certification and Commercial Services

Product certification is a formal process involving accredited testing laboratories and certification agencies that issue licenses to manufacturers indicating their products have been tested and are in conformance [105]. Certification is well known in other industries, especially for product safety, but it is a fairly recent development for photovoltaics. PV module safety certifications have been available for almost 20 years, but efforts have been made within the past 10 years to initiate certifications based on qualification testing. An example of this is the Global Approval Program for Photovoltaics (PV GAP) [106].

There are a number of independent PV laboratories that offer testing services, either as part of a formal certification program or upon request. These include:

- ASU Photovoltaic Testing Laboratory, Mesa, AZ, USA
- European Commission Joint Research Centre, Environment Institute, Renewable Energies Unit, Ispra, Italy
- TÜV Rheinland, Berlin/Brandenburg, Germany
- Underwriters Laboratories, Inc., Northbrook, IL, USA
- VDE Testing and Certification Institute, Offenbach, Germany

5 Module Degradation Case Study

To conclude this chapter, a diagnosis of a degraded polycrystalline Si module is presented as an example that uses many of the techniques outlined here. A small 20 W module was subjected to real-time outdoor weathering with a resistive

Table 3 Polycrystalline Si module I–V parameters

	V_{oc} (V)	I_{sc} (A)	FF	P_{max} (W)	R_s (Ω)
Initial	21.1	1.18	0.733	18.2	0.60
Exposed	20.8	1.15	0.687	16.4	0.43

load, and light and dark I–V measurements were made prior to exposure and at several intervals over a period of four years. At the end of this period, P_{max} under STC as measured with a pulsed Xe simulator had declined by 9.8%, as listed in Table 3. Most of this loss has occurred in the FF, which was down by 6.3%. Series resistance (R_s) values determined from dark I–V measurements did not show large increases, so a gradual degradation of the solder joints or the cell metallisation was not responsible. Examination of the light I–V curves, Figure 3, shows a 'stair step', which in a series-connected PV device typically indicates a mismatch in current output between one or more individual cells.

An attempt to locate such a problem was made with an IR camera by placing the module in forward bias (1 A and 22 V) and allowing the cells to heat for several minutes. The resulting IR image, Figure 4, was made of the module rear

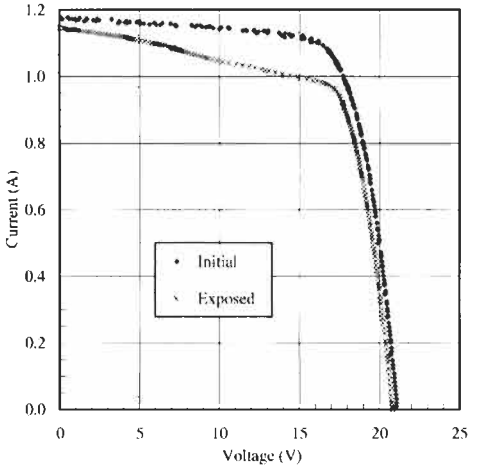

Figure 3 Light I–V curves at SRC of a polycrystalline Si module weathered outdoors for four years.

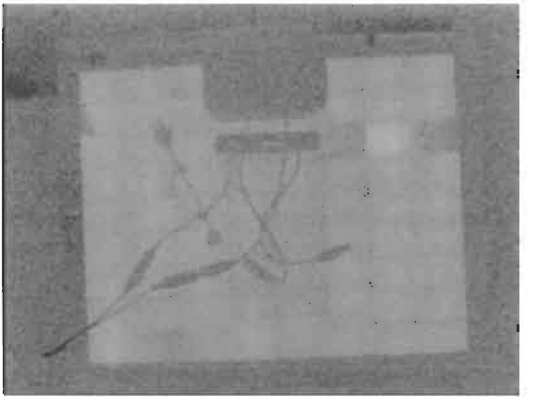

Figure 4 IR thermal image of the rear surface of the module from Figures 3 and 4. The module was placed at 1 A, 22 V in forward bias and allowed to heat for several minutes.

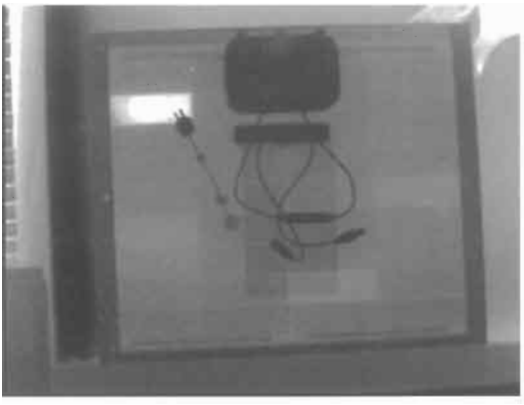

Figure 5 Another IR thermal image of the same module from Figure 3. The module was shorted for several minutes in sunlight before the image was captured.

surface through the polymeric backsheet (shadows from the junction box and the wiring are visible) and shows temperature rises of only about 1°C above the ambient. One or two cells appear to have slight temperature variations from the rest of the module, so this test was inconclusive at best. As it turns out, forward bias is not a very stressful condition for crystalline Si, and it is much easier to see hot spots when a module is shorted while illuminated in sunlight. After just a few minutes with the module in this condition, one cell developed a hot spot greater than 6°C, which was easily visible with an IR camera (Figure 5). This cell is most likely being forced into reverse bias. Looking at the hot cell in Figure 5, it appears one corner is not heating at all, and a visual examination of this cell revealed a crack in this location. Therefore, this cell has an output current about 10% lower than all the others, which caused the loss of fill factor.

Acknowledgements

Preparation of this chapter was supported by the US Department of Energy under contract No. DE-AC36-99-GO10337. Steve Rummel, Allan Anderberg, Larry Ottoson, and Tom McMahon performed and assisted with the measurements used in the module degradation case study.

Permissions

References

[1] Emery, K.A. and Osterwald, C.R. 1988. Efficiency measurements and other performance-rating methods. In: Coutts, T.J. and Meakin, J.D., Eds., *Current Topics in Photovoltaics*, Vol. 3, Academic Press, London.

[2] Emery, K. 1999. The rating of photovoltaic performance. *IEEE Transactions on Electron Devices*, Vol. ED-46, pp. 1928–1931.

[3] Emery, K.A. and Osterwald, C.R. 1986. Solar cell efficiency measurements. *Solar Cells*, Vol. 17, pp. 253–274.

[4] ASTM standard E 490: Standard Solar Constant and Zero Air Mass Solar Spectral Irradiance Tables. In: *ASTM Annual Book of Standards*. Vol. 12.02, ASTM International, West Conshohocken, PA, USA, 2002.

[5] ASTM standard G 159: Standard tables for references solar spectral irradiance at air mass 1.5: direct normal and hemispherical for a 37° tilted surface. In: *ASTM Annual Book of Standards*, Vol. 14.04, ASTM International, West Conshohocken, PA, 2002.

[6] IEC standard 60904-3: Measurement principles for terrestrial photovoltaic (PV) solar devices with reference spectral irradiance data. Photovoltaic Devices, International Electrotechnical Commission, Geneva, Switzerland, 1998.

[7] Iqbal, M. 1985. *An Introduction to Solar Radiation*, Academic Press Canada, Ontario, Canada.

[8] Riordan, C., Cannon, T., Myers, D. and Bird, R. 1985. Solar irradiance models, data, and instrumentation for PV device performance analyses. *Proc. 18th IEEE Photovoltaic Specialists Conf.*, Las Vegas, pp. 957–962.

[9] Osterwald, C.R. and Emery, K.A. 2000. Spectroradiometric sun photometry. *Journal of Atmospheric and Oceanic Technology*, September, pp. 1171–1188.

[10] Myers, D., Emery, K. and Gueymard, C. 2002. Proposed reference spectral irradiance standards to improve photovoltaic concentrating system design and performance evaluation. *Proc. 29th IEEE Photovoltaic Specialist Conf.*, New Orleans.

[11] Myers, D., Emery, K. and Gueymard, C. 2002. Terrestrial solar spectral modeling tools and applications for photovoltaic devices. *Proc. 29th IEEE Photovoltaic Specialist Conf.*, New Orleans.

[12] Myers, D.R., Emery, K.A. and Myers, D.R. 1989. Uncertainty estimates for global solar irradiance measurements used to evaluate PV device performance. *Solar Cells*, Vol. 27, pp. 455–464.

[13] Myers, D.R., Myers, D.R. and Reda, I. 2002. Recent progress in reducing the uncertainty in and improving pyranometer calibrations. *Journal of Solar Energy Engineering*, Vol. 124, pp. 44–50.

[14] ASTM standard G 130: Standard test method for calibration of narrow- and broad-band ultraviolet radiometers using a spectroradiometer. In: *ASTM Annual Book of Standards*, Vol. 14.04, ASTM International, West Conshohocken, PA, USA, 2002.

[15] ASTM standard G 138: Standard test method for calibration of a spectroradiometer using a standard source of irradiance. In: *ASTM Annual Book of Standards*, Vol. 14.04, ASTM International, West Conshohocken, PA, USA, 2002.

[16] ASTM standard E 816: Standard test method for calibration of secondary reference pyrheliometers and pyrheliometers for field use. In: *ASTM Annual Book of Standards*, Vol. 14.04, ASTM International, West Conshohocken, PA, USA, 2002.

[17] ASTM standard E 824: Standard test method for transfer of calibration from reference to field radiometers. In: *ASTM Annual Book of Standards*, Vol. 14.04, ASTM International, West Conshohocken, PA, USA, 2002.

[18] ASTM standard E 913: Standard method for calibration of reference pyranometers with axis vertical by the shading method. In: *ASTM Annual Book of Standards*, Vol. 14.04, ASTM International, West Conshohocken, PA, USA, 2002.

[19] ASTM standard E 941: Standard test method for calibration of reference pyranometers with axis tilted by the shading method. In: *ASTM Annual Book of Standards*, Vol. 14.04, ASTM International, West Conshohocken, PA, USA, 2002.

[20] ASTM standard E 948: Test method for electrical performance of photovoltaic cells using reference cells under simulated sunlight. In: *ASTM Annual Book of Standards*, Vol. 12.02, ASTM International, West Conshohocken, PA, USA, 2002.

[21] ASTM standard E 1036: Test methods for electrical performance of nonconcentrator terrestrial photovoltaic modules and arrays using reference cells. In: *ASTM Annual Book of Standards*, Vol. 12.02, ASTM International, West Conshohocken, PA, USA, 2002.

[22] IEC standard 60904-1: Measurement of photovoltaic current-voltage characteristics. *Photovoltaic Devices*. International Electrotechnical Commission, Geneva, Switzerland, 1987.

[23] Seaman, C.H. 1982. Calibration of solar cells by the reference cell method – the spectral mismatch problem. *Solar Energy*, Vol. 29, pp. 291–298.

[24] ASTM standard E 973: Test method for determination of the spectral mismatch parameter between a photovoltaic device and a photovoltaic reference cell. In: *ASTM Annual Book of Standards*, Vol. 12.02, ASTM International, West Conshohocken, PA, USA, 2002.

[25] IEC standard 60904-7: Photovoltaic devices. Part 7: computation of spectral mismatch error introduced in the testing of a photovoltaic device. International Electrotechnical Commission, Geneva, 1987.

[26] Anspaugh, B. 1987. A verified technique for calibrating space solar cells. *Proc. 19th IEEE Photovoltaic Specialist Conf.*, New Orleans, pp. 542–547.

[27] Brandhorst, H.W. 1971. Calibration of solar cells using high-altitude aircraft. In: *Solar Cells*, Gordon and Breach, London, UK.

[28] Bücher, K. 1997. Calibration of solar cells for space applications. *Progress in Photovoltaics: Research and Applications*, Vol. 5, pp. 91–107.

[29] Osterwald, C.R., Emery, K.A., Myers, D.R. and Hart, R.E. 1990. Primary reference cell calibrations at SERI: history and methods. *Proc. 21st IEEE Photovoltaic Specialists Conf.*, Kissimmee, pp. 1062–1067.

[30] ASTM standard E 1125: Test method for calibration of primary non-concentrator terrestrial photovoltaic reference cells using a tabular spectrum. In: *ASTM Annual Book of Standards*, Vol. 12.02, ASTM International, West Conshohocken, PA, USA, 2002.

[31] Osterwald, C.R., Anevsky, S., Bücher, K., Barua, A.K., Chaudhuri, P., Dubard, J., Emery, K., Hansen, B., King, D., Metzdorf, J., Nagamine, F., Shimokawa, R., Wang, Y.X., Wittchen, T., Zaaiman, W., Zastrow, A. and Zhang, J. 1999. The world photovoltaic scale: an international reference cell calibration program. *Progress in Photovoltaics: Research and Applications*, Vol. 7, pp. 287–297.

[32] ASTM standard E 1362: Test method for calibration of non-concentrator photovoltaic secondary reference cells. In: *ASTM Annual Book of Standards*, Vol. 12.02, ASTM International, West Conshohocken, PA, USA, 2002.

[33] IEC standard 60904-6: Requirements for reference solar modules. Photovoltaic Devices, International Electrotechnical Commission, Geneva, Switzerland 1994.

[34] Emery, K., Myers, D. and Rummel, S. 1988. Solar simulation – problems and solutions. *Proc. 20th IEEE Photovoltaic Specialists Conf.*, Las Vegas, pp. 1087–1091.

[35] ASTM standard E 927: Specification for solar simulation for terrestrial photovoltaic testing. In: *ASTM Annual Book of Standards*, Vol. 12.02. ASTM International, West Conshohocken, PA, USA, 2002.

[36] IEC standard 60904-9: Solar simulator performance requirements. *Photovoltaic Devices*, International Electrotechnical Commission, Geneva, Switzerland, 1995.

[37] Osterwald, C.R., Glatfelter, T. and Burdick, J. 1987. Comparison of the temperature coefficients of the basic I–V parameters for various types of solar cells. *Proc. 19th IEEE Photovoltaic Specialists Conf.*, New Orleans, pp. 188–193.

[38] Sze, S.M. 1981. *Physics of Semiconductor Devices*. Wiley, New York, USA.

[39] Fahrenbruch, A.L. and Bube, R.H. 1983. *Fundamentals of Solar Cells*. Academic Press, New York, USA.

[40] Whitfield, K. and Osterwald, C.R., 2001. Procedure for determining the uncertainty of photovoltaic module outdoor electrical performance. *Progress in Photovoltaics: Research and Applications*, Vol. 9, pp. 87–102.

[41] Osterwald, C.R. 1986. Translation of device performance measurements to reference conditions. *Solar Cells*, Vol. 18, pp. 269–279.

[42] King, D.L., Kratochvil, J.A. and Boyson, W.E. 1997. Temperature coefficients for PV modules and arrays: measurement methods, difficulties, and results. *Proc. 26th IEEE Photovoltaic Specialists Conf.*, Anaheim, pp. 1183–1186.

[43] Whitaker, C.M., Townsend, T.U., Wenger, H.J., Iliceto, A., Chimento, G. and Paletta, F. 1991. Effects of irradiance and other factors on PV temperature coefficients. *Proc. 22nd IEEE Photovoltaic Specialists Conf.*, Las Vegas, pp. 608–613.

[44] Glatfelter, T. and Burdick, J. 1987. A method for determining the conversion efficiency of multiple-cell photovoltaic devices. *Proc. 19th IEEE Photovoltaic Specialists Conf.*, New Orleans, pp. 1187–1193.

[45] Emery, K.A., Osterwald, C.R., Glatfelter, T., Burdick, J. and Virshup, G. 1988. A comparison of the errors in determining the conversion efficiency of multijunction solar cells by various methods. *Solar Cells*, Vol. 24, pp. 371–380.

[46] King, D.L., Hansen, B.R., Moore, J.M. and Aiken, D.J. 2000. New methods for measuring performance of monolithic multi-junction solar cells. *Proc. 28th IEEE Photovoltaic Specialists Conf.*, Anchorage, pp. 1197–1201.

[47] Emery, K., Meusel, M., Beckert, R., Dimroth, F., Bett, A. and Warta, W. 2000. Procedures for evaluating multijunction concentrators. *Proc. 28th IEEE Photovoltaic Specialists Conf.*, Anchorage, pp. 1126–1130.

[48] ASTM draft standard: Standard test method for measurement of electrical performance and spectral response of nonconcentrator multijunction photovoltaic cells and modules. *ASTM Annual Book of Standards*, Vol. 12.02, ASTM International, West Conshohocken, PA, USA, 2002, in press.

[49] Meusel, M., Adelhelm, R., Dimroth, F., Bett, A.W. and Warta, W. 2002. Spectral mismatch correction and spectrometric characterization of monolithic III–V multi-junction solar cells. *Progress in Photovoltaics: Research and Applications*, Vol. 10, pp. 243–255.

[50] Smith, S., Townsend, T., Whitaker, C. and Hester, S. 1989. Photovoltaics for utility-scale applications: project overview and data analysis. *Solar Cells*, Vol. 27, pp. 259–266.

[51] Whitaker, C.M., Townsend, T.U., Newmiller, J.D., King, D.L., Boyson, W.E., Kratochvil, J.A., Collier and Osborn, D.E. 1997. Application and validation of a new PV performance characterization method. *Proc. 26th IEEE Photovoltaic Specialists Conf.*, Anaheim, pp. 1253–1256.

[52] King, D.L., Kratochvil, J.A., Boyson, W.E. and Bower, W. 1998. Field experience with a new performance characterization procedure for photovoltaic arrays. *Proc. 2nd World Conf. on Photovoltaic Solar Energy Conversion*, pp. 1947–1952.

[53] Myers, K., del Cueto, J.A. and Zaaiman, W. 2002. Spectral corrections based on optical air mass. *Proc. 29th IEEE Photovoltaic Specialists Conf.*, New Orleans, in press.

[54] King, D.L., Kratochvil, J.A. and Boyson, W.E. 1997. Measuring solar spectral and angle-of-incidence effects on photovoltaic modules and solar irradiance sensors. *Proc. 26th IEEE Photovoltaic Specialists Conf.*, Anaheim, pp. 1113–1116.

[55] Kroposki, B, Emery, K., Myers, D. and Mrig, L. 1994. A comparison of photovoltaic module performance evaluation methodologies for energy

ratings. *Proc. First World Conf. on Photovoltaic Energy Conversion*, Hawaii, pp. 858–862.

[56] Marion, B., Kroposki, B., Emery, K., del Cueto, J., Myers, D. and Osterwald, C. 1999. Validation of a photovoltaic module energy ratings procedure at NREL. National Renewable Energy Laboratory Technical Report NREL/TP-520-26909, available from the Nationa Technical Information Service, Springfield, VA, USA.

[57] Chianese, D., Rezzonico, S., Cereghetti, N. and Realini, A. 2001. Energy rating of PV modules. *Proc. 17th European Photovoltaic Solar Energy Conf.*, Munich, pp. 706–709.

[58] Cereghetti, N., Realini, A., Chianese, D. and Rezzonico, S. 2001. Power and energy production of PV modules. *Proc. 17th European Photovoltaic Solar Energy Conf.*, Munich, pp. 710–713.

[59] Anderson, D., Sample, T. and Dunlop, E. 2001. Obtaining module energy rating from standard laboratory measurements. *Proc. 17th European Photovoltaic Solar Energy Conf.*, Munich, pp. 832–835.

[60] del Cueto, J.A. 2002. Comparison of energy production and performance from flat-plate photovoltaic modules deployed at fixed tilt. *Proc. 29th IEEE Photovoltaic Specialists Conf.*, New Orleans, in press.

[61] *Guide to the Expression of Uncertainty in Measurement*. International Electrotechnical Commission, Geneva, Switzerland 1995.

[62] Emery, K.A. and Osterwald, C.R. 1990. PV performance measurement algorithms, procedures, and equipment. *Proc. 21st IEEE Photovoltaic Specialists Conf.*, Kissimmee, pp. 1068–1073.

[63] Ossenbrink, H.A., Zaaiman, W. and Bishpop, J. 1993. Do multi-flash solar simulators measure the wrong fill factor? *Proc. 23rd IEEE Photovoltaic Specialists Conf.*, Louisville, pp. 1194–1196.

[64] Emery, K.A. and Field, H. 1994. Artificial enhancements and reductions in the PV efficiency. *Proc. First World Conf. on Photovoltaic Energy Conversion*, Hawaii, pp. 1833–1838.

[65] Mantingh, E.G., Zaaiman, W. and Ossenbrink, H.A. 1994. Ultimate transistor electronic load for electrical performance measurement of photovoltaic devices using pulsed solar simulators. *Proc. First World Conf. on Photovoltaic Energy Conversion*, Hawaii, pp. 871–873.

[66] Osterwald, C.R., Anevsky, S., Barua, A.K., Dubard, J., Emery, K., King, D., Metzdorf, J., Nagamine, F., Shimokawa, R., Udayakumar, N., Wang, Y.X., Wittchen, T., Zaaiman, W., Zastrow, A. and Zhang, J. 1996. Results of the PEP'93 intercomparison of reference cell calibrations and newer technology performance measurements. *Proc. 25th IEEE Photovoltaic Specialists Conf.*, Washington DC, pp. 1263–1266.

[67] Rüther, R., Kleiss, G. and Reiche, K. 2002. Spectral effects on amorphous silicon solar module fill factors. *Sol. Energy Mater. Sol. Cells*, Vol. 71, pp. 375–385.

[68] Emery, K.A., Osterwald, C.R. and Wells, C.V. 1987. Uncertainty analysis of photovoltaic efficiency measurements. *Proc. 19th IEEE Photovoltaic Specialists Conf.*, New Orleans, pp. 153–159.

[69] Heidler, K. and Beier, J. 1988. Uncertainty analysis of PV efficiency measurements with a solar simulator: spectral mismatch, non-uniformity, and other sources of error. *Proc. 8th European Photovoltaic Solar Energy Conf.*, Florence, pp. 554–559.

[70] Field, H. and Emery, K.A. 1993. An uncertainty analysis of the spectral correction factor. *Proc. 23rd IEEE Photovoltaic Specialists Conf.*, Louisville, pp. 1180–1187.

[71] King, D.L., Hansen, B.R. and Jackson, J.K. 1993. Sandia/NIST reference cell calibration procedure. *Proc. 23rd IEEE Photovoltaic Specialists Conf.*, Louisville, pp. 1095–1101.

[72] King, D.L., Hansen, B.R., Kratochvil, J.A. and Quintana, M.A. 1997. Dark current-voltage measurements on photovoltaic modules as a diagnostic or manufacturing tool. *Proc. 26th IEEE Photovoltaic Specialists Conf.*, Anaheim, pp. 1125–1128.

[73] Chegaar, M., Ouennoughi, Z. and Hoffman, A. 2001. A new method for evaluating illuminated solar cell parameters. *Solid-State Electronics*, Vol. 45, pp. 293–296.

[74] del Cueto, J.A. 1998. Method for analyzing series resistance and diode quality factors from field data of photovoltaic modules. *Sol. Energy Mater. Sol. Cells*, Vol. 55, pp. 291–297.

[75] McMahon, T.J., Basso, T.S. and Rummel, S.R. 1996. Cell shunt resistance and photovoltaic module performance. *Proc. 25th IEEE Photovoltaic Specialists Conf.*, Washington DC, pp. 1291–1294.

[76] IEC standard 60904-8: Measurement of spectral response of a photovoltaic (PV) device. *Photovoltaic Devices*, International Electrotechnical Commission, Geneva, Switzerland, 1998.

[77] ASTM standard E 1021: Test method for measuring spectral response of photovoltaic cells. In: *ASTM Annual Book of Standards*, Vol. 12.02, ASTM International, West Conshohocken, PA, USA 2002.

[78] Hartman, J.S. and Lind, M.A. 1983. Spectral response measurements for solar cells. *Solar Cells*, Vol. 7, pp. 147–157.

[79] van Steenwinkel, R. 1987. Measurements of spectral responsivities of cells and modules. *Proc. 7th European Photovoltaic Solar Energy Conf.*, p. 325.

[80] Budde, R., Zaaiman, W. and Ossenbrink, H.A. 1994. Spectral response calibration facility for photovoltaic cells. *Proc. First World Conf. on Photovoltaic Energy Conversion*, Hawaii, pp. 874–876.

[81] Osterwald, C.R., Anevsky, S., Barua, A.K., Bücher, K., Chauduri, P., Dubard, J., Emery, K., King, D., Hansen, B., Metzdorf, J., Nagamine, F., Shimokawa, R., Wang, Y.X., Wittchen, T., Zaaiman, W., Zastrow, A. and Zhang, J. 1998. The results of the PEP'93 intercomparison of reference cell calibrations and newer technology performance measurements: final report. National Renewable Energy Laboratory Technical Report NREL/TP-520-23477, available from the National Technical Information Service, Springfield, VA, USA.

[82] Field, H. 1997. Solar cell spectral response measurement errors related to spectral band width and chopped light waveform. *Proc. 26th IEEE Photovoltaic Specialists Conf.*, Anaheim, pp. 471–474.

[83] Burdick, J. and Glatfelter, T. 1986. Spectral response and I–V measurements of tandem amorphous-silicon alloy photovoltaic devices. *Solar Cells*, Vol. 18, pp. 301–314.

[84] Eisgruber, I.L. and Sites, J.R. 1996. Extraction of individual-cell photocurrents and shunt resistances in encapsulated modules using large-scale laser scanning. *Progress in Photovoltaics: Research and Applications*, Vol. 4, pp. 63–75.

[85] Agostinelli, G., Friesen, G., Merli, F., Dunlop, E.D., Acciarri, M., Racz, A., Hylton, J., Einhaus, R. and Lauinger, T. 2001. Large area fast LBIC as a tool for inline PV module and string characterization. *Proc. 17th European Photovoltaic Solar Energy Conf.*, Munich, pp. 410–413.

[86] King, D.L., Kratochvil, J.A., Quintana, M.A. and McMahon, T.J. 2000. Applications for infrared imaging equipment in photovoltaic cell, module, and system testing. *Proc. 28th IEEE Photovoltaic Specialists Conf.*, Anchorage, pp. 1487–1490.

[87] King, D.L., Quintana, M.A., Kratochvil, J.A., Ellibee, D.E. and Hansen, B.R. 2000. Photovoltaic module performance and durability following long-term field exposure. *Progress in Photovoltaics: Research and Applications*, Vol. 8, pp. 241–256.

[88] McMahon, T.J., Jorgensen, G.J., Hulstrom, R.L., King, D.L. and Quintana, M.A. 2000. Module 30 year life: what does it mean and is it predictable/achievable? *Proceedings of the NCPV Program Review Meeting*, available from the National Technical Information Service, Springfield, VA, USA.

[89] Wohlgemuth, J.H. 1994. Reliability testing of PV modules. *Proc. First World Conf. on Photovoltaic Energy Conversion*, Hawaii, pp. 889–892.

[90] Hoffman, A.R. and Ross, R.G. 1979. Environmental qualification testing of terrestrial solar cell modules. *Proc. 13th IEEE Photovoltaic Specialists Conf.*, Washington DC, pp. 835–842.

[91] Hoffman, A.R., Griffith, J.S. and Ross, R.G. 1982. Qualification testing of flat-plate photovoltaic modules. *IEEE Transactions of Reliability*, Vol. R-31, pp. 252–257.

[92] Block V solar cell module design and test specification for intermediate load applications – 1981. Jet Propulsion Laboratory report 5101-161 1981, Pasadena, CA, USA.

[93] Smokler, M.I., Otth, D.H. and Ross, R.G. 1985. The block program approach to photovoltaic module development. *Proc. 18th IEEE Photovoltaic Specialists Conf.*, pp. 1150–1158.

[94] Qualification test procedures for photovoltaic modules. Specification No. 502, Issue 1, Commission of the European Communities, Joint Research Center, Ispra Establishment, 1984.

[95] Standard for flat-plate photovoltaic modules and panels. ANSI/UL 1703-1987, American National Standards Institute, New York, USA, 1987.

[96] DeBlasio, R., Mrig, L. and Waddington, D. 1990. Interim qualification tests and procedures for terrestrial photovoltaic thin-film flat-plate modules. *Solar Energy Research Institute Technical Report* SERI/TR-213-3624, available from the National Technical Information Service, Springfield, VA, USA.

[97] IEC standard 61215: Crystalline silicon terrestrial photovoltaic (PV) modules – design qualification and type approval. International Electrotechnical Commission, Geneva, Switzerland, 1993.

[98] Ossenbrink, H., Rossi, E. and Bishop, J. 1991. Specification 503 – implementation of PV module qualification tests at ESTI. *Proc. 10th European Photovoltaic Solar Energy Conf.*, Lisbon, pp. 1219–1221.

[99] Bishop, J. and Ossenbrink, H. 1996. Results of five years of module qualification testing to CEC specification 503. *Proc. 25th IEEE Photovoltaic Specialists Conf.*, Washington DC, pp. 1191–1196.

[100] IEEE standard 1262: IEEE recommended practice for qualification of photovoltaic (PV) modules. Institute of Electrical and Electronic Engineers, New York, USA, 1995.

[101] IEC standard 61646: Thin-film terrestrial photovoltaic (PV) modules – design qualification and type approval. International Electrotechnical Commission, Geneva, Switzerland, 1996.

[102] Wohlgemuth, J.H., BP Solar, private communication.

[103] Wohlgemuth, J.H., Conway, M. and Meakin, D.H. 2000. Reliability and performance testing of photovoltaic modules. *Proc. 28th IEEE Photovoltaic Specialists Conf.*, Anchorage, pp. 1483–1486.

[104] ASTM standard E 1596: Test methods for solar radiation weathering of photovoltaic modules. *ASTM Annual Book of Standards*, Vol. 12.02, ASTM International, West Conshohocken, PA, USA, 2002.

[105] Osterwald, C.R., Hammond, R., Zerlaut, G. and D'Aiello, R. 1994. Photovoltaic module certification and laboratory accreditation criteria development. *Proc. First World Conf. on Photovoltaic Energy Conversion*, Hawaii, pp. 885–888.

[106] Osterwald, C.R., Varadi, P.F., Chalmers, S. and Fitzgerald, M. 2001. Product certification for PV modules, BOS components, and systems. *Proc. 17th European Photovoltaic Solar Energy Conf.*, Munich, pp. 379–384.

IV-2

PV System Monitoring

Bruce Cross, Energy Equipment Testing Service Ltd, Cardiff, UK

1 Introduction

There are many reasons to monitor a system as expensive and long-term as a PV installation. Careful consideration should be given to the purpose behind the monitoring before developing a specification, and the ethos should be to measure only those variables that are necessary, and the minimum frequency required to give meaningful results, for a period of time over which new information will be produced. These needs for monitoring fall into three main groups:

- User feedback
- Performance verification
- System evaluation.

1.1 User Feedback

This can range from a simple LED on the inverter lid or a user display in a domestic hallway, to a large interactive wall display in the foyer of a corporate building. The common thread to all displays is giving the users an indication that the system is functioning and, the benefits that this brings. A PV system appears, to the uninformed user, to do nothing at all - not a good public relations statement! A clear display gives much added value to the system, especially if combined with some graphic or text explaining the concepts (Figure 1).

1.2 Performance Verification

A system may have been financed on the basis of its output, and so the user needs to measure the output and compare to the claims for the system. It may also be the case that the electrical production has to be measured, in order to be sold, or that some 'green certificates' may be evaluated. The complexity and expense of such metering is determined by the number and accuracy of the measurements to be made.

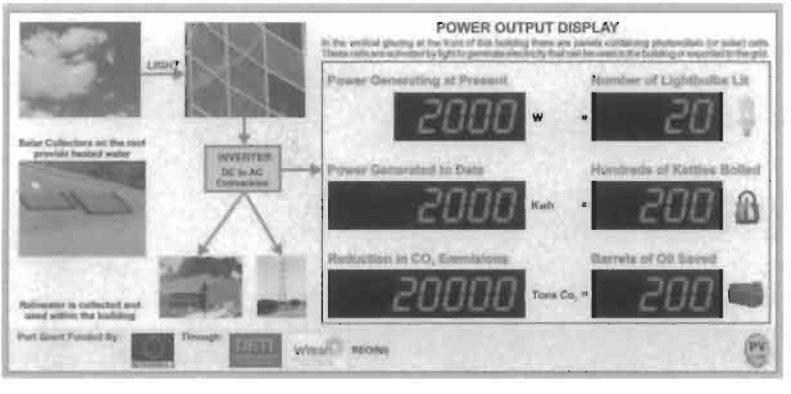

Figure 1 Public display at the William Jefferson Clinton Reading Rooms, Enniskillen, Northern Ireland, showing the PV power generation and also many consequential variables. (Photo EETS.)

High Technology Electronics
Solar Electronics
Battery Charging Systems
Cable Technology

Gamme des produits	régulateurs de charge photovoltaiques, régulateurs différentiels pour chauffes-eau solaires, régulateurs de prépaiement pour l'électrification rurale, lampes fluocompactes à CC, lampes à diodes, onduleurs sinusoidaux pour les réseaux isolés, convertisseurs CC/CC.
Profile d'entreprise	**PME à 300 employés**, certifiée d'après ISO EN DIN 9001:2000 avec des départements recherche & développement, production et vente internationale.
Maison mère	**Memmingen, Germany**

Adress Postale	87700 Memmingen, Germany Mammostrasse 1
Téléphone	+49 8331 8558 0
Fax	+49 8331 8558 12
E-mail	info@stecasolar.com
Site Web	www.stecasolar.com

Solar Thermal

Solar Photovoltaics

1.3 System Evaluation

For an unusual system it may be worthwhile to measure the detailed operation of the system in order to understand the functioning of its components in detail. This was frequently performed in the 1980s and 1990s when systems were often grant funded, and the main purpose of building the system was to improve knowledge and understanding. The operation of PV systems is now well documented, and the expense of full monitoring, and the evaluation of the data, cannot normally be justified. The European Commission used to require full monitoring of every project they supported [1], but now this level of details seems to have outlived its usefulness.

Of course, these three types of monitoring are not mutually exclusive. A display for user feedback is also necessary in a large system being fully monitored, or a system where the output is being measured [2].

2 Equipment

2.1 Displays

Displays are the backbone of monitoring. The easiest to fit is a simple indication as part of the inverter. Most PV inverter manufacturers offer an optional display. However this can place severe constraints on the placing of the inverter, which would normally be in a roof void, electrical switch room, or some other secluded place. If the display is to be effective it must be in a place where it is visible in everyday activities.

Remote displays are easier to site, and may be provided with data from the inverter itself, or by a meter in the cabling from inverter to distribution board. A significant cost to installing this is the routing of the cabling to the display, but there are instruments on the market that avoid this by utilising short-range radio transmission (see Figure 2).

Figure 2 A domestic PV output display receiving radio-linked data from a sensor next to the inverter. (Photo EETS.)

There are many different formats of data that can be displayed: the most popular are the instantaneous power being generated, and the total energy to date. However, large displays often include derived values that mean more to the public, such as numbers of lights that are being powered, or the amount of carbon production being offset (see Figure 3). A computer-based monitoring system can often embed that information within a touch screen driven information point, or to have it displayed on the website for the building.

2.2 Data Acquisition Systems

The main system tends to fall into two types: loggers and computers. The advantage of a logger is its simplicity and robust construction, but its disadvantage is its inflexibility and cost. A computer system, in contrast, may be slower to set up and commission, but has the advantage of a wider choice of operational modes and custom settings, while the cost may be less for a system based on a desktop PC.

The choice between the types may well be dictated by the type of monitoring strategy for the project: are the data to be viewed in real time? Are different types of data to be monitored at differing intervals and in differing ways?

2.3 Sensors

There is no limitation to the inputs that may be monitored for a PV System, but most systems will need to measure the input and output energy, and some environmental and system variables. A list of the more usual variables is given in Table 1.

3 Calibration and Recalibration

The system should be set up and calibrated preferably *in situ*. The need for recalibration should be determined whilst considering the length of time for the

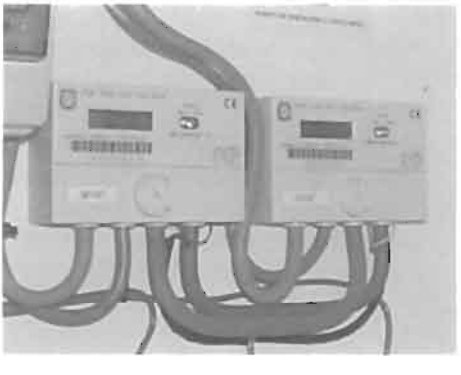

Figure 3 A pair of meters measuring import and export of electricity into a building and outputting pulse data to a monitoring system. (Photo EETS.)

Table 1 Typical monitoring variables (see also [3])

Parameter	Sensor	Accuracy	Precision	Comment
Solar radiation	Reference cell	3%	2 W/m^2	Commonly used
	Pyranometer	2%	1 W/m^2	For research only
DC current	Various	1%	0.5%	
DC voltage	Various	1%	0.5%	
Energy	Meter	1%	1 Wh	Alternative to I and V above
Ambient temperature	Thermocouple	1°C	1°C	
	PRT	0.2°C	0.2°C	
	Thermistor	1°C	1°C	
Module temperature	As ambient			
Power	AC meter	1%	0.5%	

monitoring, and the accuracy required of the system. The reference cell is particularly critical, but often the most difficult item to access. If annual recalibration is not practical back in the laboratory, an on-site comparison with a reference device nearby may be adequate. The entire monitoring system can also benefit from a comparative calibration using hand-held reference devices (ambient temperature sensors, voltage and current meters, etc.).

4 Data Storage and Transmission

The data is generally stored *in situ* using RAM for a logger, or using a hard drive for a computer system. Loggers often include removable RAM cards, discs, or other magnetic media, as a form of storage/retrieval. PCs may use multiple drives, or daily downloads, as a backup storage.

Having recorded the data, it may be transmitted back to the monitoring organisation by many means. The simplest logging systems may have to be physically carried back to the laboratory and plugged into a special reader device, or a PC serial port. Removable media allow the swapping of the storage medium on site allowing monitoring to continue uninterrupted. Such media are tapes, floppy discs, RAM cards, etc. The only disadvantages are that the new media may not be inserted correctly, or the logger may not be restarted, and the loss of data will not be noticed until the next visit.

Telephonic transmission is often used as it gives the opportunity for frequent downloading of data (reducing the length of any 'lost' periods), and also the chance to 'upload' any changes to the logging schedule. The more sophisticated loggers can initiate a call to a fax or PC to report any faults or out of range signals immediately they are detected.

The advent of the internet has allowed PCs to connect to a local portal via a local phone line, thus making downloading less expensive anywhere in the world. If a telephone line is not available at a remote site, a cellular phone connection can provide an equivalent facility.

5 Monitoring Regimes

5.1 Performance Verification

Rapidly changing variables (such as solar radiation) require frequent sampling, although generally only a mean value over a longer period is stored. The accuracy of this measurement may not be high (5% is generally used for irradiance) because of uncertainties along the calibration chain and limited accuracy of absolute reference cell measurements [4, 5]. Thus a sample every 10 sec with a mean stored every 10 min is normal. Greater accuracy of solar radiation measurement can be obtained by using a pyranomcter, which has a uniform response across the solar spectrum, but without continuous measurement of the sunlight spectrum it will not give an accurate measure of the energy available to the PV cell.

Ambient air temperature is important for correcting the output characteristic of the PV, but an accuracy of 1°C is adequate and readily achieved by most sensor types. Since ambient temperature changes so slowly, samples every 1 to 10 min are adequate.

Electrical output is readily measured using standard and inexpensive 'watt-hour' meters. Since the integration of instantaneous power to give readings of energy transmitted is a standard activity in all electrical metering, the accuracy required for PV is rarely problematic for standard instruments. The need for measurement in two directions (for the import/export location in a combined generation and load system) is unusual, and two standard meters is often less expensive than a customised single unit. The signal given from these meters is frequently a pulse, which a readily logged by most standard techniques (Figure 4).

5.2 System Evaluation

Whereas performance verification requires only simple measurements of input and output, there is no limit to the variables that may be of interest in a complex system. Since standard systems are well understood, there is little need to monitor except where new technology or systems are being utilised. Interim measurements throughout the system are required to evaluate the component efficiencies and to understand their characteristics.

Many PV inverter manufacturers offer hardware and software to create a monitoring system to display the functioning of a system. These have the advantage of being (usually) well tested and robust. However, they are not easy to modify, and so cannot often meet a very focussed specification such as is required for some national programs.

5.3 Data Gathering, Transmission and Storage

Electrical measurements of DC and AC power (including phase angle and multi-phase measurements) may be required between each component. The

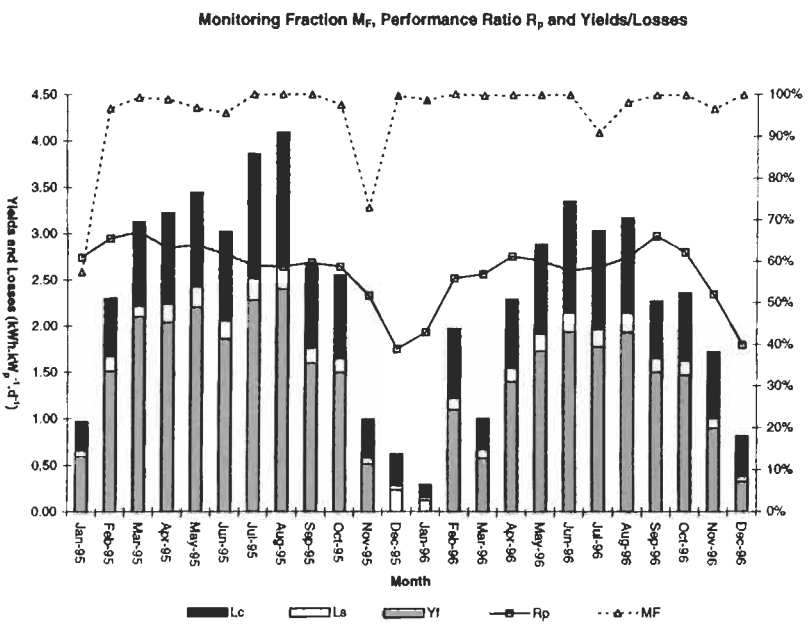

Figure 4 Typical bar graph for reporting. © ETSU. Reprinted with permission.

standard of care for signal isolation and conditioning is particularly important where high DC voltages and currents are concerned. Keeping these signals free of noise adjacent to high frequency switching devices such as inverters is challenging. The issue of fusing of these signal connections needs careful analysis, as there are a large number of fault conditions possible.

5.4 Data Analysis and Reporting

There is usually a reason for system evaluation, and this will often refer to a particular standard, such as IEC 61724 [6]. This will specify exactly the form and presentation of the output. The general variables used to compare the operation of a PV system are normalised yield values. The array energy output divided by the array nominal power gives the array yield Y_a. Similarly, the final AC energy output of the system gives the final yield Y_f. When this value is divided by the reference yield Y_r, defined as the in-plane irradiation divided by the reference irradiation. The value so obtained is the simplest way to compare the 'quality' of the PV system installed: the Performance Ratio, PR. PR is normally in the range 50–70%. A detailed discussion of the yield values and other performance indicators can be found in Chapter IIIe-2.

Energy values produced at various stages of the plant are useful for verification of particular components, as are the efficiencies at each stage but a detailed knowledge of the system is needed to make these comparisons meaningful, so they are less useful for public information. Similarly, capture losses and system losses are only relevant to detailed analysis of the system [7].

Monthly values of performance ratio, array yield, etc., have become the normal way of disseminating the performance of a PV system [8], and a comparison with existing systems is made easier if this method is continued. Such bar graphs can also be embellished with sub-categories of capture losses, system losses, etc. (see Figure 4).

References

[1] Blaesser, G. and Munroe, D. 1995. Guideline for the assessment of photovoltaic plants A: Photovoltaic system monitoring. *Report EUR 16338EN*, JRC Ispra.

[2] Testing, commissioning and monitoring guide for photovoltaic power systems in buildings, *ETSU Report S/P2/290*, Department of Trade and Industry, UK. 1998.

[3] IEC standard 61194:1992. Characteristic parameters of stand alone photovoltaic systems.

[4] IEC standard 60904-2:1988. Photovoltaic devices, Part 2 Requirements for reference solar cells.

[5] IEC standard 60904-6:1994. Part 6: Requirements for reference solar modules.

[6] IEC standard 61724:1998. Photovoltaic devices, monitoring requirements.

[7] IEC standard 61829:1995. Crystalline silicon photovoltaic array. On-site measurements of I–V characteristics.

[8] Blaesser, G. and Munroe, D. 1995. Guidelines for assessment of photovoltaic plants B: Analysis and presentation of monitoring data, *Report EUR 16339EN*, JRC Ispra.

IV-3

Calibration, Testing and Monitoring of Space Solar Cells

Emilio Fernandez Lisbona, ESA-Estec, Noordwijk, The Netherlands

1 Introduction

Solar energy is the main power source technology for most spacecraft since the 1960s. A total failure of the solar array (SA) performance will lead to complete mission loss. SA behaviour in the space environment has to be predicted in order to assure endurance during mission life.

The SA electrical performance is a basic parameter that needs to be predicted for mission life, tested on ground and monitored continuously in space. Electrical performance (EP) at beginning of life conditions is measured on ground to check power output prediction, based on performance measurements of single solar cells and before their integration on the SA. These measurements are performed with solar simulators, having adjusted their light intensity to standard AM0 illumination conditions with suitable reference solar cells. Reference cells are space calibrated using different methods that will be described in Section 2.

Endurance of the SA to the space environment has to be simulated by ground environmental testing. Different mechanical and environmental tests, together with electrical tests for degradation assessment, are performed at the different steps of development, manufacture and integration of SA components and intermediate assemblies. An overview of these tests is given in Section, mainly focused on tests at solar cell levels.

Monitoring the performance of the SA in orbit is essential to assess the predicted behaviour during the mission and this provides valuable data for verification of ground testing and further SA design improvements. Section 4 deals with the monitoring of spacecraft SA in orbit. Flight experiments are conducted to assess the performance and behaviour in space of novel solar cell or SA integration technologies. Two other important sources of data are unpredicted anomalies in orbit and investigations carried out on returned from space SAs.

2 Calibration of Solar Cells

Standard solar cells are used to set the intensity of solar simulators to standard illumination conditions, in order to electrically characterise solar cells with similar spectral response. Space calibration methods of solar cells can be extraterrestrial when performed outside the atmosphere or synthetic if they are carried out on the ground, using natural sunlight or simulated indoor illumination [1]. To prevent continuous handling operations of the expensive extraterrestrial/synthetic cells, so-called secondary working standard solar cells are calibrated for routine electrical performance testing in industry and testing laboratories.

2.1 Extraterrestrial Methods

Two calibration methods are the main suppliers of extraterrestrial standards: the high altitude balloon and the high altitude aircraft. Both methods require minimum data correction due to the small residual air mass at the altitude where the calibration is performed.

2.1.1 High Altitude Balloon

Calibrations are performed on board stratospheric balloons flying at altitudes of around 36 km, where the illumination sun conditions are very close to AM0. Cells to be calibrated are directly exposed to the sun, mounted on supports with sun trackers. Currently, two institutions, JPL-NASA in the USA [2] and CNES in France [3, 4], are conducting, on a yearly basis, these calibration campaigns. The main differences between the two calibration institutes are the position of the cells, which in the case of JPL-NASA is mounted on the balloon apex and in the case of CNES, is a gondola hanging from the balloon. Both institutes correct calibrated data taking into account the effect of temperature and the variation of illumination due to the Earth–Sun distance variation over the year. CNES also corrects its calibrated data, taking into account the effect of the residual atmosphere.

2.1.2 High Altitude Aircraft

Calibrations are performed on board of an aircraft capable of flying at altitudes of 15–16 km. Cells are mounted at the end cap of a collimating tube on a temperature controlled plate. NASA Glenn Research Centre is currently conducting more than 25 flights per calibration campaign using a Gates Learjet 25 equipped even with a spectroradiometer to measure the solar spectrum at that altitude. Data are corrected for the ozone absorption, the geocentric distance and extrapolated to the air mass value of zero [5].

2.1.3 Space Methods

The most realistic environment on which calibration of solar cells can be performed is indeed outside the atmosphere. The first constraint of these methods is their relatively high cost compared with the other two extraterrestrial methods and their lower level of maturity.

- Space shuttle: On board the space shuttle, the Solar Cell Calibration Experiment (SCCE) was conducted in two flights in 1983/84, where solar cells from different agencies, institutions and space solar cell industries around the world were calibrated and returned back to Earth [6].
- Photovoltaic Engineering Testbed: This is a NASA-proposed facility to be flown in the International Space Station, where after exposure and calibration of cells in the space environment, they are returned back to Earth for laboratory use [7].
- Lost Twin: This is an ESA-proposed method, based on the flight of several solar cells on a non-recoverable spacecraft. Cells nearly identical to the flight ones are kept on Earth. The orbiting cells are calibrated and these calibrated values are given to their respective twin cells.

2.2 Synthetic Methods

There are two methods carried out under natural sunlight conditions.

2.2.1 Global Sunlight

The cells to be calibrated and a pyranometer are placed on a horizontal surface, where simultaneous readings of spectral irradiance over the sensitivity range of the pyranometer and short circuit current of the cells are recorded in global sunlight. The calibration site environmental conditions need to fulfil several requirements relating to global and diffuse irradiance levels, solar elevation, unobstructed view over a full hemisphere, etc. The calibrated short circuit current of the cell is calculated by means of the following formula:

$$I_{sc} = I_{sg} \frac{\int (k_2 E_{g\lambda}) d\lambda}{E_{glob}} \frac{\int (k_1 s_\lambda) E_{s\lambda} d\lambda}{\int (k_1 s_\lambda)(k_2 E_{g\lambda}) d\lambda}$$

where $k_1 s_\lambda$ is the absolute spectral response of the cell, $k_2 E_{g\lambda}$ the absolute spectral irradiance of the sun at the calibration site, $E_{s\lambda}$ the AM0 spectral irradiance, E_{glob} the pyranometer irradiance reading and I_{sg} the measured short circuit current of the cell.

The final calibration value is the average of three calibrations of three different days. The former RAE (UK) performed for several years global sunlight calibrations at Cyprus [8] and presently INTA-SPASOLAB (Spain) is performed on a yearly basis and at Tenerife [9, 10].

2.2.2 Direct Sunlight

The cells to be calibrated are placed on the bottom plate of a collimation tube, a normal incidence pyrheliometer and a spectroradiometer are kept pointing to direct sunlight while measurements of short-circuit current, total irradiance and spectral irradiance are recorded. Several conditions need to be fulfilled by the calibration site and its environment, i.e. certain irradiance level, stable cell short-circuit readings, ratio of diffuse to direct irradiance, etc. The calibrated short circuit current of the cell is calculated by means of the following formula:

$$I_{sc} = \frac{I_{sd} \int E_{d\lambda} d\lambda \int E_{s\lambda} s_\lambda d\lambda}{E_{dir} \int E_{d\lambda} s_\lambda d\lambda}$$

where I_{sd} is the measured short circuit current, E_{dir} is the total solar irradiance, $E_{d\lambda}$ is the spectral solar irradiance, $E_{s\lambda}$ is the AM0 spectral irradiance and s_λ is the relative spectral response of the cell to be calibrated.

The calibrated short circuit current value is the average of three calibrations performed in three different days. CAST (China) presently performs calibrations following this method [11].

The following two methods are carried out under simulated sunlight.

2.2.3 Solar Simulator

The cell to be calibrated is illuminated by means of a steady-state solar simulator adjusted to 1 AM0 solar constant with a previously calibrated cell or a suitable detector. The spectral irradiance of the solar simulator is measured with a

spectroradiometer and the relative spectral response of the cell is measured separately. The calibrated short circuit current of the cell is calculated as follows:

$$I_{sc} = I_{sm} \frac{\int Es\lambda s_\lambda d\lambda}{\int Em\lambda s\lambda d\lambda}$$

where I_{sm} the short circuit current and $E_{m\lambda}$ the spectral irradiance, both measured under the solar simulator. NASDA (Japan) regularly performs calibrations following this method [12].

2.2.4 Differential Spectral Response

The calibrated short circuit current of the cell is calculated with its absolute spectral response together with the reference AM0 solar spectral irradiance. The absolute spectral response is obtained as follows: first, the relative spectral response of the cell to be calibrated and then for certain wavelengths the absolute differential spectral response, is determined by the ratio of the cell short circuit current to irradiance measured by a standard detector. This method was developed and is frequently presently used by PTB (Germany) for solar cell calibration [13].

2.3 Secondary Working Standards

Secondary working standard (SWS) solar cells are used to set intensity of solar simulators to standard conditions for routine measurements of identical (same spectral response) solar cells during acceptance or qualification testing. For the EP characterisation of SA, panels or coupons, SWSs are preferred for reference. SWSs are calibrated using standards obtained by the methods defined above and a continuous or pulsed light source. The measured data are corrected by means of the spectral response of both cells and the spectral irradiance of the light source and the standard AM0 spectrum, following the spectral mismatch correction method [14]. This secondary calibration method also gives relations between calibrated solar cells by different methods [15].

3 Testing of Space Solar Cells and Arrays

In order to assess the behaviour of solar cells and solar arrays for a specific space mission or environment, several tests need to be conducted at different hardware levels and phases of a project.

- Solar cells:
  - Development: To know their performance, their endurance to the space environment and therefore decide on the most appropriate solar cell candidate for specific application.

  - Design: Measured solar cell data at different environmental conditions is necessary for an accurate power prediction during the mission and therefore a suitable sizing of the solar array.
  - Qualification: Verify that the solar cells manufactured in the production line meet a set of requirements defined by the specific space mission [17].
  - Acceptance: To provide cell performance and physical data; essential for their further integration in the solar array electrical network.
- Higher levels of solar array components integration: The so-called photovoltaic assemblies (test specimens with all the components existing and integrated as in the solar array electrical network) are also tested in the development and qualification phases.
- Solar array level: Tests are performed in development phases and in the qualification phase of the flight hardware. These tests are required to see whether or not the solar array is integrated with the spacecraft body.

Tests on solar cells and solar arrays can be split in three types: Electrical, Environmental and Mechanical/Physical characteristics. The following paragraphs deal with these types of tests, focusing chiefly for their application to solar cells assemblies (SCAs), however, when relevant, their application to higher levels of solar array integration or other solar array components is described.

3.1 Electrical Tests

3.1.1 Electrical Performance

The objective of this test is to assess the corresponding electrical parameters of the solar cells and to provide data for solar generator design. The electrical current of solar cells under 1 Solar Constant AM0 equivalent illumination shall be measured and recorded at a certain voltage. A solar cell test set up consists basically of a continuous or pulsed light source, a load connected across the cell's terminals and electrical current and voltage measurement equipment. During the measurement, the temperature of the cell junction is kept at a constant temperature (25°C) and a four-point probe measurement of the cell is used in order to minimise the effects of lead and contact resistances [16].

Solar simulators need to meet certain requirements on their light beam spectrum, uniformity and stability for optimum EP measurements of photovoltaic devices [1, 17]:

- Spectrum: Maximum allowable deviations of spectral energy in certain wavelength regions of the standard AM0 spectrum define the solar simulator spectral quality classification. The spectral irradiance is measured with spectro-radiometers [18] or special filtered solar cells [19].
- Uniformity: Uniformity of the irradiance on the test area is a critical parameter for accurate measuring of panels or SA.

- Stability: The light beam stability has to be maintained under certain values, especially when no simultaneous correction is done when measuring the EP.

Continuous or pulsed light sources are used to simulate solar illumination in laboratories or test facilities:

- Continuous solar simulators are mostly based on xenon short arc lamps where the beam is filtered and collimated to achieve the above-mentioned requirements. They are mainly used for the electrical characterisation of solar cells and small coupons. Large area continuous solar simulators based on Argon discharge lamps are used to electrically characterised solar cells or panels [20]. Multi-source solar simulators are required for measuring multijunction (Mj) solar cells, in order to set equivalent AM0 illumination conditions on each sub-cell [21].
- Pulsed solar simulators are based on xenon large arc lamps where the beam usually is not filtered to meet the above requirements on the test plane. Either solar cells or large panels can be electrically characterised, being not heated during the test, but special techniques are needed for measuring slow response cells [22, 23]. When measuring Mj solar cells, a better matching of the AM0 is needed, precisely in the near infrared spectral range, where xenon large arc lamps have less radiant energy [24].

Reference cells, either primary or secondary standards, are used to set the intensity of solar simulators to standard illumination conditions. For Mj solar cells, either so-called component cells (Mj cell structures with only one active junction) [25] or methods based on mismatch factor are followed to set standard illumination conditions on each cell junction [26].

Under standard illumination conditions and constant temperature the current voltage curve of the photovoltaic device is traced by polarising at different voltages. The shape and magnitude of the I–V curve depends on the junction characteristics, shunt and series resistance, and on total radiant energy converted, regardless of wavelength composition [27]. However, for Mj solar cells, wavelength composition of the radiant energy affects the shape of the I–V curve [28].

Temperature coefficients of solar cell electrical parameters can be calculated from experimental data, by measuring the device EP at different temperatures [29, 30] (Table 1).

The solar cell EP behaviour under different angles of incidence is of most importance for SA designs with curved substrates and operation of planar SA at high tilt levels. The potential angle of incidence-dependent effects are the cosine function, Fresnel reflectivity, coverglass coatings and filters, solar cell multi-layer anti-reflecting coating, extreme angle effects and end-of-life (EOL) behaviour. Assessments of these effects for each SCA component combinations are needed for SA performance prediction [31].

Table 1 Typical EP parameters and temperature coefficients of some space solar cells. Abbreviations: Sj = single junction; Dj = double junction; Tj = triple junction

Solar cell technology	I_{sc} (mA/cm^2)	V_{oc} (mV)	P_{max} (mW/cm^2)	η (%)	$dIsc/dT$ (mA/cm^2/°C)	$dVoc/dT$ (mV/°C)	dP_{max}/dT (mW/cm^2/°C)
Si BSR	37.0	595	17.5	13.0	0.02	−2.20	−0.080
Si BSFR	39.0	610	19.0	14.0	0.03	−2.00	−0.075
Sj GaAs/Ge	32.0	1030	26.5	19.5	0.02	−1.85	−0.050
Dj GaInP/GaAs/Ge	16.3	2350	31.5	23.0	0.01	−5.50	−0.065
Tj GaInP/GaAs/Ge	16.5	2560	41.5	26.0	0.01	−6.50	−0.085

3.1.2 Relative Spectral Response

Relative Spectral Response is the short-circuit current density generated by unit of irradiance at a particular wavelength as a function of wavelength. Relative spectral response provides valuable data for improving solar cells under development, for the calculation of performance measurement errors and for solar simulator verifications. It is measured by illuminating with a narrow bandwidth (monochromator or narrow band filters) light source (pulsed or continuous) the solar cell [32], at different wavelengths in its sensitivity range, while measuring the cell short circuit current and the irradiance with a sensor. A cell with known spectral response can be used as reference, replacing the irradiance sensor [1].

To measure spectral response of Mj solar cells, each junction needs to be characterised separately by light biasing (filtered light or variable intensity lasers) of the non-measured junctions and by voltage biasing, to measure in short circuit conditions the sub-cell junction under test [33] (Figure 1).

3.1.3 Reverse Characterisation

The reverse voltage behaviour of solar cells is needed for the prediction of shadowing and hot-spot phenomena on solar cell strings. Reverse-biased cells may experience excessive heating, permanent loss of minor power output, or permanent short-circuit failure [34]. Generally, single and Mj gallium arsenide solar cells are more sensitive to reverse bias than silicon cells [35] as seen in Figure 2, driving to implement by-pass diodes on each cell for effective protection. Testing apparatus and procedures are similar to the EP ones, but current and power limitations are needed to avoid cell breakdown.

3.1.4 Capacitance Characterisation

The dynamic behaviour of solar cells may introduce specific requirements on the subsequent solar array regulator. Therefore, the capacitance of solar cells needs to be characterised following two different methods:

- Small signal or frequency domain method: This is the measured high frequency impedance around a certain bias point. Tests are performed with voltage biasing and in darkness [36].

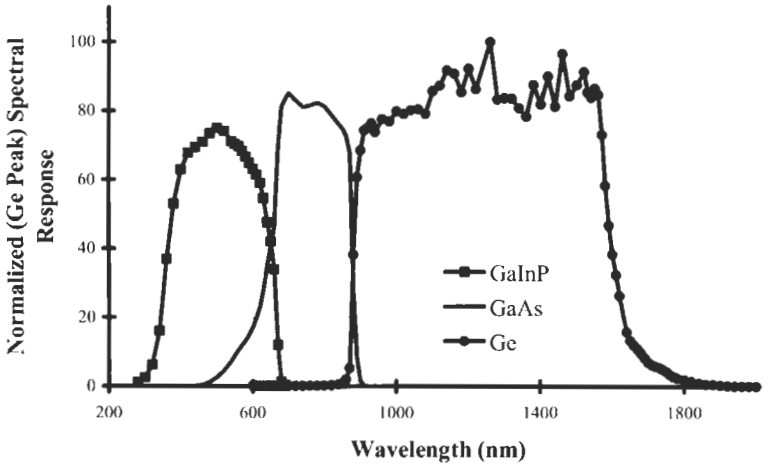

Figure 1 Spectral response of a proton-irradiated Tj solar cell.

- Large signal or time domain method: The rise of solar cell voltage between two operational points gives the solar cell capacitance by applying the formula $C = I_{sc}(t_2 - t_1)/(V_2 - V_1)$ [37], where t_2, t_1 and V_2, V_1 are the time and voltages associated with these operational points.

3.2 Environmental Tests

Environmental tests are performed to check solar array endurance to the different surroundings to which it is exposed during its complete lifetime. The most damaging environments are depicted here:

- Ground operations: Solar arrays are exposed to possible physical damage during manufacturing, integration, handling and transportation activities. During long storage periods, solar array components maybe corroded by humidity. Tests are performed at component, solar cell and SCA levels.
- Launch: Vibration, shocks, acceleration and acoustic fields affect the solar array in this phase, producing high mechanical stress levels that could produce physical damage either just after testing or in orbit. Vibration, shock and acoustic tests are performed usually at higher levels of solar array integration; panel, wing and spacecraft level.
- Space: Particles, temperature, vacuum and micrometeoroids are the main factors degrading solar arrays in space. Each factor affects different solar array components and interfaces. Tests are mainly conducted at solar cell, SCA level and coupon level.

EP and visual inspection tests are performed before and after exposure of photovoltaic devices to any environmental tests. The main environments affecting solar array performance are described below in more detail.

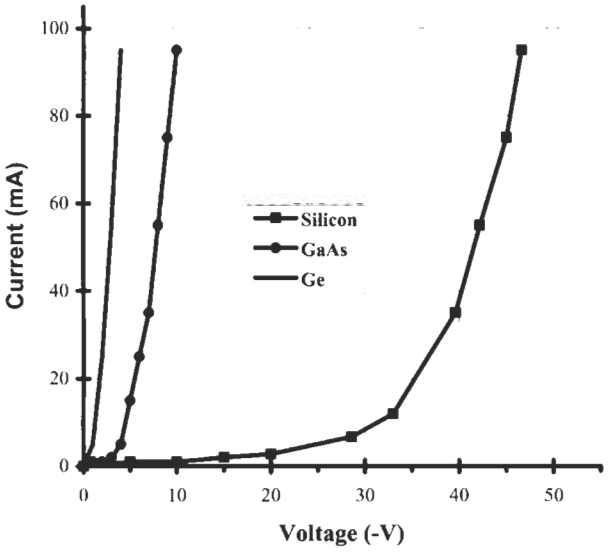

Figure 2 Reverse characteristics of some space solar cells.

3.2.1 Radiation Testing

The radiation environment in space basically comprises electrons and protons of different spectral energies. Solar cells are permanently damaged by these particles; displacement damage is produced in the cells' crystalline structure, reducing the minority carrier diffusion length and lifetimes in the cells' base region, driving a degradation of the cells' electrical parameters. For medium/high radiation environment missions, solar cell particle degradation is the key parameter for solar array sizing. Coverglasses and adhesives can be darkened by radiation reducing the array performance, by transmission losses and operational temperature increases.

Two methods are followed to predict the performance of solar cells under the space radiation environment: JPL method based on reducing all proton/electron energies from a certain space environment to an equivalent normal incidence and mono-energetic irradiation, usually 1MeV electrons [38–40] and NRL model based in the displacement damage dose methodology [41] (see Figure 3).

Solar cell radiation testing is performed on solar cell or SCAs at electron and proton irradiation facilities:

- Electrons are produced by Van der Graaff generators. Typical electron energies range from 0.6 up to 2.5 MeV and flux between 10^9 up to 1.5×10^{12} $e^-/cm^2/s$. Cells are irradiated under vacuum or inert gas conditions.
- Low energy protons (< 2 MeV) are produced by hydrogen ionising chambers and mass separators. Tandem Van der Graaff generators produced protons with energy from 2 to 10 MeV and cyclotrons and synchro-cyclotrons from 10 to 50 MeV and 50 to 155 MeV respectively. Cells are always irradiated under vacuum conditions.

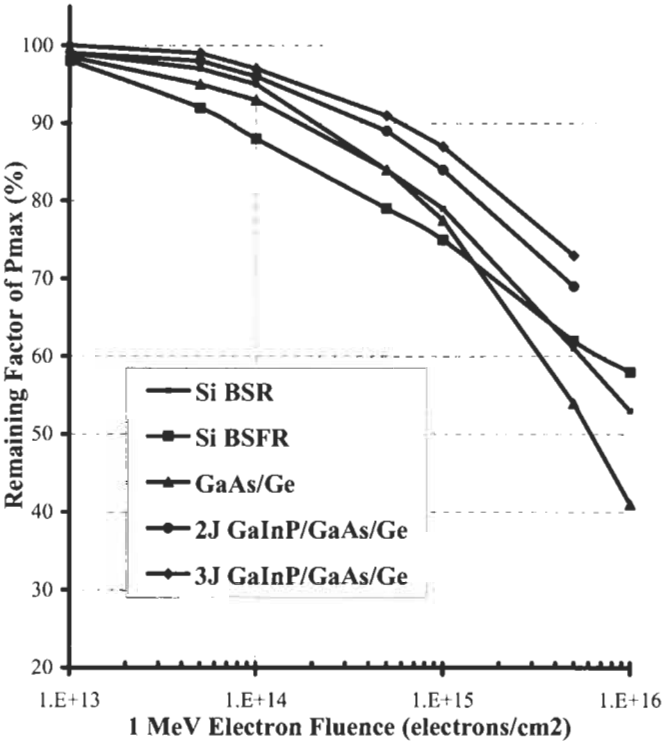

Figure 3 Power degradation of space solar cells under 1 MeV electron particles.

In general, the crystalline damage and performance degradation of irradiated solar cells is not stable for certain types. Recovery or further degradation phenomena are observed after annealing at temperatures higher than 20°C and exposure to sunlight [42, 43], suggesting performance of photon irradiation and annealing testing after particle irradiation.

3.2.2 Ultraviolet Radiation

Ultraviolet radiation can darken certain types of coated solar cell coverglass and adhesives, reducing the sunlight transmission to the solar cells, increasing solar array temperature and therefore lowering its EP [44]. Cracks on solar cell coverglasses may increase cell current degradation by 2% more for EOL [45]. Tests are conducted in vacuum chambers on coverglasses, SCAs or solar array coupons, at solar cell operational temperature in orbit, using UV light sources based on xenon arc, high-pressure mercury or halogen arc discharge lamps [46].

3.2.3 Atomic Oxygen (ATOX)

For low earth orbits (between 180 and 650 km), the presence of ATOX is a main cause of erosion of silver solar cell interconnectors [47, 48] and the kapton foil glued to the support structure outer layer [49]. ATOX durability testing on components or solar array coupons is performed on plasma asher chambers,

being air raw material that becomes a plasma of atomic oxygen and other particles [50]. ATOX dose is determined using uncoated kapton samples whose erosion is known from flying data.

3.2.4 Thermal Cycling

The temperature cycling experienced by solar arrays in orbit (eclipses) is the cause with time of fatigue cracking of harnesses, bus-bars, interconnector material and interconnector solder/weld joints [51], and also the cause of increased series resistance in the solar cell and interconnector interface. Temperature cycling tests are performed following two methods on either solar array coupons or SCAs:

- Vacuum: So-called *thermal vacuum* or *vacuum thermal cycling* provides a good simulation of the space environment, but not of the temperature rate decay in orbit [52].
- Ambient pressure: Fast temperature change rates are achieved with circulating inert gas chambers. Cost and test duration are considerably reduced compared to vacuum chambers, but failures tend to happen earlier than with vacuum chambers [53].

3.2.5 Vacuum

A space vacuum might vaporise metals (Mg, Cd and Zn) and also volatile materials like adhesives. Thermal vacuum is a standard test performed at component and up to solar array level, for endurance testing of components and interfaces. Chambers as described in [52] are commonly available in the space photovoltaic industry and test houses. Failures coming from wrong manufacturing process or contamination of materials are also quickly revealed with these tests [54].

3.1.6 Micrometeoroids

More frequent impacts from micrometeoroids and space debris (between 10^{-6} and 10^{-3} g) mainly erode coverglass and solar array exposed coatings, with small solar array performance degradation due to optical losses. Predictions are in agreement with in-orbit degradation [55] and permanent loss of solar array sections by impacts on harnesses, though these are rare [56]. Hypervelocity impacts of particles are simulated with plasma drag accelerators [57, 58] and light gas guns [59].

3.2.7 Electrostatic Discharge

Dielectric solar array surfaces, mainly solar cell coverglass and kapton layers, are subject to electrostatic charging due to geomagnetic substorm activity or by the spacecraft surrounding plasma. Subsequent sudden electrostatic discharge (ESD) effects may permanently damage solar array components [60]. Coverglasses are coated with conductive coatings (i.e. ITO) and grounded [61] to lighten charging and to give an equi-potential surface for scientific field measurements. Tests are conducted at coupon level to check adequacy of

components and interfaces [62] and at component level for the survival of the conductive coating to the mission environment [17].

3.2.8 Humidity

Accelerated humidity/temperature testing of solar cells is conducted to check the stability of solar cell contacts and anti-reflection coatings for long storage periods [63]. GaAs solar cells with AlGaAs window layers are submitted to this test in order to assure the effective protection of the anti-reflection coating to the corrosion of this window layer [64, 65].

3.3 Physical Characteristics and Mechanical Tests

Several tests are presented in this section, not only tests to check mechanical characteristics as adhesion of coatings, contacts or interconnectors, but also measurements of some physical characteristics needed for solar array sizing or essential inputs to other solar array analysis (Mass Budget, Thermal Analysis, etc). A summary is depicted in Table 2.

4 Monitoring of Space Solar Cells and Arrays

4.1 Flight Experiments

Several flight experiments have been conducted with solar cells/coupons in order to verify their endurance to the space environment and ground radiation testing assessment. Most of the flight experiments measure main electrical parameters of the cells and coupons (I_{sc}, V_{oc}, and power at certain voltage, full I–V curve), sun aspect angle and the operational temperature. In Table 3 some of the most relevant recent flight experiments are listed together with the publication reference, dates of data acquisition, orbit (apogee/perigee), cell/coupon types and main conclusions achieved.

Some flight experiments are, at the time of writing, in preparation:

- Mars array technology experiment (MATE): Several solar cell technologies shall be sent to Mars surface for checking their performance and endurance, together with instrumentation for the Mars surface (sun spectrum, dust, temperature, etc.) characterisation [79].
- Concentrator solar cell array technology flight experiment: Assessment of the performance of reflective concentrators with Mj solar cells [80].

4.2 Monitoring of Solar Array Performance in Space

Monitoring of solar arrays in space is mainly needed to verify that their performance meets the spacecraft power requirements for planned operations

Table 2 Mechanical/physical characterisation tests on space solar cells

Test name or phys./charact.	Purpose	Test method	Requirements
Visual inspection	Find solar cell or component obvious defects	Unaided eye or low magnification (5×–10×)	Several defects are not allowed at component level, relaxation criteria for higher levels of integration exist.
Interconnector adherence	Interconnector weld and cell contact adhesion	Pull test	Maximum pull force value and breakage mode.
Coating adherence	Contact and coatings adhesion	Tape peel test	Percentage of delaminated area below certain value.
Solar cell dimensions	External dimensions and contacts disposition	Microscope	Maximum dimensions provided by solar array electrical network or cell manufacturers.
Solar cell weight	Data for solar array weight budget	Balance	Maximum weight provided by solar array or cell manufacturers.
Solar cell flatness	Solar cell flatness	Profile microscope	Maximum bow provided by solar array electrical network manufacturer.
Contact thickness	Data for interconnector integration	X-ray spectroscopy	Maximum thickness provided by solar array electrical network or cell manufacturers.
Contact surface roughness	Data for interconnector integration	Roughness tester	Maximum thickness provided by solar array electrical network or cell manufacturers.
Hemispherical emittance	Emitted energy by the cell	Infrared spectrophotometer	Maximum emittance provided by solar array or cell manufacturers.
Solar absorptance	Absorbed/incident energy to the cell	Solar spectrometer	Maximum absorptance provided by solar array or cell manufacturers.

and that the design performance predictions for the complete mission are met. Reliable pre-flight data based on ground performance measurements, solar cell qualification tests and power budget calculations, based on qualification tests, is needed initially for an accurate performance evaluation in orbit. For flight data acquisition, temperature sensors, operational and short circuit sensors, and operational and open circuit voltage sensors are required, together with precise attitude and orbit data. Their quantity and precision drives the flight data quality [81]. Flight data is converted to standard conditions (1 Solar Constant and 25°C) for comparison with predicted data. In-orbit performance of some recent spacecraft is shown in Table 4, which includes relevant literature references, dates of evaluated data, orbit, SA type (array layout, power and solar cell type) and main conclusions achieved.

Table 3 Summary of recent flight experiments

Experiment	Ref.	Dates	Orbit	Cell/coupon types	Main conclusions for each cell/coupon type
Equator-S	[66], [67]	Dec. 97, May 98	Equatorial 500 km/ 67,000 km High radiation	1. GaAs/Ge 2. MBE Dj $GaInP_2$/GaAs/GaAs 3. UT[a] GaAs 4. Si NRS[b]/BSF 5. CIGS 6. CIS	1. Degradation according to modelling. 2. High radiation tolerance. 3. High radiation tolerance-thick cover. 4. Confirms ground radiation-testing data. 5. Improvement performance by light soaking effect in orbit. Degradation according to modelling. 6. Low energy protons heavily damaged uncovered cells. Degradation according to modelling.
PASP-Plus	[68–70]	Aug. 94, Aug. 95	70° Elliptic 362 km/ 2552 km High radiation	1. Si Planar & ISS[c] 2. GaAs 3. Dj AlGaAs/GaAs 4. Dj GaAs/CIS 5. InP 6. a-Si	1. Less degradation than predicted with modelling (*). 2. Degradation according to modelling (*). 3. GaAs degradation according to modelling. 4. GaAs degradation less than predicted with modelling. 5. Less degradation than predicted with modelling. 6. Positive P_{max} temp/coeff. with increasing temp.
ETS-VI (SCM)	[71]	Nov. 94, Jun. 96	Elliptic 8550 km/ 38,700 km High radiation	1. Sj GaAs/Si 2. GaAs/GaAs 3. Si BSFR 4. Si BSR	1. and 2. GaAs/Si cells more resistant to radiation damage than GaAs/GaAs.
ETS-V (SCM)	[72]	Sep. 87, Sep. 97	GEO 150°E	1. GaAs LPE 2. GaAs MOCVD 3. Si BSFR 4. Si BSR 5. Si NRS/BSFR	3. and 4. BSR are more resistant to radiation than BSFR, as in ground tests.

Table 3 (*continued*)

Experiment	Ref.	Dates	Orbit	Cell/coupon types	Main conclusions for each cell/coupon type
EURECA (ASGA)	[73]	Aug. 92, Jun. 93	LEO 510 km Circular	1. GaAs/Ge MOCVD 2. GaAs LPE 3. GaAs MOCVD	1. GaAs/Ge cells showed higher operation temperature than GaAs/GaAs. 2. No degradation of solar cells during the flight confirmed with post-flight ground measurements. 3. Post-flight analysis studied the effects on coupon components (interconnectors) of LEO environment (Large number of thermal cycles and ATOX).
LIPS-III	[74–77]	May 87, Aug. 93	LEO 1100 km 60° circular	1. Si BSR and BSFR 2. a-Si:H 3. $CuInSe_2$ 4. GaAs MOCVD and LPE 5. Sj AlGaAs/GaAs	1. BSR more resistant than BSFR. Degradation according to modelling. 2. Photodegradation main cell degradation mechanism (40% in power). 3. Extremely high radiation resistant. 4. and 5. Degradation according to modelling.
UoSAT-5	[78]	Jul. 91, Jul. 95	770 km polar Sun-sync. Low radiation	1. InP 2. ITO/InP 3. GaAs/Ge 4. Si High Eta	1. Small degradation according to modelling. 2. Anomalous degradation in voltage. 3. Small degradation according to modelling. 4. Higher degradation than 1. and 3. but fits models.

(*) Parasitic current collected by these coupons correlates with ground testing and prediction models.

[a] UT = ultra thin.

[b] NRS = non-reflective.

[c] Silicon cells of the International Space Station Array

For other abbreviations and standard solar cell terms see text or Chapter IIa-1.

Table 4 In-orbit performance of recent spacecraft.

Spacecraft (design life)	Ref.	Dates	Orbit	SA type	Main conclusions
SOHO (2.5 years)	[82]	Dec. 95, Dec. 01	LG1[a] 1.5×10^6 km from Earth	2 wings × 2 rigid panels EOL[b] power 1.4 kW Si 2 Ω cm BSR	1. Solar array design and good margin between working and P_{max} point allowed mission extension. 2. Less SA radiation degradation than predicted. 3. SA recovery after sun flares degradation.
SPOT 1 (3 years)	[83]	Feb. 86, Feb. 98	LEO[c] Sun-synchronous	2 wings × 1 flexible panel EOL[b] power 1 kW Si 1 Ω cm	1. Several loss factors have been over evaluated on the design, allowing a longer SA life. 2. SPOT 1 database shall improve EOL[b] performance predictions of coming LEO[c] spacecraft.
HS 601 HP C1 (15 years)	[84]	Aug. 97, Mar. 98	GEO[d]	2 wings × 3 rigid panels BOL[c] power 9.5 kW Dj $GaInP_2$/GaAs/Ge	1. SA power in orbit is 1.1% less than predicted. 2. Systematic errors may be the source of this discrepancy: Calibration of flight balloon standard and the calibration of ground performance testing.
INTELSAT-V (7 years)	[85]	Dec. 81, Dec. 94	GEO[d]	2 wings × 3 rigid panels EOL[b] power 1.5 kW Si BSR	1. SA power is 8–10% higher than predicted (solar flares) and 4–6% higher than predicted (no solar flares) for 13 spacecraft.
CS-3A (7 years)	[86]	Feb. 88, Nov. 88	GEO[d]	2 body mounted panels BOL[c] power 0.85 kW Sj GaAs	1. SA power is 1–5% higher than predicted.
HIPPARCOS (3 years)	[87]	Feb. 90, Jun. 93	GTO[f]	3 deployed panels EOL[b] power 325 W Si BSR 10 Ω cm	1. SA power is according to radiation degradation modelling.
IRS-1A (3 years)	[88]	Mar. 88, Mar. 95	LEO[c]	6 deployed panels EOL[b] power 0.7 kW Si BSR 10 Ω cm	1. The silver mesh interconnector survived more than 35000cy. 2. Effects of ATOX negligible on interconnectors. 3. Power degradation due to radiation matches with modelling.

Table 4 (*continued*)

Spacecraft (design life)	Ref.	Dates	Orbit	SA type	Main conclusions
Space Telescope SA (5 years)	[89]	Apr. 90, Dec. 93	LEO[c] 600 km	2 flexible wings × double roll-out 2 year life power 4.4 kW Si BSFR 10 Ω cm	1. Degradation performance is in agreement with most design loss factors. 2. Radiation fluence below initial prediction. 3. Random failures main degradation SA mechanism.
JCSAT (10 years)	[90]	Mar. 89, May 91	GEO[d]	2 telescopic cylindrical EOL[b] power 1.7 kW K7 and K3 Si	1. 1–2% less BOL[e] in-orbit performance than predicted probably due to reference standards for performance ground testing. 2. Increase performance over time probably due to radiation model more severe than in orbit. 3. Some solar flares did not produce any damage on the SA. No explanation.

[a] La Grangian Point 1.
[b] End of life.
[c] Low Earth orbit.
[d] Geosynchronous orbit.
[e] Beginning of life.
[f] Geosynchronous transfer orbit.
For other abbreviations and standard solar cell terms see text or Chapter IIa-1.

4.3 Spacecraft Solar Array Anomalies in Orbit

Another source of data for improving solar array design comes regrettably from anomalies faced by spacecraft SA in orbit. Investigations of the failure mechanism in-orbit are much more complicated due to the small quantities of data often available. However, some anomalies in orbit could be acceptably explained; a few of them are depicted here below:

4.3.1 European Communication Satellite (ECS) and Maritime European Communication Satellite (MARECS)

After 1.5 years in GEO both SA (virtually identical, two wings of three rigid panels each with silicon solar cells) started to suffer partial loss of power [60]. The failures seemed to be short-circuits between the cell network and panel structure. These failures continued intermittently until the end both missions, however, for ECS the power losses were recovered. Several potential failure modes were identified: imperfections of the Kapton insulation layer or embedded particles in between layers, insulation breakdown by electrostatic discharge, thermal cycling, corona effects, micrometeoroids or a combination of all of them. None of the potential failure modes could be identified as being responsible for the ECS and MARECS anomalies, however, several weak points in the SA design were identified, investigations continued in the direction of the most probable failure mode (ESD) [91] and some improvements were proposed aiming to lower the risk of these failures: designs should be adapted to incorporate sufficient margins in areas where uncertainties exist, parallel cell strings sections instead of single string sections and more stringent tests in manufacturing and acceptance for early failure detection.

4.3.2 X-ray Timing Explorer (XTE)

The XTE spacecraft was launched in December 1995. SA is composed of two wings of three rigid panels each, with silicon solar cells. Shortly after launch, the array showed discontinuous current drops, consistent with the loss of a part of a cell, when coming out from eclipse. The failure mechanism seems to be cell cracks not detected in ground inspections that became open in orbit due to the temperature gradients. These cracks were probably produced during the extensive tap tests, performed to detect SCA to substrate delaminations. During testing on the ground, following the same activities as for the flight SA, the qualification panel showed these effects, giving high confidence to this theory [92].

4.3.3 GPS Navstars 1–6

Six GPS Navstars satellites were placed in 20,000 km circular orbits from 1980. Mission lifetime for each spacecraft was five years and silicon solar cells K4 or K6 were in the SAs. After two years in orbit all spacecraft suffered an unexpected additional degradation of 2.5%. Investigations carried out in optical reflectors surfaces of one of the spacecraft revealed traces of contamination covering all spacecraft external surfaces. These contaminants mainly come from the

outgassing of materials from the spacecraft, leading to reflectivity degradation of the coverglasses [93].

4.3.4 Pioneer Venus Orbiter SA

Pioneer Venus orbiter was a spin-stabilised (5 rpm) cylindrical spacecraft that operated in a high eccentric near polar orbit around Venus for more than eight years. After two years orbiting, power drops correlated with string losses were observed depending on the vehicle rotating angle. This suggested failures on strings due to reverse bias of cells (no shunt diodes protected the strings) produced by cyclic shadows made by the magnetometer boom cast, not predicted and unavoidable for the mission success. Ground tests were not conclusive that the cyclic reverse bias operation ended in cell breakdowns. Therefore, other interactions, as the ATOX environment in the Venus upper atmosphere, could favour the SA degradation [94].

4.4 Post-flight Investigations on Returned Solar Arrays

Returned SAs from space are valuable opportunities to assess their predicted behaviour in the space environment. Few SAs have been returned to Earth and a brief summary of their investigation programmes and the major conclusions are outlined in subsequent paragraphs.

4.4.1 Hubble Space Telescope Solar Array 1

One wing of the Hubble Space Telescope SA was retrieved from space in December 1993, after more than 3.5 years operating in a low earth orbit. The SA of the Hubble Space Telescope consisted of two wings of a double roll-out concept using two flexible solar cell blankets on each wing. The 48760 Silicon BSFR solar cells should provide the required 4.4 kW after two years in operation.

The post-flight investigation programme carried out between 1994 and 1995 [95] had the following main objectives:

- Assess the effect of different LEO interaction and environments as: thermal fatigue, ATOX, meteoroid and space debris damage, contaminations, UV, etc.
- Explain the anomalies experienced in orbit.

During the investigation programme the SA was submitted to several tests like detailed visual inspections, EP and health checks, wipe testing etc. The SA mechanisms were also mechanically tested to study their deploy/retract performance and finally the SA was totally disassembled for detailed investigation of all its components.

The main conclusions of the post-flight investigation programme related to the SA blankets are the following:

- SA performance: 5% more power than predicted after 3.6 years in orbit, despite several anomalies (string shorts) that reduced the power by 6.7%.

Random failures are the main contributors to SA degradation. SA overall degradation excluding failures was less than predicted, mainly as radiation model used was pessimistic.

- Solar cell interconnectors: No fatigue effects on interconnection loops were detected as expected from pre-flight qualification data.
- Harness: Fatigue effects were evident on flexible data harnesses, but no full detachments were found.
- Adhesives for ATOX protection: Darkening due to UV could increase SA operational temperature.
- Micrometeoroids: More than 4000 impacts were detected on the SA, but none of them produced permanent short circuits. The loss factor applied in the design is in full agreement with the results of the observed degradation (1.8%).

4.4.2 EURECA

The European Retrievable Carrier (EURECA) was launched in July 1992 (500 km orbit) and completely retrieved in July 1993 by the Space Shuttle. The SA consists of two interchangeable wings of five rigid panels ($\sim$100 m^2) each providing initially 5 kW. Silicon BSFR 10 Ω cm solar cells of two sizes were used to manufacture the charge and load array networks. The solar array post flight investigation programme had the objectives of studying LEO environment effects and mainly the anomalies faced during the mission [96]. Main conclusions are depicted here:

- Failures by fatigue (inadequate bend radii in the stress relief loop) in the Wiring Collecting Panels (WCPs) were responsible for open circuits on solar cell strings. WPCs were never tested in a flight representative configuration, as it was not possible to detect in advance the weakness of this design.
- A short circuit on the load array produced current from the battery during eclipse to the solar array (no blocking diodes were placed between the SA and battery circuits). A large burn mark was found at the suspected location of the short circuit after retrieval.
- Kapton FEP (Fluorinated Ethylene-Propylene) coatings of the cable insulations were completely eroded in X-ray/UV direction.
- The exposed side of MoAg interconnectors was oxidised and eroded by ATOX.
- Adhesives for ATOX protection were also darkened (top surfaces converted to SiO_2) and all surfaces investigated showed contamination of carbon or silicone.

4.4.3 MIR Solar Array

In January 1998, a segment of the MIR solar array was retrieved by the space shuttle. The segment, composed of eight panels, spent 10.5 years in a 380 km orbit. The panel design is exclusive; a laminated sandwich of coverglass, glass cloth, silicon solar cells (11% efficiency), glass cloth and optical solar reflectors

(OSRs) [97]. Two post-flight investigation programmes have been conducted in the USA and Russia. The main conclusions are the following:

- Hot spots are the main reason for the 50% power degradation of the solar array. By-pass diodes were not installed on the panel, relying especially on solar cell screening for handling full reverse currents. High temperatures during the hot spots destroyed separate commutation bundles in the circuits of serial connected solar cells [98, 99].
- Large SiO_x contaminations were found on all exposed surfaces of the panel, due to outgassing of silicone adhesives, resulting in a total power loss of only 0.72%.
- The meteoroid and space debris impact produced less than 1% power loss.
- The temperature increase over life was 7°C, due to an increase of the emittance and decrease of the absorptance.
- Solar cells not influenced by the hot spots had only 10–15% power degradation.

Acknowledgements

To my wife, Maria Jesus, for her constant support and patience. My colleagues C. Signorini and R. Crabb (ESA-Estec) and T.J. Gomez (Spasolab) for their good advice and helpful comments about the contents of this chapter. All my colleagues at Estec, especially of the solar generator section, Spasolab and the space photovoltaic community for fruitful discussions about these subjects. I am grateful to ESA for its support and permission to publish this work.

References

[1] ISO/DIS 15387: Space Systems – Single-Junction Space Solar Cells – Measurement and Calibration Procedures.

[2] Anspaugh, B.E. et al. 2002. Results of the 2001 JPL balloon flight solar cell calibration program. *JPL Publication* 02-004.

[3] Pichetto, V. et al. 2002. Casolba calibration of solar cells using balloon flight. *Proc. 29th IEEE Photovoltaic Specialists Conf.*, New Orleans.

[4] Roussel, M. et al. 1984. Calibration de cellules solaires hors atmosphère. *Proc. 4th European Space Power Conf.*, ESA SP-210, pp. 257–264.

[5] Jenkins, P. et al. 1997. Uncertainty analysis of high altitude aircraft air mass zero solar cell calibration. *Proc. 26th IEEE Photovoltaic Specialists Conf.*, Anaheim, pp. 857–860.

[6] Suppa, E.G. 1984. Space Calibration of Solar Cells. Results of 2 shuttle flight missions. *Proc. 17th IEEE Photovoltaic Specialists Conf.*, Orlando, pp. 301–305.

[7] Landis, G.A. et al. 2001. Calibration and measurement of solar cells on the international space station: A new test facility. *Proc. 36th Intersociety Energy Conversion Conf.*, pp. 229–231.

[8] Davies, M.A.H. and Goodbody, C. 1991. The calibration of solar cells in terrestrial sunlight. *Proc. 2nd European Space Power Conf.*, ESA SP-320, pp. 583–587.

[9] Garcia-Cervantes, L. et al. 1998. Ground level sunlight calibration of space solar cells. *Proc. 5th European Space Power Conf.*, ESA SP-416, pp. 615–620.

[10] Garcia, L. et al. 2001. Uncertainty analysis for ground level sunlight calibration of space solar cells at Tenerife. *Proc. 17th European Photovoltaics Solar Energy Conf.*, Munich, pp. 2259–2262.

[11] Yiqiang, Y. et al. 1996. Calibration of AM0 reference solar cells using direct normal terrestrial sunlight. *Proc. 9th Asia/Pacific Photovoltaic Science and Engineering Conf.*

[12] Kawasaki, O. et al. 1994. Study of solar simulator method and round robin calibration plan of primary standard solar cell for space use. *Proc. 1st World Conf. on Photovoltaic Energy Conversion*, Hawaii.

[13] Metzdorf, J. et al. 1986. Absolute indoor calibration of large area solar cells. *Proc. 5th European Symp. on Photovoltaic Generators in Space*, ESA SP-267, pp. 397–402.

[14] ASTM E973M-96: Test method for determination of the spectral mismatch parameter between a Photovoltaic device and a Photovoltaic reference cell.

[15] Gras, A. et al. 2000. Terrestrial secondary calibration analysis. *Proc. 16th European Space Power Conf.*, pp. 1011–1014.

[16] Gras, A. et al. 1993. Generic test procedure for solar cell testing. *Proc. 3rd European Space Power Conf.*, ESA WPP-054, pp. 743–748.

[17] ESA PSS-01-604 Generic specification for silicon solar cells, 1988.

[18] Seaman, C.H. et al. 1980. The spectral irradiance of some solar simulators and its effect on cell measurements, *Proc. 14th IEEE Photovoltaic Specialists Conf.*, San Diego, pp. 494–499.

[19] Goodelle, G.S. et al. 1981. Simulator spectral characterization using balloon calibrated solar cells with narrow band pass filters. *Proc. 15th IEEE Photovoltaic Specialists Conf.*, Orlando, pp. 211–217.

[20] Thrum, T. et al. 2000. Characterizing state of the art solar panels – A new approach for large area testing. *Proc. 28th IEEE Photovoltaic Specialists Conf.*, Anchorage, pp. 1320–1323.

[21] Kilmer, L.C. 1995. A more accurate, higher fidelity dual source AM0 solar simulator design. *Proc. 4th European Space Power Conf.*, ESA SP-369, pp. 671–675.

[22] Sturcbecher, J.J. et al. 1994. The mini-flasher: a solar array test system. *Solar Energy Materials and Solar Cells*, Vol. 36, pp. 91–98.

[23] Lukschal, W. et al. 1989. A pulsed solar simulator for electrical performance tests of space solar cells/arrays. *Proc. 1st European Space Power Conf.*, ESA SP-294, pp. 689–693.

[24] Granata, J.E. et al. 2000. Triple-junction $GaInP_2$/GaAs/Ge solar cells, production status, qualification results and operational benefits. *Proc. 28th IEEE Photovoltaics Specialists Conf.*, Anchorage, pp. 1181–1184.

[25] Gras, A. et al. 2002. Analysis for multi-junction solar cell measurements at Spasolab. *Proc. 6th European Space Power Conf.*, ESA SP-502, pp. 577–580.

[26] Emery, K. et al. 2000. Procedures for evaluating multi-junction concentrators. *Proc. 28th IEEE Photovoltaic Specialists Conf.*, Anchorage, pp. 1126–1130.

[27] Rauschenbach, H.S. 1980. *Solar Cell Array Design Handbook*, Litton Educational Publishing.

[28] Adelhelm, R. et al. 2000. Matching of multi-junction solar cells for solar array production. *Proc. 28th IEEE Photovoltaic Specialists Conf.*, Anchorage, pp. 1336–1339.

[29] King, D.L. et al. 1997. Temperature coefficients for PV modules and arrays: Measurement methods, difficulties and results. *Proc. 26th IEEE Photovoltaic Specialists Conf.*, Anaheim, pp. 1183–1186.

[30] Adelhelm, R. et al. 1997. Temperature coefficients of tandem solar cells under appropriate spectra. *Proc. 14th European Photovoltaics Solar Energy Conf.*, Barcelona.

[31] Burger, D.R. et al. 1996. Angle of incidence corrections for GaAs/Ge solar cells with low absorptance coverglass. *Proc. 25th IEEE Photovoltaic Specialists Conf.*, Washington DC, pp. 243–246.

[32] Larue, J.C. 1979. Pulsed measurement of solar cell spectral response. *Proc. 2nd European Photovoltaic Solar Energy Conf.*, West Berlin, pp. 477–486.

[33] King, D.L. et al. 2000. New methods for measuring performance of monolithic Mj solar cells. *Proc. 28th IEEE Photovoltaic Specialists Conf.*, Anchorage, pp. 1197–1201.

[34] Rauschenbach, H.S. et al. 1972. Breakdown phenomena on reverse biased silicon solar cells. *Proc. 9th IEEE Photovoltaic Specialists Conf.*, Silver Springs, pp. 217–225.

[35] Baron, W.R. et al. 1987. GaAs solar cell reverse characteristics. *Proc. 19th IEEE Photovoltaic Specialists Conf.*, New Orleans, pp. 457–462.

[36] Schwander, D. 2002. Dynamic solar cell measurement techniques: New small signal measurement techniques. *Proc. 6th European Space Power Conf.*, ESA SP-502, pp. 603–608.

[37] Rueda, P. et al. 2002. Mj GaAs solar cell capacitance and its impact upon solar array regulators. *Proc. 6th European Space Power Conf.*, ESA SP-502, pp. 29–34.

[38] Tada, H.Y. et al. 1982. *The Solar Cell Radiation Handbook*. JPL publication 82-69.

[39] Anspaugh, B.E. 1996. *GaAs Solar Cell Radiation Handbook*. JPL publication 96-9.

[40] Marvin, D.C. 2000. Assessment of Mj solar cell performance in radiation environments. *Aerospace Report TOR-2000 (1210)-1*. The Aerospace Corporation.

[41] Walters, R.J. et al. 2000. Analysis and modelling of the radiation response of Mj space solar cells. *Proc. 28th IEEE Photovoltaic Specialists Conf.*, Anchorage, pp. 1092–1097.

[42] Crabb, R. 1973. Photon induced degradation of electron and proton irradiated silicon solar cells. *Proc. 10th IEEE Photovoltaic Specialists Conf.*, Palo Alto, pp. 396–403.

[43] Fischer, H. et al. 1973. Investigation of photon and thermal induced changes in silicon solar cells. *Proc. 10th IEEE Photovoltaic Specialists Conf.*, Palo Alto, pp. 404–411.

[44] Goodelle, G.S. et al. 1975. High vacuum UV test of improved efficiency solar cells. *Proc. 11th IEEE Photovoltaic Specialists Conf.*, Scottsdale, pp. 184–189.

[45] Meulenberg, A. et al. 1997. Evidence for enhanced UV degradation to cracked coverslides. *XV Space Photovoltaic Research and Technology*, pp. 213–218.

[46] Matcham, J. et al. 1998. Effects of simulated solar-UV radiation on solar cell efficiency and transparent cell components. *Proc. 5th European Space Power Conf.*, ESA SP-416, pp. 643–650.

[47] Gerlach, L. et al. 1985. Advanced solar generator technology for the Eureca low earth orbit. *Proc. 18th IEEE Photovoltaic Specialists Conf.*, Las Vegas, pp. 78–83.

[48] Dunnet, A. et al. 1991. Assessment of ATOX erosion of silver interconnects on Intelsat VI, F3. *Proc. 2nd European Space Power Conf.*, ESA SP-320, pp. 701–706.

[49] Banks, B.A. et al. 1985. Protection of solar array blankets from attack by low earth orbital atomic oxygen. *Proc. 18th IEEE Photovoltaic Specialists Conf.*, Las Vegas, pp. 381–386.

[50] Ruthledge, S.K. et al. 1991. Atomic oxygen effects on SiO_x coated kapton for photovoltaic arrays in low earth orbit. *Proc. 22nd IEEE Photovoltaic Specialists Conf.*, Las Vegas, pp. 1544–1547.

[51] Richard, D. 1981. A rational approach to design and test a space photovoltaic generator. *Proc. 15th IEEE Photovoltaic Specialists Conf.*, Orlando, pp. 554–559.

[52] Ley, W. 1976. DFVLR facility for thermal cycling tests on solar cells panel samples under vacuum conditions. *Proc. 12th IEEE Photovoltaic Specialists Conf.*, Baton Rouge, pp. 406–412.

[53] Larue, J.C. et al. 1978. Accelerated thermal cycling of solar array samples. *Proc. 1st European Symposium on Photovoltaic Generators in Space*, ESA SP-140, pp. 57–64.

[54] Norris Blake III, L. 1996. Lessons learned about fabrication of space solar arrays from thermal cycle failures. *Proc. 25th IEEE Photovoltaic Specialists Conf.*, Washington DC, pp. 329–332.

[55] Gerlach, L. et al. 1995. HST-SA1: Electrical performance evaluation. *Hubble Space Telescope Solar Array Workshop*, ESA WPP-77, pp. 257–264.

[56] Murray, J.F. et al. 1991. Space environment effects on a rigid panel solar array. *Proc. 22nd IEEE Photovoltaic Specialists Conf.*, Las Vegas, pp. 1540–1543.

[57] Paul, K.G. et al. 1995. Post-Flight particle impacts on HST solar cells. *Hubble Space Telescope Solar Array Workshop*, ESA WPP-77, pp. 493–500.

[58] Brandhorst, Jr., H.W. et al. 2002. Hypervelocity impact testing of stretched lens array modules. *Proc. 6th European Space Power Conf.*, ESA SP-502, pp. 585–590.

[59] Schneider E. 1986. Micrometeorite impact on solar panels. *Proc. 5th European Symposium on Photovoltaic Generators in Space*, ESA SP-267, pp. 171–174.

[60] Bogus, K. et al. 1985. Investigations and conclusions on the ECS Solar Array in orbit power anomalies. *Proc. 18th IEEE Photovoltaic Specialists Conf.*, Las Vegas, pp. 368–375.

[61] Stern, T.G. et al. 2000. Development of an electrostatically clean solar array panel. *Proc. 28th IEEE Photovoltaic Specialists Conf.*, Anchorage, pp. 1348–1351.

[62] Bogorad, A. et al. 1991. Electrostatic discharge induced degradation of solar arrays. *Proc. 22nd IEEE Photovoltaic Specialists Conf.*, Las Vegas, pp. 1531–1534.

[63] Bishop, C.J. 1970. The fundamental mechanism of humidity degradation in silver-titanium contacts. *Proc. 8th IEEE Photovoltaic Specialists Conf.*, Seattle, pp. 51–61.

[64] Iles, P.A. et al. 1985. The role of the AlGaAs window layer in GaAs heteroface solar cells. *Proc. 18th IEEE Photovoltaic Specialists Conf.*, Las Vegas, pp. 304–309.

[65] Mitsui, K. et al. 1984. A high quality AR coating for AlGaAs/GaAs solar cells. *Proc. 17th IEEE Photovoltaic Specialists Conf.*, Orlando, pp. 106–110.

[66] La Roche, G. et al. 2000. Evaluation of the flight data of the Equator-S mini-modules. *Proc. 16th European Photovoltaic Solar Energy Conf.*, Glasgow, pp. 945–950.

[67] Messenger, S.R. et al. 2000. A displacement damage dose analysis of the Comets and Equator-S space solar cell experiments. *Proc. 16th European Photovoltaic Solar Energy Conf.*, Glasgow, pp. 974–977.

[68] Curtis, H. et al. 1996. Final results from the PASP-Plus flight experiment. *Proc. 25th IEEE Photovoltaic Specialists Conf.*, Washington DC, pp. 195–198.

[69] Davis, V.A. et al. 1995. Parasitic current collection by PASP PLUS solar arrays. *XIV Space Photovoltaic Research and Technology*, NASA CP-10180, pp. 274–285.

[70] Guidice, D.A. 1995. High voltage space-plasma interactions measured on the PASP Plus test arrays. *XIV Space Photovoltaic Research and Technology*, NASA CP-10180, pp. 286–295.

[71] Imaizumi, M. et al. 2000. Flight degradation data of GaAs-on-Si solar cells mounted on highly irradiated ETS-VI. *Proc. 28th IEEE Photovoltaic Specialists Conf.*, Anchorage, pp. 1075–1078.

[72] Aburaya, T. et al. 2001. Analysis of 10 years' flight data of solar cell monitor on ETS-V. *Solar Energy Materials and Solar Cells*, Vol. 68, pp. 15–22.

[73] Flores, C. et al. 1994. Post-flight investigation of the ASGA solar cell experiment on Eureca. *Proc. 1st World Conf. on Photovoltaic Energy Conversion*, Hawaii, pp. 2076–2081.

[74] Burgess, R.M. et al. 1993. Performance analysis of $CuInSe_2$ and GaAs solar cells aboard the LIPS-III flight Boeing lightweight panel. *Proc. 23rd IEEE Photovoltaic Specialists Conf.*, Louisville, pp. 1465–1468.

[75] Woodyard, J.R. et al. 1996. Analysis of LIPS-III satellite a-Si:H alloy solar cell data. *Proc. 25th IEEE Photovoltaic Specialists Conf.*, Washington DC, pp. 263–266.

[76] Severns, J.G. et al. 1988. LIPS-III. A solar cell test bed in space. *Proc. 20th IEEE Photovoltaic Specialists Conf.*, Las Vegas, pp. 801–807.

[77] Kulms, H. et al. 1990. Results of the MBB LIPS-III experiment. *Proc. 21st IEEE Photovoltaic Specialists Conf.*, Orlando, pp. 1159–1163.

[78] Goodbody, C. et al. 1996. The UoSAT-5 solar cell experiment – Over 4 years in orbit. *Proc. 25th IEEE Photovoltaic Specialists Conf.*, Washington DC, pp. 235–238.

[79] Scheiman, D.A. et al. 2000. Mars array technology experiment (MATE). *Proc. 28th IEEE Photovoltaic Specialists Conf.*, Anchorage, pp. 1362–1365.

[80] Jain, J.K. et al. 2002. Concentrator solar array technology flight experiment. *Proc. 29th IEEE Photovoltaic Specialists Conf.*, New Orleans, pp. 1362–1365.

[81] Bogus, K. et al. 1993. Comparative evaluation of the in-orbit performance of ESA's satellite solar generators. *Proc. 3rd European Space Power Conf.*, ESA WPP-054, pp. 529–535.

[82] Rumler, P. et al. 2002. SOHO power system performance during 6 years in orbit. *Proc. 6th European Space Power Conf.*, ESA SP-502, pp. 141–146.

[83] Jalinat, A. et al. 1998. In orbit behaviour of SPOT 1,2 and 3 solar arrays. *Proc. 5th European Space Power Conf.*, ESA SP-416, pp. 627–631.

[84] Fodor, J.S. et al. 1998. In-orbit performance of Hughes HS 601 solar arrays. *Proc. 2nd World Conf. on Photovoltaic Energy Conversion*, Vienna, pp. 3530–3533.

[85] Ozkul, A. et al. 1994. In-orbit performance characteristics of Intelsat-V solar arrays. *Proc. 1st World Conf. on Photovoltaic Energy Conversion*, Hawaii, pp.1994–1997.

[86] Takata, N. et al. 1989. In-orbit performance of CS-3A spacecraft GaAs solar array. *Proc. 1st European Space Power Conf.*, ESA SP-294, pp. 823–828.

[87] Crabb, R.L. and Robben, A.P. 1993. In-flight Hipparcos solar array performance degradation after three and a half years in GTO. *Proc. 3rd European Space Power Conf.*, ESA WPP-054, pp. 541–549.

[88] Puthanveettil, S.E. et al. 1995. IRS-1A Solar array – In-orbit performance. *Proc. 4th European Space Power Conf.*, ESA SP-369, pp. 583–585.

[89] Gerlach, L. et al. 1995. Hubble Space Telescope and EURECA solar generators a summary of the post flight investigations. *Proc. 4th European Space Power Conf.*, ESA SP-369, pp. 5–20.

[90] Gelb, S.W. et al. 1991. In-orbit performance of Hughes HS 393 solar arrays. *Proc. 22nd* IEEE *Photovoltaic Specialists Conf.*, Las Vegas, pp. 1429–1433.

[91] Levy, L. et al. 1986. MARECS & ECS anomalies: Attempt for insulation defect production in kapton. *Proc. 5th European Symposium on Photovoltaic Generators in Space*, ESA SP-267, pp. 161–169.

[92] Gaddy, E.M. et al. 1997. The Rossi X-Ray timing explorer XTE solar array anomaly. *XV Space Photovoltaic Research and Technology*, pp.144–153.

[93] Marvin, D.C. et al. 1988. Anomalous solar array performance on GPS. *Proc. 20th IEEE Photovoltaic Specialists Conf.*, pp. 913–917.

[94] Goldhammer, L.J. et al. 1987. Flight performance of the Pioneer Venus orbiter solar array. *Proc. 19th IEEE Photovoltaic Specialists Conf.*, New Orleans, pp. 494–499.

[95] *Proceedings of the Hubble Space Telescope SA workshop.* ESA WPP-77, 1995.

[96] EURECA The European retrievable carrier. *Technical Report ESA* WPP-069, 1994.

[97] Pinkerton, R.J. 2001. MIR returned solar array. *Proc. 36th Intersociety Energy Conversion Conf.*, pp. 217–222.

[98] Letin, V.A. 2002. Optical, radiation and thermal cycling losses of power solar array returned from orbital station MIR after 10.5 years of operation. *Proc. 6th European Space Power Conf.*, ESA SP-502, pp. 713–718.

[99] Grabov, A.B. et al. 2002. A terrestrial investigation of material's degradation mechanisms in silicon solar cells, which returned from MIR space station after ten years exploitation. *Proc. 6th European Space Power Conf.*, ESA SP-502, pp. 733–740.

Part V

Economics, Environment and Business Strategy

V-1

Overview of Potential Hazards

Vasilis M. Fthenakis, National PV EHS Assistance Center,
Department of Environmental Sciences,
Brookhaven National Laboratory, Upton, New York, USA

1 Introduction

Photovoltaic (PV) technologies have distinct environmental advantages for generating electricity over conventional technologies. The operation of photovoltaic systems does not produce any noise, toxic-gas emissions, or greenhouse gases. Photovoltaic electricity generation, regardless of which technology is used, is a zero-emissions process.

However, as with any energy source or product, there are environmental, health and safety (EHS) hazards associated with the manufacture of solar cells. The PV industry uses toxic and flammable substances, although in smaller amounts than many other industries, and use of hazardous chemicals can involve occupational and environmental hazards. Addressing EHS concerns is the focus of numerous studies of the National Photovoltaic EHS Assistance Center at Brookhaven National Laboratory, which operates under the auspices of the US Department of Energy (DOE). More than 150 articles highlighting these studies are posted in the Center's website (http://www.pv.bnl.gov). This work has been done in cooperation with the US DOE PV Program and the US PV industry, which takes EHS issues very seriously and reacts proactively to concerns. Below is a summary of EHS issues pertaining to the manufacture of crystalline silicon (x-Si), amorphous silicon (a-Si), copper indium diselenide (CIS), copper indium gallium diselenide (CGS), gallium arsenide (GaAs) and cadmium telluride (CdTe), which are currently commercially available.

2 Overview of Hazards in PV Manufacture

In manufacturing photovoltaic cells, health may be adversely affected by different classes of chemical and physical hazards. In this chapter, discussion focuses on chemical hazards related to the materials' toxicity, corrosivity, flammability, and explosiveness. These hazards differ for different thin-film technologies and deposition processes. The main hazards associated with specific technologies are shown in Table 1. A listing of hazardous materials used in manufacturing is shown in Table 2.

Table 1 Major hazards in PV manufacturing

Module type	Types of potential hazards
x-Si	HF acid burns
	SiH_4 fires/explosions
	Pb solder/module disposal
a-Si	SiH_4 fires/explosions
CdTe	Cd toxicity, carcinogenicity, module disposal
CIS, CGS	H_2Se toxicity, module disposal
GaAs	AsH_3 toxicity, As carcinogenicity, H_2 flammability, module disposal

3 Crystalline Silicon (x-Si) Solar Cells

3.1 Occupational Health Issues

In the manufacture of wafer-based crystalline silicon solar cells, occupational health issues are related to potential chemical burns and the inhalation of fumes from hydrofluoric acid (HF), nitric acid (e.g., HNO_3) and alkalis (e.g., NaOH) used for wafer cleaning, removing dopant oxides, and reactor cleaning. Dopant gases and vapours (e.g., $POCl_3$, B_2H_3), also are hazardous if inhaled. $POCl_3$ is a liquid, but in a deposition chamber it can generate toxic P_2O_5 and Cl_2 gaseous effluents. Inhalation hazards are controlled with properly designed ventilation systems in the process stations. Other occupational hazards are related to the flammability of silane (SiH_4) and its byproducts used in silicon nitride deposition; these hazards are discussed in the a-Si section below.

3.2 Public Health and Environmental Issues

No public health issues were identified with this technology. The environmental issues are related to the generation of liquid and solid wastes during wafer slicing, cleaning, and etching, and during processing and assembling of solar cells. The x-Si PV industry has embarked upon programs of waste minimisation and examines environmentally friendlier alternatives for solders, slurries and solvents. Successful efforts were reported in laboratory and manufacturing scales in reducing the caustic waste generated by etching. Other efforts for waste minimisation include recycling stainless-steel cutting wires, recovering the SiC in the slurry, and in-house neutralisation of acid and alkali solutions. Finally, the content of Pb in solder in many of today's modules creates concerns about the disposal of modules at the end of their useful life. One x-Si manufacturer has developed and is using Pb-free solders, and has offered the technology know-how to others who are considering such a change [1].

4 Amorphous Silicon (a-Si) Solar Cells

Amorphous silicon, cadmium telluride, copper indium selenide and gallium arsenide are thin-film technologies that use about 1/100 of the photovoltaic material used on x-Si.

4.1 Occupational Safety Issues

The main safety hazard of this technology is the use of SiH_4 gas, which is extremely pyrophoric. The lower limit for its spontaneous ignition in air ranges from 2 to 3%, depending on the carrier gas. If mixing is incomplete, a pyrophoric concentration may exist locally, even if the concentration of SiH_4 in the carrier gas is less than 2%. At silane concentrations equal to or greater than 4.5%, the

Table 2 Some hazardous materials used in current PV manufacturing

Material	Source	TLV-TWA[a] (ppm)	STEL[b] (ppm)	IDLH[c] (ppm)	ERPG2[d] (ppm)	Critical effects
Arsine	GaAs CVD[e]	0.05	–	3	0.5	Blood, kidney
Arsenic compounds	GaAs	0.01 mg/m^3	–	–	–	Cancer, lung
Cadmium compounds	CdTe and CdS deposition; $CdCl_2$ treatment	0.01 mg/m^3 (dust); 0.002 mg/m^3 (fumes)	–	–	N/A	Cancer, kidney
Carbon tetrachloride	Etchant	5	10		100	Cancer, liver, greenhouse gas
Chloro-silanes	a-Si and x-Si deposition	5	–	800	–	Irritant
Copper	CIS deposition	1 mg/m^3 (dust); 0.2 mg/m^3 (fumes)	–	100 mg/m^3	–	
Diborane	a-Si dopant	0.1	–	40	1	CNS[f], pulmonary
Germane	a-Si dopant	0.2	–	–	–	Blood, CNS[f], kidney
Hydrogen	a-Si deposition	–	–	–	–	Fire hazard
Hydrogen fluoride	Etchant	–	C[g] 3	30	20	Irritant, burns, bone, teeth
Hydrogen selenide	CIS sputtering	0.05	–	1	–	Irritant, GI[h], flammable
Hydrogen sulfide	CIS sputtering	10	15	100	30	Irritant, CNS[f], flammable
Indium compounds	CIS deposition	0.1 mg/m^3	–	–	–	Pulmonary, bone, GI[h]
Lead	Soldering	0.05 mg/m^3	–	–	–	CNS[f], GI[h], blood, kidney, reproductive
Nitric acid	Wafer cleaning	2	4	25	–	Irritant, corrosive
Phosphine	a-Si dopant	0.3	1	50	0.5	Irritant, CNS[f], GI[h], flammable
Phosphorous oxychloride	x-Si dopant	0.1				Irritant, kidney
Selenium compounds	CIS deposition	0.2 mg/m^3		1 mg/m^3		Irritant
Sodium hydroxide	Wafer cleaning		C[g] 2 mg/m^3	10 mg/m^3	5 mg/m^3	Irritant

Table 2 (*continued*)

Material	Source	TLV-TWA[a] (ppm)	STEL[b] (ppm)	IDLH[c] (ppm)	ERPG2[d] (ppm)	Critical effects
Silane	a-Si deposition	5	–	–	–	Irritant, fire and explosion hazard
Silicon tetrafluoride	a-Si deposition	–				
Tellurium compounds	CIS deposition	0.1 mg/m^3				CNS[f], cyanosis, liver

[a] TLV-TWA: Threshold Limit Value, Time Weighted Average is defined by the American Conference of Governmental Industrial Hygienists (ACGIH) as the time-weighted average threshold concentration above which workers must not be exposed during work-shifts (8 h/day, 40 h/week).

[b] STEL: Threshold Limit Value, Short Term Exposure Level is defined by ACGIH as the maximum concentration to which workers can be exposed for a period up to 15 minutes, provided not more than four excursions per day are permitted with at least 60 minutes between exposure periods and provided that daily PEL is not also exceeded.

[c] IDLH: Immediately Dangerous to Life or Health Concentration is defined by the National Institute for Occupational Safety and Health (NIOSH) as the maximum concentration from which one could escape within 30 minutes without any escape-impairing symptoms or any irreversible health effects.

[d] ERPG-2: Emergency Response Planning Guideline-2 is defined by the American Industrial Hygiene Association (AIHA) as the concentration below which nearly al people could be exposed for up to one hour without irreversible or other serious health effects or symptoms that would impair their ability to take protective action.

[e] CVD: chemical vapour deposition.

[f] CNS: central nervous system.

[g] C: Threshold Limit Value-Ceiling is defined by ACGIH as the concentration that should not be exceeded during any part of the working exposure.

[h] GI: gastrointestinal.

–: not available.

mixtures were found to be metastable and ignited after a certain delay. In an accident, this event could be extremely destructive as protection provided by venting would be ineffective. Silane safety is discussed in detail elsewhere [2–5]. In addition to SiH_4, hydrogen used in a-Si manufacturing, also is flammable and explosive. Most PV manufacturers use sophisticated gas-handling systems with sufficient safety features to minimise the risks of fire and explosion. Some facilities store silane and hydrogen in bulk from tube trailers to avoid frequently changing gas cylinders. A bulk ISO (International Standards Organisation) module typically contains eight cylindrical tubes that are mounted onto a trailer suitable for over the road and ocean transport. These modules carry up to 3000 kg of silane. Another option is a single, 450 l cylinder, mounted on a skid, which contains up to 150 kg of silane (mini-bulk). These storage systems are equipped with isolation and flow restricting valves.

Bulk storage decreases the probability of an accident, since trailer changes are infrequent, well-scheduled special events that are treated in a precise well-controlled manner, under the attention of the plant's management, safety officials, the gas supplier, and local fire-department officials. On the other hand, if an accident occurs, the consequences can be much greater than one involving gas cylinders. Currently, silane is used mainly in glow discharge deposition at very low utilisation rates (e.g., 10%). To the extent that the material utilisation rate increases in the future, the potential worst consequences of an accident will be reduced.

Toxic doping gases (e.g., AsH_3, PH_3, GeH_4) are used in quantities too small to pose any significant hazards to public health or the environment. However, leakage of these gases can cause significant occupational risks, and management must show continuous vigilance to safeguard personnel. Applicable prevention options are discussed elsewhere [5]; many of these are already implemented by the US industry.

4.2 Public Health and Environmental Issues

Silane used in bulk quantities in a-Si facilities may pose hazards to the surrounding community if adequate separation zones do not exist. In the USA, the Compressed Gas Association (CGA) Guidelines specify minimum distances to places of public assembly that range from 80 to 450 ft depending on the quantity and pressure of silane in containers in use [6]. The corresponding minimum distances to the plant property lines are 50–300 ft. Prescribed separation distances are considered sufficient to protect the public under worst-condition accidents.

No environmental issues have been identified with this technology.

5 Cadmium Telluride (CdTe) Solar Cells

5.1 Occupational Health Issues

In CdTe manufacturing, the main concerns are associated with the toxicity of the feedstock materials (e.g., CdTe, CdS, $CdCl_2$). The occupational health hazards presented by Cd and Te compounds in various processing steps vary as a function

of the compound specific toxicity, its physical state, and the mode of exposure. No clinical data are available on human health effects associated with exposure to CdTe. Limited animal data comparing the acute toxicity of CdTe, CIS and CGS, showed that from the three compounds, CdTe has the highest toxicity and CGS the lowest [7]. No comparisons with the parent Cd and Te compounds have been made. Cadmium, one of CdTe precursors, is a highly hazardous material. The acute health effects from inhalation of Cd include pneumonitis, pulmonary edema, and death. However, CdTe is insoluble to water and, as such, it may be less toxic than Cd. This issue needs further investigation.

In production facilities, workers may be exposed to Cd compounds through the air they breathe, as well as by ingestion from hand-to-mouth contact. Inhalation is probably the most important pathway, because of the larger potential for exposure, and higher absorption efficiency of Cd compounds through the lung than through the gastrointestinal tract. The physical state in which the Cd compound is used and/or released to the environment is another determinant of risk. Processes in which Cd compounds are used or produced in the form of fine fumes or particles present larger hazards to health. Similarly, those involving volatile or soluble Cd compounds (e.g., $CdCl_2$) also must be more closely scrutinised. Hazards to workers may arise from feedstock preparation, fume/vapour leaks, etching of excess materials from panels, maintenance operations (e.g., scraping and cleaning), and during waste handling. Caution must be exercised when working with this material, and several layers of control must be implemented to prevent exposure of the employees. In general, the hierarchy of controls includes engineering controls, personal protective equipment, and work practices. Area and personal monitoring would provide information on the type and extent of employees' exposure, assist in identifying potential sources of exposure, and gather data on the effectiveness of the controls. The US industry is vigilant in preventing health risks, and has established proactive programs in industrial hygiene and environmental control. Workers' exposure to cadmium in PV manufacturing facilities is controlled by rigorous industrial hygiene practices, and is continuously monitored by medical tests, thus preventing health risks [8].

5.2 Public Health and Environmental Issues

No public health issues have been identified with this technology. Environmental issues are related to the disposal of manufacturing waste and end-of-life modules; these are discussed in Section 9 below.

6 Copper Indium Diselenide (CIS) Solar Cells

6.1 Occupational Health and Safety

The main processes for forming copper indium diselenide solar cells are co-evaporation of Cu, In and Se and selenisation of Cu and In layers in H_2Se

atmosphere. The toxicity of Cu, In and Se is considered mild. Little information exists on the toxicity of CIS. Animal studies have shown that CIS has mild to moderate respiratory track toxicity; in comparing CIS, CGS and CdTe, CIS was found to be less toxic than CdTe and somewhat more toxic than CGS.

The selenium TLV-TWA of 0.2 mg/m^3 as selenium were set to prevent systemic toxicity, and to minimise the potential of ocular and upper respiratory tract irritation. Interestingly, selenium is an essential element in the human diet and daily intakes of 500–860 μg of selenium are tolerated for long periods [9].

Although elemental selenium has only a mild toxicity associated with it, hydrogen selenide is highly toxic. It has an Immediately Dangerous to Life and Health (IDLH) concentration of only 1 ppm. Hydrogen selenide resembles arsine physiologically; however, its vapour pressure is lower than that of arsine and it is oxidised to the less toxic selenium on the mucous membranes of the respiratory system. Hydrogen selenide has a TLV-TWA of 0.05 ppm to prevent irritation, and prevent the onset of chronic hydrogen selenide-related disease. To prevent hazards from H_2Se, the deposition system should be enclosed under negative pressure and be exhausted through an emergency control scrubber. The same applies to the gas cabinets containing H_2Se cylinders in use.

The options for substitution, isolation, work practices, and personnel monitoring discussed for CdTe are applicable to CIS manufacturing as well. In addition, the presence of hydrogen selenide in some CIS fabrication processes requires engineering and administrative controls to safeguard workers and the public against exposure to this highly toxic gas.

6.2 Public Health and Environmental Issues

Potential public health issues are related to the use of hydrogen selenide in facilities that use hydrogen selenide as a major feedstock material. Associated hazards can be minimised by using safer alternatives, limiting inventories, using flow restricting valves and other safety options discussed in detail elsewhere [10]. Emissions of hydrogen selenide from process tools are controlled with either wet or dry scrubbing. Also, scrubbers that can control accidental releases of this gas are in place in some facilities. Environmental issues are related to the disposal of manufacturing waste and end-of-life modules; these are discussed in Section 9 below.

7 Gallium Arsenide (GaAs) High Efficiency Solar Cells

7.1 Occupational Health and Safety

MOCVD is today's most common process for fabricating III–V PV cells; it employs the highly toxic hydride gases, arsine and phosphine, as feedstocks. Similarly to silane and hydrogen selenide handling, the safe use of these hydrides requires several layers of engineering and administrative controls to safeguard workers

and the public against accidental exposure. Such requirements pose financial demands and risks that could create difficulties in scaling-up the technology to multimegawatt levels. One part of the problem is that today's use of the hydrides in MOCVD is highly ineffective. Only about 2–10% are deposited on the PV panels, as a 10–50 times excess of V to III (As to Ga) is required. Metal-organic compounds are used more effectively, with their material utilisation ranging from 20 to 50%. In scaling up to 10 MW/yr production using MOCVD, the current designs of flat-plate III–V modules will require approximately 23 metric tons of AsH_3, 0.7 tons of PH_3, 7 tons of metal organics, and 1500 tons of hydrogen. (These estimates are based on generic data applicable to the largest current MOCVD reactors (e.g., EMCORE Enterprise E400 and Aixtron AIX3000), and carry some unquantified uncertainty. Production for 24 hours a day by one of these reactors could provide about 100 kWp/year, so 100 such reactors will be needed for the 10 MW production-basis we are considering herein. Therefore, larger reactors will be needed at this scale, thereby introducing more uncertainty in our estimates.) These quantities can be effectively delivered only with tube trailers, each carrying 2–3 tons of gases. The potential consequences of a worst-case failure in one of these tube trailers could be catastrophic. On a positive note, however, it is more likely that terrestrial systems will be concentrators, not flat-plates, because the former would be less expensive to manufacture. PV cells have been shown to be capable of operation under concentrated sunlight, between 100 and 2000 times the one sun level (see Parts IId and IIId). A possible practical strength is 500× concentrators; the material requirements for producing such concentrators are 600 times less than those needed for flat plates.

The best way to minimise both the risks associated with certain chemicals and the costs of managing risk is to assess all alternatives during the first steps of developing the technology and designing the facility. These hydrides may be replaced in the future by the use of tertiary butyl arsine (TBAs) and tertiary butyl phosphine (TBP) [11]; it appears that there are no intrinsic technical barriers to growing PV-quality GaAs with TBAs and GaAsP, or $GaInP_2$ with TBP. Until substitutes are tested and implemented, however, it might be prudent to use arsine and phosphine from reduced-pressure containers, which are commercially available. Research efforts are being made in Europe [12] to replace hydrogen by inert nitrogen. Apparently, there is no inherent reason to prohibit such a substitution. However, since molecular hydrogen decomposes to some extent, and atoms participate in the gas-phase chemistry, the PV research community is challenged with learning how to optimise III–V growth conditions with nitrogen.

8 Operation of PV Modules

The operation of PV systems does not produce any emissions. Although tiny amounts of semiconductor materials are imbedded in the module (e.g., 7 g/m^2 for thin-film technologies), toxic compounds cannot cause any adverse health

effects unless they enter the human body in harmful doses. The only pathways by which people might be exposed to PV compounds from a finished module are by accidentally ingesting flakes or dust particles, or inhaling dust and fumes. The photovoltaic material layers are stable and solid, and are encapsulated between thick layers of glass or plastic. Unless the module is ground to a fine dust, dust particles cannot be generated. All the photovoltaic materials examined herein have a zero vapour pressure at ambient conditions. Therefore, it is impossible for any vapours or dust to be generated during normal use of PV modules.

The potential exists for exposure to toxic vapours via inhalation if the modules are consumed in residential fires and people breath the smoke from the fire [13]. However, common US residential fires are not likely to vaporise CdTe and GaAs layers; flame temperatures in roof fires are in the range 800–900°C range. The melting point of CdTe is 1041°C, and evaporation occurs at 1050°C in open air and at about 900°C under non-oxidising conditions. Sublimation occurs at lower temperatures, but the vapour pressure of CdTe at 800°C is only 2.5 torr (0.003 atm). The melting point of CdS is 1750°C and of GaAs is 1238°C. CIS starts evaporating at 600°C, and a 20% weight loss was measured at 1000°C [14].

The potential for significant photovoltaic material emissions may exist only in large externally fed industrial fires. In any case, the fire itself probably would pose a much greater hazard than any potential emissions of photovoltaic materials.

9 Photovoltaic Module Decommissioning

PV modules will have to be decommissioned at the end of their useful life, 20–30 years after their initial installation. In decommissioning these devices, the principal concern will be associated with the presence of Cd in CdTe and CdS solar films and the presence of Pb in x-Si modules if they contain Pb-based solder. If these modules end in a municipal waste incinerator (MWI), the heavy metals will gasify and a fraction of those will be released in the atmosphere. If the MWI is equipped with electrostatic precipitator (ESP) this fraction can be as small as 0.5% with the balance of the heavy metals remaining in the ash. The ash itself will have to be disposed of in controlled landfills.

If the modules end in municipal landfills, then the potential for the heavy metals to leach out in the soil exist. The leachability of metals in landfills, is currently characterised by two elution tests: the US Environmental Protection Agency (EPA) Toxicity Characterisation Leachate Profile (TCLP), and the German DEV S4 (Deutsches Einheitsverfahren). In these tests, small pieces (< 1 cm^2) of broken modules are suspended and rotated in an elutent for 24 hours. The metals present in the elutent are then measured and compared with limits prescribed by each testing protocol. If the metal concentration exceeds the limits, the modules are demonstrating the metal's leachability and may need to be recycled or disposed of in a hazardous waste landfill; if the metals are not leaching in excessive quantities the modules can be disposed of in a

commercial landfill. Some early CdTe modules have failed the TCLP and the DEV tests [15]. However, the Apollo CdTe modules produced by BP Solar were reportedly passing the TCLP. In exploratory tests with a small number of commercial x-Si modules, some modules failed the TCLP limit for Pb by about 30% [16]. Exploratory tests on CIS modules showed that they pass the test for Se. No tests are reported for GaAs modules. The a-Si modules contain very little hazardous material and easily pass the test. It should be noted that the TCLP test is conservative, as it requires breakage of the whole module to very small pieces, whereas the photovoltaic layer will often be sandwiched between two layers of glass and reasonably isolated from the environment.

The ultimate solution to the PV waste and end-of-life management is recycling of useful materials. Recent studies showed that recycling, based on current collection/recycling infrastructure and on emerging recycling technologies, is technologically and economically feasible [17]. Reclaiming metals from used solar panels in large centralised applications can be done in metal smelting/refining facilities which use the glass as a fluxing agent and recover most of the metals by incorporating them in their product streams. In dispersed operations, small quantities and high transportation costs make this option relatively expensive. Research supported by the US DOE developed technologies for hydro-metallurgical separation that may be used in both small-scale (in-house) and large-scale recycling. These options are being investigated by the photovoltaic industry as part of their proactive long-term environmental strategy to preserve the environmental friendliness of solar cells.

10 Conclusion

The manufacture of photovoltaic modules uses some hazardous materials which can present health and safety hazards, if adequate precautions are not taken. Routine conditions in manufacturing facilities should not pose any threats to health and the environment. Hazardous materials could adversely affect occupational health and, in some instances, public health during accidents. Such hazards arise primarily from the toxicity and explosiveness of specific gases. Accidental releases of hazardous gases and vapours can be prevented through choosing safer technologies, processes, and materials, better use of materials, and by employee training and safety procedures. As the PV industry vigilantly and systematically approaches these issues and mitigation strategies, the risk to the industry, the workers, and the public will be minimised.

References

[1] Fthenakis, V. and Gonsiorawski, R., 1999. Lead-free solder technology from ASE Americas, *Workshop Report BNL-67536*, 19 October 1999, Brookhaven National Laboratory, Upton, NY 11973.

[2] Fthenakis, V.M. and Moskowitz, P.D., 1990. An assessment of silane hazards. *Solid State Technology*, January, pp. 81–85.

[3] Britton, L., 1991. Improve your handling of silane. *Semiconductor International*, April.

[4] Tamanini, F., Chaffee, J.L. and Jambar, R.L., 1998. Reactivity and ignition characteristics of silane/air mixtures. *Process Safety Progress*, Vol. 17(4), pp. 243–258.

[5] Moskowitz, P.D. and Fthenakis, V.M., 1991. A checklist of safe practices for the storage, distribution, use and disposal of toxic and hazardous gases in photovoltaic cell manufacturing, *Solar Cells*, Vol. 31, pp. 513–525.

[6] CGA P-31-2000, *Safe storage and handling of silane and silane mixtures*, first edition, Compressed Gas Association, Inc., Arlington, VA, 2000.

[7] Fthenakis, V., Morris, S., Moskowitz, P. and Morgan, D., 1999. Toxicity of cadmium telluride, copper indium diselenide, and copper gallium diselenide. *Progress in Photovoltaics*, Vol. 7, pp. 489–497.

[8] Bohland, J. and Smigielski, K., 2000. First Solar's CdTe module manufacturing experience; environmental, health and safety results. *Proc. 28th IEEE Photovoltaic Specialists Conf.*, Anchorage, AK, USA.

[9] Piscator, M., 1989. The essentiality and toxicity of selenium. *Proceedings of the 4th International Symposium on Uses of Selenium and Tellurium*. Careapella, Jr., S.C., Ed.

[10] Fthenakis, V., 2001. Multi-layer protection analysis for photovoltaic manufacturing. *Process Safety Progress*, Vol. 20(2), pp. 1–8.

[11] Komeno, J., 1994. Metalorganic vapor phase epitaxy using organic group V precursors. *Journal of Crystal Growth*, Vol. 145(1–4), pp. 468–472.

[12] Juelich, 2001, MOVPE at Juelich Research Center, Website http://www.fz-juelich.de/isg/movpe/emovpe1.html.

[13] Moskowitz, P.D. and Fthenakis, V.M., 1990. Toxic materials released from photovoltaic modules during fires: Health Risks. *Solar Cells*, Vol. 29, pp. 63–71.

[14] Steinberger, H., 1997. HSE for CdTe and CIS thin film module operation, IEA expert workshop Environmental aspects of PV power systems, Report No. 97072, Niewlaar E. and Alsema, E., Ed., Utrecht University, The Netherlands.

[15] Fthenakis, V., Eberspacher, C. and Moskowitz, P., 1996. Recycling strategies to enhance the commercial viability of photovoltaics *Progress in Photovoltaics*, Vol. 4, pp. 447–456.

[16] Eberspacher, C., 1998. Disposal and recycling of end-of-life CdTe and Si PV modules, Report prepared for Brookhaven National Laboratory, February 1998.

[17] Fthenakis, V.M., 2000. End-of-life management and recycling of PV modules. *Energy Policy*, Vol. 28, pp. 1051–1058.

V-2

Energy Pay-Back Time and CO_2 Emissions of PV Systems

Erik Alsema, Department of Science, Technology and Society, Copernicus Institute for Sustainable Development and Innovation, Utrecht University, The Netherlands

1 Introduction

Photovoltaic energy conversion is widely considered as one of the more promising renewable energy technologies. It has the potential to contribute significantly to a sustainable energy supplies and it may help to mitigate greenhouse gas emissions. For this reason there is a growing support from governments for photovoltaic R&D programmes and market introduction schemes. In order to fulfil these promises PV technology has to meet two requirements: (1) PV energy generation should have an acceptable *cost/performance ratio* and (2) the *net energy yield* for PV systems should be (much) larger than zero. By a positive energy yield we mean that the energy *output* during the lifetime of the PV system must be larger than the energy *input* during the systems life cycle, i.e. for manufacturing of the components and for the installation, maintenance and decommissioning of the PV system. Of course evaluations of the CO_2 mitigation potential of PV technology should be based on expected *net* energy yields. In practice this is seldom done, leading to over-optimistic results for the CO_2 mitigation potential.

In our view, every new energy technology that is promoted as being 'renewable' or 'sustainable' should be subjected to an analysis of its energy balance in order to calculate the net energy yield. It is of great importance that such an energy analysis is not only based on data for present-generation systems but also considers expected improvements in production and energy system technology. Since energy consumption generally has significant environmental implications, the energy analysis may be considered as a first step towards a more comprehensive environmental Life Cycle Assessment (LCA) [1, 2]. Furthermore energy analysis results provide a good indication of the CO_2 mitigation potential of the considered energy technology.

Our objective in this paper is to present estimates of the energy requirements for manufacturing of PV systems and to evaluate the energy balance for a few representative examples of PV system applications. We will also investigate the effects of future enhancements in PV production technology and PV system technology in order to assess the long-term prospects of PV technology as a candidate for a sustainable energy supply and for CO_2 mitigation. We will consider mainly grid-connected PV systems, because these systems have in our view the largest potential in terms of long-term, global energy supply and CO_2 mitigation. With respect to standalone PV systems the energy balance depends very much on the specific application. Therefore, we restrict our discussion to one important type of standalone system, namely 'Solar Home Systems'.

We will begin with a brief discussion on energy analysis methodology and some general assumptions (Section 2). Then we discuss the energy requirements for the components of PV systems (Section 3). In Section 4 we present the energy balance for grid-connected PV systems, followed by an outlook for future PV systems in Section 5. In Section 6, the potential for CO_2 mitigation using PV systems will be assessed. We finish with our conclusions (Section 7).

2 Energy Analysis Methodology

In an energy analysis, a comprehensive account is given of the energy inputs and outputs involved in products or services. The overall energy performance of such products and services is determined by accounting all energy flows in the life cycle (from resource extraction through manufacturing, product use until end-of-life decommissioning). In the case of solar cells, the gross energy requirement E_{in} is determined by adding together the energy input during resource winning, production, installation, operation and decommissioning[1] of the solar cell panels and the other system components. The energy pay-back time (EPBT) can now be calculated by dividing the gross energy requirement E_{in} by the annual energy output E_{out}. The energy payback time indicates how long it takes before energy investments are compensated by energy yields. A more comprehensive discussion of the methodological aspects can found in [3] and [4].

Two important points must be noted regarding the units that we use:

- *Energy units*: Following the conventions within the disciplines of energy analysis and LCA we present all energy data in terms of the *equivalent primary energy*, so for example, inputs of electricity are calculated back to the extraction of primary energy carriers. The conversion efficiency for the electricity supply system is an often used average value, assumed here to be 0.35. This same efficiency is also used to calculate the primary energy equivalent of the electricity produced by the PV system.
- *Module energy data per m^2*: We present the energy requirements of PV modules in megajoules per square meter module area. The reason is that the energy requirements for module production are generally area dependent and not power dependent. Only after we have established the area-related energy data, we will factor in the power output per square meter module area in order to obtain the module energy requirements per Wp. As a third step, system performance and irradiation assumptions can be taken into account to evaluate the energy balance on a system level. Also some of the BOS components (e.g. supports) will be assessed on m^2 basis.

3 Energy Requirements of PV Systems

3.1 General

Over the past decade, a number of detailed studies on the energy requirements for PV modules or systems have been published [5–11]. We have reviewed and compared these and other studies and tried to establish on which data there is more or less consensus and how observed differences may be explained. Based on

[1] In our case, end-of-life energy flows, e.g. for module recycling, are not counted because of uncertainties and lack of data.

this review of available data we have established a best estimate of the energy requirement of multicrystalline silicon modules, thin film modules and other system components [4, 12, 13]. Here we will present only the main results of these analyses; for a more detailed breakdown of the solar cell production process the reader is referred to the aforementioned publications. Also the reasons for the relatively high uncertainty (~40%) in the estimates can be found there. A recent paper gives an analysis of monocrystalline silicon and CIS modules based on actual measured data at the Siemens plant [14]. The data from this paper have not been included in our earlier review study, but seem to match reasonably with our estimates below.

3.2 Crystalline Silicon Modules

First we will discuss crystalline silicon module technology, which is presently the dominant technology in the market. The production process for crystalline silicon modules is discussed in detail in Chapters IIa-1 and -2. Silicon is produced from silica (SiO_2) which is mined as quartz sand. Reduction of silica in large arc furnaces yields *metallurgical-grade silicon*, which has to be purified further to *electronic-grade silicon* before it is suitable for manufacturing of electronic components such as integrated circuits or solar cells. Moreover, both the electronics industry and the PV industry use silicon in a (mono)crystalline form. Therefore, the silicon is molten and subsequently crystallised under carefully controlled conditions so that large blocks or *ingots* of monocrystalline material are obtained. The use by the PV industry of off-spec material which is rejected by the electronics industry, raises questions about a fair allocation of energy consumption between the two end-products [15]. The ingots are sawn into smaller blocks and then into thin *wafers*. Typical wafers are 0.3 mm thick and 100–200 cm^2 in area. After processing the wafers into solar cells they are laid out into a matrix of for example 9 × 4 cells, interconnected and *encapsulated* between a glass front plate, an EVA lamination foil and a back cover foil.

In Table 1 we show the energy requirements for a typical module based on multicrystalline silicon. We can see that the silicon winning and purification process is the major energy consumer and responsible for about half of the modules energy requirement. The reason for this is that the purification is performed by a highly energy-intensive process and the purity criteria are laid down by the electronics industry, which consumes about 90% of the electronic-grade silicon. Although solar cell production would also be possible with more relaxed purity standards, dedicated purification of solar-grade silicon has up to now not been commercially feasible because of the relatively small demand for this type of silicon material [16].

The production of the silicon wafer from the electronic-grade silicon also has a significant contribution to the energy consumption, mainly because 60% of the material is lost during the formation of the multicrystalline silicon ingots and the sawing of these ingots into wafers [10]. Altogether the production of the silicon wafers requires about 3200 MJ/m^2 module area, which is about 60% of the total energy requirement for the module.

Table 1 Breakdown of the energy requirements for a typical multicrystalline silicon PV module using present-day production technology (in MJ of primary energy per m^2 module area).

Process	Energy requirements (MJ_{prim}/m^2 module)
Silicon winning and purification	2200
Silicon wafer production	1000
Cell/module processing	300
Module encapsulation materials	200
Overhead operations and equipment manufacture	500
Total module without frame)	**4200**
Module frame (aluminium)	400
Total module (framed)	**4600**

The energy requirements for cell and module processing are more modest (300 MJ/m^2) as are the energy requirements for the front cover glass, the lamination foil and the back cover foil (200 MJ/m^2). A typical aluminium frame around the module may add an extra 400 MJ/m^2, but frame materials and dimensions can vary considerably. In fact, frameless modules are also available on the market.

Also, note the relatively high energy use for overhead operations (climatisation of production facility, lighting, compressed air, etc.) and for the manufacturing of the production equipment itself (together 500 MJ/m^2). The latter is due to relatively high capital costs of solar cell manufacturing plants [17], costs which also formed the basis for our energy input estimate (cf. [4]).

Based on a conversion efficiency of 13%, we have a power output of 130 Wp/m^2 from the module, so the energy requirements of present-day mc-Si modules can be evaluated as about 32 MJ/Wp without frame and 35 MJ/m^2 with an aluminium frame.

For *mono*crystalline silicon wafers the more elaborate crystallisation process increases the energy requirements, according to our estimate with an additional 1500 MJ/m^2 [12]. However, the recent energy analysis for the Siemens monocrystalline silicon modules [14] differs from our estimates on some points. On the one hand, the silicon requirement is lower than we assumed, on the other hand processing energy in crystallisation *and* in cell and module manufacturing is considerably higher than we estimated. For one thing the overhead energy consumption in this US plant seems to be considerable[2]. Overall, the Siemens estimate for a mono-Si module with frame is 6900 MJ/m^2 (5600 kWhe/kWp), which is about 12% higher than our estimate.

3.3 Thin-Film Modules

Regarding thin-film modules, a number of contending cell types and production technologies exists and as yet it is not clear which one of these will be the leading

[2] Further comparison with, for example, European plants should show whether these data are representative for other plants, too.

technology in 10–20 years. The production technology for thin-film modules differs significantly from that for crystalline silicon modules. In general, thin film modules are made by depositing a thin (0.5–10 μm) layer of semiconductor material on a substrate (usually a glass plate). The thin-film deposition can be performed with variety of different techniques, among which are chemical vapour deposition, evaporation, electrolytic deposition and chemical bath deposition. Depending on the selected deposition technique the material properties, material utilisation rate and the energy consumption for the deposition process will vary. Processes employing elevated temperatures and/or vacuum conditions will generally have a greater energy consumption per m^2 processed substrate area. Contact layers are also deposited with chemical vapour deposition (transparent contacts) and evaporation (back contacts). The module is finally encapsulated with a second glass plate or with a polymer film. The module may be left frameless or it may be equipped with an aluminium or polymer frame.

Today, amorphous silicon (a-Si) is the leading technology in the market and Table 2 shows the break-down of energy requirements for this type of module, again expressed as MJ_{prim} per m^2 module area [4].

Table 2 shows that the material for the actual solar cell requires relatively little energy. This is, of course, because of the small cell thickness in amorphous silicon and other thin film technologies. For the rest, the energy requirements are divided about equally between module materials, processing, overhead operations and equipment manufacturing and, finally, the aluminium frame. Again, frame materials and dimensions may differ greatly between manufacturers. Polyurethane frames for example require much less energy. In this case the module encapsulation was assumed to comprise *two* glass plates because this is most common in present-day thin film technology. Switching to polymer back covers, like in crystalline silicon technology, may reduce the energy requirement by some 150 MJ/m^2. However, in the case of toxic solar cell materials such as CdTe or $CuInSe_2$ [18] this would be less desirable [19]. Assuming a conversion efficiency of 7% we arrive at an energy requirement for present amorphous silicon modules of 17 MJ/Wp without frame and 23 MJ/Wp including an aluminium frame.

Table 2 Breakdown of the energy requirement of an amorphous silicon thin film module using present-day production technology (glass-glass encapsulation; in MJ of primary energy).

Process	Energy requirements (MJ_{prim}/m^2 module)
Cell material	50
Module encapsulation material	350
Cell/module processing	400
Overhead operations and equipment manufacture	400
Total module (frameless)	**1200**
Module frame (aluminium)	400
Total module (framed)	**1600**

For other thin-film technologies (e.g. CdTe, $CuInSe_2$, organic cell), the energy requirements for processing may be different, depending on the type of deposition processes that are used to lay down the cell materials. For CIS production at Siemens [14] the energy requirement for a module is about 2300 MJ/m^2 without frame and 2870 MJ/m^2 with frame (3070 kWhe/kWp)[3]. Here again the overhead energy use seems to be considerable (about 600 MJ/m^2). Regarding CdTe modules a Japanese study suggests a fairly high processing energy for a specific CdTe deposition process [20].

Furthermore, overhead operations for specific thin films may require more energy, for example, when more extensive waste treatment is required (cadmium recovery). Nonetheless, we expect that the energy requirement of most thin film modules produced at commercial scale will fall within a range of 1000–2000 MJ/m^2, excluding the frame. Because of the smaller module sizes and the lower efficiency the energy requirements for the frame will generally be higher than for crystalline silicon modules.

3.4 Other PV System Components

The requirements for the Balance-of-System, that is all PV system components apart from the modules, will depend largely on the desired application. In grid-connected PV systems, an inverter, cables and some module support materials will be needed. In autonomous systems a battery for energy storage will be required. The energy requirements for the inverter and cabling are estimated at about 1.6 MJ/Wp, of which about 50% is for the electronic components. The energy for array supports can vary widely. In a recent study of Dutch roof installation systems we found values from 240 MJ/m^2, for a support structure based on lightweight, aluminium profiles on slanted roofs, up to 350 MJ/m^2 for a flat-roof system employing plastic support consoles [21][4]. An analysis by Frankl [6] of PV systems on rooftops and building facades in Italy found a total energy requirement around 700 MJ/m^2 for all BOS components (support, cabling and inverter). In the same study, the 3.3 MWp ground-mounted system in Serre, Italy, was analysed too and it was found to require significantly more materials and thus energy, namely 1850 MJ/m^2.

For autonomous PV systems, the storage battery is a very important component, not only with respect to the costs but also in terms of energy requirements. In our LCA study on Solar Home Systems [22], the primary energy requirements for the life cycle of a standard lead-acid starter battery of 100 Ah was estimated at 1100 MJ, *assuming an optimistic 90% recycling rate for scrap batteries*[5]. Unfortunately, the lifetime of starter batteries in Solar Home Systems is quite short: we assumed three years. This means that over a 20-year system lifetime we need 6.7 battery sets, requiring 7300 MJ of primary energy per Ah

[3] Note that the data was scaled up from 'pre-pilot' scale to commercial scale production.

[4] Notice the difference in units: the energy requirements for converter and cabling are expressed per watt, while material and thus energy requirements for array supports are related to the module area.

[5] At 0% recycling the energy requirement of the battery increases to 1900 MJ.

battery capacity. Other BOS components like cables and charge controllers contribute relatively little to the energy requirement of a Solar Home System ($< 10\%$).

4 Energy Balance of PV Systems

We will now look at the energy output of a typical PV system and evaluate the Energy Pay-Back Time. First, we will consider two types of grid-connected PV systems, namely a rooftop system and a large, ground-mounted system, and different two module technologies. We further assume a system Performance Ratio of 0.75, which is fairly representative for well-designed PV systems today [23]. As before the conversion efficiency of the conventional electricity supply system is set at 35%, so that 1 kWh of generated PV electricity will save 10.3 MJ of primary energy.

Finally we distinguish three irradiation levels (see Part I):

- high irradiation (2200 kWh/m^2/yr), as found in the south-western USA and Sahara;
- medium irradiation (1700 kWh/m^2/yr), as found in large parts of the USA and southern Europe; and
- low irradiation (1100 kWh/m^2/yr), as found in central Europe (Germany).

Given these assumptions we evaluate EPBT as the ratio of the total energy input during the system life cycle and the yearly energy generation during system operation (see Figure 1).

Figure 1 shows that the EPBT for present-day grid-connected systems is 2–3 years in a sunny climate and increases to 4–6 years (or more) under less favourable conditions. Also note that the contribution from the BOS[6] and the module frames is significant, especially for the ground-mounted systems. Regarding thin film technology, we can see that, due to their lower efficiency, the energetic advantages of present a-Si modules are partially cancelled by the higher energy requirements for frames and supports. An Energy Pay-Back Time of 2–6 years may seem rather long, but in view of the expected life time of PV systems of 25–30 years there is still a significant net production of energy.

For Solar Home Systems the concept of energy pay-back time is more ambiguous and also less interesting, because the SHS is not primarily installed for the energy it produces but rather for the service that it provides (e.g. lighting). The choice of the displaced service supply system (e.g. kerosene lamps) has a huge effect on the resulting EPBT value. Moreover, the quality of the two supply systems can be quite different, for example the light output of the kerosene lamps is much lower than for fluorescent lights and also their health effects should not be ignored. In [22] we have shown that the EPBT of an SHS in comparison with

[6] We assumed that the inverter life time was half that of the other components, so two inverters are needed over a system life cycle.

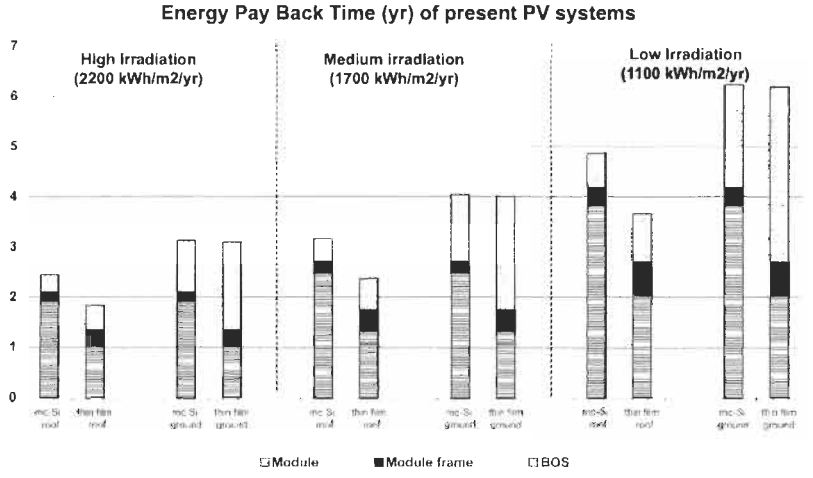

Figure 1 The Energy Pay-Back Time (in years) for present-day PV applications. Two different module technologies (multicrystalline silicon and thin-film amorphous silicon) and two types of installation (ground-mounted and roof-integrated) are distinguished.

kerosene lamps may vary between 0.8 and 2 years, depending on SHS lay-out and battery recycling rates. However, in comparison with a diesel generator set the SHS can have an EPBT of 12–20 years. Note that these results are mainly determined by the batteries with their high energy requirement and short life time.

A first conclusion from these energy balance considerations can be that grid-connected PV systems already have a significant potential for reducing fossil energy consumption, although it may take a few years of system operation before these savings can actually be cashed in. Autonomous PV systems may save on fossil energy if they replace very inefficient appliances, but they should be valued primarily for the quality of their services and less as an option to save on fossil energy.

Despite the fact that present-day, grid-connected PV systems have a clear energy-saving potential, it would very helpful if their energy balance could be improved further. Otherwise, PV technology may be considered as a less attractive option in comparison with other renewable or energy-saving technologies. Therefore, we will investigate in the next section what prospects exist for a further reduction of the energy requirements of PV.

5 Outlook for Future PV Systems

In this section we will investigate which improvements in photovoltaic technology may contribute to an improvement of the energy balance of PV systems. The general themes that will be discussed are: material efficiency, energy efficiency, new processes, and enhanced module performance. First, we will look at crystalline silicon technology. Reduction options specifically for Siemens monocrystalline silicon modules are also discussed in [24].

5.1 Crystalline Silicon Modules

We have seen that in crystalline silicon technology the silicon wafer forms the major contributor to the energy requirements of the module. This offers three avenues for reduction of energy inputs, as given below in decreasing order of probability.

1. Reduced wafer thickness. This possibility is already explored by the PV industry as it offers significant cost advantages. Wafer thickness reductions from the present-day 300–350 μm down to 200 μm or even 150 μm seem possible, so that the silicon requirements can decrease by 30–40% (wafer sawing losses will increase slightly).
2. Other wafer production methods. When blocks of crystalline silicon are sawed into thin wafers about 50% of the material is lost. Furthermore, some 40% is lost in the preceding process of block casting, so only 30% of the electronic-grade silicon ends up in the wafer. As there are only limited possibilities for reduction of the sawing losses, novel methods to produce wafers directly from molten silicon or from silicon powder have been investigated since the 1970s. The first approach is now in use in at least one commercial production line (Edge-Defined Film Growth). If such direct wafer production processes become widely employed they may lead to significant reductions in silicon requirements, possibly of the order of 40–60%.
3. Other sources for high-purity silicon feedstock. Table 2 shows us that the high-purity silicon used for solar cells is a very energy-intensive material (~1100 MJ/kg[7]). Presently, the PV industry relies fully on silicon which is rejected by the electronics industry because of insufficient quality (off-spec material). With the continued growth of the PV market the supply of off-spec silicon will soon become insufficient so that other feedstock sources will have to be developed [16]. Because standard electronic-grade silicon is too expensive for PV applications, dedicated silicon purification routes will be needed. Not much is known about the energy requirements of such solar-grade silicon processes, but it seems likely that they are lower than that of the standard process produced to the specifications of the electronics industry.

Regarding the actual cell and module production we can expect additional energy reductions from:

1. using frameless modules;
2. scaling up of production plants, resulting in more efficient processing, lower overhead, less equipment energy.

[7] Under our assumptions 2 kg of Si feedstock is needed per m^2 module with the present-day technology.

Summarising, we expect that future multicrystalline silicon production technology may achieve a reduction in energy requirements to around 2600 MJ/m^2, assuming innovations like a dedicated silicon feedstock production for PV applications, improved casting methods and reduced silicon requirements [6, 8, 11]. This kind of technology will probably become available in the next ten years. If we further assume a future module efficiency of 15% (cf. Table 3), we obtain energy requirements of 17 MJ/Wp for multicrystalline Si technology around 2010. Modules based on *mono*crystalline silicon modules will probably remain somewhat more energy-intensive, at 20 MJ/Wp [6, 15, 24].

When we look at the situation beyond 2010, then it seems difficult to achieve major energy reductions for wafer-based silicon technology. An energy-efficiency improvement in the production process of 1% per year, as is often found for established production technologies [25], seems therefore a reasonable assumption. Further improvements in the energy requirement per Wp will have to be achieved by improving module efficiency (while not increasing energy consumption). If we assume that in 2020 the efficiency of commercial mc-Si cells has been increased to 20% (the current record for small-area mc-Si cells), then module efficiency would be about 17% and thus the lowest conceivable energy requirement for Si wafer technology might be 13 MJ/Wp.

5.2 Thin-Film Modules

Because the encapsulation materials and the processing are the main contributors to the energy input, the prospects for future reduction of the energy requirement are less clearly identifiable as was the case with c-Si technology. A modest reduction, in the range 10–20%, may be expected in the production of glass and other encapsulation materials. It is doubtful whether displacement of the glass cover by a transparent polymer will lead to a lower energy requirement.

Other, existing trends which may contribute to a lower energy requirement are:

1. frameless modules;
2. thinner cells with a reduced processing time and thus a reduction in the processing energy and in the energy for equipment manufacturing;
3. an increase of production scale, leading to lower processing energy, lower equipment energy and lower overhead energy.

By these improvements we expect the energy requirement of thin film modules to decrease by some 30%, to 900 MJ/m^2, in the next ten years [5, 8, 24]. If,

Table 3. Assumptions for module efficiency development for different cell technologies (%).

	2000	2010	2020
Multicrystalline silicon	13	15	17
Thin film	7	10	15

concurrently, the module efficiency can be increased to 10%, the energy requirement on a Wp basis may reach the 9 MJ level for frameless modules.

If we try to make projections beyond 2010, we can note that further reductions in the energy requirement below 900 MJ/m^2 do not seem very probable. Like before, we assume a generic 1% per year energy-efficiency improvement in the production process. Only if completely novel module encapsulation techniques are developed, which require much less energy-intensive material, we may obtain a more significant improvement. Furthermore, new methods for cell deposition, which require less processing and less overhead operations, might help to reduce the energy input of thin-film modules. Of course, module efficiency increases will directly improve the energy input per Wp (if energy input per m^2 is constant). In this respect, significant variations may occur between different types of thin films. Moreover, significant efficiency improvements for thin film technology may be achievable. For instance, if we assume a 15% module efficiency for 2020, the energy requirement per Wp may come down to 5–6 MJ.

5.3 Other System Components

We expect that for most Balance-of-System components, there is only a limited scope for reduction of the energy requirements. The values that we have given above for roof-integrated and ground-mounted systems are representative of state-of-the art, well-designed installations that cannot be improved much unless revolutionary new concepts are introduced. We will, therefore, only assume a general 1% yearly improvement in the energy efficiency of the production processes, similar to other common materials [25]. Table 4 summarises our expectations for BOS components and for module frames.

5.4 Energy Pay-Back Time of Future Systems

With the estimates given above on the future energy requirements of modules and Balance-of-System components and using the assumptions on module efficiency developments, we can determine the expected Energy Pay-Back Time for these future technologies. In Figure 2 these results are given using the same assumptions on system performance ratio and electricity supply efficiency as before, but for only one irradiation level (1700 kWh/m^2/yr). The data for the present situation are also depicted.

Table 4. Energy requirements for Balance-of-System components and module frame [6, 21].

	Unit	2000	2010	2020
Module frame (Al)	MJ/m^2	400	0	0
Array support – central plant	MJ/m^2	1800	1700	1500
Array support – roof integrated	MJ/m^2	300	270	250
Inverter (2.5 kW)	MJ/W	1.6	1.4	1.2
Battery, lead–acid	MJ/Ah	11	10	9

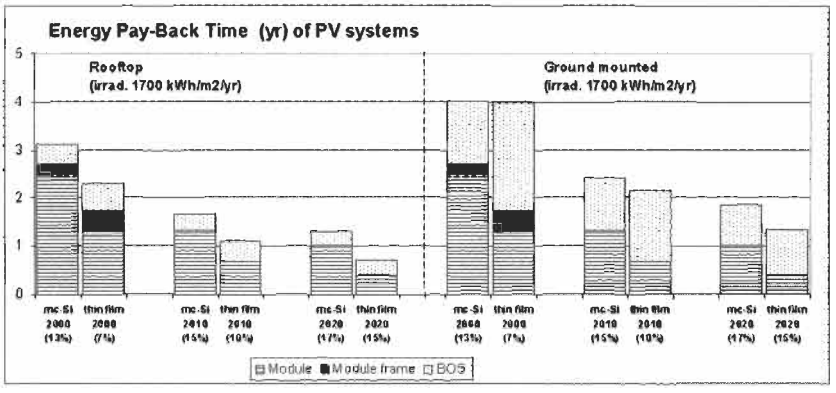

Figure 2 The Energy-Pay Back Time (in years) for two representative PV applications, both for present-day and for future (2010 and 2020) technology. The figures in parentheses denote the assumed module efficiencies for each option. Note that actual pay-back times will vary with irradiation and system performance.

We can see that according to our energy input estimates and based on our efficiency assumptions, the EPBT values of future PV technology could improve significantly to less than 1.5 years for rooftop systems and less than 2 years for ground-mounted systems. We also see that thin film modules may gain a significant advantage over c-Si technology when considering rooftop applications, *if the module efficiency can be increased to 10% or higher*. Furthermore, it is quite clear that rooftop installations have a much better potential for low Energy Pay-Back Times than ground-mounted installations.

We conclude that we see good possibilities for future developments in PV technology that result in decreasing energy requirements in component production and thus lead to an increasingly higher potential for fossil energy displacement.

6 CO_2 Emissions

Firstly we note that for PV systems, the Energy Pay-Back Time is also a quite good indicator of the CO_2 mitigation potential because generally more than 90% of the greenhouse gas emissions during the PV system life cycle are caused by energy use [26]. Emissions *not* related to energy use are only found in steel and aluminium production (for the supports and frames) and in silica reduction (for *silicon* solar cells).

To obtain the CO_2 emissions due to the production of a PV system we have to multiply all energy and material inputs with their corresponding CO_2 emission factors. This requires a detailed *life cycle assessment* of greenhouse gas emissions from solar cell manufacturing (and other life cycle stages) and from the life cycle of Balance-of-System materials. Such an analysis goes beyond the scope of this chapter. Here we will make a rough estimate of CO_2 emissions by: (1) considering only energy-related CO_2 emissions during module

production[8], (2) by evaluating all energy inputs in module production as electrical energy[9] and (3) considering only the aluminium supports employed in roof-integrated systems for the Balance-of-System components. We estimate the overall error of these approximations at a maximum of 20%.

We now arrive at a quite important point regarding the CO_2 emissions of PV systems. In comparison to most other energy technologies, the CO_2 emissions of PV occur almost entirely during system *manufacturing* and not during system *operation*. As a consequence, the CO_2 emissions of PV are determined very strongly by the *fuel mix* of the electricity supply system that is employed during the PV system production. In other words, the CO_2 emission of a PV system will depend on the CO_2 emission factor of the local utility system. In this analysis, we have assumed the present-day fuel mix of continental Western Europe (UCPTE region)[10], where about 50% of the electricity is produced by nuclear and hydro-electric plants, as well as 20% by coal, 10% by oil, and 10% by gas-fired plants. For this utility system, the CO_2 emission factor is presently about 0.57 kg per kWh produced electricity ($\sim$0.055 kg/MJ_{prim} [27]). We have taken this factor as constant for the considered time period.

Two other parameters, which may not be overlooked when evaluating CO_2 emissions of PV, are, of course, the irradiation at the site of PV system installation (cf. Section 3) and the assumed system life time. As before, we have assumed a medium high irradiation of 1700 kWh/m^2/yr and a system lifetime of 30 years. Note that because of the three parameters mentioned above, CO_2 emission estimates for PV can vary significantly between different studies.

In Figure 3 we have displayed the CO_2 emissions per kWh of supplied electricity for grid-connected rooftop PV systems. For comparison a number of conventional power generation technologies are also depicted (all status 1999). From a recent IEA study [28], we have, furthermore, included estimates for wind turbines and biomass gasification technology as well as their estimate for present-day multicrystalline-silicon PV technology in a rooftop application[11]. The results show that according to our estimates the CO_2 emissions for present PV technology are in the range 40–50 g/kWh which is considerably lower than for fossil-fuel plants but higher than for the two competing renewable energy technologies[12]. Our estimate for mc-Si

[8] Non-energy CO_2 emissions are 0.1 kg/Wp (silica reduction) or less.

[9] Primary energy use for electricity is about 90% of total primary energy consumption for crystalline silicon modules. For thin film modules this share is about 70%, but the remaining 30% is used in glass production where, by chance, the CO_2 emission is similar as our assumption for electricity production (0.055 kg/MJ of used energy).

[10] The Union for the Coordination of Production and Transmission of Electricity. It includes: Austria, Belgium, Bosnia-Herzegovina, Croatia, France, Germany, Greece, Italy, Luxembourg, Macedonia, The Netherlands, Portugal, Slovenia, Spain, Switzerland, and the Federal Republic of Yugoslavia.

[11] Corrected for the different assumptions on irradiation and system life time. The assumed fuel mix or the CO_2 emission factor of the electricity supply system is not given exactly ('current German') but their emission factor is presumably some 30% higher than ours. We did *not* correct for this difference.

[12] For biomass energy it is even argued that the CO_2 emission factor is effectively *zero* because parts of the biomass crop are not harvested and stay in the ground (trunks etc.), thus forming a CO_2 sink which compensates for the energy consumption in harvesting and transport.

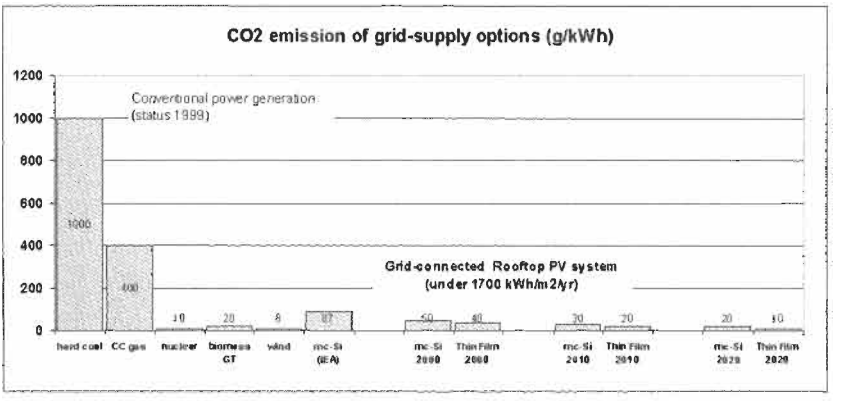

Figure 3 CO_2 emission for grid-connected rooftop PV systems now and expected in the future. For comparison we show emission data for a number of competing energy systems (coal, gas, nuclear data from [27]); wind and biomass energy estimates from a recent IEA study [28]). The PV technology estimate from the same IEA study is also shown. Note that actual CO_2 emissions for PV will vary with irradiation and system performance.

technology seems somewhat lower than that from the IEA study, but if we consider that the latter probably has assumed a 30% higher CO_2 emission factor for the utility system, the difference becomes negligible (which is to be expected as the respective energy estimates are also comparable). With improving technology, PV-related CO_2 emissions may become significantly lower, around 20–30 g/kWh in the near future, or even 10–20 g/kWh in the longer term. Only in the last case PV systems come into same range as current wind, biomass and nuclear energy.

In our LCA study of Solar Home Systems we found greenhouse gas emissions in the range 11–22 kg/Wp, or 0.6–1.2 kg/kWh. Installation of a solar lighting system could lead to GHG emission reduction around 480 kg/year if it replaces two kerosene lamps [22].

In conclusion, we can say that grid-connected PV systems can supply energy at a considerably lower CO_2 emission rate than current fossil energy technologies, but on the other hand PV is slightly at a disadvantage when compared to biomass and wind energy.

7 Conclusions

In this chapter we have reviewed the energy viability of photovoltaic energy technology. The question is whether photovoltaic (PV) systems can generate sufficient energy *output* in comparison with the energy *input* required during production of the system components. We evaluated the energy viability mainly in terms of the Energy Pay-Back Time (EPBT). For a grid-connected PV system under a medium-high irradiation level of 1700 kWh/m^2/yr, the EPBT is presently 2.5–3 years for rooftop systems and almost 4 years for large,

ground-mounted systems. The share of module frames and BOS in this figure is quite significant. Under other climatic conditions, the EPBT values will be inversely proportional to the irradiation.

Furthermore, we have shown that there are good prospects. In the coming 10 years, the EPBT of rooftop systems will decrease to less than 2 years, if certain improvements, both in production technology and in module performance are realised. For modules based on crystalline silicon, one of the requirements would be a dedicated silicon purification process with substantially lower energy consumption, while for thin film technology mainly an improved module efficiency would be necessary. Rooftop type systems will maintain their advantage over ground-mounted systems.

For standalone PV systems, like Solar Home Systems, the EPBT is in general a less meaningful indicator. If a very inefficient device like kerosene lamps is replaced by the PV system, the EPBT can be short: 0.8–2.0 years. In this case, almost 500 kg of CO_2 emissions per household per year may be saved.

In case of replacement of other supply systems, like a diesel generator, the energy balance of the PV system is less favourable. This situation will probably not change drastically in the future because the storage battery is the dominating component in these analyses.

CO_2 emissions from rooftop PV systems were calculated assuming that the PV production facility is located in Western Europe. It was found that the specific CO_2 emission at present is about 50–60 g/kWh, which is considerably lower than the emission from existing fossil-fuel electricity plants (400–1000 g/kWh). On the other hand, these CO_2 emission values for PV systems are higher than the estimate for two major competing renewable technologies, wind and biomass (< 20 g/kWh). Given the expected technology improvements, the specific CO_2 emission from PV could decrease to 20–30 g/kWh in the next ten years and perhaps even further after 2010.

Finally, we conclude from our analyses that, although the contribution of PV systems to CO_2 mitigation will probably be limited in the next decade [13], PV technology does certainly offer a large potential for CO_2 mitigation when looking beyond 2010.

References

[1] Nieuwlaar, E. and Alsema, E.A., 1997. *Environmental Aspects of PV Power Systems* – A report on the IEA PVPS Task 1 Workshop, 25–27 June 1997, Utrecht, The Netherlands, Report 97072, Dept. of Science, Technology and Society, Utrecht University.

[2] Nieuwlaar, E. and Alsema, E.A., 1998. PV Power Systems and the Environment: Results from an Expert Workshop, *Progress in Photovoltaics*, Vol. 6(2), pp. 87–90.

[3] IFIAS, International Federation of Institutes for Advanced Study, 1974. *Workshop Report no.6: Energy Analysis*. Guldsmedhyttan, Sweden.

[4] Alsema, E.A., 1998. Energy Requirements of Thin-Film Solar Cell Modules – A Review, *Renewable and Sustainable Energy Reviews*, Vol. 2(4), pp. 387–415.

[5] Alsema, E.A., 1996. *Environmental Aspects of Solar Cell Modules, Summary Report*, Report 96074, Department of Science, Technology and Society, Utrecht University.

[6] Frankl, P., Masini, A., Gamberale, M. and Toccaceli, D., 1998. Simplified Life-Cycle Analysis of PV Systems in Buildings - Present Situation and Future Trends, *Progress in Photovoltaics*, Vol. 6(2), pp. 137–146.

[7] Hagedorn, G. and Hellriegel, E., 1992. *Umwelrelevante Masseneinträge bei der Herstellung verschiedener Solarzellentypen – Endbericht – Teil I: Konventionelle Verfahren*. Forschungstelle für Energiewirtschaft, München, Germany.

[8] Kato, K., Murata, A. and Sakuta, K., 1998. Energy Payback Time and Life-Cycle CO_2 Emission of Residential PV Power System with Silicon PV Module, *Progress in Photovoltaics*, Vol. 6(2), pp. 105–115.

[9] Keoleian, G.A and Lewis, G.M., 1997. Application of life-cycle energy analysis to photovoltaic module design, *Progress In Photovoltaics*, Vol. 5, pp. 287–300.

[10] Nijs, J., Mertens, R., van Overstraeten, R., Szlufcik, J., Hukin, D. and Frisson, L., 1997. Energy payback time of crystalline silicon solar modules, in: *Advances in Solar Energy*, Vol. 11, K.W. Boer (Ed.), American Solar Energy Society, Boulder, CO, pp. 291–327.

[11] Phylipsen, G.J.M. and Alsema, E.A., 1995. *Environmental life-cycle assessment of multicrystalline silicon solar cell modules*, Report 95057, Dept. of Science, Technology and Society, Utrecht University, Utrecht.

[12] Alsema, E.A., 2000. Energy Pay-Back Time and CO_2 emissions of PV Systems, *Progress In Photovoltaics*.

[13] Alsema, E.A. and Nieuwlaar, E., 2000. Energy viability of photovoltaic systems, *Energy Policy*, Vol. 28(14), pp. 999–1010.

[14] Knapp, K.E.and Jester, T.L., 2001. Empirical investigation of the energy payback time for photovoltaic modules, *Solar Energy*, Vol. 71(3), pp. 165–172.

[15] Alsema, E.A., Frankl, P. and Kato, K., 1998. Energy Pay-back Time of Photovoltaic Energy Systems: Present Status and Prospects, *Proc. 2nd World Conference on Photovoltaic Solar Energy Conversion*, Vienna.

[16] Aulich, H.A. and Schulze, F.-W., 2002. Crystalline silicon feedstock for solar cells, *Progress in Photovoltaics: Research and Applications*, Vol. 10(2), pp. 141–147.

[17] Bruton, T. *et al.*, 1996. *Multimegawatt upscaling of silicon and thin film solar cell and module manufacturing (MUSIC FM), Final Report*, BP Solar, Sunbury-on-Thames.

[18] Fthenakis, V., Morris, S., Moskowitz, P. and Morgan, D., 1999. Toxicity of cadmium telluride, copper indium diselenide, and copper gallium diselenide, *Progress in Photovoltaics: Research and Applications*, Vol. 7(6), pp. 489–497.

[19] Alsema, E.A., Patterson, M., Baumann, A. and Hill, R., 1997. Health, Safety and Environmental Issues in Thin-Film Manufacturing, *Proc. 14th European Photovoltaic Solar Energy Conf.*, Barcelona, pp. 1505–1508.

[20] Kato, K., Hibino, T. and Komoto, K., 1999. A Life-Cycle Analysis on Thin-Film CdS/CdTe PV Modules, *Proc. 11th Photovoltaic Science and Engineering Conference*, Hokkaido, Japan.

[21] Alsema, E.A. and Nieuwlaar, E., 2002. *Life Cycle Assessment of Photovoltaic Systems in Roof-Top Installations - An LCA study focused at the contribution of Balance-of-System components* (in Dutch, with English summary), Report NWS-E-2002-04, Department of Science Technology and Society, Utrecht University, Utrecht.

[22] Alsema, E.A., 2000. *Environmental Life Cycle Assessment of Solar Home Systems*, Report NWS-E-2000-15, Dept. of Science, Technology and Society, Utrecht University, Utrecht. http://www.chem.uu.nl/nws/www/publica/e2000-15.pdf.

[23] Erge, T., Hoffman, U. and Heilscher, G., 1998. The German 1000-roofs-PV Programme – A Resume of the 5 Years Pioneer Project for Small Grid-Connected PV Systems, *Proc. 2nd World Conference on Photovoltaic Solar Energy Conversion*, Vienna, pp. 2648–2651.

[24] Knapp, K.E., Jester, T.L. and Mihalik, G.B., 2000. Energy balances for photovoltaic modules: status and prospects, *Proc. 28th IEEE Photovoltaic Specialists Conf.*, Anchorage.

[25] Beer, J. de, 1998. Potential for industrial energy efficiency improvement in the long term, Thesis, Utrecht, ISBN 90-393-1998-7.

[26] Dones, R. and Frischknecht, R., 1998. Life Cycle Assessment of Photovoltaic Systems: Results of Swiss Studies on Energy Chains, *Progress in Photovoltaics*, Vol. 6(2), pp. 117–125.

[27] Suter, P. and Frischknecht, R., 1996. *Ökoinventare von Energiesystemen, 3. Auflage*, ETHZ, Zürich.

[28] IEA, 1998. *Benign Energy? The environmental implications of renewables*, International Energy Agency, Paris.

V-3

World Photovoltaic Markets

P. D. Maycock, PV Energy Systems, Warrenton, Virginia, USA

1 Introduction

The world photovoltaic market is well established: 2001 shipments of modules all over the world exceed $1.4 billion at the factory and nearly $2.0 billion at retail. The value of installed photovoltaic systems exceeds $4 billion per year. This chapter analyses the world photovoltaic market and industry from several key perspectives. These include:

- The 2001 photovoltaic (PV) cell/module production. This section examines the world PV cell and module production by country, and by cell technology.
- The 2001 world PV market. Here we present historical and current information on photovoltaic shipments and installations throughout the world. The 2001 photovoltaic market is summarised by principal market sectors and key applications. We summarise the rapidly growing market for grid-connected systems in the USA, Japan and Germany.
- PV equipment market is summarised with a list of the principal companies involved.
- PV systems costs are analysed for three typical types of applications.

2 The 2001 Photovoltaic Cell/Module Production

World shipments of photovoltaic cells and modules reached 390.54 MWp in 2001, an increase of more than 34% over 2000. PV NEWS thanks the PV industry for their continued support in the many market surveys of PV cell and module production (the 19th survey was carried out in 2001 [1]). Readers should note that in order to avoid 'double counting' of industry output, the survey reports shipments only if the manufacturer produced the actual cells or the thin film. (If a company produced 10 MWp of cells, with 5 MWp of these cells made into modules and the other 5 MWp sold as cells, the company would be counted for shipments of 10 MWp in the survey. The company that purchased the 5 MWp of these cells would not be counted.)

2.1 Manufacturers' Production by Region/Country

Much of the 103 MWp increase in world cell/module production occurred in Japan. Japanese production increased 31%, from 127 MWp in 2000 to 171.2 MWp in 2001. For the third year in a row, all of the Japanese manufacturing capacity growth was used to serve the subsidised PV Home Systems and Institutional Buildings programme. US shipments increased from 75 MWp in 2000 to 100 MWp in 2001, primarily due to increased exports to Japan. European shipments were up 42% to 86.4 MWp. The ROW category grew from 23.4 MWp to 32.6 MWp.

The 2001 PV module shipments are summarised in Figure 1. Production by individual manufacturers, classified by region, is given in Tables 1–4.

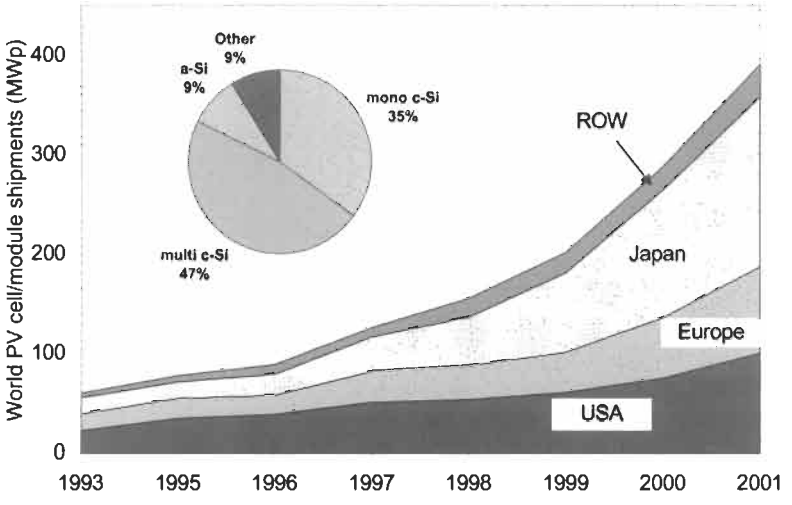

Figure 1 The photovoltaic cell and module shipments by region (main graph). The inset shows the module production by cell technology in 2001 (for details, see Table 5).

Table 1 Japanese PV cell/module production (in MWp)

Company	1994	1995	1996	1997	1998	1999	2000	2001
Sanyo	5.5	5.1	4.6	4.7	6.3	13	17	19
Kaneka	1.8	0.2	0	0	0	3.5	5	8
Kyocera	5.3	6.1	9.1	15.4	24.5	30.3	42	54
Mitsubishi	0	0	0	0	???	???	12	14
Sharp	2	4	5	10.6	14	30	50.4	75.02
Hoxan	0.4	0.5	0.8	1	1	1	1	0
Canon	–	–	0.5	2.1	2	1	0	0
Matsushita	1	1.2	1.2	1.2	1.2	1.2	1.2	1.2
Other	0.5	0.3	0	0	0	0	0	0
Total	16.5	17.4	21.2	35	49	80	128.6	171.22

2.2 Shipments and Production by Cell Technology

The sliced polycrystal silicon option gained a larger share of the world market than the single crystal option. Led by increases at Photowatt, Kyocera, and Solarex, sliced polycrystal PV cells gained 47% market share, while the single crystal option had 35%. Amorphous silicon, while increasing production to 34 MWp, saw a decrease in its market share to 8.6%. The new amorphous silicon plants, with announced, planned capacity of 25 MWp, produced less than 12 MWp in 2001. Nearly 35% of the 34 MWp of amorphous silicon produced in 2001 served the 'indoor' market – calculators, watches, scales, etc. The CIS shipments of Matsushita, 1.2 MWp, are also in the 'indoor' market. Despite the publicity about new cadmium telluride plants, only a few samples were shipped. When the 9.2 MWp 'indoor' shipments are subtracted from the

Table 2 US PV cell/module production (in MWp)

Company	1995	1996	1997	1998	1999	2000	2001
Shell Solar (Siemens Solar)	17	17	22	20	22.2	28	39
BP Solar (Solarex)	9.5	10.8	14.8	15.9	18	20.47	25.22
Solec Intl	2.6	3.5	4	4	0.6	0	0
Astropower	2.5	2.85	4.3	7	12	18	26
USSC	0.6	0.6	1.7	2.2	3	3	3.8
ASE Americas	2	3	4	4	4	4	5
Other[a]	0.45	1.1	0.2	0.6	1	1.5	1.3
Total	34.75	38.85	51	53.7	60.8	74.97	100.32

[a] Amonix, Iowa Thin Films, Evergreen, EPV, Ebara, Sunpower.

Table 3 European PV cell/module production (in MWp)

Company	1994	1995	1996	1997	1998	1999	2000	2001
RWE (ASE)	2.4	1.7	0	2	3	7	10	16
BP Solar (Spain)	6.1	7.2	8.45	11.3	4.5	5	9.16	12.16
Free Energy Europe	0.7	0.5	0.5	0.6	0.6	0.6	0.6	0.6
Intersolar (UK)	0.4	0.8	1	1.2	1.3	2	2.5	3
Photowatt-France	1.8	2.05	2.6	5.7	12	10	14	14
Eurosolare (IT)	3.5	2.7	2.5	2.5	3.2	1.5	2.3	4
Helios (Italy)	1.7	2	1.1	1.4	1.5	1.3	1.5	2.2
Isofoton (Spain)	1.5	1.5	1.6	2.7	4.2	6.1	9.5	18.02
Shell Germany							3.3	7.5
Shell Netherlands	–	–	–	2	2	2	2.2	2.8
Siemens (Germany)	0.5	0.2	0.05	0	0	2	2	2
Konkar (Croatia)	0.6	0.8	0.8	0.8	0.8	0.8	0.8	0.6
R&S (Netherlands)	0.6	0.05	0	–	–	–	–	–
Dunasolar (Hungary)	–	–	–	–	–	1.2	2.2	3
Other[a]	1.9	0.7	0.2	0.2	0.4	0.5	0.6	0.5
Total	21.7	20.2	18.8	30.4	33.5	40	60.66	86.38

[a] Western Si. (Russia), ENE (Belgium), SOVLUX, and others.

total 390 MWp, this leaves 381 MWp for terrestrial 'power' products in 2001. The 2001 production by cell technology is summarised in Table 5.

2.3 PV Module Production Costs and Material Consumption

The world production is divided into two major categories – sliced single and polycrystal silicon cells and modules and amorphous silicon thin films. To analyse the production of these modules from a materials consumption point of view, we need to summarise first the consumption per watt of module.

2.3.1 Sliced Single Crystal and Polycrystal Silicon Modules

These modules consume the following key materials: polycrystal silicon (solar grade), ethyl vinyl acetate (EVA), glass covers, aluminium or glass back sides, tabbing wire, and doping chemicals (Table 6).

Table 4 Rest of the world (ROW) PV cell/module production (in MWp)

Company	1994	1995	1996	1997	1998	1999	2000	2001
Cel (India)	1.8	1.4	1.6	2	2	2.1	1.5	1.7
Sinonar (Taiwan)			2.5	2.5	2.6	2.8	3	3
Bhel (India)	1	1.15	1	1	1	1	1	1.5
Res (India)	0.5	0.7	1	1	1.2	1.2	1	1
Heliodinamica	0.1	0.4	0.1	0	0	0	0	0
Reil (India)	0.5	0.7	0.7	–	??	??	??	??
China	1.2	1.5	1.5	1.5	1.6	2	2.5	3
Webel (India)			0.65	0.7	0.7	1.2	1.5	1.2
Udhaya (India)			0.5	0.5	0.5	0.5	0.5	0.5
BP Solar (India)					3.8	4	6.46	8.06
BP Solar(Australia)					5.1	5.5	5.76	6.96
BP Solar (Hong Kong)								1.3
BP Solar (Malaysia)								0.7
Motech								3.5
Other	0.5	0.5	0.2	0.2	0.2	0.2	0.2	0.2
Total	5.6	6.35	9.75	9.4	18.7	20.5	23.42	32.62

Table 5 Summary of the 2001 world cell/module production by cell technology (in MWp)

Technology	USA	Japan	Europe	ROW	Total	%
Single crystal flat plate	63.30	24.88	34.38	14.22	136.78	35.02
Polycrystal	18.53	116.12	35.80	14.40	184.85	47.33
Single and polycrystal total					321.63	82.35
Amorphous silicon	10.66	11.02	8.00	4.00	33.68	8.62
Amorphous silicon indoor use		(5.0)		(3.0)	(8.0)	
Crystal silicon concentrators	0.40	–	–	–	0.40	0.10
Ribbon (silicon)	5.40	–	8.2	–	13.60	3.48
Cadmium telluride[a]	0.33	1.20	–	–	1.53	0.39
Copper indium diselenide	0.70				0.70	0.18
Si on low-cost substrate	1.00		–	–	1.00	0.26
a-Si on CZ slice		18.00	–	–	18.00	4.61
Total	100.32	171.22	86.38	32.62	390.54	100.00
Total indoor use[b]					9.20	
Total terrestrial production					381.34	

[a] 1.2 MWp for indoor use.
[b] 8.0 a-Si + 1.2 CdTe.

Polycrystal silicon solar-grade feed stock is purchased by the kilogram and costs from $10 to $20/kg. If we assume a typical module efficiency of 13% (current range is 12–16%) with 300 μm thick slices, 200 μm thick kerf (saw dust), and normal yields, then the module consumes about 15–20 g of polycrystal silicon per watt. At $20/1000 g, the polycrystal silicon costs about 30–40 cents per watt.

Glass is used in the typical module as a top-side protective cover. Usually, the glass is tempered and formulated for high solar transmission. Some modules use

Table 6 Materials consumption for sliced crystal silicon

Material	Consumption per Wp	Cost per Wp	Consumption per 335 MWp
Poly-Si feedstock	15–20 g/Wp	$0.30–0.40	5025–6700 metric tons
Glass	0.0008 m/Wp	$0.03–0.04	26,800 m^2
EVA	0.0016 m/Wp	$0.04	53,600 m^2
Aluminium foil	0.0008 m/Wp	$0.05	26,800 m^2
Other materials		$0.05	

glass for both top and bottom coverage (ASE). For this analysis we assume one sheet of glass per module. Typical prices for glass bought by a 10 MWp/year producer costs $4–6 per square metre. Since a one-square-metre module at 13% efficiency produces 130 watts, the glass consumption is about 0.0008 metres per watt ($0.03–0.04 per watt).

EVA, or ethyl vinyl acetate, is used as a spacer between the cells and the top glass and back cover. A one-square-metre module uses two metres of EVA film or 0.0016 metres per watt. EVA costs about $3 per metre, totalling $6 for a one-square-metre module and costing $0.04 per watt.

Aluminium foil, or another backside material, has about the same consumption as glass – 0.0008 metres per watt.

Other materials may be used in manufacturing modules, but are not tabulated here due to process variations and their proprietary nature. Although we will not estimate the amount or cost of dopants, cleaning chemicals, conductive inks, conductive wires, etc., we estimate that the total material cost for all of these consumables is less than $0.05 per watt.

2.3.2 Amorphous Silicon Modules

There are two main types of amorphous silicon modules – based on the ECD roll-to-roll amorphous silicon on steel in a Tefzel/EVA/Tedlar package, or based on the amorphous silicon on transparent oxide-coated glass with EVA dielectric and backside glass (see Chapter IIc-1 for further details of the amorphous silicon technology). About 6 MWp of the ECD-based modules and 35 MWp of the glass/glass modules were shipped in 2001.

Amorphous Silicon on Steel (Table 7). We assume that the module efficiency is about 6%, or 60 watts per square metre.

100-micron stainless steel consumption is about 0.0185 metres per watt with a 90% active area yield. At a price of $9 per metre, the steel costs about $0.17 per watt.

EVA use consists of two layers per module for 0.033 metres per watt. At $3 per metre, EVA costs about $0.10 per watt.

Transparent tefzel use is one layer per module for 0.016 metres per watt. At $10 per square metre, this costs about $0.17 per watt.

Tedlar back use is one layer per module for 0.016 metres per watt. At $5 per metre, this is about $0.08 per watt.

Table 7 Material consumption for ECD amorphous silicon on steel

Material	Consumption per Wp	Cost per Wp	Consumption per 6 MWp
Stainless steel	0.0185 m/Wp	$0.17	110,000 m²
Tefzel	0.016 m/Wp	$0.17	96,000 m²
EVA	0.033 m/Wp	$0.10	198,000 m²
Tedlar	0.016 m/Wp	$0.08	96,000 m²

Table 8 Material consumption for amorphous silicon on glass

Material	Consumption per Wp	Cost per Wp	Consumption per 35 MWp
TCO on glass	0.0185 m/W	$0.185	647,500 m²
EVA	0.0185 m/W	$0.07	647,500 m²
glass back	0.0185 m/W	$0.07	647,500 m²

Glass/Glass Amorphous Silicon on TCO Glass (Table 8). For this module type, if we also assume the rated efficiency to be 6%, or 60 watts per square metre, then the material consumption would be:

TCO on glass, with a 90% yield of 54 watts per metre, costs about $10 per metre or $0.185 per watt.

Glass back plate, with a 90% yield of 54 watts per metre, costs $3 per metre or $0.06 per watt.

EVA with 90% yield or 54 watts per metre equals 0.0185 watts per metre. If the EVA costs $4 per square metre, then the cost per watt is $0.07.

2.4 World PV Market Experience Curve

Figure 2 shows historical PV shipments from 1975 to 2001, accumulated versus the best volume factory module price. Normally, one plots cumulative manufacturing experience versus manufacturing costs. However, the costs in the years 1975–1990 were not revealed and few analysts published their estimates of manufacturing costs. In 1990 the author started publishing and forecasting module manufacturing costs for the cell options in the market. Thus for the 1980–1990 time frame, the author estimates that costs of single crystal and poly-crystal silicon exceeded price (most manufacturers were losing money). By 1995, costs had been reduced so that some were pricing their product with profit. As the new amorphous silicon thin film factories began production in 1997, again prices (as low as $2.50 per watt) were offered with large losses being taken.

Prices for PV modules decreased dramatically from 1970 to 1990. As new plants began to produce from 1990 to 2000, prices held steady with factory module prices ranging from $3.50 per watt to $4.25 per watt for volume orders. Decreasing prices are expected from 2000 to 2010 due to cost reductions from

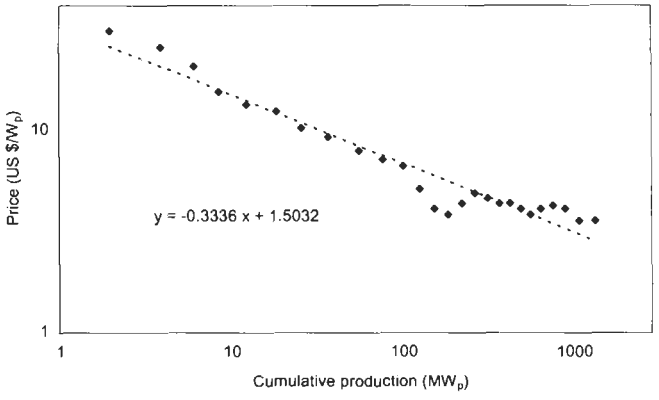

Figure 2 The 'learning curve' of the photovoltaic technology.

the introduction of amorphous silicon, copper indium diselenide, and other thin films. The market experience curve agrees well with the analysis by Anderson [2] Based on less extensive data than presented in this chapter Anderson argues that the costs of PV modules at time t (C_t, say) can be represented as a function of cumulative PV sales K_t in the form

$$C_t = C_0 K_t^{-b}$$

where C_0 is a constant and b is the learning curve coefficient. The value of b equal to 0.3336 which follows from the present analysis is consistent with Anderson's estimate of 0.3. These values indicate that the costs fall by about 20% for every doubling of the cumulative volume of sales. A recent assessment of the learning curve methodology for the PV industry has been given in [3].

3 World Photovoltaic Market Sectors by Application

For the last eight years, PV Energy Systems has attempted to summarise the World PV module shipments by principal application. We will briefly summarise each sector and provide our latest estimate of shipments for that sector. The details of the world market by sector are summarised in Figure 3.

3.1 Consumer Products

The consumer sector includes all applications for powering consumer electronics and other small, less than 5 Wp devices, including lights, signs, security systems, and portable power. The consumer electronics PV product market is now virtually saturated by Japanese-manufactured power packs for digital watches and calculators. The public has totally accepted the PV-powered calculator, 95% of which are powered by Japanese amorphous silicon solar cells (four-function hand-held calculators). More than 130 million PV-powered calculators are sold

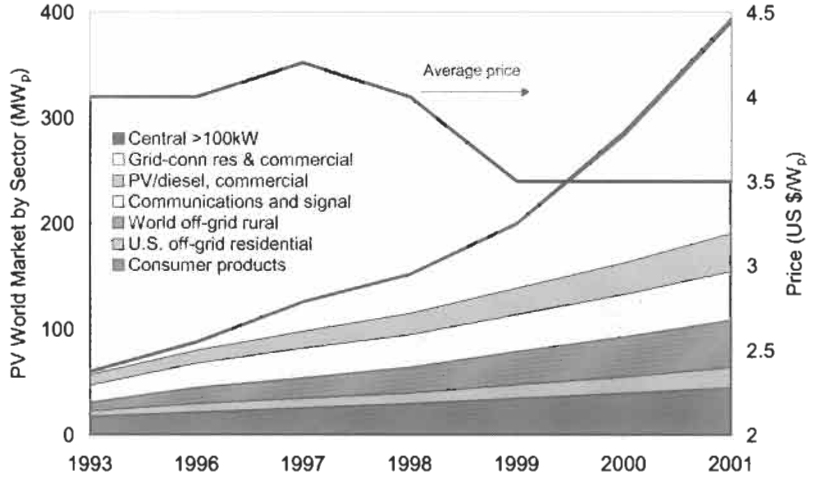

Figure 3 The world photovoltaic market divided into the principal application sectors. The average module price is also shown.

each year. Similarly, PV-powered watches are beginning to penetrate the US market. Other applications included toys, music boxes, flashlights, fans on pith helmets, clocks, and scientific kits for science fair projects. The American use of batteries, throwaway and rechargeable, is incredibly large. We estimate that 5 billion small rechargeable and throwaway batteries were purchased in 2000. It appears that the ability of PV to power both indoor and outdoor consumer portable electronics assures a much larger market than most U.S. firms have realised.

In 1986 and 1987, Chronar created a new market – portable garden and patio walk lights. In 1989 nearly 3 million of these lights were produced in Hong Kong and shipped throughout the world using amorphous silicon modules from Chronar, Solarex, and Sovonics (USSC), as well as single crystal silicon modules from Siemens Solar and polycrystal modules from Solarex and Kyocera. At this time, product failures ran as high as 50% and Chronar expectations were not met. With the Chronar bankruptcy, the market for portable lights collapsed. Fewer than one million portable garden lights, security lights, and house number lights were sold in 2000. One new lighting product from several companies, a portable fluorescent lantern powered by a 5–10 W PV module, is enjoying shipments well over 250,000 per year and will see dramatic growth as costs decrease with volume.

The present world consumption of PV-powered consumer products (if we normalise the cell output to an Air Mass 1.5 spectrum) is about 40 MWp_p annually (15% of world module shipments). Nearly 3 MWp of this product was consumed by the American market. The world market for consumer products powered by PV is in its infancy and we forecast continued explosive growth as products become commercially available. For products which feature the battery 'already in the product', the consumer market sector could develop to

a much larger market if key price points are met. As we write, new applications appear daily.

3.2 Off-the-Grid 'Residential' Systems

In 2001, most of the off-the-grid developed world PV house systems are comprised of four to eight, 4-square-foot modules, 60–100 W each, interconnected to provide 12–24 V DC systems. The loads are usually DC fluorescent lights, a music system, a water purifier, a small TV, and possibly a small pump on the well. Storage is usually by batteries with an inexpensive charge controller. The system is rack-mounted by the customer using wood or galvanised channel irons. Orientation is generally south (in the northern hemisphere) with a tilt of $\pm 10°$ from latitude. Shading is avoided, but many systems tolerate some shadows with reduced performance. The 'residence' is a small permanent residence, a vacation cottage, a motor home, houseboat, mobile trailer or other recreational vehicle. As the systems get larger, 300 Wp to 1 kWp, an inverter is often added to power some AC loads. Larger systems may power a 100-foot-deep well pump, vacuum cleaners, small tools, etc. At the 500 W and larger level, many families in moderate climates (like southern California) live a fully 'modern' life using only PV-generated electricity. A few larger systems are hybrid with a diesel or gasoline generator. PV is used most of the time and the generator used only to wash clothes or for heavy pumping.

A few systems (less than 30,000 worldwide) are fully modern stand-alone PV-powered houses. These systems typically have 5–6 days storage, diesel backup, 6–7 kWp of PV modules and cost up to $80,000. Obviously, economics is not a key factor in these large systems. They are, however, gaining much publicity for PV and tend to increase the market for small systems.

The 2001 small, off-the-grid systems are considered 'economic' by the present set of customers. Many of these people have no electricity at all other than the small amount available from batteries in cars, boats, and campers; or from small, noisy, smelly, unreliable gas or diesel generators. For example, the economics of a typical 1 kWp, $9000 system in California is nearly ideal system in that the solar flux is high (2400 hours per year at peak), the cost is very low because of low storage (2 days), and the system is DC. Further details of system costs are discussed in Section 5.

The 2000 US market is about 6 MWp annually and can grow to 20–30 MWp per year by 2005 provided module retail prices at the volume levels drop to $3 per watt. As systems become fully economic for all of the sun-belt, we could expect annual sales between 50 and 100 MWp per year.

3.3 Off-the-Grid Small Systems (less than 1 kWp)

The potential off-the-grid international market is very large compared to the US off-the-grid 'residential' market. This market has been very strong in South Africa, Spain, southern France, Italy, and Scandinavian countries primarily for outback vacation/resort homes. In developing countries, PV supplies the only

alternative for providing minimal electricity in villages. These applications range from a few fluorescent lights powered by 20–40 W modules to a 500 W system powering the essential needs of a community centre.

Community centres powered with PV bring a community closer together and provide an essential communication link with the government – and the world. It is a very powerful concept, which will enhance the objectives of most developing countries of bringing villages closer to major urban centres without further deterioration of over-burdened cities. In Panama, a 15 W fluorescent lamp with a small battery, regulator, and 20 W panel was used to provide lighting for a village meeting hall. The same system can be used for lighting small houses. In Colombia, a 500 W system now powers a village community centre. The centre has meeting rooms, radio, educational TV, and a refrigerator for storing medicines. The village community centres or small lighting systems represent government-supported markets, which are in turn dependent on international funding. We expect this market to grow quite rapidly after the initial demonstrations in various countries.

A solid, though limited, commercial market exists today for small off-the-grid stand-alone systems for lighting, entertainment and refrigeration. In French Polynesia, 12,000 island homes have PV-powered lights, a radio, and in some cases, a refrigerator. Kenya has over 60,000 off-grid small systems installed. In Honduras, the American non-profit 'SOLLUZ' has installed nearly 3000 solar home systems on a 'monthly fee' basis. SELCO, a US-based company exclusively committed to the Solar Home Market, has installed thousands of 30–40 W systems in India, Vietnam, China, Sri Lanka and South Africa.

Small off-grid commercial establishments are also installing PV systems in developing countries. For example, PV-powered refrigerators are gaining popularity in the Dominican Republic and South Africa for storing cold beer in stores and restaurants. Even where connection to the grid is feasible, unreliable grid electricity coupled with scarcity and high prices of diesel/gasoline makes PV attractive in this particular application. Even well-to-do farmers almost never have electricity in their farm houses. Small packaged systems can provide electricity for essential uses such as lighting, TV, and refrigeration. On poultry farms, longer daylight hours increase productivity of chickens. A few hours of lighting in the evening can provide higher yield of eggs, thus increasing the farmer's revenues. There are several such uses on the farm and villages that can enhance productivity and quality of life of the village residents. The major factors inhibiting sales in most of these rural markets are:

- Lack of knowledge of PV. Most buyers want to 'see and feel' a working system before deciding to buy.
- Lack of local credit for PV. In many developing countries, there are rural banks and credit unions that make small loans for farmers and small businesses. Until recently, the lack of awareness and infrastructure of PV have precluded loans. The efforts of SELCO, SOLLUZ, and others have dramatically changed this problem.

- Unavailability of distribution and service channels. This also is the cause for the lack of knowledge by consumers. Current pricing structures do not allow sufficient profit margins for the established distribution channels.
- The inability of foreign system suppliers to exchange local currency for dollars or other hard currency.
- Unavailability of proven rugged balance-of-system components that can withstand use by an unsophisticated customer.

Most leading PV manufacturers now offer packaged systems for lighting and entertainment units, medical refrigeration, stand-alone street lighting, etc. The packages come with all power supply equipment including modules, mounting hardware, regulators, and battery boxes. Batteries and load equipment are offered as optional items depending on the needs of the customer.

We expect government buys of the rural PV packages to begin as PV prices decline, but lead times associated with government projects, financing hurdles, and delays associated with the bidding process will cause a much slower development of this market. System suppliers can begin to develop distribution and service channels in key markets. As the volume increases, we expect government pressure to increase domestic content with backward integration; e.g., local frame assembly, module assembly, etc.

One excellent example of putting in place all of the critical elements listed above is the Solar Electric Light Fund (SELF), in Washington DC. The SELF process involves local selection of customers, local credit, trained local installation, service and maintenance persons, customer training, and no give-aways. The first 100–500 PV lighting systems (20–40 W peak, permitting 2–4 fluorescent lights, radio, and four hours of black and white TV) are donated to the local authority. As the systems are installed, a revolving fund is set up and new systems are procured from the private sector. SELF has installed and stimulated several thousand systems in Nepal, Sri Lanka, Zimbabwe, Kenya, Uganda, India, China, Vietnam, the Solomon Islands, Brazil, and South Africa.

In 1997, a new company, 'Solar Electric Light Company' (SELCO), was formed to move the SELF projects into the private sector. SELCO has formed sales and service companies in India (SELCO India) and Vietnam (SELCO Viet Nam). Operations in China and Sri Lanka are being finalised. SELCO has as its basic strategy the electrification of millions of homes using village service centres with local credit to permit monthly payment for the solar lighting system.

3.4 Worldwide Communication/Signal Market

The communication/signal market is the current backbone of the PV industry. PV systems have already proved to be reliable and economic for providing electricity at remote locations. As a result, PV has been routinely used for powering microwave repeaters, TV translators, radio telephones, educational TV, mobile radios, remote signalling, telemetry, and other such applications worldwide. Of the annual PV shipments (excluding central station and government projects), communication sales account for 30–35% of the total

annual revenues. The majority of the market is direct international sales. In addition, PV systems are sold to US telecommunication OEM's and systems houses, which in turn are exported to other countries.

The communications market can be divided into two sectors: military and civilian. Military sales are for border patrol and communications, including microwave repeaters, early warning systems, mobile truck-mounted power packs, mobile radios, etc. Most military tenders are by invitation only to established systems suppliers and are not widely publicised. Nevertheless, military sales in dollars account for at least 20% of the communications systems sales. The civilian communication systems offer a great promise of bringing rural communities closer, thus slowing the migration to already overpopulated urban centres. Microwave repeaters, radio telephones, TV translators, and educational TV establish a much needed communication link between the rural masses and urban centres where government agencies dealing with health, irrigation, etc., are located. Establishing these links, therefore, receives the highest priority from the government of the developing countries.

PV economics and reliability is now well accepted by international financing institutions. Recently, a telecommunications PV project in Thailand was initiated with the World Bank funding. A similar project in Colombia was financed with a loan from US Export-Import Bank. The civilian communications projects funded by the World Bank or other financial institutions are purchased by a government tender market. There will be extreme competitive pressures on all the bidders, and one should expect procurement delays and long project lifecycles associated with a government project. As the demand for PV increases, there will be continual pressure to increase domestic content and foster a domestic PV industry. Peru installed over 300 kWp in 1986, and Australia installed nearly a megawatt in 1987 and 1988 and continues regular installations. Oman installed over $20 million of PV systems in 1995–96. It appears that financing for telecommunications projects will continue to be easier in the future.

The communications market has not grown as rapidly as expected (10–15% per year rather than 25–30%), primarily due to the poor economic health of the developing countries in South America, Africa, the Middle East, and Asia. As these economies stabilise in the next few years, we will begin to see a more aggressive implementation of national communication systems in Third World countries. The majority of military communications sales have been in the Middle East, primarily in Saudi Arabia, Egypt, and Kuwait in that order. Oman, on the other hand, has powered television translators with PV, which provide TV transmission to citizens in remote villages.

In Latin America, major PV users have been Colombia, Peru, and Chile. In the first phase of the Colombian project, PV supplied electricity to two microwave repeaters and 100 radio telephones providing a communication link with 100 villages. Subsequently, most of the country has been linked with PV powered communications. In Peru, and Solarex completed 300 kWp for communications. We foresee continuing implementation in these countries and formulation of projects in other countries such as Venezuela and Ecuador.

In Asia, large potential exists in India, Pakistan, Thailand, and Indonesia. The Post and Telegraph Department of India is committed to setting up extensive communication links. Current plans call for 30,000 rural telephone stations to be operational in the next five years. PV is being thoroughly evaluated for use in microwave repeater stations as a reliable source of power. Pakistan also has similar plans for providing communication links to villages. The Telephone Organisation of Thailand (TOT) is implementing the PV telecommunications project with funding from the World Bank.

In Africa, a major user of PV has been the Post and Telegraph of South Africa, which has aggressively pursued PV over the last 10 years. In 1994/1995 South Africa installed 5000 PV-powered digital satellite phone stations for the election (15,000 PV powered phones were installed prior to the election). Tanzania awarded its first PV telecommunications project to a British systems house and will pursue more in the future. In addition, we expect PV markets for telecommunications in virtually all developing countries.

PV communication/signal sales in 2000 were in the 40 MWp range. This market could grow to 200 MWp per year by 2010.

3.5 World PV Diesel Hybrid/Replacement Market

There has been considerable interest in the concept of using the fuel in a diesel or gasoline generator as the storage for a PV system. In the early phases of the US PV programme, the DOE funded several stand-alone diesel-backed PV systems. The most notable is the 100 kWp system at Natural Bridges National Monument in Utah. The other diesel-supported hybrid is the 350 kWp at Ryhad in Saudi Arabia.

In the small generator class (less than 5 kWp), several hundred systems have been installed in the US where the diesel or gasoline generator is started automatically as power from the PV system, including its storage battery, declines. (Most systems use a small buffer storage to preclude the diesel from starting over and over again on a cloudy day.) Economic viability ranges from $2/Wp for fuel credit only to $8–9/Wp in those regions where small diesels are used as base load in the Sunbelt of the world. The product appears to be working very well in that the auto start is simple; the use of batteries means you always have enough power to turn the diesel and start it and set the ignitors. The reliability of the diesel generator increases because it is used at full load for short periods of time and its usage rate can be decreased as much as 70%, especially for those systems where the diesel is oversized and normally operates at a small fraction of its output. We find that by calling attention to the PV diesel hybrid through the installation of PV, customers get much more energy hungry than when they were running only a diesel generator because they are aware that no fuel cost is associated with the PV component. In all cases, demand has increased beyond expectations.

For applications where diesel availability is not a great problem, but the price of diesel is high, a PV–diesel hybrid system makes a very viable combination. Having diesel backup in the system ensures the availability of electricity in

periods of low insolation such as monsoon season. With PV in the system, diesel O&M costs are reduced as well as the fuel cost. The PV–diesel hybrid thus combines the attractive features of both systems.

Another advantage of PV–diesel hybrid over the stand-alone PV system, one that is most often overlooked, is the reduction in the size of the PV array to supply electricity to loads with the same reliability. A stand-alone PV system must be large enough to supply power to the load during the worst weather that can be reasonably expected. This typically means that a stand-alone system is about 20–30% larger than one designed to support the load during average weather. Thus, in periods of good insolation in summer, this 20–30% energy is wasted, or the owner gets used to summer loads that cannot be served in the wet seasons. By substituting a diesel generator for providing power during the worst weather, we not only add reliability and flexibility, but also reduce the cost of the PV system by 20–30% (or even higher in some cases). Given the high initial cost of PV systems, the PV–diesel combination can substantially reduce capital cost while maintaining reliability.

PV Energy Systems, Inc. analysed the economics of PV, wind, and diesel systems for various sizes ranging from 1.5 kWp to 80 kWp. The principal major conclusion is that PV is fully economic now against small gasoline engines, or those less than 2 kWp under most stringent economic criteria but the price must decrease for PV to be competitive in large applications.

The largest sector of the world diesel market is primarily in the Middle East. The applications include both replacement of diesel engines at existing sites, as well as new uses either as PV stand-alone or diesel hybrid systems. The applications are water pumping for drinking and irrigation; provision of electricity for farms, community centres, and rural medical clinics; and desalination. As the prices of PV systems decline, rural electrification becomes a viable and effective way for improving quality of life for villages of the Third World.

3.6 Grid-Connected Systems

Nearly 30 MWp of PV central systems with 200 kW or larger capacity were built in the 1980s, principally in the USA. These large systems proved that PV systems could provide energy of adequate quality to be used in the distribution grid. Some ten years later, European government-assisted projects began integrating PV into replacement roofs, awnings, facades, atriums, and a line of 'building integrated' architectural products began to appear. The product development was lead by Pilkington Solar in Germany and Atlantis in Switzerland. In the last four years, several hundred buildings have installed PV building products in systems ranging in size from 10 kW to two recently completed 1 MWp projects. Nearly 8 MWp of this new application for PV were built in 2000 in Germany. In the USA the building-integrated market is slowly developing in roofs for residences, a curtain wall PV product from Solarex, and an Atlantis assembly plant in Virginia.

In 1990, the German government announced the '1000 Roofs Programme', to be later extended to cover over 2000 installations. The decisive step occurred

in 1995 when the Japanese Government announced its '70,000' roofs programme, and the German '100,000 Roofs' programme, announced early in 1999 dramatically accelerated the growth of the grid connected market which now exceeds the traditional off-grid sector.

Based on an extensive survey, PV Energy Systems estimate that the grid-connected residential/commercial sector grew from 60 MWp in 1999 to over 200 MWp in 2000. Over 50 MWp of this growth occurred in Japan and Germany. Japanese installations in 2000 increased to 65 MWp, and German installations reached about 45 MWp. The remaining 10 were in the USA (4–5 MWp) and in other European countries (4–5 MWp, Figure 3).

3.6.1 US On-Grid Distributed Sector

The major photovoltaic projects in the USA consisted of new initiatives and the continuation of the projects started in the 1995–1999 time-frame. These included:

- The completion of the PVUSA (PhotoVoltaics for Utility Scale Applications) competitive procurements, where utilities teaming with customers bid the installation of photovoltaic systems with partial financial support (about 25%) from the US Department of Energy (0.5 MWp in 2001. The DOE-assisted programme (20–30% subsidy) was completed in early 2001. Nearly 9 MWp of systems were installed.
- The second year of Pioneer II, where SMUD offers photovoltaic systems for sale to customers at subsidised prices (as low as $3.50 per watt installed), The Pioneer II programme calls for 5 MWp of photovoltaics to be installed in 1999–2004. SMUD installed 1.6 MWp in 2001.
- The programme initiated by the state of California where cash rebates ($3.50 per watt) were offered to residential and commercial customers that installed grid-connected photovoltaic systems on investor-owned utility grids (1.4–1.6 MWp in 2001.
- Further refinement and definition of the US Million Solar Roofs Initiative with commitments for partnerships for new photovoltaic installations and projects.

Although detailed figures are not available for State programmes, several states have renewable energy set asides, funds for research leading to new photovoltaic industry within the state, photovoltaic school programmes, and 'Green Pricing' programmes are available. Programmes of note include:

- Arizona: Over 50 MWp of PV over ten years.
- California: Over $200 million for the support of grid-connected renewable energy electricity generation systems. Brown outs, near-bankruptcy of large investor-owned utilities, threats of increased prices started a major increase in PV UPS systems and have State planners proposing a $5.00 per watt subsidy instead of the present $3.50/watt rebate. In addition to the state rebates the state municipal utilities (Sacramento and Los Angeles)

have PV support programmes totalling $100 million over 5 years. San Francisco, after passing a bond referendum, is in the early stages of a ten year, 50 MWp PV programme.

- Illinois: Led by the strong 'Brightfields' programme in Chicago (where abandoned factories (brownfields) are converted to PV manufacturing plants (owned and operated by Spire Corporation) or installed PV systems ('brightfields'), the state of Illinois passed the largest US subsidy for PV systems, $6.00 per peak watt given.
- Ohio: Support for 50 schools to have PV systems/training modules installed on public schools.
- New York: Over $50 million to support new industry, installations, and studies to accelerate commercialisation of PV. Recently (May 2002) New York has increased the PV subsidy to $5.00 per watt for grid-connected systems.
- Virginia: $0.75 per watt cash rebate to PV module produced in the state. Capped at $6 million per year.
- North Carolina: 35% tax credit for PV systems.

The SMUD Solar Pioneer Programme. The Sacramento Municipal Utility District (SMUD) completed the PV Pioneer I (PVP I) programme where over 400 homes were equipped with SMUD-owned and maintained photovoltaic systems. The PV Pioneer II (PVP II) programme offers the sale of subsidised grid-connected photovoltaic systems to customers. Over 5 MWp of systems are planned for the next seven years. SMUD has achieved several critical milestones and continued progress in their aggressive programme of sustained, orderly development and commercialisation of photovoltaics. Key 2001 milestones include:

- In 2001, SMUD installed 1670 kWp of PV systems in the District and supplied 339 kWp to PV Partners outside the District. As of the end of 2001, SMUD has installed over 10 MWp of PV systems in some 1000 installations. For the first time, costs of fully installed systems dropped below $4.50 per watt.
- 220 PV Pioneer II systems (1200 kWp) sold to customers. Over 2000 SMUD customers have signed letters of intent to purchase net metered, grid-connected systems.
- Under SMUD's Solar Advantage Homes programme, production homebuilders offer commercially built homes with PV systems as a standard feature. The systems are now available in 15 Sacramento new home communities. More than 20 such homes were completed in 2001.
- Completion of the world's largest PV parking lot system, the 540 kWp Solarport at CalExpo.
- Rancho Seco, the worlds largest, single site, PV power plant – now 3.9 MWp.

Unlike the PVP I programme where SMUD installed and owned photovoltaic systems on customers' roofs, the PVP II customers purchase and own their

photovoltaic systems and qualify for net metering. The photovoltaic systems are sold to the customer at reduced prices that reflect the savings of SMUD's large volume purchases (modules and inverters) and the buy down provided though SMUD's Public Goods Funds (PGF). For more information contact Donald E. Osborn, Superintendent for Renewable Generation, e-mail dosborn@smud.org.

The California PV Subsidy Programme. The California Emerging Renewables Buydown Programme was started in April of 1998. The programme involves cash rebates for the installation of new renewable energy generation, including photovoltaics, small wind, and renewably fuelled fuel cells. Over 4 MW of new renewable energy generation were stimulated in 2001. The installations included 2.5 MWp of photovoltaics. The photovoltaic systems received a \$2.75–\$3.00 per watt cash subsidy (up to 50% of the total cost). Two-thirds of the 400 systems were small, less than 5 kW, grid-connected systems, mainly for residences. One-third of the systems, mostly commercial, were over 10 kW in size. The CEC has also simplified the rules and tariffs for net metering, and reduced the paperwork (four pages) for interconnection requirements for grid-connected photovoltaic systems. Net metering interconnections have become more routine and commonplace in California. At the end of 2000, California, under deregulation, suffered increase in bulk electricity prices, inadequate supply resulting in some Brown-outs. These uncertainties stimulated concern among customers, state legislators that bode well for UPS PV, especially in the summer when the peak use of electricity occurs.

3.6.2 The Japanese PV Market

We estimated that Japanese installations topped 105 MWp in 2001, making Japan the world leader in PV installations. Japan has had the most aggressive PV research and development programme since it began in the late 1970s (modelled after the US programme). Japanese PV budgets grew almost linearly from \$20 million in 1980 to over \$200 million in 2000. Virtually all funds were aimed at developing an industry capable of competing in the world PV market, and with cost reductions that would also serve the in-country market.

In the first ten years of 'Project Sunshine', major emphasis was on amorphous silicon. With the success of Siemens Solar, Solarex, and Kyocera in increasing the performance of sliced single and polycrystal silicon, the Japanese programme also started funding the crystal options. In 1995, the Japanese Ministry of International Trade and Industry (MITI) announced a major new in-country initiative, '70,000 Roofs'. The goal was to install 70,000, 3–4 kWp PV systems on homes to address summer peak loads, save imported fuel, clean the air, and establish a fully competitive Japanese PV Industry to serve both off-grid and grid-connected markets throughout the world. In the first year, the programme installed 800, 4 kWp residential systems with a 50% government subsidy, for total installations of 3.5 MWp. The FY 1997 programme resulted in 1600, 4 kWp systems to be installed. The FY 1998 programme reached 9600, 4 kWp systems installed from April 1, 1997 to March 30, 1998 – 1999 saw 1600 PV homes with 3–4 kWp resulting in over 55 MWp in calendar 2000. The

programme is open to all PV suppliers with no duties, and complements another successful Japanese PV programme, 'PV for Schools and Government buildings', which installed over 20 MWp in FY 2001.

The Japanese PV roofs programme is in its fifth year with nearly 18,000 applications for residential grid-connected PV systems in fiscal year 2000. The programme has stimulated annual sales of over 50 MWp and major increases in capacity for Kyocera, Sharp, Sanyo and Kaneka. The programme goals and the actual results are very close. Analysis of the 'economics' of the Japanese PV residential programme shows that with the 30% subsidy and ¥27/kWh electricity price many Japanese are willing to pay a premium for PV. If the programme terminates in 2002 and the PV prices decrease, the cost of PV without subsidy will once again exceed electricity price by a large margin.

In 1999, Japanese PV manufacturers reported shipment increases of 63% from 49 MWp in 1998 to 80 MWp in 1999. Kyocera, Sharp and Sanyo led this growth. Kyocera reported 1999 shipments of 30.3 MWp – 26% growth. Sharp shipments were up a whopping 114% to 30 MWp. Sanyo increased production from 6.3 MWp to 13.0 in 1999. Virtually all Sanyo growth was due to the successful introduction of the amorphous silicon film on a single crystal slice heterojunction that reached 18% cell efficiency in production.

The Japanese PV Roofs programme was started in fiscal year 1994. A government subsidy of 50% of the cost of the installed system was offered to stimulate private purchase of 3–4 kWp rood mounted, grid-connected systems. Table 9 shows the evolution of the programme. In 1993 there was virtually no Japanese market for PV residential grid-connected systems (10 homes per year or so). The subsidy started at 50% of the installed cost in 1994–1997 and was decreased to about 35% in fiscal year 1999. Despite this over 17,000 systems were for between April 1999 and March 2000 (50–65 MWp in total). The price evolution for PV systems and its components in Japan during this period is shown in Figure 4.

3.6.3 The German PV Market [4]

The German 100,000 Roofs grid connected system market, with no-interest, one-year non-payment and 99 pfennig value of PV-generated electricity created such excitement that the applications in the first four months of 2000 would call for a one-year market increase of 500% – 11 MWp of grid-connected PV in 1999 versus 70 MWp in 2000. Analysis of the economics of the German 100,000 Roofs market combined with the price-incentive programme shows fully economic PV now! The dramatic increase in applications caused a halt to the programme and revision which decreased the subsidy. Even under the revised programme, PV is nearly economic in Germany. The forecast by PV Energy News shows that, after the termination of the revised programme and expiry of the subsidy, PV will once more cease to be 'economic' compared with grid electricity. Forecasting the German PV Roofs programme will be very difficult owing to the 'political' nature of the programme.

The government provided mechanisms to stimulate PV in Germany some years back. The highly popular German '1000 Roofs' project installed 2500

Table 9. Evolution of the Japanese 70,000 Roofs Programme. Source of data: reference [5]

Fiscal year	Number of systems		Generation capacity (kWp)	
	Per year	Cumulative	Per year	Cumulative
1994	539	539	1860	1860
1995	1065	1604	3916	5776
1996	1986	3590	7536	13,312
1997	5654	9244	19,486	32,798
1998	6352	15,596	24,123	56,921
1999	15,879	31,475	57,693	114,614
2000	20,877	52,352	74,381	188,995
2001	25,151	77,503	90,993	279,989

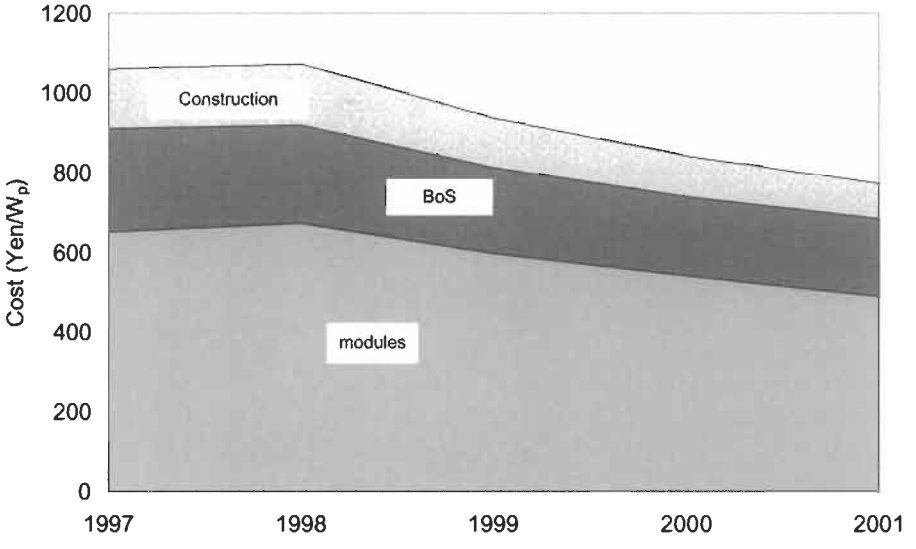

Figure 4 The evolution of PV systems price and its components for the Japanese 70,000 Roofs programme (source of data: reference [5]).

residential systems (2–4 kWp) with subsidies as high as 70%. Despite the completion of the project in 1994, private sales have continued the momentum. The German policy of paying for environmentally clean electricity and state subsidies for PV re-ignited the German grid-connected '2000 Roofs' programme. Nearly 10 MWp of PV systems were installed in Germany in 1998, prior to the announcement of the 100,000 Roofs programme (this is ten times the US PV market for similar applications). Also, Germany is clearly the world leader in the installation of building-integrated PV systems (roofs, shading, curtain wall, atria, and so on). Several megawatts of building-integrated PV were installed in Germany in the last four years. A number of projects include PV installations involving over 100,000 square feet (10,000 square metres) with over 1 MWp of PV. Even though this sector is less than 5 MWp per year, the buildings are highly

visible and much advertised. It is good business and politics to be 'green' in Germany, and PV on buildings is the most available symbol of the movement.

It is ironic that virtually all German PV production is now in the USA. Even Kyocera, using German ingot-casting technology from Wacker Chemetronics, has a significant share of the German market. Over 50 MWp of new German PV plants are under construction (most based on cast ingot polysilicon). These include a 25 MWp cell plant by ASE GmbH (about 10 MWp of cell capacity is installed in 2000 and a 25 MWp polysilicon plant by Shell Solar and former Pilkington Solar (now FLABEG). Antec has just completed a 10 MWp plant to produce cadmium telluride (see Chapter IIc-3), and EPV (USA) announced a 5 MWp copper indium diselenide plant in Saxony. We also expect major announcements of new German thin film manufacturing plants in the next three years.

The 100,000 Roof Programme. In late 1998, the German coalition government began the process of implementing the largest subsidy programme in the history of photovoltaics. The goal was to fully stimulate the PV grid-connected (residential and commercial) market. The running of the programme was assigned to the German Federal bank (KfW) to keep the amount of paperwork involved to a minimum. Assistance takes the form of a ten-year, interest-free loan to be repaid in nine annual instalments, no repayment being required in the final ear. The final instalment of 10% is waived. The KfW makes loan commitments within 5 days. Hence, the handling of the programme is very unbureaucratic. Those taking part in the programme can combine it with assistance provided under other schemes run at local level – including integration with some municipal full cost-recovery pricing schemes – so long as total assistance does not exceed 100% of the cost of finance, the German KfW assumes liability. House banks therefore have no reason to delay the extension of loans to borrowers owing to uncertainty over liability. On request, the KfW also disburses the total subsidised amount (just under 40%) immediately, thereby converting this assistance into a direct subsidy. The calculated cost of the programme to the Federal Budget was estimated to be DM1.1 billion, making it the world's biggest ever photovoltaics programme.

Despite the careful planning with attention to details, the key issues of informing the public, the role of State versus Federal subsidies, transferring the government interest subsidy to local banks, limits to sizes, standards, and so on led to confusion and delay in early 1999. However, quick action by the government, the German Bank and the Greens saved the day and the 1999 installations slightly exceeded those of 1998. Nearly 4000 systems were installed under the programme in 1999 with an installed capacity of 10 MWp. Another 4 MWp was produced for other applications and export.

Early in 2000, the government added a new subsidy for grid-connected PV systems. They offered, in addition to the zero-interest programme, 99 pfennig for PV- generated electricity (50 US cents/kWh). The combination of the two subsidies made PV fully economic at today's $8–10/Wp installed system prices. With the introduction of the new 99 pfennig payment the interest in PV soared.

The first three months had applications exceeding 30 MWp – the month of April had an additional 40 MWp of applications. This exceeded the goals of the programme and, had it continued, would have 'broken the bank', so to speak! In early May the government placed a moratorium on applications, and reformulated the scheme – they acted quickly and decisively. The goal is to set limits on the size of systems, the annual level of subsidy, etc. Their new goal of 55 MWp in 2000 of German applications (coupled with the 60 MW of Japanese applications) has created havoc in the PV industry – prices increased, delivery time increased to 4–6 months and everyone was 'sold out'. Table 10 shows the goals of the original programme and the goals of the accelerated new programme, which calls for 50 MWp of applications in the year 2000.

Many of the 'old plan' applicants are demanding that, since they met the deadlines, they should be able to participate in the original plan. The new plan will not be interest-free. It is expected that the interest rate will be 4.5%. The one year free (the tenth year) has been dropped. The new plan also has limits on the size of system.

4 PV Equipment Market

One of the fastest growing segments of the photovoltaic industry is the manufacture and sale of PV module manufacturing and test equipment. We estimate that nearly $400 million worth of PV manufacturing equipment has been sold in the last few years. As the developing world appreciates the value of PV for providing electricity to its remote villages and farms, their first realisation is that they are now importing a very capital-intensive product. In order to cut the outflow of capital, many will opt to license technology and purchase manufacturing equipment from outside the country. The US companies that decide PV is a major business opportunity are also likely to decide to license and purchase PV manufacturing capability rather than expend the incredible R&D funds required to have a competitive position.

There now are several PV module plants that purchased all of their equipment and technology from outside the country. These include China, India,

Table 10 Statistics of the German 100,000 Roofs Programme

Year	Units	MWp	
		Goal	Actual
1999	6000	18	15
2000	9000	27	45
2001	12,000	36	75
2002	17,000	51	80
2003	24,000	72	
2004	32,000	96	
Total	100,000	300	

Yugoslavia, Canada, Algeria, Wales, Hungary, and France. Several other countries are seriously looking at PV plant purchases.

4.1 Key Companies Involved

Spire Corporation has developed a complete line of single crystal silicon module manufacturing and test equipment. The equipment includes uses for cell diffusion, ion implantation, tabbing machines, laminators, and cell and module test equipment. Spire sold both separate pieces of equipment and turnkey cell and module product lines. We estimate that over 50 PV module producers use Spire equipment. Complete Spire lines were sold to Chicago Illinois (USA), Canada, China, Algeria, India, and Saudi Arabia. Spire also developed an amorphous silicon module tester that is the standard of the worldwide industry.

GT Solar (a division of GT Equipment Technologies, Inc.) is a division that offers crystal pullers, Crystal Systems casting machines, advanced furnaces, ribbon pullers, etc. The recent upsurge in ingot casting and ribbon pulling factories provide a large, growing market for the GT Solar manufacturing equipment.

Crystal Systems developed the Heat Exchange Method of forming large polycrystal ingots, which are sliced and form the basis for the polycrystal silicon solar cell option.

Global Photovoltaic Specialists offers single crystal and polycrystal equipment sold as a complete line or individually, and has sold equipment to India and China.

HCT Shaping Systems in Switzerland has sold over 300 of its multiwire silicon slicing machines to the PV industry. The semiconductor industry, in its shift to 8-inch and 12-inch slices, has also moved to wire saws. HCT now dominates the wire saw business. These advances have made thinner, less costly slicing available to the PV industry. The 500-wire-plus saws can cut hundreds of slices at once with nearly one-half the slice thickness plus kerf of the conventional internal diameter diamond saw. Notable customers include AEG (now ASE GmbH), Siemens Solar, Bayer, Photowatt, Solarex, and IBE. A new model can cut more slices and can handle a very large ingot of polycrystal material. This new machine has cut crystal and polycrystal silicon material consumption – the largest contributor to cost – by at least 50%.

Other equipment manufacturers include:

- 3T Tanakaya for crystal silicon processing equipment
- Balzers for laminators
- BMC Solartechnik for laminators
- M. SETEK for single crystal cell and module equipment
- Oxford Applied Research for laminators
- Shimadzu Corporation for thin film coaters, plasma CVD, MOCVD, and sputtering equipment
- Photec (Italy) for wire saws
- BTU Engineering for continuous belt furnaces for diffusion, antireflection coatings, etc.

5 PV System Costs

This section presents an analysis of the installed system price for three typical systems: remote off-grid systems of 40 Wp–1 kWp size, grid connected systems (1–20 kWp) and central power systems (1–10 MWp) (Table 11). This analysis is based on the module performance/cost and the Balance of Systems performance/cost described in PV Energy Systems Report Two 'PV Technology Performance and Cost, 1975–2010'. This report which includes a forecast to 2010, is available from PV Energy Systems.

5.1 Remote PV Power Systems

In 2001 costs in the USA are about 9–14 dollars per watt for AC stand alone power with battery storage installed. Multi-tier distribution and other markups tend to increase these costs and projects are often too small to gain full economies of scale from volume purchasing and effective use of installation labour. Most stand-alone PV systems sold today, ranging from 40 W Solar Home Systems in the developing world to telecommunication power systems throughout the world to 200 kWp remote military power stations are considered to be the most reliable, fully economic option available to provide the needed electricity. Over 40% of all PV applications fall into this category. Prior to 1997 the off-grid sector was over 70% of the market. The explosive growth of the grid-connected market has made the off-grid market less important.

5.2 Grid-Connected Small Systems

These systems are not required to have battery storage, but do need an inverter that can provide AC power to the customer's load and feed excess power onto the utility grid. These systems typically cost $7.00 to $9.00 per watt.

Table 11 Representative costs (in US$) of remote off-grid, and small/large grid-connected PV power systems

Cost element	Remote off-grid[c]	Small grid connected[b]		Central power systems (> 1 MWp)[a]
		Single crystal	SMUD (thin film)	
Modules	5.00–6.00	4.50–6.00	2.25–2.50	4.00–4.50
Battery	1.00–2.00	–	–	–
Charge controller	0.40	–	–	–
Inverter	0.80–1.20	0.60–0.80	0.40	0.50
Racks, wire, etc.	0.50–1.00	0.30–0.50	0.30–0.50	1.00
Labour	1.00–1.50	1.00–1.50	1.00–1.40	1.00
Profit (installer)	1.00–1.50	1.20–1.50	0.00	1.20–1.50
Total installed	9.20–13.40	7.60–10.30	3.95–5.30	7.70

[a] 2000 prices.
[b] 2001 prices.
[c] 2002 prices.

SMUD, with five year, 5 MWp purchase agreements for modules and inverters, is now installing 2 kWp grid-connected PV systems in Sacramento, California, with installed costs less than $5.00 per watt. With a SMUD subsidy of about $2.00 per watt, PV systems are being offered for sale in California at below $3 per watt. It will be interesting to see the response of the American consumer.

Recent subsidy programmes in Japan, such as the '70,000 roofs' programme, have stimulated the sale of over 100,000 3–4 kWp home systems to Japanese homeowners in the past four years. After the government subsidy, the Japanese have been paying over $5.00 per peak watt installed for their systems. Despite the less favourable solar climate in Japan than in California, the Japanese are purchasing PV. Low-cost finance (less than 5%), the high cost of electricity – about $0.30 per kilowatt hour – and a deep environmental concern appear to motivate the Japanese to purchase this new energy option.

5.3 Large Central Power Systems

The cost of large central power systems is presently in the $6000–8000 per kilowatt range. The forecast of installed costs of $2500 per kilowatt requires profitable module prices of $1.50 per watt and BOS costs of $1.00 per watt including installation and profit for the project contractor. The Balance of Systems costs (BOS) for large central power systems have been extensively analysed by design and construction firms (Black and Veatch, and Brown and Root). They conclude that BOS costs of $1.00 to $1.25 per watt installed are likely for central power systems. At these prices using investor owned utility economics (13% fixed charge rate) and the very best solar environment (2400 peak hours of sunlight per year), the cost of electricity is in the eight to ten cents per kilowatt hour range. Module costs could be reduced even further, making the USDOE goal of six cents per kilowatt hour a possibility. If the capital cost were to be reduced to a 'social' level, say 5% with a 30 year 'life' leading to a capital recovery of 7–8%, instead of the 12–15% rate used for commercial projects, then Central PV could be fully economic in the very best climates (6–8 cents per kilowatt hour) when the $2500 per kilowatt cost was reached. We note that this price level will make PV 'economic' for most grid-connected residential and commercial distributed systems.

References

[1] Maycock, P. 2002. PV NEWS, Vol. 21, Nos 2 and 3.

[2] Anderson, D. 2001. The economics of photovoltaic technologies, in: M.D. Archer and R. Hill, Eds., *Clean Electricity from Photovoltaics*, Imperial College Press, pp. 741–769.

[3] Parente, V., Goldemberg J. and Ziles, R. 2002. Comments on experience curves for PV modules, *Prog. Photovoltaics Res. Appl.*, Vol. 10, pp. 571–574.

[4] See also Maycock, P. The PV boom: where Germany and Japan lead, will California follow? *Renewable Energy World* – Review Issue 2001–2002. James and James, p. 144.

[5] Ikki, O. 2002. PV Activities in Japan, Resources Total Systems Co. Ltd., Vol. 8(5), May 2002. See also P. Maycock, PV NEWS, June 2003.

V-4

National and Regional Support Programmes

Beatriz Yordi, Directorate-General for Energy and Transport, European Commission, Brussels, Belgium

1 Introduction

In the last decade of the 20th century, the outlook for photovoltaics (PV) changed. What was a marginal technology, mainly for remote applications, has become a key technology for generating distributed power in the built environment. PV has prospects of break-even with conventional grid power for residential consumers within two decades, i.e. by around 2020. There has been a clear shift in emphasis, from primarily R&D in the 1980s towards market development and implementation in the 1990s, in both OECD and developing countries [1]. Goals, support systems and PV plans have started at national and European level, i.e. the Renewable Energy White Paper of the European Union, where the stated goal is to have 3000 MWp of PV systems installed in the EU by the year 2010 [2].

There are more and more national programmes involved in the financing of renewable energy sources and especially in PV. This chapter will try to give the rationale behind a PV support system, an overview of the different types of support systems in existence in Europe, and the 'other measures' that need to accompany an effective support system.

2 Rationale

Energy prices do not always reflect the full cost to society, because prices do not, or not completely, take into account the impacts of energy production and consumption on the environment or society. These external costs should be included in energy prices to ensure that decisions on the choice and on the volume take into account all the costs involved. In practice, governments, therefore, seek to introduce external costs associated with energy in less direct ways through regulation, taxation, incentives, tradable emissions permits and compensation costs.

In 2001, a new framework for Environmental State Aids was adopted by the Commission [3], where a possible internalisation of the avoided cost of renewable energy sources compared with conventional sources was recognised for the first time.

In the absence of an appropriated policy framework that aims at full internalisation of external cost to the environment or which improves energy demand management, reduced prices are likely to act as a disincentive to energy saving and may encourage energy consumption. The logic is now changing. Whereas before, the financial support was considered a 'subsidy', it is now moving logically towards 'compensation costs': the costs that renewable energies merit because the energy prices do not reflect the full costs.

3 Existing Support Systems in Europe

3.1 The RES Directive

Bearing in mind the need of a framework to overcome barriers and establish a stable context for renewable energy sources, the European Commission prepared

a Directive as an important part of the Community strategy to further expand the share of electricity generated from renewable energy sources in the EU. The adoption of this Directive in October 2001 [4] has been an important step towards the meeting of the EU's climate change commitments set and accepted at Kyoto.

The objective underlying this Directive is to facilitate a significant medium-term increase in renewable generated electricity (RES-E) within the EU. To achieve this goal, the Directive proposes the following:

- All Member States should introduce a system for the certification of the origin of RES-E.
- All Member States should adopt domestic targets for RES-E consumption levels on an annual basis for periods of 10 years. This measure seeks to produce a critical mass across the EU.
- Member States should consider measures to be taken to facilitate access to the grid system.
- Connection costs of renewable generators should be borne by the grid operator.
- The administrative and planning procedures that potential generators must follow should be simplified.
- Member States should ensure that benefits such as avoided systems losses will be reflected in the relevant tariff system.

Although this Directive has not set any support mechanisms for renewable energy sources, it sets the basis for a near future European support system.

3.2 The Different Support Systems

At present there are essentially two categories of direct price support systems:

1. Quota-based systems, operating notably in the UK, Ireland, the Netherlands, Italy and Belgium, are based on setting the price through competition between RES generators for the available support. Two different mechanisms which presently operate are the green certificates and the tendering schemes.

   Under a green certificate system, RES is sold at market prices. In order to finance the additional cost of producing RES electricity, and to ensure that the desired RES electricity is produced, an obligation is placed on all consumers to purchase a certain amount of green certificates from RES. Some countries, like Italy, place the obligation of the quota directly on the RES generators.

   Under a tendering procedure, the state places a series of tenders for the supply of the RES-E. The surplus cost generated by the purchase of RES-E is passed on to the end-consumer of the electricity through a specific levy.
2. Fixed-price scheme, operating presently in several EU countries, and notably Germany and Spain, and characterised by a specific price being

set for RES-E that must be paid by electricity companies, usually distributors, to domestic producers of RES. A variant of the fixed-price scheme is a fixed premium mechanism, according to which the government sets a fixed premium or an environmental bonus, paid above the normal or spot electricity price, to RES generators.

3.3 The Different Prices for Solar PV Energy in Europe

At the end of 2000, the EU's PV capacity amounted to 183.5 MW, i.e. a progression of 43.6% with respect to 1999 [5]. Germany has recently provided an example in a far-reaching Renewable Energy Act. A 113.8 MW installed capacity at the end of 2000 (including 100 MWp linked to the electrical power grid), accounted for much of this growth. It contributed to 79.5% of the supplementary capacity in the European Union, i.e. an additional 44.3 MWp. This considerable success can be explained by the German law on renewable energies. From 1 January 2000, the owners of grid-connected PV systems will be reimbursed with 99 pfennig (DM0.99 or €0.51) per kWh generated, during the lifetime of the PV installation. The following year, the reimbursement will be reduced by 5%, until a total installed capacity of 350 MWp is reached. Together with Germany's 100,000 roof programme, this will be a powerful incentive to boost PV installation in the country.

The Italian programme, which has been announced over the past three years, was finally adopted in March 2001. Around €40 million in subventions have been granted for the realisation of public, commercial and residential projects. Financing is limited to €7.7/Wp and the amount cannot exceed 75% of the total project cost.

In Spain by a royal decree of 1998, the power companies are held to purchase the electricity of photovoltaic origin at a price of €0.40/kWh for those systems with a power capacity lower than 5 kWp and €0.20/kWh for systems having capacities up to 25 MWp. The purchase price of photovoltaic electricity set in France in March 2002 is somewhat lower. Applicable for a period of 20 years, €0.15/kWh has been stipulated in continental France and €0.30/kWh in Corsica and in the French overseas departments.

The current legal-administrative position of Renewable Energy Sources is characterised by the plurality of subsequent approaches and developments. The situation in Europe is very heterogeneous with support systems varying with a factor of 10, i.e. maximum PV price for the kWh is €0.72/kWh in Austria and €0.074/kWh in Greece.

It is, therefore, vital to take stock of the situation by analysing the legislation existing throughout the community. For this reason, the Commission co-finances a project (called ENER-IURE for compiling the *legal framework* for RES in Europe) by studying, from the legal-administrative point of view, the use of the most effective legal instruments, particularly by breaking down the fiscal, administrative and legal barriers. This analysis, including financial, electricity, planning and agriculture, can be found at the following website: http://www.jrc.es/cfapp/eneriure/welcome.html.

Currently, the main instrument in Europe for the promotion of solar energy is the kWh price which takes into account the externalities of solar energy (Figure 1). The PV industry needs a stable political climate for a continuous growth. Rapid changes in subsidy levels and conditions, or in political attitudes, can seriously harm stable enlargement.

Capital co-financing is very important especially in the initial period of development. Mechanisms for paying premium rates for RES-E should be adopted in every country in order to stimulate demand and accelerate the transition of PV from a pioneering to a commercial business.

The investment support is normally linked to a limited capacity or to some technical development. The situation of this type of support in Europe is reflected in Figure 2.

Appropriated fiscal measures could be a useful instrument for internalising the external cost. Removing taxes from PV energy is currently applied for PV in Spain, Finland, Ireland, Italy and the Netherlands [6].

3.4 Other Support Systems

3.4.1 Urban Areas

PV is practically the only renewable energy source that can produce electricity in cities. However, this immediate advantage – the adaptability of PV to buildings – requires awareness on the part of construction companies, architects and city managers that does not exist at present. A big effort must be made to send the right messages to the building sector.

In the past, there were essentially only three sectors involved in the PV arena: government, the PV industry and the utilities. In recent years, other players have become increasingly active: regional and local governments and the building sector (architects, project developers, urban planners). Proper collaboration between these sectors is a necessity if PV is to be promoted in a wide range of applications.

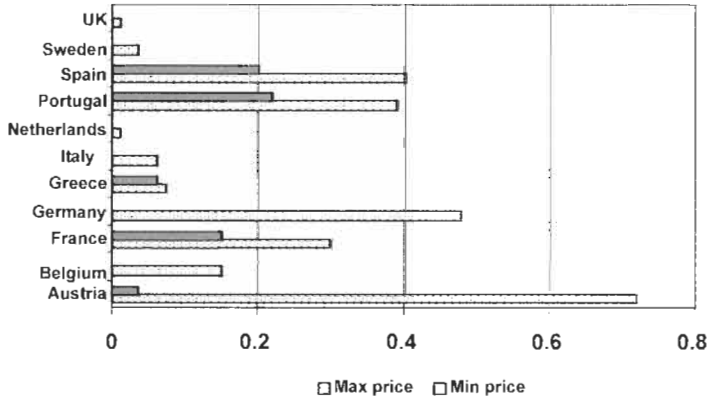

Figure 1 PV generation prices around Europe (in €/kWh).

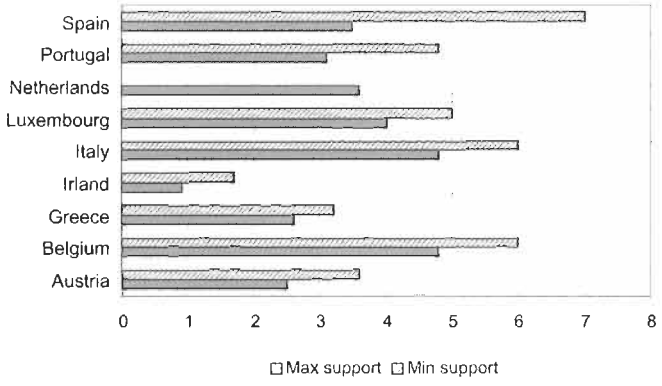

Figure 2 PV investment support in €/Wp.

Currently about the 50% of the world population lives in urban areas, while only 10% did so at the turn of this century [7]. Projections indicate that by 2025, worldwide urban population could reach 75%. By 2025 the urban population in the developing world alone will have increased to 2000 million people and half of them will have no access to basic services such as running water, electricity or sewerage.

Building-integrated solar energy is the most promising market in European countries, growing globally in the OCDE countries at a rate of 16.8% per year, and in Europe even faster, at 33% per year. The European building integrated PV (BIPV)) market was estimated to be 620 GW_p of potentially installable PV roof space [8].

In Europe, 70% of the energy used is consumed in cities, and up to 40% of the total energy demand is used in buildings. Architects and urban planners have in their hands the responsibility for nearly half of the energy consumption in Europe. PV integration should form part of an integral energy concept where the rational use of energy is considered. PV (as a cladding material, multifunctional facade or a standard envelope), together with rational use of energy, could enormously reduce the conventional energy consumption of cities. In today's conventional buildings, there is scope only for a saving potential of 22% current consumption [9]. Other forms of integration in cities, such as urban furniture, parking structures and noise barriers, are also important in this respect.

But neither the architects, nor the clients need to be brave pioneers. PV should become part of a 'normal' integration of an urban structure. It is in using this philosophy that the inclusion of PV in the municipal planning becomes decisive. The design of PV integrated into buildings should pass from the individual scale to the urban scale. This urban scale is, in general, neglected, with the result that huge potential energy savings are not made.

Support instruments should take care of considering the specific characteristics of building integrated systems and the different levels of national and local support. Appropriate municipal legislation and information about

existing support mechanisms are important for the development of a sustainable urbanism which includes PV solar energy.

PV systems do not interfere with ground occupation in cities. They can be integrated in the economy of the building, and advanced construction components are continuously emerging. The contribution of PV to cities could be substantial. The buildings of the 21st century will combine high technologies in better harmony with nature. The whole building could have an integrated energy concept in which materials, solar thermal gain, PV parts and lighting elements are as important as aesthetics or function. This Aristotelian idea of science, always in equilibrium with the environment, reconciles the idea of technical progress with a sustainable world.

Examples of sustainable plans include those implemented by the Community of Furth in Germany, the municipality of Gotland in Sweden, the municipality of Bologna in Italy and 'Barcelona renewable 2004' [10].

3.4.2 Other Support Systems: Regional Funds and Social Cohesion

Deployment of renewable energy sources can be a key feature of regional development which assists in achieving greater social and economic cohesion within a country. Grid extension, noise and pollution are avoided in PV projects. Renewable energy sources contribute to the quality of life of the users. Integration of this advanced technology in rural areas provides a performant energy service with an environmental integration. PV, although not explicitly mentioned, can benefit for regional and cohesion funds devoted to improve the quality of life of the rural areas.

Islands provide a good example of the positive local impact that PV could have, but also of the importance of non-technical barriers in the energy arena. In the majority of the Mediterranean islands, PV is cost-effective, but the existence of a conventional centralised energy system and the rigidity of administrative procedures consign renewable energies to a marginal role. But there are also good examples, such as the case of Guadeloupe Island in the Caribbean, where favourable tariffs, tax relief measures and EU initiatives have led to 30% of total energy consumption being produced by renewable energy sources.

3.4.3 RTD Funds

Other types of support give important signals in this respect. In the EU's 5th Framework programme which started in 1999, the Research and Technology Development (RTD) objectives treat renewable energy sources, particularly PV, biomass and wind, as a priority. About €100 million was devoted to renewable energy sources under this programme in 1999. Effective partnerships between the PV industry, the electrical utilities, local governments, research centres and universities were set up in order to develop common solar PV projects.

The new 6th Framework programme of the European Community for Research, Technology Development and Demonstration 2002–2006, includes in its Area of 'Sustainable development, global change and ecosystem', all the renewable energy sources, and PV is an important part of it. More details can be found at http://www.cordis.lu.

4 Other Measures. The Ideal Support Systems

A change of mentality is one of the essential requirements for integrating renewable energy sources into energy systems. To move from large centralised power stations to decentralised small systems requires more than a technical evolution. It requires a leap of imagination.

So far, financial, fiscal and administrative barriers, along with the lack of information and confidence among investors, have hindered the development of RES. For obtaining a successful development of solar PV energy, support systems need to be accompanied by the right mix of policies and measures.

1. Liberalised markets are beginning to price the external benefit of renewable energy sources. A change in exclusive economic considerations has emerged: *internalisation of environmental and external costs* is an important condition that will make a liberalised market compatible with Kyoto objectives. Competition requires market players to innovate to remain competitive. Innovation leads not only to lower prices, but also to a better use of energy sources. Liberalisation does not mean that the market is the sole king; energy policies are still needed.

   A major EU funded research study, undertaken over the past 10 years, showed that the cost of producing electricity from coal or oil would double and the cost of electricity production from gas would increase by 30% if the external costs – such as the damage to the environment and to health – were taken into account. It is estimated that these costs amount up to 1–2% of the EU's Gross Domestic Product (GDP), not including the cost of global warming. They have to be covered by society at large, since they are not included in the bills which electricity consumers pay. The EXTERNE project, which was undertaken by researchers from all EU Member States and the USA, was designed to quantify these social-environmental costs of electricity production. It is the first research project ever to put plausible financial figures against the damage resulting from different forms of electricity production (fossil, nuclear and renewable) for the entire EU. Details and figures on this extensive study could be found at http://www.externe.info/.
2. Many factors may affect the uptake of renewable energies in one country rather than another. A support system should take into account other measures that could prove crucial for the right implementation of solar energy. One of them is the existing legislation on third party grid access: *grid connection is still problematic and slow in the majority of countries.* Procedures are not clear, connection schemes are not appropriate, or there may be no possibility of low voltage connection. The user of a PV decentralised system is not comparable to a wind park owner. This obvious statement sometimes does not fit in the logic of a national system. Even a perfect financial support system will fail if a simple and affordable procedure for grid-connection is not implemented.

3. *Quantified targets* should accompany any good support system for the development of renewable policies.

   The report 'Energy and environment in the European Union', which was recently published by the European Environment Agency, examines trends over the period 1990–1999 and compares these with baseline projection to 2010. The conclusion of this report is that we need accelerated and appropriate support measures to meet the renewable energy targets in Europe. Without quantified targets, it is impossible to perform a proper monitoring of a PV policy and to propose more appropriated measures.
4. *Quality control*, good system specification, and qualified maintenance are essential too. The PV market is now crossing the ford between pioneering and mass acceptance. More than at any other time, quality plays a crucial role at this stage. Major barriers to the widespread introduction of PV vary from country to country, but usually include the difficulties of providing acceptable installers and after-sales service, assuring technical quality through national standards, and providing and distributing appropriate information.
5. A support system should take into consideration *the urban applications of PV*. It cannot throw away the very valuable assets of easy building and modularity as was discussed in Section 2.4.1.

5 Conclusions

The analysis of RES shows very different situations of the existing support systems in Europe. Notwithstanding this heterogeneous situation, there is a clear philosophy expressed by the equation that *appropriate support system means market development*. In countries where an 'internalised support system' (a financial support which establishes the price of the PV kWh as a function of the avoided cost of the same kWh produced by a conventional source of energy) has been put in place, together with grid connection simplification and an urban consideration, the development of PV is clearly visible.

References

[1] Lysen, E.H. and Yordi, B. 2001. The outlook for PV in the first century. In: *Clean electricity from photovoltaics*, Archer, M.D. and Hill, R., Eds., Imperial College Press.

[2] *Energy for the future: Renewable sources of energy. White Paper and Community Strategy and Action Plan*. COM(97) 599 final.

[3] Community guidelines on State aid for environmental protection, *Official Journal of the European Communities*, OJ 3.2.2001, C 37.

[4] *Directive 2001/77/EC on the promotion of electricity produced from renewable energy sources in the internal electricity market.* OJ 27.10.2001, L 283.

[5] *European barometer of renewable energy sources*, October 2000/February 2002 (2nd report).

[6] *PRETIR, Implementation of Renewable Energy in the European Union until 2010.* Fraunhofer Institute, 3E, Ecofys. June 2002, EC Altener programme.

[7] *Ecourbanisme*, Miguel Ruano, 2002, GG Editorial.

[8] *Photovoltaics in 2010*, Directorate-General for Energy and Transport, EPIA, ALTENER Programme, European Commission, ISBN 92-827-5347-6, 1996.

[9] *The proposal for a European Directive on the energy performance in buildings*, COM (2001) 226 final.

[10] *Renewable Energy for Europe, Campaign for Take-Off*, http://europa.eu.int/comm/energy/en/renewable/idae_site/index.html.

Appendix

APPENDIX A

Constants, physical quantities and conversion factors

Name	Symbol	Value
Astronomical unit (mean distance between the Sun and the Earth)	R_{SE}	$1.496\ 10^{11}$ m
Avogadro's number	N_{Av}	$6.023\ 10^{23}$ molecules/mol
Boltzmann constant	k_B	$1.381\ 10^{-23}$ J/K
Electron charge	q	$1.602\ 10^{-19}$ C
Electronvolt	eV	$1.602\ 10^{-19}$ J
Energy of 1 μm photon		1.240 eV
Free electron mass	m_0	$9.109\ 10^{-31}$ kg
Permitivity of free space	$\varepsilon_0 = 10^7/4\pi c^2$	$8.854\ 10^{-12}$ F/m
Permeability of free space	$\mu_0 = 4\pi\ 10^{-7}$	$1.257\ 10^{-6}$ H/m
Plank's constant	h	$6.625\ 10^{-34}$ J.s
	$\hbar = h/2\pi$	$1.055\ 10^{-34}$ J.s
Radius of the Sun	R_S	$6.96\ 10^{8}$ m
Thermal voltage at 300 K	$V_T = k_B T/q$	25.9 mV
Solid angle subtended by the Sun	ω_S	$6.85\ 10^{-5}$ sterad
	$f_\omega = \omega_S/\pi$	$2.18\ 10^{-5}$
Solar constant (mean irradiance outside Earth's atmosphere)	I_o	1367 W/m^2
Speed of light in vacuum	c	$2.998\ 10^{10}$ m/s
Stefan-Boltzmann constant	σ	$5.670\ 10^{-8}$ W/m^2 K^4
Wavelength of 1 eV photon		1.240 eV

APPENDIX B

List of principal symbols

	Quantity	Subscripted quantity		Usual units
		Symbol	Name	
A	Area			m^2, cm^2
B	Beam irradiance (without subscript)			Wm^{-2}
B	Beam irradiation[a]	B_h	Hourly beam irradiation	MJm^{-2}, Whm^{-2} [b]
		B_d	Daily beam irradiation	
		B_m	Monthly mean beam irradiation	
B	Radiative recombination constant			cm^3sec^{-1}
C	Concentration ratio			–
C	Auger recombination constant	C_{no}	... for electrons	cm^6sec^{-1}
		C_{no}	... for holes	
C_A	Normalised array size			–
C_n	Battery capacity (in energy units)			Wh
C_S	Number of days of autonomy			days
D	Diffusion constant	D_n	Electron ...	cm^2sec^{-1}
		D_p	Hole ...	
		D_a	Ambipolar ... $\{=2D_nD_p/(D_n+D_p)\}$	
D	Density of localised states (in amorphous semiconductor)	D_{Ct}	... in conduction band	cm^{-3}
		D_{Vt}	... in valence band	
		D_{DB}	... of dangling bonds	

(Appendix B continued on next page)

Appendix B (*continued*)

	Quantity	Subscripted quantity		Usual units
		Symbol	Name	
D	Diffuse irradiance (without subscript)			Wm^{-2}
D	Diffuse irradiation	D_h	Hourly diffuse irradiation	$MJ\,m^{-2}$,
		D_d	Daily diffuse irradiation	$Wh\,m^{-2}$ [b]
		D_m	Monthly mean diffuse irradiation	
d	Thickness (of antireflection coating)			μm
E	Energy	E_c	... of the edge of the conduction band	eV
		E_v	... of the edge of the valence band	
		E_g	Energy gap, band gap ($= E_c - E_v$)	
		E_F	Fermi energy	
		E_{Fn}	Electron quasi-Fermi level	
		E_{Fp}	Hole quasi-Fermi level	
		E_a	Activation energy	
		E_A	Energy generated by PV array	Wh or J
		E_{AC}	AC energy	Wh or J
EQE	External quantum efficiency			–
EOT	Equation of time			h or min
$\mathcal{E}$	Electric field			$V\,m^{-1}$
FF	Fill factor	FF_0	Fill factor of ideal solar cell characteristic	–
$F_{1/2}$	$\frac{2}{\sqrt{\pi}}\int_0^\infty \frac{x^{1/2}}{1+\exp(x-z)}dx$			
G	Global irradiance (without subscript)			Wm^{-2}
G	Global irradiation [a]	G_h	Hourly global irradiation	MJm^{-2}. Whm^{-2} [b]
		G_d	Daily global irradiation	
		G_m	Monthly mean global irradiation	
		G_o	Extraterrestrial irradiation (with further suffix indicating time interval)	
G	Carrier generation rate per unit volume			$cm^{-3}sec^{-1}$
g	Carrier generation function (generation rate per unit distance)			$cm^{-1}sec^{-1}$
H	Daily irradiation in the plane of the array [a]	H_l	Daily global irradiation in the plane of the array	$kWh\,m^{-2}$ [b]
		H_d	Daily direct irradiation in the plane of the array	

Appendix B (*continued*)

	Quantity	Subscripted quantity		Usual units
		Symbol	Name	
I	Current	I_{sc}	Short-circuit current	A
		I_{ph}	Photogenerated current	
		I_o	Diode dark saturation current	
		I_m	Current at the maximum power point	
		I_{DC}	Nominal DC current (in PV system)	
IQE	Internal quantum efficiency			–
J	Current density	J_{sc}	Short-circuit current density	Am^{-2}
		J_{ph}	Photogenerated current density	
		J_o	Diode dark saturation current density	
K	Damage constant	K_L	Diffusion length damage constant	–
		K_τ	Lifetime damage constant	cm^2sec^{-1}
k	Wave vector			cm^{-1}
KT	Clearness index	KT_h	Hourly clearness index ($=G_h/G_{oh}$)	–
		KT_d	Daily clearness index ($=G_d/G_{od}$)	
		KT_m	Monthly mean clearness index ($=(G_d)_m/(G_{od})_m$)	
L	Diffusion length	L_n	Electron diffusion length	μm
		L_p	Hole diffusion length	
L	Load (daily) energy consumption			Wh
L	Losses (system)	L_c	Array capture losses	kWh/(kWp*day)
		L_s	System losses	
L_D	Debye length			μm
ℓ	Drift (collection) length	ℓ_n	Electron drift length	μm
		ℓ_p	Hole drift length	
m	Electron mass	m_o	Free-electron mass	kg
		m_c	Density-of-states effective mass at the bottom of conduction band	
		m_v	Density-of-states effective mass at the top of valence band	

(*Appendix B continued on next page*)

Appendix B (*continued*)

	Quantity	Subscripted quantity		Usual units
		Symbol	Name	
N	Dopant or defect concentration	N_A	Acceptor concentration	cm^{-3}
		N_D	Donor concentration	
		N_B	$= N_A N_D/(N_A+N_D)$	
		N_{eff}	Effective dopant concentration	
		N_t	Concentration of carrier traps or recombination centres	
		N_{dop}	Dopant concentration	
N	Number of modules in a PV array	N_s	... connected in series	–
		N_p	... connected in parallel	
$NOCT$	Nominal operating cell temperature			K
$\mathcal{N}$	Density of states	$\mathcal{N}_C$	... in the conduction band	cm^{-3}
		$\mathcal{N}_V$	... in the valence band	
n	Electron concentration in semiconductor	n_0	....at equilibrium	cm^{-3}
		n_i	Intrinsic carrier concentration	
n_{id}	Diode ideality factor			–
$\mathbf{n}$	Refractive index	$\mathbf{n}_0$	.... of material surrounding solar cell	–
		$\mathbf{n}_{ar}$	.... of antireflection coating	
		$\mathbf{n}_{sc}$	... of a semiconductor	
P	Power	P_{max}	Power at the maximum power point	W
		P_A	Actual power produced by array	
		P_{eff}	Effective power rating of array (in stand-alone systems)	
		P_o	Nominal power of array	
		P_{AC}	AC power output	
		P_I	Nominal AC power of inverter	
PR	Performance ratio ($=Y_f/Y_r$)			–
PSH	Peak Solar Hours			h
p	Hole concentration in semiconductor	p_0	.... at equilibrium	cm^{-3}
QE	Quantum efficiency			–

Appendix B (*continued*)

	Quantity	Subscripted quantity		Usual units
		Symbol	Name	
R	Resistance	R_s	Series resistance	Ω
		R_p	Parallel (shunt) resistance	
$\mathcal{R}$	Reflection coefficient			–
r	Fresnel reflection coefficient			–
r	Normalised resistance	r_s	$= R_s I_{sc}/V_{oc}$	–
		r_p	$= R_p I_{sc}/V_{oc}$	
S	Surface recombination velocity			cm sec^{-1}
S	Sunshine duration	S_m	Monthly mean ...	h
SR	Spectral response			A W^{-1}
T	Temperature	T_s	Black body temperature of the Sun	K
		T_c	Cell temperature	
		T_a	Ambient temperature	
		T_n	= T/300	
$\mathcal{T}$	Transmission coefficient			–
t	Time			sec, hours
U	Recombination rate per unit volume	U_{rad}	Radiative ...	cm^{-3}sec^{-1}
		U_{Auger}	Auger ...	
		U_{SHR}	SHR ... (at defect)	
V	Voltage	V_{oc}	Open circuit voltage	V
		V_m	Voltage at the maximum power point	
		V_{bi}	Built-in voltage of a p-n junction	
		V_{bat}	Battery voltage	
		V_{DC}	Nominal voltage of PV system	
v	Velocity	v_{sat}	Saturation velocity	cm sec^{-1}
		v_{th}	Thermal velocity	
v_{oc}	$= qV_{oc}/k_BT$ or $qV_{oc}/n_{id}k_BT$			–

(*Appendix B continued on next page*)

Appendix B (*continued*)

	Quantity	Subscripted quantity		Usual units
		Symbol	Name	
W	Thickness of a region in solar cell	W_j	Junction width	μm
		W_e	Emitter width	
		W_b	Base width	
		W_i	Width of intrinsic region	
x	Space coordinate			m
x_g	$= E_g/k_B T_s$			–
Y	Yield	Y_A	Array yield	kWh/(kWp*day)
		Y_f	Final yield	
		Y_r	Reference yield	
α	Absorption coefficient			cm^{-1}
α_s	Solar azimuth			degrees or radians
γ_s	Solar altitude angle			degrees or radians
χ	Electron affinity			eV
δ	solar declination			degrees or radians
ε	Static dielectric constant			–
ε	Irradiance correction to mean solar distance			–
Φ	Photon flux			$cm^{-2}sec^{-1}$
ϕ	Quasi-Fermi level potential	ϕ_n	Electron ...	V
		ϕ_p	Hole	
ϕ	Potential barrier (of heterojunction)			eV
ϕ	Particle fluence			$cm^{-2}sec^{-1}$
ϕ	Latitude angle			degrees
η	Efficiency	η_C	Carnot efficiency	–
		η_{CA}	Curzon - Ahlborn efficiency	
		η_L	Landsberg efficiency	

Appendix B (*continued*)

	Quantity	Subscripted quantity		Usual units
		Symbol	Name	
		η_{PT}	Photothermal efficiency	
		η_{Amean}	Mean array efficiency	
		η_I	Inverter efficiency	
		η_{tot}	Overall PV plant efficiency	
ϑ	Collection efficiency			–
κ	Extinction coefficient			–
λ	Wavelength			μm, nm
μ	Carrier drift mobility	μ_n	Electron mobility	cm^2 V sec
		μ_p	Hole mobility	
ν	Frequency			sec^{-1}
ρ	Charge density			cm^{-3}
ρ_g	Ground albedo			
σ	Carrier capture cross section			cm^2
σ	Photoconductance			Siemens
τ	Minority carrier lifetime	τ_n	Electron lifetime	sec
		τ_p	Hole lifetime	
		τ_{rad}	Radiative lifetime	
		τ_{Auger}	Auger lifetime	
		τ_{SHR}	SHR lifetime	
		τ_{eff}	Effective	
ψ	electrostatic potential			V
ω	hour angle	ω_S	Sunset or sunrise ...	h
ω	solid angle	ω_S	... subtended by the Sun.	sterad

[a] B and G are the conventional symbols for the direct (beam) and global irradiation, as recommended by the International Solar Energy Society. IEC standard 61724:1998 recommends the symbols H_I and H_d for the daily global and direct irradiation in the plane of the array.

[b] Units $Whm^{-2}h^{-1}$ and $Whm^{-2}day^{-1}$ (or $MJm^{-2}h^{-1}$ and $MJm^{-2}day^{-1}$) are also used for the hourly and daily irradiation

APPENDIX C

Abbreviations and acronyms

AC	Alternating current
A/D	Analogue to digital
AFM	Atomic force microscopy
AGM	Absorbent glass mat
AR	Antireflection
ARC	Antireflection coating
a-Si	(Hydrogenated) amorphous silicon
AM	Air mass
AOI	Angle of incidence
APCVD	Atmospheric pressure chemical vapour deposition
ASTM	American Society for Testing and Materials
ATOX	Atomic oxygen
BCSC	Buried contact solar cell
BIPV	Building-integrated photovoltaics
BMBF	German Ministry for Research, Technology and Education
BOL	Beginning of life
BOS	Balance of system
BR	Bragg reflector
BSF	Back-surface field
BSFR	Back surface field and reflector
BSR	Back surface reflector
BST	British standard time
CAST	Chinese Academy of Space Technology
CBD	Chemical bath deposition
CDV	Committee draft for voting
CEI	Comitato Elettrotecnico Italiano (Italy)
CGA	Compressed Gas Association (USA)
CHP	Combined heat and power, co-generation
CIBSE	Chartered Institution of Building Services Engineers (UK)
CIS	Copper indium di-selenide
CIGS	Copper indium gallium di-selenide
CNES	Centre National d'Etudes Spatiales (France)

CVD	Chemical vapour deposition
CZ	Czochralski
DC	Direct current
DEV	Deutsches Einheitsverfahren (Germany)
DIN	Deutsches Institut für Normung (Germany)
Dj	Double junction
DOD	Depth of discharge
DOE	Department of Energy (USA)
DOS	Density of states
DR	Directional solidification
DTA	Differential thermal analysis
DTI	Department of Trade and Industry (UK)
DSSC	Dye sensitised solar cell
EB	Electron beam
EBIC	Electron-beam induced current
EFG	Edge-defined film fed growth
EHL	Environmental Health Laboratories
EHS	Environmental, health and safety
EMC	Electromagnetic continuous casting
ENS	Einrichtung zur Netzüberwachung mit zugerordnetem allpoligem Schaltorgan
EOL	End of life
EOT	Equation of time
EP	Electrical performance
EPA	Environmental Protection Agency (USA)
EPBT	Energy pay-back time
EPIA	European Photovoltaic Industry Association
EQE	External quantum efficiency
ESA	European Space Agency
ESD	Electrostatic discharge
ESRA	European Solar Radiation Atlas
ESTI	Eidgenossische Starkstrominspektorat (Switzerland)
ETSU	Energy Technology Support Unit for the DTI (UK)
EURECA	European Retrievable Carrier
EVA	Ethylene vinyl acetate
FF	Fill factor
FSF	Front surface field
FZ	Floating zone
GAP	Global Approval Programme (see also PV GAP)
GEO	Geostationary orbit
GDP	Gross domestic product
GMT	Greenwich mean time
HIT	Heterojunction with intrinsic thin layer (cell)
HTM	Hole transporting material
HOMO	Highest occupied molecular orbital
HV	High voltage
IBC	Interdigitated back contact
IEA	International Energy Agency
IEC	International Electrotechnical Commission
IEE	Institution of Electrical Engineers (UK)
IEEE	Institute of Electrical and Electronics Engineers (USA)
INTA	Instituto Nacional de Técnica Aeroespacial (Spain)
IPP	Independent power producers (Portugal)
IQE	Internal quantum efficiency
ISO	International Standards Organisation

ISS	International Space Station
ITO	Indium-tin oxide
JIS	Japan Industry Standard
JPL	Jet Propulsion Laboratory (USA)
JQA	Japan Quality Assurance Agency
LASS	Low angle silicon sheet
LAT	Local apparent time
LBIC	Light-beam induced current
LBSF	Local back-surface field
LCA	Life cycle assessment
LCR	Load coverage rate
LED	Light emitting diode
LEO	Low earth orbit
LLP	Loss-of-load probability
LMT	Local mean time
LOLP	Loss-of-power probability
LPCVD	Low pressure chemical vapour deposition
LPE	Liquid phase epitaxy
LPSC	Loss of power supply probability
LUMO	Lowest unoccupied molecular orbital
LV	Low voltage
MATE	Mars array technology experiment
MBE	Molecular beam epitaxy
mc	Multicrystalline
MDMO-PPV	Poly(2-methoxy-5-(3′,7′-dimethyloctyloxy) 1,4-phenylene vinylene
MEH-PPV	Poly(2-methoxy-5-2′-ethyl-hexyloxy)1,4-phenylene vinylene)
MEO	Mid-earth orbit
MG	Metallurgical grade
MINP	Metal-insulator np junction (cell)
MIS	Metal-oxide-semiconductor
MITI	Ministry of Trade and Industry (Japan)
Mj	Multijunction
MOCVD	Metalorganic chemical vapour deposition
MOS	Metal oxide semiconductor
MOVPE	Metalorganic vapour phase epitaxy
MPP	Maximum power point
MPPT	Maximum power point tracker
MSD	**M**ains monitoring units with allocated all-pole **s**witching **d**evices connected in series (also known as ENS)
MV	Medium voltage
NASA	National Aeronautics and Space Administration (USA)
NASDA	National Space Development Agency (Japan)
NEDO	New Energy and Industrial Technology Development Organisation (Japan)
NFPA	National Fire Protection Association (USA)
NIR	Near infrared
NREL	National Renewable Energy Laboratory (USA)
NRL	Naval Research Laboratory
NRS	Nonreflective
NSRDB	National Solar Radiation Data Base (USA)
O&M	Operation and maintenance
ODC	Ordered defect compound
OECD	Organisation for Economic Cooperation and Development
OECO	Obliquely evaporated contact
OLED	Organic light-emitting diode
OCVD	Open-circuit voltage decay

OMeTAD	2,2′,7,7′-tetrakis(N,N-di-p-methoxyphenylamine)-9,9′-spirobifluorene
ÖVE	Östereichische Verband für Elektrotechnik (Austria)
OVPD	Organic vapour phase deposition
PC	Point contact
PCD	Photoconductive decay
PCBM	1-(3-methoxycarbonyl)-propyl-1-phenyl-(6,6)C_{61}
PECVD	Plasma-enhanced chemical vapour deposition
PEDOT:PSS	Poly(3,4-ethylenedioxythiopene):poly(styrene sulfonate)
PERL	Passivated emitter, rear locally diffused (cell)
PESC	Passivated emitter solar cell
PET	Poly(ethylene terephalate)
PPV	Poly-phenylene vinylene
PR	Performance ratio
PRT	Platinum resistance thermometer
PSH	Peak solar hours
PTC	Performance test conditions
PV	Photovoltaic, photovoltaics
PVD	Physical vapour deposition
PVGAP	PV Global Approval Programme
PVPS	Photovoltaic Power Systems (Programme)
PVUSA	Photovoltaics for Utility Scale Applications
QE	Quantum efficiency
QSSPC	Quasi-steady-state photoconductance (method)
QSSVoc	Quasi-steady state open circuit voltage (method)
R&D	Research and development
RES	Renewable energy sources
RF	Radio frequency
RGS	Ribbon growth on substrate
RH	Relative humidity
ROCOF	Rate of change of frequency
ROW	Rest of the world
RTCVD	Rapid thermal chemical vapour deposition
RTD	Research and technology development
RTP	Rapid thermal process
SA	Solar array
SCA	Solar cell assembly
SCCE	Solar cell calibration experiment
SDL	Surface defect layer
SELF	Solar Electric Light Fund
SEM	Scanning electron microscopy
SG	Specific gravity
SRH	Shockley-Read-Hall
SHS	Solar home system(s)
SIPOS	Semi-insulating polysilicon
Sj	Single junction
SLI	Starting, lighting and ignition
SMUD	Sacramento Municipal Utility District
SOC	State of charge
SR	String ribbon
SR	Spectral response
SRC	Standard reporting conditions
SSP	Space solar power
STC	Standard test conditions
STAR	Surface texture and enhanced absorption with back reflector
SRV	Surface recombination velocity

SWE	Staebler-Wronski effect
SWS	Secondary working standard
S-Web	Supporting web
TJ	Tandem junction
Tj	Triple junction
TC	Technical committee
TCO	Transparent conducting oxide
TEC	Thermal expansion coefficient
TEM	Transmission electron microscopy
TPV	Thermophotovoltaics
TTV	Total thickness variation
UCPTE	Union for the Coordination of Production and Transmission of Electricity
UL	Underwriters Laboratory (USA)
UT	Ultrathin
UV	Ultraviolet
VDE	Verband der Elektrotechnik, Elektronik und Informationstechnik (Germany)
VdEW	Verband der Elektrizitätswirtschaft (Germany)
VHF	Very high frequency
VSE	Verband Schweizerische Elektrizitätswerke (Switzerland)
WCP	Wiring collecting panels
WET	West european time
WMO	World Meteorological Organisation
XRD	X ray diffraction
X-Si	Crystalline silicon
XTE	X-ray timing explorer
YAG	Yttrium aluminium garnet
ZMR	Zone-melt recrystalization

APPENDIX D

Bibliography

Books about solar cells, photovoltaic systems and applications

Aberle, A.G. *Crystalline Silicon Solar Cells-Advanced Surface Passivation & Analysis*, University of New South Wales, Sydney.

Andreev, V.M., Grilikhes, V.A.and Rumyantsev, V.D. *Photovoltaic Conversion of Concentrated Sunlight*, John Wiley & Sons, Chichester, 1997.

Archer, M.D. and Hill, R. *Clean Electricity from Photovoltaics*, Imperial College Press, London, 2001.

Brabec, C.J., Dyakonov, V., Parisi, J. and Sariciftci, N.S. Eds. *Organic Photovoltaics: Concepts and Realization*, Springer, Heidelberg, 2003.

Brendel, R. *Thin-Film Crystalline Silicon Solar Cells*, Wiley, Weinheim, 2003.

Bube R.H. *Photovoltaic Materials*, Imperial College Press, London, 1998

Bubenzer, A and Luther, J. *Photovoltaics Guidebook for Decision Makers*, Springer, Heidelberg, 2003.

Castañer, L. and Silvestre, S. *Modelling Photovoltaic Systems Using Pspice*, John Wiley & Sons, Chichester, 2002

Coutts, T.J. and Meakin, J.D. Eds. *Current Topics in Photovoltaics*, Academic Press, London, Vols. 1 – 4, 1985 – 1990.

Davidson, J. *The New Solar Electric Home, The Photovoltaics How-To Handbook*, Aatec Publishers, Michigan, 1987.

Derrick, A., Barlow, R.W., McNelis, B. and Gregory, J.A. *Photovoltaics: A Market Overview*, James & James Science Publishers, 1993.

Derrick, A., Francis, C. and Bokalders, V. *Solar Photovoltaic Products : A Guide For Development Workers*, Intermediate Technology Publications, London, 1991.

Fahrenbruch, A.L. and Bube, R.H. *Fundamentals of Solar Cells. Photovoltaic Solar Energy Conversion*, Academic Press, New York, 1983.

Fonash, S.J. *Solar Cell Device Physics*, Academic Press, New York, 1981.

Goetzberger, A., Knobloch J. and Voss, B. *Crystalline Silicon Solar Cells*, John Wiley & Sons, Chichester, 1998.

Green, M.A. *Solar Cells: Operating Principles, Technology and Practice*. Prentice Hall, New York, 1982.

Green, M.A. *High Efficiency Silicon Solar Cells*, Trans Tech Publications, 1987.

Green, M.A. *Silicon Solar Cells: Advanced Principles and Practice*. Centre for Photovoltaic Devices and Systems, University of New South Wales, 1995.

Green, M.A. *Third Generation Photovoltaics: Advanced Solar Energy Conversion*, Springer, Heidelberg, 2003.

Haberlin, H. *Photovoltaik*, Aarau, Switzerland, 1991 (in German).

Hill, R. Ed. *Applications of Photovoltaics*, Adam Hilger, Bristol, 1988.

Hille, G., Roth, W. and Schmidt, H. *Photovoltaic Systems (seminar coursebook)*, Frauenhofer Institute for Solar Energy Systems, Freiburg, 1995.

Hovel, H.J. Semiconductor solar cells, in: *Semiconductors and Semimetals*, R.K. Willardson and A.C. Beer, editors), Vol. 11, Academic Press, New York, 1975.

Humm, O. and Togweiler, P. *Photovoltaics in Architecture : The Integration of Photovoltaic Cells in Building Envelopes*, Birkhäuser, Basel, 1993

Iamura, M.S. , Helm, P. and Palz, W. Eds. *Photovoltaic System Technology: A European Handbook*, H.S. Stephens & Associates, Bedford, 1992.

Various chapters in Johansson, T.B., Kelly, H., Reddy, A.K.N. and Williams, R.H. Eds. *Renewable Energy: Sources for Fuel and Electricity*, Earthscan, London, 1993.

Johnston, W.D. *Solar Voltaic Cells*, Marcel Dekker Inc., New York, 1980

Komp, R.J. *Practical Photovoltaics: Electricity from Solar Cells*, Aatec Publishers, Michigan, 2002.

Lasnier, F. and Ang, T.G. *Photovoltaic Engineering Handbook*, Adam Hilger, Bristol, 1990.

Lorenzo, E. *Solar Electricity: Engineering of Photovoltaic Systems*. Progensa, Seville, 1994 (translation from the Spanish)

Luque, A. *Solar Cells and Optics for Photovoltaic Concentration*, Adam Hilger, Bristol, 1989.

Luque, A. and Araùjo, G.L. Eds. *Physical Limitations to Photovoltaic Energy Conversion*, Adam Hilger, Bristol, 1990.

Luque, A. and Hegedus, S. *Handbook of Photovoltaic Science and Engineering*, John Wiley & Sons, Chichester, 2003.

Markvart, T. Ed. *Solar Electricity (2nd edition)*, John Wiley & Sons, Chichester, 2001.

Maycock, P. and Stirewalt, E. *A Guide to the Photovoltaic Revolution. Sunlight to Electricity in One Step*, Rodale Press, Emmaus, 1985.

Mazer, J.A. *Solar Cells: An Introduction to Crystalline Photovoltaic Technology*, Kluwer Academic Publishers, Dordrecht, 1997

Messenger, R.A., and Ventre, J.G. *Photovoltaic Systems Engineering*, CRC Press, Boca Raton, USA, 1999.

Möller, H.J. *Semiconductors for Solar Cells*, Artech House, Boston, 1993.

Nelson, J. *The Physics of Solar Cells: Photons In, Electrons Out*, Imperial College Press, London, 2003

Neville, R.C. *Solar Energy Conversion (2nd edition)*, Elsevier, 1995

Novem – The Netherland Agency of Energy and the Environment. *Building With Photovoltaics*, James & James Science Publishers, London, 1997.

Overstraeten, R. van and Mertens, R.P. *Physics, Technology and Use of Photovoltaics*, Hilger, Bristol, 1986.

Partain, L.D. Ed. *Solar Cells and their Applications*, John Wiley & Sons, New York, 1995.

Perlin, J. *From Space to Earth : The Story of Solar Electricity*, Harvard University Press, Cambridge Mass., 2002.

Pulfrey, D.L. *Photovoltaic Power Generation*, Van Nostrand Reinhold Co., New York, 1978.

Randall, T. Ed. *Photovoltaics and Architecture*, Routledge – Spon Press, London, 2001.

Rauschenbach, H.S. *Solar Cell Array Design Handbook : The Principles and Technology of Photovoltaic Energy Conversion*, Van Nostrand Reinhold, New York, 1980.

Roberts, S. *Solar Electricity: A Practical Guide to Designing and Installing Small Photovoltaic Systems*, Prentice Hall, New Jersey, 1991.

Ross, M. and Royer, J. *Photovoltaics in Cold Climates*, James & James Publishers, London, 1998.

Sandia National Laboratories. *Stand-Alone Photovoltaic Systems. A Handbook of Recommended Design Practices*, US Department of Energy, 1990. Updated 1995.

Scheer, H. *A Solar Manifesto*, James & James Publishers, London, 2001.

Schropp, R.E.I and Zeman, M. *Amorphous and Microcystalline Silicon Solar Cells: Modelling, Materials and Device Technology*, Kluwer, Boston, 1998.

Smestad, G.P. *Optoelectronics of Solar Cells*, Society of Photo-Optical Instrumentation Engineers, Bellingham, 2002.

Takahashi, K. and Konagai, M. *Amorphous Silicon Solar Cells*, John Wiley & Sons, 1986.

Tao, G. *Optical Modeling and Characterization of Hydrogenated Amorphous Silicon Solar Cells*, Coronet Books, Philadelphia, 1994.

Treble, F.D. Ed. *Generating Electricity from the Sun*, Pergamon Press, Oxford, 1991

Turner, R.P. *Solar Cells and Photocells*, Howard W. Sams & Co, Indianapolis, 1975

Wenham, S.R., Green, M.A. and Watt, M.E. *Applied Photovoltaics*, Centre for Photovoltaic Devices and Systems, University of New South Wales, 1994.

Würfel, P. *Physik der Solarzellen (2nd edition)*, Spektrum, Heidelberg – Berlin, 2000 (in German; an English translation is in preparation)

Zweibel, K. and Hersch, P. *Basic Photovoltaic Principles and Methods*, Van Nostrand Reinhold Company, New York, 1984.

Books of interest which focus on topics related to photovoltaics

Born, M. and Wolf, E. *Principles of Optics (7th ed)*, Cambridge University Press, Cambridge, 1999

Brozel, M.R. and Stillman, G.E. Eds. *Properties of Gallium Arsenide (3rd edition)*, IEE/INSPEC, The Institution of Electrical Engineers, London, 1996.

Bube, R.T. *Photoconductivity of Solids*, Wiley, New York – London, 1960

Duffie, J.A. and Beckman, W.A. *Solar Engineering of Thermal Processes (2nd edition)*, John Wiley & Sons, New York, USA, 1991.

Fritzsche, H. Ed. *Amorphous Silicon and Related Materials*, University of Chicago, Chicago, 1989.

Keiser, B.E. *Principles of Electromagnetic Compatibility (5th edition)*, Artech House Inc, Ma, USA, 1985.

Lander, C.W. 1993. *Power Electronics (3rd Edition)*, McGraw-Hill, London, 1993

Landsberg, P.T. *Recombination in Semiconductors*, Cambridge University Press, Cambridge, 1991.

Levinstein, M., Rumyantsev, S. and Shur, M. Eds. *Handbook Series on Semiconductor Parameters*, Vols. 1 and 2, World Scientific, London, 1996, 1999.

Mohan, N., Undeland, T.M. and Robbins, W.P. *Power Electronics, Converters, Applications and Design (2nd Edition)*, John Wiley & Sons, New York, 1995

Pankove, J.I. *Optical Processes in Semiconductors*, Dover, New York, 1975

Palik, E.D. Ed. *Handbook of Optical Constants of Solids*, Academic Press Handbook Series, Orlando, 1985.

Palik, E.D. Ed. *Handbook of Optical Constants of Solids II*, Academic Press, San Diego, 1991.

Palz, W. Ed. *European Solar Radiation Atlas (2nd edition)*, Vols. 1 and 2, Verlag TÜV Rheinland, Köln, 1984.

Pearsall, T.P. Ed. *Properties, Processing and Applications of Indium Phosphide*, IEE/INSPEC, The Institution of Electrical Engineers, London, 2000.

Rashid, M.H. *Power Electronics, Circuits, Devices and Applications (2nd Edition)*, Prentice Hall, 1993.

Scharmer, K. and Grief, J. Co-ordinators. *European Solar Radiation Atlas (4th Edition)*. Les Presses de l' École des Mines de Paris, Paris, 2000.

Searle, T. Ed. *Properties of Amorphous Silicon and its Alloys* (EMIS Data Reviews No. 19), IEE/INSPEC, The Institution of Electrical Engineers, London, 1998.

Selberherr, S. *Analysis and Simulation of Semiconductor Devices*, Springer, Vienna – New York, 1984

Shur, M. *Physics of Semiconductor Devices*, Prentice Hall, Englewood Cliffs, 1990.

Smith, R.A. *Semiconductors (2nd edition)*, Cambridge University Press, Cambridge, 1978.

Street, R.A. *Hydrogenated amorphous silicon*, Cambridge University Press, Cambridge, 1991

Sze, S.M. *Physics of Semiconductor Devices (2nd edition)*, John Wiley & Sons, New York,, 1981.

deVos, A. *Endoreversible Thermodynamics of Solar Energy Conversion*, Oxford University Press, 1992.

Welford, W.T. and Winston, R. *The Physics of Non-imaging Concentrators*, Academic Press, New York, 1978.

APPENDIX E

International and US Standards with Relevance to Photovoltaics

Standards published by the International Electrotechnical Commission. *IEC Central Office, 3, rue de Varembé, P.O. Box 131, CH-1211 GENEVA 20, Switzerland. http://www.iec.ch/*

IEC 60364-7-712:2002. Electrical installations of buildings. Part 7-712: Requirements for special installations or locations – Solar photovoltaic (PV) power supply systems

IEC 60891:1987. Procedures for temperature and irradiance corrections to measured I-V characteristics of crystalline silicon photovoltaic devices.

IEC 60904-1:1987. Photovoltaic devices. Part 1: Measurement of photovoltaic current-voltage characteristics.

IEC 60904-2: 1989. Photovoltaic devices. Part 2: Requirements for reference solar cells.

IEC 60904-3: 1998. Photovoltaic devices. Part 3: Measurement principles for terrestrial photovoltaic (PV) solar devices with reference spectral irradiance data.

IEC 60904-5: 1996. Photovoltaic devices. Part 5: Determination of the equivalent cell temperature (ECT) of photovoltaic (PV) devices by the open-circuit voltage method.

IEC 60904-6: 1994. Photovoltaic devices. Part 6: Requirements for reference solar modules.

IEC 60904-7: 1987. Photovoltaic devices. Part 7: Computation of spectral mismatch error introduced in the testing of a photovoltaic device.

IEC 60904-8: 1998. Photovoltaic devices. Part 8: Measurement of spectral response of a photovoltaic (PV) device.

IEC 60904-9: 1995. Photovoltaic devices. Part 9: Solar simulator performance requirements.

IEC 60904-10: 1998. Photovoltaic devices. Part 10: Methods of linearity measurement.

IEC 61173:1992. Overvoltage protection for photovoltaic (PV) power generating systems. Guide.

IEC 61194:1992. Characteristic parameters of stand-alone photovoltaic (PV) systems

IEC 61215: 1993. Crystalline silicon terrestrial photovoltaic (PV) modules – design qualification and type approval.

IEC 61277:1995. Terrestrial photovoltaic (PV) power generating systems. General and guide.

IEC 61345:1998. UV test for photovoltaic (PV) modules

IEC 61427:1999. Secondary cells and batteries for solar photovoltaic energy systems. General requirements and methods of test.

IEC 61646: 1996. Thin-film terrestrial photovoltaic (PV) modules – design qualification and type approval.

IEC 61683:1999. Photovoltaic systems. Power conditioners. Procedure for measuring efficiency

IEC 61701:1995. Salt mist corrosion testing of photovoltaic (PV) modules

IEC 61702:1995. Rating of direct coupled photovoltaic (PV) pumping systems

IEC 61721:1995. Susceptibility of a photovoltaic (PV) module to accidental impact damage (resistance to impact test)

IEC 61724:1998. Photovoltaic system performance monitoring. Guidelines for measurement, data exchange and analysis.

IEC 61725:1997. Analytical expression for daily solar profiles

IEC 61727:1995. Photovoltaic (PV) systems. Characteristics of the utility interface.

IEC 61829:1995. Crystalline silicon photovoltaic (PV) array. On-site measurement of I-V characteristics

IEC/TR2 61836:1997. Solar photovoltaic energy systems – Terms and symbols

IEC/PAS 62111:1999. Specifications for the use of renewable energies in rural decentralised electrification

Draft IEC Standards

IEC 61215 Ed. 2.0 Crystalline silicon terrestrial photovoltaic (PV) modules – Design qualification and type approval

IEC 62116. Testing Procedure of Islanding Prevention Measures for Grid Connected Photovoltaic Power Generating Systems

IEC 61727 Ed. 2.0 Characteristics of the utility interface for photovoltaic (pv) systems

IEC 61730-1 Ed. 1.0 Photovoltaic module safety qualification – Part 1: Requirements for construction

IEC 61730-2 Ed. 1.0 Photovoltaic module safety qualification – Part 2: Requirements for testing

IEC 61836 TR Ed. 2.0 Solar photovoltaic energy systems – Terms and symbols

IEC 61853 Ed. 1.0 Performance testing and energy rating of terrestrial photovoltaic (PV) modules

IEC 62093 Ed. 1.0 Balance-of-system components for photovoltaic systems – Design qualification natural environments

IEC 62108 Ed. 1.0 Concentrator photovoltaic (PV) receivers and modules – Design qualification and type approval

IEC 62109 Ed. 1.0 Electrical safety of static inverters and charge controllers for use in photovoltaic (PV) power systems

IEC 62116 Ed. 1.0 Testing procedure – Islanding prevention measures for power conditioners used in grid connected photovoltaic (PV) power generation systems

IEC 62124 Ed. 1.0 Photovoltaic (PV) stand alone systems – Design verification

IEC 62145 Ed. 1.0 Crystalline silicon PV modules – Blank detail specification

IEC 62234 Ed. 1.0 Safety guidelines for grid connected photovoltaic (PV) systems mounted on buildings

IEC 62253 Ed. 1.0 Direct coupled photovoltaic pumping systems – Design qualification and type approval

IEC 62257 Ed. 1.0 Recommendations for the use of renewable energies in rural decentralised electrification

IEC 62257-1 TS Ed. 1.0 Recommendations for small renewable energy and hybrid systems for rural electrification – Part 1: General introduction to rural electrification

IEC 62257-2 TS Ed. 1.0 Recommendations for small renewable energy and hybrid systems for rural electrification – Part 2: From requirements to a range of electrification systems

PNW 82-304 Ed. 1.0 Photovoltaic module safety qualification – Part 1: Requirements for construction

PNW 82-306 Ed. 1.0 Photovoltaic module safety qualification – Part 2: Requirements for testing

PNW 82-314 Ed. 1.0 Procedures for establishing the traceability of the calibration of photovoltaic reference devices

PWI 82-1 Ed. 1.0 Photovoltaic electricity storage systems

Standards published by ASTM International (formerly American Society for Testing and Materials). *100 Barr Harbor Drive, PO Box C700, West Conshohocken, Pennsylvania, USA 19428-2959. http://www.astm.org*

E 490-00a Standard Solar Constant and Zero Air Mass Solar Spectral Irradiance Tables

E 816-95 Standard test method for calibration of secondary reference pyrheliometers and pyrheliometers for field use.

E 824-94 Standard test method for transfer of calibration from reference to field radiometers.

E 913-82(1999) Standard method for calibration of reference pyranometers with axis vertical by the shading method.

E 941-83(1999) Standard test method for calibration of reference pyranometers with axis tilted by the shading method.

E1362-99 Standard Test Method for Calibration of Non-Concentrator Photovoltaic Secondary Reference Cells

E1125-99 Standard Test Method for Calibration of Primary Non-Concentrator Terrestrial Photovoltaic Reference Cells Using a Tabular Spectrum

E948-95(2001) Standard Test Method for Electrical Performance of Photovoltaic Cells Using Reference Cells Under Simulated Sunlight

E973-02 Standard Test Method for Determination of the Spectral Mismatch Parameter Between a Photovoltaic Device and a Photovoltaic Reference Cell

E973M-96 Standard Test Method for Determination of the Spectral Mismatch Parameter Between a Photovoltaic Device and a Photovoltaic Reference Cell [Metric]

E1040-98 Standard Specification for Physical Characteristics of Nonconcentrator Terrestrial Photovoltaic Reference Cells

E1036M-96e2 Standard Test Methods for Electrical Performance of Nonconcentrator Terrestrial Photovoltaic Modules and Arrays Using Reference Cells

E1039-99 Standard Test Method for Calibration of Silicon Non-Concentrator Photovoltaic Primary Reference Cells Under Global Irradiation

E1830-01 Standard Test Methods for Determining Mechanical Integrity of Photovoltaic Modules

E1799-02 Standard Practice for Visual Inspections of Photovoltaic Modules

E1596-99 Standard Test Methods for Solar Radiation Weathering of Photovoltaic Modules

E1524-98 Standard Test Method for Saltwater Immersion and Corrosion Testing of Photovoltaic Modules for Marine Environments

E1171-01 Standard Test Method for Photovoltaic Modules in Cyclic Temperature and Humidity Environments

E1597-99 Standard Test Method for Saltwater Pressure Immersion and Temperature Testing of Photovoltaic Modules for Marine Environments

E1143-99 Standard Test Method for Determining the Linearity of a Photovoltaic Device Parameter with Respect To a Test Parameter

E1021-95(2001) Standard Test Methods for Measuring Spectral Response of Photovoltaic Cells

E1802-01 Standard Test Methods for Wet Insulation Integrity Testing of Photovoltaic Modules

E1462-00 Standard Test Methods for Insulation Integrity and Ground Path Continuity of Photovoltaic Modules

E1038-98 Standard Test Method for Determining Resistance of Photovoltaic Modules to Hail by Impact with Propelled Ice Balls

E2047-99 Standard Test Method for Wet Insulation Integrity Testing of Photovoltaic Arrays

E1328-99 Standard Terminology Relating to Photovoltaic Solar Energy Conversion

E927-91(1997) Standard Specification for Solar Simulation for Terrestrial Photovoltaic Testing

E2236-02 Standard Test Methods for Measurement of Electrical Performance and Spectral Response of Nonconcentrator Multijunction Photovoltaic Cells and Modules

E1036-02 Standard Test Methods for Electrical Performance of Nonconcentrator Terrestrial Photovoltaic Modules and Arrays Using Reference Cells

E782-95(2001) Standard Practice for Exposure of Cover Materials for Solar Collectors to Natural Weathering Under Conditions Simulating Operational Mode

E881-92(1996) Standard Practice for Exposure of Solar Collector Cover Materials to Natural Weathering Under Conditions Simulating Stagnation Mode

E822-92(1996) Standard Practice for Determining Resistance of Solar Collector Covers to Hail by Impact With Propelled Ice Balls

G113-01 Standard Terminology Relating to Natural and Artificial Weathering Tests of Nonmetallic Materials

G 130-95 Standard test method for calibration of narrow- and broad-band ultraviolet radiometers using a spectroradiometer.

G 138-96 Standard test method for calibration of a spectroradiometer using a standard source of irradiance.

G 159-98 Standard tables for references solar spectral irradiance at air mass 1.5: direct normal and hemispherical for a 37° tilted surface.

Work item WK558 Reference Solar Spectral Irradiances: Direct Normal and Hemispherical on 37 Tilted Surface

Standards published by the Institution of Electrical and Electronic Engineers. *IEEE Standards Association, PO Box 1331, 445 Hoes Lane, Piscataway NJ 08855-1331, USA. http://standards.ieee.org/*

IEEE Std 1145-1990 IEEE recommended practice for installation and maintenance of nickel-cadmium batteries for photovoltaic (PV) systems

IEEE Std 1013-1990 IEEE recommended practice for sizing lead-acid batteries for photovoltaic (PV) systems

IEEE Std 1262-1995 IEEE recommended practice for qualification of photovoltaic (PV) modules

IEEE Std 1144-1996 IEEE recommended practice for sizing nickel-cadmium batteries for photovoltaic (PV) systems

IEEE Std 1374-1998 IEEE guide for terrestrial photovoltaic power system safety

IEEE Std 1145-1999 IEEE recommended practice for installation and maintenance of nickel-cadmium batteries for Photovoltaic (PV) systems

IEEE Std 929-2000 IEEE Recommended Practice for Utility Interface of Photovoltaic (PV) Systems

IEEE Std 937-2000 IEEE Recommended Practice for Installation and Maintenance of Lead-Acid Batteries for Photovoltaic (PV) Systems

IEEE Std 1013-2000 IEEE recommended practice for sizing lead-acid batteries for photovoltaic (PV) systems

IEEE Std 1513-2001 IEEE recommended practice for qualification of concentrator photovoltaic (PV) receiver sections and modules

Draft European Standards

prEN 50312-1:1999 Photovoltaic systems. Solar home systems. Part 1. Safety. Test requirements and procedures

prEN 50312-2:1999 Photovoltaic systems. Solar home systems. Part 2. Performance. Test requirements and procedures

prEN 50313-1:1999 Photovoltaic systems. Solar modules. Part 1. Safety. Test requirements and procedures

prEN 50313-2:1999 Photovoltaic systems. Solar modules. Part 2. Performance. Test requirements and procedures

prEN 50314-1:1999 Photovoltaic systems. Charge regulators. Part 1. Safety. Test requirements and procedures

prEN 50314-2:1999 Photovoltaic systems. Charge regulators. Part 2. EMC. Test requirements and procedures

prEN 50314-3:1999 Photovoltaic systems. Charge regulators. Part 3. Performance. Test requirements and procedures

prEN 50315-1:1999 Accumulators for use in photovoltaic systems. Part 1. Safety. Test requirements and procedures

prEN 50315-2:1999 Accumulators for use in photovoltaic systems. Part 1. Performance. Test requirements and procedures

prEN 50316-1:1999 Photovoltaic lighting systems. Part 1. Safety. Test requirements and procedures

prEN 50316-2:1999 Photovoltaic lighting systems. Part 2. EMC. Test requirements and procedures

prEN 50316-3:1999 Photovoltaic lighting systems. Part 3. Performance. Test requirements and procedures

prEN 50322-1:1999 Photovoltaic systems. Part 1. Electromagnetic compatibility (EMC). Requirements for photovoltaic pumping systems

prEN 50330-1:1999 Photovoltaic semiconductor convertors. Utility interactive fail safe protective interface for PV-line commutated converters. Design qualification and type approval

prEN 50331-1:1999 Photovoltaic systems in buildings. Part 1. Safety requirements

prEN 50380:2001 Datasheet and nameplate information for photovoltaic modules

Other standards and guidelines

Qualification test procedures for photovoltaic modules. Specification No. 502, Issue 1, Commision of the European Communities, Joint Research Centre, Ispra, Italy, 1984. http://www.jrc.org/

ANSI/UL 1703-1987 Standard for flat-plate photovoltaic modules and panels. American National Standards Institute, New York, USA, 1987. http://www.ansi.org/

UL 1741-1999 Inverters, Converters, and Controllers for Use in Independent Power Systems. Underwriters Laboratories, Inc. http://www.ul.com/

NFPA 70. National Electrical Code (NEC). 1999. National Fire Protection Association, Quincy, MA 02269, USA. http://www.nfpa.org/

ISO/DIS 15387:2002 Space systems. Space solar cells. Requirements, measurements and calibration procedures. International Organization for Standardization, Geneva, Switzerland, 2002. http://www.iso.ch/

APPENDIX F

Useful web sites, journals and newsheets

There is a large and growing number of web sites, journals and newsletters with renewable energy content. This Appendix contains a cross section of those which contain useful informaion relating to photovoltaics and solar cells.

Web sites

http://www.pvpower.com/
Contains a wealth of information including PV glossary, bibliography, system design software, PV standards, units and conversion factors, and environmental safety and health information

http://www.solarbuzz.com
PV industry information with a comprehensive list of manufacturers of solar cells and PV system components.

http://www.solaraccess.com/
A renewable energy website; includes information about companies, products, jobs, education events and services.

http://www.solarenergy.org/
Web site of Solar Energy International – includes information about workshops and projects.

http://www.iea-pvps.org/
Web site of the Photovoltaic Power Systems Programme of the International Energy Agency. A wealth of information and IEA reports; many can be downloaded from the site. Newsletter of the IEA PVPS programme can be found at http://www.oja-services.nl/iea-pvps/pvpower/home.htm

http://www.pvresources.com
A (personal ?) website with much useful information

http://www.censolar.es
Web site of the Spanish Solar Energy Training Centre (in Spanish)

http://www.ises.org/ises.nsf
The web site of the International Solar Energy Society

http://www.nrel.gov/
Web site of the U.S. National Renewable Energy Laboratory

http://www.seia.org/
Web site of Solar Energy Industries Association (SEIA)

http://www.pv.unsw.edu.au/
Web site of Key Centre for Photovoltaic Engineering, UNSW. Information about its activities and courses. AM1.5 spectrum can be downloaded from http://www.pv.unsw.edu.au/am1.5.html

http://www.eurosolar.org
Web site of Eurosolar; a European renewable energy agency.

http://www.soda-is.com
Web site of the SoDa Project. Solar radiation data for a range of applications including PV, energy in buildings, vegetation, oceanography and health.

http://www.satel-light.com
Solar radiation data for Europe with a processing service for a wide range of applications. Includes an extensive glossary of terms.

http://rredc.nrel.gov/solar/
A wealth of information with solar radiation data, spectra, standards, computer programs and glossary

http://www.pv.bnl.gov
Web site of the Photovoltaic Environmental, Health and Safety Assistance Center, Brookhaven National Laboratory.

http://www.jxj.com/yearbook/index.html
Database of renewable energy suppliers and installers

http://www.ioffe.rssi.ru/SVA/NSM/Semicond/
A web sites with semiconductor data. See also M. Levinstein et al, Handbook Series on Semiconductor Parameters, in Bibliography.

http://www.semiconductors.co.uk/
A web site with general information and data concerning semiconductors

http://www.solarweb.net
A Spanish renewable energy web site. A useful summary of the regulations for grid connection in Spain can be found at http://www.solarweb.net/fotovoltaica.php

Journals

Progress in Photovoltaics published by Wiley.
http://www3.interscience.wiley.com/

Solar Energy Materials and Solar Cells published by Elsevier.
http://www.elsevier.nl/locate/solmat

Photon International.. Solar Verlag GmbH, Wilhelmstrasse 34, D-52070 Aachen, Germany. http://www.photon-magazine.com/

Solar Energy published by Pergamon. Official Journal of the International Solar Energy Society. http://www.elsevier.com/locate/solener

Newsletters

PV News: editor: Paul Maycock; PV Energy Systems, 4539 Old Auburn Road, Warrenton, VA 20187 USA; Phone/Fax: 540-349-4497; e-mail pvenergy@crosslink.net; http://www.pvenergy.com.

Photovoltaics Bulletin: editor Gail Purvis; Elsevier Advanced Technology, P.O. Box 150, Kidlington, Oxford 0X5 1AS UK; Phone: +44 1865 843 194; Fax: +44 1865 943 971; e-mail: g.purvis@elsevier.com; http://www.pvbulletin.com

Photovoltaic Insider's Report: editor: Richard Curry; 1011 W. Colorado Blvd., Dallas, TX 75208 USA; phone and fax 214-942-5248; e-mail rcurry@pvinsider.com; http://www.pvinsider.com.

PV Network News; editor: Paul Wilkins; 2303 Cedros Circle #l; Santa Fe NM 87505 USA; Phone: 505-473-1067; e-mail: pvpaulset@aol.com

The Solar Letter; editor: Allan L. Frank; ALFA Publishing, 9124 Bradford Rd., Silver Spring, MD 20901 USA; phone 301-565-2532; fax 301-565-3298.

Editorial Index

Editorial Index

As the emphasis toward sustainable and renewable energy resources grows world-wide, so interest in the capture and use of solar energy is increasing dramatically. Solar cells have been known and used for many years, but recent advances in their design and manufacture have resulted in renewed interest in their more widespread use.

Although several textbooks and monographs on photovoltaics are available, this **Practical Handbook of Photovoltaics** is a unique source of reference where all the relevant information on solar cell manufacture, system design and related topics can be found in a readily-accessible form. Edited by two leading researchers in the field, with contributions from an international pool of academic and industrial specialists, this book is targeted at designers, manufacturers and end-users of PV components, systems and integration, plus fundamental and applied researchers in the field of photovoltaics.

ALSO OF INTEREST:

Photovoltaics Bulletin: an international technology and business newsletter dedicated entirely to the photovoltaic sector of the global renewable energy industry.

12 issues per year. ISSN 1473 – 8325

www.pvbulletin.com

ISBN: 1 85617 390 9

ISBN 1-85617-390-9

9 781856 173902 >